Materials Horizons: From Nature to Nanomaterials

Sushil Kumar
D. K. Aswal *Editors*

Recent Advances in Thin Films

Springer

Materials Horizons: From Nature to Nanomaterials

Series Editor

Vijay Kumar Thakur, School of Aerospace, Transport and Manufacturing, Cranfield University, Cranfield, UK

Materials are an indispensable part of human civilization since the inception of life on earth. With the passage of time, innumerable new materials have been explored as well as developed and the search for new innovative materials continues briskly. Keeping in mind the immense perspectives of various classes of materials, this series aims at providing a comprehensive collection of works across the breadth of materials research at cutting-edge interface of materials science with physics, chemistry, biology and engineering.

This series covers a galaxy of materials ranging from natural materials to nanomaterials. Some of the topics include but not limited to: biological materials, biomimetic materials, ceramics, composites, coatings, functional materials, glasses, inorganic materials, inorganic-organic hybrids, metals, membranes, magnetic materials, manufacturing of materials, nanomaterials, organic materials and pigments to name a few. The series provides most timely and comprehensive information on advanced synthesis, processing, characterization, manufacturing and applications in a broad range of interdisciplinary fields in science, engineering and technology.

This series accepts both authored and edited works, including textbooks, monographs, reference works, and professional books. The books in this series will provide a deep insight into the state-of-art of Materials Horizons and serve students, academic, government and industrial scientists involved in all aspects of materials research.

More information about this series at http://www.springer.com/series/16122

Sushil Kumar · D. K. Aswal
Editors

Recent Advances in Thin Films

Springer

Editors
Sushil Kumar
CSIR-National Physical Laboratory
New Delhi, India

D. K. Aswal
CSIR-National Physical Laboratory
New Delhi, India

ISSN 2524-5384 ISSN 2524-5392 (electronic)
Materials Horizons: From Nature to Nanomaterials
ISBN 978-981-15-6115-3 ISBN 978-981-15-6116-0 (eBook)
https://doi.org/10.1007/978-981-15-6116-0

This Springer imprint is published by the registered company Springer Nature Singapore Pte Ltd.
The registered company address is: 152 Beach Road, #21-01/04 Gateway East, Singapore 189721, Singapore

Preface

Thin film is a two-dimensional layer of material deposited using controlled processes on some supporting surface. There are a variety of thin films based on its structures such as amorphous thin films, crystalline/polycrystalline/nanocrystalline thin films, nanostructured thin films, nanocomposite thin films, multilayer and supperlattice structures and monolayers. Advances in deposition processes and characterization tools for these thin films during last five decades or so have enabled a wide range of breakthroughs in technological applications such as optical coatings, magnetic recording media, electronic semiconductor devices, light emitting devices, hard coatings on cutting tools, thin-film solar cells and thin-film sensors.

Noticeable advancements have taken place in already progressing field of thin films and related technology in recent past. Ultra-thin films, monolayers, nanomaterials, hybrid thin films, organic and polymer thin films, etc. recently added to the inventory of class of thin-film materials have given new dimension in realization of exceptional properties. These thin films have well-determined structures and functionalities which have further opened up the avenue for advancement of devices.

The present book entitled *Recent Advances in Thin Films* is a collection of 22 review articles from experts who presented their recent R&D work in 17th International Conference on Thin Films (ICTF-17), working specifically in the field of surface engineering, hard coatings, epitaxial growth, magnetic materials, photovoltaic and sensors. The book also covers an overview of recent advances in development of thin film based newer devices and applications such as hydroelectric cell, electrocaloric cooling devices and hybrid flexible sensors. All the chapters contain in-depth studies and analysis of recent aspects of thin films as material and its use for devices. The book is not only useful for researchers in the area under discussion in various chapters but also for Ph.D. students, graduate and undergraduate students specializing in condensed matter physics and material science. Particularly, the chapter "Thin Film and Significance of Its Thickness" will be interesting to students for right understanding of thin film definition and significance of thin film thicknesses in various devices.

The other chapters of the book deal with recent advancement in growth, characterization and device applications of thin films. Chapter "Ultra-Thin Films on Complex Metallic Alloy Surfaces: A Perspective" gives an overview of ultra-thin films on complex alloy surfaces. The next four chapters ("Growth Defects in PVD Hard Coatings"–"Synthesis, Stability and Self-Diffusion in Iron Nitride Thin Films: A Review") are mainly focused on growth aspect of hard coatings, epitaxial gallium nitride thin films, non-magnetic cobalt in cobalt thin films and iron nitride thin films. Chapter "Photoelectron Energy Loss Spectroscopy: A Versatile Tool for Material Science" discussed new insight in photoelectron energy loss spectroscopy tool for thin-film material characterization. Chapter "MoS_2- and MoO_3-Based Ultrathin Layered Materials for Optoelectronic Applications" is about MoS_2- and MaO_3- based ultra-thin layered materials for optoelectronic applications. The next three chapters ("Optoelectronic Properties of Nanocrystalline Silicon-Based Superlattice Structures"–"Organic Thin Films: Langmuir Monolayers and Multilayers") discussed about thin-film multilayer and superlattice structures. Chapters "Thin Films for Electrocaloric Cooling Devices"–"Conducting Polymers and Their Composites Adding New Dimensions to Advanced Thermoelectric Materials" are about overview of newer applications of thin films such as hydroelectric cell, electrocaloric cooling devices and polymer-based thermoelectric materials, respectively. The next four chapters ("HWCVD: A Potential Tool for Silicon-Based Thin Films and Nanostructures"–"Nanostructured Black Silicon for Efficient Thin Silicon Solar Cells: Potential and Challenges") are about photovoltaic applications of various kinds of solar cells such as silicon, dye sensitized, perovskite and polymer. Particularly, chapter "Nanostructured Black Silicon for Efficient Thin Silicon Solar Cells: Potential and Challenges" discussed about recent advancement in the use of various thin-film layers in nanostructured black silicon solar cells. The last four chapters ("Chemiresistive Sensors for H_2S Gas: State of the Art"–"Vanadium Oxide Thin Films for Optical and Gas Sensing Applications") of the book cover recent development in a variety of thin film based sensors.

We are thankful to all the eminent contributors who made extraordinary efforts in preparing their respective chapters. We hope this book will be an important reference book for a wide scientific community doing R&D work in thin film in universities, research institutions and industries.

New Delhi, India
December 2019

Sushil Kumar
D. K. Aswal

Contents

About the Editors

Dr. Sushil Kumar is presently Senior Principal Scientist and Head – Photovoltaic Metrology Group at CSIR-National Physical Laboratory (NPL), New Delhi and also recognized as Professor of Physical Sciences at Academy of Scientific & Innovative Research (AcSIR). His research interests cover solar cells, thin film coatings and plasma processing and related instrumentation. He was a visiting fellow at Ecole Polytechnique – Palaiseau, Paris, France during 2002-2003. He received his Ph.D in 1997 from the Institute of Technology (now IIT-BHU), Banaras Hindu University, Varanasi with research focusing on the stress relieved diamond like carbon thin films. He has significantly contributed over the years in process development for growth of nanostructured diamond like coatings, and silicon thin films and their related instrumentation. He has published more than 100 research papers in peer-reviewed international journals and also holds three international patents on deposition of diamond-like carbon films (USA and European Patents) and nanostructured silicon films (USA patent). Some well recognized academic awards he received includes: BOYSCAST fellowship by the Department of Science and Technology, Government of India and Young Scientist Award, CSIR, INDIA. Recently, he has also developed a laboratory for organic solar cells testing and validation at CSIR-NPL. His current research focuses on the development of products for rural household and recycling of solar modules.

Dr. D. K. Aswal is currently Director, CSIR- National Physical Laboratory (CSIR-NPL), New Delhi, Director, Central Electronics Engineering Research Institute (CEERI, Pilani) and Chairman, National Accreditation Board for Testing and Calibration Laboratories (NABL), India is maintaining lien with his position as "Outstanding Scientist" at Bhabha Atomic Research Centre (BARC), Department of Atomic Energy (DAE), Government of India, Mumbai. Dr. Aswal, during 2012-2015, has also served as Secretary, Atomic Energy Education Society (AEES), Mumbai, which is an autonomous institution under DAE. Dr. Aswal joined BARC through the training school batch of the year 1986 after completing M.Sc. in Physics (Gold medalist) from Garhwal University in 1985. He obtained his Ph.D. in Physics from Mumbai University and subsequently carried out post-doctoral research work

at the Research Institute of Electronics, Hamamatsu, Japan. He is a condensed matter physicist of international repute and has made several outstanding contributions in the areas of molecular electronics, physics of organic films and their applications, thermoelectric power generators and gas sensors. He has had visiting professor/scientist positions at several international institutes/universities viz. Institut d'Electronique de Microelectronique et de Nanotechnologie (France), Sizuoka University (Japan), Commissariat à l'Energie Atomique (France), Weizmann Institute of Science (Israel), University of Yamanashi (Japan), University of Paris VII (France), Karlsruhe institute of Technology (Germany), and the University of South Florida (USA). He is a recipient of several national and international awards/fellowships including Fellow of National Academy of Sciences, India (NASI), Academician, Asia Pacific Academy of Materials, Distinguished Faculty Award of Homi Bhabha National Institute (HBNI), Materials Research Society of India (MRSI) Medal, Homi Bhabha Science and Technology Award, DAE-SRC Outstanding Research Investigator Award, Paraj: Excellence in Science award, JSPS fellowship (Japan), BMBF fellowship (Germany), EGIDE fellowship (France). He has edited three books, contributed 20 book chapters, published over 275 journal papers, filed three patents and secured the trademark of Bhartiya Nirdeshak Dravya (BND) – the Indian Certified Reference Materials. His current focus is to enhance the metrological capabilities of India at par with international standards for continuous improvement of the quality and safety of life in the country and making CSIR-NPL as a growth engine of the nation by supporting industries and strategic sectors through apex calibration facilities.

Thin Film and Significance of Its Thickness

Sushil Kumar and D. K. Aswal

Abstract Thin film is a two dimensional material layer deposited on a substrate in order to achieve properties that cannot be easily achieved or not realized at all by the same material in its bulk form. The distinct property of a thin film is resulting from the unique way of making it, in the form of progressive addition of atoms or molecules. Thickness is the fundamental property of thin film and is closely linked to other properties which scale differently with thickness. Thus, thin films are not defined by their thickness alone. Thin films have a range of properties, based on their thickness used in a number of applications such as in optical coatings, tribological coatings, quantum well structures based on supper lattices, magnetic multilayers, nanoscale coatings, etc. Here effort is made to revisit the definition of thin film by highlighting significance of its thickness and briefly discussed the role of thicknesses in some of the applications such as monolayer, nanoscale coatings and multilayer and superlattice structures.

1 Thin Film and Its Thickness

If we go back in the history of mankind, thin-film material coating traces may be observed well before 2000 years. Making of thin foil of gold by a goldsmith is a well-known artwork in early days of development of humankind. It was being made by beating or slicing of gold or any other metal like a silver block until it reaches a thickness to be called as a thin layer or foil. In those era goldsmiths have developed variety of ways to apply thin layer of metals like gold or silver on statue and sculptors or other common surfaces to look like precious. However, this kind of material cannot be called as a thin film. Definition of thin film is not straight forward and thus, one should not define thin film in terms of its thickness. There is no way to define that thickness below which a film becomes thin. Essentially thin film is a two dimensional material formed by a method using atom-by-atom or molecule-by-molecule or ion-by-ion condensation process and having one of its dimensions negligible compared to

S. Kumar (✉) · D. K. Aswal
CSIR—National Physical Laboratory, Dr. K.S. Krishnan Marg, New Delhi 110012, India
e-mail: skumar@nplinidia.org

S. Kumar and D. K. Aswal (eds.), *Recent Advances in Thin Films*, Materials Horizons: From Nature to Nanomaterials, https://doi.org/10.1007/978-981-15-6116-0_1

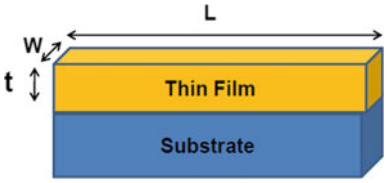

Fig. 1 Thin film as two dimensional materials having one of its dimensions negligible compared to other two dimensions ($t << \ldots W$ and L; t, L and W are thickness, length and width respectively)

the other two dimensions. Now point is that how much should be the third dimension; about a micron, less than a micron, few microns or something else. Here it is again emphasized that it is not simply in terms of thickness, which define thin film rather a two dimensional material on some support material called "substrate" as shown in Fig. 1 with distinct properties resulting from a unique way of making it in the form of progressive addition of basic building blocks, i.e. atoms or molecules one-by-one or layer-by-layer.

One can question, do we have a class of thick films and how they are different from thin films? This can be answered in a way they are prepared. A "thin" film is prepared by deposition of atoms, molecules and ions from the gaseous or liquid phase. On the other hand a "thick" film is prepared by deposition of particles consisting of a bunch of atoms/molecules, e.g. wall paint. Thick films are obtained by the processes like screen printing, doctor blade, etc., having a thickness of several microns and usually more when applied in applications. The nature of these thick films which are also used in printed circuits and for other applications is quite different from the thin film. One should not be uncertain that "thin" films can be thicker than "thick" films. The thickness of thin-film material may be few nanometers to about several micrometers for a specific application. The thickness may be few atoms onto a "substrate" surface or on some other layer already deposited. Thus, there is no well-defined limit of thickness to the end of the thin-film stage or any indication of its transition to the thicker film region. According to material's thickness, sometimes it can be wrongly classified into thin film, thick film and bulk.

Generally the physical limit of a film is determined by its thickness below which certain anomalies appear in film properties, however, this differs for different physical phenomena. For example, the resistivity of metal is determined by the mean free path of electron conduction which appears very low at thickness 50 nm where applied voltage produces high field because of non-linear behaviour of the field. Electrical resistivity increases abruptly for almost all metallic films below a certain thickness. The scaling of thickness with electrical resistivity is true when structural defects and impurities present in the body of film remain the same. A film which is optically thin may be of the order of the wavelength of light, say 500 nm or so reflected from the top surface and the bottom surface to observe optical interference as shown in Fig. 2a. The optical interference is observed when film thicknesses of single or multilayer dielectric thin films are below the wavelength of light. This is due to constructive or destructive interference between waves reflected/transmitted from the various

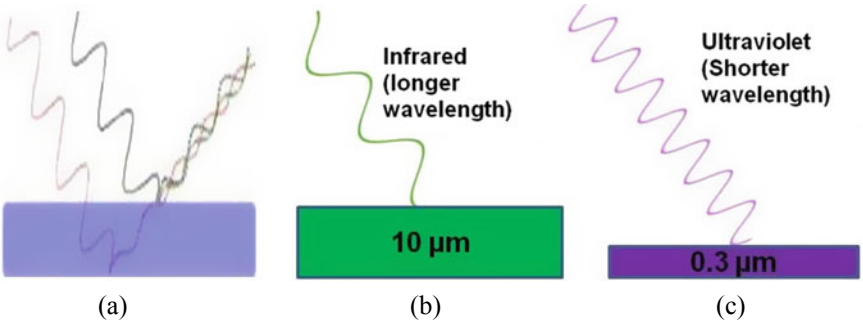

Fig. 2 A film which is optically thin may be of the order of wavelength of light **a** reflected from top surface and bottom surface to observer interference **b** in infrared (longer wavelength, 10 micron) or **c** thickness of thin film of order in ultraviolet (shorter wavelength, 0.3 micron)

boundaries (or interface) separating optical media of different refractive indices. The optical thin film may be regarded as one whose thickness is of the same order as the wavelength of the light interacting with the film material. If an infrared light having longer wavelength, say 10 microns interact with a film material of thickness of same order may be called as thin film for optical application to this particular wavelength of light (Fig. 2b). This is true for any wavelength of light and its interaction with the same order of film thickness as shown in Fig. 2c, for the thickness of thin film of order in ultraviolet, i.e. shorter wavelength, 0.3 micron. This means that a film of thickness 10 microns can be considered as a thin film when it interacts with infrared light of wavelengths few microns to several tens of microns, but if the same film interacts with ultraviolet light say wavelength less than 0.3 micron, then this film cannot be considered as thin film.

Thickness is one of the significant thin-film parameters as properties of any thin film depends on the thickness. As such there are many parameters that may affect thin-film materials structure and on which different properties such as mechanical, optical, magnetic, electrical, etc., depends. Several research papers are published where the thickness dependent studies were performed on a variety of thin-film materials [1–7].

Most of the basic research on thin films is generally confined to a limited range of thickness from a few nanometers to about a micron depending on the properties to be investigated. On the other hand for technological applications where the reliability of performance is important, thus, criteria for the thickness limit at lower range is usually higher than a few nanometres and can be high as several micrometers. Therefore, precise measurement of thickness of thin film is extremely vital. As such there are various ways to measure thickness of a thin film like using stylus profilometry, interferometry, ellipsometry, spectrophotometric measurements, X-ray microanalysis, cross-sectional imaging by electron microscopy, etc. It is also possible to measure the thickness of a film during its growth in progress using quartz crystal thickness monitor or optical interferometry etc.

Thin-film materials can be deposited by various ways having similar properties; however, the difference may be in (a) and (b) of following three steps involved in vapour based thin-film deposition process:

(a) How the starting precursors such as atoms, ions, molecules, clusters, etc., are created?
(b) How these atoms, ions, molecules, cluster, etc., transported in an environment towards substrate?
(c) How these atoms, ions, molecules, clusters, etc., get condensed on the substrate for the formation of thin film?

These three steps process: (a) creation, (b) transportation and (c) condensation of atoms, ions, molecules, clusters, etc., involved in the deciding the thin-film structures as depicted in Fig. 3. Mode of creation depends on a suitable form of energy (electrical/thermal/photon) applied to the source. Thin film deposited in such a way is characterized with certain structural properties, largely as amorphous, polycrystalline and/or crystalline or maybe mix phases.

Thin-film deposition process is usually divided into two broad categories—Chemical Vapour Deposition (CVD) and Physical Vapour Deposition (PVD). CVD is a process wherein a volatile fluid or gaseous precursor produces a chemical change on a substrate surface by a chemical process leaving a chemically deposited material in the form of a coating. Thermal CVD, plasma CVD, metal-organic CVD, etc., are commonly used to produce solid materials in industries. Physical Vapour Deposition is a process, wherein a material is released from a source and deposited on a

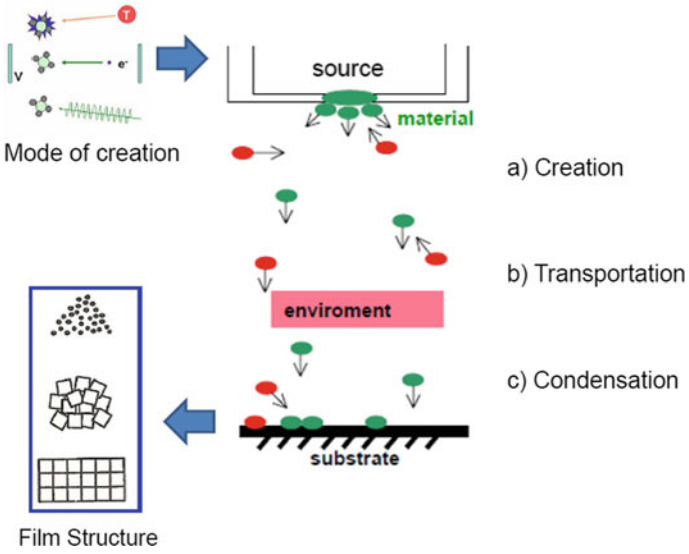

Fig. 3 Three steps process: **a** creation, **b** transportation and **c** condensation of atoms, ions, molecules, clusters etc. involved in deciding the thin film structure

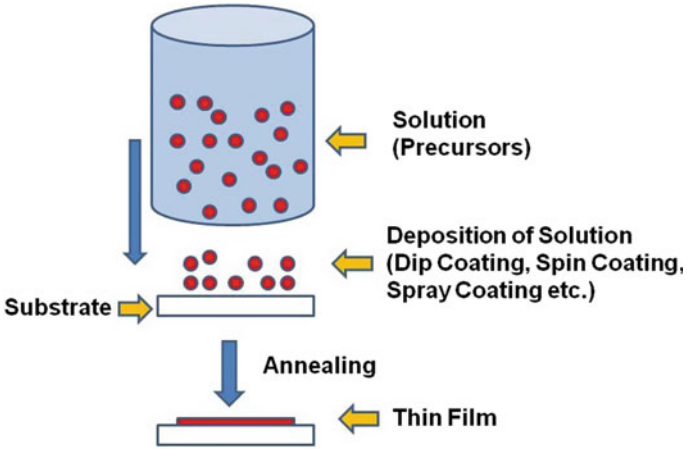

Fig. 4 Schematic of solution based thin film deposition process

substrate surface using mechanical, electromechanical or thermodynamic processes. The most common techniques of PVD are thermal evaporation, sputtering, laser ablation, molecular beam epitaxy (MBE), etc. In all these vapour deposition processes, deposition of thin films are carried out by condensation of precursors such as atoms, ions, molecules, etc., as two dimensional material layer on some substrate and properties of deposited layer scale differently with thickness. There are solution based processes like sol-gel, spin-coating, dip coating, spray coating, electrode deposition, Longmuir–Blodgett method, etc., are also being used for deposition of thin films as shown schematically in Fig. 4.

Thin-film deposition processes are at the heart of today's manufacturing industry and it is important to mention that specific thickness of thin film is required for a specific application in microelectronics, solar panels, sensors, disk drives, optical devices, etc., and even used in thin film based batteries. In subsequent subsections criticality of the thickness of thin films for specific applications is discussed briefly.

2 Monolayer and Its Transition to Thin Film

The term "Monolayer" means single layer material of atoms or molecules deposited on a substrate surface. However, the material on a surface to form a monolayer does not guarantee a uniform monolayer of coverage. Thus, this is also important to understand that in synthesis of a thin film how many layers of atoms or molecules one can consider in a monolayer. This may not be correct in the assumption of a monolayer as some materials deposit in ways that are not uniform. Usually spin-coating method has been and assumed to provide a single layer of molecules/atoms and not been cross-checked for the resultant thickness of the deposited material. Deposition methods

like molecular beam epitaxy, Langmuir–Blodgett method and atomic layer deposition allow thin films to be deposited just one layer of molecules/atoms. More precisely, use of the general term for monolayer is "uniform monolayer", when the amount of material that is deposited on a surface uniformly to confirm the formation of a uniform single layer. Casually it is also said that monolayer is a thin layer of material and in that case the term "thin layer" does not specify any particular number of layers of atoms/molecules. The term "thin layer" is generally comparative and the term used as "mono-layer of a thin film" adds more confusion.

It should also be noted that thin films rarely grow in uniform layers. The structure of a real film often happens to be imperfect due to early stages of growth features such as their seeds/nuclei and other defects. High-resolution techniques like STM and high-resolution AFM may be used for the measurement of height/diameter of atoms/molecules to illustrate the possible number of layers of atoms or molecules. HRTEM can be used to view the position of the single atoms, i.e., the crystallographic structure of the layer/film under investigation. Monolayer of a molecule like lipid, DNA will consist of multiple layers of atoms. Monolayer of grapheme consists of carbon atoms arranged with the two dimensional honeycomb crystal structure.

Let us try to understand monolayer in terms of adsorbates site. The adsorbates normally do not occupy any position on the surface, but only specific adsorption sites depending upon the favourable thermodynamical condition. The fractional coverage of an adsorbate is normally defined as F_A = (Number of occupied adsorption sites (Na))/(Total number of available adsorption sites (N)) and when $F_A = 1$ is referred to as a lattice-saturated atomic layer or simply monolayer. If adsorbate particles, i.e. atoms or molecules bond to each other on a surface to form a structure occupying all available adsorption sites and arranged in a one-layer fashion, e.g. a close-packed layer of its own crystal structure, such layer is also define as a monolayer, which is called "geometric monolayer".

One has to be careful when using terms like monolayer/atomic layer/thin film, and should not be confused with likeness. Therefore, the concept of a monolayer is a physical assembly of a layer on surface that result in ordered two dimensional (2D) molecular structures, i.e. also known as supramolecular assembly of nanomaterials. A non-covalent force is responsible for assembly of these nanostructures which is chemically designed using functional molecular precursors. These structures can be further used as templates for the formation of subsequent ordered layers. The 2D molecular structure interacts with the surface for stabilizing the molecular overlayer and with increasing thickness; a 2D molecular layer will eventually adopt the 3D structure. It is important to understand how this transition from 2D to 3D occurs and at what thickness? It is to be noted that in most applications the functional organic 2D layer is realized when it becomes 3D structure as thin film, e.g. in organic electronics, organic photovoltaics, sensors, etc. [8]. In the recent past the number of research articles published on monolayer formation and study of its properties for various applications considering these as thin films [9–12]. Grapheme monolayer exhibiting as ultrathin film with outstanding properties has been demonstrated for potential application for flexible supercapacitors [10]. There is an excellent review article written on molecular electronics overview specific to charge transport across

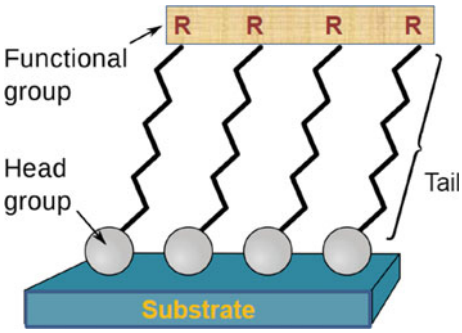

Fig. 5 Self assembled monolayer with functional group

molecular monolayers by Vilan et al. [12]. A study was carried out on graphene transistors on conventional SiO_2/Si substrates by modification with organic molecule octadecyltrichlorosilane (OTS) self-assembled monolayers [13]. Figure 5 shows a typical representation of self-assembled monolayer which is formed by two-step process: an initial fast step of adsorption and a second slower step of monolayer organization. Self-assembled monolayers of organic molecules are molecular assemblies formed spontaneously on surfaces by adsorption process and are organized into ordered domains. In conclusion, it is important to precisely look into the thickness of a layer before naming it as a monolayer.

3 Nano-Scale Coatings

A thin layer coating with the thickness of a few tens to a few hundreds of nanometers which is deposited on the surface for improving some property or for adding new functionality is called nano-scale coating or nano coating. The thickness of these coatings are not only in nano-scale but particles may also be dispersed into the matrix in the nanosize range of coatings have nanosized grains/phase. Nano-scale coatings are technologically attractive for different applications due to its extraordinary properties such as high hardness, toughness, anti-abrasive, wear resistance, optical transparency, better adhesion between coating layer and substrate, more flexibility, more durability, etc. These coatings are applied on surfaces to act as corrosion protection, moisture protection, friction reduction, antifouling and antibacterial protection, dust self-cleaning, heat and radiation resistance, etc. Ceramic based nanocoating is a proof-coat against fluctuation in temperature and rough weather used on various products such as vehicles, aircraft, ceramic tiles, glass windows, etc., which enhances durability and long-lasting of these materials/products. Nanocoating is also resistant to oxidisation arising from ultraviolet damage of materials/products. It is well-known that the properties of any thin film or bulk material are nearly the average of all the forces affecting the atoms it consists. On the other hand the large surface to volume ratio affects the nano-scale coatings which make the materials more reactive. This

nanocoating is hydrophobic (water repellent), oleophobic (oil repellent) surface layer that repels water, oil, dirt and other dry particles from which they are applied.

There are various techniques available for deposition of nano-scale coatings, such as sol-gel, layer-by-layer, self-assembly, dip coating, spin-coating, plasma-enhanced or assisted chemical vapour deposition, ion-beam assisted deposition techniques, electrochemical deposition, vapour deposition, magnetron sputtering, atomic layer deposition, etc. In any of these deposition processes the nanoparticles organize themselves to form a coating and bond with the surface after product material application. When the surface of the product material is smooth and not absorbent, the nanoparticles combine with the surface, so liquids are repelled taking contaminants with them. With porous surfaces, the nanoparticles fill up the pores from the inside in the product material.

Nano-scale coatings for biomedical applications such as ultralow dose BMP-2-Driven regeneration of bone defects is excellently demonstrated [14]. Excellent improvement of structure and quality of nano-scale multilayered, a composite coating on cutting tools is shown by Vereschaka et al. [15]. The carbide tool in longitudinal turning (continuous cutting) and end symmetric milling, and intermittent cutting of steel C45 and hard-to-cut nickel alloy of NiCr20TiAl showed advantages of the tool with nano-scale multilayered composite coating as compared to the tool without coating [15]. Kun Wang et al. have shown the critical thickness of a surface-functionalized coating for enhanced lithium storage [16]. In this study they have used nano-scale polypyrrole (PPY)-coated FeS_2 as a cathode for Li-ion batteries and demonstrated that critical thickness of 5 nm at which the PPY-coated FeS_2 cathode exhibited remarkable superior high-rate capability and long-term stability as compared to those with other coating thicknesses owing to the achievement of optimal electrical conductivity and ion diffusion efficiency. This study opens a new avenue for the further enhancement of the performance of energy storage devices. Flexible thin-film batteries are shown for powering smart cards and radio frequency identification tags. A novel empirical method based on energy-dispersive X-ray spectroscopy (EDX) analysis is proposed as non-destructive thickness quantification for nano-scale coatings on Li-Ion battery cathode material by Wuye Ouyang and Clifford S. Todd to evaluate the protection layer thickness on the scale of tens of nanometers and carbon layer coatings of 1–10 nm thickness were successfully quantified by them using this method [17]. In conclusion, the role of thickness in nano-scale coating in the realization of the functionality of thin-film coatings and surfaces is well appreciated.

4 Superlattice and Multilayer Structures

Material structure with stacks of several distinct layers is a multilayer structure. Properties of each incorporated layer material influence on properties of multilayer as a

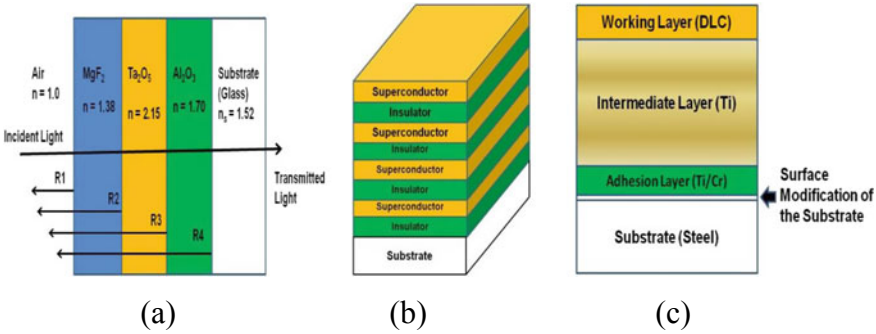

Fig. 6 Schematic of design of **a** optical coating **b** magnetic multilayer (*S*: superconductor and *X*: insulator) **c** tribological coating

whole. The overall properties of a multilayer structure depends on various parameters such as on the structure of layer materials, properties of each layer, structure in the interface, number of layers, thickness of each layer, etc. The multilayer structure may consist of several repetitions of two layers. The layer of different structural morphology with distinct properties is deposited one-upon the other for obtaining desired properties which otherwise may not possible with a single material. Multilayer structures offer multifunctional characteristics which are widely used in making of coating products such as in optical coatings for optical filters, multimode optical fibres, beam splitters, antireflection coatings, etc.; tribological coatings for wear/corrosion resistance, low friction, resistance to fracture, etc.; magnetic multilayers such as GMR (Giant magnetoresistance) used to read data in hard disk drives, random-access memory, etc. Optical multilayer coatings are developed after optimization of design specification by choosing the number of layers, type of material and thickness of each layer. Three-layer optical coating design involving layers of MgF_2 ($n = 1.38$), Ta_2O_5 ($n = 2.15$) and Al_2O_3 ($n = 1.70$) is shown in Fig. 6a. It is important to know an accurate refractive index and thickness values of each layer involved in multilayer coating for its excellent performance in accordance with the specification of spectral reflectance/transmittance. The basic structure of magnetic multilayers consist of a ferromagnetic metal (like Fe, Co, Ni and their alloys) and a non-magnetic metal (like Cr, Ru, Cu, Ag, Au, etc.) with the thickness of each layer usually in range 1–10 nm and the number of layers range from 3 to 100 [18]. Magnetic properties of Co/Ni multilayer structures with Co thickness in the range of 0.16–0.26 nm and Ni thickness from 0.47 to 0.75 nm shown potential towards the realization of STT-RAM (Magnetoresistive spin-transfer torque random access memory) [19]. Superconducting multilayer structures consist of alternating one dimensional layers (actually it is ultrathin layers) of superconductor and insulator as shown in Fig. 6b. Another superconducting or normal metal/ferromagnet layer can be used in place of an insulating layer in the design of superconducting multilayer as shown in Fig. 6b. Tribological coatings are designed to accomplish hardness with elastic modulus and plasticity in coatings. Wear protection of super hard coatings can be

increased by incorporation of multilayer designs as shown in Fig. 6c, such as using tri-layers involving adhesion layer (Ti/Cr), intermediate layer (Ti) and working/load-bearing layer (Diamond like Carbon, DLC). In another design, multilayer consisting of hard and soft layers, such as Ti/DLC can also be incorporated [20]. The effect of coating thickness on the tribological performance, namely friction and wear were studied by Lara et al. [21].

Superlattice structures consist of periodic stacking of very thin alternating layers of two different materials usually semiconductors that usually lattice matched. Ultra-thin thickness of two alternating layers is used as a modulation period in superlattice structures. These layered structures are used for tailoring bandgap for the making of novel electronic and photonic devices. Superlattice structures of semiconductors of different bandgaps result into an offset of the energy band which appears at the heterojunction. When the thickness of the layer becomes very thin as comparable with the de Broglie wavelength of the carrier (electron/hole) then quantum size effects dominate and these structures are known as quantum well structures. The important feature of these superlattice is that the barriers are very thin and so wavefunctions of adjacent quantum wells overlap strongly. Thus, electrons in superlattice are delocalized which can easily tunnel out. Quantum size effect is observed in GaAs based superlattice structures when layer thickness become close to 10 nm [22]. The superlattice structure consisting of AlGaAs and GaAs layers alternately (four layers each) on GaAs substrate is shown in Fig. 7a and the corresponding formation of quantum wells is presented in Fig. 7b. Layers of this level of thickness are commonly grown using epitaxial methods such as molecular beam epitaxy (MBE) and metal organic chemical vapour deposition (MOCVD).

The estimated value of band-offset helps in understanding of properties of the superlattice structures and in designing electronic and photonic devices based on these structures. N. Dwivedi et al. have developed structurally driven enhancement

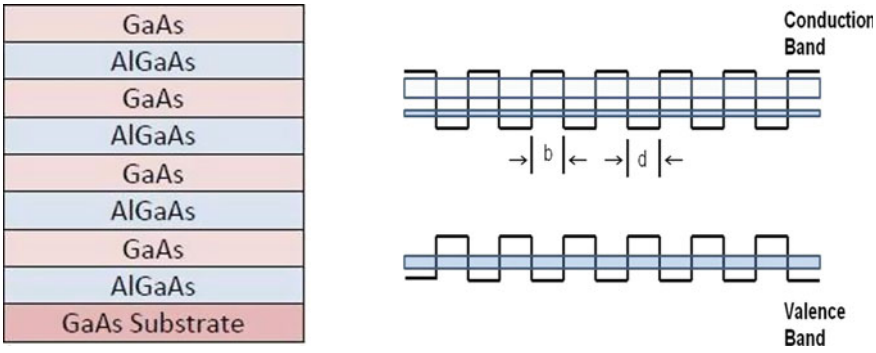

Fig. 7 Schematic of **a** superlattice structures and **b** corresponding formation of quantum wells, where *d* and *b* represent the thickness of the quantum well and barrier regions respectively

of resonant tunneling and nanomechanical properties in diamond-like carbon superlattices [23]. In conclusion, precise and controlled inclusion of thicknesses of layer is a crucial parameter for the design of superlattice and multilayer structures.

5 Conclusions

Revisit in the definition of thin film presented to emphasize the significance of its thickness. Reason for not defining thin film in terms of its thickness is primarily because of different properties scale differently with thickness. Thin-film properties vary from properties of corresponding bulk material because of its small thickness, large surface to volume ratio and unique physical structure which depends on the growth process. The phenomena like optical interference, electronic tunnelling through an insulating layer, high resistivity and low-temperature coefficient of resistance in metals, increase in the critical magnetic field of superconductors, etc., arises in the thin film below a certain thickness. Role of thin-film thickness in the design of superlattice and multilayer structures, optical coatings, tribological coatings is well appreciated. Study of thickness depended properties of newer thin-film materials can make one understand wonderful science.

References

1. A.E. Al-Salami, A. Dahshan, E.R. Shaaban, Optik **150**, 34 (2017)
2. R. Rajalakshmi, S. Angappane, J. Alloys Compounds **615**, 355 (2014)
3. Y. Akaltun, Thin Solid Films **594**, 30 (2015)
4. J. Potocnik, M. Nenadovic, N. Bundaleski, M. Popovic, Z. Rakocevic, Opt. Mat. **62**, 146 (2016)
5. D. Li, X. Song, J. Xu, Z. Wang, R. Zhang, P. Zhou, H. Zhang, R. Huang, S. Wang, Y. Zheng, D.W. Zhang, L. Chen, Appl. Surf. Sci. **421**, 884 (2017)
6. B. Hymavathi, B.R. Kumar, T.S. Rao, Opt. Quant. Electron. **49**, 13 (2017)
7. A. El-Denglaweya, M.M. Makhloufa, M. Dongolb, Results Phys. **10**, 714 (2018)
8. Z.P.L. Laker, A.J. Marsden, O.D. Luca, A.D. Pia, L.M.A. Perdigão, G. Costantini, N.R. Wilson, Nanoscale **9**, 11959 (2017)
9. B. Fabre, Chem. Rev. **116**, 4808 (2016)
10. G.F. Wang, H. Qin, X. Gao, Y. Cao, W. Wang, F.C. Wang, H.A. Wu, H.P. Cong, S.H. Yu, Chem **4**, 896 (2018)
11. F. Borghi, A. Podest'a, C. Piazzoni, P. Milani, Phys. Rev. Appl. **9**, 044016 (2018)
12. A. Vilan, D.K. Aswal, D. Cahen, Chem. Rev. **117**, 428 (2017)
13. S.Y. Chen, P.H. Ho, R.J. Shiue, C.W. Chen, W.H. Wang, Nano Lett. **12**, 964 (2012)
14. Z.A. Cheng, A.A. Perez, C.G. Garcia, H. Donnelly, V.L. Hernandez, V. Jayawarna, P. Childs, D.W. Shields, M. Cantini, L.R. Cantu, A. Reid, J.F.C. Windmill, E.S. Addison, S. Corr, W.G. Marshall, M.J. Dalby, M.S. Sanchez, Adv. Sci. **6**, 1800361 (2019)
15. A.A. Vereschaka1, A.S. Vereschaka, A.D.L. Batako, B.J. Mokritskii, A.Y. Aksenenko, N.N Sitnikov, Nanomater. Nanotechnol. **7**, 1 (2017)
16. K. Wang, S.P. Huang, Y. Wu, N.N. Cai, N. Li, Q. Xiao, Z. Sun, Nanoscale **11**, 16277 (2019)
17. W. Ouyang, C.S. Todd, Anal. Chem. **89**, 2816 (2017)
18. J. Inoue, *Nanomagnetism and Sprintonics*, T. Shinjo (ed.) (Elsevier, 2009) p. 15

19. M. Arora, N.R.L. Hone, T. Mckinnon, C. Coutts, R. Hübner, B. Heinrich, D.M. Broun, E. Girt, J. Phys. D: Appl. Phys. **50**, 505003 (2017)
20. N. Dwivedi, S. Kumar, H.K. Malik, ACS Appl. Mater. Inter. **3**, 4268 (2011)
21. L.C. Lara, H. Costa, J.D. Biasoli de Mello, Ind. Lubr. Tribol. **67**, 460 (2015)
22. S. Kasap, P. Capper (eds.), *Springer Handbook of Electronic and Photonic Materials* (Imprint, Springer International Publishing, 2017)
23. N. Dwivedi, R. McIntosh, C. Dhand, S. Kumar, H.K. Malik, S. Bhattacharyya, ACS Appl. Mater. Inter. **7**, 20726 (2015)

Ultra-Thin Films on Complex Metallic Alloy Surfaces: A Perspective

Vincent Fournée, Julian Ledieu, Émilie Gaudry, Hem-Raj Sharma, and Ronan McGrath

Abstract Complex metallic alloys (CMAs) may be defined as those intermetallic compounds having large (>~nm) unit cell dimensions. This includes quasi crystals as a special case, the unit cell being infinite. The discovery of quasi crystals motivated the study of CMAs, and the surface science community became active in the field once stable samples of sufficient size were produced. While the initial surface science activity centred on clean surface preparation, increasingly the formation of thin films, both metallic and molecular grew in importance. In this chapter, we give a brief introduction to this topic and then focus on several current areas of interest. These include the growth and characterization of ultra-thin metallic films of diverse architectures, the formation through deposition of novel molecular overlayers and thin films, complex intermetallics such as surface alloys and the potential use of intermetallic surfaces for catalytic reactions.

Keywords Quasi crystal · Complex metallic alloy

1 Introduction

Quasi crystals are physical systems that possess long-range order but without translational symmetry. The synthesis of the first quasi crystal, the metastable Al_6Mn alloy by Dan Shechtman in 1982 [1], and the subsequent controversy surrounding this discovery are well documented (e.g. [2]). In the subsequent decades, many more solid quasi crystals were discovered, and a large and diverse research community came together in an effort to understand their structure, physical properties and potential for applications [3]. Indeed, quasi crystallinity was later found in a large

V. Fournée · J. Ledieu · É. Gaudry
Institut Jean Lamour, UMR 7198 CNRS et Université de Lorraine, Nancy, France
e-mail: vincent.fournee@univ-lorraine.fr

H.-R. Sharma · R. McGrath (✉)
Surface Science Research Centre, The University of Liverpool, Liverpool L693BX, UK
e-mail: mcgrath@liverpool.ac.uk

S. Kumar and D. K. Aswal (eds.), *Recent Advances in Thin Films*, Materials Horizons: From Nature to Nanomaterials, https://doi.org/10.1007/978-981-15-6116-0_2

variety of physical systems, including dendritic liquid crystals [4], ABC-star polymers [5], binary nanoparticle superlattices [6], colloids [7], mesoporous silica [8] and oxide thin films [9]. New and surprising phenomena in quasi crystal systems continue to be reported; for example in 2018, the Al-Zn-Mg quasi crystal was found to be superconducting [10].

Once stable quasi crystals were discovered and produced in large enough samples [11, 12], they became suitable for surface science studies. Among the first such studies were those of the tenfold surface of the decagonal phase [13, 14] using scanning tunnelling microscopy (STM) and low energy electron diffraction (LEED). The fivefold surfaces of icosahedral quasi crystals and the tenfold surfaces of decagonal quasi crystals, in particular, have received the most attention [15].

This focus on quasi crystals in turn sparked an increasing focus on their approximants [16]. Approximants are periodic crystals close in stoichiometry to quasi crystals. They tend to have large unit cells and local structure within the unit cell similar to their quasi crystalline counterparts. They are attractive to study because of their periodicity—many structural (diffraction) and theoretical (density functional theory) techniques are based on a periodic formalism. Studying approximants can yield important knowledge that can be applied to the understanding of quasi crystals themselves [17]. Again, the surfaces of approximants have received considerable interest [18, 19].

In time, the phrase complex metallic alloys (CMAs) began to be used to describe quasi crystals, their approximants and other alloy structures [20] with large numbers of atoms in the unit cells. Dubois has identified the presence of a pseudogap in the electronic structure at the Fermi edge as a necessary but not sufficient differentiator between CMAs and other alloy systems [21].

Once excellent surfaces could be prepared, there followed a considerable interest in the nature of epitaxial processes on CMA surfaces, and in the structure and properties of the overlayers and thin films which result [22–24]. This interest was motivated partly by the importance of thin films in technological processes, but was also curiosity-driven: would thin films and molecular overlayers adopt the structure of the substrate, or order according to the structure of the bulk? This question has been answered in part—many elements and molecules do adopt the structure of the substrate, at least in the first layer; indeed for some elements, the quasi crystalline architecture persists beyond a single layer [25].

This chapter is not intended to be a comprehensive review of the literature; rather we describe a number of topics of current interest to the CMA thin-film community. We discuss the growth of multilayer quasi crystalline thin films, molecular adsorption and architectures on CMA surfaces, CMAs as surface alloys and the application of CMA surfaces in catalysis. We conclude with a perspective and future look.

2 Growth of Multilayer Quasi crystalline Thin Films on Ag-In-Yb Surfaces

In this section, we report studies of growth of quasi crystalline thin films of single elements on surfaces of the icosahedral (*i*)-Ag-In-Yb quasi crystal. All three high symmetry surfaces (two-, three- and fivefold) of this system have been studied [26–28] and used as a template to grow thin films of various elements such as Pb, Bi, In and Sb. Here, we will limit our discussion on the growth of Pb and Bi on the fivefold surface [25, 29].

The *i*-Ag-In-Yb quasi crystal is isostructural to the binary *i*-Cd-Yb phase, where Cd is replaced by Ag and In. The atomic structure of this system can be explained by the rhombic triacontahedral (RTH) cluster. The RTH cluster is formed by five successive atomic shells: a tetrahedron (innermost, 4 Cd atoms), a dodecahedron (12 Cd atoms), an icosahedron (30 Yb atoms), an icosidodecahedron (32 Cd atoms) and a rhombic triacontahedron (92 Cd atoms) [30]. A RTH cluster bisected perpendicular to the fivefold axis is shown in Fig. 1a (first shell not shown). For clarity, we have shown different atomic shells in different colours.

Although the three-dimensional shells are believed to be the building blocks of *i*-Cd-Yb, the structure can still be explained using a notion of the atomic plane. Figure 1b shows the atomic density distribution along the fivefold axis, for the ideal (unrelaxed) Cd-Yb model [30]. For simplicity, we define a region with a non-zero density as a plane. The density of the densest atomic planes is comparable to that of the closed-packed Yb surface [26]. Some of the atomic planes are marked in Fig. 1b. These planes are important for the discussion of the structure of the thin films. The atomic planes are formed by atoms of specific shells of the RTH cluster. For example, plane 1 is formed by atoms of the third and fourth shells, while plane 2 is formed by atoms of the fifth shell.

When the surface of i-Ag-In-Yb is prepared using the common sputter-annealing methods, it produces a step-terrace structure, as revealed by scanning tunnelling microscopy (STM) [26]. The terraces are formed at bulk planes intersecting the centres of the RTH clusters (for example, plane 1 in Fig. 1b). These surface terminating planes have a moderate atomic density. The structure of a surface terminating plane, superimposed with the structure of other planes, is shown in Fig. 1c, d. The structure can be mapped by a Penrose P1 tiling of edge length 2.50 nm with vertices located at the centres of the RTH clusters.

The atomic sites above the surface plane are vacant. Interestingly, these sites will be occupied by the adatoms (Pb or Bi) when deposited on the surface, mimicking the structure of the RTH cluster (Fig. 1e). The structure of the film thus can be characterized by layers of atoms, and the structure of each layer can be deduced from the bulk structure.

Figure 2a, b shows STM images taken from the first and second layers of Bi, respectively [29]. It was found that the first layer is formed by fifth shell atoms (which form planes 5 and 6). The most common features observed in the first layer by STM are pentagonal stars, pentagons and crescent shapes (marked in Fig. 2a).

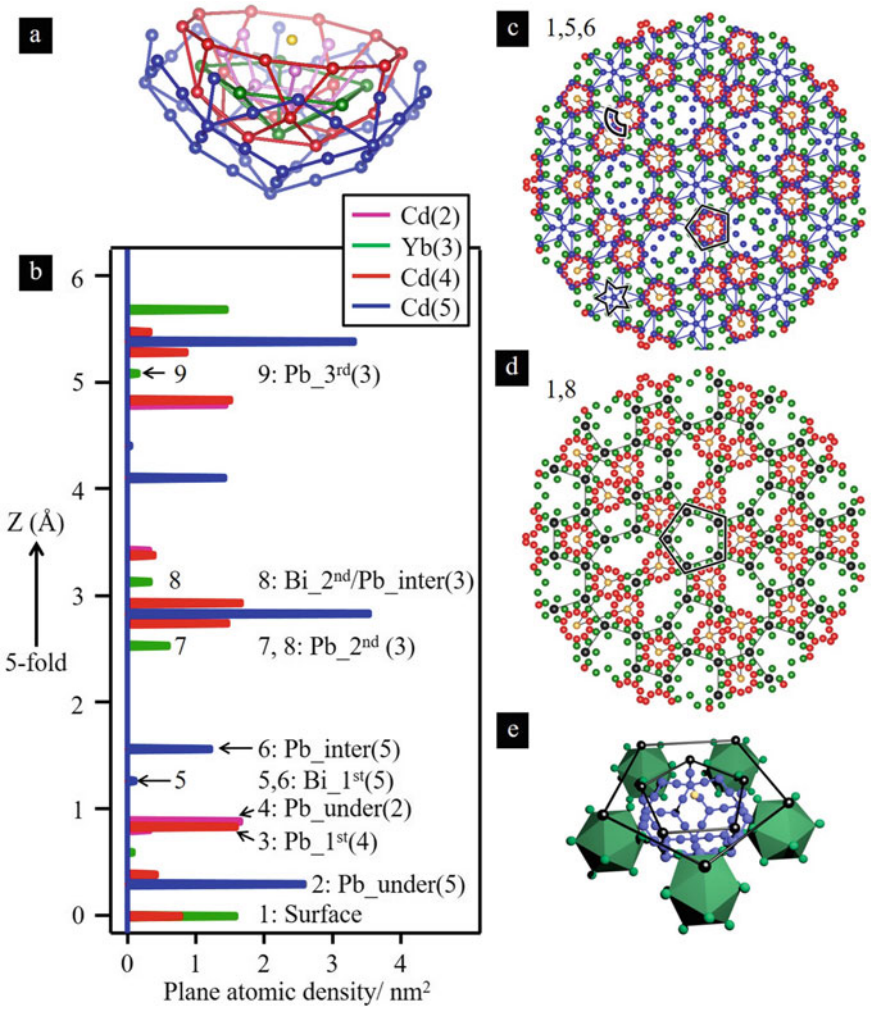

Fig. 1 **a** An RTH cluster, the building block of the i-Cd-Yb quasi crystal, bisected perpendicular to the fivefold axis [30]. Atoms of different shells are coloured differently. **b** Atomic density distribution along the fivefold axis deduced from the idea model structure of i-Cd-Yb. The density is estimated in slabs of 0.01 nm thickness. Plane 1 represents the surface. Other planes indicated by numbers are occupied by Pb or Bi adatoms. The number in parentheses indicates the nth shell of the RTH cluster. **c** Structure of surface (plane 1) superimposed with planes 5 and 6, which explains the first layer of Bi. **d** Structure of surface (plane 1) superimposed with plane 8, which produces the second layer of Bi. A Penrose P1 tiling of 2.5 nm edge length is superimposed in (**c**) and (**d**). **e** Surface truncated RTH clusters with Bi atoms atop. Black spheres represent Bi atoms. Only relevant shells are shown for clarity. Reprinted from [29] © 2018 Elsevier

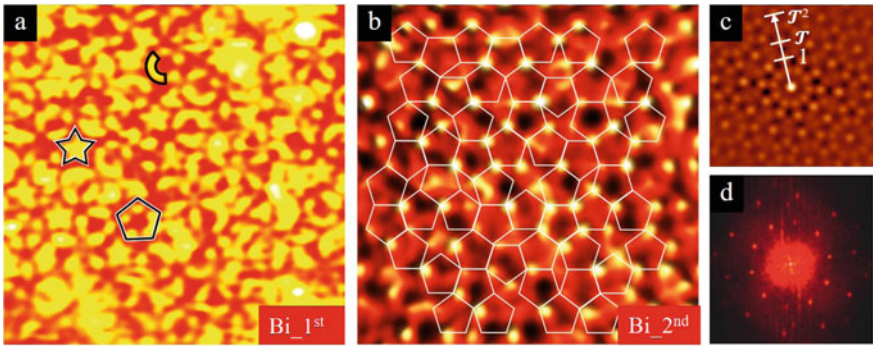

Fig. 2 **a**, **b** STM images of the first-layer (20 nm × 20 nm) and second-layer (20 nm × 20 nm) Bi formed on the fivefold surface of i-Ag-In-Yb. Common features are highlighted in (**a**). **c** Autocorrelation and **d** fast Fourier transform of the STM image (**b**). A Penrose P1 tiling of 2.5 nm edge length is superimposed in (**b**). Reprinted from [29] © 2018 Elsevier

These features match very well with those in planes 5 and 6 (Fig. 1c), in terms of height, size, orientation and location with respect to the surface plane. Similarly, the second layer Bi atoms are located at the vertices of a Penrose P1 tiling of 2.5 nm. This structure can be explained by Yb atoms of the third shell (plane 8). The autocorrelation pattern and the fast Fourier transform (FFT) of the STM image display tenfold symmetry with maxima located at τ-scaling distances (Fig. 2c, d), confirming long-range quasi crystalline order of the film. The adsorption sites for Bi atoms identified by STM are similar to those established by density functional theory (DFT) calculations [31].

Lead atoms deposited on the surface also occupy the cluster sites, displaying layers of different heights. STM images of first, second and third layers of Pb are shown in Fig. 3a, b and c, respectively [25]. These layers are formed at planes 2 (fourth shell), 7/8 (third shell) and 3 (third shell), respectively. DFT calculations

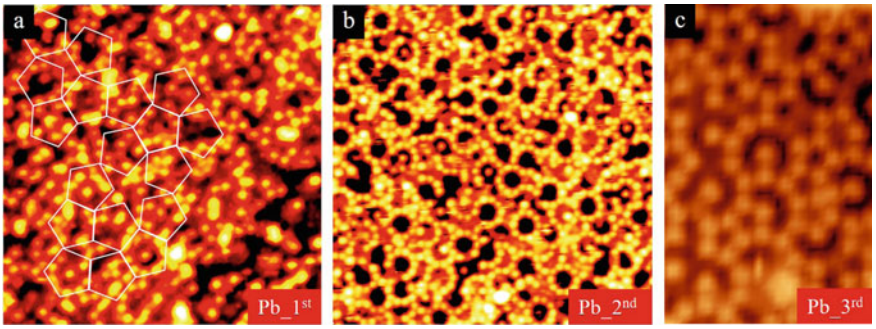

Fig. 3 **a–c** STM images of the first- (30–30 nm), second- (20 nm × 20 nm) and third-(23 nm × 15 nm)layer Pb formed on the fivefold surface of *i*-Ag-In-Yb [25]. A Penrose P1 tiling of 2.5 nm edge length is superimposed in (**a**).

have identified other layers, denoted by Pb-under and Pb-inter in Fig. 1b [25]. The Pb-under layer, which is underneath the first layer, is formed after the first layer is completed and thus this layer is not observed by STM. The existence of these under- and intermediate-layers is vital for the stability of the other layers, and thus the film as a whole. The formation of the layered structure is also confirmed by x-ray photoemission spectroscopy (XPS) [25].

The atomic density of a single layer is very low such that the distance between Pb atoms in the layer is larger than the nearest neighbour distance of Pb in its natural face-centred cubic structure. However, the Pb–Pb distance in neighbouring layers is short enough (comparable to the fcc Pb–Pb distance) to have a strong interaction between the adatoms, stabilizing such 3D films [25]. The same observation is true for Bi films [29].

The nature of thin-film growth on i-Ag-In-Yb is unique. A certain number of elements (Pb, Bi, Sb and Sn) grown on Al-based quasi crystals are also found to develop quasi crystalline structure. However, quasi crystalline order is limited up to one atomic layer [32–35], in contrast to three-dimensional quasi crystalline growth on *i*-Ag-In-Yb. After completion of the monolayer, the adsorbate develops its natural periodic structure [36–38]. Some other systems, for example Cu or Co on the *i*-Al-Pd-Mn surface, yield atomic rows spaced in a Fibonacci sequence at coverage above a few atomic layers [39–41]. Below this critical coverage, no order is observed. The structure within the atomic rows is periodic.

3 Intermetallic Surfaces as Templates for Complex Molecular Architectures

The formation of molecular thin films on metal surfaces typically occurs out of thermodynamic equilibrium. It involves molecular adsorption from the gas phase to the surface, random diffusion of the molecules between local minima of the potential energy surface (which is a thermally activated process to overcome surface diffusion barriers) and island nucleation or attachment to a pre-existing island. If the deposition flux is high and the substrate temperature is low, the diffusivity of the molecules is low and they will be easily trapped into metastable adsorption sites or captured by pre-existing nuclei. In this case, the corrugation of the potential energy surface cannot efficiently drive the molecular self-assembly. On the other side, if the deposition flux is low and the substrate temperature is high, then the diffusivity of the molecules is high and the molecules can more easily explore the potential energy surface and reach the deepest adsorption sites before nucleating into islands. These deposition conditions are therefore more favourable to take benefit from the templating effect of the substrate and drive molecular self-assembly into a long-range ordered structure.

The first attempts to grow molecular films on quasi crystalline surfaces were performed by room temperature deposition of fullerene C_{60} on the fivefold surface of the icosahedral Al-Pd-Mn quasi crystal [42] or the tenfold surface of the decagonal

Al-Ni-Co quasi crystal [43]. STM images of these surfaces dosed with a fraction of a monolayer showed individual immobile molecules rather than the formation of islands, suggesting that the molecules are trapped in adsorption sites and cannot diffuse further at this temperature. Nevertheless, common distances separating individual molecules were found to exhibit τ-scaling relationships characteristic of the bare quasi crystalline substrate, suggesting that local ordering takes place at low coverage. However, upon further deposition, a disordered film is obtained producing no diffraction pattern. Post-annealing treatment of the as-deposited films did not produce any structural change, and the molecules were found to desorb above 600 K.

Two recent studies reported the growth of ordered quasi periodic C_{60} films templated on quasi crystalline substrates obtained after high-temperature deposition [44, 45]. Smerdon et al. [44] reported the growth of a C_{60} film deposited on the fivefold surface of the Al-Cu-Fe icosahedral quasi crystal held at a temperature comprised between 770 and 970 K. In this temperature regime, a complete monolayer cannot be obtained due to a reduced sticking coefficient and/or possible molecular desorption taking place. STM investigations of the film revealed individual molecules trapped in a set of deeper adsorption sites and forming a discontinuous film (see Fig. 4a). The fast Fourier transform and autocorrelation function of the position map of individual C_{60} exhibited a tenfold rotational symmetry and τ-scaling relationships characteristic of quasi-periodic systems (see Fig. 4b). Some of the molecules appeared brighter than others, corresponding to a height difference of 1.4 Å with respect to dimer molecules. It was concluded that this height difference is due to molecules adsorbed at two different types of adsorption sites. The complete analysis of the STM images led to a scenario in which bright C_{60} molecules partially occupy a pentagonal lattice with edge length equal to 1.2 nm connecting Fe surface atoms embedded in an otherwise almost pure Al top layer [46]. The dim molecules were

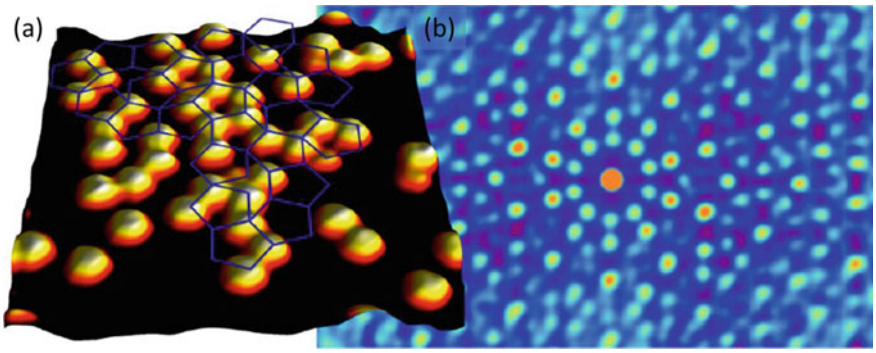

Fig. 4 **a** STM image (11×13 nm^2) showing individual C_{60} molecules deposited on the fivefold surface of the *i*-Al-Cu-Fe. They are located at the node of a quasi-periodic tiling. **b** autocorrelation pattern of the position map of the molecules extracted from an STM image, showing tenfold symmetry of the layer. Adapted with permission from J. A. Smerdon, K. M. Young, M. Lowe, S. S. Hars, T. P. Yadav, D. Hesp, V. R. Dhanak, A. P. Tsai, H. R. Sharma, and R. McGrath, Nano Letters 14, 1184 (2014). Copyright (2014) American Chemical Society

ascribed to C_{60} adsorbed on top of subsurface Fe atoms located at about 2.1 Å below the top plane, implying some surface reconstruction.

Another study reported the growth of dense, long-range quasi periodically ordered C_{60} layers grown on various quasi crystalline surfaces held between 623 and 673 K [45]. This temperature range is still above the multilayer desorption temperature but low enough to allow saturation of the first layer. It is high enough to facilitate molecular diffusion and sampling of the potential energy surface and still low to avoid fragmentation or polymerization of the C_{60} as verified by core-level photoemission spectroscopy. Molecular films were grown on the fivefold surfaces of Al-Pd-Mn and Al-Cu-Fe icosahedral quasi crystals as well as on the tenfold surfaces of the Al-Cu-Co and Al-Ni-Co decagonal quasi crystals. The long-range quasi-periodic order was demonstrated by the LEED patterns exhibiting sharp diffraction spots and either five- or tenfold rotational symmetry. Fast Fourier transform and autocorrelation of STM images are characterized by rings of ten spots with diameters related by t-scaling relationships, in agreement with the LEED patterns. The structure of the film can be interpreted by the adsorption of the molecules at specific sites of the substrate exhibiting a local fivefold symmetry. Both decagonal phases are described by the packing of partially overlapping columnar clusters extending along the tenfold axis, perpendicular to the surface plane (see Fig. 5). The cluster centres truncated by the surface constitute fivefold symmetric sites located at the nodes of a quasi-periodic tiling made of pentagonal (P), star (S) and boat (B) tiles, with an edge length equal to 2 nm [47]. Additional fivefold symmetric sites form inverted pentagons with edge length equal to 1.2 nm inside the P tiles. The decoration of these specific sites with C_{60} perfectly reproduces the experimentally observed film structure. It leads to a dense molecular film, with a packing density of one C_{60} per nm^2 and the shortest intermolecular distances of about 1 nm, i.e. similar to the van der Waals radius. The molecules have different contrasts in the STM images, corresponding to a height difference of 0.1 to 0.2 nm, but these values are strongly bias dependent suggesting some electronic origin. It may be due to differences in the local chemistry surrounding the various adsorption sites and/or to different adsorption configurations of the molecules.

A similar self-assembly occurs for C_{60} deposited on the fivefold surfaces of Al-Cu-Fe and Al-Pd-Mn icosahedral phases, leading to dense molecular films with long-range quasi-periodic order. In these cases, the molecules appear either bright or dim at negative bias in STM images, corresponding to a height difference of about 0.1 nm. The most common motifs are 1.2 nm edge length pentagonal tiles made by five bright C_{60} centred by either a bright or a dim molecule. These bright and dim motifs are pointing in the opposite direction on the same terrace and they keep the same orientation across terraces. The structure of the films can again be explained by preferential adsorption at specific sites of the substrate characterized by a local fivefold symmetry. Both icosahedral phases are described as a packing of pseudo-Bergman and pseudo-Mackay type clusters. The surface terminations of both phases correspond to dense Al-rich planes of the bulk structure. The most frequent motifs observed by STM have been termed ‘white flowers’ (WF) and ‘dark stars’ (DS). They both correspond to truncated clusters or clusters hanging down from the surface

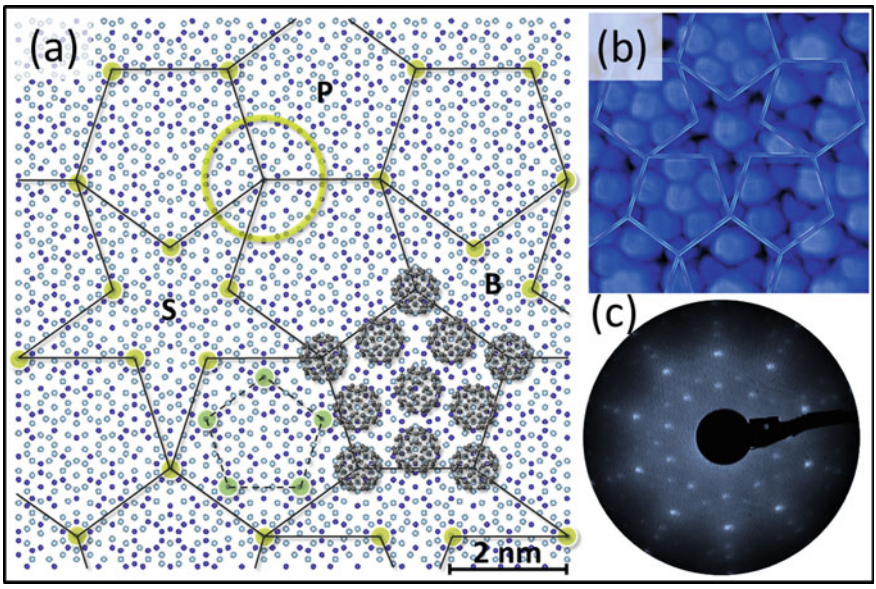

Fig. 5 **a** Structure model of the d-Al-Cu-Co decagonal phase perpendicular to the tenfold axis. Al atoms appear as light blue circles and transition metal atoms (Cu/Co) as dark blue circles. The cluster centres are highlighted as yellow circles. The yellow ring delimits the 2 nm wide cluster units. The tiling connecting the cluster centres appears as dark lines. It consists of pentagonal (P), star (S) and boat (B) tiles with 2 nm edge length. The green circles inside the P tile at the bottom of the figure indicate additional fivefold symmetric sites. They define a smaller pentagon with edge length 1.2 nm (dotted dark line). The decoration of the P tile by C_{60} molecules (in grey) is illustrated. **b** A portion of the quasi-periodic tiling with 2 nm edge length superimposed on an STM image of the C_{60} film. **c** LEED pattern of the C_{60} film formed on that surface, recorded at a primary beam energy of 48 eV. Adapted from [45]

plane, but the DS motifs have a central vacancy. Both motifs exhibit local fivefold symmetry. The WF are located at the nodes of a tiling made of pentagons, stars and rhombi with an edge length equal to 1.26 nm [48–50]. Some of the pentagonal tiles have a DS motif in their interior, all pointing in the same direction. It was thus concluded that the molecular self-assembly occurs through preferential adsorption of the C_{60} at these specific sites, the dim molecules corresponding to C_{60} adsorbed at DS sites, i.e. on top of a vacancy. This growth scenario perfectly matches with all experimental observations. It was further verified by performing submonolayer deposition experiments, allowing to image both the substrate structure and the C_{60} positions in order to determine the adsorption sites.

For both icosahedral and decagonal substrates, the driving force promoting the molecular self-assembly is the preferential adsorption at specific sites exhibiting local fivefold symmetry. Considering that symmetry matching between the molecules and the substrate is an important factor in determining the adsorption configuration, and these results suggest that the molecules adsorb with a C pentagonal face down at these fivefold symmetric sites. Ab initio DFT calculations have then been

performed in the case of C_{60}/Al-Pd-Mn in order to determine adsorption energies of C_{60} molecules at different adsorption sites and for various adsorption configurations. These calculations were performed using a structure model of a periodic approximant which contains both the WF and DS local configurations. The most stable adsorption configurations were found to correspond to C_{60} contacting the surface with a pentagonal face aligned with the five Al atoms forming the DS motif or aligned with Al pentagon centred by a Mn atom for the WF motif. The DFT calculations indicate that the bonding is quite different at DS and WF sites. At DS sites, the bonding is rather directional between the 5 C-Al pairs. The C atoms involved are not those forming the bottom pentagonal face but are C atoms involved in adjacent hexagonal faces. At WF sites, the bonding charge is localized at the interface between the pentagonal C face and the Mn atom at the centre of the WF motif. The calculated densities of states show a broadening of the molecular orbitals as well as an energy shift consistent with a charge transfer from the substrate to the molecules. New electronic states appear at the Fermi level as a result of sp and spd hybridization between C and substrate atoms, the film becoming metallic. It is to be noted that C_{60} adsorption with a C pentagonal face contacting the surface is rather unusual compared to noble metal surfaces but may be quite general for quasi crystalline substrates or possibly their approximants due to the existence of local fivefold symmetric configuration.

Additional growth experiments have been reported using different types of molecular building blocks. One is the growth of corannulene $C_{20}H_{10}$ on the fivefold surface of the Ag-In-Yb quasi crystal at room temperature [51]. Corannulene molecules are bowl-shaped, consisting of a fragment of a C_{60} and they have C5v symmetry. This system also self-assembles into a quasi-periodic pattern which appears to be driven again by symmetry matching, in the sense that the specific adsorption sites identified are characterized by their local fivefold symmetry.

A totally different picture was found for pentacene molecules deposited on the same surface [44]. Pentacene are polycyclic aromatic hydrocarbon molecules consisting of five linearly fused benzene rings; it is an organic semiconductor. The room temperature diffusivity of the pentacene was found high enough to lead to a quasi-periodic distribution of the molecules as demonstrated by the autocorrelation function of the molecular positions map. Pentacene molecules do not have fivefold symmetry contrary to C_{60} and therefore symmetry matching between molecules and substrate does not play a significant role. From the analysis of the STM data, it was concluded that pentacene molecules are anchored on pairs of Yb surface atoms, which are quasi-periodically distributed. Therefore, the chemical affinity between the molecules and the various species present in the surface planes is the key factor driving the self-assembly in this particular case.

In conclusion, quasi crystalline surfaces are both structurally and chemically complex and they have been used successfully as templates for the self-assembly of molecular building blocks into quasi-periodically ordered thin films. So far, mainly prototype molecules like C_{60} have been used, but there is a full range of more complex molecules carrying various functional properties awaiting for further growth experiments. These are considered as interesting model systems to understand the structure/properties relationship linked to the long-range quasi-periodic order.

4 Complex Intermetallics as Surface Alloys: An Alternative

Most of the structural works performed on complex intermetallic surfaces have been achieved using centimetre-sized single crystals of high structural quality and purity. Such specimens can be obtained by conventional growth techniques. Once polished and oriented, they are investigated using surface science techniques under ultra-high vacuum conditions. Depending on the intermetallics targeted, it is not always possible to obtain large enough samples due to, for instance, growth limitations (temperature, phase diagram constraints…) or elemental costs. Hence, an alternative approach consists in the deposition of pure elements on unary, binary or even ternary systems aiming to form the desire complex phases as surface alloys. The crystallographic and electronic surface structures of the terminating layers can then be characterized in situ. Sometimes the growth of surface intermetallic compounds can be fortunate originating from the alloying between adsorbates and substrate elements. As will be described below, this has often occurred while studying the growth of atomic thin films on aperiodic systems [52–56].

Elemental adsorption on a binary intermetallic compound represents also a great opportunity to follow the initial nucleation and growth of complex metallic alloys, including the propagation of aperiodic long-range order. In addition to the determination of the clean surface structure, the formation of complex intermetallic compounds as surface alloys allows characterization down to the atomic level of the interfaces between the matrix (here the substrate) and the grown phase. Such fundamental studies could in fine bring new solutions to issues encountered in the field of coating technology. Regarding complex metallic alloys, we will refer here to delamination and reactive diffusion upon post-annealing treatment often identified as technological bottlenecks [57]. Hence, an atomistic description of the interfacial structure between both antagonists could lead to the design of specific buffer layers to accommodate the strain related to lattice mismatch and/or to release internal stress due to thermal expansion coefficient differences between the two phases.

Although extensive works on single and multilayer surface alloys have been reported [58], the surface characterization of Al-based (complex) intermetallic compounds formed upon adsorption is much more limited. We will start with studies where intermetallic compounds have been formed while trying to grow quasi-periodic thin films.

Due to its tendency to self-assemble into decagonal- and icosahedral-shaped clusters, the adsorption of Au atoms was carried out on the decagonal Al-Ni-Co surface [52]. Submonolayer deposition of Au adatoms at room temperature leads to the formation of an Al-Au surface alloy without any orientational order as evidenced by x-ray photoelectron diffraction (XPD) and reflection high-energy electron diffraction (RHEED) experiments. Upon annealing the dosed sample to 350–400 K, the surface structure changes can be interpreted as an epitaxial layer consisting of twinned $AuAl_2$ crystals with (110)-oriented surface (see Fig. 6a) [52]. The twin azimuthal orientations replicate the tenfold symmetry of the underlying template. For 10 ML thick Au layers, the thin film is described as a polycrystalline Au layer using RHEED

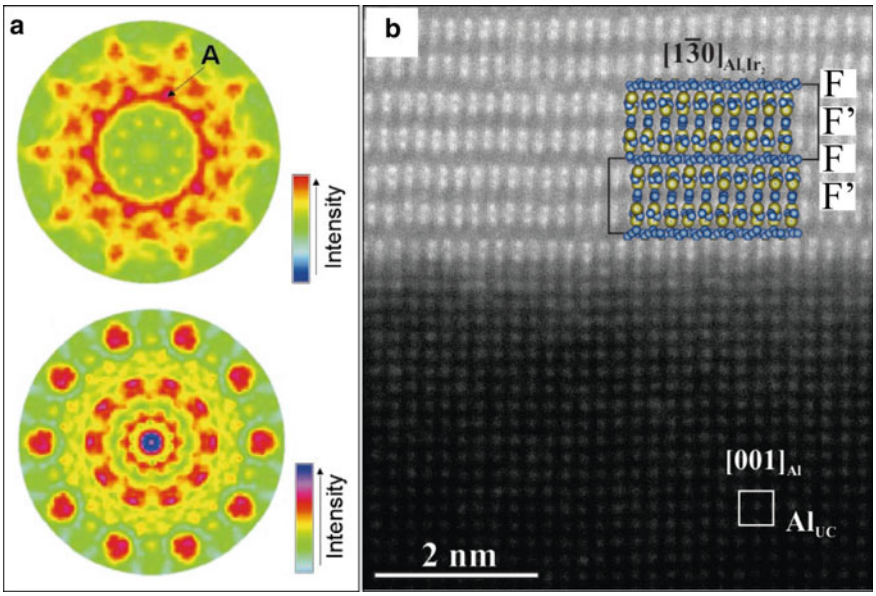

Fig. 6 **a** Stereographic projection (top) and single scattering cluster simulations (bottom) XPD images for Au 4f from the Au-dosed and annealed decagonal Al-Ni-Co surface and from an epitaxial $AuAl_2$ layer, respectively. **b** Atomically resolved HAADF-STEM image of the precipitate/matrix interface with the superimposed structural units of Al_9Ir_2 and Al substrate viewed in the $[1\bar{3}0]_{Al_9Ir_2}$ and $[001]_{Al}$projections, respectively. **a** Reprinted with permission from [52] M. Shimoda, T. Sato, A. Tsai, J.Q. Guo, Phys. Rev. B, 62, 11,288 (2000), https://doi.org/10.1103/PhysRevB.62.11288, copyright (2000) by the American Physical Society, and **b** reprinted with permission from [66] J. Kadok, K. Pussi, S. Šturm, B. Ambrožič, É. Gaudry, M.C. de Weerd, V. Fournée, J. Ledieu, Physical Review Materials 2(4), 043, 405 (2018), https://doi.org/10.1103/PhysRevMaterials.2.043405, copyright (2018) by the American Physical Society

measurements. The structure is unchanged upon annealing the Au thick film until adatom re-evaporation occurs [54]. The same scenarios apply to Au adsorption on the fivefold Al-Pd-Mn surface [53] and for Pt adsorption on the decagonal Al-Ni-Co surface with the formation of a Pt polycrystalline film regardless of the film thickness [59]. However, the Au and Pt growth modes are altered if the quasi crystalline substrate is pre-covered by an In layer [53, 54, 59]. Indeed, the Au polycrystalline thick film deposited at room temperature on the In pre-covered surface transforms upon annealing to 350–400 K to the $AuAl_2$ structure as demonstrated by RHEED and X-ray photoelectron spectroscopy (XPS) analysis. As already observed for submonolayer deposition [52], XPD images reveal a tenfold symmetry pattern consistent with an epitaxial layer model of multiply twinned $AuAl_2$ (110)-oriented crystals [54]. Based on XPS analysis, there is clear evidence for In diffusion across the thick Au overlayer at 300 K. With annealing, the initial In 3d core-level intensity is restored. Indium is then considered here as a surfactant promoting Frank–van der Merwe over Stranski–Krastanov type growth. Similar mechanisms are observed while dosing Pt

and Au adatoms on In pre-covered Al-Ni-Co and Al-Pd-Mn surfaces, respectively. In the former case, the structure of the annealed Pt thick film (490 K) results in an epitaxial layer of multiply twinned $PtAl_2$ crystals [59].

Still aiming at forming pseudomorphic overlayers, another intermetallic phase has been grown on similar quasi crystalline substrates. Located in the same column of the Periodic Table as Au, the adsorption of Cu atoms on complex metallic alloy surfaces has led to the formation of a unique intermetallic compound, namely the complex Hume-Rothery Al_4Cu_9 phase. The lattice parameter of this simple cubic γ-brass phase is equal to 8.71 Å (space group $P\bar{4}3$ m). At room temperature, the adsorption of Cu adatoms on the fivefold and twofold Al-Pd-Mn quasi crystalline surfaces yields quasi-periodic structures [39, 60]. Once annealed to 570 K, the thick Cu film (25 ML) crystallizes into five periodic domains rotated from each other by 72°, i.e. following the directional order of the fivefold substrate [55]. XPS, XPD and LEED analysis reveal that the domains correspond to the (110) surface-oriented Al_4Cu_9 structure [56]. This is also the conclusion drawn when Cu adsorption is carried out on the fivefold Al-Cu-Fe surface. Contrary to the Cu/Al-Pd-Mn system, the formation of β-Al(Cu, Fe)(110) domains is initially observed at room temperature from 1 to 8 ML [61]. Within this coverage regime, the β-phase is also the stable phase up to 573 K. Then, the growth of five Al_4Cu_9(110) domains appears for 20 ML thick Cu film annealed to 558 K, i.e. there is a minimal Cu thickness required for the growth of the Al_4Cu_9 phase as a surface alloy.

Interestingly, this γ-brass phase is also the one that appears upon the adsorption of Al atoms on a simple Cu(111) surface. In this case, the formation of Al_4Cu_9(110) domains occurs only if the nominal Al thickness is above 12 ML. The STM measurements combined with ab initio calculations demonstrate that the γ-Al_4Cu_9 surface is bulk-terminated at puckered planes [62]. This conclusion is in agreement with the surface plane selection identified across the Al_4Cu_9(110) surface using a single crystal [63].

As explained at the beginning of this section, elemental adsorption on a binary complex metallic alloy could represent an alternative route to grow ternary quasi-periodic surface phases and to possibly monitor in situ the propagation of long-range order. To this end, Cu adatoms have been deposited on the $Al_{13}Co_4$(100) surface [64]. The latter crystal which is considered as an approximant to the decagonal quasi crystal was an apparently ideal candidate for aperiodic surface alloy formation. Instead, the results indicate the formation of a β-Al(Cu, Co) phase above 3 ML Cu deposition at 300 K. For higher temperature (473 K), the β-Al(Cu, Co) is also formed but it is replaced by a γ-Al_4Cu_9 phase above 7.5 ML Cu deposition [64]. One of the striking features lies here in the domain orientations of both β- and γ-phases. The orientation of the γ-Al_4Cu_9 domains reported in previous studies tends to match with the atomically densest directions of the surface plane. Hence, five domains and two sets of threefold rotational domains are formed on fivefold surfaces and on Cu(111), respectively. For the Cu/$Al_{13}Co_4$(100) case, the two (110) domains identified across the surface are rotated from each other by 72°. Moreover, the growth proceeds $4 \pm 1°$ off the [011] and [$01\bar{1}$] directions of the orthorhombic substrate. At this stage, these peculiar growth directions could only be related to the orientation of the bipentagonal

motifs present on the clean $Al_{13}Co_4(100)$ surface. These motifs correspond to the elementary pentagonal bipyramid clusters, i.e. building blocks of the bulk structure. These different studies demonstrate the stability of the γ-Al_4Cu_9 phase as a surface alloy. It also shows that the phase will be formed as long as a critical amount of Al and Cu elements is reached within the surface region. The surface structural complexity has little influence on the γ-Al_4Cu_9 phase growth except for the domain orientations.

Aside from model adsorption studies performed under ultra-high vacuum conditions, the formation of complex intermetallic compounds is also encountered in industrial processes. To improve their oxidation and corrosion resistance, steel and cast iron can be hot-dip coated with pure Al or Al alloys of varying compositions. The resulting coating which is dependent on the chemical composition of the bath consists of an outer layer and an inner intermetallic layer which can be further subdivided into two zones. Using a pure Al bath, the intermetallic layer adjacent to the cast iron (first zone) contains the Al_5Fe_2 phase, while in the second zone, the Al_3Fe is identified (Si atoms being present in both phases in different amounts) [65]. The resulting interfaces between the different antagonists vary quite drastically from an irregular tongue-like morphology between the cast iron and the Al_5Fe_2 layer to a more regular interface between the Al outer layer and the Al_3Fe phase. The interfacial microstructure and composition will in fine dictate the coating physical and chemical properties.

Depending on the applications, protective coatings may be designed to sustain harsh conditions, including for instance high-temperature conditions and/or excessive oxidizing environments. Given its highmelting temperature and due to its oxidation resistance, Al-Ir based coating has been considered as a protective coating in gas turbine engines [67]. Although several methods are focussing on improving deposition processes, little is known on the surface structure of Al-Ir alloys and compounds. This is true for the interfacial structure between Al-Ir and the supporting substrate also.

To this end, the adsorption of Ir atoms on the Al(100) clean surface has been recently carried out under ultra-high vacuum conditions. The objectives were to determine (i) which Al-Ir phases will initially appear; (ii) the associated surface structure and (iii) the corresponding interface structure between the single crystal and the surface alloys formed. A reverse strategy by adsorbing Al on Ir(111) surface had been previously chosen to study the Ir-rich side of the phase diagram [68]. The layer-by-layer growth mode reported at 300 K preceded the formation of Ir_4Al surface aluminide obtained for high-temperature deposition (1100–1500 K). For the Ir/Al(100) system, a higher intermixing length is already expected at room temperature [69]. This is confirmed by experimental and theoretical results revealing the diffusion of Ir adatoms within the surface selvedge at room temperature [66]. Ir adsorption above 623 K leads to the growth of Al-Ir domains exhibiting a unit cell equal to $\sqrt{5}$ times the Al(100) surface unit cell. After a careful analysis of the Al-Ir binary system and in agreement with dynamical LEED analysis, the grown phase has been assigned to the Al_9Ir_2 compound. The surface of the $Al_9Ir_2(001)$ oriented

domain is bulk-terminated at pure Al planes in accordance with ab initio calculations demonstrating that Ir adatoms located within the topmost surface layer are energetically unfavored.

Regarding the Al_9Ir_2 growth orientation with respect to the Al(100) substrate, it can be described for one domain by the following epitaxial relation: $(100)_{Al}[001]_{Al} \| (001)_{Al_9Ir_2}[1\bar{3}0]_{Al_9Ir_2}$.

As shown using STM, LEED and transmission electron microscopy (TEM) techniques, these specific domain orientations originate from the alignment of local Al motifs present in the $Al_9Ir_2(001)$ planes with the Al(100) surface unit cell. Atomic resolution high-angle annular dark-field scanning TEM (HAADF-STEM) images reveal a coherent growth and a sharp interface between Al_9Ir_2 precipitates and the Al matrix (see Fig. 6b) [66]. The absence of dislocations within the measurements is related to the low strain due to lattice mismatches close to 0.4% between the two antagonists.

From the work presented in this section, it is clear that the surface characterization of complex intermetallic grown as surface alloys is still in its infancy. It is also true for interfacial structural characterization, which should play a crucial role when intermetallic compounds are envisaged as a protective or functionalized coating. Furthermore, the introduction of intermetallic phases as buffer layers between substrates and coatings may represent an interesting alternative to circumvent adhesion or delamination issues [61].

5 Complex Intermetallic Surfaces and Recent Developments in Catalysis

The interest in (complex) intermetallics as catalysts has increased significantly in the past few years, as documented in recent numerous reviews [70–73]. Indeed, their surfaces present several main advantages compared to simple metals and alloys. They are stable, with possible surface segregation being generally suppressed, due to the strong bonding network occurring in the bulk materials. Site isolation, i.e. the spatial separation of catalytically active sites at the surface, which is known to be an important factor for reaction selectivity, is commonly achieved on complex intermetallic surfaces. Synergistic effects are also expected when combining different chemical elements in ordered alloys, like the ones highlighted using PdZn and PdCd as selective catalysts for methanol steam reforming [74, 75]. While pure Cu is traditionally used for this reaction, PdZn and PdCd lead to similar high selectivity towards the formation of CO_2. It is attributed to the similar valence electronic densities of states of Cu and the 1:1 compounds. PdZn and PdCd can then be considered as replacing Cu for this reaction.

Due to the large number of intermetallic compounds known so far—more than 6000 binaries have been synthesized and characterized up to now, one expects to find new competitive intermetallic catalysts by a careful selection of their atomic

and electronic surface structures. Several families of intermetallics have already been identified as stable, reactive and selective catalysts. Most of them combine noble metals—the catalytically active sites—with elements from different areas of the periodic table, for example sp metals like Al, Ga or Sn. A few noble metal-free catalysts do exist, promising for the reduction of costs and environmental impacts.

In the following sub-sections, two families of (complex) intermetallic compounds are discussed, in relation to the hydrogenation of acetylene and butadiene. The case of quasi crystals or approximants used as catalysts after a leaching process [76–81] is not developed, since the catalytic material obtained after the chemical treatment generally consists of metallic nanoparticles dispersed on an oxide, thus leading to mechanisms for the reactivity distinct from the ones valid for ideal intermetallic surfaces.

5.1 Pd- and Pt-Based Intermetallic Catalysts

One of the typical intermetallic compound surfaces used as a catalyst is probably $Pt_3Sn(111)$. For the semi-hydrogenation of butadiene, the activities of its $p(2 \times 2)$ or $(\sqrt{3} \times \sqrt{3})$ surfaces were found to be one order of magnitude lower than that of Pt(111) but the selectivity into butenes is largely increased by comparison to pure Pt (98–100%) [82]. Theoretical studies on surface alloys showed that the presence of Sn at the surface weakens the chemisorption of unsaturated hydrocarbon molecules [83]. More complex intermetallics—as least when evaluated with the number of atoms in the cell—were also identified as potential catalysts for selective semi-hydrogenation reactions (Fig. 7), like Pd_3Ga_7, Pd_2Ga and PdGa [84–87]. Selectivity is expected to increase with the number of Ga atoms in the vicinity of the active Pd atoms, and it has been demonstrated on $Pd_2Ga(010)$ [88]. Other compounds with similar compositions, like $Ga_{2+x+y}Sn_{4-x}Pd_9$ do not present attractive performance [89], highlighting the challenge to predict the catalytic properties from the knowledge of the bulk structure.

The surface structure is a decisive factor for catalytic performance [90–93]. In the cases of GaPd (and Al-Pd), corrugated surfaces with slightly protruding transition metal atoms forming a triangular arrangement with two neighbouring Al/Ga atoms are indeed highlighted as catalytically attractive surfaces, allowing the transition from the di-σ bonded adsorption configuration for acetylene to a π-bonded adsorption of ethylene. The mechanism follows the one proposed by Horiuti and Polanyi in 1934 [94] and consists of three steps: (i) adsorption of the unsaturated molecule on the hydrogenated catalyst surface, (ii) hydrogen migration to the β-carbon of the unsaturated molecule and formation of a σ-bond between the catalyst surface and α-C and finally (iii) reductive elimination of the hydrogenated molecule. The large distances between the isolated active sites avoid undesired side-reactions such as oligomerization.

Hydrogenated surfaces are a clear requirement for this mechanism. On simple transition metal surfaces, atomic hydrogen is adsorbed on top sites. On GaPd or

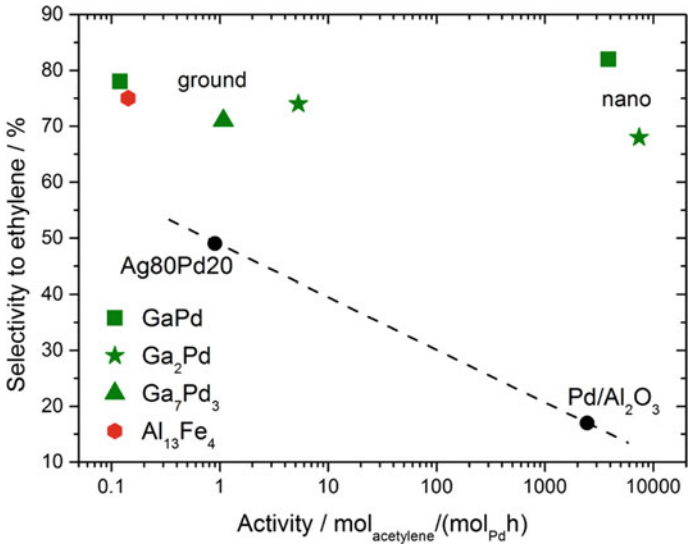

Fig. 7 Comparison of several intermetallic catalysts to supported 5% Pd/Al_2O_3 and the unsupported substitutional alloy $Ag_{80}Pd_{20}$. The dashed line is a guide to the eye. This figure is reproduced from ref [72]. (https://doi.org/10.1088/1468-6996/15/3/034803) under the licence Creative Commons Attribution 3.0 licence

AlPd surfaces, H is generally adsorbed on transition metal top sites, with a few exceptions. For example, a Ga–H top interaction has been identified on PdGa(100) [95], highlighting that surface Ga atoms are not only a spacer, but part of the active site, as already postulated by Krajcı et al. [71, 96].

5.2 Non-noble Intermetallic Catalysts

Highly active catalysts towards hydrogenation reactions are usually based on Pt-group metals. There are not many solutions available today to replace these noble metals. Non-precious metal catalysts, especially those based on nickel (such as Raney nickel), have been developed as economical alternatives, but they are less active and/or selective than Pt-group metals and prone to deactivation [97, 98]. Al-based complex intermetallic compounds like γ-Al_4Cu_9 or $Al_{13}TM_4$ (TM = Co, Fe) have recently been identified as potential catalysts for hydrogenation reactions [86, 99–101]. For the semi-hydrogenation of acetylene, $Al_{13}Fe_4$ presents a high conversion and a high ethylene-selectivity of 81–84% (reaction conditions: 0.5% C_2H_2, 5% H_2, 50% C_2H_4 in He, 30 ml min^{-1} total flow, 200 °C). For the hydrogenation of butadiene, the γ-Al_4Cu_9(110) surface is active and 100% selective to butenes (2–20 mbar and temperatures of 110–180 °C).

Table 1 Dissociation, activation and desorption energies for the semi-hydrogenation of acetylene on complex Al-Co intermetallic surfaces. E_a^{dis} and E_a^i are the activation energies for H_2 dissociation and C_2H_x hydrogenation, respectively. $E_d^{C_2H_4}$ is the ethylene desorption energy. Energies are given in kJ mol^{-1}

Surface	Model	$H_2 \rightarrow 2H$	$C_2H_x \rightarrow C_2H_{x+1}$			$C_2H_4\uparrow$
		E_a^{dis}	$E_a^{x=2}$	$E_a^{x=3}$	$E_a^{x=4}$	$E_d^{C_2H_4}$
$Al_5Co_2(2\bar{1}0)$	P_B [106]	15	60	50	60	87
Al_5Co_2 $(2\bar{1}0)$	$P_{B\text{-}4}Co$ [106]	–	80	87	64	105
$Al_{13}Co_4(100)$	[103]	17	63	61	80	70
$Al_{13}Co_4(100)$	[105]	52	78	83	111	89

As already mentioned, the presence of atomic hydrogen on the intermetalic surfaces is mandatory for the Horiuti and Polanyi mechanism. The dissociative adsorption of H_2 on γ-$Al_4Cu_9(110)$ is the rate-limiting step. It is likely caused by the high concentration of Cu in the topmost surface (Cu:Al is 12:6), H_2 dissociation occurring with a non-negligible barrier on pure Cu (47 kJ/mol [102]). Hydrogen dissociation is much easier when transition metals protrude at the surface, as in the case of the $Al_{13}Co_4(100)$ surface model obtained by bulk truncation (17 kJ/mol) [103]. However, the combination of surface science studies and theoretical calculations point towards a dense Al-rich topmost layer for $Al_{13}Co_4(100)$ [104], leading to a rather high H_2 dissociation barrier (~52 kJ/mol) [105]. These observations highlight again the importance of surface structure on catalytic performances (Table 1).

In summary, intermetallic compound surfaces are promising for applications in catalysis. An enthalpic driving force usually prevents surface segregation, but sp metals are subject to oxidation and therefore the surface of the intermetallic may deviate strongly from the bulk in the presence of oxygen. Their surfaces however provide isolation for the active site, which makes them at least interesting model systems to further investigate single-atom catalysts [107].

6 Conclusions

We have presented a topical review of several areas of current interest relating to the structure and properties of surfaces of quasi crystals and other complex metallic alloys and the formation of ultra-thin atomic and molecular films on these surfaces. Interest in these areas varies from fundamental curiosity about the behaviour of adsorbing materials on these surfaces to their potential for applications in economically important areas such as corrosion resistance and catalysis. We hope to have demonstrated that the surfaces of complex metallic alloy surfaces, though not receiving perhaps the same levels of attention as simpler elemental and alloys surfaces, nonetheless merit an increasing level of scrutiny from the international surface science community.

Acknowledgement This work was partly supported by the Engineering and Physical Sciences Research Council and the European Integrated Centre for the Development of New Metallic Alloys and Compounds. We dedicate this chapter to the memory of our colleague, mentor and friend An Pang Tsai who passed away in early 2019 after a short illness.

References

1. D. Shechtman, I. Blech, D. Gratias, J.W. Cahn, Phys. Rev. Lett. **53**, 1951 (1984)
2. I. Hargittai, J. Mol. Struct. **976**(1–3), 81 (2010)
3. J.M. Dubois, *Useful Quasicrystals* (World Scientific, Singapore, 2005)
4. X.B. Zeng, G. Ungar, Y.S. Liu, V. Percec, S.E. Dulcey, J.K. Hobbs, Nature **428**(6979), 157 (2004)
5. K. Hayashida, T. Dotera, A. Takano, Y. Matsushita, Phys. Rev. Lett. **98**(19), 195502 (2007)
6. D.V. Talapin, E.V. Shevchenko, M.I. Bodnarchuk, X.C. Ye, J. Chen, C.B. Murray, Nature **461**(7266), 964 (2009)
7. S. Fischer, A. Exner, K. Zielske, J. Perlich, S. Deloudi, W. Steurer, P. Lindner, S. Förster, Proc. Natl. Acad. Sci. **108**(5), 1810 (2011)
8. C. Xiao, N. Fujita, K. Miyasaka, Y. Sakamoto, O. Terasaki, Nature **487**, 349 (2012)
9. S. F¨orster, K. Meinel, R. Hammer, M. Trautmann, W. Widdra, Nature **502**, 215 (2013)
10. K. Kamiya, T. Takeuchi, N. Kabeya, N. Wada, T. Ishimasa, A. Ochiai, K. Deguchi, K. Imura, N.K. Sato, Nat. Commun. **9**(1), 154 (2018)
11. A.P. Tsai, A. Inoue, T. Masumoto, J. Mat. Sci. Lett. **6**, 1403 (1987)
12. A.P. Tsai, Acc. Chem. Res. **36**(1), 31 (2003)
13. A. Kortan, R. Becker, F. Thiel, H. Chen, Phys. Rev. Lett. **64**, 200 (1990)
14. E.G. McRae, R.A. Malic, T.H. Lalonde, F.A. Thiel, H.S. Chen, A.R. Kortan, Phys. Rev. Lett. **65**, 883 (1990)
15. P.A. Thiel, R. McGrath, Surfaces of quasicrystals and complex metallic alloys, in *Handbook of Surface and Interface Science* (Wiley, Berlin).
16. A.I. Goldman, R.F. Kelton, Rev. Mod. Phys. **65**(1), 213 (1993)
17. Z. He, H. Li, H. Ma, G. Li, Sci. Rep. **7**, 40510 (2017)
18. D. Naumovíc, Prog. Surf. Sci. **75**(3–8), 205 (2004)
19. J.A. Smerdon, J.K. Parle, R. McGrath, B. Bauer, P. Gille, Zeit. Kristallographie **224**, 13 (2009)
20. S.S. Hars, H.R. Sharma, J.A. Smerdon, T.P. Yadav, A. Al-Mahboob, J. Ledieu, V. Fournée, R. Tamura, R. McGrath, Phys. Rev. B **93**(20), 205428 (2016)
21. K. Urban, M. Feuerbacher, J. Non-Crystalline Solids **334–335**, 143 (2004)
22. J.M. Dubois, An introduction to complex metallic alloys and to the CMA Network of Excellence, in *Complex Metallic Alloys*, vol. 1, book section 1 (World Scientific, Singapore, 2007), pp. 1–29
23. J.A. Smerdon, H.R. Sharma, J. Ledieu, R. McGrath, J. Phys. Condens. Matter **20**, 314005 (2008)
24. J.A. Smerdon, L.H. Wearing, J.K. Parle, L. Leung, H.R. Sharma, J. Ledieu, R. McGrath, Philos. Mag. **88**, 2073 (2008)
25. R. McGrath, J.A. Smerdon, H.R. Sharma, W. Theis, J. Ledieu, J. Phys.-Condens. Matter **22**(8), 084022 (2010)
26. H.R. Sharma, K. Nozawa, J.A. Smerdon, P.J. Nugent, I. McLeod, V.R. Dhanak, M. Shimoda, Y. Ishii, A.P. Tsai, R. McGrath, Nat. Commun. **4**, 2715 (2013)
27. H.R. Sharma, M. Shimoda, K. Sagisaka, H. Takakura, J.A. Smerdon, P.J. Nugent, R. McGrath, D. Fujita, S. Ohhashi, A.P. Tsai, Phys. Rev. B **80**(12), 121401 (2009)
28. C. Cui, P.J. Nugent, M. Shimoda, J. Ledieu, V. Fournée, A.P. Tsai, R. McGrath, H.R. Sharma, J. Phys. Condens. Matter **26**(1), 015001 (2014)

29. C. Cui, P.J. Nugent, M. Shimoda, J. Ledieu, V. Fournée, A.P. Tsai, R. McGrath, H.R. Sharma, J. Phys. Condens. Matter **24**(44), 445011 (2012)
30. S. Hars, H. Sharma, J. Smerdon, S. Coates, K. Nozawa, A. Tsai, R. McGrath, Surf. Sci. **678**, 222 (2018)
31. H. Takakura, C.P. Gómez, A. Yamamoto, M. de Boissieu, A. Tsai, Nat. Mat. **6**, 58 (2007)
32. K. Nozawa, Y. Ishii, J. Phys. Conf. Ser. **809**(1), 012018 (2017)
33. K.J. Franke, H.R. Sharma, W. Theis, P. Gille, P. Ebert, K.H. Rieder, Phys. Rev. Lett. **89**(15), 156104 (2002)
34. H.R. Sharma, M. Shimoda, A.R. Ross, T.A. Lograsso, A.P. Tsai, Phys. Rev. B **72**(4), 045428 (2005)
35. J. Ledieu, L. Leung, L.H. Wearing, R. McGrath, T.A. Lograsso, D. Wu, V. Fournée, Phys. Rev. B. **77**, 073409 (2008)
36. J.A. Smerdon, J.K. Parle, L.H. Wearing, T.A. Lograsso, A.R. Ross, R. McGrath, Phys. Rev. B **78**, 075407 (2008)
37. V. Fournée, H.R. Sharma, M. Shimoda, A.P. Tsai, B. Ünal, A.R. Ross, T.A. Lograsso, P.A. Thiel, Phys. Rev. Lett. **95**(15), 155504 (2005)
38. H.R. Sharma, V. Fournée, M. Shimoda, A.R. Ross, T.A. Lograsso, P. Gille, A.P. Tsai, Phys. Rev. B **78**(15), 155416 (2008)
39. J.A. Smerdon, N. Cross, V.R. Dhanak, H.R. Sharma, K.M. Young, T.A. Lograsso, A.R. Ross, R. McGrath, J. Phys. Condens. Matter **22**(34), 345002 (2010)
40. J. Ledieu, J.T. Hoeft, D.E. Reid, J.A. Smerdon, R.D. Diehl, T.A. Lograsso, A.R. Ross, R. McGrath, Phys. Rev. Lett. **92**, 135507 (2004)
41. J.A. Smerdon, J. Ledieu, J.T. Hoeft, D.E. Reid, L.H. Wearing, R.D. Diehl, T.A. Lograsso, A.R. Ross, R. McGrath, Philos. Mag. **86**, 841 (2006)
42. K. Pussi, M. Gierer, R.D. Diehl, J. Phys. Condens. Matter **21**, 474213 (2009)
43. J. Ledieu, C.A. Muryn, G. Thornton, R.D. Diehl, T.A. Lograsso, D.W. Delaney, R. McGrath, Surf. Sci. **472**(1–2), 89 (2001)
44. E.J. Cox, J. Ledieu, V.R. Dhanak, S.D. Barrett, C.J. Jenks, I. Fisher, R. McGrath, Surf. Sci. **566–568**, 1200 (2004)
45. J.A. Smerdon, K.M. Young, M. Lowe, S.S. Hars, T.P. Yadav, D. Hesp, V.R. Dhanak, A.P. Tsai, H.R. Sharma, R. McGrath, Nano Lett. **14**(3), 1184 (2014)
46. V. Fournée, E. Gaudry, J. Ledieu, M.C. deWeerd, D. Wu, T. Lograsso, ACS Nano **8**(4), 3646 (2014)
47. T. Cai, J. Ledieu, R. McGrath, V. Fournée, T.A. Lograsso, A.R. Ross, P.A. Thiel, Ultra-thin films on complex metallic alloy surfaces: a perspective. Surf. Sci. **526**(1–2), 115 (2003)
48. D. S., F. F., S. W, Acta Crystallographica Section B **67**(1), 1 (2011)
49. Z. Papadopolos, G. Kasner, J. Ledieu, E.J. Cox, N.V. Richardson, Q. Chen, R.D. Diehl, T.A. Lograsso, A.R. Ross, R. McGrath, Phys. Rev. B **66**, 184207 (2002)
50. B. Ünal, C.J. Jenks, P.A. Thiel, J. Phys. Condens. Matter **21**(5), 055009 (2009)
51. M. Krajčí, J. Hafner, J. Ledieu, V. Fournée, J. Phys. Conf. Ser. **226**, 012005 (2010)
52. N. Kalashnyk, J. Ledieu, E. Gaudry, C. Cui, A. Tsai, V. Fournée, Nano Res. **11**(4), 2129 (2018)
53. M. Shimoda, T.J. Sato, A.P. Tsai, J.Q. Guo, Phys. Rev. B **62**(17), 11288 (2000)
54. M. Shimoda, J.Q. Guo, T.J. Sato, A.P. Tsai, Jpn. J. Appl. Phys. **40**(10), 6073 (2001)
55. M. Shimoda, J.Q. Guo, T.J. Sato, A.P. Tsai, Surf. Sci. **482–485**, 784 (2001)
56. J. Ledieu, J.T. Hoeft, D.E. Reid, J.A. Smerdon, R.D. Diehl, N. Ferralis, T.A. Lograsso, A.R. Ross, R. McGrath, Phys. Rev. B **72**(3), 035420 (2005)
57. M. Bielmann, A. Barranco, P. Ruffieux, O. Gröning, R. Fasel, R. Widmer, P. Gröning, Adv. Eng. Mat. **7**, 392 (2005)
58. J.M. Dubois, Chem. Soc. Rev. **41**, 6760 (2012)
59. U. Bardi, Rep. Prog. Phys. **57**, 939 (1994)
60. M. Shimoda, T.J. Sato, A.P. Tsai, J.Q. Guo, Surf. Sci. **507**, 276 (2002)
61. D. Reid, J.A. Smerdon, J. Ledieu, R. McGrath, Surf. Sci. **600**(18), 4132 (2006)

62. T. Duguet, J. Ledieu, J.M. Dubois, V. Fournee, J. Phys.-Condens. Matter **20**(31), 314009 (2008)
63. T. Duguet, É. Gaudry, T. Deniozou, J. Ledieu, M.C. de Weerd, T. Belmonte, J.M. Dubois, V. Fournée, Phys. Rev. B **80**(20) (2009)
64. É. Gaudry, A.K. Shukla, T. Duguet, J. Ledieu, M.C. deWeerd, J.M. Dubois, V. Fournée, Phys. Rev. B 82(8) (2010)
65. R. Addou, A.K. Shukla, S.A. Villaseca, É. Gaudry, T. Deniozou, M. Heggen, M. Feuerbacher, R. Widmer, O. Gröning, V. Fournée, J.M. Dubois, J. Ledieu, New J. Phys. **13**, 103011 (2011)
66. R. Mola, T. Bucki, K. Wcislo, Arch. Foundry Eng. **14**, 85 (2014)
67. J. Kadok, K. Pussi, S. Sturm, B. Ambrozic, É. Gaudry, M.C. deWeerd, V. Fournée, J. Ledieu, Phys. Rev. Mater. **2**(4), 043405 (2018)
68. R. Darolia, U.S. Patent 6,630,250, B1, Oct. 7 (2003)
69. N. Gall', E. Rut'kov, A. Tontegode, Phys. Solid State **48**, 369 (2006)
70. J.D.R. Buchanan, T.P.A. Hase, B.K. Tanner, P.J. Chen, L. Gan, C.J. Powell, W.F. Egelhoff, Phys. Rev. B **66**, 104427 (2002)
71. S. Furukawa, T. Komatsu, ACS Catal. **7**, 735 (2017)
72. M. Krajčí, J. Hafner, ChemCatChem **8**, 34 (2016)
73. M. Armbrüster, R. Schlögl, Y. Grin, Sci. Technol. Adv. Mater. **15**, 034803 (2014)
74. J. Hafner, M. Krajčí, Acc. Chem. Res. **47**, 3378 (2014)
75. A. Tsai, S. Kameoka, K. Nozawa, M. Shimoda, Y. Ishii, Acc. Chem. Res. **50**, 2879 (2017)
76. A.P. Tsai, S. Kameoka, Y. Ishii, J. Phys. Soc. Jpn. **73**, 3270 (2004)
77. B.P. Ngoc, C. Geantet, M. Aouine, G. Bergeret, S. Raffy, S. Marlin, Int. J. Hydrog. Energy **33**, 1000 (2008)
78. T. Tanabe, S. Kameoka, A.P. Tsai, Catal. Today **111**, 153 (2006)
79. S. Kameoka, T. Tanabe, A. Tsai, Catal. Today **93–5**, 23 (2004)
80. M. Yoshimura, A. Tsai, J. Alloy Compd. **342**, 451 (2002)
81. H. Takakura, J. Guo, A. Tsai, Philos. Mag. Lett. **81**, 411 (2001)
82. S. Kameoka, S. Wakabayashi, E. Abe, A.P. Tsai, Catal Lett **146**, 1309 (2016)
83. Y. Jugnet, R. Sedrati, J. Bertolini, J. Catal. **229**, 252 (2005)
84. C. Becker, J. Haubrich, K. Wandelt, F. Delbecq, D. Loffreda, P. Sautet, J. Phys. Chem. C **112**, 14693 (2008)
85. M. Armbrüster, K. Kovnir, M. Behrens, D. Teschner, Y. Grin, R. Schlögl, J. Am. Chem. Soc. **132**, 14745 (2010)
86. K. Kovnir, J. Osswald, M. Armbrüster, D. Teschner, G. Weinberg, U. Wild, A. Knop-Gericke, T. Ressler, Y. Grin, R. Schlögl, J. Catal. **264**, 93 (2009)
87. J. Osswald, R. Giedigkeit, R.E. Jentoft, M. Armbrüster, F. Girgsdies, K. Kovnir, T. Ressler, Y. Grin, R. Schlögl, J. Catal. **258**, 210 (2008)
88. J. Osswald, K. Kovnir, M. Armbrüster, R. Giedigkeit, R.E. Jentoft, U. Wild, Y. Grin, R. Schlögl, J. Catal. **258**, 219 (2008)
89. M. Krajčí, J. Hafner, J. Phys. Chem C **118**, 12285 (2014)
90. O. Matselko, U. Burkhardt, Y. Prots, R. Zimmermann, M. Armbruester, R. Gladyshevskii, Y. Grin, Eur. J. Inorg. Chem. **29**, 3542 (2017)
91. M. Krajčí, J. Hafner, J. Phys. Chem. C **116**, 6307 (2012)
92. M. Krajčí, J. Hafner, J. Catal. **295**, 70 (2012)
93. M. Krajčí, J. Hafner, Phys. Rev. B **87**, 035436 (2013)
94. M. Krajčí, J. Hafner, J. Catal. **312**, 232 (2014)
95. M. Polanyi, J. Horiuti, J. Trans, Faraday Soc. **30**, 1164 (1934)
96. P. Bechthold, J. Ardenghi, O. Nagel, A. Juan, E. González, P. Jasen, Int. J. Hydrog. Energy **39**, 2093 (2014)
97. M. Sandoval, P. Bechthold, V. Orazi, E. González, A. Juan, P. Jasen, Appl. Surf. Sci. **435**, 568 (2018)
98. A.B. Mekler, S. Ramachandran, S. Swaminathan, M.S. Newman, Org. Synth. **5**, 743 (1973)
99. C.F.H. Allen, J. VanAllan, Org. Synth. **3**, 827 (1955)
100. L. Piccolo, L. Kibis, M.C.D. Weerd, E. Gaudry, J. Ledieu, V. Fournée, ChemCatChem (2017)

101. M. Armbrüster, K. Kovnir, M. Friedrich, D. Teschner, G. Wowsnick, M. Hahne, P. Gille, L. Szentmiklosi, M. Feuerbacher, M. Heggen, F. Girgsdies, D. Rosenthal, R. Schlögl, Y. Grin, Nat. Mater. **11**, 690 (2012)
102. M. Armbrüster, K. Kovnir, Y. Grin, R. Schlögl, P. Gille, M. Heggen, M. Feuerbacher, European Patent **09157875**, 7 (2009)
103. C. Diaz, E. Pijper, R.A. Olsen, H.F. Busnengo, D.J. Auerbach, G.J. Kroes, Science **326**, 832 (2009)
104. M. Krajčí, J. Hafner, J. Catal. **278**, 200 (2011)
105. É. Gaudry, C. Chatelier, G. McGuirk, L.S. Loli, M.C.D. Weerd, J. Ledieu, V. Fournée, R. Felici, J. Drnec, G. Beutier, M. de Boissieu, Phys. Rev. B **94**, 165406 (2016)
106. D. Kandaskalov, V. Fournée, J. Ledieu, E. Gaudry, J. Phys. Chem. C **121**(34), 18738 (2017)
107. M. Meier, J. Ledieu, V. Fournée, E. Gaudry, J. Phys. Chem. C **121**, 4958 (2017)
108. T. Yamada, T. Kojima, E. Abe, S. Kameoka, Y. Murakami, P. Gille, A.P. Tsai, J. Am. Chem. Soc. **140**, 3838 (2018)

Growth Defects in PVD Hard Coatings

Miha Čekada, Peter Panjan, Aljaž Drnovšek, Matjaž Panjan, and Peter Gselman

Abstract Growth defects are imperfections in coating microstructure at the size level in the order of 0.1–1 μm. Though they are encountered in most techniques of thin film deposition, this paper is generally limited to hard protective coatings deposited by physical vapor deposition. Most results have been obtained by magnetron sputtering. The starting point of a growth defect is a seed, which may have a geometrical origin; it may be an inclusion or a foreign particle. Methods to analyze individual growth defects are presented, with an emphasis on focused ion beam. Using this technique, types of defects are discussed based on seed type, their evolution, and consequences, particularly in terms of corrosion resistance. Experiments involving a single growth defect are presented too. A different approach is a statistical analysis on growth defect density, predominately limited to nodular defects. Stylus profilometry is proposed as the principle technique; however, poor reproducibility should be taken into account and thus interpretation taken accordingly.

1 Introduction

1.1 Background

In a typical thin film study, the primary interest is in the film properties, such as mechanical, electrical, optical, etc. In an applied study, this interest is narrowed down to a short list of relevant properties. These properties should be homogeneous in both lateral directions, though some variation can be tolerated. For instance, a minor variation of reflectivity in a general-purpose optical coating is not an issue.

M. Čekada (✉) · P. Panjan · A. Drnovšek · M. Panjan · P. Gselman
Jožef Stefan Institute, Jamova 39, 1000 Ljubljana, Slovenia
e-mail: miha.cekada@ijs.si

P. Gselman
Interkorn d.o.o., Gančani 94, 9231 Beltinci, Slovenia

A. Drnovšek
Montanuniversität Leoben, Franz-Josef-Straße 18, 8700 Leoben, Austria

S. Kumar and D. K. Aswal (eds.), *Recent Advances in Thin Films*, Materials Horizons: From Nature to Nanomaterials, https://doi.org/10.1007/978-981-15-6116-0_3

However, a sharp localized decrease of reflectivity in a laser application can cause a catastrophic failure due to heating in this particular spot [1, 2]. A similar daily experience is pitting corrosion on steel protected by a galvanic coating. In this case, a minute defect in the coating integrity can cause a major structural damage.

Thin films deposited by Physical Vapor Deposition (PVD) are no exception to this effect. Imperfections on the substrate surface, substrate contamination, impurities in the film, etc., have a similar influence on the coating quality as in other deposition techniques. In addition, there is the specific microstructure, typically strongly columnar, which causes additional inhomogeneity at the microscopic level. In some types of PVD, particularly cathodic arc evaporation, the emission of microdroplets is an inherent part of the process and greatly increases the non-uniformity of the film [3].

The term »defect« is a very broad one with different meanings in different areas of research. It can be applied to a point defect in the crystal lattice, or can be colloquially used as a structural deficiency in an engineering environment. In thin films, the term »growth defect« has become established to include all the localized imperfections in film microstructure which arise during the film growth. This definition excludes wear, cracks, delamination, etc., as a consequence of film application. Nevertheless, an existing growth defect may evolve during application. As by definition, the growth defects are a feature of thin film growth; the vertical size of growth defects has an upper limit in the film thickness, though they can be much larger in the lateral direction. The lower size limit is somehow arbitrary; often only those growth defects are considered which can have a sizable effect on applications.

The growth defects are a common sight on a PVD coating surface; Fig. 1 shows such a case. The most common growth defect type is the nodular defect (shown on the left of Fig. 1), indeed, sometimes the terms »nodular defect« and »growth defect« are used interchangeably.

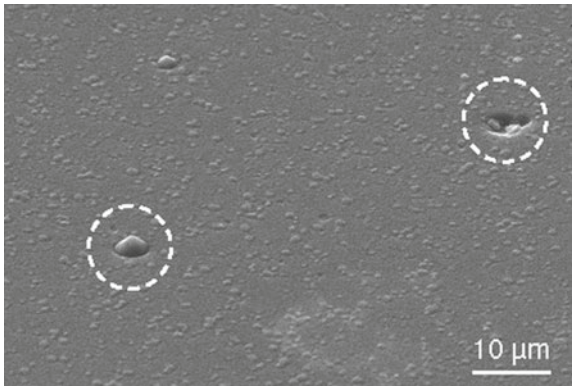

Fig. 1 SEM image of a PVD coating surface; there is a typical nodular defect on the left and a depression on the right

1.2 History

Whenever a thin film property is evaluated, the operator performs the measurement on a defect-free area. For instance, a nanohardness measurement requires a flawless film surface; therefore, the indentation is made far from any defect. The growth defects are thus well known in the PVD community, but they tend to be avoided. The number of publications is thus quite limited.

The nodular defects were discovered in 1969 by studying the metallic films deposited by electron beam evaporation [4]. Three years later, the growth defects were also observed on films deposited by sputtering [5]. At that time, the formation mechanism was explained for the first time [6] while SEM was used for observation of defects [7]. The early works were based on either metallic or dielectric films, predominantly for optical applications; see a review of papers in [8]. Detailed growth explanations were given [9], and first computer simulations were run [10]. Consequent modeling was augmented by experimental verification using nanolayer coatings [11]. Later, works were primarily associated with the problems as a consequence of growth defects, i.e., how to limit the growth defect formation. A thorough overview of growth phenomena in amorphous carbon coatings, including the growth defects, is given in [12]. The main fields of application are optical coatings (problems with local overheating at growth defects) [1, 2], microelectronics, and corrosion.

Corrosion in particular is an important aspect since localized corrosion (pitting, stress, opening …) is often more important than a homogeneous corrosion. A growth defect is thus a suitable starting point for the corrosion process. Several papers have been dedicated to this topic for the past two decades. Corrosion mechanisms were proposed taking place at the growth defect [13]; the same group also observed wear patterns during erosion tests [14]. Early papers already suggested that the corrosion resistance of hard coatings strongly depends on the behavior at the growth defects rather than the properties of the homogeneous coating [15]. Studies were conducted on multilayer coatings with an emphasis on porosity influence [16] and growth defect microstructure [17]. For an authoritative overview on corrosion protection of hard coatings, see [18], where a sizeable part is devoted to the influence of growth defects on corrosion resistance.

In recent years, there has been a renewed interest in growth defects, partially also driven by new techniques suitable for growth defect study, such as focused ion beam or advanced topography evaluation methods [19]. In combination with corrosion behavior, tribological studies were made as well [20]. Another interesting study is oriented toward the role of growth defects during cavitation erosion [21].

1.3 Motivation

As explained in the previous subsection, the motivation for growth defect studies has been driven by applications most affected by growth defect induced phenomena. On

the other hand, one can also look at the deposition aspect. In this regard, the cathodic arc evaporation is the main method with a strong issue of growth defects. The cathodic spot is typically only a few micrometers in diameter where a current of 100 amps causes local melting of the target material. This is associated with microdroplet formation, and these droplets (0.1–1 μm size range) fall on the growing film.

There has been a lot of research on how to minimize the droplet formation or the droplet incorporation into the growing film [22–24]. Standard remedy in the latter direction is the filtered arc technique, but it is accompanied by a substantial drop in deposition rate [25]. The droplet formation can be reduced by improved arc power supply; this is essentially an electrical engineering topic rather than thin film physics. This approach has considerably lowered the roughness of coatings in industrial production which makes the microdroplet formation a less relevant problem than what it used to be.

A competitive PVD technology is the magnetron sputtering. A major advantage compared to cathodic arc evaporation is the absence of melting-induced microdroplets. The surface of magnetron sputtered coating is not perfect either, but the overall defect density is far lower compared to cathodic arc evaporation (Fig. 2). This makes magnetron sputtering a useful tool to study growth defects. The (relatively few) growth defects are the ones inherent to the PVD in general, rather than in the case of cathodic arc where the majority of growth defects is associated to this technique alone. In magnetron sputtering, the growth defects have been associated

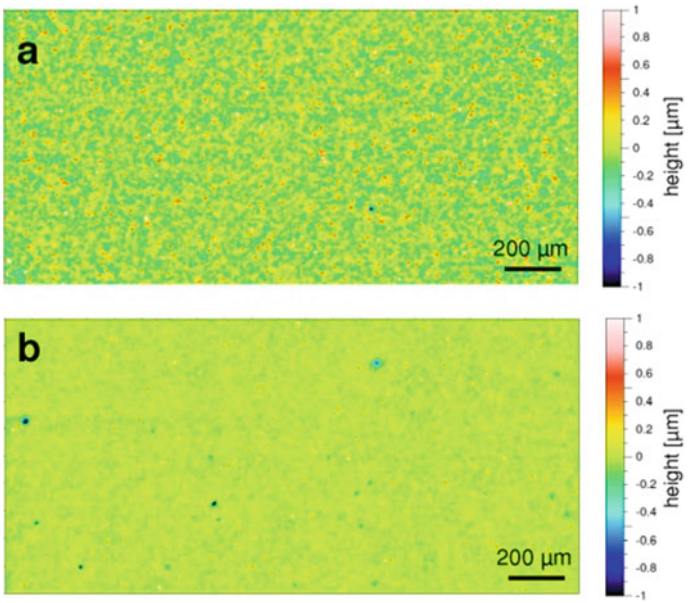

Fig. 2 Surface topography of the same coating type (TiAlN) but deposited by cathodic arc evaporation (**a**) and magnetron sputtering (**b**); both images at same scale

with arcing [26]. For an overview of arcing in sputtering, see, e.g., [27]. Yet another PVD technology where growth defects have been studied is the PLD [28].

In summary, the growth defects are a well-known feature, at least phenomenologically, but the interest in scientific community is relatively limited. This interest is more concentrated on the applied side rather than the formation mechanism and associated statistical phenomena (growth defect density). We can only guess how much interest there is in the industry, but their findings are typically kept secret.

In this chapter, we will try to answer two groups of questions. The first one is related to single growth defects: to understand the origin of growth defect formation and to understand the growth mechanisms. The second group of questions is associated to the whole surface: how to detect the growth defects and how to evaluate their density. Most of the work in this paper is based on transition metal nitride hard coatings deposited on standard tool materials (steels and cemented carbides). This is a rather limited class of materials; however, it is a strongly applied case. Thus, these results are far more relevant compared to idealistic cases such as metals on silicon single crystals.

2 Analytics of Single Growth Defects

In this section, we discuss methodologies to evaluate a particular growth defect. This can be either top view or in cross-section. First, the rather limited standard techniques are shortly addressed followed by a more detailed explanation of the possibilities offered by Focused Ion Beam (FIB).

2.1 Standard Experimental Methods

As shown at low magnification in Fig. 1, SEM can be routinely used for imaging of growth defects [30]. Figure 3a shows a detail of an intact nodular defect; however, it does not give much more information than pure top view. As will be shown later, the topography of the nodular defect top is more or less similar irrespective of the origin, provided the nodular defect is no larger than a few micrometers. Microchemical analysis such as EDS can be applied on the defect, but in most cases the results are inconclusive. In a typical coating thickness of several micrometers, the penetration depth of the electron beam is too low to get a reliable signal from the defect initiation point (the so-called seed). Even if the coating thickness is low enough, it remains unclear whether any additional elemental peaks originate from the seed or from the substrate.

An interesting combination includes a short glow discharge pretreatment of the sample using a standard GDOES spectrometer. This treatment exposes the growth defects due to different etching rates and enhances the image. Consequent SEM

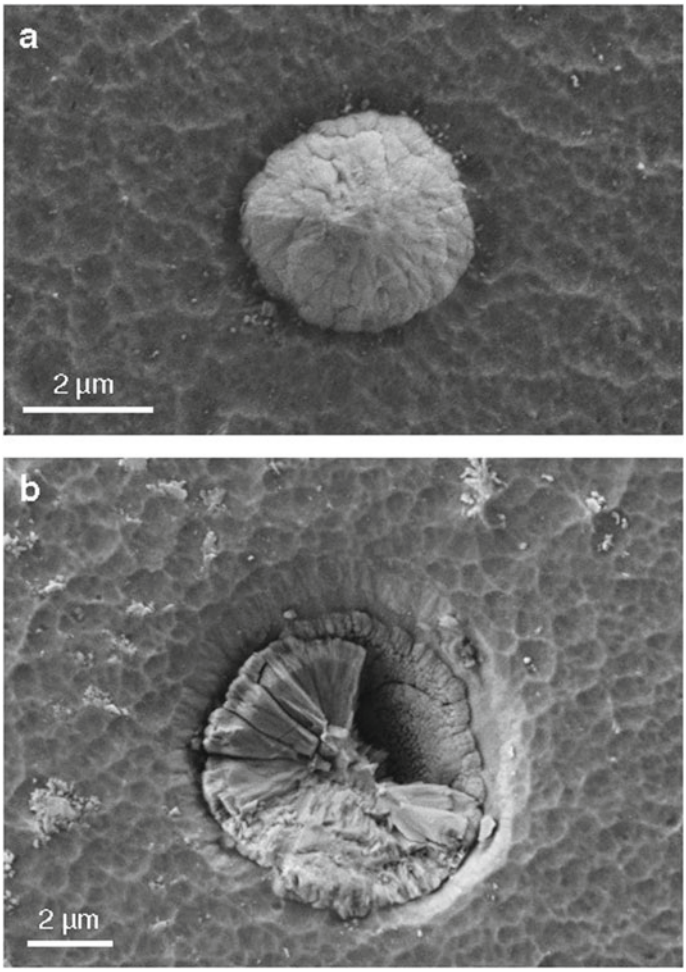

Fig. 3 SEM top view of two nodular defects: **a** intact defect, **b** partly expunged defect with the seed exposed; TiAlN coating in both cases (figures taken from [29], p. 216, Fig. 3bd)

observation reveals the different sizes of the growth defects and their distribution [31].

If the nodular defect disintegrates, its internal structure can become visible. As shown on Fig. 3b, such a case provides lots of additional information. The shaded area of reduced thickness is visible around the former defect cap; a strongly columnar growth radiating from the seed is well apparent too, as well as the seed itself. The latter can be directly probed by point analysis using EDS. Depending on geometry, size, and orientation that may not be a very precise microchemical analysis; however, presence of a foreign element can easily be proven. On the other hand, if the seed chemical composition equals that of the substrate or coating, not much information

can be extracted from EDS. For instance, a proof of Cr, Fe, and N in the defect within a CrN-deposited steel is hardly useful at all.

Other methods can be used in addition to SEM, but they are only of limited applicability. Using an AFM, a precise topography of a single nodular defect can be acquired, but it is experimentally challenging due to high aspect ratio [30]. Anyway, it remains an open question what kind of information a precise nodular defect topography can give. Optical microscopy is limited by the magnification to a statistical evaluation of defect density; it can offer some limited information only for excessively large growth defects. Additional disadvantage of optical microscopy is its inability to differentiate between nodular defects (hills) and pinholes (craters); both appear as dark spots. The contrast can be enhanced by polishing, and one of the methods is to use the standard ball-cratering technique, which is routinely applied for coating thickness measurement. To some extent, depth distribution of growth defect appearance can be deduced [32].

In contrast to top view, a cross-section is an interesting option. The main problem in observing growth defects in cross-section is the relatively low probability that a defect will be reached at all. Standard metallographic cross-section preparation (cutting-grinding-polishing) will yield a straight line which might incidentally cross a growth defect, but more likely it will not. If the coating is deliberately deposited on a thin brittle substrate, an attractive option is to prepare the cross-section by breaking rather than cutting. In addition to speed and simplicity compared to standard metallographic cross-section, there is another advantage: the growth defects are the mechanically weak points of the coating, so the fracture path will more likely propagate next to the growth defects. An even more challenging process is to catch a growth defect in TEM sample preparation [3, 33].

Figure 4 shows two examples of cross-sections hitting the growth defects. In Fig. 4a, the fracture path propagated slightly in front of the growth defect, ensuring that the complete defect remained embedded in the coating. This enables us to observe the total side view from the seed up to the cap. The opposite case is presented in Fig. 4b; in this case, the fracture path was slightly behind the growth defect, which caused a complete removal. We can only observe the negative image of the removed defect. Yet, in this particular case, it is clearly seen that the seed was located at the substrate surface.

2.2 Focused Ion Beam

Focused Ion Beam (FIB) is nowadays an established technique for studying depth profile of near-surface material, subsurface analytics, and preparation of TEM lamellae. It turns out to be extremely useful for studying single growth defects [34, 35].

Figure 5 shows the general concept of operation. First, a suitable growth defect is selected using standard SEM conditions (Fig. 5a). Then, targeted ion etching is applied in front of the growth defect (Fig. 5b), which forms an oblique trough. Ion

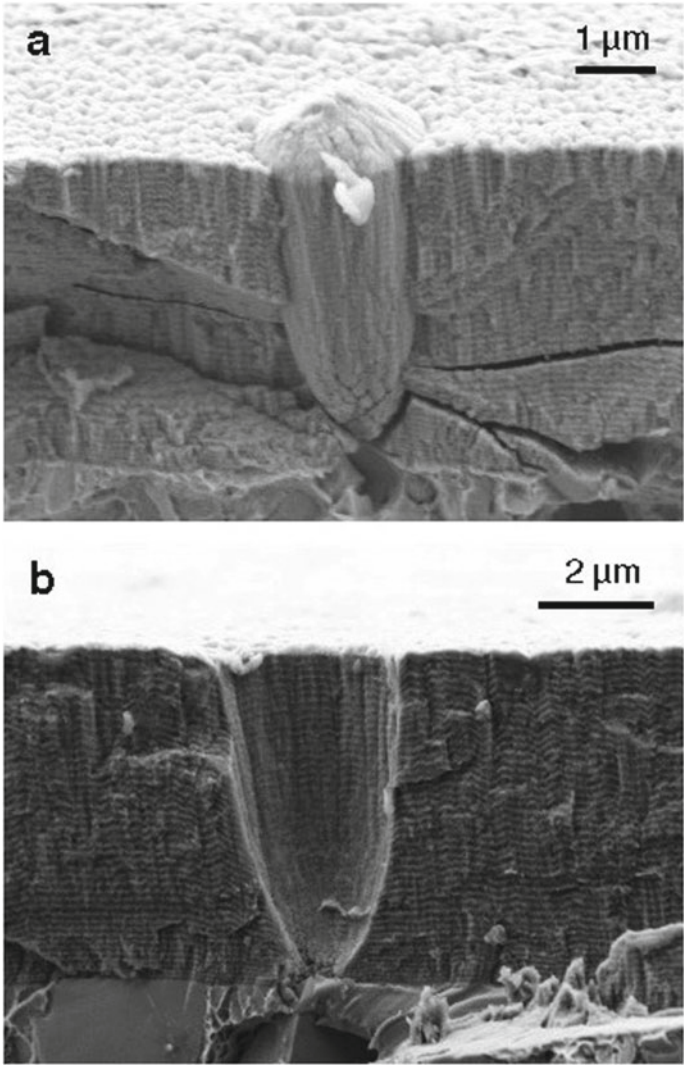

Fig. 4 SEM side view of the coating cross-section prepared by breaking the sample: **a** the defect has remained embedded in the coating (taken from [30], p. 255, Fig. 2d), **b** the defect has fallen off during the breaking; TiAlN/CrN multilayer coating in both cases

etching is in progress as long as necessary to form a suitable cross-section across the growth defect (Fig. 5c). As a last stage, ion polishing is applied at low currents to smoothen up the surface. The final result of etching is a full cross-section, containing the complete growth defect (including the seed) and part of the neighboring undisturbed substrate and film (Fig. 5d). The interface between the defect and the undisturbed film is also clearly visible. This aspect is particularly important in studying

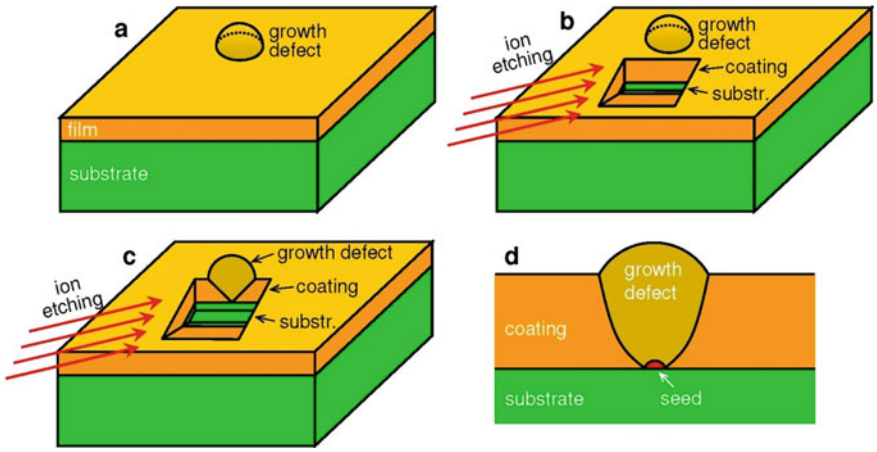

Fig. 5 Principle of preparing an FIB cross-section: **a** pinpointing the growth defect, **b** ion etching the initial trough, **c** continuing the ion etching across the growth defect, **d** final prepared cross-section used for imaging and analysis

the corrosion-induced damage. One can also clearly see the microstructure of the complete growth defect. Optionally, a platinum cap is deposited above the growth defect and immediate neighborhood before etching; the purpose is to limit etching on the cross-section area only.

On this cross-section, standard SEM analysis can be made: imaging using electrons (or ions), and EDS. The latter is particularly useful as it can be pinpointed directly on the seed, for instance, which gives a much better result compared to the hazy areas of interest in Figs. 3b and 4a. Evaluating the seed, chemical composition thus becomes a routine operation.

In contrast to optimized preparation of a single cross-section, one can prepare several consecutive slices, thus covering the whole defect in both lateral directions. Figure 6 shows such a case when a defect was probed in total. Such a slicing is the background for a 3D reconstruction of the growth defect, further discussed in Sect. 4.

3 Structure of Single Growth Defects

This section is dedicated to growth defect origin, their internal structure, growth, and shape. First, we take a quick look at the pinholes while the bulk of the section is devoted to the nodular defects. Corrosion-associated phenomena are discussed at the end, followed by 3D reconstruction methodology. Several papers have proposed a classification of growth defect types, primarily based on their overall appearance [32, 36]. While this is particularly useful from the applied point of view, in this section we prefer to follow the evolution rather than the final outcome.

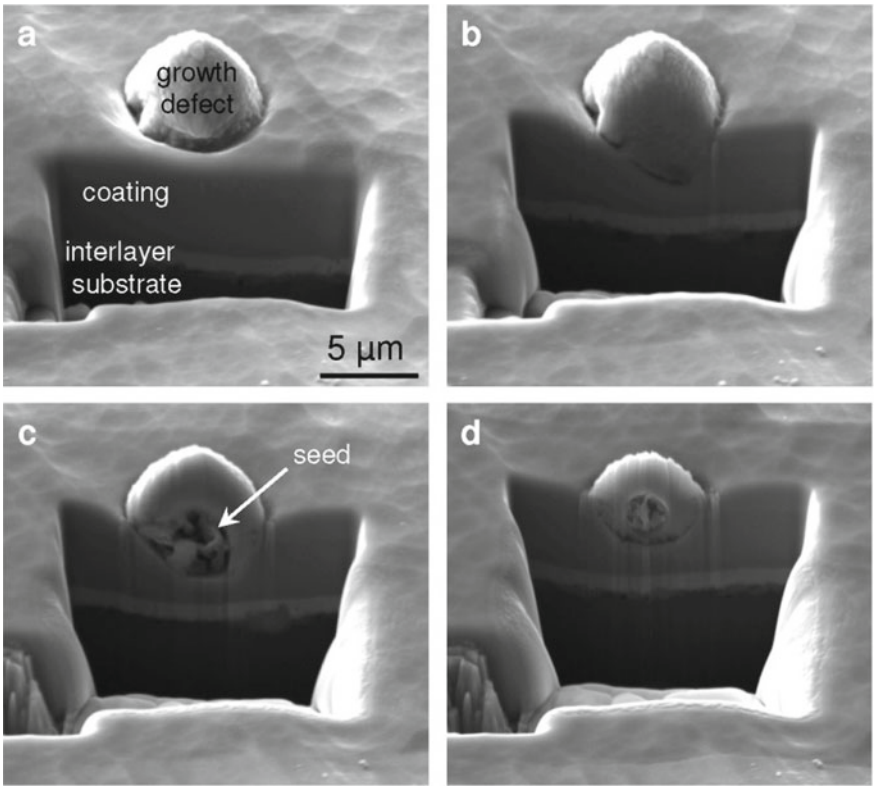

Fig. 6 Example of preparing an FIB cross-section: **a** initial trough in front of the growth defect (cf. Fig. 5b) (taken from [35], p. 2304, Fig. 2a), **b** progressive etching has reached the growth defect, **c** after consecutive etching a full growth defect cross-section is obtained (cf. Fig. 5c) (taken from [35], p. 2304, Fig. 2b), **d** last remains of the growth defect; CrN coating on Al alloy substrate with a Ni interlayer

3.1 Pinholes

The pinholes are discontinuities in the coating microstructure in the form of thin channels extending from the coating surface down to the substrate. In the broadest sense of word, even a border between two columns is a pinhole. In contrast, the narrow meaning requires a measurable physical opening, a visible void channel as a prerequisite for a pattern to be called a pinhole. Often a pinhole might not be directly open, but due to its microstructure, it can act as a shortcut for diffusion.

The usual origin of pinhole formation is geometrical: a narrow but deep crater, where the shading effect prevents the film growth on the crater walls. Rather than the crater size, its aspect ratio is the important parameter. A laterally large but shallow crater will not develop a pinhole. An instructive example is shown on Fig. 7a. The functional crater in this case is actually intergranular void, possibly formed

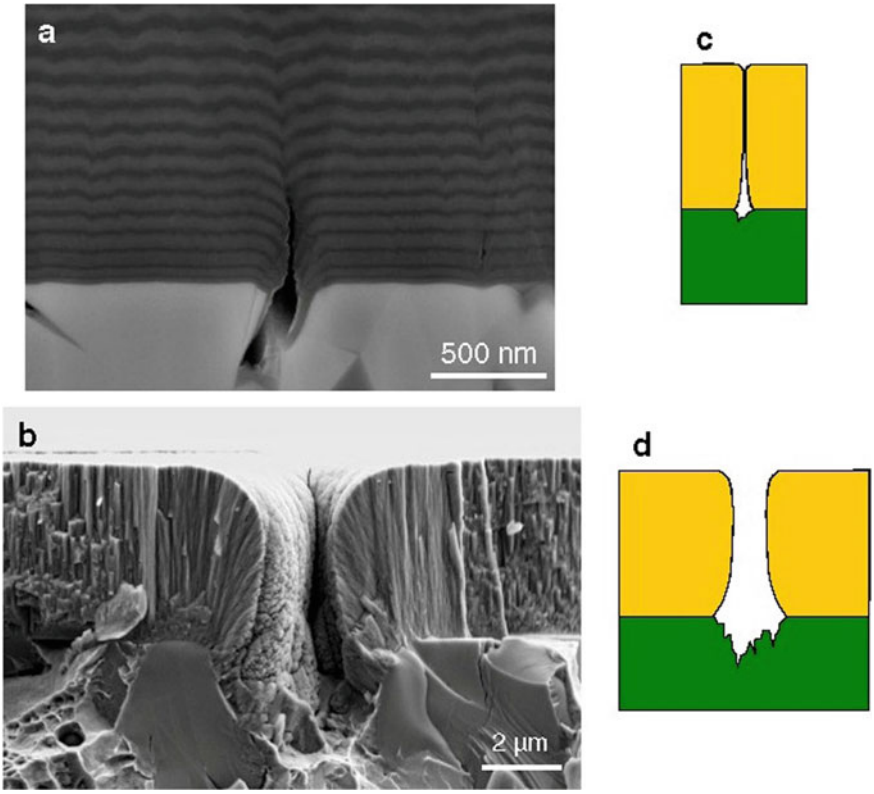

Fig. 7 Two types of pinholes: **a** closed pinhole, **b** open pinhole; the respective schemes are shown in **c** and **d**. (Coating type: TiAlN/CrN in closed pinhole, TiAlN in open pinhole.) (**c** taken from [31], p. 796, Fig. 2c)

by polishing or selective etching. There is a very thin film on the crater walls, but too thin to cover the whole wall. During the following coating growth, the two sides of the partly coated crater nudge together; they even appear to touch and close the opening. However, a microstructural discontinuity is preserved through the growing coating, extending up to the coating surface. This is called a closed pinhole and is schematically shown on Fig. 7c. A closed pinhole is virtually invisible from a top view, but the diffusion speed is far greater than in the undisturbed coating; thus, it can act as a starting point for pitting corrosion.

If the width of the initial geometrical crater is comparable to the final coating thickness, the pinhole will not be able to close up during the coating growth. In this case, an open pinhole will form (Fig. 7b, d). If the coated object is put in an aqueous medium where the coating is supposed to act as a protection, there will be a direct contact with the corroding solution and no protection is offered whatsoever. Pitting corrosion will start immediately.

Note that in the two examples in Fig. 7 the initial craters have a similar aspect ratio. Their main difference is the lateral size which determines whether a closed or an open pinhole will form.

3.2 *Nodular Defects*

Nodular defects are the most common type of growth defects. Using sufficient magnification, they appear as hillocks on the coating surface, having the shape of a spherical cap. They are typically several micrometers in diameter, but may be much larger in some cases, up to a few tens of micrometers. Their vertical height is a few hundred nanometers, and seldom higher than a micrometer or so. Though generally circular in planar projection, they may be of an elongated, elliptical shape. Irregular shapes are not uncommon, particularly in very large defects.

Groups of growth defects are quite common, far exceeding the statistical probability based on overall defect density. Coalescing growth defects are also a relatively common feature.

The starting point of the growth defect formation is the seed (Fig. 8). There are several possible seed types:

(1) geometric irregularity on the substrate surface
(2) inclusion in the substrate (carbide, sulfide)
(3) foreign particle (several possible origins).

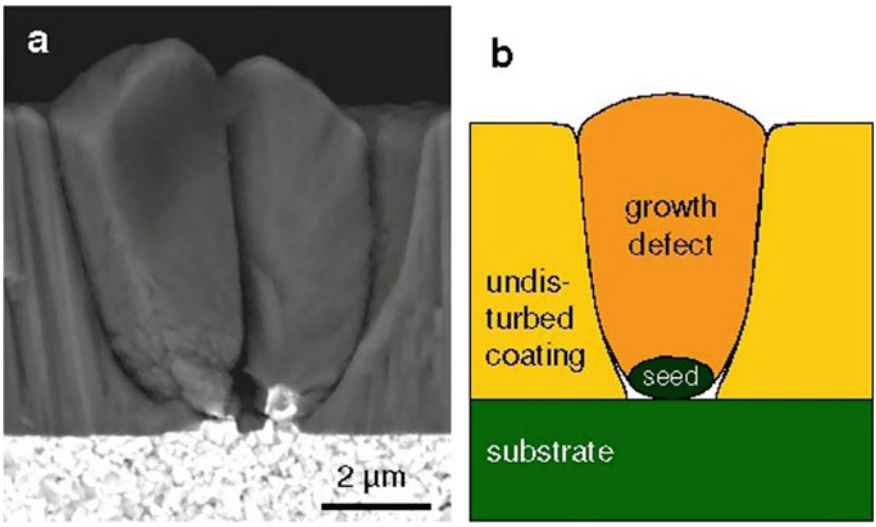

Fig. 8 Basic structure of a growth defect: **a** SEM image (TiAlN coating) (taken from [37], p. 353, Fig. 4a), **b** scheme

In the latter case, the seed may be present on the substrate surface before deposition, or it may appear later, during the coating growth. Typical seed size is in the range of 100 nm, but may be larger. It is important to stress that the overall shape of the growth defect is generally similar regardless of seed type. In the following text, different seed types will be discussed in more detail. The consecutive defect-growing pattern will be discussed afterwards.

3.2.1 Geometric Irregularity

The substrate surface is never completely flat. Careful surface preparation includes grinding with progressively finer gradation, followed by polishing. Obeying the rules of preparation, we will generally be able to finish up with a smooth surface without noticeable irregularities. However, the final surface quality can easily be compromised by deviations from the good practice: using worn grinding plates, too short or too long treatment at a particular stage, applying too strong load, etc. As a consequence, burs can appear, wear traces, carbides (partly) torn out, etc. Negligent sample manipulation during handling, cleaning, and mounting can also leave traces in geometry. No doubt, the density of possible geometric seeds for growth defect formation can be greatly reduced by proper handling, but cannot be entirely omitted.

A typical example of a geometric irregularity is shown in Fig. 8. The cemented carbide surface (WC-Co) has a well apparent irregularity, possibly a scratch. Though the particle on top of the right ridge might be of a foreign origin, the two ridges are definitely part of the substrate. As such, they acted as seeds for growth defect initiation.

In most cases, the geometric irregularity has no difference in chemical composition, compared to the remaining substrate. The seed has a purely geometrical origin.

3.2.2 Inclusion

Modern functional materials are rarely homogenous. For instance, steel contains the ferrous matrix and several types of inclusions, such as carbides, sulfides, and oxides. The microstructure of the growing coating can depend on the substrate chemistry and crystal structure. So even if the inclusions at the surface are completely geometrically level with the matrix, there may be a different growth mode at the site of an inclusion compared to the coating grown on the matrix.

However, the inclusions can stand out of the surface (or vice versa) due to substrate preparation. Because the carbide and oxide inclusions are harder than the matrix, they tend to have a lower removal rate during polishing. The sulfide inclusions on the other hand (e.g., MnS) are softer, so their removal rate is higher. The substrate surface thus typically has slightly elevated/depressed plateaus which act like geometrical irregularities, similar to the ones discussed in the beginning of this section. A comparable effect arises during ion etching. In this case, it is not directly obvious whether a

particular inclusion type will stand out of the matrix or vice versa; this depends on the sputtering rate at the particular ion etching conditions [30, 38]. The total geometrical extension from the matrix level (either positive or negative) thus depends both on the differences in polishing rate and ion etching rate. Typical values are up to a few hundred nanometers.

Three different cases are possible. If the net etching rate of the inclusion is higher than that of the matrix, the inclusion appears like a shallow crater within the substrate level (Fig. 9a). The contact between the crater floor (inclusion) and the neighboring plateau (matrix) is in a shade which is similar to a narrow crater—starting point for a pinhole formation (cf. Fig. 7a). In the case presented in Fig. 9a, there is an additional effect of poor contact to the inclusion surface, causing strong columnar growth with extensive pinholes. The final outcome is a combination of nodular defects and a mesh of pinholes.

If the net etching rate of the inclusion does not differ to one of the matrix, there is no geometric effect at all (Fig. 9b). The only difference to the coating growth is related to the inclusion chemistry and crystal structure, if at all. A net lower etching rate of the inclusion is, geometrically speaking, analogous to a flat foreign particle (Fig. 9c). It acts like a common seed discussed before, yielding a standard nodular defect.

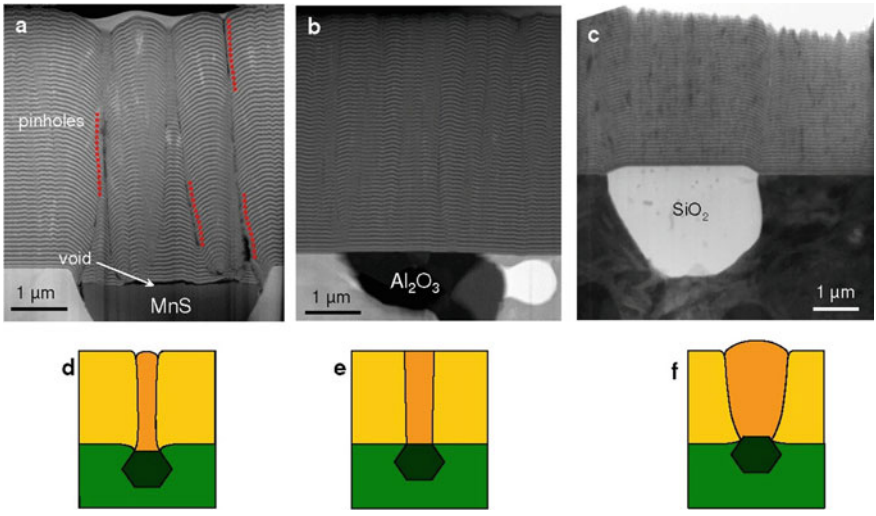

Fig. 9 Three cases of inclusions regarding the etching rate: **a** higher than the matrix (taken from [39], p. 324, Fig. 2, right), **b** same as the matrix, **c** lower than the matrix; (**d–f**) respective schemes; TiAlN/CrN multilayer coating

3.2.3 Foreign Particle

Similar to the concept of a completely flat surface, a completely clean surface is another goal which can never be entirely met. There are several steps to ensure a proper surface cleanliness: the cleaning procedure itself, consequent rinsing and drying, a dust-free environment in the lab, regular sand blasting of the deposition chamber, etc. Nevertheless, in an industrial environment, many of these steps may become too time-consuming and thus expensive; therefore, the measures taken tend to be optimized in order to achieve a reasonable cleanliness. This depends on coating application, thus a hard coating facility will not have such a stringent environment compared to, say, microelectronics.

Based on our experience in doing well over a hundred FIB cross-sections of individual defects, the vast majority of seed sources belong to two types. The first is the one having the same chemical composition as the undisturbed coating (Fig. 10a, CrN, in this particular case). This means that a fragment of the growing coating delaminated from a spot somewhere in the deposition chamber and fell on the surface where it stuck. That stuck fragment served as the seed for the emerging growth defect. The fragment may even originate from a previous deposition of the same type, which would be impossible to distinguish from the current growing coating. Yet another explanation is a microdroplet ejected from the cathode. This is the mechanism for the majority of growth defects at cathodic arc deposition. In contrast to the coating fragments which have identical chemical composition as the undisturbed coating, a microdroplet is predominantly metallic or substoichiometric, say, $CrN_{0.5}$ in this case

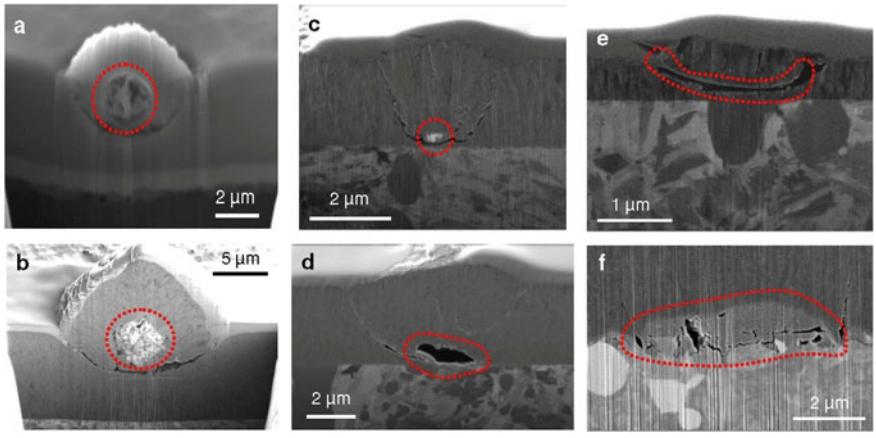

Fig. 10 Types of seeds as foreign particles based on their chemical composition: **a** same as the coating (CrN in this case) (taken from [35], p. 2304, Fig. 2c); **b** iron (TiAlN coating) (taken from [39], p. 325, Fig. 3, bottom left); **c** copper (CrN coating) (taken from [29], p. 216 Fig. 4c); **d** calcium-based (TiAlN coating) (taken from [39], p. 325, Fig. 3, bottom right); **e** silicon (TiN coating) (taken from [29], p. 216, Fig. 4d); **f** iron oxide (TiAlN/CrN multilayer coating) (taken from [37], p. 354 Fig. 6i)

[3]. Using EDS, this nitrogen deficiency is difficult to prove due to excessive beam spot size compared to the size of the seed.

The second very common seed type is based on iron (Fig. 10b). Though visually there is hardly any difference, the EDS point analysis of the seed spot showed the presence of iron. This is a fragment of any of the many steel components in the deposition chamber. These are primarily the complex-shaped fixtures, especially the moving parts in contact, but may also originate from the steel substrates. The iron-based seeds are relatively easy to prove as iron is typically not a coating component; however, one has to make sure the iron signal does not originate from the substrate surface.

The majority of seeds are either coating materials or iron, with the latter originating from the substrate or from a component of the deposition chamber. Several other types have been found in minute quantities. Their advantage is the distinct chemical composition (neither coating material nor substrate) which can be extracted even in the case of very small seeds, where only a small part of the EDS signal originates from the seed itself. A textbook case is the copper signal from a very small seed in Fig. 10c; the copper anode ring is the only meaningful explanation for the appearance of a copper-based fragment in this particular deposition chamber. A signal of calcium, and in minor extent some other alkaline elements (Fig. 10d), is probably an indication of the cleaning agent residue. Previous depositions of a different type, such as the silicon flake in the TiN coating (Fig. 10e), can also be confirmed based on the operational history. Indeed, before TiN deposition, silicon was deposited a day before in this deposition chamber. In the last case (Fig. 10f), the additional signal of oxygen at the interface proves that iron oxide is the seed; the sample was partly corroded before deposition.

The preceding classification did not take in account the position of the seed in the coating; or put it another way, the timing of the seed generation. While the cleaning agent residue and the oxidized steel is definitely a surface feature (Fig. 10d, f), other cases can appear either before or during the deposition. The emission of a fragment can occur during substrate-heating phase due to large thermal stress, during etching or during deposition. Some particles may even originate during the pumping phase, especially during the turbulent rough pumping where dust remnants can be raised from the uncleaned corners of the deposition chamber.

Even observing the growth defects in cross-section, it may not be entirely obvious whether a growth defect not touching the substrate indeed originates form within the coating. While that may be obvious in Fig. 11b because the seed is definitely located close to the coating surface, this is not the case in Fig. 11a. A high magnification is necessary to prove the seed location. In low magnification, the same picture may be also interpreted as an off-axis cross-section of the growth defect, where the seed is located at the substrate but not visible in the picture.

As already mentioned, the majority of growth defects in cathodic arc evaporation originate during the coating deposition. In magnetron sputtering, on the other hand, the primary origin is at the seeds at the substrate surface. This is not due to an increase of the substrate-based seeds but a consequence of a far larger density of coating-based seeds in cathodic arc.

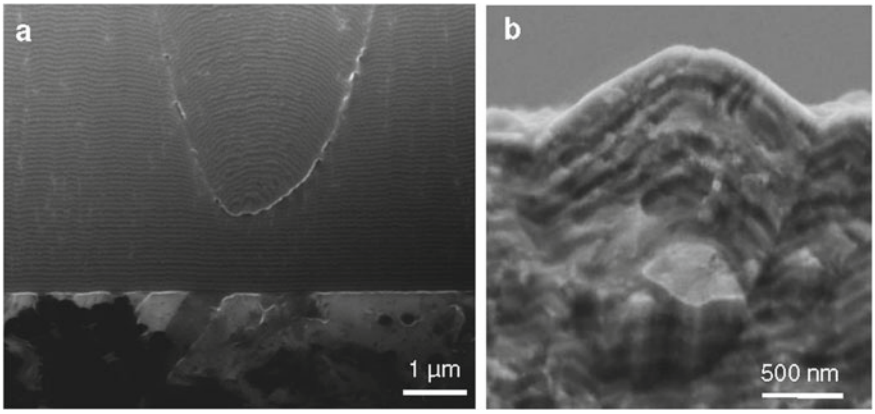

Fig. 11 Examples of a seed not located at the interface: **a** lower part of the coating (taken from [31], p. 795, Fig. 1b); **b** close to the coating surface (taken from [31], p. 255, Fig. 2c); TiAlN/CrN multilayer coating

So far, the discussion has been based only on the seed composition. A short comment on the influence of seed shape and size is necessary too. The examples in Figs. 10 a, c, and d show relatively small seeds; they all enable the growth of similar nodular defects with a similar circular cap protruding from the coating surface. The seed shown in Fig. 10b is much larger; consequently, the aspect ratio of the nodular defect is lower: the circular cap is almost as high as wide, in contrast to the gentle slope of the previously mentioned cases. However, a gentle slope does not necessarily mean a small seed. The case in Fig. 10e shows a large seed but having a very flat, elongated shape. This is a typical flake, often formed by delamination from an existing coating somewhere in the deposition chamber. Due to its flat shape, the flake will probably stick parallel to the substrate; therefore, the nodular defect height will not be excessive, despite the flake's large lateral size. A low but laterally large nodular defect will form, possibly with a very irregular shape (Fig. 12).

3.3 Nodular Defect Growth

As mentioned in the previous subsection, the initial point of nodular defect growth is a seed. Having typically an irregular shape, it will almost always cause a shade in part of the substrate. The area just underneath the seed is completely obscured, thus there the coating is not deposited at all (Fig. 13). There is a gradual transition between the completely obscured area and the completely undisturbed area. In Fig. 13, this transition is apparent by the increasing thickness of individual layers starting from the direct seed contact point away in both directions.

The seed surface, regardless of its origin, should be considered as a part of the substrate surface upon which the coating grows. The contours of coating growth in

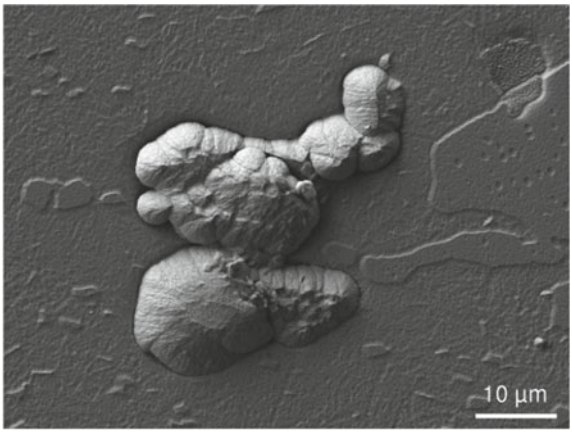

Fig. 12 A very large, irregularly shaped nodular defect

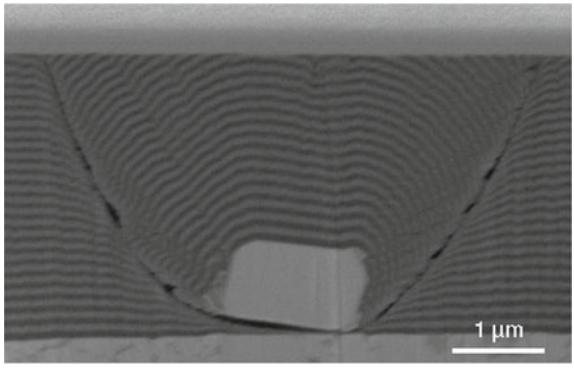

Fig. 13 A typical seed (composition: iron) and the overgrowing TiAlN/CrN multilayer coating; note the loose contact between the growth defect and the undisturbed coating

Fig. 13 clearly follow the seed shape as if it were part of the substrate. Nevertheless, two important differences stand out compared to the undisturbed coating. First, the complex seed shape causes a strong columnar growth. And second, there is a clear boundary between the seed-based coating and the undisturbed coating. The pore between the seed and the substrate effectively causes a pinhole (see Subsection 3.1). It is a closed pinhole, extending from the seed/substrate contact up to the surface. A standard closed pinhole originates in a narrow opening (a point in first approximation); the pinhole itself is a linear object. In the case of a nodular defect seed, the pinhole starting point is a ring (encircling the seed), and the pinhole is a planar object with a shape of a cylinder, or better, a cone section.

Consecutive growth above the seed depends on the local geometry as well as general coating growth dynamics. Compact growth conditions will be followed at the nodular defect too. Likewise, a generally porous coating will have excessively porous nodular defects. These conditions depend on bias voltage, plasma density, and other parameters encountered in PVD.

Figure 14 shows two extreme cases. On one hand, there is a compact coating (Fig. 14a) with no visible porosity in the nodular defect microstructure. However, the microstructure remains highly columnar with strongly oriented radially growing columns. The opposite case is shown in Fig. 14b. The individual columns are poorly bound; in essence, there is a pinhole between each pair of neighboring columns. Far worse conditions are at the contact with the undisturbed coating, where there is essentially one large open pinhole. The adhesion of such a nodular defect is very poor, and it will be easily expunged from the growing coating.

The case in Fig. 14b is rather extreme, but the pattern is valid generally for all nodular defects. The contact between the seed and the substrate surface is very

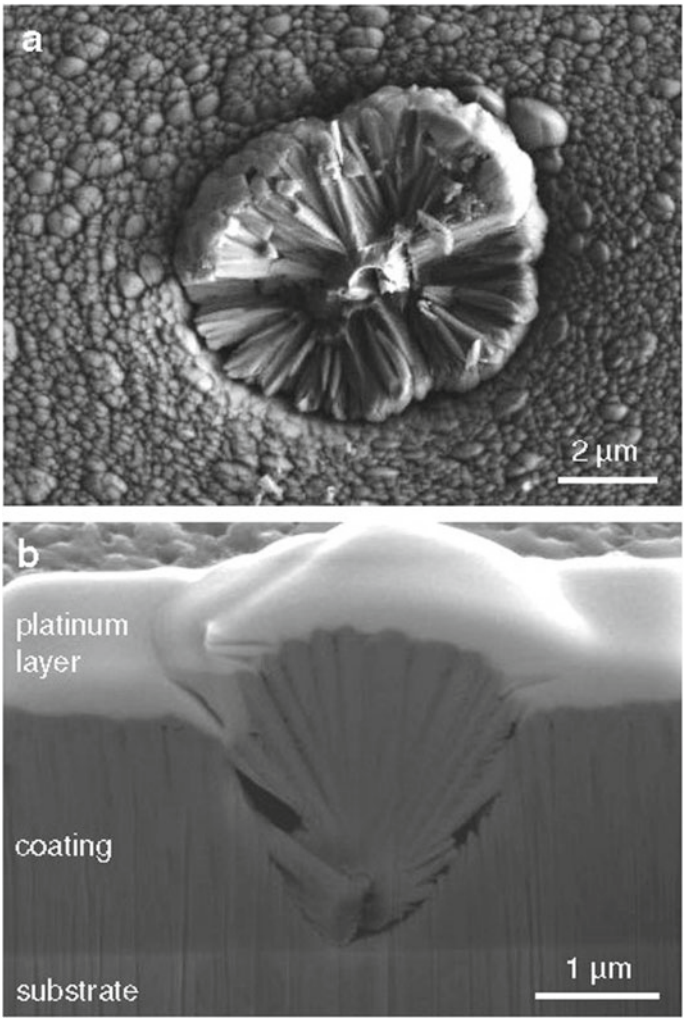

Fig. 14 Radial columnar growth: **a** top view of a relatively compact microstructure (TiAlN coating); **b** cross-section of a case of a very porous nodular defect microstructure (TiN coating)

poor as there is no coating at all. And the contact between the nodular defect and the undisturbed coating is poor as well because the border is essentially a circular pinhole. PVD coatings are in most cases in compressive stress and the resulting force inevitably points into the perpendicular direction, finally causing the nodular defect to break free. When this failure will happen depends on the geometrical and microstructural conditions at the nodular defect border. It also depends on the internal stress, which increases with thickness. Thus, during the deposition, with increasing coating thickness, the stress-to-cohesion difference decreases. After it reaches the threshold, the nodular defect is expunged.

What remains out of such nodular defect removal is a crater. Side view of such a crater is shown in Fig. 15a. (In a cross-section like this one, it is difficult to tell, whether the defect was expunged before sample preparation or the expunging is a consequence of the preparation process; the outcome is identical.) Often, the internal cohesion of the nodular defect is inferior to the cohesion at the boundary. In this case, only a part of the nodular defect is broken off, like the case shown in Fig. 14a. Both figures show cases where the nodular defect removal occurred after the deposition had been completed. This may have been during the cooling stage, where the internal stress was augmented by the thermal stress. On the other hand, the nodular defect removal can take place during the deposition too. In this case, the coating will continue to grow even on the crater floor or remnant defect. Same principles will apply: due to irregular topography of the crater floor (or remnant defect), the microstructure of the overgrowing coating will be highly columnar and porous with poor cohesion. The story will essentially repeat.

In large defects (see e.g. Fig. 12), the origin is likely a large flake, lying parallel to the surface. If this defect is removed during the deposition, a large crater remains behind having a flat bottom and relatively steep walls (Fig. 15b).

In summary, the nodular defect starts with a seed. There are several seed types: geometric irregularity on the substrate surface (Fig. 16a), an inclusion in the substrate (Fig. 16b), or a foreign particle, either adhered on the substrate surface (Fig. 16c) or embedded during the coating growth (Fig. 16d). In all these cases, the consequent growth mechanisms are similar, yielding similar nodular defects, which are generally indistinguishable from a top view. The overall shape does not depend much on the seed type, neither its chemical composition. If the internal stress overcomes the adhesion of the nodular defect, it is expunged from the coating (Fig. 16e). In the case, this happens during the coating deposition rather than at the end, the remaining crater is covered by the additional growing coating (Fig. 16f).

3.4 Corrosion at a Growth Defect

If two metals in a contact are exposed to a corrosive medium, the more electronegative component dissolves first. In coating technology, this is regularly applied by depositing the more electronegative coating (e.g., zinc) on the base substrate (e.g., iron). During the component lifetime, the coating is slowly consumed even if there are

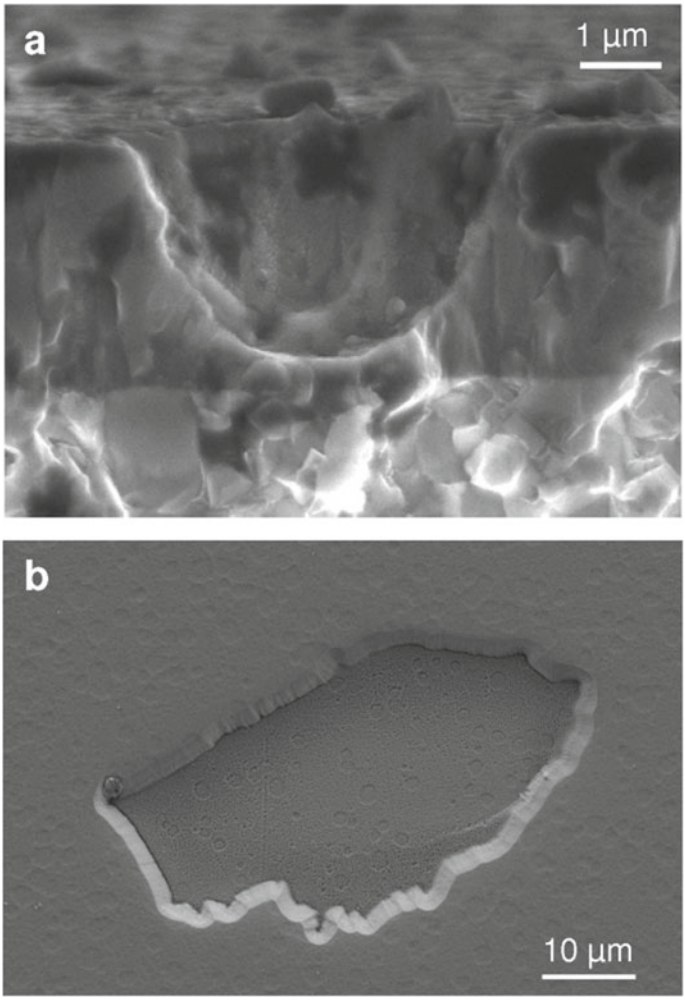

Fig. 15 Remnant of a site where a nodular defect has been expunged (coating: TiAlSiN): **a** cross-section at a standard nodular defect, **b** a large dish-like remnant of a very large defect (taken from [30], p. 255, Fig. 3, insert 2)

pinholes extending down to the substrate (Fig. 17a). The dashed area shows the part of the coating which will be dissolved. In the opposite case, when a less electronegative coating is deposited on the substrate (e.g., nickel on iron), it is the substrate which will first be consumed. Though the coating may act as a barrier toward the corrosive medium, any pinhole extending down to the substrate will cause the reaction to take place at the substrate. This means the substrate will be consumed rather than the coating (Fig. 17b, dashed area), which will in this case offer no protection any more.

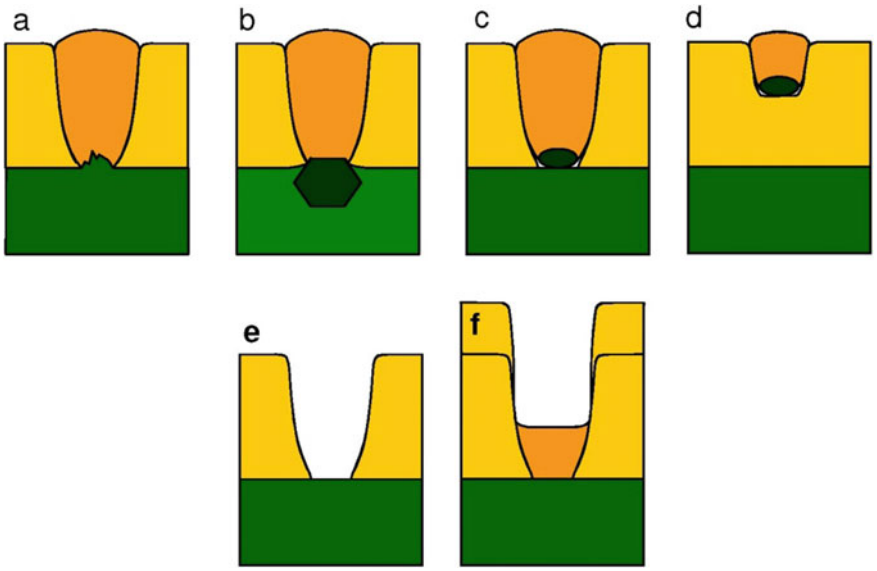

Fig. 16 Schematic overview of different seeds causing the nodular defect growth: **a** geometric irregularity, **b** inclusion, **c** foreign particle on the substrate, **d** foreign particle during growth. Further steps due to large internal stress: (**e**) expulsion of the nodular defect; (**f**) later growth

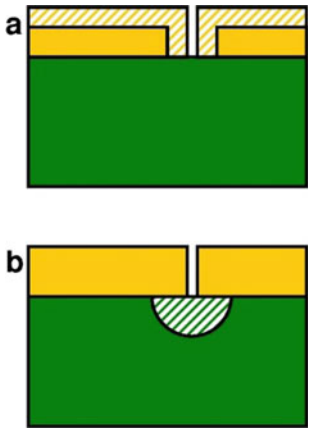

Fig. 17 Corrosion attack at a pinhole if the coating is **a** more electronegative than the substrate, **b** less electronegative than the substrate

Transition metal nitride coatings, which are the common choice for tool protection, are chemically more electronegative than the steel, thus the (electrochemically unwelcome) case from Fig. 17b applies. Two examples are shown here where standard hard coatings (CrN and AlTiN) were deposited on the steel substrate. Both samples were then exposed to 0.1 M NaCl. Afterwards, the samples were investigated by SEM, and selected spots were analyzed by FIB.

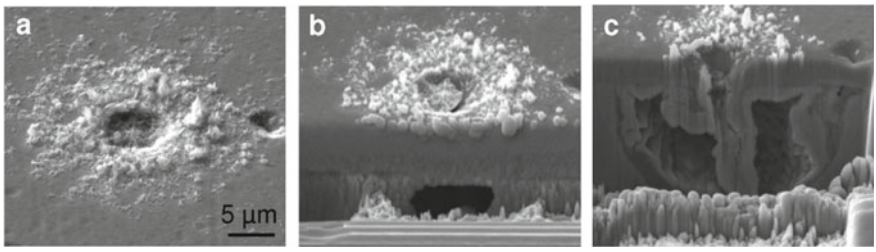

Fig. 18 FIB cross-section over a pinhole in the CrN coating exposed to a corrosion medium: **a** original surface, **b** starting the cross-section, **c** section across the pinhole center

The first example is the CrN coating, well known for its superior chemical inertness compared to other standard hard coatings. Figure 18a shows the coating surface centered at an apparent shallow crater, surrounded by the debris. It seams likely to be the site of a corrosion attack, where the debris is residue of the dissolution reaction which formed the crater. There is no indication that the reaction took place any deeper than the top part of the coating. It seems purely as a superficial damage.

By starting the FIB cross-sectioning, a void appears deep below the coating even before reaching the crater (Fig. 18b). By continuing the sectioning toward the crater center, it becomes evident that intense pitting corrosion occurred (Fig. 18c). The situation is a textbook example of the case schematically shown in Fig. 17b. In the crater center, there is a pinhole which enabled the diffusion of the chloride medium toward the substrate. The latter then started to react and the reaction continued unhindered, limited only by the reaction rate at the solution/substrate interface. The important summary is the size of the consumed substrate volume. Though the visible crater is no more than 6 μm in diameter and perhaps a micrometer deep (coating thickness is 3 μm), the dissolved volume is 15 μm deep and 25 μm wide. The top view of the relatively minor damage is thus counter-intuitive and strongly underestimates the actual damage hidden below the surface [36].

The other example shows the AlTiN coating, where two defects were analyzed by FIB (Fig. 19a). Though appearing larger, the shallow crater at the right is limited to the topmost part of the coating only. However, the relatively small crater on the left already shows extensive damage in the substrate even at this cross-section, far away from the crater. Continuing the sectioning toward the crater center, two observations stand out (Fig. 19b). First, there is a very narrow pinhole in the coating. This is essentially the only damage on the coating itself; however, even such a narrow pinhole enabled the chloride medium to penetrate toward the substrate and initiate the chemical reaction.

The second observation is the site where the pinhole started. At this particular spot, there are three large carbide grains. The central and right grain are located at such a position that during surface preparation (grinding, polishing), the two were placed directly next to each other with a small crater in-between. This crater acted as a starting point for pinhole formation during the coating growth. The extensive

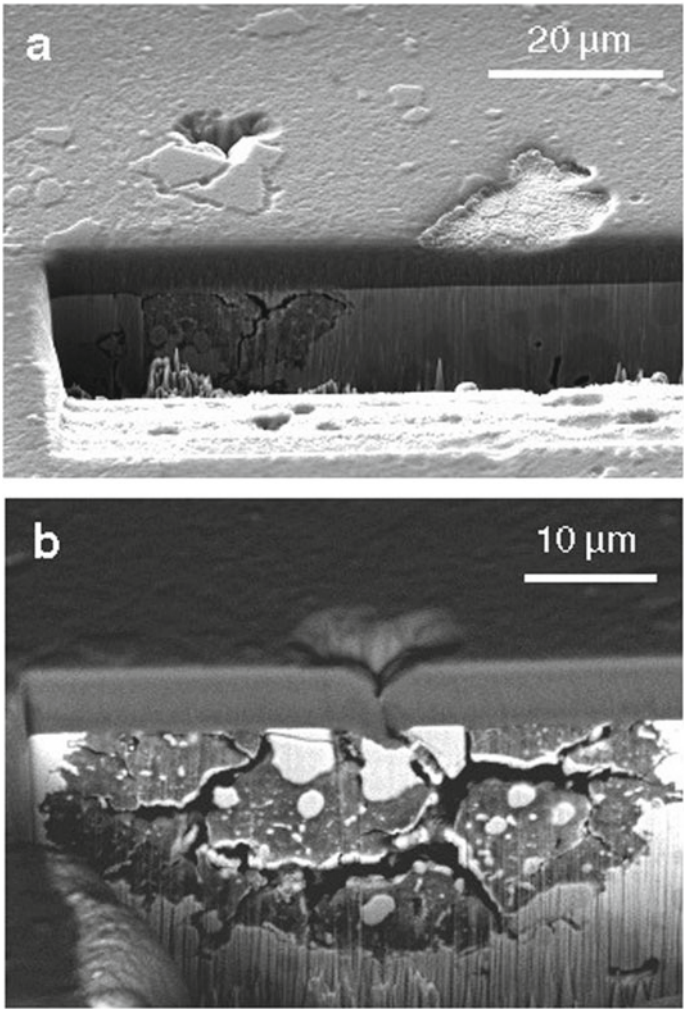

Fig. 19 FIB cross-section over a pinhole in the AlTiN coating exposed to corrosion medium: **a** starting the cross-section, **b** section across the pinhole center

corrosion damage is therefore not a consequence of a material failure as such, but rather due to a coincidental contact of two carbide grains just at the substrate surface.

Corrosion is not the only phenomenon where the growth defects act as shortcuts for a chemical process. Oxidation is a similar case. There are reports proving nodular defects rather than pinholes as starting points for high-temperature oxidation [40, 41]. In these publications, the CrVN-based coatings were analyzed; V_2O_5 patches started to appear around the nodular defects.

3.5 3D Reconstruction of a Growth Defect

Most growth defect cross-sections using FIB, presented in this paper so far, were made with a goal to show an optimum overview across the center of the defect. This is obtained in three steps:

(1) rough removal of material; typical current of 20 nA
(2) polishing; 1 nA
(3) imaging; 1 pA when using ions, or standard imaging using electrons.

In the cases presented so far, these steps were repeated a few times, to get a rough picture of the growth defect in the direction of imaging (e.g., Fig. 18). A logical extension of this principle is to perform a targeted, stepwise imaging in order to acquire the images of the complete growth defect. For instance, a 10 μm wide defect can be sliced ten times with a 1 μm step size (Fig. 20a). This example shows the TiAlN coating, exposed to NaCl solution. The images can be interpreted manually with some basic evaluation of size possible.

However, a promising alternative is to perform automatic image evaluation. This contains several steps in image enhancement, calibration, and post-calculation using specialized software [42]. With proper care, the evaluation can be performed giving the result of a 3D model of individual components. In the presented example (Fig. 20b), only the coating (yellow) and the corroded area (black) are shown. The crater on the coating surface is visible, as well as the pinholes protruding through the coating. In addition to the visual result, explicit values can be calculated such as volumes of individual components. In the presented example, the crater volume is 12 μm^3 and the corroded volume is 23 μm^3.

These are useful results; nevertheless, the method is very time-consuming and requires specialized software. Thus, it might be applied only in limited cases.

3.6 Single Defect Systematic Observation

In the preceding subsections, the individual growth defects were randomly chosen. Their position can be saved in the microscope's coordinate system; but once the sample is taken out of the microscope, this information is lost, and the very same growth defect can practically not be found again. Their location can be marked in advance by drawing scratches or some other marks, but they tend to be poorly

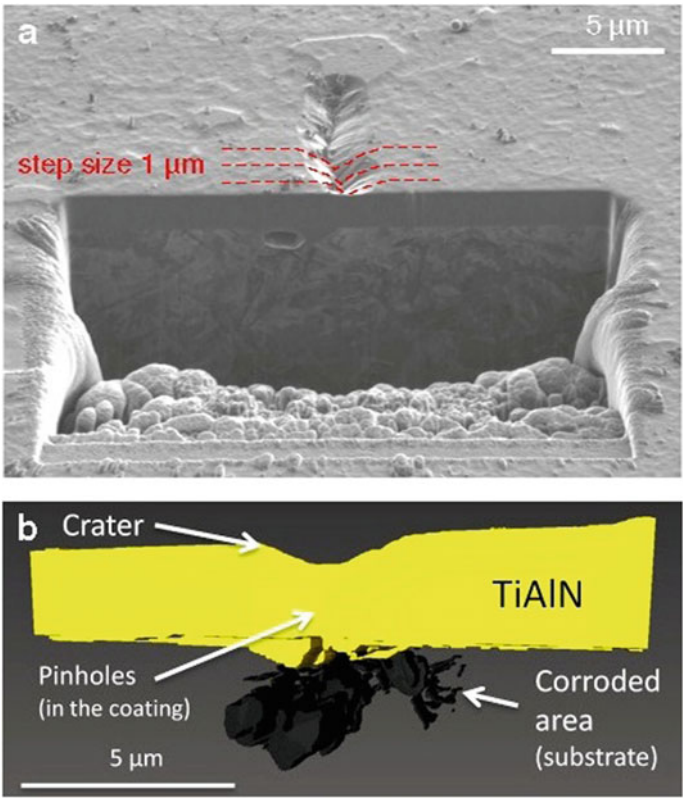

Fig. 20 3D reconstruction of a growth defect: **a** preparing the slices (taken from [42], p. 352, Fig. 1), **b** reconstructed model (taken from [42], p. 353, Fig. 3)

defined at high magnification. Automated marks such as Vickers indentations are an alternative but any such interference with sample surface can ruin the experiment in the case of corrosion studies. An indentation small enough would probably not influence the corrosion experiment, but such a mark would not be visible at low magnification and thus difficult to find.

A better alternative is to construct a local coordinate system of the sample. For that purpose, we need two points (not areas), which can easily be found both at low and at high magnification. We can use edges of a rectangular sample, for instance. In the case of a round, flat sample, there are no suitable points for that purpose, so we should prepare them on our own. In our experience, the most suitable tool is a Rockwell indenter which makes large but pointed indentations. In order to prevent mixing them up, we make three indentations on one side (take the middle one as a reference) and one indentation on the other (Fig. 21). Since the indentations are at the edge of the sample, they do not interfere much with the experiment taking place at the center of the sample.

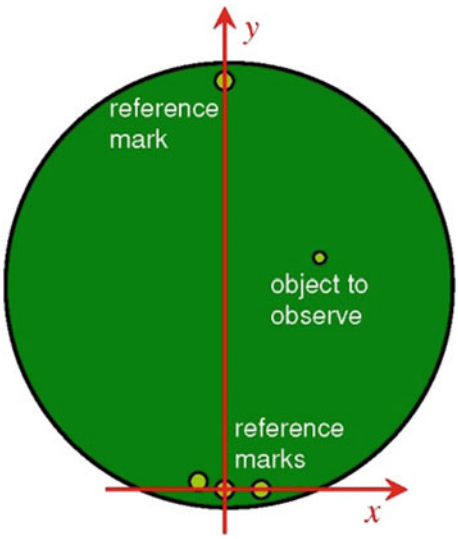

Fig. 21 Construction of the sample coordinate system

In the native coordinate system of the sample, the coordinates of the middle indentation are (0, 0) and the coordinates of the opposite one (0, d), where d is the distance between them. Say, the coordinates of an interesting object are (x, y). When we put the sample into a microscope, the coordinates of the two reference marks should be evaluated first using the microscope's coordinate system: (x_1', y_1') and (x_2', y_2'), where $d = \sqrt{(x_1' - x_2')^2 + (y_1' - y_2')^2}$. Finding the desired object in the new coordinate system involves simple linear algebra. The coordinates of the object in the new coordinate system (x', y') can be calculated as

$$\begin{pmatrix} x' \\ y' \end{pmatrix} = \begin{pmatrix} \cos\phi & -\sin\phi \\ \sin\phi & \cos\phi \end{pmatrix} \begin{pmatrix} x \\ y \end{pmatrix} + \begin{pmatrix} x_0 \\ y_0 \end{pmatrix} \tag{1}$$

where ϕ is the rotation and (x_0, y_0) the shift from the old to the new coordinate system. Using the reference indentation locations, the direct expressions are

$$\begin{aligned} x' &= \frac{y_2' - y_1'}{d} x + \frac{x_2' - x_1'}{d} y + x_1' \\ y' &= \frac{x_1' - x_2'}{d} x + \frac{y_2' - y_1'}{d} y + y_1' \end{aligned} \tag{2}$$

Using this simple procedure, one can easily find any motif on any scale-equipped microscope. Figure 22 shows an example of a flat surface, where the very same motif was observed by three techniques.

This methodology is especially useful when observing the evolution of a single growth defect during a certain experiment. The initial observation includes imaging

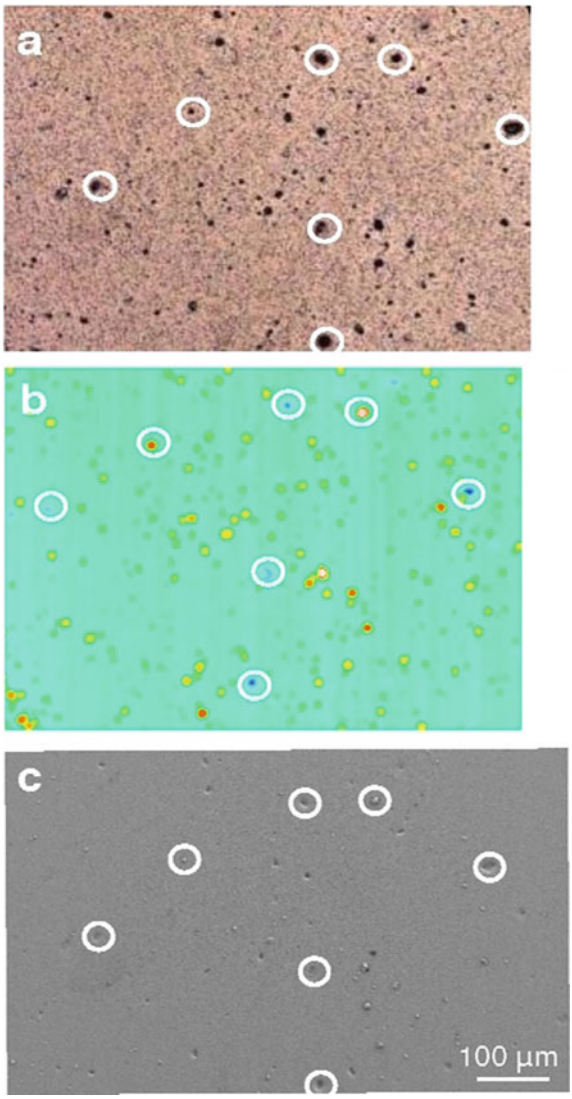

Fig. 22 Imaging of the same motif using **a** optical microscope, **b** profilometer, **c** SEM; same prominent growth defects are encircled

(e.g., by SEM) and recording the coordinates. Then, the first step of the experiment is made. Afterwards, the sample is returned into the microscope. Using the orientation methodology, we find the very same growth defect, perform the imaging, and run another experiment. Examples of such repeated observation of identical spots are shown in [31, 38, 39]. Observing this alternating process (experiment/observation), we are able to follow consecutive evolution of this growth defect for as many steps as necessary.

An example of this concept is shown in Fig. 23. The sample was exposed to a pin-on-disk test. The same motif can be directly compared: before and after test. We can directly observe that the nodular defect no. 1 (Fig. 23a) was completely removed during the test. The defect no. 2 was only partly broken, while the defect no. 3 disintegrated completely. These results have given important conclusions on the role of growth defects in the running-in phase of a tribological test [43].

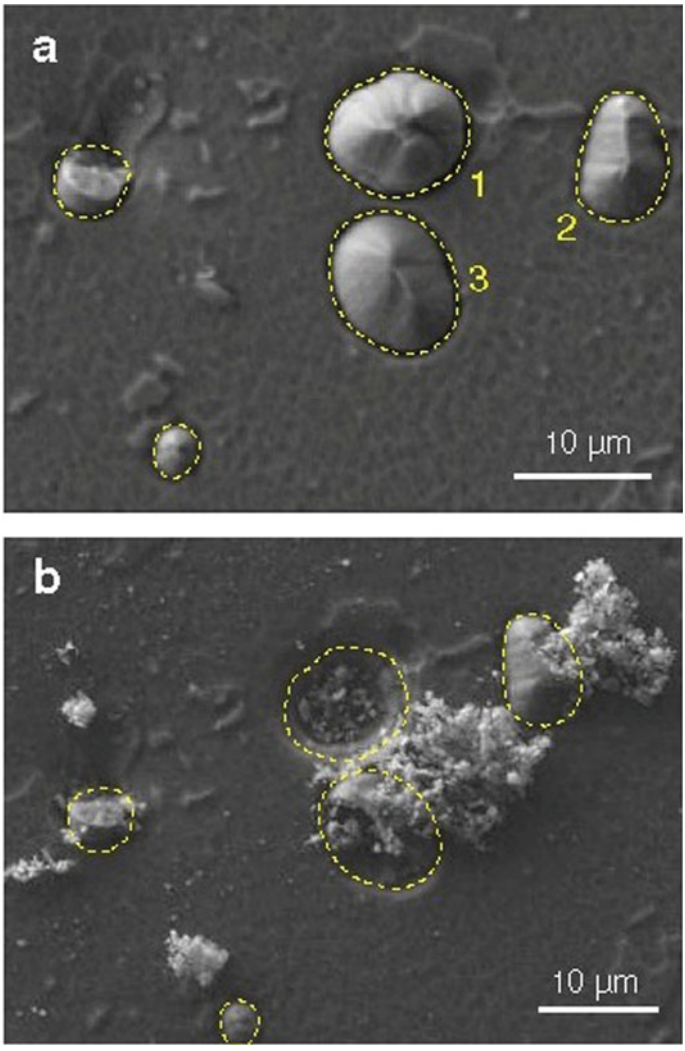

Fig. 23 The same motif before experiment (**a**) and after eight passes of pin-on-disk test (**b**); TiAlN coating

4 Growth Defect Density

In the preceding section, the main emphasis was given on a single growth defect, its structure, evolution, and evaluation. In this section, we will take a broader look on the sample as a whole, trying to evaluate relevant statistical parameters describing the growth defect density.

4.1 Principle of Measurement

The concept of defect density is at first glance clear: the number of growth defects per unit area. If we recall Fig. 22, though individual growth defects are well visible as discrete spots, there is quite a strong variation in their properties. The most apparent variation is in height, not so much in diameter; one can also find groups of defects, double defects, etc. Thus, the question is: How can we evaluate the growth defect density on a given surface?

Among the images given so far, the majority of them were obtained by SEM. However, it is difficult to tell the difference between various heights, and difficult to automate the counting procedure. Though instructive in observation of one single defect topography, AFM takes an area too small for proper statistical relevance. A mathematically identical technique (though using a different principle of operation) is the stylus profilometer. In our experience, this is by far the most useful tool. There are some limitations, such as poor ability for proper evaluation of craters, but it gives a reproducible topography which enables proper counting of growth defects. Yet another alternative is the confocal optical microscopy. It enables a contact-less scanning of the surface but can give false peaks due to light scattering on the defects in the size range of light wavelength.

The images shown in this section and consequent evaluation were acquired by a diamond stylus (diameter 2 μm) scanning an area 1 mm × 1 mm at a resolution of 2 μm (both in x and y). The effective height resolution is about 5 nm. Typical acquisition time is 2 h, but the actual workload is limited to setting up the start of the measurement; the rest is done automatically. The Taylor-Hobson Talysurf Series 2 unit was used for all the measurements.

4.2 Principle of Evaluation

As said in the previous section, the definition of a growth defect, whether to include it into the count or not, is arbitrary. The lateral size is inevitably linked to the lateral resolution of the profilometer. Say, a 5 μm wide defect will always be recorded using a 2 μm resolution, but not necessarily using a 10 μm resolution. Things can

get more complicated if a different resolution is used along the scan line than the distance between the scan lines.

But the parameter most open to decision is the minimum height of the peak to be regarded as a defect. There is no physically useful gauge about that, but the threshold value should definitely be larger than the step height of protrusions at carbide inclusions (which is typically about 200 nm). A reasonable removal of waviness should be ensured too, such as using the Gaussian filter. The remaining waviness should be at least a few times lower than the threshold. In our experience, a reasonable threshold is 0.5 μm [37]; unless otherwise stated, this was used throughout the experiments shown in this section.

The raw topography after measurement is shown in 3D perspective view on Fig. 24a. Note the strong exaggeration in z-scale. The sharp peaks are in most cases the nodular defects, though this cannot be directly proven from the topography alone. An alternative presentation of the same topography is a top view, shown in Fig. 24c. Though these two images are informative for a visual inspection, they cannot provide any meaningful number. For this purpose, all the values below the threshold (0.5 μm) should be omitted (Fig. 24b). For proper counting of defects or acquiring additional statistical parameters, a top view of "islands" is the most appropriate (Fig. 24d). A similar procedure can be done on valleys, using a negative image in height.

The software for topography evaluation ([44] in our case) offers many statistical parameters to be extracted from the profile of Fig. 24d: number of peaks, their

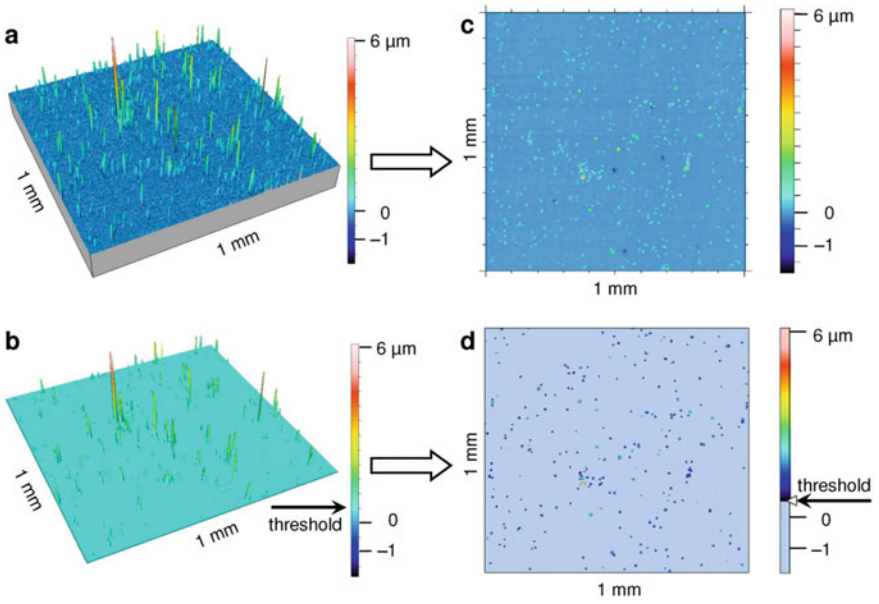

Fig. 24 Different ways of presenting the topography with defects: **a** 3D view of the complete topography, **b** 3D view of only that part with the height above +0.5 μm, **c, d** respective top view of both 3D images

average height, average area, average volume, etc. In our experience, the most useful parameter is the number of peaks per unit area. The problem with other parameters (particularly average volume) is their sensitivity to excessively large peaks which can substantially influence the average value. For instance, one very large defect can have more volume than all the rest together. If the number of defects is taken instead, that influence is negligible.

The density evaluated using these conditions gives a value of about 300 mm^{-2} for magnetron sputtered hard coatings and about 3000 mm^{-2} for those prepared by cathodic arc. These are the numbers the following discussion will be centered around. For comparison, the defect density on a bare substrate is usually zero; sometimes non-zero values are acquired, but usually below 5 mm^{-2}.

There is yet another influence which should be taken into account. The stylus has a finite tip, in first approximation a sphere (in our case, 2 μm diameter). In a hypothetical very sharp peak (Fig. 25a), the profile measured by the gauge will be broader than in reality, though the height will be correct. In a narrow crater, on the other hand (Fig. 25b), its size will be underestimated in both directions. Thus, the method is primarily suitable for nodular defect density evaluation and not for pinholes or craters.

As discussed above, the 0.5 μm threshold is arbitrary, but it does give useful results for typical PVD hard coatings. Their usual thickness is in the range 2.5–5 μm, thus the threshold height is 10–20% of the coating thickness in relative terms. Perhaps the relative thickness would be a more appropriate parameter, but it is more difficult to use because each sample would have to be evaluated for thickness first. However, for thinner films, we cannot stick to the 0.5 μm threshold, especially when the thickness is comparable to the threshold value. To evaluate this dependence, it is useful to calculate the defect density in dependence of the threshold height.

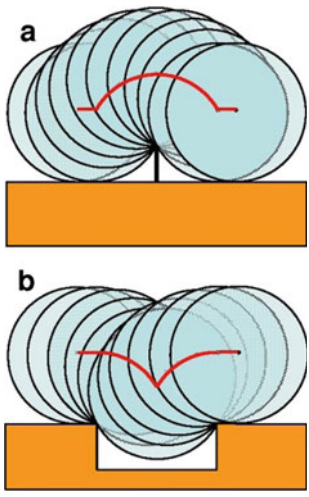

Fig. 25 Cases of improper shape recording by a stylus: **a** sharp peak, **b** narrow crater

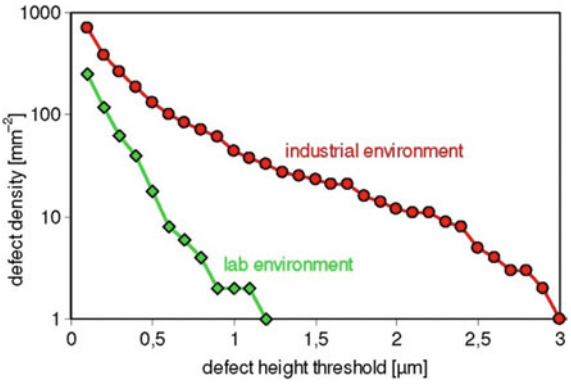

Fig. 26 Density of defects in dependence of chosen height threshold, for two deposition environments (taken from [29], p. 215, Fig. 1a)

Figure 26 shows a comparison of two nominally identical coatings, deposited in different deposition environments [29]. The red line applies to the standard industrial deposition system, operating in the usual high vacuum regime. The green line is the case of a laboratory deposition system in ultra high vacuum. If a large threshold height is taken, above 0.5 µm, the difference between the two environments is large indeed. This can logically be explained by a lack of large seeds in the extremely clean ultra high vacuum environment. Quite unexpectedly, using very low threshold heights (e.g., 0.2 µm), the difference closes up. This means that the origin of very small defects is not related to the cleanliness of the chamber but is a pertinent property of PVD process itself.

4.3 Reproducibility of Results

The relatively smooth curves presented in Fig. 26 hint that the extracted defect density is a robust, reproducible value. However, these curves apply to one profile only, evaluated using different threshold heights. Another scan at a different spot on the same sample may give a different curve. Indeed, the scattering of results, even when using the same threshold height, can be substantial. Therefore, it is important to make several measurements and perform proper statistical evaluation of results.

An example of a large set of measurements on nominally identical samples is given in Fig. 27. Rather than the defect density, the distribution of defect densities is given, divided into classes with a width of 50 defects/mm^2. The points show the number of measurements per each class, and the line is the fit using the formula [31]

$$y = y_0 \left(\frac{x}{x_0} \right)^n \exp\left(-\frac{x}{x_0} \right) \tag{3}$$

In this way, we can calculate the average defect density over the whole set of measurements. There is no need to emphasize that for this chart to be obtained a large number of measurements had to be conducted, so this is definitely not a method of

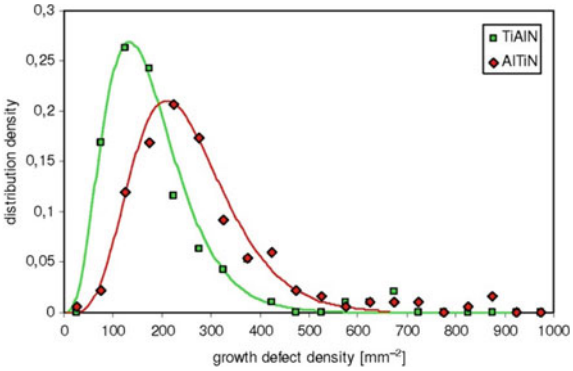

Fig. 27 Distribution of defect density for two sets of samples: coated by single-layer TiAlN and nanolayer AlTiN

choice to evaluate the quality of a particular coating type. However, a grand average does prove a difference between the two evaluated coatings, which cannot be shown on a single sample alone.

Nevertheless, one scan alone may be a good starting point for the initial coating quality check. In other words, if the defect density of one sample is excessively high compared to the grand average, this may be an indication of poor coating quality. In Fig. 27, the potentially problematic batches are the ones with a defect density above 500 mm^{-2} (for TiAlN) and above 600 mm^{-2} (for AlTiN). These isolated cases stick out of the distribution tail.

Similar minor difference can be proven between different substrates, different rotation modes, and different deposition chambers [31, 37]; except when using cathodic arc where the difference is substantial. The result shown above that the AlTiN coating has a third higher defect density than the TiAlN coating does not say much. But such results may help reduce the defect density for a certain amount, which might be beneficial for an application. Figure 28 shows a similar thorough analysis, but this time it evaluates the dependence on chamber position. This dependence is

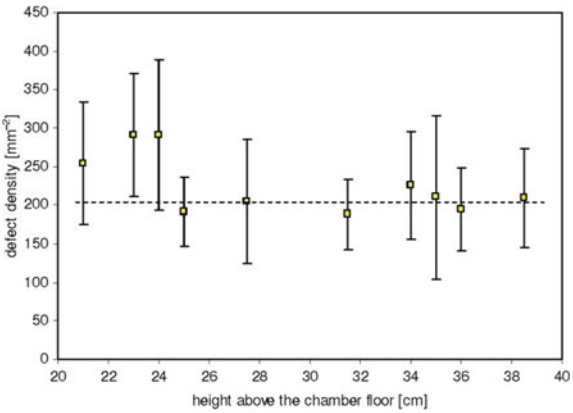

Fig. 28 Density of defects in dependence of sample vertical position in the deposition chamber

minimal; however, it proves that samples deposited at the lower part of the chamber do have a higher defect density. The take-home message in this case is clear that in sensitive applications it is advisable to avoid the bottom positions.

The discussion so far has been limited to peaks in the profile, i.e., primarily nodular defects. Using stylus profilometry, crater density is generally underestimated (see Fig. 25b). In addition, unless there was intensive expunging of nodular defects, the number of peaks is far greater than the number of craters. This is reflected in results; nevertheless, the density of craters tends to correlate well with the density of peaks [32]. Average roughness S_a generally correlates with peak density as well.

4.4 Local Variations

The relatively poor reproducibility of evaluated defect densities can be attributed to two major contributions. One is the temporal variation (batch-to-batch), linked to target wear-out, chamber cleanliness, batch content, etc. The other is related to spatial inhomogeneity of defect density within the same batch, or even on the surface of the same sample. Being a statistical value, the defect density will inevitably vary on the surface, particularly at a small scale. Note, for instance, Fig. 24d, which appears relatively homogeneous at the lateral scale of 1 mm, would give a variable result if taken at the scale of, say, 0.2 mm. The open question remains whether such an inhomogeneous lateral pattern can be observed in larger scale as well.

For instrumental constrains, it is difficult (and especially, very time-consuming) to conduct a measurement at 10 mm scale. An alternative option is to make a mesh of several measurements and stitch them together into one profile. For evaluation of the lateral inhomogeneity, we opted for one large measurement, followed by segmentation. Figure 29a shows a simplified topography extracted from one measurement of the area 8 mm × 3 mm. Each dot presents one defect (in most cases, these are the nodular defects). It is visually directly clear that the defects tend to cluster in areas with the typical size in the 1 mm range.

To get a number rather than visual estimation, we divided the area into sections (0.5 mm × 0.5 mm) and counted the number of defects per each section. A filtering was performed to smoothen up the topography, and a density map was constructed as the final result (Fig. 29b). It shows the defect density per cell (i.e., to get the density per mm^2, the value should be multiplied by four). Even after filtering the map, the defect density effectively varies for one order of magnitude. Note that the values presented here were extracted from relatively small sections with an area of 0.25 mm^2 only. Taking a larger scan area, such as the typical 1 mm^2 or larger, narrows down the scattering substantially.

From the statistical point of view, we cannot directly explain the origin of this clustering. But based on the origin of seeds (see Subsection 3.2), the most likely explanation is arcing. The contact of the arc with the surface is an area of locally strongly elevated temperature, which increases the mechanical stress, which in turn causes spallation, delamination, or droplet formation. The emission of these particles

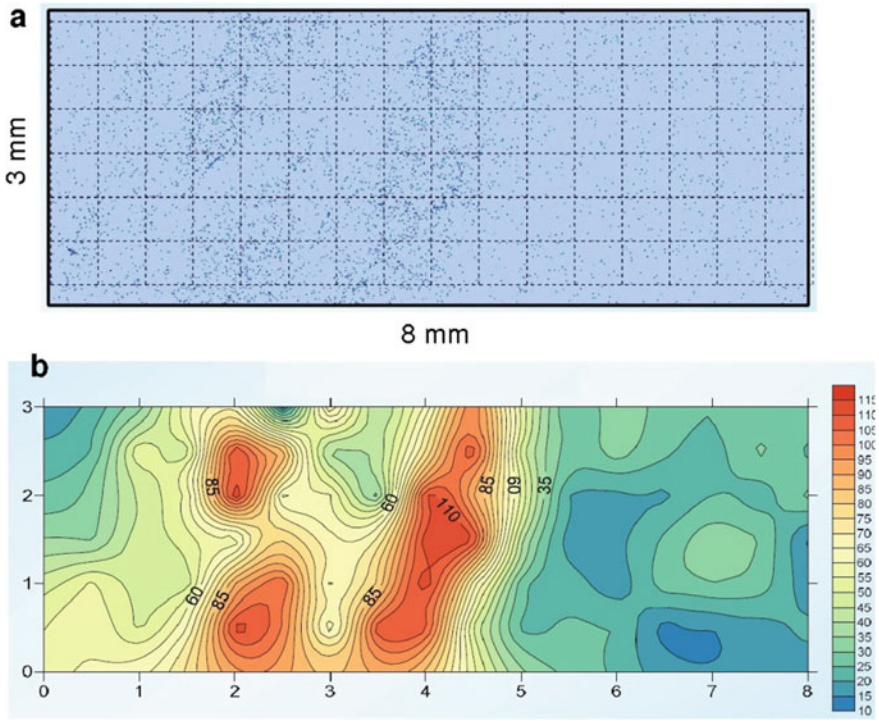

Fig. 29 Defect density map for a large area on a sample (8 mm × 3 mm): **a** direct presentation of defects including the sectioning mesh, **b** contour plot of defect density (taken from [37], p. 251, Fig. 1)

is highly localized in the area of arc appearance, thus it affects only a minor part of the substrate surface. An arc during the etching phase causes seed formation at the substrate surface, while an arc during the coating phase is the origin of seeds embedded in the growing coating. A side result of this analysis shows that an arc affects an area in the lateral size of a millimeter or so.

A similar analysis was conducted by another group [19]. A different measuring method was used, a confocal optical microscope rather than a profilometer. Being an optical method, they experienced a problem with the dust (which is not relevant for a stylus). A lower height threshold was taken, only 0.2 μm. Scanning was done on a large area with a similar segmentation on sections. Despite the different experimental approach, the results were similar, as they found out a large lateral scattering of defect density including clustering of high-defect areas. The main motivation of the study was linked to corrosion resistance, where they first analyzed the as-deposited sample, then put it into a corrosive medium, followed by a repeated analysis of the surface. Special attention was paid to the question, whether local pitting corrosion was linked to a previously existing growth defect. The following conclusion is very important: *» […] all corrosion pits found on these samples were caused by identifiable growth*

defects. This reversely means that the microstructure of the undisturbed growing coating is irrelevant for the corrosion behavior of the studied samples.« [19]

5 Conclusions

This review has emphasized two concepts in growth defect studies. From an individual growth defect perspective, it needs to be stressed that the majority of them are nodular defects. They all start with a seed which may have different origins (geometric imperfection, inclusion, foreign particle), but the consequential evolution takes place regardless of the seed type. Thus, the final shape and size of the nodular defect is similar and therefore difficult to evaluate other than geometrical properties. The method of choice is the Focused Ion Beam (FIB) which allows making a cross-section of the desired growth defect. This enables us to extract the seed nature (location, size, composition), and in the case of advanced sectioning, a 3D reconstruction of the defect. By introducing a coordinate system on the sample surface, one can find a desired growth defect in any microscope. This is a useful tool to study a single growth defect before and after an experiment and to follow the evolution of that defect at several stages of this experiment.

In contrast to the single defect concept, an ensemble of growth defects can be evaluated on a statistical basis. For this purpose, we suggest positive experience using the contact profilometer. The growth defect density (mm^{-2}) is a quantity, expressed as the number of peaks above 0.5 μm height in a given area. Care must be taken in interpretation because of poor reproducibility. If taken properly, this quantity can be a useful gauge of the coating quality.

Acknowledgements This work was supported by Slovenian Research Agency (program P2-0082, projects M2-0125, L2-4173, L2-4239, L2-4249, L2-5470, and BI-HR/14-15-022). We also acknowledge funding from the European Regional Development Funds (CENN Nanocenter, OP13.1.1.2.02.006).

References

1. X. Liu, D. Li, Y. Zhao, X. Li, J. Shao, Characteristics of nodular defect in HfO_2/SiO_2 multilayer optical coatings. Appl. Surf. Sci. **256**, 3783–3788 (2010)
2. X. Cheng, J. Zhang, T. Ding, Z. Wei, H. Li, Z. Wang, The effect of an electric field on the thermomechanical damage of nodular defects in dielectric multilayer coatings irradiated by nanosecond laser pulses. Light Sci. Appl. **2**, e80 (2013)
3. M.-H. Shiao, F.-S. Shieu, A formation mechanism for the macroparticles in arc ion-plated TiN films. Thin Solid Films **386**, 27–31 (2001)
4. B.A. Movchan, A.V. Demchishin, Investigation of the structure and properties of thick vacuum condensates of nickel, titanium, tungsten, and aluminum oxide. Fiz. Met. Metalloved. **28**(4), 653–660 (1969)

5. D.M. Mattox, G.J. Kominiak, Structure modification by ion bombardment during deposition. J. Vac. Sci. Technol. **9**(1), 528–531 (1972)
6. T. Spalvins, W.A. Brainard, Nodular growth in thick-sputtered metallic coatings. J. Vac. Sci. Technol. **11**(6), 1186–1192 (1974)
7. T. Spalvins, Characterization of defect growth structrures in ion-plated films by scanning electron microscopy. Thin Solid Films **64**(1), 143–148 (1979)
8. K.H. Guenther, Nodular defects in dielectric multilayers and thick single layers. Appl. Opt. **20**(6), 1034–1038 (1981)
9. M.J. Brettm R.N. Tait, S.K. Dew, S. Kamasz, A.H. Labun, T. Smy, Nodular defect growth in thin films. J. Mater. Sci. **3**, 64–70 (1992)
10. S. Müller-Pfeiffer, H.-J. Anklam, Computer simulation of hillock growth. Vacuum **42**, 113–116 (1991)
11. D.G. Stearns, P.B. Mirkarimi, E. Spiller, Localized defects in multilayer coatings. Thin Solid Films **446**, 37–49 (2004)
12. J. Vetter, M. Stüber, S. Ulrich, Growth effects in carbon coatings deposited by magnetron sputtering. Surf. Coat. Technol. **168**, 169–178 (2003)
13. H.W. Wang, M.M. Stack, S.B. Lyon, P. Hovsepian, W.-D. Münz, The corrosion behaviour of macroparticle defects in arc bond-sputtered CrN/NbN superlattice coatings. Surf. Coat. Technol. **126**, 279–287 (2000)
14. H.W. Wang, M.M. Stack, S.B. Lyon, P. Hovsepian, W.-D. Münz, Wear associated with growth defects in combined cathodic arc unbalanced magnetron sputtered CrN/NbN superlattice coatings during erosion in alkaline slurry. Surf. Coat. Technol. **135**, 82–90 (2000)
15. H.A. Jehn, Improvement of the corrosion resistance of PVD hard coating–substrate systems. Surf. Coat. Technol. **125**, 212–217 (2000)
16. S.H. Ahn, J.H. Lee, J.G. Kim, J.G. Han, Localized corrosion mechanisms of the multilayered coatings related to growth defects. Surf. Coat. Technol. **177–178**, 638–644 (2004)
17. D.B. Lewis, S.J. Creasey, C. Wüstefeld, A.P. Ehiasarian, PEh. Hovsepian, The role of the growth defects on the corrosion resistance of CrN/NbN superlattice coatings deposited at low temperatures. Thin Solid Films **503**, 143–148 (2006)
18. M. Fenker, M. Balzer, H. Kappl, Corrosion protection with hard coatings on steel: past approaches and current research efforts. Surf. Coat. Technol. **257**, 182–205 (2014)
19. M. Balzer, Identification of the growth defects responsible for pitting corrosion on sputter-coated steel samples by large area high resolution mapping. Thin Solid Films **581**, 99–106 (2015)
20. C. Petrogalli, L. Montesano, M. Gelfi, G.M. La Vecchia, L. Solazzi, Tribological and corrosion behavior of CrN coatings: roles of substrate and deposition defects. Surf. Coat. Technol. **258**, 878–885 (2014)
21. G.T.P. Azar, C. Yelkarasi, M. Ürgen, The role of droplets on the cavitation erosion damage of TiN coatings produced with cathodic arc physical vapor deposition. Surf. Coat. Technol. **322**, 211–217 (2017)
22. R.R. Aharonov, M. Chhowalla, S. Dhar, R.P. Fontana, Factors affecting growth defect formation in cathodic arc evaporated coatings. Surf. Coat. Technol. **82**, 334–343 (1996)
23. W.-D. Münz, D. Lewis, S. Creasey, T. Hurkmans, T. Trinh, W.v. Ijzendorn, Defects in TiN and TiAlN coatings grown by combined cathodic arc/unbalanced magnetron technology. Vacuum **46**, 323–330 (1995)
24. S. Creasey, D.B. Lewis, I.J. Smith, W.-D. Münz, SEM image analysis of droplet formation during metal ion etching by a steered arc discharge. Surf. Coat. Technol. **97**, 163–175 (1997)
25. P.J. Martin, R.P. Netterfield, T.J. Kinder, Ion-beam-deposited films produced by filtered arc evaporation. Thin Solid Films **193–194**, 77–83 (1990)
26. C. Mitterer, O. Heuzè, V.-H. Derflinger, Substrate and coating damage by arcing during sputtering. Surf. Coat. Technol. **89**, 233–238 (1997)
27. A. Anders, Physics of arcing, and implications to sputter deposition. Thin Solid Films **502**, 22–28 (2006)

28. J.M. Lackner, W. Waldhauser, B. Major, J. Morgiel, L. Major, H. Takahashi, T. Shibayama, Growth structure and growth defects in pulsed laser deposited Cr–CrN_x–CrC_xN_{1-x} multilayer coatings. Surf. Coat. Technol. **200**, 3644–3649 (2006)
29. M. Čekada, N. Radić, M. Jerčinović, M. Panjan, P. Panjan, A. Drnovšek, T. Car, Growth defects in magnetron sputtered PVD films deposited in UHV environment. Vacuum **138**, 213–217 (2017)
30. M. Čekada, P. Panjan, D. Kek-Merl, M. Panjan, G. Kapun, SEM study of defects in PVD hard coatings. Vacuum **82**, 252–256 (2008)
31. P. Panjan, M. Čekada, M. Panjan, D. Kek-Merl, F. Zupanič, L. Čurković, S. Paskvale, Surface density of growth defects in different PVD hard coatings prepared by sputtering. Vacuum **86**, 794–798 (2012)
32. P. Panjan, M. Čekada, M. Panjan, D. Kek-Merl, Growth defects in PVD hard coatings. Vacuum **84**, 209–214 (2010)
33. P.B. Mirkarimi, D.G. Stearns, Investigating the growth of localized defects in thin films using gold nanospheres. Appl. Phys. Let. **77**(14), 2243–2245 (2000)
34. J.M. Cairney, S.G. Harris, L.W. Ma, P.R. Munroe, E.D. Doyle, Characterisation of TiN and TiAlN thin films deposited on ground surfaces using focused ion beam milling. J. Mat. Sci. **39**, 3569–3575 (2004)
35. P. Panjan, D. Kek Merl, F. Zupanič, M. Čekada, M. Panjan, SEM study of defects in PVD hard coatings using focused ion beam milling. Surf. Coat. Technol. **202**, 2302–2035 (2008)
36. D. Kek Merl, P. Panjan, M. Panjan, M. Čekada, The role of surface defects density on corrosion resistance of PVD hard coatings. Plasma Process. Polym **4**, 5613–5617 (2007)
37. P. Panjan, P. Gselman, D. Kek-Merl, M. Čekada, M. Panjan, G. Dražić, T. Bončina, F. Zupanič, Growth defect density in PVD hard coatings prepared by different deposition techniques. Surf. Coat. Technol. **237**, 349–356 (2013)
38. P. Panjan, A. Drnovšek, J. Kovač, Tribological aspects related to the morphology of PVD hard coatings. Surf. Coat. Technol. **343**, 138–147 (2018)
39. P. Panjan, A. Drnovšek, Influence of growth defects in PVD hard coatings on their wear, corrosion and oxidation resistance, in *The Thirteenth International Symposium on Sputtering and Plasma Processes (ISSP)*, Kyoto (2015), pp. 323–328
40. P. Panjan, A. Drnovšek, J. Kovač, M. Čekada, M. Panjan, Oxidation processes in vanadium-based single-layer and nanolayer hard coatings. Vacuum **138**, 230–237 (2017)
41. P. Panjan, A. Drnovšek, J. Kovač, P. Gselman, T. Bončina, S. Paskvale, M. Čekada, D. Kek Merl, M. Panjan, Oxidation resistance of CrN/(Cr,V)N hard coatings deposited by DC magnetron sputtering. Thin Solid Films **591**, 323–329 (2015)
42. P. Gselman, T. Bončina, F. Zupanič, P. Panjan, D. Kek Merl, M. Čekada, Characterization of defects in PVD TiAlN hard coatings. Mater. Technol. **46**, 351–354 (2012)
43. A. Drnovšek, P. Panjan, M. Panjan, M. Čekada, The influence of growth defects in sputter-deposited TiAlN hard coatings on their tribological behavior. Surf. Coat. Technol. **288**, 171–178 (2016)
44. TalyMap Gold, Taylor Hobson Ltd. (2012)

Growth Dynamics of Epitaxial Gallium Nitride Films Grown on c-Sapphire Substrates

Shibin Krishna, Neha Aggarwal, Lalit Goswami, and Govind Gupta

Abstract In the present scenario, semiconducting material based devices with new capabilities are redefining the existing technologies. The developments in III-Nitride thin-film technology have produced significant advances in high-performance optoelectronic and photovoltaic devices. However, the quality of the material is an important factor for the fabrication of nitride-based efficient devices. For instance, a large difference in the covalent bond radius of Gallium and Nitrogen atoms results in high dislocation densities in the III-Nitride compound, Gallium Nitride (GaN) which is sturdily ruled by residual strain in the GaN films. Another main source of residual strain is the lack of an appropriate lattice-matched substrate that will critically impact the optoelectrical performance of the fabricated devices. So, this chapter illuminates the solution to key challenges and elaborate on various parameters to grow GaN by using plasma-assisted molecular beam epitaxy (PAMBE) technique. Numerous efforts have been made for improving the quality of GaN semiconductor for high performance of device operation. This chapter elucidates the role of the growth variables towards high-quality epitaxial GaN films and discusses the stress-relaxation controlled defect minimization in detail. Also, it provides an in-depth understanding towards structural and interface quality of multilayered GaN/AlN heterostructure grown on c-plane sapphire substrate. Therefore, this chapter contributes distinctly to understanding the growth dynamics in GaN films and subsequently in GaN/AlN based multilayered heterostructures for next-generation promising nitride-based devices.

1 Introduction

The rise in energy demand with the availability of limited natural resources is a promising challenge for the global economy. Eventually, the world is approaching towards complex consequences where energy crisis would decide the outcome of

S. Krishna · N. Aggarwal · L. Goswami · G. Gupta (✉)
Sensor Devices & Metrology Division, CSIR-National Physical Laboratory, New Delhi 110012, India
e-mail: govind@nplindia.org

S. Kumar and D. K. Aswal (eds.), *Recent Advances in Thin Films*, Materials Horizons: From Nature to Nanomaterials, https://doi.org/10.1007/978-981-15-6116-0_4

upcoming technology. The processes and methodologies for developing future technologies have to be responsible for intricate environmental concerns [1]. So, the mainstream necessity of leading technology demands such materials that enable semiconductor devices to be capable of redefining the existing technologies without disturbing the eco-balance. The biocompatible III-nitride semiconductor material system can significantly endow this endeavour and its exceptional material properties provide high-performance applications in the latest optoelectronic and photovoltaic device technology [2–6]. Among III-Nitrides, GaN emerges out to be the most suitable candidate for realizing such optoelectronic devices that are capable of operating in harsh environmental conditions [7, 8].

1.1 Properties of GaN Semiconductor

The various properties of GaN which are marking its existence as an attractive semiconducting material for numerous applications are tabulated in Table 1. Because of its advantageous properties such as wide direct energy band gap, excellent radiation hardness and high thermal conductivity, GaN is a verified material for short wavelength emitters (LEDs and diodes lasers) and detectors [9–13].

Mainly, the crystal structures for group-III nitrides are classified into: cubic zinc blende and hexagonal wurtzite. Both can coexist under various parameters used for the crystal growth [15]. The cubic structure is thermodynamically metastable and the wurtzite structure is thermodynamically stable. Figure 1a shows the hexagonal wurtzite and zinc blende structures of GaN and the various planes of GaN are represented in Fig. 1b.

Table 1 Basic properties of GaN semiconductor [14]

Physical property	GaN
Band gap energy, E_g (eV)	3.44
Thermal conductivity at 300 K (W/cm K)	2.1
Thermal expansion coefficient (300 K)	
a ($\times 10^{-6}$ K^{-1})	5.59
c ($\times 10^{-6}$ K^{-1})	3.17
Lattice constant (300 K)	
a (Å)	3.189
c (Å)	5.185
Bond length (Å)	1.94
Melting point (°C)	>2500
Density (g/cm^3)	6.10
Heat capacity at 300 K (J/mol K)	35.3
Breakdown field at 300 K (cm^{-1})	3–5 $\times$ 10^6

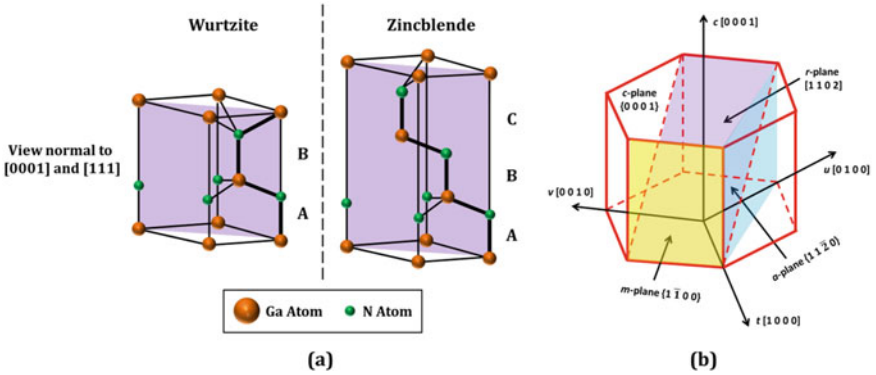

Fig. 1 **a** The three-dimensional view of a stick-and-ball stacking model of GaN crystals with 2H wurtzite and 3C zinc blende polytypes; **b** schematic representation of different planes (c-, a-, r- and m-planes) of GaN

In GaN wurtzite hexagonal system, c-plane is on the top of the hexagonal unit. This plane is called polar-oriented plane, where the termination is either Ga or N ions, so there is always a net charge on this plane. The m- and a- plane (yellow and blue colour planes Fig. 1b) are at the sidewall of the hexagonal system, they belong to non-polar-oriented planes. Here, the termination is both by Ga and N ions, so the net charge will be neutralized. While r-plane (violet colour plane in Fig. 1b) is a semi-polar oriented surface where the termination is dominated either by Ga or N ions leading to semi-polarity on the surface.

1.2 Growth Kinetics and Its Mechanism

The epitaxial growth of GaN has been reported by using a variety of methods, including metal organic chemical vapour deposition (MOCVD), high-pressure vapour epitaxy (HPVE), molecular beam epitaxy (MBE), etc. Each of these are suited for a particular application. Here, MBE is a physical vapour deposition technique where the materials undergo Solid/Liquid → Gas → Solid phases. Since the growth is performed in ultra-high vacuum (UHV), so the contaminations are minimized and also allow better doping incorporation. Besides, the lower growth rate allows precise control over the thickness and forms a very sharp interface between the layers. During the MBE growth, various physical processes occur which are explained below.

The growth kinetics is affected by a variety of factors including substrate material, impinging flux of adatoms, surface interaction with the adatoms, nitrogen flux and the growth temperature. The growth mechanism can be explained by adatoms residing on the surface of a substrate which involves the existence of several surface phenomena. These include adatom adsorption on the surface, desorption from the

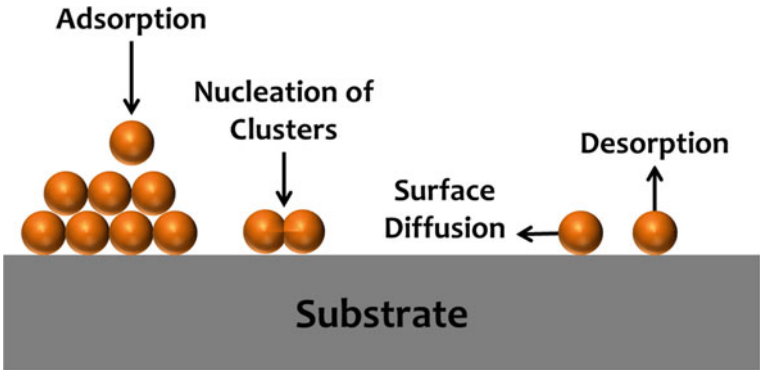

Fig. 2 A schematic representing various microscopic kinetic processes of growth

surface, surface diffusion and nucleation headed for cluster formation (Fig. 2). The basic growth kinetics is based on surface diffusion which is explained as follows. When adatom arrived at the target surface (substrate), the incident atoms generally lose their momentum perpendicular to the surface, while receiving kinetic energy from the substrate for their in-plane diffusive motions, and the energy depends on the substrate temperature. Such diffusion may be described by a two-dimensional 'random-walk' model on the surface by 'hopping' from one site to another. While the free random-walk of the adatoms will stop due to some other kinetic effects on the surface such as nucleation, adatom attachment, desorption from the substrate, etc. which are illustrated in Fig. 2 [16]. The mobility of such diffusing adatoms can be related by mean displacement as given below:

$$r_s = a \exp\left(\frac{E_{\text{des}} - E_{\text{sd}}}{2k_B T}\right) \tag{1}$$

where r_s is the 'mean displacement' of the diffusion, and T is substrate temperature. E_{des}, E_{sd} are the activation energies of the surface desorption and diffusion, respectively. The k_B is the Boltzmann constant, while 'a' is the adsorption site spacing which is determined by the lattice of the surface. Therefore, a proper substrate temperature to maintain the sufficient diffusion on the surface leads to an improvement in the surface morphology.

From the past few years, a numerous crystal-growth technique, substrate-type and orientation have been tried in an effort to grow high-quality group-III Nitride thin films. Considerable efforts have been focused on the high-quality epitaxial growth of GaN on various substrates such as Silicon, SiC and different orientations of Sapphire (c, a, r and m-plane), etc. However, c-plane sapphire substrate is widely used for the epitaxial growth of various Nitride semiconductors as it has a good epitaxial relationship with hexagonal Nitride structure and is comparatively a cost-effective substrate. The in-plane epitaxial relationship between GaN and Sapphire is: $[0001]_{\text{GaN}} \parallel [0001]_{\text{sapphire}}$. The lattice and thermal expansion mismatch of GaN on

Sapphire is found to be 13% (in-plane rotation of 30°) and 33%, respectively. Thus, this chapter focuses on demonstrating the growth kinetics and defect generation in GaN grown on sapphire substrates.

Due to the absence of a suitable lattice-matched substrate to GaN, heteroepitaxial approach has been adopted, i.e. thin film of GaN to be grown on sapphire or other foreign substrates. When grown on sapphire, GaN usually comprises a high density of threading dislocations (of the order of 10^{10} cm^{-2}) due to large lattice constant as well as thermal expansion coefficient mismatches between GaN and sapphire [17–19]. Apart from threading dislocations, there exist many other structural defects such as, voids, surface pits, inversion domain and stacking mismatch boundaries. These defects disturb the periodicity of grown crystal structure and thereby, affect the optoelectronic properties of the devices fabricated on these films. Since, large number of dislocations, sturdily ruled by the strain present in the GaN structure (due to huge difference in covalent bond radius of the Ga and N atoms [20]), remains a key challenge for a high-performance device application. Thus, the scarcity of suitable substrate (having comparable lattice constant) is found to be the major cause of residual strain which directly impact the optoelectrical performance of the fabricated devices [21]. Several efforts have been impelled for designing highly crystalline GaN semiconductor for efficient device operation [22–24]. So far, researchers have been experimenting with several techniques to reduce the density of dislocations [25, 26]. In an approach, the AlN interlayers were introduced to curtail threading dislocation densities (TDD) and projected its influence on the stress developed in grown GaN structures [27]. While, another approach correlated the growth temperature and stress in GaN crystals grown on SiC templates [28]. Lately, our group has exemplified the stress relaxation for reducing various defects in GaN grown by PAMBE on GaN epilayer (MOCVD grown GaN template, Lumilog) [29]. Furthermore, another study correlating the structural, optical and electrical properties with defect states has been illustrated in the GaN films grown on a-plane ($11\bar{2}0$) sapphire substrates [30, 31]. Although, Wang et al. demonstrated the reduction of threading dislocation density by insertion of superlatticed structure [26]. However, a clear correlation of stress and surface defects in GaN film grown by PAMBE on c-plane (0001) sapphire substrate has not been understood so far. This chapter deals with the growth of epitaxial GaN and GaN/AlN heterostructure on c-plane sapphire as well as elucidates various structural and optical properties of the grown GaN films. Herein, the role of growth temperature is illustrated enrouting defect minimization by releasing the lattice stress in epitaxial GaN films grown on c-plane sapphire substrates. Besides, the correlation of electronic structure and surface defects with stress-relaxed GaN films are also discussed in detail. In addition, growth of a multi-interlayered GaN/AlN/GaN/AlN/GaN heterostructure on c-plane sapphire and its comprehensive structural analysis is presented in detail. This chapter contributes distinctly in understanding the defect reduction in GaN films and subsequently impact of various growth parameters towards developing efficient nitride-based devices. The chapter has been classified into two sections, epitaxial growth of GaN on c-plane sapphire substrate as a first part, secondly: epitaxial growth of GaN/AlN multilayered heterostructure on c-plane sapphire substrate.

2 Epitaxial GaN Growth

2.1 Growth Conditions

The growth/substrate temperature is found to imprint a strong impact on the properties and dynamics of GaN films grown on c-sapphire substrate. Generally, the heteroepitaxial growths were started by nitridation of sapphire substrate (i.e. exposing the substrate to nitrogen plasma) at low substrate temperature (450 °C) where the oxygen atoms in sapphire (Al_2O_3) have been replaced by nitrogen atoms due to lower bond energy of Al–O compared to Al–N bond. This is an essential step as the presence of oxygen species at the interface may create a monolayer of Ga–O at the heterointerface which can perplex the GaN epitaxial growth and thereby, cause a detrimental impact on the device efficiency. Thus, the substrate is exposed to nitrogen plasma resulting in forming a monolayer of strained AlN. This facilitates the subsequent growth of GaN on a better chemically matched substrate. A low temperature (LT) GaN buffer layer was deposited at 530 °C under Ga-rich conditions where it will act as a cushion layer for the epitaxial GaN film. The LT buffer layer will form a polycrystalline crystallography of GaN with sufficient Ga adatoms where it will play the main role for the two-dimensional (2D) mode of growth. Finally, the epitaxial GaN films were grown on c-plane sapphire substrate at different growth temperatures of 715, 730, 745 and 760 °C to exemplify the role of growth temperature on growth kinetics and processes.

Then, the crystallinity, surface morphology, optical and structural properties of the grown GaN film need to be explored in detail using various characterization tools such as reflection high-energy electron diffraction (RHEED), high-resolution X-ray diffraction (HRXRD), field emission scanning electron microscopy (FESEM), atomic force microscopy (AFM), photoluminescence (PL) and Raman spectroscopy (RS).

2.2 Nucleation—Surface Diffusion: RHEED Analysis

A real-time tool to monitor the growth of crystalline layers during the growth processes is RHEED. It also guides towards atomic-level analysis of various structures of crystal surfaces. The basic principle of RHEED is demonstrated in Fig. 3. The electrons from an electron gun are incident on the sample where diffraction takes place from the atoms at the surface of the sample and a fraction of the diffracted electrons interfere constructively at specific angles to form regular patterns on a fluorescent screen which was recorded via a charged coupled device (CCD) camera detection device. The electrons interfere according to the position of the atoms on the sample surface, giving an indication of the growth mode.

Relation of RHEED patterns with respective growth mode:

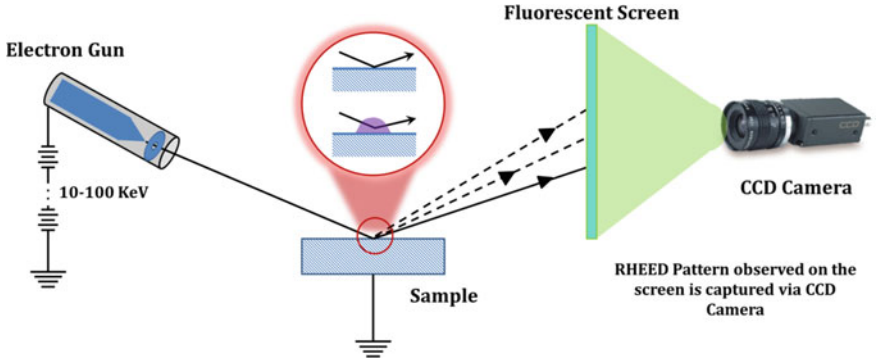

Fig. 3 The working phenomenon of RHEED technique

- Ideal surface (2D layer): Circular arrays of elongated spots or Streaky pattern.
- Amorphous layer: No diffraction pattern.
- Three-dimensional (3D) surface: The electrons transmitted through the surface and scattered in different directions resulting in the Spotty RHEED pattern on the screen.

Here, the PAMBE grown GaN was in situ observed by RHEED to monitor its growth dynamics and mode. RHEED images of all GaN samples along $(11\bar{2}0)$ zone axes are shown in Fig. 4, where sharp streaky (1×1) RHEED patterns were obtained indicating that growth proceeds in two-dimensional mode for all the samples [32].

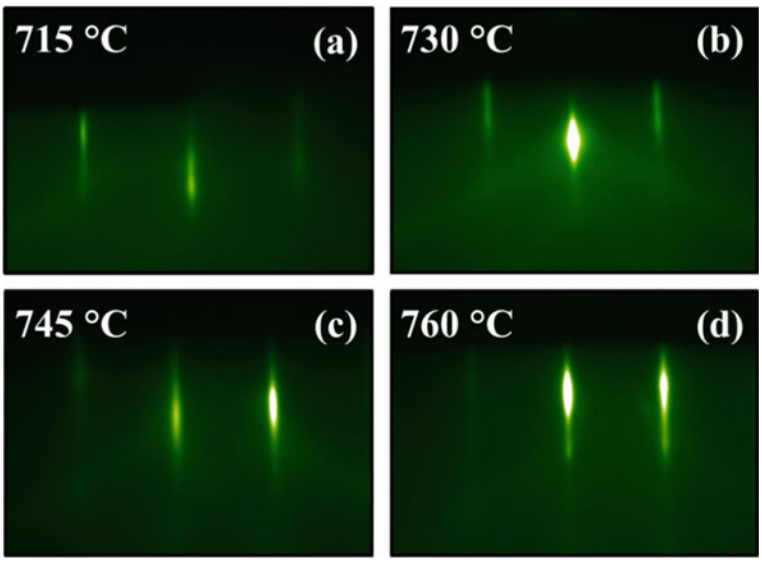

Fig. 4 RHEED patterns along $(11\bar{2}0)$ zone axis from the PAMBE grown GaN films

These patterns estimate the interplanar spacing of the planes by calculating the camera length of diffraction system. Based upon these evaluations, it was confirmed that GaN growth on c-plane sapphire follows an epitaxial orientation relationship of (0001) GaN ‖ (0001) sapphire. Henceforth, certain nucleation and surface dynamics could result in high crystallinity GaN structure to be grown epitaxially along c-direction on c-plane sapphire substrates.

2.3 Structural Quality of GaN Thin Films

To analyse the structural properties of any material, XRD is an essential tool and for thin films, HRXRD is utilized. HRXRD is a non-destructive technique that is based on the elastic scattering of X-rays from the electron clouds of individual atoms in the crystal structure of the epitaxial thin film. This technique enables us to measure the information such as atomic structure, lattice mismatch, strain and relaxation, disorientation, curvature, layer thickness, composition, inhomogeneity, dislocation density and crystallite size. In general, the HRXRD technique is not utilized mainly for determining the crystal structure, but to investigate any deviations from an ideal crystal orientation which can be impelled by defects, strain or impurities. Here, the HRXRD measurements were performed to analyse the impact of a key growth parameter, i.e. growth temperature on various physical properties and defect reduction in the GaN films.

A crystal lattice is formed by the 3D distribution of atoms arranged in a series of parallel planes parted from one another by interplanar spacing, d which depends on the nature of material. For the parallel planes of atoms (Fig. 5), when a monochromatic X-ray beam of wavelength 'λ' is targeted on a crystalline material with an angle 'θ', constructive interference only occurs when Bragg's law is satisfied. Bragg's

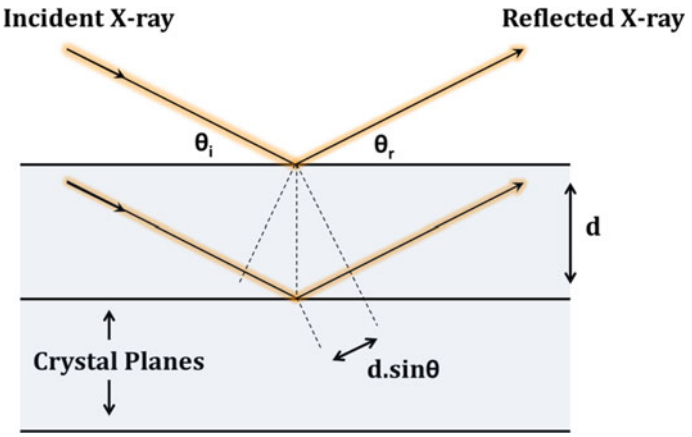

Fig. 5 A schematic illustration of Bragg's law of diffraction

equation is given by

$$n\lambda = 2d \sin\theta \tag{2}$$

where $1/d_{hkl}^2 = (4/3) \times \left((h^2 + hk + k^2)/a^2\right) + \left(l^2/c^2\right)$ for a hexagonal symmetry system, h, k and l are the Miller indices; θ is the angle of diffraction. By using this Eq. (2), the lattice parameters 'a' and 'c' can be calculated.

Figure 6a, b shows the HRXRD ($2\theta - \omega$) scans along (0002) and (10–12) diffraction planes of GaN film grown by PAMBE. The HRXRD spectra represents two distinct peaks in Fig. 6a, which corresponds to GaN (0002) and (0004) plane of diffractions along with two sharp peaks ascribing to (0006) and (0012) orientation of the sapphire substrate. The presence of first- and second-order X-ray diffractions of GaN reveals the epitaxial growth of highly crystalline GaN film along the c-direction on c-plane sapphire substrate. The peak positions of GaN (0004) and GaN (11–22) in $2\theta - \omega$ scans of Fig. 6 were used to estimate the lattice constants (c and a) by using the Bragg's law given in Eq. (2) and the calculated lattice parameters are provided in Table 2. It was observed that calculated lattice constant value, c, initially decreases with increasing the growth temperature while at elevated temperature, less compressively stressed value of lattice constant has been noticed. For GaN film grown at 715 °C, the lattice is under tensile stress whereas in other GaN films, the lattice is

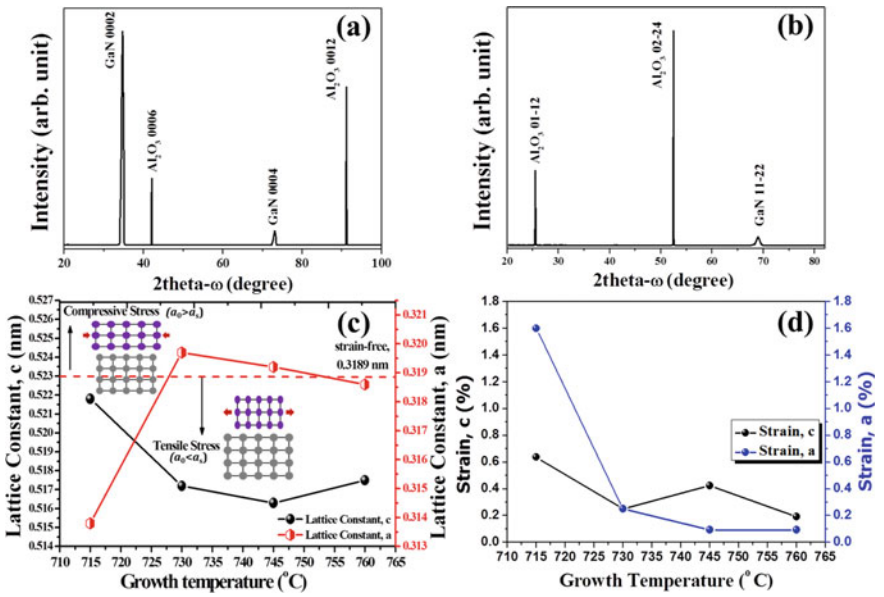

Fig. 6 **a** HRXRD ($2\theta - \omega$) symmetric scan of GaN epitaxial film and **b** HRXRD ($2\theta - \omega$) asymmetric scan of GaN epitaxial film grown on c-sapphire (Reproduced from Ref. [32], with permission from the PCCP Owner Societies), **c** variation of lattice parameters (a and c) versus growth temperature, **d** plots of growth temperature versus strain along a and c lattices

Table 2 The experimentally evaluated lattice parameters (c and a) and dislocation densities (screw and edge) of the grown GaN epitaxial films [32]

Growth temperature (°C)	Lattice constant c (nm)	Lattice constant, a (nm)	Screw dislocation densities, D_{screw} ($\times 10^8$ cm^{-2})	Edge dislocation densities, D_{edge} ($\times 10^9$ cm^{-2})
715	0.5218	0.3138	9.5	7.3
730	0.5172	0.3197	3.1	3.3
745	0.5163	0.3192	8.7	8.2
760	0.5175	0.3186	8.6	7.9

found to be compressively stressed. Figure 6c represents a plot showing variation in the lattice parameters with growth temperature and compared the experimentally observed values with fully relaxed GaN film ($c_0 = 0.5185$ nm and $a_0 = 0.3189$ nm) [14]. It was inferred that the samples grown at 730 °C and 760 °C have lattice constant value near to strain-free values [32].

Figure 6d represents the variation in strain along c- and a-axis with changing growth temperatures. It was observed that the strain values are higher at lower substrate temperature and minimum at elevated temperature. It could be due to higher thermal energy leading to the equilibrium condition for the growth of less lattice strained GaN films. Often, the quality of epitaxial growth is primarily determined by the lattice constant mismatch with the immediate substrate below it. Though, lattice mismatch is defined as the difference between the lattice constant of two crystals with different lattice planes. Lattice mismatch usually prevents the growth of a defect-free epitaxial film. If a film grows coherently on a thick substrate, uniform stress will build up due to a lattice mismatch. The stress state of heteroepitaxial layers depends on whether the in-plane lattice space of the epitaxial film is greater or smaller than that of the substrate. Figure 7 illustrates two cases of strain: compressive ($a_{film} > a_{substrate}$) and tensile ($a_{film} < a_{substrate}$). The strain developed in grown films produces various optical defects which create charge scattering centres and non-radiative trap centres in the electronic band structure of the GaN films [22, 23].

In order to quantify the defects density in grown samples, their structural properties were further investigated through ω-scans along symmetric (002) and asymmetric

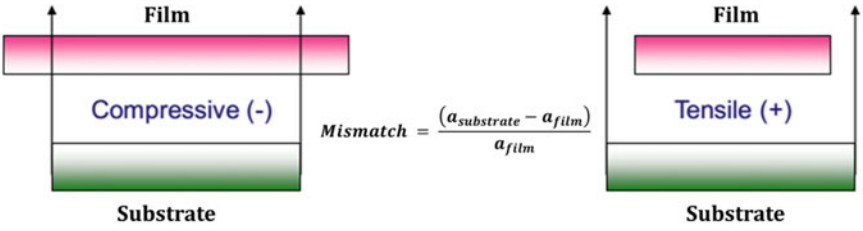

Fig. 7 Schematic diagrams showing compressive strain state (when $a_{substrate} < a_{film}$) and tensile strain (when $a_{substrate} > a_{film}$)

(102) plane of diffraction as shown in Fig. 8a, b, respectively. The full-width half maximum (FWHM) values from symmetric scan (002) of GaN grown at 715 °C, 730 °C, 745 °C and 760 °C are 994, 564, 948 and 944 arcsec, respectively while from the asymmetric scan (102), FWHM values are estimated to be 1694, 1151, 1795 and 1761 arcsec, respectively [32]. The peak broadening of ω-scans is mainly attributed to the presence of dislocations in epitaxial films. The dislocations are abrupt alterations in the systematic ordering of atoms along a dislocation line in any crystal lattice. The lines are characterized by the Burgers vector b, which describes the unit slip distance in terms of magnitude and direction. There are broadly two types of dislocations (Fig. 9). When an extra plane of atoms is introduced into an existing part of a crystal lattice, it is said to be an edge dislocation. Thus, the part of crystal lattice having extra atoms would be under compressive stresses, while the part with the correct number of atoms would be under tensile stresses.

And, when the planes amend with respect to each other due to shear, it is defined as screw dislocations [33]. The Burgers vector ($\bar{b}$) is perpendicular to the dislocation line in edge type while in screw type, $\bar{b}$ is parallel to the dislocation line [34]. Thus, they have a certain impact on growth kinetics and further on the structural as well as optoelectrical properties which will be now discussed in this section.

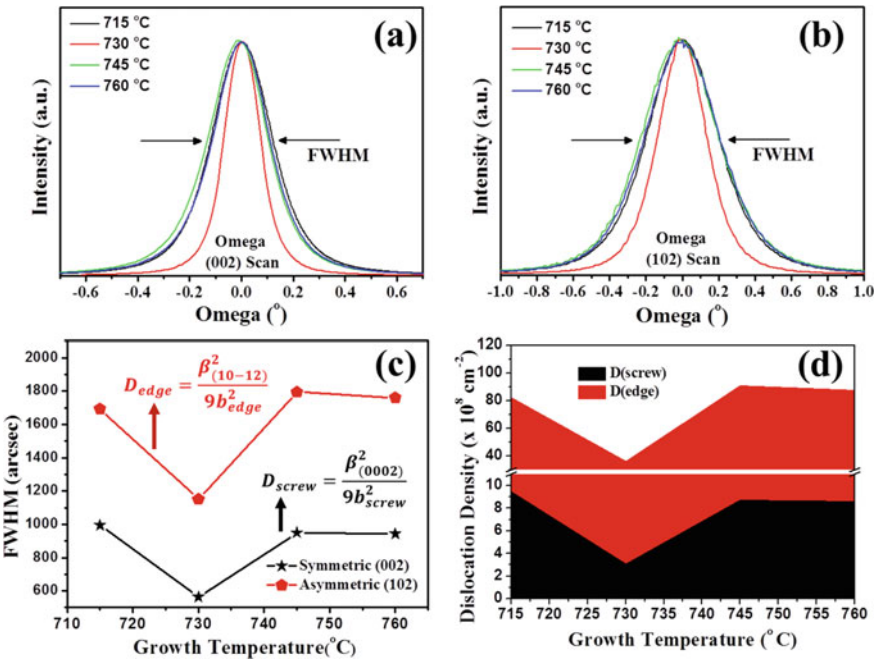

Fig. 8 The HRXRD omega scans along **a** (002) plane of diffraction and **b** (102) plane of diffractions; **c** a couple of profiles comparing the FWHM values against growth temperature; **d** variation in dislocations density with varying growth temperature

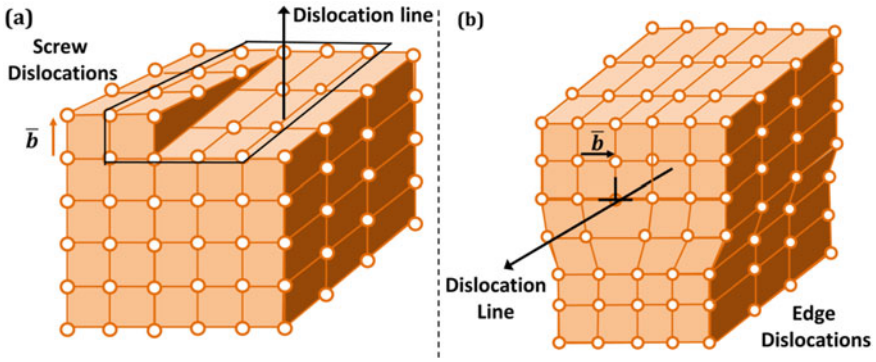

Fig. 9 The demonstration of **a** screw and **b** edge dislocations in a crystal lattice

A comparative FWHM plot of both symmetric and asymmetric scans is presented in Fig. 8c. The determined FWHM values are observed to be lowest in GaN epitaxial film grown at an optimum growth temperature of 730 °C which indicates that it contains minimum threading dislocations (TD). The total TD density can be quantified by summing the separate components of the screw (D_{screw}) and edge (D_{edge}) dislocations which are given by the following equations [35]:

$$D_{\text{screw}} = \frac{\beta^2_{(0002)}}{9b^2_{\text{screw}}} \tag{3}$$

$$D_{\text{edge}} = \frac{\beta^2_{(10-12)}}{9b^2_{\text{edge}}} \tag{4}$$

where β is FWHM (in radians) measured from (0002) and (10–12) plots of HRXRD ω-scans and b is the Burgers vector length ($b_{\text{screw}} = 0.5185$ nm, $b_{\text{edge}} = 0.3189$ nm). Both the screw and edge dislocation densities from (0002) and (10–12) plane reflections for all the samples are calculated and plotted in Fig. 8d. A reduction in TD density with a strain-relaxed lattice of GaN at an optimum growth temperature (730 °C) is ascribed to the single-crystalline, epitaxial GaN film growth.

Next, to evaluate the uniform atomic concentration and elemental distribution of the grown film, secondary ion mass spectroscopy (SIMS) depth profile was performed on GaN thin film grown at an optimized growth temperature of 730 °C. SIMS is a technique in which the surface of the sample is bombarded with ion beam resulting in the emission of secondary ions that can then be collected by a detector unit.

In Fig. 10a, a stable SIMS spectrum of Ga and N ions were clearly observed all the way through the film with no oxygen (below the detection limit) incorporation within the film. Further, the cross-sectional FESEM image (Fig. 10b) revealed the total thickness of 643 ± 10 nm which is highly in accordance with the thickness value obtained from SIMS analysis [32].

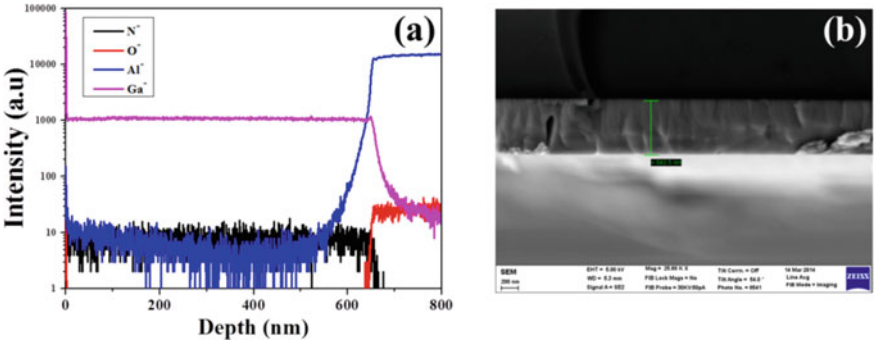

Fig. 10 **a** The SIMS depth profile and **b** FESEM cross-sectional view of grown GaN film at 730 °C

2.4 Morphological Examination of GaN Thin Films

The surface of a thin film plays a key role in determining the performance of any device since a better surface morphology implies good 2D growth and better interfaces for effective current transport. The surface of grown thin films has been probed closely by AFM to study the impact of growth temperature on its growth kinetics. AFM is a high-resolution microscopic technique having a resolution of fractions of a nanometer which is determined to be, nearly 1000 times better and precise than the optical diffraction limit. As shown in a schematic representation of its basic phenomenon in Fig. 11, AFM comprises a cantilever having a very sharp and nanoscale tip to scan over the sample's surface. As the tip approaches the surface, a confined space attractive force develops between the tip and the surface to deflect the cantilever towards the surface. However, as the cantilever approaches further close

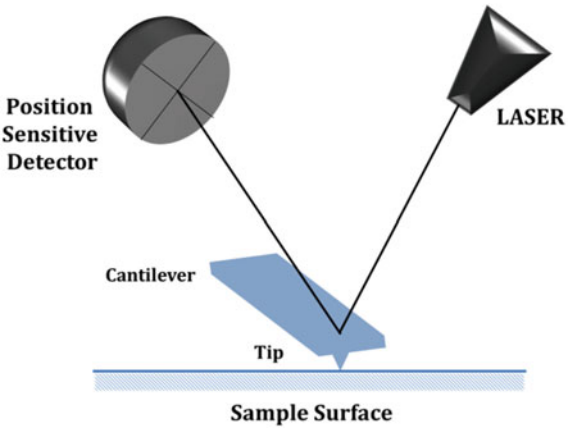

Fig. 11 The phenomenon behind AFM imaging technique

to the surface, such that the tip comes in contact with it (contact-mode), an increasingly repulsive force develops and dominates the cantilever to deflect away from the surface. These deflections and deviations are tracked using a position-sensitive photodiode (PSPD). Thus, when AFM tip passes over an elevated surface feature, it results in a subsequent deflection in cantilever which is recorded by the PSPD.

Finally, an accurate topographic map of the surface features can be achieved by maintaining a constant laser position via a feedback loop to control the height of the tip. Figure 12a–d shows the AFM images of respective GaN films at different growth temperatures. It was witnessed that surface morphology of GaN grown at a lower temperature of 715 °C is relatively smoother in addition to low pit density and pit depth which is associated with Ga-rich growth. The observed root mean square (r.m.s.) roughness of all of the samples were represented in Fig. 12e and it was observed to be minimum for GaN films (at 715 °C and 730 °C) grown under Ga rich condition (due to lower substrate temperature). It is clear from the aforesaid explanation that growth at 715 °C and 730 °C possesses smoother surface morphology with a reduced number of pits as compared to growth performed at comparatively higher temperatures of 745 °C and 760 °C. The vital parameters to arbitrate the surface quality include average pit density and average pit depth for all the grown GaN films which are compared in Fig. 12f and also tabulated in Table 3 for guiding towards optimized growth dynamics of GaN films. It was investigated that the formation

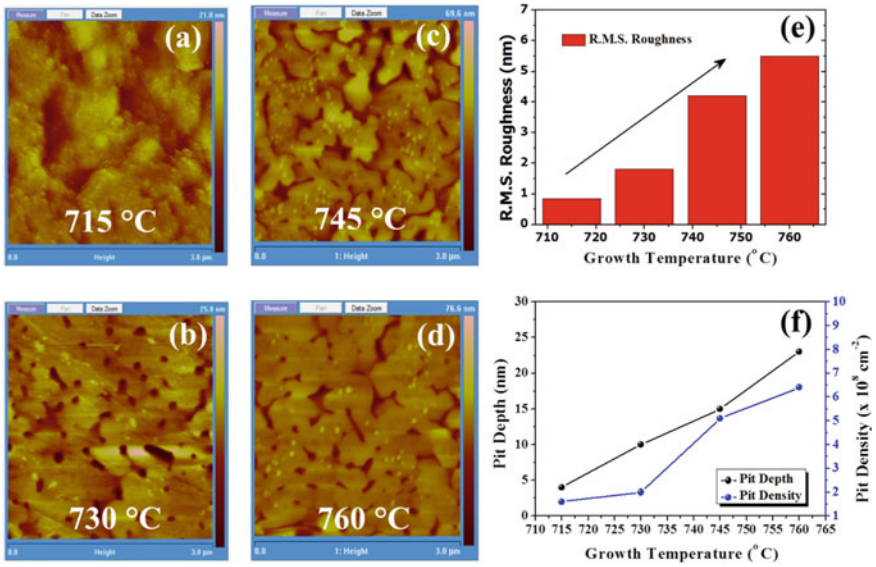

Fig. 12 **a–d** shows the AFM images of GaN grown on c-plane sapphire substrate at 715 °C, 730 °C, 745 °C and 760 °C, respectively (Reproduced from Ref. [32], with permission from the PCCP Owner Societies); **e** shows a histogram depicting trend of r.m.s. roughness with increasing growth temperature; **f** the couple of profiles represent the avg. pit depth and pit density variation versus growth temperature

Table 3 Values of average pit density, pit size, pit depth and r.m.s. roughness for grown GaN films

Growth temperature (°C)	Avg. pit density (cm^{-2})	Avg. pit size (nm)	Avg. pit depth (nm)	R.m.s. roughness (nm)
715	1.6×10^8	70–250 ± 10	4	0.84
730	2×10^8	140 ± 10	10	1.8
745	5.1×10^8	160 ± 10	15	4.2
760	6.4×10^8	160 ± 10	23	5.5

of surface pits are results of strain relaxation in the heteroepitaxy of GaN films, as the mismatch between grown film and the substrate is large (lattice mismatch in GaN/c-sapphire is ~13% and thermal expansion coefficient mismatch is ~33%). It has been observed that by reducing the substrate temperature we can improve the morphological quality, however the crystallinity may not be good. Both qualities should be compensated for efficient device performance.

2.5 Band Gap and Optical States Evaluation

The band gap and optical properties need to be analysed to evaluate the optoelectronic applicability of grown GaN films which were analysed by using photoluminescence (PL) spectroscopy. PL is a non-destructive luminescence technique used to probe the electronic structure of semiconducting materials. In PL spectroscopy, a light source with energy larger than or equal to the semiconductor band gap is shined on the requisite material to excite electrons from the valence band into the conduction band (Fig. 13).

After completing their lifetime, the electrons and holes recombine either directly from conduction to valence band or involving different excitonic levels existing in the energy band gap (Fig. 13). The emitted radiation is concentrated and focused by lenses to direct onto the monochromator where the light disperses into separate

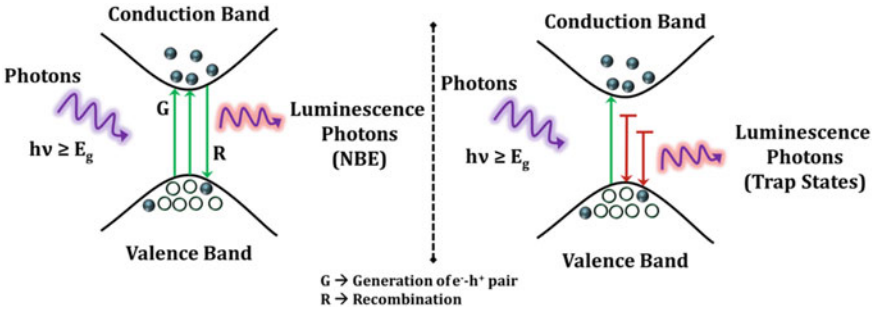

Fig. 13 A representation of the basic principle behind photoluminescence spectroscopy

wavelengths. Then, the dispersed light is recorded by a CCD-based detector and intensity versus wavelength plot is observed on a computer screen. Here, the CCD camera based detector is used over a photomultiplier tube because it allows simultaneous data collection over a large spectral range in every measurement. In this context, PL spectroscopy has been performed to examine the variation in optical properties of the GaN films with distinct growth temperatures. A sharp and narrow near-band-edge (NBE) emission peak has been perceived in the room temperature (RT)—PL spectra (shown in Fig. 14a) of the grown GaN films which are attributed to the radiative transition of an excited electron from the conduction band to valence band governing the band gap of the material. The NBE peak position for defect-free, bulk GaN film was reported at 3.41 eV [36]. Henceforth, a blue shift of 10, 8, 11 and 10 meV was witnessed upon closely observing the NBE emission of GaN grown at 715 °C, 730 °C, 745 °C and 760 °C, respectively [23]. The blue-shifted NBE emission value is comparable to the earlier reported stress-relaxed homo-epitaxial growths of GaN films [14]. The observed shift could be due to the Burstein–Moss effect or an indication of strain. Thus, detailed Raman studies were carried out to affirm if the shift was originated from strain/stress. Besides, the FWHM values of NBE emission can be used to ascertain the quality of GaN films which were evaluated to be 65, 45, 60 and 60 meV for GaN grown at 715 °C, 730 °C, 745 °C and 760 °C, respectively (Fig. 14b).

The acclaimed NBE peak and its narrow FWHM in film grown at 730 °C indicates that high-quality GaN has been grown at an optimized substrate temperature of 730 °C. Further, the defects mediated optical states present in between the energy band gap were analysed and presented as the defect band (DB) emission which basically evolves as yellow band (YB) emission in GaN. Figure 14b shows the intensity ratio of DB to NBE emission band and the defect-related band emission was perceived to be higher in GaN grown at 715 °C while it was significantly diminished for the growth carried out at 730 °C. The origin of YB emission is still not clear; various models

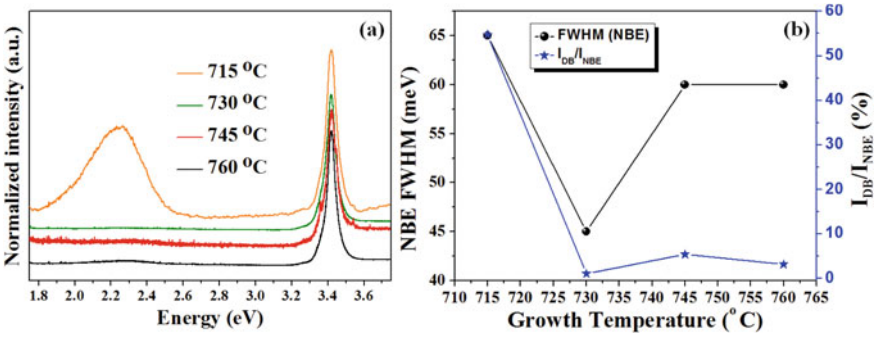

Fig. 14 **a** RT–PL spectra of GaN films grown at varied growth temperatures (Reproduced from Ref. [32] with permission from the PCCP Owner Societies); **b** the profiles demonstrates the FWHM of NBE emission band and intensity ratio of defect band to NBE emission band versus growth temperature

have been proposed to explain its source including transitions between shallow and deep levels of donors and acceptors [37, 38]. Although, it was reported that the gallium vacancies are majorly responsible for YB emissions, [37] in this study, a high YB emission at lower substrate temperature (715 °C) has eliminated the possibility related to gallium vacancies. So, the possible reason could be the transition from deep donor level to valance band minima. Notably, the intensity of YB emission from all other GaN films is lower than that grown at 715 °C and found to be minimal in GaN grown at 730 °C. The detailed RT-PL analysis illustrates that high-quality GaN film with good optical properties can be grown at optimized growth temperature which possess the least amount of defects as ascertained by the lower FWHM value of PL NBE peak [32].

2.6 *Stress Analysis in GaN Films*

The stress present in the grown GaN film greatly affects the quality of the thin film and thus needs to be quantified which has been performed via RS. Since Raman scattering technique is an inelastic light scattering process deriving vibrational molecular spectroscopy. In RS, a laser photon packet is scattered by a sample molecule that gains (or loses) energy during this process (Fig. 15). The amount of energy lost/gained can be observed as a change in the energy of irradiating photon. This energy change is characteristic of a particular bond in the molecule. RS can be assumed as a technique for developing a precise spectral fingerprint (unique to a particular molecule), which can gauge physical properties such as crystalline phase and orientation and intrinsic stress.

Hence, RS has been utilized here to scrutinize the correlation of defects minimization on stress relaxation in the grown GaN films. Usually, GaN forms a hexagonal wurtzite structure and according to group theory, single-crystalline GaN has eight sets

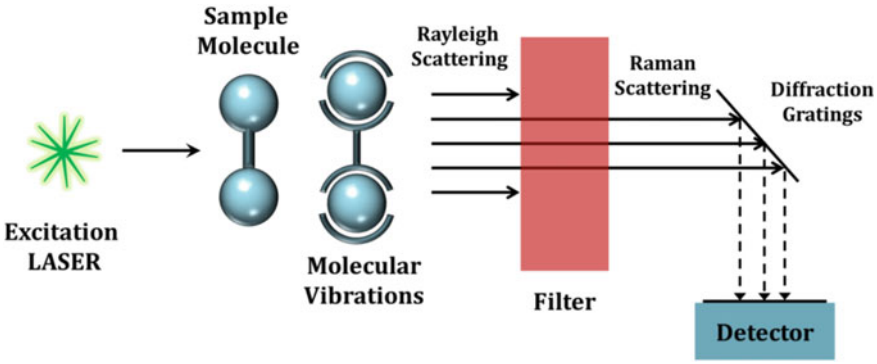

Fig. 15 The basic principle behind Raman spectroscopy

of phonon modes: $2A_1 + 2B_1 + 2E_1 + 2E_2$ [39]. Although in backscattering geometry, only E_2 (high) and A_1 (LO) are the two Raman active modes which appear due to atom displacement in c-plane and atoms relative motion along the c-axis, respectively [40]. Among them, the FWHM and intensity of E_2 (high) mode reveals the quality of the grown film and the shift in its wavenumber is allocated to quantify the stress/strain present in the GaN film [41]. So, we eminently observe on the wavenumber shift in the E_2 (high) phonon mode peaks under distinct growth temperatures. Figure 16a shows the RT—Raman spectra of the GaN films being discussed in this chapter. The frequency positions of E_2 (high) phonon modes are plotted in Fig. 16b with respect to growth temperatures and the values are found to be 568.97, 568.84, 569.12 and 569.47 cm^{-1} for GaN grown at 715 °C, 730 °C, 745 °C and 760 °C, respectively. Generally, the up-shift in E_2 (high) mode phonon frequencies ascribes to compressive stress while a down-shift represents the presence of tensile stress with respect to stress-free bulk GaN (567.6 cm^{-1}) [42]. Thus, the witnessed up-shift in the experimental data indicates that the stress present in all the samples is compressive in nature. Further, the obtained in-plane compressive stress (σ) is quantified by using the following equation [29]:

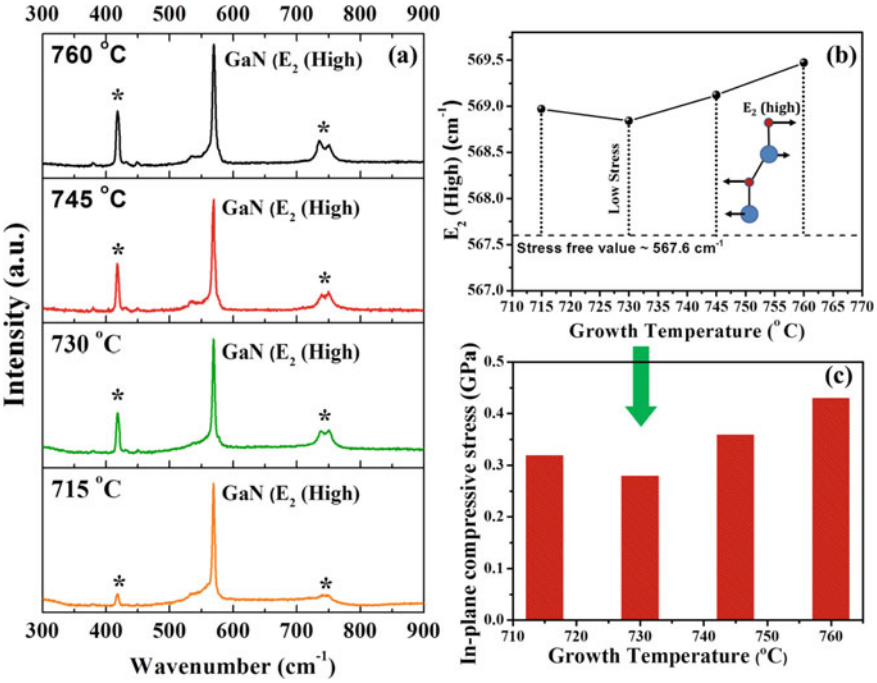

Fig. 16 **a** Micro-Raman spectra of GaN films grown on c-sapphire at different growth temperatures (Reproduced from Ref. [32] with permission from the PCCP Owner Societies); **b** the plot showing E_2 (high) modes of all the GaN films compared with the stress-free value to evaluate stress; **c** the variation in compressive stress versus growth temperature

$$\sigma = \Delta\omega/4.3\,\text{GPa} \tag{5}$$

where $\Delta\omega$ is the experimentally obtained value of Raman frequency shift from the stress-free position.

The quantified stress is found to be minimum (0.28 GPa) for GaN film grown at 730 °C while a higher stress values of 0.32, 0.36 and 0.43 GPa have been calculated for the GaN films grown at 715 °C, 745 °C and 760 °C, respectively [32]. Figure 16c represents a histogram plot revealing variation in the in-plane compressive stress with the growth temperature. These results from Raman analysis are in accordance with the HRXRD results where a compressive strain was realized in these hetero-epitaxially grown GaN films on c-sapphire. Next in this chapter, the role of multiple interlayers has been explored towards the better growth dynamics of GaN thin film on the sapphire substrate.

3 Epitaxial Growth of GaN/AlN Multilayered Heterostructure

Since the heterostructure growth leads to a large disparity in lattice constants and thermal expansion constants. Thus, the AlN interlayers are widely introduced as a buffer layer during the growth process of epitaxial GaN because of only a small mismatch of ~2.4% in the lattice parameters of AlN and GaN [43]. Amano et al. were among the first few researchers who introduced the concept of thin AlN interlayers for achieving thick crack-free AlGaN layers on GaN [44]. While inserting a multilayered AlN layer in between GaN, it can also effectively reduce the stress in the growing film along with reduced pit formation. This section of the chapter reveals the growth of GaN/AlN double-barrier heterostructure (DBH) by using PAMBE to scrutinize the role of multiple interlayers for epitaxial GaN growth and examine their structural progression in detail.

The growth of a multilayer heterostructure has been performed on thermally cleaned c-oriented sapphire substrate in the Riber compact-21 PAMBE system. Initially, the nitridation of sapphire substrate is carried out which produces few monolayers of AlN followed by the growth of GaN buffer layer over a thin Ga wetting layer (~1 nm) at lower substrate temperature. Then, AlN (30 nm)/GaN (70 nm)/AlN (30 nm)/GaN (70 nm) heterostructure was successfully grown on 200-nm-thick GaN epitaxial layer at a base chamber pressure of 1.3E–5 Torr using fixed RF plasma power of 500 W. The epitaxial GaN and AlN films were grown at a substrate temperature of 730 °C and 810 °C, respectively. A time-correlated stepwise growth phase diagram for the GaN/AlN multilayered heterostructure is provided in Fig. 17.

The impact of multiple interlayers on the surface of GaN during the growth has been monitored by in-situ RHEED technique which confirmed the 2D GaN over layer growth and the patterns observed at different zone axis are shown in Fig. 18. The sharp streaky 1 × 1 reconstructed RHEED patterns confirm the two-dimensional growth of

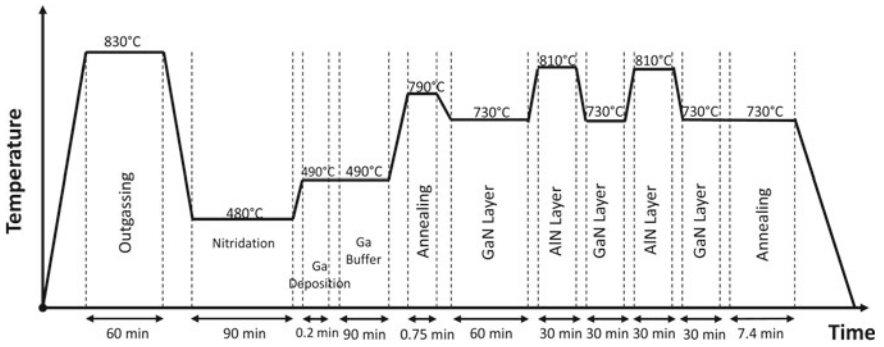

Fig. 17 A time-correlated growth processes involved for the GaN/AlN heterostructure

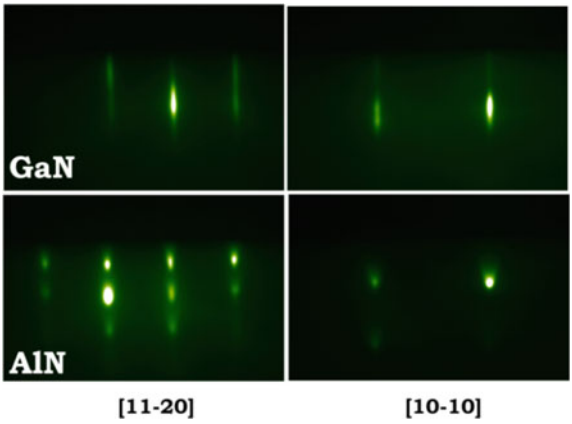

Fig. 18 The RHEED patterns of grown DBH along [11–20] and [10–10] azimuthal planes

GaN, while a three-dimensional (3D) growth mode was witnessed for the AlN layer. According to RHEED analysis, it is noteworthy to explain that both the epitaxial AlN layer was grown in 3D mode. It is because of the AlN layer thickness that has not reached up to a critical value, where the nucleation and strain relaxation occurs. Below this critical thickness, the layer will be in the three-dimensional mode of growth. However, in the case of GaN layer, the critical thickness was achieved resulting in a layer by layer growth along with the introduction of threading dislocations propagated from the AlN interlayer. A detailed morphological evolution of GaN film in accordance with threading dislocation will be explained later in this section.

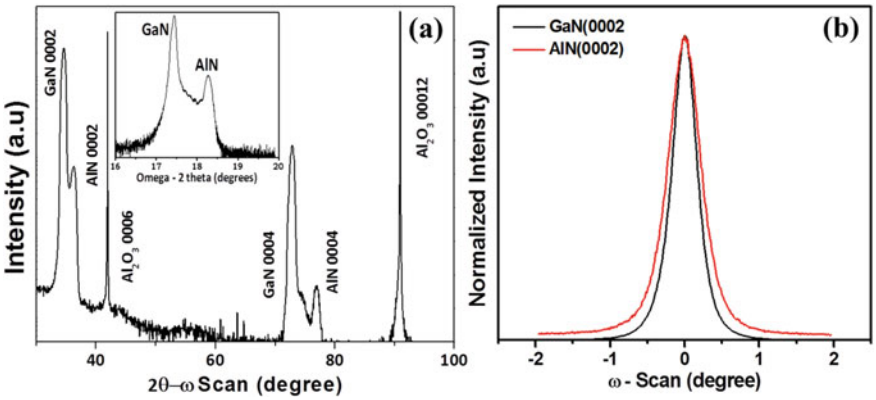

Fig. 19 **a** $2\theta - \omega$ scan of the GaN/AlN DBH (inset shows the $\omega - 2\theta$ scan), **b** ω-scans along symmetric (0002) plane of diffraction of GaN and AlN. (Reprinted from [45], Copyright 2017, with permission from Elsevier)

3.1 Evaluation of GaN Grown on Multiple AlN Interlayers in DBH

The HRXRD $2\theta - \omega$ scan of the grown GaN/AlN multilayered heterostructure is shown in Fig. 19a. A sharp and high-intensity X-ray diffraction peaks were observed along (0002) plane of diffraction of GaN and AlN located at 34.6° and 36.3°, respectively.

The presence of first-order (0002) and second-order (0004) plane of diffractions for both GaN and AlN unveils that high crystalline quality GaN and AlN layers have been epitaxially grown in the heterostructure. The peak position of GaN and AlN in the $\omega - 2\theta$ scan acquired along (0002) plane of diffraction is provided in the inset of Fig. 19a which is used to estimate the lattice constant (c) value of 5.1806 Å and 4.9456 Å, respectively. It was observed that the estimated lattice parameter values are close to the strain bulk GaN and AlN films [46, 47]. Detailed structural properties were further inspected through ω-scans wherein, the FWHM value of GaN and AlN along the symmetric plane of diffraction was evaluated to be 0.38° and 0.52°, respectively (Fig. 19b). Further, the TD density can be quantified by using Eq. (3) and the screw dislocation density evaluated for GaN film is 1.8 E9 cm^{-2} while for AlN film is 3.6 E9 cm^{-2}.

Further, the structural and morphological quality of grown multi-interlayered heterostructure was examined by high-resolution transmission electron microscopy (HRTEM). Figure 20a shows the cross-sectional TEM image revealing the interface analysis of the GaN and AlN layers in the heterostructure grown on c-plane sapphire substrate. The bottom-most GaN film was observed to be ~200 nm thick while the thickness of 30 nm and 70 nm are obtained for alternating AlN and GaN films, respectively. Moreover, the magnified HRTEM image of GaN and AlN interface in heterostructure is represented in Fig. 20b. It demonstrates a sharp and clear interface

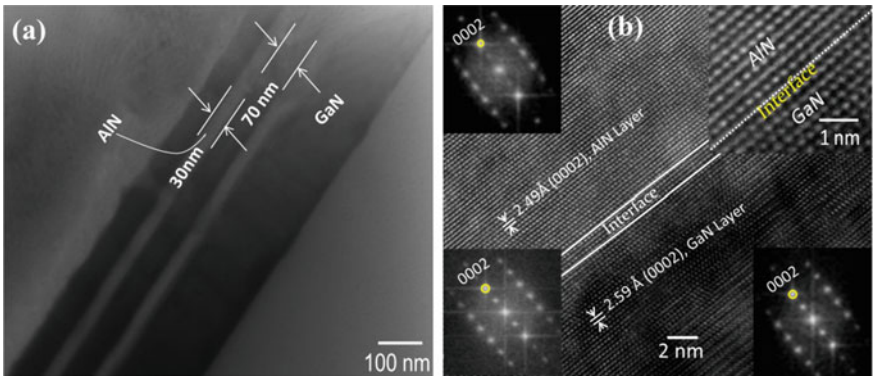

Fig. 20 **a** Cross-sectional TEM image of the grown GaN/AlN/GaN/AlN/GaN/Al_2O_3 heterostructure; **b** HRTEM images reveal the analysis of GaN and AlN interface. Inset top-right shows the magnified image of AlN/GaN interface, inset top-left and bottom-right represent the FFT pattern of selected area HRTEM image of AlN and GaN, respectively. Inset bottom-left displays the FFT pattern of AlN/GaN interface. (Reprinted from [45], Copyright 2017, with permission from Elsevier)

with a well-ordered crystal lattice of AlN and GaN in the grown heterostructure. Thus, a heterointerface without any cracking and minimum threading dislocations was successfully realized by optimizing the growth conditions. Besides, the HRTEM image in the top-right inset of Fig. 20b reveals the single-crystalline structure with epitaxial growth along (0002). The fast Fourier transform (FFT) images (top-left and bottom-right inset of Fig. 20b) are captured from the corresponding atomic-scale image of Fig. 20b, which governs the presence of c-plane orientation of AlN and GaN having an inter-planar spacing of 2.49 Å and 2.59 Å, respectively. The observed values are in good agreement with the hexagonal wurtzite structure of GaN and AlN films [46]. From the interface analysis via FFT image (bottom left inset of Fig. 20b), it is interesting to observe that the highly intense pattern reveals that the growth directions are consistently grown to be along c-axis, and therefore signifying an excellent configuration of AlN and GaN films.

The more detailed interface analysis and the elemental distribution in the heterostructure have been performed by SIMS as shown in Fig. 21. Sharp interfaces between GaN and AlN are clearly observed with a minimum metallic (Ga or Al) diffusion at the interface of the double-barrier heterostructure. Moreover, the depth profile of grown multi-interlayered heterostructure obtained via SIMS is in accord with the thickness of the different GaN and AlN layers as studied from HRTEM analysis.

This was also observed in the elemental mapping of the grown heterostructure (inset of Fig. 21) which reveals a clear distribution of different material layers. Moreover, it is clearly visible that the unintentional doping concentration through the heterostructure is below the detection limit. Such highly crystalline heterostructure with sharp interfaces and negligible elemental contamination are essential for enhanced current transport in devices.

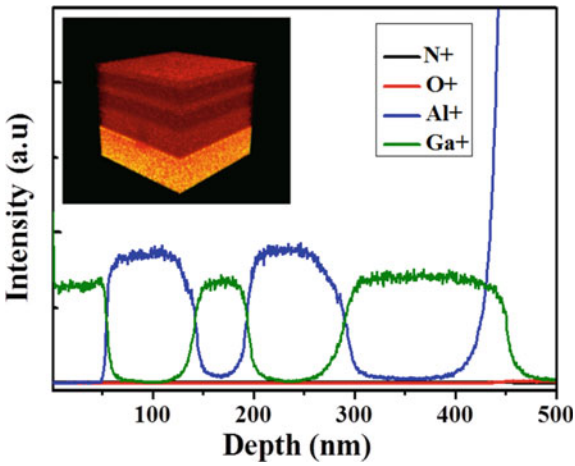

Fig. 21 The SIMS spectra of the grown multi-interlayered DBH; inset shows the elemental distribution mapping in the heterostructure

The morphological properties of grown multilayer heterostructure were also scrutinized by FESEM. Figure 22a shows the cross-sectional FESEM image of the GaN/AlN-based heterostructure grown on Al_2O_3 substrate. A sharp and uniform heterostructure has been affirmed by the insertion of multiple AlN interlayers as shown in the FESEM image. Inset of Fig. 22a represents the magnified image of the GaN/AlN DBH showing the intermediate AlN layers sandwiched between GaN layers. The thickness of 200 nm was observed for the epitaxial bottom GaN layer while the alternative AlN and GaN layers thickness were obtained to be

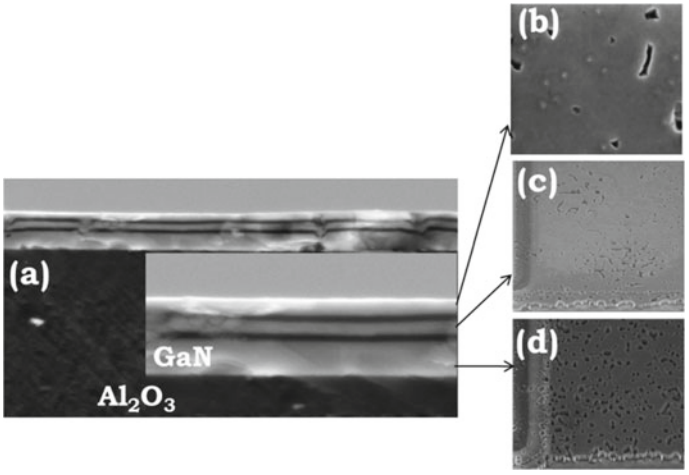

Fig. 22 **a** Cross-sectional FESEM image of the grown GaN/AlN DBH; inset shows the magnified image at the interface; **b**, **c** and **d** FESEM image of GaN film evolved at different growth regimes

30 nm and 70 nm, respectively. The FESEM cross-sectional images are consistent with TEM images. Furthermore, the morphological evaluation of GaN layers in the grown heterostructure and the effect of AlN layer insertion will be discussed below. Figure 22b, c and d represents the FESEM images of top, middle and bottom GaN layers, respectively. Interestingly, it is noteworthy that the bottom GaN layer (Fig. 22d) abides high pit density while from the middle to top GaN layer; the pit density was significantly decreased. Since the bottom GaN layer undergoes strain relaxation by the formation of threading dislocations due to the high lattice constant and thermal expansion coefficient mismatch. This leads to high pit generation on the growing GaN layer. However, the AlN layer insertion relaxes the lattice and obviously thereby, reduces the pit density in the middle GaN layer (Fig. 22c). The AlN multi-interlayered structure reduced the developed strain due to the low lattice mismatch between GaN and AlN (2.4%) as compared to the GaN/Sapphire (13%). It was observed that the pit density of the top GaN layer (Fig. 22b) has been considerably reduced by inserting another AlN layer. Though the thickness of the grown layers are in few tens of nm, still we can achieve high crystalline quality and minimize pit density on the surface of GaN layers to improve the growth dynamics of GaN on sapphire substrates via PAMBE.

4 Summary

The growth kinetics of GaN thin films is found to be strongly dependent on a key growth parameter, i.e. growth temperature. The impact of growth temperature on the induced stress with defect states in the heteroepitaxial GaN film grown on c-sapphire (0001) by PAMBE is discussed. An optimized temperature was employed to attain reduced defect, stress-relaxed GaN films and successfully grown a minimum compressively stressed thin film. The thermal stability of stress-relaxed GaN films has been explained at elevated temperatures, where thermal expansion of lattice occurred. The stress-relaxed GaN film pertain to a minimum threading dislocation density along with a highly intense, narrow NBE emission with reduced defects band related optical trap states. The stress relaxation induces enhancement in the topographical properties by reducing the pit density and surface roughness. This chapter would contribute significantly towards understanding how the growth conditions impact the growth kinetics for epitaxial GaN thin films. Furthermore, another step towards better growth dynamics is achieved by incorporating the multiple AlN interlayers between the substrate and epitaxial GaN thin film. This has been achieved by growing GaN/AlN/GaN/AlN/GaN DBH on c-plane sapphire substrate by PAMBE. The chapter illustrated the importance of multiple interlayers in terms of improvising the structural and morphological quality of GaN films. By utilizing this approach, good crystalline quality as well as sharp interfaces was clearly witnessed in GaN. The different GaN layers in the DBH were topographically probed by FESEM and it was revealed that the insertion of AlN layer can reduce the pit generation in the epitaxially grown GaN layer since the AlN layer relaxes the strain due to lattice mismatch

between substrate and GaN. The structure suggested in this study opens up the ways to fabricate cost-effective and highly efficient solid-state devices with few tens of nm dimensions. And, utilization of good quality GaN films/heterostructures creates a path towards numerous device applications which will be a highly feasible field of interest in the near future.

Acknowledgments We sincerely acknowledge Director CSIR-NPL, New Delhi, India for his perpetual encouragement and support. Neha would like to thank CSIR for providing financial support under CSIR-Research Associateship.

References

1. The Future Availability of Natural Resources, World Economic Forum (November 2014)
2. M. Henini, M. Razeghi, *Optoelectronic Devices: III Nitrides* (Elsevier Ltd., 2004)
3. A.G. Bhuiyan, K. Sugita, A. Hashimoto, A. Yamamoto, InGaN solar cells: present state of the art and important challenges. IEEE J. Photovolt. **2**, 276–293 (2012)
4. N. Aggarwal, S. Krishna, A. Sharma, L. Goswami, D. Kumar, S. Husale, G. Gupta, A highly responsive self-driven UV photodetector using GaN nanoflowers. Adv. Electron. Mater. **3**, 1700036 (2017)
5. S. Krishna, A. Sharma, N. Aggarwal, S. Husale, G. Gupta, Ultrafast photoresponse and enhanced photoresponsivity of Indium Nitride based broad band photodetector. Sol. Energy Mater. Sol. Cells **172**, 376–383 (2017)
6. A. Gundimeda, S. Krishna, N. Aggarwal, A. Sharma, N.D. Sharma, K.K. Maurya, S. Husale, G. Gupta, Fabrication of non-polar GaN based highly responsive and fast UV photodetector. Appl. Phys. Lett. **110**, 103507 (2017)
7. N. Aggarwal, S. Krishna, M. Mishra, K.K. Maurya, G. Gupta, Influence of active nitrogen species on surface and optical properties of epitaxial GaN films. J. Alloy. Compd. **661**, 461–465 (2016)
8. R.W. Chuang, S.P. Chang, S.J. Chang, Y.Z. Chiou, C.Y. Lu, T.K. Lin, Y.C. Lin, C.F. Kuo, H.M. Chang, Gallium nitride metal-semiconductor-metal photodetectors prepared on silicon substrates. J. Appl. Phys. **102**, 073110 (2007)
9. S.-W. Chen, H. Li, C.-J. Chang, T.-C. Lu, Effects of three-dimensional strain distribution on the performance of GaN-based light-emitting diodes on patterned sapphire substrates. Jpn. J. Appl. Phys. **58**, SC1036 (2019)
10. S. Mariana, Gc, G. Hamdana, F. Yu, K. Strempel, H. Spende, N. Yulianto, T. Granz, J.D. Prades, E. Peiner, H.S. Wasisto, A. Waag, Vertical GaN nanowires and nanoscale light-emitting-diode arrays for lighting and sensing applications. ACS Appl. Nano Mater. **2**, 4133–4142 (2019)
11. E. Di Russo, N. Cherkashin, M. Korytov, A.E. Nikolaev, A.V. Sakharov, A.F. Tsatsulnikov, B. Bonef, I. Blum, J. Houard, G. Da Costa, D. Blavette, L. Rigutti, Compositional accuracy in atom probe tomography analyses performed on III-N light emitting diodes. J. Appl. Phys. **126**, 124307 (2019)
12. N. Aggarwal, S. Krishna, S.K. Jain, A. Arora, L. Goswami, A. Sharma, S. Husale, A. Gundimeda, G. Gupta, Impact on photon-assisted charge carrier transport by engineering electrodes of GaN based UV photodetectors. J. Alloy. Compd. **785**, 883–890 (2019)
13. S. Krishna, N. Aggarwal, A. Gundimeda, A. Sharma, S. Husale, K.K. Maurya, G. Gupta, Correlation of donor-acceptor pair emission on the performance of GaN-based UV photodetector. Mater. Sci. Semicond. Process. **98**, 59–64 (2019)
14. L. Liu, J.H. Edgar, Substrates for gallium nitride epitaxy. Mater. Sci. Eng. R Rep. **37**, 61–127 (2002)

15. C.H. Hong, D. Pavlidis, S.W. Brown, S.C. Rand, Photoluminescence investigation of GaN films grown by metalorganic chemical vapor deposition on (100) GaAs. J. Appl. Phys. **77**, 1705–1709 (1995)
16. G. Antczak, G. Ehrlich, Jump processes in surface diffusion. Surf. Sci. Rep. **62**, 39–61 (2007)
17. S.D. Lester, F.A. Ponce, M.G. Craford, D.A. Steigerwald, High dislocation densities in high efficiency GaN-based light-emitting diodes. Appl. Phys. Lett. **66** (1995)
18. W. Qian, M. Skowronski, M.D. Graef, K. Doverspike, L.B. Rowland, D.K. Gaskill, Microstructural characterization of α-GaN films grown on sapphire by organometallic vapor phase epitaxy. Appl. Phys. Lett. **66**, 1252 (1995)
19. T. Yao, S.-K. Hong (Eds.), *Oxide and Nitride Semiconductors: Processing, Properties, and Applications* (Springer-Verlag, Berlin, Heidelberg, 2009)
20. J.C.R. Neugebauer, C.G. Van de Walle, Atomic geometry and electronic structure of native defects in GaN. Phys. Rev. B **50**, 8067–8070 (1994)
21. S. Nakamura, M. Senoh, S.-I. Nagahama, N. Iwasa, T. Yamada, T. Matsushita, H. Kiyoku, Y. Sugimoto, T. Kozaki, H. Umemoto, M. Sano, K. Chocho, InGaN/GaN/AlGaN-based laser diodes grown on GaN substrates with a fundamental transverse mode. Jpn. J. Appl. Phys. **37**, L1020–L1022 (1998)
22. H.Y. Shih, M. Shiojiri, C.H. Chen, S.F. Yu, C.T. Ko, J.R. Yang, R.M. Lin, M.J. Chen, Ultralow threading dislocation density in GaN epilayer on near-strain-free GaN compliant buffer layer and its applications in hetero-epitaxial LEDs. Sci. Rep. **5**, 13671 (2015)
23. S. Nakamura, M. Senoh, S.-I. Nagahama, N. Iwasa, T. Yamada, T. Matsushita, H. Kiyoku, Y. Sugimoto, InGaN multi-quantum-well-structure laser diodes with cleaved mirror cavity facets. Jpn. J. Appl. Phys. **35**, L217–L220 (1996)
24. S.C. Jain, M. Willander, J. Narayan, R.V. Overstraeten, III–nitrides: growth, characterization, and properties. J. Appl. Phys. **87**, 965 (2000)
25. T. Akasaka, T. Nishida, Y. Taniyasu, M. Kasu, T. Makimoto, N. Kobayashi, Reduction of threading dislocations in crack-free AlGaN by using multiple thin $Si_xAl_{1-x}N$ interlayers. Appl. Phys. Lett. **83**, 4140–4142 (2003)
26. T. Wang, Y. Morishima, N. Naoi, S. Sakai, A new method for a great reduction of dislocation density in a GaN layer grown on a sapphire substrate. J. Cryst. Growth **213**, 188–192 (2000)
27. J. Chaudhuri, J.T. George, D.D. Kolske, A.E. Wickenden, R.L. Henry, Z. Rek, Reduction of dislocation density in GaN films on sapphire using AIN interlayers. J. Mater. Sci. **37**, 1449–1453 (2002)
28. L. Zhang, J. Yu, X. Hao, Y. Wu, Y. Dai, Y. Shao, H. Zhang, Y. Tian, Influence of stress in GaN crystals grown by HVPE on MOCVD-GaN/6H-SiC substrate. Sci. Rep. **4**, 4179 (2014)
29. N. Aggarwal, S. Krishna, L. Goswami, M. Mishra, G. Gupta, K.K. Maurya, S. Singh, N. Dilawar, M. Kaur, Extenuation of stress and defects in GaN films grown on a metal-organic chemical vapor deposition-GaN/c-sapphire substrate by plasma-assisted molecular beam epitaxy. Cryst. Growth Des. **15**, 2144 (2015)
30. S. Krishna, N. Aggarwal, G.A. Reddy, P. Dugar, M. Mishra, L. Goswami, N. Dilawar, M. Kumar, K.K. Maurya, G. Gupta, Probing the correlation between structure, carrier dynamics and defect states of epitaxial GaN film on (11–20) sapphire grown by RF-molecular beam epitaxy. RSC Adv. **5**, 73261–73267 (2015)
31. S. Krishna, N. Aggarwal, M. Mishra, K.K. Maurya, M. Kaur, G. Sehgal, S. Singh, N. Dilawar, B.K. Gupta, G. Gupta, Epitaxial growth of high In-content $In_{0.41}Ga_{0.59}N$/GaN heterostructure on (11–20) Al_2O_3 substrate. J. Alloy. Compd. **658**, 470 (2016)
32. S. Krishna, N. Aggarwal, M. Mishra, K.K. Maurya, S. Singh, N. Dilawar, S. Nagarajan, G. Gupta, Correlation of growth temperature with stress, defect states and electronic structure in an epitaxial GaN film grown on c-sapphire via plasma MBE. Phys. Chem. Chem. Phys. **18**, 8005–8014 (2016)
33. F.K. Yam, L.L. Low, S.A. Oh, Z. Hassan, Gallium nitride: an overview of structural defects, in *Optoelectronics: Materials and Techniques*, ed. by P. Predeep (IntechOpen, National Institute of Technology, Norway, 2011)
34. W.F. Smith, *Principles of Materials Science and Engineering* (McGraw-Hill, 1996)

35. M.A. Moram, M.E. Vickers, X-ray diffraction of III-nitrides. Rep. Prog. Phys. **72**, 036502 (2009)
36. M.A. Reshchikov, H. MorkoC, Luminescence properties of defects in GaN. J. Appl. Phys. **97**, 061301 (2005)
37. J.C.R. Neugebauer, C.G. Van de Walle, Gallium vacancies and the yellow luminescence in GaN. Appl. Phys. Lett. **69**, 503–505 (1996)
38. D.M. Hofmann, D. Kovalev, G. Steude, B.K. Meyer, A. Hoffmann, L. Eckey, R. Heitz, T. Detchprom, H. Amano, I.I. Akasaki, Properties of the yellow luminescence in undoped GaN epitaxial layers. Phys. Rev. B: Condens. Matter **52**, 16702–16706 (1995)
39. A. Tabata, R. Enderlein, J.R. Leite, S.W. da Silva, J.C. Galzerani, D. Schikora, M. Kloidt, K. Lischka, Comparative Raman studies of cubic and hexagonal GaN epitaxial layers. J. Appl. Phys. **79**, 4137–4140 (1996)
40. M.S. Liu, L.A. Bursill, S. Prawer, K.W. Nugent, Y.Z. Tong, G.Y. Zhang, Temperature dependence of Raman scattering in single crystal GaN films. Appl. Phys. Lett. **74**, 3125–3127 (1999)
41. Z.C. Feng, W. Wang, S.J. Chua, P.X. Zhang, K.P.J. Williams, G.D. Pitt, Raman scattering properties of GaN thin films grown on sapphire under visible and ultraviolet excitation. J. Raman Spectrosc. **32**, 840–846 (2001)
42. V.Y. Davydov, Y.E. Kitaev, I.N. Goncharuk, A.N. Smirnov, J. Graul, O. Semchinova, D. Uffmann, M.B. Smirnov, A.P. Mirgorodsky, R.A. Evarestov, Phonon dispersion and Raman scattering in hexagonal GaN and AlN. Phys. Rev. B **58**, 12899–12907 (1998)
43. M.Z. Mohd Yusoff, A. Mahyuddin, Z. Hassan, Y. Yusof, M.A. Ahmad, C.W. Chin, H.A. Hassan, M.J. Abdullah, Plasma-assisted MBE growth of AlN/GaN/AlN heterostructures on Si (111) substrate. Superlattices Microstruct. **60**, 500–507 (2013)
44. H. Amano, M. Iwaya, N. Hayashi, T. Kashima, S. Nitta, C. Wetzel, I. Akasaki, Control of dislocations and stress in AlGaN on sapphire using a low temperature interlayer. Phys. Status Solidi (B) **216**, 683–689 (1999)
45. S. Krishna, A.G. Reddy, N. Aggarwal, M. Kaur, S. Husale, D. Singh, M. Singh, R. Rakshit, K.K. Maurya, G. Gupta, Enhanced current transport in GaN/AlN based single and double barrier heterostructures. Sol. Energy Mater. Sol. Cells **170**, 160–166 (2017)
46. O. Lagerstedt, B. Monemar, Variation of lattice parameters in GaN with stoichiometry and doping. Phys. Rev. B **19**, 3064–3070 (1979)
47. S. Iwama, K. Hayakawa, T. Arizumi, Ultrafine powders of TiN and AlN produced by a reactive gas evaporation technique with electron beam heating. J. Cryst. Growth **56**, 265–269 (1982)

High-Density Non-magnetic Cobalt in Cobalt Thin Films

B. N. Dev and Nasrin Banu

Abstract Volume contraction or higher density of any bulk material is usually obtained by placing the material under high-pressure conditions. For materials in the form of thin films, a compressed (higher density) state may be obtained during growth without the necessity of any external pressure. Here, we present cobalt thin films, grown on silicon, which show the formation of high-density layers within the film. Normal cobalt is ferromagnetic. Theoretical calculations have shown that cobalt can be non-magnetic when its density increases beyond a specific value. Formation of this high-density (HD) non-magnetic (NM) state of cobalt in cobalt thin films has been revealed and confirmed via various experiments. The non-magnetic state of cobalt is of great interest. Ferromagnetism and superconductivity are known to be antagonistic. When ferromagnetic normal cobalt becomes non-magnetic, it raises the possibility of being a superconductor. Indeed both experiments and theory have shown the high-density non-magnetic cobalt to be a superconductor. The cobalt films have grown in a trilayer structure—HDNM Co/normal Co/HDNM Co. Thus, it is a self-organized superconductor (S)/ferromagnet (F)/superconductor (S) hybrid structure. S/F/S hybrid structures have potential applications in areas like spintronics and quantum information technology.

1 Introduction

Cobalt has many important, strategic and irreplaceable industrial uses. Regarding its source, while it is widely scattered in the Earth's crust, what is of great interest is the presence of cobalt in the Earth's core where a high-pressure condition exists. Due to the existence of magnetism in the Earth's core, the studies of structure and

B. N. Dev (✉)
Department of Physics and School of Nano Science and Technology, Indian Institute of Technology Kharagpur, Kharagpur 721302, India
e-mail: bhupen.dev@gmail.com; bhupen.dev@phy.iitkgp.ac.in

N. Banu
Department of Condensed Matter Physics and Materials Science, Tata Institute of Fundamental Research, Homi Bhabha Road, Navy Nagar, Colaba, Mumbai 400005, India

S. Kumar and D. K. Aswal (eds.), *Recent Advances in Thin Films*, Materials Horizons: From Nature to Nanomaterials, https://doi.org/10.1007/978-981-15-6116-0_5

magnetism of cobalt, and 3*d* transition metals in general, at reduced volume (under high pressure) have been of great interest [1]. Bulk Co is ferromagnetic and it has a hexagonal close packed (hcp) structure under normal pressure and temperature. Structural phase transition to face-centred cubic (fcc) structure has been found to occur under high pressure. Theoretical calculations have shown that with decreasing atomic volume, which would occur under high pressure, the magnetic moment of Co decreases and the magnetic moment of a fcc Co nearly vanishes when the atomic volume is reduced by a factor of ~1.4 [2]. That is, this high-density state of Co is non-magnetic.

Structural transition from hcp to fcc was observed in experiments on bulk Co under high pressure [1]. A mixed phase of hcp and fcc was observed for the range of pressure of 90–150 GPa. Around 150 GPa, which corresponds to a density of ~1.4 times the normal density, a complete transition to fcc structure was observed. However, no measurements of the magnetic state of this high-density Co were made, perhaps for the apparent difficulty of such measurements under such a high-pressure condition.

Magnetism of bulk Co under high pressure has been recently investigated [3]. The magnetic moment was found to decrease with the increase in pressure. The complete extinction of ferromagnetism above 130 GPa in a mixed hcp-fcc phase was reported [3]. This work also reports that the fcc structure is theoretically predicted to lose magnetic moment at a lower pressure compared to hcp. There is some uncertainty (20%) in the values of the critical pressure for the extinction of magnetism for both phases; the pressure ranges are 70–120 GPa and 90–180 GPa for the fcc and the hcp phase, respectively. A pressure of 70 GPa corresponds to a density of about 1.25 times the normal density of Co. Non-hydrostatic pressure was also found to be important for loss of magnetism at a relatively lower pressure (lower density) as it appears to promote hcp to fcc transition.

Materials in the form of thin films may display unusual properties, which are not observed in their bulk form under identical or similar conditions. For example, bulk cobalt has a face-centred cubic (fcc) structure at temperatures above 417 °C [4] or under high pressure [1]. On the other hand, thin films of cobalt may exist in fcc structure at room temperature and at normal pressure, and their properties vary widely with respect to bulk cobalt [5]. Bulk Bi is superconducting under high pressure with a superconducting transition temperature, T_c, of about 8 K [6]. However, at ambient pressure, bulk Bi is superconducting with an extremely small T_c of about 0.5 mK [7]. On the other hand, at ambient pressure, thin films of Bi are superconducting with a T_c of about 5–6 K [8]. Thin films provide extra degrees of freedom, which may change the thermodynamic variables required to get certain phase transitions in thin films. Thus, thin films provide an interesting playground for exploring many unexpected properties of the corresponding bulk materials.

A thin-film approach was attempted for finding a high-density non-magnetic state of Co, as it was already known that polycrystalline thin films can produce compressive stress in a thin film [9] thereby producing a higher material density by mimicking a high-pressure-like situation. If a high-density state of Co is formed in the Co thin films, it would be straightforward to investigate its magnetic state by directly probing

the total spin moment using a technique like polarized neutron reflectivity (PNR). (It may be noted that X-ray magnetic circular dichroism (XMCD), the technique used for investigation of magnetism of Co under high pressure, cannot measure the total spin moment [3]). Experiments carried out on Co thin films have indeed revealed the existence of high-density non-magnetic Co, and the results were first reported in 2015 [10]. These results were further established in several subsequent investigations [11–13].

However, discovering a high-density non-magnetic state of Co in thin films was not the end goal. Magnetism and superconductivity and their antagonism are topics of enormous scientific interest. Ferromagnetic materials like 3*d* transition metals (Fe, Co and Ni) are not superconductors. A non-magnetic state of these materials could make them superconductors. Indeed a high-density non-magnetic state of bulk Fe, obtained under high pressure, was found to be superconducting with a $T_c = 2$ K [14]. So, a high-density non-magnetic state of Co may display superconductivity and it is easy to make the required measurements on thin films rather than in a high-pressure experiment. Indeed, experiments carried out on high-density non-magnetic Co in thin films have shown superconductivity with a T_c of about 5 K [15].

Experimental results on revealing the high-density (HD) non-magnetic (NM) state of Co in Co thin films, the film thickness dependence and the substrate dependence of the formation of the HDNM state and several other properties of the HDNM Co in Co thin films are presented below.

2 Revealing the High-Density Non-magnetic State of Co in Thin Films

X-ray reflectivity (XRR) and polarized neutron reflectivity (PNR) techniques provide the information about the material density as a function of depth in thin films. In addition, PNR provides magnetic moment density. XRR and PNR are non-destructive techniques. From these techniques, the depth-dependent density of the sample, averaged over the lateral dimensions of the entire sample, can be obtained with subnanometer depth resolution [16–18]. At each depth, there may be lateral density variation. That is indeed the case for the Co thin film discussed here (see Sect. 2.3). However, XRR and PNR provide only laterally averaged density at each depth. XRR and PNR involve measurement of the X-ray/neutron radiation reflected from a sample surface as a function of wave vector transfer **Q** (i.e. the difference between the outgoing and the incoming wave vectors). For specular reflectivity (R) (angle of incidence = angle of reflection), the magnitude of **Q** is $Q = (4\pi/\lambda)\sin\theta$, where θ is the grazing angle of incidence and λ is the wavelength of X-ray/neutron. The reflectivity as a function of wave vector transfer, $R(Q)$, is quantitatively related to the square of the Fourier transform of the depth profile $\rho(z)$ of the scattering length density (SLD) (the z-direction is normal to the film surface) [16–18]. For XRR, $\rho_x(z)$ is the electron SLD (ESLD), which is proportional to the electron density (or mass

density) depth profile. For PNR, $\rho(z)$ consists of nuclear and magnetic SLDs (NSLD and MSLD) such that

$$\rho^{\pm}(z) = \rho_n(z) \pm CM(z) \tag{1}$$

where $C = 2.9109 \times 10^{-9}$ Å^{-2} m/kA, and $M(z)$ is the magnetization (kA/m) depth profile whereas the suffix 'n' indicates nuclear [16–18]. The sign $+(-)$ is determined by the condition when the neutron beam polarization is parallel (opposite) to an applied magnetic field, and the corresponding reflectivities are $R^{\pm}$. ESLD in XRR and NSLD in PNR are proportional to material density. So the ESLD and NSLD depth profiles reflect the density depth profile.

The mass density depth profiles were obtained from XRR data by fitting a model $\rho(z)$ for which the computed reflectivity best fits the data. The reflectivity was calculated using the formalism of Parratt [19] and least-squares fitting was used to fit the data. The parameters of the model were adjusted to minimize the value of reduced χ^2—a weighted measure of goodness of fit [20]. To fit XRR data, different model structures consisting of layer(s) representing regions with different ESLD were considered [16–18]. The parameters of the model also included layer thickness and interface (or surface) roughness [16–18]. Similarly, PNR data were fitted to a model of $\rho^{\pm}(z)$, for which the computed reflectivity best fits the $R^{\pm}$ data. For this, different model structures consisting of layer(s) representing regions with different NSLD and MSLD were considered.

In this section, we discuss a thin cobalt film (25 nm nominal thickness), deposited in a high vacuum (low 10^{-7} mbar) by electron-beam evaporation method on a piranha-cleaned, HF-etched Si(111) substrate (a 100 mm diameter wafer). Then the cobalt film was taken out of the vacuum chamber. The exposure of the film to air, when taken out of the vacuum chamber, led to surface oxidation. XRR and PNR experiments were carried out for obtaining the mass density and the magnetic moment density depth profiles. Transmission electron microscopy (TEM) experiments were carried out to investigate crystallinity, strain corresponding to high-density condition and other characteristics of the high-density state.

2.1 X-ray Reflectivity Investigation to Explore High-Density Cobalt

A schematic of an X-ray reflectivity experiment is shown in Fig. 1. It should be noted that it is a specular reflection [the angle of reflection equal to the angle of incidence (θ)]. In a typical XRR experiment, the value of θ is very small (usually in the range of 0–2°). The reflected X-rays are collected under the specular condition as the angle of incidence (or equivalently, the value of $\mathbf{Q}$) is varied. $\mathbf{Q} = \mathbf{k}' - \mathbf{k}$, where $\mathbf{k}$ and $\mathbf{k}'$ are the wave vectors of the incident and the reflected X-rays, respectively. The magnitudes of the wave vectors are $k = k' = 2\pi/\lambda$, where λ is the wavelength

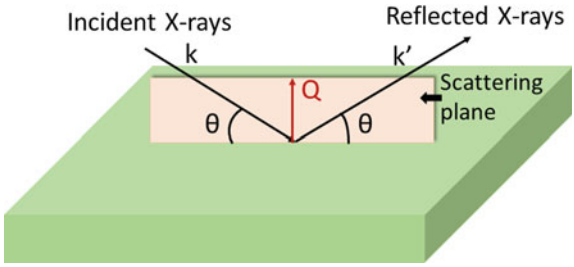

Fig. 1 Scattering geometry in an X-ray reflectivity experiment. The directions of **k**, **k′** and **Q** are shown by arrows. See text for details

of X-rays. The direction of **Q** is perpendicular to the surface of the sample and its magnitude is $Q = (4\pi/\lambda)\sin\theta$ (Fig. 1).

The results of the analysis of XRR data from the Co thin film sample mentioned above, obtained from measurements with Cu Kα X-rays ($\lambda = 1.54$ Å), are shown in Fig. 2. It is well known that a surface oxide layer is formed when a cobalt film, deposited in a vacuum chamber, is taken out and exposed to air. So, initially, a three-layer model—cobalt-oxide/cobalt/substrate was considered for calculating the

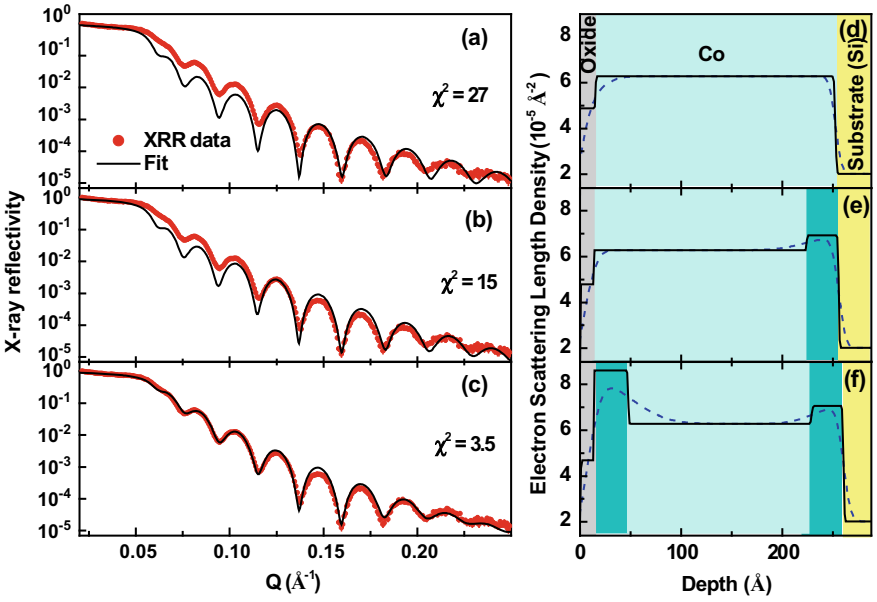

Fig. 2 X-ray reflectivity data (circles) and fits (solid lines) (**a**, **b**, **c**) considering three electron scattering length density (ESLD) models (**d**, **e**, **f**). (**d**) A uniform density normal Co layer, (**e**) a uniform density normal Co layer and a high-density (HD) Co layer at Co/substrate interface and (**f**) a uniform density normal Co layer and HD Co layers at both Co/substrate and Co/oxide interfaces. The ESLD depth profiles in (**d**), (**e**) and (**f**) correspond to fits in (**a**), (**b**) and (**c**), respectively. The solid line histogram depth profiles do not contain the effect of surface/interface roughness. The dashed line depth profiles include the effect of roughness. (From Ref. [12] supplementary materials)

Table 1 Layer structures and the depth-dependent parameters obtained from the analysis of XRR data from the Co film. The roughness values indicate the roughness at the upper interface of the corresponding layer. (From Ref. [12], supplementary material)

Layers	Thickness (Å)	ESLD (10^{-5} Å^{-2})	Roughness (Å)
CoO	13 ± 2	4.68 ± 0.10	7 ± 2
HD Co	35 ± 3	8.56 ± 0.20	8 ± 2
Co	183 ± 5	6.28 ± 0.10	24 ± 4
HD Co	34 ± 3	7.20 ± 0.15	13 ± 3
Si substrate	–	2.05 ± 0.05	5 ± 2

reflectivity and fitting the data. The calculation includes the contribution of surface and interface roughness. Figure 2a shows the reflectivity data and the fitted curve. The corresponding ESLD depth profile for this three-layer model is shown in Fig. 2d. The unacceptable fit in Fig. 2a indicates that the actual layer structure is different from that in Fig. 2d. The fit improves (Fig. 2b) when a thin layer at the Co/Si interface region, with a density higher than that of normal Co (Fig. 2e), is allowed. The best fit (Fig. 2c) is obtained when the model includes two additional layers of materials, both with densities higher than that of normal Co, at the oxide/Co and Co/Si interfaces (Fig. 2f).

Rutherford backscattering spectrometry (RBS) experiments ruled out the possibility of the presence of any other elements that could be responsible for this high-density layers near the two interfaces [12, 21], establishing the identity of these high-density layers as high-density (HD) Co. The parameters obtained from the best fit of the XRR data are shown in Table 1, and the layer structure is schematically shown in Fig. 3. As discussed later, these HD Co layers are also non-magnetic (NM). Comparison of the ESLDs of the HD Co layers and normal Co provides the density of the upper HD Co layer as 8.56/6.28 or 1.36 times the density of normal Co. The density of the lower HD Co layer is 7.20/6.26 or 1.15 times the density of normal Co. As discussed in Sect. 2.3, the HD Co has fcc structure.

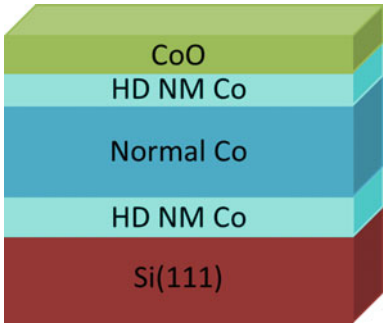

Fig. 3 The layer structure in the sample, as obtained from XRR and PNR results, is shown schematically

2.2 Polarized Neutron Reflectivity (PNR) Analysis

A typical PNR experimental geometry is schematically shown in Fig. 4. It is similar to that of X-ray reflectivity except for the fact that a neutron has a magnetic moment, which can be aligned in the desired direction. Two alignment conditions—parallel and antiparallel to a magnetic field (H) applied to the sample—are used in PNR experiments. Reflectivity is measured for each alignment.

PNR experiments were carried out on the same sample as the one used in XRR experiment using the sole neutron reflectometer available in India at DHRUVA, Bhabha Atomic Research Centre, Mumbai, India [22]. The results are shown in Fig. 5. Figure 5a shows, from a theoretical work, how the magnetic moment of Co

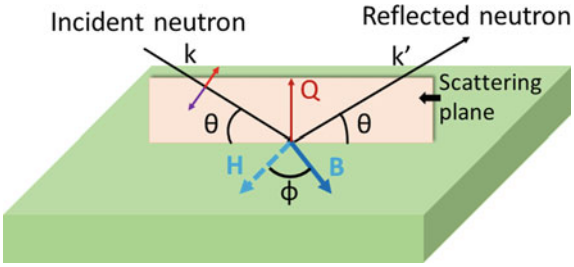

Fig. 4 The scattering geometry in a PNR experiment. **H** is the applied magnetic field in the sample plane. **B** is magnetic induction, which may have an angle with **H**. The directions of **k**, **k**′ and **Q** are shown by arrows, as in X-ray reflectivity. The magnitude of **Q** is $(4\pi/\lambda)\sin\theta$, λ being the wavelength of neutrons. The short arrows on the incident beam indicate the neutron beam polarization

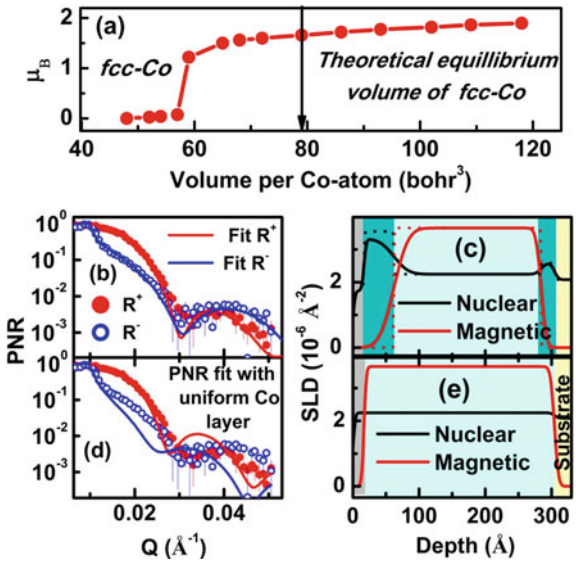

Fig. 5 **a** Theoretical prediction of magnetic moment (μ_B) variation with atomic volume of fcc Co. **b** PNR data (filled and open circles) and fits (solid lines) considering nuclear and magnetic scattering length density (NSLD and MSLD) models shown in (**c**), which corresponds to HD Co layers at interfaces. **d** PNR data and fits considering the NSLD and MSLD models corresponding to a uniform density of normal Co, shown in (**e**). Solid line depth profile includes the effect of surface/interface roughness, while the dotted profile does not. (From Ref. [12])

in the fcc structure changes with decreased atomic volume (increased mass density) of Co. The equilibrium volume of both hcp and fcc Co is 78.27 bohr^3/atom [2], as marked by an arrow in Fig. 5a. According to Fig. 5a, the magnetic moment is expected to nearly vanish at 57 bohr^3/atom, which corresponds to a mass density of about 1.37 times the normal density of Co. PNR data and two different fits are shown in Fig. 5b, d for the nuclear SLD (NSLD) and magnetic SLD (MSLD) profile models shown in Fig. 5c and e, respectively. A uniform NSLD and MSLD depth profile for normal Co, as shown in Fig. 5e, does not fit the PNR data (Fig. 5d) over the entire Q-range, suggesting that the uniform density depth profile of Co is unacceptable. The best fit for PNR data (Fig. 5b) is obtained from the NSLD/MSLD depth profile in Fig. 5c. The extracted parameters from the best fit are not shown here. However, some relevant values are discussed and compared below. Like ESLD in XRR, NSLD depth profile in PNR corresponds to a mass density depth profile. The NSLD value, as obtained from PNR for the mid-region of the depth profile in Fig. 5c, is $(2.26 \pm 0.07) \times 10^{-6}$ Å^{-2}. This NSLD value is consistent with normal Co (confer Table 2). For the Co layers near the oxide/Co and Co/Si interfaces, the NSLD values are $(3.30 \pm 0.15) \times 10^{-6}$Å^{-2} and $(2.70 \pm 0.14) \times 10^{-6}$ Å^{-2}, respectively. The possible alloys/compounds at these interfaces and their NSLD values are listed in Table 2. The observed NSLD values for the interfaces are inconsistent with these alloys/compounds. Considering also the results obtained from XRR, RBS and secondary ion mass spectrometry (SIMS) analysis [12, 23], it was confirmed that these layers at the interfaces are high-density Co layers (3.30/2.26 or 1.46 times and 2.70/2.26 or 1.19 times the density of normal Co). PNR results also show that the HD Co layer at both interfaces has nearly zero MSLD or magnetic moment density (Fig. 5c). This indicates that the HD Co is also non-magnetic. The normal Co layer in the middle shows a magnetization value of ~1250 kA/m [MSLD $(3.65 \pm 0.12) \times 10^{-6}$ Å^{-2}], which is marginally lower than its bulk value (~1400 kA/m). The difference in densities observed for HD Co layers in XRR and PNR experiment was attributed mainly to the fact that the PNR data were obtained from a sample area of 5×5 cm^2, while the XRR data were obtained from a sample area of about 1×1 cm^2. Some lateral non-uniformity, over a sample area of about 80 cm^2 (sample diameter 10 cm), is not unexpected.

It is desirable to have XRR and PNR data over a large range of Q values. While the range of Q values for XRR data (Fig. 2) is reasonably large, this range is small for the PNR data (Fig. 5). The low neutron flux at the DHRUVA reactor was inadequate for collecting PNR data over a larger Q-range. In order to obtain greater confidence in the extracted depth profile model, the PNR experiment was repeated with a better neutron source, at the Magnetism Reflectometer [24] at the spallation neutron source

Table 2 Calculated theoretical [17] values of scattering length density (SLD) of bulk Co, cobalt oxides and cobalt silicides for X-rays (ρ_x, ESLD) and neutron (ρ_n, NSLD) (From Ref. [12])

Element/Compound	Co	CoO	Co_3O_4	CoSi	$CoSi_2$
ρ_x (10^{-5} Å^{-2})	6.30	4.76	4.56	5.00	4.1
ρ_n (10^{-6}Å^{-2})	2.27	4.29	4.69	3.01	2.99

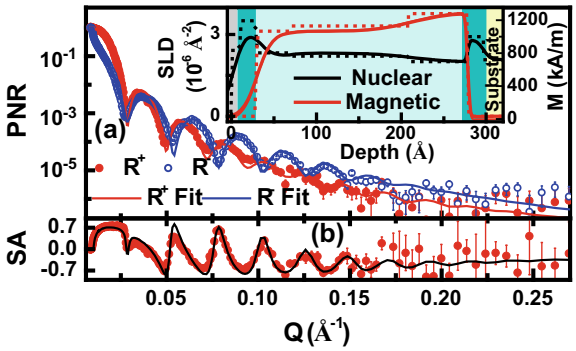

Fig. 6 **a** PNR data (circles) and the best fits (solid lines) corresponding to NSLD and MSLD depth profiles shown in the inset. SLD histograms are also shown in the inset as dashed lines. **b** SA data (circle) with the best fit (solid line) corresponding to the profiles in the inset. (From Ref. [12])

(SNS), Oak Ridge National Laboratory (ORNL), USA. This allowed collection of PNR data over a larger Q-range, which provides a higher spatial resolution. The much higher neutron flux at SNS compared to DHRUVA also allowed the use of smaller samples (1×1 cm^2) at SNS compared to those (5×5 cm^2) at DHRUVA. The results from the experiment at SNS are shown in Fig. 6. The NSLD and the MSLD [inset of Fig. 6a] depth profiles are similar to those in Fig. 5. These profiles also show higher NSLD with no ordered ferromagnetism in Co layers near the oxide/Co and the Co/Si interfaces. This again establishes that these two layers are high-density non-magnetic (HDNM) Co. Some differences in the details of the NSLD and the MSLD depth profiles are seen in the results obtained from the measurement at DHRUVA and those from SNS, ORNL. The reasons for the difference are twofold. First, that data from DHRUVA represent information averaged over about 5×5 cm^2 of the sample area, while those from SNS is averaged over an area of about 1×1 cm^2. The small sample in the second case was a piece from the former large-area sample. Some non-uniformity over the sample area is expected. Secondly, the higher Q-range covered at SNS provided better spatial resolution for a refinement of the parameters for fitting the PNR data. Both the experiments at DHRUVA and ORNL, in spite of the difference in the Q-ranges, endorse the existence of HDNM Co layers near both the interfaces.

Fitting the spin asymmetry (SA) data provides further confidence in the depth profile model. Spin asymmetry is defined as $(R^+ - R^-)/(R^+ + R^-)$, where $R^{\pm}$ are spin-dependent reflectivity. Figure 6b shows the SA data and the corresponding fit for the SLDs in Fig. 6a. Several other models for NSLD and MSLD depth profiles were considered [12]. However, these models do not fit the SA data. Thus all the three reflectometry results, XRR, PNR at DHRUVA and PNR at ORNL clearly confirm the existence of high-density (HD) non-magnetic (NM) Co at both oxide/Co and Co/substrate interfaces. The structure of the film, as obtained from XRR and PNR measurements and depicted in Fig. 3, may be written as CoO(2 nm)/HDNM Co(3 nm)/normal Co(18 nm)/HDNM Co(3 nm)/Si.

2.3 Transmission Electron Microscopy

Transmission electron microscopy (TEM) can throw light on the crystallinity, structure, lateral uniformity and strain state of a material. According to Ref. [9], a compressive (denser) state of material can form in a polycrystalline thin film. For the Co film in the discussion, TEM shows that the film is polycrystalline. The TEM image in Fig. 7 shows polycrystalline grains. Figure 7a shows a relatively higher density grain (dark), which is fcc, as the fast Fourier transform (FFT) of the image of this grain in Fig. 7b shows. The fcc (111) planar spacing within the grain is 1.83 Å. Just outside the grain boundary, the planar spacing is 2.06 Å. So, the lattice contraction within the dark grain is about 11%, amounting to a density increase of about 43% for isotropic contraction. Figure 7d, e shows dislocations and bent lattice planes at the grain boundary regions. These are effects of lattice mismatch well known in heteroepitaxial growth. Figure 7f illustrates the mechanism for the growth of compressively stressed grains [9].

Figure 7a indicates a lateral variation of density of the Co grains. Figure 7g shows a scanning transmission electron microscopy high-angle annular dark-field (STEM-HAADF) image, where grains of very high density look much brighter. That the brighter spots are indeed higher density Co grains compared to their surroundings is revealed by the Co–K-fluorescence map, shown in the inset. Intense fluorescence is observed from the bright grains. It has been mentioned earlier that XRR and PNR techniques provide laterally averaged density over the whole sample area for each depth. These techniques are not capable of providing information on lateral non-uniformity. TEM reveals the lateral non-uniformity of the high-density grains.

Figure 7h shows a cross-sectional TEM image of the sample, where the Co film and the Si substrate are easily identified. The FFT pattern from Si shows fcc structure as expected. The FFT pattern from the mid-depth region of the Co film shows hcp structure. Normal Co has hcp structure and is ferromagnetic. This is consistent with the XRR and PNR results, which show that, in the mid-depth region, Co has the density of normal hcp Co and it is ferromagnetic. The FFT from the region near the top oxide/Co interface shows fcc structure of Co. From XRR and PNR results, this region is HD Co and expected to be fcc according to theoretical calculations. The cross-sectional STEM-HAADF image in Fig. 7i shows the Co film bright. X-ray fluorescence yields of Si, Co and O along line ‘1’ in (i) are shown in Fig. 7j. From Fig. 7j, it is clear that Co fluorescence yield is higher near the Si/Co and Co/oxide interfaces compared to the yield from the mid-depth region. This is also consistent with XRR and PNR results, which show HD Co near these interfaces. Thus, we have a consistent picture of non-magnetic HD Co formation in the Co film from XRR, PNR and TEM results.

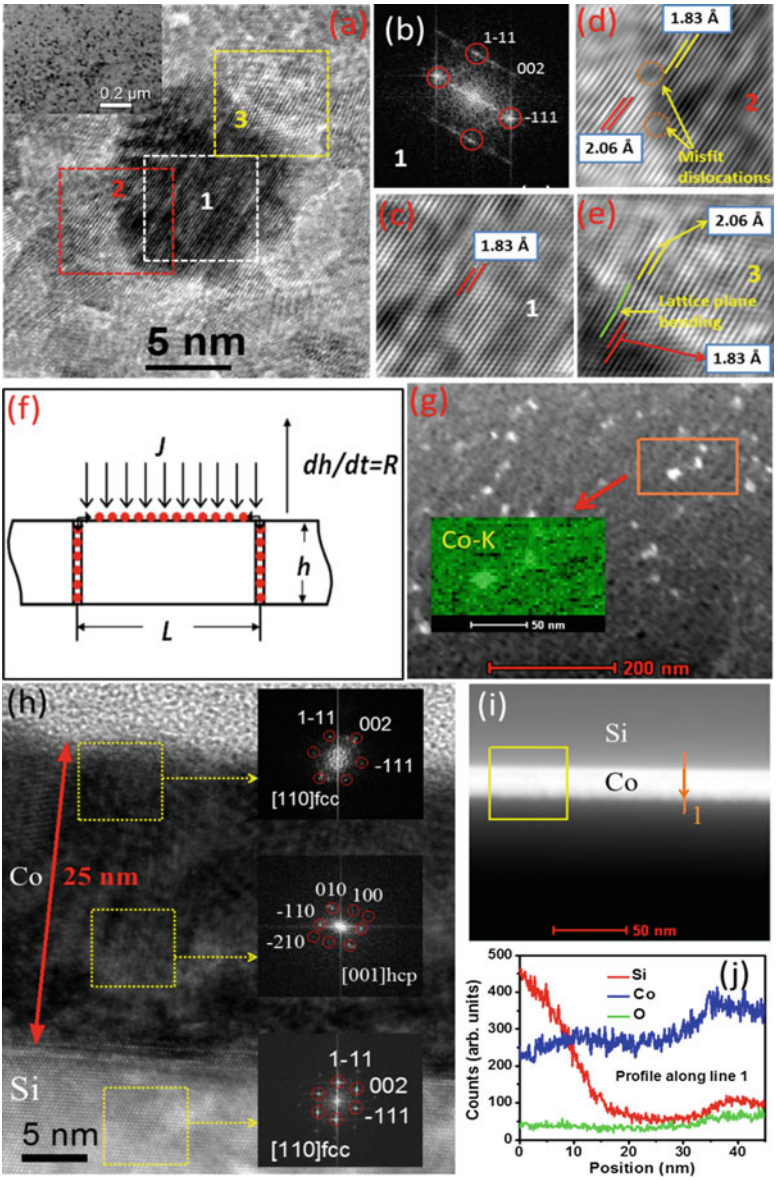

Fig. 7 **a** A high-resolution TEM plan view image. **b** FFT pattern from the marked part of the darker grain (region 1) in (**a**) shows fcc structure. **c** A high-resolution image from region 1 shows fcc (111) planes with a planar spacing of 1.83 Å indicating a lattice contraction corresponding to higher density. (**d**, **e**) High-resolution images of the grain boundary regions (regions 2 and 3 in (**a**)) of the high-density grain. The planar spacing is 2.06 Å just outside the high-density grain. **f** The mechanism of formation of high-density grains. **g** Plan view STEM-HAADF image. Inset: Co fluorescence map from the boxed region. **h** Cross-sectional TEM image showing the full thickness of the Co layer. FFT from the mid-depth region of the Co film shows hcp structure, while that from the top region shows fcc structure. **i** Cross-sectional STEM-HAADF image. **j** Drift corrected X-ray fluorescence yields of Si, Co and O along line '1' in (**i**). (From Ref. [12])

3 X-ray Absorption Behaviour of High-Density Cobalt

X-ray absorption spectroscopy (XAS) is a well-adapted technique for studying materials under high pressure [25, 26], which usually corresponds to high density. This method is sensitive to pressure-induced structural and electronic modifications in materials. The Co/Si thin-film system contains different densities and structures at different depths: CoO(2 nm)/HDNM Co(3 nm)/normal Co(18 nm)/HDNM Co(3 nm)/Si. This is a part of the sample discussed in Sect. 2. It is necessary to access different depths of the film and collect X-ray absorption data from that depth. Different depths of the film are accessed by removing thin layers of material from the top of the sample by ion beam sputtering.

3.1 Soft X-ray Absorption Spectroscopy

In situ depth-dependent soft X-ray absorption spectroscopy (SXAS) measurements on the Co thin film sample were carried out by sputtering the sample with an Ar^+ ion beam (5 keV, 40 μA, at 45°). Sputtering time was calibrated using a standard thin film sample of Co (50 nm) on a Si substrate. SXAS spectra were obtained by detecting the total electron yield [27].

SXAS results from the CoO(2 nm)/HDNM Co(3 nm)/normal Co(18 nm)/HDNM Co(3 nm)/Si sample [27] are shown in Fig. 8. SXAS measurements were carried out as a function of depth by sputtering the sample at a rate of about 0.4 Å/s. Sputtering time is proportional to depth. SXAS spectra were taken at Co L-edge. Pre- and post-edge normalized SXAS spectra, taken at different depths, are shown in Fig. 8. The depth values, which are obtained by converting sputtering time to depth, are shown alongside the spectra. A close scrutiny of the spectra reveals that there is a peak shift to a slightly higher energy for HD Co compared to normal Co. Figure 9a shows the derivative spectra from 33 to 48 Å depths, corresponding to HD Co, and from 58 to 96 Å depths, corresponding to normal Co. The inset in Fig. 9a clearly shows a peak shift (~0.3 eV) to higher energy for the HD Co. Figure 9b shows the L_{III} absorption peaks from the CoO, normal Co and the two HD Co regions. The peak shift in the HD Co, compared to normal Co, is clearly seen in Fig. 9b. Here, the HD Co is also non-magnetic, as known from PNR measurements. For non-magnetic Co, lower energy states in the *d* band will be filled with up-spin and down-spin. So the empty states available for the transition will be at higher energies. This would increase the L-edge energy. A shift of L-edge to higher energy has also been observed for other materials in high-pressure experiments [25, 26, 28–30], which additionally show a decrease in absorption cross section with increasing pressure or at higher densities.

For experiments on bulk samples whether the experiment is at high pressure or at normal pressure, the corresponding densities of the material are constant over the whole sample volume. In such cases, the measured absorption cross sections for different densities can be directly compared. In the present case of thin film,

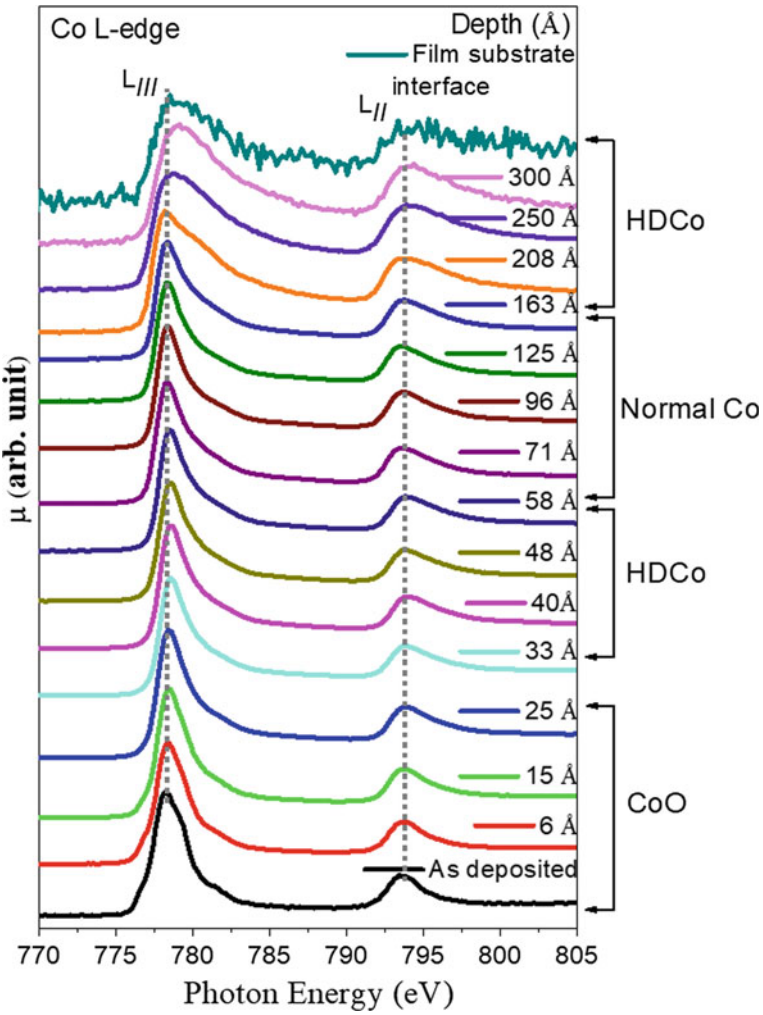

Fig. 8 SXAS spectra taken at Co L_{III}- and L_{II}-edges at different depths of the CoO(2 nm)/HD Co(3 nm)/normal Co(18 nm)/HD Co(3 nm)/Si sample. The layers corresponding to different depth regions are also marked on the right. Data from the top surface, marked as 'As deposited', and from various depths (6 Å, 15 Å, … 300 Å) are shown. (From Ref. [27])

the oxide state, HD state and normal state of Co—all exist in the same sample at different layers and the interfaces between layers are rather rough (confer Table 1) [12]. This, in addition to some variation in the sputtering yield from different depths, would introduce some uncertainties in comparing the intensities of the absorption peaks, which are proportional to absorption cross sections. That is why the intensities of the absorption peaks from the HD Co and normal Co regions have not been compared. However, variation in absorption cross section is expected. An alternative

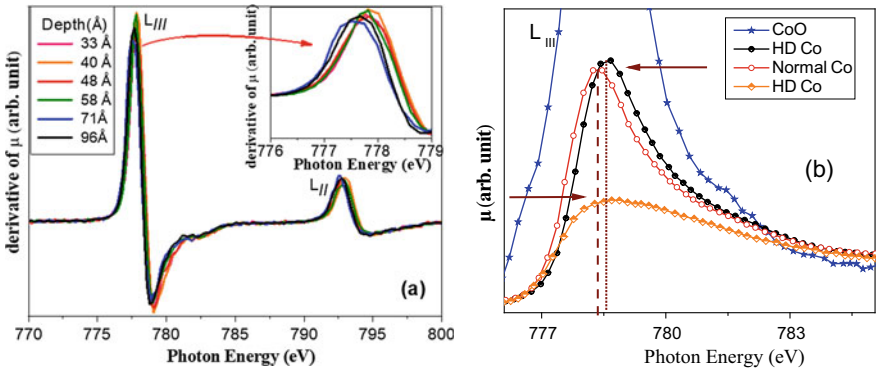

Fig. 9 **a** Derivative of SXAS pattern at the Co L-edges of the sample, following CoO removal, through the first HD Co layer up to the HD Co/normal Co interface (58 Å) and some depth into the normal Co. Inset shows the shift of the peak to higher energy in the HD Co region. **b** Enlarged view around the L_{III}-edge absorption peak from different layers. The vertical dashed line shows the peak position for normal Co, and the arrows show the shift in the absorption edge towards higher energy for HD Co compared to the normal Co. (From Ref. [27])

method, electron energy loss spectroscopy, was thus applied for the comparison of the absorption cross sections in Co of different densities. This is discussed in Sect. 3.2.

3.2 Electron Energy Loss Spectroscopy

Electron energy loss spectroscopy (EELS) experiments were carried out together with the TEM measurements, the results of which have been presented in Sect. 2.3. EELS results [27] are presented in Fig. 10. Figure 10a is the same as Fig. 7g. As there are lateral variations of density of Co, seen in this image, EELS measurements were made at various points—the brighter spots representing very high-density Co and the darker spots representing relatively lower density Co. EELS spectra from a dark spot (point 1, encircled red) and a bright spot (point 2, encircled blue within the rectangular box) are presented in Fig. 10b. The lower peak height in the spectrum from the brighter (higher density Co) spot indicates a lower absorption cross section compared to lower density Co. (It should be noted that the X-ray absorption spectrum and the electron energy loss spectrum are similar). This is consistent with the results of high-pressure XAS experiments on bulk samples of several materials, where a reduction in absorption cross section with increasing pressure (or increasing density) was observed [26, 28–30].

From Sects. 3.1 and 3.2, we notice that both the features, namely, a shift of an absorption edge towards higher energy and a decrease in absorption cross section at higher densities, observed in high-pressure experiments on bulk materials, have also been observed for high-density Co in the thin film. High-density Co has properties different from normal Co. We have already seen that HD Co is non-magnetic unlike

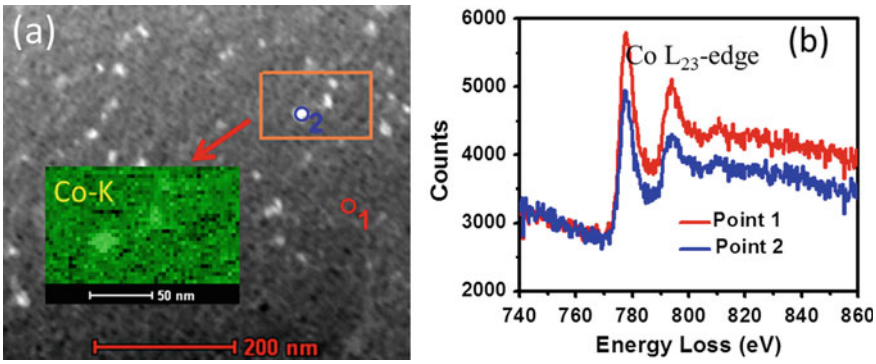

Fig. 10 **a** Plan view STEM-HAADF image. Co–K X-ray fluorescence map, obtained by energy dispersive X-ray (EDX) analysis from the boxed region, is shown in the inset. Intense fluorescence is seen from the denser (bright) grains. **b** EELS spectra from point 1 (red, from lower density Co grain) and point 2 (blue, from higher density Co grain) marked in (**a**). (From Ref. [27])

normal Co, which is ferromagnetic. Details of the SXAS experiments have also indicated different surface chemistry of high-density Co compared to normal Co [27].

4 Thin Films with Protective Coating

So far we have discussed the case of a Co film that was taken out of the vacuum chamber after growth, so that a surface oxide layer has grown upon exposure to air. In this section, we consider Co thin films with a protective gold coating. Before the Co thin film samples were taken out of the vacuum chamber, an ultra-thin (~2 nm) Au film was deposited on them, which has prevented oxidation of the surface of the Co thin films. Other conditions of growth were kept the same as the one discussed above. We first discuss a Co thin film with a nominal thickness of 25 nm in the structure: Au(2 nm)/Co(25 nm)/Si(111) [13]. The XRR and the PNR data (obtained at DHRUVA), theoretical fits and the corresponding ESLD, NSLD and MSLD depth profiles for this sample [13] are shown in Fig. 11. The extracted parameters from XRR and PNR results are shown in Tables 3 and 4, respectively.

The deviation between the values of the parameters (compare Tables 3 and 4), extracted from XRR and PNR data arises mainly for two reasons: (i) XRR results represent the parameter values averaged over an area of 1 cm^2 (sample size 1 × 1 cm^2), whereas the PNR results represent an average over 25 cm^2 (sample size 5 × 5 cm^2), and (ii) data obtained over a large Q-range in XRR provide better precision compared to the PNR data (Q-range smaller by a factor of about 5).

PNR experiment was repeated on a part of this sample (cut from the large wafer sample) at the SNS at ORNL. The results [13] are shown in Fig. 12 and Table 5.

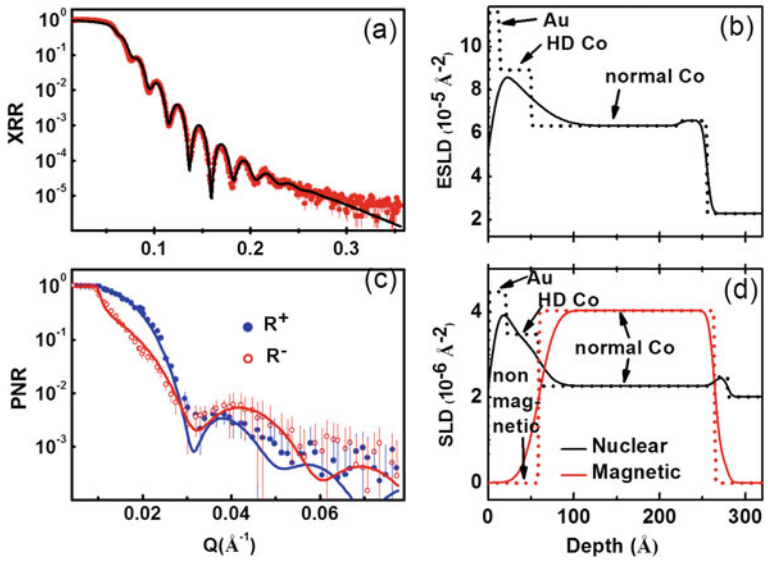

Fig. 11 **a** XRR data (circle) and the fitted curve (solid line). **b** The ESLD depth profile (solid line) that produces the best fit in (**a**). The dotted line (histogram) in (**b**) represents the depth profile without the interface roughness. **c** PNR data (circle) and the fitted curves (solid line). **d** NSLD (black) and MSLD (red) depth profiles (solid lines) that provide the best fits shown in (**c**). The dotted lines (histogram) in (**d**) represent the depth profiles without including the interface roughness. (From Ref. [13])

Table 3 Parameters, such as layers, their thicknesses, ESLDs and surface/interface roughness obtained from the analysis of the XRR data. (From Ref. [13])

Layer	Thickness (Å)	ESLD (10^{-5} Å^{-2})	Roughness (Å)
Au	13 ± 2	11.7 ± 0.30	10 ± 2
HD Co	35 ± 3	8.97 ± 0.20	12 ± 3
Co	170 ± 5	6.40 ± 0.30	20 ± 4
HD Co	32 ± 3	6.65 ± 0.35	5 ± 2
Si sub	–	2.08 ± 0.05	5 ± 2

Table 4 Different layers and their thickness, NSLD, MSLD and surface/interface roughness parameters, as obtained from the analysis of the PNR data. (From Ref. [13])

Layer	Thickness (Å)	NSLD (10^{-6} Å^{-2})	MSLD (10^{-6} Å^{-2})	Roughness (Å)
Au	17 ± 3	4.50 ± 0.25	0	10 ± 2
HD Co	35 ± 3	3.50 ± 0.20	0	11 ± 3
Co	195 ± 10	2.26 ± 0.12	4.04 ± 0.27	17 ± 5
HD Co	20 ± 5	2.50 ± 0.25	0	5 ± 2
Si sub	–	2.05 ± 0.05	0	5 ± 2

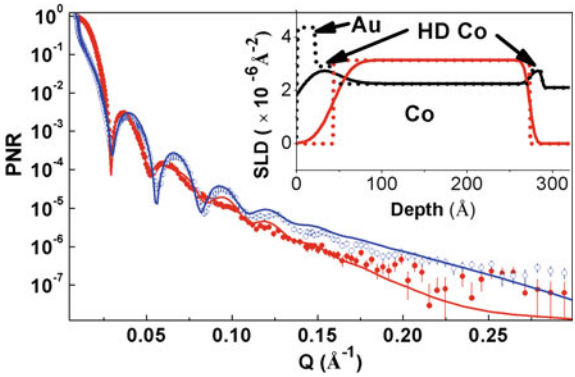

Fig. 12 PNR data (circle) and the fitted curves (solid line). Inset shows NSLD (black solid line) and MSLD (red solid line) depth profiles that provide the best fit to the data. The dotted lines (histogram) in the inset represent the depth profiles without including the interface roughness. (From Ref. [13])

Table 5 Different layers and their thickness, NSLD, MSLD and surface/interface roughness parameters, as obtained from the analysis of the SNS-PNR data. (From Ref. [13])

Layer	Thickness (Å)	NSLD (10^{-6} Å^{-2})	MSLD (10^{-6} Å^{-2})	Roughness (Å)
Au	21 ± 2	4.40 ± 0.20	0	22 ± 4
HD Co	22 ± 3	3.00 ± 0.30	0	25 ± 4
Co	230 ± 13	2.25 ± 0.18	3.20 ± 0.23	15 ± 2
HD Co	15 ± 3	2.76 ± 0.12	0	5 ± 1
Si sub	–	2.05 ± 0.10	0	3 ± 1

The deviation between the values of the parameters (compare Tables 4 and 5), extracted from the PNR data from DHRUVA and SNS, arises mainly for two reasons: (i) PNR results from SNS represent the parameter values averaged over an area of 1 cm^2 (sample size 1 × 1 cm^2), whereas the PNR results from DHRUVA represent an average over 25 cm^2 (sample size 5 × 5 cm^2), and (ii) data obtained over a large Q-range at SNS provide better precision compared to the PNR data at DHRUVA (Q-range smaller by a factor of about 5).

The above results confirm that similar HDNM Co layers, as observed in the case of the film with CoO at the top, are obtained even with the Au-capping layer [13]. Thus, Au-capping layer has no effect on the formation of the HDNM Co layers.

After knowing that a Au-capped Co layer also shows the formation of HDNM Co layers, investigations were carried out on a few other Au-capped Co films of different thicknesses, namely 22, 12 and 4 nm to study the dependence of HDNM Co growth on the thickness of the film [13]. All of these Co films were deposited on Si(111) substrate under the same conditions. For all the Co films with a protective Au coating investigated, from 25 nm down to 4 nm, HDNM Co growth was observed and the growth pattern is similar in all cases. A HDNM Co layer has grown on the Si substrate, normal Co has grown on this HDNM Co, and on top of the normal Co again, a HDNM Co layer has grown. This is the same pattern of growth observed where the topmost layer was CoO [12] instead of Au [13].

Compared to the other cases, it was noticed that for the 4 nm Co film, the MSLD value for the mid-depth region of the Co film, i.e. for normal Co, is much smaller [13]. It is indeed much smaller than the value expected for saturation magnetization of normal Co. Prior to the PNR measurements, a couple of samples (25 nm and 22 nm films) were investigated by superconducting quantum interference device (SQUID) magnetometry. An in-plane magnetic anisotropy was found in these samples, and the easy axis of magnetization was identified. During PNR measurement, the applied magnetic field (1.7 kOe) on the sample was along this direction. Having completed PNR measurements on all samples, the thinnest sample (4 nm) was investigated by SQUID and found that the in-plane easy axis of magnetization was different from the assumed easy axis based on SQUID measurement on the thicker samples. That means that during the PNR experiment, the magnetic field was not applied along the easy axis for the 4 nm Co film, and consequently, the applied field could not saturate the magnetization. This is apparently the reason for the observed low MSLD value for normal Co in the 4 nm film, the details of which are available in Ref. [13].

Results show that the capping of the Co film by Au has no significant effect on the formation of the HDNM Co layers within the Co thin film. As the surface oxidation (Sect. 2) or Au-capping occurred after the growth of the Co film had been completed, it is clear that the HDNM phase of Co has formed during the film growth and neither surface oxidation nor Au-capping has an effect on this growth. Also, irrespective of the film thickness, HDNM Co layers are always formed near the bottom and the top of the Co layer under the growth conditions used in these cases. A different growth condition may lead to a different layer structure in the film. Some indications of that have been obtained in recent XRR experiments carried out at the Indian beamline at the Photon Factory, Japan [31].

5 Substrate Dependence of Growth of HDNM Co

5.1 Co Films on SiO_2

In this case, a SiO_2 layer was first grown on Si(111) prior to Co deposition. But other than the substrate, the deposition conditions are exactly similar to the previous cases and this film also had a capping layer of Au as the samples discussed in Sect. 4. The as-grown nominal layer structure was Au(2 nm)/Co(25 nm)/SiO_2/Si(111) [13]. Here, the substrate SiO_2 is amorphous, while in the cases of Sects. 2, 3, and 4, the substrate is single-crystalline Si(111). XRR and PNR results from this sample are shown in Fig. 13 and Tables 6 and 7.

Comparing Fig. 13b, d, we notice that the major difference between the ESLD and the NSLD depth profiles appears in the SiO_2 film region. This is because the ESLD values for SiO_2 and Si (below the SiO_2 film) are comparable, while the NSLD value for SiO_2 is much larger than that of Si (compare Tables 6 and 7). The Co layer shows the usual MSLD, as expected from normal ferromagnetic hcp Co. MSLD from Au,

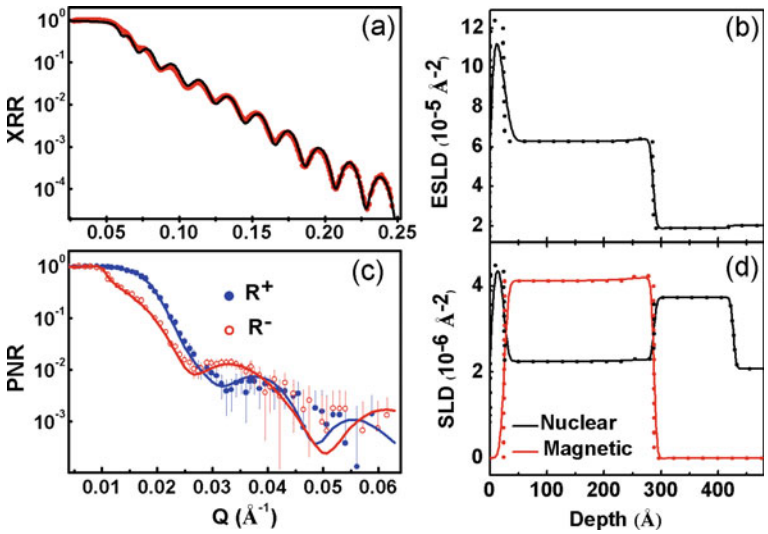

Fig. 13 **a** XRR data (circle, red) and the fitted curve (line, black). **b** The ESLD depth profile (solid line) that produces the best fit in (**a**). **c** PNR data (circle) and the fitted curves (solid line). **d** NSLD and MSLD depth profiles that provide the best fits shown in (**c**). The dashed line depth profiles (histogram) in (**b**) and (**d**) do not include the effect of roughness. (From Ref. [13])

Table 6 Parameters, such as layers, their thicknesses, ESLDs and surface/interface roughness values obtained from the analysis of the XRR data. (From Ref. [13])

Layer	Thickness (Å)	ESLD (10^{-5} Å^{-2})	Roughness (Å)
Au	23 ± 2	12.00 ± 0.40	7 ± 2
Co	260 ± 12	6.35 ± 0.30	12 ± 3
SiO_2	130 ± 8	1.92 ± 0.10	5 ± 2
Si sub	–	2.10 ± 0.10	5 ± 2

Table 7 Different layers and their thickness, NSLD, MSLD and surface/interface roughness parameters, as obtained from the analysis of the PNR data. (From Ref. [13])

Layer	Thickness(Å)	NSLD(10^{-6} Å^{-2})	MSLD(10^{-6} Å^{-2})	Roughness(Å)
Au	23 ± 3	4.48 ± 0.25	0	7 ± 2
Co	263 ± 10	2.24 ± 0.12	4.10 ± 0.27	11 ± 4
SiO_2	136 ± 7	3.70 ± 0.25	0	5 ± 2
Si sub	–	2.04 ± 0.05	0	5 ± 2

SiO_2 and Si layers is zero as they do not have a magnetic moment. The results show that no HDNM Co layers have formed within the Co film when the film is grown on SiO_2.

The experiment was repeated on this sample at the SNS, ORNL. The results are shown in Fig. 14 and Table 8.

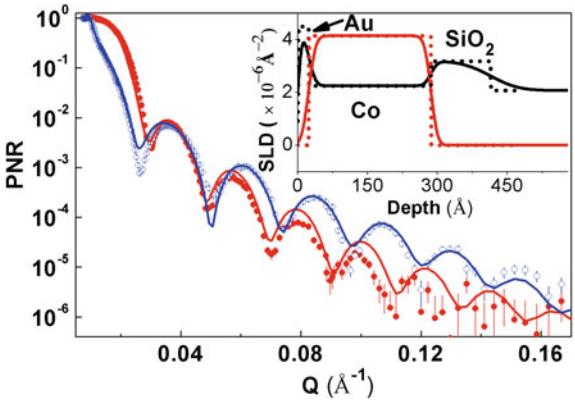

Fig. 14 PNR data (red and blue circles) and the fitted curves (*solid lines*). Inset shows the NSLD (black solid line) and MSLD (*red solid line*) depth profiles that provide the best fit to the data. Depth profiles without taking into account surface and interface roughness are shown by dashed lines (*histogram*). (From Ref. [13])

Table 8 Different layers and their thickness, NSLD, MSLD and surface/interface roughness parameters, as obtained from the analysis of the SNS-PNR data. (From Ref. [13])

Layer	Thickness (Å)	NSLD (10^{-6} Å^{-2})	MSLD (10^{-6} Å^{-2})	Roughness (Å)
Au	23 ± 1	4.50 ± 0.23	0	7 ± 2
Co	263 ± 8	2.25 ± 0.16	4.14 ± 0.25	12 ± 3
SiO_2	128 ± 5	3.18 ± 0.12	0	11 ± 3
Si sub	–	2.07 ± 0.10	0	25 ± 15

The results obtained from measurements over a small Q-range at DHRUVA are quite similar to those obtained from measurements over a large Q-range at SNS, ORNL. Here also, the results from SNS represent the values averaged over 1 × 1 cm^2, while those from DHRUVA represent an average over 5 × 5 cm^2, both samples being parts of the same original sample.

The results from the sample where the Co film is grown on SiO_2 show that the formation of HDNM Co strongly depends on the substrate. We have seen the formation of HDNM Co in all cases where the film was deposited directly on Si(111) substrate.

We notice that in all cases where HDNM Co has formed, it has formed in a HDNM Co/normal Co/HDNM Co structure. HDNM Co has shown superconductivity [15]. As normal Co is ferromagnetic, when the HDNM Co is superconducting, a superconductor(S)/ferromagnet(F)/superconductor(S) hybrid structure is formed.

5.2 [CoO/Co]$_2$/Si(111)

In this example of [CoO/Co/CoO/Co] layers on Si(111), the first Co layer was grown on clean single-crystalline Si(111) substrate and exposed to air thus forming a top oxidized Co layer forming a CoO/Co/Si(111) structure. A second Co layer was

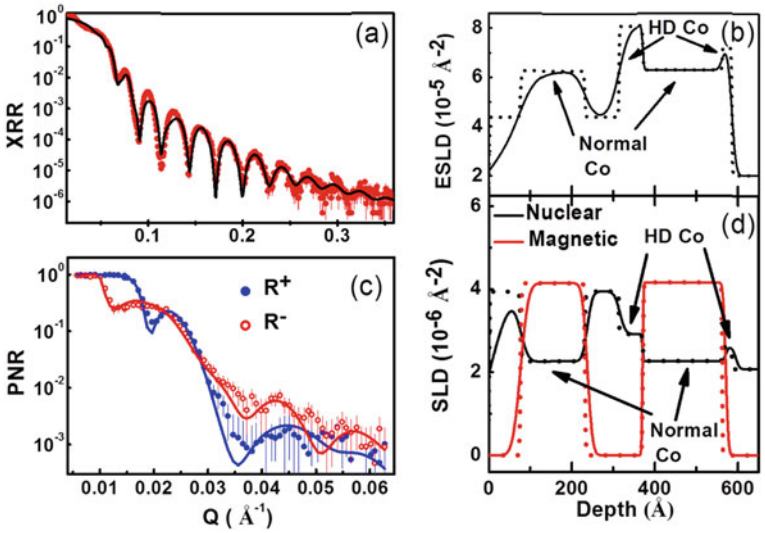

Fig. 15 **a** XRR data and the fitted curve. **b** The ESLD depth profile (solid line) that produces the best fit. The dotted histogram represents the profile without taking into account the surface and interface roughness. **c** PNR data (filled and open circles) and the fitted curves (solid lines). **d** NSLD (black solid line) and MSLD (red solid line) depth profiles that provide the best fit. The dotted histograms show the depth profile without taking into account surface and interface roughness. (From Ref. [13])

grown on amorphous CoO top layer forming a Co(2)/CoO/Co(1)/Si(111) structure [13]. So, the first Co layer, Co(1), was grown on crystalline Si(111) substrate and the second Co layer, Co(2), was deposited on amorphous CoO. Upon exposure to air, this became a CoO/Co(2)/CoO/Co(1)/Si(111) structure.This means, within the same sample, the substrate dependence of the HDNM Co growth was investigated. XRR and PNR results from this sample [13] are shown in Fig. 15a, c. Figure 15b shows the ESLD depth profile. It is clear that HD Co layers are formed in the Co(1) film grown on Si(111), just like the cases in Sects. 2, 3, and 4. There is no formation of HD Co in the Co(2) film. In the ESLD depth profile, the values of ESLD for the outer CoO and Co layers appear to be smaller than those for the inner CoO and Co layers. This is mainly the effect of much larger roughness of the outer CoO (72 Å) and Co (27 Å) layers (see Table 9). PNR results also confirm the presence of HDNM Co in the Co(1) film and the absence in the Co(2) film. The NSLD depth profile in Fig. 15d shows two HD Co layers at the interfaces of the Co(1) layer. The CoO layer on the HD Co layer shows a much higher NSLD value. Indeed it should be about 1.9 times the NSLD value of normal Co (see Table 2). The Co(2) film on CoO has an NSLD value of normal Co and it has no HD Co at its interfaces. The top CoO layer shows a smaller NSLD compared to the deeper CoO layer. This is an effect of larger roughness (see Table 10) of the top CoO layer. When the roughness effect is not included, the NSLDs for both the CoO layers are the same, as the dotted

Table 9 Parameters, such as layers, their thicknesses, ESLDs and surface/interface roughness obtained from the analysis of the XRR data. (From Ref. [13])

Layer	Thickness (Å)	ESLD (10^{-5} Å^{-2})	Roughness (Å)
CoO	76 ± 3	4.41 ± 0.2	72 ± 4
Co	155 ± 6	6.27 ± 0.14	27 ± 3
CoO	82 ± 5	4.41 ± 0.13	17 ± 2
HD Co	57 ± 4	8.09 ± 0.12	20 ± 2
Co	191 ± 6	6.32 ± 0.15	3 ± 1
HD Co	23 ± 2	7.21 ± 0.14	7 ± 2
Si sub	–	2.08 ± 0.05	8 ± 1

Table 10 Parameters, such as layers, their thicknesses, NSLDs, MSLDs and surface/interface roughness obtained from the analysis of the PNR data. (From Ref. [13])

Layer	Thickness (Å)	NSLD (10^{-6} Å^{-2})	MSLD (10^{-6} Å^{-2})	Roughness (Å)
CoO	75 ± 3	3.93 ± 0.14	0	41 ± 7
Co	161 ± 5	2.27 ± 0.12	4.14 ± 0.12	15 ± 2
CoO	78 ± 3	3.95 ± 0.13	0	9 ± 3
HD Co	54 ± 4	2.91 ± 0.12	0	10 ± 2
Co	200 ± 5	2.27 ± 0.11	4.16 ± 0.11	2.0 ± 0.5
HD Co	24 ± 2	2.6 ± 0.10	0	5 ± 1
Si sub	–	2.08 ± 0.05	0	6 ± 2

profile shows. The zero MSLD values in the HD Co layers of Co(1) show that they are non-magnetic. Small differences between XRR and PNR results are again due to averaging over small (XRR) and large (PNR) sample areas. From XRR and PNR results, it is clear that HD Co is not formed in the Co(2) film grown on CoO. So, Co films grown on the oxides, either SiO_2 (Sect. 5.1) or CoO, do not show any HD Co formation. This is consistent with earlier investigations where Co films were grown on various oxide substrates [32, 33].

Experiment on this sample was also carried out at the SNS, ORNL. The results are shown in Fig. 16 and Table 11. The results show the same feature, namely, the presence of HDNM Co layers at the interfaces of Co(1) film and the absence of HD Co in the Co(2) film.

The oxide substrates, namely SiO_2 and CoO, are amorphous. When the cobalt films are grown on Si, the local epitaxy apparently guides the growth and is responsible for the formation of HD NM cobalt layers. For growth on amorphous substrates, there is no local epitaxy and HD NM cobalt layers are not formed. In order to get a proper understanding of the HDNM Co growth, more studies under different growth conditions are necessary.

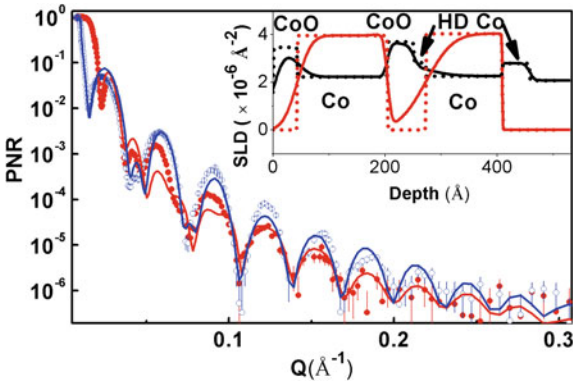

Fig. 16 PNR data [R^+ (*red circle*) and R^- (*blue circle*)] and the fitted curves (*solid lines*). The inset shows NSLD (*black solid line*) and MSLD (*red solid line*) depth profiles that provide the best fit. The dashed line profiles do not include the effect of roughness. (From Ref. [13])

Table 11 Parameters, such as layers, their thicknesses, ESLDs, MSLDs and surface/interface roughness obtained from the analysis of the SNS-PNR data. (From Ref. [13])

Layer	Thickness (Å)	NSLD (10^{-6} Å^{-2})	MSLD (10^{-6} Å^{-2})	Roughness (Å)
CoO	43 ± 7	3.46 ± 0.20	0	16 ± 5
Co	161 ± 9	2.22 ± 0.11	3.96 ± 0.15	20 ± 3
CoO	47 ± 8	3.69 ± 0.14	0	6 ± 2
HD Co	21 ± 5	2.83 ± 0.12	0	8 ± 3
Co	136 ± 11	2.26 ± 0.10	3.96 ± 0.16	38 ± 4
HD Co	48 ± 5	2.8 ± 0.13	0	2 ± 1
Si sub	–	2.08 ± 0.06	0	6 ± 2

6 Stability of the High-Density Co Layers

One may wonder if the high-density state of Co is stable or would relax to normal density over time. The first results of XRR and PNR measurements at DHRUVA reactor on high-density Co, discussed in Sect. 2, were reported in early February, 2015 [10] on the sample prepared in late 2014. The Co film was on a 100 mm Si wafer. Small pieces from this sample were cut and used for various experiments (PNR at spallation neutron source at ORNL, TEM, EELS, RBS, SIMS, SXAS [27]) over about four years. The high-density Co still did not disappear. The samples discussed in Sect. 4 were also prepared at the same time as that in Sect. 2, and experiments were carried out over a couple of years. All results indicate that high-density Co in the thin film is fairly stable. The stability of both high density as well as its non-magnetic state under moderate annealing temperature was also verified. PNR measurements were carried out at ORNL on annealed samples. Field annealing at 473 K for 30 min with 1T magnetic field, followed by PNR measurement at room temperature, did not reveal any significant change of the HDNM Co layers. As Co and Si are reactive, they would form cobalt silicide at a higher temperature. In order to avoid cobalt silicide formation, a higher annealing temperature was avoided. PNR measurements

at 70 K did not show any change of density or magnetic state of high-density Co [12, Supplementary material].

All these indicate that the high-density non-magnetic Co in thin films is quite stable.

7 Superconductivity and the Hybrid Structure

The Co film containing HDNM Co, discussed in Sects. 2 and 3, have been investigated for exploring superconductivity [15]. A four-probe measurement of resistivity has shown a superconducting transition with a T_c of about 5 K. When a magnetic field is applied, T_c shifts to lower values with increasing magnetic field—a clear characteristic of superconductivity—with a critical field of ~2.2 T. Point contact measurement also showed superconductivity with somewhat different parameters—a T_c of ~9 K and a critical field of ~3.5 T in both resistivity and conductance measurement. The higher value of T_c in point contact measurement is apparently a pressure-induced effect from making the point contact. Superconducting T_c was calculated within the BCS theory for fcc Co corresponding to the observed density of HD Co. It clearly shows the loss of magnetic moment as observed in experiments (HDNM Co). However, the estimated T_c was ~0.3 K. This calculation corresponds to hydrostatic pressure or uniform compression of the material. However, a uniform compression is not expected in a thin film. From the knowledge of heteroepitaxial growth of thin films on single-crystalline substrates, where a biaxial strain is usual, a biaxial strain has been introduced in the calculation. This shows a T_c of ~5 K, comparable to the observed value. In this case, phonon softening causes an enhancement of electron–phonon coupling leading to an enhancement of T_c.

Considering that HDNM Co is superconducting, the HDNM Co/normal Co/HDNM Co trilayer structure (Fig. 3) is a superconductor (S)/ferromagnet (F)/superconductor (S) hybrid structure. S/F/S structures [34] have applications in spintronics, quantum information technology and superconducting digital and quantum circuits [35]. S/F/S structures have also shown quantum phase transition [36]. The Co films discussed here represent self-organized S/F/S hybrid structures and offer themselves for further explorations for various other objectives.

More details of the results discussed here, including theoretical formalism, experimental techniques and analyses, on the high-density non-magnetic cobalt and its superconductivity [15] are available in Ref. [37].

8 HDNM Co/Normal Co/HDNM Co Growth Mechanism

In earlier experiments, where cobalt films were grown on various (amorphous) oxide substrates, no high-density non-magnetic cobalt was found. The absence of HD NM cobalt discussed in Sect. 5, when the films are grown on oxides, is consistent with

earlier results. For direct deposition of cobalt on silicon (after removal of oxide), local epitaxial growth of cobalt grains at the Co/Si interface, the consequent strain in these grains and the additional atomic diffusion into the grain boundaries [9] are apparently responsible for the growth of HD NM cobalt layer at the Co/Si interface.

While investigations of epitaxial growth of cobalt silicides on Si are abundant in literature [38, 39], investigations of Co growth on clean Si are rare. Such investigations have to be limited to below 375 °C, beyond which Co reacts with Si to form cobalt silicide [40]. Growth of very thin layers of Co on clean Si under ultra-high vacuum condition has been investigated, and grain growth has been observed although aspects of epitaxial growth, either local or global, are not available [41]. One may ask whether epitaxial growth is at all possible with the large lattice mismatch between Co and Si. It is definitely not impossible. Indeed epitaxial growth has been observed in many cases where large (up to 25%) lattice mismatch is involved [42] via coincident site epitaxy or tilted epitaxy [43]. For large lattice mismatched systems, epitaxy often occurs via coincidence site lattice matching. Epitaxial growth of fcc Co nanostructures on different planes of Al_2O_3, where large lattice mismatches are involved, has been observed [44].

For Co growth on oxides, the initial epitaxial grain growth would be absent. A tentative model of the HDNM Co/normal Co/HDNM Co trilayer structure growth is described below. Co has larger surface free energy compared to Si which would favour Co island growth on Si instead of a uniform layer growth. Lateral growth of islands into grains and diffusion of further deposited Co into grain boundaries produce compressed grains leading to HD Co. Following this, Co grows on Co layer, and no difference in surface free energy is involved. So, this Co is expected to grow as a uniform layer, although polycrystalline. Diffusion into grain boundaries is not prominent at this stage. Towards the end of the deposition process, apparently diffusion into grain boundaries is again responsible for the HD Co growth. This diffusion process can be influenced by growth at different vacuum conditions in the growth chamber. Co growth at a chamber pressure of 3×10^{-5} mbar has shown the absence of the top HD Co layer. This Co film, exposed to air, has shown Si/HD Co/normal Co/CoO structure [31]. More extensive investigations on growth under different conditions are necessary for a proper understanding of the growth mechanism of HD Co and the HDNM Co/normal Co/HDNM Co trilayer structure.

9 Conclusions and Outlook

For bulk materials, a higher density condition is usually achieved by placing the material under high pressure. For thin films, a high-density state may be obtained without the application of any external pressure, although the density may not be uniform over the entire volume of the film. The formation of compressed (higher density) material was earlier demonstrated experimentally. In the present case of Co thin films on Si, high-density (HD) Co layers have formed within the film. Additionally, these HD Co layers are non-magnetic (NM) in contrast to normal Co, which is

ferromagnetic. Similar to the earlier observation of X-ray absorption behaviour of materials at a higher density, HD Co has also shown a shift of L-absorption-edge to higher energy along with a reduced absorption cross section in comparison to normal Co.

Growth of Co thin films on single-crystalline Si has produced HDNM Co layers. However, growth on amorphous (oxide) substrates, like SiO_2 and CoO, has not produced HDNM Co. This shows the importance of growth on single-crystalline substrates for the growth of HDNM Co. However, the details of the growth mechanism of the observed trilayer structure HDNM Co/normal Co/HDNM Co in the Co thin films are still not properly understood. Future investigations in this direction are necessary.

Because of long-range ferromagnetic order in the transition metals Fe, Co and Ni, they are not superconductors at ambient pressure. However, superconductivity was found in Fe when a dense non-magnetic state of Fe was formed under high pressure [14]. HDNM Co layers, found in Co thin films, have also shown superconductivity [15]. In materials with long-range magnetic interaction, thin films may offer the possibility of observing superconductivity under ambient pressure and open new possibilities for applications. Hybrid structures of superconductors (S) and ferromagnets (F), such as S/F and S/F/S hybrid structures, are being investigated for potential applications in spintronics and quantum information technology [45] and exploring basic science of quantum transitions [36]. These structures are fabricated by the successive deposition of layers of different superconducting and ferromagnetic materials. The Co films with HDNM Co are self-organized superconductor–ferromagnet hybrid structures—HDNM Co (S)/normal Co (F)/HDNM Co (S). These self-organized hybrid S/F/S structures, obtained in a single deposition of Co thin film, and over a range of thickness, offer themselves for investigations of various properties of S/F/S structures.

References

1. C.S. Yoo, H. Cynn, P. Söderlind, V. Iota, Phys. Rev. Lett. **84**, 4132 (2000)
2. S.F. Matar, A. Houari, M.A. Belkhir, Phys. Rev. B **75**, 245109 (2007)
3. R. Torchino, C. Marini, Y.O. Kvashnin, I. Kantor, O. Mathon, G. Garbarino, C. Meneghini, S. Anzellini, F. Occelli, P. Bruno, A. Dewaele, S. Pascarelli, Phys. Rev. B **94**, 024429 (2016)
4. N. Greenwood, A. Earnshaw, *Chemistry of the Elements* (Pergamon, New York, 1990), p. 1292
5. C.M. Schneider, P. Bressler, P. Schuster, J. Krishner, J.J. de Miguel, R. Miranda, Phys. Rev. Lett. **64**, 1059 (1990)
6. S. Sankaralingam, G. Subramoniam, S. Pauline, R. Asokamani, High Press. Res. **6**, 219 (1991)
7. O. Prakash, A. Kumar, A. Thamizhavel, S. Ramakrishnan, Science **355**, 52 (2017)
8. V.I. Petrosyan, V.N. Molin, O.I. Vasin, P.A. Skripkina, S.I. Stenin, E.G. Batyev, Sov. Phys.-JETP **39**, 485 (1974)
9. E. Chason, B.W. Sheldon, L.B. Freund, J.A. Floro, S.J. Hearne, Phys. Rev. Lett. **88**, 156103 (2002)
10. N. Banu, S. Singh, A. Roy, S. Basu, B. N. Dev, Polarized neutron reflectivity study of an ultrathin cobalt film on Si(111) with Au capping. Paper presented in the 5th Conference on Neutron Scattering, Mumbai, India, 2–4 February 2015, in *Abstracts* p. 122

11. N. Banu, S. Singh, B. Satpati, A. Roy, S. Basu, P. Chakraborty, Hema C. P. Movva, V. Lauter, B. N. Dev, Evidence of formation of superdense nonmagnetic cobalt, arXiv:1602.05713 (2016)
12. N. Banu, S. Singh, B. Satpati, A. Roy, S. Basu, P. Chakraborty, H.C.P. Movva, V. Lauter, B.N. Dev, Evidence of formation of superdense nonmagnetic cobalt. Sci. Rep. **7**, 41856 (2017). https://doi.org/10.1038/srep41856
13. N. Banu, S. Singh, A. Roy, S. Basu, P. Chakraborty, H.C.P. Movva, V. Lauter, B. Satpati, B.N. Dev, Nanotechnology **29**, 195703 (2018)
14. K. Shimizu, T. Kimura, S. Furomoto, K. Takeda, K. Kontani, Y. Onuki, K. Amaya, Nature **412**, 316 (2001)
15. N. Banu, M. Aslam, A. Paul, S. Banik, S. Das, S. Datta, A. Roy, I. Das, G. Sheet, U.V. Waghmare, B.N. Dev, Superconductivity of cobalt in thin films, arXiv:1710.06114 (2017); Europhys. Lett. (in press)
16. H. Zabel, Appl. Phys. A **58**, 159 (1994)
17. M.R. Fitzsimmons, C. Majkrzak, *Modern Techniques for Characterizing Magnetic Materials* (Springer, New York, 2005), Ch. 3, pp. 107–155
18. S. Singh, S. Basu, M. Gupta, C.F. Majkrzak, P. A. Kienzle, Phys. Rev. B **81**, 235413 (2010)
19. L.G. Parratt, Phys. Rev. **95**, 359 (1954)
20. W.H. Press, B.P. Flannery, S.A. Teukolsky, W.T. Vetterling, *Numerical Recipes in Fortran: The Art of Scientific Computation*, 2nd edn. (Cambridge University Press, Cambridge, 1992)
21. W.K. Chu, J. W. Mayer, M.A. Nicolet, *Backscattering Spectrometry* (Academic Press, 1978), pp. 124–126
22. S. Basu, S. Singh, J. Neutron Res. **14**, 109 (2006)
23. A. Benninghoven, F.G. Rudenauer, H.W. Werner, *Secondary Ion Mass Spectrometry: Basic Concepts, Instrumental Aspects, Applications, and Trends* (Wiley, New York, 1987)
24. V. Lauter, H. Ambaye, R. Goyette, W.-T. Hal Lee, A. Parizzi, Physica B **404**, 2543 (2009)
25. J.P. Itie, F. Baudelet, A. Congeduti, B. Couzinet, F. Farges, Polian. J. Phys.: Condens. Matter **17**, S883 (2005)
26. J.-P. Rueff, S. Raymond, M. Taguchi, M. Sikora, J.-P. Itié, F. Baudelet, D. Braithwaite, G. Knebel, D. Jaccard, Phys. Rev. Lett. **106**, 186405 (2011)
27. N. Banu, P. Kumar, N. Pandey, B. Satpati, M. Gupta, B.N. Dev, Thin Solid Films **675**, 177 (2019)
28. F. Nasreen, D. Antonio, D. Van Gennep, C.H. Booth, K. Kothapalli, E.D. Bauer, J.L. Sarrao, B. Lavina, V. Iota-Herbei, S. Sinogeikin, J. Phys. Condens. Matter **28**, 105601 (2016)
29. J.-P. Rueff, J.-P. Itié, M. Taguchi, C.F. Hague, J.-M. Mariot, R. Delaunay, J.-P. Kappler, N. Jaouen, Phys. Rev. Lett. **96**, 237403 (2006)
30. C. Donnerer, M. Moretti Sala, S. Pascarelli, A.D. Rosa, S.N. Andreev, V.V. Mazurenko, T. Irifune, E.C. Hunter, R.S. Perry, D.F. McMorrow, Phys. Rev. B **97**, 035106 (2018)
31. S. Chaudhuri, B.N. Dev (unpublished)
32. F. Radu, M. Etzkom, R. Siebrecht, T. Schmitte, K. Westerholt, H. Zabel, Phys. Rev. B **67**, 134409 (2003)
33. S.G.E. Velthuis, A. Berger, G.P. Felcher, BK. Hill, E. Dan Dahlberg, J. Appl. Phys. **87**, 5046 (2000)
34. I.F. Lyuksyutov, V.L. Pokrovsky, Adv. Phys. **54**, 67 (2005)
35. A.K Feofanov, V.A. Oboznov, V.V. Bol'ginov, J. Lisenfeld, S. Poletto, V.V. Ryazanov, A.N. Rossolenko, M. Khabipov, D. Balashov, A.B. Zorin, P.N. Dmitriev, V.P. Koshelets, A.V. Ustinov, Nature Physics **6**, 593 (2010)
36. N. Pompeo, K. Torokhtil, C. Cirillo, A.V. Samokhvalov, E.A. Ilyina, C. Attanasio, A.I. Buzdin, E. Silva, Phys. Rev. B **90**, 064510 (2014)
37. N. Banu, Dissertation, University of Calcutta, 2017
38. J.C. Mahato, D. Das, R.R. Juluri, R. Batabyal, A. Roy, P.V. Satyam, B.N. Dev, Appl. Phys. Lett. **100**, 263117 (2012); and references therein
39. J.C. Mahato, D. Das, N. Banu, B. Satpati, B. N. Dev, Nanotechnology **28**, 425603 (2017); and references therein
40. Y. Yalisove, R.T. Tung, J. Vac. Sci. Technol. **A7**, 1472 (1989). and references therein

41. T.D. Lowes, M. Zinke-Allmang, Scanning Microsc. **12**, 119 (1998)
42. D.K. Goswami, K. Bhattacharjee, B. Satpati, S. Roy, G. Kuri, P.V. Satyam, B.N. Dev, App. Surf. Sci. **253**, 9142 (2007). and references therein
43. D. Das, J.C. Mahato, Bhaskar Bisi, B. Satpati, B.N. Dev, Appl. Phys. Lett. **105**, 191606 (2014)
44. S. Kim, H. Yoon, H. Lee, Y. Jo, S. Lee, J. Choo, B. Kim, J. Mater. Chem. C **3**, 100 (2015)
45. B. Baek, W.H. Rippard, S.P. Benz, S.E. Russek, P.D. Dresselhaus, Hybrid superconducting-magnetic memory device using competing order parameters. Nature Commun (2014). https://doi.org/10.1038/ncomms4888

Synthesis, Stability and Self-Diffusion in Iron Nitride Thin Films: A Review

Mukul Gupta

Abstract Nitrides of 3*d* ferromagnetic metals (Fe, Co and Ni) or transition metal nitrides (TMNs) appearing late (Group 8–10) in the 3*d* series are emerging compounds in a wide range of areas such as spintronics, magnetic devices, hard coatings, catalysts for hydrogen and oxygen evolution reaction for electrochemical water splitting, ion batteries, high energy density materials, etc. Some of these TMNs can be synthesized using non-equilibrium processes such as physical vapour deposition or under extremely high pressure and high temperatures. Thermodynamical constraints arisen due to high enthalpy of formation not only make the synthesis of late TMNs difficult, but also thus formed TMNs are also metastable. The thermal stability of late TMN is closely related to metal and nitrogen self-diffusion processes. We performed both Fe and N self-diffusion measurements in various Fe-N compounds and also explored ways to control it through effective dopants. It was found that in magnetic Fe-N compounds (N$at.\% < 25\%$), N self-diffusion is orders of magnitude faster than Fe, but in non-magnetic Fe-N compounds (N$at.\% \approx$30 and 50%), it was surprisingly found to be the other way round. The mechanism related to self-diffusion processes in different Fe-N phases is presented and discussed. This chapter is divided into five sections. In Sect. 1, after a brief introduction of TMNs, different phases and the structure of iron nitrides have been discussed with a brief timeline and applications. Synthesis of different iron nitride thin films using reactive sputtering process, their thermal stability and the effect of dopant on the thermal stability is presented in Sect. 2. Section 3 presents methods and techniques for self-diffusion measurements. In Sect. 4, detailed self-diffusion measurements in magnetic as well as non-magnetic Fe-N compounds are given and also the effect of dopants on self-diffusion process is discussed. This chapter ends with conclusions presented in Sect. 5.

M. Gupta (✉)
UGC-DAE Consortium for Scientific Research, University Campus, Khandwa Road, Indore 452001, India
e-mail: mgupta@csr.res.in

S. Kumar and D. K. Aswal (eds.), *Recent Advances in Thin Films*, Materials Horizons: From Nature to Nanomaterials, https://doi.org/10.1007/978-981-15-6116-0_6

1 Introduction

1.1 Transition Metal Nitrides

In recent years, transition metal nitrides (TMNs) have emerged as active materials for applications in numerous fields. TMNs can be categorically divided into broad branches as 'early' or 'late' on the basis of their appearance in the periodic table along a *d* (3*d*-, 4*d*- or 5*d*-) series. For example, elements of IUPAC group 3–6 can be termed as early while group 8–10 as late. Group 7 elements (e.g. Mn, Tc, Re) lie in between them. Some of early TMNs (e.g. 3*d*: TiN, CrN; 4*d*: NbN, MoN; 5*d*: TaN, WN) are refractory and their thin films are often used as diffusion barriers. They also exhibit several interesting properties such as super-hardness, decorative coatings, corrosion resistance, superconductivity, plasmonic properties etc [1–7]. Generally, early TMNs can be synthesized easily in the chemical formula of MN (i.e. mononitride) having a rock salt type structure. The di-metal nitride (M_2N) phase with hexagonal structure has also been observed in some early TMNs, viz. Cr_2N [8, 9], Nb_2N [10]. Due to the ease of formation (using conventional methods) and interesting properties, early TMNs have been studied for several decades and have been subject to several research reviews [2–7].

Late TMNs, on the other hand adopt a more complex structure and can be formed in a wide composition range, e.g. M_8N ($M_{16}N_2$), M_4N, M_3N, M_2N and MN. In addition to these, N richer compounds such as M_3N_4 [11, 12], MN_2 [13], MN_4 and even higher N phases have been predicted theoretically [14]. Some TMNs with x exceeding 1 in TMN_x have been evidenced experimentally under extreme conditions (high pressure and high temperature), e.g. PtN_2 [15], FeN_2 and FeN_4 [16], CoN_2 [17], CrN_2 [18], NiN_2 [19], OsN_2 [20], RuN_2 [21], RhN_2 [22], N-rich Pt and Pd [23] etc. Compared to early TMNs, late TMNs are rather difficult to synthesize in a single phase and they are not thermally stable. Some of the late TMNs, e.g. $Fe_{16}N_2$ has been intensively explored due to its giant magnetic moment (even defying the Slater–Pauling curve) and application as rare-earth free permanent magnet [24]. Tetra iron nitride (Fe_4N) compound has also received considerable attention due to its larger (than Fe) magnetic moment and high spin-polarization ratio [25]. Similarly, tetra cobalt nitride (Co_4N) has also been studied recently [26]. Tri- and bimetal nitrides of Fe, Co and Ni have also been explored for their magnetic properties [27–30]. On the other hand, mononitride of TM can be considered as most fundamental nitrides and have been studied theoretically by several researchers [31]. Experimentally, it turns out that mononitrides of FeN and CoN can be synthesized in the form of thin films under ambient pressure and temperatures but in case of Ni, the N concentration does not increase beyond that of Ni_2N [32]. Recently, FeN and CoN compounds gained significant interests as they are promising energy materials. They can be used as a catalyst in electrocatalysis and water splitting in oxygen and hydrogen evolution reaction [33–38], for mesoscopic and perovskite solar cells [39], non-aqueous supercapacitor [40] and high- capacity anode in Li-ion batteries [41, 42].

In recent years, TM nitrides and carbides have been reviewed by several co-workers [2–7]. Very recently, Sun et al. [1] presented a map of ternary metal nitrides and it has been emphasized that such nitride compounds can open new possibilities in several emerging area such as solid-state lighting, hard coatings, catalysts, superconductors, etc. It was pointed out that compared to metal oxides the research on metal nitrides is still in the nascent stage. This becomes clear by comparing the International Crystal Structure Database (ICSD), where more than 4000 ternary metal oxides have been registered but only fewer than 400 ternary metal nitrides [1]. Such discrepancy between metal oxides and nitrides can be primarily linked to the the bonding strength of oxygen and nitrogen. The bond enthalpy of triply bonded N_2 at about 1000 kJ mol^{-1} is about twice that of O_2 [44]. This, combined with the fact that the formation energies of metal nitrides are small and their thermal stability is poor, the research work in metal nitrides did not evolve at the same pace as evidenced in the case of metal oxides. However, recent developments in experimental and computation capabilities can provide ample possibilities to discover new metal nitrides.

The distinction between early and late TMNs can be readily understood considering bonding energies expressed as enthalpies of formation (ΔH_f°), which represents the energy gained in the formation of a compound. In a seminal work, Häglund et al. [43] studied bonding properties of 3*d*-, 4*d*- and 5*d*-TM carbides and nitrides. The enthalpies of formation at zero temperature ($\Delta^0 H(0)$) of metal monocarbide (MC) and mononitride (MN) were compared and they show a similar behaviour across the 3*d*-, 4*d*- or 5*d* series. As one moves along the 3*d*-series, $-\Delta^0 H(0)$ is maximum for Ti and reduces continuously as shown in Fig. 1(left). The bonding energies $-\Delta E_{\text{bond}}$ also follow a similar trend (Fig. 1(right)). The behaviour of $-\Delta^0 H(0)$ and $-\Delta E_{\text{bond}}$ has been interpreted in terms of changes in the nature of bonding along the *d*-series. In early TMs, the filling of bonding *p*-*d* hybridized states yield larger $-\Delta^0 H(0)$ and $-\Delta E_{\text{bond}}$ and the formation of a 'bonding' character of electronic density of states (DOS). As one moves along a *d*-series, this changes to 'anti-bonding' and finally to a 'non-bonding' character for the late TMNs. The differences in the thermal stability of early and late TMNs can be well explained due to such differences in the bonding character between them. It is known that early TMNs, e.g. ScN, TiN, VN are refractory compounds with their melting temperatures exceeding 2000 K but late TMNs, e.g. FeN and CoN show thermal instabilities even when heated at a moderate temperature of 500 K. This understanding of the enthalpy of formation (hereafter refereed as ΔH_f°) is important to understand the synthesis, thermal stability and self-diffusion processes in Fe-N compounds which will be described in this work.

1.2 Phases of Iron Nitride

Iron nitride (Fe-N) alloys and compounds belong to the family of late TMNs and are expected to be found in a broad composition range in which N atomic percentage ($at.\%$) can vary from as little as a fraction of a $at.\%$ to as high as $80 at.\%$. Major

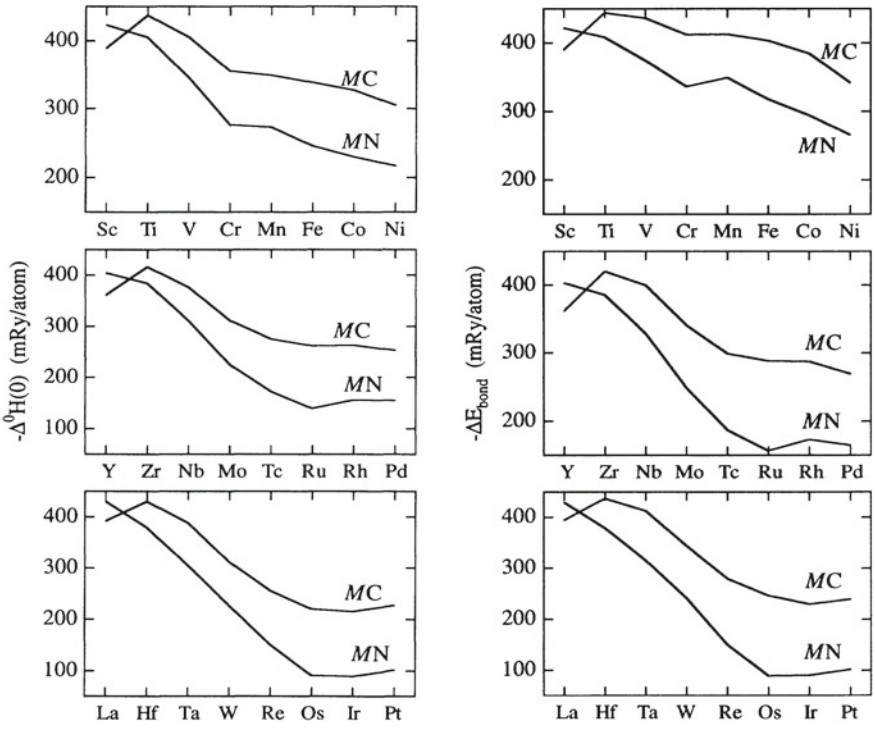

Fig. 1 Calculated enthalpies of formation at 0 K, $\Delta^0 H(0)$ (left), and bonding energies $-\Delta E_{\text{bond}}$ (right), for 3*d*-, 4*d*- and 5*d*-TM carbides and nitrides (reproduced with permission from Ref. [43])

Fe-N phases that are theoretically predicted or realized experimentally are listed in Table 1. They are generally referred as α-Fe(N), $\alpha''-Fe_{16}N_2$, γ'-Fe_4N, $\varepsilon - Fe_{3-y}N$ ($1 \geq y \geq 0$), $\zeta - Fe_2N$, γ''-FeN, γ'''-FeN. In this work, we drop prefix (e.g. α, γ) and denote a Fe-N phase without such prefixes. Among these, phases that are formed with $Nat.\% \leq 50$ have been synthesized in bulk or in the form of thin films. Phases with $Nat.\%$ exceeding 50 have been predicted theoretically, and very recently some of them have been evidenced experimentally under extremely high pressure and high temperature (HPHT) [16, 45].

The Fe-N system has been critically reviewed in several works, and for a comprehensive overview, the reader is referred to seminal works by Coey and Smith on magnetic nitrides [46]. More recently, S. Bhattacharya presented a review of iron nitrides at reduced dimensions with an emphasis on their synthesis protocols, structure and magnetic properties [47]. A review of the high magnetic moment thin films including $Fe_{16}N_2$ for microscale and nanotechnological applications has been given by Scheunert [24]. In this work, we will not categorically review the iron nitride system, rather present the results on the phase formation, thermal stability and self-diffusion measurements on some iron nitride phases that are formed with

Table 1 An overview of Fe-N phases formed at different N concentration (N atomic %) along with their nominal structure(s)

Composition	Phase	N$at.\%$	Structure
Fe	Ferrite (α)	0	bcc
Fe(N)	Ferrite (α)	0–9	bcc
Fe(N)	Martensite (α')	10	bct
Fe(N)	Austenite (γ)	11	fcc
$Fe_{16}N_2$	α''	11.1	bct
Fe_4N	γ'	20	fcc (inverse Perovskite)
Fe_2N_{1-x} ($0 \leq x < 1$)	ϵ	18–32	Hexagonal
Fe_2N	ζ	33.3	Orthorhombic
FeN	Mononitride	50	ZB, RS, NiAs, MnP - type
Fe_3N_4		57	Spinel
FeN_2		66.6	Orthorhombic
FeN_4		80	Triclinic

N$at.\% \approx 10, 20, 30$ and 50% corresponding to $Fe_{16}N_2$, Fe_4N, $Fe_{2.2}N$ and FeN phases, respectively.

1.3 Structure, Applications and Brief Timeline of Iron Nitrides

1.3.1 Early Works (1900–1950)

The earliest published work in the Fe-N system can be traced back to the year 1905 [48] but substantial amount of work was carried out between 1920–1930, which helped in establishing the phase diagram of Fe-N [49–55]. Through these works, major Fe-N phases like α-Fe(N), Fe_8N, Fe_4N, Fe_3N and Fe_2N were synthesized by heating iron powder $\approx 600\,^\circ$C in the presence of nitrogen, ammonia and hydrogen gases. The dissociation of ammonia yielded nascent nitrogen that diffuses into hot iron leading to the formation of different Fe-N phases. The composition of such phases can be tuned with the available amount of N during the synthesis process. Through these methods, Fe-N compounds with a maximum amount of 11 wt.% or about $33at.\%$ i.e. up to Fe_2N could be obtained. The Fe-N system received renowned interests around the year 1950 due to its application in ferrous metallurgy and the phase diagram of Fe-N was more carefully drawn by Pranjape et al. [56] and detailed works were carried out by Jack [57–59]. In fact, all Fe-N phases that are formed

below N $at.\% \leq 50$ in Table 1 have been identified in the phase diagram of Jack [59], including the $\alpha''-Fe_{16}N_2$ phase. The structure of these compounds will be discussed below.

1.3.2 $Fe_{16}N_2$ Phase

Between 1950 and 1970, the focus on Fe-N was limited to their usage in steel industry and tribological properties. Although the $Fe_{16}N_2$ phase was already evidenced by Jack in 1951 [59], this compound received immense attention after the discovery of a giant magnetic moment in thin films containing a mixture of $\alpha''-Fe_{16}N_2$ and Fe by Kim and Takahashi [60]. This suddenly made the Fe-N system a *tour de force* due its potential usage as a rare-earth free permanent magnet and in computer memory devices. This compound exhibited to possess a magnetic moment of $3.0\mu_B$ per Fe atom—the highest value observed in any material at room temperature. The structure of $Fe_{16}N_2$ is shown in Fig. 2. The interstitial incorporation of nitrogen induces the tetragonal distortion with three different Fe sites, namely: Fe-I (4e), Fe-II(4d), Fe-III(8h) and N occupies the 2a site (see Fig. 2). The nearest neighbour of N (2a) is the Fe(4e) and Fe(8h) in the crystal lattice. Later in the year 1991, Sugita et al. prepared epitaxial thin films of $Fe_{16}N_2$ and found even higher moment at $3.2\mu_B$ per Fe atom at room temperature which increases to $3.5\mu_B$ per Fe atom at lower temperatures. Such observations about a giant magnetic moment could not be explained taking into account theoretical considerations.

In a report by Lai et al. [62], the strong correlation effect on all iron sites in the $Fe_{16}N_2$ were taken into account for the high moment. However, it has been argued considering such correlation effects, it would not be possible to retain metallic state of $Fe_{16}N_2$. Subsequently, Sakuma et al. [63] proposed that the charge transfer model, in which N atoms serve as charge hopping sites, predicted that an effective 'double-exchange' process resulted in high spin configuration of Fe and long-range ferromagnetic ordering [63]. However, no clear evidence was presented revealing the most negatively charged N site as compared to other sites in the iron nitrides. Further, the concept of partial localization of Fe 3d states in $Fe_{16}N_2$ was predicted by Ji et al.

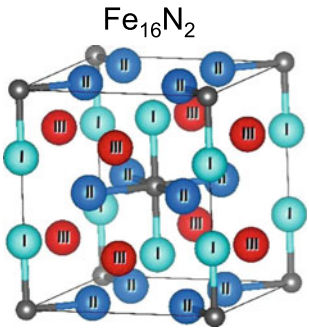

Fig. 2 Crystal structure of body-centered tetragonal (bct) $Fe_{16}N_2$, lattice parameter $a = 5.72$ Å, $c = 6.29$ Å, space group: I4/mmm (no.139) [61]. Here large circle denotes Fe atoms and smaller one N atom. Wyckoff positions are: Fe (I)-4e, Fe (II)-8h, Fe (III)-4d, N-2a (0, 0, 0), (0.5, 0.5, 0.5)

[64] and also confirmed experimentally by the same group using magnetic circular dichroism measurements. In the year 2012, Sims et al. [65], calculated an average spin moment of 2.9, 2.6–2.7 and 2.7 μ_B per Fe atom, using hybrid functional method, the GW approximation and the GGA+U method, respectively. However, it is to be noted that Fe moment on fcc Fe was also greatly overestimated by these methods. In a very recent report, Bhattacharjee et al. [66] predicted that the giant magnetization of $Fe_{16}N_2$ can be understood by considering a combination of double-exchange (between 8h and 4d sites) and superexchange interactions (among the localized Fe sites). Briefly, it can be said that challenges to reproduce giant magnetization and theoretical understanding has led to a so-called *40-year-old mystery* in $Fe_{16}N_2$ [64]. Floods of experimental and theoretical works appeared after the discovery of giant magnetic moment [67] but $\alpha''-Fe_{16}N_2$ is still a controversial compound due to issues related to its magnetization and thermal stability [68].

1.3.3 Tetra Iron Nitride (Fe_4N) Phase

The timeline of Fe_4N appears to be rather smooth and the dramatic developments that were evidenced in $Fe_{16}N_2$ seems to be missing in Fe_4N. Though Fe_4N was already evidenced in 1930 [54, 55], research work on this system is still taking place to understand its magnetization. The earliest interest in the synthesis and the study of Fe_4N were motivated by its application as a catalyst for the production of ammonia and in the surface treatment of steels [55]. The structure of Fe_4N is already well established to be an fcc anti-perovskite with LP = 3.79 Å as shown in Fig. 3.

As compared to (hypothetical) fcc Fe, the LP of Fe_4N is about 9% larger [70] due to insertion N at body- centered positions. Such insertion leads to a magneto-volume effect resulting in higher (than Fe) magnetization in Fe_4N. Together with high magnetization, Fe_4N exhibit a half-metallic character and its spin-polarization ratio can reach to almost 100% [71]. These qualities make Fe_4N an attractive choice for spintronic application to the extent that it may be considered as an alternative to Heusler alloys [72]. Fe_4N has been synthesized both in bulk as well as in the form of thin films. Its structure matching very well with theoretical predictions has been

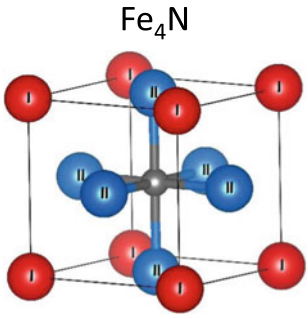

Fig. 3 Crystal structure of face-centered cubic tetra iron nitride (Fe_4N). Lattice parameter a = 3.79 Å, space group (No.): Cubic; Pm-3m (No, 221) Wyckoff Positions: Fe (I)-4a, Fe (II)-3c, N-4b [69]

achieved and confirmed with neutron diffraction [73] and Mössbauer spectroscopy measurements [74], however the magnetization of Fe_4N seems to vary a lot in thin films produced in different works, e.g. Atiq et al. [75] observed a very high moment $\approx 2.9\,\mu_B$ per Fe atom whereas values as low as $1.3\,\mu_B$ have also been reported [76], however in most of other works the value was found between these extremes [77] and close to the theoretical value of $2.35\mu_B$ [25]. In 2009, Blancá et al. [78] reviewed magnetization of Fe_4N both from theoretical and experimental view points and concluded that the large magnetization ($2.9\,\mu_B$) value observed by Atiq et al. [75] is not an intrinsic property of Fe_4N but it could have emerged due to some experimental artefacts. The lower values of magnetization found in otherwise perfect Fe_4N thin films is a concern and as evidenced recently, it may be caused by interdiffusion between film and substrate as Fe_4N films are generally grown at higher temperature ($\approx$700 K) [77]. It is to be foreseen that Fe_4N can suitably replaced Fe in magnetic devices due its chemical inertness and interesting magnetic properties.

1.3.4 Tri and Bi Iron Nitride ($Fe_{3-y}N$ and Fe_2N) Phases

The Fe-N compounds formed between N$at.\%$ 25 and 33 are termed as $\varepsilon - Fe_{3-y}N$ and when N$at.\%$ = 33, the $\zeta - Fe_2N$ phase can be obtained. The 'ϵ' phase exhibits the largest homogeneity range in the phase diagram of Fe-N (see Fig. 5) and has a hexagonal close-packed (hcp) structure as shown in Fig. 4. When N$at.\%$ = 25, stoichiometric Fe_3N phase is formed, however with a rise in N$at.\%$ an anisotropic distortion of the hexagonal lattice results in transformation into the orthorhombic $\zeta - Fe_2N$ phase, when N$at.\%$ = 33. In Fe_3N, N occupies the 1/3 of the corner-sharing octahedral units in an hcp lattice of Fe, whereas in Fe_2N, N occupies the 1/2 of the octahedral sites [27] as shown in Fig. 4. The magnetic state of these phases is somewhat debated [28]. Theoretically, the magnetic moment of Fe_3N and Fe_2N has been predicted to be 1.99 and 1.43 μ_B [27], however experimentally phases with the

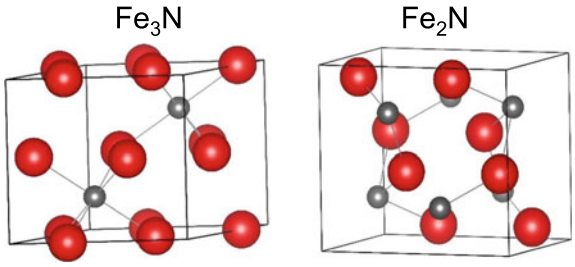

Fig. 4 (Left): Crystal structure of hexagonal Fe_3N, lattice parameter a = 4.658 Å, c = 4.322 Å, space group: $P6_322$ (No. 182) [69]. Wyckoff positions are Fe-6g (x, 0, 0), N-2c (1/3, 2/3, 1/4). (Right): Crystal structure of Orthorhombic Fe_2N, lattice parameter $a = 4.437$, $b = 5.541$, $c = 4.843$Å. Space group (No.): Pbcn (No. 60), Wyckoff positions; Fe-8d (0.2491, 0.1281, 0.082675), N-4c (0, 0.364, 1/4) [82]. Here large circle denotes Fe atoms and smaller one N atom

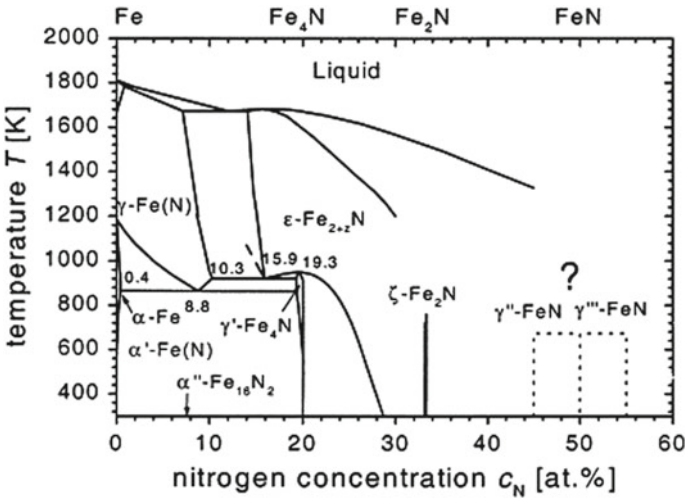

Fig. 5 Phase diagram of Fe-N system modified after realization of FeN phases. Reproduced with permission from Ref. [90]

values of y between 0 and 0.5 (in $Fe_{3-y}N$) were found to be magnetic and whereas phases with y = 0.8, 0.92 and 1 in $Fe_{3-y}N$, have been found non-magnetic at room temperature [29].

Even though $Fe_{3-y}N$ phases are most homogenous in the phase diagram of Fe-N, they have received much less attention than other Fe-N phases such as $Fe_{16}N_2$, Fe_4N or FeN. The reason for such discrepancy may be due to a challenging synthesis process to produce $Fe_{3-y}N$ in bulk [30]. However, $Fe_{3-y}N$ phases with controllable stoichiometry can be suitably obtained in the reactive sputtering process and there seems to be a renowned interest in sputter-deposited $Fe_{3-y}N$ films in recent years [79–81].

1.3.5 Iron Mononitride (FeN) Phase

The Fe-N phase diagram was updated in the year 1987 by Wriedt et al. [83] taking into account magnetic transformations in Fe-N system. Around the mid-1980, a new Fe-N phase having an equiatomic ratio of Fe and N, i.e. iron mononitride (FeN) was discovered by Oueldennaoua et al. [84]. They deposited samples using reactive rf sputtering on liquid nitrogen cooled substrates and associated a rock salt (RS - NaCl) type structure with a lattice parameter of 4.53 Å and the composition of their samples was found to be $FeN_{0.97}$. This was the first time that a Fe-N phase exceeding N*at.%* 33 (i.e. Fe_2N) was evidenced. Subsequently, several efforts were made to reproduce the mononitride phase and it was amply demonstrated by Nakagawa et al. in 1991 [85], Suzuki et al. in 1993 [86], Hinomura et al. in 1998 [87]. In a series of works published by Schaaf et al. between 1995 and 2002 [29, 88–90], the synthesis

of FeN was reported and they were termed as 'new cubic nitrides'. Subsequently, the phase diagram of Fe-N system was modified. Their structural and magnetic properties were studied and it appeared that FeN can be formed in the RS and/or zinc blende (ZB–ZnS) structures as shown in Fig. 6. In both cases, FeN was found to be non-magnetic at room temperature but RS-FeN was claimed to be ferromagnetic (FM) or antiferromagnetic (AFM) at low temperatures (≈5 K). During this time, theoretical works also started to appear to understand the structural and magnetic ground state of FeN [91–94]. Through these theoretical works, it appeared that RS-type FeN with an FM or AFM magnetic structure is preferred.

With the advent of this century, efforts were made to synthesize the mononitride FeN thin films using a variety of thin-film deposition methods, viz. ion beam sputtering [96–98], dc/rf magnetron sputtering [95, 99–108], pulsed laser deposition (PLD) [109–112], high power impulse magnetron sputtering [113], nitrogen plasma assisted molecular beam epitaxy (MBE) [114–118] and under high pressure and high temperature [16, 17, 45, 119, 120]. From these experimental works, it was observed that the LP of FeN was found to be either about 4.33 or 4.50 Å. Generally, FeN with a LP of 4.33 Å was associated with the ZB and 4.50 Å with the RS-type structure. However, in most of these works, no magnetic order could be found down to 5 K [95, 104, 117], and therefore the existence of the RS-type FeN was questioned. It was concluded that irrespective of its LP (4.3 or 4.5 AA), the structure of FeN is ZB type and differences in the value of LP are related with defects and vacancies in it. Recent first-principles calculations also seem to agree this point of view and predict that at T = 0 K and P = 0 GPa, the preferred phase in FeN is ZB type, but above 50 GPa a phase transition from ZB to RS type is expected [121]. Very recently ultra-thin films of FeN were studied by growing them at 100 K and performing in situ magnetization measurements (using ^{57}Fe nuclear resonance scattering) and it was found that a magnetic phase emerges in FeN thin films when their thickness is below ≈5 nm [122].

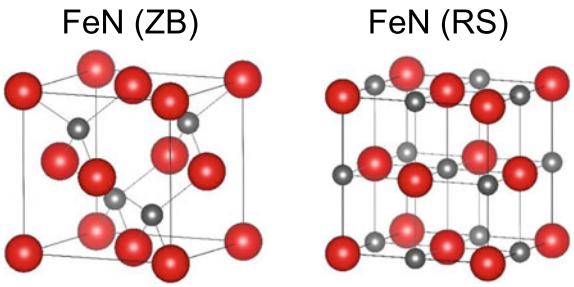

Fig. 6 (Left): Crystal structure of cubic FeN with zinc blende (ZB) structure, lattice parameter a = 4.33 Å, space group: F-43m (No.216) [14, 95]. Wyckoff Positions are: Fe-4a (0, 0, 0), N-4c (1/4, 1/4, 1/4). (Right): Crystal structure of FeN with rock-slat (RS) structure, lattice parameter a = 4.452 Å. Space group (No.): Fm-3m (No.225), Wyckoff positions: Fe-4a (0, 0, 0), N-4b (1/2, 1/2, 1/2) [14, 95]. Here large circle denotes Fe atoms and smaller one N atoms

From the applications points of views, nowadays FeN is becoming a very interesting compound as it can be used as an effective catalyst in chemical reactions due to its oxidation resistance [123, 124] and also in biomedical applications [14]. FeN can also be used as a precursor to produce lower N Fe-N phases such as Fe_4N [108, 114, 125, 126] Still, the fundamental understanding of FeN is not well-understood with respect to its structural and magnetic ground state and needs further attention.

1.3.6 N-Rich Iron Nitride Phases

After the experimental discovery of pernitride phase of Pt, i.e. PtN_2 [15] in 2004 by laser heating of Pt under high pressure in a diamond anvil cell, it was realized that such phases might also exist in other metals. As mentioned already in Sect. 1.1, pernitrides of several other metals have been reported. Recently, the discovery of single-bonded cubic nitrogen polymorphs [127, 128] have paved ways to seek these materials for high energy density applications.

In the Fe-N system, some N-rich phases were predicted long back, e.g. in the year 2002, Ching et al. [11, 12] made prediction about the cubic spinel nitride Fe_3N_4, however this phase remains to be realized experimentally. Similarly in 2011, the pernitride FeN_2 [13] phase was predicted and very recently, it was experimentally

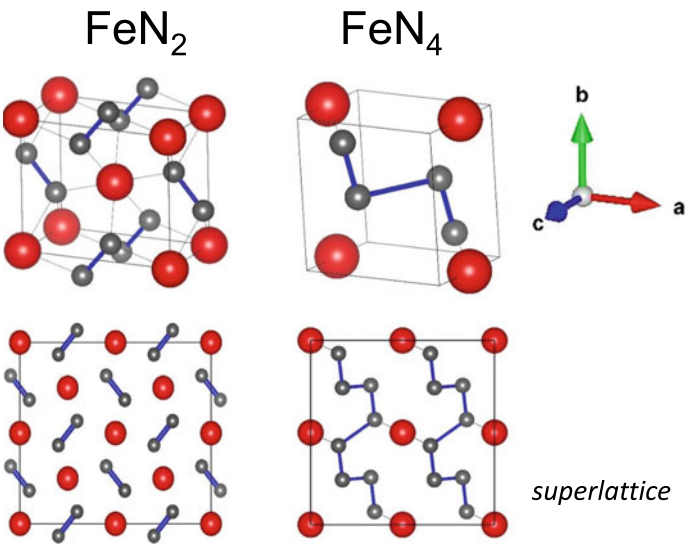

Fig. 7 (Left): Crystal structure of orthorhombic FeN_2, lattice parameter a = 4.431, b = 3.722, c = 2.421 Å, space group: Pnnm (No.58). Wyckoff positions are: Fe (0, 0, 0), N (−0.4025, 0.1335, 0) [14, 16]. (Right): Crystal structure of Triclinic FeN_4, lattice parameter a = 2.509, b = 3.524, c = 3.541 Å, space group: P-1 (No.2). Wyckoff positions are: Fe (0.5, 0, 0), N1 (0.160, −0.346, −0.487), N2 (0.060, −0.303, −0.859) [14, 16]. Here large circle denote Fe atoms and smaller one N atoms

realized [16, 45] by heating a iron foil under high pressure (≈50 GPa) and high temperature (≈2000 K). By further increasing the pressure above 100 GPa, the FeN_4 phase was also evidenced by Bykov et al. [16]. The iron pernitride FeN_2 phase was also synthesized by Laniel et al. [45]. The structure FeN_2 is predicted to be hexagonal (R-3m) and marcasite (Pnnm), but experimentally only marcasite phase has been observed [16, 45, 45]. A schematic diagram of FeN_2 and FeN_4 primitive unit cell and superlattice structures is shown in Fig. 7. Laniel et al. [45] found a partial phase transition from marcasite (Pnnm) to hexagonal (R-3m), implying its metastable nature. This marcasite FeN_2 under ambient condition is expected to exhibit a bulk modulus of 344(13) GPa, highest among all iron nitrides predicted theoretically. The structure of FeN_2 consists of FeN_6 octahedrons with slight distortions and rotations allowing N-N bonds. Structural refinements give the bond distance of these N-N chains in between single and double bonds and the presence of these $(N_2)^3$ dimer is ultimately held responsible for the large bulk modulus value. In addition, even higher N phases like FeN_6 and FeN_8 have been theoretically predicted [14], but they remain to be realized experimentally hitherto. Since these N-rich phases contain polymeric N chains, they are viable as cheap high energy density material.

2 Synthesis and Thermal Stability of Iron Nitrides

Iron nitrides have been synthesized using chemical as well as physical processes. As mentioned before, the dissociation energy of N_2 molecule is large, about twice that of O_2, and this not only makes the formation of iron nitrides more challenging, also the interactions in iron nitrides are dominated by Fe–Fe interactions unlike Fe-O in iron oxides. Weakly bonded Fe atoms generate less negative enthalpies of formation (ΔH_f°) and as compared to oxides, many more nitrides of iron appear. For example in FeN_x, x = 0.11 ($Fe_{16}N_2$), 0.2 (Fe_4N), 0.25 to 0.33 ($Fe_{3-y}N$, $0 \leq y < 1$), 0.33 (Fe_2N), 0.5 (FeN), 0.66 (FeN_2), 0.8 (FeN_4). On the other hand only very limited number of iron oxides can be found, e.g. in FeO_x, x = 1 (FeO), 1.33 (Fe_3O_4) and 1.5 (Fe_2O_3). The lowest value of ΔH_f° in iron oxides is for Fe_3O_4 at -1116 kJ mol^{-1} but in iron nitrides it is about 25 times higher, e.g. about -45 kJ mol^{-1} for $Fe_3N_{1.22}$ and FeN [44]. In other nitrides ΔH_f° is even higher (less negative or even positive), e.g. +85±47 kJ mol^{-1} in $Fe_{16}N_2$, −12±20 kJ mol^{-1} in Fe_4N, −34±8 kJ mol^{-1} in Fe_2N [44].

Due to unfavourable energetics, synthesis of Fe-N compounds by simple dissociation of N_2 is not favoured. Therefore, to prepare Fe-N compounds, ammonia (NH_3) is used together with some iron precursor kept at high temperatures (≈400–600°C). The dissociation of ammonia to atomic nitrogen (and subsequently to molecular nitrogen) is given by $2NH_3 \rightarrow 2N + 6H \rightarrow N_2 + 3H_2$. The atomic N diffuses into the hot iron surface and leads to the formation of iron nitrides. The composition of thus formed iron nitrides can be tailored by varying the temperature and the amount of NH3 gas. Using such methods Fe-N compounds such as $Fe_{16}N_2$, Fe_4N, $Fe_{3-y}N$ and Fe_2N were

formed and already included in the Fe-N phase diagram established around 1950 [56–59]. On the other hand, using thin-film deposition methods, particularly sputtering it became possible to form a variety of Fe-N compounds at low temperatures. In the sputtering process, typical adatom energy is about 20–30 eV [129] and during the condensation process at a substrate, this energy is lost within picosecond time scale leading to quenching rates of the order of 10^{16} K/s [130]. This makes the sputtering process a highly non-equilibrium process and utilizing these, it may be possible to achieve the formation of some Fe-N phases which is otherwise difficult to achieve. Reactive sputtering processes, therefore, have been one of the most frequently used processes to synthesize Fe-N thin films [95, 99–108]. We will take a few examples from our earlier works to understand the formation of Fe-N phases in reactive sputtering processes.

2.1 Synthesis of Iron Nitride Thin Films by Reactive Sputtering

Figure 8a, b shows an evolution of Fe-N phases in the reactive sputtering process at substrate temperature (Ts) of 300 K (no intentional heating) and at Ts = 423 K. Starting with pure Fe, the reactive N_2 gas flow R_{N_2}(=pN/(pN+pAr), with pN and pAr being the individual gas flows of N_2 and Ar gases measured from a mass flow controller was varied in a way that the total gas flow remains constant at 50 sccm. Samples were deposited on an amorphous quartz (SiO_2) substrate. As can be seen that at 300 K [106], the phases formed are Fe, Fe(N), $Fe_{3-y}N$, Fe_2N and FeN but this behaviour slightly changes to Fe, Fe(N), Fe_4N, $Fe_{3-y}N$ and FeN at 423 K [113].

From the behaviour shown in Fig. 8a, b, it can be observed (i) reactive sputtering at room temperature initially leads to formation of an amorphous and a nanocrystalline phase of Fe-N in which N atoms occupy the interstitial spaces within the bcc-Fe (α-Fe). A mechanism leading to such effects has been described in detail in Ref. [101] (ii) at Ts = 300 K, prominently the $Fe_{3-y}N$ phase is formed between R_{N_2} = 30 to 70%, and thereafter the Fe_2N and FeN phases are formed. (iii) the formation of Fe_4N phase does not take place at 300 K but it seems to evolve only when the substrate temperature is raised (this is contrary to Co_4N phase that is formed only when the Ts = 300 K [26, 70]). (iv) formation of the $Fe_{16}N_2$ phase does not take place either at Ts = 300 or 423 K.

It is known that the formation of $Fe_{16}N_2$ phase may take place after thermal annealing. Therefore, further optimization of R_{N_2} was carried out at as can be seen from Fig. 9, at R_{N_2} = 15%, peaks corresponding to $Fe_{16}N_2$ along with α-Fe can be seen in the as-deposited samples but the peak corresponding to (004) reflection of $Fe_{16}N_2$ grows in intensity at 400 and 450 K but it almost diminished when the annealing temperature was raised above 450 K [131]. At further higher temperatures, this sample becomes a mixture of Fe and Fe_4N.

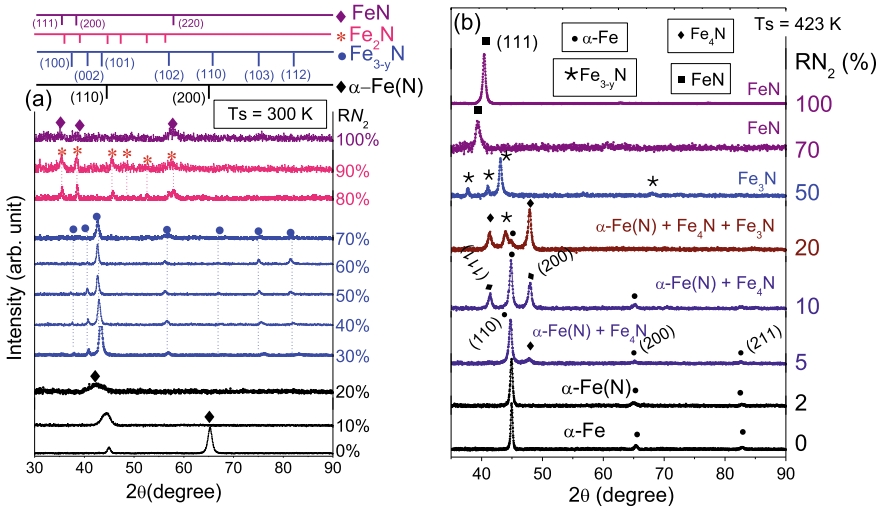

Fig. 8 X-ray diffraction patterns of Fe-N thin films deposited at different nitrogen gas flows (R_{N_2}) grown at room temperature (300 K) (**a**) and at 423 K (**b**). **a** is reproduced with permission from Ref. [106]

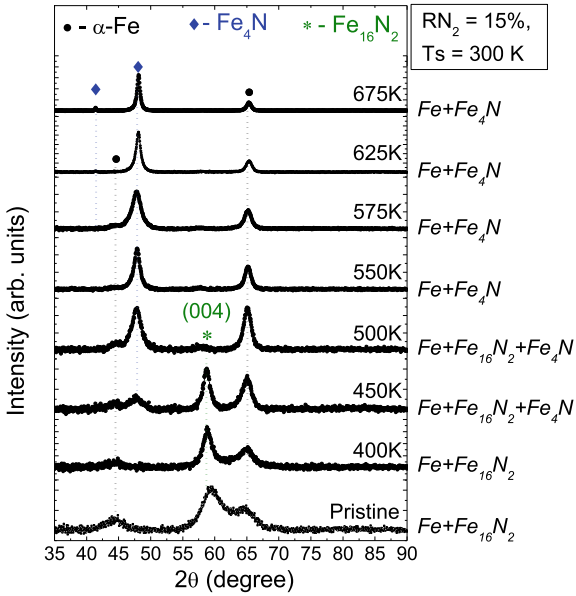

Fig. 9 X-ray diffraction patterns of Fe+$Fe_{16}N_2$ phase formed with R_{N_2} = 15% in the as-deposited state and after annealing at different temperatures

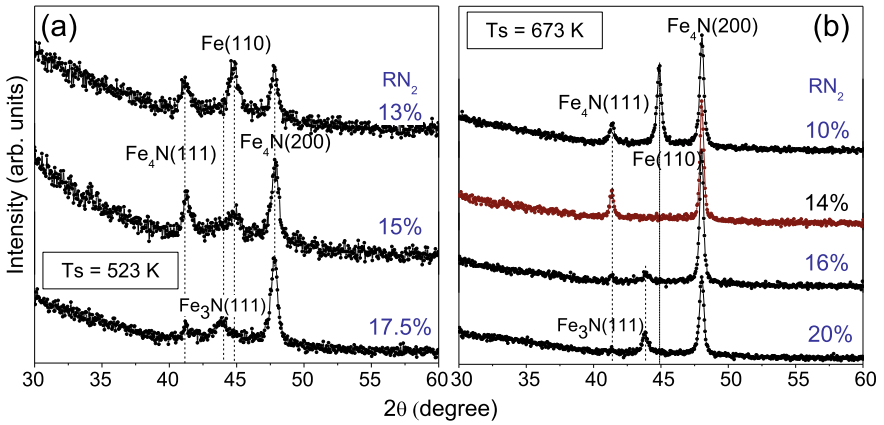

Fig. 10 X-ray diffraction patterns of Fe-N thin films deposited at different nitrogen gas flows (R_{N_2}) grown at substrate temperature (Ts) = 523 K (**a**) and at 673 K (**b**)

To further study the growth of a single phase Fe_4N, the substrate temperature was raised to 523, 598 and 673 K and again the R_{N_2} was varied in close intervals to optimize the growth of Fe_4N phase. As can be seen from Fig. 10a, at R_{N_2} = 13%, Fe is present as an impurity but raising the R_{N_2} to 17.5%, results in impurity of $Fe_{3-y}N$. Even at an intermediate flow of 15%, impurities due to Fe or $Fe_{3-y}N$ can be seen in Fig. 10a. By further raising the Ts to 598 K (not shown), single phase Fe_4N could not be formed, however by raising the Ts to 673 K, it can be seen from Fig. 10b that single phase Fe_4N can be obtained. This indicates that the formation of a polycrystalline Fe_4N phase on an amorphous SiO_2 substrate is difficult but can be achieved by the optimization of Ts and R_{N_2}. More details about the optimization of Fe_4N can be found in Ref. [132]. In addition, the formation of an epitaxial Fe_4N phase can be obtained with the assistance of suitable lattice matching by using single-crystalline substrates such as MgO, $SrTiO_3$, $LaAlO_3$ or underlayers such as Cr, Cu, Ag, etc. [78, 133–137].

Further, in order to grow the iron mononitride FeN phase, it seems that some substrate heating is essential. From Fig. 8a, b, it can be seen that at Ts = 300 K a disordered FeN phase is formed when R_{N_2} = 100%, but at Ts = 423 K, though the presence of FeN phase can be seen at R_{N_2} = 70%, at R_{N_2} = 100%, the stoichiometric and well crystalline FeN phase seems to form. From the XRD data shown in Fig. 8b the only peak appearing there can be identified as FeN (111) and its lattice parameter (LP) and grain size (GS) come out to be 4.457(2) Å and 18 nm in R_{N_2} = 70% sample and in R_{N_2} = 100% sample, the values LP and GS become 4.323(3) Å and 31 nm. As already discussed in Sect. 1.3.5, the LP of FeN can vary approximately between 4.5 and 4.3 Å and it appears that higher values of LP are found probably in off-stoichiometric and not so well crystalline samples.

As it appears from Fig. 8b that sputtering of iron by N_2 alone as processing gas is the best suitable recipe for the growth of FeN film. Therefore, we kept R_{N_2} fixed at

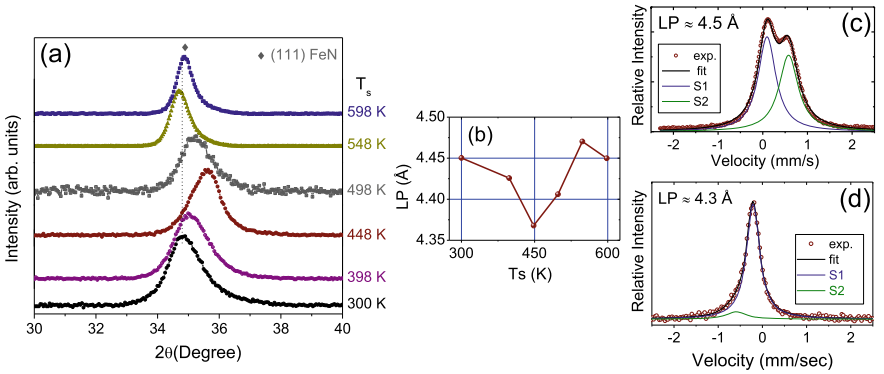

Fig. 11 X-ray diffraction patterns of Fe-N thin films deposited at different substrate temperatures (Ts) using $R_{N_2} = 100\%$ (**a**). The variation of lattice parameter (LP) as a function of Ts (**b**). Conversion electron Mössbauer spectroscopy (CEMS) pattern of FeN thin films with LP ≈4.5 Å(**c**) and LP ≈4.3 Å(**d**)

100% and varied the Ts in small steps between 300 and 600 K and XRD pattern of these samples are shown in Fig. 11a. In all these XRD patterns, the peak corresponding to (111) reflection of FeN can be seen and from this, we calculated the LP and the variation of LP with Ts is shown in Fig. 11b. At lower Ts (300 and 398 K), the LP is large (LP ≈4.5 Å) and it decreases to ≈4.3 Å at Ts = 448 K. But surprisingly, it starts to increase again when Ts is raised beyond 450 K. Such occurrence of minima in the LP of FeN with Ts is a new finding in this compound and it appears that the stoichiometry of FeN phase critically depends on the Ts. When the temperature is lower than a value, it is not sufficient to establish the long-range ordering and stoichiometry but if it increases beyond this critical Ts, diffusion process becomes dominant leading to defects in FeN. To study the local structure of FeN, CEMS is the best technique and CEMS spectrum of a FeN sample is well established to be consisting of an asymmetric peak profile. The fitting of such CEMS can be done using a number of combinations of singlet (S) and/or doublet (D): (i) two S [85, 95, 104, 115] (ii) one S and one D [115, 116, 138] (iii) two S and one D [89]. The component S with isomer shift (IS) ≈0 mm/s (relative to α-Fe) is due to Fe coordinated to four N atoms as expected in FeN with ZB-type structure. But the second component (either S or D) seems to be not so well defined and has been understood as defects or vacancies in FeN. We did CEMS measurements on samples with LP of about 4.5 and 4.3 Å and found that CEMS spectra various significantly with LP of FeN as shown in Fig. 11c, d. In case of a sample with LP of 4.5 Å, we can see that both singlets S1 and S2 are of comparable strength but in the sample with LP of about 4.3 Å, S2 almost disappears. Therefore, it can be concluded that a single phase and stoichiometric FeN phase can be formed in a narrow substrate temperature range only and the existing debate regarding the LP of FeN can be understood due to its sensitivity to growth temperature. The details of fitting of CEMS are described in Refs. [122, 139].

From the results presented on the synthesis of iron nitride thin films using the reactive sputtering process, it can be seen that most of the phases such as amorphous and nanocrystalline Fe(N), $Fe_{16}N_2$, Fe_4N, $Fe_{3-y}N$, Fe_2N, and FeN can be synthesized by suitably varying the growth conditions. Essentially, by fine-tuning the amount of N_2 gas and growth temperature, it is possible to achieve any of these Fe-N phases in correct stoichiometry with an exception to $Fe_{16}N_2$ phase. The issues related to the thermal stability of Fe-N phases are described in the next Sect. 2.2.

2.2 Thermal Stability of Iron Nitrides

The thermal stability of Fe-N samples was studied by doing thermal annealing of Fe-N samples across the Fe-N phase diagram. Results obtained from such studies will be presented and discussed briefly here and more details can be found in Refs. [96–98, 101, 103–105, 131, 140, 141] Fig. 12a–d shows XRD patterns of pristine (at 300 K) and annealed samples, deposited at R_{N_2} = 2, 5, 10 and 20%, respectively [101]. The phases that are formed with R_{N_2} = 2 and 5% are nanocrystalline Fe(N) in which N atoms gradually occupy the interstitial positions within the bcc-Fe. As can be seen from Fig. 12a, b, even after annealing these samples at 423 K, they become unstable and peaks corresponding to $Fe_{16}N_2$ can be seen. On the other hand, when R_{N_2} is raised to 10%, this sample attains an amorphous phase (Fig. 12c) and this phase is surprisingly much more stable than nanocrystalline phases. This amorphous phase remains stable up to 523 K and after annealing at 573 and 673 K, peaks corresponding to $Fe_{3-y}N$ can be seen. As will be discussed later in Sect. 4, somewhat better thermal stability of amorphous (compared to nanocrystalline) phase can be due to different diffusion processes. In the nanocrystalline phase, diffusion takes place via grain boundaries and in an amorphous phase due to the absence of such grain boundaries, the diffusion mechanism is a collective type involving a large group of atoms [131, 142]. Since grain boundaries diffusion is much faster than collective- type process, the improved thermal stability upon attaining an amorphous phase can be understood.

The sample deposited with R_{N_2} = 20% is a mixture of amorphous Fe(N) and $Fe_{3-y}N$ and after annealing at 423 K, it attains $Fe_{3-y}N$ phase that remains stable at 573 K as shown in Fig. 12d. Further, the thermal stability of Fe_4N phase was also studied. Since this phase is synthesized at 673 K, it remains stable when annealed for a short time below the synthesis temperature, however it shows signs of instability when kept at growth temperature (673 K) at longer times. Such instabilities were observed in Ref. [143] and also in our recent work, it was observed that when the post-deposition annealing time was increased to 60 min, Fe starts to appear in the XRD pattern, though its presence could not be seen when the post-deposition annealing time was 30 min [132]. Therefore, it appears that even during the growth of a Fe_4N phase at a high Ts of 673 K, some N out diffusion is taking place. Also at such high growth temperatures, interdiffusion from the substrate can also influence the properties of Fe_4N films [77].

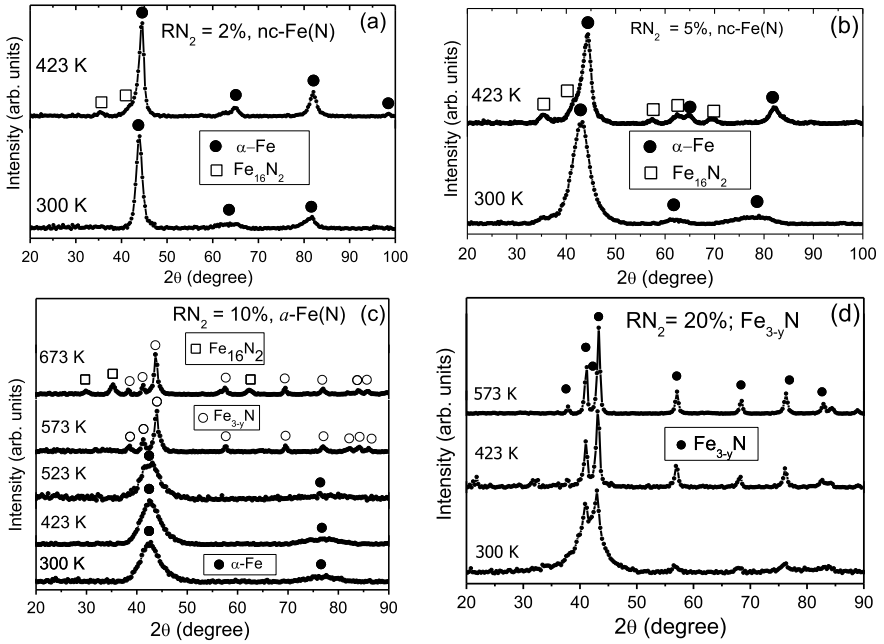

Fig. 12 X-ray diffraction patterns of Fe-N thin films deposited at 300 K and annealed at different temperatures (**a**) nanocrystalline (nc) Fe(N) film formed with R_{N_2} = 2% (**b**) nanocrystalline (nc) Fe(N) film formed with R_{N_2} = 5% (**c**) amorphous (*a*) Fe(N) film formed with R_{N_2} = 10% (**d**) $Fe_{3-y}N$ film formed with R_{N_2} = 20%. Reproduced with permission from Ref. [101]

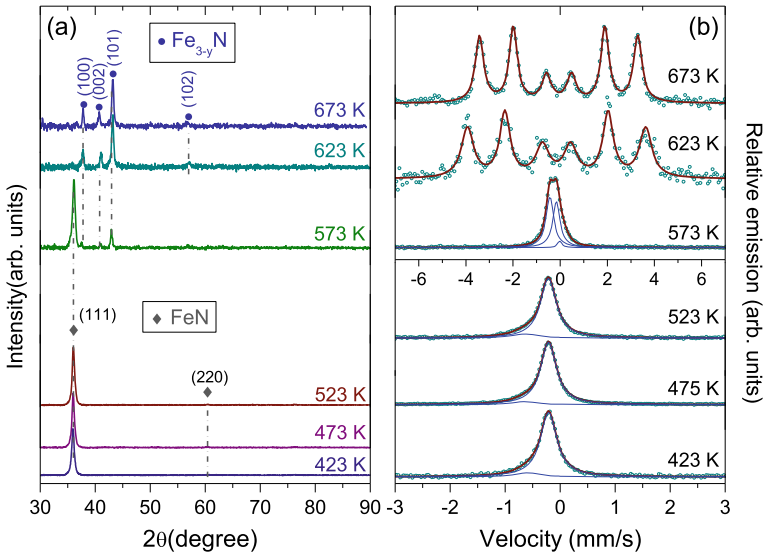

Fig. 13 X-ray diffraction (**a**) and conversion electron Mössbauer spectroscopy (**b**) patterns of FeN thin films deposited at 423 K and annealed at different temperatures

Thermal stability of mononitride FeN phase was also studied. Single-phase and stoichiometry FeN films were grown at optimized growth temperature ≈423 K and thereafter they were annealed at different temperatures as shown in Fig. 13. As can be seen here, both XRD and CEMS pattern of FeN film remains similar after annealing them at 473 and 523 K. However, above 573 K, they become unstable and the $Fe_{3-y}N$ phase start to emerge. After annealing at even higher temperatures (not shown), the $Fe_{3-y}N$ phase also becomes unstable and N completely diffuses out from Fe-N leaving behind pure Fe. From the thermal stability behaviour discussed in the section, it appears that in magnetic nitrides the amorphous phase formed with interstitial incorporation of N and the mononitride phases show thermal stability up to 523 K, other disorder phases are unstable even at 423 K. The $Fe_{3-y}N$ phase in different composition remains stable up to 673 K. In order to understand the thermal stability of iron nitrides, we performed Fe and N self-diffusion measurements in various Fe-N compounds. As will be discussed in Sect. 4, in magnetic Fe-N compounds, N diffusion is faster than Fe and can be understood due to smaller size of N, but in non-magnetic Fe-N compounds, it becomes other way round. In order to suppress the fast N diffusion in magnetic Fe-N, it is possible to use a suitable dopant. The effect of dopant of the thermal stabling of FeN is discussed in the next section.

2.3 *Effect of Doping on Thermal Stability of Iron Nitride Thin Films*

From the results shown in Sect. 2.2, it becomes clear that Fe-N compounds are metastable and they start to show instabilities even when annealed at a moderately low temperature of 423 K or in some cases above 523 K. Such thermal instability of Fe-N compounds is not unexpected due to large (less negative) ΔH_f° as explained in Sect. 1.1 for late TMNs. In order to enhance the thermal stability, it, therefore, becomes essential to dope the Fe-N system in such a way that the dopant does not influence the nature of a Fe-N phase yet enhances its stability. The obvious choice of a dopant is a material whose ΔH_f° is much smaller than Fe-N and this dopant must act like a diffusion barrier so that the thermal stability of Fe-N can be enhanced. To achieve this, we used several dopants like Al, Ti, Zr and optimized the best dopant for the Fe-N system [106, 131, 144, 145] and from these works, it was found that Al is the best suitable dopant when used in a small amount (≈3–5%). The criteria for choosing the best dopant is not only the small values of ΔH_f°(e.g. $\Delta H_f^\circ = -360$, -338, and -321 for ZrN, TiN and AlN, respectively) but their atomic size also matters. Al with the the smallest size was found to be the most effective dopant as it suppresses the lattice distortions that are generally caused by larger (than Fe) dopants.

The effect of dopants on the thermal stability will be discussed later in this section and its influence on Fe and N self-diffusion process in Sect. 4.3. However, before discussing the role of dopants on the thermal stability, it is essential to know if these

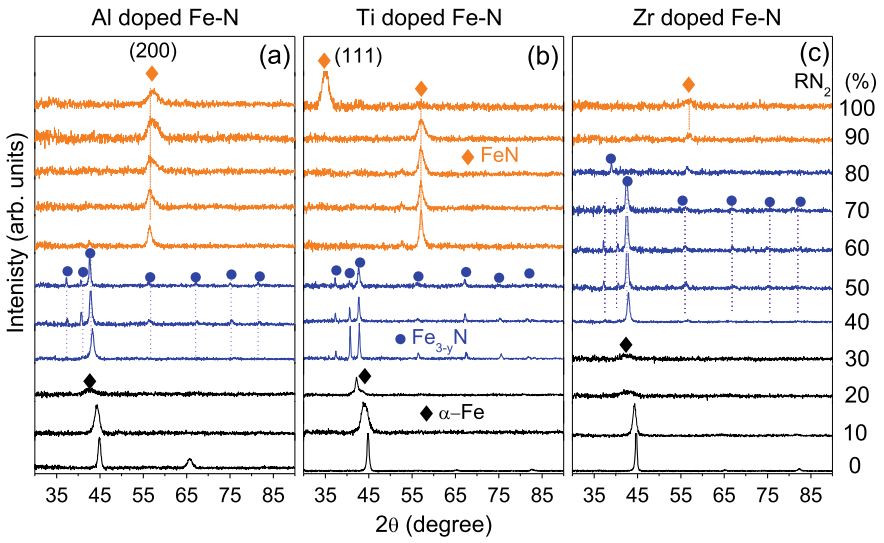

Fig. 14 X-ray diffraction patterns of Fe-N thin films deposited at 300 K for various R_{N_2} values between 0 and 100%(similar to un doped case shown in Fig. 8a) with about 2–3% doping of Al (**a**), Ti (**b**) and Zr (**c**)

dopants affect the phase formation of Fe-N. Figure 14a, b and c, respectively, show the effect of Al, Ti and Zr dopants on the Fe-N phases formed with different R_{N_2} at Ts = 300 K. The amount of dopant used was about $3at.\%$. In absence of any dopant (Fig. 8a), the evolution of FeN phases was Fe $\rightarrow$ Fe(N) $\rightarrow$ $Fe_{3-y}N$ $\rightarrow$ Fe_2N $\rightarrow$ FeN as R_{N_2} increases from 0 to 100%. After doping also, the evolution of Fe-N phases remains almost similar but some minor differences can be seen (i) with doping the Fe_2N phase could not be seen (ii) the appearance of FeN phase already starts at with much smaller amount of R_{N_2} with Al and Ti doping (iii) the preferred orientation of FeN also gets affected. However, it can be clearly seen from Fig. 14 that nitrides of Al, Ti or Zr cannot be seen in the XRD pattern and they do not as such affect the formation of Fe-N phases.

The effect of doping on the thermal stability was studied on a Fe-N sample deposited using R_{N_2} =10% at Ts = 300 K. Samples were annealed in a high vacuum furnace for 1 h at each temperature. Without any doping, the Fe-N phase formed is nanocrystalline bcc Fe(N) in which N atoms occupy the interstitial positions. Undoped Fe(N) becomes thermally unstable when annealed above 423 K as shown in Fig. 12, however after doping with about $3at.\%$ of Al or Zr, the nanocrystalline Fe(N) phase becomes stable up to 625 K as shown in Fig. 15a, b. In fact doping of different amounts of Al, Ti and Zr was tried and in all cases a thermally stable state could be achieved as shown in Fig. 15c. In the undoped sample, the grain growth already starts to take place above 423 K but such grain growth could not be seen up to 673 K with dopants. So it appears that any dopant is suitable in Fe-N system to

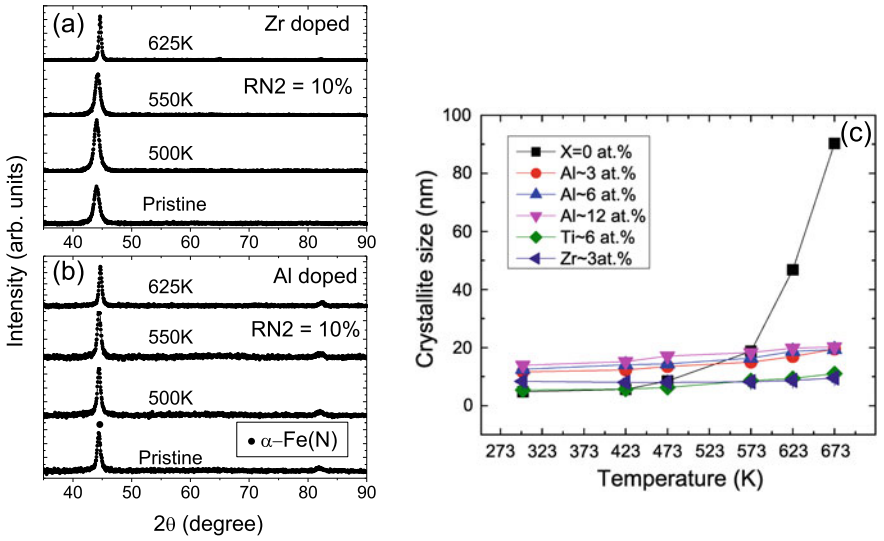

Fig. 15 X-ray diffraction patterns of Fe-N thin films deposited at 300 K with R_{N_2} =10% with $3at.\%$ Zr doping (**a**) and $3at.\%$ Al doping (**b**). The effect of various doping on crystallite size is compared in (**c**)

enhance the thermal stability. However, from the self-diffusion measurements, it was found that Al is most effective as dopant as it suppresses both Fe and N self-diffusion.

The effect of doping on the mononitride FeN phase was also studied. The dopants like Al, Ti and Zr do not affect the thermal stability of the FeN phase at all and this is not surprising owing to target poisoning issues. Since the FeN phase is formed when the $R_{N_2} \approx 100\%$ and in this situation, elements with high affinity towards N, e.g. Al, Ti and Zr become poisoned due to formation of a nitride layer on to themselves. In this situation, the effective sputtering from such targets becomes negligibly low [146–148] and henceforth they cannot be doped in FeN. In fact a series of FeN samples with doping of Al, Ti and Zr were deposited and it was found (not shown) that their thermal stability remained analogous to undoped FeN. Therefore, Ag and C were used as a dopant in FeN. It is known that Ag and C are largely not miscible with Fe and during the reactive sputtering process they do not get poisoned. Following the growth procedure described in Sect. 2.1, FeN samples were deposited at substrate temperature Ts = 423 K and XRD patterns of pristine and vacuum-annealed samples at different temperatures (for 1 h at each) are compared in Fig. 16. As can be seen here, the undoped FeN film remains stable up to 523 K and reflection corresponding to the Fe_3N phase can be seen in the 573 K annealed samples. In Ag- or C-doped FeN films, it can be seen that they become stable up to 573 K but after annealing at 623 K the Fe_3N phase starts to emerge. So with Ag or C doping the thermal stability of FeN improves marginally. Moreover,by comparing the XRD pattern of pristine sample, it can be seen that the peak shape of the undoped sample was somewhat asymmetric (marked by an arrow in Fig. 16a), but with Ag or C doping the peak shape becomes

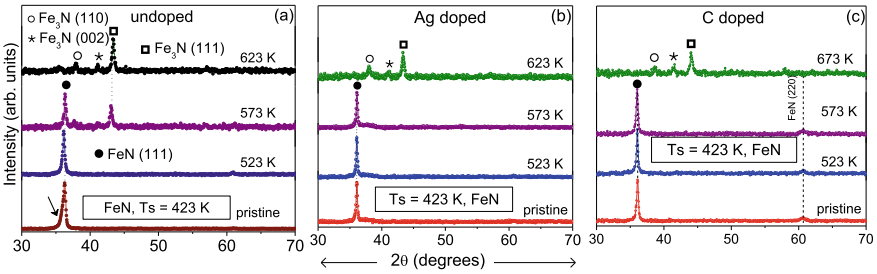

Fig. 16 X-ray diffraction patterns of iron mononitride FeN thin films deposited at substrate temperature Ts = 423 K with R_{N_2} =100% without any doping (**a**), following a similar process but with Ag doping (**b**) and C doping (**c**). XRD patterns of pristine and isochronally annealed samples at different temperatures are compared

symmetric. In addition, the peak corresponding to FeN(111) also becomes narrower with Ag or C doping. These results clearly demonstrate the possibilities to achieve a defect free and stable FeN phase with Ag or C doping.

The thermal stability of iron nitrides is closely related with atomic self-diffusion and dopants have a role to play in improving the thermal stability. The details of the self-diffusion process will be discussed in Sect. 4 but before presenting results on self-diffusion processes, it is essential to know about the methodology and techniques suitable for measuring the self-diffusion process. The details of these techniques are presented in the next Sect. 3.

3 Methodology and Techniques for Self-Diffusion Measurements in Thin Films

Atomic self-diffusion is one of the most basic phenomena which is responsible for several physical and chemical process including phase transformation and solid-state reactions. Even when no defect, gradient or vacancies are present, atomic diffusion is an inevitable process that can occur through an atomic exchange process. In absolute terms, the measurement of self-diffusion is not possible as one would need a 'probe' to locate such a process. In a homogenous medium, it would not be possible to distinguish between similar atoms, one would need a probe that is similar to the host but can be differentiated, as required. In this context, the isotope of host element is viable since the chemical properties of host and isotopes are similar but their mass difference allows them to be differentiated using suitable techniques. Therefore, isotope diffusion can be approximated as self-diffusion. Diffusion is a process that can be activated by external conditions such as pressure, temperature, etc. On this basis, a self-diffusion process can be defined as the measure of atomic diffusivity of any atomic species in a solid in the absence of any chemical potential gradient. For

a detailed review of diffusion in solids, the reader is referred to a review article by Faupel et al. [142] and a monograph by Mehrer [149].

Further, the poor thermal stability of iron nitrides is also a concern and requires diffusion measurements to be carried out at very low temperatures down to ≈500 K or even below. Therefore, it is often required that diffusion lengths of the order of sub to few nm need to be probed and typical diffusivity 10^{-23} m^2 s^{-1} or smaller needs to be measured. Traditionally, self-diffusion measurements are carried out using radiotracer methods, secondary ion mass spectrometry (SIMS) and nuclear-reaction analysis (NRA) [142]. However, the the depth resolution of these methods is typically 5–10 nm. Therefore, probing diffusion lengths below ≈10 nm is not reliable using traditionally used techniques. In this respect, reflection of neutron from a smooth surface which is known as neutron reflectivity (NR) is a versatile technique that can be utilized to probe self-diffusion processes at much smaller length scales than that with traditional techniques. Also since neutron scattering length (SL) vary significantly among most isotopes, NR becomes a unique technique to probe self-diffusion processes at very short length scale even down to sub-nm regime. For example, in case of neutrons, the SL for ^{natural}Fe (or Fe hereafter) is 9.45 fm, for ^{57}Fe 2.3 fm, for ^{natural}N (or N hereafter) is 9.36 fm and for ^{15}N 6.6 fm, therefore isotope labelling using either ^{57}Fe or ^{15}N allows to probe Fe self-diffusion in Fe-N system.

The usage of NR for diffusion measurements was introduced by Greer et al. [150–152] and has been used in several works. Similar to NR, another technique that can be used with the same precision is nuclear resonance reflectivity (NRR) at a large (≥6 GeV) synchrotron radiation (SR) source. The NRR is analogous to Mössbauer spectroscopy but performed under grazing incidence at an SR source. However, unlike neutrons, the NRR is restricted to a Mössbauer active nuclei (e.g. ^{57}Fe). The usage of NRR for self-diffusion measurements was demonstrated in our group [98, 140, 153, 154] and subsequently, NRR has also been used in several works to probe self-diffusion in chemically homogenous multilayers and thin films. Though NR is more versatile, neutron flux, in general, is a concern, this problem can be amply resolved in NRR. For example in using ^{57}Fe isotope, NRR technique can be used even when the individual layer thickness is few nm, NR is more suitable when the thickness increase to about 10 nm and SIMS is suitable when thicknesses reach tens to hundreds of nm. Therefore, combining NRR, NR and SIMS; Fe self-diffusion ranging from a fraction of nm to several hundreds of nm can be probed. In the next section, we will briefly discuss the methodology of SIMS, NR and NRR for self-diffusion measurements in Fe-N thin films.

3.1 Self-Diffusion Measurements Using SIMS Depth Profiling

Secondary ion mass spectrometry (SIMS) is a technique that provides a 'direct' depth profile of a thin film sample by sequential removal of a surface using a sputter

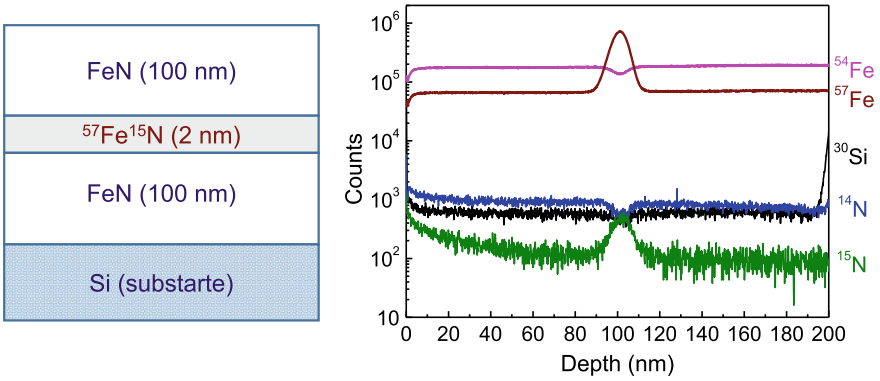

Fig. 17 Schematic representation of a FeN (100 nm)/$^{57}Fe^{15}N$ (2 nm)/ FeN (100 nm) sample deposited on a Si substrate (left) and SIMS depth profiling of ^{14}N, ^{15}N, ^{30}Si, ^{54}Fe and ^{57}Fe showing a peak for ^{15}N and ^{57}Fe distribution (right)

ion source. By its virtue, it is a destructive technique and during the measurements, it is possible that the surface gets modified due to the impingement of primary ion (typical energy few keV) beam falling on to the sample. However, using low beam current (typically a few hundred nA), the heating of the sample due to ion bombardment can be avoided. The primary ion beam sputters the surface of a sample and produces secondary ions that are detected using a suitable mass spectrometer. Generally, the mass resolution of a typical SIMS system is good enough to distinguish neighbouring masses, e.g. ^{14}N or ^{15}N, ^{56}Fe or ^{57}Fe in case of Fe-N. However, the depth resolution of SIMS is typically 5 nm. This is primarily limited by the fact that secondary ions generated in a sputtering process do not come only from the surface, but also from some region underneath. The extent of such depth depends upon the geometry, intensity and the energy primary ion beam. Therefore, even from the best SIMS system, achieving a depth resolution better than a few nm becomes tedious. Nevertheless, the depth resolution of SIMS is sufficient to probe diffusion lengths exceeding beyond a few nm in a sample.

In order to probe self-diffusion in this film samples, it is required that one or more tracer layer(s) to be placed between thick layers as shown schematically in Fig. 17. In this sample, a 2 nm enriched $^{57}Fe^{15}N$ layer is sandwiched between natural FeN layers. Typical experimental SIMS depth profile of this sample is also shown in Fig. 17. In this experiment, depth profiles corresponding to masses ^{14}N, ^{15}N, ^{30}Si, ^{54}Fe, and ^{57}Fe are shown and the sample was sputtered till the intensity of substrate (^{30}Si) start to increase. The sputter time can be converted to depth either by measuring the depth of the crater using a profilometer or using the sputter time to depth conversion factor if the thickness of the sample was known a priori. As one would expect, the depth profile of both ^{15}N and ^{57}Fe yield a peak. Using this depth profile as a reference, broadening due to diffusion of ^{15}N and ^{57}Fe into Fe-N will yield N and Fe self-diffusion coefficients.

In such cases where diffusing species (diffusant or diffuser) is allowed to spread into two material bodies ideally occupying spaces between $+\infty$ and $-\infty$, the thin film solution to non-steady-state diffusion or Fick's second law of diffusion is applicable [149]. The tracer concentration C at a penetration depth x at time t is given by [149, 155]

$$c(x,t) = \frac{M}{2\sqrt{\pi Dt}} \exp\left(-\frac{x^2}{4Dt}\right), \tag{1}$$

where M is a constant denoting the number of diffusing particles per unit area, and D is diffusion coefficient. The quantity $2\sqrt{Dt}$ is a characteristic diffusion length. This solution is also known as Gaussian solution comparing the standard deviation (σ) of Gaussian depth profile before ($t = 0$) and after time t, time-averaged diffusivity $\langle D \rangle$ can be obtained using

$$\langle D \rangle(t) = \frac{\sigma_t^2 - \sigma_0^2}{2t}. \tag{2}$$

At a given temperature, at initial times diffusion takes places rapidly and decays exponentially given by [97, 156]

$$\langle D \rangle(t) = \frac{A\tau}{t}(1 - e^{-t/\tau}) + D_R, \tag{3}$$

where D_R is diffusivity obtained in the relaxed state and τ is time taken to achieve the relaxed state. After obtaining D_R at a temperature T, it becomes possible to calculate the pre-exponential factor D_0 and activation energy (E) using

$$D_R = D_0 \exp\left(-\frac{E}{k_B T}\right), \tag{4}$$

where k_B is Boltzmann constant. Therefore, one needs to calculate the D_R at various temperatures and the logarithmic of Eq. 4 becomes a linear equation and a straight line fit to diffusivity data follows an Arrhenius behaviour yielding E and D_0. Taking into account the available self and impurity diffusion data in amorphous crystalline alloys, it has been established that an universal correlation exists between E and D_0 [142, 157]. Such relation between E and D_0 is known as isokinetic relation, given by [158]

$$\ln D_0 = \ln A + \frac{E}{B}, \tag{5}$$

here A and B are constants. Comparing the E and D_0 correlation, one can differentiate between the type of diffusion mechanisms that takes place in a given material. In general, it has been found that the slope of such correlation is distinctly different in amorphous and crystalline alloys [142]. Following an approach adopted by Shewmon [155], the pre-exponential factor D_0 can be written as

$$\ln D_0 = \ln(ga^2 f \nu_0) + \frac{\Delta S}{k_B}, \tag{6}$$

where g is a geometrical factor, a is the effective jump distance with frequency ν_0 and ΔS is entropy term. Combining Eqs. 5 and 6, we get [159]

$$A = ga^2 f \nu_0; B = k_B E/\Delta S. \tag{7}$$

with the known values of E and B from an experiment, it becomes possible to estimate ΔS. In general the values of ΔS have been typically found between 2.5 and $7.5\,k_B$ in crystalline alloys, whereas in amorphous alloys these values were found to be much large, between 19 and $56\,k_B$. In case of nanocrystalline thin films, these values lie typically between 8 and $15\,k_B$. Broadly, by estimating ΔS one can estimate the type of diffusion mechanism—low values ΔS indicate vacancy-type diffusion process generally found in crystalline alloys and much higher values observed in case of amorphous alloys are indicative of a collective-type diffusion mechanism in which a large group of atoms collectively participate in the diffusion process.

Here, Eqs. 1 and 2 are specific to diffusion measurements using SIMS depth profiling whereas Eqs. 3, 4, 5, 6 and 7 are applicable irrespective of the technique used to determine diffusion coefficient. We will now briefly discuss ways to measure self-diffusion using neutron and nuclear resonance reflectivity techniques.

3.2 Self-Diffusion Measurements Using Neutron Reflectivity

The grazing angle reflection of hard X-rays (wavelength $\lambda \approx 1$ Å) and also of neutrons of similar wavelengths are well-established elastic scattering techniques commonly referred as X-ray reflectivity (XRR) and neutron reflectivity (NR). At grazing angles, the length scales that are probed increase immensely and X-rays or neutrons are no longer sensitive to crystal lattice as in X-ray or neutron diffraction. Therefore, irrespective of long-range ordering, XRR and NR can be equally used in a single crystalline, polycrystalline or an amorphous thin film. Both XRR and NR rely on the principle of total external reflection that takes place below a critical angle, above this critical angle X-rays or neutrons penetrate deep inside a sample and get reflected again when a change in number density occurs. The first experiment on total reflection of X-rays from smooth and flat surfaces was carried out way back in 1923 by Compton [160]. Parratt [161] developed theory for XRR in 1954, which is based on Fresnel reflection and transmission and treated in a similar way for X-rays and neutrons. With further developments in theory and instrumentation, XRR become a popular technique to probe thin films and multilayers for their density, thickness (with an accuracy of about 0.2 nm) and surface/interface roughness [162]. Both XRR and NR techniques have been described in several books, e.g. [163–165] and in this work, we will focus on their utility for determination of diffusion.

The primary difference between XRR and NR is based on their interaction with matter. While X-ray interacts with electrons, the interaction of neutrons takes place from nuclei. Therefore, X-ray scattering depends on the number of electrons (i.e. Z) present in a sample, neutron scattering lengths (nSL) have been found to vary randomly across the periodic table. In addition, since the mass of different isotopes are different, nSL can vary appreciably even for neighbouring masses, e.g. for ^{natural}Fe, nSL = 9.45 fm, for ^{57}Fe, nSL = 2.3 fm, for ^{natural}N, nSL = 9.36 fm and for ^{15}N, nSL = 6.6 fm. Similarly, nSL can vary for isotopes of different elements and a database for nSL can be found in Ref. [166]. In addition, it is known that neutron possesses a magnetic moment and in case of ferromagnetic samples they also interact with unpaired electrons through a dipole–dipole interaction which is known as magnetic scattering. The amplitudes of nuclear and magnetic scattering are comparable, therefore magnetism of a magnetic sample can also be probed by performing polarized neutron reflectivity (PNR) measurements [167]. In fact combing the sensitiveness of neutron to isotopes and magnetism, simultaneous information about the self-diffusion as well as magnetism can be probed by doing PNR measurements. This was amply demonstrated in case of $[FePt|^{57}FePt]_{10}$ chemically homogeneous multilayer (CHM). It was found that the structural/magnetic ordering and iron self-diffusion processes are concurrent in this system [168].

For measuring diffusion using XRR or NR, is it preferable (through not necessary) to prepare the sample in the form of a multilayer with a repeating sequence of elements A and B in the form of $[A|B]_m$, where m is number by which A and B are repeated. Typically m is taken anywhere between 10 and 100, depending upon the thickness and SL of layer A and B. Such repetition is analogous to a single crystal and gives rise to Bragg peaks in the reflectivity pattern. In the year 1985, Greer et al. [169] introduced such methods for investigation of atomic (inter)-diffusion using X-ray scattering from synthetic modulated structures. Subsequently, Mizoguchi et al. [170] calculated the variation in the X-ray intensity upon diffusion, given by

$$I(t) = I(0) \exp\left(-\frac{8\pi^2 n^2 D(T) t}{d^2}\right), \tag{8}$$

where I_0 is the intensity of the nth-order Bragg peak at time $t = 0$; D is the diffusivity at temperature T, and d is the bilayer periodicity. As a sample is annealed, diffusion across the interfaces takes place and the average scattering length contrast get suppressed leading to a fall in the the intensity of Bragg peak. After calculating D from Eqs. 3, 4, 5, 6, 7 and 8 can be used to get various parameters.

Equation 8 is equally valid in case of XRR and NR, the only difference is that in the case of XRR interdiffusion is probed from composition modulated multilayer whereas in NR isotopic modulation or chemically homogenous multilayers (CHMs) yield self-diffusion. The usage of NR to determine self-diffusion was demonstrated by Greer et al. [150–152] in amorphous $[NiZr|^{62}NiZr]$ multilayers. Soon after in 1997, Baker et al. [171] applied NR to study Boron self-diffusion in amorphous $[^{11}B|^{10}B]$ samples. We used NR to measure Fe self-diffusion in amorphous and nanocrystalline FeZr [159, 172, 173] thin films, Fe and N self-diffusion in Fe-N [103, 131], Fe

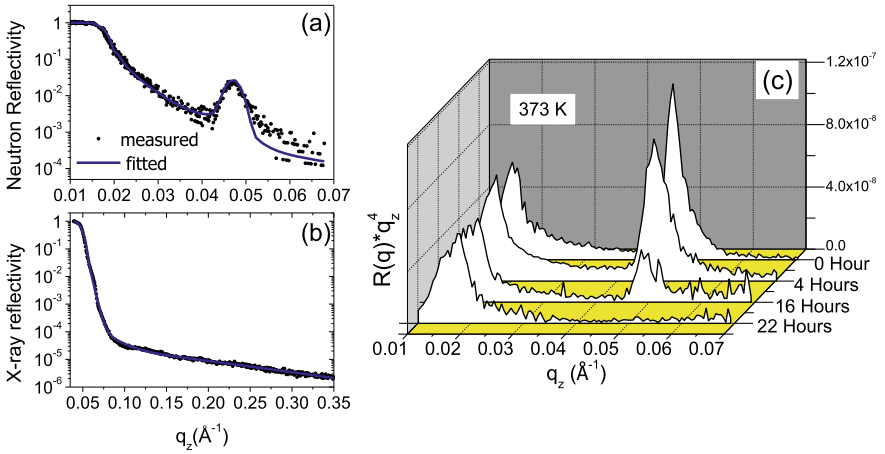

Fig. 18 Neutron (**a**) and X-ray (**b**) reflectivity pattern of FeZr (9 nm)|^{57}FeZr (5 nm)]$_{20}$ chemically homogenous multilayer (CHM). The presence (absence) of well-resolved Bragg peak in NR (XRR) is indicative of chemical homogeneity between FeZr and ^{57}FeZr, as expected. Typical neutron reflectivity profiles (multiplied by a factor of q_z^4 to get a flat background in (**b**)) observed at T = 373 K after different annealing times. Reproduced with permission from Ref. [159]

self-diffusion in FePt [168], N self-diffusion in Co-N [26], Schmidt et al. used NR to study N self-diffusion in amorphous Si_3N_4 [174, 175], Ge self-diffusion in crystalline [^{70}Ge/Ge] multilayers [176], N self-diffusion in amorphous silicon carbonitrides (Si-C-N) [177], Li self-diffusion in lithium niobate single crystals ($LiNbO_3$) [178]. Such a demonstration of usage of NR to measure self-diffusion measurements in a variety of systems having amorphous, polycrystalline or single-crystalline structures clearly exhibit that NR has now become an established technique to study self-diffusion processes in thin films and multilayers.

Prior to self-diffusion measurements from a CHM, it is required that XRR measurements must be carried out to ensure the absence of any unforeseen chemical contrast. This was amply demonstrated in case of our initial usage of NR to measure Fe self-diffusion in amorphous [FeZr (9 nm)|^{57}FeZr (5 nm)]$_{20}$ CHM [159] as shown in Fig. 18. As expected, the XRR pattern of this sample remains analogous to a homogenous film of 140 nm FeZr film, whereas the presence of a well-defined Bragg peak confirms the isotopic periodicity. Subsequently, this film was annealed at 373 K for 4, 16 and 22 h and as can be seen that after 22 h complete Fe self-diffusion takes place in this CHM.

3.3 *Self-Diffusion Measurements Using Nuclear Resonance Reflectivity*

Similar to NR, nuclear resonance reflectivity (NRR) from CHMs can be used as a sensitive technique to study self-diffusion of a Mössbauer isotope (e.g. ^{57}Fe). Although, the way in which interaction of neutron and nuclear resonance scattering (NRS) takes place is entirely different, the information about self-diffusion process can be measured with a similar precession (depth resolution ≈0.2 nm). What makes NRR even more effective (than NR) is the enormous flux available at large synchrotron radiation (SR) sources (e.g. SP-ring-8 in Japan, Advance Photon Source in the USA, PETRA III in Germany and European Synchrotron Radiation Facility in France). By doing NRR measurements, it becomes possible to probe ultrathin films on very small size samples, which is rather difficult to achieve in NR due to rather the poor flux of neutron sources.

NRS measurements are analogous to Mössbauer spectroscopy (MS), while MS measurements are performed using a radioactive source, NRS measurements at an SR source can be performed by tuning the incident X-ray beam energy to nuclear resonance (e.g. 14.4 keV for ^{57}Fe). It is known that the electronic scattering is prompt, taking place in a picosecond time scale, NRS is delayed in time depending on the lifetime (τ_0) of the excited state of the nucleus (for ^{57}Fe, τ_0 = 141 ns). Therefore, if the pulse separation between successive SR pulse is larger than τ_0, the time-integrated measurements are performed similar to XRR measurements, yield NRR. In comparison to X-ray scattering, at nuclear resonance, the total scattering amplitude (f) becomes $f = f^e + f^n$, where f^e is electronic and f^n is nuclear scattering amplitude. The refractive index (n) of the sample is given by [154, 179, 180]:

$$n = 1 + \frac{\lambda_0^2}{2\pi} \sum_i \sigma_i (f_i^e + f_i^n), \tag{9}$$

where λ_0 is the wavelength of incident X-rays and σ_i is the atomic density of ith species. The inset of Fig. 19a compares the refractive index as a function of energy in natural line width units (Γ_0) for a single line (unsplit) resonance for electronic and nuclear contrast. As $\Gamma_0 \rightarrow 0$, large variations can be seen in the nuclear contrast, whereas the electronic part remains unaffected, as expected. It becomes clear that f^n is significant only in a narrow energy range (≈ μeV) around the nuclear transition energy. This gives rise to a strong scattering contrast even exceeding the electronic contrast over an order of magnitude (e.g. for the case shown in Fig. 19a, the values of nuclear and electronic components when $\Gamma_0 \rightarrow 0$ are -2.2×10^{-4} and -5.7×10^{-6}, respectively). Since the chemical composition in a CHM is identical, no contrast can be present due to the electronic scattering, the only contrast that arises is due to Mössbauer active nuclei. This can be amply demonstrated by comparing electronic (XRR) and nuclear (NRR) reflectivity as shown in Fig. 19a for an amorphous [$FeN_{0.7}$ (3 nm)|$^{57}FeN_{0.7}$ (2 nm)]$_{10}$ CHM. Here, both XRR and NRR measurements were performed simultaneously and their actual counts rates are compared. As can be seen

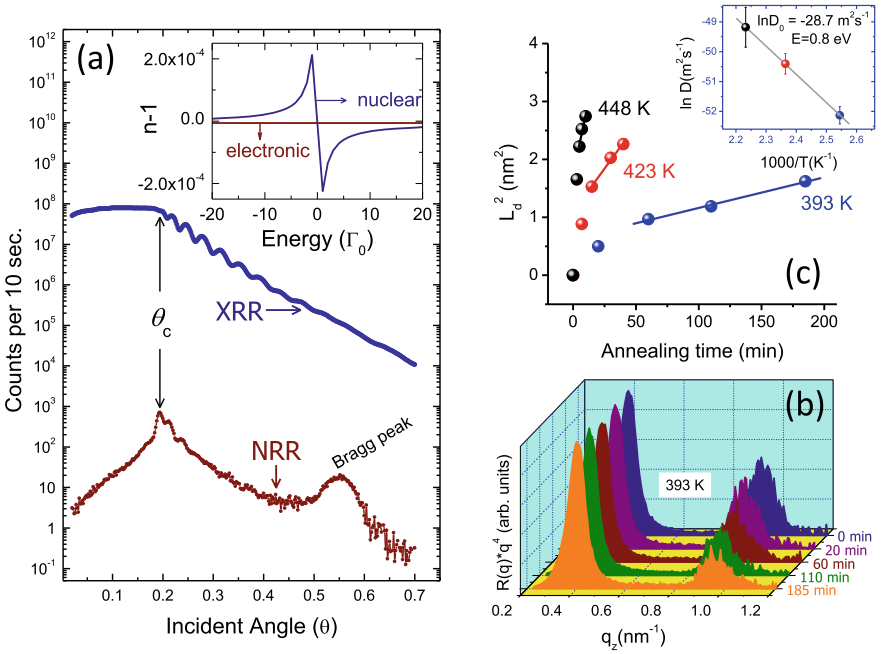

Fig. 19 **a** Electronic (XRR) and nuclear resonance reflectivity (NRR) from an amorphous $[FeN_{0.7}|^{57}FeN_{0.7}]_{10}$ CHM, performed simultaneously at NRS beamline (BL09XU) of SP-ring 8 SR source. The position of critical angles in XRR and NRR is marked as θ_c, and the presence (absence) of a Bragg peak due to isotope periodicity can be seen in the NRR (XRR) patterns. The inset of **a** compares the refractive index as a function of energy in natural line width units (Γ_0) for an unsplit resonance for electronic and nuclear contrasts. **b** NRR pattern of an amorphous [FeN(Zr) (4 nm)| ^{57}FeN(Zr)]$_{20}$ CHM in the as-deposited state (0 min) and after annealing at 393 K for different times. Reflectivity (R(q)) in NRR pattern was multiplied by a factor of q^4 to remove the decay due to Fresnel reflectivity **c** compares obtained diffusivity as a function of annealing times at 393, 423 and 448 K and the inset of **c** shows Arrhenius behaviour of diffusivity given by Eq. 4 yielding pre-exponential factor D_0 and activation energy E. **b** and **c** were reproduced with permission from Ref. [153])

from Fig. 19a, unlike XRR, the critical angle (θ_c) appears like a 'peak' in NRR and this happens due to an interplay between the electronic and nuclear scattering at θ_c [181, 182].

The NRR pattern obtained from such CHM can be used to measure Fe self-diffusion. Such measurements are demonstrated in Fig. 19b for an amorphous [FeN(Zr) (4 nm)| ^{57}FeN(Zr)]$_{20}$ sample after annealing the sample at 393 K for different annealing times. It may be noted that NRR profiles have been multiplied by a factor of q_z^4 to get a flat background. This allows more convincing realization of data and estimation of intensity at the Bragg peak. As can be seen in Fig. 19b, as annealing time increases, the intensity at Bragg peak decreases gradually whereas the intensity at θ_c remains unaffected. Similar to the case described for NR, using Eq. 8 instanta-

neous diffusion can be calculated and thereby using Eq. 3 diffusivity in the relaxed state can be obtained. By performing such experiments at different temperatures, the evolution of diffusion length was obtained and is shown in Fig. 19c. We can see that the diffusion length increases at a faster rate in the beginning but after some time it becomes constant. This type of behaviour is typically associated with the structural relaxation in the system. The slope of the curve in Fig. 19c can be used to calculate the diffusivity in the relaxed state and then using Eq. 4, the pre-exponential factor (D_0) and activation energy E can be calculated.

As mentioned already, the NRR measurements are performed in time integral mode, in addition grazing incidence NRS measurements can also be performed in these samples at a fixed angle of incidence. This mode is known as time differential mode or simply known as NRS of SR [183–187]. This mode is a time response of hyperfine interactions present in the sample. As a nucleus interacts with the surrounding electrons, the splitting of the excited and/or ground state takes place, in the time spectra this results in a beating pattern known as Quantum beats. Time-resolved NRS measurements provide a wealth of information about the magnetism of sample and have been described in detail in Ref. [183].

From this brief description of SIMS, NR and NRR, it becomes clear that these techniques can be suitability used for Fe self-diffusion in Fe-N system. By the virtue of these techniques, the typical diffusion length that can be probed in NRR are up to few nm, say between 0.2 and 10 nm, in NR this typically changes to 2–20 nm and in SIMS 10–1000 nm. Therefore, by combining these techniques it is possible to cover a vast range for measurements of self-diffusion in thin-film samples. In addition, both SIMS and NR can also be used to probe N self-diffusion also. We performed Fe self-diffusion measurements using all three methods described here and N self-diffusion using NR and SIMS in some Fe-N compounds. These self-diffusion measurements are discussed in Sect. 4.

4 Self-Diffusion Studies in Iron Nitride Thin Films

In this section, we will present experimental results that were carried out in different Fe-N phases with their nominal composition around $Fe_{16}N_2$, Fe_4N, $Fe_{3-y}N$ ($y \approx 0.8$) and FeN [97, 98, 103, 105, 131, 140, 141, 153, 179]. The synthesis and thermal stability of these phases have already been described in Sect. 2. Essentially, $Fe_{16}N_2$ and Fe_4N phases are magnetic while $Fe_{3-y}N$ ($y \approx 0.8$) and FeN were non-magnetic at 300 K. From the measurements of Fe and N self-diffusion in Fe-N, it was found that diffusion processes were significantly different in magnetic and non-magnetic Fe-N compounds and they will be discussed separately in Sects. 4.1 and 4.2, respectively.

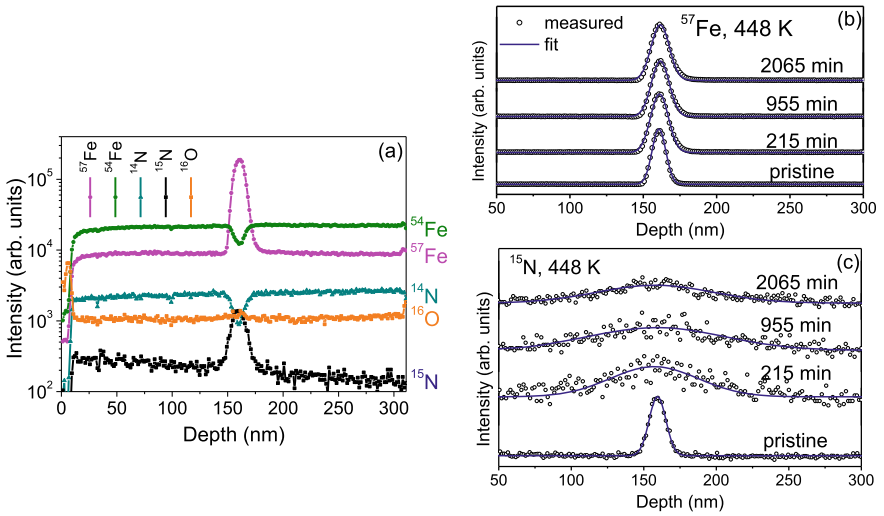

Fig. 20 SIMS depth profile (raw data) of a [FeN (120 nm)|^{57}Fe^{15}N (9 nm)|FeN (120 nm)] tri-layer sample showing distinguished peaks corresponding to ^{57}Fe and ^{15}N contrasts and dips in ^{54}Fe and ^{14}N profiles (**a**). ^{57}Fe (**b**) and ^{15}N (**c**) depth profiles of this sample after annealing at different times (reproduced with permission from Ref. [141])

4.1 Self-Diffusion Studies in Magnetic Iron Nitride Thin Films

Fe and N self-diffusion measurements were carried out in amorphous and nanocrystalline Fe-N compounds formed with N$at.\% \approx$10 which is the nominal composition for $Fe_{16}N_2$ phase. As discussed in Sect. 2, by doing a little variation of R_{N_2} an amorphous or a nanocrystalline phase of Fe-N can be formed and the thermal stability of the amorphous phase was found to be slightly better in the amorphous Fe-N phase. Amorphous Fe-N samples with a tri-layer structure [Fe-N (120 nm)|^{57}Fe-^{15}N (9 nm)|Fe-N (120 nm)] and a CHM with [Fe-N (22 nm)|^{57}Fe-N (8 nm)]$_{10}$ were deposited under identical deposition conditions on a Si substrate and (Fe+N) and Fe diffusion was measured using SIMS and NR [141].

Using SIMS, it is possible to measure self-diffusion of both Fe and N simultaneously. Raw SIMS depth profiles of the samples for ^{57}Fe, ^{54}Fe, ^{15}N, ^{14}N and ^{16}O are compared in Fig. 20a. After annealing, these depth profiles get broadened due to self-diffusion. ^{57}Fe and ^{15}N depth profiles measured after annealing at 448 K are shown in Fig. 20b, c for different annealing times. As can be clearly seen, the ^{57}Fe profile becomes only a little broadened even after annealing for 2065 min but the ^{15}N profile get significantly broadened just after 215 min. This behaviour clearly indicates that N is diffusing several times faster than Fe. By measuring the difference in broadening before and after annealing time-averaged diffusivity can be calculated using Eq. 2. Similarly, such measurements have also been carried out 498 K and diffusivity in

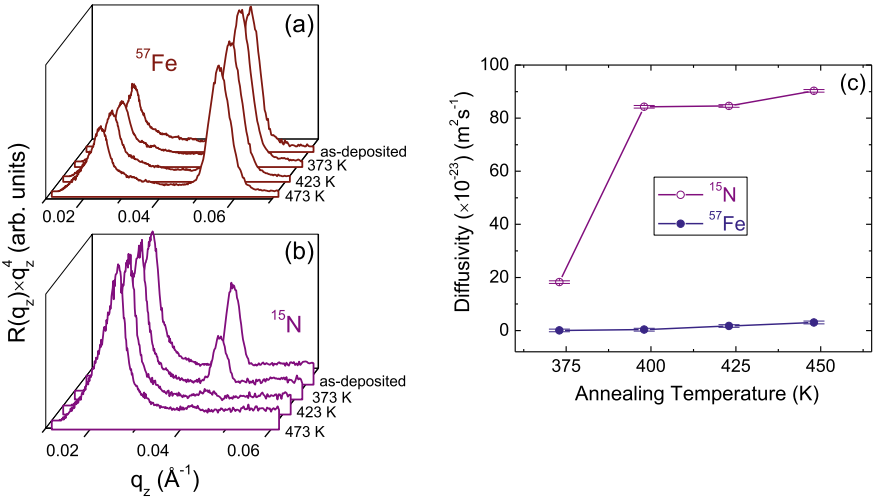

Fig. 21 Neutron reflectivity patterns of nanocrystalline [Fe-N (6 nm)|^{57}Fe-N (6 nm)]$_{10}$ (**a**) and [Fe-N (9 nm)|Fe-^{15}N (9 nm)]$_{25}$ (**b**) in the as-deposited state and after annealing at different temperatures. The y-axis has been multiplied by a factor of q_z^4 [131]. Obtained values of Fe and N diffusivity are compared in (**c**), here solid lines are a guide to the eye

the relaxed state was calculated using Eq. 3. From this analysis, it was found that diffusivity of N was about 2 orders of magnitude faster than that of Fe. But it was interesting to note that the time taken to achieve a relaxed state was almost similar for Fe and N self-diffusion- about 7000 s at 448 K and 2000 s at 498 K [141].

In order to measure diffusivity more precisely, NR measurements were carried out to measure Fe self-diffusion in [FeN (22 nm)|^{57}FeN (8 nm)]$_{10}$. A Bragg peak corresponding to the bilayer period was observed and after annealing at different temperatures and different times, it was found that the activation energy (E) and pre-exponential factor (D_0) comes out to be 0.5±0.3 eV and exp(−40±8 m^2 s^{-1}), respectively. Subsequently, using Eqs. 5, 6 and 7, it was found that value of entropy, ΔS was about $10k_B$, which indicates that the diffusion mechanism was similar to other metal–metal and metal–metalloid amorphous alloys, involving a large group of atoms [141].

Fe and N self-diffusion measurements were also carried out in a nanocrystalline Fe-N phase having N $\approx 11at.\%$ by doing NR measurements in CHM of [Fe-N (6 nm)|^{57}Fe-N (6 nm)]$_{10}$ and [Fe-N (9 nm)|Fe-^{15}N (9 nm)]$_{25}$ [131] as shown in Fig. 21. Here, it can be seen that up to an annealing temperature of 473 K, Fe self-diffusion was negligible but N self-diffusion was significantly high and gets completed at 423 K. In fact N self-diffusion was so fast that measuring a sample after a year amounted to the diffusivity of about 2×10^{-25} m^2 s^{-1} at 300 K [131] whereas extrapolated values of Fe diffusivity at 300 K are expected to be much smaller [141]. The measurement of diffusivity down to 2×10^{-25} m^2 s^{-1} demonstrates the capability of NR technique to measure such a small value of diffusivity.

It was even more interesting to find out that the relaxation time for N self-diffusion in nanocrystalline Fe-N was about 250 s at 415 K [131]. Compared to this, in amorphous Fe-N phase, the relaxation was about 8000 s at 448 K. Since relaxation time decreases with increasing annealing temperature, higher relaxation time at even higher temperature clearly indicates differences in the diffusion process [141]. As pointed out by Faupel et al. [142], in amorphous alloys a collective diffusion mechanism involving many atoms is prevalent but in a nanocrystalline phase the presence of large amount of grain boundaries leads to the motion of a much smaller group of atoms. This eventually explains why the relaxation time was significantly larger in amorphous Fe-N as compared to nanocrystalline Fe-N of similar composition.

Self-diffusion of Fe was also measured in Fe_4N samples using a CHM of $[Fe_4N\ (25\,nm)\ |\ ^{57}Fe_4N(5\,nm)]_{10}$. Since the formation of Fe_4N starts to take place around a substrate temperature of 500 K [188], this sample was deposited at Ts = 523 K. Due to growth at high temperature, during the growth itself significant diffusion takes place, however a well-resolved Bragg peak in the NR pattern (not shown) paved ways to elucidate Fe self-diffusion in this sample by doing isothermal annealing for 1 h at 573, 623 and 673 K. The values of Fe diffusivity in Fe_4N were found to be 3.1×10^{-24}, 2.5×10^{-23}, and $2.9\times10^{-23}\,m^2\ s^{-1}$, respectively, at 573, 623 and 673 K and the activation energy E comes out to be 0.8 eV. The extrapolated value of Fe diffusivity at room temperature (300 K) comes out to be $8\times10^{-30}m^2\ s^{-1}$.

From the Fe and N self-diffusion data obtained in Fe-N, the thermal stability can be understood. Following the dense random packing model for metal–metalloid systems, it is anticipated that metal atom forms a dense packing in which metalloid atoms occupy the interstitial sites. The thermal stability of such a system is highest when the metalloid concentration is about 20% [189]. In case of Fe-N compounds with $N at.\% \approx 11$, i.e. around the $Fe_{16}N_2$ phase, it can be expected that there are several vacant interstitial sites available for N atoms to hop without affecting its thermal stability. We can see that N self-diffusion practically gets over even when Fe self-diffusion process starts to take place (see Figs. 20 and 21). It is also interesting to note the thermal stability of Fe-N phases is not affected by N self-diffusion, but at the onset of Fe self-diffusion. However, when Fe self-diffusion becomes appreciable, N atoms start to diffuse out from Fe-N leaving behind N deficient Fe-N or pure Fe. Therefore, to improve the thermal stability of Fe-N alloys and compounds, it appears that Fe self-diffusion should be suppressed. The effect of dopants on the Fe and N self-diffusion is presented in Sect. 4.3.

4.2 Self-Diffusion Studies in Non-Magnetic Iron Nitride Thin Films

In this section, we will present and discuss Fe and N self-diffusion processes in non-magnetic iron nitride samples, namely $Fe_{3-y}N$ (y = 0.77) or $Fe_{2.23}N$ and the

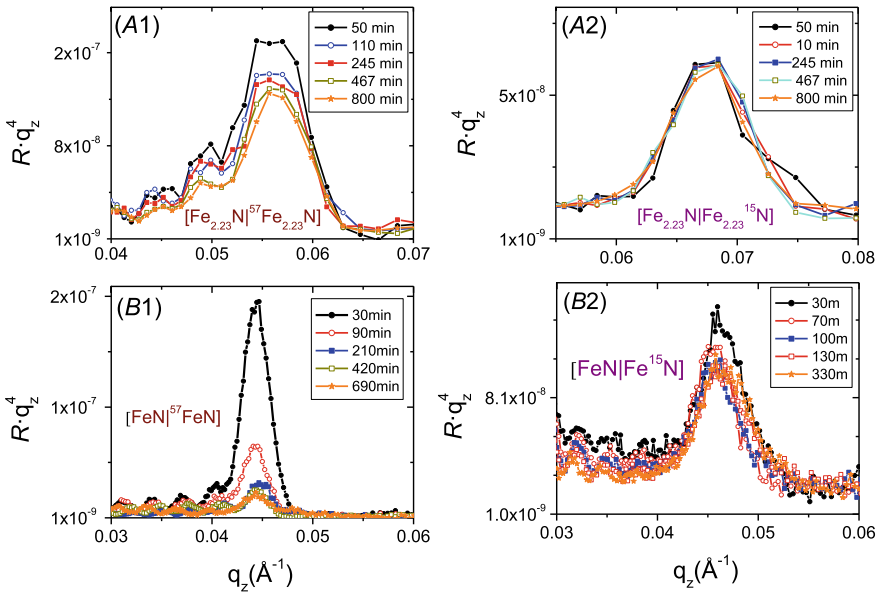

Fig. 22 Neutron reflectivity patterns measured after annealing at 373 K (**A1**,**A2**) and at 463 K (**B1**,**B2**) for different annealing times in sample **A1**: $[Fe_{2.23}N(7.5\,nm)|^{57}Fe_{2.23}N(4.5\,nm)]_{10}$ (for Fe self-diffusion in $Fe_{2.23}N$), **A2**: $[Fe_{2.23}N(6.4\,nm)|Fe_{2.23}{}^{15}N(3.2\,nm)]_{10}$ (for N self-diffusion in $Fe_{2.23}N$), **B1**: $[FeN(10.2\,nm)|^{57}FeN(5.2\,nm)]_{10}$ (for Fe self-diffusion in FeN) and **B2**: $[FeN(10.6\,nm)|Fe^{15}N(5.2\,nm)]_{10}$ (for N self-diffusion in FeN). Reproduced with permission from Ref. [103]

mononitride, FeN phase [103, 105]. For this purpose, following CHM samples were prepared and studied using NR:

$A1$: $[Fe_{2.23}N(7.5\,nm)|^{57}Fe_{2.23}N(4.5\,nm)]_{10}$, for Fe self-diffusion in $Fe_{2.23}N$
$A2$: $[Fe_{2.23}N(6.4\,nm)|Fe_{2.23}{}^{15}N(3.2\,nm)]_{10}$, for N self-diffusion in $Fe_{2.23}N$
$B1$: $[FeN(10.2\,nm)|^{57}FeN(5.2\,nm)]_{10}$, for Fe self-diffusion in FeN
$B2$: $[FeN(10.6\,nm)|Fe^{15}N(5.2\,nm)]_{10}$, for N self-diffusion in FeN

Figure 22 ($A1$, $A2$) compares the NR profiles of samples $A1$, $A2$ obtained after annealing for different times at 373 K. As discussed already in Sect. 3.2 and from Eq. 8, the decay in the intensity of Bragg peak occurs due to interdiffusion in such multilayer samples. As can be seen there, in sample $A1$, Fe self-diffusion already starts to take place after the shortest annealing time of 110 min and after 800 min, the intensity of the Bragg peak decays significantly. However, it was surprising to note that the Bragg peak in sample $A2$ remains intact even after the highest annealing time of 800 min. It may be noted that both samples ($A1$, $A2$ or $B1$, $B2$) were always annealed together in a vacuum furnace so that the comparison of Fe and N self-diffusion can be done accurately. Similarly, such time-dependent NR measurements were also carried out at other temperatures as well. Following a similar procedure, samples $B1$, $B2$ were also studied and representative NR patterns after annealing at

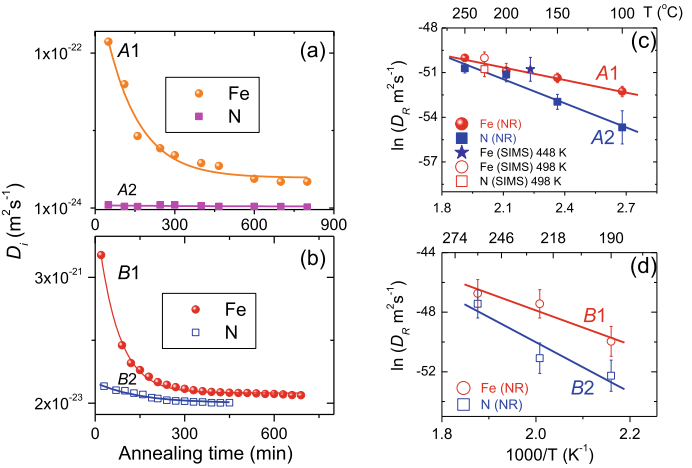

Fig. 23 Instantaneous diffusivity (D_i) in samples $A1$, $A2$ after annealing at 373 K (**a**) and in samples $B1$, $B2$ after annealing at 463 K (**b**). Arrhenius behaviour of diffusivity in the relaxed state (D_R) in samples $A1$, $A2$ (**c**) and $B1$, $B2$ (**d**). Reproduced with permission from Ref. [103]

463 K are shown in Fig. 22. Here again, we observe a similar trend that Fe diffusion seems to be much faster than N.

Further, following the procedure described in Sect. 3, the instantaneous diffusivity (D_i) and the relaxed state diffusivity (D_R) were calculated. A plot of D_i with annealing time is shown in Fig. 23a, b for samples ($A1$, $A2$) and ($B1$, $B2$), respectively. Here also it can be clearly seen that N self-diffusion was much smaller compared to Fe self-diffusion. By performing such measurements at different temperatures, it was found that D_R follows an Arrhenius-type behaviour as shown in Fig. 23c, d and using Eq. 4, E and D_0 were calculated. It was found that the E for Fe self-diffusion was 0.25 eV in $A1$ and 1.0 eV in $B1$ and for N self-diffusion, it was 0.46 eV in $A2$ and 1.5 eV in $B2$. In both samples higher activation energy for N diffusion clearly suggests that N self-diffusion in these samples is slower than Fe. This behaviour is in stark contrast with the behaviour observed in magnetic Fe-N samples presented in previous Sect. 4.1. Also, it is well known that in a binary or multi-component alloys or compound, generally it is expected that smaller atoms would diffuse rapidly [142] (similar to the case observed in magnetic Fe-N samples). However, the diffusion process in non-magnetic Fe-N samples seem to be completely defying such atomic size dependence [103].

In the quest to seek the origin of such anomalous diffusion, iron mononitride (FeN) samples were again studied using NR as well as SIMS depth profiling [105]. Trilayer and CHM samples were prepared with their structure as: [FeN (7.9 nm)|^{57}FeN (7.9 nm)]$_{10}$ (for Fe self-diffusion with NR), [FeN (7.3 nm)|Fe^{15}N (7.3 nm)]$_{10}$ (for N self-diffusion with NR) and [FeN (100 nm)|^{57}Fe^{15}N (2 nm)|FeN (100 nm)] (for simultaneous Fe and N diffusion using SIMS). NR and SIMS depth profile measurements on these samples are shown in Fig. 24a–d. As can be seen here that after

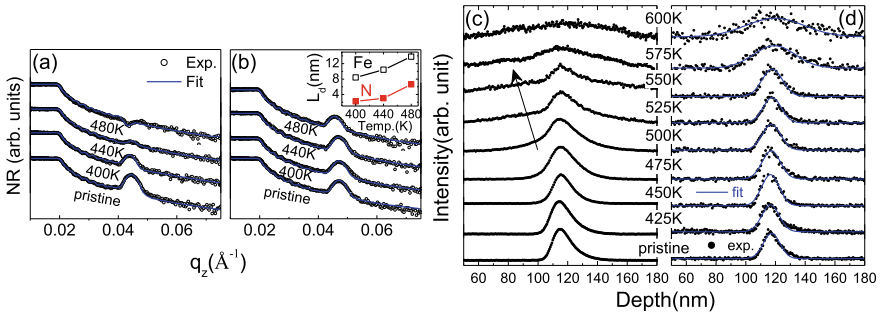

Fig. 24 NR pattern of sample [FeN (7.9 nm)|^{57}FeN (7.9 nm)]$_{10}$ (**a**) and that of sample [FeN (7.3 nm)|Fe^{15}N (7.3 nm)]$_{10}$ (**b**) in the pristine state and after annealing for 2 h each at different temperatures. The inset of **b** compared diffusion length L_d obtained from the fitting these NR patterns. SIMS depth profiles of sample [FeN (100 nm)|^{57}Fe^{15}N (2 nm)|FeN (100 nm)] for ^{57}Fe (**c**) and ^{15}N (**d**) after annealing for 1 h each at different temperatures. Here scattered points are experimental data and solid lines are fit to them. Reproduced with permission from Ref. [105]

annealing at 440 K, the Bragg peak corresponding to Fe contrast disappears in sample [FeN (7.9 nm)|^{57}FeN (7.9 nm)]$_{10}$, whereas it remains intact even after annealing at 480 K in sample [FeN (7.3 nm)|Fe^{15}N (7.3 nm)]$_{10}$. The fitting of NR patterns was carried out using an interdiffused layer and so obtained diffusion lengths L_d are plotted in the inset of Fig. 24b. These results clearly signify that indeed Fe is diffusing faster than N in FeN, in agreement with results obtained in previously studied samples *B*1, *B*2 shown in Fig. 23b, d. In addition, SIMS depth profile measurements carried out in sample: [FeN (100 nm)|^{57}Fe^{15}N (2 nm)|FeN (100 nm)] are shown in Fig. 24c, d, respectively, for ^{57}Fe and ^{15}N in the pristine and isochronally annealed samples for 1 h at each temperature. By increasing the annealing time, the width of ^{57}Fe becomes much broader than that of ^{15}N, due to faster Fe diffusion. Moreover, it is to be noted that the ^{15}N profiles can be fitted to a Gaussian, ^{57}Fe profiles show an additional slope above 475 K marked by an arrow in Fig. 24c. This is an indication of a diffusion process taking place through the grain boundaries as well. Following the detailed analysis presented in Ref. [105], the volume diffusion D_V and grain boundary diffusion (D_{gb}) processes can be separated as shown in Fig. 25a–c. As can be seen there, the D_{gb} of Fe is about 3 orders of magnitude higher compared to D_V of Fe. Moreover, D_{gb} of Fe starts to rise at much lower temperatures.

Further, since isochronal annealing only provides a snapshot picture, therefore isothermal annealing was also performed at different temperatures and again SIMS measurements were carried out. They are representatively shown in Fig. 25d, e for ^{57}Fe and ^{15}N depth profiles taken after annealing of different times at 525 K. Here again, N profiles can be fitted to Gaussian, but Fe profiles were evaluated considering grain boundary and volume diffusion as shown in Fig. 25f. Here also it can be seen that after attaining relaxation, D_{gb} of Fe is about 2 orders of magnitude larger as compared to D_V of Fe. Interestingly, the D_V of N is even smaller than D_V of Fe. Similar isothermal annealing measurements were also performed at other temperatures as

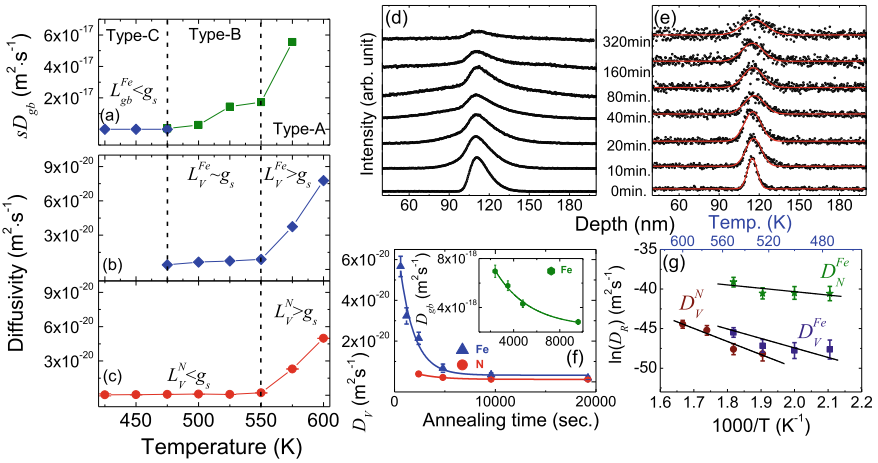

Fig. 25 Variation in grain boundary diffusion (D_{gb}) of Fe (**a**), volume diffusion (D_V) of Fe (**b**) and D_V of N (**c**). SIMS depth profiles of sample [FeN (7.3 nm)|$Fe^{15}N$ (7.3 nm)]$_{10}$ after isochronal annealing treatments for different times at 525 K for ^{57}Fe (**d**) and ^{15}N (**e**). Obtained D_V for Fe and N showing a relaxation behaviour. Inset: Variation in D_{gb} of Fe (**f**). Arrhenius behaviour of grain boundary diffusion of Fe and volume diffusion of Fe and N (**g**). Reproduced with permission from Ref. [105]

well and obtained diffusivity in the relaxed state are plotted in Fig. 25g and they follow Arrhenius-type behaviour. Using Eq. 4, it was found that E of the D_V of Fe and N are about 1.0 and 1.4 eV but E of the D_{gb} of Fe was about 0.6 eV. As expected, the E of Fe for grain boundary diffusion is significantly smaller than the volume diffusion. However, it was somewhat surprising to note that the value of E for volume diffusion of N is larger than the volume diffusion of Fe. Therefore, the discrepancy in the Fe and N self-diffusion process cannot be explained considering the D_{gb} alone. It seems that the higher Fe diffusion may also take place due to larger metal–metal bonds distances as compared to shorter Fe-N bonds, e.g. the bond Fe-Fe bond length in FeN is about 3.046 Å but Fe-N bond lengths are much shorter at 1.865 Å [11]. Since bond energies are inversely proportional to bond length, weaker Fe-Fe bonds may get broken rather easily leading to faster Fe self-diffusion. Therefore, it appears that the thermal instability of magnetic as well non-magnetic iron nitrides is more correlated with Fe self-diffusion process. Since the end result of thermal stability appears in terms of N deficient phases, it is generally believed that the thermal stability of iron nitrides is related to N diffusion. In the next section, we will present the effect of dopants in controlling the diffusion process in iron nitrides.

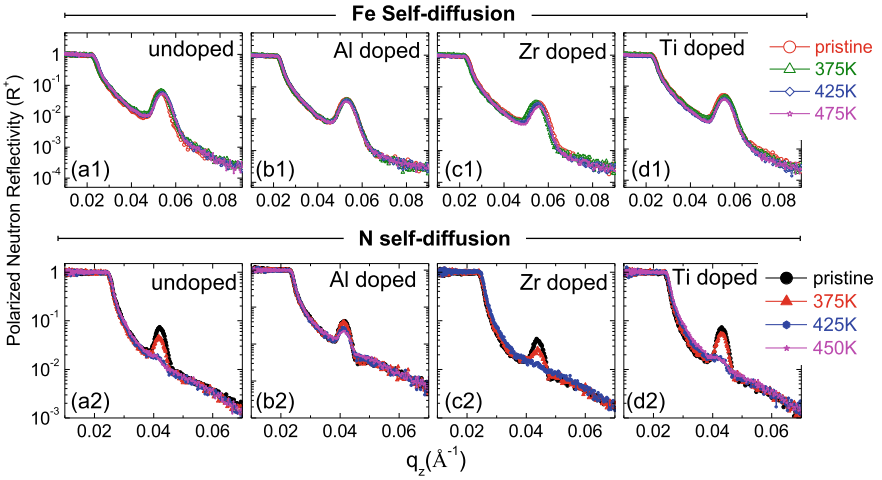

Fig. 26 Polarized neutron reflectivity (PNR) showing only the spin up (R^+) part in samples [Fe-X-N(6 nm)|^{57}Fe-X-N(6 nm)]$_{\times 10}$ (for Fe self-diffusion) and [Fe-X-N(9 nm)|Fe-X-^{15}N(9 nm)]$_{\times 25}$ (for N self-diffusion) with X = 0 (**a1,a2**), X = Al (**b1,b2**), X = Zr (**c1,c2**) and X = Ti (**d1,d2**) in the pristine state and after annealing isochronally for 1 h at each temperature. Reproduced with permission from Ref. [131]

4.3 Effect of Dopants on Self-Diffusion Process in Iron Nitride Thin Films

The effect of doping on the thermal stability with dopants like Al, Ti, Zr has already been discussed in Sect. 2.3 in magnetic iron nitride phases. In this section we will discuss the correlation, if any between the thermal stability and self-diffusion process. CHM samples with a nominal structure: [Fe-X-N(6 nm)|^{57}Fe-X-N(6 nm)]$_{\times 10}$ (for Fe self-diffusion) and [Fe-X-N(9 nm)|Fe-X-^{15}N(9 nm)]$_{\times 25}$ (for N self-diffusion) were prepared with X = 0 (undoped), Al, Ti, and Zr. The N*at*.% in these samples was about 11% corresponding to that of $Fe_{16}N_2$ phase. Figure 26 compares PNR pattern of these samples in the pristine state and after annealing them at different temperatures. Comparing the PNR patterns for Fe self-diffusion in sample [Fe-X-N(6 nm)|^{57}Fe-X-N(6 nm)]$_{\times 10}$, it can be seen from Fig. 26a1–d1 that the profile of pristine and annealed (up to 475 K) samples are similar irrespective of doping. This essentially indicates that Fe self-diffusion at these temperatures is negligible. On the other hand, N self-diffusion measured in [Fe-X-N(9 nm)|Fe-X-^{15}N(9 nm)]$_{\times 25}$ sample shows significant variations as shown in Fig. 26a2–d2. Here, it can be seen that undoped as well as Ti- and Zr-doped samples, the Bragg peak almost disappears signifying substantial N self-diffusion is taking place even at a moderately low temperature of 425 K but in the Al- doped sample, the presence of Bragg peak, though with slightly reduced intensity can be prominently seen even at higher temperature of 450 K. This behaviour immediately indicates that N self-diffusion gets suppressed only with Al doping.

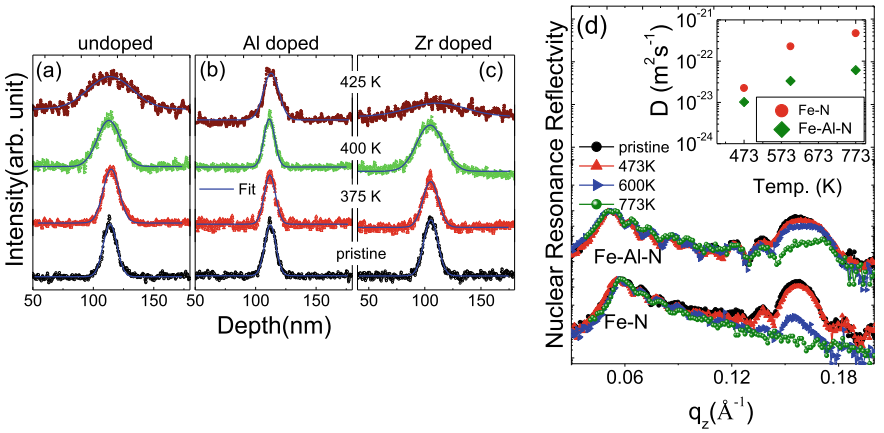

Fig. 27 SIMS depth profile of ^{15}N in [Fe-X-N(110 nm)|Fe-X-^{15}N(2 nm)|Fe-X-N(110 nm)], with X = 0 (**a**), Al (**b**), Zr (**c**) in the pristine state and after annealing at different temperatures (**d**). NRR patterns of CHM sample with structure [Fe-X-N (2 nm)/|^{57}Fe-X-N(2 nm)]$_{\times 10}$, with X = 0 and Al in the pristine state and after annealing at different temperatures. Inset of **d** compared diffusivity of Fe-undoped and Al-doped Fe-N samples. Reproduced with permission from Ref. [131]

Since, N self-diffusion is significantly fast in these samples, to study the N self-diffusion at a larger length scale SIMS measurements were performed in the trilayer sample: [Fe-X-N(110 nm)|Fe-X-^{15}N(2 nm)|Fe-X-N(110 nm)], with X = 0, Al, Zr. ^{15}N depth profiles in this samples are compared in Fig. 27a, b and c in undoped, Al- and Zr-doped samples, respectively, in the pristine state and after annealing for 1 h at 375, 400 and 425 K. From here it can be seen that ^{15}N profiles start to become broad at the lowest annealing temperature of 375 K and after annealing at 425 K, it becomes significantly broad indicating fast N self-diffusion in the undoped samples, similar to the case already presented in Sect. 4.1. However, with Al doping, ^{15}N profiles remain sharp but with Zr doping they become even broader compared to the undoped sample. This behaviour again signifies that only with Al doping N diffusion gets suppressed. Time-dependent N diffusion was also measured by doing isothermal annealing for different times at different temperatures and it was found that relaxation time in the undoped sample was about 250 s and increases to about 2500 s in Al-doped sample. Such slower relaxation with Al doping also signifies that Al is an effective dopant in suppressing N self-diffusion in this sample [131].

To completely understand the role Al doping, Fe diffusion was also measured in these sample with NRR (see Sect. 3.3) and using a rather thin CHM sample with structure [Fe-X-N (2 nm)/|^{57}Fe-X-N(2 nm)]$_{\times 10}$, with X = 0 and Al. NRR measurements in the undoped and Al-doped samples are shown in Fig. 27d in the pristine state and after annealing at 473, 600 and 773 K. As can be seen that after annealing at 473 K the Bragg peak intensity in undoped and Al- doped samples remain similar to their pristine state indicating Fe diffusion is negligible (also seen from PNR measurements shown in Fig. 26). However, annealing at higher temperatures results in

significant Fe self-diffusion in this sample, e.g. at 600 K, the intensity of Bragg peak reduces significantly and disappears completely at 773 K. But in Al-doped sample, Fe diffusion is indeed smaller. Diffusivity of Fe is compared in the inset of Fig. 27d and the suppression in Fe diffusivity amounts to about an order of magnitude at the highest annealing temperature.

Combining Fe and N self-diffusion measurements, obtained using NR, SIMS and NRR, a picture about the effect of dopant on the diffusion mechanism can be drawn. In the sample with about $11 at.\%$ N, N atoms occupy the interstitial positions in Fe. Thus it is expected that N atoms would diffuse through an interstitial-type diffusion process in which they try to find that most suitable equilibrium sites by crossing a saddle point barrier. In the undoped sample, the absence of any impeding force leads to rapid redistribution without affecting the thermal stability. But with Al doping, the Fe lattice gets compressed by about 0.5%, and therefore volume available for interstitial sites also get reduced resulting in suppression of N diffusion. On the other hand doping of a larger (than Fe) atom like Zr expands the Fe lattice by about 2%, and therefore the availability of interstitial sites gets augmented leading to faster N diffusion as compared to that in the undoped sample. On the other hand, the role of dopants on the Fe self-diffusion process is entirely different as compared to the N self-diffusion. As can be seen from Fig. 15 in Sect. 2.3, the doping of both Al and Zr resulted in similar stability, however crystallite size in Al- doped samples was larger than in Zr-doped samples. Since the ΔH_f° for nitride formation of dopants like Al and Zr is much lower than Fe, this results in the formation of AlN or ZrN phase in the grain boundary regions in Fe-N leading to suppression of Fe self-diffusion. From the comparison of crystallite size, it appears that a larger size dopant like Zr also affects the grain growth by causing expansion of the Fe lattice, on the other hand since Al compresses the lattice, it does not adversely affect Fe-N phase formation. Also since N self-diffusion is only suppressed by Al doping, it is indeed the best dopant to control the diffusion processes in Fe-N without adversely affecting the formation of Fe-N phases.

Similarly, the effect of dopants on the diffusion process was also studied in the mononitride FeN phase. As mentioned already, Ag and C are effective dopants in FeN. From the results presented in Sect. 4.2, it was observed that Fe diffusion was faster than N diffusion in FeN. With Ag doping, it was found that Fe diffusion gets suppressed significantly. The effect of doping on the diffusion process in the mononitride composition is still under investigation.

5 Conclusions

In this chapter after presenting a general introduction of TMNs from the point of view of their emerging applications, a detailed description of different phases of iron nitrides was discussed. A brief timeline of Fe-N was given that includes historical developments in it. Subsequently, synthesis of different iron nitride phases using the reactive nitrogen sputtering process was presented in detail and the pathways

to obtain a stoichiometric Fe-N phase were found through a delicate optimization of process parameters. Results on the thermal stability of Fe-N compounds having composition across its phase diagram were presented and ways to improve the thermal stability through doping in magnetic and non-magnetic Fe-N phases were presented. Since the thermal stability is closely related to atomic diffusion, results on Fe and N self-diffusion process in magnetic as well as non-magnetic Fe-N phases were presented in detail. Also, a methodology to obtain self-diffusion coefficients using secondary ion mass spectroscopy, neutron reflectivity and nuclear resonance reflectivity was discussed in detail. The effect of dopants on the self-diffusion of Fe and N was also presented in detail. The overall picture that emerges from diffusion measurements can be summarized by comparing the extrapolated values of diffusivity at room temperature (300 K) in different Fe-N phases. We find that these values for Fe self-diffusion in their nominal composition are: $2.5\times10^{-26}\,m^2\,s^{-1}$ in $Fe_{16}N_2$; $8\times10^{-30}\,m^2\,s^{-1}$ in Fe_4N; $2.9\times10^{-24}\,m^2\,s^{-1}$ in $Fe_{2.23}N$; $3\times10^{-28}\,m^2\,s^{-1}$ in FeN. The values of N self-diffusion in $Fe_{2.23}N$ and FeN were much smaller than that of Fe at $5.8\times10^{-26}\,m^2\,s^{-1}$and $1.2\times10^{-32}\,m^2\,s^{-1}$, respectively. Across different Fe-N phases, the Fe self-diffusion was found to be lowest in the Fe_4N composition formed with about $20at.\%$ N but N self-diffusion in the mononitride composition was found to be even smaller.

Acknowledgments This article is dedicated to Prof. Ajay Gupta. Contributions from Akhil Tayal, Nidhi Pandey, Seema and Niti are gratefully acknowledged. The author would like to thank Rachana Gupta, Sujoy Chakravarty, A. K. Taygi, S. M. Amir and V. R. Reddy for their support in this work. Thanks are due to Jochen Stahn, Thomas Gutberlet, Andrew Wildes in NR measurements; Y. Yoda, H.-C. Wille, R. Rüffer in NRR measurements. We are thankful to Layanta Behera for the help provided in sample preparation, SIMS and XRD measurements. Our special thanks are due to Michael Horisberger for depositing ^{15}N enriched Fe-N samples without that, it would not have been possible to measure N self-diffusion in this work. Nidhi and Seema are acknowledged for proofreading this article. We wish to thank the Department of Science and Technology, India (SR/NM/Z- 07/2015) for the financial support and Jawaharlal Nehru Centre for Advanced Scientific Research (JNCASR) for managing the project. A part of this work was performed at AMOR, Swiss Spallation Neutron Source, Paul Scherrer Institute, Villigen, Switzerland. Financial support received from Indo Swiss Joint Research Programme (Grant No. INT/SWISS/JUAF(9)/2009) is also acknowledged. We wish to thank B. A. Dasannacharya, P. Chaddah, A. K. Sinha, V. Ganesan, A. Banerjee and D. M. Phase for their support.

References

1. W. Sun, C.J. Bartel, E. Arca, S.R. Bauers, B. Matthews, B. Orvañanos, B.R. Chen, M.F. Toney, L.T. Schelhas, W. Tumas, J. Tate, A. Zakutayev, S. Lany, A.M. Holder, G. Ceder, Nat. Mater. **18**, 732 (2019)
2. P. Patsalas, N. Kalfagiannis, S. Kassavetis, G. Abadias, D. Bellas, C. Lekka, E. Lidorikis, Mater. Sci. Eng. R Rep. **123**, 1 (2018)
3. B. Saha, A. Shakouri, T.D. Sands, Appl. Phys. Rev. **5**(2), 021101 (2018)
4. R. Ningthoujam, A. Tyagi, S. Banerjee (eds.), *Materials Under Extreme Conditions* (Elsevier, Amsterdam, 2017), pp. 337–375
5. Y. Zhong, X. Xia, F. Shi, J. Zhan, J. Tu, H.J. Fan, Adv. Sci. **3**(5), 1500286 (2016)

6. R. Ningthoujam, N. Gajbhiye, Prog. Mater. Sci. **70**, 50 (2015)
7. A. Salamat, A.L. Hector, P. Kroll, P.F. McMillan, Coordin. Chem. Rev. **257**(13), 2063 (2013)
8. C. Mitterbauer, C. Hébert, G. Kothleitner, F. Hofer, P. Schattschneider, H. Zandbergen, Solid State Commun. **130**(3), 209 (2004)
9. M.A. Gharavi, G. Greczynski, F. Eriksson, J. Lu, B. Balke, D. Fournier, A. le Febvrier, C. Pallier, P. Eklund, J. Mater. Sci. **54**(2), 1434 (2019)
10. B. Gajar, S. Yadav, D. Sawle, K.K. Maurya, A. Gupta, R.P. Aloysius, S. Sahoo, Sci. Rep. **9**, 8811 (2019)
11. W.Y. Ching, Y.N. Xu, P. Rulis, Appl. Phys. Lett. **80**(16), 2904 (2002)
12. Y.N. Xu, P. Rulis, W.Y. Ching, J. Appl. Phys. **91**(10), 7352 (2002)
13. M. Wessel, R. Dronskowski, Chem.: Eur. J. **17**(9), 2598. https://doi.org/10.1002/chem.201003143
14. L. Wu, R. Tian, B. Wan, H. Liu, N. Gong, P. Chen, T. Shen, Y. Yao, H. Gou, F. Gao, Chem. Mater. **30**(23), 8476 (2018). https://doi.org/10.1021/acs.chemmater.8b02972
15. E. Gregoryanz, C. Sanloup, M. Somayazulu, J. Badro, G. Fiquet, H.k. Mao, R.J. Hemley, Nat. Mater. **3**, 294 (2004). https://doi.org/10.1038/nmat1115
16. M. Bykov, E. Bykova, G. Aprilis, K. Glazyrin, E. Koemets, I. Chuvashova, I. Kupenko, C. McCammon, M. Mezouar, V. Prakapenka, H.P. Liermann, F. Tasnádi, A.V. Ponomareva, I.A. Abrikosov, N. Dubrovinskaia, L. Dubrovinsky, Nat. Commun. **9**, 2756 (2018). https://doi.org/10.1038/s41467-018-05143-2
17. K. Niwa, T. Terabe, D. Kato, S. Takayama, M. Kato, K. Soda, M. Hasegawa, Inorg. Chem. **56**(11), 6410 (2017). https://doi.org/10.1021/acs.inorgchem.7b00516. PMID: 28509545
18. Z. Zhao, K. Bao, F. Tian, D. Duan, B. Liu, T. Cui, Phys. Rev. B **93**, 214104 (2016). https://doi.org/10.1103/PhysRevB.93.214104
19. K. Niwa, R. Fukui, T. Terabe, T. Kawada, D. Kato, T. Sasaki, K. Soda, M. Hasegawa, Eur. J. Inorg. Chem. **2019**(33), 3753 (2019). https://doi.org/10.1002/ejic.201900489
20. J.A. Montoya, A.D. Hernandez, C. Sanloup, E. Gregoryanz, S. Scandolo, Appl. Phys. Lett. **90**(1), 011909 (2007). https://doi.org/10.1063/1.2430631
21. K. Niwa, K. Suzuki, S. Muto, K. Tatsumi, K. Soda, T. Kikegawa, M. Hasegawa, Chem. Eur. J. **20**(43), 13885 (2014). https://doi.org/10.1002/chem.201404165
22. K. Niwa, D. Dzivenko, K. Suzuki, R. Riedel, I. Troyan, M. Eremets, M. Hasegawa, Inorg. Chem. **53**(2), 697 (2014). https://doi.org/10.1021/ic402885k. PMID: 24393052
23. G.M. Veith, A.R. Lupini, L. Baggetto, J.F. Browning, J.K. Keum, A. Villa, L. Prati, A.B. Papandrew, G.A. Goenaga, D.R. Mullins, S.E. Bullock, N.J. Dudney, Chem. Mater. **25**(24), 4936 (2013). https://doi.org/10.1021/cm403224m
24. G. Scheunert, O. Heinonen, R. Hardeman, A. Lapicki, M. Gubbins, R.M. Bowman, Appl. Phys. Rev. **3**(1), 011301 (2016). https://doi.org/10.1063/1.4941311
25. M. Meinert, J. Phys.: Condens. Matter **28**(5), 056006 (2016)
26. N. Pandey, M. Gupta, R. Gupta, Z. Hussain, V.R. Reddy, D.M. Phase, J. Stahn, Phys. Rev. B **99**, 214109 (2019). https://doi.org/10.1103/PhysRevB.99.214109
27. M. Sifkovits, H. Smolinski, S. Hellwig, W. Weber, J. Magn. Magn. Mater. **204**(3), 191 (1999). https://doi.org/10.1016/S0304-8853(99)00296-6
28. K.S. Rao, H. Salunke, J. Magn. Magn. Mater. **449**, 582 (2018). https://doi.org/10.1016/j.jmmm.2017.10.041
29. P. Schaaf, C. Illgner, M. Niederdrenk, K.P. Lieb, Hyperfine Interact. **95**, 199 (1995)
30. Z. Schnepp, M. Thomas, S. Glatzel, K. Schlichte, R. Palkovits, C. Giordano, J. Mater. Chem. **21**, 17760 (2011). https://doi.org/10.1039/C1JM12842F
31. V.F. Hlynsson, E. Skúlason, A.L. Garden, J. Alloys Compd. **603**, 172 (2014). https://doi.org/10.1016/j.jallcom.2014.02.153
32. D. Vempaire, F. Fettar, L. Ortega, F. Pierre, S. Miraglia, A. Sulpice, J. Pelletier, E.K. Hlil, D. Fruchart, J. Appl. Phys. **106**(7), 073911 (2009). https://doi.org/10.1063/1.3238290
33. Y. Wang, B. Zhang, W. Pan, H. Ma, J. Zhang, ChemSusChem **10**(21), 4170 (2017). https://doi.org/10.1002/cssc.201701456

34. Y. Zhang, B. Ouyang, J. Xu, G. Jia, S. Chen, R.S. Rawat, H.J. Fan, Angew. Chem. **55**(30), 8670 (2016). https://doi.org/10.1002/anie.201604372
35. X. Peng, C. Pi, X. Zhang, S. Li, K. Huo, P.K. Chu, Sustain. Energy Fuels **3**, 366 (2019). https://doi.org/10.1039/C8SE00525G
36. Z. Chen, X. Duan, W. Wei, S. Wang, B.J. Ni, J. Mater. Chem. A (2019). https://doi.org/10.1039/C9TA03220G
37. Z. Wu, D. Nie, M. Song, T. Jiao, G. Fu, X. Liu, Nanoscale **11**, 7506 (2019). https://doi.org/10.1039/C9NR01794A
38. Z. Ye, P. Zhang, X. Lei, X. Wang, N. Zhao, H. Yang, Chem.: Eur. J. **24**(36), 8922 (2018). https://doi.org/10.1002/chem.201706028
39. J.S. Kang, J.Y. Kim, J. Yoon, J. Kim, J. Yang, D.Y. Chung, M.c. Kim, H. Jeong, Y.J. Son, B.G. Kim, J. Jeong, T. Hyeon, M. Choi, M.J. Ko, Y.E. Sung, Adv. Energy Mater. **8**(13), 1703114. https://doi.org/10.1002/aenm.201703114
40. B. Das, M. Behm, G. Lindbergh, M. Reddy, B. Chowdari, Adv. Powder Technol. **26**(3), 783 (2015). Special issue of the 7th World Congress on Particle Technology. https://doi.org/10.1016/j.apt.2015.02.001
41. B. Das, M.V. Reddy, G.V.S. Rao, B.V.R. Chowdari, J. Mater. Chem. **22**, 17505 (2012). https://doi.org/10.1039/C2JM31969A
42. B. Das, M.V. Reddy, B.V.R. Chowdari, Nanoscale **5**, 1961 (2013). https://doi.org/10.1039/C2NR33675H. URL http://dx.doi.org/10.1039/C2NR33675H
43. J. Häglund, A.F. Guillermet, G. Grimvall, M. Körling, Phys. Rev. B **48**(16), 11685 (1993)
44. F. Tessier, A. Navrotsky, R. Niewa, A. Leineweber, H. Jacobs, S. Kikkawa, M. Takahashi, F. Kanamaru, F.J. DiSalvo, Solid State Sci. **2**, 457 (2000)
45. D. Laniel, A. Dewaele, G. Garbarino, Inorg. Chem. **57**(11), 6245 (2018). https://doi.org/10.1021/acs.inorgchem.7b03272. PMID: 29505253
46. J.M.D. Coey, P.A.I. Smith, J. Magn. Magn. Mat. **200**(1–3), 405 (1999). https://doi.org/10.1016/S0304-8853(99)00429-1
47. S. Bhattacharyya, J. Phys. Chem. C **119**(4), 1601 (2015). https://doi.org/10.1021/jp510606z. URL http://dx.doi.org/10.1021/jp510606z
48. E. Baur, G.L. Voerman, Z. physik. Chem. **52**, (1905)
49. A. Fry, Stahl 1t. Eisen. **43**, 1271 (1923)
50. C.B. Sawyer, Trans. AIME **69**, 798 (1923)
51. G. Hägg, Nature **121**(3056), 826 (1928)
52. G. Hägg, Nature **122**, 314 (1928)
53. R. Brill, Naturwissenschaften **16**, 593 (1928). https://doi.org/10.1007/BF01505045
54. S. Epstein, H.C. Cross, E.C. Groesbeck, I.J. Wymore, J. Res. (U.S. Natl. Bur. Stand.) **3**, 1005 (1929)
55. P.H. Emmett, S.B. Hendricks, S. Brunauer, J. Am. Chem. Soc. **52**(4), 1456 (1930). https://doi.org/10.1021/ja01367a024
56. V.G. Paranjpe, M. Cohen, M.B. Bever, C.F. Floe, J. Met. **2**, 261 (1950)
57. K.H. Jack, Proc. Royal Soc. A **195**, 34 (1948)
58. K.H. Jack, Acta Cryst. **3**(5), 392 (1950). https://doi.org/10.1107/S0365110X50001075
59. K.H. Jack, Proc. Royal Soc. A **208**, 200 (1951). https://doi.org/10.1098/rspa.1951.0154
60. T.K. Kim, M. Takahashi, Appl. Phys. Lett. **20**, 492 (1972)
61. D. Sun, E. Jiang, D. Sun, Thin Solid Films **298**(1), 116 (1997). https://doi.org/10.1016/S0040-6090(96)09059-1
62. W.Y. Lai, Q.Q. Zheng, W.Y. Hu, J. Phys.: Condens. Matter **6**(18), L259 (1994). https://doi.org/10.1088/0953-8984/6/18/001
63. A. Sakuma, J. Appl. Phys. **79**(8), 5570 (1996). https://doi.org/10.1063/1.362245
64. N. Ji, X. Liu, J.P. Wang, New J. Phys. **12**(6), 063032 (2010). https://doi.org/10.1088/1367-2630/12/6/063032
65. H. Sims, W.H. Butler, M. Richter, K. Koepernik, E. Şaşıoğlu, C. Friedrich, S. Blügel, Phys. Rev. B **86**, 174422 (2012). https://doi.org/10.1103/PhysRevB.86.174422

66. S. Bhattacharjee, S.C. Lee, Sci. Rep. **9**, 8381 (2019). https://doi.org/10.1038/s41598-019-44799-8
67. M. Takahashi, H. Shoji, J. Magn. Magn. Mater. **208**(3), 145 (2000). https://doi.org/10.1016/S0304-8853(99)00536-3
68. S. Kikkawa, Y. Masubuchi, Prog. Solid State Ch. **51**, 19 (2018). https://doi.org/10.1016/j.progsolidstchem.2017.06.001
69. H. Jacobs, D. Rechenbach, U. Zachwieja, J. Alloys Compd. **227**(1), 10 (1995). https://doi.org/10.1016/0925-8388(95)01610-4
70. M. Gupta, Seema, N. Pandey, S. Amir, S. Pütter, S. Mattauch, J. Magn. Magn. Mater. **489**, 165376 (2019). https://doi.org/10.1016/j.jmmm.2019.165376
71. S. Kokado, N. Fujima, K. Harigaya, H. Shimizu, A. Sakuma, Phys. Rev. B **73**, 172410 (2006). https://doi.org/10.1103/PhysRevB.73.172410
72. H. Li, X. Li, D. Kim, G. Zhao, D. Zhang, Z. Diao, T. Chen, J.P. Wang, Appl. Phys. Lett. **112**(16), 162407 (2018). https://doi.org/10.1063/1.5023698
73. B.C. Frazer, Phys. Rev. **112**, 751 (1958). https://doi.org/10.1103/PhysRev.112.751
74. J. Gallego, S.Y. Grachev, M. Passeggi Jr., F. Sacharowitz, D. Ecija, R. Miranda, D. Boerma, Phys. Rev. B **69**(12), 121404 (2004)
75. S. Atiq, H.S. Ko, S.A. Siddiqi, S.C. Shin, Appl. Phys. Lett. **92**(22), 222507 (2008). URL http://scitation.aip.org/content/aip/journal/apl/92/22/10.1063/1.2940599
76. J. Feng-Xian, Z. Ye, Z. Guo-Wei, Z. Jun, F. Jiu-Ping, X. Xiao-Hong, Chin. Phys. Lett. **32**, 087501 (2015)
77. N. Pandey, S. Pütter, S.M. Amir, V.R. Reddy, D.M. Phase, J. Stahn, A. Gupta, M. Gupta, Phys. Rev. Mater. **3**, 114414 (2019)
78. E.L.P.y. Blancá, J. Desimoni, N.E. Christensen, H. Emmerich, S. Cottenier, Phys. Status Solidi (b) **246**(5), 909 (2009). https://doi.org/10.1002/pssb.200844401
79. H. Fang, X. Peng, Y. Li, Z. Tao, Mater. Res. Express **6**(10), 106443 (2019). https://doi.org/10.1088/2053-1591/ab410a
80. Z. Tao, H. Fang, L. Chen, J. Chen, X. Xiu, R. Zhang, J. Cryst. Growth **506**, 160 (2019). https://doi.org/10.1016/j.jcrysgro.2018.10.044
81. D.M. Zhang, L.Y. Yuan, D.W. Zhao, G.K. Li, L. Ma, C.M. Zhen, D.L. Hou, Thin Solid Films **677**, 90 (2019). https://doi.org/10.1016/j.tsf.2019.03.022
82. D. Rechenbach, H. Jacobs, J. Alloys Compd. **235**(1), 15 (1996). https://doi.org/10.1016/0925-8388(95)02097-7
83. H.A. Wriedt, N.A. Gokcen, R.H. Nafziger, Bull. Alloy Phase Diagrams **8**(4), 355 (1987). https://doi.org/10.1007/BF02869273
84. A. Oueldennaoua, E. Bauer-Grosse, M. Foos, C. Frantz, Scripta Metall. **19**, 1503 (1985)
85. H. Nakagawa, S. Nasu, H. Fujii, M. Takahashi, F. Kanamaru, Hyperfine Interact. **69**, 455 (1991). https://doi.org/10.1007/BF02401863
86. K. Suzuki, H. Morita, T. Kaneko, H. Yoshida, H. Fujimori, J. Alloys Compds. **201**, 11 (1993). https://doi.org/10.1016/0925-8388(93)90854-G
87. T. Hinomura, S. Nasu, Hyperfine Interact. **111**(1), 221 (1998). https://doi.org/10.1023/A:1012614019538
88. M. Niederdrenk, P. Schaaf, K.P. Lieb, O. Schulte, J. Alloys Compd. **237**, 81 (1996)
89. L. Rissanen, M. Neubauer, K.P. Lieb, P. Schaaf, J. Alloys Compds. **274**, 74 (1998)
90. P. Schaaf, Prog. Mater. Sci. **47**(1), 1 (2002). https://doi.org/10.1016/S0079-6425(00)00003-7
91. B. Eck, R. Dronskowski, M. Takahashi, S. Kikkawa, J. Mater. Chem. **9**, 1527 (1999). https://doi.org/10.1039/A809935I
92. A. Filippetti, W.E. Pickett, Phys. Rev. B **59**(13), 8397 (1999). https://doi.org/10.1103/PhysRevB.59.8397
93. Y. Kong, J. Phys.: Condens. Matter **12**(18), 4161 (2000)
94. A. Kartsev, O.D. Feya, N. Bondarenko, A.G. Kvashnin, Phys. Chem. Chem. Phys. **21**, 5262 (2019). https://doi.org/10.1039/C8CP07165A

95. I. Jouanny, P. Weisbecker, V. Demange, M. Grafouté, O. Peña, E. Bauer-Grosse, Thin Solid Films **518**(8), 1883 (2010). https://doi.org/10.1016/j.tsf.2009.07.039
96. M. Gupta, A. Gupta, S. Chaudhari, D. Phase, V. Ganesan, M.R. Rao, T. Shripathi, B. Dasannacharya, Vacuum **60**, 395 (2001). https://doi.org/10.1016/S0042-207X(00)00148-2
97. M. Gupta, A. Gupta, S. Rajagopalan, A.K. Tyagi, Phys. Rev. B **65**(21), 214204 (2002). https://doi.org/10.1103/PhysRevB.65.214204
98. A. Gupta, M. Gupta, B.A. Dasannacharya, Y. Yoda, S. Kikuta, M. Seto, J. Phys. Soc. Jpn **73**(2), 423 (2004). https://doi.org/10.1143/JPSJ.73.423
99. X. Wang, W. Zheng, H. Tian, S. Yu, W. Xu, S. Meng, X. He, J. Han, C. Sun, B. Tay, Appl. Sur. Sci. **220**(1–4), 30 (2003). 10.1016/S0169-4332(03)00752-9. URL http://www.sciencedirect.com/science/article/pii/S0169433203007529
100. D. Peng, T. Hihara, K. Sumiyama, J. Alloys Compd. **377**(1), 207 (2004). https://doi.org/10.1016/j.jallcom.2003.12.045
101. R. Gupta, M. Gupta, Phys. Rev. B **72**, 024202 (2005). https://doi.org/10.1103/PhysRevB.72.024202
102. V. Demange, T.H. Loi, P. Weisbecker, E. Bauer-Grosse, Thin Solid Films **494**, 184 (2006). https://doi.org/10.1016/j.tsf.2005.08.196
103. M. Gupta, A. Tayal, A. Gupta, R. Gupta, J. Stahn, M. Horisberger, A. Wildes, J. Appl. Phys. **110**(12), 123518 (2011). https://doi.org/10.1063/1.3671532
104. M. Gupta, A. Tayal, A. Gupta, V.R. Reddy, M. Horisberger, J. Stahn, J. Alloys Compd. **509**(33), 8283 (2011). https://doi.org/10.1016/j.jallcom.2011.04.139
105. A. Tayal, M. Gupta, A. Gupta, P. Rajput, J. Stahn, Phys. Rev. B **92**, 054109 (2015). https://doi.org/10.1103/PhysRevB.92.054109
106. A. Tayal, M. Gupta, N. Pandey, A. Gupta, M. Horisberger, J. Stahn, J. Alloys Compd. **650**, 647 (2015). https://doi.org/10.1016/j.jallcom.2015.06.253
107. K. Jantasom, M. Horprathum, P. Eiamchai, S. Limwichean, N. Nuntawong, V. Patthanasettakul, P. Chindaudom, C. Thanachayanont, P. Songsiriritthigul, Mater. Today: Proc. **4**(5, Part 2), 6173 (2017). https://doi.org/10.1016/j.matpr.2017.06.112
108. Q. Lu, M. Xie, G. Han, B. Zheng, Y. Song, J. Qiang, X. Wang, Z. Wu, P. Yan, W. Liu, J. Magn. Magn. Mater. **474**, 76 (2019). https://doi.org/10.1016/j.jmmm.2018.10.119
109. M. Gupta, A. Gupta, P. Bhattacharya, P. Misra, L. Kukreja, J. Alloys Compd. **326**, 265 (2001). https://doi.org/10.1016/S0925-8388(01)01316-0
110. F. Sun, J. Liu, Y. Yang, H. Yu, Mater. Sci. Eng. B **122**(1), 29 (2005). https://doi.org/10.1016/j.mseb.2005.04.010
111. R. Usui, Y. Yamada, Y. Kobayashi, Hyperfine Interact. **205**(1), 13 (2012). https://doi.org/10.1007/s10751-011-0473-7
112. Y. Yamada, R. Usui, Y. Kobayashi, Hyperfine Interact. **219**(1), 13 (2013). https://doi.org/10.1007/s10751-012-0664-x
113. A. Tayal, M. Gupta, A. Gupta, V. Ganesan, L. Behera, S. Singh, S. Basu, Surf. Coat. Technol. **275**, 264 (2015). https://doi.org/10.1016/j.surfcoat.2015.05.008
114. C. Navío, J. Alvarez, M.J. Capitan, F. Yndurain, R. Miranda, Phys. Rev. B **78**(15), 155417 (2008). https://doi.org/10.1103/PhysRevB.78.155417
115. D.M. Borsa, D.O. Boerma, Hyperfine Interact. **151**(1), 31 (2003). https://doi.org/10.1023/B:HYPE.0000020403.64670.02
116. E. Andrzejewska, R. Gonzalez-Arrabal, D. Borsa, D. Boerma, Nucl. Inst. Meth. in Phys. Res. B **249**(1), 838 (2006). https://doi.org/10.1016/j.nimb.2006.03.150
117. J. Pak, W. Lin, K. Wang, A. Chinchore, M. Shi, D.C. Ingram, A.R. Smith, K. Sun, J.M. Lucy, A.J. Hauser, F.Y. Yang, J. Vac. Sci. Technol. A **28**(4), 536 (2010). https://doi.org/10.1116/1.3425805
118. M. Naito, K. Uehara, R. Takeda, Y. Taniyasu, H. Yamamoto, J. Cryst. Growth **415**, 36 (2015). https://doi.org/10.1016/j.jcrysgro.2014.12.022
119. D. Laniel, A. Dewaele, S. Anzellini, N. Guignot, J. Alloys Compd. **733**, 53 (2018). https://doi.org/10.1016/j.jallcom.2017.10.267

120. W.P. Clark, S. Steinberg, R. Dronskowski, C. McCammon, I. Kupenko, M. Bykov, L. Dubrovinsky, L.G. Akselrud, U. Schwarz, R. Niewa, Angew. Chem. Int. Ed. **56**, 25 (2017)
121. S. Li, X. Cui, Z.F. Liu, T.L. Song, J. Alloys Compd. **771**, 322 (2019). https://doi.org/10.1016/j.jallcom.2018.08.220
122. M. Gupta, N. Pandey, Niti, V.R. Reddy, D.M. Phase, K. Schlage, H.C. Wille, A. Gupta, Hyperfine Interact. **240**(1), 99 (2019). https://doi.org/10.1007/s10751-019-1633-4
123. M. Zheng, X. Chen, R. Cheng, N. Li, J. Sun, X. Wang, T. Zhang, Catal. Commun. **7**(3), 187 (2006). https://doi.org/10.1016/j.catcom.2005.10.009
124. Z. Yang, S. Guo, X. Pan, J. Wang, X. Bao, Energy Environ. Sci. **4**, 4500 (2011). https://doi.org/10.1039/C1EE01428E
125. C. Navío, J. Álvarez, M.J. Capitan, J. Camarero, R. Miranda, Appl. Phys. Lett. **94**, 263112 (2009). https://doi.org/10.1063/1.3159630
126. C. Navío, M.J. Capitán, J. Álvarez, R. Miranda, F. Yndurain, New J. Phys. **12**(7), 073004 (2010)
127. W. Sun, A. Holder, B. Orvañanos, E. Arca, A. Zakutayev, S. Lany, G. Ceder, Chem. Mater. **29**(16), 6936 (2017). https://doi.org/10.1021/acs.chemmater.7b02399
128. L. Zhang, Y. Wang, J. Lv, Y. Ma, Nat. Rev. Mater. **2**, 17005 (2017). https://doi.org/10.1038/natrevmats.2017.5
129. D. Lundin, K. Sarakinos, J. Mater. Res. **27**, 780 (2012)
130. K. Wasa, *Handbook of Sputtering Technology*, 2nd edn. (William Andrew Publishing, Oxford, 2012). https://doi.org/10.1016/B978-1-4377-3483-6.00013-9
131. A. Tayal, M. Gupta, N.P. Lalla, A. Gupta, M. Horisberger, J. Stahn, K. Schlage, H.C. Wille, Phys. Rev. B **90**, 144412 (2014). https://doi.org/10.1103/PhysRevB.90.144412
132. N. Pandey, M. Gupta, R. Rawat, S. Amir, J. Stahn, A. Gupta, Phys. B Condens. Matter **572**, 36 (2019). https://doi.org/10.1016/j.physb.2019.07.039
133. H. Li, X. Li, D. Kim, G. Zhao, D. Zhang, Z. Diao, T. Chen, J.P. Wang, Appl. Phys. Lett. **112**(16), 162407 (2018)
134. Y. Komasaki, M. Tsunoda, S. Isogami, M. Takahashi, J. Appl. Phys. **105**(7), 07C928 (2009)
135. A. Narahara, K. Ito, T. Suemasu, Y. Takahashi, A. Ranajikanth, K. Hono, Appl. Phys. Lett. **94**(20), 202502 (2009)
136. K. Ito, G.H. Lee, K. Harada, M. Suzuno, T. Suemasu, Y. Takeda, Y. Saitoh, M. Ye, A. Kimura, H. Akinaga, Appl. Phys. Lett. **98**(10), 102507 (2011). https://doi.org/10.1063/1.3564887
137. I. Dirba, M.B. Yazdi, A. Radetinac, P. Komissinskiy, S. Flege, O. Gutfleisch, L. Alff, J. Magn. Magn. Mater. **379**, 151 (2015)
138. E. Fratczak, J. Prieto, M. Moneta, J. Alloys Compd. **586**, 375 (2014). https://doi.org/10.1016/j.jallcom.2013.09.200
139. M. Niti, N. Gupta, V.R. Pandey, I. Reddy, H.C. Sergueev, A,G. Wille, Phys. B Condens. Matter **572**, 94 (2019). https://doi.org/10.1016/j.physb.2019.07.040
140. M. Gupta, A. Gupta, S. Chakravarty, T. Gutberlet, H.C. Wille, O. Leupold, R. Rüffer, Mater. Res. Soc. Symp. Proc. **840**, 15 (2005)
141. S. Chakravarty, M. Gupta, A. Gupta, S. Rajagopalan, A. Balamurugan, A. Tyagi, U. Deshpande, M. Horisberger, T. Gutberlet, Acta Mater. **57**, 1263 (2009). https://doi.org/10.1016/j.actamat.2008.11.008
142. F. Faupel, W. Frank, M.P. Macht, H. Mehrer, K. Rätzke, H. Schober, S.K. Sharma, H. Teichler, Rev. Mod. Phys. **75**, 237 (2003)
143. S. Atiq, H.S. Ko, S.A. Siddiqi, S.C. Shin, J. Alloys Compd. **479**, 755 (2009). https://doi.org/10.1016/j.jallcom.2009.01.041
144. R. Gupta, A. Tayal, S.M. Amir, M. Gupta, A. Gupta, M. Horisberger, J. Stahn, J. Appl. Phys. **111**(10), 103520 (2012). https://doi.org/10.1063/1.4718579. http://link.aip.org/link/?JAP/111/103520/1
145. A. Tayal, M. Gupta, A. Gupta, M. Horisberger, J. Stahn, Thin Solid Films **536**, 39 (2013). https://doi.org/10.1016/j.tsf.2013.03.026
146. S. Berg, E. Särhammar, T. Nyberg, Thin Solid Films **565**(Supplement C), 186 (2014). https://doi.org/10.1016/j.tsf.2014.02.063

147. S. Berg, T. Nyberg, Thin Solid Films **476**(2), 215 (2005)
148. D. Depla, S. Heirwegh, S. Mahieu, R. De Gryse, J. Phys. D: Appl. Phys. **40**(7), 1957 (2007)
149. H. Mehrer, *Diffusion in Solids* (Springer, Berlin, Heidelberg, 2007)
150. A. Greer, J. Magn. Magn. Mater. **126**(1), 89 (1993). https://doi.org/10.1016/0304-8853(93)90552-D
151. A. Greer, Appl. Surf. Sci. **86**(1), 329 (1995). https://doi.org/10.1016/0169-4332(94)00399-8
152. J. Speakman, P. Rose, J. Hunt, N. Cowlam, R. Somekh, A. Greer, J. Magn. Magn. Mater. **156**(1), 411 (1996). *Proceedings of the Second International Symposium on Metallic Multilayers*. https://doi.org/10.1016/0304-8853(95)00918-3
153. A. Gupta, M. Gupta, S. Chakravarty, R. Rüffer, H.C. Wille, O. Leupold, Phys. Rev. B **72**, 014207 (2005). https://doi.org/10.1103/PhysRevB.72.014207
154. A. Gupta, Appl. Surf. Sci. **256**(2), 552 (2009). https://doi.org/10.1016/j.apsusc.2009.08.034. Physics at Surfaces and Interface
155. P.G. Shewmon, *Diffusion in Solids* (Mc Graw-Hill, New York, 1963)
156. Y. Loirat, J.L. Boequet, Y. Limoge, J. Non-Cryst Solids **262**, 252 (2000)
157. V. Naundorf, M.P. Macht, A. Bakai, N. Lazarev, J. Non-Cryst, Solids **224**(2), 122 (1998). https://doi.org/10.1016/S0022-3093(97)00465-1
158. W. Linert, R.F. Jameson, Chem. Soc. Rev. **18**, 477 (1989). https://doi.org/10.1039/CS9891800477
159. M. Gupta, A. Gupta, J. Stahn, M. Horisberger, T. Gutberlet, P. Allenspach, Phys. Rev. B **70**(18), 184206 (2004). https://doi.org/10.1103/PhysRevB.70.184206
160. A. Compton, Phil. Mag. **45**, 1121 (1923)
161. L.G. Parratt, Phys. Rev. **95**, 359 (1954)
162. K.S. Krassimir N. Stoev1, Spectrochim. Acta B **54**, 41 (1999)
163. M. Tolan, *X-ray Scattering From Soft-Matter Thin Films: Materials Science and Basic Research* (Springer, New York, 1998)
164. J. Daillant, A. Gibaud (eds.), *X-ray and Neutron Reflectivity: Principals and Applications* (Springer, Berlin, 1999)
165. J. Als-Nielsen, D. McMorrow, *Elements of Modern X-ray Physics* (Wiley, New York, 2001)
166. V.F. Sears, Neutron News **3**(3), 26 (1992). https://doi.org/10.1080/10448639208218770
167. H. Zabel, Mater. Today **9**(1), 42 (2006). https://doi.org/10.1016/S1369-7021(05)71337-7
168. M. Gupta, A. Gupta, J. Stahn, T. Gutberlet, New J. Phys. **10**(5), 053031 (2008)
169. A. Greer, F. Spaepen, Materials science and technology series, in *Synthetic Modulated Structures*, ed. by L.L. Chang, B. Giessen (Academic Press, 1985), pp. 419–486
170. T. Mizoguchi, S. Tanabe, M. Murata, J. Magn. Magn. Mater. **126**(1), 96 (1993). https://doi.org/10.1016/0304-8853(93)90553-E
171. S.M. Baker, G.S. Smith, N.J.S. Brown, M. Nastasi, K. Hubbard, Phys. Rev. B **55**, 7255 (1997). https://doi.org/10.1103/PhysRevB.55.7255
172. A. Gupta, M. Gupta, U. Pietsch, S. Ayachit, S. Rajagopalanl, A. Balamurgan, A. Tyagi, J. Non-Cryst, Solids **343**(1), 39 (2004). https://doi.org/10.1016/j.jnoncrysol.2004.07.051
173. M. Gupta, A. Gupta, S. Chakravarty, R. Gupta, T. Gutberlet, Phys. Rev. B **74**(10), 104203 (2006). https://doi.org/10.1103/PhysRevB.74.104203
174. H. Schmidt, M. Gupta, M. Bruns, Phys. Rev. Lett. **96**(5), 055901 (2006). https://doi.org/10.1103/PhysRevLett.96.055901
175. H. Schmidt, M. Gupta, T. Gutberlet, J. Stahn, M. Bruns, Acta Mater. **56**(3), 464 (2008). https://doi.org/10.1016/j.actamat.2007.10.005
176. E. Hüger, U. Tietze, D. Lott, H. Bracht, D. Bougeard, E.E. Haller, H. Schmidt, Appl. Phys. Lett. **93**(16), 162104 (2008). https://doi.org/10.1063/1.3002294
177. E. Hüger, H. Schmidt, J. Stahn, B. Braunschweig, U. Geckle, M. Bruns, A. Markwitz, Phys. Rev. B **80**, 220101 (2009). https://doi.org/10.1103/PhysRevB.80.220101
178. J. Rahn, E. Hüger, L. Dörrer, B. Ruprecht, P. Heitjans, H. Schmidt, Phys. Chem. Chem. Phys. **14**, 2427 (2012). https://doi.org/10.1039/C2CP23548J
179. A. Gupta, S. Chakravarty, P. Rajput, M. Gupta, R. Rüffer, in *ICAME 2007*, ed. by N.S. Gajbhiye, S.K. Date (Springer, Berlin Heidelberg, 2009), pp. 23–30

180. J.P. Hannon, G.T. Trammell, M. Mueller, E. Gerdau, R. Rüffer, H. Winkler, Phys. Rev. B **32**, 6363 (1985). https://doi.org/10.1103/PhysRevB.32.6363
181. L. Deák, G. Bayreuther, L. Bottyán, E. Gerdau, J. Korecki, E.I. Kornilov, H.J. Lauter, O. Leupold, D.L. Nagy, A.V. Petrenko, V.V. Pasyuk-Lauter, H. Reuther, E. Richter, R. Röhloberger, E. Szilágyi, J. Appl. Phys. **85**(1), 1 (1999). https://doi.org/10.1063/1.369470
182. A.Q.R. Baron, J. Arthur, S.L. Ruby, A.I. Chumakov, G.V. Smirnov, G.S. Brown, Phys. Rev. B **50**, 10354 (1994). https://doi.org/10.1103/PhysRevB.50.10354
183. R. Röhlsberger, *Nuclear Condensed Matter Physics with Synchrotron Radiation*, vol. 208 (Springer, 2004)
184. K. Schlage, R. Röhlsberger, J. Electron Spectros. Relat. Phenomena **189**, 187 (2013). https://doi.org/10.1016/j.elspec.2013.02.005
185. G.V. Smirnov, Hyperfine Interact. **97**(1), 551 (1996). https://doi.org/10.1007/BF02150198
186. R. Rüffer, CR Phys. **9**(5), 595 (2008). https://doi.org/10.1016/j.crhy.2007.06.003
187. R. Rüffer, A.I. Chumakov, Hyperfine Interact. **97**(1), 589 (1996). https://doi.org/10.1007/BF02150199
188. X. Li, M.S. Osofsky, K.L. Jensen, H. Li, J.P. Wang, AIP Adv. **7**(9), 095001 (2017). https://doi.org/10.1063/1.4991963
189. D. Polk, Acta Metall. **40**, 485 (1972)

Photoelectron Energy Loss Spectroscopy: A Versatile Tool for Material Science

Christian Godet, Denis G. F. David, Victor Mancir da Silva Santana, Jailton Souza de Almeida, and Didier Sébilleau

Abstract X-ray photoelectron spectroscopy (XPS) used in quantitative chemical analysis of solid surfaces requires subtraction of a broad background, arising from various energy loss mechanisms, to obtain reliable core-level peak intensities. Besides single-electron excitation, collective electron oscillations (plasmons) can be excited in the bulk and at the surface. Photoelectron energy loss spectroscopy (XPS-PEELS) is a non-destructive tool useful for both process control and thin-film metrology. This review emphasizes its versatility to elucidate material research issues. The energy loss function (ELF) is useful for thin-film growth optimization since it gives insight in valence electron density, hardness, optical band gap and interface properties such as adhesion and wetting. XPS-PEELS also provides depth and width of implanted atom profiles in solid targets, e.g. Ar nanobubbles in Al. Special emphasis is given to the retrieval of electronic properties from XPS-PEELS data. Since the ELF, $\langle \mathrm{Im}[-1/\varepsilon(q,\omega)]\rangle_{\boldsymbol{q}}$ is related to the q-averaged dielectric function, $\langle \varepsilon(q,\omega)\rangle_{\boldsymbol{q}}$, the latter can be obtained by taking into account multiple bulk and surface plasmon excitations. This task is rather simple in wide band gap materials, where the ELF and the no-loss peak are clearly separated, as illustrated by amorphous silicon, amorphous carbon or Al oxide data. In contrast, in metals or small band gap materials, the broad asymmetric photoemission peak overlaps the ELF and low-energy features in the ELF may be lost. A Fourier transform (FT) method is proposed to analyse PEELS data, with the objective of retrieving such low-energy excitations, e.g. interband transitions. This FT method is compared with an empirical method based on a smooth cutoff of the zero-loss peak, using PEELS data obtained from Al_2O_3. Current developments of a quantum mechanical theory are crucial to obtain the respective contributions of *intrinsic* and *extrinsic* plasmon excitation (along with their interference) and to assess some approximations performed in classical treatments.

C. Godet (✉) · V. M. da S. Santana · D. Sébilleau
Univ Rennes, CNRS, Institut de Physique de Rennes - UMR 6251, 35000 Rennes, France
e-mail: christian.godet@univ-rennes1.fr

D. G. F. David · V. M. da S. Santana · J. S. de Almeida
Instituto de Física, Universidade Federal da Bahia, Campus Universitário de Ondina, 40.210-340 Salvador, Bahia, Brazil

S. Kumar and D. K. Aswal (eds.), *Recent Advances in Thin Films*, Materials Horizons: From Nature to Nanomaterials, https://doi.org/10.1007/978-981-15-6116-0_7

1 Introduction

X-ray Photoelectron Spectroscopy (XPS) has been widely developed over the past 50 years for quantitative chemical analysis of solid surfaces, using core-level peak intensities obtained after subtraction of a broad background arising from energy loss to electronic excitations in a solid or at its surface [1–9]. Since the probability for inelastic scattering increases with the path length of photoelectrons on their way towards the solid surface, this background *signal* contains useful information about the depth distribution of the photoionized atoms [10–13] as well as the inelastic scattering cross section or energy loss function (ELF) of the medium crossed by the photoelectrons.

Photoelectron energy loss spectroscopy (XPS-PEELS) is thus a valuable non-destructive tool in material science with threefold interest: (i) improved analysis of zero-loss peak (ZLP) intensities in particular in the case of multiple environments of a given emitter species, with different binding energies; (ii) determination of the energy loss function of a homogeneous solid allowing identification of crystalline allotropes or estimation of the atom density of amorphous materials; (iii) insight into the depth distribution of atom concentration at inhomogeneous solid surfaces.

The high surface sensitivity of XPS is related to a strong inelastic scattering cross section; its decrease as a function of photoelectron kinetic energy, E_0, provides an increase in the photoelectron inelastic mean free path (IMFP), i.e. the average distance an electron travels between successive inelastic collisions measured along its flight path [1, 14, 15]. The IMFP can be tuned in synchrotron-based XPS characterizations [16, 17]. Surface sensitivity can be independently increased by angle-resolved photoemission using grazing emission angles.

Besides single-electron excitation (from occupied to unoccupied electronic states), collective oscillation of valence electrons (plasmons) can be excited in the bulk, as well as at the solid surface. Owing to the collective nature of plasma oscillations, low-loss spectra are best described in terms of the complex dielectric function, $\varepsilon(\bar{h}\omega)$, of the solid. As detailed below, the retrieval of electronic properties from XPS-PEELS data, in the framework of a dielectric theory of plasmon excitation, gives access to the dielectric function (DF) $\varepsilon(q, \omega)$, over a broad energy range (tens of eV). On the one hand, this retrieved DF allows identification of allotropic phases by comparison with ab initio calculations or optical measurements [18]. On the other hand, it provides guidelines for predicting surface wettability or interface binding strength in composite materials, through the evaluation of the dispersive Hamaker energy [19, 20].

Detailed understanding of plasmon excitation and decay mechanisms is also important for a variety of applications, including the determination of the stopping power for charged particles deceleration during ion implantation or irradiation of biological fluids [21, 22], the reduction of carrier mobility in doped electronic devices [23, 24] and the manipulation of light-electron interactions in metallic nanostructures such as plasmonic spin pumping [25].

In this review, the physics of plasmon excitation by photoelectrons will be briefly explained (Sect. 2) with some emphasis on the concepts of *intrinsic* and *extrinsic* plasmon excitation, dispersion of plasmon energy, IMFP, Bethe–Born sensitivity factor and ZLP line shape. In Sect. 3, the actual and potential applications of XPS-PEELS will be addressed, both in the field of *process control* to optimize thin-film growth parameters or implantation profiles and in *thin-film metrology* to elucidate material research issues, including a variety of microscopic or macroscopic physical properties: valence electron density, optical gap, hardness … Some practical examples will be given to illustrate the ongoing research in various fields of material science. In Sect. 4, some useful tools for XPS-PEELS data analysis will be compared to retrieve the ELF and the dielectric function. Finally, in Sect. 5, some interesting directions will be proposed for future investigations, in particular quantum modelling issues to evaluate interference effects between the intrinsic and extrinsic plasmon excitation mechanisms and to assess the validity of some classical model approximations.

2 Physics of Plasmon Excitation

Plasma oscillation in a bulk metal is characterized by the collective longitudinal oscillation of conduction electrons originating from the inertia of electrons and the Coulomb restoring force from the background positive charge. The oscillation frequency ω_P depends on the density of loosely bound electrons, i.e. those for which $E_P = \bar{h}\omega_P$ is large compared with their binding energy; the free-electron plasmon energy is given by [26–28]

$$\bar{h}\omega_{\mathrm{P}} = \bar{h}\left(\frac{4\pi n e^2}{m}\right)^{1/2} \tag{1}$$

The plasmon energy is conventionally obtained from the maximum in the bulk energy loss function (ELF), $S_{\mathrm{B}}(\bar{h}\omega)$, which is proportional to the imaginary part of the inverse dielectric function, $\mathrm{Im}[-1/\varepsilon(q, \omega)]$, corresponding to $\mathrm{Re}[\varepsilon(q, \omega)] \approx 0$ [29]. Collective excitations of valence electrons also exist at the solid-vacuum boundary, where longitudinal waves of charge density run along the surface as a polarization wave; at a planar boundary, the surface energy loss function (SELF), $S_{\mathrm{S}}(\bar{h}\omega)$, proportional to $\mathrm{Im}[(1/\varepsilon(q, \omega)) - 4/(1 + \varepsilon(q, \omega))]$, is peaked at $\sqrt{2}E_P$, corresponding to $\mathrm{Re}[\varepsilon(q, \omega)] \approx -1$.

In XPS-PEELS, a plasmon can be excited either by the core hole potential created upon photoionization of the atom (*intrinsic* plasmon) or by the longitudinal electric field of the excited electron on its way out of the solid (*extrinsic* plasmon) [3, 30, 31]. Although quantum theory shows that extrinsic and intrinsic mechanisms do interfere [32, 33], classical theories neglect the interference effect on ELF and IMFP values. In a three-step model of photoemission [34], different mechanisms contribute to

XPS spectra: the primary event is the excitation of a core electron by X-ray photon absorption at a particular atom in the solid, then the ejected photoelectron with kinetic energy E_0 travels through the material and, after crossing the solid boundary, it is collected by the detector at a particular kinetic energy value ($E \leq E_0$).

Due to the presence of a core hole, the interpretation of XPS-PEELS data is thus more complex than that of Reflection Electron Energy Loss Spectroscopy (REELS), where a mono kinetic electron beam is used at a unique incidence angle. However, in REELS measurements, detection of reflected electrons at a given exit angle requires at least one large angle elastic scattering event, because inelastic scattering only produces a minor angular deflection of electron trajectory, on the order of $\theta_T(T) = 2T/E_0$, where E_0 is the initial kinetic energy and T is the energy loss [26]. Hence, REELS analysis must take into account the path length increase brought by elastic scattering at large deflection angles [35] whereas the latter effect can usually be neglected in XPS-PEELS, in first approximation, if the photoelectron kinetic energy, E_0, is large enough. Interestingly, besides providing quantitative chemical composition of solid surfaces and detailed information on the emitter atom environment, XPS-PEELS can be readily performed on powders, or core–shell nanostructures [36, 37].

In the framework of a dielectric theory of plasmon excitation, the differential scattering cross section per unit range of energy loss, per unit solid angle, is in the Born approximation

$$\frac{d^2\sigma}{d\Omega dE} \approx \frac{1}{q^2}\mathrm{Im}\left[\frac{-1}{\varepsilon(q,\omega)}\right] \tag{2}$$

where $\varepsilon(q, \omega)$ is the characteristic DF of the solid for momentum transfer q and energy transfer $\hbar\omega$. The inelastic electron scattering allows experimental determination of the frequency- and wave-vector-dependent dielectric screening function $\varepsilon(q, \omega)$, which describes the response of the electrons in the solid to an applied charge-density fluctuation. Hence, the single bulk plasmon (SBP) energy loss distribution in XPS-PEELS contains valuable information related to the q-averaged DF $\langle\varepsilon(q, \omega)\rangle_q$ over a broad energy range.

In contrast with optical measurements which provide the dielectric function $\varepsilon(q = 0, \omega)$, in XPS-PEELS and REELS experiments, the relevant bulk losses are governed by a weighted average, $\langle\mathrm{Im}[-1/\varepsilon(q, \omega)]\rangle_q$, over the range of transferred wave numbers, q, allowed by energy and momentum conservation laws. For electrons travelling through an infinite medium, the differential inverse inelastic mean free path (DIIMFP) is the probability density per unit path length, $K(E_0, \bar{h}\omega)$, of losing an energy $\bar{h}\omega$:

$$K\left(E_0, \bar{h}\omega\right) = \frac{1}{\pi a_0 E_0}\int_{q^-}^{q^+}\frac{dq}{q}\mathrm{Im}\left[\frac{-1}{\varepsilon(\omega)}\right]. \tag{3}$$

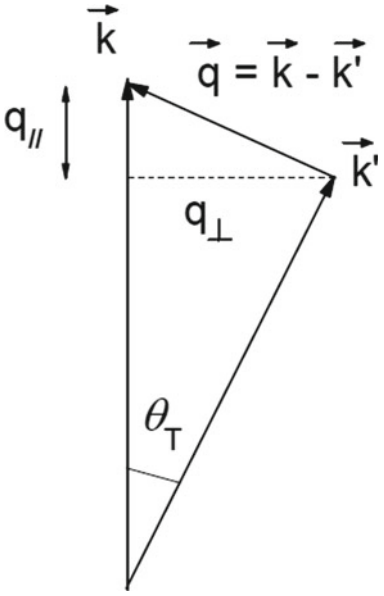

Fig. 1 Schematic illustration of inelastic scattering of an electron with initial momentum k; the momentum q and the energy T are transferred to some excitation in the solid, e.g. a plasmon

where a_0 is the Bohr radius, E_0 is the initial kinetic energy of the photoelectron, q is the wave vector transferred from the electron and

$$q_{\pm} = (2m_0/\bar{h}^2)^{1/2}[E_0^{1/2} \pm (E_0 - \bar{h}\omega)^{1/2}] \tag{4}$$

are q vector limits imposed by energy and momentum conservation during inelastic scattering (Fig. 1).

In addition, a cutoff scattering angle, θ_C, is introduced to account for plasmon decay to single-particle excitations (Landau damping) above a critical wave vector transfer, q_C, corresponding to equal phase and group velocities [26]. Hence, for an abrupt cutoff, the inverse inelastic mean free path (IIMFP) is given by [38, 39]

$$\frac{1}{\lambda_p} = \int_0^{E_{MAX}} K(E_0, T)dT = \int_0^{\infty} \frac{f_C(T)}{2\pi^2 a_0 E_0} \mathrm{Im}\left(-\frac{1}{\varepsilon(T)}\right)dT \tag{5}$$

where the Bethe–Born sensitivity factor $f_C(T)$:

$$f_C(T) = 2\pi \int_0^{\theta c} \frac{\theta d\theta}{\theta^2 + (\theta_T)^2} = \pi \mathrm{Ln}\left(\left(\frac{\theta c}{\theta_T}\right)^2 + 1\right) \tag{6}$$

depends weakly on $\theta_T(T)$, with $\theta_C \approx q_C/k_0$ for small $\theta_T(T)$. Hence,

$$K(E_0, T) = \frac{1}{2\pi^2 a_0 E_0} \mathrm{Im}\left(-\frac{1}{\varepsilon(T, q)}\right) \pi \ \mathrm{Ln}\left[1 + \left(\frac{\theta_C}{\theta_T}\right)^2\right] \tag{7}$$

This dielectric formulation of the DIIMFP (3–7) must take into account the dispersion in $\boldsymbol{\varepsilon}(E, q)$ that is the effect of momentum q transferred from the photoelectron to plasmon excitation. Its exact q-dependence being unknown, a general dispersion law for the ELF peak energy at small q is given by

$$E = E_P(q = 0) + \alpha^0 \frac{\bar{h}^2}{m} q^2 \tag{8}$$

Dispersion effects can be illustrated by experimental and theoretical results obtained with aluminium metal. Al is representative of free-electron like materials, in which the ELF shows a predominant peak due to well-defined volume plasmons with energy E_P close to the free-electron value given by (1), with square root dependence on the electron density [40–46]. In addition, the Al $2p$ core level is sharp due to the relatively long lifetime of the $2p$ core hole and weak coupling to phonons [47]. In Al metal, the plasmon energy observed in electron energy loss spectroscopy (EELS) is linear with q^2, out to about 17 nm^{-1}, with E_P $(q = 0) = 15.0$ eV and $\alpha^\circ = 0.38 \pm 0.02$ [44]. This quadratic dispersion persists beyond the critical wave vector, $q_\mathrm{C} = 11.4\ \mathrm{nm}^{-1}$, well into the single-particle excitation region.

Dispersion is first considered in the framework of the Lindhard–Mermin formalism, which describes the response of a degenerate free-electron gas to an external (longitudinal) perturbation [48–50]. The Lindhard dielectric function, $\varepsilon_\mathrm{L}(q, \omega)$, consists in a delta function (describing plasmon excitations) and a continuous part (describing electron–hole excitations); it can be derived from the quantum perturbation theory [48] or following the random phase approximation (RPA) [28]. Mermin introduced the damping rate (inverse relaxation-time) of the plasmons in the Lindhard longitudinal DF in a physical way which fulfils the conservation of the local number of particles. Plasmon damping may result from either interband transitions (Landau damping) or electron–phonon interaction. The Mermin loss function is based on a free-electron model and the width of the loss feature increases with q, while fulfilling the Bethe sum rule

$$\int_0^\infty d\omega\, \omega\, \mathrm{Im}\left(-\frac{1}{\varepsilon(q, \omega)}\right) = \frac{\pi}{2} \omega_P^2 \tag{9}$$

for all q values, as well as the Kramers–Kronig sum rule [50, 51].

As shown in Fig. 2, in the Lindhard–Mermin model, the ELF peak disperses and loses strength with increasing normalized wave number (q/k_F). In Al metal, $E_\mathrm{P} = 15.3$ eV, $k_\mathrm{F} = 17.5\ \mathrm{nm}^{-1}$ and $\Gamma = 1.6$ eV. Above the critical wave vector, $q_\mathrm{C} = 11.4\ \mathrm{nm}^{-1}$ ($q_C/k_\mathrm{F} = 0.65$) the integrated intensity of the ELF drops and the plasmon is no longer a well-defined excitation. For $q < q_\mathrm{C}$, one obtains a dispersion parameter $\alpha^\circ{}_\mathrm{LM} = 0.52 \pm 0.02$ for the *median* ELF energy in (8).

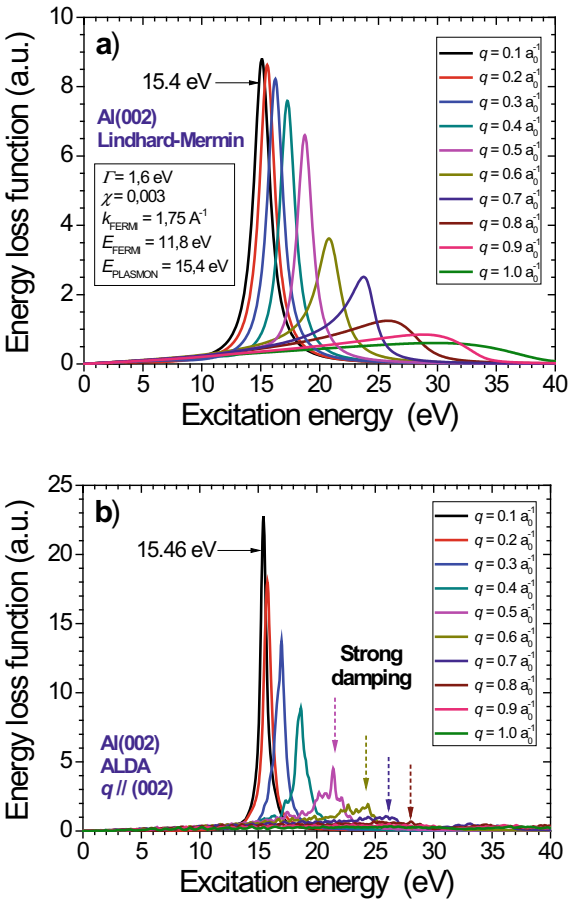

Fig. 2 Energy loss function of Al obtained with: **a** the Lindhard–Mermin formalism using $E_P = 15.4$ eV, $k_F = 17.5$ nm^{-1} and $\Gamma = 1.6$ eV); **b** a TD-DFT code (EXCITING) in the local density approximation for wave vector q //(002). The ELF peak energy follows a quadratic q-dependence for $q < q_C$ (8)

The dispersion of the bulk plasmon loss function of Al single crystal has also been obtained from a time-dependent density functional theory (TD-DFT) code (EXCITING software [52, 53]). The ground state was obtained with 30 × 30 × 30 k vectors in the Brillouin zone, while the excited spectrum was calculated with 16 × 16 × 16 k vectors in the Brillouin zone, 9 base functions and 40 empty conduction bands. Very weak anisotropy effects were found for q wave vectors in the directions (002), (110) and (111). For $q < q_C$, the ELF dispersion $E(q)$ follows a q-dependence stronger than given by (8). Using a more comprehensive dispersion law, valid also for larger q values [54]:

$$\omega_P(q) = \omega_P(q = 0) + Aq^2 + Bq^4 \tag{10}$$

the adjusted coefficients, $A = 2.8$ eV Å^2 and $B = 5.6$ eV Å^4, give a large dispersion parameter $\alpha^\circ_{EXC} = 0.80 \pm 0.05$ at low q values, as compared to that derived from the

Lindhard–Mermin model. The quite large slope in $E(q)$ and the narrow ELF width as compared to the ELF retrieved from XPS-PEELS (Sect. 4) indicate that lifetime effects should be incorporated in the Exciting calculation, e.g. using the self-energy derived from GW calculations [55].

Since dispersion effects strongly influence the ELF, $\langle \mathrm{Im}[-1/\varepsilon(q,\omega)]\rangle_{\boldsymbol{q}}$, measured by XPS-PEELS, as shown in this section, some q-averaged dielectric function, $\langle \varepsilon(q,\omega)\rangle_{\boldsymbol{q}}$, will be retrieved in Sect. 4 by taking into account multiple bulk and surface plasmon excitations.

3 A Versatile Tool for Material Science

The actual and potential applications of XPS-PEELS cover two main fields: (i) *process control* to optimize thin-film growth parameters or implantation profiles in solid targets and (ii) *thin-film metrology* to elucidate material research issues, including a variety of microscopic or macroscopic physical properties: valence electron density, optical gap, hardness. The dielectric function retrieval methods will be treated in Sect. 4.

3.1 Process Control

For an ideal metal, the ELF peak energy is proportional to the square root of the valence electron density (1). In real materials including semiconductors and insulators, this characteristic remains qualitatively valid and the loss energy provides a straightforward signature for identification of allotropes with identical composition, as well as surface-sensitive guidelines for optimizing the growth parameters in thin-film deposition.

Core-level photoemission spectra of Si_3N_4 in the hexagonal β phase and in the high-pressure cubic phase show a large difference in plasmon energy, associated to Si 2*p* and 2*s* and N 1*s* core lines in XPS [56]. In the hexagonal phase, Si atoms are in tetrahedral configurations linked by planar 3-coordinated N atoms, while in the metastable cubic phase (spinel structure), Si atoms occupy half of the octahedral holes and one-quarter of the tetrahedral holes in a cubic close-packed array of nitrogen atoms. The primary plasmon satellites found at 23.45 and 26.10 eV, in the β and cubic phases, correspond to the expected electron density ratio of 1.26.

In covalent semiconductors and insulators, the energies of plasmon satellites and their intensities relative to the core lines are usually identical for the different atom core levels (e.g. Si 2*p* and 2*s* vs. N 1*s* photoemission spectra in Si_3N_4) [56] because both atoms contribute to the valence electron density, which provides strong coupling between core holes on both elements and the valence electrons. In contrast, in ionic oxides such as MgO, where *all* the valence electron density is essentially localized

on O ions, the plasmon satellites are much stronger in O 1*s* photoemission than in the metal core-level photoemission [57].

The sensitivity of the ELF in amorphous semiconductors is illustrated by the complex structure of amorphous carbon (a-C) films obtained by plasma-enhanced chemical vapour deposition (PECVD) or physical vapour deposition (PVD). Since the growth mechanisms are highly sensitive to the deposition process, a wide range of C atom densities can be obtained, corresponding to variable sp^2 versus sp^3 hybridization with possible structuration as sp^2-C clusters at the nm scale [58]. Previous work compared the PEELS characteristics of sputtered, pulsed laser deposited (PLD) and plasma deposited a-C films, corresponding to increasing $sp^3/(sp^2 + sp^3)$ hybridization ratio [38].

Figure 3 shows the C 1*s* core-level peak along with the first plasmon satellite; removal of multiple order satellites due to the self-convolution of the ELF (Fig. 4) provides the $\sigma + \pi$ plasmon energy values ranging from 24 to 31 eV. The ZLP tailing overlaps the ELF distribution in sp^2-rich a-C films, while better separation is observed in the wide band gap hydrogenated carbon film (a-C:H). This study confirms the interest of XPS-PEELS as compared to REELS experiments, since the former provides an accurate estimate of the amount of sp^2 and sp^3 C atom configurations, due to the large difference in their binding energies, $E_B(sp^3) - E_B(sp^2) = 0.77 \pm 0.05$ eV [59].

The above examples correspond to the bulk properties of materials which are homogeneous on a depth scale of several IMFP values. The interest of XPS-PEELS for process control has also been demonstrated in the study of the topmost surface

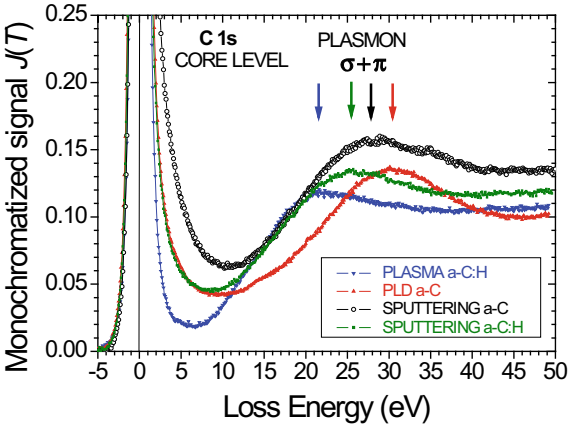

Fig. 3 XPS-PEELS spectra at normal emission angle ($\alpha = 0°$) for different a-C films with variable sp^2-sp^3 content and ($\sigma + \pi$) plasmon energy. Raw XPS spectra were numerically monochromatized to obtain normalized loss spectra $J(T)$ using X-ray source satellites $K\alpha_3/K\alpha_{1,2} = 0.08$ and $K\alpha_4/K\alpha_{1;2} = 0.04$ at −8.4 and −10.2 eV, respectively. From Ref. [38] reprinted by permission from Elsevier, Applied Surface Science (2016)

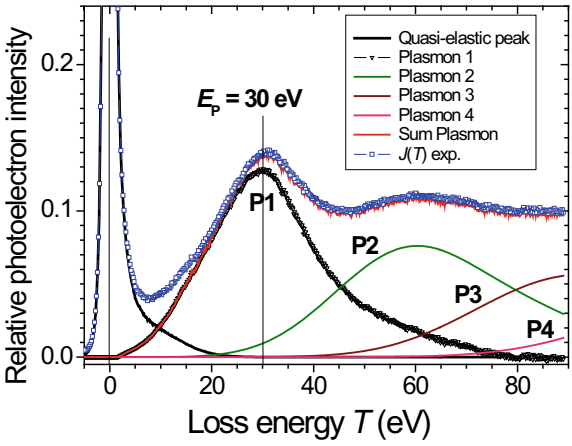

Fig. 4 Deconvolution of plasmon losses in PLD a-C ($\alpha = 0°$) up to fourth order after removal of the ZLP by the smooth cutoff method (sigmoid function (16) with $\Delta E_{SIG} = 10$ eV, $E_G = 1.3$ eV). From Ref. [38] reprinted by permission from Elsevier, Applied Surface Science (2016)

termination, in the prediction of interface properties and in the characterization of shallow ion implantation profiles.

XPS-PEELS is sensitive to the surface reconstruction of crystalline materials, as illustrated by annealing of boron-doped microcrystalline diamond films, with a mixture of (111) and (100) preferential orientations [60]. Comparison of ELF characteristics in the as-grown state, with a partially hydrogenated surface, and after annealing at 1150 °C in an ultra-high vacuum has shown some weak attenuation of the bulk ($\sigma + \pi$) plasmon of the diamond at 34.5 eV without evidence for surface graphitization. The new features which appear at 10 ± 1 eV and 19 ± 1 eV in the energy loss distribution are well described by simulation of surface plasmon excitations in graphite-like materials; alternatively, they also coincide with experimental interband transition losses, respectively, attributed to $\pi \rightarrow \sigma^*$ and $\sigma \rightarrow \pi^*$ single-electron transitions, in some graphene layers [61].

Some interface characteristics, such as wetting properties of solid surfaces, self-assembly or binding strength of nanocomposite materials, can be investigated using the DF retrieved from XPS-PEELS [20] or EELS [19] data, over a very broad energy range. This approach has also been considered in the field of tribology of magnetic disk coatings [62, 63]. The Lifshitz theoretical formalism [64, 65] provides dispersion forces between electrically neutral macroscopic bodies based on their dielectric functions, $\varepsilon(q, \omega)$. The van der Waals (vdW) interaction energy per unit area as a function of separation distance, L, between parallel planar half-spaces 1 and 2 separated by intervening medium 3, is given by $E_{132} = -A_{132}(L)/12\pi\ L^2$, where the Hamaker energy $A_{132}(L)$ is a function of the respective Kramers–Krönig (KK) transforms of $\mathrm{Im}[\varepsilon(\omega)]$ and thus requires knowledge of $\varepsilon(q, \omega)$ over several tens of eV. Predictive formulas were derived for a wide family of amorphous carbon films in contact with water or diiodomethane [20].

The depth distribution of implanted atoms in solid targets is important to monitor sputter-cleaning experiments, fusion wall damage, metal nitridation processing and doping profiles in electronic devices. In XPS, core-level peak intensity carries little

information on the total amount or depth distribution of implanted atoms, in contrast with their energy loss distribution [11]. In the case of dilute emitter atoms embedded in a solid matrix, besides angular dependence of the host/matrix relative core-level peak intensities [66], complementary insight can be gained into energy losses experienced by photoelectrons emitted from implanted atom core levels along their path through the matrix to the solid surface.

Valuable information on implantation profiles is obtained from the relative intensities of first-order and second-order plasmon excitation peaks at variable emission angles, after decomposition of energy loss spectra [67]. This method is sensitive to average depth (ion range) and width (straggling) of the profile, but not to higher moments of the distribution, as illustrated by the case study of noble gas ion implantation into a metal matrix, which is known to provide subsurface nanobubbles [66, 68, 69]. Interestingly, for shallow implantation of argon ions ($E_{\mathrm{ION}} = 2.0$ keV, 35° incidence, 3 ML) into Al(002) matrix, it has been observed that the average depth ($d_{\mathrm{PEELS}} = 2.04 \pm 0.1$ nm) of Ar bubbles obtained from energy loss spectra of Ar $2p$ photoelectrons ($E_{\mathrm{KIN}} = 1011$ eV, IMFP = 2.15 nm) is significantly smaller than the average depth calculated from the Monte Carlo SRIM code ($d_{\mathrm{SRIM}} = 3.8$ nm). This discrepancy has been attributed to significant sputtered thickness (≈1.7 nm) of Al due to a large Ar^+ sputtering yield ($Y = 2.8$ at 35° off-normal incidence) combined with possible diffusion of argon-vacancy complexes towards the surface during Ar ion implantation, overlooked in SRIM simulations [67].

Finally, it is worth reporting the empirical relationship found between hardness measured by indentation methods and plasmon energy derived from valence EELS [70] or XPS-PEELS. For covalent semiconductors and a wide family of carbon materials (soot and films), the observed correlation is consistent with the enthalpy density theory [71, 72], which states that the hardness of homogeneous bulk materials is proportional to the sum of the local bond strengths per unit volume. The outstanding hardness of diamond is thus explained by its large atom density and strong binding energy (7.0 eV) between sp^3 hybridized carbon atoms.

3.2 Thin-Film Metrology

Some useful guidelines for accurate analysis of XPS-PEELS data are given in the following. We particularly consider: (a) the behaviour at the onset of the energy loss distribution which corresponds to the electronic band gap energy; (b) the ELF normalization procedure which requires additional information from optical measurements or theoretical input; (c) the shift of the ELF peak value with respect to its predicted value for an electron gas of the same average electron density resulting from the interplay between plasmon excitation and interband transitions.

3.2.1 Optical Gap Region

A major interest of XPS-PEELS for insulating materials is its ability to evidence the onset of the energy loss distribution which coincides with the forbidden band gap. In contrast, in semi-metals and narrow gap semiconductors, overlapping of ZLP tail and ELF distribution prevents a simple determination of the optical gap, as illustrated in Fig. 3 for sp^2-rich a-C films, while better separation is observed in the wide band gap a-C:H film.

The band gap of metal oxides can be measured using the XPS O 1*s* energy loss spectra, down to very small film thickness ($d \approx 2$ nm) limited by increasing contributions of energy losses arising from the underlying substrate with a smaller band gap. In addition, the oxide band gap combined with the valence band offset (also measured by XPS) provides the value of the conduction band offset. Energy band alignment diagrams have thus be obtained in a number of metal–oxide–semiconductor (MOS) and semiconductor heterojunction devices, e.g. Ta_2O_5 and ZrO_2 evaporated on Si [73], Al_2O_3 and HfAlO grown by atomic layer deposition on 4H–SiC for high-power applications [74], Al:ZnO sputtered on Cu_2SnS_3 for heterojunction solar cells [75].

In the latter XPS-PEELS studies, as well as in REELS spectra, the optical gap is usually obtained from some extrapolation in the linear loss region near the leading edge [73, 76]. In the following, we show that this procedure is justified if the surface excitation parameter (SEP) is not too large. The measured XPS-PEELS signal is given by

$$S_B(T) = \mathrm{Im}\left[\frac{-1}{\varepsilon(\omega)}\right] f_C(T) \text{ and } S_S(T) = \mathrm{Im}\left[\frac{1}{\varepsilon(\omega)} - \frac{4}{1+\varepsilon(\omega)}\right] g(T) \qquad (10)$$

for bulk and surface plasmon excitations, respectively, where $f_C(T)$ and $g(T)$ are angular response integrals (Bethe–Born factors) which, respectively, decrease as a function of loss energy as $T^{-1/8}$ and T^{-1}, as determined previously [38]. For both Drude, Lorentz and Tauc–Lorentz dielectric functions, $\varepsilon(T) = \varepsilon_1(T) + i\varepsilon_2(T)$, the ***bulk*** plasmon ELF is proportional to Im $\varepsilon(\omega)$, hence it is linear as a function of loss energy at low T. In the case of the ***Tauc–Lorentz model***, $S_P(T) = S_B(T) + S_S(T) \approx a_{TL}(T - E_{GAP}) + b_{TL}(T)$, while $S_B(T) = S_S(T) = 0$ for $T \leq E_{GAP}$. Assuming that $f_C(T)$ is practically constant near E_{GAP}, the bulk plasmon expression is linear above E_{GAP}. The latter result was used to obtain a neat separation between the ZLP and the energy loss region in the case of the model semiconductor a-Si:H [77].

In contrast, the surface plasmon expression shows a fast increase above E_{GAP} and tends, as in the case of the Lorentz dielectric function, to a quasi-constant value for $T \gg E_{GAP}$ (Fig. 5). This effect is emphasized by the strong energy dependence of $g(T)$ as T^{-1}. If the surface excitation parameter (SEP) is large, this non-linearity may lead to some underestimation of the electronic band gap obtained from a linear extrapolation.

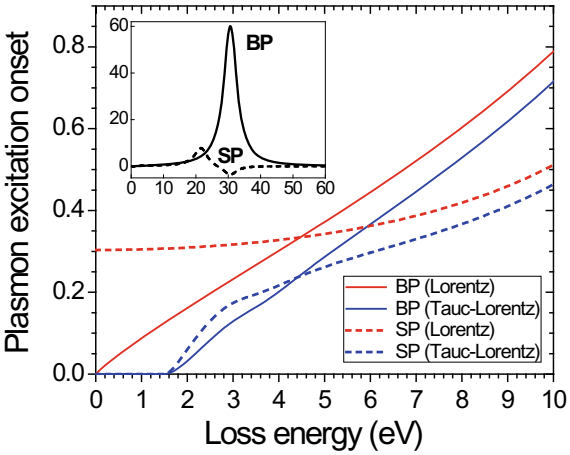

Fig. 5 Onset of bulk and surface plasmon excitations for the Lorentz (L) and Tauc–Lorentz (TL) approximations. The model parameters were adjusted to the energy loss function of dense amorphous carbon films (inset) with a gap of 1.6 eV in the TL model

3.2.2 ELF Normalization

As far as optical properties are concerned, since XPS-PEELS experiments only give a relative ELF intensity with respect to the ZLP intensity, some normalization of the ELF strength (or equivalently of the DIIMFP and IMFP parameters) is usually performed using the value of Re $\varepsilon(\omega \to 0)$ measured independently by optical methods, such as spectroscopic ellipsometry [38], and the Kramers–Krönig relation:

$$\frac{2}{\pi}\int_0^\infty \mathrm{Im}\left(-\frac{1}{\varepsilon(T)}\right)\frac{dT}{T} = 1 + \mathrm{Re}\left(-\frac{1}{\varepsilon(0)}\right) \approx 1 - \frac{1}{\varepsilon_1} \tag{11}$$

The normalized loss function is then converted using Kramers–Krönig integration according to

$$1 + \mathrm{Re}\left(-\frac{1}{\varepsilon(T)}\right) = \frac{2}{\pi}\int_0^\infty \mathrm{Im}\left(-\frac{1}{\varepsilon(X)}\right)\frac{XdX}{X^2 - T^2} \tag{12}$$

Other sum rules are useful to determine the effective electron number per atom participating in the plasma oscillation:

$$N_2 = \frac{2\varepsilon_0 m_0}{\pi \bar{h}^2 N_{AT}}\int_0^\infty \mathrm{Im}\left(-\frac{1}{\varepsilon(T)}\right)TdT \tag{13}$$

The latter equation is known as the oscillator strength or f-sum rule.

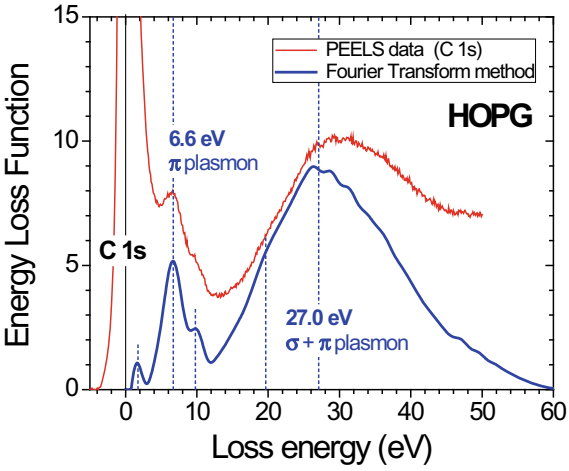

Fig. 6 Energy loss spectrum of highly oriented pyrolyzed graphite (HOPG) obtained from C 1*s* photoelectrons ($\alpha = 0°$) derived from the Fourier transform method

3.2.3 Interplay Between Plasmon and Interband Transitions

Both plasmon line shape and peak energy can be affected by the interband transitions and the core-level polarization, which basically modify the energy value at which $\mathrm{Re}[\varepsilon] \approx 0$ [26, 46, 78, 79]. A rough estimate of the shift of the plasmon energy with respect to its predicted value, ω_{EG}, for an electron gas of the same average electron density, is given by

$$\omega_P^2 = \frac{\omega_{EG}^2 + \omega_N^2}{1 + \chi_B} \tag{14}$$

where χ_B is the polarizability of deeper bound shells and ω_N is the eigenfrequency of the electrons participating in plasma oscillation.

Amorphous carbon and graphitic materials nicely illustrate the interplay between plasmon behaviour and interband transitions. In Fig. 6, XPS-PEELS data for HOPG measured at normal emission angle were analysed using the Fourier transform method (see Sect. 4.2). Two main loss peaks appear at 27.0 eV and 6.6 eV, corresponding, respectively, to the $\sigma + \pi$ and π plasmon excitations, while a smaller peak and a shoulder, respectively, appear at 9.8 eV and 19.7 eV. For the $\sigma + \pi$ plasmon, the core-level polarizability is negligible and the average $\sigma \rightarrow \sigma^*$ energy (bonding–antibonding splitting) is about 14 eV; using (1), the conduction electron density (4.48×10^{23} cm^{-3}) of graphite gives $\omega_{EG} = 25$ eV, hence $\omega_P = 28.5$ eV; this calculation is in good agreement with experiment, taking into account the fact that HOPG anisotropy has been overlooked. For the π plasmon excitation, the average $\pi \rightarrow \pi^*$ energy is about 5 eV hence the π electron density of graphite (1.12×10^{23} cm^{-3}) gives $\omega_{EG} = 12.5$ eV; the large decrease of the electron gas value to the π plasmon experimental value of 6.6 eV can be understood by taking into account

the large polarizability of σ states, $\chi_B \approx 3$, which increases Re[ε] (i.e. enhances screening).

Following systematic comparison between EELS data and X-ray reflectivity measurements of the atom density in amorphous carbons [79], some corrections of the measured plasmon energy have been proposed, either using an average electron effective mass or some independently measured value of $\varepsilon(0)$. Such corrections are important for hydrogen-rich a-C:H films.

4 Retrieval of the Dielectric Function from XPS-PEELS Data

In Sect. 2, we have emphasized that, in XPS-PEELS, the measured energy losses corresponding to a particular core-level photoelectron result from intrinsic, extrinsic and interference mechanisms, giving some ELF peak near the energy E_P, and multiple satellites resulting from successive inelastic events expressed by the n-fold self-convolution of the ELF distribution. In addition, the primary ELF is broadened as a consequence of the extended range of accessible values of the momentum transfer q, given by energy and momentum conservation rules, further limited by a critical q_C value above which plasmons decay into electron–hole pairs. In summary, in energy loss spectroscopy, the ELF appears as a q-averaged energy loss distribution $\langle \mathrm{Im}[-1/\varepsilon(q,\omega)] \rangle_q$.

4.1 Quantitative Analysis of XPS-PEELS Data

The experimental photoelectron flux, $J(E)$, measured in XPS is ideally separated into a sum of the primary photoelectron peak, $F(E)$, and energy losses obtained by convolution of $J(E)$ with the DIIMFP, $\lambda_P(E')K(E'-E)$ [5, 6, 80]:

$$J(E) = F(E) + \int_0^\infty dE' J(E') \lambda_P(E') K(E'-E) \tag{15}$$

In the literature, quantitative analysis of XPS-PEELS experiments has followed two complementary directions: (i) the accurate recovery of the line shape and intensity of the ZLP or primary peak $F(E)$; (ii) the retrieval of q-averaged ELF or q-averaged dielectric function. As a matter of fact, the latter approach has been essentially applied to REELS, since it is simpler to isolate the elastic peak in REELS (no core hole) than in XPS (one core hole) or Auger (two holes) spectra, where additional broadening of the elastic peak results from shake-up excitations that typically extend tens of eV on the low kinetic energy side of the zero-loss peak [81–84]. In addition, there are as many primary electron energies in XPS as there are orbitals of

different binding energy, hence the spectral loss distributions are superimposed in the XPS-PEELS spectrum.

In the first approach, the mathematical description of energy loss processes (last term on the right-hand side of (15)) must take into account the n-fold self-convolution of the bulk ELF, along with the surface ELF. Additional refinements have been developed in the simulation of electron spectra for spectral analysis (SESSA) in order to account for elastic scattering which increases the photoelectron path length; using DIIMFP derived from optical data or from Tougaard's universal model [8], partial intensities can be obtained from Monte Carlo calculations for each population of photoelectrons that have suffered n inelastic collisions [13]. Some limitations of such a model have been pointed out due to neglected surface and core hole effects which may contribute to enhanced losses at small energies [9].

A semi-classical dielectric response model has been proposed for quantitative analysis of electron energy loss in XPS (QUEELS-XPS) [85, 86]. The starting point is the determination of the complex dielectric function $\varepsilon(q, \omega)$, or alternatively the energy loss function $\mathrm{Im}[-1/\varepsilon(q, \omega)]$. A model dielectric function expanded in Drude–Lindhard-type oscillators with a quadratic dispersion relation is derived from a multi-parameter fitting of ancillary optical ($q = 0$) or REELS data [85, 86]. However, empirical adjustment appears necessary because a model with only Drude–Lindhard oscillators does not allow to correctly fit the region of small energy losses [9]. Theoretical inelastic cross sections (including bulk and surface excitations) are further calculated according to a semi-classical response model which describes the interactions of electrons with semi-infinite media in terms of the dielectric properties of the bulk solid and incorporates the effects of the surface and of the static core hole [85, 86]. The XPS spectrum is finally reconstructed by convolution of the differential inverse inelastic mean free path (DIIMFP) by a primary spectrum, $F(E)$, taken as a sum of Voigt components.

Since the dispersion parameter and the critical q_C value are not known precisely, even in quasi free-electron metals, it may appear as a better choice to retrieve directly the q-averaged energy loss distribution $\langle \mathrm{Im}[-1/\varepsilon(q, \omega)] \rangle_q$, without making particular hypothesis on either the dielectric function shape or the dispersion coefficient, which is particularly hazardous in the study of new materials. In this recently developed approach [38], it is stressed that no arbitrary baseline is subtracted from XPS-PEELS data since all energy loss mechanisms, i.e. plasmon collective excitations and single-electron excitations, are included in the ELF. The electron analyzer sensitivity is assumed to be constant over a typical 100 eV-loss window. Any algorithm must take into account multiple bulk and surface plasmon excitations, with the additional constraint that bulk and surface ELF distributions (see Sect. 3.b) should be self-consistent, i.e. result from the same dielectric function if the solid is homogeneous. This task is rather straightforward in wide band gap materials where the ELF and the no-loss peak are clearly separated, as illustrated in this report by amorphous silicon (Fig. 7), amorphous carbon (Fig. 4) or aluminium oxide (Fig. 13) examples.

In the case of amorphous semiconductors, empirical approaches for ZLP subtraction have been proposed and compared previously [77] but more physically relevant methods are clearly desirable. As shown in Fig. 7, the main advantage of a 'smooth

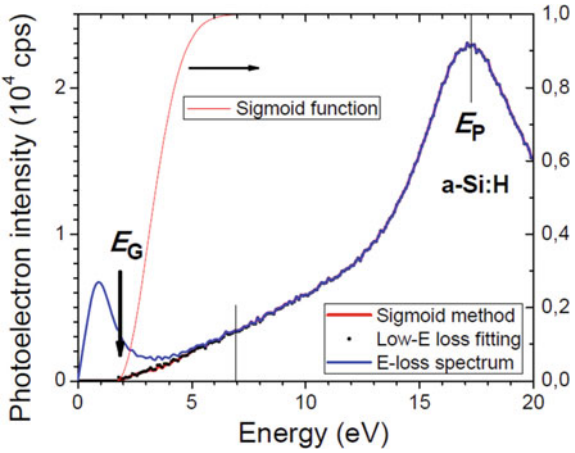

Fig. 7 Separation of asymmetrical ZLP and energy losses of a-Si:H by two methods: (i) removal of a symmetrical ZLP function and *subtraction* of the low-energy ZLP tailing as fitted by some analytic function; (ii) sigmoid method where the measured XPS-PEELS spectrum is *multiplied* by a smooth cutoff function (16) ($\Delta E_{\mathrm{SIG}} = 2.0$ eV, $E_{\mathrm{G}} = 1.7$ eV). Both results are overlapped; however, in the smooth cutoff method, the noise is completely suppressed in the loss energy range 0–7 eV. From Ref. [77] reprinted by permission from Elsevier, Journal of Non-crystalline Solids (2012)

cutoff method' is the reduction of the noise level, in contrast with subtraction procedures, because the XPS signal is multiplied by a monotonic function, e.g. a sigmoid function [77]:

$$\sigma(T) = 0 \quad \text{for } T \leq E_G \text{ and}$$
$$\sigma(T) = 1 - \exp\left(-\left(\frac{T - E_G}{\Delta E_{SIG}}\right)^2\right) \quad \text{for } T > E_G \tag{16}$$

In contrast, in metals or materials with a small electronic band gap, the broad asymmetric photoemission peak overlaps bulk and surface ELF distributions and low-energy features in the ELF may be lost as a result of ZLP subtraction operation. Such detrimental effects may be attenuated by using an appropriate 'guess' ZLP line shape, e.g. the Doniach–Sunjic distribution [87] or, in the case of crystalline solids, a calculated ZLP line shape using the joint density of states in the conduction band within Mahan–Nozières–de Dominicis (MND) theory [88–90].

4.2 Retrieval of the DF: Fourier Transform Method

Since the XPS intensity measured over a broad range towards lower kinetic energies results from the convolution of four spectral distributions (photoemission line shape,

multiple plasmon loss probability, non-monochromatic X-ray source and Gaussian broadening of the photoelectron kinetic energy analyzer), a Fourier Transform (FT) method is a natural way to analyse PEELS data in metals [91]. The last two functions are experimentally available [92], while the former ones require a combined experimental and theoretical approach. Using the Doniach–Sunjic line shape for the ZLP, the only adjustable parameters are the singularity index and the broadening energy Γ (inverse lifetime due to plasmon decay to electron–hole pairs). After correction for surface plasmon excitations, q-averaged distributions of the ELF and the dielectric function are obtained, the major hypothesis being that intrinsic and extrinsic loss functions have the same energy distribution. Note that, in line with previous works [40], we assume that the signal above the flat background on the low binding energy side of the ZLP should be entirely assigned to the plasmon excitations and single-electron transitions.

Using carefully designed FT methods [91], the objective of keeping low-energy features can be effectively reached, as illustrated by results obtained from Al(002), showing interband transitions at small loss energies. This FT method was applied to XPS spectra taken on a freshly etched monocrystalline Al(002) surface, using a non-monochromatic Mg Kα source (Fig. 8), where equally spaced peaks due to well-defined volume plasmon excitations are observed up to 6th order (Fig. 9) [40–43].

Several simplifying assumptions have been used. In first approximation, intrinsic and extrinsic plasmon excitation mechanisms are considered separately, i.e. with no interference, but with identical ELF distributions [3, 30, 31]. Successive extrinsic plasmon excitations are assumed to be independent events. Hence, the intensity I_n of the nth-order plasmon line is given by $I_n = (b^n/n!)\,I_0 + a\,I_{n-1}$, where I_0 is the intensity of the zero-loss peak, $b_n = (b^n/n!)$ is the creation rate for an intrinsic plasmon and $a(I_{n-1}/I_0)$ is the creation rate for an extrinsic plasmon. In the case of Al metal, the low b value ($b \approx 0.11$, $a \approx 0.66$) [3, 30, 31] makes intrinsic plasmon

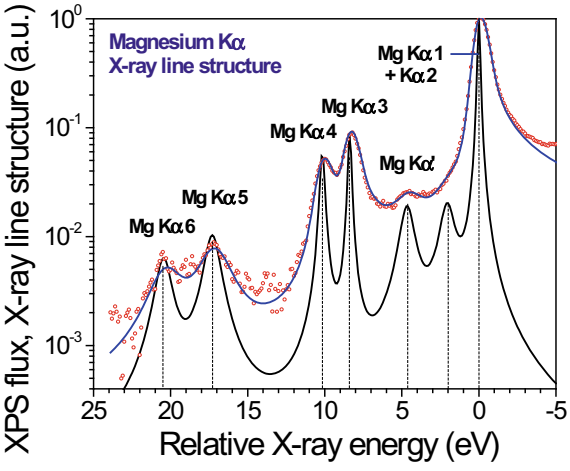

Fig. 8 The spectral distribution of the Mg Kα X-ray source is given by a sum of seven Lorentzians (*black line*); peak position E_i, amplitude A_i, and full-width at half maximum Γ_i parameters were obtained from fitting a convolution product $XRS(E)*DS(E)*G(E)$ (*blue*) to experimental Al 2*p* satellites (*red*). From Ref. [91] reprinted by permission from Springer, Brazilian Journal of Physics (2018)

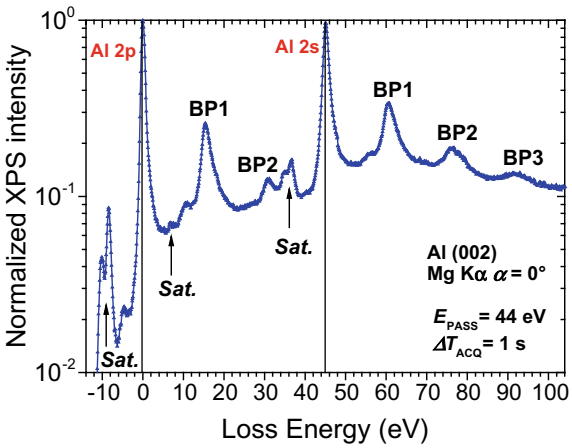

Fig. 9 Raw XPS-PEELS data for a clean Al(002) surface, obtained with non-monochromatic Mg source; loss energies are referenced to Al 2*p* core level and XPS intensities are normalized to the no-loss peak maximum. From Ref. [91] reprinted by permission from Springer, Brazilian Journal of Physics (2018)

excitation negligible beyond first order, hence we have $I_1 = (b + a)\, I_0$ for the first-order plasmon and $I_n = a I_{n-1}$ $(n > 1)$. These basic principles are translated into convolution products which make the FT algorithm quite efficient, provided that suitable noise reduction methods are implemented. The measured spectrum is thus given by the convolution $EXP(E) = G(E) \otimes XR(E) \otimes J(E)$ of the X-ray source and Gaussian spectrometer broadening functions with the photoelectron flux $J(E)$, expressed as a sum $J(E) = ZLP(E) + BP1(E) + BP2(E) + BP3(E) \ldots$ of ZLP and nth-order bulk plasmon losses $\mathrm{BP_n}(E)$. In the Fourier space,

$$F[J(E)] = F[ZLP(E)] + aF[ELF(E)]F[J(E)] + bF[ELF(E)]F[ZLP(E)]. \tag{17a}$$

One recognizes that the second term on the right-hand side represents the sum of all extrinsic losses while the last term is the first-order intrinsic loss. This equation gives the FT of $ELF(E)$:

$$F[ELF(E)] = \frac{F[J(E)] - F[ZLP(E)]}{aF[J(E)] + bF[ZLP(E)]} \tag{17b}$$

and the ELF in the energy space is obtained using the inverse Fourier transform.

Figure 10 shows the bulk ELF of Al crystal obtained after correction for surface plasmon excitation. This q-averaged bulk loss function, $\langle \mathrm{Im}[-1/\varepsilon(E, q)] \rangle_q$, of Al(002) differs from the optical value $\langle \mathrm{Im}[-1/\varepsilon(E, q = 0)] \rangle$ and is well described by the Lindhard–Mermin dispersion relation [48–50].

A quality criterion of the inversion algorithm is given by the capability of observing interband transitions very close to the ZLP, namely at 0.65 and 1.65 eV in $\varepsilon(\omega, q)$ (Fig. 11) in good agreement with optical spectra and ab initio calculations of aluminium [93, 94].

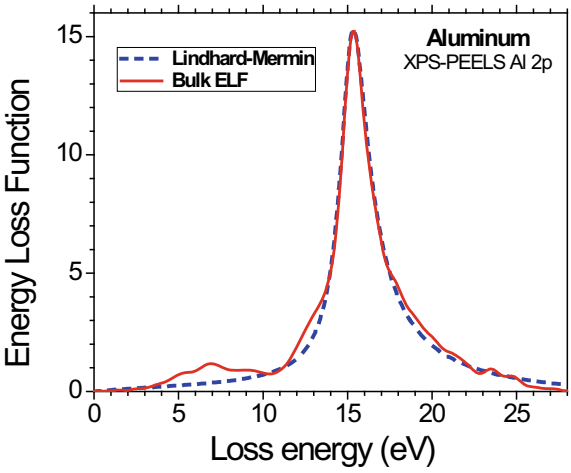

Fig. 10 Bulk loss functions for Al(002) obtained by FT analysis of PEELS data (*red bold line*) and the Lindhard–Mermin model with $\Gamma_{\mathrm{LM}} = 1.6$ eV, $\chi_{\mathrm{core}} = 0.003$ (*blue dashed line*). From Ref. [91] reprinted by permission from Springer, Brazilian Journal of Physics (2018)

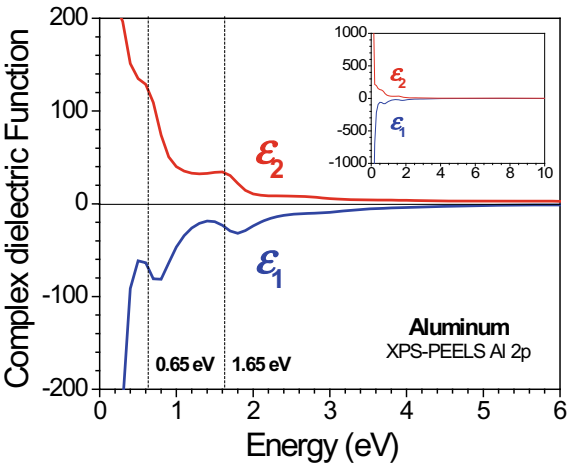

Fig. 11 Effective dielectric function $\varepsilon(\omega, q)$ of Al(002) at low energy, showing structures at 0.65 ± 0.1 eV and 1.65 ± 0.1 eV. From Ref. [91] reprinted by permission from Springer, Brazilian Journal of Physics (2018)

4.3 Comparison Between ZLP Subtraction and Fourier Transform

The FT method has been compared with the empirical method based on a smooth cutoff of the asymmetric zero-loss peak, using PEELS data obtained from Al oxide thin films prepared by ion beam assisted deposition (IBAD) (Fig. 12) [95]. The ZLP is composed of two O 1*s* peaks due to different chemical environments. In the smooth cutoff method, optically determined values were used in the sigmoid expression ($E_{\mathrm{GAP}} = 5.5$ eV) and the ELF strength normalization ($n_{\mathrm{OPT}} = 1.9$). The resulting ELF distributions (Fig. 13) have identical peak energies ($E_{\mathrm{P}} = 25.2$ eV vs. 24.8 eV) and loss distribution shape, in particular at small loss energies near the forbidden

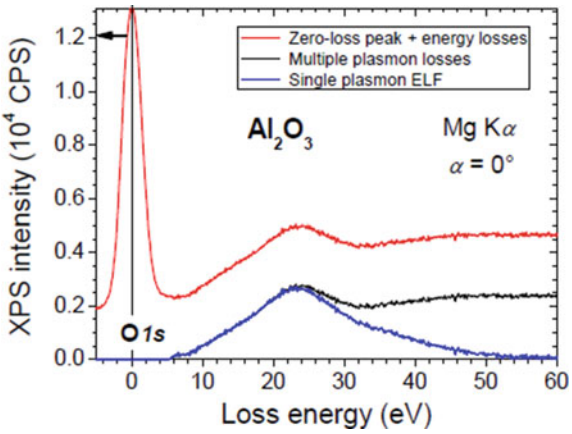

Fig. 12 XPS-PEELS analysis of Al oxide (O/Al = 1.87) grown by ion beam assisted deposition (São Paulo University) showing ZLP separation using *multiplication* by a smooth cutoff function (16) and retrieval of the bulk ELF (*blue curve*). XPS was measured with a monochromatic Al Kα (1486.6 eV) source (Escalab MK2, LAS – Chemistry Institute – UFBa); the broad O 1*s* peak results from different environments (possibly Al-O and Al-O-H with respective binding energies at 531.0 eV and 532.6 eV)

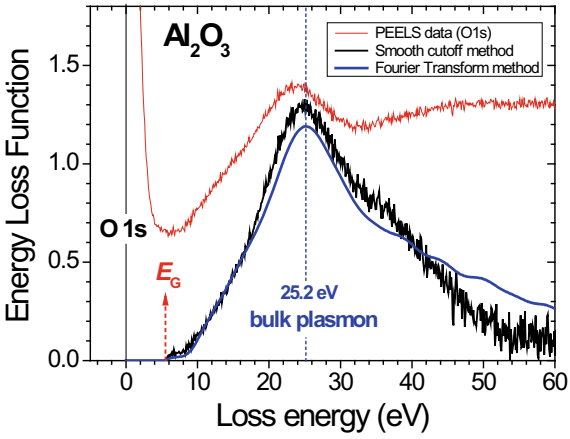

Fig. 13 Bulk plasmon ELF of Al oxide (O/Al = 1.87) retrieved from XPS-PEELS data analysis of the O 1*s* core level (*red*) using the smooth cutoff method (sigmoid (16) with $E_G = 5.5$ eV, $\Delta E_{SIG} = 0.5$ eV) (*black line*) and the Fourier transform method with Hanning filter (*blue line*)

band gap. Some discrepancy appears above 45 eV, possibly because the multiple losses incorporate intrinsic and extrinsic plasmon excitations in the FT method.

Interestingly, the ELF distribution of Al_2O_3 obtained previously by a VUV method ($q = 0$, optical limit) [19] is significantly narrower than XPS-PEELS results, while valence EELS spectrum has intermediate width [96]. Note that in VEELS, the q-range for ELF integration depends on the angular deflection and the analyzer resolution, e.g. with 100 keV primary electron beam, a spectrometer collection angle of 9 mrad corresponds to an integration over scattering vectors out to $q = 2.4$ nm^{-1} [96]. Since

previous high-resolution EELS experiments were typically performed using q_{VEELS} = 2.0 nm^{-1}, the dispersive behaviour of plasmon excitation is probably not fully captured in VEELS experiments ($q_{VEELS} \ll q_C$). Overall, these results validate the concept of q-induced ELF broadening [50].

5 Future Developments of XPS-PEELS

State-of-the-art analysis of XPS-PEELS data would benefit from a better theoretical description of the ZLP line shape. In the screening process, the positive photo hole produces excitations in the Fermi sea of conduction electrons, hence possible excitation energies range between zero (directly at E_F) and the bandwidth of the metal under investigation [3]. The Mahan–Wertein–Citrin model [90] requires a DFT calculation of the joint density of states in the conduction band. Although this approach has been well explored in crystalline materials, particularly in metals, similar developments would be interesting for amorphous semi-metals, such as amorphous carbon or carbon soots [97].

Interband transitions may also affect the loss distribution in the low energy loss region [98]. They have been evidenced in XPS-PEELS characterizations of Al(002) at 1.65 and 0.65 eV, i.e. very close to the ZLP [91]. Some explicit incorporation of single-electron excitations in model ELF distributions would likely improve theoretical reconstructions of experimental spectra.

From the experimentalist point of view, synchrotron X-ray sources provide excellent signal-to-noise ratio and the possibility to investigate buried interfaces using hard X-ray photoelectron spectroscopy (HAXPES) with a larger inelastic mean free path of core-level photoelectrons [17, 98, 99]. However, classical laboratory X-ray sources remain valuable instruments for reactive surfaces when installed in an excellent UHV environment; such spectra obtained with low-energy resolution will benefit from the recently developed FT algorithm which provides smart elimination of source satellites and electron analyser broadening [91].

Model systems may be interesting to test current algorithms. Interestingly, implanted noble gas nanobubbles in a metal target, e.g. Ar in Al, allow separation of two effects: (i) the apparent binding energy depends on bubble diameter through variable screening of the Ar 2p core hole by conduction electrons of the metal, (ii) the relative intensity of extrinsic losses in the metal host matrix is related to the bubble depth and photoelectron emission angle. The role of internal surface versus external surface remains a subject for future investigations, e.g. to understand whether the absence of a signature of bubble surface plasmon (BSP) peaks is due to some q-induced broadening and/or to some coupling of the BSP modes related to the very high bubble density (typically 10^{20} cm^{-3}) [69].

Materials with anisotropic dielectric functions (HOPG, boron nitride, transition metal dichalcogenides, black phosphorus …) and their monolayer components (graphene, nanotubes) deserve more fundamental investigations to enhance their strong application potential [78, 100, 101, 102]. Finally, structures with

inhomogeneous composition or nanostructured geometry (nanoparticles, core–shell systems …) [36, 37] will require new developments to assess plasmon excitation by photoelectrons in such complex systems.

Coincidence electron spectroscopies (*e*, 2*e*) offer new avenues to investigate elementary mechanisms of plasmon decay. Using low-energy electron impact on Al(200) surfaces, secondary electron emission was measured in time coincidence with loss features in the spectrum of reflected electrons, demonstrating that plasmons excited by electron energy losses predominantly decay via creation of single-electron–hole pairs that act as a source for the secondary electrons [103]. This study is crucial for potential applications such as information transport and hot electron production issues, e.g. chemical reactivity, catalysis, photovoltaics.

Current research is devoted to the development of a quantum mechanical theory, required to obtain the respective contributions of *intrinsic* and *extrinsic* plasmon excitation (and their interference) and to assess the approximations performed in classical treatments. The quantum Landau formula originally derived by Hedin et al. [104] can explain overall plasmon loss features in core-level photoemission spectra, where elastic scatterings before and after the losses are completely neglected. Significant steps have been performed in this direction by the Chiba University group [32, 33, 105, 106]. Figure 14 summarizes recent theoretical results for depth-integrated first-order plasmon excitation spectra in Al: (i) both intrinsic and extrinsic excitations are important to describe plasmon losses, (ii) the extrinsic terms are much larger than the intrinsic ones, (iii) as a whole, intrinsic and interference terms contribute to some broadening of the purely extrinsic ELF, essentially towards higher loss energy values (in the case of Al). Future efforts should also consider a combined approach incorporating elastic and inelastic scattering to describe plasmon excitation in crystalline materials where inelastic photoelectron diffraction has been observed [107, 108, 109].

6 Conclusions

This review shows that photoelectron energy loss spectroscopy (XPS-PEELS) is a valuable non-destructive tool to elucidate material science issues, with threefold interest: (i) improved accuracy in the determination of the zero-loss peak (ZLP) intensities for compositional analysis; (ii) insight in the depth distribution of inhomogeneous atom concentrations; (iii) determination of the energy loss function and dielectric function of a solid surface. Some useful guidelines have been proposed for an empirical analysis of wide band gap materials. However, the Fourier transform method is necessary to extend XPS-PEELS analysis to metals and low band gap semiconductors with present some substantial spectral overlap of the ZLP with surface/bulk plasmon excitations. In this FT analysis, no hypothesis is made either on the dielectric function shape or on the dispersion coefficient; no arbitrary adjustment of the baseline is necessary, i.e. the loss signal is entirely assigned to plasmon excitations and interband transitions, although the latter is usually negligible. The FT

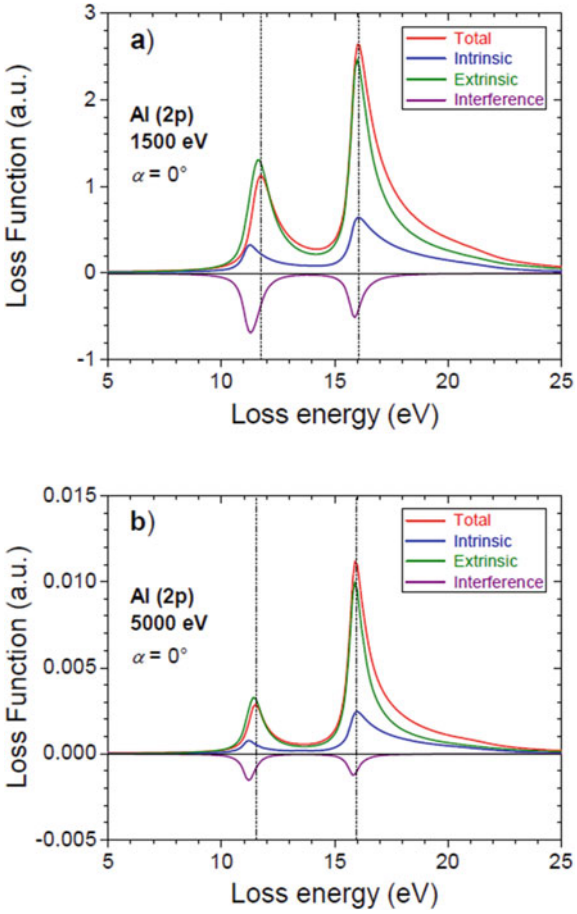

Fig. 14 Quantum calculation of depth-integrated surface (12 eV) and bulk (16 eV) losses due to plasmon excitation in Al, for electron kinetic energies of 1500 eV (**a**) and 5000 eV (**b**). Intrinsic (*blue curve*) and extrinsic (*green curve*) plasmon excitations were calculated separately, along with their (negative) interference (*purple curve*), at normal emission angle. Energy is measured relative to the Al 2*p* elastic peak. The relative surface loss peak intensity decreases with increasing photoelectron kinetic energy. As compared with the purely extrinsic distribution (*green*), the total loss distribution (*red*) is slightly broadened towards large loss energy (reprinted with permission from Prof. K. Niki, Chiba University)

method provides the *q*-averaged ELF and DF distributions, under the strong hypothesis that intrinsic and extrinsic loss functions have identical energy distributions and do not interfere. Quantum theoretical developments are required to assess the classical hypothesis and to extend the XPS-PEELS capabilities to inelastic photoelectron diffraction.

Acknowledgments We are grateful to Prof. M.G. Carneiro Rocha and P. Bargiela (LAS – Chemistry Institute – UFBa) for XPS measurements on aluminum oxide. We also wish to thank A. Le Pottier and B. Lépine for technical help in surface preparation. We are indebted to Prof. T. Fujikawa, K. Niki and M. Kazama for their permission for using theoretical results on photoelectron energy loss distributions. This collaborative work was promoted by Prof. A. Ferreira da Silva (UFBa). One of us (C.G.) acknowledges the CNPq agency (Brazil) for a visiting researcher grant from the *Ciência Sem Fronteiras* programme. One of us (D.D.) is grateful to the CAPES agency (Brazil) for a senior researcher grant. One of us (V.S.) is grateful to the CAPES agency and Rennes Métropole (France) for Ph.D. grants.

References

1. D.J. Briggs, M.P. Seah (eds.), *Practical Surface Analysis, Auger and X-ray Photoelectron Spectroscopy*, vol. 1 (Wiley, Chichester, 1990)
2. P. Schattschneider, *Fundamentals of Inelastic Electron Scattering* (Springer-Verlag, Berlin, 2003)
3. S. Hüfner, *Photoelectron Spectroscopy: Principles and Applications*. Springer series in Solid-State Sciences, vol. 82 (Springer, Berlin, 1995)
4. C.S. Fadley, Basic concepts of X-ray photoelectron spectroscopy in *Electron Spectroscopy: Theory, Techniques, and Applications*, vol. II, ed. by C.R. Brundle, A.D. Baker (Academic Press, London, 1978)
5. S. Tougaard, P. Sigmund, Influence of elastic and inelastic scattering on energy spectra of electrons emitted from solids. Phys. Rev. B **25**, 4452 (1982). https://doi.org/10.1002/sia.740090210
6. S. Tougaard, Quantitative analysis of the inelastic background in surface electron spectroscopy. Surf. Interface Anal. **11**, 453–472 (1988). https://doi.org/10.1016/0368-2048(90)85022-2
7. W.S.M. Werner, Partial intensity analysis (PIA) for quantitative electron spectroscopy. Surf. Interface Anal. **23**, 737–752 (1995). https://doi.org/10.1002/sia.2103
8. S. Tougaard, Universality classes of inelastic electron scattering cross-sections. Surf. Interface Anal. **25**, 137–154 (1997). https://doi.org/10.1002/(SICI)1096-9918(199703)25:3%3c137:AID-SIA230%3e3.0.CO;2-L
9. N. Pauly, F. Yubero, S. Tougaard, Quantitative analysis of satellite structures in XPS spectra of gold and silver. Appl. Surf. Sci. **383**, 317–323 (2016). https://doi.org/10.1016/j.apsusc.2016.03.185
10. S. Tougaard, Surface nanostructure determination by X-ray photoemission spectroscopy peak shape analysis. J. Vac. Sci. Technol. A **14**, 1415–1423 (1996). https://doi.org/10.1116/1.579963
11. S. Hajati, S. Coultas, C. Blomfield, S. Tougaard, XPS imaging of depth profiles and amount of substance based on Tougaard's algorithm. Surf. Sci. **600**, 3015–3021 (2006). https://doi.org/10.1016/j.susc.2006.05.020
12. S. Tougaard, F. Yubero, Software package to calculate the effects of the core hole and surface excitations on XPS and AES. Surf. Interface Anal. **44**, 1114–1118 (2012). https://doi.org/10.1002/sia.4855
13. W. Smekal, W.S.M. Werner, C.J. Powell, Simulation of electron spectra for surface analysis (SESSA): a novel software tool for quantitative Auger-electron spectroscopy and X-ray photoelectron spectroscopy. Surf. Interface Anal. **37**, 1059–1067 (2005). https://doi.org/10.1002/sia.2097
14. M.P. Seah, W.A. Dench, Quantitative electron spectroscopy of surfaces: a standard database for electron inelastic mean free paths in solids. Surf. Interface Anal. **1**, 2–11 (1979). https://doi.org/10.1002/sia.740010103

15. S. Tanuma, C.J. Powell, D.R. Penn, Calculations of electron inelastic mean free paths. VIII. Data for 15 elemental solids over the 50–2000 eV range. Surf. Interface Anal. **36**, 1–14 (2004). https://doi.org/10.1002/sia.740210302
16. S.A. Flodstrom, R.Z. Bachrach, R.S. Bauer, J.C. McMenamin, S.B.M. Hagström, Investigation of plasmon sidebands by synchrotron radiation tuning of electron escape depth. J. Vac. Sci. Technol. **14**, 303–306 (1977). https://doi.org/10.1116/1.569147
17. P. Risterucci, O. Renault, E. Martinez, B. Detlefs, J. Zegenhagen, G. Grenet, S. Tougaard, Inelastic background analysis of HAXPES spectra: towards enhanced bulk sensitivity in photoemission. Surf. Interface Anal. **46**, 906–910 (2014). https://doi.org/10.1002/sia.5484
18. A. Schleife, C. Rödl, F. Fuchs, J. Furthmüller, F. Bechstedt, Optical and energy loss spectra of MgO, ZnO, and CdO from *ab initio* many-body calculations. Phys. Rev. B **80**, 035112 (2009). https://doi.org/10.1103/PhysRevB.80.035112
19. R.H. French, Origins and applications of london dispersion forces and Hamaker constants in ceramics. J. Am. Ceram. Soc. **83**, 2117–2146 (2000). https://doi.org/10.1111/j.1151-2916.2000.tb01527
20. C. Godet, D. David, Derivation of Hamaker dispersion energy of amorphous carbon surfaces in contact with liquids using photoelectron energy-loss spectra. Braz. J. Phys. **47**, 594–605 (2017). https://doi.org/10.1007/s13538-017-0521-0
21. I. Abril, R. Garcia-Molina, C.D. Denton, F.J. Pérez-Pérez, N.R. Arista, Dielectric description of wakes and stopping powers in solids. Phys. Rev. A **58**, 357–366 (1998). https://doi.org/10.1103/PhysRevA.58.357
22. I. Abril, C.D. Denton, P. de Vera, I. Kyriakou, D. Emfietzoglou, R. Molina-Garcia, Effect of Bethe surface description on the electronic excitations induced by energetic proton beams in liquid water and DNA. Nucl. Instrum. Meth. Phys. Res. B **268**, 1763–1767 (2010). https://doi.org/10.1016/j.nimb.2010.02.069
23. M.V. Fischetti, Effect of the electron-plasmon interaction on the electron mobility in silicon. Phys. Rev. B **44**, 5527–5534 (1991). https://doi.org/10.1103/physrevb.44.5527
24. M. Fischetti, Long range Coulomb interactions in small Si devices. Part II: effective electron mobility in thin oxide structures. J. Appl. Phys. **89**, 1232–1250 (2001)
25. K. Uchida, H. Adachi, D. Kikuchi, S. Ito, Z. Qiu, S. Maekawa, E. Saitoh, Plasmonic generation of spin currents. Nat. Comm. **6**, 5910 (2015). https://doi.org/10.1038/ncomms6910
26. R. Raether, *Excitation of Plasmons and Interband Transitions by Electrons*. Springer Tracts in Modern Physics, vol. 88 (Springer, Berlin, 1980)
27. J. Daniels, C.V. Festenberg, H. Raether, K. Zeppenfeld, Springer Tracts in Modern Physics, vol. 54 (Springer-Verlag, Berlin, 1970), p. 77
28. D. Pines, *Elementary Excitations in Solids* (Benjamin, New York, 1964)
29. R. Hobbiger, J.T. Drachta, D. Kreil, H.M. Böhm, Phenomenological plasmon broadening and relation to the dispersion. Solid State Commun. **252**, 54–58 (2017). https://doi.org/10.1016/j.ssc.2017.01.011
30. P. Steiner, H. Höchst, S. Hüfner, Analysis of the plasmon structure in XPS experiments of simple metals. Phys. Lett. A **61**, 410–412 (1977). https://doi.org/10.1016/0375-9601(77)90350-4
31. P. Steiner, H. Höchst, S. Hüfner, XPS investigation of simple metals I. Core level spectra. Z. Phys. B **30**, 129–143 (1978). https://doi.org/10.1007/BF01320978
32. T. Fujikawa, M. Kazama, H. Shinotsuka, Theoretical study of plasmon losses in core-level photoemission spectra. J. Surf. Sci. Nanotech. **6**, 263–268 (2008). https://doi.org/10.1380/ejssnt.2008.263
33. H. Shinotsuka, T. Uwatoko, T. Konishi, T. Fujikawa, Theoretical study of plasmon loss peaks in core-level photoemission spectra: energy and angular dependence. J. Surf. Anal. **14**, 332–335 (2008)
34. C.N. Berglund, W.E. Spicer, Photoemission studies of copper and silver: theory. Phys. Rev. A **136**, 1030–1044 (1964). https://doi.org/10.1103/PhysRev.136.A1030
35. W.S.M. Werner, Electron transport in solids for quantitative surface analysis. Surf. Interface Anal. **31**, 141–176 (2001). https://doi.org/10.1002/sia.973

36. M. Chudzicki, W.S.M. Werner, A.G. Shard, Y.C. Wang, D.G. Castner, C.J. Powell, Evaluating the internal structure of core–shell nanoparticles using X-ray photoelectron intensities and simulated spectra. J. Phys. Chem. C **119**, 17687–17696 (2015). https://doi.org/10.1021/acs.jpcc.5b04517
37. G. Maidecchi, C.V. Duc, R. Buzio, A. Gerbi, G. Gemme, M. Canepa, F. Bisio, Electronic structure of core–shell metal/oxide aluminum nanoparticles. J. Phys. Chem. C **119**, 26719–26725 (2015). https://doi.org/10.1021/acs.jpcc.5b07678
38. D. David, C. Godet, Derivation of dielectric function and inelastic mean free path from photoelectron energy-loss spectra of amorphous carbon surfaces. Appl. Surf. Sci. **387**, 1125–1139 (2016). https://doi.org/10.1016/j.apsusc.2016.06.044
39. L. Calliari, S. Fanchenko, Reflection electron energy loss spectroscopy: role of the Bethe-Born factor. Surf. Interface Anal. **44**, 1104–1109 (2012). https://doi.org/10.1002/sia.4827
40. W.J. Pardee, G.D. Mahan, D.E. Eastman, R.A. Pollak, L. Ley, F.R. McFeely, S.P. Kowalczyk, D.A. Shirley, Analysis of surface- and bulk-plasmon contributions to X-ray photoemission spectra. Phys. Rev. B **11**, 3614–3616 (1975). https://doi.org/10.1103/PhysRevB.11.3614
41. R. Pollak, L. Ley, F. McFeely, S. Kowalczyk, D. Shirley, Characteristic energy loss structure of solids from X-ray photoemission spectra. J. El. Spec. Relat. Phenom. **3**, 381–398 (1974). https://doi.org/10.1016/0368-2048(74)80022-8
42. T.J. Baird, C.S. Fadley, S.M. Goldberg, P.J. Feibelman, M. Sunjic, The angular dependence of plasmon loss features in XPS spectra from polycrystalline aluminum: clean surfaces and effects of oxygen adsorption. Surf. Sci. **72**, 495–512 (1978). https://doi.org/10.1016/0039-6028(78)90366-7
43. C. Biswas, A.K. Shukla, S. Banik, V.K. Ahire, S.R. Barman, Plasmons in core-level photoemission spectra of Al(111). Phys. Rev. B **67**, 165416 (2003). https://doi.org/10.1103/PhysRevB.67.165416
44. P.E. Batson, J. Silcox, Experimental energy-loss function, Im$[-1/\varepsilon(q, \omega)]$, for aluminum. Phys. Rev. B **27**, 5224–5240 (1983). https://doi.org/10.1103/PhysRevB.27.5224
45. D.J. Planes, R. Molina-Garcia, I. Abril, N.R. Arista, Wavenumber dependence of the energy loss function of graphite and aluminum. J. El. Spec. Relat. Phenom. **82**, 23–29 (1996). https://doi.org/10.1016/S0368-2048(96)03043-5
46. D.Y. Smith, E.J. Shiles, M. Inokuti, The optical properties of aluminum, in *Handbook of Optics*, ed. by E. Palik (Academic Press, New York, 1985), pp. 369–408
47. M. Borg, M. Birgersson, M. Smedh, A. Mikkelsen, D.L. Adams, R. Nyholm, C.O. Almbladh, J.N. Andersen, Experimental and theoretical surface core-level shifts of aluminum (100) and (111). Phys. Rev. B **69**, 235418 (2004). https://doi.org/10.1103/PhysRevB.69.235418
48. J. Lindhard, On the properties of a gas of charged particles. K. Dan. Vidensk. Selsk. Mat. Fys. Medd. **28**, 8 (1954)
49. N.D. Mermin, Lindhard dielectric function in the relaxation-time approximation. Phys. Rev. B **1**, 2362–2363 (1970). https://doi.org/10.1103/PhysRevB.1.2362
50. P.C. Gibbons, S.E. Schnatterly, J.J. Ritsko, J.R. Fields, Line shape of the plasma resonance in simple metals. Phys. Rev. B **13**, 2451–2460 (1976). https://doi.org/10.1103/physrevb.13.2451
51. M. Vos, A model dielectric function for low and very high momentum transfer. Nucl. Instrum. Meth. Phys. Res. B **366**, 6–12 (2016). https://doi.org/10.1016/j.nimb.2015.09.091
52. A. Gulans, S. Kontur, C. Meisenbichler, D. Nabok, P. Pavone, S. Rigamonti, S. Sagmeister, U. Werner, C. Draxl, Exciting—a full-potential all-electron package implementing density-functional theory and many-body perturbation theory. J. Phys. Condens. Mat. **26**, 363202 (2014). https://doi.org/10.1088/0953-8984/26/36/363202
53. Exciting website http://exciting-code.org/
54. L. Serra, F. Garcias, M. Barranco, N. Barberán, J. Navarro, Bulk-plasmon dispersion relations in metals. Phys. Rev. B **44**, 1492–1498 (1991). https://doi.org/10.1103/physrevb.44.1492
55. M. Cazzaniga, N. Manini, L.G. Molinari, G. Onida, Ab-initio self-energy corrections in systems with metallic screening. Phys. Rev. B **77**, 035117 (2008). https://doi.org/10.1103/PhysRevB.77.035117

56. R.G. Egdell, V.E. Henrich, R. Bowdler, T. Sekine, On the difference in valence electron plasmon energy and density of states between beta- and cubic Si_3N_4. J. Appl. Phys. **94**, 2611–2615 (2003). https://doi.org/10.1063/1.1619568
57. S. Kohiki, M. Arai, H. Yoshikawa, S. Fukushima, Energy Loss Structure of X-ray Photoelectron Spectra of MgO and α-Al_2O_3. J. Phys. Chem. B **103**, 5296–5299 (1999). https://doi.org/10.1021/jp9901996
58. C. Godet, T. Heitz, J.E. Bourée, B. Drévillon, C. Clerc, Growth and composition of dual-plasma polymer-like amorphous carbon films. J. Appl. Phys. **84**, 3919–3932 (1998). https://doi.org/10.1063/1.368570
59. A. Zebda, H. Sabbah, S. Ababou-Girard, F. Solal, C. Godet, Surface energy and hybridization studies of amorphous carbon surfaces. Appl. Surf. Sci. **254**, 4980–4991 (2008). https://doi.org/10.1016/j.apsusc.2008.01.147
60. D. David, M.A. Pinault-Thaury, D. Ballutaud, C. Godet, Sensitivity of photoelectron energy loss spectroscopy to surface reconstruction of microcrystalline diamond films. Appl. Surf. Sci. **273**, 607–612 (2013). https://doi.org/10.1016/j.apsusc.2013.02.087
61. A. Siokou, F. Ravani, S. Karakalos, O. Frank, M. Kalbac, C. Galiotis, Surface refinement and electronic properties of graphene layers grown on copper substrate: an XPS, UPS and EELS study. Appl. Surf. Sci. **257**, 9785–9790 (2011). https://doi.org/10.1016/j.apsusc.2011.06.017
62. R.R. Dagastine, L.R. White, P.M. Jones, Y.T. Hsia, Effect of media overcoat on van der Waals interaction at the head-disk interface. J. Appl. Phys. **97**, 126106 (2005). https://doi.org/10.1063/1.1941464
63. T.E. Karis, X.C. Guo, J.Y. Juang, Dynamics in the bridged state of a magnetic recording slider. Tribol. Lett. **30**, 123 (2008). https://doi.org/10.1007/s11249-008-9319-0
64. E.M. Lifshitz, The theory of molecular attractive forces between solids. Sov. Phys. JETP **2**, 73 (1956)
65. I.E. Dyaloshinski, E.M. Lifshitz, L.P. Pitaevski, General theory of van der Waals' forces. Adv. Phys. **10**, 165 (1961). https://doi.org/10.1080/00018736100101281
66. R.S. Dhaka, C. Biswas, A.K. Shukla, S.R. Barman, A. Chakrabarti, Xe and Ar nanobubbles in Al studied by photoemission spectroscopy. Phys. Rev. B **77**, 104119 (2008). https://doi.org/10.1103/physrevb.77.104119
67. C. Godet, V.M.S. Santana, D. David, Depth distribution of noble gas atoms implanted in Al matrix: a photoelectron energy loss spectroscopy study. Thin Solid Films **659**, 70–80 (2018). https://doi.org/10.1016/j.tsf.2018.05.038
68. R.S. Dhaka, S.R. Barman, X-ray photoemission studies on rare gas bubbles in aluminium with annealing temperature. Surf. Coat. Technol. **203**, 2380–2382 (2009). https://doi.org/10.1016/j.surfcoat.2009.02.079
69. R.S. Dhaka, S.R. Barman, Plasmon excitations by photoelectron emission from rare gas nanobubbles in aluminum. Phys. Rev. Lett. **104**, 036803 (2010). https://doi.org/10.1103/physrevlett.104.036803
70. J.M. Howe, V.P. Oleshko, Application of valence electron energy-loss spectroscopy and plasmon energy mapping for determining material properties at the nanoscale. J. Electron Microsc. **53**, 339–351 (2004). https://doi.org/10.1093/jmicro/dfh044
71. S. Neuville, A. Matthews, A perspective on the optimisation of hard carbon and related coatings for engineering applications. Thin Solid Films **515**, 6619–6653 (2007). https://doi.org/10.1016/j.tsf.2007.02.011
72. D.F. Shriver, P.W. Atkins, C.H. Langford, *Inorganic Chemistry* (Oxford University Press, Oxford, 1989), p. 337
73. S. Miyazaki, Characterization of high-*k* gate dielectric/silicon interfaces. Appl. Surf. Sci. **190**, 66–74 (2002). https://doi.org/10.1016/s0169-4332(01)00841-8
74. R. Suri, C.J. Kirkpatrick, D.J. Lichtenwalner, V. Misra, Energy band diagram of Al_2O_3/4H-SiC and HfAlO/4H-SiC constructed using valence band offset and bandgap values as determined by XPS. Appl. Phys. Lett. **96**, 042903 (2010). https://doi.org/10.1063/1.3291620
75. S. Dias, S.B. Krupanidhi, Determination of band offsets at the Al:ZnO/Cu_2SnS_3 interface using X-ray photoelectron spectroscopy. AIP Adv. **5**, 047137 (2015). https://doi.org/10.1063/1.4919111

76. D. Tahir, S. Tougaard, Electronic and optical properties of Cu, CuO and Cu2O studied by electron spectroscopy. J. Phys. Cond. Mat. **24**, 175002 (2012). https://doi.org/10.1088/0953-8984/24/17/175002
77. D. David, C. Godet, H. Sabbah, S. Ababou-Girard, F. Solal, V. Chu, J.P. Conde, Derivation of the near-surface dielectric function of amorphous silicon from photoelectron loss spectra. J. Non-Cryst. Solids **358**, 2019 (2012). https://doi.org/10.1016/j.jnoncrysol.2012.01.026
78. A.G. Marinopoulos, L. Reining, A. Rubio, V. Olevano, *Ab initio* study of the optical absorption and wave-vector-dependent dielectric response of graphite. Phys. Rev. B **69**, 245419 (2004). https://doi.org/10.1103/physrevb.69.245419
79. A.C. Ferrari, A. Libassi, B.K. Tanner, V. Stolojan, J. Yuan, L.M. Brown, S.E. Rodil, B. Kleinsorge, J. Robertson, Density, sp^3 fraction, and cross-sectional structure of amorphous carbon films determined by X-ray reflectivity and electron energy loss spectroscopy. Phys. Rev. B **62**, 11089–11103 (2000). https://doi.org/10.1103/physrevb.62.11089
80. S. Tougaard, Energy loss in XPS: fundamental processes and applications for quantification, non-destructive depth profiling and 3D imaging. J. El. Spec. Relat. Phenom. **178–179**, 128–153 (2010). https://doi.org/10.1016/j.elspec.2009.08.005
81. M.P. Seah, Background subtraction III. The application of REELS data to background removal in AES and XPS. Surf. Sci. **471**, 185–202 (2001). https://doi.org/10.1016/s0039-6028(00)00906-7
82. S. Tougaard, I. Chorkendorff, Differential inelastic electron scattering cross sections from experimental reflection electron-energy-loss spectra: application to background removal in electron spectroscopy. Phys. Rev. B **35**, 6570 (1987). https://doi.org/10.1103/physrevb.35.6570
83. S. Tougaard, Algorithm for analysis of low-energy-resolution REELS; determination of inelastic electron scattering cross-sections and applications in quantitative XPS. Surf. Sci. **464**, 233–239 (2000). https://doi.org/10.1016/s0039-6028(00)00684-1
84. M. Vos, P.L. Grande, Extracting the dielectric function from high-energy REELS measurements. Surf. Interface Anal. **49**, 809–821 (2017). https://doi.org/10.1002/sia.6227
85. A.C. Simonsen, F. Yubero, S. Tougaard, Quantitative model of electron energy loss in XPS. Phys. Rev. B **56**, 1612–1619 (1997). https://doi.org/10.1103/PhysRevB.56.1612
86. F. Yubero, S. Tougaard, Quantification of plasmon excitations in core-level photoemission. Phys. Rev. B **71**, 045414 (2005). https://doi.org/10.1103/PhysRevB.71.045414
87. S. Doniach, M. Sunjic, Collective excitations in X-ray spectra of metals. J. Phys. C **3**, 285 (1970). https://doi.org/10.1088/0022-3719/3/2/010
88. G.D. Mahan, Collective excitations in X-ray spectra of metals. Phys. Rev. B **11**, 4814 (1975). https://doi.org/10.1103/PhysRevB.11.4814
89. P. Nozières, C.T. de Dominicis, Singularities in the X-ray absorption and emission of metals. III. One-body theory exact solution. Phys. Rev. **178**, 1097 (1969). https://doi.org/10.1103/physrev.178.1097
90. G.K. Wertheim, P.H. Citrin, Fermi surface excitations in X-ray photoemission line shapes from metals. In *Photoemission in Solids I*. Topics in Applied Physics, vol. 26 ed. by M. Cardona, L. Ley (Springer, Berlin, Heidelberg), pp. 197–236. https://doi.org/10.1007/3540086854_5
91. V.M. Santana, D. David, J.S. Almeida, C. Godet, Photoelectron energy loss in Al(002) revisited: retrieval of the single plasmon loss energy distribution by a fourier transform method. Braz. J. Phys. **48**, 215–226 (2018). https://doi.org/10.1007/s13538-018-0566-8
92. C. Klauber, Magnesium Kα X-ray line structure revisited. Appl. Surf. Sci. **70–71**, 35–39 (1993). https://doi.org/10.1016/0169-4332(93)90393-p
93. D.Y. Smith, B. Segall, Intraband and interband processes in the infrared spectrum of metallic aluminum. Phys. Rev. B **34**, 5191–5198 (1986). https://doi.org/10.1103/physrevb.34.5191
94. K.H. Lee, K.J. Chang, First-principles study of the optical properties and the dielectric response of Al. Phys. Rev. B **49**, 2362–2367 (1994). https://doi.org/10.1103/physrevb.49.2362

95. T. Borrely dos Santos, Controle de propriedades de filmes finos através da assistência de feixe iônico. Master thesis, Universidade de São Paulo, USP, Brazil (2017)
96. H. Müllejans, R.H. French, Interband electronic structure of a near-Σ11 grain boundary in α-alumina determined by spatially resolved valence electron energy-loss spectroscopy. J. Phys. D Appl. Phys. **29**, 1751–1760 (1996). https://doi.org/10.1088/0022-3727/29/7/010
97. T.T.P. Cheung, X-ray photoemission of polynuclear aromatic carbon. J. Appl. Phys. **55**, 1388–1393 (1984). https://doi.org/10.1063/1.333229
98. D. David, C. Godet, F. Johansson, A. Lindblad, Quantitative analysis of plasmon excitations in hard x-ray photoelectron spectra of bulk black phosphorus. Appl. Surf. Sci. **505**, 144385 (2020). https://doi.org/10.1016/j.apsusc.2019.144385
99. F. Offi, W.S.M. Werner, M. Sacchi, P. Torelli, M. Cautero, G. Cautero, A. Fondacaro, S. Huotari, G. Monaco, G. Paolicelli, W. Smekal, G. Stefani, G. Panaccione, Comparison of hard and soft X-ray photoelectron spectra of silicon. Phys. Rev. B **76**, 085422 (2007). https://doi.org/10.1103/physrevb.76.085422
100. L. Calliari, S. Fanchenko, M. Filippi, Effective medium theory for REELS analysis of amorphous carbon films. Surf. Interface Anal. **42**, 1066–1071 (2010). https://doi.org/10.1002/sia.3232
101. R.R. Dagastine, D.C. Prieve, L.R. White, Calculations of van der Waals forces in 2-dimensionally anisotropic materials and its application to carbon black. J. Colloid Interface Sci. **249**, 78–83 (2002). https://doi.org/10.1006/jcis.2002.8239
102. A.G. Marinopoulos, L. Reining, V. Olevano, A. Rubio, T. Pichler, X. Liu, M. Knupfer, J. Fink, Anisotropy and interplane interactions in the dielectric response of graphite. Phys. Rev. Lett. **89**, 076402 (2002). https://doi.org/10.1103/physrevlett.89.076402
103. W.S.M. Werner, A. Ruocco, F. Offi, S. Iacobucci, W. Smekal, H. Winter, G. Stefani, Role of surface and bulk plasmon decay in secondary electron emission. Phys. Rev. B **78**, 233403 (2008). https://doi.org/10.1103/physrevb.78.233403
104. L. Hedin, J. Michiels, J. Inglesfield, Transition from the adiabatic to the sudden limit in core-electron photoemission. Phys. Rev. B **58**, 15565–15582 (1998). https://doi.org/10.1103/physrevb.58.15565
105. K. Niki, N. Yamamura, Y. Ohori, M. Kazama, T. Fujikawa, L. Kövér, Theoretical study of plasmon losses from Li 1*s* level in core-level photoemission spectra. Surf. Interface Anal. **46**, 924–926 (2014). https://doi.org/10.1002/sia.5504
106. M. Kazama, H. Shinotsuka, Y. Ohori, K. Niki, T. Fujikawa, L. Kövér, Plasmon losses in core-level photoemission spectra studied by the quantum Landau formula including full multiple scattering. Phys. Rev. B **89**, 045110 (2014). https://doi.org/10.1103/physrevb.89.045110
107. J. Osterwalder, T. Greber, S. Hüfner, L. Schlapbach, Photoelectron diffraction from core levels and plasmon-loss peaks of aluminum. Phys. Rev. B **41**, 12495–12501 (1990). https://doi.org/10.1103/physrevb.41.12495
108. G.S. Herman, C.S. Fadley, Inelastic photoelectron diffraction. Phys. Rev. B **43**, 6792–6795 (1991). https://doi.org/10.1103/physrevb.43.6792
109. T. Greber, J. Osterwalder, S. Hüfner, L. Schlapbach, Enhanced plasmon-loss emission along Al[011] chains upon heating. Phys. Rev. B **44**, 8958–8961 (1991). https://doi.org/10.1103/physrevb.44.8958

MoS_2- and MoO_3-Based Ultrathin Layered Materials for Optoelectronic Applications

Hongfei Liu

Abstract The success in exfoliation and later chemical vapour deposition (CVD) of graphene, i.e. single-layer nanosheets of carbon atoms crystallized in hexagonal structure, triggered extensive investigations in non-graphene two-dimensional (2D) materials, driven by their dimension-reduction-induced physically unique and technologically useful properties. This chapter discusses the synthesis of semiconducting MoS_2- and MoO_3-based 2D materials, addressing their fabrication issues in recent bottom-up deposition techniques and/or post-deposition exfoliation processes. Typical applications of the 2D MoS_2–MoO_3 nanosheets composite thin films in optoelectronic devices are also presented and discussed. Through these discussions, we attempt to provide the readers a perspective on recent developments of MoS_2- and MoO_3-based 2D materials as well as their future opportunities towards practical applications in optoelectronic devices.

Keywords 2D materials · MoS_2 · MoO_3 · WS_2/MoS_2 heterostructure · MoS_2–MoO_3 nanosheets composite · CVD · Reactive magnetron sputtering · Exfoliation

1 Introduction

Theoretical studies about the possibility of weather crystals can be nucleated and grown in the form of single atomic layered films can be traced back to over 100 years ago [1] Experimentally realization of ultrathin films consisting of a few layers of atoms was unsuccessful until the beginning of this century when graphene was exfoliated from graphite by using scotch tapes [2]. It is a nice excitation that this breakthrough in 2004, after the long-term explorations towards single-crystal two-dimensional (2D) materials, won the 2010 Nobel Prize in Physics. This research excitation in 2D materials is, more or less, strengthened when one thinks of the fact that the realization of GaN-based light-emitting diodes (LEDs) in 1993 took

H. Liu (✉)
Institute of Materials Research and Engineering (IMRE), A*STAR (Agency for Science, Technology and Research), 2 Fusionopolis Way, Singapore 138634, Singapore
e-mail: liuhf@imre.a-star.edu.sg

S. Kumar and D. K. Aswal (eds.), *Recent Advances in Thin Films*, Materials Horizons: From Nature to Nanomaterials, https://doi.org/10.1007/978-981-15-6116-0_8

21 years to win the 2014 Nobel Prize in Physics. As a consequence, tremendous research interest has been retriggered in 2D materials, covering those of metallic, semiconducting and insulating atomic layered nanosheets as well as their hybrid heterostructures [3–8]. Typical examples, among many others [9], are graphene [2, 5], Xene (X = Si, Ge, or Sn) [10], black-phosphorus/arsenic (BP/BA) [11–14], transition metal dichalcogenides (TMDCs) [15–22], α-phase molybdenum trioxide (α-MoO_3) [23–29], gallium sulphide (GaS) [30–32], boron nitride (BN) [33, 34], etc. [9].

It is necessary to mention that 2D materials here are different in concept from those of traditional ultrathin crystal structures, e.g. III–V semiconductor quantum heterostructures [35, 36], although the latter ones may have a thickness in the range of a few atomic layers while the former ones can be heterostructurally stacked up to a thickness over tens of nanometers [37, 38]. The distinction is recognized by the type of bonding that tightens the adjacent atomic layers along the thickness direction of the film. In this view, 2D materials distinguish themselves by the interlayer van der waals (VDW) bonds [9, 39]. Thermodynamically when the thickness of a VDW crystal is reduced approaching a few atomic layers via breaking the interlayer VDW bonds, still can the crystal stably sustain in the form of nanosheets [1, 9]. In contrast, when the thickness is reduced in those traditional ultrathin quantum structures approaching a few atomic layers the interactions between the interlayer and intralayer chemical bonds tend to reconstruct the crystals, e.g. via surface reconstruction [40], making their free-standing 2D nanosheets unavailable.

It is well known that when the thickness of a VDW crystal is reduced approaching a few atomic layers, its electronic structure deviates away from that of the bulk due to quantum confinement effect. A typical example is the indirect-to-direct band gap change of MoS_2 when its layer thickness is reduced from multiple layers to single layer [41]. As the thickness of MoS_2 is reduced approaching a few atomic layers, its conduction and valence bands increase in their energy levels. However, the energy increments as a function of the thickness reductions are not uniform in the reciprocal space that eventually give rise to the band gap transition from indirect to direct [41]. This situation is similar for BP/BA but different for 2D α-MoO_3 [12–14]. The thickness-reduction-induced increments in the electronic band energies of α-MoO_3 are quite uniform, not only in the reciprocal space but also for the conduction and valence bands, leading to the absence of changes in the direct ($E_d = 3.3$ eV) and indirect ($E_{in} = 2.2$ eV) band gap energies as well as the intact optical conductivity in the photon energy range of $E_{ph} < 3.8$ eV [24].

Although the breakthrough in producing high-quality graphene nanosheets was realized by mechanical exfoliations employing the scotch tape method [2], this top-down method has the disadvantage of being unreliable in controlling the yield of large area and single-layer nanosheets. In this light, various exfoliations, other than the scotch tape method, have been explored and developed for producing graphene and non-graphene 2D nanosheets from their bulk crystals. These exfoliation techniques include electrochemical intercalation, mechanical shear, ultrasonication, etc. [30, 42–44]. The general principle is to break the interlayer VDW interactions in a liquid media by applying external stress. To this end, the single-step exfoliations

can be hybridized to improve the efficiency [26, 45]. These liquid or wet-chemical processes are fundamentally feasible scaled up for mass production of 2D materials [42]. However, so-produced 2D nanosheets suffer from contaminations and less control in crystal quality, which hindered their integrations with conventional thin-film technologies in semiconductor industry [46, 47].

To develop more controllable methods for producing 2D materials from their parent bulks, top-down thinning processes of VDM crystals have been widely studied, including chemical etching in both solution and gaseous phases [48–50], plasma etching [51, 52], lasing thinning [53–55], etc. [56–58]. From the application point of view, the top-down thinning process is generally a downstream fabrication step that follows the deposition of 'thick' parent VDW layers on a desired substrate. This downstream material thinning step can be omitted one day when the deposition method is improved enough to produce the desired 2D materials with reliable controls of the layer thickness and crystal quality. Nevertheless, from the point of view of materials science and engineering, the exploration and development of such top-down thinning processes will not stop since they can provide great helps towards understanding the fundamental and comprehensiveness of 2D materials with respect to their structures and properties [48–53, 56, 57].

To develop a suitable bottom-up growth method for 2D materials that can be compatible with conventional thin-film technologies, the 2D community has been trying most, if not all, of the common available material synthesis methods. These methods, except those following the wet-chemical route (e.g. hydrothermal synthesis), can be basically catalogued into three groups in terms of their growth mechanisms. The first group is dominated by physical depositions that include sputtering [22, 59–61], pulsed laser deposition (PLD) [62–65] and molecular beam epitaxy (MBE) [66–68]; the second group is dominated by chemical depositions that include chemical vapour deposition (CVD) [16, 17, 20, 69, 70], atomic layer deposition (ALD) [71–74] and metalorganic chemical vapour deposition (MOCVD) [75–78] and the third group includes those of multiple-stepped growth that consists of materials deposition and conversion, e.g. thermal vapour sulfurization (TVS) of 2D TMDCs [19, 73, 79–83]. This group does not have a clear-cut boundary from the former two because the source materials can be deposited by either physical or chemical methods. This is why the multiple-stepped growth methods are flexibly named in the literature [17, 20, 84], sometimes after the source material deposition method, sometimes after the material conversion method.

Along with the great developments in 2D materials over the last decade, their applications have seen increasing opportunities in electronic and optoelectronic devices [85–91]. These device applications of 2D materials are strongly depending on their individual characteristics. The metallic character of graphene nanosheets makes them a nature candidate for fabricating transparent conductive coatings, replacing ITO, in display, photovoltaic, LED, etc., applications [90–92]. Graphene, with its huge response to external electric fields, can be an active layer for flexible field-effect transistors [93–95]. The subnanometer thickness and the tunable Fermi level of graphene can be engineered, in conjunction with high-k dielectrics, for plasmonic and metamaterial applications, e.g. in the frequency range of THz [87, 90,

96–98]. Atomic nanosheets of TMDCs, α-MoO_3, black-phosphorus/arsenic, together with their heterostructures, are typical semiconductor 2D materials that have been extensively studied for applications in electric-field transistors, sensor and photovoltaic devices, LEDs, as well as photocatalyst for energy harvesting applications [55, 85, 86, 89, 99–101].

Since 2D materials have been extensively investigated over the last decade and a lot of excellent reviews have been written on the fundamentals, material processes/syntheses and device designs/fabrications of various 2D materials and heterostructures, we would like to distinguish this chapter by recent developments of MoS_2- and α-MoO_3-based 2D materials as well as their hybrid structures. The dominant focus is placed on the most recent issues encountered with the development of such semiconductor 2D materials and heterostructures towards their electronic and optoelectronic applications.

2 Synthesis and Characterization of MoS_2-Based 2D Materials

2.1 Unique 2D TMDCs and General Bottom-Up Growth Methods

Semiconductor single-layer MoS_2 is one of the most important 2D materials that overcomes the zero-band gap shortcoming of graphene and greatly widens its application in electronic and optoelectronic devices. In crystallography, a single-layer MoS_2 crystal consists of three 60°-rotation-symmetric sublayers, one of Mo atoms sandwiched by the other two of S atoms, crystallized via covalent bonding. The three sublayers organized, without forming surficial dangling bonds, either in a trigonal prismatic (2H) structure or an octahedral (1T) structure with the sublayers of S atoms rotated 180° or 0° with respect to each other. The electronic structure of the 2H-phase exhibits the semiconductor character while that of 1T-phase exhibits metallic character. The metal-to-semiconductor phase transition of 2D MoS_2 tends to occur at elevated temperatures [102]. The electronic band gap energy (both the direct and the indirect ones) of semiconductor 2D MoS_2 exhibits a strong correlation with the thickness in the range of a few atomic layers [41].

To bottom-up grow 2D TMDC nanosheets on desired substrate, thermal vapour sulfurization (TVS) is probably one of the earliest methods that were employed [16, 17, 103]. This method has long been developed for converting thin films deposited on thermal stable substrates into sulphides [29, 80, 104–107], or improving the crystal qualities of pre-deposited sulphide thin films [108–110], by chemical reactions in sulphur species contained (e.g. S, H_2S, etc.) vapour environment at elevated temperatures. The thermal vapour deposition (TVD) method, using MoO_3 powder as the Mo-specie sources, was employed around the same time as that of TVS [20], and later on MOCVD growth emerged [75, 76], for producing TMDCs nanosheets. It has

been mentioned above that both the TVS and TVD methods are, sometimes, named CVD in the literature. Here, we discuss these methods separately and highlight their current issues in obtaining large area, single layer and single-crystal 2D TMDCs.

2.2 Growth of 2D TMDCs by TVS

The typical TVS method consists of source materials' deposition and post-deposition heat treatment under sulphur species environment at elevated temperatures. This method is feasible to control the alloying and/or doping of the final products in the film deposition stage. For producing 2D TMDCs, the source material, usually sub-10 nm thick, can be Mo and/or W metal, Mo-and/or W-oxide, Mo- and/or W-sulphide, etc., while the deposition should be controllable for desired film thickness. We have compared the TVS process of Mo and MoO_x thin films, which were deposited by magnetron sputtering on c-plane sapphire substrates, under sulphur vapour environment. During the sputtering deposition, the substrate was kept at room temperature to improve the thickness uniformity of the Mo film.

Typical backscattering Raman spectra and atomic-force microscopy (AFM) images taken from the 2D MoS_2 samples produced by TVS of Mo ultrathin films are presented in Fig. 1. One sees that the TVS temperature window, in which the Mo thin films can be converted to crystalline MoS_2, is quite broad, i.e. covering, at least, the range of 650–950 °C. The crystallinity, the lateral grain size and the surface coverage of the resultant MoS_2 nanosheets are strongly dependent on the TVS temperature and the initial thickness of the Mo films. In general, an increased TVS temperature tends to improve the surface mobility of the reaction species and thus the increase crystal quality as well as the increased lateral grain sizes; however, the surface coverage might be reduced, especially when the thickness of the initial Mo films is reduced, due to the increased evaporations at higher temperature. In contrast, the surface mobility of the reaction species could be reduced by increasing the initial thickness of the Mo films at certain TVS temperatures, leading to reduced lateral grain sizes of the resultant MoS_2 nanosheets.

By replacing the initial Mo films with $Mo_{1-x}W_x$ alloys, via, for example, co-sputtering, 2D $Mo_{1-x}W_xS_2$, instead of 2D MoS_2, can be obtained after TVS. Our experimental results with the W concentration increasing from 0 through 25%, 51 %, 87 % to 100 % (determined by X-ray photoelectron spectroscopy, XPS) reveal an absence of any phase separations between MoS_2 and WS_2 during the TVS at elevated temperatures (up to 950 °C). The Mo and W atoms were randomly alloyed in the 2D $Mo_{1-x}W_xS_2$ nanosheets, which were evidenced by the apparent band bowing (i.e. a redshift in the band gap energy) when the W concentration is increased from 0 to ~25 %. Figure 2 presents the band bowing phenomenon of the 2D $Mo_{1-x}W_xS_2$ nanosheets produced by TVS, which was spectroscopically manifested by the redshifts in the optical absorptions of the intrinsic excitons A (the one at lower energy of the two prominent absorption peaks). Also shown in Fig. 2 are the Raman spectra and a photograph of a 2-in. 2D $MoWS_2$-on-sapphire wafer, as well as

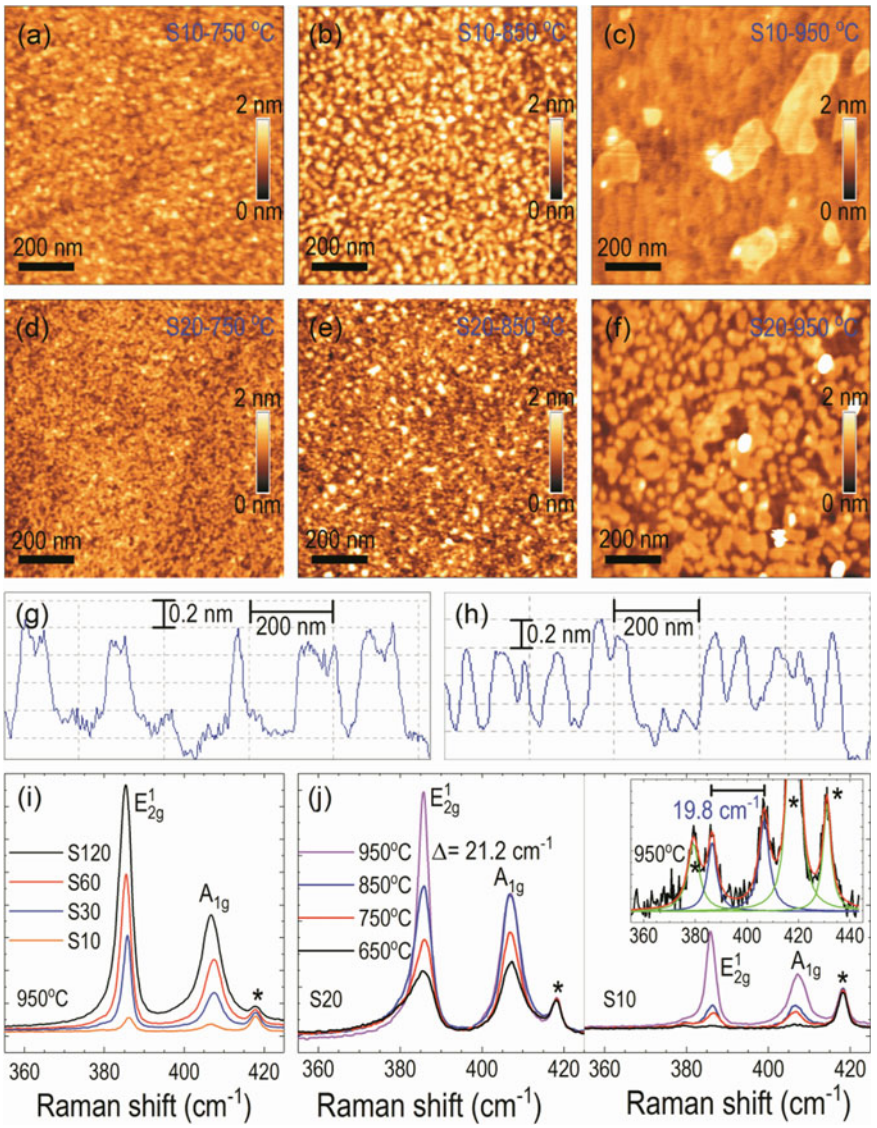

Fig. 1 AFM results and Raman spectra of 2D MoS_2 produced from Mo-on-Sapphire thin films, named after their sputtering deposition durations in second, by TVS (20 min) at varied temperatures: **a** S10 at 750 °C, **b** S10 at 850 °C, **c** S10 at 950 °C, **d** S20 at 750 °C, **e** S20 at 850 °C, **f** S20 at 950, **g** S10 at 950 °C, **h** S20 at 950 °C, **i** S120, S60, S30, S10 at 950 °C and **j** S20 and S10 at 650, 750, 850 and 950 °C. The inset highlights the fitting of the Raman features for S10 at 950 °C. The asterisks indicate the Raman features from the sapphire substrate. Figures partly reproduced from Ref. [19] with permission, Copyright 2014, IOP Publishing Ltd.

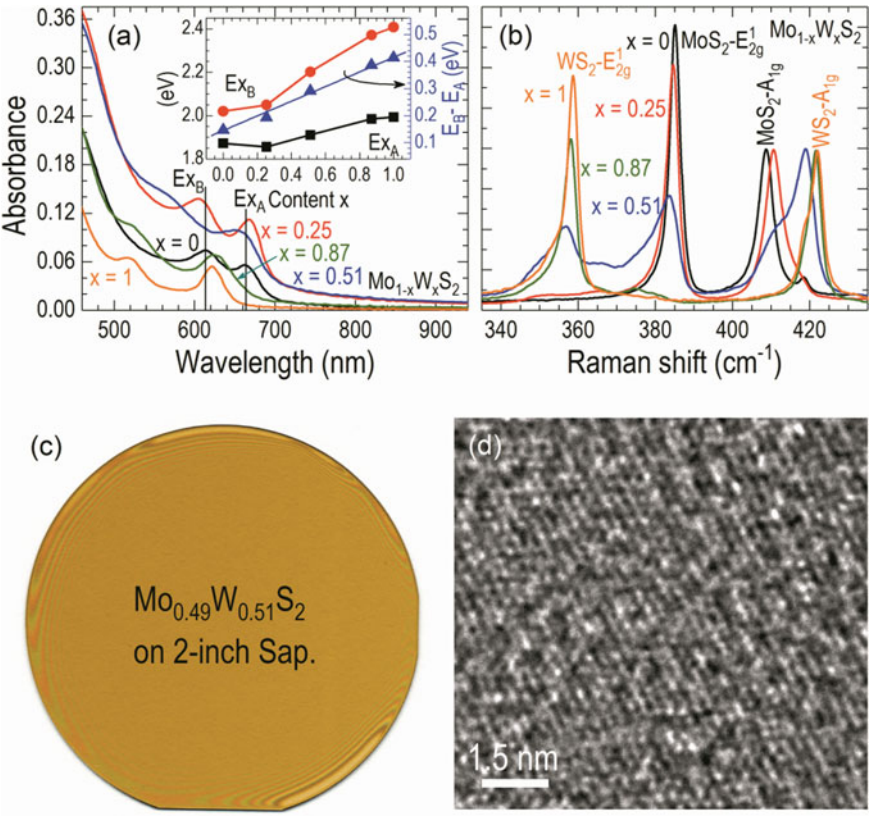

Fig. 2 Results of TVS growth of 2D $Mo_{1-x}W_xS_2$ on 2-in. diameter sapphire substrates at 950 °C for 20 min: **a** Absorbance spectra, **b** Raman spectra, **c** typical photograph of 2D $Mo_{1-x}W_xS_2$ with $x = 0.51$ and **d** Typical HRTEM image of so-grown 2D TMDCs. The inset shows the energy of the intrinsic excitons A and B, as well as their separations, as a function of W composition. Figures partly reproduced from Ref. [18] with permission, Copyright 2014, The Royal Society of Chemistry

a high-resolution transmission-electron microscopy (HRTEM) image, recorded from such TVS produced 2D $MoWS_2$ samples. They indicate the wafer-scale uniform and microscale ordered 2D crystallites. By the compositional engineering of MoS_2 and WS_2, via alloying Mo and W of the initial metallic source material, the direct band gap of the TVS produced 2D $Mo_{1-x}W_xS_2$ can be tailored in the range of 1.85–1.99 eV.

The substrate material may also have important effects on the TVS growth of 2D TMDCs when using the metallic films as the initial source species. Figure 3 shows our experimental results collected from the MoS_2 nanosheets produced by TVS of an ultrathin Mo film on a Si substrate. The photograph and the Raman spectrum provide evidence that the wafer-scale nanosheet is multilayer crystalline MoS_2. The microscale images recorded by AFM and scanning electron microscopy (SEM) show an orange-skin-like morphology of the MoS_2-on-Si, which is different from those

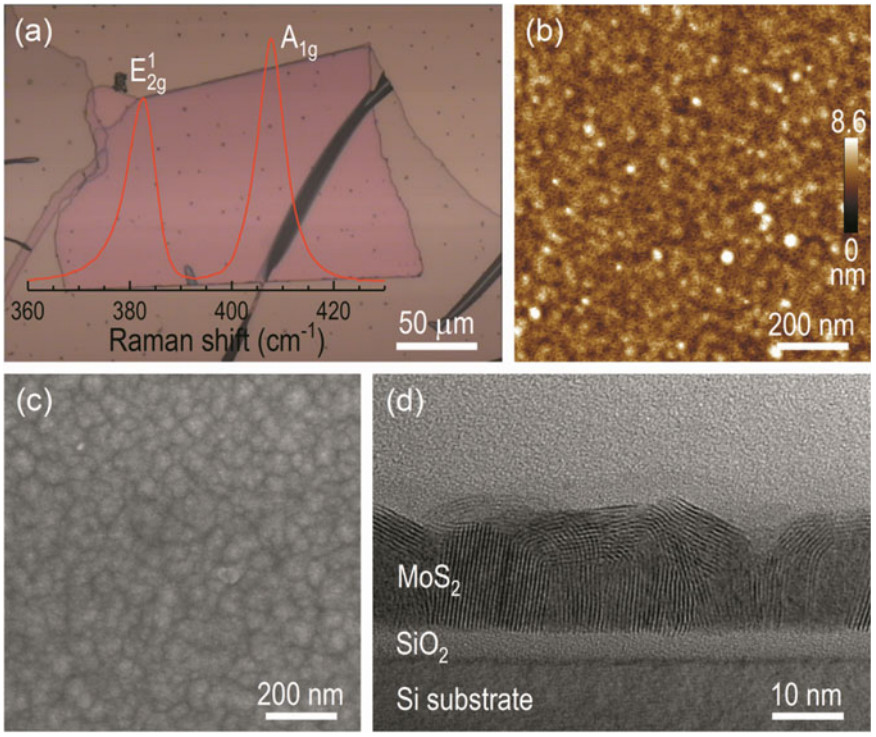

Fig. 3 Wafer-scale MoS_2 nanosheets produced by TVS (at 900 °C for 30 min) of Mo thin films deposited on Si substrates: **a** photograph and Raman spectrum, **b** AFM image from the surface free of folding, **c** SEM image from the surface free of folding and **d** cross-sectional HRTEM image showing the vertical MoS_2 nanosheets. Figures partly reproduced with permission from Ref. [103], Copyright 2015, WILEY-VCH

of MoS_2-on-sapphire produced by the same TVS process. The cross-sectional TEM images reveal that the distinct surface morphology of the 2D MoS_2-on-Si is associated with its distinct growth mechanism. During the TVS at elevated temperatures, the Mo atoms in the deeper layer beneath the surface tend to form clusters before being sulfurized by the inward diffusion of the sulphur species from the film surface, typically through the grain boundaries. The later on sulfurization of the Mo clusters gave rise to the bell-like structures with their mouths opening on the residual SiO_2 on the Si substrate. The bell walls, formed by multiple VDW layers, aligned nearly perpendicular to the film surface, while the bending of the VDW layers downwards to the film surface formed the observed orange-skin like morphology. Such vertical aligned 2D MoS_2 nanosheets could have important consequence in photoassisted catalyst applications due to the abundance of the dangling bonds at the crystal edges on the film surfaces [111–113]. These dangling bonds of 2D materials are potential reaction sites that can also be engineered for novel functions.

It has been mentioned above that to suppress the atomic clustering, so as to improve the surface smoothness, of the metallic films during sputtering, the substrate has to be kept at low temperatures, i.e. room temperature in our study. Unfortunately, one sees in Fig. 3 that still can the atomic clustering occur during the TVS process at elevated temperatures, especially when the thickness of the metallic film is increased to improve the surface coverage of the 2D nanosheets. In this light, MoO_3 thin films deposited by magnetron sputtering were studied for the TVS growth of 2D MoS_2 [19]. We found that the deposition temperature of the initial MoO_3 films by sputtering plays an important role in the crystal quality of the resultant 2D MoS_2 after the TVS process. Mixture of two-monolayer-thick triangular and hexagonal MoS_2 flakes with well-developed crystal edges have been obtained by TVS of the MoO_3 films deposited at room temperature. Unfortunately, the surface coverage of so-obtained 2D MoS_2 flakes is quite small. In comparison, a same TVS process for the MoO_3 films deposited at 700 °C can significantly increase the surface coverage while keeping the layer thickness of MoS_2 unchanged. In both cases, the individual MoS_2 flake sizes are about 100 nm, which has to be greatly improved for their applications in electronic and optoelectronic devices.

2.3 Growth of 2D TMDCs by TVD

The thermal vapour deposition (TVD) method is occasionally named thermal vapour transfer (TVT) in the literature that takes place in a tube-furnace reactor. Usually, two heating zones are necessary for a TVD reactor. One is to evaporate the source precursors and the other is to deposit the source species on desired substrates where they react, driven by heat, to form the desired films. The reaction species are carried by inert gas such as argon and/or nitrogen and transferred from the evaporation zone to the deposition zone. To minimize the chemical reactions between the source species before reaching the substrate, so as to control the quality of the crystal growth, the arrangement and distance between the source materials and the substrate in the tube reactor have to be dedicatedly designed and optimized [103]. The initial growth stage with this method, from the crystal growth point of view, is more likely a self-assembly nucleation process, which brings many issues towards large area and uniform 2D compound materials.

To optimize the TVD process for 2D MoS_2 using sulphur and MoO_3 powders as the source materials, we have developed a dispersive growth mode [21]. A schematic diagram of the growth setup, together with the typical photoluminescence (PL) and Raman spectrum collected from so-grown 2D MoS_2, is shown in Fig. 4. By encapsulating the substrate surface with a shadow mask, the reaction species can only be transferred onto the growing front below the mask through the gap between the mask and the substrate. The crystal nucleations on the substrate initiate near the edge of the mask facing the flow of the evaporated source species [see Fig. 4b]. The photograph in Fig. 4c shows an absent of crystal nucleations, and thus unavailable reactions species, at the areas away from the growth front below the mask. A combination

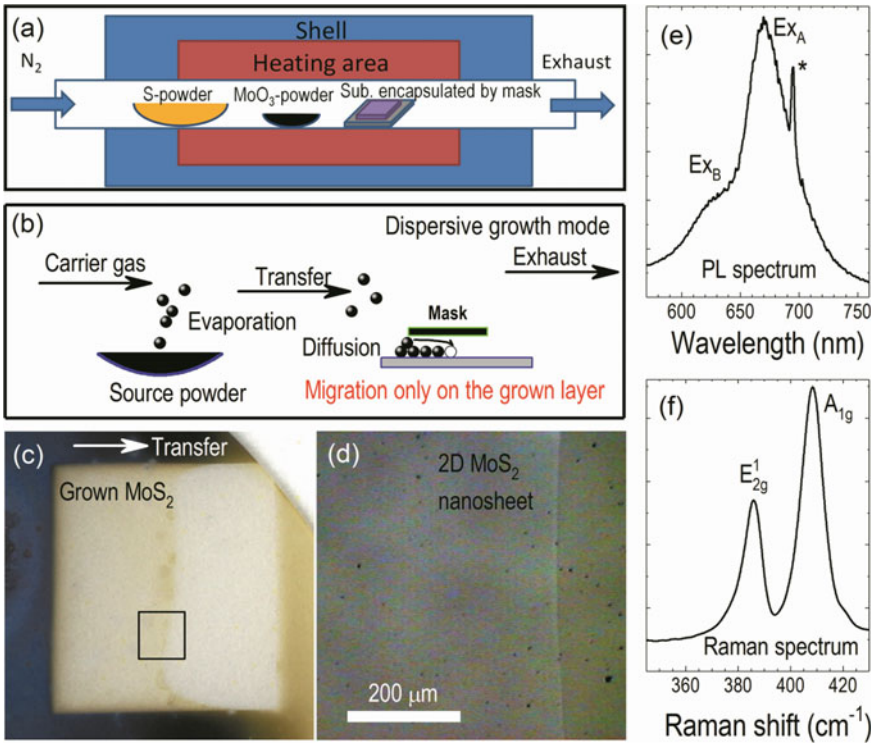

Fig. 4 Growth of 2D MoS_2 nanosheets by TVD using sulphur and MoO_3 powders as the source materials in a dispersive mode: **a** the growth setup, **b** the mechanism that controls the transfer of source species to the growth front via diffusing on the grown layer, **c** photograph of a 2D MoS_2 nanosheet grown by the dispersive mode on sapphire using a Si wafer (1×1 cm^2) as the encapsulating mask, **d** a highlight of the sharp growth front at the location indicated by the box in **c**, **e** PL spectrum collected from the MoS_2 nanosheet and **f** Raman spectrum collected from the MoS_2 nanosheet. Figures reproduced with permission from Ref. [21], Copyright 2015, Nature Publishing Group

of the photograph and the Raman spectrum shows that a uniform single-layer MoS_2 nanosheet has been grown below the mask on the left and closer to the powder MoO_3 source [see Fig. 4c, d]. These observations indicate that the migration of reaction species below the mask is most likely on surface of the grown MoS_2 nanosheets, where there are no dangling bonds and thus absence of nucleations at high temperatures (e.g. 950 °C). When the reaction species reach the growth front, they are captured by the dangling bonds and grow into the nanosheet, which advances the growth front below the mask towards the right side. Because the nucleation and the migration of the reaction species (i.e. adatoms) are spatially controlled by applying the mask encapsulation, the sensitivity of the crystal growth to the process parameters (e.g. the load of the powder source) is significantly weakened. As a result, the growth

of 2D TMDCs can be more feasibly controlled via adjusting the growth temperature and/or the growth duration.

To increase the wafer size and to make the growth more compatible with conventional semiconductor thin-film technologies, we have further modified the dispersive growth mode by shifting the mask from encapsulating the substrate surface to standing in the vaporized source flow just before the substrate. In this way, the reaction species are transferred onto the substrate surface via diffusing from the supersaturated gas phase through a boundary layer. Similar to most of the reported TVD methods, the process control in this modified dispersive TVD growth is a bit difficult. Our preliminary experimental results, shown above in Fig. 5, demonstrate the capability of this method to grow high-quality uniform single-layer MoS_2 nanosheets on a quarter of 2-in. diameter sapphire substrate. Unfortunately, although the PL and Raman spectra [see Fig. 5f], together with their peak intensity mappings [see Fig. 5b and c, respectively], show excellent crystal quality of the continuous wafer-scale single-layer MoS_2 nanosheet, one sees that the single-layer nanosheet consists of in-plane close-packaged grains. The grain boundaries manifest themselves as the dark lines in the PL intensity mapping [see Fig. 5b] because the crystal defects are rich at the grain boundaries that weaken the PL emissions wherein. The in-plane close packaging of the grains, averagely about 10 μm in size, is randomly and exhibits no collective orientation. This random in-plane orientation of the grains is confirmed

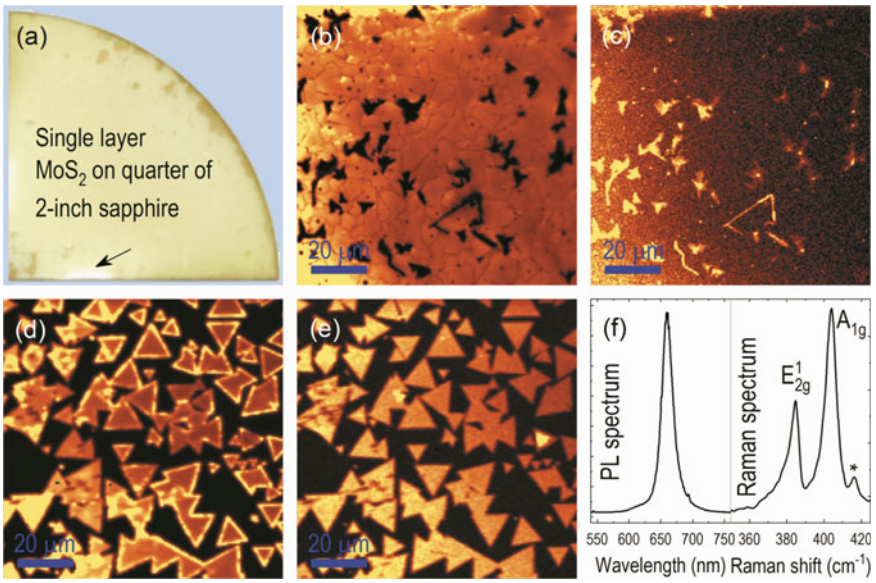

Fig. 5 Dispersive growth of single-layer MoS_2 nanosheets on a quarter of 2-in. diameter sapphire substrate: **a** photograph, **b**, **c** PL and Raman intensity mappings at the centre area of the wafer, **d**, **e** PL and Raman intensity mappings at the wafer edge indicated by the arrow, where the wafer was hold by a quartz block during growth and **f** PL and Raman spectra collected from the centre area of the wafer

by the well-developed triangular flakes [see the PL and Raman intensity mapping shown in Fig. 5d and e, respectively] grown at the edge of the wafer, indicated by the arrow in Fig. 5a, where the sample was held by a quartz block during growth. This is a common issue in recent growth of semiconducting 2D TMDCs towards their electronic applications. The abundant grain boundaries negatively affect the charge transport and thus the device performance via scattering the carriers of the MoS_2 nanosheet; they also contribute the unreliability when fabricating integrated circuits based on such 2D nanosheets. We believe that the best bet to overcome this issue, from the growth control point of view, should be MOCVD [75, 76], although its development for growing 2D materials is still at the beginning stage [114–116].

3 Synthesis and Process of α-MoO_3 Single Crystals Towards 2D Nanosheets

3.1 Unique α-MoO_3 and Its Synthesis by TVD

The earlier investigations on MoO_3 mainly focused on its catalyst applications. The multiple valance states of Mo, as a transition metal, in MoO_3 make it effective in selectively oxidizing hydrocarbons and alcohols [117–119]. MoO_3, as a semiconductor, has a wide band gap (~3.0 eV), a large work function (~6.8 eV) and a high dielectric constant (>200). These unique electrical properties of MoO_3 have been intensively applied in electronic and optoelectronic devices, e.g. via making MoO_3 as a component layer to effectively collect and transport holes [120–122]. It has been proposed that MoO_3, in heterostructures, can dope holes to its adjacent graphene layers without introducing any structural defects, so that the high carrier mobility of the graphene layer can be kept intact [122–124].

Orthorhombic α-phase MoO_3 is a VDW crystal with its individual single layers consisted of two sublayers of Mo-centred and O-cornered MoO_6 octahedrons along its [010]-axis. The [001] and [100] crystal axes of α-MoO_3 are aligned in-plane, sharing an O-corner and an inclined edge of adjacent octahedrons. In recent years, synthesis and post-synthesis process of α-MoO_3 VDW crystals have been attracting increasing research interest towards their 2D nanosheets for potential applications in transparent, flexible and wearable electronics and/or energy storage devices [125–127]. By intercalating the VDW lattice with hydrogen, a carrier mobility of up to 1100 cm^2/Vs has been obtained for of α-MoO_3 atomic layers [23].

The synthesis and defect engineering of α-MoO_3 crystals have been intensively studied by various thin-film techniques in recent years [128–132]. In a similar way to the TVD synthesis of MoS_2 except for the sulphur source, we have carried out the crystal growth of α-MoO_3 in a tube-furnace reactor using MoO_3 powder solely as the source material. The MoO_3 powder was heated at 1000 °C in the hot zone and the vaporized species were transferred by nitrogen to the synthesis zone in the downstream, where the temperature is lower than 600 °C. The TVD setup for the

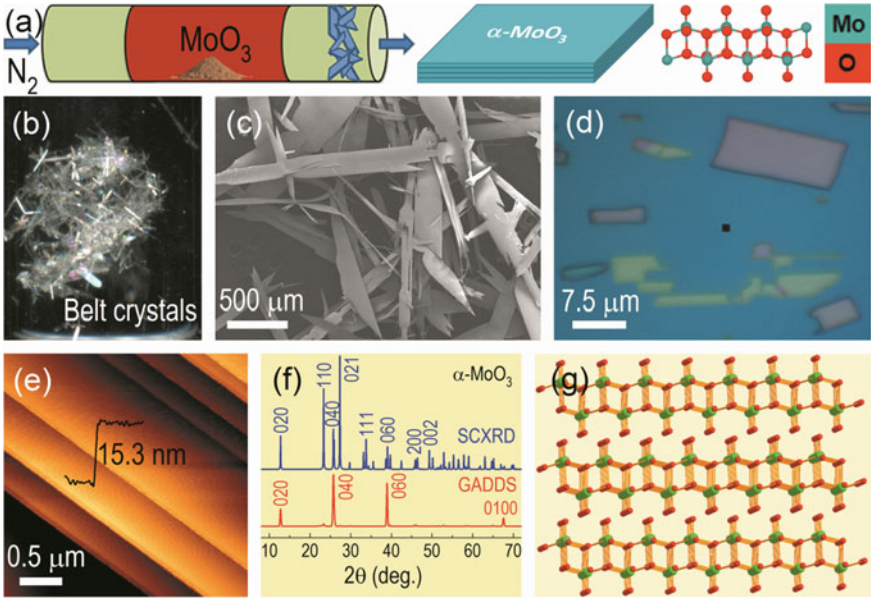

Fig. 6 TVD synthesis of α-MoO_3 crystals using MoO_3 powder as the source materials: **a** schematic diagram of the growth setup, the [010]-oriented layered structures, and a single-layer structure viewed along its [100]-axis, **b**, **c** Photograph and SEM image of the obtained α-MoO_3 belt crystals, **d** Optical microscopic image of the α-MoO_3 flakes with varied layer thicknesses, **e** AFM image showing the VDW stacking of the α-MoO_3 layers along their [010]-axis, **f** XRD patterns collected from a single belt crystal by SCXRD and from the belts gathered on substrate by GADDS and **g** the α-phase crystal structure derived from the SCXRD measurements. Figures reproduced with permission from Ref. [27], Copyright 2018, American Chemical Society

growth of α-MoO_3 is schematically shown in Fig. 6a, together with the [010]-oriented layered structure and a single-layer α-phase MoO_3 view along its [100]-axis.

Figure 6b–e show the morphology and topography properties of the obtained α-MoO_3 crystals, they are in belt shapes [see Fig. 6b–d] that consisted of individual layers, stacking along the surface normal direction. Presented in Fig. 6f are the XRD patterns collected from a single belt using a single crystal X-ray diffractometer (SCXRD, KAPPA APEX) as well as those from a collection of belts on a substrate by a general area detector diffraction system (GADDS, Bruker-D8). The former are the overall results of more than thousands of XRD scans from different angles respect to the belt, which is sensitive to the crystal structure. Not only phase impurity but also variation in orientation cause failure in the SCXRD measurements. The success in the derivation of the SCXRD patterns provides evidence that the belt is a single crystal while the patterns, together with a theoretical calculation, give rise to the crystal structure shown in Fig. 6g, which is indeed α-phase MoO_3 with its [010]- and [001]-axis along the belt-surface and -length directions, respectively. In comparison, the GADDS method has the advantage of being accurate in identifying impurity phases. A comparison between the GADDS and SCXRD results in Fig. 6f indicates

a high phase purity of the TVD-grown α-MoO_3 crystals. The lattice parameters, derived from the SCXRD measurements, are $a = 3.9527$ Å, $b = 13.8146$ Å, $c = 3.6903$ Å and $\alpha = \beta = \gamma = 90°$. These lattice constants, when compared with those of JCPDF 05-0508 ($a = 3.9628$ Å, $b = 13.855$ Å, $c = 3.6964$ Å), are compressively stressed and the strains are anisotropic at $\varepsilon_a = -0.25\%$, $\varepsilon_b = -0.29\%$ and $\varepsilon_c = -0.17\%$.

3.2 *Defects Engineering of α-MoO_3 Single Crystal Belts*

Defects engineering of α-MoO_3 crystals via releasing oxygen atoms from the surface and energetically reorganizing the oxygen vacancies (V_O) in the crystal lattice can have important consequences in tuning the electronic structure of α-MoO_3 for novel functions. In general, two types of methods have been developed for the defects engineering of α-MoO_3 [27, 28, 133–136]. One is physically kicking out the surficial oxygen atoms, for example, by heating and/or bombarding by energetic particles in oxygen-free environment [136]. The resultant V_O introduce defect energy levels in the band gap of α-MoO_3, the hybridization of the defect levels as the increase in V_O density leads to the reduction in the band gap of the parent crystal, i.e. oxygen-deficient MoO_{3-x}. The other is chemically reacting with hydrogen and/or hydrocarbon species to form H_xMoO_3 precipitates [133–135]. The alloying of hydrogen into the lattice of MoO_3 also introduces defect energy levels in the band gap, an increase in the hydrogen alloying composition tends to hybrid the defect levels with the conduction bands of the α-MoO_3 matrix, giving rise to the reduced band gap of H_xMoO_3 in compared with that of α-MoO_3.

Experimentally distinguishing the type of oxygen deficiencies in α-MoO_3 is, sometimes, difficult because both the above-mentioned oxygen releasing mechanisms could occur simultaneously. A typical example is observing the defects in TEM chamber where the electron-beam bombardments could energetically kick out the surface oxygen atoms while the residual hydrocarbon contaminations could induce the surficial reduction reactions [28]. In this light, we have employed confocal Raman scattering technique via mapping the intensity of the V_O-related lattice vibrational mode. For this study, we have carried out low-temperature heat treatments for single crystal α-MoO_3 belts in an oxygen-free environment, which was realized by soaking the crystal belts in liquid sulphur at 300 °C for 8 h.

Figure 7 presents the comparisons of the single crystal α-MoO_3 belts before and after the low-temperature treatments using the setup schematically shown in Fig. 7a where free oxygen can be rapidly eliminated at the initial treatment stage via chemical reactions with sulphur. Figure 7b–d shows the Raman scattering enhancements at the belt edges, when compared with those at the centre areas of the belts, and these enhancements are typically observed from those modes sensitive to V_O, indicating that V_O is rich at the edge areas of the as-grown belts. Figure 7e shows an image taken by optical microscopy (OM) from the treated belt, which exhibits regular patterns along the intersections between the (302) atomic planes and the surface,

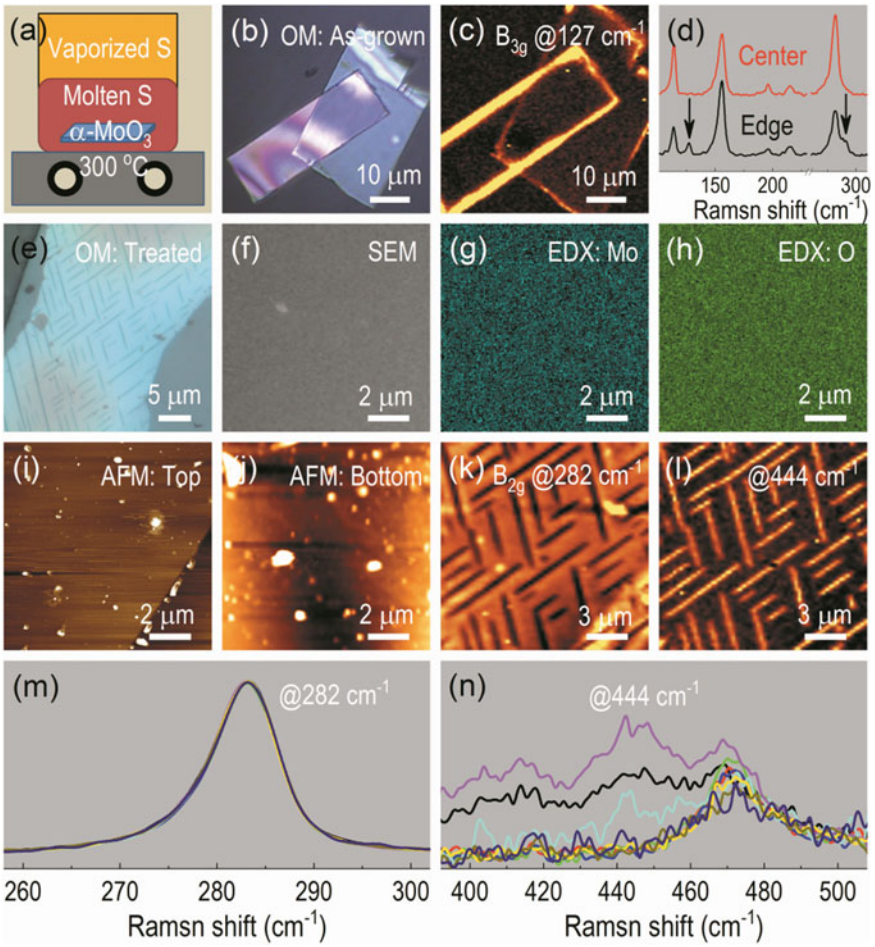

Fig. 7 Post-growth low temperature treatment of single crystal α-MoO_3 belts in liquid sulphur at 300 °C: **a** schematic diagram of the setup, **b** Optical microscopy (OM) image of typical as-grown belts, **c** Ramam scattering intensity mapping of the B_{3g} mode at 127 cm^{-1}, showing the scattering enhancement at the edge areas of the as-grown belts, **d** Spectral comparison of the Raman scattering at the centre- and edge area of the as-grown belts, **e** OM of the treated belt, showing the appearance of regular defects, **f**–**h** SEM image and EDX mapping for Mo and O collected from a same area at the surface of the treated belt, **i**, **j** AFM images recorded from the top and bottom surfaces of the treated belt, **k**, **l** Raman scattering intensity mappings of the modes at 282 and 444 cm^{-1}, **m**, **n** Spectral comparisons of the modes at 282 and 444 cm^{-1} collected at the defects and their surrounding areas, the spectra were normalized to the intrinsic α-MoO_3 modes. Figures partly reproduced with permission from Ref. [28], Copyright 2018, American Chemical Society

i.e. the (010) atomic planes, of the α-MoO_3 belt. These patterns are undetectable, from both the top and bottom surfaces of the belt, by both SEM/EDX [see Fig. 7f, g] and AFM [see Fig. 7i, j]. These results indicate that the observed patterns are structural defects formed in the crystal along its (302) atomic planes. The low-temperature heat treatment-induced (302) planar defects were further confirmed by the Raman scattering as shown in Fig. 7k–n. One sees that after normalizing the spectra collected from the defects and their surroundings the intrinsic α-MoO_3 mode at ~282 cm^{-1} (B_{2g}) in Fig. 7m does not exhibit any variations while the additional mode at ~444 cm^{-1} in Fig. 7n emerged along with the defects. Their intensity mappings, shown in Fig. 7k and l, respectively, provide direct evidence that the intrinsic α-MoO_3 mode has been weakened, while the additional mode has been enhanced, by the planar defects. Also seen in Fig. 7m is that the V_O-induced mode at ~290 cm^{-1} is absent at the planar defects.

It has been generally accepted that the formation of planar defects in α-MoO_3 is usually associated with oxygen deficiencies, e.g. an increase in the density of V_O and thermal-induced rearrangements of V_O in the crystal lattice of α-MoO_3 can give rise to its crystallographic shear (CS) along certain atomic planes [136]. As a result, the V_O is consumed by forming the CS, manifesting as the planar defects [137]. We also found that the planar defects monotonically decrease in density when moving away from the edge towards the centre of the belt crystal [28]. This observation indicates that the formations of CS are dominated by the intrinsic V_O rather than those recreated on the surface via releasing the surficial oxygen atoms. Another striking observation is that the planar defects are regularly distributed with certain separations between adjacent ones, which suggests that the migration of intrinsic V_O is much faster along the in-plane directions than along the [010]-axis, i.e. the layer thickness direction.

To engineer the surface defects of the single crystal α-MoO_3 belts, we have employed low-energy plasma treatments at room temperature in oxygen and argon atmospheres, respectively. Hydrogen contaminations from residual gas (e.g. moisture) are most likely unavoidable due to the low vacuum system used in this work. It has been reported that the presence of atomic hydrogen, even at room temperature, could reduce α-MoO_3, resulting in H_xMoO_3 acicular precipitates on the crystal surface. The H_xMoO_3 precipitates tend to topotactically align themselves along the [203]-axis of the MoO_3 (010) atomic planes [134, 137, 138]. The phenomenon has been clearly observed in our experiments when switching the plasma treatment atmosphere between argon and oxygen. The reactions between the residual hydrogen with α-MoO_3 can be enhanced by the argon plasma while the produced H_xMoO_3 precipitates can be reoxidized by the oxygen plasma [27, 28]. These conclusions have been confirmed by the plasma treatment-induced shifts in the absorption edge of the α-MoO_3 crystal belts. The absorption edge shifts to lower energies upon an argon plasma treatment while the shift turns back by switching to an oxygen plasma treatment. It is worth mentioning that the crystal belts do not exhibit any apparent thickness reductions upon the employed low-energy plasma treatments.

3.3 *Thinning of α-MoO_3 Single Crystal Belts Towards 2D Nanosheets*

Although the studies on α-MoO_3-based 2D materials have emerged soon after those of TMDC-based 2D materials, the effort that has been made on the former is much less than on the latter. Theoretically, it has been well understood that when the thickness of 2D TMDCs is reduced to single VDW layers, their indirect band gap [dominated by the hybridizations of the transition metal (TM) and the chalcogenide atoms] converts to direct band gap [dominated by the TM atoms] due to the varied effect of interlayer coupling as well as that of the quantum confinements [41]. This phenomenon has been unambiguously confirmed by various experimental studies. However, this situation is different for α-MoO_3, where the theoretical calculations reveal no band gap changes, not only for the direct band gap but also for the indirect band gap, when its thickness is reduced to single VDW layers [24]. Unfortunately, consolidate experimental evidence that can support this theoretical prediction is missing in the literature [24, 25]. On the contrary, our experiments provide evidence that there is a huge blue shift in the absorption edge of the single crystal α-MoO_3 belts when the thickness is thinned down towards 2D nanosheets. Meanwhile, an apparent mode softening up to 5 cm^{-1} of the Mo-O-Mo stretching mode at about 818 cm^{-1} (A_g) has been observed for the 2D α-MoO_3 nanosheets as compared with that of the bulk [26, 27]. To thin down the layer thickness of the crystal belts, we have employed a few methods including mechanical exfoliation, gas-phase etching and aqueous mechanical exfoliations assisted by bovine serum albumin (BSA).

Figure 8 shows the morphology, topography and spectroscopy results collected from a mechanical exfoliated α-MoO_3 flake and α-MoO_3 single crystal belts with varied thicknesses. The inset in Fig. 8b is the geometric structure of the flake derived from the comparisons amongst the OM image, the AFM image and the Raman intensity mapping of the A_g mode around 818 cm^{-1} [see Fig. 8a, b and c, respectively], which shows a single VDW layer, i.e. of ~1.4 nm thick, at the edge on the left. The normalized Raman spectra in Fig. 8e show an apparent softening of the A_g mode at ~818 cm^{-1} for the single VDW layer as compared with those of the bulk crystals. The mode softening of the α-MoO_3 single VDW layer is also confirmed by the Raman frequency mapping as shown in Fig. 8d, which was simultaneously recorded with the intensity mapping in Fig. 8c. A plotting of the Raman intensities as a function of their corresponding frequencies derived from the mappings as shown in Fig. 8c, d is presented in Fig. 8f. One can see that the A_g mode frequency exhibits an apparent and sharp softening as the mode intensity is decreased lower than 1500 counts. Physically, the Raman mode intensity is proportional to the layer thickness, especially for the confocal Raman mapping, where the data collecting conditions are kept constant. In this light, the Raman mode softening at the edge of the α-MoO_3 flake provides direct evidence for the thickness reduction of α-MoO_3 approaching 2D nanosheets realized by the mechanical exfoliation.

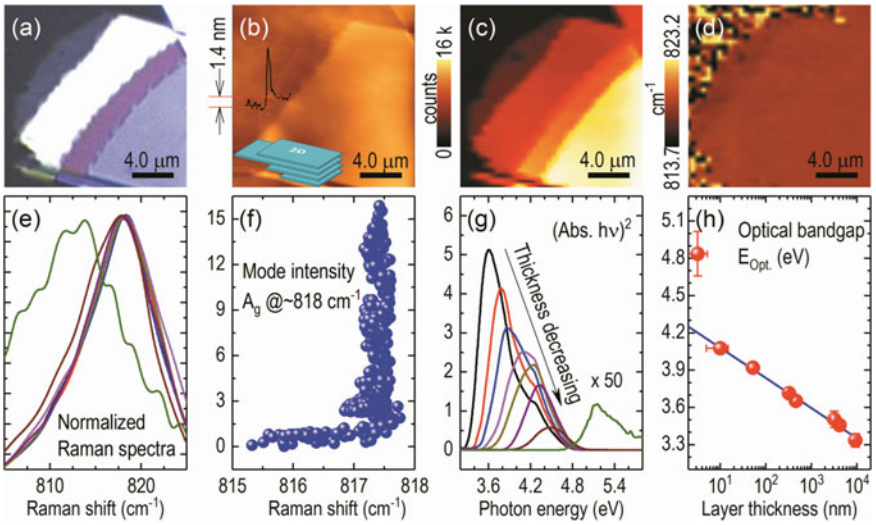

Fig. 8 Mechanical exfoliation of the single crystal α-MoO_3 belts using scotch tapes: **a** Optical microscopy (OM) image of a piece of α-MoO_3 after a few round of scotch tape exfoliations, **b** AFM image of the α-MoO_3 flake, showing the single VDW layer at the edge, **c**, **d** confocal Raman intensity and frequency mappings of the A_g mode at around 818 cm^{-1}, **e** normalized Raman spectra collected from α-MoO_3 belts with varied thickness as well as the single VDW layer at the edge of the flake, **f** mode intensity varied as a function of the mode frequencies derived from the mappings in (**c**, **d**), **g** absorption spectra in the form of (abs. × $h\nu$)^2 collected from the samples in (**e**) and **h** optical band gap energies as a function of the layer thickness of α-MoO_3 derived from the absorption spectra in (**g**). The inset shows the geometric structure derived for the α-MoO_3 flake from the comparisons between the AFM and OM images and the Raman intensity mapping. Figures partly reproduced with permission from Ref. [26], Copyright 2017, Tsinghua University Press and Springer

Figure 8h shows a semi-log plot of the optical band gap energies, E_{Opt}, derived from the absorption spectra of the α-MoO_3 single crystal belts as well as the exfoliated 2D nanosheet, as a function of their thicknesses. One sees that when the layer thickness is larger than 10 nm, the E_{Opt} of α-MoO_3 exhibits a linear increase with the decrease in the layer thickness. However, when the layer thickness is decreased lower than 10 nm, i.e. approaching the single VDW layer, the increment of E_{Opt} is much larger than that following the linear relationship. The thickness-reduction-induced increase of E_{Opt} has also been observed in γ-In_2Se_3 thin films with the thickness larger than 10 nm and attributed to the quantum confinement effect caused by the crystallites of the polycrystals [139]. However, the α-MoO_3 belts in our work are single crystal and the thickness of 10 nm is bigger than the critical size that exhibits quantum confinement effect. In this regard, we have carried out finite difference time domain (FDTD) calculations for the absorption spectrum of α-MoO_3 with the previously reported optical refractive index [140]. The calculations indeed show a linear relationship for the semi-log plot of E_{Opt} as a function of the layer thickness in the range of 10–10^4 nm [27], indicating that the thickness-reduction-induced increase in the E_{Opt} of α-MoO_3 is most likely caused by the light interferences at the surface

of the single crystal belts rather than changes in the electronic structures. On the other hand, the much larger increment in the E_{Opt} of the single VDW layer [see Fig. 8h], which deviates from the linear fittings by up to 600 meV, has further been observed for the 2D α-MoO_3 nanosheets produced by gaseous chemical etching and BSA-assisted aqueous exfoliations.

Gaseous XeF_2 and HF have been employed for thinning down the single crystal α-MoO_3 belts via chemical etching on their surfaces. Our experiments show that HF is more effective than XeF_2 in the chemical etching and the etching of α-MoO_3 can be realized layer by layer on the crystals free of surface defects [27]. Figure 9a

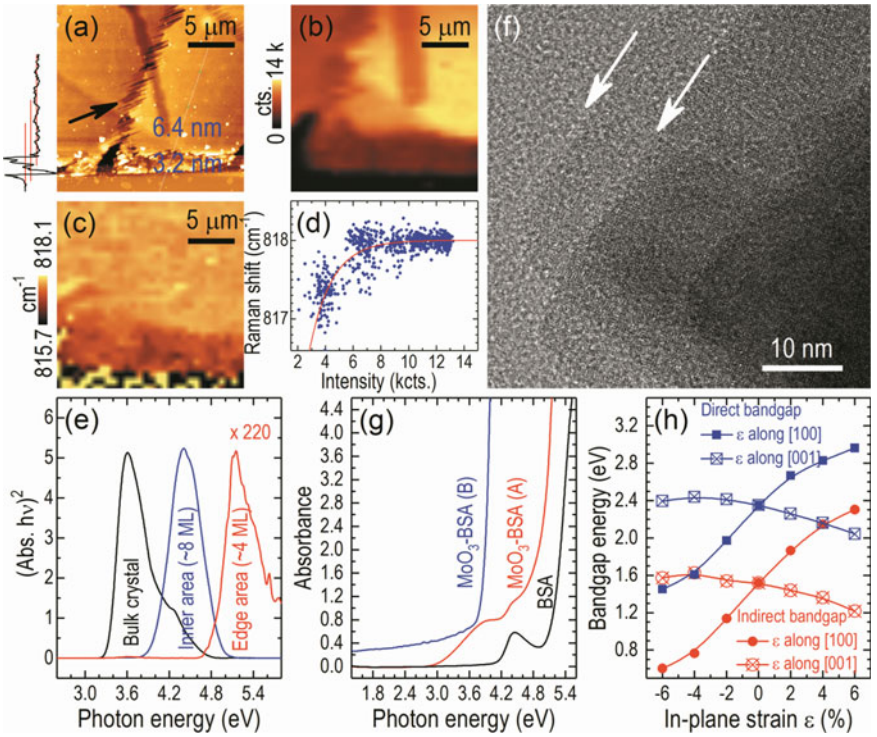

Fig. 9 Gaseous chemical etching and BAS-assisted aqueous exfoliation of α-MoO_3 single crystal belts towards 2D nanosheets: **a** AFM image taken from the α-MoO_3 nanosheet after chemical etching by gaseous HF, the height profile reveals a thickness of 6.4/3.2 nm for the inner/edge area, i.e. around 8/4 VDW layers thick, **b**, **c** Raman intensity and frequency mappings of the nanosheets produce by the HF-etching, **d** plot of the Raman intensities as a function of their corresponding frequencies derived from the mappings, **e** optical absorption spectra in the form of (Abs. × $h\nu$)^2 collected a bulk α-MoO_3 belts and the inner/edge area of the nanosheet produced by the HF-etching, **f** HRTEM image taken from the 2D α-MoO_3 flakes produced by BSA-assisted aqueous exfoliations, **g** optical absorption spectra collected from the aqueous exfoliated 2D α-MoO_3 flakes and the BSA solution and **h** Band gap energies calculated using the periodic DFT method for 2D α-MoO_3 flakes with varied anisotropic in-plane strains. Figures partly reproduced with permission from Ref. [26], Copyright 2017, Tsinghua University Press and Springer

shows an AFM image taken from a HF-etched α-MoO_3 on a sapphire wafer. The surface height profiling indicates that the inner and edge areas are of 6.4 (~8 VDW layers) and 3.2 nm (~8 VDW layers) thick, respectively. The Raman intensity and frequency mappings, shown in Fig. 9b and c, respectively, were measured for the A_g mode at about 818 cm^{-1} of the HF-etched nanosheet; their correlations are plotted in Fig. 9d, which confirm the mode softening when the thickness of α-MoO_3 is reduced approaching to ~4 VDW layers. Presented in Fig. 9e are the absorption spectra in the form of (Abs. × $h\nu$)^2 collected from a bulk α-MoO_3 crystal and the HF-etched nanosheet at the inner and edge areas. One sees that the absorption edge is significantly blue shifted after the HF-etching and the thinner the nanosheet the larger the blue shift.

The aqueous exfoliations were processed by carrying out ultrasonication of the α-MoO_3 crystal belts in BSA solutions. The BSA molecules tend to attach their branch ends to the surface of the crystals while floating their main body in the solution. By applying ultrasound energy to the BSA molecules surrounding the crystals through the solution, the surface layer of the crystal can be mechanically peeled off or exfoliated. Once the surface layer is peeled off, the exposed surface of both the parent crystal and the peeled layer will be attached by the BSA molecules. By controlling the centrifugation rate of the sonicated samples, the layer thickness of the exfoliated nanosheets can be separated. Figure 9f presents a HRTEM image taken from an aqueous exfoliated α-MoO_3 nanosheet, from which the single-layer nanosheet and the boundary between the single- and multiple-layer nanosheets are clearly distinguished as those indicated by the arrows. Presented in Fig. 9g are the absorbance spectra collected from the MoO_3-BSA samples A and B with varied layer thickness of the nanosheets, the spectrum of the BSA solution is also presented for comparison. It is seen that the more exfoliated sample A exhibits a huge blue shift in its absorption edge as compared with the less exfoliated sample B.

Theoretically, impurities and/or defects tend to red shift, rather than blue shift, the absorption edge of the host semiconductors. This is indeed what we have discussed above that both the oxygen deficiencies and the hydrogen reductions can narrow down the band gap of α-MoO_3 crystals. Besides, the theoretical calculations suggest no band gap changes of α-MoO_3 when its thickness is thinned down to a single VDW layer [24]. On the other hand, lattice strain has been well known as a mechanism that can cause band gap changes as well as Raman mode shifts of crystalline semiconductors [141–143]. In fact, Cai et al. have already observed a red shift of the Raman mode at ~818 cm^{-1} for 2D α-MoO_3 as compared with that of the bulk crystal and they attributed the red shift to an in-plane lattice expansion of the few-layer α-MoO_3 [125]. Interestingly, one sees in Fig. 9a that regular linear structural defects, indicated by the arrow, have been created on the HF-etched α-MoO_3 nanosheet. These gas-phase etching-induced regular structural defects suggest an occurrence of isotropic in-plane strain relaxation and/or redistribution when the α-MoO_3 layer is thinned down towards 2D nanosheets. In this light, we have calculated the electronic structures for α-MoO_3 nanosheets by introducing varied uniaxial in-plane strains, i.e. strains along the [100]- and [001]-axis, respectively.

Figure 9h presents the band gap energies derived from the electronic band structures of nanosheet α-MoO_3 calculated using the periodic density functional theory (DFT) with varied uniaxial in-plane strains. One sees that both the direct and indirect band gap energies exhibit similar variation behaviours as a function of the in-plane uniaxial strains. They increase with the lattice expansion in [100] direction while decrease with the lattice expansion along the [001] direction. This result, together with the regular linear structural defects formed on the surface of the α-MoO_3 nanosheets, provides clues to an in-plane redistribution and/or an anisotropic relaxation of the residual lattice strains when the thickness of the [010]-oriented α-MoO_3 is reduced towards nanosheets. This unique of 2D α-MoO_3 nanosheets might also be useful in band gap tailoring of not only themselves but also their adjacent layers in 2D heterostructures for additional functions and/or improved performances.

4 Hybrids of 2D TMDCs and α-MoO_3 for Optoelectronic Applications

4.1 Methods for 2D WS_2/MoS_2 Heterostructures and 2D MoS_2–MoO_3 Composites

Heterostructures of 2D materials have been intensively studied in recent years, and the typical studies are focused on vertical stacking of different 2D nanosheets, lateral epitaxy of heterojunctions and hierarchical hybrids of 2D materials [7, 144–147]. The vertical 2D heterostructures are usually fabricated by transfer of 2D nanosheets while the 2D nanosheets, as the building blocks, can be those produced by exfoliations and/or depositions [148, 149]. The vertical 2D heterostructures can also be produced by monolithic growth methods via switching the reaction species through controlling the precursor sources in a similar way to those for the growth of conventional semiconductor heterostructures [22, 150]. In comparison, the lateral 2D heterostructures are mainly grown by depositions, typically CVD, either using the single-step synthesis that is based on in-plane phase separations or the two-step synthesis that switches the source precursors from one step to another [6, 150]. Wet-chemical synthesis is the dominant method that has been employed to composite the hierarchical hybrids of 2D materials [147].

Magnetron sputtering has long been developed in our research group not only for traditional semiconductor thin films but also for 2D TDMCs [60, 110, 151, 152]. With this technique, we have also explored monolithic growth of 2D WS_2/MoS_2 heterostructures without any post-growth sulfurization [22]. It is worth mentioning that the source precursors of the employed reactive sputtering are supplied from metal target and sulphur powder, both are installed in the vacuum chamber of the sputtering reactor. During growth, argon is fed into the chamber as the working gas; its plasma via controlled discharging is guided by the magnetic field to bombard the metal target, so as to produce the TM reaction species. The sulphur powder is loaded

in a Knudsen-cell-like evaporator and its partial pressure during the sputtering growth can be controlled by the cell temperature. The substrate temperature was generally kept at about 750 °C for the growth of the 2D TMDC layers.

Figure 10 presents the results of a patterned growth of 2D MoS_2 and WS_2/MoS_2 heterostructure by the above-mentioned reaction magnetron sputtering. Figure 10a, b shows the OM and AFM images collected at the boundary area of the 2D WS_2/MoS_2 heterostructure and the monolayer thick MoS_2. The height profile shown in the inset in Fig. 10b indicates that the WS_2 is also about a monolayer thick. Figure 10c–e presents the element distributions of W, Mo and S, respectively, measured by time-of-flight secondary ion-mass spectroscopy (TOF-SIMS) across the boundary area between the 2D MoS_2 and the 2D WS_2/MoS_2 heterostructure. Figure 10f, g shows the PL (normalized) and Raman spectra collected from the monolayer MoS_2

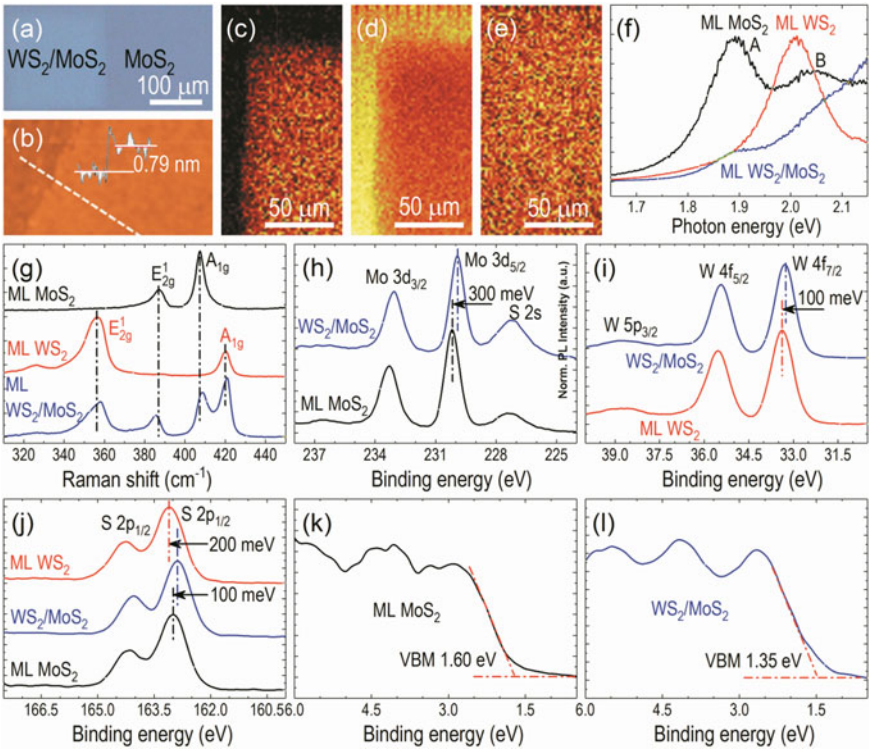

Fig. 10 Growth of 2D MoS_2 and WS_2/MoS_2 heterostructures by reactive magnetron sputtering using metal targets and sulphur powder as the source materials: **a** microscopy image showing the growth of 2D MoS_2 and WS_2/MoS_2 heterostructure, **b** AFM image showing the monolayer thickness of the grown layer, **c**, **d**, **e** elemental mappings of W, Mo, and S measured by time-of-flight secondary ion-mass spectroscopy, **f** normalized PL spectra, **g** Raman spectra, **h**, **i**, **j** core levels of Mo3d, W4f, and S2p collected by XPS and **k**, **l** valance band spectra collected by XPS. Figures reproduced with permission from Ref. [22], Copyright 2018, The Royal Society of Chemistry

and WS_2/MoS_2 heterostructure, as well as a monolayer WS_2, indicating their high-quality crystalline structures. The relative mode shifts in the Raman features of MoS_2 in the 2D WS_2/MoS_2 heterostructure with respect to those in the single MoS_2 layer provide evidence for the presence of interlayer coupling and exciton relaxation at the heterointerface. Further, TEM studies and theoretical simulations confirmed that the interlayer coupling between WS_2 and MoS_2 is associated with the in-plane alignment of their crystallographic orientations, i.e. the twist angle of the heterostructural stacking [22].

Figure 10h–j presents the core levels of Mo3d, W4f and S2p collected by XPS from the single-layer MoS_2, the 2D WS_2/MoS_2 heterostructure and the single-layer WS_2. They, together with the valence band maxima (VBM) of the single-layer MoS_2 shown in Fig. 10k and the 2D WS_2/MoS_2 heterostructure shown in Fig. 10l, reveal a type-II band alignment of the 2D WS_2/MoS_2 heterojunction. The band offsets across the heterojunction of the 2D WS_2/MoS_2 heterostructure, in terms of the separations between the VBM and the core levels [153, 154], are 0.41 and 0.25 eV for the conduction and valance band, respectively [22].

To synthesize MoS_2–MoO_3 nanosheets composite films, we have employed a wet-chemical intercalation and exfoliation method [155]. For this process, MoS_2 powder (0.6 g) was intercalated using an n-butyllithium solution (0.8 mL) in an argon environment. After removal of the excess lithium and organic residuals by washing in hexane for a few times, the material was exfoliated by ultrasonication in deionized water (1 mg/mL), followed by centrifugation at 2000 rpm for 5 min so that the larger MoS_2 blocks can be removed. The resultant solution was diluted to 0.1 mg/ML for the deposition of thin films on desired substrates. In this work, we have deposited the exfoliated nanosheets with a thickness of about 2 μm on a cellulose ester membrane through a vacuum filtering process.

Figure 11 presents the experimental results of the obtained MoS_2–MoO_3 nanosheets composite on the cellulose membrane. The top-view SEM image in Fig. 11a shows the porous structured layer, consisted of loosely stacked nanosheet composites, with a lateral dimension of a few hundred micrometres. The intercalation of lithium ions into the VDW gaps of MoS_2 gives rise to the fragments of the multiple layer nanosheets. The top-view SEM images with increased magnifications in Fig. 11b, c show the winkle up of the nanosheets due to the compressive strain developed during the chemical exfoliation for the 2D layered film structures with reduced thickness-to-area ratios. Microscale flakes are also seen as shown in Fig. 11d, their elemental distributions mapped by energy-dispersive X-ray spectroscopy (EDX), aiming at S [Fig. 11e], Mo [Fig. 11f] and O [Fig. 11g], indicate that they are O-rich and Mo/S-poor and attributable to remaining lithium oxides and/or hydroxides developed along with the intercalations. The EDX mappings also reveal the coexistence of Mo and O in the areas free of microscale flakes, which is further validated by XPS and identified, in terms of their valance states, as of the presence of MoO_3 on the surface of MoS_2 of the film [155]. Figure 11h shows a cross-sectional SEM image while Fig. 11i, j shows the cross-sectional TEM images recorded with varied magnifications. They show that the overall layer [~2 μm thick, see Fig. 11h] consists of thin nanosheet stacks of ~10 nm thick [see Fig. 11i] while

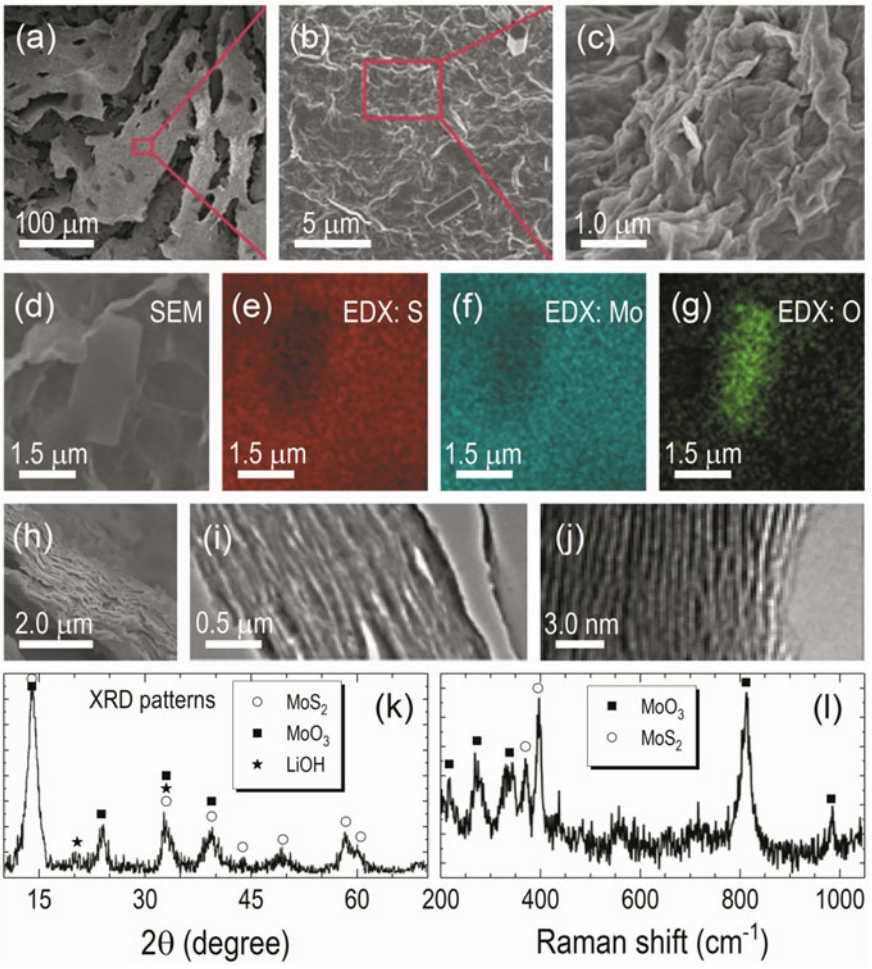

Fig. 11 Synthesis of MoS_2–MoO_3 nanosheets composites using the wet-chemical method: **a**, **b**, **c** top-view field-emission SEM images collected from the 2D MoS_2–MoO_3 composites at varied magnifications, **d**, **e**, **f**, **g** SEM image and element distributions of S, Mo, and O measured by energy-dispersive X-ray spectroscopy (EDX), **h** Cross-sectional SEM image, **i**, **j** Cross-sectional TEM images collected at varied magnifications and **k**, **l** XRD patterns and Raman spectrum collected from the wet-chemical processed 2D MoS_2–MoO_3 nanosheets composite. Figures reproduced with permission from Ref. [155], Copyright 2019, American Chemical Society

the thin stacks consist of nanosheets of ~0.63 nm thick [i.e. a single VDW layer of MoS_2, see Fig. 11j].

The XRD patterns in Fig. 11k and the Raman spectrum in Fig. 11l provide evidence that the wet-chemical processed nanosheets consisted of crystalline MoO_3 (JCPDS no. 05-0508) and MoS_2 (JCPDS no. 65-1951), as well as a small amount of LiOH. Detailed XPS analyses revealed that both the 2H- and 1T-phase are existing with

the MoS_2 crystals due partly to the 2H-to-1T phase changes [102, 156]. They also revealed the presence of MoO_3, which is consistent with the XRD and Raman spectroscopic studies as shown in Fig. 11i and j, respectively. The presence of MoO_3 can be attributed to surficial oxidation of the MoS_2 nanosheets. The complex phase structure and the chemical composition of the nanosheets composite are strongly depending on the process time, intercalation efficiency, restacking of the exfoliated nanosheets, etc. [157]. The phase compositions of the obtained 2D MoS_2–MoO_3 nanosheets composite are 1T-MoS_2:2H-MoS_2:MoO_3 = 1:4.6:2.5 in weight ratios. These compositions could play important roles in device performance and can be tuned by controlling the intercalation and exfoliation processes.

4.2 Flexible Multiband Photodetector Based on 2D MoS_2–MoO_3 Composites

To fabricate photodetectors with the 2D MoS_2–MoO_3 nanosheets composite deposited on flexible cellulose ester membranes, rectangular PEDOT:PSS electrodes (5.4 mm × 1.0 mm), which have the advantages of being flexible, transparent and physical/chemical stable, etc., were prepared by inkjet-printing [155]. The spatial separation between the pairs of electrode pads is 1.0 mm, and the overlap of the electrode on the composite film is about 1.0 mm that forms an active area of 1.0 × 1.0 mm^2. The electrodes, after being printed on the composite-on-membrane, were annealed at 100 °C for 30 min to improve the conductivity. The device performance was characterized by I–V tests in a voltage range of −6.5 to 6.5 V with a scanning rate of 0.1 V/s. Its photoresponse was tested by switching the on/off states at an interval of 30 s. For this test, the device was biased at a constant voltage, i.e. 5 V and illuminated by lasers with the wavelength of 405 nm (purple), 532 nm (green) and 650 nm (red), respectively. The power densities on the surface of the device are 6.21 and 5.09 and 0.968 mW/mm^2 for the purple, green and red laser illuminations, respectively.

Figure 12 presents the schematic structures of the photodetector device and its I–V performance under dark and laser illuminations at the wavelength of 405, 532 and 650 nm, respectively. One sees that the I–V profiles of the junction between the PEDOT:PSS electrode and the composite film exhibit a linear behaviour in Fig. 12b, indicating the formation of ohmic contact. The laser illuminations significantly reduce the resistance of the device via generating photocarriers and thus the photocurrent [105]. As is mentioned above that nanosheet wrinkles are formed on the surface of the composite film, which could interact with incident light with enhanced efficiencies through multiple reflections that, in turn, facilitates the light absorptions and the generation of photocarriers.

Figure 12c presents the time-resolved photocurrents collected at a bias of 5 V of the device, which shows a stable and repeatable response to the on/off switches of the laser illuminations. The maximum photocurrents generated by the purple,

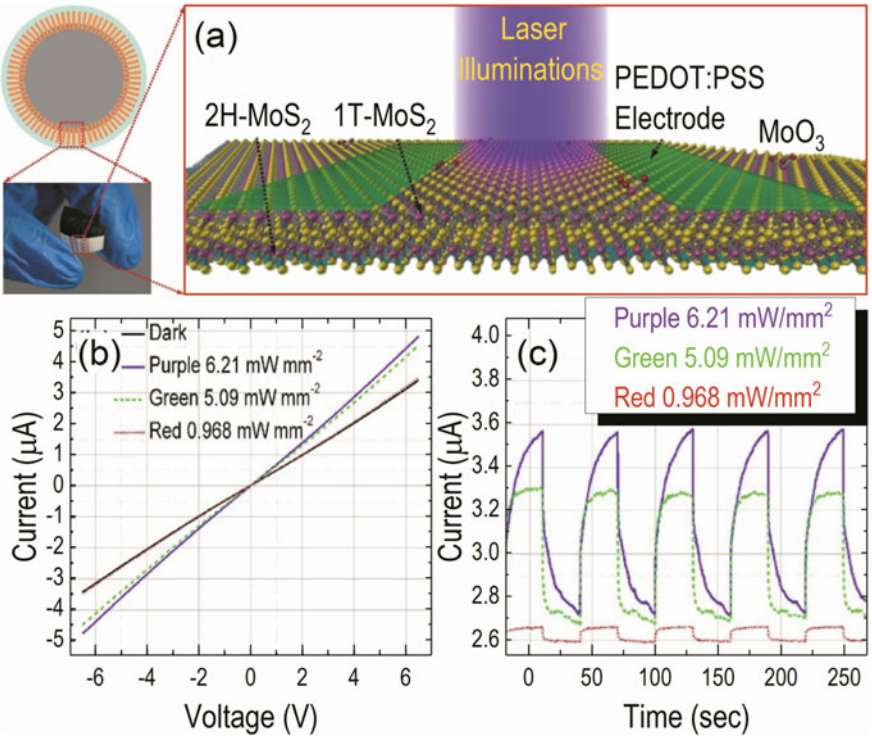

Fig. 12 Schematic diagrams (**a**), *I*–*V* curves (**b**) and time-resolved photocurrent biased at 5 V (**c**) of the multiple bands photodetector fabricated on flexible cellulose ester membranes using the wet-chemical exfoliated 2D MoS_2–MoO_3 nanosheets composite and the inkjet-printed PEDOT:PSS electrodes. Figures reproduced with permission from Ref. [155], Copyright 2019, American Chemical Society

green and red lasers are 3.56, 3.31 and 2.66 μA, respectively. A detailed analysis of the time-resolved photocurrents revealed a faster response (i.e. in the range of ~5 s) of the device to green and red laser illuminations while a slow response (i.e. in the range of ~15 s) to the purple ones. These comparisons, together with the relative photocurrent densities induced by the different wavelength illuminations, are ascribed to the enhanced photoelectrons generated by both MoS_2 and MoO_3. The inclusions of the 1T-phase MoS_2 in the composite film might also improve its electric conductivity and enhance its charge transport efficiency.

Table 1 summarizes the device performance of the photodetector fabricated on the flexible eater membrane using the 2D MoS_2–MoO_3 nanosheets composite film and the inkjet-printed PEDOT:PSS electrodes; comparisons were made by changing the laser illumination wavelength. One sees that the photodetector shows the best performance except for the slow switching characters, under the 405-nm laser illuminations as compared with those under 532- and 650-nm laser illuminations. Also seen is that the responsivity of so-fabricated photodetector is comparable to others

Table 1 Device performance of the multiband photodetector fabricated on the flexible cellulose ester membranes using the wet-chemical exfoliated 2D MoS_2–MoO_3 nanosheets composite and the inkjet-printed PEDOT:PSS electrodes. The performances of some typical MoS_2-based photodetectors reported in recent literature are also listed for comparison. Table reproduced with permission from Ref. [155], Copyright 2019, American Chemical Society

Laser	λ (nm)	Photocurrent biased at 5 V (μA)		Time (s)		Quantum efficiency (%)		Responsivity (mA/W)
		Maximum	Absolute	Response	Recovery	External	Internal	
Purple	405	3.56	0.835	17.5	15.3	0.041	0.063	0.134
Green	532	3.31	0.636	4.3	5.6	0.029	0.042	0.125
Red	650	2.66	0.070	6.4	4.9	0.014	0.020	0.072
Recently reported in the literature [158–161]								
Liquid-exfoliated MoS_2 under UV-visible–NIR [158]							0.036	
Inkjet-printed MoS_2 under visible [159]							~0.10	
Solution-derived MoS_2 under UV-visible [160]							0.063	
Solution-processed MoS_2 under broadband light (biased at 15 V) [161]							0.10	

recently reported in the literature although the illumination conditions might be different [158–161]. It is worth mentioning that the device does not show any significant degradation in its photodetection performance after being bent for up to 600 cycles, demonstrating the flexible and robust device characters as desired.

5 Conclusion and Outlook

In this chapter, we have introduced the latest advances in MoS_2-based 2D TMDCs, 2D α-MoO_3, as well as their 2D hybrid structures and composites towards optoelectronic applications. For the MoS_2-based 2D TMDCs, we have overviewed the emergence and development of bottom-up synthesis methods, including TVS, TVD and CVD, to attain high-quality, large area and uniform single-layer TMDCs nanosheets. Through the discussions about the TVS and TVD methods developed in our group for 2D TMDCs, we demonstrated that the TVS method can deliver larger area and uniform 2D nanosheets that can be feasibly controlled in doping densities and alloying compositions during the source film deposition stage. However, the crystal quality of such 2D nanosheets is relatively low due to the small grain sizes, typically in the range of 10–30 nm. Also demonstrated by the TVS method is that vertical aligned 2D nanosheets can be obtained, which could have important consequence for photocatalytic applications with the dangling bonds, being rich at the edge of the nanosheets on the film surface, as the active reaction sites.

For the TVD method, we have developed a dispersive growth that controls the nucleation sites and the transport of reaction source species, i.e. via migrating on the grown surface of the 2D nanosheets, to grow large area, high-quality single-layer

MoS_2 crystals. The encapsulating mask used to control the crystal nucleation sites as well as the transport of the source species can also be shifted away from the surface of the substrate to standing in its upstream. With this method (and its fine tunings), the grain size of the single-layer 2D nanosheets can be significantly increased to a few tens of microns and nanosheets can be grown in wafer scale, i.e. up to 2-in. diameter. Unfortunately, the crystal grains, although continuously in-plane merged in singe layers, do not have a collective in-plane orientation; crystal defects are formed at the grain boundaries. This is one of the biggest issues that have to be solved before systematically integrating such 2D materials into conventional industrialized semiconductor technologies.

Compared to the extensive studies and the abundant new knowledge obtained on 2D TDMCs, the investigation on 2D α-MoO_3 is still at the beginning stage. In general, the theoretical studies reveal none or minor changes in the electronic band gaps of α-MoO_3 crystals when its thickness is reduced from bulk to approaching a few van der Waals layers. However, experimental evidence that can support this prediction is lacking in the literature. We have employed TVD method and successfully synthesized high-quality single crystal α-MoO_3 belt crystals. These crystal belts were further treated under oxygen-free environment, i.e. liquid sulphur, for defects engineering. The defect engineering was also studied by carrying out the plasma treatments and switching the working gas between argon and oxygen. Gaseous phase chemical etching, mechanical exfoliation and aqueous exfoliation methods have been explored to make 2D α-MoO_3 nanosheets from the belt crystals, they provide clear evidence for the absorption edge blue shift and the Raman mode softening of the 2D α-MoO_3 as compared with those of the bulk crystal. We have attributed the observed changes, via theoretical calculations, to an anisotropic in-plane strain relaxation or redistribution. Further dedicated experiments are needed to validate the strain evolutions upon thickness reductions of 2D α-MoO_3.

Hybrids of 2D TMDCs and 2D α-MoO_3 have also been presented and discussed based on reactive magnetron sputtering growth 2D WS_2/MoS_2 heterostructures and wet-chemical process of 2D MoS_2–MoO_3 composite films. Metal targets and sulphur powder were installed in the sputtering reactor for supplying the reaction species while the wet-chemical method is based on lithium ions intercalation and chemical exfoliation of MoS_2 powders. XPS studies revealed that the 2D heterostructure with a single-layer WS_2 monotonically grown on a single-layer MoS_2 forms a type-II heterojunction; the offsets in the conduction and valance bands of the 2D WS_2/MoS_2 heterostructure are 0.41 and 0.25 eV, respectively. The XPS, XRD and Raman scattering studies of the 2D MoS_2–MoO_3 nanosheets composites revealed that they consist of 1T-MoS_2, 2H-MoS_2 and MoO_3 at a weight ratio of 1:4.6:2.5. The inclusions of 1T-phase MoS_2 are due to the chemical process induced 2H-to-1T phase changes of MoS_2 while those of MoO_3 are due to partial oxidations of the MoS_2 nanosheets.

To demonstrate the optoelectronic application of the 2D MoS_2–MoO_3 nanosheets composite, we have coated them on flexible cellulose ester membranes followed by inkjet-printing of PEDOT:PSS electrodes to fabricate a photodetector. The ohmic contact between the composite and the PEDOT:PSS electrodes of the fabricated

photodetector can be improved by annealing at 100 °C for 30 min. The fabricated photodetector was tested under laser illuminations at the wavelength of 405, 532 and 650 nm, respectively. The results demonstrated high sensitivities of the designed cellulose membrane-supported 2D MoS_2–MoO_3 nanosheets composite film in response to the specific illuminations at certain wavelengths. The test of device bending for up to 600 cycles does not show any significant performance degradations, demonstrating the desired flexibility and robustness for potential applications in wearable electronics. Nevertheless, the device structures and the material qualities of the 2D nanosheets composite, including its phase structures and chemical compositions, are the key factors that could be optimized to further improve the device performance.

References

1. P. Miró, M. Ghorbani-Asl, T. Heine, Adv. Mater. **25**, 5473 (2013)
2. K.S. Novoselov, A.K. Geim, S.V. Morozov, D. Jiang, Y. Zhang, S.V. Dubonos, I.V. Grigorieva, A.A. Firsov, Science **306**, 666 (2004)
3. W. Guo, X. Liu, Nat. Nanotechnol. **9**, 413 (2014)
4. G.S. Duesberg, Nat. Mater. **13**, 1075 (2014)
5. A.K. Geim, K.S. Novoselov, Nat. Mater. **6**, 183 (2007)
6. Y. Gong, J. Lin, X. Wang, G. Shi, S. Lei, Z. Lin, X. Zou, G. Ye, R. Vajtai, B.I. Yakobson, H. Terrones, M. Terrones, B.K. Tay, J. Lou, S.T. Pantelides, Z. Liu, W. Zhou, P.M. Ajayan, Nat. Mater. **13**, 1135 (2014)
7. D. Jariwala, T.J. Marks, M.C. Hersam, Nat. Mater. **16**, 170 (2016)
8. H. Liu, A.B. Chew, L.K. Tan, J. Teng, D. Chi, J. Vac. Sci. Technol. A **34**, 021517 (2016)
9. K.S. Novoselov, D. Jiang, F. Schedin, T.J. Booth, V.V. Khotkevich, S.V. Morozov, A.K. Geim, Proc. Natl. Acad. Sci. U.S.A. **102**, 10451 (2005)
10. A. Molle, J. Goldberger, M. Houssa, Y. Xu, S.-C. Zhang, D. Akinwande, Nat. Mater. **16**, 163 (2017)
11. Z. Hu, T. Niu, R. Guo, J. Zhang, M. Lai, J. He, L. Wang, W. Chen, Nanoscale **10**, 21575 (2018)
12. B. Liu, M. Köpf, A.N. Abbas, X. Wang, Q. Guo, Y. Jia, F. Xia, R. Weihrich, F. Bachhuber, F. Pielnhofer, H. Wang, R. Dhall, S.B. Cronin, M. Ge, X. Fang, T. Nilges, C. Zhou, Adv. Mater. **27**, 4423 (2015)
13. O. Osters, T. Nilges, F. Bachhuber, F. Pielnhofer, R. Weihrich, M. Schöneich, P. Schmidt, Angew. Chem. Int. Ed. **51**, 2994 (2012)
14. Y. Cai, G. Zhang, Y.-W. Zhang, Sci. Rep.**4**, 6677 (2014)
15. S. Manzeli, D. Ovchinnikov, D. Pasquier, O.V. Yazyev, A. Kis, Nat. Rev. Mater. **2**, 17033 (2017)
16. Y. Zhan, Z. Liu, S. Najmaei, P.M. Ajayan, J. Lou, Small **8**, 966 (2012)
17. Y.-C. Lin, W. Zhang, J.-K. Huang, K.-K. Liu, Y.-H. Lee, C.-T. Liang, C.-W. Chu, L.-J. Li, Nanoscale **4**, 6637 (2012)
18. H. Liu, K.K.A. Antwi, S. Chua, D. Chi, Nanoscale **6**, 624 (2014)
19. H. Liu, K. K. Ansah Antwi, J. Ying, S. Chua, and D. Chi, Nanotechnology **25,** 405702 (2014)
20. Y.-H. Lee, X.-Q. Zhang, W. Zhang, M.-T. Chang, C.-T. Lin, K.-D. Chang, Y.-C. Yu, J.T.-W. Wang, C.-S. Chang, L.-J. Li, T.-W. Lin, Adv. Mater. **24**, 2320 (2012)
21. H. Liu, D. Chi, Sci. Rep. **5**, 11756 (2015)
22. W. Yang, H. Kawai, M. Bosman, B. Tang, J. Chai, W.L. Tay, J. Yang, H.L. Seng, H. Zhu, H. Gong, H. Liu, K.E.J. Goh, S. Wang, D. Chi, Nanoscale **10**, 22927 (2018)

23. S. Balendhran, J. Deng, J.Z. Ou, S. Walia, J. Scott, J. Tang, K.L. Wang, M.R. Field, S. Russo, S. Zhuiykov, M.S. Strano, N. Medhekar, S. Sriram, M. Bhaskaran, K. Kalantar-zadeh, Adv. Mater. **25**, 109 (2013)
24. A.J. Molina-Mendoza, J.L. Lado, J.O. Island, M.A. Niño, L. Aballe, M. Foerster, F.Y. Bruno, A. López-Moreno, L. Vaquero-Garzon, H.S.J. van der Zant, G. Rubio-Bollinger, N. Agraït, E.M. Pérez, J. Fernández-Rossier, A. Castellanos-Gomez, Chem. Mater. **28**, 4042 (2016)
25. D. Wang, J.-N. Li, Y. Zhou, D.-H. Xu, X. Xiong, R.-W. Peng, M. Wang, Appl. Phys. Lett. **108**, 053107 (2016)
26. H. Liu, Y. Cai, M. Han, S. Guo, M. Lin, M. Zhao, Y. Zhang, D. Chi, Nano Res. **11**, 1193 (2018)
27. H. Liu, C.J.J. Lee, Y. Jin, J. Yang, C. Yang, D. Chi, J. Phys. Chem. C **122**, 12122 (2018)
28. H. Liu, C.J.J. Lee, S. Guo, D. Chi, Langmuir **34**, 14003 (2018)
29. H. Liu, R.B. Yang, W. Yang, Y. Jin, C.J.J. Lee, Appl. Surf. Sci. **439**, 583 (2018)
30. A. Harvey, C. Backes, Z. Gholamvand, D. Hanlon, D. McAteer, H.C. Nerl, E. McGuire, A. Seral-Ascaso, Q.M. Ramasse, N. McEvoy, S. Winters, N.C. Berner, D. McCloskey, J.F. Donegan, G.S. Duesberg, V. Nicolosi, J.N. Coleman, Chem. Mater. **27**, 3483 (2015)
31. X. Wang, Y. Sheng, R.-J. Chang, J.K. Lee, Y. Zhou, S. Li, T. Chen, H. Huang, B.F. Porter, H. Bhaskaran, J.H. Warner, ACS Omega **3**, 7897 (2018)
32. B.J. Carey, J.Z. Ou, R.M. Clark, K.J. Berean, A. Zavabeti, A.S.R. Chesman, S.P. Russo, D.W.M. Lau, Z.-Q. Xu, Q. Bao, O. Kavehei, B.C. Gibson, M.D. Dickey, R.B. Kaner, T. Daeneke, K. Kalantar-Zadeh, Nature Commun.**8**, 14482 (2017)
33. Y. Lin, J.W. Connell, Nanoscale **4**, 6908 (2012)
34. K. Zhang, Y. Feng, F. Wang, Z. Yang, J. Wang, J. Mater. Chem. C **5**, 11992 (2017)
35. H.F. Liu, V. Dixit, N. Xiang, J. Appl. Phys. **99**, 013503 (2006)
36. H.F. Liu, C.S. Peng, E.-M. Pavelescu, S. Karirinne, T. Jouhti, M. Valden, M. Pessa, Appl. Phys. Lett. **82**, 2428 (2003)
37. M. Velický, P.S. Toth, Appl. Mater. Today **8**, 68 (2017)
38. Z. Wang, Q. Jingjing, X. Wang, Z. Zhang, Y. Chen, X. Huang, W. Huang, Chem. Soc. Rev. **47**, 6128 (2018)
39. P. Ajayan, P. Kim, K. Banerjee, Phys. Today **69**, 7 (2016)
40. T. Konishi, S. Tsukamoto, Nanoscale Res. Lett. **5**, 1901 (2010)
41. K.F. Mak, C. Lee, J. Hone, J. Shan, T.F. Heinz, Phys. Rev. Lett. **105**, 136805 (2010)
42. H. Tao, Y. Zhang, Y. Gao, Z. Sun, C. Yan, J. Texter, Phys. Chem. Chem. Phys.**19**, 921 (2017)
43. W. Cao, J. Wang, M. Ma, J. Phys. Chem. Lett. **10**, 981 (2019)
44. J.N. Coleman, M. Lotya, A. O'Neill, S.D. Bergin, P.J. King, U. Khan, K. Young, A. Gaucher, S. De, R.J. Smith, I.V. Shvets, S.K. Arora, G. Stanton, H.-Y. Kim, K. Lee, G.T. Kim, G.S. Duesberg, T. Hallam, J.J. Boland, J.J. Wang, J.F. Donegan, J.C. Grunlan, G. Moriarty, A. Shmeliov, R.J. Nicholls, J.M. Perkins, E.M. Grieveson, K. Theuwissen, D.W. McComb, P.D. Nellist, V. Nicolosi, Science **331**, 568 (2011)
45. G. Guan, S. Zhang, S. Liu, Y. Cai, M. Low, C.P. Teng, I.Y. Phang, Y. Cheng, K.L. Duei, B.M. Srinivasan, Y. Zheng, Y.-W. Zhang, M.-Y. Han, J. Am. Chem. Soc. **137**, 6152 (2015)
46. L. Lin, H. Peng, Z. Liu, Nat. Mater. **18**, 520 (2019)
47. D. Neumaier, S. Pindl, M.C. Lemme, Nat. Mater. **18**, 525 (2019)
48. F. Rahman, T. Ahmed, S. Walia, E. Mayes, S. Sriram, M. Bhaskaran, S. Balendhran, 2D Mater. **4**, 035008 (2017)
49. K.K. Amara, L. Chu, R. Kumar, M. Toh, G. Eda, APL Mater. **2**, 092509 (2014)
50. S. Fan, J. Qiao, J. Lai, H. Hei, Z. Feng, Q. Zhang, D. Zhang, S. Wu, X. Hu, D. Sun, W. Ji, J. Liu, ACS Appl. Mater. Interfaces. **11**, 9213 (2019)
51. H. Park, G.H. Shin, K.J. Lee, S.-Y. Choi, Nanoscale **10**, 15205 (2018)
52. H. Zhu, X. Qin, L. Cheng, A. Azcatl, J. Kim, R.M. Wallace, ACS Appl. Mater. Interfaces. **8**, 19119 (2016)
53. A. Castellanos-Gomez, M. Barkelid, A.M. Goossens, V.E. Calado, H.S.J. van der Zant, G.A. Steele, Nano Lett. **12**, 3187 (2012)
54. L. Hu, X. Shan, Y. Wu, J. Zhao, X. Lu, Sci. Rep. **7**, 15538 (2017)

55. J. Park, M.S. Kim, B. Park, S.H. Oh, S. Roy, J. Kim, W. Choi, ACS Nano **12**, 6301 (2018)
56. K.S. Kim, K.H. Kim, Y. Nam, J. Jeon, S. Yim, E. Singh, J.Y. Lee, S.J. Lee, Y.S. Jung, G.Y. Yeom, D.W. Kim, ACS Appl. Mater. Interfaces. **9**, 11967 (2017)
57. Z.J. Han, A.T. Murdock, D.H. Seo, A. Bendavid, 2D Mater. **5**, 032002 (2018)
58. S. Biccai, S. Barwich, D. Boland, A. Harvey, D. Hanlon, N. McEvoy, J.N. Coleman, 2D Mater. **6**, 015008 (2018)
59. H. Samassekou, A. Alkabsh, M. Wasala, M. Eaton, A. Walber, A. Walker, O. Pitkänen, K. Kordas, S. Talapatra, T. Jayasekera, D. Mazumdar, 2D Mater. **4**, 021002 (2017)
60. J. Tao, J. Chai, X. Lu, L.M. Wong, T.I. Wong, J. Pan, Q. Xiong, D. Chi, S. Wang, Nanoscale **7**, 2497 (2015)
61. W.C. Wong, S.M. Ng, H.F. Wong, W.F. Cheng, C.L. Mak, C.W. Leung, Solid-State Electron.**138**, 62 (2017)
62. Z. Yang, J. Hao, J. Mater. Chem. C **4**, 8859 (2016)
63. J.D. Yao, Z.Q. Zheng, G.W. Yang, Prog. Mater. Sci. 100573 (2019)
64. G. Siegel, Y.P.V. Subbaiah, M.C. Prestgard, A. Tiwari, APL Mater. **3**, 056103 (2015)
65. M.I. Serna, S.H. Yoo, S. Moreno, Y. Xi, J.P. Oviedo, H. Choi, H.N. Alshareef, M.J. Kim, M. Minary-Jolandan, M.A. Quevedo-Lopez, ACS Nano **10**, 6054 (2016)
66. S.M. Poh, S.J.R. Tan, H. Wang, P. Song, I.H. Abidi, X. Zhao, J. Dan, J. Chen, Z. Luo, S.J. Pennycook, A.H. Castro Neto, K.P. Loh, Nano Lett. **18**, 6340 (2018)
67. J. Hall, B. Pielić, C. Murray, W. Jolie, T. Wekking, C. Busse, M. Kralj, T. Michely, 2D Mater. **5**, 025005 (2018)
68. M.-W. Chen, D. Ovchinnikov, S. Lazar, M. Pizzochero, M.B. Whitwick, A. Surrente, M. Baranowski, O.L. Sanchez, P. Gillet, P. Plochocka, O.V. Yazyev, A. Kis, ACS Nano **11**, 6355 (2017)
69. D. Dumcenco, D. Ovchinnikov, K. Marinov, P. Lazić, M. Gibertini, N. Marzari, O.L. Sanchez, Y.-C. Kung, D. Krasnozhon, M.-W. Chen, S. Bertolazzi, P. Gillet, A. Fontcuberta i Morral, A. Radenovic, A. Kis, ACS Nano **9**, 4611 (2015)
70. Z. Cai, B. Liu, X. Zou, H.-M. Cheng, Chem. Rev. **118**, 6091 (2018)
71. W. Hao, C. Marichy, C. Journet, 2D Mater. **6**, 012001 (2018)
72. Y. Kim, J.-G. Song, Y.J. Park, G.H. Ryu, S.J. Lee, J.S. Kim, P.J. Jeon, C.W. Lee, W.J. Woo, T. Choi, H. Jung, H.-B.-R. Lee, J.-M. Myoung, S. Im, Z. Lee, J.-H. Ahn, J. Park, H. Kim, Sci. Rep. **6**, 18754 (2016)
73. H. Liu, J. Mol. Eng. Mater.**04**, 1640010 (2016)
74. H.G. Kim, H.-B.-R. Lee, Chem. Mater. **29**, 3809 (2017)
75. V. Kranthi Kumar, S. Dhar, T.H. Choudhury, S.A. Shivashankar, S. Raghavan, Nanoscale **7**, 7802 (2015)
76. K. Kang, S. Xie, L. Huang, Y. Han, P.Y. Huang, K.F. Mak, C.-J. Kim, D. Muller, J. Park, Nature **520**, 656 (2015)
77. H. Jeong, D.Y. Kim, J. Kim, S. Moon, N. Han, S.H. Lee, O.F.N. Okello, K. Song, S.-Y. Choi, J.K. Kim, Sci. Rep. **9**, 5736 (2019)
78. D. Andrzejewski, M. Marx, A. Grundmann, O. Pfingsten, H. Kalisch, A. Vescan, M. Heuken, T. Kümmell, G. Bacher, Nanotechnology **29**, 295704 (2018)
79. S. Hussain, M.A. Shehzad, D. Vikraman, M.F. Khan, J. Singh, D.-C. Choi, Y. Seo, J. Eom, W.-G. Lee, J. Jung, Nanoscale **8**, 4340 (2016)
80. H. Liu, A. Iskander, N.L. Yakovlev, D. Chi, Mater. Lett. **160**, 491 (2015)
81. H. Liu, Vacuum **154**, 44 (2018)
82. A.L. Elías, N. Perea-López, A. Castro-Beltrán, A. Berkdemir, R. Lv, S. Feng, A.D. Long, T. Hayashi, Y.A. Kim, M. Endo, H.R. Gutiérrez, N.R. Pradhan, L. Balicas, T.E. Mallouk, F. López-Urías, H. Terrones, M. Terrones, ACS Nano **7**, 5235 (2013)
83. J.-G. Song, G.H. Ryu, S.J. Lee, S. Sim, C.W. Lee, T. Choi, H. Jung, Y. Kim, Z. Lee, J.-M. Myoung, C. Dussarrat, C. Lansalot-Matras, J. Park, H. Choi, H. Kim, Nat. Commun. **6**, 7817 (2015)
84. L.K. Tan, B. Liu, J.H. Teng, S. Guo, H.Y. Low, K.P. Loh, Nanoscale **6**, 10584 (2014)
85. J. Cheng, C. Wang, X. Zou, L. Liao, Adv. Opt. Mater. **7**, 1800441 (2019)

86. D. Jariwala, S.L. Howell, K.-S. Chen, J. Kang, V.K. Sangwan, S.A. Filippone, R. Turrisi, T.J. Marks, L.J. Lauhon, M.C. Hersam, Nano Lett. **16**, 497 (2016)
87. R. Degl'Innocenti, L. Xiao, D.S. Jessop, S.J. Kindness, Y. Ren, H. Lin, J.A. Zeitler, J.A. Alexander-Webber, H.J. Joyce, P. Braeuninger-Weimer, S. Hofmann, H.E. Beere, D.A. Ritchie, ACS Photon. **3,** 1747 (2016)
88. J.-K. Huang, J. Pu, C.-L. Hsu, M.-H. Chiu, Z.-Y. Juang, Y.-H. Chang, W.-H. Chang, Y. Iwasa, T. Takenobu, L.-J. Li, ACS Nano **8**, 923 (2014)
89. R. Cheng, D. Li, H. Zhou, C. Wang, A. Yin, S. Jiang, Y. Liu, Y. Chen, Y. Huang, X. Duan, Nano Lett. **14**, 5590 (2014)
90. Q. Bao, K.P. Loh, ACS Nano **6**, 3677 (2012)
91. D. Schall, D. Neumaier, M. Mohsin, B. Chmielak, J. Bolten, C. Porschatis, A. Prinzen, C. Matheisen, W. Kuebart, B. Junginger, W. Templ, A.L. Giesecke, H. Kurz, ACS Photon. **1**, 781 (2014)
92. G. Jo, M. Choe, S. Lee, W. Park, Y.H. Kahng, T. Lee, Nanotechnology **23**, 112001 (2012)
93. M. Yankowitz, J. Jung, E. Laksono, N. Leconte, B.L. Chittari, K. Watanabe, T. Taniguchi, S. Adam, D. Graf, C.R. Dean, Nature **557**, 404 (2018)
94. F. Schwierz, Proc. IEEE **101**, 1567 (2013)
95. F. Schwierz, in *Graphene Transistors—A New Contender for Future Electronics* (2010), p. 1202
96. L. Ju, B. Geng, J. Horng, C. Girit, M. Martin, Z. Hao, H.A. Bechtel, X. Liang, A. Zettl, Y.R. Shen, F. Wang, Nat. Nanotechnol. **6**, 630 (2011)
97. A. Ishikawa, T. Tanaka, Appl. Phys. Lett. **102**, 253110 (2013)
98. S. Ogawa, M. Shimatani, S. Fukushima, S. Okuda, K. Matsumoto, Opt. Express **26**, 5665 (2018)
99. M.M. Furchi, A. Pospischil, F. Libisch, J. Burgdörfer, T. Mueller, Nano Lett. **14**, 4785 (2014)
100. Q.H. Wang, K. Kalantar-Zadeh, A. Kis, J.N. Coleman, M.S. Strano, Nat. Nanotechnol. **7**, 699 (2012)
101. B. Liu, A. Abbas, C. Zhou, Adv. Electron. Mater. **3**, 1700045 (2017)
102. G. Eda, H. Yamaguchi, D. Voiry, T. Fujita, M. Chen, M. Chhowalla, Nano Lett. **11**, 5111 (2011)
103. H.F. Liu, S.L. Wong, D.Z. Chi, Chem. Vap. Deposition **21**, 241 (2015)
104. H.F. Liu, Y.D. Wang, M. Lin, L.T. Ong, S.Y. Tee, D.Z. Chi, RSC Adv. **5**, 48647 (2015)
105. H.F. Liu, K.K.A. Antwi, N.L. Yakovlev, H.R. Tan, L.T. Ong, S.J. Chua, D.Z. Chi, ACS Appl. Mater. Interfaces **6**, 3501 (2014)
106. H.F. Liu, K.K.A. Antwi, Y.D. Wang, L.T. Ong, S.J. Chua, D.Z. Chi, RSC Adv. **4**, 58724 (2014)
107. H. Liu, S. Guo, R.B. Yang, C.J.J. Lee, L. Zhang, ACS Appl. Mater. Interfaces **9**, 26201 (2017)
108. K.R. McClay, P.G. Ellis, Mineral. Mag. **47**, 527 (2018)
109. H.F. Liu, A. Huang, D.Z. Chi, J. Phys. D Appl. Phys. **43**, 455405 (2010)
110. H. Liu, D. Chi, J. Vac. Sci. Technol. A **30**, 04D102 (2012)
111. C. Liu, D. Kong, P.-C. Hsu, H. Yuan, H.-W. Lee, Y. Liu, H. Wang, S. Wang, K. Yan, D. Lin, P.A. Maraccini, K.M. Parker, A.B. Boehm, Y. Cui, Nat. Nanotechnol. **11**, 1098 (2016)
112. D. Kong, H. Wang, J.J. Cha, M. Pasta, K.J. Koski, J. Yao, Y. Cui, Nano Lett. **13**, 1341 (2013)
113. H. Wang, Z. Lu, S. Xu, D. Kong, J.J. Cha, G. Zheng, P.-C. Hsu, K. Yan, D. Bradshaw, F.B. Prinz, Y. Cui, Proc. Natl. Acad. Sci. **110**, 19701 (2013)
114. M. Heuken, A. Grundmann, H. Kalisch, A. Vescan, *Hydride-Free MOCVD of 2D MoS2 and 2D WS2 for Optoelectronic Applications (Conference Presentation)*, Vol. 10940 (SPIE, 2019)
115. S. Cwik, D. Mitoraj, O. Mendoza Reyes, D. Rogalla, D. Peeters, J. Kim, H.M. Schütz, C. Bock, R. Beranek, A. Devi, Adv. Mater. Interfaces **5,** 1800140 (2018)
116. B. Kalanyan, W.A. Kimes, R. Beams, S.J. Stranick, E. Garratt, I. Kalish, A.V. Davydov, R.K. Kanjolia, J.E. Maslar, Chem. Mater. **29**, 6279 (2017)
117. P.L. Gai, Philos. Mag. A **43**, 841 (1981)
118. S. Barber, J. Booth, D.R. Pyke, R. Reid, R.J.D. Tilley, J. Catal. **77**, 180 (1982)
119. Z. Li, Y. Li, E. Zhan, N. Ta, W. Shen, J. Mater. Chem. A **1**, 15370 (2013)

120. M. Kröger, S. Hamwi, J. Meyer, T. Riedl, W. Kowalsky, A. Kahn, Org. Electron. **10**, 932 (2009)
121. Y. Nakayama, K. Morii, Y. Suzuki, H. Machida, S. Kera, N. Ueno, H. Kitagawa, Y. Noguchi, H. Ishii, Adv. Func. Mater. **19**, 3746 (2009)
122. Z. Chen, I. Santoso, R. Wang, L.F. Xie, H.Y. Mao, H. Huang, Y.Z. Wang, X.Y. Gao, Z.K. Chen, D. Ma, A.T.S. Wee, W. Chen, Appl. Phys. Lett. **96**, 213104 (2010)
123. L. D'Arsié, S. Esconjauregui, R. Weatherup, Y. Guo, S. Bhardwaj, A. Centeno, A. Zurutuza, C. Cepek, J. Robertson, Appl. Phys. Lett. **105**, 103103 (2014)
124. M. Kröger, S. Hamwi, J. Meyer, T. Riedl, W. Kowalsky, A. Kahn, Appl. Phys. Lett. **95**, 123301 (2009)
125. L. Cai, C.J. McClellan, A.L. Koh, H. Li, E. Yalon, E. Pop, X. Zheng, Nano Lett. **17**, 3854 (2017)
126. M.B. Sreedhara, A.L. Santhosha, A.J. Bhattacharyya, C.N.R. Rao, J. Mater. Chem. A **4**, 9466 (2016)
127. S. Balendhran, S. Walia, H. Nili, J.Z. Ou, S. Zhuiykov, R.B. Kaner, S. Sriram, M. Bhaskaran, K. Kalantar-zadeh, Adv. Func. Mater. **23**, 3952 (2013)
128. M. Epifani, P. Imperatori, L. Mirenghi, M. Schioppa, P. Siciliano, Chem. Mater. **16**, 5495 (2004)
129. M. Chen, C.M. Friend, E. Kaxiras, J. Am. Chem. Soc. **123**, 2224 (2001)
130. S. Yazdani, R. Kashfi-Sadabad, T.D. Huan, M.D. Morales-Acosta, M.T. Pettes, Langmuir **34**, 6296 (2018)
131. R. Naouel, H. Dhaouadi, F. Touati, N. Gharbi, Nano-Micro Lett. **3**, 242 (2011)
132. H.-U. Kim, J. Son, A. Kulkarni, C. Ahn, K.S. Kim, D. Shin, G.Y. Yeom, T. Kim, Nanotechnology **28**, 175601 (2017)
133. R. Kashfi-Sadabad, S. Yazdani, T.D. Huan, Z. Cai, M.T. Pettes, J. Phys. Chem. C **122**, 18212 (2018)
134. A. Borgschulte, O. Sambalova, R. Delmelle, S. Jenatsch, R. Hany, F. Nüesch, Sci. Rep. **7**, 40761 (2017)
135. K. Eda, J. Solid State Chem. **98**, 350 (1992)
136. L.A. Bursill, J.S. Anderson, Proc. R. Soc. Lond. A Math. Phys. Sci. **311**, 267 (1969)
137. R. L. Smith, Thesis, Carnegie Mellon University, 1998
138. R.L. Smith, G.S. Rohrer, J. Catal. **173**, 219 (1998)
139. C.-H. Ho, Y.-C. Chen, RSC Adv. **3**, 24896 (2013)
140. L. Lajaunie, F. Boucher, R. Dessapt, P. Moreau, Phys. Rev. B **88**, 115141 (2013)
141. H.F. Liu, S.J. Chua, J. Appl. Phys. **106**, 023511 (2009)
142. H.F. Liu, H.L. Seng, J.H. Teng, S.J. Chua, D.Z. Chi, J. Cryst. Growth **402**, 155 (2014)
143. H.F. Liu, S.B. Dolmanan, L. Zhang, S.J. Chua, D.Z. Chi, M. Heuken, S. Tripathy, J. Appl. Phys. **113**, 023510 (2013)
144. A. Pant, Z. Mutlu, D. Wickramaratne, H. Cai, R.K. Lake, C. Ozkan, S. Tongay, Nanoscale **8**, 3870 (2016)
145. W.-T. Hsu, Z.-A. Zhao, L.-J. Li, C.-H. Chen, M.-H. Chiu, P.-S. Chang, Y.-C. Chou, W.-H. Chang, ACS Nano **8**, 2951 (2014)
146. S.L. Wong, H. Liu, D. Chi, Prog. Cryst. Growth Charact. Mater. **62**, 9 (2016)
147. C. Tan, X. Cao, X.-J. Wu, Q. He, J. Yang, X. Zhang, J. Chen, W. Zhao, S. Han, G.-H. Nam, M. Sindoro, H. Zhang, Chem. Rev. **117**, 6225 (2017)
148. M.Z. Bellus, F. Ceballos, H.-Y. Chiu, H. Zhao, ACS Nano **9**, 6459 (2015)
149. H. Fang, C. Battaglia, C. Carraro, S. Nemsak, B. Ozdol, J.S. Kang, H.A. Bechtel, S.B. Desai, F. Kronast, A.A. Unal, G. Conti, C. Conlon, G.K. Palsson, M.C. Martin, A.M. Minor, C.S. Fadley, E. Yablonovitch, R. Maboudian, A. Javey, Proc. Natl. Acad. Sci. **111**, 6198 (2014)
150. Y. Gong, S. Lei, G. Ye, B. Li, Y. He, K. Keyshar, X. Zhang, Q. Wang, J. Lou, Z. Liu, R. Vajtai, W. Zhou, P.M. Ajayan, Nano Lett. **15**, 6135 (2015)
151. H.F. Liu, C.C. Tan, G.K. Dalapati, D.Z. Chi, J. Appl. Phys. **112**, 063114 (2012)
152. H.F. Liu, S.J. Chua, G.X. Hu, H. Gong, N. Xiang, J. Appl. Phys. **102**, 083529 (2007)
153. H.F. Liu, G.X. Hu, H. Gong, K.Y. Zang, S.J. Chua, J. Vac. Sci. Technol. A **26**, 1462 (2008)

154. H. F. Liu, K.K. Ansah Antwi, C.S. Chua, J. Huang, S.J. Chua, D.Z. Chi, ECS Solid State Lett. **3**, P131 (2014)
155. Y. Wei, V.-T. Tran, C. Zhao, H. Liu, J. Kong, H. Du, ACS Appl. Mater. Interfaces **11**, 21445 (2019)
156. Z. Yin, X. Zhang, Y. Cai, J. Chen, J.I. Wong, Y.-Y. Tay, J. Chai, J. Wu, Z. Zeng, B. Zheng, H.Y. Yang, H. Zhang, Angew. Chem. Int. Ed. **53**, 12560 (2014)
157. Y. Yu, G.-H. Nam, Q. He, X.-J. Wu, K. Zhang, Z. Yang, J. Chen, Q. Ma, M. Zhao, Z. Liu, F.-R. Ran, X. Wang, H. Li, X. Huang, B. Li, Q. Xiong, Q. Zhang, Z. Liu, L. Gu, Y. Du, W. Huang, H. Zhang, Nat. Chem. **10**, 638 (2018)
158. D.-S. Tsai, K.-K. Liu, D.-H. Lien, M.-L. Tsai, C.-F. Kang, C.-A. Lin, L.-J. Li, J.-H. He, ACS Nano **7**, 3905 (2013)
159. J. Li, M.M. Naiini, S. Vaziri, M.C. Lemme, M. Östling, Adv. Func. Mater. **24**, 6524 (2014)
160. Y. Lee, J. Yang, D. Lee, Y.-H. Kim, J.-H. Park, H. Kim, J.H. Cho, Nanoscale **8**, 9193 (2016)
161. G. Cunningham, U. Khan, C. Backes, D. Hanlon, D. McCloskey, J.F. Donegan, J.N. Coleman, J. Mater. Chem. C **1**, 6899 (2013)

Optoelectronic Properties of Nanocrystalline Silicon-Based Superlattice Structures

Pratima Agarwal and Asha Yadav

Abstract Superlattice structures consist of alternate layers of two different materials, each having a fixed thickness. These structures thus have an additional periodicity along the growth direction and thus behave like a quasi-crystal with a periodicity much larger than that in single-crystal materials having a periodicity of the order of lattice constant of crystal and exhibit several interesting phenomena. The optical, electrical and other physical properties of these structures are significantly different from those of individual layers. In the present article, we present some interesting experimental results observed for nc-Si/a-Si:H-based superlattice structures. Though the lattice constant and electron affinity of nc-Si/a-Si:H are nearly matched, their structural, electrical and optical properties are significantly different. Our studies show that the electrical transport properties of these structures can be tuned by controlling the thickness of the individual layer. The superlattice structures with thick individual layers show excess conductivity in dark after exposure to light. On the other hand, strong photoluminescence (PL) signal in the visible range is observed for the structures with thin individual layers and the PL peak energy depends upon the thickness of the nc-Si layer. The nc-Si/a-Si:H superlattice structures can be used for silicon-based photonic devices in the integrated circuits.

1 Introduction

Superlattice structures are a new class of materials, which consists of alternate layers of two different materials each having a fixed thickness. The unit building block of these superlattice structures is a set of two layers, and the structure is formed by periodically repeating this building block along one direction (Fig. 1). The structures thus behave as quasi-crystal with a periodicity which is much larger than the lattice constant of the individual layer. The two layers in these materials are typically a few nanometers thin along the direction of the superlattice growth, whereas in the

P. Agarwal (✉) · A. Yadav
Department of Physics and Center for Energy, Indian Institute of Technology Guwahati, Guwahati 781039, India
e-mail: pratima@iitg.ac.in

S. Kumar and D. K. Aswal (eds.), *Recent Advances in Thin Films*, Materials Horizons: From Nature to Nanomaterials, https://doi.org/10.1007/978-981-15-6116-0_9

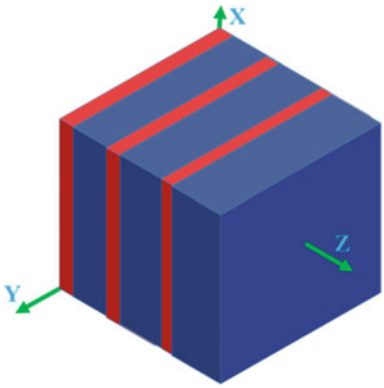

Fig. 1 Schematic of a superlattice structure

other two dimensions these could be infinitely large (a few mm or cm). This way, the transport of charge carries is anisotropic and the electrical properties can be tuned by choosing the thickness of the individual layer. The optoelectronic properties of these quasi-crystals are very different than those of individual layers. These structures have attracted the attention of both the theorist as well experimentalist due to their unique and tunable properties.

The semiconductor superlattice structures can be divided into two classes, (i) Compositional superlattice (heterogeneous) structures, where the alternate layers are made of two different semiconductors, having different band gaps, electron affinity, etc. and (ii) doping-modulated (homogeneous) structures, where the individual layers are differently doped semiconductor (variation in dopant type or doping concentration), for example, n-p-n-p-…, n-i-n-i-… or p-i-p-i.. structures. In the first case (heterogeneous structures), the conduction and valance band edges are discontinuous at the interface, whereas in the other case (homogeneous structures), though there is a band bending at the interface, both Ec and Ev remain continuous. In both cases, a potential well/potential barrier structure for carriers is formed. Most of these structures are fabricated using semiconductors having nearly similar lattice constant thus avoiding the interfacial strain and defects, which influence the carrier transport. A number of superlattice structures have also been fabricated with the amorphous semiconductor to study their transport and optical properties.

The superlattice structures have attracted the attention of both theorists and experimentalists due to their unique and tunable properties. The theoretical studies on compositional superlattice semiconductors have predicted many interesting phenomena such as Wannier stark hopping, sequential and resonant electron tunnelling, Bloch oscillations, Fabry–Perot Oscillations, enhanced conductivity and metal–insulator transition [1–7].

Doping-modulated superlattice structures (homogeneous), consisting of periodically varying the dopant type or concentration, such as n-i-p-i.. or n-p-n-p structures have also been studied both theoretically as well experimentally [8–10]. Such superlattice structures are free from band discontinuity at the interface. Some other interesting experimental phenomena observed for these semiconductor superlattice

structures include the persistent photoconductivity [10–12], tunable visible photoluminescence [13, 14] and electroluminescence [14, 15], tunable absorption coefficient [16] which arise due to spatial separation of electrons and hole, carrier confinement and spatially modulated energy band gap. Semiconductor superlattice structures have also been proposed as semiconductor parametric oscillators for sub-terahertz and terahertz radiation source [17], mid-infrared detector [7], infrared screen projector system [18]. Most of these studies are performed on III-V compound superlattice structures such as GaAs/GaAlAs, InAs/GaSb.

In addition to semiconductor superlattice structures, similar periodic structures could also be formed using alternate layers of materials of different refractive index or alternate layers of materials having different elastic constants. All these structures exhibit interesting optical, mechanical and electronic properties, which include extremely high carrier mobility, enhanced optical properties, high photosensitivity, low thermal conductivity, high transmittance, etc. which can be tuned by carefully choosing the thickness, band gap, doping or refractive index of the constituent layers. The superlattice structures made of different refractive index layers are used as Dielectric Bragg Mirrors [19] and exhibit photon equivalent of Bloch oscillations of electrons in the crystal lattice. Another interesting superlattice structure made of alternate metal and insulator layers has been proposed for high-speed transistor [20, 21]. Metal–semiconductor superlattice structures have also been proposed as thermionic refrigerators for integrated cooling of optoelectronic devices [22, 23].

With the advancement of the thin-film technology, which allows the growth of an atomically smooth thin layer of materials, it is possible to fabricate such multilayer structures with high precision for high-speed optoelectronic and photonic devices. A number of techniques are used to fabricate such structures such as molecular beam epitaxy, co-evaporation and co-sputtering, Pulsed laser deposition, radio frequency-Plasma Enhanced Chemical Vapour Deposition (rf-PECVD), hot wire chemical vapour deposition (HWCVD), low-pressure CVD, ion implantation, etc. Using these techniques, it is possible to fabricate semiconductor superlattice structures showing desirable optoelectronic properties, by carefully choosing the composition, doping profile and thickness of individual layers. The variation in one or more of these parameters changes the width or height of the potential well and the optoelectronic properties can be tuned due to carrier confinement and spatial separation of electron and holes in different layers. In these structures, the electron transport is anisotropic and optoelectronic properties are very different when measured in a direction, parallel or perpendicular to these layers. It is also possible to tailor the effective refractive index and optical transmission and reflection of these structures as well as the absorption coefficient.

In the past two decades, a lot of research efforts are focused on semiconductor nanostructures due to their tunable optoelectronic transport and luminescent properties. Among these, nanostructures made of silicon such as porous silicon and ultrathin nanocrystalline silicon films, are particularly of more interest because they exhibit visible photoluminescence. Bulk silicon is an indirect band gap material with an energy band gap of 1.1 eV, and thus exhibits a very poor luminescence signal in the infrared range, which restricts its use in photonics industries in spite of being the

most favourite material for the microelectronics industry and solar cell industry. The efficient visible photoluminescence in porous silicon prepared by electrochemical etching [24], suggested that it is possible to make silicon-based photonic devices if the size of the Si crystal is reduced significantly to the nano-dimension level. Other Si nanostructures have also shown photoluminescence in the visible range of electromagnetic spectra [14, 15, 25, 26]. The reduction in the size of Si crystals not only increases the band gap of Si but also relaxes the k-selection rule allowing the direct band to band transition. The peak emission wavelength of these transitions can be controlled by controlling the size of the Si nanocrystals. This discovery of light emission from nc-Si is an important breakthrough in the scientific research community since it has opened a new possibility of synthesis of Si-based light-emitting electronic devices. Si nanocrystals offer a viable pathway for the fabrication of direct band gap materials with tunable band gap depending upon the size of the Si nanocrystallites. Various methods have been employed to produce ultra-fine silicon nanocrystals such as low-pressure chemical vapour deposition, laser ablation, electrochemical anodization, rf-magnetron sputtering, rf-PECVD, microwave CVD, gas-phase synthesis, etc.

Another method to produce Si nanocrystals with the controlled size is by fabricating multilayer structures such as a-Si/SiO_2, nc-Si/SiO_2, Si/SiO_2, etc. in which a very thin layer of Si is sandwiched between two layers of other materials such as SiO_2 or SiN_x [14, 25, 27]. The entire structure is subsequently annealed at high temperature to form Si nanocrystals embedded in an amorphous matrix. In such structures, SiO_2 acts as a good size controlling layer, however due to large band offset between Si and SiO_2, which influences the carrier transport, this is not a very suitable material for device application. A superlattice structure with lower band offset such as a-Si:H/nc-Si:H is desirable to increase carrier mobility for high-speed thin-film transistors. Large photocurrent enhancement is also reported in these a-Si:H/nc-Si:H superlattice structures [16]. The optical absorption enhancement from photonic and plasmonic effects has also been reported by several groups in the nanostructured a-Si:H and nc-Si:H thin film [16].

In the present article, we present some interesting experimental results observed for nc-Si/a-Si:H-based superlattice structures [13, 28, 29]. We have chosen this system because it is easier to fabricate these structures by tuning the deposition parameters in an rf-PECVD or HWCVD system. Further, the lattice constant and electron affinity for the two layers are nearly matched, though their optical absorption and electrical conductivity could be very different. The presence of atomic hydrogen during the deposition of such structures passivates the interfacial and coordination defects. These structures have shown nanophotonic and nanoplasmonic enhancements in thin-film silicon solar cells [16]. The article also includes a brief discussion on the band structure, electronic transport and optoelectronic properties of semiconductor superlattice structure and dielectric superlattice structures.

1.1 Electronic Band Structure and Electrical Transport in Superlattice Structures

Figure 2 shows the conduction and valence band bending for a number of heterogeneous semiconductor junctions. When a superlattice structure (Fig. 3a) is fabricated using these heterogeneous semiconductors (composition modulated semiconductor superlattice structures), the band bending and charge accumulation may vary depending upon the band gap and electron affinity of the two semiconductors. In these structures, the carriers are confined in the narrow regions and if the widths of the constituent layers are comparable to the electron mean free path, the entire electron system may behave as a quantum system in presence of nearly ideal interfaces.

In case of compositional superlattice structures, the alternate layers of low and high band gap materials impose an additional periodic potential with a period much larger than that of the lattice potential. The conduction band energy diagram for a free electron appears to be similar to the periodic potential seen by an electron in the crystal lattice, with the lattice constant ***a*** being replaced by the periodicity ***d*** of the superlattice. The periodic spatial variation of Ec in these superlattice structures results in the formation of energy bands (mini bands) in the conduction band having width and separation as shown in Fig. 3b. The energy width Δ of these mini bands

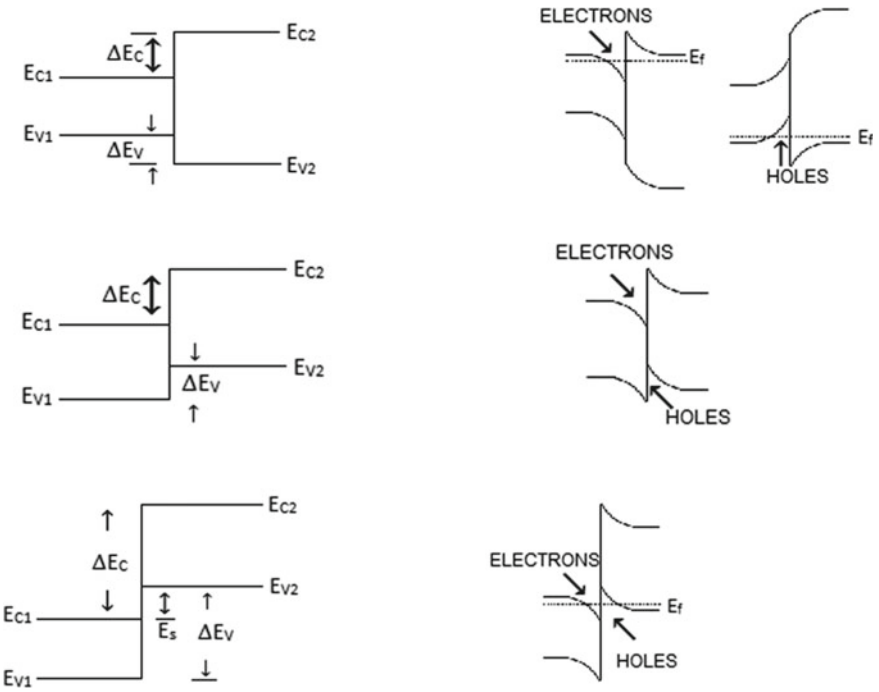

Fig. 2 Band bending at the junction of two different semiconductors

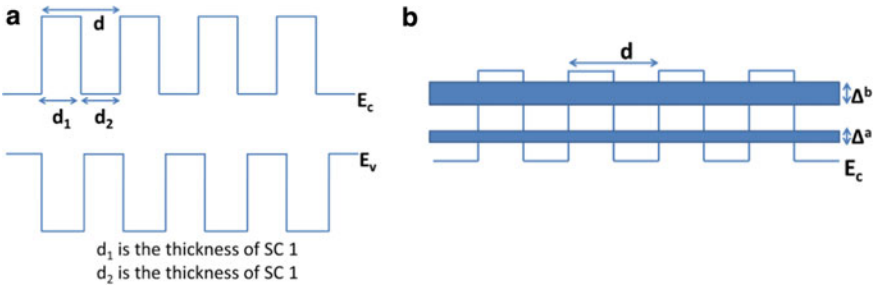

Fig. 3 **a** Schematic compositional superlattice structure, **b** formation of minibands in conduction band in these compositional superlattice structures

and the extension $2\pi/d$ of Brillouin zone in case of superlattice structure are now much smaller than the bandwidth and $2\pi/a$, the extension of Brillouin zone in the crystal lattice as lattice constant $a << d$, the periodicity in superlattice structure. Also as $d \gg a$, the Bloch Oscillations time ($\sim h/eEd$) is much smaller compared to the corresponding scattering time (h/eEa) in crystal lattice, where E is the external electric field. The thickness of individual layers govern the band structure and thus the electron transport and mobility of charge carriers.

When an external electric field is applied to the superlattice structures along the z-direction, the conduction band and minibands in these structures bend the same way as Ec and Ev for any semiconductor, as shown in Fig. 4. and electric current flows through it along the direction of the electric field. The magnitude of the current is determined by the band structure of the semiconductor, scattering process, external electric field strength as well as equilibrium carrier distribution. For low electric field, the current is linearly proportional to the electric field, however, when the field is high, the scattering processes may dominate resulting in the non-linear variation of current with applied electric field and phenomenon such as Wannier stark hoping and sequential tunnelling are observed [1–3].

In case of homogenous/doping-modulated superlattice structures, such as p-n-p-n layers, the band diagram is slightly different than what is discussed above. The most important feature of these structures is that the band edges are continuous unlike the compositional superlattice structures. The periodic variation in doping results in bending of bands as shown in Fig. 5. The interface between the individual layers is

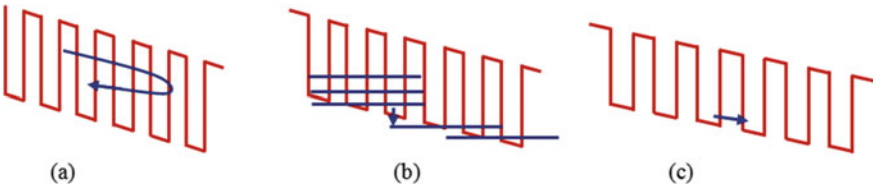

Fig. 4 Carrier transport in superlattice structures **a** miniband conduction, **b** Wannier stark hopping, **c** sequential tunnelling

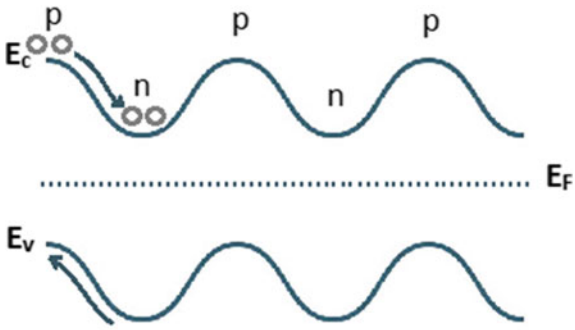

Fig. 5 Band bending at the interfaces between doping-modulated semiconductors

now depleted of free carriers (electrons and holes). The periodic variation in potential in such structures arise due to immobile ionized dopants in the depletion region and is electrostatic in nature, which is partially compensated by the free electrons and holes in the n- and p-doped regions, respectively. The maxima of the valance band and minima of the conduction band in such superlattice structures are spatially separated and the structures seem to have an indirect band gap in real space with the band gap value smaller than the parent semiconductor (Fig. 5). The optical band gap and optical absorption can thus be tuned by tuning the doping concentration and the period of superlattice structure. The effective band gap of these superlattice structures is smaller than that of unmodulated semiconductor material [10]. Under illumination, the photogenerated electrons and holes are spatially separated due to inbuilt potential reducing the recombination probability very significantly. It is also possible to alter the electron and hole concentration in these structures by carrier injection or extraction via an appropriate lateral electrode [9]. The photogenerated as well injected charge carriers have a very large lifetime and strong photoluminescence and electroluminescence signals are observed [16]. The structures also show interesting phenomenon such as persistent photoconductivity [10–12, 30–32].

1.2 Persistent Photoconductivity in Doping-Modulated Superlattice Structures

An interesting phenomenon exhibited by the doping-modulated superlattice structure is higher dark conductivity after brief exposure to illumination (Fig. 6). The phenomenon is termed as persistent photoconductivity as the current after cutting off the illumination does not fall back the equilibrium dark value instantaneously, rather decays slowly and takes a long time, a few minutes to a few hours, to return to the equilibrium dark value. The excess dark current is a fraction of photocurrent in the presence of illumination. In other words, the phenomenon suggests that in this case, recombination life time of a fraction of photogenerated electron–hole pair is enhanced which shows up as enhanced carrier concentration and thus larger current

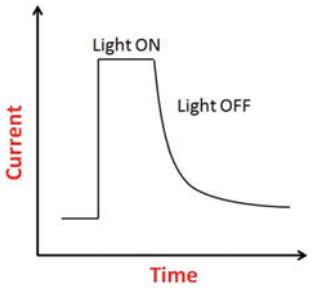

Fig. 6 Schematic diagram showing the PPC in semiconductors

in dark. The phenomenon has been observed for a number of superlattice structures such as doping-modulated GaAs [10, 30] and a-Si:H [12, 31, 32]-based superlattice structures. The phenomenon has also been reported for composition modulated GaAs/GaAlAs superlattice structures and some other thin films like CdS [33, 34], ZnCdSe [35, 36], CdSSe [36], Zn0 **[**37**],** nanowires, porous Silicon [38], compensated a-Si:H films [31], etc. In case of doping-modulated GaAs structures, the PPC was observed at low temperature (4 K) and it persists for several hours. Whereas for a-Si:H-based doped superlattice structures, PPC was observed even at room temperature. In case of compositionally modulated GaAs/$Ga_{0.7}Al_{0.3}As$, it was observed at 4.2 K and 77 K. For GaAs, PPC is believed to arise due to spatial separation of photogenerated e-h pair as a result of band bending, which delays their recombination. In case of doping-modulated a-Si:H n-p-n-p structure, centres created by Phosphorus–Boron complexes trap the carriers, as these are in poor communication with rest of materials, and a higher current is observed after cutting off the illumination. Whereas in case of n-i-p-i structures, the holes are trapped in the acceptor like centres (AX) in the p-type regions and leave behind electrons in n-type region which results in observed PPC. The presence of dangling bonds is also believed to be responsible for the observed PPC in amorphous p-n-p-n structures. In all these a-Si:H-based superlattice structures, the observed PPC is attributed to one or more of the following: (i) presence of random local potential fluctuation arising due to compositional inhomogeneities [32], (ii) p-n junction field at the interface causing the photogenerated electron–hole pair to spatially separate before these recombine [32], (iii) presence of defect centres which capture electrons and present a barrier against the re-trapping of photoexcited carriers [12]. For several other systems, the PPC is assigned to the trapping of charge carriers in the defect states. The excess current in all these cases initially falls of rapidly followed by a slow non-linear decay. The initial rapid decay is due to the recombination of closely spaced carriers, whereas the non-linear slow decay is due to de-trapping of carriers and subsequent recombination [39].

1.3 Photoluminescence in Semiconductor Superlattice Structures

An interesting phenomenon observed for superlattice structures is tunable photoluminescence in visible and near-infrared range [40–42]. A red shift in peak emission wavelength is reported for the AlAs/GaAs superlattice structures, grown by molecular beam epitaxy, when the thickness of the GaAs layer is increased. The emission peak position for these structures is at a lower wavelength as compared to bulk GaAs. The FWHM of the main emission peak is also observed to be smaller than for bulk GaAs due to the stepwise density of states in these one-dimensional quantum wells [40, 41]. Shih et al. [40] reported two distinct peaks in the PL spectra of AlAs/GaAs superlattice structures at 4 K, which are attributed to transitions involving light and heavy holes. The position of these emission peaks shifts to a higher wavelength when the thickness of the AlAs layer is increased keeping the GaAs layer thickness constant. In these superlattice structures, essentially a periodic quantum well is formed in the GaAs layer as the band gap of AlAs is more than that of GaAs. In these structures, the carriers are confined in one-dimensional quantum well and thus its energy states are raised beyond the band gap of corresponding bulk semiconductors. The emission wavelength is controlled by controlling the width of the quantum well [40, 41]. In case of doping-modulated (Sn-doped AlAs/GaAs) superlattice structures, the PL peak energy (wavelength) is also found to depend upon the doping concentration, PL peak is blue shifted when the doping concentration is reduced [41, 42]. Photoluminescence has also been reported in Si/SiO_2, Si/Si_3N_4, SiO/SiO_2, and silicon-rich nitride/ultrathin silicon nitride superlattice structures. In all these structures, the thermal annealing at high temperatures led to the formation of nc-Si resulting in broad PL peak around 500–900 nm [14, 25, 27, 43, 44]. Tunable PL has also been observed in ZnS/ZnSe based superlattice structures [45]. It has been shown that the PL peak position depends upon the layer thickness as well as annealing temperature.

1.4 Optical Properties of Dielectric Superlattice Structures

Another interesting feature of the superlattice structures is that the optical transmission and reflection in such structures can be tuned. Figure 7 shows the propagation of electromagnetic waves through such structures. When an electromagnetic wave propagates through such structures, partial reflection and transmission takes place at each interface due to mismatch in the refractive index. The amplitude of resultant transmitted or reflected wave depends upon the reflection and transmission coefficient as well as the phase difference introduced by each of these layers. The specular reflectance and transmittance of these structures can be calculated using transfer matrix method [46–48].

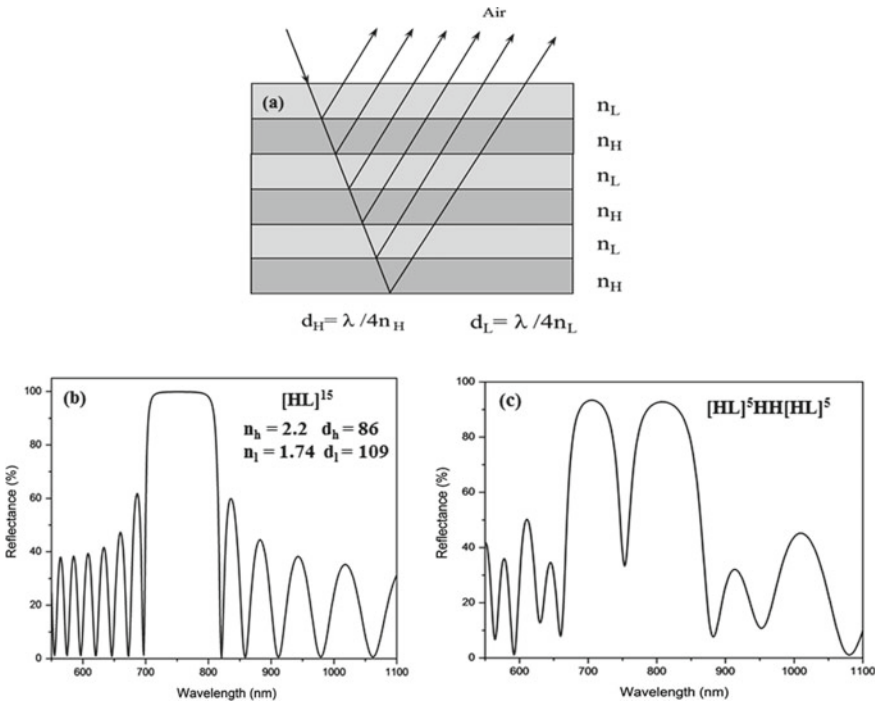

Fig. 7 **a** Light propagation through a multilayer structure made of different refractive index layers, **b** the reflectance spectra of a 15 period multilayer structure, **c** drop in reflectance at centre of band when an extra high refractive index layer is introduced. (The refractive index, thickness of individual high[H] and low[L] refractive index layer and complete structure is mentioned in the figure) [49]

If thickness and refractive index are adjusted such that $n_1 d_1 = n_2 d_2 = \lambda/4$, reflectance is significantly enhanced for a narrow band around λ, as shown in Fig. 7 [49]. In such structures, the number of layers defines the maximum reflectance, whereas the width is controlled by the mismatch between the refractive index of two layers. Inserting an extra layer of low or high refractive index results in a sharp dip in reflectance at that λ (Fig. 7) and if using a femtosecond laser, the oscillations equivalent to Bloch oscillations of electrons in crystal lattice can be seen. These structures behave as one-dimensional photonic crystals and are known as dielectric Bragg mirrors. The region of high reflectance is terms as photonic band gap.

2 Materials and Methods

To study the electronic transport and optical properties of a-Si:H/nc-Si:H-based superlattice structures, we fabricated a number of such superlattice structures by varying the thickness of a-Si:H and nc-Si:H layers using both HWCVD and rf-PECVD techniques. The structures having thick individual layers (70 and 175 nm

each) of a-Si:H and nc-Si:H were fabricated using HWCVD techniques whereas for thin (5–30 nm) layers of a-Si:H and nc-Si:H, rf-PECVD technique is used. In HWCVD structures, the bottom layer is a-Si:H and a pair of a-Si:H layer and nc-Si layer is defined as one period. Two such structures consisting of 2 and 5 periods with 70-nm-thick individual layer and one 2 period structure with 175-nm-thick individual layers were studied in detail. The combination was chosen to study the influence of the number of layers with a thickness of individual layer at 70 nm (Case I, total thickness as well as the number of interfaces are different), and influence of thickness of each layer keeping the number of periods same (case II) and total thickness of structure constant (Case III). For rf-PECVD samples, bottom layer was nc-Si and alternate a-Si:H/nc-Si layers were deposited to fabricate the superlattice structure having an extra nc-Si layer at the top of the structure. In these structures fabricated using rf-PECVD, the thickness of nc-Si layer was varied from 5 to 30 nm, keeping the a-Si:H film thickness constant of 10 nm. Figure 8 shows the schematic of the superlattice structure fabricated by both HWCVD and rf-PECVD. These structures were deposited on Corning 1737 Borosilicate glass, undoped c-Si and ITO-coated glass substrates for different measurements. To change the microstructure of the films from amorphous to nanocrystalline silicon, hydrogen and silane flow rates were changed, which resulted in a change in the ratio of two gases. Prior to deposition of superlattice structures, single layer a-Si:H and nc-Si films were deposited to estimate the deposition rate, microstructure, and optical band gap of the films. The deposition parameters of single layer a-Si:H and nc-Si:H films prepared using HWCVD and rf-PECVD samples are listed in Tables 1 and 2. In superlattice structures, the thickness of the individual layer was varied by varying the deposition time only. The details of the thickness of individual layers, number of layers and total thickness of different structures by rf-PECVD are listed in Table 3.

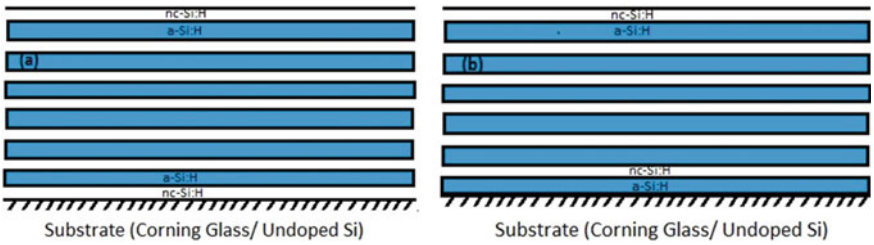

Fig. 8 Schematic of a-Si:H/nc-Si:H superlattice structures **a** rf-PECVD and **b** HWCVD

Table 1 Deposition parameters of single layer of a-Si:H and nc-Si:H thin films prepared using HWCVD technique [28]

Sample no.	P.P (mbar)	SFR (sccm)	HFR (sccm)	[R] (%)	T_s (°C)	T_f (°C)
a-Si:H	0.02	2.7	1	27	200	1900
nc-Si:H	0.2	2.6	15	85		

Table 2 Deposition parameters of single layer of a-Si:H and nc-Si:H thin films prepared using rf-PECVD technique (P.P is process pressure, SFR (sccm) and HFR (sccm) refer to silane and hydrogen flow rates in standard cubic centimetre per min, R is the hydrogen dilution($[H_2]/[H_2] + [SiH_4]$)) [13]

Type	P.P (mbar)	SFR (sccm)	HFR (sccm)	[R] (%)	rf power (W)	T_s (°C)
a-Si:H	0.76	8	10	55	80	250
nc-Si:H	0.68	4	96	96		

Table 3 Deposition parameters of a-Si:H/nc-Si:H superlattice structures thin films using rf-PECVD technique

Sample no.	Thickness (nm) nc-Si/a-Si/total	No. of individual layers nc-Si:H/a-Si:H
PE99	5/10/50	4/3
PE115	10/10/70	4/3
PE137	20/10/110	4/3
PE138	30/10/150	4/3
PE93	20/10/170	6/5

Single-layer films were characterized using X-ray diffraction (XRD) and transmission electron microscope (TEM) to confirm that films are amorphous or nanocrystalline. The microstructure of the films was also confirmed by micro Raman spectroscopy. The band gap of single layer a-Si:H and nc-Si:H was estimated using the Tauc plot from UV–Vis–NIR transmission spectra and the thickness of films were measured using surface profilometer of single-layer films. Electrical characterizations, such as dark and photoconductivity, activation energy were performed on these single-layer films using Ag paste as electrodes in coplanar geometry. The PPC studies were also performed in coplanar geometry, whereas to estimate the density of states (DOS), space-charge-limited current (SCLC) measurements were performed on (ITO/a-Si:H/Ag) and (ITO{a-Si:H/nc-Si:H}$_n$/Ag) in transverse geometry. Keithley 2450 source metre was used for these measurements and 100 W halogen lamp was used for illumination. The photoluminescence measurements were carried out using diode-pumped solid-state laser at an excitation wavelength of 405 nm and laser power 30 W. All these details are given elsewhere also [28, 29, 50].

3 Results and Discussion

3.1 Single-Layer a-Si:H and Nc-Si:H

The XRD pattern of Si thin films prepared at different hydrogen dilution of silane [R] using both techniques (rf-PECVD and HWCVD) is shown in Fig. 9. The XRD pattern was recorded using CuKα radiation ($\lambda = 1.54$ Å) in the scanning range from 10 to

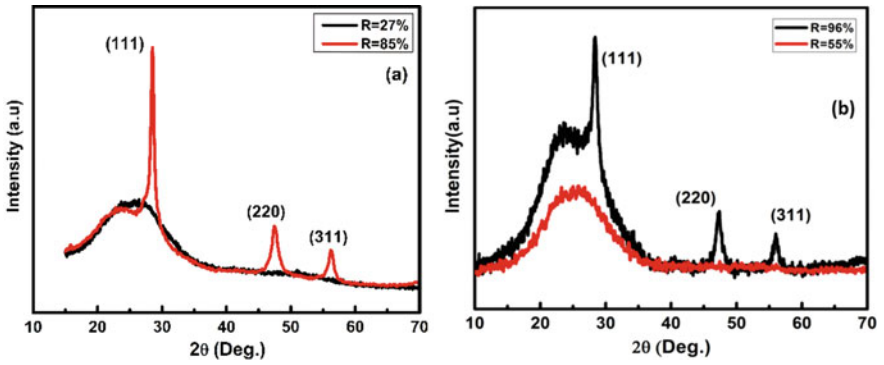

Fig. 9 The XRD pattern of single-layer a-Si:H and nc-Si:H thin films **a** HWCVD [28] and **b** rf-PECVD [13]

70°. For both deposition techniques, the films deposited at low hydrogen dilution are amorphous in nature with a broad peak around 28°. As hydrogen dilution is increased, sharp peaks corresponding to (111), (220) and (311) planes of crystalline silicon appeared. We observed a strong peak at $2\Theta = 28°$ in both cases and less intense peak at $2\Theta = 45°$ and $2\Theta = 56°$. These results indicate that the crystallites have a preferable orientation in <111> direction for nc-Si films.

To further confirm the microstructure and calculate the fraction of the nanocrystalline phase, the Raman scattering spectra (Fig. 10) were recorded for these films using 'Ar-ion laser' with excitation wavelength, 488 nm, in the scanning range of 300–600 cm^{-1}. In order to avoid any possibility of laser-induced crystallization [51], the low laser power density (~127 kW/cm^2) was used. The films (both HWCVD as well as rf-PECVD) prepared at low [R] show the broad peak centred at 480 cm^{-1} corresponding to the transverse optic mode (TO) of amorphous silicon, whereas films prepared at higher [R] show sharp peak near about 520 cm^{-1} corresponding to TO mode of phonon vibration of c-Si in both cases. To estimate the crystalline volume

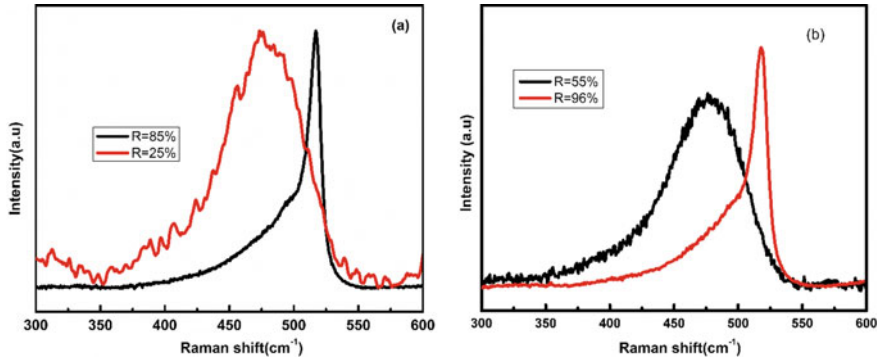

Fig. 10 Raman spectra of single-layer a-Si:H and nc-Si:H thin films **a** HWCVD and **b** rf-PECVD

fraction in the nc-Si films, the Raman peaks were deconvoluted in three components; two Gaussian (at 480 cm^{-1} and 495 cm^{-1} corresponding to TO mode of a-Si:H and grain boundaries respectively) and one Lorentzian peak (at 511 cm^{-1} corresponding to nc-Si) as described elsewhere [51]. The estimated total crystalline volume fraction for nc-Si films deposited by both techniques is about 64%.

The optical band gap was estimated from UV-Vis-NIR transmission spectra of thick single layer a-Si:H (110 nm) and nc-Si:H (95 nm) film prepared using rf-PECVD and was found to be 1.8 and 2.1 eV, respectively, while for the HWCVD films, the band gap was found to be 1.9 and 2.1 eV for a-Si:H (160 nm) and nc-Si:H (410 nm) films. Dark and Photo Conductivity measurement at room temperature in coplanar geometry were also performed to estimate the photosensitivity of these films. The amorphous films (deposited at lower hydrogen dilution) showed high photosensitivity of 4 order in magnitude, whereas, nc-Si films (deposited at higher [R]) showed low photosensitivity of ~1 order in magnitude, which is the characteristic features of amorphous and nanocrystalline silicon thin films. The above results confirm that with the change in H_2 dilution there is a structural transition from amorphous to nanocrystalline film irrespective of the deposition techniques.

3.2 Persistent Photoconductivity (PPC) on Nc-Si/a-Si:H Superlattice Structures

As discussed in Sect. 1.2, persistent photoconductivity (PPC) is an interesting phenomenon observed in a number of superlattice structures as discussed above. In PPC, current does not fall back to initial dark value after switching OFF the illumination, instead it shows a slow exponential decay. In this section, a detailed study on persistent photoconductivity in a-Si:H/nc-Si:H superlattice structures (where none of the layers is doped) has been presented. To understand the origin of PPC in these structures, the measurements were performed to measure the extent of excess current (%PPC), PPC decay time constant and its dependence on exposure time, number of periods, individual layer thickness and lateral electric field in superlattice structures. The measurements were performed on both thick and thin layer structures fabricated using HWCVD and rf-PECVD techniques, respectively. The electrode geometry used for these measurements is shown in Fig. 11.

Figure 12 shows the current transient for single layer a-Si:H and nc-Si films and also for three different superlattice structures under illumination and after switching off the light. All the samples have been in the as-deposited state without any post-deposition treatment. As can be seen from these figures, for all the samples, an almost instantaneous increase in current is observed as soon as the light is turned on due to excess carriers generated during illumination. The subsequent nature of the transient is, however, slightly different for different samples. For a-Si:H, a slow decay in current while the light is ON is observed followed by a rapid decrease in current to its dark value (Fig. 12a), which is known as Staebler–Wronski effect in a-Si:H.

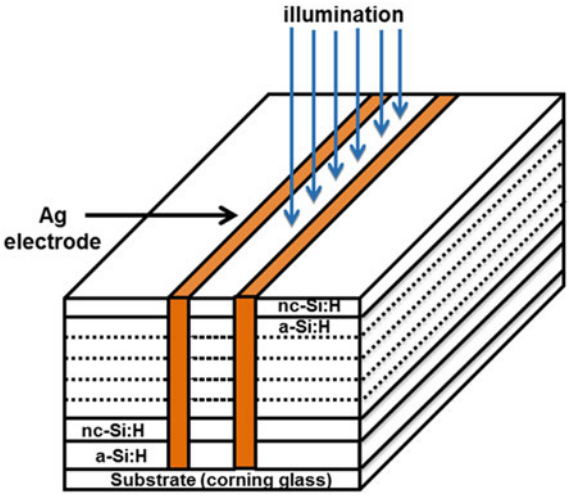

Fig. 11 Schematic diagram of a-Si:H/nc-Si:H superlattice structure and electrode geometry [50]

For nc-Si, the current remains almost constant during illumination and decreases instantaneously to dark value when the light is OFF (Fig. 12a) showing no sign of excess current. For superlattice structures, however, the nature of this transient is quite different (Fig. 12b–d). For all these structures, an initial rapid rise in current followed by an almost linear slow increase is observed while the light is ON. When the light is OFF, the excess current after the initial rapid decrease decays slowly approaching its dark value. This nature of current transient is the same for different subsequent exposure time, and each time, the current settles to a slightly higher value than the previous stage.

The slow decay part of the photocurrent after turning OFF the illumination is well described by single exponential decay function:

$$I = I_o \exp^{\frac{-t}{\tau}} \tag{1}$$

where I_o is the pre-exponential factor and τ is the decay time constant. The time constant for different structures and exposure times are listed in Table 4. It is observed that the decay time constant is high for the structure having more number of layers.

The PPC (%) is determined using relation as given below:

$$\text{PPC}(\%) = \frac{\Delta I_d}{I_d} \tag{2}$$

where I_d is the dark current measured just before switching ON the illumination and ΔI_d is the excess dark current after 180 s of switching OFF the light. These values are also listed in Table 4. The PPC % is more for the structure having more number of layers.

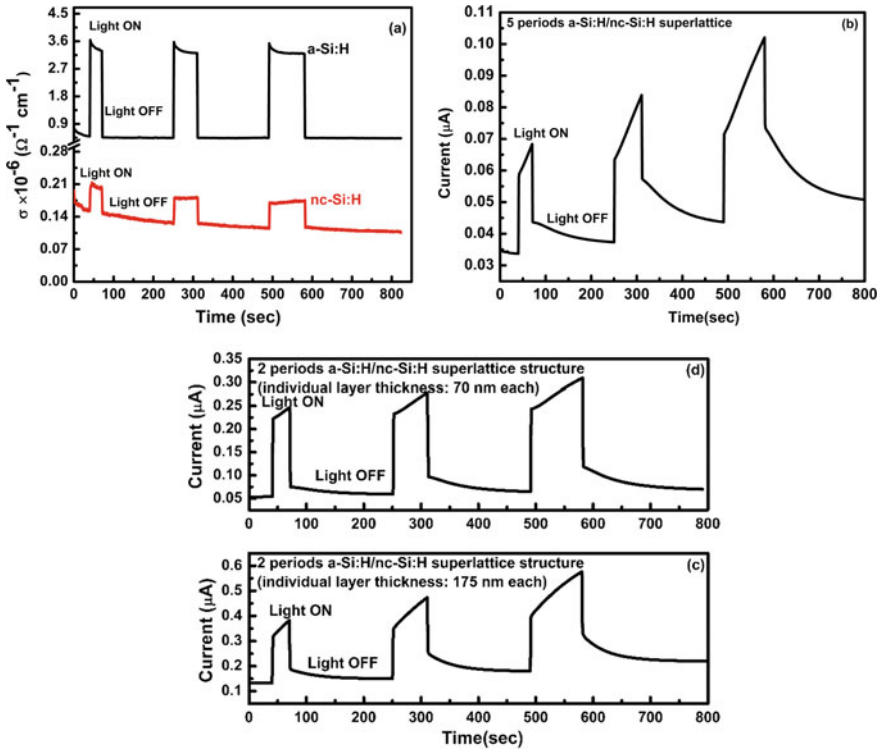

Fig. 12 Rise and decay of photoconductivity of as deposited **a** single-layer a-Si:H and nc-Si:H thin films and rise and decay of photocurrent of **b** 5 periods (70-nm-thick each layer), **c** 2 periods (175-nm-thick each layer) and **d** 2 periods (70-nm-thick each layer) of a-Si:H/nc-Si:H superlattice [28]

Table 4 The values of dark current, photocurrent, PPC and the decay time constant of the thick individual superlattice structures prepared by HWCVD technique [28]

Type (individual layer thickness)	Annealed temperature	I_{dark} (μA) at RT	I_{photo} (μA) at RT	I_{ppc} μA) at RT	PPC (%)	τ (sec)		
						Light exposure time		
						30 (sec)	60 (sec)	90 (sec)
5 periods (70 nm)	As deposited	0.03	0.06	0.04	33	91.20	80.54	76.14
	70 °C	0.29	0.52	0.35	20	45.96	45.95	46.01
	120 °C	1.77	2.45	1.93	9	47.03	47.31	47.75
2 periods (175 nm)	As deposited	0.13	0.32	0.15	15	44.20	42.70	41.80
2 periods (70 nm)	As deposited	0.053	0.220	0.059	11	69.29	67.19	64.77

The PPC has been earlier reported for a number of semiconductor superlattice structures, including doping-modulated (n-p-n-p-n-p) a-Si:H-based structures. In these doping-modulated structures, PPC is believed to be due to trapping of the carriers at the centres made by P-B complexes, which are in poor communication with the rest of the material [31]. Several models have been proposed to understand the origin of PPC in semiconductors in the past [31, 52–54]. In our case, the role of P-B complex or AX or DX is ruled out as these superlattice structures are made without any doping. Further, the extent of PPC and its decay constant is found to depend upon the number of layers and individual layer thickness. Since there is a small difference in band gap and significant difference in dark conductivity of the two layers, trapping of photogenerated charge carriers at the interface or the separation of carriers due to band bending caused by in-homogeneities thus appears to be the more likely cause of the observed PPC [28]. Also, there could be a large number of interface states present in these structures due to the presence of dangling bonds in a-Si:H and grain boundaries in nc-Si layers. In order to further understand the role of these states, the PPC measurements were carried out again at room temperature after annealing these structures at 70 °C and 120 °C, respectively. Figure 13 shows the current transient for 5 period structure after annealing. The structure was chosen as this showed the maximum PPC and largest decay time constant in the as-deposited state. The PPC% and decay time constant are listed in Table 4. It is observed that both PPC% and decay time constant decreased after annealing.

In order to further understand the origin of the observed PPC, the electric field dependence of photoconductivity (Fig. 14a) and PPC are also measured for the structure annealed at 120 °C. It is observed that the photocurrent varies linearly with the applied field; however, the extent of PPC reduces with the increase in the applied field as shown in Fig. 14b.

The observed PPC in these structures can be explained by trapping of one type of photogenerated carriers at the interface states. As a-Si:H and nc-Si have a slightly different band gap, the band bending at the interface is likely to be there. Assuming that the electron affinity for the two layers is not different, the schematic band picture

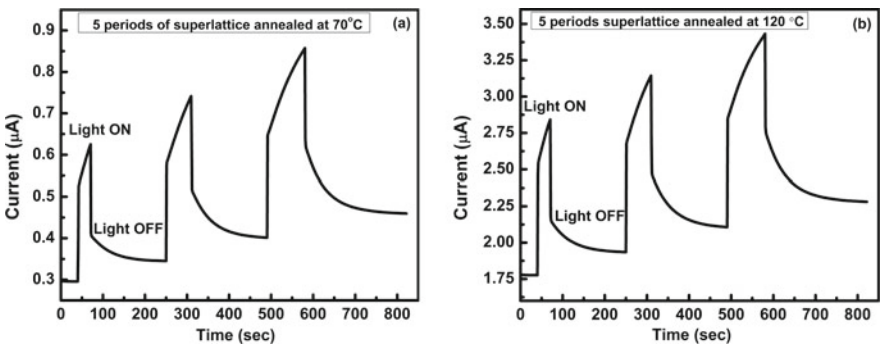

Fig. 13 Rise and decay of photocurrent (measured at RT) of 5 periods of superlattice structure annealed at **a** 70 °C and **b** 120 °C [28]

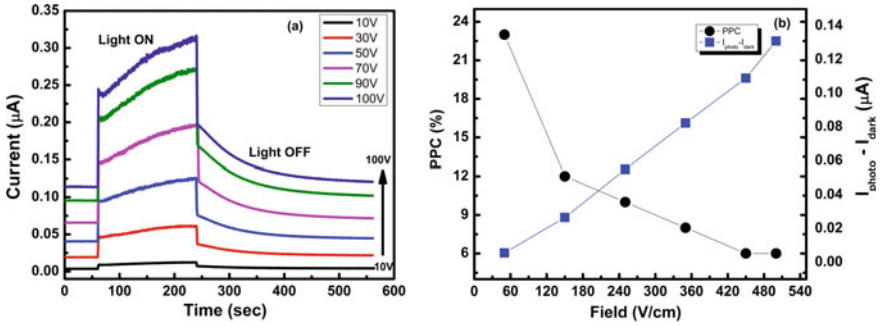

Fig. 14 **a** Rise and decay of the photocurrent with the variation of external applied field, **b** Variation of PPC (%) and photocurrent with the change of external applied field in 5-period superlattice structures [28]

at the junction is likely to be similar to that is shown in Fig. 15. In this picture, though there is no discontinuity for the conduction band at the interface, a band discontinuity is seen for the valence band. The electrons in the nc-Si:H region can move freely to the a-Si:H region, however, the holes in a-Si:H region are likely to be trapped in the interface states. When the light is shone, the photogenerated carriers are generated, some of these carriers recombine instantaneously whereas, other drift towards the interfaces due to the field at the junction. Thus, the electrons and holes are physically separated preventing their recombination. When the light is OFF, these trapped carriers are remitted to the extended states and recombine slowly resulting in a slow exponential decay of the photocurrent. As the number of such interfaces is increased, more such carriers are trapped resulting in larger excess current (PPC) and slower decay of current. When the thickness of the individual layer is large (175 nm), more carriers are generated in a-Si:H layer and PPC % is slightly more than for structures having thin layers (70 nm) but the same number of interfaces. The model can also explain the electric field dependence of PPC in these structures. Though current is measured in lateral direction, normal to these interfaces, the photogenerated carriers are likely to move also along the interfaces due to the inbuilt field at the interfaces (Fig. 16) which may not be very high as in case of p-n junction. For a low electric field in the lateral direction, the built-in

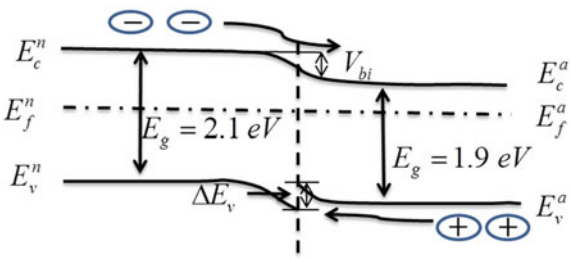

Fig. 15 Schematic band diagram of a-Si:H/nc-Si:H superlattice structure [28]

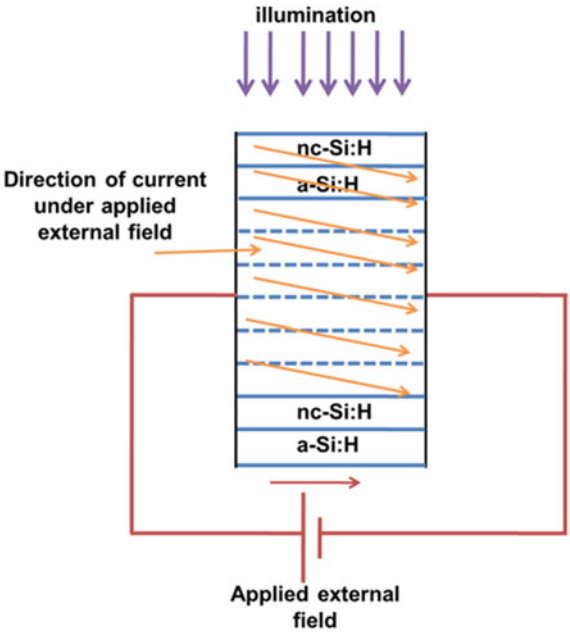

Fig. 16 Direction of current under the applied external field in the superlattice structure [28]

field at the interfaces could be sufficiently large to drag a fraction of photogenerated carriers towards the interfaces where these are trapped, before these are swept in lateral direction. At higher lateral fields, more carriers are swept by the external field in lateral direction and the observed PPC is low. The origin of PPC is understood in terms of competition between carriers transport in the lateral direction due to the external field and along the depth due to band bending at a-Si:H/nc-Si:H interfaces. Carriers trapped in the interfaces states or the separations of carriers due to band bending are likely to be responsible for observed PPC [28].

Since both % PPC and decay time constant were found to depend on individual layer thickness also (Refer the results for 2 period structures having individual layer thickness as 175 and 70 nm each in Table 4), these studies were also conducted on the thin layer a-Si:H-and nc-Si:H-based superlattice structures prepared using rf-PECVD techniques, where individual layer thickness could be tuned to as low as 5–10 nm. This individual layer thickness is compared with the width of the band bending region at the interfaces.

Figure 17 shows the rise and decay of photocurrent for the individual layers (110-nm-thick a-Si:H layer and 95-nm-thick ncSi layer) and superlattice structures prepared using the rf-PECVD technique. For single-layer films (Fig. 17), once again, the current transient was similar to that for films deposited by HWCVD techniques and no PPC was observed either for a-Si:H or nc-Si films. However, in case of superlattice structures of 7 layers (Fig. 18a) with nc-layer thickness in the range of 5–20 nm (with the total thickness of 50–110 nm), though an increase in current was observed for all the structures (despite the total thickness being very less), the current

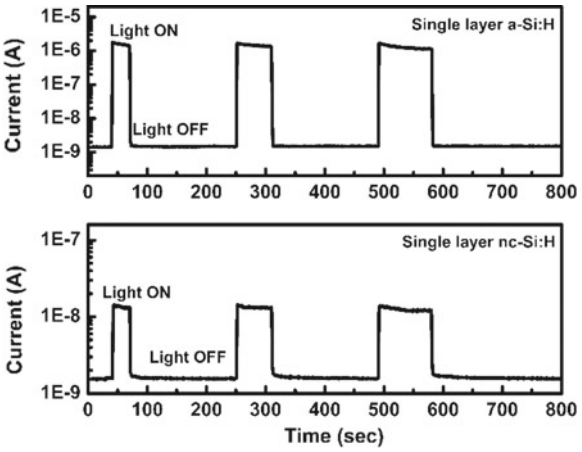

Fig. 17 Rise and decay of the photocurrent across a single layer of a-Si:H and nc-Si:H thin films [13]

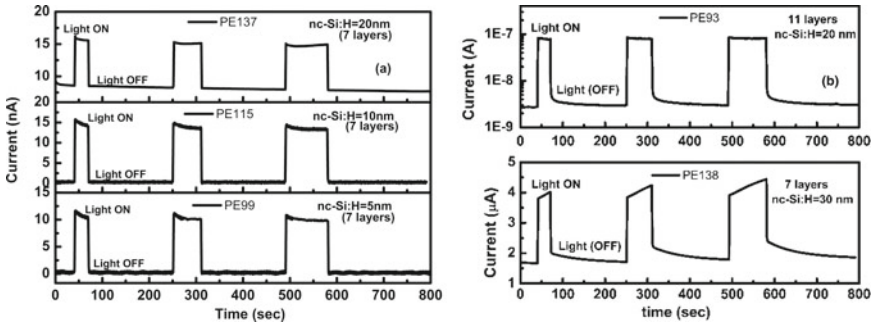

Fig. 18 Rise and decay of the photocurrent in a-Si:H/nc-Si:H superlattice with nc-Si:H layer thickness of **a** 5 nm, 10 nm, 20 nm (7 layers) and **b** 30 nm (7 layers) and 20 nm (11 layers) structures [13]

decayed instantaneously to its dark value as soon as the light was OFF and no PPC was observed. However, in the structures with (Fig. 18b, c) nc-Si:H layer thickness of 30 nm (total thickness of 150 nm) and the superlattice structure of 11 layers with nc-Si:H layer thickness of 20 nm (total thickness of 170 nm), a slow decay of excess current was observed, after the initial rapid decrease, when the light was OFF. PPC illustrated by the appreciable excess current when the light is turned OFF (Fig. 18b, c). The values of dark current, photocurrent, PPC (%) and decay time constant for these structures are listed in Table 5.

Though the observed PPC (%) for superlattice structures having thin individual layer (rf-PECVD) is small compared to that with thick sublayers of a-Si:H and nc-Si:H films prepared using HWCVD technique, it can be seen that in this case also, PPC% increases with increase in the number of layers from 7 (total thickness of

Table 5 The values of dark current, photocurrent, PPC and the decay time constant of the thin superlattice structures prepared by rf-PECVD technique [13]

No. of layers thickness (nm)	I_{dark} (μA)	I_{photo} (μA)	I_{ppc} μA)	PPC (%)	τ (sec)		
					Exposure time		
					30 (sec)	60 (sec)	90 (sec)
7-layer nc-Si:H 30 nm	1.67	3.77	1.71	2	67.97	69.68	72.10
11-layer nc-Si:H:20 nm	2.72×10^{-3}	8.22×10^{-3}	3.0×10^{-3}	10	21.24	23.00	26.24

150 nm) to 11 (total thickness 170 nm). For 7-layer supper lattice structures, no PPC is observed when nc-Si layer is only 20 nm (total thickness of $\leq$110 nm) and very small PPC is observed for nc-Si layer with a thickness of 30 nm (Total thickness (150 nm). The absence of PPC for these superlattice structures with low total thickness as well as low individual layer thickness could be due to (i) insufficient absorption of light (when the total thickness is low) resulting in very few photogenerated carriers and (ii) due to possible tunnelling of carriers between a-Si:H and nc-Si:H layers when the thickness of nc-Si:H is low (5–10 nm). As the layer thickness is increased, the band bending, depletion width, and thickness of the undepleted region are likely to change. This may not allow all the carriers to tunnel through and some of these may get trapped at the interface in between a-Si:H and nc-Si:H layers resulting in observed PPC. With an increase in the number of layers, the number of such interfaces as well as total thickness increases which result in the observed PPC for 11-layer structure with 20-nm-thick nc-Si:H layers and no PPC for 7-layer structure with 20-nm-thick nc-Si:H layers [13].

3.3 Space-Charge-Limited Conduction (SCLC) in nc-Si/a-Si:H Superlattice Structures

In an earlier section, we have observed that the superlattice structures consisting of alternate layers of nc-Si and a-Si:H show PPC when current is measured in coplanar geometry normal to the direction of superlattice structures. Other studies on similar structures also report an enhancement in photosensitivity, carrier mobility and photonics and plasmonic properties [16, 55, 56]. In all these multilayer structures, the interface states between the sub-layers act as trapping and recombination centres and control the carrier transport. The role of these interface states become much more significant, if the carrier transport is along the direction in which the superlattice structures are fabricated. In addition to these interface states, the nc-Si as well as a-Si:H layers have short-range order only and are characterized by the

density of states in the band gap region. For any device fabrication, a knowledge of the density of states and interface states are very necessary.

A number of techniques have been reported to measure the density of states which include field-effect measurements [57–60], capacitance–voltage measurements [61, 62], isothermal capacitance transient spectroscopy [63], transient current spectroscopy [64], transient voltage spectroscopy [65], etc. All these transient techniques involve a complicated analysis as carriers from different trap states have different evolution times as well. Steady-state space-charge-limited current (SCLC) measurement [66–70] is a simple method of estimating the density of states as this does not involve any transient measurements and current is measured as a function of the applied field. As the carriers are trapped in the defect states, the shift in the position of Fermi level with applied field results in a non-linear variation of current, which is used to estimate the density of defect states.

In this section, we present our SCLC studies on single-layer a-Si:H and nc-Si films and nc-Si/a-Si:H superlattice structures. The HWCVD fabricated structures having thick nc-Si and a-Si:H layers (70 nm each) with two different periods (2 and 5 periods) have been used for these studies. The structures with very thin layers of a-Si:H and nc-Si could not be used for these studies as for even the smallest voltages, which could be applied from the source metre, the electric field was too large.

We used a Schottky diode configuration, *ITO (Indium Tin Oxide)/a-Si:H/Ag* and *ITO{a-Si:H/nc-Si:H}$_n$/Ag*, for these measurements, where *ITO/a-Si:H* acted as a Schottky junction, whereas *Ag/a-Si:H* and *Ag/nc-Si:H* acted as an ohmic junction. The measurements were performed in sandwich geometry. The *I-V* characteristics in the non-linear region were used to estimate the DOS in single-layer a-Si:H and a-Si:H/nc-Si:H superlattice structures [29]. In single-layer films, the injected charge from the metal to semiconductor (Ag to a-Si:H) was trapped in the DOS in the band gap, whereas in superlattice structures, the charge redistributed itself between the defect states in the band gap region as well as at the interface between the nc-Si:H and a-Si:H layers.

Den Boer's step by step method [71]. is considered as the simplest method for estimating the DOS because in this case, the spatial variation in DOS is neglected. When the voltage difference changes from V_1 to V_2, the shift in the Fermi energy level $\left(E_{fn}\right)$ is given as follows:

$$\Delta E_{fn} = kT \ln\left(\frac{I_2 V_1}{I_1 V_2}\right) \tag{3}$$

In the non-linear region of *I-V*, the charge density Q_t injected into the trap states is related to the change in voltage $\Delta V = (V_2 - V_1)$ as follows:

$$Q_t = \frac{\varepsilon_s \chi \Delta V}{d} = qd \int_{E_{fn}}^{E_{fn}+\Delta E_{fn}} g(E)dE = qdg(E)\Delta E_{fn} \tag{4}$$

The factor χ accounts for the non-uniformity of the space charge and is taken as a constant ($\chi = 2$), ε_s is the semiconductor permittivity ($\varepsilon_s = 105.31 \times 10^{-12}$ Fm^{-1}; dielectric constant of silicon = 11.9), q is the electronic charge, d is the thickness of the film and $g(E)$ is the DOS distribution in the a-Si:H film around the Fermi level.

For a sufficiently small ΔV, $g(E)$ can be assumed to be constant between E_{fn} and $E_{fn} + \Delta E_{fn}$. From Eq. (4), the DOS is given by

$$g(E) = \frac{\chi \varepsilon_s \Delta V}{q d^2 \Delta E_{fn}} \tag{5}$$

Using the values of ΔV and ΔE_{fn}, the distribution of the DOS can be estimated using Eq. (5).

Figures 19a, b and 20a, b show the dark *I-V* curves in sandwich geometry for single as well as superlattice structures at room temperature (RT) after annealing it at 150 °C. For single-layer nc-Si films, the I-V curve is found to be linear over the

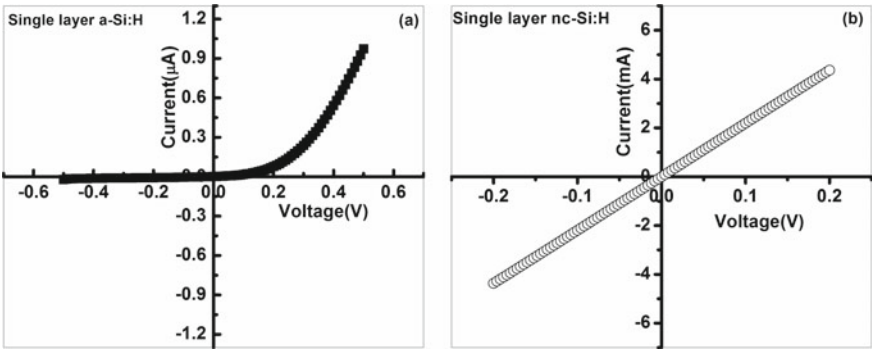

Fig. 19 I-V across single layer **a** a-Si:H and **b** nc-Si:H in sandwich geometry [29]

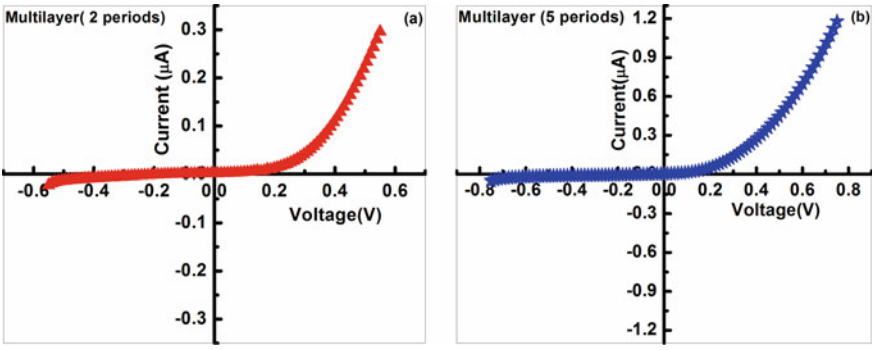

Fig. 20 I-V across total a-Si:H/nc-Si:H **a** 2 periods and **b** 5 periods superlattice structures in sandwich geometry [29]

measured range of voltage (4×10^3 V/cm), whereas in case of amorphous silicon films, a non-linear variation in current with voltage, with rectifying nature (ITO/a-Si:H junction is rectifying) is observed. In this case, in forward bias condition, the current increased exponentially with the applied field, with a diode ideality factor being ~2. The conductivity of a-Si:H and nc-Si:H in this sandwich geometry is found to be different by several orders of magnitude, 4.3×10^{-9} $\Omega^{-1}\text{cm}^{-1}$ and 1.1×10^{-5} $\Omega^{-1}\text{cm}^{-1}$, respectively (Electric field $<1\times10^4$ V/cm); the dark conductivity of nc-Si:H films at 300 K is more than 3 orders of magnitude higher as compared to a-Si:H films under forward bias condition. Dark *I-V* characteristics of a-Si:H/nc-Si:H (2 and 5 periods) superlattice structures at RT after annealing these films at 150 °C are also found to be asymmetric and non-linear similar to a-Si:H film with the diode ideality factor being ~2 and current having the same order of magnitude as that for single layer a-Si:H film. Since the conductivity of nc-Si:H layer is much higher, where the thickness of both a-Si:H and nc-Si layer is same, it can be assumed that the nc-Si layer in these structures behave like short-circuit elements and the resistive path for carriers is only due to a-Si:H layers and the depletion region at the interface, most of it being on a-Si:H side only.

In order to estimate the density of states in the single layer of these superlattice structures, it is necessary to know the voltage drop across single layer in these multilayer structures. As nc-Si layer offers much smaller resistance (more like short-circuit element), it can be assumed that the entire voltage is dropped across a-Si:H layers. With this approximation, equivalent *I-V* curve for one pair of a-Si:H/nc-Si:H structure in both the superlattice structures are replotted, dividing the voltage by a factor of 2 and 5, respectively, for 2 and 5 period structures, respectively. Whereas the current is same as earlier since the resistance offered by these layers are connected in series in sandwich geometry. The I-V curves for single-layer a-Si:H films and across single pair of a-Si:H/nc-Si in superlattice structures on log–log scale are shown in Fig. 21. The *I-V* curves obey power law, i.e. $I \alpha V^m$, with different values of exponent in different regions of the curve, a characteristic of space-charge-limited conduction. The value of m for different regions is shown in Fig. 21a–c. In the low-field region, where the current is Schottky limited, the exponent is less than 1. Further for electric field $>10^4$ V/cm, the current increased sharply with the exponent greater than 2.0, which could be due to the onset of space-charge-limited conduction in these structures.

To estimate the shift in Fermi level (Eq. 3) and the density of state (Eq. 5), the region with $m > 2$ of *I-V* characteristics are used. Further, to measure the variation of DOS as a function of the shift in Fermi energy, the initial field ($>1\times10^4$ V/cm) was kept constant for the given samples. The variation of DOS with the change in ΔE_{fn} is shown in Fig. 22a for both single as well as superlattice structures. It is observed that DOS is high for the superlattice structures than that for single layer a-Si:H film. Further, DOS does not depend on ΔE_{fn} for single-layer a-Si:H film, however, a little variation with ΔE_{fn} is observed for superlattice structures. The average value of DOS over the entire range of ΔE_{fn} is also estimated from the slope of ΔV verse ΔE_{fn} (Fig. 22b using Eq. 5 and the values of $g(E)$ are listed in Fig. 22b. It is observed that ΔV verse ΔE_{fn} curves overlap for both superlattice structures

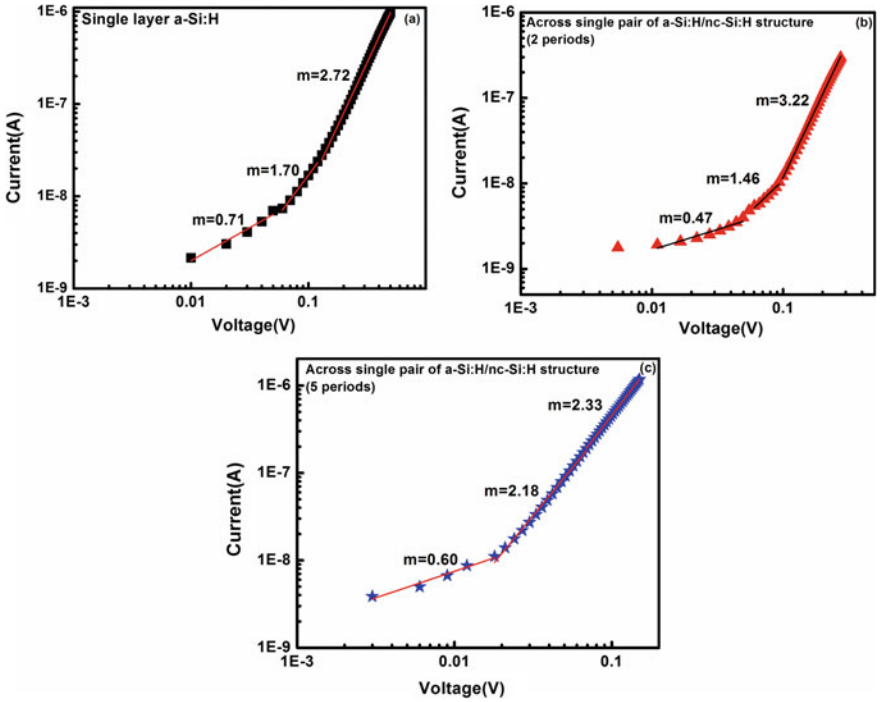

Fig. 21 I-V across **a** single layer a-Si:H film, across a single pair of a-Si:H/nc-Si:H **b** 2 periods and **c** 5-period superlattice structures [29]

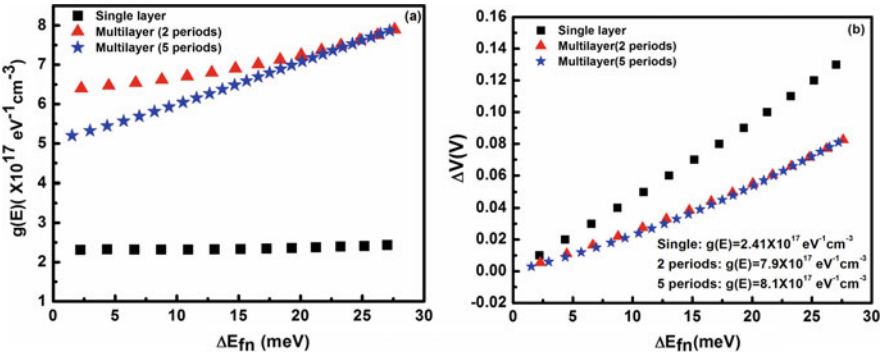

Fig. 22 **a** Variation of DOS and **b** ΔV verse ΔE_f across single, 2-period and 5-period superlattice structures (across single pair of a-Si:H/nc-Si:H) [29]

irrespective of number of layers. It has also been observed that the DOS obtained across superlattice structures of both the periods (2 and 5) is almost same and is higher by a factor of 5 as compared to single-layer a-Si:H film.

In our case, the DOS obtained across a-Si:H film was ~10^{17} $eV^{-1}cm^{-3}$, typical of a-Si:H samples, however for both the superlattice structures it was ~10^{18} $eV^{-1}cm^{-3}$. It may, therefore, be assumed that the observed difference in DOS in case of single-layer and superlattice films (Fig. 22a) might arise due to the presence of interface states between a-Si:H and nc-Si:H layers in these superlattice structures. These interface states are also found to be responsible for observed PPC in these superlattice structures as discussed in the PPC section.

The higher DOS in superlattice structure can be understood by drawing the equivalent band diagram and the charge transport across this. Figure 23 shows the band diagram of a-Si:H/nc-Si:H superlattice structure with ITO as the base electrode and Ag as the top electrode. In a-Si:H/nc-Si:H superlattice structure, the difference in band gaps of nc-Si:H and a-Si:H results in band bending giving rise to a built-in electric field at the interface, which controls the charge transport across the interface and affect the carrier recombination kinetics. The rectifying junction at ITO/a-Si:H interface also results in built-in electric field under no bias condition. In absence of any bias, the current density from semiconductor to ITO $\left(J_{sc;ITO}\right)$ must be equal and opposite of current density from ITO to semiconductor $\left(J_{ITO;sc}\right)$. Under the influence of external bias, which forward biases the ITO semiconductor (ITO/a-Si:H) contact, the bands in the a-Si:H side are raised in energy relative to those of ITO and the electric field at this junction decreases, therefore the charge carriers are able to cross the barrier without any obstacles, resulting in increase in $J_{ITO;sc}$ under the applied field. If we further increase the external voltage, the bands at the ITO semiconductor junction as well as a-Si:H and nc-Si:H interface approach to become flat and thus the carrier (electrons) from nc-Si:H layer (highly conducting) to a-Si:H (low conducting) could easily tunnel towards ITO. In this process, some of the electrons get trapped in the bulk density of states of a-Si:H as well as the interface states between a-Si:H and nc-Si:H. This could be the reason behind the higher value of DOS in the superlattice

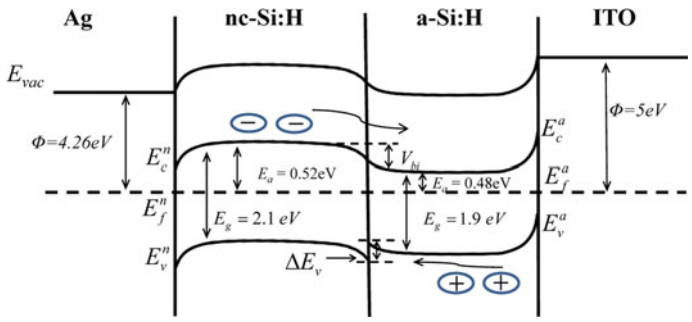

Fig. 23 Schematic band diagram of Ag/nc-Si:H/a-Si:H/ITO superlattice structure. The value of band gap and activation energies are obtained from transmission spectroscopy and conductivity measurements, respectively. The electron affinity of Si is taken as 4.05 eV [29]

structures as compared to single-layer a-Si:H film, which is estimated assuming no trapping of charge carriers at the interface.

The conjecture that the excess DOS in superlattice structures is due to the interface state between nc-Si:H and a-Si:H gets further support from the observed PPC in these superlattice structures which has been understood in terms of carrier trapping at the interface states; PPC (%) is found to increase with an increase in the number of interface states in these superlattice structures as discussed in PPC section. In case of SCLC measurements, the DOS for superlattice structures does not depend upon the number of layers in the given structure as these are calculated for a single pair of nc-Si:H/a-Si:H layers. Further, these values are different than those for single layer a-Si:H films as no such interface states exist in case of single-layer film. The results show that the existence of the interface states in these superlattice structures could be the reason behind the observed PPC as well as the higher DOS in these a-Si:H/nc-Si:H superlattice structures [29].

3.4 Tunable Photoluminescence in nc-Si/a-Si:H Superlattice Structures

Silicon is the most favourite material for the fabrication of microelectronic devices and integrated circuits. However, the use of silicon in photonic devices is limited due to its low band gap in IR range and also being an indirect band gap material, its photoluminescence is almost negligible. With the advancement in technology, it is sought to integrate the microelectronics and micro-photonics and optoelectronic devices on a single chip, however, indirect band gap of silicon presents a barrier to this concept. Quantum theory predicts that it is possible to tune the band gap of silicon in the visible range by suitably controlling the size of nanocrystallites and realize the integration of microelectronic and photonic devices. Several allotropes of silicon such as porous silicon and nc-Si prepared using chemical routes are known to have a strong PL signal in the visible range [24, 72–76]. However, the process of fabrication of these nanostructures restricts its use in integrated circuits and integrating these nanocrystallites of Si in a single-chip device is still a problem. Other methods for fabricating nc-Si have been explored. These include the formation of nc-Si in Si/SiO_2-based superlattice structures, which can be fabricated using chemical vapour deposition route. Several superlattice structures such as nc-Si/SiO, a-Si/SiO_2 and Si/SiO_2, a-Si/SiO_2 fabricated and annealed at high temperature (~1000 °C) have exhibited photoluminescence in visible range [14, 15, 25]. In all these superlattice structures small size nanocrystallites of Si could be formed, by annealing at high temperature, converting a part of a-Si or thin Si layer into nanocrystallites. All these structures have SiO_2 as one of the layers, which has a large band offset with silicon and also its growth requires high-temperature processing. A superlattice structure with a small band offset such as a-Si:H/nc-Si:H superlattice structure is desirable to

enhance the carrier mobility along with high optical absorption, photonic and plasmonic effects. In this section, we discuss how the photoluminescence signal can be tuned by controlling the thickness of nc-Si in a-Si:H/nc-Si superlattice structures. The structures used for these studies were fabricated by the rf-PECVD method at a low substrate temperature of 250 °C and no post-deposition annealing or any other processing was done. These structures were fabricated on undoped c-Si wafers and alkali-free borosilicate glass (Corning 1737) substrates, those fabricated on glass substrates were also used for PPC studies discussed in the earlier section. The PL spectra were recorded using solid-state laser (excitation wavelength 405 nm) with a laser power of 30 mW [13].

Figure 24 shows the PL spectra recorded for blank Si substrates as well as single-layer a-Si:H (10 nm) and nc-Si (5 nm) films. Apart from a peak at ~450 nm (2.78 eV), no photoluminescence signal is observed for either blank substrates or thick as well thin single-layer films. The peak at 2.78 eV is characteristic of SiO_2, a thin layer of which is always present on the samples and substrates. The PL spectra for superlattice structures on c-Si and glass substrates, having 4 alternating layers of nc-Si and 3 layers of a-Si:H, are shown in Fig. 25 along with the spectra for an 11-layer-thick structure. The thickness of a-Si:H layer, in all these structures, is fixed at 10 nm, whereas that of nc-Si is varied between 5 and 30 nm. These structures are the same

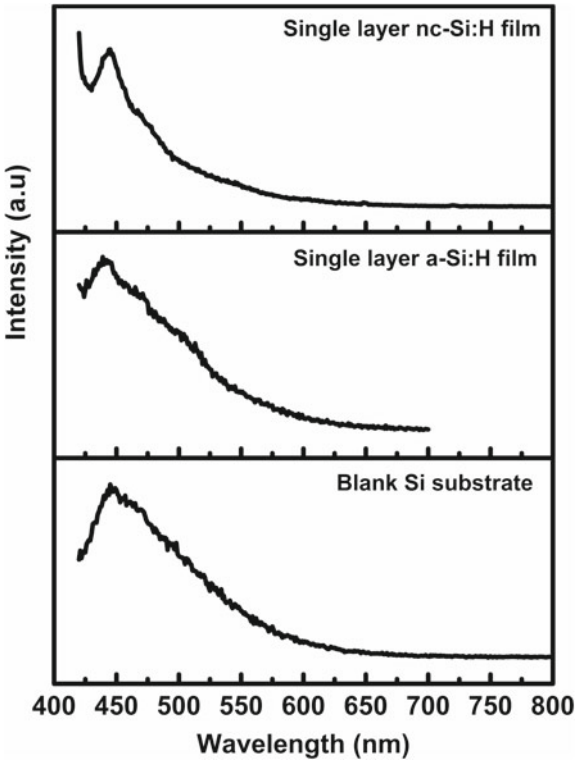

Fig. 24 PL spectra of single-layer a-Si:H (10 nm) and nc-Si:H (5 nm) thin films on silicon substrate and blank Si substrate [13]

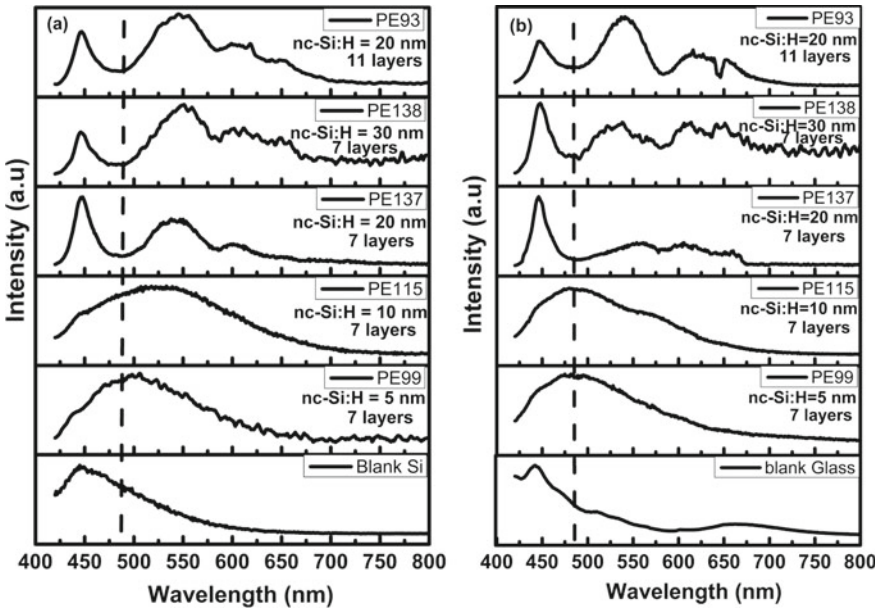

Fig. 25 PL spectra of a-Si:H/nc-Si:H superlattice structures on **a** silicon and **b** glass substrates [13]

as those used for PPC studies and were fabricated simultaneously on glass as well as c-Si substrates. As is evident from these figures, PL spectra of all these structures have a broad peak in the visible range (for nc-Si layer up to 10 nm thick) and distinct peaks when the nc-Si layer is 20–30 nm. The spectra for structures on both substrates are qualitatively identical with some change in peak intensity.

Since a broad peak in spectroscopy is often a convolution of several overlapping peaks, the PL spectra were deconvoluted to get the information about different peaks. While deconvolution, a peak at 2.78 eV corresponding to SiO_2 was pinned. One of the deconvoluted spectra on each substrate is presented in Fig. 26. The position of different peaks along with its full width at half maxima (FWHM) and maximum intensity is compiled in Table 6. It is observed that for all the spectra two peaks, one around 2.25 eV and another around 2.06 eV is observed. The structures with very thin nc-Si (5–10 nm) show a peak around 2.45–2.55 eV, which is replaced by a peak at 1.91 eV, when the thickness of nc-Si layers is changed to 20–30 nm. Further, in all these structures, the most intense peak is the one centred at the highest energy. In order to investigate if the peak positions also depend upon the number of layers in superlattice structures, PL measurements were also performed on a 11-layer superlattice structure having 20-nm-thick nc-Si layers. Interestingly, the positions of different peaks in the deconvoluted spectra and its FWHM were found to be the same as that for 7-layer superlattice structure with 20-nm-thick nc-Si layers, both for c-Si as well as glass substrates.

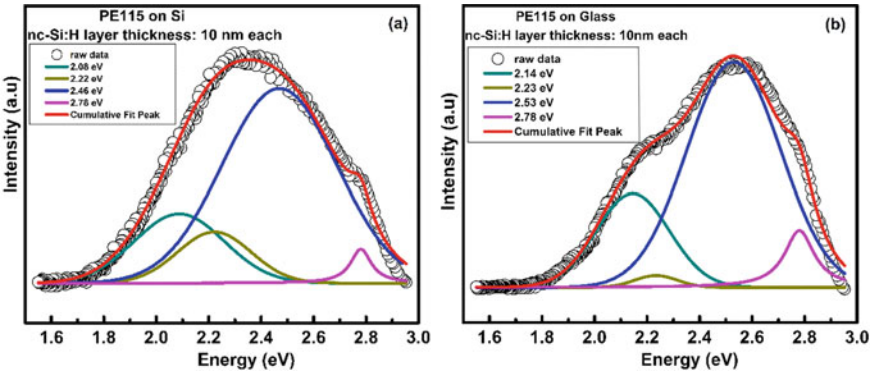

Fig. 26 The deconvoluted PL spectra of superlattice structure films (nc-Si:H layer thickness of 10 nm) with peak position on **a** Si and **b** glass substrates

Table 6 The PL peak position, FWHM and peak intensity of superlattice structures on glass and Si substrates [13]

Sample no.	On Si substrate			On glass substrate		
	Peak position (eV)	FWHM (eV)	Max ht. (a.u.)	Peak position (eV)	FWHM (eV)	Max ht. (a.u.)
PE99 nc-Si:H = 5 nm (7 layer)	2.78	0.19	153	2.78	0.15	11244
	2.53	0.43	1158	2.57	0.36	35718
	2.26	0.35	382	2.34	0.24	11206
	2.09	0.44	200	2.16	0.34	13583
PE115 nc-Si:H = 10 nm (7 layer)	2.78	0.09	2145	2.78	0.13	8085
	2.46	0.51	12271	2.53	0.42	31969
	2.22	0.33	3243	2.23	0.19	1688
	2.08	0.40	4378	2.14	0.32	13319
PE137/PE93 nc-Si:H = 20 nm (7 layers/11 layers)	2.78/2.78	0.12/0.13	15738/4649	2.78/2.78	0.11/0.19	13827/13445
	2.28/2.27	0.25/0.29	10019/6079	2.24/2.30	0.33/0.23	3837/23007
	2.03/2.03	0.10/0.09	2512/2094	2.01/2.01	0.13/0.10	2602/9718
	1.91/1.91	0.24/0.16	1161/1832	1.89/1.89	0.07/0.15	2059/6673
PE138 nc-Si:H = 30 nm (7 layers)	2.77	0.11	537	2.77	0.12	694
	2.26	0.26	815	2.33	0.28	380
	2.03	0.10	352	2.03	0.13	225
	1.91	0.15	296	1.90	0.22	251

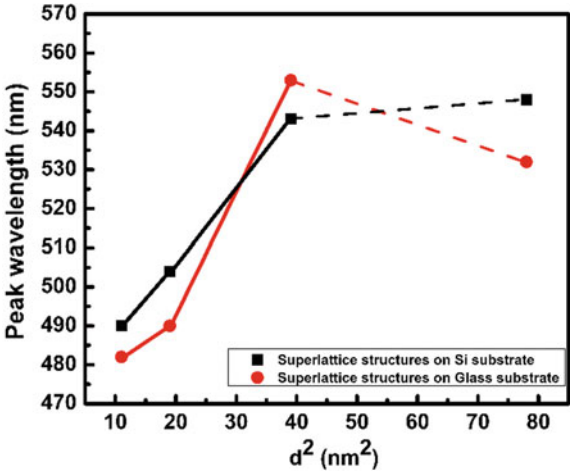

Fig. 27 PL peak position λ versus d^2 on silicon and Corning glass substrate [13]

It is interesting to observe a shift in PL peak position with the thickness of nc-Si layer in these multilayer structures, especially when single-layer films do not show any PL. It appears to be originated from the Si nanocrystallites embedded in the matrix of the amorphous phase in nc-Si layer, the size of which depends upon the thickness of nc-Si. In order to estimate the typical size of the nanocrystallites in nc-Si layer, single-layer nc-Si films with thickness varying between 5 and 30 nm were deposited under identical conditions and Raman measurements were performed on these thin films [50]. The Raman spectra for all these films were characterized by an intense peak near 520 cm^{-1}. The peak at 520 cm^{-1} corresponds to the TA mode of Si in c-Si and a shift from this position towards lower wavenumber is a measure of crystallite size [77]. The size of nanocrystallites (d) in these thin single-layer nc-Si films are estimated to be 3.35, 4.44, 6.26 and 8.88 nm for 5-, 10-, 20- and 30-nm-thick films, respectively, which suggests a systematic increase in the size of nanocrystallites with the thickness of the films. Figure 27 shows the peak wavelength (corresponding to the most intense peak) as a function of Si nanocrystallite size (d), estimated from Raman measurements on thin single-layer nc-Si films. It is observed that peak wavelength varies as d^2, for nc-Si layer thickness up to 20 nm for superlattice structures fabricated on Si substrates. It may appear that for structures fabricated on glass substrates, the variation is not linear, but it may be noted here that the size of nanocrystallites on glass substrates may be slightly different. For 30-nm-thick nc-Si layers, the peak wavelength does not follow this linear relation. A linear variation of peak wavelength with the size of nanocrystallites is in accordance with the quantum confinement model of Brus [78], which predicts the confinement energy of the nanocrystals to be proportional to the reciprocal of the square of the diameter of crystallites. A systematic shift in the absorption edge is also observed in the transmission spectra of these films (Fig. 28), which also suggests an increase in band gap with a decrease in thickness of the films, indicating a decrease in the size of the nanocrystallites. For 30-nm-thick nc-Si layer, small intensity peaks in PL spectra are seen due to

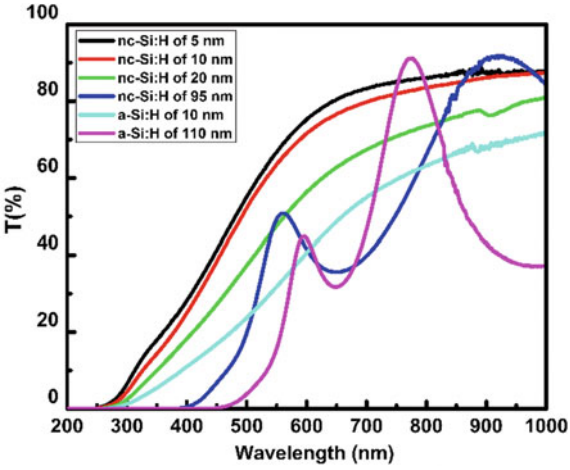

Fig. 28 UV-Vis-NIR transmission spectra of single-layer a-Si:H and nc-Si:H thin films [13]

smaller size particles, however, a significant fraction of these crystallites are bigger in size and the most intense peak is observed at around 1.9 eV, which is almost same as the band gap of a-Si:H films in these structures. From these observations, the origin of high energy peaks in PL spectra appears to be due to presence of small size Si nanocrystallites in nc-Si layer, however, the same phenomenon is unable to explain the origin of low-energy (1.9 eV) peak. In order to understand the origin of this peak, we revisited the PPC data on these film, which was appreciable for superlattice structures having 30-nm-thick nc-Si layers. It appears that some of the carriers trapped in the interface states and responsible for the PPC when recombine radiatively give rise to the PL peak around 1.9 eV along with small intensity PL peaks at higher energy also, which is likely to be due to small size nanocrystallites in these nc-Si layers. When the thickness of nc-Si layer is small, the carriers are not trapped in the interface states, rather these can easily tunnel through and hence no low-energy PL peak is observed when the thickness of nc-Si layer is small [13]. These observations suggest that it is possible to tune the peak wavelength in PL spectra of nc-Si-based superlattice structures by controlling the thickness of nc-Si. The fabrication of superlattice structures thus offers a unique process of tuning the size of nanocrystallites and PL peak position.

4 Summary

Semiconductor superlattice structures exhibit interesting and tuneable optoelectronic properties. Most of these superlattice structures are fabricated using two different semiconductors having a large band offset at the interface. Our studies show that it is possible to fabricate the superlattice structures using different isomorphs like a-Si:H and nc-Si, which do not have much conduction band offsets but a large difference

in electrical conductivity and band gap. It is thus possible to tune the electrical transport and optoelectronic properties of these structures by carefully choosing the thickness of the individual layer. The thick individual layer structures exhibit persistent photoconductivity, whereas the thin individual layer structures can be used for tuning the photoluminescence peak, making these structures a good candidate for photonic and plasmonic applications. The interface states in these structures also have a role in controlling the optoelectronic and transport properties.

Acknowledgments Financial support for fabricating rf-PECVD system was received from Department of Science and Technology (DST) [Grant No. DST/TM/SERI/2K11/78(G)]; and Defence Research and Development Organization (DRDO) [Grant No. ERIP/ER/0900376/M/01/1297], New Delhi, India. The Hot wire CVD system was fabricated through the financial support from Department of Science and Technology (DST) [Grant No. DSTSR-S2-CMP-32-2003]. The study was sponsored by the Council of Scientific and Industrial Research (CSIR), New Delhi, India [80(0082)/13/EMR(II)]. We also acknowledge the Department of Physics, IIT Guwahati and Centre for Instrument Facility (CIF), IIT Guwahati for different characterization facilities and other support. We also acknowledge the fruitful discussions with (Late) Professor Satish Chandra Agarwal (IIT Kanpur) and Professor Rana Biswas (Iowa state University, Ames, USA).

References

1. L. Esaki, R. Tsu, IBM J. Res. Dev. **14**, 61 (1970)
2. L. Eskai, IEEE J. Quantum Electron. **22**, 1611 (1986)
3. A. Wacker, Phys. Rep. **3**(357), 1 (2002)
4. B. Movaghar, Semicond. Sci. Technol. **2**, 185 (1987)
5. N. Chen, X. Li, X. Wang, S. Xie, W.Q. Tian, S. Zhang, H. Sun, IEEE Trans. Nanotechnol. **17**, 140 (2018)
6. H. Xu, B. Chen, F. Jin, Z. Guo, G. Gao, F. Chen, W. Wu, Mater. Res. Express **3**, 126403 (2016)
7. H.J. Haugan, F. Szmulowicz, K. Mahalingam, G.J. Brown, S.R. Munshi, B. Ullrich, Appl. Phys. Lett. **87**, 261106 (2005)
8. G.H. Döhler, Physica Status Solidi (b) **52**, 533 (1972)
9. G.H. Döhler, J. Vac. Sci. Technol. **16**, 851 (1979)
10. G.H. Döhler, H. Künzel, K. Ploog, Phys. Rev. B **25**, 2616 (1982)
11. M. Hundhausen, L. Ley, R. Carius, Phys. Rev. Lett. **53**, 1598 (1984)
12. J. Kakalios, H. Fritzsche, Phys. Rev. Lett. **53**, 1602 (1984)
13. A. Yadav, P. Agarwal, R. Biswas, J. Mater. Sci.: Mater. Electron. **30**, 4696 (2019)
14. P. Photopoulos, A.G. Nassiopoulou, D.N. Kouvatsos, A. Travlos, Mater. Sci. Eng., B **69–70**, 345 (2000)
15. D.J. Lockwood, Z.H. Lu, J.M. Baribeau, Phys. Rev. Lett. **76**, 539 (1996)
16. S. Pattnaik, N. Chakravarty, R. Biswas, V. Dalal, D. Slafer, Sol. Energy Mater. Sol. Cells **129**, 115 (2014)
17. B.I. Sthal, Ph.D. thesis submitted to University of Rosensburg, Germany, 2008
18. D.T. Norton Jr, Ph.D. thesis submitted to University of Iowa, Iowa, 2013
19. M.B.H. Breese, D. Mangaiyarkarasi, Opt. Express **15**, 5537 (2007)
20. Y. Nakata, M. Asada, Y. Suematsu, Electron. Lett. **22**, 58 (1986)
21. Y. Nakata, M. Asada, Y. Suematsu, Surf. Sci. **174**, 519 (1986)
22. G.D. Mahan, L.M. Woods, Phys. Rev. Lett. **80**, 4016 (1998)
23. L.W. Whitlow, T. Hirano, J. Appl. Phys. **78**, 5460 (1995)
24. L.T. Canham, Appl. Phys. Lett. **57**, 1046 (1990)

25. L. Tsybeskov, K.D. Hirschman, S.P. Duttagupta, M. Zacharias, P.M. Fauchet, J.P. McCaffrey, D.J. Lockwood, Appl. Phys. Lett. **72**, 43 (1998)
26. M. Zacharias, L. Tsybeskov, K.D. Hirschman, P.M. Fauchet, J. Bläsing, P. Kohlert, P. Veit, J. Non-Cryst. Solids **227–230**, 1132 (1998)
27. Y.-H. So, S. Huang, G. Conibeer, M.A. Green, Thin Solid Films **519**, 5408 (2011)
28. A. Yadav, P. Agarwal, Superlattices Microstruct. **85**, 776 (2015)
29. A. Yadav, P. Agarwal, Mater. Sci. Semicond. Process. **61**, 5 (2017)
30. K. Ploog, G.H. Döhler, Adv. Phys. **32**, 285 (1983)
31. S.C. Agarwal, S. Guha, J. Non-Cryst. Solids **77–78**, 1097 (1985)
32. S.C. Agarwal, S. Guha, Phys. Rev. B **32**, 8469 (1985)
33. G.S. Paul, P. Agarwal, J. Appl. Phys. **106**, 103705 (2009)
34. D. Azulay, O. Millo, S. Silbert, I. Balberg, N. Naghavi, Appl. Phys. Lett. **86**, 212102 (2005)
35. J.Y. Lin, H.X. Jiang, Phys. Rev. B **41**, 5178 (1990)
36. H.X. Jiang, J.Y. Lin, Phys. Rev. Lett. **64**, 2547 (1990)
37. D. Cammi, C. Ronning, Adv. Condens. Matter Phys. **2014**, 5 (2014)
38. M.N. Islam, P.S. Dobal, H.D. Bist, S. Kumar, Solid State Commun. **107**, 43 (1998)
39. H.J. Queisser, D.E. Theodorou, Phys. Rev. B **33**, 4027 (1986)
40. Y.C.A. Shih, B.G. Streetman, Appl. Phys. Lett. **62**, 2655 (1993)
41. T. Ishibashi, Y. Suzuki, H. Okamoto, Jpn. J. Appl. Phys. **20**, L623 (1981)
42. V.K. Kononenko, H.W. Kunert, I.S. Manak, D.V. Ushakov, J. Appl. Spectrosc. **70**, 115 (2003)
43. S. Tong, X.N. Liu, X.M. Bao, Appl. Phys. Lett. **66**, 469 (1995)
44. L. Khriachtchev, S. Novikov, J. Lahtinen, J. Appl. Phys. **92**, 5856 (2002)
45. K. Ou, S. Wang, M. Huang, Y. Zhang, Y. Wang, X. Duan, L. Yi, J. Lumin. **199**, 34 (2018)
46. M.B.A.E. Wolf, Cambridge University Press, Cambridge, 1999
47. E. Hecht, *Optics*, 4th edn. (Addison Wesley, San Francisco, 2002), p. 425–500
48. A.K. Ghatak, K. Thyagarajan, *Optical electronics* (Cambridge University Press, Cambridge, 1989), p. 57
49. J.A. Pradeep, Ph.D. thesis submitted to IIT Guwahati, India, 2011
50. A. Yadav, Ph.D. thesis submitted to IIT Guwahati, India, 2018
51. A. Yadav, P. Agarwal, Mater. Today: Proc. **4**, 12722 (2017)
52. A. Kastalsky, J.C.M. Hwang, Solid State Commun. **51**, 317 (1984)
53. M. Hundhausen, L. Ley, Phys. Rev. B **32**, 6655 (1985)
54. F.C. Su, S. Levine, P.E. Vanier, F.J. Kampas, Appl. Phys. Lett. **47**, 612 (1985)
55. K.H. Jun, K.S. Lim, J. Non-Cryst. Solids **261**, 268 (2000)
56. V.L. Dalal, A. Madhavan, J. Non-Cryst. Solids **354**, 2403 (2008)
57. A. Madan, P.G. Le Comber, W.E. Spear, J. Non-Cryst. Solids **20**, 239 (1976)
58. G.W. Neudeck, A.K. Malhotra, J. Appl. Phys. **46**, 239 (1975)
59. N.B. Goodman, H. Fritzsche, H. Ozaki, J. Non-Cryst. Solids **35–36**, **Part 1**, 599 (1980)
60. W.E. Spear, P.G. Le Comber, J. Non-Cryst. Solids **8–10**, 727 (1972)
61. T. Tiedje, C.R. Wronski, B. Abeles, J.M. Cebulka, Solar Cells **2**, 301 (1980)
62. M. Hirose, T. Suzuki, G.H. Dohler, Appl. Phys. Lett. **34**, 234 (1979)
63. Y.T.H. Okushi, S. Yamasaki, H. Oheda, K. Tanaka, J. Phys. Colloques **42**, C4 (1981)
64. J. Beichler, H. Mell, K. Weber, J. Non-Cryst. Solids **59–60**, **Part 1**, 257 (1983)
65. N.M. Johnson, J. Non-Cryst. Solids **59–60**, **Part 1**, 265 (1983)
66. E. Bhattacharya, S. Guha, K.V. Krishna, D.R. Bapat, J. Appl. Phys. **53**, 6285 (1982)
67. H.S. Soh, C. Lee, J. Jang, M.Y. Jung, S.S. Yoo, Appl. Phys. Lett. **63**, 779 (1993)
68. S.B. Husain, M. Zulfequar, M.A. Majeed Khan, M. Husain, Curr. Appl. Phys. **4**, 445 (2004)
69. A. Bozhko, M. Shupegin, T. Takagi, Diam. Relat. Mater. **11**, 1753 (2002)
70. Z. Çaldıran, M. Şinoforoğlu, Ö. Metin, Ş. Aydoğan, K. Meral, J. Alloy. Compd. **631**, 261 (2015)
71. W.D. Boer, J. Phys. Colloques **42**, C4 (1981)
72. V. Lehmann, U. Gösele, Appl. Phys. Lett. **58**, 856 (1991)
73. W.L. Wilson, P.F. Szajowski, L.E. Brus, Science **262**, 1242 (1993)
74. S. Furukawa, T. Miyasato, Phys. Rev. B **38**, 5726 (1988)

75. D.C. Hannah, J. Yang, N.J. Kramer, G.C. Schatz, U.R. Kortshagen, R.D. Schaller, ACS Photonics **1**, 960 (2014)
76. O. Yukio, T. Keiji, T. Fumitaka, M. Hiroaki, K. Kenji, Jpn. J. Appl. Phys. **31**, L365 (1992)
77. S. Veprek, F.A. Sarott, Z. Iqbal, Phys. Rev. B **36**, 3344 (1987)
78. L.E. Brus, J. Chem. Phys. **80**, 4403 (1984)

Evolutionary Design, Deposition and Characterization Techniques for Interference Optical Thin-Film Multilayer Coatings and Devices

S. Jena and N. K. Sahoo

Abstract Nano and subnanometric thin-film multilayer interference optical coatings and devices have been playing key as well as essential roles in the manipulation and transport of electromagnetic radiations in various areas of applications such as lasers, telecommunications, smart windows, astronomy, aerospace, environmental monitoring, display, lighting, etc. There are surmounting challenges in the field of optical coatings due to increasing demands of optics in various fields, therefore innovative millstones are continuously explored, especially in investigations on complex multilayer design of challenging filters, development of advance deposition and characterization techniques, searching of news materials, and tuning of microstructure of thin-film coatings. This book chapter presents the overview of recent trends in design, deposition and characterization methods relevant to multilayer optical coatings.

1 Introduction

Interference is the fundamental concept behind modern thin-film optics. The common examples of interference patterns are rainbow in water bubbles and oily substances on water noticed by human civilizations since ancient times. Interference phenomena of light occur in nature as the colours observed in feathers and wings of birds and many insects. Figure 1 gives an example of coloration in butterfly caused due to multilayer interference. The explanation of colours in nature or materials in thin-film forms is now easy as the concept of interference is well understood. In ancient times, people struggled to explain the reason behind colours as the theory of nature of light was not advanced at that time. In 1665, Hooke [1] suggested that the iridescence in

S. Jena (✉) · N. K. Sahoo
Atomic & Molecular Physics Division, Bhabha Atomic Research Centre, Mumbai 400085, India
e-mail: shuvendujena9@gmail.com; shujena@barc.gov.in

N. K. Sahoo
e-mail: sahoonk@gmail.com

N. K. Sahoo
Presently at Eden Garden Apartment, Kharghar, Navi Mumbai 410210, India

S. Kumar and D. K. Aswal (eds.), *Recent Advances in Thin Films*, Materials Horizons: From Nature to Nanomaterials, https://doi.org/10.1007/978-981-15-6116-0_10

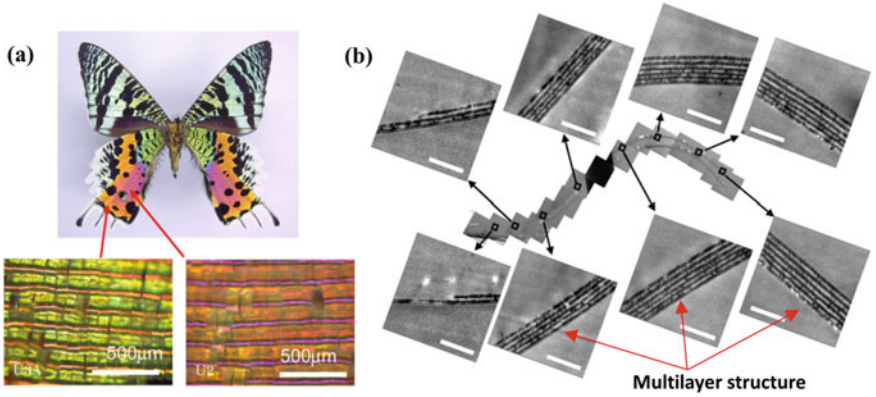

Fig. 1 Colour mixing in the wing of Madagascan sunset moth and its **a** optical microscope images at two different colouring regions. **b** Cross-sectional TEM images of a cover scale in the longitudinal direction, and the inserted images are the magnified views at various positions (reproduced from [8] with permission). The images show that the distal part of the wing cover scale is highly curved like a hemisphere, while the proximal parts are flat. The magnified images clearly show the multilayer structures. The number of layers varies from two to six layers with a position from bottom to top of the wing scale. The thickness of the dark layer is around 170 ± 20 nm and the white layer is distributed from 100 to 150 nm. The colour mixing is due to multilayer reflection caused by interference

peacock feathers was due to the thin alternating layers of plate and air, while Newton suggested it is due to the thinness of the transparent part of the feathers [2]. In 1704, Newton first established a systematic study on interference and tried to extract the film thickness information with his pioneering technique known as 'Newton's rings' [3]. In 1801, Young [4] provided the principle of the interference of light and produced a satisfactory explanation for it. In 1816, Augustin-Jena Fresnel formulated the wave theory of light. Subsequently, Maxwell [5] and Hertz [6] explained the electromagnetic nature of light in. At the same time, the field of interferometry was on significant progress, leading to the invention of the Fabry–Perot interferometer in the year 1899 [7]. By the end of the nineteenth century, there was a considerable progress in understanding the interference phenomena in thin films and multilayer coatings.

The thin-film multilayer optics made rapid progress in the 1930s. The use of metallic thin film to reduce the internal reflection of glass plates was reported by Rouard [9] in 1932. In 1934, Pfund [10] made high reflective ZnS thin films and noted that TiO_2 might be a better option. Halide [11] and fluorite [12] thin films as anti-reflection coatings were demonstrated by 1936. Several factors were responsible for such rapid expansion of the field. But the two most important factors are World War II and the development of lasers. War triggered to improve the light transmission in optical instruments, such as binocular telescopes, and periscopes, especially for use at sea [13]. The optical coatings were a highly secret project during that period. Few companies started work on anti-reflection coatings and achieved light gain over 40%

by 1941, which were coated on all submarine periscopes and binoculars. As a result, the binoculars got an additional 30–45 min of clear sighted at dusk and dawn [14]. World War II brought large number of scientists together to boost the development of technology. Many of the scientists became principal figures in the field of optical coatings after the world war. A substantial number of companies like Balzers AG, Denton Vacuum, Leybold AG, etc. were emerged to produce the coatings, or the coating system, or both [13]. After World War II, the most triggering factor for the development of optical coatings was laser. The key component of a laser is a resonator that needs high reflecting mirrors. Earlier, silver coating was used as a high reflecting mirror at both ends of the polished laser rod. Silver has absorption loss as well as it would be damaged or eroded most often making it difficult for use in lasers. For better lifetime of laser resonators, dielectric multilayer mirrors emerged as replacement of the metallic coatings. The use of laser in different spectroscopic experiments lead to the invention of different optical filters that were not realized before. In this process with time, the thin-film coatings delivered various precision optical components and devices required for the development of technology in different fields of science and engineering.

Optical multilayer coatings such as anti-reflection coatings, high reflection mirrors, beam splitters, beam combiners, bandpass filters, etc. are effectively utilized in various fields such as manufacturing of optical and scientific instruments, lasers, synchrotron radiation and emission–absorption spectroscopy, medical science and astronomy [15]. Today's technology demands complex optical instruments. To meet such demands, the surface of the optical components is coated with specially designed multilayer coatings to achieve tailored spectral properties. The geometric structure and the properties of the individual layers in a multilayer significantly affect the spectral properties of the multilayer coating, even when each layer is assumed to be optically isotropic and homogenous with smooth surface and interfaces. In real coatings, the thin film layers may exhibit inhomogeneity in thickness as well as refractive index and also, there exist finite surface and interface roughness of the layers.

There is no clear definition of thin film. For example, a coating which is termed as thin-film protective coating may be much thicker than an extreme UV interference coating, and at the same time it may be much thinner than a THz mirror coating. Generally, thin films are thin layers of materials having thickness from fractions of a nanometer to several micrometres. In case of thin-film optics, the thin layer is assumed to be infinitely extended in two directions, while its spatial extension is small enough in the third direction so that its thickness in this direction is much smaller than the coherence length of the light. In reality, no thin-film layer extends to infinity in its plane, but it is much larger than the extension along the film axis. This difference creates significant battle between models based on ideal and real structure films. In addition to that, there is always a fixed number of atoms at the interface and they are different than those present in the bulk. The ratio between surface and bulk atoms significantly influences the material properties, which can be realized through the following practical examples. Real optical thin-film coatings with their macroscopic counterpart that exist in nature are presented in Fig. 2, which is found exciting as well as amazing. It clearly shows that there exists a great resemblance

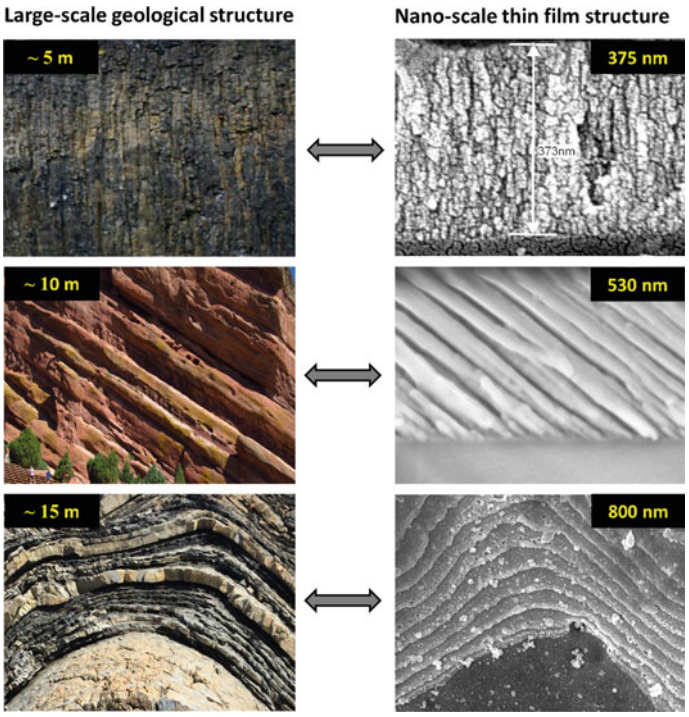

Fig. 2 Comparison between large-scale geological structure (*on left*) and nanoscale thin-film structure (*on right*). *First row*: The *left* image is the basaltic pit columns at Rhoen, Bavaria, Germany [16] and the *right* image is the cross-sectional FESEM image of the electron beam evaporated ZrO_2 thin film. *Second row*: The *left* image is the Red Rocks at Colorado, USA [17], and the *right* image is the cross-sectional FESEM image of the oblique angle deposited HfO_2 thin film [18]. *Third row*: The *left* image is the alternating layers of Devonian sandstone and mudstone at Cape Liptrap, Victoria, Australia [19], and the *right* image is the cross-sectional FESEM image of laser-induced damage structure of HfO_2/SiO_2 multilayer coating [20]

in the topography of nanoscale real thin films and multilayer coatings with their large-scale geological structure. All the coatings are prepared using electron beam evaporation technique, and they exhibit columnar structure with finite porosity in the film or multilayer. In Fig. 2, the right side of the first row presents the columnar growth structure of 373-nm-thick ZrO_2 thin film. Surprisingly, it exhibits similar appearance as the basaltic columnar rock structure in a mining at Rhoen, Bavaria, Germany as shown in the left of the 1st row. The left of the second row in Fig. 2 shows the structure of famous Red Rocks, Colorado, USA, made of assembly of rocks having height more than 10 m. Its thin-film nanostructure counterpart, i.e. cross-sectional morphology of oblique angle deposited HfO_2 thin film is presented in the right side of second row, which shows tilted columnar structure like the Red Rocks structure. Even more exciting is the structures presented in the third row. The

left side presents a large-scale geological rock made of brittle and ductile deformation of alternating layers of Devonian sandstone and mudstone at Cape Liptrap, Victoria, Australia, and its exact microscopic counterpart is presented in the right side which shows the cross-sectional morphology of the laser-induced damage structure of electron beam evaporated HfO_2/SiO_2 multilayer coating made of alternate layers of HfO_2 and SiO_2. In spite of their apparent geometrical resemblance, the physical properties of the nanoscale materials are significantly different from their large-scale counterparts. This can be realized by comparing the surface-to-volume ratio between a large-scale and nanoscale columnar structure. A column can be considered as a cylinder with height (h) and diameter (D). The surface-to-volume ratio is given by $S/V = (2/h) + (4/D)$. For a nanoscale thin-film structure, D is assumed to be 100 nm and h is ~500 nm. For a large-scale structure, D ~1 m and h ~10 m. The calculation clearly shows that the surface effects relative to the volume effects in the nanoscale structure are ~10^7 times higher as compared to that of large-scale columnar structure. Therefore, surface effects are dominant in case of thin films or nanostructured materials. Primarily, the surface features define the physical difference between thin film and bulk. The quasi two-dimensional structure of a thin film is exploited to replace the volume functionality by surface functionality, which is a viable approach in a world with limited resources [15]. For optical coating applications, the control of thickness, grain size and distributions, stoichiometry and structure of the thin films are very much essential.

The thin-film properties are sequentially combined to make multilayer interference coatings with each thin-layer thickness comparable to the wavelength of visible light. Generally, a multilayer optical coating is designed by quarter-wave stack of high refractive index and low refractive index materials, which is then refined for the desired spectral characteristics. A simple example of an optical thin film coating is anti-reflection coatings for ophthalmic glasses. The optical coatings are essential for almost all fields of science and technology dealing with light. The complex design aspect with advanced deposition systems plays a crucial role in the progress of optical coatings. Nowadays, interference filters can be made of hundreds and even thousands of layers that are also commercially available. The field of optical thin films is well documented by several researchers in the form of review articles [21], books and chapters [3, 15, 22–27]. In addition to this, thin-film optical coating design courses and short courses are regularly carried out at various conferences [28–30]. A large number of researchers, experts and industries have been working to design and develop modern optical coatings as per the technology demands. A clear procedure needs to be followed in order to design a multilayer coating targeting some desired spectral characteristics usually transmission, reflection and absorption. In many applications, these properties are required as a function of a given combination of external parameters such as wavelength (λ), angle of incidence (θ) and polarization (TE and TM) of incident light. To meet the desired spectrum, a thin-film designer has to play with following parameters in a multilayer, i.e. number of layers (N), refractive index (n), extinction coefficient (k) and thickness (d) of the layers, and optical constants of incident medium and substrate [31], which can be tackled by graphical, analytical and numerical methods. Analytical methods are

usually fast, but they are not efficient in case the materials are strongly absorbing or highly dispersive [32]. Graphical methods help to identify approximate multilayer designs, which can be used as the starting designs for further refinement using advanced computers [33]. In most numerical methods, the design of a multilayer structure targeting the desired spectrum is based on the use of merit functions [32]. Though the history of using a digital computer for optical coating design was more than half a century, the significant progress was made in the first part of this period when attempts were made to develop different types of design approaches and mathematical optimization routines for computational designing of optical coatings. These developments were documented by Dobrowolski, who approached two ways, i.e. refinement and synthesis techniques to design optical coatings [34]. The refinement approach normally requires a starting design that is not quite satisfactory, and gradually improves to match the desired performance. By contrast, the synthesis approach frequently generates its own starting design and then followed by refinement, which is generally used for complex optical coatings [35]. A multilayer optimization example is given below in Fig. 3a which presents a refined design spectral characteristic of a passband filter along with its target spectrum. Figure 3b shows the starting design of a multilayer structure and its final optimized design structure to get the spectrum that is close to the targeted spectrum. Though various books, chapters, research papers and review articles are devoted to optical coating design in the past, reports on systematic presentations of different optimization approaches used for designing complex multilayer coatings are rare. In this chapter, different optimization techniques with their advantages and limitations for designing multilayer optical coatings will be discussed with suitable examples.

To achieve the desired spectral characteristics of a multilayer coating, one needs knowledge of all aspects of design, requirement of materials and deposition techniques used for the production of such coatings. Materials are deposited layer by layer on transparent optical grade substrates using both physical vapour deposition (PVD) and chemical vapour deposition (CVD) techniques. The most common PVD

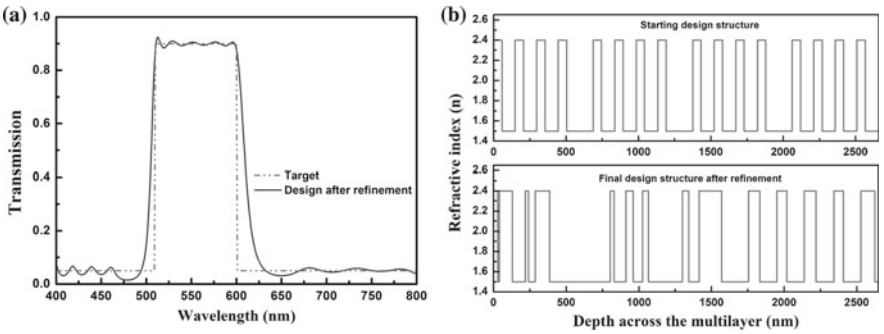

Fig. 3 **a** Target (dotted line) and design (solid line) spectra of a passband filter. **b** Refractive index profile of a starting design structure with its final design structure after refinement which gives the design spectrum (solid line) as shown in the left figure

techniques used for deposition of optical coatings are techniques evaporation and sputtering. Materials having inorganic elements or compounds are usually deposited using PVD process with or without reactive gases, while the techniques like CVD, dip coating and spin coating requires liquid inorganic and organic compound, and gases for the deposition process to happen [36]. Generally, transparent dielectric refractory oxides, halides, sulphides, selenides, tellurides and chalcogenides are widely used for optical coating applications, which are deposited using mostly PVD techniques. During evaporation, the parent materials get decomposed and the final coating may lead to non-stoichiometry thin films. Therefore, evaporation is performed under a reactive environment to ensure the resultant coating exhibits the required stoichiometry. The residual gas pressure in terms of moisture present in the evaporation material significantly affects the evaporation process as well as the structure of thin-film layers. Hence, preheating or outgassing of the evaporation materials are must prior to the deposition. Moreover, there are also several other factors that can affect the properties of thin-film coatings. An attempt is made to cover various aspects of deposition techniques with their advantages and disadvantages related to thin-film optical coatings in the later part of this book chapter.

The cleanness of a deposition system and better quality thin-film coatings require materials that should fulfil a series of criteria before being used as a coating material. They are basically chemical purity, stoichiometry in case of alloys, homogeneity of the grains or particles, density, etc. Chemical purity of the materials or targets is one of the important criteria which should be at least 99.99%. Fluoride materials such as MgF_2, BaF_2, AlF_3, CaF_2, LaF_2, etc. are used to develop filters or mirrors required for deep ultraviolet–vacuum ultraviolet laser applications since they exhibit transparency in the UV region having optical band gap close to 10 eV [21, 37]. Dielectric refractory oxides such SiO_2, HfO_2, TiO_2, ZrO_2, Ta_2O_5, Al_2O_3, etc. are an important class of optical coating materials as they exhibit wide transparent spectral range from visible to near-infrared region with a good variety of refractive indices [21, 38]. In addition to this, they form hard, abrasion-resistant and chemically and environmentally stable thin-film coatings. Since most of the oxides get dissociated at high temperatures, therefore it is advised to provide oxygen during the evaporation process of oxide materials as per the needs. ZrO_2 and HfO_2 are very commonly used high-index coating materials because of their high UV transmission and higher laser-induced damage threshold. The absorption of both hafnia and zirconia is only significant below the wavelength of 250 nm; therefore they are very useful for UV optical coatings [39]. SiO_2 is the common low refractive index and high band gap material used for the fabrication of different optical filters [39]. In addition to that, SiO_2 thin film can be used as a corrosion resistance layer of metals [40]. TiO_2 (n ~2.4) is a high refractive index material mostly used in the visible range as it begins to absorb light below 450 nm [39]. TiO_2 is very useful for applications such as self-cleaning and defogging windows [41]. Some complex coatings require material refractive index values that do not exist in conventional pure coating materials. For example, there is a gap between refractive index values of 1.63 (Al_2O_3) and 1.85 (Y_2O_3). Two materials of different refractive index values can be mixed to get the desired refractive indices, and are called as mixed oxide thin films [42]. The mixed oxide film helps to tune grain

morphology, structure, film density and residual stress in coatings. There are reports on the mixed films of ZrO_2–MgO, ZrO_2–SiO_2, ZrO_2–MgF_2, TiO_2–SiO_2, HfO_2–SiO_2 and Ta_2O_5–TiO_2. The range of refractive index for the mixed films is roughly 2.05–1.7 for ZrO_2–MgO, 2.05–1.45 for ZrO_2–SiO_2, 2.1–2.55 for Ta_2O_5–TiO_2 and 2.05–1.36 for ZrO_2–MgF_2 [43]. There are also commercially available mixed oxide materials such as SiO_2–Al_2O_3, ZrO_2–TiO_2, ZrO_2–Al_2O_3, TiO_2–La_2O_3 and Ta_2O_5–Al_2O_3 [36]. Sulphides, selenides and tellurides such as ZnS, CdS, SbS_3, ZnSe, CdSe, Sb_2Se_3, ZnTe, CdTe and PbTe, are important infrared coating material [21]. They are evaporated from resistively heated boats made of tungsten or molybdenum. Most of the sublimated materials decompose during evaporation, but finally, recombine on the surface of the substrate, and the recombination is controlled by substrate heating. Today, ZnS and ZnSe are mainly used for anti-reflection coatings for infrared region, decorative coatings and holographic applications [44–46]. Telluride materials are mainly useful for electro-optical applications [47]. Metal–dielectric mixture known as cermets is used for solar coatings or absorbing coatings. Besides the above, there exist numerous materials used for optical coatings.

Once thin films or multilayer optical coatings are prepared, the next step is to see whether they show the required structure, optical properties, surface morphology, stress and laser damage threshold, which are very much essential for developing stable multilayer optical coatings. The film optical properties such as refractive index, extinction coefficient, and optical band gap are the most important parameters for the design and development of optical filters. The interface in a multilayer gets affected by the crystal structure of thin layers. Generally, crystalline films generate rough interfaces as compared to that of amorphous films. Hence, the crystal structure of thin-film coatings is very crucial for developing low-loss optical filters. Surface morphology gives surface features such as roughness and grain sizes. Therefore, control of surface morphology of coatings is essential to get the least surface scattering. Generally, finer grain size distributed morphology is desired to get dense films with least surface roughness, resulting in stable optical coatings with least scattering. Under mechanical shocks, intense pulsed laser fields or environmental disturbances, cracking or peeling of thin coating layers may occur, which can adversely affect the performance of the thin-film coating devices. To avoid it, the optimization of the mechanical properties of the thin films is of great concern. In particular, residual stress in coatings is related to the coating stability, i.e. peeling, cracking and curling of the films [48]. Therefore, determination of residual stress of thin films is very crucial for developing stable optical coatings. The dielectric multilayer coatings are widely used for laser applications. For high-power lasers, the multilayer coatings should withstand laser power without being damaged. Therefore, the laser damage threshold of thin films and multilayer coatings is of high importance. There are several other properties such as electronic, magnetic, non-linear optical properties, etc. which are also important as per the coating applications. Here, we will restrict to discuss the characterization techniques that are relevant for optical coatings only.

Conventionally, the field of thin-film multilayer optical coatings is interdisciplinary in nature, which combines optics, electrodynamics, quantum mechanics and material science into a specific research area known as applied optics. The recent

updates in the novel design, characterization and production of thin films and multilayer optical coatings are found to be less clearly arranged as a result a new researcher faces trouble and gets confused in the rapidly changing scientific environment. The present book chapter will try to cover from simple to complex coating designs, widely used coating deposition methods and all necessary characterization techniques to qualify and quantify the performance of an optical coating.

2 Basics of Thin Films and Multilayer

2.1 Single Layer

We will briefly review some of the key concepts and basic mathematical formulations of thin films, which are very much essential for designing thin-film optical coatings. Figure 4a shows schematic of a thin-film structure considering multiple reflections from both the front and back surfaces of the film. The light reflected from the first surface of the film is denoted as r_{12} and the transmitted part has r_{23} reflected from the second surface of the film. Again, the light is reflected when it falls back on the first surface and part of this reflected light r_{21} is again reflected when it falls on the second surface. The resultant amplitude reflectance considering all the reflections from the two interfaces is given by [22]

$$r = r_1 + r_2 + r_3 + \cdots = \frac{r_{12} + r_{23}e^{-i\varphi}}{1 + r_{21}r_{23}e^{-i\varphi}} \tag{1}$$

Here $\varphi = (4\pi/\lambda)nd\cos\theta$ is the phase difference between r_1 and r_2 caused by the optical thickness of the film, and θ is the angle of incidence of light. The Fresnel amplitude reflection coefficients at first and second interfaces of the thin film are given by

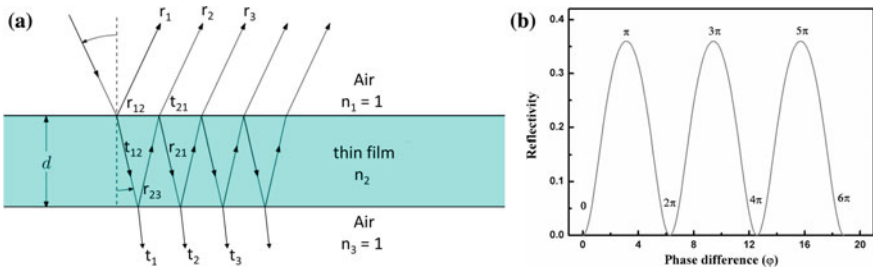

Fig. 4 **a** Schematic of a thin film with multiple reflections, and **b** variation of reflectivity of the thin film with phase difference between r_1 and r_2

$$r_{12} = \frac{n_1 - n_2}{n_1 + n_2},\ r_{21} = \frac{n_2 - n_1}{n_2 + n_1} \text{ and } r_{23} = \frac{n_2 - n_3}{n_2 + n_3} \tag{2}$$

Figure 4b shows the variation of reflectivity with the phase difference for a thin film having refractive index $n = 2$ placed in air medium having refractive index $n = 1$. This figure shows that the reflectivity is a maximum of 0.35 for $\varphi = \pi, 3\pi$ and 5π, while the reflectivity is zero for $\varphi = 0, 2\pi, 4\pi$ and 6π. The phase difference of π and 2π correspond to optical path difference of $\lambda/4$ and $\lambda/2$, respectively. If the film having a thickness of one-quarter-wave optical thickness (QWOT), i.e. $nd = \lambda/4$ at the wavelength of consideration λ, the film appearance would be white. As the film becomes thicker close to $\lambda/2$ or thinner close to zero, then it would appear as black as it shows no reflection. This is the reason which leads to colour mixing in water bubbles. Water bubble has a thickness of many QWOTs with respect to the visible light. The bubble shows more QWOTs in blue light than the red light for a given thickness. Hence, the blue and red lights are at different phases and exhibit different reflectivity. This creates a rainbow in soap bubbles. The half-wave optically thick ($nd = \lambda/2$) layers are absentee layers, while the QWOT layers are used to enhance the reflectivity in a multilayer coating design. These are the basic principle of the reflectance or circle diagram as documented by Apfel [33]. QWOTs are used either to increase or decrease the reflectance using high or low refractive index layers as per the requirement.

The design of multilayer coatings considers the properties of individual single layers to give a desired spectral performance. Incident light having coherence length of incident light ($\lambda^2/2\pi\,\Delta\lambda$) greater than the optical thickness (nd) of a layer is considered as monochromatic for the thin layer. Therefore, interference of light due to multiple reflections within the layers cannot be neglected. So, their electric field amplitudes are added to get the net reflection and transmission to its adjacent layers. If the optical thickness is greater than the coherence length, the phases of the internally multiple reflected lights are random, therefore the interference of light can be ignored. As a result, intensities of light instead of amplitudes of the electric field of the light inside or outside of the thick layer are added to get the net reflection and transmission [49]. Depending on the thickness of a film, the optical response of the film is treated as either coherently or incoherently. In the present case, the thicknesses of the thin films are considered being comparable to the wavelength of light, hence should be treated coherently. The optical response of single-layer thin films of high-index and low-index materials should be discussed before moving to multilayer optics. Therefore, the spectral properties of single-layer films are discussed below, so that one would get an idea about the importance of single-layer geometric and optical parameters. The effects of refractive index, film thickness, angle of incidence and polarization of light on the spectral reflection and transmission of single-layer films are computed and plotted in Figs. 5 and 6.

High as well as low refractive index thin films are assumed to be coated on a glass substrate having refractive index n ~1.5 and light is incident normal to the films. Figure 5a clearly shows that the reflectivity increases and transmission decreases for a significant part of the spectrum with an increasing refractive index from 1.8

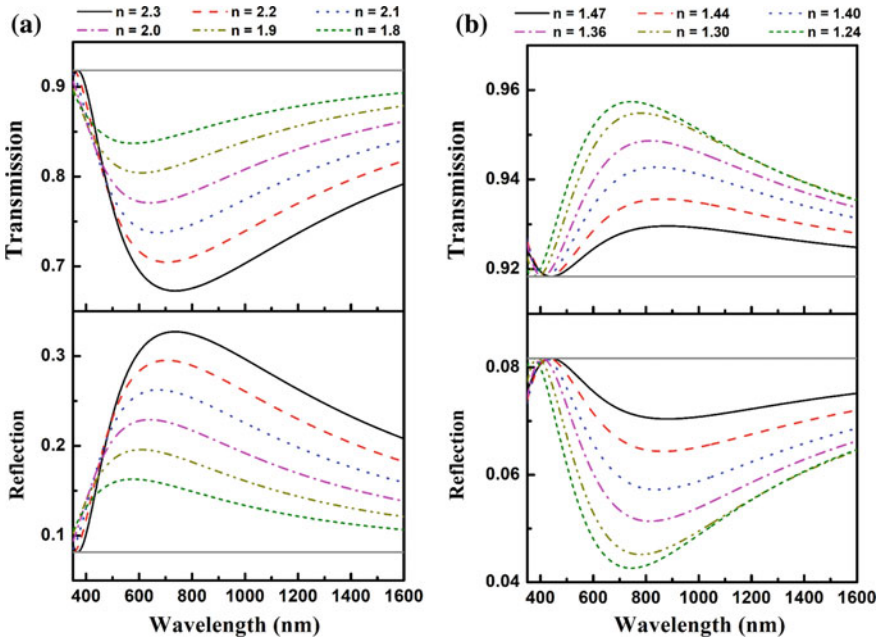

Fig. 5 Optical spectrum of **a** high refractive index thin films ($d = 80$ nm), **b** low refractive index thin films ($d = 140$ nm) with varying refractive index (n) values

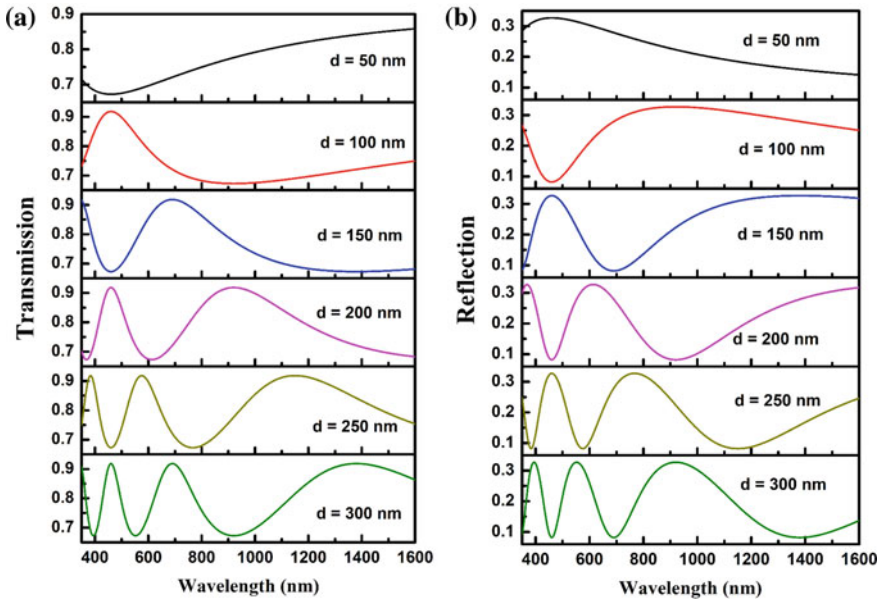

Fig. 6 Thickness dependent **a** transmission and **b** reflection spectrum of a high refractive index ($n = 2.3$) coating on glass substrate

to 2.3, but there is a very small change in reflection as well as transmission at a wavelength around 350 nm, as it is close to half-wave position. The peak reflectivity or least transmission position is the quarter-wave position for high-index thin films. Figure 5b shows the anti-reflection properties of the low-index thin-film coatings. The transmission of the low-index-coated glass increases or the reflectivity decreases with decreasing refractive index values from 1.47 to 1.24. The lowest reflection point indicates the quarter-wave position, while again the reflectivity does not change at the half-wave position in the spectrum. Figure 6 shows that the number of interference fringes increases both in reflection and transmission spectra with increasing thickness of a dielectric thin film having a refractive index value of $n = 2.3$. In real coatings, the thickness may even affect the refractive index, band gap, roughness and structure of the thin-film coatings [50–52]. Hence, control of thickness is essential to achieve the desired spectral performance of optical coatings.

Now, let us consider the effect of angle of incidence and polarization of light on the optical response of dielectric thin films. Light is basically an electromagnetic wave in which the electric and magnetic field vibrates perpendicular to each other in space and time. The light is considered plane-polarized or linearly polarized light if its electric field vibrates in a fixed plane in space, named as plane of vibration. Most of laser light are plane-polarized, while the light from the sun is found to be unpolarized. When unpolarized light is incident on the dielectric thin films, it can be decomposed into two components, i.e. S-polarization and P-polarization. If the electric field of light is polarized perpendicular (parallel) to the plane of incidence, then it is called as S-polarized (P-polarized) light. The spectral reflection or transmission of both the polarizations depends on the angle of incidence. It is well known that the reflection of P-polarized light (TM wave) drops to zero at a definite angle, known as Brewster's angle, and the reflected light becomes plane or linearly polarized with only the S-polarization. Figure 7 shows the angle of incidence dependent reflection and transmission spectra of thin films with varying refractive index values from 2.3 to 1.5 for both the polarizations of light. The Brewster's angle shifts to a higher angle with an increasing refractive index value of the films. The reflection increases or the transmission decreases with increasing angle of incidence for S-polarized light. In the case of p-polarized light, the reflection gradually decreases with the angle of incidence and becomes zero at Brewster's angle, and then increases drastically with further increasing angle of incidence of light.

2.2 Multilayer

Before designing multilayer coating based optical filters and mirrors, the basic theory of multilayer structure needs a revisit to formulate the design problems. In the past, various methods such as recurrence equations, Smith, Kard and admittance charts, vector methods and analogies with electrical and microwave filters have been used to design optical multilayer coatings [53]. These methods were efficient for coatings with a few layers. But the most versatile approach that is suitable for designing both

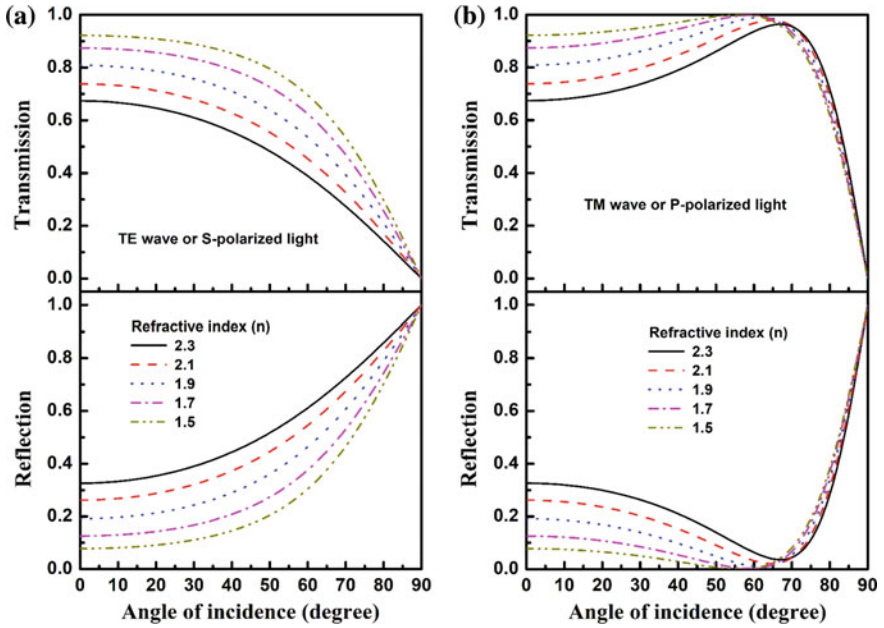

Fig. 7 Angle of incidence dependent transmission and reflection of a thin film ($d = 80$ nm) with varying refractive index values for **a** S- and **b** P-polarization light of $\lambda = 700$ nm

simple and complex optical coatings was proposed by Abeles [54] and then pioneered by Weinstein [55] is based on the matrix formulation derived using Maxwell's equations [53]. Figure 8 illustrates the schematic of a multilayer coating consists of m homogenous and isotropic layers. The z-axis is in the direction from the incident medium (air) to the substrate, and the layers are numbered along the z-axis. All the layers are assumed to be transparent in nature for the sake of simplicity. The thickness and refractive index of the layers are denoted by $(d_1, n_1), (d_2, n_2), \ldots, (d_m, n_m)$. The refractive index of the substrate and incident medium (air) is denoted as n_s and n_0, respectively.

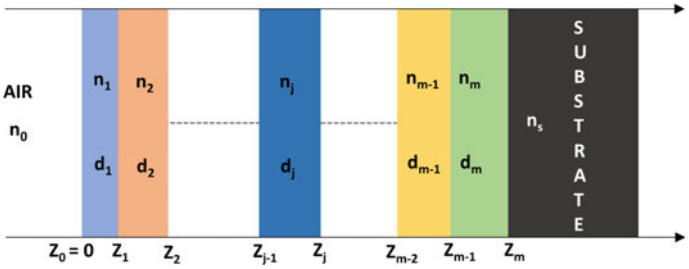

Fig. 8 Schematic of a multilayer coating structure

Using the continuity conditions, the electric and magnetic fields at any two positions z and $z + d_j$ in the jth layer can be related by a transfer matrix as proposed by Abeles [24, 25, 54]

$$M_j = \begin{pmatrix} \cos k_j d_j & \frac{i}{\eta_j} \sin k_j d_j \\ i\eta_j \sin k_j d_j & \cos k_j d_j \end{pmatrix} \tag{3}$$

where d_j is the thickness of the jth layer, ω is the angular frequency of the incident light, $k_j = (2\pi/\lambda) n_j \cos\theta_j = (2\pi/\lambda) n_j \sqrt{1 - \left(\sin^2\theta / n_j^2\right)}$ is the propagation wave-vector in the z-axis, n_j is the refractive index and θ_j is the incident angle of the jth layer, θ is the angle of incidence and c is the speed of light in vacuum. Using Snell's law $n_j \sin\theta_j = n_0 \sin\theta$, we obtain the pseudo-indices $\eta_j = n_j \cos\theta_j = n_j \sqrt{1 - \left(\sin^2\theta / n_j^2\right)}$ for S-polarized (TE wave) light, and $\eta_j = n_j / \cos\theta_j = n_j \Big/ \sqrt{1 - \left(\sin^2\theta / n_j^2\right)}$ for P-polarized (TM wave) light. The electric and magnetic field amplitudes are continuous at the boundaries of the layers, therefore the field can be estimated from its boundaries at $z_0 = 0$ to z_m by multiplying all the transfer matrices, known as the characteristic matrix (M) of a multilayer given by [24]

$$M = M_1 M_2 M_3 \ldots M_m = \begin{pmatrix} m_{11} & m_{12} \\ m_{21} & m_{22} \end{pmatrix} \tag{4}$$

The amplitude of transmission coefficient (t) and reflection coefficient (r) are expressed through the matrix elements by the equations [25, 56]

$$t = \frac{2\eta_0}{(\eta_0 m_{11} + \eta_s m_{22}) + (\eta_0 \eta_s m_{12} + m_{21})} \tag{5}$$

$$r = \frac{(\eta_0 m_{11} - \eta_s m_{22}) + (\eta_0 \eta_s m_{12} - m_{21})}{(\eta_0 m_{11} + \eta_s m_{22}) + (\eta_0 \eta_s m_{12} + m_{21})} \tag{6}$$

The transmitted and reflected intensities, T and R, are calculated from the amplitude coefficients by the equations given below:

$$T = \frac{\mathrm{Re}(\eta_s)}{\mathrm{Re}(\eta_0)} |t|^2, \; R = |r|^2 \tag{7}$$

The above equations are used to compute reflection, and transmission in a multilayer coating for any angle of incidence for both polarizations of light. The reflection of two multilayer structures, one having periodic bilayer and other having periodic tri-layer with varying number of periods (N), are calculated and plotted in Fig. 9. The figure shows that the reflectivity of the multilayer increases with an increasing

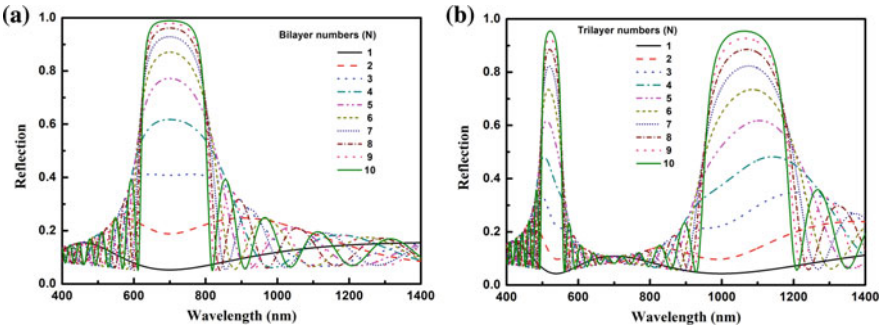

Fig. 9 **a** Reflection spectra of a $(HL)^N$ multilayer structure with varying bilayer numbers N from 1 to 10, where the refractive index of the H and L layers are 2 and 1.46, respectively. **b** Reflection spectra of a $(HML)^N$ multilayer structure with varying tri-layer numbers N from 1 to 10, where the refractive index of the H, M and L layers are 2, 1.8 and 1.46, respectively. In both cases, the design wavelength is considered to be 700 nm, and the optical thickness of all the layers is quarter-wave at $\lambda_0 = 700$ nm

number of periods. The periodic tri-layer shows two high reflection bands, while the periodic bilayer shows only one high reflection band for $N = 10$. Figure 10 shows the variation of reflectivity of a multilayer quarter-wave stack with different angles of incidence for S- and P-polarized lights. The peak reflectivity as well as bandwidth of the reflection profile increases with angle of incidence for S-polarized light, while it decreases for P-polarized light. The central wavelength of the reflection spectrum undergoes blueshift with increasing angle of incidence for both polarizations. But beyond Brewster's angle, the peak reflectivity for P-polarized light again increases. These equations remain valid and used even for metal–dielectric multilayer, where the materials are absorbing in nature. These are the fundamental formulations for designing any multilayer coatings, where the computation aims to find the number of layers, the refractive indices and thicknesses of each layer in a multilayer that

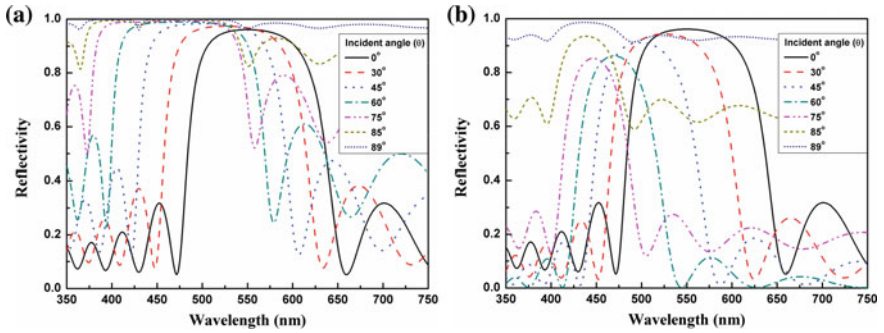

Fig. 10 Angle of incidence dependent reflectivity of a $(HL)^8$ multilayer for **a** S-polarized, and **b** P-polarized light, respectively, where the refractive index of the quarter-wave H and L layers are 2 and 1.46, respectively, at $\lambda_0 = 550$ nm

deliver the target spectrum. The detailed utilities of these equations will be explored further in the simple and complex design of optical coatings in the next part.

3 Design of Multilayer Optical Coating Devices

3.1 Simple Designs

Early days of design of optical coatings were basically done using the concept of quarter-wave optical thickness (QWOT = nd = $\lambda_0/4$), where λ_0 is the wavelength of consideration. If a thin film has QWOT, then the path travelled by the light from the first surface to second and back to the first would be half-wavelength ($\lambda_0/2$), i.e. the phase difference $\varphi = 180°$. Here, the two reflections are added to give maximum reflectivity. Similarly, QWOT low-index layers coated on high-index substrate gives low reflection. The QWOT is regarded as the building block for designing most of the optical coatings. Some of the QWOT-based simple designs for various optical coatings and filters are illustrated below.

The simplest coating is a single-layer coating on both sides of a substrate to reduce its reflection, known as anti-reflection coating. The single layer is having QWOT with refractive index equal or close to the square root of the index of the substrate ($n_s = 1.52$ for glass), i.e. $n = 1.23$. Excluding porous coatings, no conventional coating material has such low refractive index values. The material MgF_2 has the least refractive index value of $n = 1.38$, which is frequently used for anti-reflection coatings on high-index substrates. This single-layer coating on glass substrate does not entirely reduce its reflection to zero. For that reason, people approached double-layer QWOT coating (Air/LH/substrate/HL/air) to get zero reflection at the design wavelength. The refractive index of the high-index second layer (H) is chosen using the equation $n_2 = n_1\sqrt{n_s / n_0}$ for a QWOT double layer. With $n_0 = 1$, $n_1 = 1.38$ (L layer) and $n_s = 1.52$ (glass substrate), the value of $n_2 = 1.70$ (H layer). Using these parameters, the reflection spectrum is computed and plotted in Fig. 11a. The figure shows that the reflectivity is zero at the design wavelength of $\lambda_0 = 1000$ nm. The coating shows perfect anti-reflection at the design wavelength. The aim of this coating is to enhance the transmission and simultaneously reduce the reflection of light in various optical components in the widest possible spectral region. Particularly, the optics in lasers needs such anti-reflection coatings to be loss free.

The other simple QWOT design is the design of high reflection (HR) mirrors. As QWOT layer gives maximum reflection, hence many more QWOT layers are required to get high reflection. The HR mirror is designed by a multilayer stack made of alternate QWOT layers of high- and low-index materials. Figure 11b shows the reflection spectrum of an HR mirror having design structure Air/$(HL)^{10}$/Glass with a refractive index of H and L layers as 2.36 (TiO_2 layer) and 1.46 (SiO_2 layer), respectively. The half-width ($\Delta\lambda$) of the high reflection band depends on the refractive index contrast between the high- and low-index layers, and can be calculated by

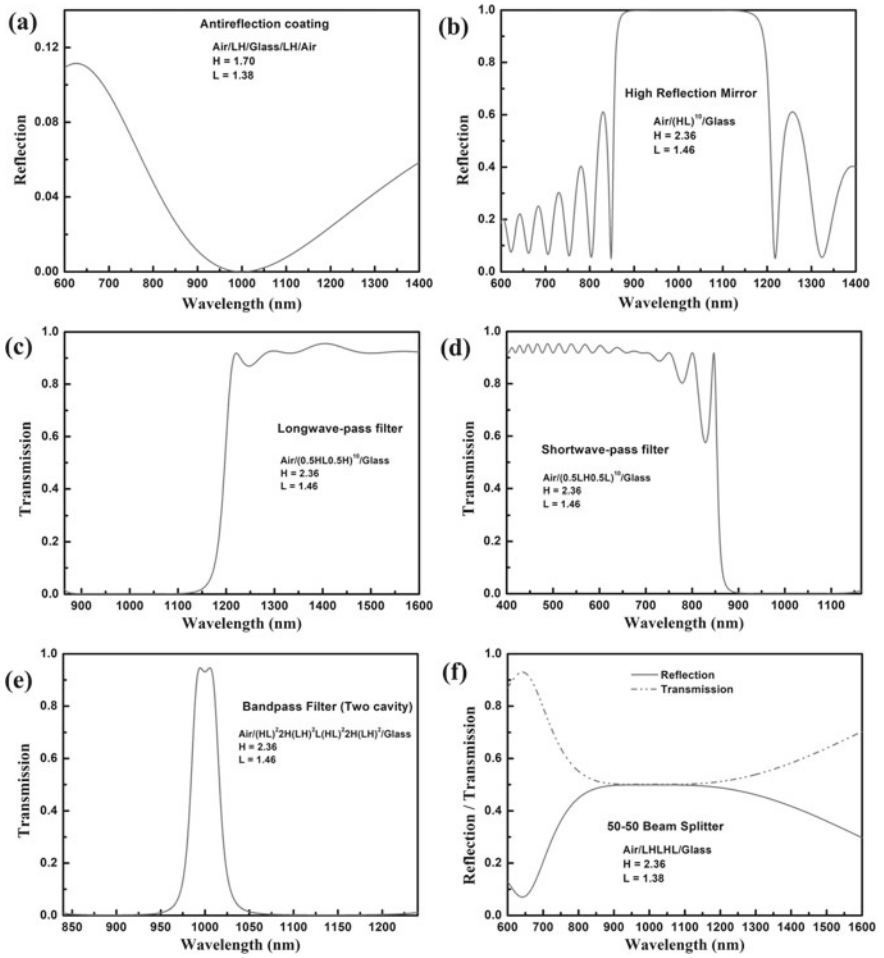

Fig. 11 Simple quarter-wave design of various optical coatings and devices targeted at the central wavelength of $\lambda_0 = 1000$ nm: **a** Anti-reflection coating **b** High reflection mirror, **c** Long wave pass filter, **d** Short wave pass filter, **e** bandpass filter, and **f** beam splitter. The design structure of all the coatings as well as materials refractive index values are mentioned in the inset of the plots. H and L represent the high and low refractive index layers, respectively

$\Delta\lambda = (2/\pi)\sin^{-1}[(n_H - n_L)/(n_H + n_L)]$. Wider the refractive index contrasts between the materials, larger the width of high reflection band. The design wavelength as well as other materials can be chosen as per the requirement. Heterogeneous multilayer structure can be made to design wideband high reflection mirrors covering the entire visible spectrum.

Figure 11c, d shows the transmission spectrum of a long wave pass and short wave pass filters along with their design structure mentioned in the inset of the plots. The starting design is a quarter-wave stack with maximum

number of layers to get a block band. Then half-wave high-index layers are matched if the stack starts and ends with QWOT low-index layers to design long wave pass filters, and vice versa for short wave pass filter. The two possibilities are (i) $\frac{H}{2}LHLHLH \ldots LHL\frac{H}{2}$, and (ii) $\frac{L}{2}HLHLHL \ldots HLH\frac{L}{2}$. These arrangements can be replaced by $\frac{H}{2}L\frac{H}{2}\frac{H}{2}L\frac{H}{2}\frac{H}{2}L\frac{H}{2}\frac{H}{2}L \ldots \frac{H}{2}\frac{H}{2}L\frac{H}{2}$, and $\frac{L}{2}H\frac{L}{2}\frac{L}{2}H\frac{L}{2}\frac{L}{2}H\frac{L}{2}\frac{L}{2} \ldots H\frac{L}{2}\frac{L}{2}H\frac{L}{2}$, respectively, which can be further written as $\left[\frac{H}{2}L\frac{H}{2}\right]^N$ and $\left[\frac{L}{2}H\frac{L}{2}\right]^N$ [3]. Here N is the period of the multilayer stack. The stack $\frac{H}{2}L\frac{H}{2}$ and $\frac{L}{2}H\frac{L}{2}$ are the basic period for long wave pass and short wave pass filters, respectively. In pass band of both the filters, the multilayer stack behaves as if it is an inhomogeneous single layer. There exist ripples in the pass band of the filters. There are various ways one can reduce the ripples. The easiest one is to choose a combination having an equal admittance comparable to that of the substrate with a condition that the reflection loss due to the substrate is not very high. Presently, the most common technique to remove the ripples is by computer refinement which is discussed later in more detail.

Narrow bandpass filter is made by simple quarter-wave design, in which a half-wave optically thick layer (absentee layer) is inserted between two QWOT multilayer stacks. The QWOT multilayer increases the reflection while the reflection at the half-wave point does not change and remains the same as the substrate. As a result, the high reflection band becomes wider and the low reflection band becomes narrower, which is the origin of the narrow bandpass filter. The design structure of a narrow bandpass filter is $(HL)^N$ HH $(LH)^N$ or $(LH)^N$ LL $(HL)^N$. We can wider the passband by merging multiple such structures using QWOT coupling layers. Figure 11e shows the transmission spectrum of a bandpass filter in which structures of two narrow bandpass filters are merged to get a two-cavity bandpass filter. Therefore, the design structure of the filter is Air/$(HL)^2$ HH $(LH)^2$ L $(HL)^2$ HH $(LH)^2$/Glass. This structure gives a broader transmission band with steeper skirts as compared to the base narrow bandpass filter. The small ripple can be eliminated by anti-reflection coated matching layers.

Neutral beam splitter is another multilayer coating that can be designed with a simple QWOT multilayer structure. Beam splitter reflects a part of the light and transmits the rest of the light. The beam splitters are specified by the ratio of transmission to reflection, and 50/50 beam splitter is the most widely used. The design of beam splitters is relatively simple. By using the QWOT multilayer stack, 80/20, 60/40, 30/70, etc. beam splitters can be designed as per the requirement just by tuning the number of layers or refractive index of the materials. Figure 11f shows the transmission and reflection spectrum of 50/50 beam splitter made by five QWOT layers. The structure of the beam splitter is Air/LHLHL/Glass at the design wavelength of 1000 nm. The bandwidth of the beam splitter can be further improved by computer refinement using different optimization techniques, which will be discussed in detail in the next part. There are several other optical filters or mirrors which can be made using simple designs.

3.2 Complex Designs

During the initial days, the optical coatings were designed by direct analysis of optical properties of single and multilayer thin films. Especially, anti-reflection coatings and high reflection mirrors were designed by that method, which are discussed in the previous part. Later, it was realized that such a design approach has limited capabilities and only certain simple optical coating designs can be done using that direct approach. In 1958, Philip Baumeister [57] considered the coating design as an optimization problem and introduced the concept of merit function that evaluates the closeness between the designed and target spectral properties. Baumeister designed a good cutoff filter without increasing the number of layers from the starting design using the damped least-squares method in his optimization. The merit function is a function of all the building parameters of the system such as the number of layers (N), thickness (d), refractive index (n) and extinction coefficient (k) of the incident medium, substrate and thin-film layers in case of optical coatings. It estimates a weighted mean square deviation between the present and the target spectrum, and is given by [35]

$$F = \sqrt{\frac{1}{m}\sum_{j=1}^{m}\left[\frac{S_j - S_j^T}{\Delta S_j}\right]^2} \tag{8}$$

The function F is the standard merit function, m is the number of targets, S_j is spectral properties of interest (reflection/transmission), S_j^{T} is the target spectral properties and ΔS_j is the design tolerance. An optimization procedure is used to adjust the thickness and refractive index of the layers to minimize the merit function. The merit function value converges to one if all the optimized quantities differ from their target values within the tolerance limit [31]. The target specifications such as reflection, transmission, polarization, angle of incidence, etc. must be provided. The target can be defined for a particular wavelength or over a wavelength range depending on the applications. Optimization of the merit function is now commonly used for the design of multilayer coatings.

Based on the merit function approach, the design of optical coating is crudely divided into two classes: numerical refinement and thin-film synthesis. The procedure *Refinement* was first proposed by Baumeister and it requires a starting design that is close to the required spectral performance. The initial designs start by taking approximate solutions derived from the fundamental principles or earlier experience, and by semi-analytical methods. Then, the construction parameters such as refractive index and thickness of layers are optimized to minimize the merit function. Several optimization routines are detailed in the book authored by William H. Press [58]. Various first-order optimization methods that use the gradient of the merit function are generally implemented for the refinement. The details of these optimization methods are described elsewhere [25]. The gradient is basically a vector component of partial derivatives of merit function with respect to the design parameters. Figure 12 shows

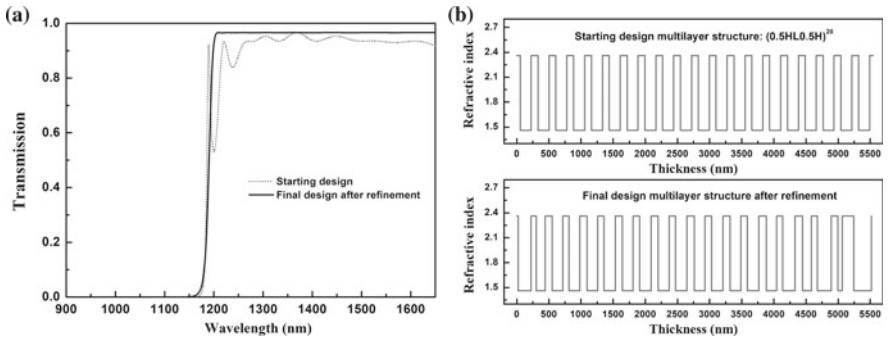

Fig. 12 **a** Design of a long wave pass edge filter by refinement process: the dotted line represents the starting design spectrum, and the solid line represents the final design spectrum. **b** Refractive index profile across the depth of the multilayer for the starting design, and final design after refinement

the use of the refinement process to design the ripple-free long wave pass edge filter. The target transmission is more than 96% in the spectral region 1220–1700 nm and zero transmission in the spectral region 900–1180 nm. This filter is designed by 41 alternate layers of high- and low-index materials ($n_H = 2.36$, and $n_L = 1.46$) at the central wavelength of 1000 nm. The refractive index of the substrate and incident air medium are $n_s = 1.52$, and $n_0 = 1$. The starting design of the refractive index profile and the final design of the refractive index profile after refinement is plotted in Fig. 12b. The transmission spectrum of the starting design (dotted line) and final design (solid line) of the filter are plotted in Fig. 12a. The refinement process hardly takes a few seconds to complete in modern computers. This example shows that refinement is a tremendously efficient approach if a proper starting design is guessed or known. Nowadays, modern computers enable refinement process to design some coatings with unknown starting designs, if the number of layers involved in a design is relatively small up to 10–20, then the refinement process can be started with random designs. Unfortunately, the refinement process limits itself once it reaches a local minimum and the design cannot be more better. If the optimized design does not match the target, then the refinement process again reinitiated with a better and new starting design, otherwise one must go for a synthesis process that allows further optimization by inserting new additional layers in the design, which is generally required for complex optical coating designs.

Synthesis method is effective and it does not require a starting design, as it generates its own starting design automatically. Take an example of a rugate filter which can be synthesized by starting from a single homogeneous layer to a refractive index gradient layer. Most often synthesis is followed by refinement, but it is not always true. Synthesis methods are approached either analytically, semi-analytically or numerically. The semi-analytical methods are primarily built on equivalent layers, polynomial synthesis, buffer layers, effective interfaces or admittance diagrams [24–27]. Most often, these approaches deliver the coating designs composed of groups of quarter-wave layers. Such designed filters are easy to fabricate than highly optimized

optical designs, because the QWOT layers can be easily controlled by an optical monitor system. Rather complex coatings are designed following this approach. In thin-film synthesis, the key point is to get a starting point in the multi-parameter design system which is close enough to minimize the merit function, as a result an adequate solution to the design problem can be obtained. Early thin-film synthesis methods were based on Dobrowolski's comprehensive search, gradual evolution and minus filter methods, Southwell's flip-flop technique and Tang's statistical search. The *comprehensive search method* is very computation intensive and effective for designs that can be resolved with a comparatively lesser number of layers [59, 60]. The *gradual evolution method* is applicable to designs that have a large number of layers to get a solution, because the solution is gradually evolved by adding a number of layers to design in several stages [59, 60]. The *minus filter method* decomposes a required spectral transmission into a number of minus filters that are placed in series, each having suitable attenuation and half-width [60]. The *flip-flop method* subdivides the starting design of two dielectric layers into many thin layers of equal optical thickness and iteratively flips the refractive index of each layer until the best configuration is achieved. The process is very fast as the optical thickness of the individual layers of the design is not varied during these calculations [60]. The *statistical search method* is based on a statistical sampling of the layer parameters and the sampling is restricted up to which the merit function stays below a certain level. The most successful numerical thin-film synthesis methods in recent years are approached by needle method, step method, inhomogeneous refinement and Fourier transform method, which are briefly discussed below.

3.2.1 Needle Method

Needle method is the most widespread and effective thin- film synthesis technique to date. This method was first conceived by Tikhonravov et al. in 1982 [25], and gained popularity in the middle of the 1990s. It successfully solved various complex design problems at a normal and oblique angle of light incidence. The needle optimization technique can handle all kinds of materials (dielectric, semiconducting and metal) [61]. The correct implementation of basic analytical formulas is essential for the effectiveness of this technique, otherwise it can give erroneous results. The needle method is presented qualitatively in Fig. 13, where thin layers (needles) are inserted at the optimal positions of the multilayer coating, and their thickness is adjusted by refinement. The needles are inserted till an acceptable solution is obtained or the insertion of additional needles does not improve the merit function further. The inserting positions of the needles are determined by taking the first derivative of the merit function (F) with respect to the thickness of an extremely small thin layer as a function of the position where it is inserted. In principle, all positions, where $\mathrm{d}F/\mathrm{d}d_{\mathrm{n}}$ is negative, are considered as suitable positions for the insertion of new layers as shown in Fig. 13b. Generally, single needle at a time is inserted at the position where $\mathrm{d}F/\mathrm{d}d_{\mathrm{n}}$ is the most negative, and the positions are indicated on the z-axis by dotted lines. In case of two material coating designs, the newly inserted layers

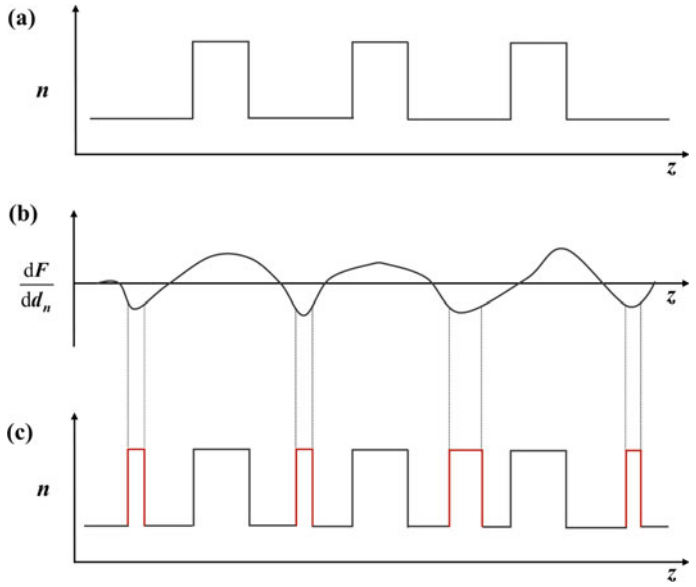

Fig. 13 **a** Refractive index profile before insertion of layers, **b** the gradient of the merit function that determines the thickness and position of the new layers to be inserted and **c** refractive index profile after insertion of the needles

exhibit opposite refractive indices to those material layers where the insertions are made. The refractive index profile of the new design attained after the insertion of new layers is illustrated in Fig. 13c.

In general, the synthesis process adopting needle optimization comprises of a sequential insertion of new layers in the existing multilayer. Subsequently, optimizations of the multilayer structure with respect to layer thickness are sequentially followed. The insertion of a needle in the jth layer can be presented by the matrix M_j in a multilayer like Eq. (3) having a thickness corresponding phase shift φ_j. Subsequently, the needle layer represented by the matrix M_n generates two sublayers represented by matrices $M_{j,2}$ and $M_{j,1}$ with phase shifts of $\varphi_{j,2}$ and $\varphi_{j,1}$ such that $\varphi_j = \varphi_{j,1} + \varphi_{j,2}$ and $M_j = M_{j,2} M_n M_{j,1}$. The influence of the insertion of needle layer with refractive index n_n and infinitesimal thickness d_n can be evaluated as [62]

$$\left.\frac{\mathrm{d}M_j}{\mathrm{d}d_n}\right|_{d_n=0} = M_{j,2} \left.\frac{\mathrm{d}M_n}{\mathrm{d}d_n}\right|_{d_n=0} M_{j,1} \tag{9}$$

To speed up the calculations, the above equation can be rewritten as

$$\left.\frac{\mathrm{d}M_j}{\mathrm{d}d_n}\right|_{d_n=0} = \frac{1}{2}\left[\left(\frac{\eta_j}{\eta_n} + \frac{\eta_n}{\eta_j}\right)\frac{\mathrm{d}M_j}{\mathrm{d}\varphi_j} + \left(\frac{\eta_j}{\eta_n} - \frac{\eta_n}{\eta_j}\right)\begin{pmatrix} 1 & 0 \\ 0 & -1 \end{pmatrix}\frac{\mathrm{d}M_j(\Delta\varphi_j)}{\mathrm{d}\Delta\varphi_j}\right]\frac{\mathrm{d}\varphi_n}{\mathrm{d}d_n} \tag{10}$$

where η_n is the pseudo-index of the needle, $\varphi_n = (2\pi / \lambda) n_n d_n \cos\theta_n$ is the phase shift in the needle, and $\Delta\varphi_j = \varphi_{j,1} - \varphi_{j,2}$. Equation (10) is much faster to compute as compared to Eq. (9) as there is no matrix multiplication, and the term $\frac{dM_j}{d\varphi_j}$ and $\frac{dM_j(\Delta\varphi_j)}{d\Delta\varphi_j}$ are independent of the needle layer material, and $\frac{dM_j}{d\varphi_j}$ are independent of the needle location.

The best results using needle method obtained when needles are inserted one needle at a time, but we sometimes insert more than one needle at a time to save time which leads to increasing the overall optical thickness of the coating. A drawback of the needle method is the generation of undesirable very thin layers, which is difficult to deposit using conventional evaporation processes. Recently, both commercial as well as free source software have implemented simple procedures to remove the thin layers below a certain value. Overall, the needle method is a powerful technique for thin-film coating design. Verly [64] proposed the modified needle method which is applicable if there exists a continuous range of refractive indices. In those cases, the derivative of the merit function is computed for many possible refractive indices and the optimal index and its position are determined. Figure 14 illustrates the use of the needle method to obtain target designs which are not possible by conventional quarter-wave designs. The starting 21 QWOT layer designs are refined and then followed by needle optimization, and the reflection and refractive index profile of the final 57-layer design are plotted in Fig. 14a, and b, respectively. The final design gives a ripple-free spectrum with suppressed sidelobes. Figure 14c shows the capability of needle optimization to design the Taj Mahal like complex filter using 61 sequential layers of Na_2O_5 and SiO_2, respectively, and the refractive index profile resulting in the Taj Mahal like filter is presented in Fig. 14d. Another very challenging spectral profile using needle optimization is presented in Fig. 14e along with its refractive index profile plotted in Fig. 14f, where a very successful attempt was made by the authors to design the spectral reflectance contour like famous Indus buildings, RRCAT, Indore [65], using 296 sequential layers of HfO_2 and SiO_2, respectively.

3.2.2 Step Method

The step method proposed by Larouche and Martinu [66] is like the modified needle method, where small refractive index steps instead of needles are introduced in suitable positions. But instead of inserting thin layers as in the case of needle method, the current layers are divided into a large number of layers by inserting negligible small refractive index steps as illustrated in Fig. 15. A layer is divided into two layers by decreasing, and increasing the refractive index of its first and second part, respectively, making a rising step as demonstrated in Fig. 15a. The opposite index profile is made in both the parts, creating a falling step. Then, the derivative of the merit function (F) with respect to the index step height (Δn) is computed for both rising and falling steps as a function of the position as presented in Fig. 15b. The new small index step layers are inserted where the derivative of the merit function is minimal as shown in Fig. 15c. The filter design is re-optimized, and the procedure

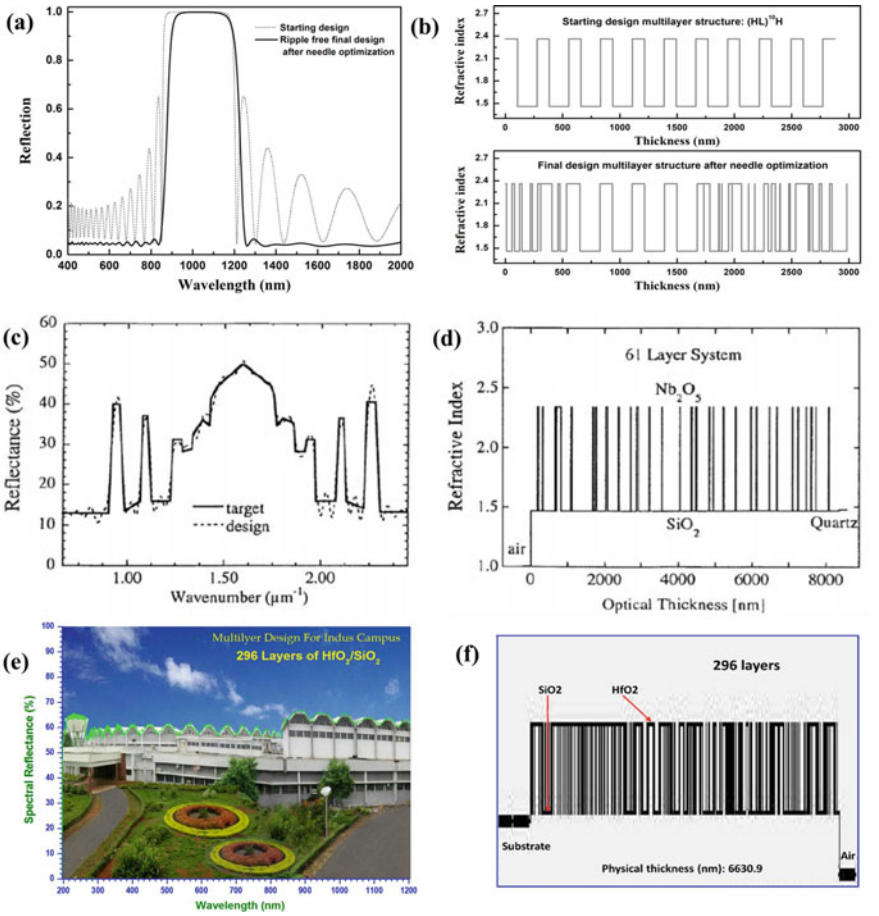

Fig. 14 **a** Use of needle method to design high reflection mirror with suppressed sidelobes: starting (dotted line) and final (solid line) design spectrum, and their corresponding **b** refractive index profiles. Another example of needle method to achieve a complex target like **c** Taj Mahal with its design curve made of sequential 61 layers of Na_2O_5 and SiO_2 and the corresponding **d** refractive index profile of the Taj Mahal filter after needle optimization (reproduced from [63] with permission), **e** Indus campus like filter design using 296 layers of HfO_2 and SiO_2 materials and its needle optimized (**b**) refractive index profile with a total thickness of 6631 nm

is repeated until getting a reasonable solution [66]. The derivative of the merit function is computed only by calculating the derivative of the characteristic matrix of a multilayer, as it determines the spectral response of the multilayer.

Let us consider the jth layer in a multilayer is divided into two sublayers. The effect of the addition of a step in a multilayer can be realized by taking the derivative of the layer matrix with respect to the infinitesimal step index height (Δn_j) as

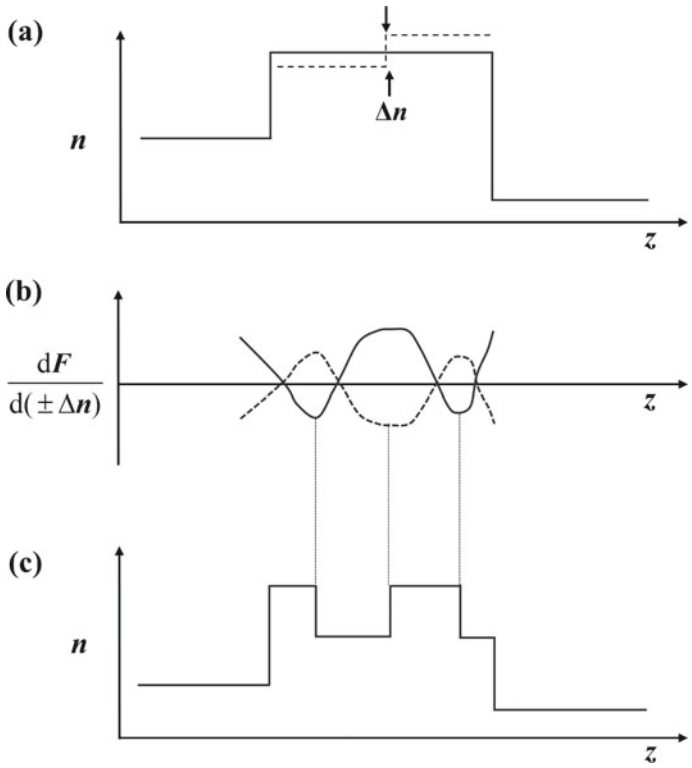

Fig. 15 Graphical illustration of step method: **a** additional parameter can be added to the refinement process by inserting new index steps in the existing layers; **b** the derivative of the merit function (dF/d(± Δn)) is computed for rising (dotted line) and falling (solid line) steps as a function of positions; and **c** the new steps are inserted at the positions where dF/d(± Δn) is minimum

$$\left.\frac{\mathrm{d}M_j}{\mathrm{d}\Delta n_j}\right|_{\Delta n_j=0} = M_{j,2}\left.\frac{\mathrm{d}M_{j,1}}{\mathrm{d}\Delta n_j}\right|_{\Delta n_j=0} + \left.\frac{\mathrm{d}M_{j,2}}{\mathrm{d}\Delta n_j}\right|_{\Delta n_j=0} M_{j,1} \tag{11}$$

If the refractive index difference Δn is equally distributed on both the sublayers as shown in Fig. 15a, then the refractive index of first and second sublayers are decreased, and increased, respectively, by $\Delta n/2$. So, the above equation can be written as

$$\left.\frac{\mathrm{d}M_j}{\mathrm{d}\Delta n_j}\right|_{\Delta n_j=0} = \frac{1}{2}\left[M_{j,1}\frac{\mathrm{d}M_{j,2}}{\mathrm{d}n_j} - \frac{\mathrm{d}M_{j,1}}{\mathrm{d}n_j}M_{j,2}\right] \tag{12}$$

To speed the computation, Eq. (12) can be expressed as

$$\left.\frac{\mathrm{d}M_j}{\mathrm{d}\Delta n_j}\right|_{\Delta n_j=0} = \frac{1}{2}\left[\frac{\mathrm{d}M_j}{\mathrm{d}\varphi_j}\frac{\mathrm{d}\Delta\varphi_j}{\mathrm{d}n_j} + \left(\frac{\mathrm{d}M_j(\Delta\varphi_j)}{\mathrm{d}\eta_j} + \frac{1}{\eta_j}(cos\varphi_j - cos\Delta\varphi_j)\begin{pmatrix}-1 & 0\\ 0 & 1\end{pmatrix}\right)\frac{\mathrm{d}\eta_j}{\mathrm{d}n_j}\right] \tag{13}$$

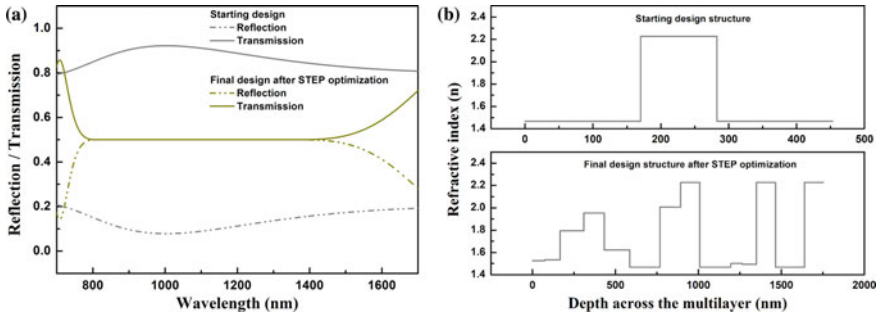

Fig. 16 Illustration of step method to design a 50/50 broadband beam splitter: **a** Transmission and reflection spectrum of the starting and final design of a beam splitter, and **b** Refractive index profile of the starting and final design after step optimization

Equation (13) is much quicker to compute than Eq. (10) because of no involvement of matrix multiplication and $\frac{dM_j}{d\varphi_j}$ is independent of step position. The specifics of the theoretical formulation of the methods can be found elsewhere [66]. One can insert a step in a finite thick layer to improve the merit function excluding the situation where its refractive index is $n_{\min}$ or $n_{\max}$. An optimal design is possible with homogeneous layers of intermediate indices and finite thicknesses except $d\eta/dn = 0$. The optimized filter either comprises homogeneous layers of maximum contrast in refractive index or of graded-index layers. The step method is very much effective for designing filters at oblique angle of incidence with P-polarized light and it is available in OpenFilter software [62]. It is an efficient synthesis method as demonstrated in Fig. 16. The target is to obtain a 50/50 broadband beam splitter having bandwidth of 800–1400 nm. The starting design was a three-layer structure made of two low-index layers and one high-index layers as shown in Fig. 16b, which gives 10/90 beam splitting at design wavelength of 1000 nm. The step method resulting the final refractive index profile as shown in Fig. 16b delivered the targeted beam splitter. The reflection and transmission spectrum of the 50/50 wideband beam splitter is shown in Fig. 16a.

3.2.3 Inhomogeneous Refinement

Inhomogeneous refinement method divides an inhomogeneous film into a large number of thin layers, whose refractive indices and thicknesses are refined [67–69]. This is the method where the difference between synthesis and refinement is somewhat vague. The inhomogeneous film shows the continuous variation of refractive index, and the multilayer designs are basically quasi-inhomogeneous coatings made of many thin homogeneous layers. The optical response of such coatings is equivalent to an inhomogeneous thin film of average refractive index having optical thicknesses smaller than the operating wavelength. In this method, the starting design can be relatively simple, and no special assumption for its refractive index structure such as a sequence of materials, number of layers, etc. is required except for a rough

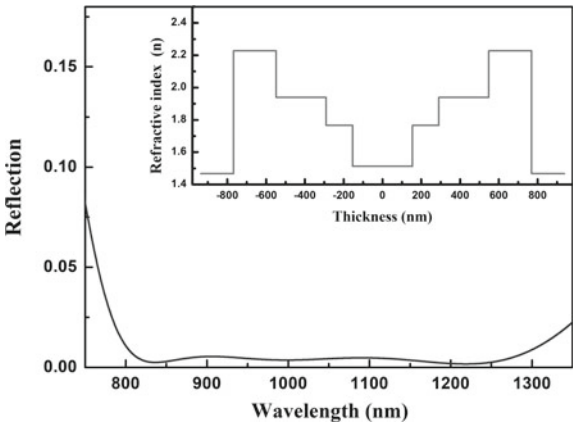

Fig. 17 Broadband anti-reflection (BBAR) coating designed by inhomogeneous refinement. The inset plot presents the inhomogeneous refractive index profile of the design

estimation of the overall optical thickness [68]. The layer thicknesses are separated by their average values, while their refractive indices are adjusted without scaling. The advantage of this refinement process is that it is considerably fast, but needle optimization is much more versatile. Generally, the inhomogeneous refinement process rapidly converges to the target solution, while the needle optimization is more effective for tuning the design close to the process ending. This method is mostly used for the synthesis of all-dielectric filters. Figure 17 illustrates the use of an inhomogeneous refinement method to design a broadband anti-reflection coating having a bandwidth of 800–1300 nm. The inhomogeneous refractive index profile generating the final design is plotted in the inset plot of Fig. 17. This optimization method is available in almost all commercial as well as open-source software.

3.2.4 Fourier Transform Method

Fourier transform method (FTM) is perhaps the first effective method to design filters with any arbitrary spectral shape. This method was developed by Delano in 1966 [70] and Sossi [71], and later advanced by Dobrowolski [72]. It does not assume anything about the layer thicknesses, refractive indices of the layer materials or number of individual layers of the filter designs. The FTM directly relates the refractive index profile with a complex spectral function (Q-function) that depends on the target spectrum. The complex Q-function is defined as

$$\tilde{Q}(k) = Q(k)e^{i\psi(k)} \tag{14}$$

Here, Q and Ψ are the amplitude and phase functions of the complex Q-function, respectively, and $k = 2\pi/\lambda$ is the wavenumber. The refractive index profile as a function of depth $n(x)$ is derived using the inverse Fourier transform [72] as follows:

$$\ln\left[\frac{n(x)}{n_m}\right] = \frac{2}{\pi}\int_0^{\infty} \frac{Q(k)}{k}\sin(\psi(k) - kx)dk \tag{15}$$

where x is a variable which is twice the optical thickness, and $n_m = \sqrt{n_{\min} n_{\max}}$ is the mean refractive index. The variable x is expressed as

$$x = 2\int_0^{z} n(u)du \tag{16}$$

Here, z is the physical thickness of the layers, and u is the integration variable. In case of real coatings, the Q-function is expressed for a definite and limited range of wavelengths. Various analytically simple Q-functions have been proposed by several researchers [70, 73–76] as follows:

$$\begin{aligned} Q &= \sqrt{\frac{R}{T}}, \\ Q &= \sqrt{\frac{1}{2}\left(\frac{1}{T} - T\right)}, \\ Q &= \frac{1}{2}\ln\left(\frac{1+\sqrt{R}}{1-\sqrt{R}}\right), \\ \tilde{Q} &= \frac{r}{t}, \end{aligned} \tag{17}$$

where R and T are reflection and transmission spectra, respectively, of the coating, and r and t are the amplitude of reflection and transmission coefficients, respectively. The last term of Eq. (17) is known as Delano's Q-function and its phase part is $\psi \approx \arg(r/t)$. This phase part can be exploited to control the shape of the refractive index profile. Verly [76] have obtained surprisingly good results, and designed good high reflectance rugate filter by Q-phase optimization only. The FTM to design optical filters has two important drawbacks: (i) the Q-functions are only approximate, and (ii) it does not consider the dispersion in the refractive index. Therefore, there will be a difference between the target and FTM designed spectrum. The former is taken care by iteratively correcting the Q-function [75]. The later is resolved by scaling the wavelength by the optical thickness in the Fourier transform and multiplying the Q-function with a wavelength-dependent correction factor [77]. Despite its limitations, the FTM can quickly generate useful inhomogeneous multilayer design. A common application of the FTM is the design of single or multi-wavelength reflecting mirrors termed 'rugate filters', which are usually defined as optical coatings having a continuous variation of refractive index in the direction perpendicular to the film plane [78]. If a Q-function is defined for a single wavelength (single-band rugate filter), then its Fourier transform gives a sinusoidal refractive index profile. For multiband rugate

filter, the refractive index profile can be defined by multiplying multiple sinusoidal profiles as follows:

$$\ln\left[\frac{n(x)}{n_m}\right] = \prod_{j=1}^{N} \bar{Q}_j \sin\left(\frac{2\pi x}{\lambda_j} + \varphi_j\right)\omega(x) \tag{18}$$

where λ_j are the central wavelengths of the band, φ_j are phase shifts that allow one to centre the refractive index profile, N is the number of bands and

$$\bar{Q}_j = \frac{1}{2}\ln\frac{n_m + \Delta n_j/2}{n_m - \Delta n_j/2} \tag{19}$$

are the reduced Q-functions which govern the amplitude of the band index profile Δn_j, and $\omega(x)$ is an apodization function that limits the range of refractive index profile to finite. The amplitude of the refractive index profile decides the bandwidth of the rugate filter, while the reflectivity of the filter is decided by both amplitude of refractive index profile and the number of periods. Figure 18 illustrates the Fourier transform method to design multi-band rugate filters. The refractive index profile of a

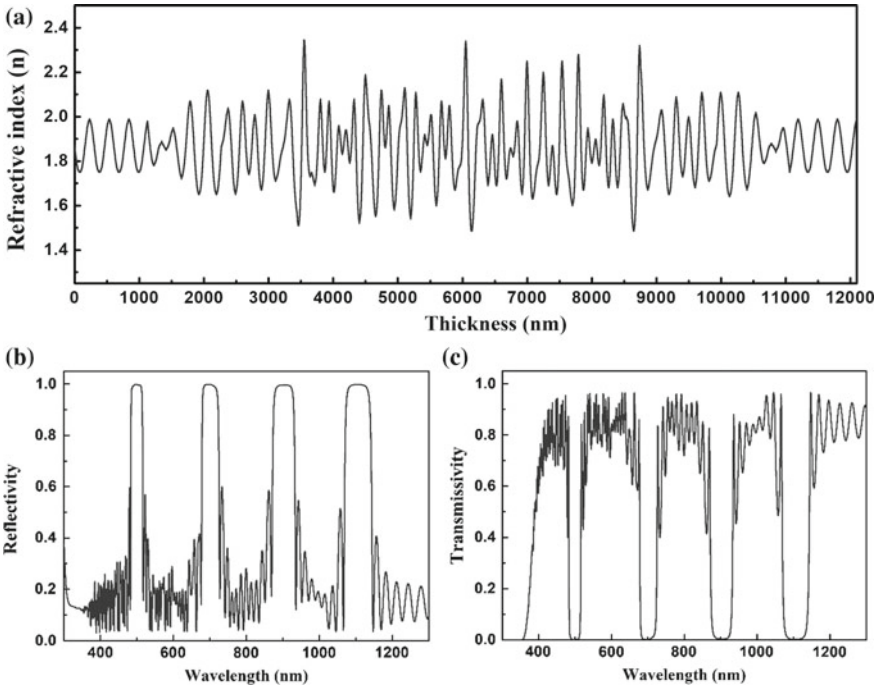

Fig. 18 **a** Refractive index profile of a quadruple-band rugate filter made of TiO_2–SiO_2 mixture, **b** transmission and **c** reflection spectra of the rugate filter with bands at 500, 700, 900 and 1100 nm

four-band rugate filter made of TiO_2-SiO_2 mixture, and the corresponding reflection and transmission spectra of the rugate filter are shown in Fig. 18. It is realized that the FTM can rapidly produce useful inhomogeneous multilayer designs. Generally, the synthesis gradually evolve in quasi-multilayer when the refractive index modulation reaches its extremum. The hybrid solutions can be considered as starting designs for conventional refinement. This method eliminates the high-frequency contributions, consequently reduces the number of thin layers, which are difficult to deposit.

For thin-film synthesis, one needs global minimum seeking optimization routines for the design of optical coatings. In the past, different optimization routines such as modified gradient, damped least square, adaptive random search, golden section, modified complex, Hooke and Jeeves pattern search, basic Powell's conjugate search, generalized simulated annealing, Monte Carlo simulated annealing, etc. are used to refine the performance of the optical multilayer coatings [79]. It was noticed that no optimization routine delivered best on all the problems, and therefore all commercial codes or free software provide a choice of several optimization routines. There are several commercial [80] or free software [62] available for the design of multilayer optical coatings. OpenFilter [62] is the most famous open-source software that has a complete design environment, including popular design methods and easy-to-use graphical user interface. It gives the opportunity to the thin-film optical coating community to develop new features using the fully functional open-source software.

4 Deposition of Thin Films and Multilayer Coatings

Thin films and multilayer coatings are deposited using one of several deposition techniques. The deposition techniques are broadly classified under two headers such as physical vapour deposition (PVD) and chemical vapour deposition (CVD) techniques [81–84]. For optical interference coatings, the PVD processes are much preferred as compared to that of the CVD. Therefore, the chapter limits its discussion to the PVD processes only. The PVD methods involve the evaporation of materials from a solid or liquid source in the form of atoms or molecules in a high vacuum environment, and the vapours condense on the substrate to form a thin film. The basic PVD processes are evaporation and sputtering. The variants of these processes are bias sputtering, ion plating, pulsed laser deposition, ion-assisted deposition, oblique angle deposition, co-deposition, etc. Modern PVD coating systems are highly automated and installed in humidity-controlled clean rooms.

4.1 Evaporation

In 1912, Pohl and Pringsheim [85] made metallic mirrors through vacuum distillation that laid out the foundation of evaporation process. Evaporation process is usually performed in a vacuum typically 10^{-4}–10^{-8} mbar depending on the purity

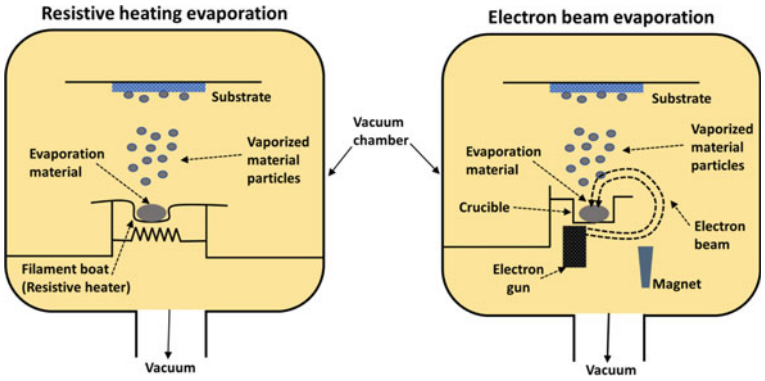

Fig. 19 Schematic of resistive heating and electron beam evaporation techniques

of the film, the tolerable contamination level, deposition rate, depositing species and reactivities of the residual gas. In evaporation methods, materials are heated (<1500 °C) to form vapours in several ways using direct resistance, electron beam, radiation, lasers, or an arc discharge. The simplest method is to use a refractory metal boat as a heater by passing an electric current through it known as resistive heating evaporation as shown in Fig. 19. In some cases, the substrate is heated at temperatures of 150–350 °C before the start of deposition. The complete system consists of a vacuum chamber along with necessary vacuum pumps, pressure gauges, thickness controller and monitor, substrate holder, substrate heaters, power supplies to melt the materials placed on the metal boat, etc. Since the boat's resistance is low, therefore high currents (>several hundreds of amperes) at low voltages (<10 V) are needed to heat them [82]. Tantalum, molybdenum and tungsten are popular refractory metals for the manufacturing of the boats. Boats often suffer from corrosive interaction with the heated charge. Premelting and wetting of the evaporation materials on the heated boat are necessary prior to the deposition as it provides good thermal contact between the evaporant and the boat surface, and removes volatile impurities and contaminants from the evaporant as well as from the boat surface. The boats often affect the vapour distribution when the temperature reaches their melting points, and some materials start reacting with the boat surface degrading the boat itself, consequently it is difficult to deposit high-melting point materials using the resistive heating technique. Therefore, people gradually shifted towards electron beam heating to avoid the disadvantages, and it became the most preferred deposition process for most materials to prepare highly pure thin-film coatings, especially refractory oxide materials. Except for some cases of metallic coatings, resistive heating techniques are rarely used. The schematic of an electron beam evaporation process is shown in Fig. 19.

In the electron beam evaporation process, the evaporation material is kept in a metallic crucible (mostly copper because of its good electrical as well as thermal conductivity), and is heated by energetic electron beams to vapourize it. The electrons emitted from a hot filament (usually tungsten) are accelerated towards the

evaporant by providing a potential of typically 4–20 kV. The beam current could be of several amperes; as a result, the heat generated in the crucible is massive and capable of melting virtually any evaporant. The crucible is generally water-cooled in order to prevent the possible reaction between the evaporant and the crucible. The hot filament and the electrodes are positioned under the crucible to avoid their corrosion by the evaporant. The electron beam is bent through angle more than a semicircle (mostly 270°) and focused on the evaporant in the crucible using a magnetic field [86]. Moreover, small electromagnets are added to scan the beam over the evaporant to increase the area of heated materials. High deposition rates as well as fast rate changes can be obtained by electron beam evaporation process and it can have multiple crucibles resulting in vapourization of more than one material using the same electron gun. As per our experience, all refractory oxide materials such as SiO_2, HfO_2, ZrO_2, TiO_2, Ta_2O_5, etc. can be effectively deposited using a reactive electron beam evaporation process. Using a double electron gun, mixed oxide coatings can also be deposited to get tunable refractive indices by vapour-phase mixing of two materials deposited by the two guns separately. A hybrid process such as a combination of resistive heating as well as electron beam evaporation process can be implemented to deposit metal/dielectric multilayer coatings. Optically transparent heat reflecting mirror made of HfO_2/Ag/HfO_2 has been prepared by the hybrid process and its reflection and transmission spectrum are shown in Fig. 20a. For refractory oxide coatings, oxygen is supplied during deposition known as reactive process and tunable refractive indices can be obtained as shown in Fig. 20b by co-evaporation of HfO_2 and SiO_2 using reactive EB evaporation. Earlier multilayer filters or devices were fabricated mostly using electron beam evaporation. The evaporated coatings generally exhibit columnar or porous structure because of less energetic evaporated atoms deposited on the substrate (typically 0.1 eV), as a result, the filter stability and optical performance were compromised. Later, it was realized that if we can improve the energy of the evaporated atoms, then dense coatings can be prepared,

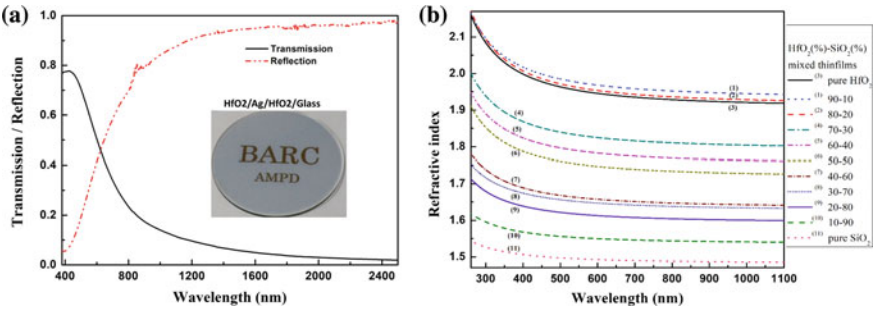

Fig. 20 **a** Fabrication of optically transparent heat reflecting mirror using HfO_2/Ag/HfO_2 tri-layer coating on glass substrate using hybrid evaporation techniques, where the Ag layer is deposited using the resistive heating technique, and the HfO_2 layer is deposited using reactive electron beam evaporation technique, and **b** Tunable refractive indices in HfO_2-SiO_2 mixed oxide thin films deposited by electron beam co-evaporation process (reproduced from [87] with permission)

which was subsequently achieved by ion-assisted deposition process. In this process, energetic ion beams (>few hundred electron volts) are bombarded with electron beam evaporated atoms on the substrate as a result the atoms gain energy and improve the film quality by making it highly dense with good adhesion to the substrate as compared to that of conventional electron beam process. Mostly, argon ions are used as the bombarding species. Since the films prepared by the ion-assisted deposition (IAD) are almost pore-free, hence they are less sensitive to moisture. As a result, moisture-induced shifts in the optical spectrum of the optical coatings or filters can be completely avoided resulting in stable optical constants of the coatings. This is the main reason for which the IAD was rapidly adopted by the optical coating community. Several researchers as well as optical coating manufacturing companies are still using ion-assisted electron beam evaporation method to develop various filters and coatings.

Conventional evaporation processes are less energetic process without the ion beam assistance. As a result, the coatings exhibit columnar porous structure, subsequently coating instability and drift. The limited mobility of the adatoms is the origin of the columnar structure as explained by Movchan and Demchishin [88]. Experiment as well as computer simulation confirmed that the key mechanism for film densification is momentum transfer due to bombardment [89–91], which makes ion-assisted deposition and sputtering more demanding. The energy of the film-forming particles decides the physical properties of the deposited films. The energy of such particles in case of evaporation is ∼0.1–0.5 eV, while it is significantly higher for magnetron sputtering, ion plating and ion beam sputtering, i.e. ∼1–100 eV [92]. Sputtering is an energetic process; therefore, the sputtered particles form smooth, adhesive and dense coatings.

4.2 Sputtering

Sputtering is an old method but was not much used to deposit optical coatings until the second half of twentieth century. In this process, atoms are ejected from a target material by bombarding energetic particles like atoms or ions (usually inert) to the solid target. The ejected atoms condense on a substrate and form a thin film. It is a purely momentum transfer process. The main advantages of sputtering are (a) high uniformity in film thickness, (b) good adhesion to the substrate, (c) better reproducibility of films and (d) stoichiometric film as target [93]. The sputtered atoms have an energy of a few tens of eV. Based on the source of discharge, sputtering can be classified into magnetron (DC, pulsed DC and RF) sputtering and ion beam sputtering (IBS).

Magnetron sputtering process as shown in Fig. 21 can be categorized as DC, pulsed DC or RF depending on the use of power supply. In simple sputtering techniques, the deposition rate is low and contamination in films occurs due to the relatively high working pressure. To overcome these problems, the magnetron configuration is used where a permanent magnet (or electromagnet) with a magnetic field of a few

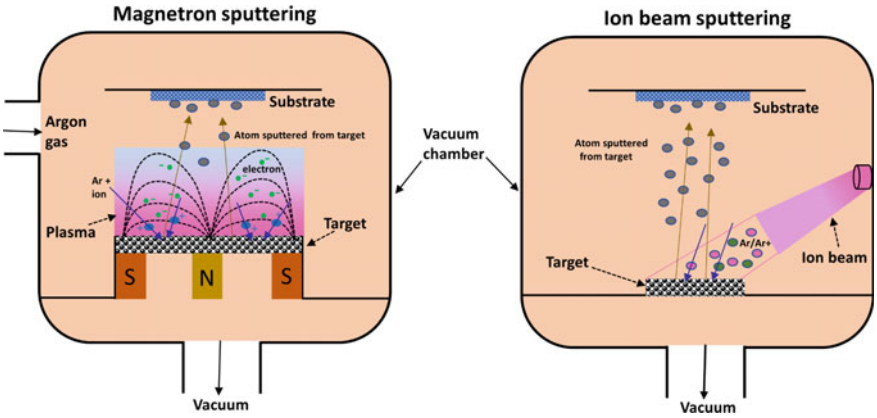

Fig. 21 Schematic of magnetron sputtering and ion beam sputtering techniques

hundred gausses is incorporated, to generate magnetic flux lines parallel to the target surface. This field makes the electrons to form a closed loop, and increases the collision cross section between the electrons and the sputtering gas. Therefore, sputtering can be done at a lower working pressure of 10^{-4} torr, which results in effectively higher deposition rates with low contamination of the deposited films. DC sputtering utilizes a DC gaseous discharge. The vacuum chamber walls and the substrate can be considered as anode, while target (deposition source) acts as cathode. The power supply is simply a high-voltage DC source. DC sputtering is primarily used for deposition of metals, while it fails in case of insulators because of positive charge build up on the target surface. It can be avoided by the bombardment of both positive ions and electrons simultaneously to the insulator surface, which is done by providing an RF potential to the target. The electrons oscillating in the alternate electric field gain sufficient energy from the RF potential to make ionizing collisions, and subsequently maintain self-sustained discharge plasma. The target becomes negatively self-biased as the electrons exhibit higher mobility compared to the ions. The target repels the electrons and a sheath enriched in positive ions is formed in front of the target surface. Sputtering happens as these ions bombard the target material. The RF power of a few hundred watts to kilowatt is applied between the electrodes at a frequency of 13.56 MHz [82]. RF sputtering system needs an impedance matching network between the sputtering chamber and the power supply to deliver maximum power to the chamber [94], which is the key difference from the DC sputtering system. For deposition of oxide dielectric optical coatings, reactive sputtering is the most suitable process. But the reacting gas tends to react with the sputtering target as well, which leads to build up of insulating materials known as target poisoning, which was subsequently eliminated by asymmetric bipolar pulsed DC (ABPDC) magnetron sputtering [95] technique. In pulsed DC sputtering, a pulsed reverse bias is added to the normal pulsed DC working in the frequency range of hundreds of kilohertz. As a result, during the negative cycle of the voltage (e.g. −400 V), the argon ions strike the target and

cause sputtering of aluminium. At the same time, insulating Al_2O_3 films is also redeposited on the metallic target and it collects low-energy ions on its surface, which reduces the sputtering of insulating films from the target surface. As the charge builds up, the ions get repulsion from the Ar^+ ions and the positive capacitor voltage. On reversing the polarity to +100 V, the electrons flow to the target surface and discharge ions on insulating layers resulting in capacitor voltage −100 V. The reversal is typically held for 1–10 μs. When the voltage returns to sputter mode (−400 V) again, the effective voltage on the plasma side of the parasitic capacitor becomes −500 V (−400 V ± 100 V). Thus, the argon ions strike the insulator with extra energy and sputter the insulating surface of the target first, which ultimately eliminates the target poisoning [95]. The effectiveness of ABPDC indeed depends on its pulse frequency, which falls in the range 25–300 kHz. A positive voltage of 25–50 V is usually effective and safe for deposition of refractory oxide coatings. The utility of magnetron sputtering to fabricate complex designed Taj Mahal filter is illustrated in Fig. 22a. The figure shows the measured spectral response of the Taj Mahal filter along with its design spectrum. It clearly shows the accuracy of magnetron sputtering process that enables to produce such complex filter which exactly meets the designed target.

Ion beam sputtering (IBS) has the capability to solve many challenges related to different sputtering processes. The schematic of the IBS is shown in Fig. 21, in which the neutral ion beam derived from an ion source is bombarded to target only and sputter the target material. Dielectric refractory oxide materials can be easily sputtered to fabricate optical coating devices as there is no target-charge problem. Generally, ion currents in the range of 10–500 mA with ion energies 0.5–2.5 keV are used in IBS [96] depending on the material and required coating properties. The working pressure close to the substrate can be dropped down to 1×10^{-5} mbar as the ions are produced in an isolated vessel of the ion source. Therefore, impurities like implantation of gas atoms or molecules in the sputtered film reduce significantly. The geometrical and ion beam parameters like ion incidence angle, emission angle, ion

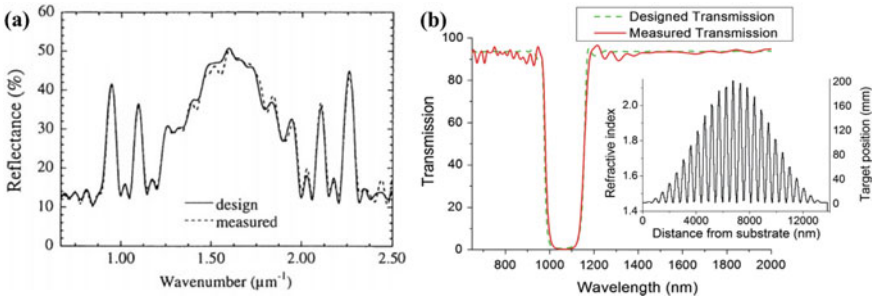

Fig. 22 **a** Design and measured reflection spectrum of a Taj Mahal filter prepared by magnetron sputtering and **b** design and fabricated transmission spectrum of a rugate filter prepared using ion beam sputtering. The inset plot shows the refractive index profile achieved by the ion beam sputtering process as a result the measured transmission matches with that of the design (reproduced from [63, 97] with permission)

species, ion beam energy, etc. can be varied to tailor the coating properties [92]. Since the ion beam source, target and substrate are spatially separated, so the intervention of plasma in the IBS process is completely avoided, and the sputtered atoms travel to the substrate without any hindrance. As a result, the IBS produces exceptionally high-quality coatings with high density and adhesion. Therefore, IBS becomes popular and alternative to several other deposition techniques. Usually, a second ion source directly bombards the growing film which provides additional control of coating properties, particularly intrinsic stress, called as dual ion beam sputtering (DIBS) process. The IBS is a very slow process as the rate of deposition offered by the process is very low. Moreover, the ion beam sources and their related components are much more complex than the magnetron or evaporation sources. However, IBS is must go coating system where superior quality films with the highest level of purity and the lowest possible optical losses are desired. The utility of IBS is demonstrated through an example as shown in Fig. 22, in which a rugate filter is made by the IBS process. This figure shows that the measured transmission spectrum is almost matching with that of the designed one, which indicates that both the refractive index as well as the thickness of a thin layer can be precisely controlled by the IBS process. The refractive index modulation profile across the depth of the multilayer is shown in the inset plot, which is deposited by IBS.

4.3 Oblique Angle Deposition

Oblique angle deposition (OAD) has been widely implemented in electron beam evaporation, pulsed laser deposition, as well as sputtering systems to produce nanostructured porous coatings [98]. Generally, this OAD process [99] is a hybrid PVD process in which incoming flux of adatoms is allowed to strike a substrate at an angle with or without substrate rotation as shown in Fig. 23. Deposition using OAD can be made using either top-down or bottom-up nanofabrication process [100]. Significantly unique microstructure like pillar, zigzag, helix, tilted columns, etc. leading to tunable physical and chemical properties can be obtained by varying substrate rotation and the angle of deposition of OAD [101]. Typically, if the angle of deposition is $\geq 80^{\circ}$, then the process is called as glancing angle deposition (GLAD). In OAD/GLAD, the substrate is inclined to the evaporated or sputtered atoms, thus making oblique deposition geometry as shown in Fig. 23. When the vapour flux reaches to the substrate at an angle, the vapour atoms initially condense on the substrate naturally to form microscopic nuclei. Subsequently, the incoming vapour flux is restricted to condense behind the nuclei because of ballistic shadowing, as a result, the nuclei grow and become tilted columns. These tilted columns increase the voids or generate a porous microstructure, which can be tunable across the film thickness in a controlled manner as per the requirement. Porous sculptured coatings prepared by OAD show optical anisotropy as well as lower refractive index than dense materials, which can be tailored by varying deposition angles, materials and deposition process parameters. The peculiar nanostructure itself is the origin of optical

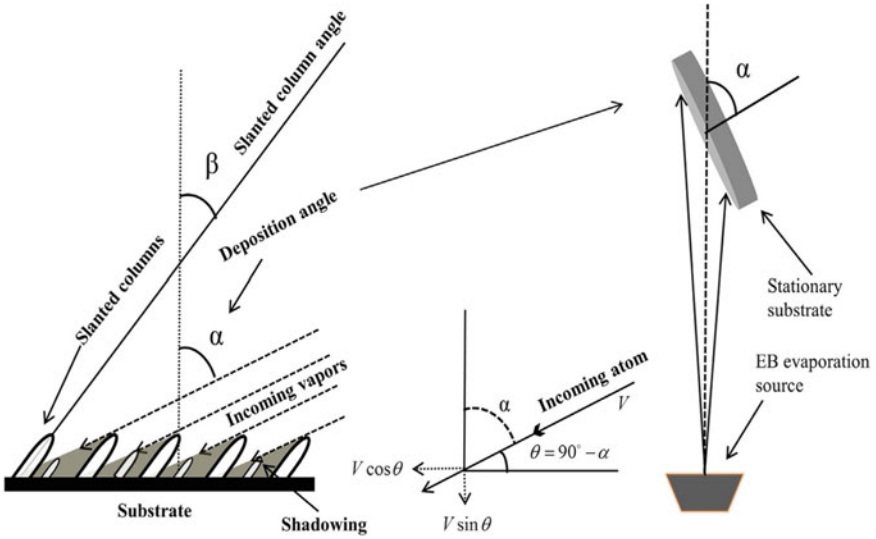

Fig. 23 Schematic of film growth and deposition process of oblique angle deposition technique (reproduced from [103] with permission)

anisotropy, while the porous nature is responsible for the lower refractive index. Such properties of porous thin films have various applications in optical devices such as wideband anti-reflection coatings, high reflection mirror, optical retardation plates, microsensors, circular polarization filters, and negative-index metamaterials [102]. Tunable refractive indices are possible using a single material by varying the angle of depositions as shown in Fig. 24b for OAD HfO_2 thin film. It is clear that the film

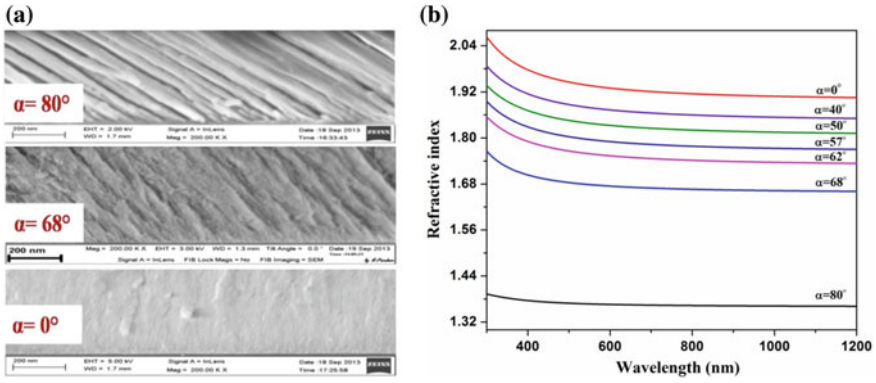

Fig. 24 Angle of deposition dependent **a** microstructure (cross-sectional FESEM image) of electron beam evaporated HfO_2 thin film, and **b** the corresponding refractive index spectra (reproduced from [18, 103] with permission)

refractive index decreases with increasing angle of deposition because of increasing porosity as shown in Fig. 24a.

In recent years, controlled sculptured coatings with their theoretical formulations have been established to design and develop various multilayer coating devices. Oliver et al. [104] used GLAD MgO coating to fabricate a quarter-wave retarder at a wavelength of 351 nm. Andy et al. [105] have enhanced the birefringence of TiO_2 thin films to almost double ($\Delta n = 0.22$) using the OAD technique. A. Lakhtakia et al. [106] prepared multi-section chiral sculptured thin films that act as spectral reflection holes for fluid sensor applications. Tunable refractive indices across layer thickness are possible by varying the deposition angle α in a controlled manner as illustrated in Fig. 24, which can be exploited to develop optical filters. The figure shows that the OAD HfO_2 thin film deposited using electron beam evaporation becomes porous with a tilted columnar structure with an increasing angle of deposition, which subsequently affects the film refractive index and it decreases from 1.96 to 1.38 at a wavelength of 550 nm with increasing angle of deposition. The GLAD process enables extraordinary flexibility in designing optical coating devices as almost any refractive index profiles are possible using this technique. Narrow bandwidth ($\Delta\lambda = 50$ nm) reflection filter has been fabricated by Robbie et al. [107] using single-material MgF_2, in which the refractive index of MgF_2 is varied sinusoidally along thickness by varying angle α between 51° and 81°. Yumei Zhu and Jiao [108] developed a multi-stopband filter by exploiting the mix index profile (sinusoidal + step) of OAD TiO_2 thin films. Kennedy and Brett [109] achieved a transmission of 99.9% for glass substrate deposited with graded-index layer of SiO_2 thin film. Apart from optical rugate filters, many researchers have reported work on 2D and 3D photonic crystal [110], luminescent devices [111] and liquid crystal devices [112] utilizing OAD optical thin films.

5 Characterization of Thin Film and Multilayer Coatings

5.1 Optical Properties

Optical properties include transmission, reflection, absorption, scattering, etc. are very important for the spectral performance of thin film and multilayer coating based optical devices. The information of optical constants of the coating materials is essential for the design and development of multilayer optical coating devices, which are determined by several different methods. They are based on interferometry, spectrophotometric measurements of reflection and/or transmission, laser calorimetry, attenuated total reflection, polarimetry and spectroscopic ellipsometry [113]. The most widely used methods for optical coatings are spectrophotometry, and spectroscopic ellipsometry, which are discussed as follows.

5.1.1 Spectrophotometry

The optical properties of thin films and spectral performance of multilayer coating devices are evaluated by spectrophotometry, which measures transmission, reflection and absorption spectrum of a material. The optical properties such as refractive index, absorption coefficient, band gap and thickness of optical thin films can be extracted from the transmission as well as the reflection spectrum. The spectral performance of a multilayer depends on the optical dispersion parameters, i.e. the refractive index $n(\lambda)$ and the extinction coefficient $k(\lambda)$, and thickness (d) of individual thin layers. Therefore, the determination of the optical constants is of huge importance prior to any optical filter design. There are numerous methods for the determination of the optical properties of thin films. But we will focus on two routinely used methods such as the Envelope/Swanepoel method [114, 115] and Inverse synthesis method [116], in which optical constants and film thickness are derived from single transmission measurement only [117]. In the following section, we briefly describe the general procedure of the two methods with their advantage and disadvantage.

Envelope method has been developed and refined by several workers after the work of Manifacier et al. [114]. It uses the interference fringes to derive optical constants and thickness of the film. The extremes of the measured transmission spectrum occur according to the condition

$$2nd = m\lambda \tag{20}$$

where m is an integer for maxima and half-integer for minima and λ is the corresponding wavelength. T_{M} and T_{m} define the envelopes passing tangentially through the maxima and minima as shown in Fig. 25. The refractive index of the transparent substrate can be calculated from its measured transmission spectrum T_s via the relation

$$n_s = \frac{1}{T_s} + \sqrt{\frac{1}{T_s^2} - 1} \tag{21}$$

Above the strong absorption region, the expression for the refractive index of the thin film at a wavelength of different extreme points is given by

$$n = \sqrt{N + \sqrt{N - n_s^2}} \tag{22}$$

where

$$N = 2n_s \frac{T_M - T_m}{T_M T_m} + \frac{n_s^2 + 1}{2} \tag{23}$$

Using Eq. (1), we can estimate the film thickness by the relation

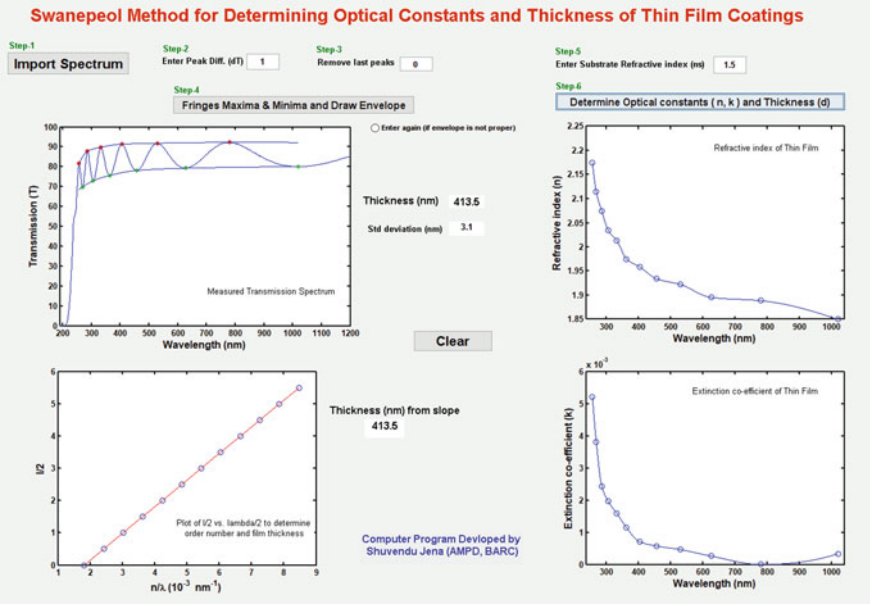

Fig. 25 Screenshot of a GUI computer program to determine refractive index, extinction coefficient, and thickness of thin-film coatings using the Swanepoel method. The code is used to derive the optical constants and thickness of ZrO_2-MgO thin-film coating from its measured transmission spectrum as shown in the figure

$$d = \frac{\lambda_1 \lambda_2}{2[\lambda_1 n(\lambda_1) - \lambda_2 n(\lambda_2)]} \tag{24}$$

where λ_1 and λ_2 are the wavelengths of two adjacent maxima (or minima). Since there could be errors in making exact smooth envelopes T_M and T_m, hence the preliminary calculated values of the refractive index (n_{in}) and thickness (d_{in}) of the films calculated from Eqs. (23) and (24) could be inaccurate. The more accurate refractive index and thickness of the thin film can be obtained by further executing the steps as follows. At first, take the average value of d_{in} obtained from every two adjacent extremes and use it in Eq. (20) to estimate the order number (m_{in}) for each extreme and round off the obtained m_{in} to the nearby integer or half-integer. These rounded values are considered as the exact order number m_{fn} corresponding to each maxima or minima. Then, use m_{fn} and n_{in} in Eq. (20) again to calculate the accurate thickness d_{fn} for each extreme excluding first maximum and minimum present in the strong absorption region. Now the average value of d_{fn} is considered as the final thickness of the film. Finally, the final thickness and the exact m values are used in Eq. (20) to calculate the accurate refractive index n_{fn} for each extreme. The refractive index as a function of wavelength $n(\lambda)$ can be then obtained by fitting the estimated values as using suitable dispersion models such as Cauchy or Sellimier dispersion equations [118]. The extinction coefficient (k) is given by

$$k = \frac{\alpha}{4\pi}\lambda = -\frac{\lambda}{4\pi d}\ln\left[\frac{(n+1)(n+n_s)(\sqrt{T_M}-\sqrt{T_m})}{(n-1)(n-n_s)(\sqrt{T_M}+\sqrt{T_m})}\right] \tag{25}$$

The calculated extinction coefficient at each extreme is fitted using a suitable dispersion model to get $k(\lambda)$. The Envelope method works well for thick films as they show a large number of interference fringes. It is not effective for absorbing film as interference fringes vanish unlike at the absorption edge. It is also not suitable if there are local absorption bands in between interference fringe extremes. The accuracy of the method decreases with decreasing film thickness. Because with decreasing thickness, the spacing between interference extremes increases, this makes interpolation between extremes more difficult [117]. Instead of all these pitfalls, the Envelope method is widely used as a routine analysis technique for the determination of optical constants of transparent or semiconducting optical thin-film materials. The complete process of the Envelope method is demonstrated in a MATLAB-based GUI program that determines thickness, refractive index and extinction coefficient (medium-strong absorption region) of a representative ZrO_2–MgO thin film as shown in Fig. 25. It estimates the parameters following the above-mentioned procedure.

Inverse synthesis method is approached by a multi-wavelength spectral fitting technique in which the measured spectrum is fitted with a theoretically generated spectrum using valid optical dispersion models. Ideally, optical constants of thin-film coatings of any materials can be determined using this method. Here, we have restricted its utility for optical coatings only. For simplicity, the optical thin-film coating having a refractive index (n), extinction coefficient (k) and thickness (d) deposited on a transparent substrate having a refractive index (n_s) is assumed to be isotropic and homogenous. The substrate is smooth and thick enough to avoid its surface interference effects on the measured spectrum of the thin-film coating. With the above assumptions, the transmission of a single-layer absorbing thin film on a transparent substrate is given by [119]

$$T = \frac{Ax}{B - Cx + Dx^2} \tag{26}$$

where

$$A = 16n_s(n^2 + k^2)$$

$$B = [(n+1)^2 + k^2][(n+1)(n+1)_s^2 + k^2]$$

$$C = 2\cos(\varphi)[(n^2 - 1 + k^2)(n^2 - n_s^2 + k^2) - 2k^2(n_s^2 + 1)] - k[2(n^2 - n_s^2 + k^2) + (n_s^2 + 1)(n^2 - 1 + k^2)]2\sin(\phi)$$

$$\phi = \frac{4\pi nd}{\lambda} \quad \alpha = \frac{4\pi k}{\lambda} \quad x = e^{(-\alpha d)}$$

In the above equations, λ is the wavelength. The measured transmission data provides a set of experimental data $(\lambda_i, T_i^{\text{Exp}})$, $i = 1, 2, 3, \ldots, N$. From this experimental data, n, k and d have to be determined. For all $i = 1, 2, 3, \ldots, N$, it must satisfy the equation: $T_i^{\text{Cal}}[\lambda_i, n_s(\lambda_i), n(\lambda_i), k(\lambda_i), d] = T_i^{\text{Exp}}$. The three unknowns $n(\lambda)$, $k(\lambda)$ and d, are estimated through the optimization process. The starting guess value for d is taken from the in situ measured film thickness. The wavelength dependency of $n(\lambda)$ and $k(\lambda)$ are generally expressed by different dispersion models such as (i) Cauchy–Urbach model [120] (ii) Wimple–De Domenico model (single oscillator model) [121] (iii) Adachi model [122] (iv) Forouhi and Bloomer model [123] (v) Tauc–Lorentz model [124] (vi) Cody–Lorentz model [125], etc. Then the fitting is done by minimizing the squared difference (χ^2) between the experimental and theoretically generated transmission data given by

$$\chi^2 = \frac{1}{(2N - P)} \sum_{i=1}^{N} \left[\left(T_i^{\text{Exp}} - T_i^{\text{Cal}} \right)^2 \right] \tag{27}$$

where T_i^{Exp} and T_i^{Cal} are the experimental and calculated transmissions, respectively. N and P are the number of data points and model parameters, respectively. The optimization is performed using the Levenberg–Marquardt algorithm [126]. The illustration of this method is shown in Fig. 26a, where the measured transmission spectrum of a HfO_2 thin film has been best fitted with the theoretically generated data using an appropriate dispersion model. The model parameters are used to derive the film refractive index and extinction coefficient spectra as plotted in Fig. 26b.

In case of a multilayer coating, each layer information can be obtained by numerical inverse synthesis of the measured optical spectrum of the multilayer. The measured spectrum is fitted with a theoretically generated data which includes layer thickness, and refractive indices as optimization parameters. In this approach, a merit function containing experimentally measured and theoretically generated parameters is given by [127]

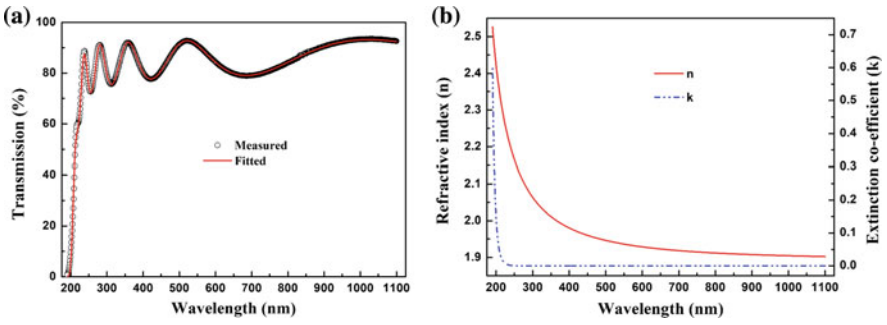

Fig. 26 **a** Measured transmission spectrum fitted with theoretical one for a representative HfO_2 thin film, and **b** the refractive index and extinction coefficient of the thin film derived from the fitting parameters

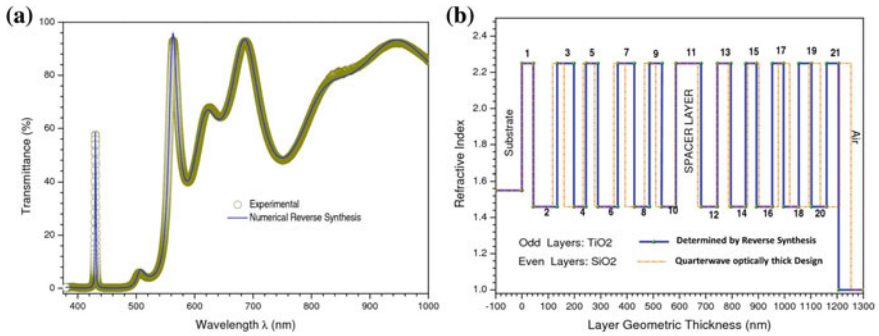

Fig. 27 **a** Analysis of the spectral characteristic of a 21-layer TiO_2/SiO_2 multilayer Fabry–Perot filter using numerical reverse synthesis method and **b** the layer thickness profile of the multilayer structure derived from the reverse synthesis method along with the optical monitored thickness profile [127]

$$M(p) = \left[\frac{1}{L}\sum_{i=1}^{L} W_i \left(\frac{D_i}{\delta F_i}\right)^m\right]^{1/m} \tag{28}$$

$$D_i = F_i^T(\exp) - F_i^C(d_i, n_i, k_i, \phi_i, \lambda), (1 \le i \le L) \tag{29}$$

where $M(p)$ dynamic merit function, L and F are the number of data points and the number of parameters to be optimized, respectively, and W_i and δF_i are the weight and tolerance factors. T and C are the targeted and the computed value. The parameters d, n, k, φ and λ represent layer thickness, refractive index, extinction coefficient, phase factor and wavelength, respectively. An example of this approach considering a Fabry–Perot interference filter is illustrated in Fig. 27. The Fabry–Perot filter is prepared by the sequential deposition of 21-QWOT layers of TiO_2 and SiO_2 using reactive EB evaporation. The peak position of the filter matched very well with the design, but not the peak transmission value. The reverse synthesis of the filter was made to understand the change. The measured transmission of the filter is fitted with the simulated spectrum as shown in Fig. 27a. The derived thickness of each layer of TiO_2 and SiO_2 in the multilayer is plotted in Fig. 27b along with that of QWOT design. It clearly shows that there is a thickness difference in each layer except the first and the spacer layer, as a result the peak position does not change as it is decided by the spacer layer, while its amplitude changes as it depends on the thickness of each layer.

5.1.2 Spectroscopic Ellipsometry

Spectroscopic ellipsometry is widely used as a high precision characterization tool to probe optical properties and thickness of thin films. It measures the change in polarized light reflectivity of a thin film. As linearly polarized light becomes 'elliptical'

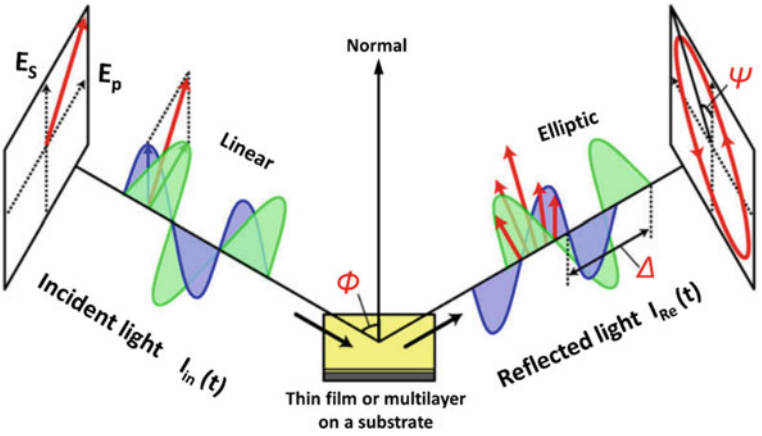

Fig. 28 Schematic illustration of a spectroscopic ellipsometry setup (reproduced from [129] with permission)

upon reflection as shown in Fig. 28, hence it is termed as 'ellipsometry'. Remarkable high thickness sensitivity of ~0.1 Å can be obtained in conventional spectroscopic ellipsometry [128].

In ellipsometry, change in amplitude and phase difference between parallel (p) and perpendicular (s) components of the electric field of light reflected from the sample surface are measured. The plane-polarized light is incident on the sample surface close to the Brewster angle to achieve better amplitude ratio (ψ) and phase difference (Δ) between the reflected 'p' and 's' components of light. The basic ellipsometry equation that includes the complex reflectance ratio (ρ) of thin film as a function of (ψ, Δ) is expressed as [128, 130]

$$\rho = \frac{r_p}{r_s} = \tan(\psi)\exp(i\Delta) = f(n_s, k_s, n, k, d, \theta, \lambda) \tag{30}$$

where (n, k), and (n_s, k_s) are the refractive index, and extinction coefficient of the substrate and film, respectively. θ and λ are the angle of incidence and wavelength of light, respectively. d is the thickness of the film. In rotating polarizer type ellipsometry, the time-dependent light intensity $I(t)$ at each wavelength is expressed by the equation [128, 130].

$$I(t) = I_0(1 + \alpha\cos(2\omega t) + \beta\sin(2\omega t)) \tag{31}$$

where I_0 is the proportional constant of the reflected light that is proportional to the intensity of incident light, ω is the angular frequency of the polarizer and α and β are the normalized Fourier coefficients. In rotating polarizer ellipsometry, (α, β) are first determined from the Fourier analysis of measured light intensities. Then the parameters (ψ, Δ) are extracted by substituting the measured (α, β) using the

following equations [130]:

$$\tan\psi = \sqrt{\frac{1+\alpha}{1-\alpha}}|\tan P| \text{ and } \cos\Delta = \frac{\beta}{\sqrt{1-\alpha^2}} \tag{32}$$

Here P is the polarizer angle. In the present analysis, the directly measured ellipsometry parameters α and β (at polarizer/analyser angle of 45°) have been fitted considering the appropriate sample structure and dispersion model. The complex refractive index of most optical thin-film coatings can be described by either of the following models: Tauc–Lorentz model, Adachi model, Drude model, Drude–Lorentz model, Cauchy–Urbach model, Forouhi and Bloomer model and Cody–Lorentz model. The complex dielectric constant of the void rich layer is estimated mostly using Bruggeman effective medium approximation. Then best-fit between the measured and calculated data are obtained by minimizing a common root mean square deviation (RMSD) function as follows:

$$RMSD = \sqrt{\frac{1}{2N-P}\sum_{i=1}^{N}\left[\left(\alpha_i^{Exp}-\alpha_i^{Cal}\right)^2+\left(\beta_i^{Exp}-\beta_i^{Cal}\right)^2\right]} \tag{33}$$

where N and P are the number of data points and the number of fitting parameters, respectively. The optimization is done using the Levenberg–Marquardt algorithm. Figure 29 illustrates the utility of spectroscopic ellipsometry to measure optical constants (n, k) and thickness (d) of thin-film coatings with EB evaporated ZrO_2 thin film as an example. The measured spectra of ellipsometric parameters are best fitted with theoretically generated spectra, and the fitting parameters are used to derive refractive index (n), extinction coefficient (k) and thickness of the film as shown in Fig. 29b.

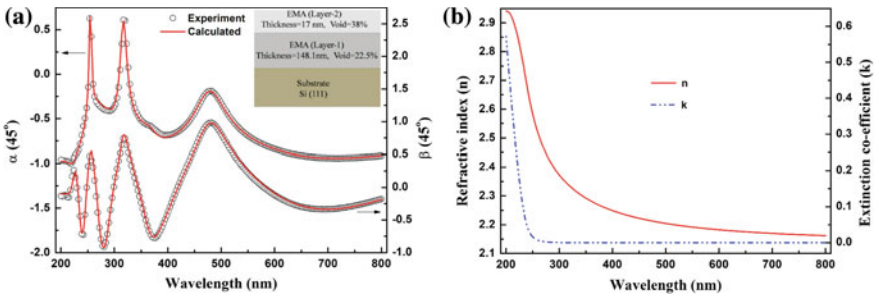

Fig. 29 **a** Measured ellipsometric spectra parameters (α and β) at analyzer angle of 45° along with their corresponding best fitted spectra of magnetron sputtered ZrO_2 thin film using suitable optical dispersion models as shown in the inset of the plot, and **b** derived refractive index and extinction coefficient of the ZrO_2 thin film using the fitting parameters [131]

5.2 Microstructure

Microstructures including crystal phase, density or porosity, surface morphology, etc. are very important for the stability and performance of optical coatings. Hence, they need to be thoroughly understood. Various characterization techniques such as X-ray diffraction, X-ray reflectivity, atomic force microscopy (AFM), scanning electron microscopy (SEM) and transmission electron microscope (TEM), etc. are utilized to probe the microstructure of thin films and multilayer coatings. Some of the essential techniques are briefly discussed here.

X-ray diffraction (XRD) [132] is a powerful non-destructive technique, which provides information on crystal structure, phase, texture, crystallite size and crystal defects. When monochromatic X-ray beams (typically $\lambda = 1.5406$ Å) diffracted from different planes of a sample interfere constructively, it results in diffraction peaks at specific angles. The atomic arrangements in the lattice define the peak intensities. As a result, the XRD pattern reveals the atomic arrangements in a given material. The ICDD (International Centre for Diffraction Data) database helps to identify the phase of a wide range of crystalline materials. In the diffraction pattern, 2θ position represents the angle of diffraction of a particular plane from which the d-spacing as well as lattice parameter can be derived by using Bragg's equation $2d \sin\theta = n\lambda$ [132]. Where n is the order of diffraction, λ is the wavelength of x-ray, d is the distance between atomic planes and θ is the Bragg's angle. The crystallite size (D) is estimated from the diffraction peak using Scherrer formula as $D = 0.9\lambda/\beta \cos\theta$, where β is the FWHM of the peak. The average strain (ε) value is estimated by the change in d-spacing with respect to the d-spacing in JCPDS file by the equation: $\varepsilon = \Delta d/d$. In case of optical coatings, the preferred phase of a thin film in a multilayer is amorphous, but it could be polycrystalline depending on the materials as well as the deposition process. Generally, the film deposited using the evaporation process under low substrate temperature shows an amorphous phase, while the film prepared by sputtering exhibits polycrystalline phase as illustrated in Fig. 30a for HfO_2 thin film. Therefore, phase identification is very essential as the same thin-film coating prepared by different deposition processes or the same process at different process parameters may have different crystalline phases.

Grazing incidence X-ray reflectivity (XRR) measurement gives precise information about film density, layer thickness, electron density and surface and interface roughness of very thin films and nanometric multilayer. The complex refractive index (η) of material for X-rays is expressed as [133]

$$\eta = 1 - \delta - i\beta \tag{35}$$

where

$$\delta = r_0\left(\frac{N_A Z}{2\pi A_W}\right)\lambda^2\rho \text{ and } \beta = \frac{\mu\lambda}{4\pi} \tag{36}$$

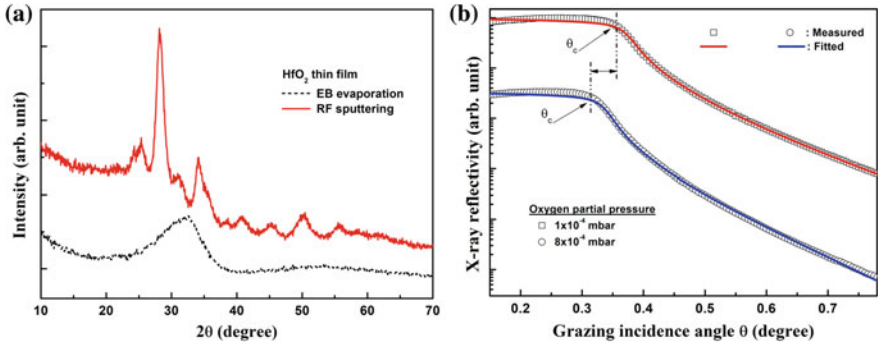

Fig. 30 **a** X-ray diffraction pattern of HfO_2 thin film prepared by EB evaporation, and RF magnetron sputtering, show amorphous and polycrystalline structure, respectively [134, 135]. **b** X-ray reflectivity curves of HfO_2 thin film prepared at different oxygen partial pressure show different critical angles, and exhibit different film densities [134]

here r_0 is the classical electron radius (2.82×10^{-15} m), N_A is the Avogadro number, and ρ, Z, A_W and μ are the density, atomic number, atomic weight and linear absorption coefficient of the element, respectively. The quantity $[N_A(\rho Z/A_W)]$ represents the density of electron of the element. X-ray gets total external reflection from any material surface at grazing incident angle as the refractive index of all known materials is slightly less than one in the X-ray region. But, as the grazing incident angle (θ) exceeds the critical angle (θ_c), the X-ray reflectivity drops drastically because the X-ray gets transmitted or absorbed in the layer. The critical angle is related to the refractive index correction factor δ by the approximate expression $\theta_c = \sqrt{\delta}$, which strongly depends on the bulk density of the material as well as the X-ray wavelength. The reflectivity of a thin film can be derived using Fresnel's boundary conditions. The X-ray reflectivity of a thin-film multilayer is determined by Parratt formalism. For rough surface and interfaces, the Fresnel's reflectivity is modified by incorporating a 'Debye–Waller-like' factor as given below [133]:

$$R = R_0 \exp\left(-\frac{q^2\sigma^2}{2}\right) \tag{37}$$

where $q = 4\pi \sin\theta/\lambda$ is the wave-vector transfer, R is the rough surface reflectivity and R_0 is the smooth surface reflectivity and σ is the surface RMS roughness. Thus, accurate estimation of density ρ and surface roughness σ can be obtained by fitting the grazing incidence X-ray reflectivity of the thin-film surface near its critical angle. The film density varies with the deposition process as well as with the process parameters. For example, the thin film prepared by the evaporation process shows lower film density as compared to that prepared by sputtering. The decrease in film density with increasing oxygen pressure in the case of oxide optical coatings such as HfO_2, ZrO_2, TiO_2, etc. are reported by several researchers. Therefore, accurate film density is very much essential for developing stable multilayer coatings, otherwise

a shift in spectral response could be possible because of less dense layers in the multilayer. The use of XRR to measure thin film density is illustrated in Fig. 30b, where the measured XRR spectra of EB evaporated HfO_2 thin films prepared at different oxygen partial pressures are fitted with theoretical spectra and the obtained film densities are different and found to be 8.5 and 7 g/cm^3 for deposition oxygen pressure of 1×10^{-4} and 8×10^{-4} mbar, respectively.

TEM [136] is the most sophisticated technology used to see directly the structure of each thin layer in a multilayer coating. It works on a similar concept like an optical microscope but uses electron instead of a photon as the source. In TEM, much smaller wavelength electrons (0.03 Å) are used, which gives a much higher resolution. This technique images electrons that are transmitted through the sample. For that, the electrons need a very high accelerating voltage (>100 keV) and the sample should be very thin (typically <100 nm) so that electrons can pass through it [137]. TEM can even image single rows of atoms and has higher resolution than SEM. It can also quantify dislocation density, sizes of nanoparticles, inclusions, voids, and provides medium-long range ordering information through electron diffraction [138]. The crystal structure of each layer along with their thickness and cross-sectional microstructure of multilayer optical coatings can also be probed using a transmission electron microscope (TEM) as demonstrated in Fig. 31. Low magnification cross-sectional TEM images of the HfO_2/SiO_2 multilayer mirror provide information about layer thickness as well as layer grain structure, while the high magnification images reveal the polycrystalline phase of HfO_2 layers and amorphous nature of SiO_2 layers. The orientations of different phases in a different direction can be clearly seen from

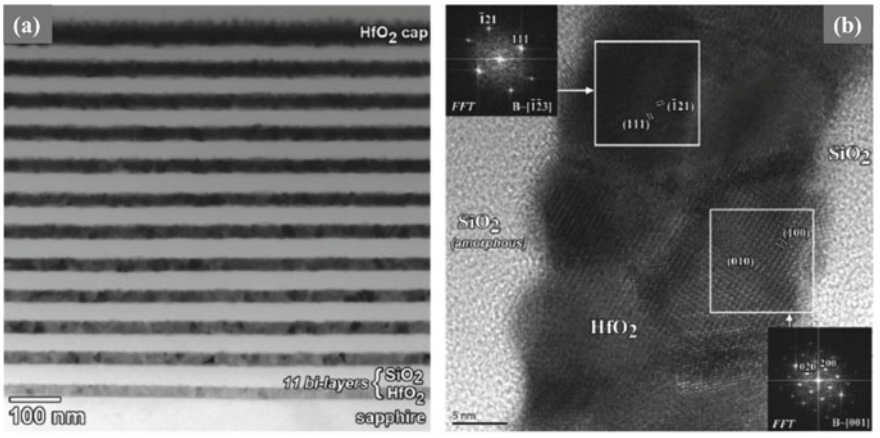

Fig. 31 Cross-sectional TEM images of a HfO_2/SiO_2 multilayer mirror: **a** Low and **b** high magnification. The images clearly show the polycrystalline phase of the HfO_2 and amorphous nature of the SiO_2 layers. The insert images in (**b**) are the fast Fourier transformations (FFT) of the lattice which clearly show the orientations of different crystalline phases (reproduced from [139] with permission)

the high magnification images. TEM helps to see directly the real structure of the multilayer coatings.

AFM [140] is considered as one of the best surface characterization techniques to probe surface morphology of any kind of materials. It measures surface roughness as well as average surface grain size. For optical coatings, the loss due to scattering at surface or interfaces in a multilayer because of surface or interface roughness is not desired, therefore the target is to deposit thin layer coatings with smooth surface or interfaces. Roughness is one of the important parameters that is used for quality checks of optical coatings. After deposition of every multilayer coating device, the surface roughness measurement of the coating is a must in order to ensure its optical grade quality, which is often done using AFM. Lesser the roughness, better the optical quality coatings. AFM uses van der Waals force between atoms of the tip apex ad the surface to create surface morphology, which eliminates the resolution limitations associated with optical microscopy. It is capable of measuring the vertical dimension (height or depth) of the sample surface, while optical and electron microscope does not have this scope.

A schematic diagram of a typical AFM system is shown in Fig. 32 and its operation is governed by three basic components: cantilever tip, piezoelectric scanner and feedback loop control system. A sharp tip is mounted at the end of a cantilever, which is attached at one end to a piezoelectric scanner. The force detection is based on the beam deflection method. A diode laser reflected from the back side of gold coated cantilever is detected by a position-sensitive quadrant photodiode detector, which determines the bending of the cantilever. As the tip is scanned across the sample, the tip-sample interaction force is measured by the cantilever. A desired tip-sample force is maintained by a feedback loop control system called the set point. If the measured force is larger or smaller than the set point, the piezoelectric scanner

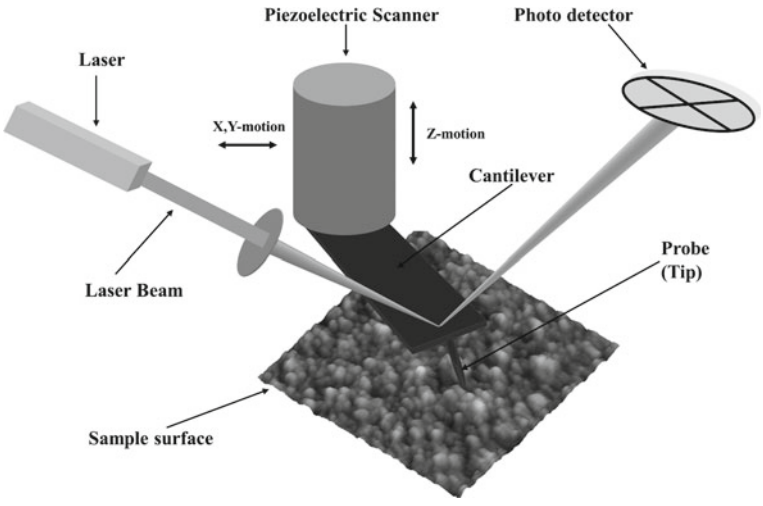

Fig. 32 Schematic working diagram of AFM (reproduced from [141] with permission)

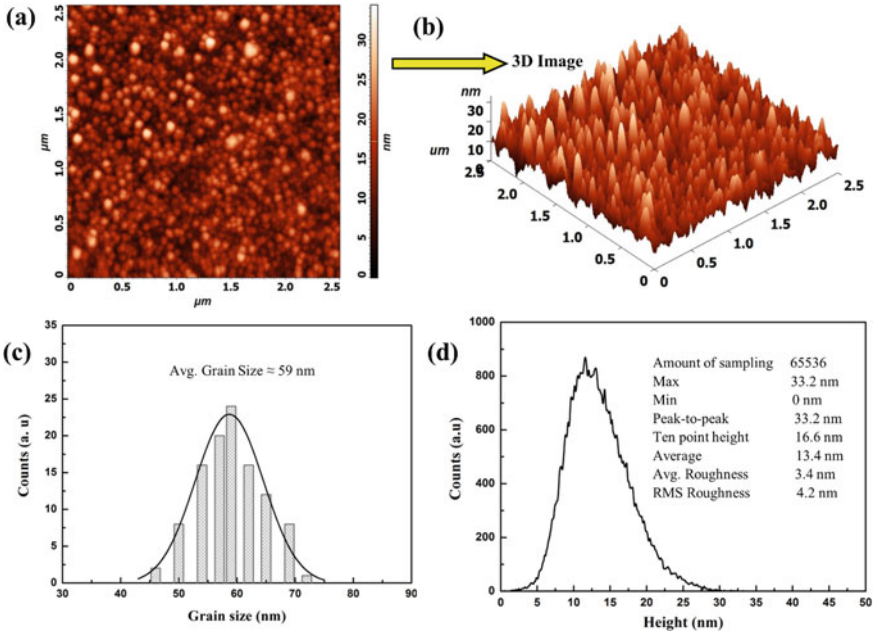

Fig. 33 Representative **a** 2D, **b** 3D AFM surface morphology for determination of **c** grain size and **d** surface roughness of HfO_2 thin film [141]

in the z-direction moves the probe either towards or away from the surface to bring the force back to the set point. The displacement of the piezo-scanner is proportional to the height of the sample. A surface topography can be produced by recording the displacement of the piezo-scanner as a function of position. The surface roughness and grain size [142] are derived from the vertical height and the lateral size of the particles in the AFM image. Root mean square (rms) surface roughness describes the smoothness of optical surfaces. A cross-sectional line across any part of an image can be processed to see the lateral size of grains, and the vertical profile along that line gives roughness. The mean grain size can be determined by taking numerous cross-sectional line profiles for different grains. Figure 33a and b show the 2D and 3D AFM topography of EB evaporated HfO_2 thin film. The grains are spherical in size with uniform size distribution. The estimated average grain size and rms roughness are found to be 58 nm and 4.2 nm as shown in Fig. 33c and d, respectively.

5.3 Residual Stress

The mechanical stability of optical coatings is one of the important factors which can hinder their performance. In particular, excessive stress in coatings leads to cracks,

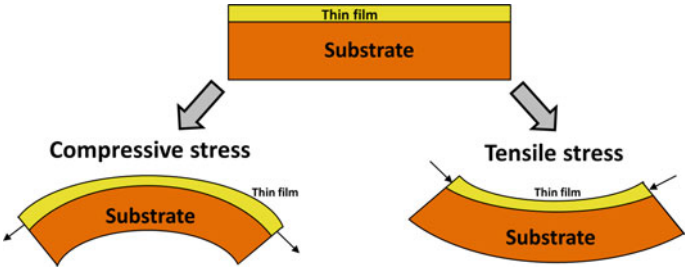

Fig. 34 The schematic illustrates the nature of stress in thin film by looking at the substrate curvature. If the curvature is positive (concave), then the residual stress in the film is tensile and if he curvature is negative (convex), then the film stress is compressive

delamination and deformation, that significantly affect the performance and durability of the coated optical components [143]. Therefore, knowledge of residual stress in thin-film coatings is essential for developing mechanically stable optical coatings. Stress can be either tensile or compressive as illustrated in Fig. 34. Tensile (compressive) stress makes the thin-film coating to contract (expand) parallel to its surface. The residual stress in the film strongly depends on deposition parameters such as rate of deposition, working pressure, residual gas pressure, substrate temperature, microstructure, material type, etc. Apart from this, the thickness-induced microstructure of individual thin layers also influences the stresses in multilayer coatings. The total stress in a multilayer is the combination of stresses generated due to individual layers and interfaces. The nature of interfacial stress in a multilayer strongly depends on the thickness of individual layers, material combinations and interface microstructure. Hence control over residual mechanical stress is very crucial for better performance of these optical coatings.

There are numerous experimental techniques [144] by which residual stress in a thin-film coating can be determined. But the substrate curvature method is the most preferred one because of its ease and quite fast process. Moreover, the additional knowledge of the film's elastic properties such as biaxial elastic modulus, Poisson's ratio, etc., are not required that are usually unknown. The curvature of the substrate before and after thin-film deposition is used for the determination of stress in films. The substrate curvature resulting in tensile and compressive stress in a thin-film coating is illustrated in Fig. 34. Considering a thin stressed film deposited on a thick initially stress-free substrate, the residual stress in the film can be determined using the substrate curvature by the Stoney's equation [145] as follows:

$$\sigma = \frac{1}{6}\left(\frac{E_s}{1-\upsilon_s}\right)\left(\frac{1}{R_a}-\frac{1}{R_b}\right)\left(\frac{t_s^2}{t_f}\right) \tag{38}$$

Here, R_b and R_a are radii of curvature of the substrate before and after coating, respectively, E_s and υ_s are Young's modulus and Poisson's ratio of the substrate, respectively, and t_s and t_f are the thicknesses of the substrate and the film, respectively.

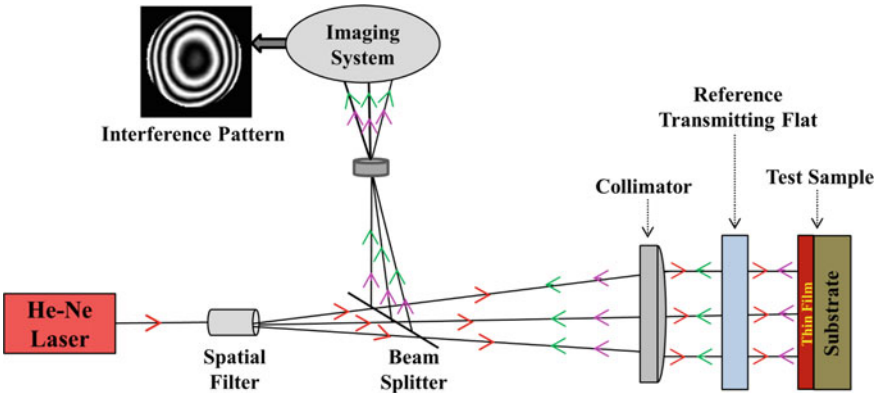

Fig. 35 Schematic diagram of laser interferometer setup for substrate curvature measurement (reproduced from [146] with permission)

The above equation is valid for $t_f << t_s$. It further assumes that the stress in the film is isotropic and homogeneous, and the substrate deformation is small as compared to its thickness. Here, the positive stress value is assigned for tensile stress, whereas the negative is for compressive stress.

Laser interferometer is one of the most accurate techniques for substrate curvature measurement more precisely [131, 147]. It measures surface profile with a precision more than $\lambda/10$ at $\lambda = 632.8$ nm. The schematic of a typical interferometer is shown in Fig. 35, in which a cavity made of a reference flat and a test coating sample is illuminated by a well collimated He–Ne laser ($\lambda = 632.8$ nm). The reference flat surface having a flatness of $\lambda/20$ reflects some of the laser light back into the interferometer, which becomes the reference wavefront. The remaining laser light passes through the reference flat on to the sample [146]. Subsequently, the two wavefronts superimpose to give bright and dark interference patterns. The data to estimate the sample surface error is acquired by taking numerous 'snapshots' of the interference patterns, which are subsequently processed to derive the phase of the wavefront at each point that yields the surface shape profile. The sag of the spherical shape component of the sample surface is derived by Zernike polynomial fitting [148]. The substrate surface curvature (R) is computed using the formula [149] $R = (r^2 + s^2)/2s$, where r is the radius of circularly shaped substrate aperture (typically r is taken ~20 mm) and s is the sag in the curvature profile. The obtained curvature is used in Eq. (38) to estimate stress in a coating. The importance of stress in a coating is illustrated in Fig. 36. It shows that the stress in EB evaporated HfO_2 thin film is tensile in nature, while that prepared by RF magnetron sputtering is compressive in nature. The stress in the HfO_2 coating varies with deposition process parameters (oxygen pressure) as shown in Fig. 36. Therefore, residual stress in a coating should be optimized properly to produce stable optical coating devices.

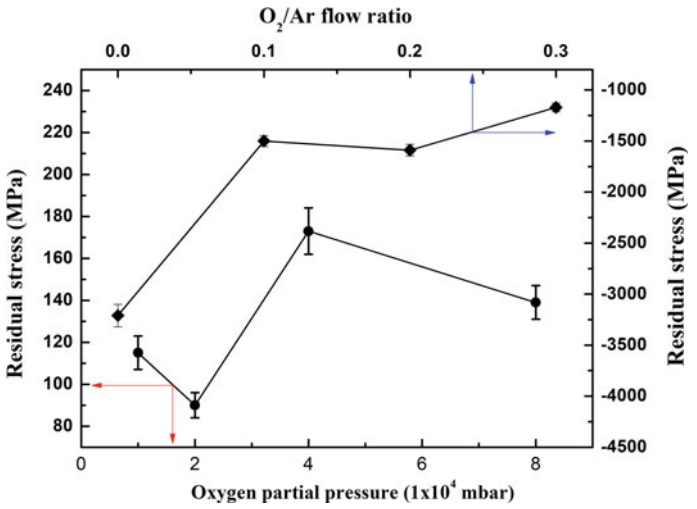

Fig. 36 Residual stress of the thin films made of the same material can show different nature of stress depending on their preparation methods. The residual stress in the EB evaporated HfO_2 thin films is tensile in nature, and it varies from 90 to 173 MPa with varying oxygen partial pressure [134]. The residual stress in the RF sputtered HfO_2 thin film is compressive nature and it varies from −1170 to −3210 MPa with varying O_2/Ar flow ratio [135]

5.4 Laser-Induced Damage Threshold

Laser systems are composed of many optical components, whose surfaces are coated with thin film or multilayer of optical coating materials and many of these lasers need high peak power for frequency conversion application in non-linear optical technology. The optical components for all such laser systems entail low optical losses, high efficiency, accurate optical properties and mainly high laser-induced damage threshold (LIDT) [150–152]. The damage threshold of the optical thin film or multilayer is the main limiting factor in designing a high-power laser system. Consequently, the research and development related to LIDT of thin film and multilayer coatings is widely supported by the scientific community for advancement of modern optics technology [153]. The laser fluence at which damage occurs in a coating is defined as LIDT of the coating [154]. Numerous factors such as damage criteria, test procedure, laser wavelength, laser pulse, spatial and temporal beam profile, number of shots, etc. [155]. In addition, it is highly necessary to distinct between bulk and thin film properties of a material to be investigated. Because, the basic properties of thin optical coatings such as refractive index, band gap, density, etc. vary significantly from their bulk counterpart depending on the types of the deposition process and their process parameters [156]. Therefore, the study of laser-induced damage threshold is quite a difficult job because of the involvement of such a complex process and various correlated parameters [157]. In this context, various

experimental setups have been developed worldwide at different labs to understand the laser-induced damage phenomena.

In the initial days, LIDT measurement methods were less understood by the researchers. In 1980, the LIDT measurements were thoroughly established by performing a prolonged round-robin on optical coatings for the laser wavelength of 1064 nm [155]. It resulted in the development of ISO-11254 [158] standard for the reliable measurement of LIDT values. The schematic of a standard laser damage measurement facility as per ISO-11254 is shown in Fig. 37. For pulsed lasers, two international standard methods are followed. One is single-shot (1 on 1 test) and the other is a multiple shot method [153]. The 1 on 1 test uses only one single shot on each unexposed site of the sample, whereas, the multiple shot test uses multiple shots in the same location of the sample. For both methods, it is important to know the spot-size and energy of the beam and the pulse duration. The beam size and the energy of the laser radiation are precisely measured by the laser beam profilometer and the energy metre, respectively. A focusing lens is used to focus the laser light into a precise spot to achieve sufficient energy density for damaging typical optical coatings. Generally, optical microscopy has been used to monitor the online damage event.

For 1 on 1 test, the measurement is done by multiple examinations of a coating with laser pulses of varying laser fluence or energy density from lower to higher values that initiate the damage. Then the damaged coating is investigated with an optical microscope or electron microscope to detect the damaged locations. Subsequently, the damage probability is estimated by taking the ratio of the number of damaged spots to the total number of spots exposed to laser at a specific energy density. The laser-induced damage threshold is defined by the maximum laser fluence at which the extrapolated probability is zero. For practical use of coatings, the 1 on 1 testing is least relevant. However, it is still considered by various optics manufacturing companies to demonstrate the damage resistance capability of their optical components. For S

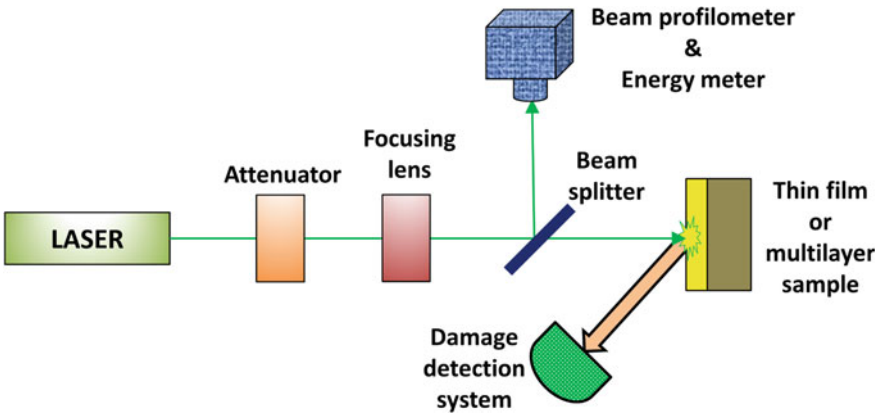

Fig. 37 Schematic illustrations of laser-induced damage threshold measurement setup

on 1-test, trains of pulses with well-defined laser fluence are used at each test position of a coating surface. Online damage is detected by in situ microscopy imaging as the laser-induced damage may be caused in the coating before a certain number S of pulses. The in situ imaging helps to estimate the number of pulses N of a certain laser fluence at which the damage occurs. Damage probabilities versus number of pulses of different energy densities are plotted and the characteristic probability curves are extrapolated to a large number of pulses in the range 10^9–10^{12} to determine the life time of the coatings. Recently, a revised project for the standard series 11254 is elaborated to deliver more practical information to the community. The laser-induced bulk damage and several other damage detection methods are elaborated in the recent revised series with project number 21254 [153].

Gallais and Commandré [159] have reported an extensive femtosecond laser damage threshold measurement of various bulk and thin-film optical materials including oxides, fluorides, mixture of two dielectric materials, semiconductors, ionic crystals, and metallic films. Most of them are optical thin-film coatings such as HfO_2, SiO_2, ZrO_2, Ta_2O_5, Al_2O_3, Nb_2O_5, Sc_2O_3, Y_2O_3, AlF_3, MgF_2, Ag and Pt. The material SiO_2 has the highest internal LIDT as compared to the rest of the considered materials. Al_2O_3–AlF_3 mixture exhibits the highest LIDT among mixed material coatings. High laser damage threshold beam combiner has been developed by process optimization using an electron beam evaporation process as compared to that made by the sputtering process [160] (Fig. 38).

LIDT of a multilayer coating can be improved by slightly modifying the electric field distribution without losing its spectral performance, which can be done either changing the layer thicknesses or adding overcoat layers [162–164]. The optimization of standing wave electric field distribution in multilayer coatings used for high-power lasers is very important. It is well known that absorption at film interfaces is far larger than the other parts of the film, therefore the normalized electric field intensity should be kept minimum at the interfaces to get higher LIDT of the

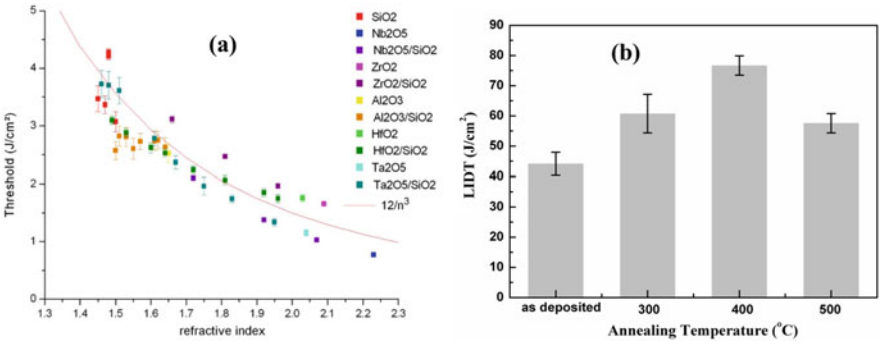

Fig. 38 **a** Measured LIDT (laser wavelength $\lambda = 1030$ nm and laser pulse $\tau = 500$ fs) as a function of the refractive index of the thin films at a wavelength of 1030 nm (reproduced from [161] with permission). **b** Measured LIDT ($\lambda = 532$ nm and $\tau = 7$ ns) of HfO_2/SiO_2 multilayer high reflection mirrors at different annealing temperatures [20]

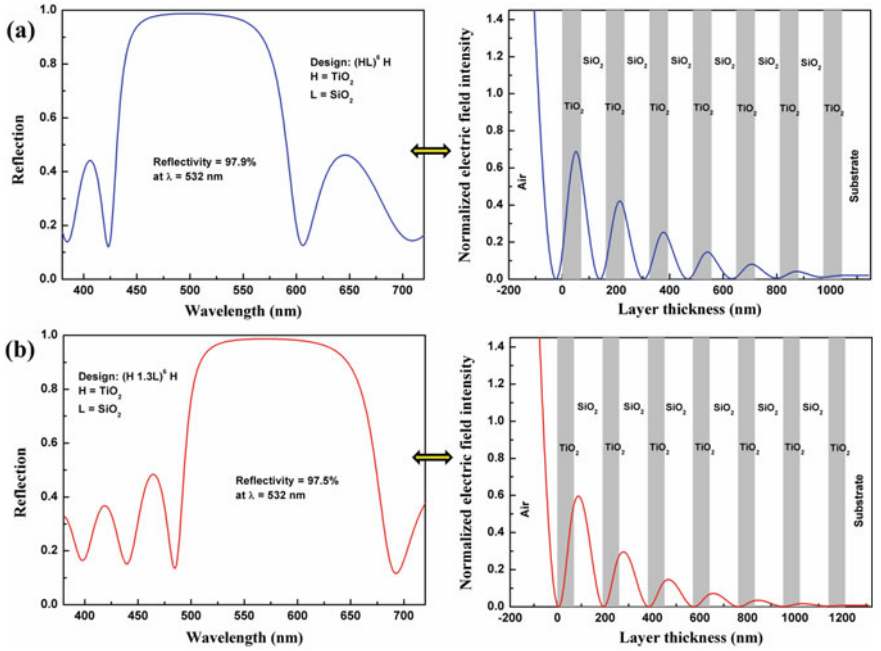

Fig. 39 Illustrations of designing of mirrors targeting high laser-induced damage threshold. Reflectivity and electric field distribution profile across the depth of multilayer for **a** conventional quarter-wave multilayer mirror, and **b** non-quarter-wave multilayer mirror

coatings. Moreover, high-index thin films exhibit lower LIDT than the low-index thin films. Therefore, the peak of the field intensity should be kept in the low-index layers to get higher LIDT. The illustration of the electric field optimization to get a higher LIDT high reflection laser mirror at a laser wavelength of 532 nm is shown in Fig. 39. Since SiO_2 is a low-index and high band gap material, while TiO_2 is a high-index and low band gap material, therefore SiO_2 shows higher intrinsic LIDT than TiO_2. The multilayer laser mirror is designed by a stack of alternate layers of TiO_2 and SiO_2 thin film layers. Figure 39a and b show the reflectivity and normalized electric field intensity of a quarter-wave stack and an optimized non-quarter-wave stack of TiO_2/SiO_2 multilayer, respectively. The quarter-wave and non-quarter-wave multilayer mirrors show reflectivity of 97.9% and 97.5%, respectively, at a wavelength of 532 nm. But the electric field intensity peaks appear in the high-index TiO_2 thin layers in case of quarter-wave design, while the peaks appear in the low-index SiO_2 layers in case of non-quarter-wave design. Moreover, the field intensity at the high-index layer interfaces is relatively higher for quarter-wave design as compared to that of non-quarter-wave design. Consequently, the LIDT of the electric field optimized non-quarter-wave multilayer TiO_2/SiO_2 mirror must be higher than that of quarter-wave mirror.

6 Conclusion

Technological advancement in computers and numerical methods and the developments of advanced deposition and characterization techniques have enabled us to produce complex multilayer optical coatings and devices with a great precision, which was unreal 50 years back. As a result, extensive use of optical thin-film coatings can be seen in a variety of consumer products and sophisticated scientific and technological equipment. It is usually perceived that the design part of thin-film multilayer coating devices is a simpler task. But it is not always so when the target is to design complex filters. A number of innovative and revolutionary design techniques like the needle method and Fourier transform method greatly ease the designer's job. The existing design methods/tools that are useful to tackle complex coating designs are reviewed in this chapter, which will be helpful for the beginners of this field. Access to parallel computing facilities has excited researchers to go for computer-intensive modelling to design multilayer coatings. The optical coating design is extending itself gradually by involving novel concepts like cermets, metamaterials, terahertz region, mixed materials and photonic crystals, which is undoubtedly the future direction. A design is realized to a real coating device through suitable deposition techniques. The history of deposition of optical coatings is very old, but it rapidly expanded in the twentieth century as there is a huge demand for coatings on optical instruments because of military need in World War II and mirrors for the development of high-power lasers. Subsequently, the development of vacuum process established thermal evaporation deposition technique; as a result, optical coating became essential features virtually in every aspect of optics. Thermal evaporation techniques such as resistive heating and electron beam evaporation are still important processes but now they are complemented or replaced by several new techniques such as sputtering, pulsed laser deposition, plasma-enhanced chemical vapour deposition process, etc. Now the number of deposition processes becomes so large that it is almost impossible to list all the processes used for optical coatings. The current chapter has focused on the most widely used techniques for optical coatings such as electron beam evaporation, magnetron sputtering, and ion beam sputtering for deposition of optical coatings. In addition to that, a hybrid deposition technique named oblique angle deposition method used to produce porous sculptured coatings is briefly discussed. Every deposition process has its advantages as well as disadvantages. No single technique is best for the deposition of all optical coatings. The deposition method is chosen depending on the application of coatings. The increasing demands of optics in various technologies always need continuous development of novel deposition techniques. The deposited thin film/multilayer coatings are tested and qualified through various characterization techniques prior to their use. Characterization plays a vital role for manufacturing high-quality optical coatings. The performance of multilayer optical coating devices strongly depends on various properties of the individual layers, which need to be thoroughly characterized. The important properties of optical coatings are optical properties, structure, surface topography, stress, adhesion and laser damage threshold. Spectrophotometer and spectroscopic ellipsometry are used

to probe optical properties of the coatings, while the coating microstructure is characterized using X-ray diffraction, X-ray reflectivity, SEM, TEM and AFM. Substrate curvature method is one of the precise measurement techniques for the determination of residual stress in coatings. The laser-induced damage threshold value of optical coating devices decides their utility for high-power laser applications. Efforts to endeavour new design, deposition and characterization methods will continue to make further advancement in the field of optical coatings.

References

1. R. Hooke, *Micrographia: Or Some Physiological Descriptions of Minute Bodies Made by Magnifying Glasses, with Observations and Inquiries Thereupon* (Courier Corporation, 2003)
2. I. Newton, *Opticks, or, a Treatise of the Reflections, Refractions, Inflections & Colours of Light* (Courier Corporation, 1952)
3. H. A. Macleod, *Thin-Film Optical Filters* (CRC Press, 2010)
4. T. Young, II. The Bakerian Lecture. On the theory of light and colours. Philos. Trans. R. Soc. London **12** (1802)
5. J.C. Maxwell, *A Treatise on Electricity and Magnetism* (Clarendon Press, Oxford, 1873)
6. H. Hertz, *Electric Waves: Being Researches on the Propagation of Electric action with Finite Velocity Through Space* (Dover Publications, 1893)
7. C. Fabry, Theorie et applications d'une nouvelle methods de spectroscopie intereferentielle. Ann. Chim. Ser. **7**(16), 115 (1899)
8. S. Kinoshita et al., Physics of structural colors. Rep. Prog. Phys. **71**, 076401 (2008)
9. P. Rouard, Sur le pouvoir réflecteur des métaux en lames très minces. CR Acad. Sci. Paris **195**, 869 (1932)
10. A. Pfund, Highly reflecting films of zinc sulphide. J. Opt. Soc. Am. A **24**, 99 (1934)
11. G. Bauer, Absolutwerte der optischen Absorptionskonstanten von Alkalihalogenidkristallen im Gebiet ihrer ultravioletten Eigenfrequenzen. Ann. Phys. **411**, 434 (1934)
12. J. Strong, On a method of decreasing the reflection from nonmetallic substances. J. Opt. Soc. Am. A **26**, 73 (1936)
13. A. Macleod, The early days of optical coatings. J. Opt. A-Pure Appl. Op. **1**, 779 (1999)
14. R.A. Denton, The manufacture of military optics at the Frankford Arsenal during WW II. Opt. News **15**, 24 (1989)
15. A. Piegari, F. Flory, *Optical Thin Films and Coatings: From Materials to Applications* (Woodhead Publishing, 2018)
16. https://www.alamy.it/fotos-immagini/basalt-mining.html
17. https://www.colorado.com/articles/red-rocks-amphitheatre-5-things-see-do
18. R. Tokas et al., Oblique angle deposition of HfO_2 thin films: quantitative assessment of indentation modulus and micro structural properties. Maer. Res. Express **2**, 035010 (2015)
19. https://blogs.agu.org/mountainbeltway/2018/04/27/friday-fold-cape-liptrap/
20. S. Jena et al., Annealing effects on microstructure and laser-induced damage threshold of HfO_2/SiO_2 multilayer mirrors. Appl. Opt. **55**, 6108 (2016)
21. H. Pulker, Characterization of optical thin films. Appl. Opt. **18**, 1969 (1979)
22. O. Stenzel, *The Physics of Thin Film Optical Spectra* (Springer, Heidelberg, 2005)
23. O. Stenzel, *Optical Coatings: Material Aspects in Theory and Practice* (Springer Science & Business, 2014)
24. A. Thelen, *Design of Optical Interference Coatings* (McGraw-Hill Companies, 1989)
25. S.A. Furman, A. Tikhonravov, *Basics of Optics of Multilayer Systems* (Atlantica Séguier Frontieres, 1992)
26. N. Kaiser, H.K. Pulker, *Optical Interference Coatings* (Springer, 2013)

27. P.W. Baumeister, *Optical Coating Technology* (SPIE Press Book, 2004)
28. P. Baumeister, Evaluation of the solutions for two design problems presented at the 1998 optical interference coatings conference. Appl. Opt. **39**, 2230 (2000)
29. J. Dobrowolski et al., Topical meeting on optical interference coatings (OIC'2001): manufacturing problem. Appl. Opt. **41**, 3039 (2002)
30. M. Tilsch, K. Hendrix, Optical interference coatings design contest 2007: triple bandpass filter and nonpolarizing beam splitter. Appl. Opt. **47**, C55 (2008)
31. J. Dobrowolski, Computer design of optical coatings. Thin Solid Films **163**, 97 (1988)
32. L. Li, J. Dobrowolski, Computation speeds of different optical thin-film synthesis methods. Appl. Opt. **31**, 3790 (1992)
33. J.H. Apfel, Graphics in optical coating design. Appl. Opt. **11**, 1303 (1972)
34. A.V. Tikhonravov, M.K. Trubetskov, Modern design tools and a new paradigm in optical coating design. Appl. Opt. **51**, 7319 (2012)
35. J. Dobrowolski, R. Kemp, Refinement of optical multilayer systems with different optimization procedures. Appl. Opt. **29**, 2876 (1990)
36. M. Friz, F. Waibel, Coating materials, in *Optical Interference Coatings* (Springer, 2003), p. 105.
37. D. Ristau et al., Ultraviolet optical and microstructural properties of MgF 2 and LaF 3 coatings deposited by ion-beam sputtering and boat and electron-beam evaporation. Appl. Opt. **41**, 3196 (2002)
38. F. Rainer et al., Materials for optical coatings in the ultraviolet. Appl. Opt. **24**, 496 (1985)
39. M. Friz, F. Waibel, Coating materials, in *Optical Interference Coatings*, ed. by N. Kaiser, H.K. Pulker (Springer-Verlag, 2003), pp. 105
40. S. Ono et al., Improvement of corrosion resistance of metals by an environmentally friendly silica coating method. J. Sol-Gel Sci. Techn. **29**, 147 (2004)
41. L. Bergamonti et al., Photocatalytic self-cleaning TiO_2 coatings on carbonatic stones. Appl. Phys. A **122**, 1 (2016)
42. A. Feldman et al., Modifying structure and properties of optical films by coevaporation. J. Vac. Sci. Technol. A **4**, 2969 (1986)
43. J.-S. Chen et al., Mixed films of TiO_2–SiO_2 deposited by double electron-beam coevaporation. Appl. Opt. **35**, 90 (1996)
44. U. Gangopadhyay et al., Low cost CBD ZnS antireflection coating on large area commercial mono-crystalline silicon solar cells. Appl. Surf. Sci. **230**, 364 (2004)
45. A. Kabir et al., Holographic imaging using the phase coherent photorefractive effect in ZnSe quantum wells. Appl. Phys. Lett. **93**, 063504 (2008)
46. P.K. Nair et al., Metal sulfide thin films on glass as solar control, solar absorber, decorative, and photographic coatings, in *Reflective and Refractive Optical Materials for Earth and Space Applications*, vol. 1485 (1991), p. 228
47. D.B. Chenault et al., Electro-optic coefficient spectrum of cadmium telluride. Appl. Opt. **33**, 7382 (1994)
48. G. Abadias et al., Stress in thin films and coatings: Current status, challenges, and prospects. J. Vac. Sci. Technol. A Vac. Surf. Films **36**, 020801 (2018)
49. M.M.A.-G. Jafar, Comprehensive formulations forthe total normal-incidence optical reflectance and transmittance of thin films laid on thick substrates. Eur. Int. J. Sci. Technol. **2**, 214 (2013)
50. Q.-Y. Cai et al., Evolution of optical constants of silicon dioxide on silicon from ultrathin films to thick films. J. Phys. D **43**, 445302 (2010)
51. J. López et al., Thickness effect on the optical and morphological properties in Al_2O_3/ZnO nanolaminate thin films prepared by atomic layer deposition. Superlattices Microst. **90**, 265 (2016)
52. J.-P. Xu et al., The thickness-dependent band gap and defect features of ultrathin ZrO_2 films studied by spectroscopic ellipsometry. Phys. Chem. Chem. Phys. **18**, 3316 (2016)
53. J. Dobrowolski, Numerical methods for optical thin films. Opt. Photonics News **8**, 24 (1997)

54. F. Abelès, Recherches sur la propagation des ondes électromagnétiques sinusoïdales dans les milieux stratifiés-Application aux couches minces. Ann. Phys. Paris **12**, 596 (1950)
55. W. Weinstein, Computations in thin film optics. Vacuum **4**, 3 (1954)
56. S. Jena et al., Tunable mirrors and filters in 1D photonic crystals containing polymers. Phys. E **114**, 113627 (2019)
57. P. Baumeister, Design of multilayer filters by successive approximations. J. Opt. Soc. Am. A **48**, 955 (1958)
58. W. Press et al., *Numerical Recipes* (Cambridge U. Press, Cambridge, 1986), Chap 12, p. 454
59. J.A. Dobrowolski et al., Fifty years of optical interference coatings at the national research council of Canada. Opt. Photon. News **18**, 24 (2007)
60. J. Dobrowolski, The impact of computers on the design and manufacture of optical multilayer coatings during the past 50 years, in *Proceedings of the Annual Technical Conference—Society of Vacuum Coaters*, vol. 50 (2007), p. 289.
61. A.V. Tikhonravov et al., Application of the needle optimization technique to the design of optical coatings. Appl. Opt. **35**, 5493 (1996)
62. S. Larouche, L. Martinu, OpenFilters: open-source software for the design, optimization, and synthesis of optical filters. Appl. Opt. **47**, C219 (2008)
63. B.T. Sullivan et al., Manufacture of complex optical multilayer filters using an automated deposition system. Vacuu **51**, 647 (1998)
64. P.G. Verly, Modified needle method with simultaneous thickness and refractive-index refinement for the synthesis of inhomogeneous and multilayer optical thin films. Appl. Opt. **40**, 5718 (2001)
65. http://www.rrcat.gov.in/organization/cat/aboutus.html#
66. S. Larouche, L. Martinu, Step method: a new synthesis method for the design of optical filters with intermediate refractive indices. Appl. Opt. **47**, 4321 (2008)
67. P.G. Verly, Optical coating synthesis by simultaneous refractive-index and thickness refinement of inhomogeneous films. Appl. Opt. **37**, 7327 (1998)
68. P. Verly et al., Efficient refinement algorithm for the synthesis of inhomogeneous optical coatings. Appl. Opt. **36**, 1487 (1997)
69. A.V. Tikhonravov et al., New optimization algorithm for the synthesis of rugate optical coatings. Appl. Opt. **45**, 1515 (2006)
70. E. Delano, Fourier synthesis of multilayer filters. J. Opt. Soc. Am. A **57**, 1529 (1967)
71. L. Sossi, *A Method for the Synthesis of Multilayer Dielectric Interference Coatings* (STIN, 1977), p. 229
72. J. Dobrowolski, D. Lowe, Optical thin film synthesis program based on the use of Fourier transforms. Appl. Opt. **17**, 3039 (1978)
73. L. Sossi, On the theory of the synthesis of multilayer dielectric light filters. Transl. into ENGLISH from Izv. Akad. Nauk Est. SSR, Fiz. Mat. (USSR) **25**(2), 171–176 (1977)
74. B.G. Bovard, Fourier transform technique applied to quarterwave optical coatings. Appl. Opt. **27**, 3062 (1988)
75. P. Verly, J. Dobrowolski, Iterative correction process for optical thin film synthesis with the Fourier transform method. Appl. Opt. **29**, 3672 (1990)
76. P.G. Verly, Optimum phase for rugate filter synthesis by Fourier transforms. Appl. Opt. **50**, C124 (2011)
77. S. Larouche, L. Martinu, Dispersion implementation in optical filter design by the Fourier transform method using correction factors. Appl. Opt. **46**, 7436 (2007)
78. B.G. Bovard, Rugate filter theory: an overview. Appl. Opt. **32**, 5427 (1993)
79. N. Sahoo, K. Apparao, Modified complex method for constrained design and optimization of optical multilayer thin-film devices. Appl. Phys. A **59**, 317 (1994)
80. J. Kruschwitz, Software tools speed optical thin-film design. Laser Focus World **39**, 157 (2003)
81. M. Ohring, *Materials Science of Thin Films* (Academic press, 2001)
82. D.M. Mattox, *Handbook of Physical Vapor Deposition (PVD) Processing* (William Andrew, 2010)

83. K. Seshan, *Handbook of Thin Film Deposition* (William Andrew, 2001)
84. P.M. Martin, *Handbook of Deposition Technologies for Films and Coatings: Science, Applications and Technology* (William Andrew, 2009)
85. R. von Pohl, P. Pringsheim, Über die Herstellung von Metallspiegeln durch Distillation im Vakuum. Verhandl. Deut. Physik. Ges **14**, 506 (1912)
86. M. Ohring, Thin-film evaporation processes, in *Materials Science of Thin Films* (2nd Ed.) (Academic Press, San Diego, 2002), p. 95
87. S. Jena et al., Optical properties and laser damage threshold of HfO_2–SiO_2 mixed composite thin films. Appl. Opt. **53**, 850 (2014)
88. B. Movchan, A. Demchishin, Structure and properties of thick condensates of Nickel, Titanium, Tungsten, Aluminium oxides, and Zirconium oxides in vacuum Fiz. Metal. Metalloved. **28**, 653–60 (1969)
89. E.H. Hirsch, I.K. Varga, Thin film annealing by ion bombardment. Thin Solid Films **69**, 99 (1980)
90. K.H. Müller, Model for ion-assisted thin-film densification. J. Appl. Phys. **59**, 2803 (1986)
91. J.D. Targove, H.A. Macleod, Verification of momentum transfer as the dominant densifying mechanism in ion-assisted deposition. Appl. Opt. **27**, 3779 (1988)
92. C. Bundesmann, H. Neumann, Tutorial: The systematics of ion beam sputtering for deposition of thin films with tailored properties. J. Appl. Phys. **124**, 231102 (2018)
93. J. George, *Preparation of Thin Films* (CRC Press, 1992)
94. J.E. Mahan, *Physical Vapor Deposition of Thin Films* (Wliey, 2000)
95. J. Sellers, Asymmetric bipolar pulsed DC: the enabling technology for reactive PVD. Surf. Coat. Tech. **98**, 1245 (1998)
96. M. Becker et al., Materials processing using radio-frequency ion-sources: Ion-beam sputter-deposition and surface treatment. Rev. Sci. Instrum. **90**, 023901 (2019)
97. H. Liu et al., Ion beam sputtering mixture films with tailored refractive indices. Opt. Laser Technol. **55**, 21 (2014)
98. M.M. Hawkeye et al., *Glancing Angle Deposition of Thin Films: Engineering the Nanoscale* (Wiley, 2014)
99. A. Barranco et al., Perspectives on oblique angle deposition of thin films: from fundamentals to devices. Prog. Mater Sci. **76**, 59 (2016)
100. R. Messier et al., Engineered sculptured nematic thin films. J. Vac. Sci. Technol. A **15**, 2148 (1997)
101. B. Dick et al., Controlled growth of periodic pillars by glancing angle deposition. J. Vac. Sci. Technol. B **21**, 23 (2003)
102. K. Sobahan et al., Nanostructured optical thin films fabricated by oblique angle deposition. Adv. Nat. Sci. Nanosci. **1**, 045005 (2011)
103. R. Tokas et al., Effect of angle of deposition on micro-roughness parameters and optical properties of HfO_2 thin films deposited by reactive electron beam evaporation. Thin Solid Films **609**, 42 (2016)
104. J. Oliver et al., Glancing-angle–deposited magnesium oxide films for high-fluence applications. Opt. Mater. Express **6**, 2291 (2016)
105. A.C. van Popta et al., Birefringence enhancement in annealed TiO_2 thin films. J. Appl. Phys. **102**, 013517 (2007)
106. A. Lakhtakia et al., Sculptured-thin-film spectral holes for optical sensing of fluids. Opt. Commun. **194**, 33 (2001)
107. K. Robbie et al., Inhomogeneous thin film optical filters fabricated using glancing angle deposition. Electron. Lett. **33**, 1213 (1997)
108. Y. Zhu, H. Jiao, Rugate filter with multi-channel grown by glancing angle deposition. Optik **123**, 1501 (2012)
109. S.R. Kennedy, M.J. Brett, Porous broadband antireflection coating by glancing angle deposition. Appl. Opt. **42**, 4573 (2003)
110. M. Summers et al., Fabrication of 2D–3D photonic crystal heterostructures by glancing angle deposition. Photon. Nanostruct. Fundam. Appl. **7**, 76 (2009)

111. P.C. Hrudey et al., Highly ordered organic Alq3 chiral luminescent thin films fabricated by glancing-angle deposition. Adv. Mater. **18**, 224 (2006)
112. K. Robbie et al., Chiral nematic order in liquid crystals imposed by an engineered inorganic nanostructure. Nature **399**, 764 (1999)
113. E.D. Palik, *Handbook of Optical Constants of Solids* (Academic Press, 1998)
114. J.C. Manifacier et al., A simple method for the determination of the optical constants n, k and the thickness of a weakly absorbing thin film. J. Phy. E **9**, 1002 (1976)
115. R. Swanepoel, Determination of the thickness and optical constants of amorphous silicon. J. Phy. E **16**, 1214 (1983)
116. J.A. Dobrowolski et al., Determination of optical constants of thin film coating materials based on inverse synthesis. Appl. Opt. **22**, 3191 (1983)
117. P. Dirk, S. Philippe Frederic, Methods for the determination of the optical constants of thin films from single transmission measurements: a critical review. J. Phys. D Appl. Phys. **36**, 1850 (2003)
118. D.Y. Smith et al., A generalized Cauchy dispersion formula and the refractivity of elemental semiconductors. J. Phys. Condens. Matter **13**, 3883 (2001)
119. J.-M. González-Leal et al., Influence of substrate absorption on the optical and geometrical characterization of thin dielectric films. Appl. Opt. **41**, 7300 (2002)
120. D.V. Likhachev, A practical method for optical dispersion model selection and parameters variations in scatterometry analysis with variable n&k's. Thin Solid Films **562**, 90 (2014)
121. S.H. Wemple, M. DiDomenico, Behavior of the electronic dielectric constant in covalent and ionic materials. Phy. Rev. B **3**, 1338 (1971)
122. S. Adachi, Model dielectric constants of GaP, GaAs, GaSb, InP, InAs, and InSb. Phy. Rev. B **35**, 7454 (1987)
123. A.R. Forouhi, I. Bloomer, Optical dispersion relations for amorphous semiconductors and amorphous dielectrics. Phy. Rev. B **34**, 7018 (1986)
124. G.E. Jellison, F.A. Modine, Parameterization of the optical functions of amorphous materials in the interband region. Appl. Phys. Lett. **69**, 371 (1996)
125. J. Price et al., Spectroscopic ellipsometry characterization of HfxSiyOz films using the Cody-Lorentz parameterized model. Appl. Phys. Lett. **85**, 1701 (2004)
126. N.M. Kamble et al., Determination of the optical constants of HfO_2–SiO_2 composite thin films through reverse fitting of transmission spectra. Vacuum **86**, 422 (2011)
127. N.K. Sahoo et al., Postanalyses of an optical multilayer interference filter using numerical reverse synthesis and Rutherford backscattering spectrometry. Appl. Opt. **52**, 2102 (2013)
128. H. Fujiwara, *Spectroscopic Ellipsometry: Principles and Applications* (Wiley, 2007)
129. D. Yokoyama et al., Horizontal orientation of linear-shaped organic molecules having bulky substituents in neat and doped vacuum-deposited amorphous films. Org. Electron. **10**, 127 (2009)
130. R. Azzam, N. Bashara, *Ellipsometry and Polarized Light* (Amsterdam, 1977)
131. R. Tokas et al., Study of ZrO_2 thin films deposited at glancing angle by radio frequency magnetron sputtering under varying substrate rotation. Thin Solid Films **645**, 290 (2018)
132. B.D. Cullity, S.R. Stock, *Elements of X-ray Diffrcation* (3rd ed.) (2001)
133. A. Gibaud, S. Hazra, X-ray reflectivity and diffuse scattering. Curr. Sci. **78**, 1467 (2000)
134. S. Jena et al., Influence of oxygen partial pressure on microstructure, optical properties, residual stress and laser induced damage threshold of amorphous HfO_2 thin films. J. Alloys Compd. **771**, 373 (2019)
135. S. Jena et al., Effect of O_2/Ar gas flow ratio on the optical properties and mechanical stress of sputtered HfO_2 thin films. Thin Solid Films **592**, 135 (2015)
136. E. Ruska, The development of the electron microscope and of electron microscopy. Rev. Mod. Phys. **59**, 627 (1987)
137. C.B. Carter, D.B. Williams, *Transmission Electron Microscopy: Diffraction, Imaging, and Spectrometry* (Springer, 2016)
138. L. Reimer, *Transmission Electron Microscopy: Physics of Image Formation and Microanalysis* (Springer, 2013)

139. K.J. Leonard et al., The role of microstructure on the optical performance of neutron irradiated dielectric mirrors. J. Nucl. Mater. **445**, 281 (2014)
140. G. Binnig et al., Atomic force microscope. Phys. Rev. Lett. **56**, 930 (1986)
141. S. Jena et al., Characterization of optical thin films by spectrophotometry and atomic force microscopy. SMC Bulletin **6**, 1 (2015)
142. R. De Oliveira et al., *Measurement of the Nanoscale Roughness by Atomic Force Microscopy: Basic Principles and Applications* (INTECH Open Access Publisher, 2012)
143. J.B. Oliver et al., Stress compensation in hafnia/silica optical coatings by inclusion of alumina layers. Opt. Express **20**, 16596 (2012)
144. G.N. Strauss, Mechanical stress in optical coatings, in *Optical Interference Coatings* (Springer, 2003), p. 207.
145. X. Feng et al., On the Stoney formula for a thin film/substrate system with nonuniform substrate thickness. J. Appl. Mech. **74**, 1276 (2007)
146. S. Jena et al., Study of aging effects on optical properties and residual stress of HfO_2 thin film. Optik **185**, 71 (2019)
147. A. Majhi et al., Evaluation of microstructure and residual stress in W/B4C multilayer optics. J. Appl. Phys. **124**, 115306 (2018)
148. D. Malacara, *Optical Shop Testing* (Wiley, 2007)
149. R.S. Sirohi, *Wave Optics and Its Applications* (Orient Blackswan, 1993)
150. R.M. Wood, *Laser-Induced Damage of Optical Materials* (CRC Press, 2003)
151. T. Walker et al., Pulsed laser-induced damage to thin-film optical coatings-Part I: Experimental. IEEE J. Quantum Electron. **17**, 2041 (1981)
152. T. Walker et al., Pulsed laser-induced damage to thin-film optical coatings-Part II: Theory. IEEE J. Quantum Electron. **17**, 2053 (1981)
153. D. Ristau et al., Laser damage thresholds of optical coatings. Thin Solid Films **518**, 1607 (2009)
154. X. Zu et al., Comparative studies of laser-induced damage of several single-layer optical films. Nucl. Instrum. Methods Phys. Res. B **266**, 3195 (2008)
155. K.H. Guenther, R.G. Menningen, 1.06-μm laser damage of optical coatings: regression analyses of round-robin test results. Appl. Opt. **23**, 3754 (1984)
156. A.J. Glass, A.H. Guenther, Laser induced damage in optical materials: 7th ASTM symposium. Appl. Opt. **15**, 1510 (1976)
157. A. Bananej et al., The effect of porosity on the laser induced damage threshold of TiO_2 and ZrO_2 single layer films. Opt. Laser Technol. **42**, 1187 (2010)
158. J. Becker, A. Bernhardt, ISO 11254: an international standard for the determination of the laser-induced damage threshold, in *Laser-Induced Damage in Optical Materials: 1993*, vol. 2114 (1994), p. 703
159. L. Gallais, M. Commandré, Laser-induced damage thresholds of bulk and coating optical materials at 1030 nm, 500 fs. Appl. Opt. **53**, A186 (2014)
160. M. Nand et al., Development of high damage threshold multilayer thin film beam combiner for laser application. AIP Conf. Proc. **1731**, 080051 (2016)
161. B. Mangote et al., Femtosecond laser damage resistance of oxide and mixture oxide optical coatings. Opt. Lett. **37**, 1478 (2012)
162. M. Chorel et al., Robust optimization of the laser induced damage threshold of dielectric mirrors for high power lasers. Opt. Express **26**, 11764 (2018)
163. S. Melnikas et al., Enhancement of laser-induced damage threshold in chirped mirrors by electric field reallocation. Opt. Express **25**, 26537 (2017)
164. M. Zhu et al., Influence of SiO_2 overcoat layer and electric field distribution on laser damage threshold and damage morphology of transport mirror coatings. Opt. Commun. **319**, 75 (2014)

Organic Thin Films: Langmuir Monolayers and Multilayers

Sarathi Kundu

Organic thin films are playing an important role in our daily life. These films are used as a coating layer for transmission of light, different optical control constituents in microelectronics, detectors for sensing organic, inorganic and gas molecules in biosensor devices, etc. Organic thin films are also used as display materials and electronic circuit elements in transistors, optoelectronic devices, biochips, etc. In addition to the technological applications and having immense importance in materials science, organic thin films are also useful to study different physical phenomena in reduced dimensions.

There are different experimental techniques available by which structures and novel properties of such organic thin films are investigated. Scanning tunnelling microscopy (STM), atomic force microscopy (AFM), Brewster angle microscopy (BAM), fluorescence microscopy (FM), UV-Vis spectroscopy, Fourier transform infrared (FTIR) spectroscopy, Photoluminescence (PL) spectroscopy, sum frequency generation (SFG) spectroscopy, X-ray and neutron scattering techniques are commonly used to investigate the structures and properties of such thin films. As the film thickness varies between 10 and 1000 Å, it is therefore quite obvious that the selection of specific technique mostly depends upon the film thickness and constituent molecules. Organic thin films made of different fatty acids, lipids, polymers, biopolymers, liquid crystals, etc. have been used to build novel pattern or architecture in the nanometer length scale and to explore structure-induced property modifications. Moreover, investigation of the structures and patterns formation is also a very fascinating area to study to tune the specific property of the thin-film materials in confined geometry.

S. Kundu (✉)
Soft Nano Laboratory, Physical Sciences Division, Institute of Advanced Study in Science and Technology, Paschim Boragaon, Garchuk, Guwahati 781035, Assam, India
e-mail: sarathi.kundu@gmail.com

S. Kumar and D. K. Aswal (eds.), *Recent Advances in Thin Films*, Materials Horizons: From Nature to Nanomaterials, https://doi.org/10.1007/978-981-15-6116-0_11

In this chapter, organic thin films of fatty acids and fatty acid salts for different physicochemical conditions are reviewed extensively. Different characterization techniques are also explained briefly for better understanding.

1 Molecular Crystal and Different Types of Organic Thin Films

For the description of the physical properties of a solid body, the strength of attraction among the particles (atoms or molecules) of which the crystal is formed may be compared with the forces of attraction among the composite parts (electrons and atoms, respectively) of these particles. If the inter-particle forces are significantly smaller than the intra-particle forces, then during the formation of a solid body, these particles remain essentially unchanged. Such solid bodies are defined as *molecular crystals* [1]. If the magnitude of energy of inter-particle forces is close to chemical energies (the bond energies of atoms in a molecule or of electrons in an atom), then the particles lose their individuality, and the crystals can be identified as the *valence*, *metallic* or *ionic* type [2]. In the valence or covalent bonding, the degree of overlap between the electronic wave functions of the neighbouring atoms, and thus the strength of the bonding, is dependent not only on the separation but also on the bond angles. On the other hand, metallic or ionic bonding is non-directional. The main difference between the latter two is that in the metallic bond, the wave function spreads over a distance that is large compared with the interatomic separation, whereas for the ionic bond, the overlap is extremely small. For molecular crystals, mainly van der Waals force of attraction acts between the molecules. Such crystals can form with atoms having closed electron shells, or with saturated molecules. Molecular crystals generally occur for organic substances. Not only bulk crystals, organic monolayers and multilayers are also formed by this type of van der Waals interactions. Inorganic monolayer and multilayer depositions by molecular beam epitaxy (MBE) [3] and metal organic chemical vapour deposition (MOCVD) [4] always need ultra-high-vacuum (UHV) conditions, temperature control, short switching times between different sources, etc. Also, only a specified range of materials can be grown on a particular substrate, which, moreover, has always to be crystalline. It is known that the growth of inorganic crystals or films, i.e. possessing valence or metallic bonds is extremely dependent on environmental conditions. This is due to the comparable strengths of inter- and intra-particle bonds in these crystals, which places stringent restrictions on environmental conditions during growth. On the other hand, for organic molecules, presence of weak van der Waals interactions and strong covalent bonds within molecules allows organic monolayers and multilayers to grow easily under ambient conditions, and on any substrate, including liquids (which are called subphases), although for making some special kinds of organic films selective environments are necessary.

There are mainly four ways by which crystalline organic films can be made.

(a) *Langmuir films* or *Langmuir monolayers* are made up of amphiphilic molecules spread on a liquid surface like water [5, 6]. The hydrophilic 'head' part of each molecule has an affinity to water, while the hydrophobic 'tail' part towards air side.
(b) *Langmuir–Blodgett (LB) films* are formed when Langmuir monolayer is transferred onto a solid substrate [7]. Multilayers are deposited by repeated up- and down-strokes of the substrate through the monolayer-covered water surface.
(c) *Organic molecular beam deposition (OMBD)* or *organic molecular beam epitaxy (OMBE)* is nearly similar to the evaporation technique under ultra-high-vacuum (UHV) for inorganic materials. For example, aromatic molecules such as perylene-derivatives are typical systems for OMBD [8, 9]. Such organic samples are loaded into sublimation cells and then allowed to grow on a solid substrate which is kept at a particular temperature. The chamber pressure and the cell temperature are maintained in such a way that molecular decomposition does not take place and the powder sources are sublimed to achieve the desired growth [10].
(d) *Self-assembled monolayers (SAMs)* usually grown from the gaseous phase or solution represent a further class of organic thin films. The defining feature is the chemisorptions (or, generally, strong interaction) of the headgroups with a specific affinity to the substrate [11].

It should however be noted that the boundaries between some of these techniques are not rigid. For example, the difference between Langmuir monolayers and SAMs are not absolutely sharp. Langmuir monolayers can form both on liquid and solid substrates through weak bonds, whereas, SAMs form only on solid substrates and are chemisorbed, i.e. strongly bound [11].

2 Organic Films on Liquid Surfaces

Organic monolayers or films can be formed on the water surface by choosing *amphiphilic molecules* [5–7]. Amphiphilic molecules have two parts: hydrophilic part usually called 'head' is soluble in water and hydrophobic part usually called 'tail' is insoluble in water. When such molecules are spread on the water surface, a monomolecular layer forms where the heads touch the water surface and the tails stay towards the air. The monomolecular layer thus formed is generally called a *Langmuir monolayer* [5–7]. Long-chain fatty acids, alcohols, lipids, etc. are the most common examples of such molecules. These molecules, also known as *surfactants*, can form stable monolayer depending upon the balance between hydrophilicity and hydrophobicity of headgroups and tails, respectively.

Surface tension is the most important physical property that is obtained from the Langmuir monolayer. But the quantifiable quantity is the surface pressure [12], which is the difference between the surface tension of pure water and the surface tension of film covered water. Surface pressure [13] is thus defined as

$$\pi = \gamma_0 - \gamma_f \tag{1}$$

where γ_0 and γ_f are the surface tensions of pure water and film covered water surface, respectively.

To form a film on the water surface, amphiphiles are dissolved in some solvent and then the solution is spread on water. It is required that the solvent should be capable of dissolving and spreading the film-forming molecules on the water surface and then could be evaporated completely keeping the film free from any contamination. Usually, the spreading solvent chosen has lower surface tension than water, is volatile, i.e. evaporate within a reasonably short time within which the solution has covered the water surface. The solvent has also to be lighter than water and insoluble in water. The extent to which a drop of liquid (1) placed on a solid or another liquid (2) spreads is given by Young's equation

$$\gamma_{1V} \cos\theta = \gamma_{2V} - \gamma_{12} \tag{2}$$

where the interfacial tensions (γ's) are for the various interfaces between the substrate or subphase (2), liquid (1) and vapour (V) phases, and θ is the contact angle between the (1) and (2) at the 1–2-V interface. There is no finite contact angle for complete wetting, i.e. the liquid spreads completely on the substrate or subphase. In this context, a quantity called the spreading coefficient is defined as [14]

$$S_{1/2} = \gamma_1 - \gamma_2 - \gamma_{12} \tag{3}$$

where $S_{1/2}$ is the spreading coefficient for liquid (1) on liquid (2), γ_1 and γ_2 are the corresponding surface tensions and γ_{12} is the interfacial tension. If the value of $S_{1/2}$ is positive, spreading occurs, but if it is negative, liquid (1) dewets and rests as a lens on liquid (2).

There are several properties of the monolayer that are well studied viz. surface pressure, surface potential [5, 13, 15] and surface viscosity [5, 7, 13]. But the well-studied and well-characterized properties of a Langmuir monolayer is surface pressure (π) and its variation with surface area [16], temperature [6, 16], metal ions [17, 18], subphase pH [19], compression rate [20], time [21], etc. The basic information that is obtained from a Langmuir monolayer is its surface pressure (π)—area per molecule (A) isotherm. The schematic of a typical π–A isotherm for a Langmuir monolayer is shown in Fig. 1. Langmuir monolayers are considered as two-dimensional model systems. They can be formed easily and are frequently used for studying structures [6], structural changes [6] and phase transitions in two dimensions [22, 23]. Langmuir monolayers are also used as precursors for LB films on solid substrates [24, 25] and used as templates for bio-mimetic growth, i.e. to grow specially oriented crystals from supersaturated aqueous salts below the Langmuir monolayer [26, 27]. The most advantage in working with Langmuir monolayers is that the structures and properties can be modified easily by changing different physical and chemical parameters like surface pressure [16], temperature [6, 16], subphase pH [19], dissolved metal ions and ion concentration [28], etc. It has also

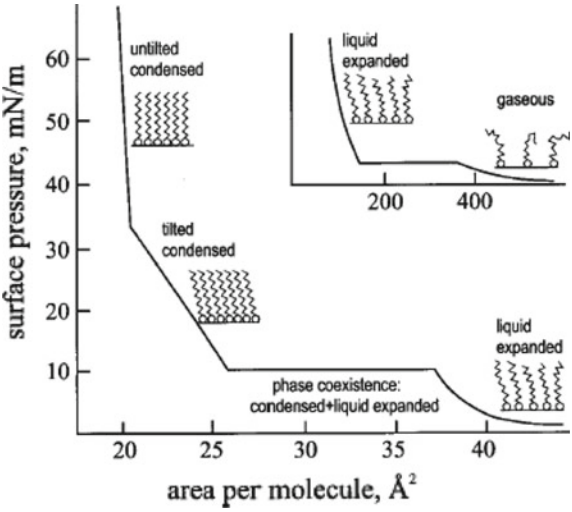

Fig. 1 Schematic of the surface pressure versus area per molecule isotherm. Phase transitions are shown by the flat part and kink in the isotherm. (Reproduced from Kaganer et al. [6])

been explored that in the presence of inorganic materials inside aqueous subphase, the structural and physical aspects of Langmuir monolayers become rich. For example, long-chain fatty acids Langmuir monolayers in the presence of divalent metal ions show rich two-dimensional structures and patterns both for the organic and inorganic parts at the air–water interface. Super lattice peaks are observed in the grazing incidence diffraction pattern of the fatty acid monolayer in the presence of Cd^{2+} ions in the water subphase [29, 30]. Super lattice peaks are also observed with the peaks of fatty acid monolayer in the presence of Mg^{2+}, Mn^{2+} and Pb^{2+} ions in the aqueous subphase [31, 32]. However, on the other hand, the presence of certain metal ions like Co^{2+}, Cu^{2+} and Ba^{2+} inside water subphase induces a high-pressure structural phase of the monolayer at lower surface pressure without forming a super lattice structure by the metal ions [32]. For certain experimental conditions, new type of chemical bond is also formed between the hydrophilic part and metal ions [33]. In presence of metal ions inside the aqueous subphase, the monolayer becomes much more ordered [34], changes their viscoelastic properties [35] and in addition helps the monolayer to transfer easily on some solid substrate [36], i.e. for monolayer and multilayer deposition.

Amphiphiles with more than one tail per headgroup, such as preformed fatty acid salts of trivalent metals, for example ferric stearate, produce a significant change in the structural and physical property compared with the conventional stearic acid monolayer with and without ferric ions in the water subphase. A 'Y and inverted Y' type of structure, as shown in Fig. 2, is assumed to form on the water surface by such preformed fatty acid salt molecules that matchs with the π–A isotherm and X-ray reflectivity measurements [37]. Instead of forming a monolayer where all three stearate tails of the ferric stearate molecules are towards air (i.e. asymmetric configuration with respect to headgroups), a monomolecular layer (conventional bilayer) is formed where tails are on both sides of the headgroups (i.e. symmetric

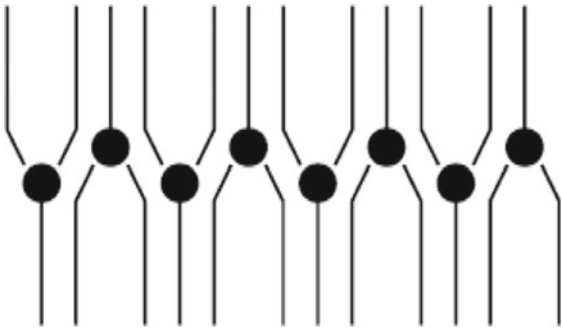

Fig. 2 'Y and inverted Y' configuration formed by the preformed ferric stearate film on the water surface

configuration with respect to headgroups). Different lipids and esters having two or three tails can also form a monolayer on the water surface. Lipids like DMPE, DPPE, DSPC [38–41] and different esters [42, 43] form monolayer film on the water surface and their thermodynamic behaviours and the molecular packing has been explored. Like fatty acids and lipids, long-chain alkanes [44], proteins [45–47] and organo-coated nanoparticles [48–51] also form organic films on the water surface.

3 Organic Multilayers

Organic multilayers formed on water or solid substrates have total film thickness in a multiple of the monolayer thickness. There are different processes by which monolayers and multilayers can be formed on solid substrates from monolayers. Multilayers can also be formed on the water surface from monolayers.

3.1 Multilayers Formed by Vertical Deposition

In this deposition process, a multilayer is formed by passing a solid substrate through the monolayer-covered water surface alternately upwards and downwards. Organic monolayer and multilayer films deposited by this up- and down-strokes of the substrate are called Langmuir–Blodgett (LB) films [13]. These LB films can be useful to explore physical and chemical phenomena in confined geometries and in preparing of model biological membranes [6, 7, 13, 34, 52–54]. LB films are considered as an ideal system to study the two- to three-dimensional melting transition [55], two-dimensional magnetic property [56, 57], etc. In addition, LB films are also used as a template for the formation of the nanostructure materials [58]. Different quantum dots like CdS, PbS and ZnS [59] or CdS nanosheets [60] are also produced inside the organic matrix of LB films.

In LB deposition, a layer is deposited during each up- and down-stroke. In the up-stroke, polar headgroups of the deposited molecules are oriented towards the substrate surface, while in the down-stroke, hydrophobic tails of the deposited molecules are oriented towards the substrate. As a result, the headgroups are adhered to the headgroups of the previous layer during the up-stroke and the tails are attached to the tails of the previous layer during the down-stroke, which is usually obvious for the deposition of amphiphilic molecules. There are several outcomes on the molecular orientation depending upon the dipping direction. First, a bi-layer is the basic unit of an ideal LB multilayer. Second, the first layer can be deposited only in the up-stroke of the hydrophilic substrate and in the down-stroke of the hydrophobic substrate. Third, hydrophobic tails and hydrophilic headgroups will be the outermost layer in air and water, respectively.

These three consequences can be regarded as the postulates of the molecular structure of LB films [34]. Structures and structural modifications inside LB films depend upon the energetics of amphiphilic interactions. For example, although generally monolayer is transferred during both up- and down-strokes (Y-type deposition) of the substrate, but under certain conditions depending upon the hydrocarbon tail length of the molecules and pH of the subphase water and dissolved metal ions, film deposition is possible only during the down-stroke (X-type deposition) or the up-stroke (Z-type deposition). These three types of depositions are shown in Fig. 3, 4 and 5, respectively. However, for the multilayer films formed using X-type or Z-type deposition methods, the basic structural unit is monolayer instead of a bi-layer as formed during Y-type deposition. Although, X-ray diffraction study shows that multilayers made using X-type deposition may have the usual bi-layer unit structure [61]. This implies that the molecular rearrangement takes place during or after the transfer process to attain a more energetically favourable configuration. Using reflectivity (X-ray and neutron) and AFM analysis, it has been observed that apart from the first layer, molecules reorient themselves from asymmetric to a symmetric configuration in particular for amphiphiles having more than one tail per headgroup [62].

In LB films, much more ordered structure is formed in the out-of-plane direction, i.e. nearly perfect periodic structure is maintained along the surface normal (z-direction) [57, 63, 64]. However, most LB films such as LB films of fatty acid salts always have some inherent defects, which are known as ‘pinhole-type defects’ [34, 65]. Pinhole-type defects make the film less ordered in the plane of headgroups (x–y plane), and domains of at most micron length scales can be achieved. The molecular packing inside the crystalline domains of the LB films depends upon the hydrocarbon chain length, cations attached with the headgroups and substrate nature [34, 66]. Using X-ray scattering and atomic force microscopy, the surface morphology, in-plane correlations and growth mechanisms are investigated. Both liquid-like and self-affine correlations are evidenced from the interfaces of LB films [67–69]. The growth mechanism was explained using linear stochastic theory considering one-dimensional deposition followed by two-dimensional desorption [68]. The competitive effects between the surface roughening from pinholes and the smoothening due to the surface tension dictate the interface morphology in LB films [69]. Different efforts

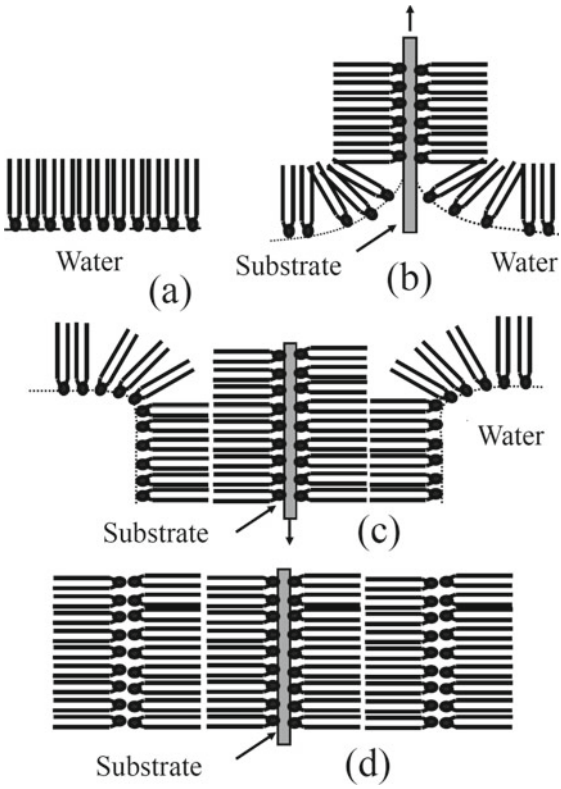

Fig. 3 Y-type Langmuir–Blodgett film deposition

are made for obtaining defects-free better LB films, however, the most successful results are obtained by Takamoto et al. [70]. It has been observed that although in LB films, the basic structural unit is bi-layer but for fatty acid salts of multivalent ions, i.e. for amphiphilic molecules having more than one tail per headgroup, two different molecular configurations exist that can form bi-layer unit. One is *asymmetric configuration* where two molecules are attached by the head–head or tail–tail attachment where all tails stay on the same side of the metal-bearing headgroups. The other one is *symmetric configuration* where the attachment of two molecules is such that tails remain in both sides of the metal-bearing headgroups and the attachment takes place through the tail–tail interaction. It has been observed by X-ray scattering experiments [71, 72] that apart from the first layer, the symmetric molecular configuration exists in all the layers, i.e. tails are on both sides of the headgroups [73]. Using X-ray and neutron scattering, the symmetric bi-layer configuration of deposited fatty acid salts has also been observed [62]. Thus, except the first layer where molecules are in asymmetric configurations, all other layers are formed by the molecules which are in symmetric configurations.

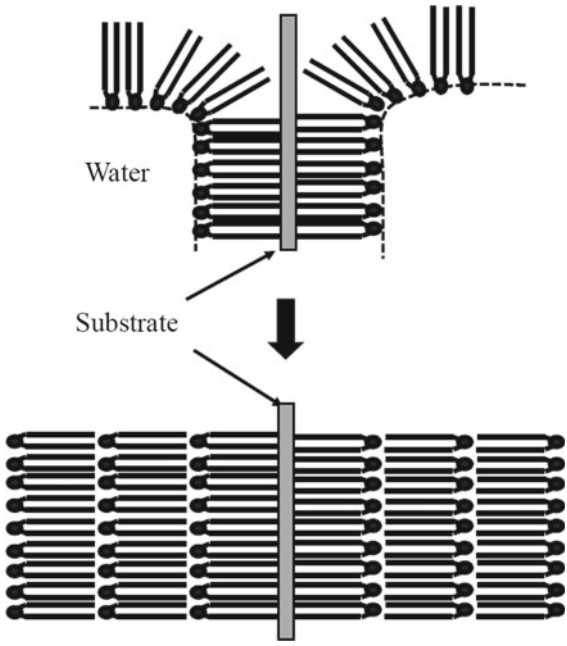

Fig. 4 X-type deposition

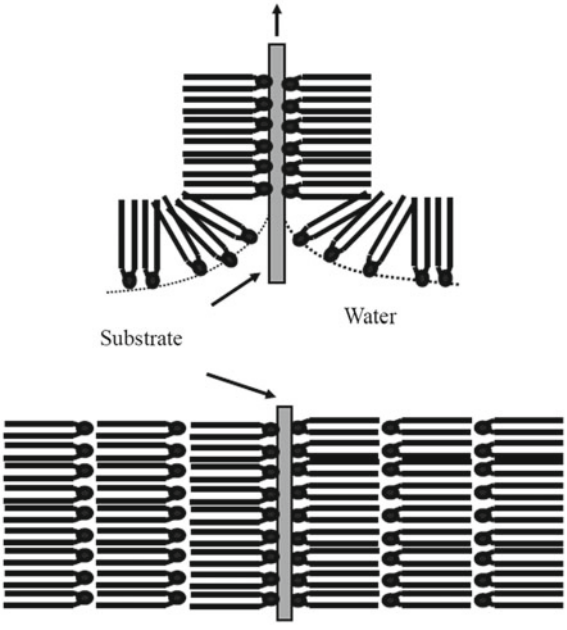

Fig. 5 Z-type deposition

3.2 Multilayer Formed by Horizontal Deposition

For the very viscous and rigid compact monolayers, conventional LB deposition process does not work as the transfer process becomes very weak. LB deposition also not works if it is required to deposit at a lower surface pressure of the monolayer. To overcome these problems, alternative deposition processes are considered. Actually, three different horizontal deposition techniques are developed which provide considerable good results. In the first deposition scheme employed by I. Langmuir and V. J. Schaefer (called as LS—method) [74], always hydrophobic substrate is required and the monolayer film is 'lifted by the tails' from the top, as shown schematically in Fig. 6.

In this LS method, the hydrophobic substrate is kept parallel to the monolayer surface and monolayer transfer takes place when the substrate touches the monolayer from the top. However, during this deposition process, frequent overturning of constituent molecules has also been reported [75]. However, for both LB and LS deposition techniques, the local molecular organization, fraction of various phases, size of domains, etc. can change during the transfer process.

The second horizontal deposition technique is the inverse Langmuir–Schaefer (ILS) method [76] where only the hydrophilic substrate is required and the film is picked up onto the hydrophilic substrate by keeping it below the film inside the water and draining out the water at the desired rate. The schematic of the trough design is shown in Fig. 7. Attachment of optical microscopy with this kind of trough helps to examine the surface morphology during transfer. This method makes it possible to transfer rigid films on a solid surface. In this method, a special kind of trough is required with an arrangement for highly controlled removal of water.

The third horizontal deposition technique was started by Kato et al. [77]. In this technique also, the hydrophilic solid substrate was used and that substrate was kept almost horizontal beneath the water surface before the monolayer was spread. The

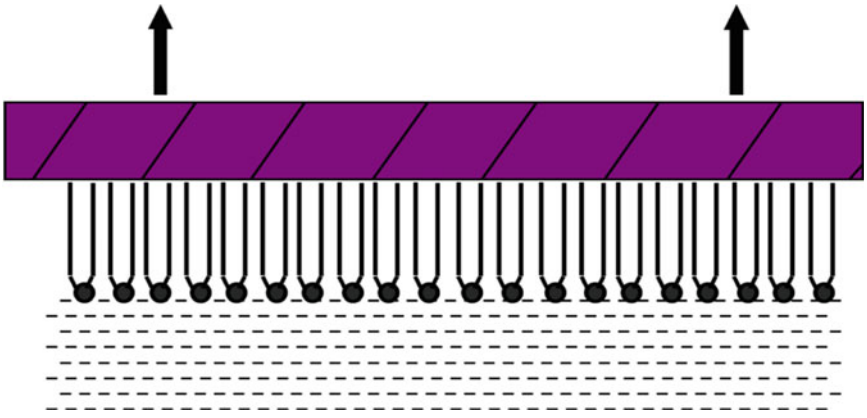

Fig. 6 Horizontal lifting (Langmuir–Schaefer) technique for depositing floating monolayers

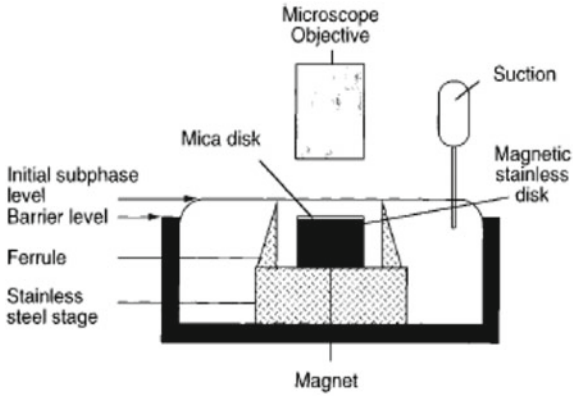

Fig. 7 Schematic of the inverse Langmuir–Schaefer (ILS) deposition system. (Reproduced from Lee et al. [76])

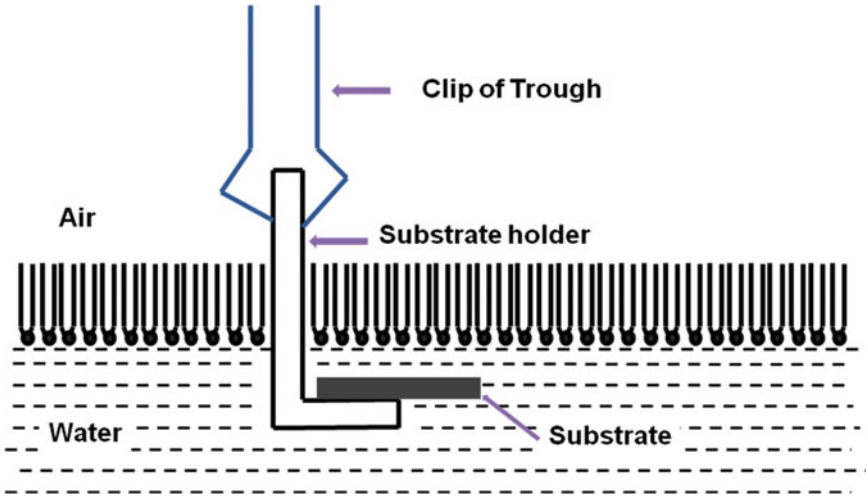

Fig. 8 Schematic diagram of the film deposition technique by MILS method where the substrate is kept below the monolayer

substrate was then raised up slowly and horizontally when the monolayer achieves desired conditions. Transmission electron microscopy (TEM) and AFM are used to reveal the three-dimensional structure of the deposited films from which the nucleation and growth mechanism of fatty acid Langmuir monolayers have been proposed [78, 79].

The fourth technique is the modified inverted Langmuir–Schaefer (MILS) method used by Kundu et al. [80, 81] and is nearly similar to the third technique [77]. This is a very simple method and can be employed easily with any LB trough. The MILS method is schematically shown in Fig. 8. During deposition by MILS method, at first, the water surface is cleaned properly and then an L-shaped Teflon substrate holder is immersed into the water so that the hydrophilic substrate is kept parallel to

and nearly 10–15 mm below the air–water interface. Then, the monolayer-forming molecules are spread on the water surface and the monolayer is compressed at the desired surface pressure. Finally, the substrate holder is taken out from water to air with the desired speed. In MILS method, like ILS method, deposition is possible from very low pressure to very high (collapse) pressure of the monolayer which could not be possible using the LB technique.

Structure and morphology of all the monolayer and multilayer films deposited by all types of horizontal deposition techniques are analysed by X-ray and neutron scattering, AFM, or FTIR spectroscopy just like the characterization of LB films. Here, it is important to mention that among all the horizontal deposition techniques, multilayers of desired thickness are formed only by the Langmuir–Schaefer method. In the other horizontal deposition techniques, monolayers or multilayers that are formed on the water surface are transferred onto the solid substrate but the formation of multilayered films of desired thickness is not possible.

3.3 Multilayer Formation on Water and Deposition on Solid Surface

Multilayer is formed on the water surface after monolayer collapse. In a Langmuir monolayer, the amphiphilic molecules are in a metastable state [13], so a transition from the two-dimensional (2D) monolayer to a three-dimensional (3D) multilayer can occur when the surface pressure reaches a particular value called the *collapse pressure* (π_c) [5] and the 3D structures are formed perpendicular to the water surface. However, in general, the π_c is dependent on the monolayer compression rate, showing the essential metastable nature of Langmuir monolayers. Collapse can occur by showing two different signatures in the π–A isotherm. For the first one, called as 'constant pressure collapse', the π is kept constant (a plateau is observed in the isotherm) after π_c and for the second, called as 'constant area collapse', the surface pressure drops suddenly (a strong spike is observed in the isotherm) after π_c. Structural and morphological information of all these collapsed states is obtained by different microscopic, spectroscopic and scattering techniques to understand the collapse mechanism and kinetics. Theoretical approaches have also been employed to explain the structure, morphology and kinetics of these three-dimensional states formed from the monolayer [82].

There are mainly two ways by which three-dimensional states are investigated. In the first one, monolayer and its collapsed states are investigated on the water surface by microscopy, spectroscopy or by scattering techniques (X-ray and neutron). In the second, multilayer films formed after the collapse are transformed on a solid substrate by vertical and horizontal deposition techniques and then analysed by AFM, FTIR, X-ray and neutron scattering, etc. The different mechanisms of morphological 2D–3D transformation of insoluble monolayers of long-chain alkanoic acids, esters and salt derivatives are studied directly on the water surface by using BAM [83]. By phase

contrast microscopy, the collapse of fatty acid monolayer is examined [84] where a transition from constant area to constant pressure collapse is observed by changing the pH of the water subphase [85]. Different collapse patterns are also observed for such films by changing pH and metal ion concentration [86]. All these optical tools help to observe the collapse pattern in 2D, i.e. no information is observed in the out-of-plane direction.

X-ray and neutron specular scattering gives information about the out-of-plane structures of the collapsed films on the water surface [87]. Monolayer to tri-layer transformation occurs in constant pressure collapse of 10,12 pentacosanoic acid (PCA) as indicated by X-ray scattering [87]. Also collapsed films of 10,12 pentacosanoic acid (PCA) are transferred on solid substrate and information is obtained [20, 87] by AFM. Structural and morphological change due to 3-D transformation of the fatty acid monolayer is also analysed by AFM [79] and TEM [78]. Collapsed structure and hence the collapse mechanism of 2-hydroxi-tetracosanoic acid (2-OH TCA) were proposed after obtaining the electron micrographs of the collapsed films [88]. Among different proposed collapse mechanisms, in 'Ries' mechanism [88] for monolayer collapse, the collapse starts with buckling in the monolayer that grows to large amplitude with compression, fold over and then breaks into a bi-layer on top of the monolayer. Whereas, in 'folding and sliding' [87, 89] mechanism, the collapse happens by folding the monolayer at first and then sliding of that folded monolayer over the rest of the monolayer. The above two mechanisms by which multilayers are formed due to collapse have been shown schematically in Fig. 9. For certain molecular layers, monolayer can also be collapsed by buckling that has been observed by using optical fluorescence microscopy where buckled regions can coexist with the flat monolayer and then that can be reversibly incorporated again into the monolayer after the expansion of the monolayer [90]. Collapse by reversible folding [91] of the 2-hydroxi-tetracosanoic acid (2-OH TCA) monolayer has also

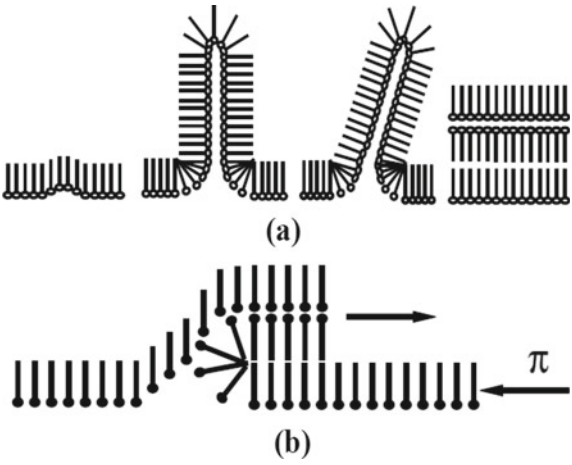

Fig. 9 Multilayer formation on the water surface. **a** Ries mechanism, **b** Folding and sliding mechanism. (Reproduced from Gourier et al. [87])

been observed by light scattering microscopy. Besides this, the formation of spontaneous assembly of lignoceric acid molecules at air–water interface and nearly at zero surface pressure has been observed indicating a strong interaction between long hydrocarbon tails of the molecules [92]. Also in the presence of divalent cations, this acid monolayer exhibits many isolated domains of collapsed regions at zero pressure [92], which indicates more strong attractive forces between the molecules. The delicate balance between head–head and tail–tail interactions may cause a structural instability in the monolayer and hence the different collapse transitions occur [92]. Both in-plane and out-of-plane structures after monolayer collapses are studied through X-ray reflectivity (XRR), neutron reflectivity (NR), GIXRD, AFM, etc. on both water and solid surfaces [80, 81, 93–95]. In general, monolayer collapse occurs at higher surface pressure ($\pi_c \geq 50$ mN/m) through two different ways [5, 13, 80, 81, 95, 96] as stated before, i.e. 'constant area collapse' where π suddenly drops just after π_c and 'constant pressure collapse' where π remains nearly constant after π_c. Different structures and morphologies are identified from the collapsed fatty acid monolayers after deposition on solid substrates in the presence of different divalent metal ions inside water. From those structural and morphological information, collapse mechanism and related growth modes are proposed.

4 Different Techniques for Thin-Film Characterization

4.1 X-Ray and Neutron Scattering

For X-rays and neutrons, the refractive index (n) of any materials is slightly less than 1 [97–99], i.e. n can be defined as

$$n = 1 - \delta - i\beta \tag{4}$$

where δ and β are related with the scattering length density and absorption of the materials. For X-rays, $\delta = \frac{\lambda^2}{2\pi} r_e \rho_e$ and $\beta = \frac{\mu\lambda}{4\pi}$, where λ is the X-ray wave length, r_e is the electron scattering length, ρ_e is the average electron density and μ is the linear absorption coefficient of the materials, whereas for neutrons, those values are related with the neutron wavelength, scattering length (b_i), nuclear number density (N_i) and neutron absorption cross section (σ_i) of the materials. Hence, there exists a *critical angle* of incidence, θ_c, below which X-rays and neutrons will be reflected totally and only an *evanescent wave* will exist within a few Angstroms of the surface. The scattering depth of the evanescent wave in the medium can be varied by changing the incident angle and it depends upon the imaginary component of the wave vector in the medium. The low scattering cross section of the X-rays helps to penetrate matter to a much greater extent than electrons or ion beams and hence can provide detailed structural information about the buried interfaces of a material. However, for neutrons, different isotopes of the same element give different scattering cross sections and

are therefore mostly used for getting information from the biological samples. For any material at grazing angle of incidence, the X-ray and neutron scattering becomes less sensitive to individual atoms and therefore continuous electron density profile $\rho_e(\vec{r})$ or nuclear scattering length density profile $b_i N_i(\vec{r})$ are used. Thus, at grazing incidence, the scattering becomes surface-sensitive and can be used to probe the structure of surfaces and interfaces. Both X-ray and neutron scattering techniques provide nearly the same information from the surfaces and interfaces of the thin films but each technique has specific advantages and disadvantages. Availability of intense rotating anode sources, synchrotron sources and advanced design of beam optics using Göbel mirrors helps to increase the signal to noise ratio in the feeble scattering from interfaces, and thus to obtain the structural and morphological information of surfaces and interfaces. Intense monochromatic neutrons beam are also obtained from the different nuclear reactors which are also used to explore the structures of the thin films [100, 101]. Mainly four different measurement techniques exist by which structural information is obtained. These techniques are X-ray or neutron specular reflectivity, diffuse or off-specular scattering, grazing incidence diffraction and grazing incidence small-angle X-ray and neutron scattering. The different types of information regarding surface scattering are shown schematically in Fig. 10 for different $\vec{q}$ ranges.

In specular reflectivity experiment [53, 102], where the incident and reflected rays are in the plane normal to the surface and the incident angle is same as the scattered angle, the scattering vector $\vec{q}$ is perpendicular to the substrate surface which provides information about the average electron or nuclear number density as a function of the depth (z). In the GID technique, on the other hand, large $\vec{q}_{||}$ with high in-plane angle (ψ) is achieved and as a result, atomic locations are obtained in the ordered sample [32]. For having a better understanding of correlation in an interface and between interfaces, off-specular diffuse scattering technique [53, 102] is used which

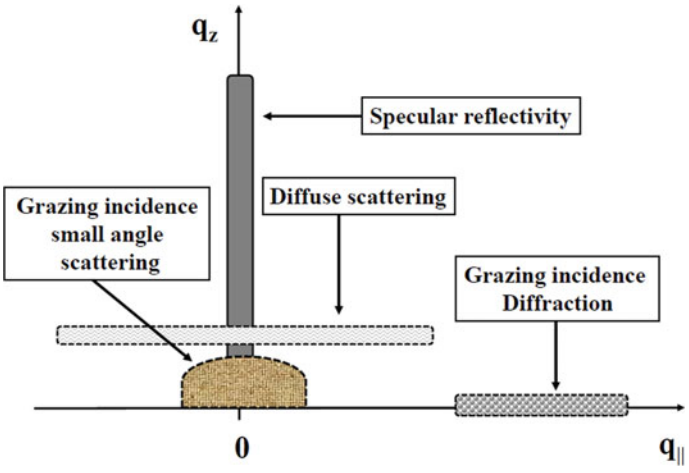

Fig. 10 Schematic of the different scan-regions in reciprocal space

has the scattering plane identical to the specular plane but the incident and scattered angles are not equal. It is sensitive to in-plane morphology and for that generally diffuse scattering data are collected to extract morphological information through height–height correlation in a multilayer. The geometry in the grazing incidence small-angle scattering is basically the same as grazing incidence diffraction but for small scattered angles, both in the in-plane and out-of-plane directions [103]. The theoretical details of X-ray and neutron scattering are explained elsewhere [97–99].

An ideal three-dimensional crystal can be defined by the lattice vectors $\vec{R}_n = n_1\vec{a}_1 + n_2\vec{a}_2 + n_3\vec{a}_3$, where ($\vec{a}_1$, $\vec{a}_2$, $\vec{a}_3$) are the basis vectors of the lattice and (n_1, n_2, n_3) are integers. It is well known from the diffraction theory [104–106] that the diffraction pattern from an ideal three-dimensional crystal consists of discrete points lying on a reciprocal lattice, where the intensity peaks at each of these points and is zero elsewhere. The intensity scattered by a crystal having N_1, N_2 and N_3 unit cells along the three crystal axes takes the form

$$I_{hkl} = AF_{hkl}^2 N_1^2 N_2^2 N_3^2 \tag{5}$$

where $F(\vec{q})$ is called the structure factor. The structure factor can be written as

$$F(\vec{q}) = \sum_{j=1}^{N_c} f_j(\vec{q}) \exp(i\vec{q} \cdot \vec{r}_j) \tag{6}$$

where the sum is over all the atoms within one unit cell and $f_j(\vec{q})$ is the atomic form factor. Like a three-dimensional crystal, an ideal two-dimensional crystal can be defined by the lattice vectors $\vec{R}_n = n_1\vec{a}_1 + n_2\vec{a}_2 + \hat{z}$, where there is no lattice periodicity in the third direction. In a three-dimensional reciprocal space, it gives a two-dimensional lattice of rods, which are the chief characteristic of diffraction from surfaces. But there is a deviation from this ideal picture as solid surfaces are generally a combination of a two-dimensional layer plus the bulk. The modified rods generated from a convolution of the two-dimensional rods and the distribution of intensity from the bulk is called crystal truncation rods (CTR) [107]. Intensity distribution along the rod for ideal and truncated crystals can be written as

$$I_{2D} = AF^2 N_1^2 N_2^2 \tag{7}$$

$$I_{CTR} = AF^2 N_1^2 N_2^2 \frac{1}{2\sin^2(\vec{q} \cdot \vec{a}_3/2)} \tag{8}$$

For quasi-two-dimensional organic monolayers like Langmuir monolayer, the scattered intensity follows the ideal distribution given by Eq. (8). However, the lattice is made up of extended molecules with complicated electron distributions of their own and hence, in reciprocal space, the scattering pattern is obtained by the product of structure factor and form factor where the structure factor is the translational order of the molecular centres in the monolayer plane and the form factor is the

contribution of an individual molecule. For 2D lattice, the structure factor is a set of discontinuous δ-function (called as 'Bragg rods') perpendicular to the plane of the monolayer. The form factor of a long rod-like molecule (like long-chain fatty acid molecule) is maximum in a plane perpendicular to its long axis, which is called as 'reciprocal disc'. The intersections between first-order Bragg rods and reciprocal disc provide six diffraction peaks or maxima. For the untilted molecules, the reciprocal disc and hence all the diffraction peaks are positioned in the monolayer plane. In a plane having sixfold symmetry, the all six equal length first-order momentum transfer vectors $\vec{q}$ overlap completely in powder averaging. However, if the lattice is distorted from hexagonal symmetry, then the degeneracy is lifted. Thus, when the unit cell is stretched or shrunk in the nearest neighbour direction of the molecule, two distinct first-order momentum transfer vectors generate two peaks (one degenerate, $\vec{q}_{\mathrm{d}}$ and the other is non-degenerate, $\vec{q}_{\mathrm{n}}$) in the reciprocal space. Due to the molecular tilting of the long-chain molecules, such degeneracy may also be lifted. Depending upon both tilt magnitude and tilt direction, the peaks move out of the monolayer plane. For the nearest neighbour (NN) tilt, two peaks are observed, one is non-degenerate in-plane peak and the other one is degenerate out-of-plane peak. When the molecular tilt is in the next nearest neighbour (NNN) direction, all $\vec{q}$ move out of the plane. If the tilt direction is intermediate between NN and NNN, or if the unit cell distortion is asymmetrical or chiral, then a total three distinct first-order peaks are found [6]. All the diffraction peaks can be assigned in crystallographic notation considering either a hexagonal or a centred rectangular unit cell. After assigning the three first-order peaks, the shape of the unit cell in reciprocal space and hence the real-space lattice is completely determined.

X-ray and neutron specular reflectivity yields information about interfacial roughness, film thickness and density of different sublayers of a thin film [53, 97–99]. In Parratt's formalism, the reflectivity $R(q_z)$ obtained from a thin film of thickness d over a substrate [108] can be written as $R(q_z) = rr^*$, where

$$r_0 = \frac{r_{1,2} + r_{2,3}}{1 + r_{1,2} r_{2,3}}, \tag{9}$$

with r_{12} and r_{23} are the reflectance for the vacuum–film and film–substrate interfaces, respectively. For n such thin stratified layers of thickness d, one arrives at a recursive formula in terms of Fresnel reflectance given by

$$r^F_{n-1,n} = \frac{r_{n,n+1} + F_{n-1,n}}{1 + r_{n,n+1} F_{n-1,n}} \exp(-i q_{n-1,n} d_{n-1}), \tag{10}$$

where

$$F_{n-1,n} = \frac{q_{n-1,z} - q_{n,z}}{q_{n-1,z} + q_{n,z}}. \tag{11}$$

For the nth stratified layer, the wave vector can be defined as $q_{n,z} = (q_z^2 - q_{n,c}^2)^{1/2}$. Including the roughness σ_n of the nth stratified layer, the Fresnel reflectance for the interface between nth and $(n-1)$th stratified layer can finally be written as

$$r_{n-1,n} = r_{n-1,n}^F \exp(-0.5 q_{n-1,z} q_{n,z} \sigma_n^2). \tag{12}$$

In general, the electron density variation inside a sample of thin film is determined by assuming a model and then comparing the simulated profile with the experimental XRR data. The electron density profile (EDP), i.e. electron density (ρ) variation along the substrate normal (z-direction) is extracted after fitting the experimental data. For the data fitting, each film is divided into a number of sublayers having different thicknesses and electron densities, and also including roughness at each interface.

Using X-ray and neutron reflectivity, not only the out-of-plane structure but also the molecular reorganization after deposition is explained [62]. The self-affine in-plane interfacial correlation functions for LB multilayers have been observed by Gibaud et al. using X-ray scattering [67]. However, the logarithmic in-plane correlation was also obtained in cadmium arachidate LB films, which is the characteristic of capillary waves on liquid surfaces [60, 109]. Both self-affine and logarithmic in-plane interfacial correlations are observed by X-ray diffuse scattering and AFM studies [68]. Li et al. [69], using X-ray diffuse scattering and AFM, obtained the logarithmic interfacial correlation function of LB films of different thicknesses. Packing structures of Langmuir monolayers and LB multilayers are measured precisely by the GID technique. A different crystalline packing is obtained for Langmuir monolayers on water depending upon the temperature and pressure [6]. Nearly hexagonal packing is observed for LB monolayer, whereas for LB multilayer, well-ordered orthorhombic packing is identified [110]. Shih et al. [111] used the GID technique to determine the structures of heneicosanoic acid monolayer deposited from the L_2, S and LS phases of the monolayer on a silicon oxide substrate. However, from all the three deposited phases, only an untilted hexagonal packing, i.e. LS phase is observed. Distorted hexagonal packing is observed for LB monolayer by Dupres et al. [112]. Dupres et al. [113] have also obtained the depth-dependent in-plane structural variation in thin LB films by using the GID technique. A centred rectangular unit cell for $PbSt_2$ multilayer has been identified by GID [114, 115], while Malik et al. [71] found that for LB multilayer, each layer was shifted laterally by 1/4 of a lattice spacing relative to the lower layer. Using GID, Peng et al. [116] observed the monoclinic structure of cadmium atoms in fatty acid salts of cadmium and the chains also have the monoclinic structure without the centred symmetry. A 5×1 superstructure was also found to be present in the film [116].

4.2 Scanning Probe Microscopy

Scanning probe microscopy (SPM) is another very useful technique for obtaining different surface characteristics of various materials [34, 117]. Real-space surface

information obtained from the images achieved using this SPM technique actually support the reciprocal space information obtained from the scattering techniques. In this class of microscopic technique, commonly a sharp tip acting as an appropriate probe is scanned in a raster fashion over the surface of the material to be studied. There are different types of forces that exist between the tip and sample surface and accordingly, different techniques were also evolved under this SPM family. Among SPM family, atomic force microscopy (AFM) is used widely as it can provide information from any types of surfaces, i.e. useful for all metallic, non-metallic, hard and soft surfaces. On the other hand, scanning tunnelling microscopy (STM) is used only for the conducting surfaces as STM works through the tunnelling of electrons between the metallic tip and conducting surface. All SPM techniques can only probe the top surfaces of thin films and multilayers, whereas the X-ray scattering technique is sensitive to both top surfaces and interfaces. High-resolution AFM also gives the information about the packing structures of the constituent molecules. Garnaes et al. [118] and Schwartz et al. [119, 120] used AFM to measure the in-plane lattice parameters, which obtained as centred rectangular of dimensions 4.8×7.5 Å^2 and is consistent with the results obtained from the scattering experiments. They also provided the first direct evidence that the unit cell contains two non-identical molecules consistent with herringbone packing [34]. The molecular resolution images of LB films of CdA_2, MnA_2 and PbA_2 were obtained by Zasadzinski et al. [36]. The lattice symmetry of these films was also obtained from the Fourier transform of the images and the alternating bright and dim spots confirmed a rectangular lattice. The real-space lattice structure corresponded to a two-molecule unit cell with a herringbone packing. The lattice parameters measured by AFM were very similar to that observed for thick films of $PbSt_2$ [114] and thin films of CdA_2 [110] as measured by X-ray diffraction [36]. More stable and defect-free structures of LB films were observed by depositing at pH > 8.5. Only one type of crystalline grain (herringbone structure) was observed when the LB was deposited at pH $\approx$ 7, but numerous small crystallites possessing herringbone, hexagonal and pseudo-herringbone packing were observed when LB deposition was performed at pH $\approx$ 8.8 [70].

4.3 Fourier Transform Infrared (FTIR) Spectroscopy

FTIR spectroscopy [121, 122] probes the vibrational frequencies of a molecule. A molecular bond having a permanent dipole moment interacts with the infrared radiation and gives absorption peaks corresponding to its normal mode of vibrations. From these peak positions, the information about the packing structures of the molecules is obtained [123, 124]. FTIR spectroscopy has been extensively used to determine the molecular packing in LB films [125–127] and also in Langmuir monolayers [54, 128, 129]. The information about the new kind of bond formations in the Langmuir monolayers is also obtained by FTIR spectroscopy [33, 95, 130, 131].

In addition to the above-mentioned characterization techniques, other techniques like Brewster angle microscopy (BAM) [132–134], fluorescence microscopy

(FM) [135], sum frequency generation spectroscopy [136–138], Raman spectroscopy [139–142], etc. are also used to characterize the Langmuir monolayers and Langmuir–Blodgett films.

5 Conclusions

Amphiphilic molecules having hydrophilic polar or ionic headgroups and hydrophobic hydrocarbon tails can show interesting self-assembled ordered structures such as monolayers, bilayers as well as lameller or multilayer structures. It has been observed, in particular, that a planar fatty acid Langmuir monolayer, which shows crystalline phases at high pressure, shows 'folding' behaviour when it collapses at nearly constant pressure in the presence of certain metal ions in the aqueous subphase. Depending upon its elastic property that depends upon the physicochemical conditions, the monolayer starts to fold and the trilayer structure is formed due to the folding and sliding of the molecules. Multilayers can be formed spontaneously through Ries mechanism on the water surface when the monolayer is compressed after π_c. These multilayers, though structurally identical with the LB multilayers, differ in the mode of growth from the LB multilayer where the periodicity of the layers is achieved by dipping a substrate through the monolayer-covered water surface repeatedly. It is known that in the absence of multivalent metals in the headgroups, the formation of LB multilayers is difficult. The presence of multivalent metals in the headgroups modifies the intrinsic elastic properties of the amphiphilic monolayer and accordingly, the structures, growth and collapse behaviours modify. Multilayers with well-defined one-dimensional periodicity can form by both compression of the Langmuir monolayer beyond critical surface pressures or by repeated dipping through the monolayer. Different X-ray and neutron scattering techniques, and in addition specific microscopic and spectroscopic methods, help to explore the structures and properties of such organic thin films.

References

1. A.I. Kitaigorodsky, *Molecular Crystals and Molecules* (Academic Press, New York, 1973)
2. H. Ibach, H. Lüth, *Solid-State Physics: An Introduction to Theory and Experiment* (Narosa, New Delhi (Reprint), 1992)
3. M.A. Herman, H. Sitter, *Molecular Beam Epitaxy: Fundamentals and Current Status*, 2nd edn. (Springer Series in Materials Science, 1997)
4. R.F. Bunshah (ed.), *Handbook of Deposition Technologies for Films and Coatings Science, Technology, and Applications* (Noyes Publications, New Jersey, 1994)
5. G.L. Gaines, *Insoluble Monolayers at Liquid-Gas Interfaces* (Interscience, New York, 1966)
6. V.M. Kaganer, H. Möhwald, P. Dutta, Rev. Mod. Phys. **71**, 779 (1999)
7. A. Ulman, *Introduction to Ultrathin Organic Films* (Academic Press, New York, 1991)
8. S.R. Forrest, Chem. Rev. **97**, 1793 (1997)
9. E. Umbach, M. Sokolowski, R. Fink, Appl. Phys. A **63**, 565 (1996)

10. F.F. So, S.R. Forrest, Y.Q. Shi, W.H. Steier, Appl. Phys. Lett. **56**, 674 (1990)
11. F. Schreiber, Prog. Surf. Sci. **65**, 151 (2000)
12. I. Langmuir, J. Am. Chem. Soc. **39**, 1848 (1917)
13. M.C. Petty, *Langmuir-Blodgett Films: An Introduction* (Cambridge University Press, New York, 1996)
14. W.D. Harkins, *Physical Chemistry of Surface Films* (Reinholds, New York, 1952)
15. M. Yazdanian, H. Hu, G. Zografi, Langmuir **6**, 1093 (1990)
16. S. Ställberg-Stenhagen, E. Stenhagen, Nature **156**, 239 (1945)
17. M. Shih, T. Bohanon, J. Mikrut, P. Zschack, P. Dutta, J. Chem Phys. **96**, 1556 (1992)
18. C. Böhm, F. Leveiller, D. Jacquemain, H. Möhwald, K. Kjaer, J. Als-Nielsen, I. Weissbuch, L. Leiserowitz, Langmuir **10**, 830 (1994)
19. A. Datta, J. Kmetko, A.G. Richter, C.-J. Yu, P. Dutta, Langmuir **16**, 1239 (2000)
20. C. Ybert, W. Lu, G. Möller, C.M. Knobler, J. Phys. Chem. B **106**, 2004 (2002)
21. Y.-L. Lee, K.-L. Liu, Langmuir **20**, 3180 (2004)
22. V.M. Kaganer, E.B. Loginov, Phys. Rev. Lett. **71**, 2599 (1993)
23. V.M. Kaganer, E.B. Loginov, Phys. Rev. E **51**, 2237 (1995)
24. K.B. Blodgett, J. Am. Chem. Soc. **57**, 1007 (1935)
25. K.B. Blodgett, I. Langmuir, Phys. Rev. **51**, 964 (1937)
26. S. Mann, D.D. Archibald, J.M. Didymus, T. Douglas, B.R. Heywood, F.C. Meldrum, N.J. Reeves, Science **261**, 1286 (1993)
27. J. Kmetko, C. Yu, G. Evmenenko, S. Kewalramani, P. Dutta, Phys. Rev. Lett. **89**, 186102 (2002)
28. A. Datta, J. Kmetko, C.-J. Yu, A.G. Richter, K.-S. Chung, J.-M. Bai, P. Dutta, J. Phys. Chem. B **104**, 5797 (2000)
29. F. Leveiller, D. Jacquemain, M. Lahav, L. Leiserowitz, M. Deutsch, K. Kjaer, J. Als-Nielsen, Science **252**, 1532 (1991)
30. F. Leveiller, C. Böhm, D. Jacquemain, M. Lahav, H. Möhwald, L. Leiserowitz, K. Kjaer, J. Als-Nielsen, Langmuir **10**, 819 (1994)
31. J. Kmetko, A. Datta, G. Evmenenko, M.K. Durbin, A.G. Richter, P. Dutta, Langmuir **17**, 4697 (2001)
32. J. Kmetko, A. Datta, G. Evmenenko, P. Dutta, J. Phys. Chem. B **105**, 10818 (2001)
33. Y. Ren, K.-I. Iimura, T. Kato, Langmuir **17**, 2688 (2001)
34. D.K. Schwartz, Surf. Sci. Rep. **27**, 241 (1997)
35. R. Ghaskadvi, S. Carr, M. Denim, J. Chem. Phys. **111**, 3675 (1999)
36. J. Zasadzinski, R. Viswanathan, L. Madsen, J. Garnaes, D.K. Schwartz, Science **263**, 1726 (1994)
37. A. Datta, M.K. Sanyal, A. Dhanabalan, S.S. Major, J. Phys. Chem. B **101**, 9280 (1997)
38. R.M. Kenn, K. Kjaer, H. Möhwald, Colloids Surf. A **117**, 171 (1996)
39. C. Böhm, C. H. Möhwald, L. Leiserowitz, J. Als-Nielsen, K. Kjaer. Biophys. J. **64**, 553 (1993)
40. G. Brezesinski, A. Dietrich, B. Struth, C. Böhm, W.G. Bouwman, K. Kjaer, H. Möhwald, Chem. Phys. Lipids **76**, 145 (1995)
41. S.A. Kane, Langmuir **18**, 9853 (2002)
42. M. Lundquist, Chem. Scr. **1**, 197 (1971)
43. W.J. Foster, M.C. Shih, P.S. Pershan, J. Chem. Phys. **105**, 3307 (1996)
44. S.P. Weinbach, I. Weissbuch, M. Lahav, L. Leiserowitz, K. Kjaer, W.G. Bouwman, J.A. Nielsen, Adv. Mater. **7**, 857 (1995)
45. A. Tronin, T. Dubrovsky, C. De Nitti, A. Gussoni, V. Erokhin, C. Nicolini, Thin Solid Films **238**, 127 (1994)
46. S. He, M. Huang, W. Ye, D. Chen, S. He, L. Ding, Y. Yao, L. Wan, J. Xu, S. Miao, J. Phys. Chem. B **118**, 12207 (2014)
47. B.K. Sah, S. Kundu, Colloids Surf., B **159**, 696 (2017)
48. M. Fukuto, R.K. Heilmann, P.S. Pershan, A. Badia, R.B. Lennox, J. Chem. Phys. **120**, 3446 (2004)

49. D.G. Schultz, X.-M. Lin, D. Li, J. Gebhardt, M. Meron, P.J. Viccaro, B. Lin, J. Phys. Chem. B **110**, 24522 (2006)
50. M.K. Bera, M.K. Sanyal, S. Pal, J. Daillant, A. Datta, G.U. Kulkarni, D. Luzet, O. Konovalov, Euro. Phys. Lett. **78**, 56003 (2007)
51. S. Kundu, Langmuir **27**, 3930 (2011)
52. G.G. Roberts, *Langmuir-Blodgett Films* (Plenum Press, New York, 1990)
53. J.K. Basu, M.K. Sanyal, Phys. Rep. **363**, 1 (2002)
54. J.B. Peng, G.T. Barnes, I.R. Gentle, Adv. Colloid Interface Sc. **91**, 163 (2001)
55. M.K. Mukhopadhyay, M.K. Sanyal, A. Datta, M. Mukherjee, T. Geue, J. Grenzer, U. Pietsch, Phys. Rev. B **70**, 245408 (2004)
56. E. Hatta, T. Maekawa, K. Mukasa, Y. Shimoyama, Phys. Rev. B **60**, 14561 (1999)
57. M.K. Mukhopadhyay, M.K. Sanyal, M.D. Mukadam, S.M. Yusuf, J.K. Basu, Phys. Rev. B **68**, 174427 (2003)
58. P. Facci, A. Diaspro, R. Rolandi, Thin Solid Films **327**, 532 (1998)
59. A.G. Milekhin, L.L. Sveshnikova, S.M. Repinsky, A.K. Gutakovsky, M. Friedrich, D.R.T. Zahn, Thin Solid Films **422**, 200 (2002)
60. J.K. Basu, M.K. Sanyal, Phys. Rev. Lett. **79**, 4617 (1997)
61. R.C. Ehlert, J. Coll. Sci. **20**, 387 (1965)
62. M.K. Sanyal, M.K. Mukhopadhyay, M. Mukherjee, A. Datta, J.K. Basu, J. Penfold, Phys. Rev. B **65**, 033409 (2002)
63. M.V. Frieling, H. Bradaczek, Acta Cryst. A **46**, 227 (1990)
64. Y. Sasanuma, H. Nakahara, Thin Solid Films **261**, 280 (1995)
65. Th Geue, M. Schultz, U. Englisch, R. Stömmer, U. Pietsch, J. Chem. Phys. **110**, 8104 (1999)
66. D.K. Schwartz, R. Viswanathan, J.A. Zasadzinski, J. Am. Chem. Soc. **115**, 7374 (1993)
67. A. Gibaud, N. Cowlam, G. Vignaud, T. Richardson, Phys. Rev. Lett. **74**, 3205 (1995)
68. J.K. Basu, S. Hazra, M.K. Sanyal, Phys. Rev. Lett. **82**, 4675 (1999)
69. X.-H. Li, M. Li, Z.-H. Mai, Phys. Rev. B **69**, 235407 (2004)
70. D.Y. Takamoto, E. Aydil, J.A. Zasadzinski, A.T. Ivanova, D.K. Schwartz, T. Yang, P.S. Cremer, Science **293**, 1292 (2001)
71. A. Malik, M.K. Durbin, A.G. Richter, K.G. Hung, P. Dutta, Phys. Rev. B **52**, R11654 (1995)
72. U. Englisch, F. Peñacorda, I. Samoilenko, U. Pietsch, Phys. B **248**, 258 (1998)
73. A.I. Kitaigorodsky, *Organic Chemical Crystallography* (Consultants Bureau, New York, 1961)
74. I. Langmuir, V.J. Schaefer, J. Am. Chem. Soc. **60**, 1351 (1938)
75. T. Kato, Jpn. J. Appl. Phys. **27**, L2128 (1988)
76. K.Y.C. Lee, M.M. Lipp, D.Y. Takamoto, E. Ter-Ovanesyan, A. Zasadzinski, A.J. Waring, Langmuir **14**, 2567 (1998)
77. T. Kato, Jpn. J. Appl. Phys. **26**, L1377 (1987)
78. T. Kato, N. Matsumoto, M. Kawano, N. Suzuki, T. Araki, K. Iriyama, Thin Solid Films **242**, 223 (1994)
79. D. Vollhardt, T. Kato, M. Kawano, J. Phys. Chem. **100**, 4141 (1996)
80. S. Kundu, A. Datta, S. Hazra, Langmuir **21**, 5894 (2005)
81. S. Kundu, A. Datta, S. Hazra, Phys. Rev. E **73**, 051608 (2006)
82. D. Vollhardt, U. Retter, J. Phys. Chem. **95**, 3723 (1991)
83. A. Angelova, D. Vollhardt, R. Ionov, J. Phys. Chem. **100**, 10710 (1996)
84. E. Hatta, H. Hosoi, H. Akiyama, T. Ishii, K. Mukasa, Eur. Phys. J. B **2**, 347 (1998)
85. E. Hatta, J. Nagao, Phys. Rev. E **67**, 041604 (2003)
86. E. Hatta, T.M. Fischer, J. Phys. Chem. B **106**, 589 (2002)
87. C. Gourier, C.M. Knobler, J. Daillant, D. Chatenay, Langmuir **18**, 9434 (2002)
88. H.E. Ries Jr., Nature **281**, 287 (1979)
89. E.S. Nikomarov, Langmuir **6**, 410 (1990)
90. M.M. Lipp, K.Y.C. Lee, D.Y. Takamoto, J.A. Zasadzinski, A.J. Waring, Phys. Rev. Lett. **81**, 1650 (1998)

91. W. Lu, C.M. Knobler, R.F. Bruinsma, M. Twardos, M. Dennin, Phys. Rev. Lett. **89**, 146107 (2002)
92. E. Hatta, Langmuir **20**, 4059 (2004)
93. D. Vaknin, W. Bu, S.K. Satija, A. Travesset, Langmuir **23**, 1888 (2007)
94. W. Bu, D. Vaknin, Langmuir **24**, 441 (2008)
95. K. Das, B.K. Sah, S. Kundu, Phys. Rev. E **95**, 022804 (2017)
96. S. Kundu, D. Langevin, Colloids Surf. A **325**, 81 (2008)
97. Jens Als-Nielsen, Des McMorrow, *Elements of Modern X-ray Physics* (Wiley, UK, 2011)
98. J. Daillant, A. Gibaud, *X-Ray and Neutron Reflectivity: Principles and Applications* (Springer, Berlin, 1999)
99. M. Tolan, *X-Ray Scattering from Soft Matter Thin Films* (Springer, Berlin, 1999)
100. Y. Gerelli, L. Porcar, G. Fragneto, Langmuir **28**, 15922 (2012)
101. M. Belicka, Y. Gerelli, N. Kucerka, G. Fragneto, Soft Matter **11**, 6275 (2015)
102. M.K. Sanyal, Radiat. Phys. Chem. **51**, 487 (1998)
103. D.-M. Smilgies, A.T. Heitsch, B.A. Korgel, J. Phys. Chem. B **116**, 6017 (2012)
104. R.W. James, *The Optical Principles of the Diffraction on X-rays* (G. Bell and Sons, London, 1948)
105. B.E. Warren, *X-ray Diffraction* (Addison-Wesley, Massachusetts, 1969)
106. J.M. Cowley, *Diffraction Physics* (North Holland, Amsterdam, 1984)
107. I.K. Robinson, D.J. Tweet, Rep. Prog. Phys. **55**, 599 (1992)
108. L.G. Parratt, Phys. Rev. **95**, 359 (1954)
109. M.K. Sanyal, J.K. Basu, A. Datta, Phys. B **248**, 217 (1998)
110. P. Tippmann-Krayer, R.M. Kenn, H. Möhwald, Thin Solid Films **210–211**, 577 (1992)
111. M.C. Shih, J.B. Peng, H.G. Hung, P. Dutta, Langmuir **9**, 776 (1993)
112. V. Dupres, S. Cantin, F. Perrot, P. Fontaine, M. Goldmann, J. Chem. Phys. **116**, 3822 (2002)
113. V. Dupres, S. Cantin, F. Benhabib, F. Perrot, P. Fontaine, M. Goldmann, Phys. Rev. E **66**, 012701 (2002)
114. M. Prakash, J.B. Peng, J.B. Ketterson, P. Dutta, Chem. Phys. Lett. **128**, 354 (1986)
115. M. Prakash, P. Dutta, J.B. Ketterson, B.M. Abraham. Chem. Phys. Lett. **111**, 395 (1984)
116. J.B. Peng, G.T. Barnes, I.R. Gentle, G.J. Foran, J. Phys. Chem. B **104**, 5553 (2000)
117. F.J. Giessibl, Rev. Mod. Phys. **75**, 949 (2003)
118. J. Garnaes, D.K. Schwartz, R. Viswanathan, J.A. Zasadzinski, Nature **357**, 54 (1992)
119. D.K. Schwartz, J. Garnaes, R. Viswanathan, S. Chiruvolu, J.A. Zasadzinski, Phys. Rev. E **47**, 452 (1993)
120. D.K. Schwartz, J. Garnaes, R. Viswanathan, J.A. Zasadzinski, Science **257**, 508 (1992)
121. B.C. Smith, *Fundamentals of Fourier Transform Infrared Spectroscopy* (CRC Press, New York, 1996)
122. K. Nakamoto, *Infrared and Raman Spectra of Inorganic and Coordination Compounds* (Wiley, New York, 1986)
123. R.F. Holland, J.R. Nielsen, J. Mol. Spec. **9**, 436 (1962)
124. R.A. MacPhail, H.L. Strauss, R.G. Snyder, C.A. Elliger, J. Phys. Chem. **88**, 334 (1984)
125. C. Naselli, J.F. Rabolt, J.D. Swalen, J. Chem. Phys. **82**, 2136 (1985)
126. H.D. Sikes, D.K. Schwartz, Science **278**, 1604 (1997)
127. P.K. Nayak, S.S. Talwar, S.S. Major, R.S. Srinivasa, Colloids Surf. A **187**, 284 (2006)
128. Y. Ren, M.M. Hossain, K.-I. Iimura, T. Kato, Chem. Phys. Lett. **325**, 503 (2000)
129. T.Y. Kim, D.J. Ahn, Matterials. Sci. Eng. C **24**, 205 (2004)
130. S. Kundu, A. Datta, S. Hazra, Chem. Phys. Lett. **405**, 282 (2005)
131. K. Das, S. Kundu, Colloids Surf. A **468**, 56 (2015)
132. E. Teer, C.M. Knobler, J. Chem. Phys. **106**, 1913 (1997)
133. H. Tanaka, T. Akatsuka, T. Murakami, Y. Ogoma, K. Abe, Y. Kondo, J. Biochem. **12**, 206 (1997)
134. I. Prieto, R.M.T. Martin, L. Camacho, D. Möbius, Langmuir **14**, 4175 (1998)
135. B. Moore, C.M. Knobler, D. Broseta, F. Rondelez, J. Chem. Soc. Faraday Trans. II **82**, 1753 (1986)

136. G. Ma, H.C. Allen, Langmuir **22**, 5341 (2006)
137. W. Sung, S. Seok, D. Kim, C.S. Tian, Y.R. Shen, Langmuir **26**, 18266 (2010)
138. N. Takeshita, M. Okuno, T.-A. Ishibashi, Phys. Chem. Chem. Phys. **19**, 2060 (2017)
139. A. Saito, Y. Urai, K. Itoh, Langmuir **12**, 3938 (1996)
140. R. Capelletti, M.P. Fontana, C.A. Nicolae, R. Paradiso, R. Bonnett, R.F. Wilkins, Mol. Cryst. Liq. Cryst. **266**, 35 (1995)
141. G.G. Siu, Y.L. Liu, S.S. Xie, J.M. Xu, T.K. Li, L.G. Xu, Thin Solid Films **274**, 147 (1996)
142. J.R. Chamberlain, J.E. Pemberton, Langmuir **13**, 3074 (1997)

Thin Films for Electrocaloric Cooling Devices

Gunnar Suchaneck and Gerald Gerlach

Abstract Currently, many publications report on the electrocaloric effect and its application for cooling devices. This work focusses now on the prospects of using ceramic thin films in electrocaloric cooling. We introduce the electrocaloric effect and examine electrical properties, mechanical boundary conditions as well as the film microstructure affecting electrocaloric activity. Further, multilayer ceramic capacitors are introduced as a promising device concept for electrocaloric refrigeration, and limitations of the related heat transfer in electrocaloric devices will be discussed. Finally, ceramic thin films and bulk ceramics are compared with regard to electrocaloric cooling.

1 Introduction

A general definition of thin films is not yet available. Generally, the thickness of thin films is proposed to be in the order of the wavelength of light [1]. The International Union of Pure and Applied Chemistry (IUPAC) defines solid and liquid thin films as layers that have a thickness of at least one atom or molecule. It recommends to apply the term 'thin' only to films whose thickness is of the order of a characteristic scale or smaller [2]. Wikipedia specifies a thin film as a layer of material ranging from fractions of a nanometer (monolayer) to several micrometres in thickness [3]. In this chapter, we denote thin films as those films whose thickness d is less than 10 μm, i.e. not much larger than a characteristic value d_t where the breakdown strength changes from a thickness-independent, intrinsic regime to a thickness-dependent, extrinsic regime (cf. Sect. 3.1).

There are a number of recent reviews of the electrocaloric (EC) effect [4–6] and its application in refrigerators [7, 8], as well as a book on this topic [9]. Here, the most recent review is devoted to ceramic multilayer capacitors fabricated by tape casting and screen printing [5]. However, the application aspects of thin films are still poorly studied.

G. Suchaneck (✉) · G. Gerlach
Institute for Solid State Electronics, Dresden, TU, Germany
e-mail: gunnar.suchaneck@tu-dresden.de

S. Kumar and D. K. Aswal (eds.), *Recent Advances in Thin Films*, Materials Horizons: From Nature to Nanomaterials, https://doi.org/10.1007/978-981-15-6116-0_12

The usage of thin films instead of bulk materials allows the application of high electric fields with voltages compatible with the standard-silicon CMOS (complementary metal-oxide semiconductor) technology. Simultaneously, it is assumed to yield a higher adiabatic temperature change. The resulting giant EC effect was expected to lead to a breakthrough in the EC refrigeration technology [10, 11].

However, the cooling capacity of thin films was considered to be too small for any practical application due to their mass limitations. Therefore, the use of EC thin films for mid- and large-scale cooling applications was claimed to be unlikely [6]. On the other hand, the average cooling power of an EC element is independent of its heat capacity when the cycle time is chosen to be proportional to the thermal relaxation time of the EC element [12]. Thin-film devices are then limited by the time constants of their thermal interfaces (heat switches or heat transfer fluids) [13].

In this work, EC cooling will be reviewed from the perspective of thin films. In Sect. 2, the EC effect is introduced. Section 3 is devoted to thin-film properties affecting the EC effect—the dielectric strength limiting the EC effect, the dielectric permittivity determining the dielectric strength, the mechanical stress and the grain size. Section 4 considers multilayer ceramic capacitors fabricated by ceramic tape and screen printing technologies which are unusual in thin-film manufacture. In Sect. 5, limitations of heat transfer in EC devices are discussed. Finally, Sect. 6 compares ceramic thin films and bulk ceramics with regard to EC cooling.

2 Electrocaloric Effect

An electric field E applied to a dielectric material induces a change in electric polarization and, thus, a change in entropy in the material. The EC effect is a reversible temperature change ΔT_{EC} when polarization or depolarization takes place adiabatically or, equivalently, an entropy change ΔS_{EC} when they are carried out isothermally. The entropy change determines the heat $Q = T \cdot \Delta S_{EC}$ absorbed or rejected during an isothermal step. With regard to $Q = c \cdot \Delta T_{EC}$, where c is the volumetric specific heat, the adiabatic temperature change and the isothermal entropy change are related by $c \cdot \Delta T_{EC} = T \cdot \Delta S_{EC}$.

A Clausius–Clapeyron contribution to ΔT_{EC} takes its origin from the latent heat of a first-order ferroelectric–paraelectric phase transition to $\Delta T_{EC,PT}$ [14]

$$\Delta T_{EC,PT} = \frac{T}{c_P} \cdot \frac{dE_{cr}}{dT} \cdot \Delta P, \tag{1}$$

where ΔP is the polarization discontinuity at the phase transition, E_{cr} the critical electric field, at which the phase transition occurs and c_P the specific heat at constant P. It increases with the Curie temperature T_C as $\Delta T_{\mathrm{EC,PT}} \sim T_C^{3/2}$ [15] and amounts to 1.4 K for $BaTiO_3$ exhibiting a T_C of 120 °C [14]. During cycling of ferroelectrics through their phase transition temperatures, a large part of the entropy change involves the creation and destruction of domains what are not fully reversible.

The entropy change ΔS of a second-order ferroelectric–paraelectric phase transition possessing no latent heat is about 1 J/molK. This yields an EC temperature change ΔT_{EC} of about 5 K [16]. In the absence of a phase transition, the EC effect induced by the application of an electric field is given by [17]:

$$\Delta T_{EC} = -\frac{T}{c}\int_{E_1}^{E_2}\left(\frac{\partial P_r(T)}{\partial T} + \varepsilon_0 E\frac{\partial \varepsilon(E,T)}{\partial T}\right)_E dE, \tag{2}$$

where T is the temperature, P_r the remanent polarization, c_E the volumetric specific heat at constant E considered to be constant, $c_E \approx c$, and ε the dielectric permittivity. Practical applications require a ΔT_{EC} of at least 5 K [18]. Generally, the EC effect will be large in any insulating material with a highly temperature-dependent dielectric susceptibility $\chi(T) = \partial P / \partial T = \varepsilon(T) - 1$ [19]. Above the temperature T_m of maximum dielectric permittivity, relaxor ferroelectrics provide a large and reversible polarization change due to contributions to polarization not present in ordinary ferroelectrics. This increases the predicted upper limit of the EC effect up to about 50 K [20]. Consequently, lead-containing $PbMg_{1/3}Nb_{2/3}O_3$–$PbTiO_3$ (PMN-PT) relaxor ferroelectric thin films were considered to be promising for EC application [21]. Experimentally, values of ΔT_{EC} up to 40 K were reported for thin-film relaxor ferroelectrics or polymers, whereas ΔT_{EC} values obtained in bulk materials amounted only to several Kelvin [4, 6, 22].

Another approach to achieve high entropy changes is the use of compositions near an invariant critical point (ICP) at which multiple phases can coexist [23]. Here, an increased number of polar states are available and the electric field for switching among different polar states becomes relatively small. Correspondingly, application-suitable ΔT_{EC} values obtained in $BaZr_xTi_{1-x}O_3$ ceramics at room temperature were attributed to the coexistence of four phases, i.e. paraelectric cubic, ferroelectric tetragonal, orthorhombic and rhombohedral phases near ICP [24].

Other serious candidates for solid-state refrigerants would be antiferroelectric materials [25].

A large EC effect is obtained for ferroelectrics and relaxor ferroelectrics exhibiting a slim *P-E* hysteresis (small remnant polarization and coercive field) and a weak dependence of the dielectric permittivity on the electric field [26]. For a negligible remnant polarization, the maximum entropy change is then given by

$$\Delta S_{EC}^{\max} = -\frac{3\varepsilon_0[\varepsilon(0)]^2}{2\alpha C}\cdot(1+\alpha E_{BD}^2)^{1/3} \approx -\frac{3\varepsilon_0[\varepsilon(0)]^2}{2\alpha^{2/3}C}E_{BD}^{2/3}, \tag{3}$$

where $\varepsilon(0)$ is the low-field value of ε, C the Curie constant derived from its temperature dependence, E_{BD} the dielectric breakdown field (dielectric strength) and α an empirical coefficient describing the field dependence of ε for a second-order phase transition [27]:

$$\varepsilon(E) \approx \frac{\varepsilon(0)}{\left(1+\alpha E^2\right)^{1/3}}. \tag{4}$$

Theoretically, the $\Delta T_{EC} \sim E^{2/3}$ field dependence was derived from the Landau–Ginzburg–Devonshire equation in [28]. Experimentally, a 2/3-power law of the EC temperature change, $\Delta T_{EC} \sim E^{2/3}$, was obtained for $PbSc_{0.5}Ta_{0.5}O_3$ in [29]. However, the EC effect was attributed here to the Clausius–Clapeyron contribution of a long-term-annealed material with a high degree of ordering of scandium and tantalate ions.

Relaxor ferroelectric $0.71Pb(Mg_{1/3}Nb_{2/3})O_3$–$0.29PbTiO_3$ (PMN–PT) (011) single crystals, (Pb,La)(Zr,Ti)O_3 ceramic thin films and poly(vinylidene fluoride–trifluoroethylene–chlorofluoroethylene) (P(VDF–TrFE–CFE))/poly(vinylidene fluoride–trifluoroethylene) (P(VDF–TrFE)) terpolymer/copolymer blends obey the 2/3-power law of ΔT_{EC} at higher electric fields, $E > 50$ V/μm [30]. Note that calculations for ultra-thin ($d = 2.4$ nm) $BaTiO_3$ films based on a multiscale thermodynamic model [23] predicted a weaker field dependence, $\Delta T_{EC} \sim E^{0.45}$, making the enhancement of ΔT_{EC} not so significant. On the other hand, ultra-thin films will conduct too much leakage or tunnelling current which is detrimental to the EC effect.

To compare different materials as solid-state refrigerants, the EC coefficient $\partial T/\partial E \approx \Delta T_{EC}/\Delta E$ is more appropriate [6]. It is related to the pyroelectric coefficient π by Maxwell´s relation [31]:

$$-\left(\frac{\partial T}{\partial E}\right)_S = \left(\frac{\partial D}{\partial S}\right)_E = \frac{T}{c_E}\left(\frac{\partial D}{\partial T}\right)_E = \frac{T\pi_E}{c_E}, \tag{5}$$

where D is the dielectric displacement. Equation 5 is the differential form of Eq. 2. The field dependence of $\Delta T_{EC}/\Delta E$ is then given by

$$\frac{\Delta T_{EC}}{\Delta E} \sim E^{-1/3}, \tag{6}$$

i.e. the EC material exhibits a high EC coefficient at low electric fields which becomes lower at higher fields. The EC coefficient is an intrinsic material property. On the other hand, in thin films, the polarization behaviour is significantly affected by the clamping conditions of the film on the substrate [32] and by the misfit strain [33] both deteriorating $\Delta T_{EC} \big/ \Delta E$.

3 Thin-Film Properties Affecting the Electrocaloric Effect

3.1 Dielectric Strength of Thin Films

Following Eq. 2, higher values of the EC temperature change, ΔT_{EC} values, are obtained by the application or removal of higher electric fields. Even for this reason, EC cooling has regained attention in 2006, when Mischenko et al. could show that large electrical fields can be applied to antiferroelectric $PbZr_{0.95}Ti_{0.05}O_3$ thin films [10]. They observed that—close to the ferroelectric Curie temperature of 222 °C—a field change from 77.6 to 29.5 V/μm induced an adiabatic temperature change of 12 K as it was determined from the integrated pyroelectric effect described by Eq. 2. Therefore, the dielectric strength was considered to be a key parameter for the high-performance EC materials [6, 18, 28].

Bulk ceramic materials are limited by their lower dielectric breakdown field (dielectric strength of the material) where the breakdown mechanism is dominated by extrinsic breakdown instead of the intrinsic avalanche breakdown mechanism typical for thinner films. Dielectric breakdown as an electron avalanche was first considered theoretically by von Hippel [34]. Recently, calculations based on density functional perturbation theory and on the direct integration of electronic scattering probabilities over all possible final states, with no adjustable parameters, have shown that von Hippel´s avalanche model is able to predict properly the intrinsic breakdown for covalently bonded and ionic materials [35]. On the other hand, the electrical breakdown of metal-oxide dielectrics is fixed by the arising local electric field and the chemical bond strength. Therefore, only a certain energy density, equivalent to a limit in electrostatic pressure, might be stored in a dielectric. This results in an empirical relationship [36]:

$$E_{BD} \approx \frac{2450}{\sqrt{\varepsilon_r}} \frac{V}{\mu m}. \tag{7}$$

For instance, E_{max} of ferroelectric ceramics with $\varepsilon = 1000$ amounts to ca. 80 V/μm. In thin films, the electric field is distributed more uniformly over the film thickness, and fewer hot spots appear compared to ceramic samples. Here, the situation is more similar to an ideal crystal lattice and the breakdown is more likely caused by an electron ionization avalanche, which is the highest limit for the dielectric strength of a particular material. Current–voltage studies of very thin (~77 nm) barium titanate single crystals ($\varepsilon = 2700$) showed an estimated breakdown value of 800 V/μm [37], about one order of magnitude higher than predicted by Eq. 7. Optimized $BaTiO_3$ ceramics prepared with Ba-excess or Nb-doping possessed a dielectric strength of 70 V/μm [38]. Thus, Eq. 7 is an appropriate estimate for the maximum dielectric strength. However, it does not account for the reduction of dielectric strength by the microstructure of real ceramics including pores, microcracks, strain field, impurity phases causing hot spots, etc.

When the film thickness exceeds a transition-thickness d_t, the breakdown strength changes from a thickness-independent, intrinsic regime to a thickness-dependent, extrinsic regime [39]. The value of d_t represents the characteristic length of a breakdown-initiating conducting filament which is approximately between 1 μm and 20 μm for Al_2O_3, TiO_2, $SrTiO_3$ and $BaTiO_3$ and what is almost one order of magnitude higher for polymers (d_t = 10–100 μm) [40, 41]. For wide band-gap dielectrics, e.g. ABO_3 perovskites, the dependence of the extrinsic breakdown field upon dielectric thickness d generally obeys a power-law dependence [41–43]

$$E_{BD} \propto (\varepsilon_r d)^{-1/2}. \tag{8}$$

In [44], the validity of Eq. 8 was proven experimentally for a large number (4100) of $BaTiO_3$-based multilayer capacitors with Ni base-metal electrodes. The data averaged over the lateral area showed for $6 < d < 22$ μm a power-law dependence with an exponent of $n = -0.50 \pm 0.06$. This gives evidence that the value of d_t for typical lead-free EC materials is at the most about 5 μm. By replacing thickness by grain size, a power law of the breakdown field similar to Eq. 8 was obtained in $BaTiO_3$ ceramics [45]. Grain boundaries contribute to dielectric breakdown similar to electrodes, i.e. they provide a path of least resistance. Otherwise, less grain boundary area (larger grains) leads to an increase in the voltage drop on each grain boundary leading to a lower apparent dielectric strength of each grain boundary [46]. Following Eq. 8 and the definition of thin films in this chapter, the dielectric strength of thin films which are free of extended defects will be only a little bit smaller than the electron avalanche limit.

Porosity degrades the electrical reliability performance of dielectric thin films, i.e. higher porosity leads to lower breakdown voltage. Quantitatively, this effect was characterized by a statistical approach where the breakdown occurs along a path containing a maximum of voids and a minimum of solid ceramics [47]. For the corresponding defect model, the breakdown field of a porous material is given by

$$E_{BD} = E_{BD}(0) \cdot \left(1 - \frac{x_m}{n}\right), \tag{9}$$

where $E_{BD}(0)$ is the breakdown field strength of the pore-free material, n the number of hypothetical cubes in a column, x_m the maximum number of voids in a column determined by

$$N P_n(x_m) = 1, \tag{10}$$

with N the number of columns $N \approx (L/d)^2$, L the lateral sample dimension, $P_n(x)$ the probability of finding a column of n cubes containing x voids:

$$P_n(x) = \binom{n}{x} \cdot \left[1 - \frac{\rho}{\rho_0}\right]^x \cdot \left[\frac{\rho}{\rho_0}\right]^{n-x} \tag{11}$$

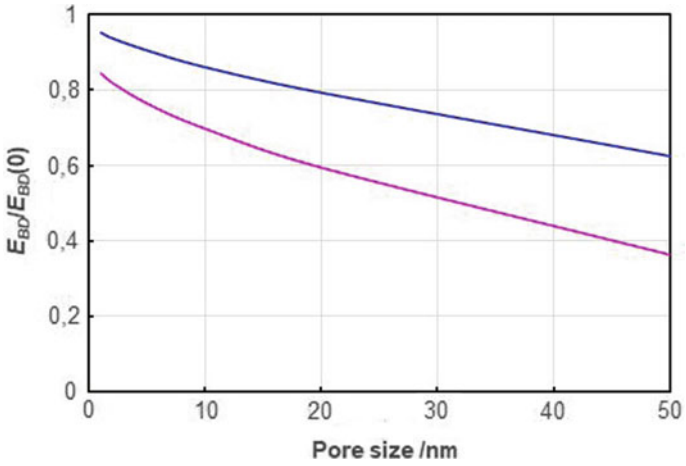

Fig. 1 The effect of pores size on dielectric strength for materials with 2% (blue) and 10% porosity (magenta), respectively

ρ the density of the porous and ρ_0 the theoretical density of the void-free material, respectively. Figure 1 illustrates the deterioration of the breakdown field with pore size calculated using Eqs. 9–11 for ceramic materials exhibiting 2% and 10% porosity, respectively. As the result, porosities exceeding 2% and pore sizes larger than 20 nm are detrimental to EC applications.

The dielectric strength is further reduced by other microstructural defects [18]. With the exception of antiferroelectrics, EC materials are piezoelectrics, i.e. large mechanical strains are generated during the cycling of the electric field generating microcracks as weak points for the breakdown. Impurity phases cause field enhancement and a thermal expansion mismatch to the host phase [38]. Impurity phases in lead-containing ceramics—such as residues of PbO or PbO-rich phases—and local oxygen-deficiency reducing the host phase form hot spots and provide conductive channels for the electric breakdown. Additionally, lead oxides can melt or decompose under the application of high electric fields [18]. Other parameters affecting the breakdown field are the contact surface between the material and the electrodes defining electric field inhomogeneities, the finishing of the surface, the size and quality of electrodes, etc. Since both dielectric and mechanical strength are correlated via porosity, dielectric strength measurements of ceramics is affected also by the mechanical strength [48]. The latter can be evaluated by appropriate nanoindentation measurements [49].

3.2 *Dielectric Permittivity*

Since the maximum of ΔT_{EC} occurs in the *T*-*E* plot along a line of minimum inverse capacitance [19], a high ε value may serve as criteria for a large EC effect. Figure 2 compares the relative dielectric permittivities ε of single-crystal $BaTiO_3$ [50], of polycrystalline $BaTiO_3$ ceramics [51] and of 233 nm thick $BaTiO_3$ thin films deposited by RF ceramic-target sputtering at 650 °C onto silicon (low compressive stress of −47 MPa) and sapphire (high compressive stress of −401 MPa), respectively [52]. Figure 2 illustrates that the dielectric permittivity of ceramics is smaller than the one of single crystals. This is attributed to a low-permittivity layer appearing at grain boundaries. In fine-grained $BaTiO_3$ ceramics, ε in the ferroelectric state shows a maximum at a critical grain size of about 0.8 μm where the highest density of 90° domain walls is obtained [53]. In the paraelectric state, ε is almost independent of grain size [54].

The microstructure of thin films is determined by a number of deposition and process parameters which control the energy delivered to the film surface. The relationship between substrate temperature, kinetic energy of the ions and deposition rate has been summarized in various structure zone models. The most commonly used is the Thornton structure zone model [54, 55]. In agreement with these models, perovskite (111)-textured $PbZr_{0.2}Ti_{0.8}O_3$ thin films sputter-deposited onto platinized Si-wafers exhibit a columnar structure with column diameters in the order of 100 nm

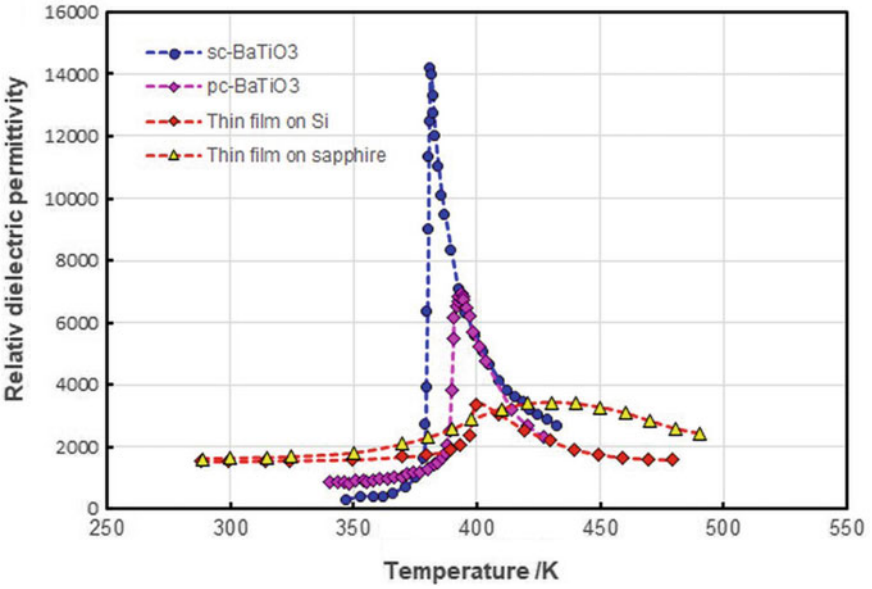

Fig. 2 Temperature dependence of the relative dielectric permittivity of $BaTiO_3$ for single crystals [50], ceramics [51] and thin films [52]

consisting of domain strips of 20–40 nm width. For a film thickness $d > 100$ nm, the domain configuration is almost independent of film thickness [56, 57].

Also, low-permittivity and ferroelectrically inactive layers are present at the interfaces. Thus, the dielectric permittivity of thin films decreases with thickness since the interfacial-dead-layers cause a thickness dependence of the dielectric permittivity following a series-capacitor model [58]

$$\varepsilon = \left(\frac{1 - d_i/d}{\varepsilon_b} + \frac{d_i/d}{\varepsilon_i} \right)^{-1}, \tag{12}$$

where d, d_i, ε_b and ε_i are the film thickness, the interfacial-dead-layer thickness, the dielectric constant of the film bulk and the dielectric constant of the interfacial-dead-layer, respectively.

Other extrinsic effects influencing thin-film properties are (i) mechanical boundary conditions, (ii) electrostatic boundary conditions, (iii) processing-induced defects, (iv) deviations of stoichiometry, (v) the presence of secondary phases, etc. [28, 59]. For instance, in the case depicted in Fig. 2, the compressive film stress shifts the peak of relative permittivity to higher temperatures—to 402 K for the silicon substrate and to 430 K for the sapphire substrate.

The presence of secondary phases has a deleterious effect on dielectric properties. Secondary phases have been reported to reduce the dielectric properties of PMN-PT [60]. Due to the presence of Ba_2TiO_4 in Ba-rich compositions of $BaTiO_3$, both the dielectric permittivity ε and $d\varepsilon/dT$ decrease [61, 62]. Therefore, stoichiometry must be carefully controlled during film deposition since the solubility limit of excess BaO in $BaTiO_3$ is very small [63]. This is best done by reactive multitarget sputtering [64, 65].

Following the thermodynamic theory of ferroelectrics [66], a first-order phase transition shifts to higher temperature with larger electric fields. This temperature shift is easily calculated by means of Eq. 5 assuming $T = T_C$ and $\Delta D/\Delta S \approx \Delta P/\Delta S$ [31]. With further increasing electric field, a tricritical point T_{tri} is reached where the transition becomes second order. Here, the polarization discontinuity ΔP at phase transition is replaced by an always more blurred $P(T)$ curve [66], the dielectric stiffness is raised, i.e. the crystal lattice resists to more polarization in response to further increasing electric fields and the peak of dielectric permittivity is shifted to higher temperature both with a 2/3-power-law field dependence [31]. Thus, at a rather high electric field, the dielectric permittivity-versus-temperature characteristics of $BaTiO_3$ are largely reduced both for single crystals [67], ceramics [51] and thin films [68] due to the intrinsic tuneable properties of the ferroelectrics [27].

3.3 Mechanical Stress

Thin films epitaxially grown on a substrate are two-dimensionally clamped. This changes the temperature-dependent coefficient of the thermodynamic potential and changes the ferroelectric–paraelectric phase transition from first order in mono-domain bulk crystals to second order in mono-domain clamped thin films [69]. Both reduce the EC effect. In the latter case, the Clausius–Clapeyron contribution to ΔT_{EC} disappears. Calculations demonstrate that perfect mechanical clamping in $BaTiO_3$ thin-film structures results in a reduction of EC response but reduces its sensitivity to temperature [32]. At $T_{EC}^{\max} = 390$ K, it is found that $\Delta T_{EC}/\Delta E$ of laterally clamped $BaTiO_3$ is about 80% of the value observed for a bulk crystal. A tensile misfit strain shifts the maximum in the EC response to lower temperatures, increasing both its magnitude and its dependence on temperature, while a compressive misfit strain has the opposite influence [70]. First-principle calculations [71] showed that the EC effect in clamped BST ceramics is suppressed by about 40%. Thus, the control of film/substrate misfit strain provides a mean of optimizing an EC device.

Thermal strains which develop in the film due to the differences in the coefficients of thermal expansion between film and substrate upon cooling from the film growth (or annealing) temperature might be tuned choosing different substrates ($SrTiO_3$, MgO, $LaAlO_3$, $0.29LaAlO_3{:}0.35Sr_2TaAlO_6$ (LSAT), $DyScO_3$, metallized Si or sapphire, etc.) [72]. A principal effect of the tensile strains is to shift the zero-field values of the Curie temperature T_C to lower temperatures. For $BaTiO_3$ films, the thermal strains are sufficient to shift the zero-field T_C to room temperature.

The EC effect can be tuned by mechanical stress or pressure. A significant enhancement and broadening of the EC response is predicted in $BaTiO_3$ thin films under compressively loaded conditions [73]. Under tensile stresses, the EC peak moves towards higher temperatures with a slight enhancement [74].

A statistical mechanical lattice model considers relaxor ferroelectrics as constituted from various types of clusters with localized vibrational modes with a frequency defined by a cluster Debye temperature [75]. It predicts significant enhancement of ΔT_{EC} with pressure. The same result was obtained by first-principle calculations for $LiNbO_3$ [19].

3.4 Grain Size

In bulk $BaTiO_3$ ceramics, the grain size has a strong effect on the low-frequency dielectric permittivity at room temperature [76]. With decreasing grain sizes below approximately 10 μm, ε first increases up to a maximum at approximately 0.8 μm attributed to domain wall contributions and then it decreases with a further reduction of the grain sizes. The temperature T_m of maximum dielectric permittivity does not shift significantly with temperature for decreasing grain sizes [77], if no impurities are incorporated during synthesis. Chemical-solution-deposited $BaTiO_3$ thin films

of different grain sizes synthesized on platinized Si substrates fit into the dielectric permittivity-versus-grain size diagram of bulk ceramics [53]. Here, the value of ε of fine-grained films increasing with grain size is related to a decreasing fraction of low-permittivity grain boundaries. Sputtered thin films usually exhibit a columnar texture, indicating that the nucleation and growth of the crystallites initiate from the substrate. These films will be in an intermediate state between, for instance, tetragonal 4 mm symmetry of single crystals and ∞m symmetry of ceramics. In films possessing such a columnar structure, grain boundaries lie perpendicular to the electrodes so that the presence of a low-permittivity layer at the grain boundaries reduces only the overall permittivity with regard to a parallel connection of capacitors. In fine-grained films fabricated by chemical-solution deposition with a subsequent annealing procedure, grain boundaries exist parallel to the electrodes. They are connected in series with the bulk of the grain significantly reducing the dielectric permittivity. Therefore, a remarkable impact of grain size on the EC effect is expected only in the latter case.

In accordance with a larger ε value, large grain sizes will favour a large EC response [78]. On the other hand, processing conditions have an impact not only on grain size, but also on stoichiometry, etc. Thus, an apparent dependence of the EC effect on grain size is obtained in bulk PMN-PT ceramics caused by a lead-deficiency in more coarse-grained samples which were annealed at higher temperature [79].

Theoretically, the EC coefficients of $Ba_{0.6}Sr_{0.4}TiO_3$ thin films on $LaAlO_3$ and MgO substrates at room temperature below a thickness of 200 nm strongly depend on film thickness [80]. A decrease of grain size in $BaTiO_3$ nanoceramics (grain size <50 nm) reduces significantly the temperature where the maximum EC effect is obtained [81].

4 Multilayer Ceramic Capacitors

The main disadvantage of thin films is their attachment to substrates, which significantly reduces the cooling power [82]. A solution that does not require a substrate and keeps the high breakdown field of films in a bulk material is the use of multilayer ceramic capacitor (MLCC) structures with internal metallic electrodes. MLCCs provide an efficient heat transfer between the EC elements (large surface-to-volume ratio, high thermal conductivity of vertically interdigitated metallic electrodes), they avoid arcing as a frequent failure mechanism and they are extremely reliable [83]. The MLCC concept was developed by Herbert [84] and introduced in the early 1980s by Murata Manufacturing Co. for the fabrication of base-metal monolithic capacitors [85]. It was previously used to evaluate the high-field EC effect of $PbSc_{0.5}Ta_{0.5}O_3$ [86], $(Cd_{0.83}Pb_{0.17})_2Nb_2O_7$ [87] and $BaTiO_3$ [51, 88]. MLCCs are now in high-volume production (some 5×10^{11} pieces per year) by means of sheeting green ceramic tapes and screen printing technology [89]. On the other hand, they are not optimized for EC applications.

Commercial MLCCs are an attractive EC component in proof-of-concept refrigerator prototypes [17]. They combine a suitable thermal mass with an operating

Table 1 Characteristics of prototypes of EC coolers using MLCCs as refrigerant

Refrigerant	Thermal interface	T, K	E, V/μm	ΔT_{EC} (°C)	f, Hz	$\dot{q}$ (Wcm^{-2})	Reference
Y5V $BaTiO_3$[a]	Aceton	298	86	0.55	0.1	0.083	Sato [106]
Y5V $BaTiO_3$[a]	Hydrofluoroethers	298	~50	0.6	0.25	0.0012[b]	Hehlen et al. [107]
Y5V $BaTiO_3$[a]	MEMS[c]-shaped Si with liquid lubricant	300	27.7	0.5	0.33	0.036	Wang et al. [108]
$Ba(Zr,Ti)O_3$	Silicone fluid	298	20	0.54	0.025	0.007	Sette et al. [109]

[a]doped $BaTiO_3$ formulation with a specification −30 °C/+85 °C, $\Delta C/C_0 = -82/+22\%$
[b]estimation of maximum value
[c]microelectromechanical system

voltage in the order of 100 V as well as with the high dielectric strength obtained in thin films (cf. Sect. 3.1). A compilation of MLCC EC properties is given in Table 1 in [4]. MLCCs can be stacked in series to achieve a higher temperature span of the refrigerator. Moreover, MLCC arrays may be operated between a common heat source and sink to increase cooling power. Nevertheless, cooling powers achieved so far with MLCCs amount to only a few up to several 10 mW/cm^2 (cf. Table 1).

5 Limitations of Heat Transfer in EC Devices

The thermodynamical cycle that best is addressed to the EC refrigeration is the reverse Brayton cycle [11, 17]. It consists of two adiabatic and two isofield stages:

- Adiabatic polarization by increasing the electric field, the EC material experiences EC heating.
- Heat rejection to a heat sink under a constant electric field.
- Adiabatic depolarization by decreasing the electric field, the material experiences EC cooling.
- Heat absorption from a load under a constant or zero electric field returning to the initial state.

Heat is transferred from the load or to the heat sink either

- via controlled heat switches as well as uncontrolled thermal rectifiers, or
- by pumping a gaseous or liquid heat transfer agent through the solid refrigerant.

The main requirements of EC thin films driven by a reverse Brayton cycle are [28]:

- a maximum temperature coefficient $d\varepsilon/dT$ of dielectric permittivity (>100 K^{-1}) or, correspondingly, a large latent heat of a first-order phase transition,
- a temperature of maximum dielectric permittivity or a Curie temperature near the operational temperature range,
- large dielectric strength (>100 V/μm) and low electrical ageing,
- low dielectric losses (<2%),
- sufficient thermal conductivity and large heat capacity of the EC refrigerant, and
- a positive slope of $d\varepsilon/dT$, i.e. $d^2\varepsilon/dT^2 > 0$, in order to prevent EC element heating during the successive thermodynamic cycles.

In a first approximation, the cycles can be modelled as a harmonic temperature oscillation with an angular heat modulation frequency ω. Harmonic temperature oscillations are described by a highly damped wave exhibiting a complex wave vector [90].

$$k = \sqrt{\frac{i\omega}{D}} = (1+i)\sqrt{\frac{\omega}{2D}}. \tag{13}$$

The main parameter of such a strongly damped wave is its penetration depth

$$d_p = \sqrt{\frac{2D}{\omega}}, \tag{14}$$

where D is the thermal diffusivity.

Figure 3 compares the EC material thickness d necessary to provide a given specific cooling power,

$$\frac{dq}{dt} = \frac{c \cdot d \cdot \Delta T_{EC}}{\tau_c}, \tag{15}$$

where d is the thickness of the EC material, with d_p, Eq. 14, in dependence on the cycle time τ_c.

The comparison in Fig. 3 illustrates that in ceramics with a thickness in the order of 1 mm, an inefficient heat transfer limits device performance at the appropriate low frequencies. Also, small thermal penetration depths make bulky solid-state refrigerants impractical. Therefore, EC cooling should be adapted to large areas. Then, the specific cooling power is related to the cooled area. Thin-film and thick-film ceramics as well as multilayer ceramic capacitors with a limited total thickness are favourable for EC device applications when sufficiently fast heat switches or rectifiers with high thermal contrast or high rectification ratio become available. Here, a heat switch is a two-terminal element where, at the same temperature drop, the heat flow depends on a non-thermal control parameter (electric field, magnetic field, pressure, etc.) while a thermal rectifier exhibits a magnitude of the forward heat flow which is greater than the magnitude of the reverse heat flow [91]. In the case of thermal switches, the cycle time should be low enough that the heat cannot leak out of the refrigerant ($\tau_c < R_{\text{off}}$

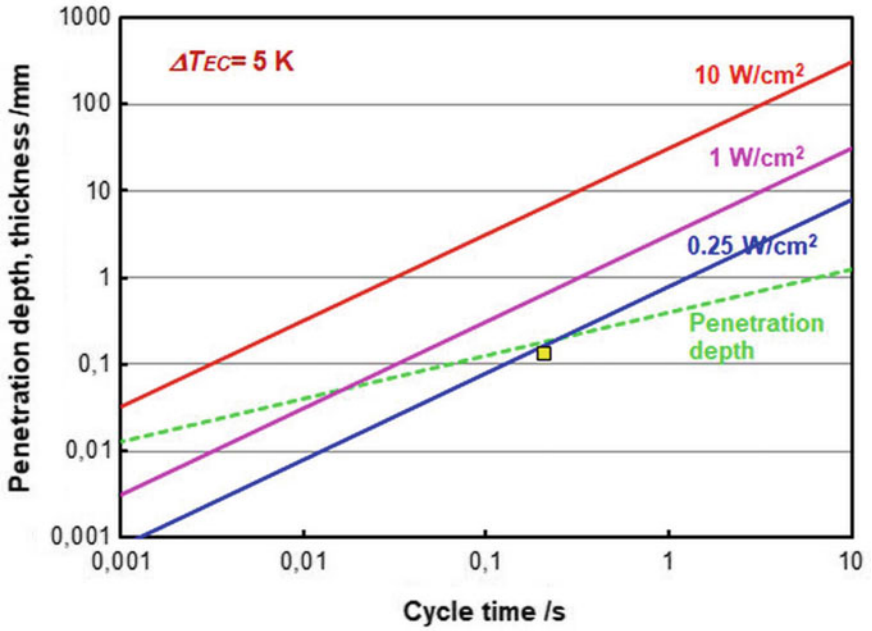

Fig. 3 EC material thickness necessary for a given cooling power and thermal wave penetration depth versus EC device operating frequency. The square shows data of Y5V $BaTiO_3$/Ni multilayer ceramic capacitors with a cooling power of 0.25 W/cm^2 geometrically optimized by FEM [105]

$\cdot C_{th}$), but high enough that the refrigerant can be fully loaded and exhausted ($\tau_c > R_{\text{on}} \cdot C_{th}$). Here, R_{off} and R_{on} are the thermal resistances of the heat switch in off- and on-state, respectively, and C_{th} is the heat capacity (thermal mass) of the refrigerant.

Considering only heat losses caused by heat switches, the maximum relative efficiency of EC refrigerators is given by [92]

$$\Phi_{\text{switch}} = \left(\frac{\sqrt{K} - 1}{\sqrt{K} + 1} \right)^2, \tag{16}$$

where $K = \kappa_{\text{on}}/\kappa_{\text{off}}$ is the conductivity contrast of the heat switches and κ_{on} and κ_{off} are the thermal conductivities of the heat switch in the on and off states, respectively. Thus, if $K > 10$, then EC cooling exceeds the efficiency of thermoelectric cooling. For $K > 100$, it offers a refrigeration efficiency comparable to magnetic cooling (about 70%). Shaped silicon heat switches provide a thermal contrast ratio in the range of $K = 34, \ldots, 59$ at switching times in the order of 30 ms [93]. They were fabricated by microelectromechanical systems (MEMS) technology and comprise a silicon oil/silver or polystyrol nanoparticle lubricant enabling good thermal contact in the on-state, where the lubricant film dominates the on-state thermal resistance. A Hg-droplet-array heat switch, also manufactured by MEMS technology, showed $K >$

200 due to the high thermal conductivity of liquid mercury [94]. Arrays of vertically aligned carbon nanotubes yield $K = 27$. The switching time of such devices is in the order of 10 ms [94]. A device where a flexible EC polymer acts as both the electrostatic heat switch and the EC material showed switching times of 30 ms and repeatable thermal performance over 30,000 cycles [95]. However, it requires actuating and driving voltages of about 1 kV. All solid-state thermal rectifiers possess still thermal contrasts values K of less than 1.5 what is far from application [96, 97].

Transient heat transfer is characterized by the dimensionless Fourier number

$$Fo = \frac{D \cdot t}{L^2}, \tag{17}$$

where $t \leq \tau_c/2$ is the characteristic time and L the heat transfer length. It represents the ratio of the heat conduction rate to the rate of thermal energy storage in a solid [98]. Complete heat absorption or rejection steps were realized in EC device prototypes for $Fo \sim 8, \ldots, 10$ [95, 99]. This imposes additional constraints on the cycle time.

6 Thin Films Versus Bulk Materials in EC Cooling

The reported EC temperature changes ΔT_{EC} of bulk ceramics are still below the value at least 5 K required for practical applications. Thin films come into play in refrigeration technology primarily due to their high breakdown strength exceeding 100 V/μm [22]. Higher electric fields induce larger polarization changes and, consequently, larger EC temperature changes. The EC temperature changes ΔT_{EC} amount to 31 K at $\Delta E = 75$ MV/m for PMN-PT thin films (240 nm) [100] and more than 40 K at $\Delta E = 125$ MV/m for $Pb_{0.92}La_{0.08}Zr_{0.65}Ti_{0.35}O_{3-\delta}$ thin films (450 nm) [22]. Also, thin films provide values of ΔT_{EC} which are sufficient for practical cooling applications over a broad temperature range (cf. Fig. 1 in [101]). Data for lead-free $BaZr_xTi_{1-x}O_3$ is available solely for quite low electric fields [24]. Here, an extrapolation to comparable fields based on the 2/3-power law according to Sect. 2 predicts a material performance worthy of experimental examination. Figure 4 summarizes published EC coefficients $\Delta T_{EC}/\Delta E$ of thin films measured at electric fields $E \geq 10$ V/μm in dependence on temperature. For comparison, all data were scaled to a field of $E = 80$ V/μm by means of Eq. 6. Large negative values for $\Delta T_{EC}/\Delta E$ were obtained in antiferroelectric PLZT [102] and in $(1-x)Bi_{0.5}Na_{0.5}TiO_3$-$xBaTiO_3$ (BiNT-BT) near the ferroelectric–antiferroelectric phase transition [103]. All separately indicated examples illustrate that phase structure tuning is an important tool for EC performance improvement.

Compositionally graded antiferroelectric $Pb_{1-x}La_xZr_{0.85}Ti_{0.15}O_{3-\delta}$ films deposited on $LaNiO_3$/Si(100) substrates show higher dielectric constants, larger saturation polarizations and a large EC temperature change [110]. The maximum EC effect at room temperature—28 K at 90 V/μm—was obtained for an 'upgraded' composition by varying the La content from 8 mol% at the substrate interface to 14 mol% at

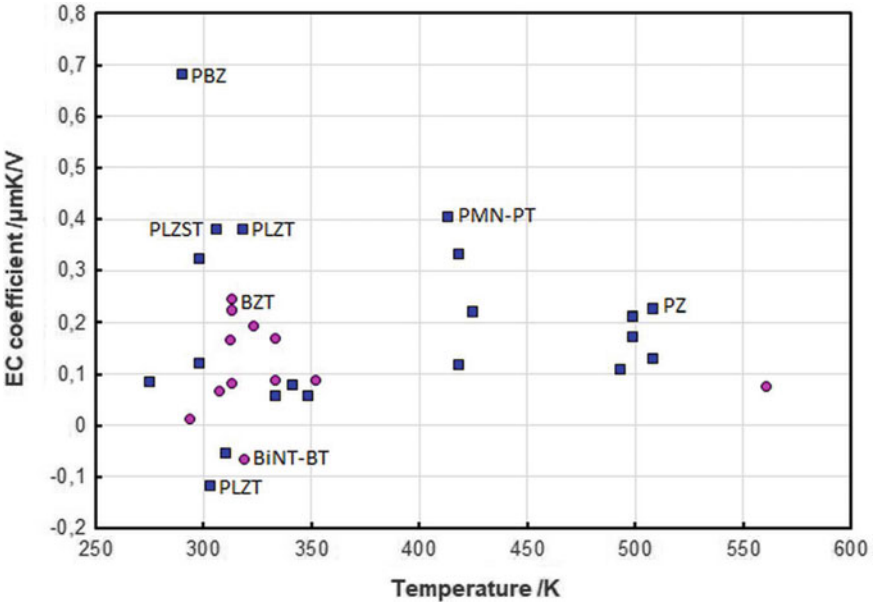

Fig. 4 EC coefficients of thin films at 80 V/µm in dependence on temperature for: *PBZ*—nanoscale antiferroelectric and ferroelectric two-phase, relaxor $Pb_{0.8}Ba_{0.2}ZrO_3$ [104], *PLZST*—antiferroelectric–ferroelectric phase transition point of $Pb_{1-x}La_xZr_ySn_zTi_{1-y-z}O_{3-\delta}$ at the morphotropic phase boundary of orthorhombic and tetragonal phases [104], *PLZT*—relaxor $Pb_{1-x}La_xZr_yTi_{1-y}O_{3-\delta}$ [22], *PMN-PT*—relaxor PMN-PT [9, 100], *PZ*—antiferroelectric $PbZrO_3$ [6] and *BZT*—$BaZr_xTi_{1-x}O_3$ (BZT) with compositions that are between the multiphase point at $x \approx 0.15$ where rhombohedral, orthorhombic, tetragonal and cubic phases coexist and the ferroelectric-relaxor crossover at $x \approx 0.23$ [24, 104]

the top surface. However, a smaller EC effect compared to the equivalent bulk sample was observed at lower fields up to values of 10, …, 20 V/µm. This is a consequence of the fact that here much larger fields are required to induce comparable values of the polarization than in a bulk material since the coercive field in thin films exceeds the one in the bulk by more than one order of magnitude. Contrarily, for the field values above a coercive field of ~20 V/µm, ΔT_{EC} in thin films exceeds the ones observed in the bulk samples [9]. Similarly, an enhanced EC response was found in $BaZr_xTi_{1-x}O_3$ based bilayer films with composition gradient over a broad temperature range [104]. A $BaZr_{0.17}Ti_{0.83}O_3/BaZr_{0.20}Ti_{0.80}O_3$ bilayer exhibited a value of $\Delta T_{EC} = 4.9$ K at an electric field strength of 10 V/µm and a temperature of 40 °C. The improvement of the EC properties was attributed to strain coupling between the two layers and to the induction of multiple phases.

Single thin films have a very small volume V so that the heat $Q = c \cdot V \cdot \Delta T_{EC}$ transferred per cycle is too small to satisfy the requirement of cooling power for mid- and large-scale cooling applications. This represents an important hindrance for using thin films as a solid-state refrigerant. The cooling power obtained from a

single thin film will be competitive with bulk ceramics at cycle times less than 10 ms (cf. Fig. 3).

To overcome this problem, multilayer stacks of thin films can be applied which increase the volume of the refrigerant without compromising the electric breakdown field of each capacitor. By fabricating thin films using a MLCC technology, the film thickness of each layer can be reduced to less than 2 μm [89], which allows for the application of high electric fields with relatively small voltages compatible with the semiconductor integrated circuit technology. Since ceramics are good thermal insulators, the internal interdigital electrodes should be directed parallel to the heat flow to provide a faster heat transfer. This adds additional challenges to fabrication technology. Bulk ceramics are usually not compatible with silicon technology.

7 Conclusions

Thin films of ceramic materials provide EC temperature changes over a certain temperature range that are sufficient for practical applications. The EC properties of thin films can be optimized by tuning phase structure, composition and composition gradients in an appropriate way. The very small volume of thin films and, thus, the small amount of heat transferred during one cooling cycle is compensated by the use of multilayer structures comprising interdigitated internal electrodes. Here, the overall thickness is limited by the penetration depth of thermal oscillations. Consequently, EC cooling is aimed at large area cooling in niche markets, such as lithium ion automotive battery cooling in countries with a hot climate, food cooling in trucks, wine coolers and room air conditioning.

Currently, the application of ceramic thin films as refrigerators is hindered by the absence of appropriate thermal interfaces, i.e. thermal switches or rectifiers as well as heat transfer media operating at frequencies well over 100 Hz. Interfacial thermal resistance and contact thermal resistance are very critical in determining the device performance. Here, further basic research is needed.

References

1. W.A. Pliskin, S.J. Zanin, in *Handbook of Thin Film Technology*, ed. by L.I. Maissel, R. Glang (McGraw Hill, New York, 1970)
2. L. Ter Minassian-Saraga, Pure Appl. Chem. **66**, 1667 (1994)
3. Thin film. https://en.wikipedia.org/wiki/Thin_film. Accessed 27 Feb 2020
4. P.S. Alpay, J. Mantese, S. Trolier-McKinstry, Q. Zhang, R.W. Whatemore, MRS Bull. **39**, 1099 (2014)
5. X. Moya, E. Defay, N.D. Mathur, S. Hirose, MRS Bull. **43**, 291 (2018)
6. M. Valant, Prog. Mater Sci. **57**, 980 (2012)
7. M. Ožbolt, A. Kitanovski, J. Tušek, A. Poredoš, Int. J. Refrig. **40**, 174 (2014)
8. S. Qian, D. Nasuta, A. Rhoads, Y. Wang, Y. Geng, Y. Hwang, R. Rademacher, I. Takeuchi, Int. J. Refrig. **62**, 177 (2016)

9. T. Correia, Q. Zhang (eds.), *Electrocaloric Materials: New Generation of Coolers* (Springer, Berlin, Heidelberg, 2014)
10. A.S. Mischenko, Q. Zhang, J.F. Scott, R.W. Whatmore, N.D. Mathur, Science **311**, 1270 (2006)
11. J. Scott, Annu. Rev. Mater. Res. **41**, 229 (2011)
12. G. Suchaneck, G. Gerlach, Phys. Scr. **90**, 094020 (2015)
13. G. Suchaneck, in *2016 Joint IEEE International Symposium on Application of Ferroelectrics, European Conference on Polar Dielectrics, and Piezoelectric Force Microscopy Workshop (ISAF/ECAPD/PFM)* (Darmstadt, 21–25 August 2016)
14. E. Birks, M. Dunce, A. Sternberg, Ferroelectrics **400**, 336 (2010)
15. M.A. Arkhipov, Dissertation, Moscow Power Engineering Institute, 1995
16. G. Suchaneck, G. Gerlach, A. Deyneka, L. Jastrabik, S. Davitadze, B. Strukov, MRS Proc. **718**, D8.4 (2002)
17. G. Suchaneck, O. Pakhomov, G. Gerlach, in *Refrigeration*, ed. by O. Ekren (IntechOpen, London, 2017), p. 19
18. M. Valant, A.-K. Axelsson, F. Le Goupil, N. McN, N.M. Alford, Mater. Chem. Phys. **136**, 277–280 (2012)
19. M.C. Rose, R.E. Cohen, Phys. Rev. Lett. **109**, 187604 (2012)
20. G. Suchaneck, G. Gerlach, Mater. Today Proc. **3**, 622 (2016)
21. T.M. Correia, J.S. Young, R.W. Whatmore, J.F. Scott, N.D. Mathur, Q. Zhang, Appl. Phys. Lett. **95**, 182904 (2009)
22. S.G. Lu, B. Rožič, Q.M. Zhang, Z. Kutnjak, X. Li, E. Furman, L.J. Gorny, M. Lin, B. Malič, M. Kosec, R. Blinc, R. Pirc, Appl. Phys. Lett. **97**, 162904 (2010)
23. Z.K. Liu, X. Li., Q.M. Zhang, Appl. Phys. Lett. **101**, 082904 (2012)
24. X.S. Qian, H.J. Ye, Y.T. Zhang, H. Gu, X. Li, C.A. Randall, C.A. Zhang, Adv. Funct. Mater. **24**, 1300 (2014)
25. Y. Liu, J.F. Scott, B. Dkhil, APL Mater. **4**, 064109 (2016)
26. G. Suchaneck, G. Gerlach, Ferroelectrics **516**, 1 (2017)
27. K.M. Johnson, J. Appl. Phys. **33**, 2826 (1962)
28. G. Suchaneck, G. Gerlach, MRS Proc. **1581**, Mrss13-1581-ccc03-03 (2013)
29. Y.V. Sinyavsky, N.D. Pashkov, Y.M. Gorovoy, G.E. Lugansky, L. Shebanov, Ferroelectrics **90**, 213 (1989)
30. S.G. Lu, Z.H. Cai, Y.X. Ouyang, Y.M. Deng, S.J. Zhang, Q.M. Zhang, Ceram. Int. **41**, S15 (2015)
31. M.E. Lines, A.M. Glass, *Principles and Applications of Ferroelectrics and Related Materials* (Oxford University Press, Oxford, 1977). Chapter 5
32. G. Akcay, S.P. Alpay, J.V. Mantese, G.A. Rossetti Jr., Appl. Phys. Lett. **90**, 252909 (2007)
33. J.H. Qui, Q. Jiang, J. Appl. Phys. **103**, 084105 (2008)
34. A. von Hippel, Z. Phys. **67**, 707 (1931)
35. Y. Sun, S.A. Boggs, R. Ramprasad, Appl. Phys. Lett. **101**, 132906 (2012)
36. J. McPherson, J.-Y. Kim, A. Shanware, H. Mogul, Appl. Phys. Lett. **82**, 2121 (2003)
37. F.D. Morrison, P. Zubko, D.J. Jung, J.F. Scott, P. Baxter, M.M. Saad, R.M. Bowman, J.M. Gregg, Appl. Phys. Lett. **86**, 152903 (2005)
38. X. Xu, G.E. Hilmas, J. Am. Ceram. Soc. **89**, 2496 (2006)
39. A.F. Joffé, Trans. Faraday Soc. **24**, 65 (1927)
40. E.J. Garboczi, Phys. Rev. B **38**, 9005 (1988)
41. C. Neusel, G.A. Schneider, J. Mech. Phys. Solids **63**, 201 (2014)
42. F. Forlani, N. Minnaja, Phys. Status Solidi B **4**, 311 (1964)
43. J.J. O'Dwyer, *The Theory of Electrical Conduction and Breakdown in Solid Dielectrics* (Clarendon, Oxford, 1973)
44. A.D. Milliken, A.J. Bell, J.F. Scott, Appl. Phys. Lett. **90**, 112910 (2007)
45. T. Tunkasiri, G. Rujijanagul, J. Mater. Sci. Lett. **15**, 1767 (1996)
46. H.Y. Lee, K.H. Cho, H.-D. Nam, Ferroelectrics **334**, 165 (2006)
47. R. Gerson, T.C. Marshall, J. Appl. Phys. **30**, 1650 (1959)

48. A. Kishimoto, K. Koumoto, H. Yanagida, M. Nameki, Eng. Fract. Mech. **40**, 927 (1991)
49. X.J. Zheng, Y.C. Zhou, J.Y. Li, Acta Mater. **51**, 3985 (2003)
50. W.J. Merz, Phys. Rev. **91**, 513 (1953)
51. A.I. Karchevskii, Soviet Phys. Solid State **3**, 2249 (1962)
52. S.B. Desu, Phys. Status Solidi A **141**, 119 (1994)
53. R. Waser, O. Lohse, Integr. Ferroelectrics **21**, 27 (1998)
54. R. Messier, A.P. Giri, R.A. Roy, J. Vac. Sci. Technol., A **2**, 500 (1984)
55. J.A. Thornton, Ann. Rev. Mater. Sci. **7**, 239 (1977)
56. D. Kiselev, I. Bdikin, A. Movchikova, A. Kholkin, G. Suchaneck, G. Gerlach, MRS Proc. **966**, 0966-T07-02 (2013)
57. G. Suchaneck, T. Sandner, A. Deyneka, G. Gerlach, L. Jastrabik, Ferroelectrics **298**, 309 (2004)
58. B.T. Lee, C.S. Hwang, Appl. Phys. Lett. **77**, 124 (2000)
59. T.M. Shaw, S. Trolier-McKinstry, P.C. McIntyre, Ann. Rev. Mater. Sci. **30**, 263 (2000)
60. E.R. Leite, A.M. Scotch, A. Khan, T. Li, H.M. Chan, M.P. Harmer, S.-F. Liu, S.-F. Park, J. Am. Ceram. Soc. **85**, 3018 (2002)
61. A. Beauger, J.C. Mutin, J.C. Niepce, J. Mater. Sci. **19**, 195 (1984)
62. J.-K. Lee, K.-S. Hong, J.-W. Jang, J. Am. Ceram. Soc. **84**, 2001 (2001)
63. S. Lee, C.A. Randall, Z.-K. Liu, J. Am. Ceram. Soc. **91**, 1748 (2008)
64. G. Suchaneck, E. Chernova, A. Kleiner, R. Liebschner, L. Jastrabík, D.C. Meyer, A. Dejneka, G. Gerlach, Thin Solid Films **621**, 58 (2017)
65. V.S. Vidyarthi, W.-M. Lin, G. Suchaneck, G. Gerlach, C. Thiele, V. Hoffmann, Thin Solid Films **515**, 3547 (2007)
66. A.F. Devonshire, Adv. Phys. **3**, 85 (1954)
67. N. Novak, R. Pirc, Z. Kutnjak, Phys. Rev. B **87**, 104102 (2013)
68. B.H. Hoerman, G.M. Ford, L.D. Kaufmann, B.W. Wessels, Appl. Phys. Lett. **73**, 2248 (1998)
69. N.A. Pertsev, A.G. Zembilgotov, A.K. Tagantsev, Phys. Rev. Lett. **80**, 1988 (1998)
70. G. Akcay, S.P. Alpay, G.A. Rossetti, J.F. Scott, J. Appl. Phys. **103**, 024104 (2008)
71. S. Prosandeev, I. Ponomareva, L. Bellaiche, Phys. Rev. B **78**, 052103 (2008)
72. J. Zhang, S.P. Alpay, G.A. Rossetti, Appl. Phys. Lett. **98**, 132907 (2011)
73. Y. Liu, I.C. Infante, X.J. Lou, D.C. Lupascu, B. Dkhil, Appl. Phys. Lett. **104**, 012907 (2014)
74. Y. Liu, J. Wei, P.-E. Janolin, I.C. Infante, J. Kreisel, X.J. Lou, B. Dkhil, Phys. Rev. B **90**, 104107 (2014)
75. L.J. Dunne, M. Valant, A.-K. Axelsson, G. Manos, N. McN, N.M. Alford, J. Phys. D Appl. Phys. **44**, 375404 (2011)
76. G. Arlt, D. Hennings, G. de With, J. Appl. Phys. **58**, 1619 (1985)
77. K. Kinoshita, A. Yamaji, J. Appl. Phys. **47**, 371 (1976)
78. B.A. Tuttle, D.A. Payne, Ferroelectrics **37**, 603 (1981)
79. M. Vrabelj, H. Uršič, Z. Kutnjak, B. Rožič, S. Drnovšek, A. Benčan, V. Bobnar, L. Fulanović, B. Malič, J. Eur. Ceram. Soc. **36**, 75 (2016)
80. J.H. Qiu, Q. Jiang, J. Appl. Phys. **103**, 034119 (2008)
81. J.H. Qiu, Q. Jiang, J. Appl. Phys. **105**, 034110 (2009)
82. M. Quintero, L. Ghivelder, L. Gomez-Marlasca, F. Parisi, Appl. Phys. Lett. **99**, 232908 (2011)
83. S. Kar-Narayan, N.D. Mathur, Appl. Phys. Lett. **95**, 242903 (2009)
84. J.M. Herbert, Proc. IEE **112**, 1474 (1965)
85. Y. Sakabe, K. Minai, K. Wakino, Jpn. J. Appl. Phys. **20S4**, 147 (1981)
86. L. Shebanovs, K. Borman, W.N. Lawless, A. Kalvane, Ferroelectrics **273**, 137 (2002)
87. W.N. Lawless, C.F. Clark, Phys. Rev. B **36**, 459 (1987)
88. Y. Bai, G.-P. Zheng, K. Ding, L. Qiao, S.-Q. Shi, D. Guo, J. Appl. Phys. **110**, 094103 (2011)
89. H. Kishi, Y. Mizuno, H. Chazono, Jpn. J. Appl. Phys. **42**, 1 (2003)
90. H.J. Carslaw, J.C. Jaeger, *Conduction of Heat in Solids*, 2nd edn. (Oxford University Press, New York, 1959)
91. G. Wehmeyer, T. Yabuki, C. Monachon, J. Wu, C. Dames, Appl. Phys. Rev. **4**, 041304 (2017)
92. R.I. Epstein, K.J. Malloy, J. Appl. Phys. **106**, 064509 (2006)

93. Y. Wang, D.E. Schwartz, S.J. Smullin, Q. Wang, M.J. Sheridan, J. Microelectromech. Syst. **26**, 580 (2017)
94. J. Cho, C. Richards, D. Bahr, J. Jiao, R. Richards, J. Micromech. Microeng. **18**, 105012 (2008)
95. R. Ma, Z. Zhang, K. Tong, D. Huber, R. Kornbluh, Y.S. Ju, Q. Pei, Science **357**, 1130 (2017)
96. W. Kobayshi, T. Teraoka, I. Terasaki, Appl. Phys. Lett. **95**, 171905 (2009)
97. T. Majdi, S. Pal, I.K. Puri, Int. J. Therm. Sci. **117**, 260 (2017)
98. T.L. Bergmann, A.S. Lavine, F.P. Incropera, D.P. Dewitt, *Fundamentals of Heat and Mass Transfer*, 7th edn. (Wiley, Hoboken (NJ, 2011)
99. D. Guo, J. Gao, Y.-J. Yu, S. Santhanam, A. Slippey, G.K. Fedder, A.J.H. McGaughey, S.-C. Yao, Int. J. Heat Mass Transf. **72**, 559 (2014)
100. D. Saranya, A.R. Chaudhuri, J. Parui, S.B. Krupanidhi, Bull. Mater. Sci. **32**, 259 (2009)
101. C. Aprea, A. Greco, A. Maiorino, C. Masselli, Int. J. Refrig **69**, 369 (2016)
102. W. Geng, Y. Liu, X. Meng, L. Bellaiche, J.F. Scott, B. Dkhil, A. Jiang, Adv. Mater. **27**, 3165 (2015)
103. X.-C. Zheng, G.-P. Zheng, Z. Lin, Z.-Y. Jiang, Thin Solid Films **522**, 125 (2012)
104. Y. Hou, L. Yang, X. Qian, T. Zhang, Q.M. Zhang, Appl. Phys. Lett. **108**, 133501 (2016)
105. S. Crossley, J.R. McGinnigle, S. Kar-Narayan, N.D. Mathur, Appl. Phys. Lett. **104**, 082909 (2014)
106. W. Sato, Heat transfer and thermal engineering, in *ASME 2013 International Mechanical Engineering Congress and Exposition*, vol. 8B (San Diego, California, USA, 2013), pp. 15–21
107. M.P. Hehlen, A.H. Mueller, N.R. Weisse-Bernstein, R.I. Epstein, in *Proceedings of SPIE 8638, Laser Refrigeration of Solids VI.*, ed. by R.I. Epstein, D.V. Seletskiy, M. Sheik-Bahae (SPIE, Bellingham (WA), 2013), p. 86380D
108. Y.D. Wang, S.J. Smullin, M.J. Sheridan, Q. Wang, C. Eldershaw, D.E. Schwartz, Appl. Phys. Lett. **107**, 134103 (2015)
109. D. Sette, A. Asseman, M. Gérard, H. Strozyk, R. Faye, E. Defay, APL Mater. **4**, 091101 (2016)
110. Y. Liu, X.-P. Peng, X. Lou, H. Zhou, Appl. Phys. Lett. **100**, 192902 (2012)

Colossal Humidoresistance Inducement in Magnesium Ferrite Thin Film Led to Green Energy Device Invention: Hydroelectric Cell

Jyoti Shah, Rekha Gupta, and R. K. Kotnala

Abstract The scarcity of energy is a major constraint in economic growth of any country. Day-by-day increasing demand of energy is deteriorating our environment quality. In order to combat environmental pollution threat, clean and green energy sources are critically enforced. Naturally occurring relative humidity has been probed in the form of humidity sensor. Highly resistive ceria doped magnesium ferrite thin film exhibited a colossal decrease in resistance of the order of 10^7 with only environmental humidity change from 10 to 95%RH. Such huge colossal humidoresistance of magnesium ferrite paved way to research on energy harvesting from water molecule dissociation at room temperature. Nanoporous and oxygen-deficient lithium substituted magnesium ferrite has been processed to make it highly sensitive towards water molecule dissociation into OH^- and H^+ ions. Electrochemistry has been adapted to collect these dissociated ions by two dissimilar electrodes zinc anode and silver inert cathode. The redox reactions on these electrodes generated power and the device is named 'Hydroelectric Cell'. The working principle of hydroelectric cell has been also validated in other ferrite and different metal-oxides such as Fe_3O_4, Fe_2O_3, SnO_2, TiO_2, ZnO, Al_2O_3, MgO and SiO_2. The redox reactions at electrodes of hydroelectric cell provide eco-friendly and commercially viable byproducts hydrogen and zinc hydroxide.

1 Introduction

Relative humidity (%RH) is an attribute of the environment, most generally recognized by its important role as a determinant in climate, weather, human comfort and commercial goods. Humidity is frequently apparent by its effect on common hygroscopic materials such as wood, textiles, paper and foodstuffs. The measurement and control of humidity play an important role in pharmaceuticals, engineering, meteorology and agriculture. Thus, monitoring and control of relative humidity is of utmost important to maintain the quality of industrial production and its energy

J. Shah · R. Gupta · R. K. Kotnala (✉)
CSIR—National Physical Laboratory, New Delhi, 110 012, India
e-mail: rkkotnala@gmail.com

S. Kumar and D. K. Aswal (eds.), *Recent Advances in Thin Films*, Materials Horizons: From Nature to Nanomaterials, https://doi.org/10.1007/978-981-15-6116-0_13

saving. Humidity is monitored by its effect rather than measured directly since moisture content of air is typically only 1% by weight. The mass of water vapour is difficult to measure thus a simple measurement, relative humidity is used. Relative humidity (%RH) is the percentage of the amount of water that the air can hold at a given temperature. The following equation is used to calculate the percent relative humidity.

$$\%\mathrm{RH} = \frac{P_a}{P_s} \times 100$$

where P_a = actual pressure of water vapour

P_s = saturated pressure of water vapour.

For smart technologies, fast and a wide range of humidity sensors are on high demand. For such smart electronic sensors highly sensitive metal-oxides are needed that change their resistance or capacitance quickly with humidity. In resistive type sensor, surface resistivity of metal-oxide changes quickly with varying humidity present in air. The fundamental requirement for water vapour sensing by metal-oxide is surface oxygen defects and porous microstructure. The surface resistance of metal-oxide decreases due to protonic conduction in physisorbed water layer over chemisorbed OH^- layer. Magnesium ferrite has been processed in such a way to create oxygen vacancies and porosity for sensing high humidity [1]. The change in resistance of defective magnesium ferrite by lithium substitution has been observed three order of magnitude from 10 to 90%RH at room temperature. Humidity sensitivity of magnesium ferrite has been abundantly improved by translating it to thin film [2]. Humidity sensing is a surface phenomenon thus water vapour sensing is pronounced in thin films due to high oxygen vacancies generated at film surface by controlled oxygen partial pressure. A colossal ~10^7order decrease in surface resistance of magnesium ferrite thin film for 10–95%RH has been observed by Ce doping [3]. The gigantic increase in surface conduction leads to an idea of current collection from humidity sensor. The concept of energy harvesting from water vapour present in air by highly sensitive magnesium ferrite thin film paved way to do R & D on 'Humidity Cell'. Ultimately a breakthrough achieved in 2015 when a green energy device, 'Hydroelectric Cell' has been invented [4, 5]. In hydroelectric cell (HEC) highly sensitive surface towards water molecule, Li-substituted magnesium ferrite has been fabricated with two dissimilar electrodes zinc and silver to collect the dissociated OH^- and H^+ ions as shown in Fig. 1. Hydroelectric cell is the rare combination of material science, nanotechnology and electrochemistry. Hydroelectric cell generates electricity by water molecule dissociation without electrolyte/photon/temperature followed by collection of ions.

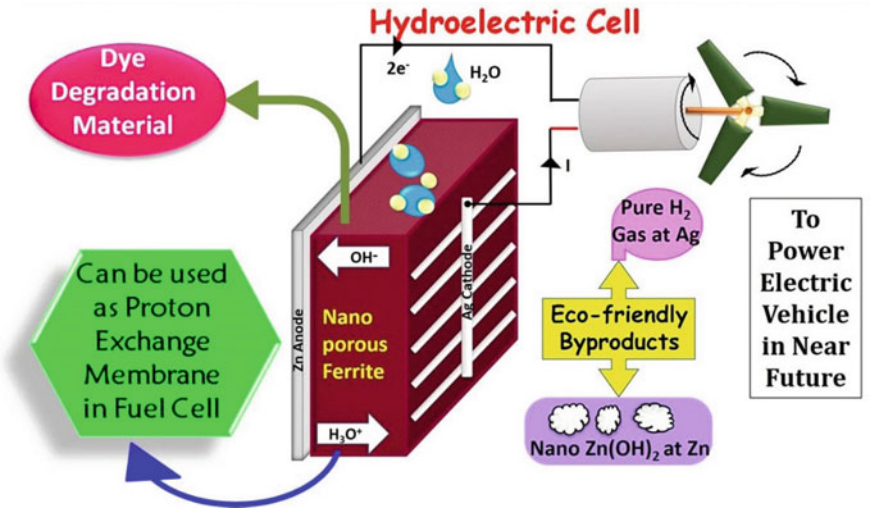

Fig. 1 Schematic diagram of Hydroelectric cell representing its configuration and various applications

2 Change in Resistance of Magnesium Ferrite with Relative Humidity (Humidoresistance)

The primary characteristic of humidity sensitive materials is their surface sensitivity for H_2O adsorption and porous microstructure. A broad variety of materials from conducting to semiconducting oxides and polymers has been explored for humidity sensor applications [6, 7]. The main limitations of past studied humidity-sensitive materials have been exhitbiting their less sensitivity at low humidity, water solubility at high humidity, drift in overall impedance and hysteresis modifications. Spinel ferrites have shown better sensitivity towards humidity and gas sensing due to their inherent defect chemistry and porous microstructure [8]. Magnesium ferrite ($MgFe_2O_4$) is an attractive spinel ferrite for humidity sensing applications due to its oxygen defects, porous microstructure and high electrical resistivity (~10^7 Ωcm) that support large humidity variations. The inherent imbalance between metal cations and non-stoichiometric presence of oxygen, increases the surface sensitivity of $MgFe_2O_4$ towards humidity.

The humidity sensitive properties of $MgFe_2O_4$ and doped $MgFe_2O_4$ mainly with Li, Ce, Pr, Sn, Mo, Ni and Mn have been investigated by many groups [1, 9–12]. The purpose of doping has been to promote porosity, defect density and decrease in the ceramic grain size. Increase in sensitivity of $MgFe_2O_4$ towards low humidity has been observed by CeO_2 addition in magnesium ferrite [8]. It was observed that surface sensitivity enhances due to oxygen vacancy promotion. A good linearity of log R in a wide relative humidity (RH) range was obtained by 4 wt% cerium oxide addition. The effect of Li doping on $MgFe_2O_4$ was found to promote nano size grain

formation, increased surface charge density and smaller pore size distribution [1]. At 20 mol% lithium doping in $MgFe_2O_4$, the highest humidity sensitivity has been observed. In one of the studies, Pr doping in $MgFe_2O_4$, resulted in least humidity hysteresis over the entire range of RH due to fast complete desorption [10]. Co-doping of Sn and Mo in $MgFe_2O_4$ led to nanocrystalline microstructure with high surface area and enhanced humidity sensitivity [11]. Change in surface resistance of material due to humidity present in air is named as humidoresistance [13].

3 Colossal Humidoresistance (CHR)

Resistive type humidity sensors measure change in humidity and translate it into change in electrical resistance of the material surface [14]. Ceramic humidity sensors based on porous metal-oxides and semiconductors adsorb moisture present in air and form an immobile chemisorbed layer of OH^- ions on the surface of material. Further, adsorption of water leads to formation of physiosorbed layer of water molecules leading to formation of H_3O^+ and OH^- ions on material surface. Ionic conduction occurs via Grotthuss chain reaction when H_3O^+ releases a H^+ ion to neighbouring water molecule, which accepts it while releasing another proton and so forth [15]. A significant drop in resistance (~10^7), colossal humidoresistance (CHR) due to high surface conduction by humidity has been observed in ceria added magnesium ferrite thin films.

Colossal humidoresistance (CHR) $= \frac{R(0\%\text{RH}) - R(95\%\text{RH})}{R(95\%\text{RH})}$, where R(0%RH) is surface resistance of sample at 0% relative humidity and R(95%RH) is resistance of sample at 95% relative humidity.

3.1 Magnesium Ferrite Thin Film as CHR Sensor

Ceria doped magnesium ferrite thin film exhibited remarkable sensitivity for atmospheric humidity [3]. Oxygen deficient, porous thin films of pure and 1 wt% cerium doped magnesium ferrite was fabricated by pulsed laser deposition technique. Since humidity sensitivity is primarily a surface phenomenon, humidoresistance has been observed to be a pronounced effect in thin films [16]. Cerium doping in $MgFe_2O_4$ (Ce:MgF) thin film resulted in large enhancement in defects and oxygen vacancies in film microstructure leading to extensive adsorption of water vapours on surface. Pure magnesium ferrite (MgF) thin film showed three-order decrease in resistance from 230 GΩ at 10%RH to 184 MΩ at 95%RH, while 1 wt% Ce:MgF thin film represented 1.8 TΩ at 10%RH which deceased to 754 KΩ at 95%RH exhibiting approximately a seven-order decrease in resistance. These results correspond to CHR ~2.8×10^3 in pure MgF thin film while CHR ~3×10^6 in Ce:MgF thin film. CHR plots of pure and cerium doped MgF thin films are shown in Fig. 2. It was observed that cerium doping induced increase in surface defects and porosity of doped MgF

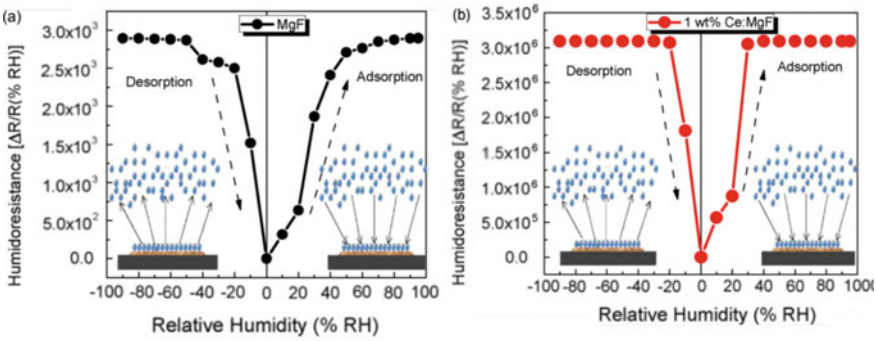

Fig. 2 **a** CHR response of $MgFe_2O_4$ thin film and **b** Ce doped $MgFe_2O_4$ thin film. Reproduced from Kotnala et al. [3]

films resulting in increased water adsorption and chemidissociation on Ce:MgF film surface. In addition to surface ionic conduction, higher humidity results in capillary condensation inside active pores of Ce:MgF thin film. High activity of ceria segregated at grain boundaries of these nanopore surfaces promote conduction via physiosorbed layers of water resulting in colossal response of humidoresistance in Ce:MgF film as compared to pure MgF film.

4 Conceptualization of CHR Sensor into Electricity Generation Emerged as Revolutionary Path Breaking Hydroelectric Cell

The colossal humidoresistance observed in Ce doped MgF thin film exhibited the potential of ferrite material to dissociate water molecules at room temperature without any external stimuli. CHR paved way to do research on energy harvesting by humidity present in air. In order to implicate this concept, highly sensitive composition 20% Li-substituted $MgFe_2O_4$ (Li: MgF) was optimized to synthesize it 30% porous and 165 m^2/g specific surface area (Kotnala et al. 2016). The average pore diameter ~4.2 nm and total pore volume ~0.74 cc/g were detected by brunauer–emmett–teller (BET) surface area measurement technique. Lithium substitution was found to enhance sensitivity of MgF pellet towards water molecule adsorption and chemidissociation. Electrode chemistry has been adopted to capture ions produced in CHR sensor realized into hydroelectric cell. The water molecule chemidissociation and physidissociation phenomenon are the basic mechanism in both devices. In CHR sensor, protonic conduction takes place entirely on the surface of Ce:MgF film. The protons were collected by silver (Ag) electrodes deposited on top film surface. In hydroelectric cell, for collection of OH^- and H^+ ions two dissimilar zinc (Zn) and silver (Ag) electrodes were attached on opposite surface of Li:MgF square pellet.

In the presence of dissociated OH^-/H^+ ions on cell surface, an electrode potential (0.98 V) is generated due to redox reactions on Zn/Ag electrode which force the ions to flow across the cell pellet. Proton (H^+) conduction takes place on the surface of cell via physiosorbed H_2O molecules towards Ag electrode similar to CHR sensor. Unlike to CHR sensor, hydroxide (OH^-) ions are forced to move through the pellet towards Zn plate under electrode potential in hydroelectric cell. These OH^- ions react with Zn plate to produce $Zn(OH)_2$ by releasing two electrons in external circuit then collected by Ag electrode to release H_2 gas. The electron flow in external circuit leads to current generation by water dissociation.

4.1 Spontaneous Water Dissociation by HEC at Room Temperature

Hydroelectric cell (HEC) works on the principle of water molecule dissociation on nanoporous oxygen-deficient ferrite/oxide pellet surface. Polar water molecules are initially attracted towards the surface oxygen vacancies and unsaturated metal cations. As soon as they approach defects, chemidissociation of water molecules occurs to form the first layer of hydroxide ions. Chemidissociated surface hydroxyl ions further provide high surface charge to physiosorbed water molecules and proton hops in physisorbed layer. Subsequently, the hopping protons get trapped inside the open nanopores present on and inside the material surface. Large concentration of protons inside nanopores provide enough electrostatic potential to further physidissociate water molecules spontaneously. Thus, dissociation of water is sustained by the ferrite material.

4.1.1 Role of Oxygen Defects and Nanoporosity

Li-substituted magnesium ferrite (MgLiF) HEC synthesis process was optimized to avail unsaturated surface cations, oxygen vacancies and nanopores deriving maximum chemidissociation of water on the surface of cell pellet. Substitution of smaller monovalent Li ion at divalent Mg ion site in $MgFe_2O_4$ matrix results in a negative charge at defect site. Oxygen vacancies are generated to maintain charge equilibrium along with local lattice distortions. Distortion in $MgFe_2O_4$ spinel lattice due to strain induced by lithium substitution has been visualized in captured lattice images by high resolution transmission electron microscopy (HRTEM) [4]. Moiré fringe pattern was obtained due to overlapped interference of strained fringes of defects in ferrite lattice. It was observed from HRTEM images that most defective octahedral lattice (311) planes were exposed on the surface of MgLiF particles. The octahedral sites and grain boundaries were observed to be the most defective due to higher enthalpy of Li ion ($E_{Li}^{+} \sim -41$Kj/mol) to occupy octahedral site as compared to Mg ($E_{Mg}^{+} \sim -25.1$ kJ/mol) and Fe $\left(E_{Fe}^{+} \sim -22.4\text{kJ/mol}\right)$ ions

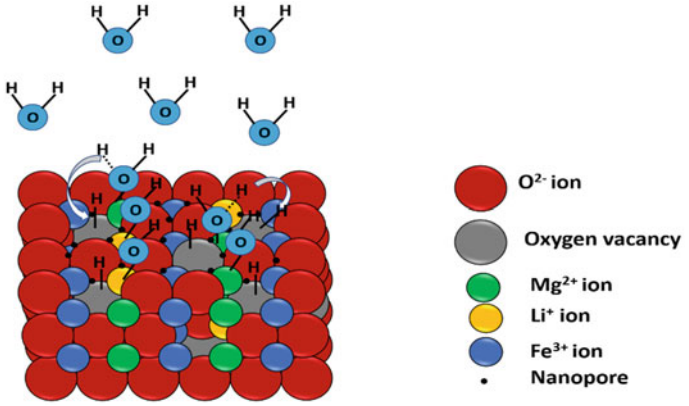

Fig. 3 Water molecule adsorption and dissociation on unsaturated Mg, Li ions and oxygen vacancies in (111) plane of $Mg_{0.8}Li_{0.2}Fe_2O_4$ spinel lattice

[17]. This oxygen-deficient and octahedrally coordinated unsaturated surface plane adsorbs H_2O molecules and chemidissociate them into H^+ and OH^- ions via bonding of H^+ ion to metal cation and OH^- ion gets hitched to adjacent oxygen vacancy site. This first chemisorb layer of H^+/OH^- ions on MgLiF surface further attracts more water molecules to get physiosorbed via hydrogen bonding and multiple physiosorbed layers of H_2O molecules form on MgLiF surface. The water molecule adsorption and dissociation mechanism on (111) surface plane of MgLiF is systematically shown in Fig. 3. The dissociated H^+ ions transport towards Ag electrode via hopping through hydrogen bonded network of physiosorbed H_2O molecule by Grotthus mechanism. Each H_2O molecule accepts one H^+ and forms H_3O^+ ion, this H_3O^+ ion further releases a proton to next physiosorbed H_2O molecule and H^+ ion hops on physiosorbed H_2O molecules. On the other side, OH^- ions move towards Zn anode via capillary diffusion by interconnected pores and grain boundaries. Dissociated H_3O^+ ions also get trapped inside the nanopores resulting in a strong electrostatic potential developed inside nanopore. A typical cylindrical nanopore of dimension 100 nm length and 50 nm diameter produces electrostatic field of the order of E ~2.16 $\times$ 10^4 V/cm calculated by electrostatic Gauss theorem. This electric field is sufficient enough to further dissociate the physiosorbed water molecules spontaneously and produce a huge amount of dissociated H^+ and OH^- ions. The collection of the dissociated ion via respective Ag cathode and Zn anode results in current flow in an external circuit.

4.1.2 Direct Imaging of Surface H^+/OH^- Ions by Electrostatic Force Microscopy (EFM)

Chemidissociation of water molecules into H^+ and OH^- ions on MgLiF surface generates a space charge layer of ions on pellet. Over chemidissociated ions in the

topmost layer of ferrite, is physisorbed water layer in which proton hops to adjacent water molecules. The local electric field gradient generated due to distribution of ions at surface was evidently mapped by charged probe in electrostatic force microscopy (EFM). The EFM image of wet HEC pellet with 1 μm^2 scanning area showed a charged MgLiF surface due to presence of dissociated H^+ and OH^- ions. The cantilever tip was biased simultaneously with +0.6 and −0.6 V dc voltage, kept lesser than water molecule dissociation voltage, 1.23 V at room temperature. The EFM images of wet MgLiF pellet are shown in Fig. 4. It was observed that on reversing polarity of DC bias from positive to negative, a clear colour contrast change in EFM image is produced demonstrating attractive and repulsive forces generated by surface charge. The electric field gradient generated by the electrostatic surface charge changes the oscillating frequency of cantilever and induces a phase shift as shown in EFM images. On applying −0.6 V bias voltage, a bright contrast image demonstrated the presence of attractive forces due to presence of hydronium ions on physiosorbed water layers. The same scanning area demonstrated a repulsive force and darker image when +0.6 V bias voltage was applied. These results were direct evidence of dissociation of water molecules on the surface of MgLiF pellet.

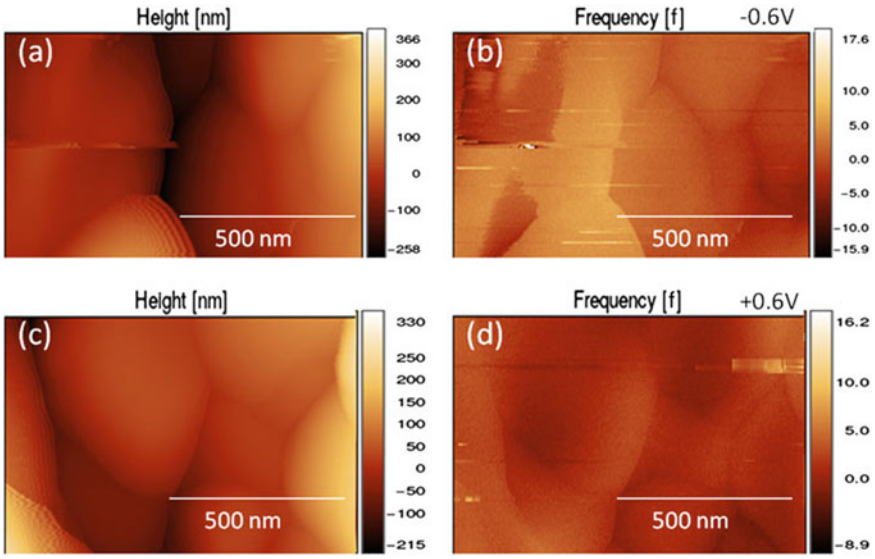

Fig. 4 Atomic force microscopic images (**a**) and (**b**) showing topography of the pellet surface along with colour bar in nanometer and corresponding area electrostatic force microscopy images with a dc bias of −0.6 (**c**) and +0.6 V (**d**) at tip, respectively. Colour bar shows developed voltage in volts. Reproduced from Kotnala et al. [4]

4.2 Ion Collection by Dissimilar Electrodes

Silver-Zinc (Ag-Zn) electrode chemistry was used to collect the dissociated ions for direct current flow in an external circuit. Silver electrode was used to collect H^+ by reduction reaction and zinc electrode collected OH^- ions by oxidation reaction. Comb patterned silver cathode of 0.1 μm thickness was initially sputtered and screen printed at later stage on one face of square pellet while opposite face was covered with 0.3 mm Zn plate as anode. The silver electrode acted as inert cathode due to the absence of Ag ions, while zinc played anode role due to oxidation reaction occurring on it. At anode, formation of zinc hydroxide releases two electrons by the reaction: $Zn + 2\ OH^- = Zn(OH)_2 + 2e^-$, these electrons flow towards Ag cathode in external circuit. Hydronium ion combines with these electrons at Ag electrode resulting in nascent hydrogen by the reaction: $2H_2O + 2e^- = H_2\uparrow + 2H_2O$, where hydrogen gas evolved at Ag cathode. The electrons flow from Zn to Ag in external circuit and ions move through cell pellet acting as a solid hydronium exchange electrolyte to respective electrodes. To confirm electrochemical reaction in HEC, reaction products ε-$Zn(OH)_2$ and ZnO obtained in water were confirmed by XRD analysis. Hydrogen gas released at Ag electrode was confirmed by using a hydrogen detector MQ sensor in an air tight vessel containing three operating HEC's. A small (1-inch square) and large (2-inch diameter) pellet of $Li_{0.2}Mg_{0.8}Fe_2O_4$ material coated with comb patterned silver electrodes of 1 μm thickness on one surface and opposite surface covered with zinc electrode of 3 mm thickness is shown in Fig. 5.

4.2.1 Reaction Mechanism

The redox reactions occurring at cathode and anode in hydroelectric cell are described below

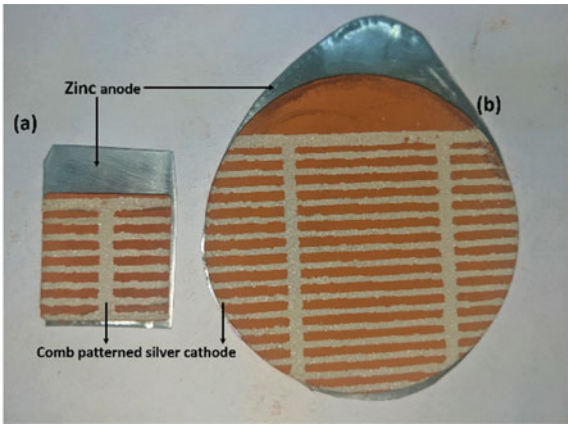

Fig. 5 MgLiF HEC's of **a** 1-inch square pallet, **b** 2-inch diameter circular pallet

Water dissociation at MgLiF surface:

$4H_2O \leftrightarrow 2OH^- + 2H_3O^+$

Reduction reaction at cathode (Ag):

$2H_3O^+ + 2e^- \rightarrow H_2 \uparrow + 2H_2O$

Cathode reaction potential ($E_{cathode}$) $= +0.22$ V

Oxidation reaction at anode (Zn):

$2OH^- + Zn \rightarrow Zn(OH)_2 + 2e^-$

Anode reaction potential (E_{anode}) $= -0.76$ V

The overall reaction potential:

$\boldsymbol{E_{cell} = E_{cathode} - E_{anode}} = 0.22 - (-0.76) = 0.98$ V

Gibb's free energy of reaction is given by: $\Delta G = -n\,F\,E_{cell}$, where n is number of electrons involved in reaction, F is faraday constant = 96.5 kJ/mol and E_{cell} is cell voltage = 0.98 V.

Theoretical Specific energy of HEC is −189.08 kJ/mol equating to 802.77-watt hr/kg. Byproducts of the cell reaction H_2 gas as well as $Zn(OH)_2$ nanopowder are environment friendly.

4.2.2 Eco-friendly Byproducts of HEC

The eco-friendly operation of green energy device hydroelectric cell is further aided by its non-hazardous and toxin-free byproducts. The two byproducts during power generation from a hydroelectric cell are highly pure hydrogen (H_2) gas and zinc hydroxide nanoparticles. Both byproducts are safe for environment and having high commercial values. Whereas, highly pure H_2 gas can be collected for clean fuel applications. $Zn(OH)_2$ nanoparticles can be easily converted into ZnO nanoparticles which is on high demand in semiconducting, gas sensing and optoelectronic applications.

4.3 Electrical Power Generation by Hydroelectric Cell Device

Hydroelectric cell acts as a small portable source of direct power generator by water as a fuel. A one-inch square ferrite HEC presently generates short-circuit current (I_{sc}) 70 mA and open-cell voltage (V_{oc}) 0.98 V. The output current in hydroelectric cell is dependent upon surface area of pellet. Two-inch square ferrite pellet is presently generating 110 mA short-circuit current and 0.9 V open-cell voltage. The voltage–current characteristics and impedance response of hydroelectric cell manifest ionic current flow in the pellet and at electrode interface.

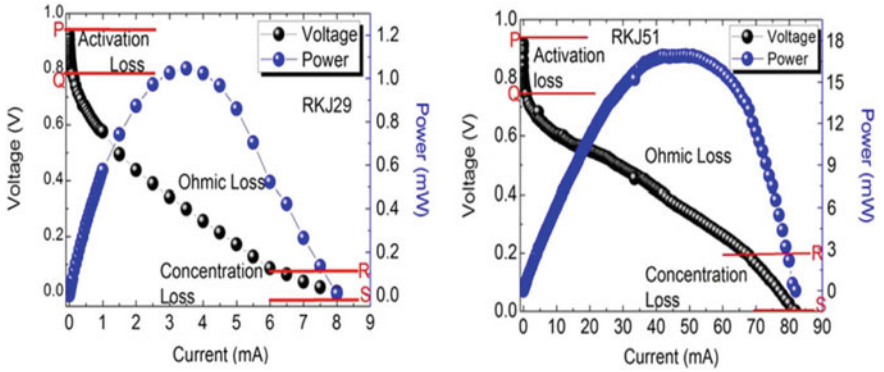

Fig. 6 Polarization curve and energy generated by RKJ29 & RKJ51 cell dipped in deionized water. Reproduced from Kotnala et al. [4]

4.3.1 Operating Characteristics of HEC

The operating characteristics of HEC were examined by standard V–I polarization plots representing cell voltage behaviour with operating current. Hydroelectric cell square pellets were prepared in two different sizes RKJ29 of surface area ~4.8 cm^2 and RKJ51of surface area ~17 cm^2. The different polarization regions of cell operation namely activation polarization, ohmic polarization and concentration polarization were observed as shown in Fig. 6. The polarization curve was subdivided into three regions PQ, QR and RS. The actual open-circuit voltage of RKJ29 was V_{oc} ~0.98 V and for RKJ51 ~0.92 V. Activation loss region PQ is the voltage required to overcome the activation potential barrier at electrode interface and for reaction occurring at MgLiF surface. A linear drop in voltage QR represented internal ohmic resistance for ionic current flow through the cell primarily due to high resistivity of ferrite, DI water and electrode contact resistance. Concentration loss region RS was dominated by mass transport limitation due to high concentration of ions at high current density. The maximum current obtained by RKJ29 cell (I_{sc}) ~8 mA and RKJ51 cell I_{sc} ~82 mA corresponded to peak out power P_{out} ~7.8 mW for RKJ29 and P_{out} ~74 mW for RKJ51. The dynamic behaviour of MgLiF HEC was analyzed by electrochemical impedance spectroscopy. Hydroelectric cell turns chemical energy into electrical energy with an efficiency of about 90%. In fact, it is the most efficient way to produce electricity by water molecule dissociation.

4.3.2 Ionic Conduction by Electrochemical Impedance Spectroscopy

Electrochemical impedance spectroscopy provides a direct insight of dynamic conduction mechanism by different charges like ions, electrons or interfacial charges present in a medium. Different relaxation times of different charge carriers result in a unique combination of resistance–capacitance, RC element where $\tau = RC$ is time

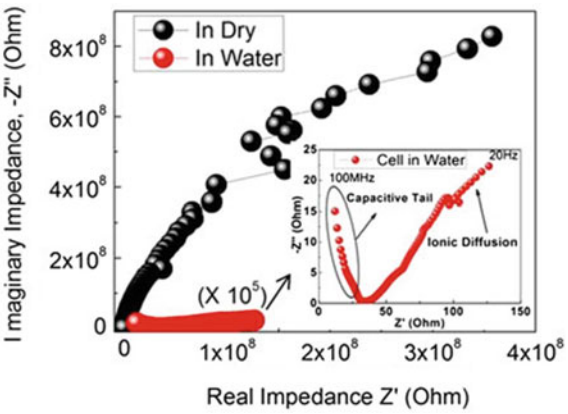

Fig. 7 Nyquist plot of RKJ29 cell in dry argon and in water (inset) showing low-frequency tail as a result of H_3O^+ ion diffusion and high-frequency capacitive tail as a result of formation of passive film $Zn(OH)_2$ at Zn anode. Reproduced from Kotnala et al. [4]

constant. Separate semicircles are observed for each RC circuit in different frequency bands representing a unique conduction mechanism. The impedance response of hydroelectric cell in dry and wet state is shown in Fig. 7. A dry cell (RKJ29) showed high impedance ~10^8 Ω while ionic current flow on the surface of HEC by water molecule dissociation reduced the resistance of ferrite pallet from 10^8 to 10^2 Ω. Low-frequency tail due to Warburg diffusion of H_3O^+ ions articulated surface ionic conduction at Ag electrode. On the other hand, high-frequency capacitive arc resulted from passive layer of $Zn(OH)_2$ formation at Zn electrode by reaction of Zn with OH^- ions. These plots also confirmed the reaction of Zn electrode with OH^- ions and H^+ ion conduction at Ag electrode.

5 Green Energy Harvesting from Water Dissociation

Energy plays a key role to support expanding economy and developing infrastructure of modern world. The rapid depletion of conventional energy resources based on oil, coal, natural gas and increasing energy demand has encouraged the intensive research for more efficient energy technologies that are self-replenished continuously by nature. Utilization of wind, hydrothermal and geothermal energy requires large scale power plants to set up. Among other green energy resources solar and fuel cells technologies are growing fast. However, these technologies are expensive and involve tedious manufacturing process. Alternative promising and facile green energy resources are immensely required for future energy portfolio. In this direction, many attempts have been made by researchers to produce green energy by water molecule splitting. The state of art of water splitting has been mainly focused to produce hydrogen by electrocatalysis, photocatalysis and photobiological processing [18, 19]. Since water dissociation is an endothermic reaction, input energy and hefty processing is required for hydrogen production by water splitting.

Table 1 A comparison chart of power output of different water batteries

Battery type	Open circuit voltage (V_{OC}) V	Output power density (P_{out}) W/cm^2	Reference
Zirconia planer battery	–	2.3×10^{-10}	Doroshkevich et al. [22]
Mixed entropy battery	0.1	13.8×10^{-6}	Mantia et al. [23]
Soil battery	0.24	43×10^{-6}	Meng et al. [21]
Sea water battery	0.4–0.5	2×10^{-3}	Hasvold [50]
$Li_{0.2}Mg_{0.8}Fe_2O_4$ hydroelectric cell	0.92	4.3×10^{-3}	Kotnala et al. [4]
Graphene oxide battery	0.7	0.4	Wei et al. [20]

Till now very few attempts have been focused on spontaneous dissociation of water to produce green energy but the output energy has been obtained very low [20–25]. Graphene oxide-based battery like planer energy source was demonstrated by Di Wei producing open-circuit voltage (V_{OC}) of 0.7 V and power output (P_{out}) ~0.4 W/cm^2 [20]. Cement-based ceramic batteries have been reported to produce V_{OC} ~0.7 V and P_{out} ~1.4 μW/cm^2 [21]. Zirconia nanoparticles-based planer battery has been reported to produce P_{out} ~2.3 μW/cm^2 [22]. Saltwater batteries and seawater batteries have also been reported utilizing K^+ and Na^+ ions for conduction [23–25]. The major drawback of all these batteries is their low output power and electrolytic action. A revolutionary invention of harvesting green energy from water splitting without electrolyte, acid/alkali, temperature or any light radiation has been achieved by Dr. R K Kotnala & Dr. Jyoti Shah from hydroelectric cell (HEC) [4]. Hydroelectric cell (HEC) is fabricated using low-cost raw material lithium substituted magnesium ferrite ($Mg_{0.8}Li_{0.2}Fe_2O_4$) besides easy processing step and a common setup. This cell simply runs by dissociation of water molecules at room temperature without using any electrolyte or light radiation. HEC of area 17 cm^2 generated short-circuit current of 82 mA and emf of 92 mV with maximum output power of 4.3 mW/cm^2. This value is typically four orders higher than reported value of output power 1.4 μW/cm^2 produced by water in ceramic matrix and 2.3 μW/cm^2 by water in zirconia matrix [21, 22]. This cell possess immense potential to replace the conventional renewable resources like solar cell and fuel cell to generate electricity without any hazards to environment. A key comparison of various water-based electricity generation processes is illustrated in Table 1.

6 Fabrication of Different Metal-Oxide Hydroelectric Cells for Harvesting Green Energy from Water

Metal-oxides are abundantly available in nature and majorly are non-toxic. These materials play a promising role in emerging energy technologies by the virtue of their

intriguing physical and chemical properties. These materials offer vital technological utility in new generation solid-state sensors, antibacterial agents, electrochemical reactions and solar power generation [26–28]. The process of water interaction with metal-oxide surface has been focused on various applications in electrochemistry, catalysis, geology and corrosion studies. The complex surface morphology of metal-oxides comprises various local structural phases, undercoordinated surface atoms, defects and dangling bonds. Oxygen vacancies have been the most common point defects observed at oxide surface. The increase in surface reactivity of metal-oxides by oxygen vacancies has been systematically utilized in sensor, catalytic and spintronic applications but recently Kotnala et al. reported hydroelectricity generation as a versatile property of metal-oxides [29]. Energy generation by hydroelectric cell using water molecule dissociation on oxygen deficient nanoporous ferrite surface is integrated and extended to various metal-oxides. Water dissociation at metal-oxide surface is found to be strongly influenced by defect density, Lewis acid strength (electronegativity) of metal cation and porosity of the sample surface. Metal-oxides have been explored in order to obtain high power output from hydroelectric cell due to their low-cost availability and high surface reactivity. Green electricity generation has been evidenced by different metal-oxide fabricated as hydroelectric cell.

6.1 Magnetite HEC

Magnetite (Fe_3O_4) commonly occurs in the earth's uppermost mental and soil. Inverse spinel Fe_3O_4 is one of the most important ferrimagnetic materials of magnetic industry. The ionic structure of magnetite can be represented as $[Fe^{3+}]_t\,[Fe^{3+}\,Fe^{2+}]_o\,O_4^{2-}$, where Fe^{3+} occupies half tetrahedral (t) and half octahedral (o) sites and Fe^{2+} occupies octahedral sites in inverse spinel (Fd3m) cubic structure [30]. Naturally occurring oxygen vacancies and valence fluctuations of Fe^{3+} and Fe^{2+} ions at magnetite surface attract water molecules towards its surface and chemidissociates it into H^+ and OH^- ions. A highly efficient hydroelectric cell synthesized by magnetite nanoparticles was reported by Jain et al. [31]. Oxygen deficient Fe_3O_4 nanoparticles of average 11 nm size were prepared by chemical coprecipitation method. Mesoporous magnetite HEC surface was analyzed consisting of pores of average diameter ~9.81 nm and specific surface area ~89.78 m^2/g by BET surface area study. The average porosity of Fe_3O_4 HEC was calculated to be 46% by volumetric analysis. Spin density of ~8.24×10^{24} spins/g was calculated by electron spin resonance (ESR) spectra indicating high density of unsaturated surface bonds responsible for H_2O chemidissociation on HEC surface. Further physidissociation of H_2O molecules by electric field developed inside the nanopores due to trapped ions and collection of dissociated ions by zinc anode and silver cathode resulted in electric current flowing in external circuit. This mesoporous magnetite HEC was found to deliver peak output power (P_{out}) ~38.5 mW and open-circuit voltage (V_{oc}) ~0.77 V. The short-circuit current (I_{sc}) was obtained 50 mA in a typical 4.8 cm^2 cell.

6.2 Hematite HEC

Reddish brown hematite (α-Fe_2O_3) is a very important iron ore found in sedimentary rocks. Hematite has a similar structure to corundum where Fe^{3+} ions are densely packed in an octahedral coordination with oxygen ions in hexagonal close packing [32]. The structure can be thought of stackings of octahedrally coordinated Fe^{3+} sheets between two close-packed layers of oxygen ions. Interaction of water molecule with hematite surface has been defining the surface chemistry of these materials, whereas heterocatalytic dissociation of H_2O molecule has been observed energetically favourable as compared to molecular adsorption [33]. Preferable water molecule dissociation at octahedral Fe^{3+} sites led to devising a cheap hematite-based hydroelectric cell for green electricity generation reported by Jain et al. [34]. The hematite nanoparticles were prepared by annealing magnetite nanoparticles in inert atmosphere (Ar gas) at 500 °C for 2 h. High oxygen vacancy concentration was obtained by annealing Fe_3O_4 nanoparticles in Ar gas as compared to air. Average pore size ~16.8 nm and specific surface area ~72.2 m^2/g was analyzed by BET surface area measurement in 27.4% porous hematite HEC pellet. Hematite HEC delivered peak output power (P_{out}) ~27.6 mW and open-circuit voltage (V_{oc}) ~0.92 V. The short-circuit current I_{sc} ~30 mA was obtained in a typical 4.8 cm^2 hematite cell.

6.3 Tin Oxide HEC

Tin oxide (SnO_2) has been widely used in humidity and gas sensing applications due to its high surface reactivity and semiconducting nature [35]. SnO_2 is highly sensitive to defects and dopants which increase surface conduction by inducing charge carriers. Low defect formation energy, high electronegativity (1.96) of Sn atom and easy reduction of Sn^{4+} to Sn^{2+} due to non-stoichiometry further enhances catalytic activity of surface to attract water molecules. Water molecules get chemidissociated at Sn^{4+} atom adjacent to defect site and form terminal Sn-OH bond via proton transfer to nearby oxygen vacancy. Tin oxide-based hydroelectric cell was synthesized by simple solid-state reaction method [29]. The average pore size of 3.4 nm and specific surface area ~4.9 cm^2/g was observed in 6% porous SnO_2 cell. The peak output power (P_{out}) ~16.65 mW, open-circuit voltage (V_{oc}) ~0.75 V and short-circuit current (I_{sc}) ~22.2 mA was obtained in SnO_2 HEC. High ionic conduction obtained in SnO_2 HEC was accounted to faster diffusion of dissociated ions via grain boundaries due to low grain boundary impedance to ionic conduction.

6.4 Aluminium Oxide HEC

Aluminium oxide (Al_2O_3) is one of the very important industrial ceramic due to its high thermal and chemical stability. Corundum structure of Al_2O_3 consists of naturally occurring oxygen vacancies in form of F and F^+ centres where $\frac{1}{3}$ of possible octahedral cation sites are vacant [36]. Due to high Lewis acid strength and reduced nearest neighbour coordination of Al ion by cation vacancies, a high concentration of chemidissociated ions was observed on Al_2O_3 HEC pellet surface [29]. Further low grain boundary impedance and defective lattice of alumina promoted H^+ and OH^- ion hopping towards respective Ag and Zn electrodes resulting in electricity generation. The peak output power (P_{out}) ~6.04 mW was delivered by 15.78% porous Al_2O_3 HEC of pore size ~6.6 nm and specific surface area ~10.96 m^2/g. The open-circuit voltage (V_{oc}) ~0.93 V and short-circuit current (I_{sc}) ~6.5 mA were obtained in Al_2O_3 HEC.

6.5 Zinc Oxide HEC

Partially covalent and partially ionic nature of Zinc oxide (ZnO) results in its many interesting physical and chemical properties. Water wettability of ZnO surface has been utilized in reverse water gas shift reactions for methanol production. Photoinduced hydrophilic ZnO surface has been utilized in photocatalytic reactions and hydrogen generation [37]. One of the very interesting applications of zinc oxide for electricity generation by hydroelectric cell was reported by Kotnala et al. [28]. Oxygen deficient ZnO surface with 30.9% porosity and 3.44 nm pore diameter was observed to generate P_{out} ~4.50 mW and V_{oc} ~0.90 V. Oxygen vacancies were induced in ZnO powder prepared by a simple solid-state reaction method. Initial chemidissociation of H_2O molecules at Zn^{2+} cation site near oxygen vacancies was further enhanced by physidissociation of physiosorbed H_2O molecules at ZnO pellet surface. The short-circuit current (I_{sc}) ~5 mA was obtained by collecting the dissociated ions by respective electrodes. The low value of current obtained in ZnO was accounted to high grain boundary impedance of ZnO and low specific surface area ~1.699 m^2/g as compared to other oxides studied. Non ohmic resistive loss was obtained in V–I polarization plots due to impeded motion of OH^- ions by grain boundaries and disconnected nanopores.

6.6 Titanium Dioxide HEC

Titanium dioxide (TiO_2) has been a model material for studying water interaction with oxide surface. Photoinduced water splitting at TiO_2 surface has been widely used for hydrogen generation applications [38]. High sensitivity of TiO_2 for atmospheric

humidity has also been utilized in humidity sensor applications [39]. For hydroelectric cell application, TiO_2 powder was prepared by solid-state reaction method [28]. Oxygen vacant, anatase phase formation of TiO_2 was analyzed by Raman and Photoluminescence spectra. The average pore diameter ~3.07 nm and specific surface area ~11.182 m^2/g was observed by BET analysis. The total porosity of TiO_2 HEC pellet was measured 30.8% by Archimedes method. Electricity generation by water splitting in TiO_2 hydroelectric cell resulted in P_{out} ~2.07 mW and V_{oc} ~0.90 V. Reduced value of current (I_{sc}) ~2.3 mA in TiO_2 as compared to other oxides was accounted to limiting surface conduction of H^+ ions due to large number of grain boundaries present at the surface.

6.7 Magnesium Oxide HEC

The simple structure of magnesium oxide serves as prototype for studying chemical reactions of oxide surface [40]. The interaction of H_2O with MgO has been long studied to determine water to oxide surface interaction energies. Dissociative chemisorption of water on MgO surface also led to current generation in the form of hydroelectric cell [28]. Oxygen deficient MgO powder was prepared having 20.5% porosity by typical solid-state processing. BET surface area analysis showed pore diameter ~3.279 nm and specific surface area ~5.670 m^2/g. High bulk resistance observed by impedance spectroscopy and maximum number of grain boundaries resulted in low current in MgO hydroelectric cell, I_{sc} ~1.5 mA. The out power (P_{out}) ~1.41 mW and open-circuit voltage V_{oc} ~0.94 V was delivered by MgO hydroelectric cell. Maximum number of ions was analyzed in dissociated bound state on the surface of MgO by dielectric loss spectroscopy due to higher associative adsorption of water as compared to dissociative one.

6.8 Silicon Dioxide HEC

Interaction of water with silicon dioxide (SiO_2) is of fundamental interest due to common occurrence of both materials in environment. Dissociative chemisorption of water at silica surface and rupture of Si-O-Si bonds has been observed on silica glasses as well as earth crust silicate mineral [41]. SiO_2–water interaction on silicon dioxide hydroelectric cell was investigated to generate electricity by water splitting [28]. The silica powder was processed through solid-state reaction method for HEC fabrication. The observed porosity of silica particles was 10.3% with pore diameter ~3.279 nm and specific surface area ~5.670 m^2/g. Dissociative chemisorption of H_2O molecules at porous silica surface resulted in P_{out} ~1.05 mW and V_{oc} ~0.96 V in SiO_2 HEC. However, a high bulk ionic impedance leading to very slow diffusion of OH^- ions towards Zn anode was analyzed by impedance spectroscopy. A low value of current (I_{sc}) ~1.1 mA was accounted to reduced water splitting due to slow reaction

Table 2 Comparison of power output of metal-oxide/ferrite HEC's of cell size 1-inch^2 (area ~4.48 cm^2)

S. no	Material	V_{OC} (V)	I_{SC} (mA)	P_{out} (mW)
1.	Magnetite (Fe_3O_4)	0.77	50	38.5
2.	Hematite (α-Fe_2O_3)	0.92	30	27.6
3.	Tin Oxide (SnO_2)	0.75	22.2	16.65
4.	Magnesium Ferrite ($MgFe_2O_4$)	0.98	8	7.84
5.	Aluminium Oxide (Al_2O_3)	0.93	6.5	6.045
6.	Zinc Oxide (ZnO)	0.9	5	4.5
7.	Titanium Oxide (TiO_2)	0.90	2.3	2.07
8.	Magnesium Oxide (MgO)	0.94	1.5	1.41
9.	Silicon Oxide (SiO_2)	0.96	1.1	1.056

of Si with water to form silanol (Si-OH) and further $Si(OH)_4$ complex formation. Open macropores and large number gain boundaries that further reduced dissociated ion movement and reduced current to a very low value as compared to other oxides. A comparison of current and voltage outputs of all ferrite and metal-oxide hydroelectric cells of area 4.48 cm^2 is specified in Table 2.

These results propose enormous opportunities for various other materials to be explored for hydroelectric cell fabrication to obtain green electricity at higher scale. Apart from various other oxides, nitrides, carbides and sulphides of metal can also be investigated. Functional materials like multiferroics, ceramic composites and thermoelectrics may also enhance power output of cell. Porous materials like zeolite, silicates and porous glasses also can be investigated for hydroelectric cell formation.

7 Commercially Viable Byproducts of Hydroelectric Cell

The green electricity generation by hydroelectric cell also produces byproducts during redox reactions at cathode and anode. The two byproducts, pure hydrogen gas and zinc hydroxide nanoparticles are commercially useful, whereas hydroelectric cell provides a new mechanism to generate pure hydrogen gas and ZnO nanoparticles.

7.1 Green Synthesis of Uniformly Distributed ZnO Nanoparticles in Deionized Water

Zinc oxide is a multifunctional material having its many technological applications in cosmetics, electronics, magnetics and optics [42]. Till now zinc oxide has been synthesized by many physical and chemical routes but a distinct green route for ZnO

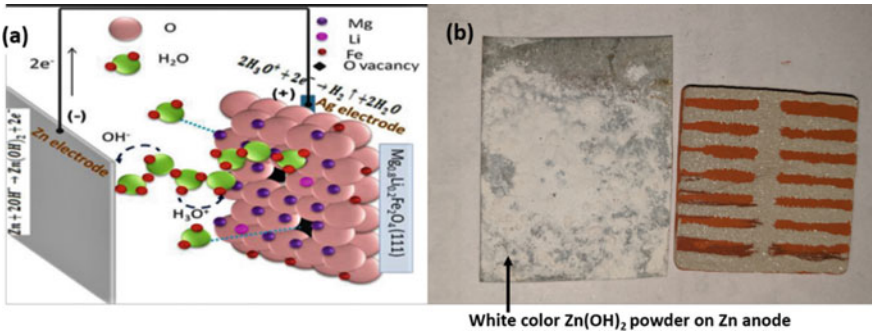

Fig. 8 **a** Schematic diagram of $Zn(OH)_2$ formation during cell operation, **b** Zinc plate covered with $Zn(OH)_2$ nanoparticles during continuous MgLiF HEC operation for 3 h

nanoparticles synthesis was reported by shah et al. by hydroelectric cell [43]. Water splitting on MgLiF hydroelectric cell resulted in current flow out of cell and formation of $Zn(OH)_2$ at anode surface due to reaction of Zn plate with OH^- ions. HEC is operated at low current of 0.3 mA and cell voltage of 0.9 V for 3 h. Zinc hydroxide nanoparticles were synthesized at Zn plate as a byproduct during electrical power generation by HEC and collected as anode mud from zinc plate. These nanoparticles were annealed at 250 °C for pure ZnO nanoparticles formation. The yield of ZnO nanoparticles was 0.017 g (60 $\mu A/cm^2$) without an electrolyte compared with a reported yield of 0.17 g (5 mA/cm^2) with a hybrid electrochemical–thermal method [44]. The ZnO nanoparticles in a narrow size distribution range from 5 to 20 nm were obtained from current generation by HEC. The direct bandgap of ZnO nanoparticles obtained in this process was 3.41 eV. Figure 8 represents $Zn(OH)_2$ nanopowder collected at Zn anode after hydroelectric cell operation for 3 h.

7.2 Highly Pure, Eco-Friendly Hydrogen Production by HEC

Hydrogen generation is focus of current green energy research due to its potential application as an efficient clean energy fuel for cooking, transport and industrial applications [45, 46]. Hydrogen fuel produces the highest energy per unit mass as compared to other fuels which is about 3 times of gasoline or any other hydrocarbon fuel (H_2 = 150 MJ/kg, Gasoline = 45 MJ/kg, LPG = 12.9 MJ/kg). Hydrogen burns cleanly and produces water vapours only as byproduct, so it reduces carbon emission and global warming. The non-toxic nature of hydrogen avoids any harm or destruction to human health. This aspect makes it preferred fuel compared to other sources like nuclear energy and natural gas, which are extremely hazardous to harness safely. The most common methods for hydrogen generation are electrolysis of water and natural gas reforming [47]. These processes suffer with high energy inputs as well as high cost for production. The other methods include photocatalytic water

Table 3 Amount of hydrogen (H_2) gas collection (mmol/hr) by applying external voltage (1–4 V)

H_2 gas	1 V	2 V	3 V	4 V
mmol/hr	1.426	1.623	1.780	1.856

splitting and photobiosynthesis using artificial bacteria but all of them use either external radiation UV/IR or electrolyte [48]. The generation of H_2 gas by hydroelectric cell is facile technique without using any light source or electrolyte [49]. Water molecule dissociation property of hydroelectric cell was used to produce hydrogen as a byproduct. External electric voltage was applied to HEC for hydrogen evolution reaction. Collection of H_2 gas was recorded per hour by using a fresh 4.48 cm^2 cell for each applied voltage. The amount of hydrogen gas collected per hour at different applied voltages in is given in Table 3.

The experimental setup is shown in Fig. 9. The collected gas was detected by gas chromatography (GC). Prior to H_2 detection GC was injected with pure N_2 gas, N_2 in helium and O_2 in helium to confirm N_2 and O_2 peak retention time. For confirmation of H_2 gas retention time, pure H_2 (99.999%) gas diluted with air and argon (99.999%) was inserted into column of gas chromatograph as a carrier gas. Out of the two-peak observed immediate after H_2 gas insertion, the first peak obtained with retention time 0.919 min. and second one with retention time 1.132 min. The gas collected from HEC was inserted into GC after confirming the reference standards. The gas showed a peak with retention time 0.938, confirming it to be pure H_2 matching with reference hydrogen standard. The collection of hydrogen gas was increased with increased applied voltage. The increased current density and larger surface area of metal-oxide/ferrite hydroelectric cells further produce larger volume of hydrogen gas by this facile method. Presently, large-area cells in parallel combination are able to produce hydrogen close to commercial methods by applying very low power 5 W.

Fig. 9 Experimental setup image of H_2 gas collection by hydroelectric cell on applying 2 volts

8 Advantages and Applications of HEC

HEC offers many advantages as compared to other available renewable energy sources, and the most important one is its green energy generation, where the residues are also non-toxic and its low-cost component raw materials. The key advantages of hydroelectric cell are

- It is portable green energy source which is compact and lightweight (2 gm for small 1-inch^2 cell).
- It requires only few drops of water (500 μL) to produce energy and no other toxic chemicals are required.
- Unlike solar cell it can work in day or night and can run small scale devices like LED and Fan at present.
- The two byproducts of HEC, hydrogen gas and $Zn(OH)_{-2}$ nanoparticles are high value industrial commercial products and environment friendly.
- It generates highly pure 99.98% H_2 gas by a simple and cost-effective technique.
- No tedious manufacturing process is involved in fabrication of HEC.

Hydroelectric cell finds its applications in power generation at geographically tough regions like rural areas, farms, forests and mountains. It can be utilized for domestic and residential applications in decentralized mode. After scaling up, hydroelectric cell can be used to fulfill energy needs of automotive industry. Another important application of HEC is to produce high-quality H_2 gas by facile process. Hydroelectric cell can be used at large scale for consumer applications especially in rural areas.

9 Conclusions and Future Directions

The colossal humidoresistance response of nanoporous magnesium ferrite led to invention of revolutionary green energy source, hydroelectric cell. Oxygen deficient, undercoordinated and nanoporous microstructure of ferrite and metal-oxides have efficiently generated green energy by using few drops of water only. Power output of metal-oxides HEC's can be improved further by optimizing the processing conditions. Facile processing and simple setup of hydroelectric cell fabrication for green electricity generation make it an outstanding technology. A small cell of surface area ~4.48 cm^2 generated current I_{sc} ~50 mA at voltage V_{oc} ~0.77 V in magnetite HEC to produce maximum output power P_{out} ~8.59 mW/cm^2. Metal-oxides used in fabrication of hydroelectric cell are biodegradable, in fact it would improve fertility of the soil. Electrodes used in HEC fabrication may be reused after drain out of the cell. Hydroelectric cell for green electricity production by water dissociation is an emerging technology that has a high potential to replace conventional green energy sources like solar cell and fuel cell. Simple working principle and cost-effective production of hydroelectric cell make it a suitable technology

for enormous industrial and residential applications. Validation of hydroelectric cell working principle in almost 25 compounds has been confirmed. There are abundant compounds available that can be further explored for achieving better efficiency and economic version of hydroelectric cell. Green electricity production by hydroelectric cell would play a key role in the mitigation of pollutant gases released in the environment. Highly pure hydrogen production by cost-effective hydroelectric cell technique is highly favourable alternative for industrial-scale hydrogen production. Highly pure hydrogen is specifically used in fuel cell operation so hydroelectric cell can be integrated with fuel cell for hydrogen gas supply. Protonic conduction in nanoporous magnesium ferrite can be explored as proton exchange membrane as an alternative to highly expensive Nafion used in fuel cells.

References

1. R.K. Kotnala, J. Shah, B. Singh, S. Singh, S.K. Dhawan, A. Sengupta, Sens. Actuators B Chem. **129**, 909 (2008)
2. R.K. Kotnala, J. Shah, M.C. Mathpal, K.C. Verma, S. Singh, Thin Solid Films **519**, 6135 (2011)
3. R.K. Kotnala, J. Shah, R. Gupta, Sens. Actuators B Chem. **181**, 402 (2013)
4. R.K. Kotnala, J. Shah, Int. J. Energy Res. **40**, 1652 (2016)
5. R.K. Kotnala, J. Shah, R.K. Kotnala, J. Shah, India Patent 792DEL2015 and U.S. Patent Appl. US20160285121A12016
6. T.A. Blank, L.P. Eksperiandova, K.N. Belikov, Sens. Actuators B Chem. **228**, 416 (2016)
7. Z. Chen, C. Lu, Sensor Lett. **3**, 274 (2005)
8. A. Šutka, K.A. Gross, Sens. Actuators B Chem. **222**, 95 (2016)
9. J. Shah, R.K. Kotnala, B. Singh, H. Kishan, Sens. Actuators B Chem. **128**, 306 (2007)
10. J. Shah, M. Arora, L.P. Purohit, R.K. Kotnala, Sens. Actuators A Phys. **167**, 332 (2011)
11. N. Rezlescu, C. Doroftei, E. Rezlescu, P.D. Popa, Sens.Actuators B Chem. **115**, 589 (2006)
12. V. Jeseentharani, M. George, B. Jeyaraj, A. Dayalan, K.S. Nagaraja, J. Exp. Nanosci. **8**, 358 (2013)
13. R.K. Kotnala, J. Shah, *Handbook of Magnetic Materials*, ed by. K.H.J. Buschow (Elsevier, 2015), p. 291
14. H. Santha, M. Packirisamy, I. Stiharu, X. Li, G. Rinaldi, Sens. Rev. **25**, 271 (2005)
15. N. Agmon, Chem. Phys. Lett. **244**, 456 (1995)
16. E. Traversa, G. Gnappi, A. Montenero, G. Gusmano, Sens Actuators B Chem. **31**, 59 (1996)
17. P.V. Kovtunenko, Glass Ceram. **54**, 143 (1997)
18. Y. Li, J.Z. Zhang, Laser Photonics Rev. **4**, 517 (2010)
19. H. Ahmad, S.K. Kamarudin, L.J. Minggu, M. Kassim, Renew. Sust. Energ Rev. **43**, 599 (2015)
20. D. Wei, Sci. Rep. **5**, 15173 (2015)
21. Q. Meng, D.D.L. Chung, Cem. Concr. Compos. **32**, 829 (2010)
22. A.S. Doroshkevich, E.B. Asgerov, A.V. Shylo, A.I. Lyubchyk, A.I. Logunov, V.A. Glazunova et al., Appl. Nanosci. **9**, 1 (2019)
23. F. La Mantia, M. Pasta, H.D. Deshazer, B.E. Logan, Y. Cui, Nano Lett. **11**, 1810 (2011)
24. D.P. Leonard, Z. Wei, G. Chen, F. Du, X. Ji, ACS Energy Lett. **3**, 373 (2018)
25. S. Park, B.S. Kumar, K. Kim, S.M. Hwang, Y. Kim, J. Mater. Chem. A **4**, 7207 (2016)
26. R. Yu, Z. Ma, P.G. Bruce, Chem Soc Rev **41**, 4909 (2012)
27. A. Harriman, I.J. Pickering, J.M. Thomas, P.A. Christensen, J. Chem. Soc. Faraday Trans. **84**, 2795 (1988)
28. J. Jiang, Y. Li, J. Liu, X. Huang, C. Yuan, X.W. Lou, Adv. Mater. **24**, 5166 (2012)

29. R.K. Kotnala, R. Gupta, A. Shukla, S. Jain, A. Gaur, J. Shah, J. Phys. Chem. C **122**, 18841 (2018)
30. M.E. Fleet, J. Solid State Chem. **62**, 75 (1986)
31. S. Jain, J. Shah, S.R. Dhakate, C. Sharma, G. Gupta, R.K. Kotnala, J. Phys. Chem. C **122**, 5908 (2018)
32. L.A. Bursill, J.L. Peng, X.D. Fan, Aust. J. Chem. **45**, 1527 (1992)
33. S.K. Geochimica et al., Geochim. Cosmochim. Acta **75**, 2043 (2011)
34. S. Jain, J. Shah, N.S. Negi, C. Sharma, R.K. Kotnala, Int. J. Energy Res. **43**, 1 (2019)
35. C. Wang, L. Yin, L. Zhang, D. Xiang, R. Gao, Sensors **10**, 2088 (2010)
36. P. Lamparter, R. Kniep, Physica B Condens. **234**, 405 (1997)
37. M. Reli, M. Edelmannová, M. Šihor, P. Praus, L. Svoboda, K.K. Mamulová, H. Otoupalíková et al., Int. J. Hydrog. Energy **40**, 8530 (2015)
38. A. Fujishima, X. Zhang, D.A. Tryk, Surf. Sci. Rep. **63**, 515 (2008)
39. Y. Zhang, W. Fu, H. Yang, Q. Qi, Y. Zeng, T. Zhang, R. Ge, G. Zou, Appl. Surf. Sci. **254**, 5545 (2008)
40. K. Refson, R.A. Wogelius, D.G. Fraser, M.C. Payne, M.H. Lee, V. Milman, Phys. Rev. B **52**, 10823 (1995)
41. M. Nogami, Y. Abe, Phys. Rev. B **55**, 12108 (1997)
42. Z.L. Wang, J. Phys. Condens. Matter **16**, R829 (2004)
43. J. Shah, R.K. Kotnala, J. Phys. Chem. Solids **108**, 15 (2017)
44. K.G. Chandrappa, T.V. Venkatesha, K. Vathsala, C. Shivakumara, J. Nanoparticle Res. **12**, 2667 (2010)
45. S. Sharma, S.K. Ghoshal, Renew. Sustain. Energy Rev. **43**, 1151 (2015)
46. T.N. Veziro, F. Barbir, Int. J. Hydrog. Energy **17**, 391 (1992)
47. I. Dincer, Ibrahim. Int. J. Hydrog. Energy **37**, 1954 (2012)
48. I. Dincer, C. Acar, Int. J. Hydrog. Energy **40**, 11094 (2015)
49. J. Shah, S. Jain, A. Shukla, R. Gupta, R.K. Kotnala, Int. J. Hydrog. Energy **42**, 30584 (2017)
50. Ø. Hasvold, H. Henriksen, E. Melv, G. Citi, B.Ø. Johansen, T. Kjønigsen, R. Galetti, J. Power Sourc. **65**, 253 (1997)

Conducting Polymers and Their Composites Adding New Dimensions to Advanced Thermoelectric Materials

Meetu Bharti, Ajay Singh, K. P. Muthe, and D. K. Aswal

Abstract Thermoelectric materials can provide a solution to the alarming situation of the energy crisis and global warming by harnessing natural as well as waste heat. Recently many studies are being focused on efficient thermoelectric materials such as chalcogenides, clathrates, half-alloys, skutterudites, etc. However, the chapter presented here discusses the scope of conducting polymers as an emerging class of thermoelectric materials. Conducting polymers owing to their nature friendliness, flexibility, reduced manufacturing and processing cost and low thermal conductivity have recently carved out a special place in the arena of thermoelectricity. Though these organic materials cannot substitute conventional inorganic materials at higher temperatures (in terms of efficiency and stability) but their non-toxicity, plentiful availability and solution processability enable them to overshadow their inorganic counterparts for low-temperature heat recovery programmes. Moreover, their amenability to blend with inorganic materials results in hybrid composites which derive the properties of both the organic and inorganic realms and can be used to develop efficient thermoelectric power generators. Also, diverse morphologies and structures of the conducting polymers can be easily manipulated through many ways such as doping, chain alignment, nanostructuring, etc. to tune their charge trans-

M. Bharti (✉) · A. Singh (✉) · K. P. Muthe · D. K. Aswal
Technical Physics Division, Bhabha Atomic Research Centre, Trombay, Mumbai 400085, India
e-mail: meetubharti@yahoo.com

A. Singh
e-mail: ajay@barc.gov.in

M. Bharti
All India Jat Heroes' Memorial College, Rohtak, Haryana 124001, India

D. K. Aswal
CSIR-National Physical Laboratory, New Delhi 110012, India

S. Kumar and D. K. Aswal (eds.), *Recent Advances in Thin Films*, Materials Horizons: From Nature to Nanomaterials, https://doi.org/10.1007/978-981-15-6116-0_14

port characteristics. The best thermoelectric figure-of-merit (ZT) ~0.4 (at 300 K) obtained in case of many polymers (PEDOT:PSS and P3HT) suggests that these conducting polymers with their advantages can be a good alternative of Bi_2Te_3 -based alloys (with the highest ZT ~1) that are established thermoelectric materials till date in the lower temperature range (<150 °C). Besides this, conducting polymers can be deposited over large surface areas to be used on curved surfaces (for tapping body/appliance heat), thus providing an additional advantage, which the rigid and brittle Bi_2Te_3 -based alloys cannot provide. With the knowledge of state-of-the-art techniques existing in the field of organic electronics and materials manipulation at nanoscale conducting polymers can really furnish new dimensions to advanced thermoelectric materials. Evolution of high-performance polymer-fabric composites and free-standing films indicates a bright future for conducting polymers-based smart and wearable but inexpensive devices. The chapter attempts to reveal recent advancements that have been attained through conducting polymers in the domain of thermoelectric power generation. In addition, critical analysis of all the problems that may occur while designing conducting polymer based thermoelectric devices is also presented.

Graphical Abstract The potential shown by conducting polymers in the field of thermoelectric power generation can certainly pave towards the novel design of flexible, wearable and smart devices, which are much needed in this modern era to harness waste and natural heat near room-temperature applications.

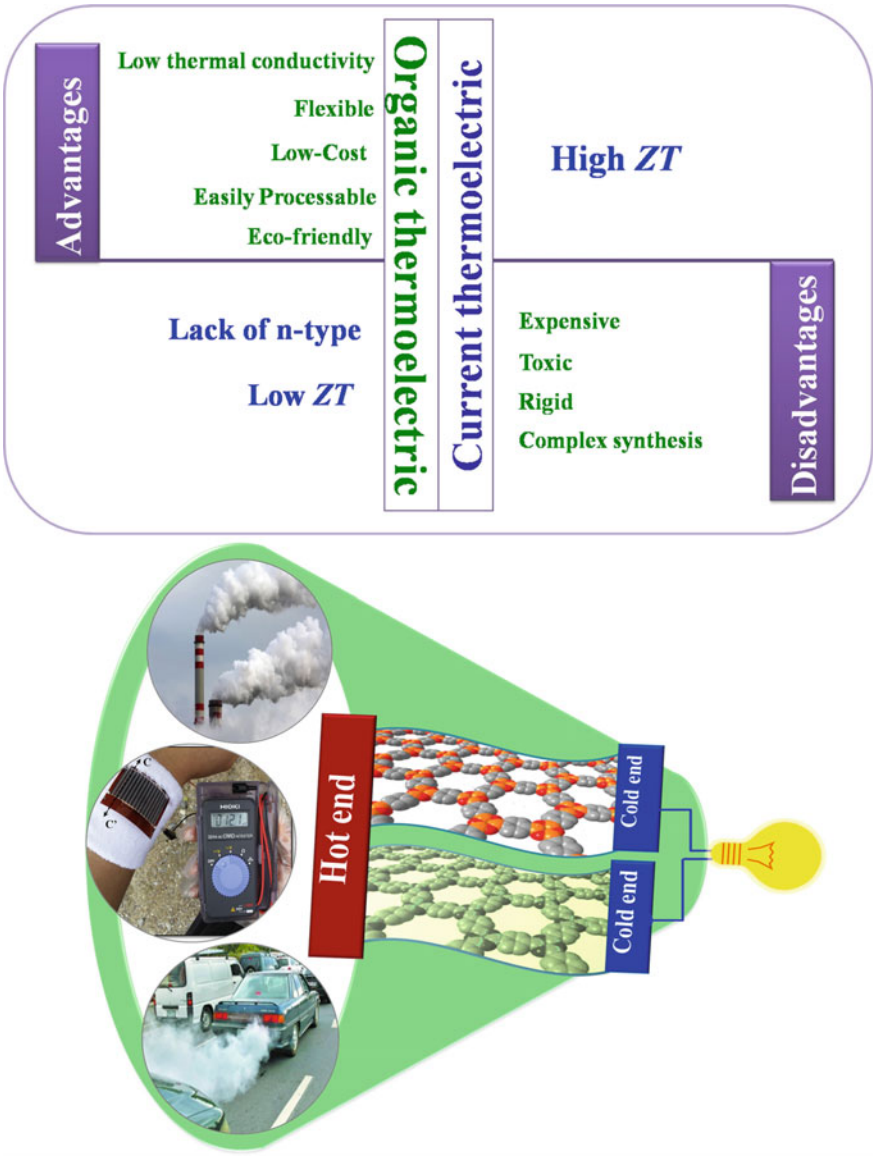

Keywords Thermoelectricity · Flexible/wearable thermoelectric · Conducting polymers · Organic thermoelectrics · Seebeck coefficient · Thermal conductivity

1 Introduction

Worldwide research groups are striving hard to find out the alternative energy solutions to meet the leaping energy demands of this modern era of industrialization and urbanization. However, still, the majority of the power production sector relies on the non-replenishing resources which are not only expensive but also harmful for the environment. Therefore, thermoelectricity which deals with the conversion of thermal difference into electrical energy can harness waste/surrounding heat and emerge as a green and clean tool for small-scale power generation [1–3]. In view of the wastage of nearly 70% of the world's total energy in form of heat, thermoelectric power generation can have a much greater impact than we can think of [2]. For instance, some of its implications are: it can tap heat energy at the initial stage of emissions (root level) resulting in the reduction of pollution as well as global warming; minimize energy (heat) loss by making use of industrial and automotive exhausts; and serve at remote/unattended places of operation particularly where other energy conversion technologies are not so effective such as in case of space/indoor applications [4]. Recently, in addition to the focus on the development of efficient thermoelectric materials and devices, a novel concept of integrating this technology with other power production technologies such as solar plants/hydel plants/oceanic power conversion centres, is on the wish-list of many research groups [5]. With such integration, one type of technology can work complementary to the other when energy conversion is not feasible through the second one and thus, overall efficiency can be improved. But to realize such ideas practically, one must design and develop promising thermoelectric materials that can be configured into potential devices to harvest heat of usually existing curved surfaces. A lot of studies are being focussed on finding efficient thermoelectric materials such as chalcogenides, clathrates, half huesler alloys, skutterudites, etc. for specific temperature zones [4]. Established existing inorganic thermoelectric materials can also be classified according to the temperature zones as: (i) for low-temperature range (<250 °C): Bi_2Te_3 and Sb_2Te_3; (ii) mid-temperature range (250–650 °C): PbTe and TAGS-85; and (iii) high-temperature range (>650 °C): SiGe alloys [4, 6]. But such inorganic-based thermoelectric materials have certain constraints such as they are expensive, toxic and in addition, lack flexibility and also involve complex synthesis.

Therefore, in pursuit of efficient and novel thermoelectric materials, many advantages of conducting polymers such as nature friendliness, flexibility, reduced manufacturing and processing cost and low thermal conductivity have attracted the focus of worldwide research groups [6–8]. The present chapter, therefore, has been inclined to critically discuss the relevance of conducting polymers (CPs) in the emerging field of organic thermoelectrics. Also, conducting polymers due to being flexible can be the most suitable materials for enwrapping around curved hot surfaces (i.e. having a wearable form) to tap their heat; and furthermore, their solution processability allows easy blending with inorganic materials to integrate the advantages of both the organic and inorganic realms [9].

The present chapter has also summarized the outcome of our own investigations on the thermoelectric performance of some selective polymers such as Polypyrrole, Poly(3,4-ethylenedioxythiophene): poly(styrenesulfonate), i.e. PEDOT:PSS, Poly(3-hexylthiophene) (P3HT). Films of these CPs were synthesized and also, inorganic dopants were added to synthesize composites to examine their significance as potential materials for thermoelectric applications. Various methods were devised to transform the substrate-adherent films of these polymers in the free-standing form so that the futuristic application of harvesting heat from curved surfaces can be realized. However, measurement of thermoelectric performance of conducting polymers based films (substrate-adherent as well as free-standing) demands much concern regarding proper metallic interconnects (with low contact resistance) and effectual heat flow through the films [4, 6, 9]. Not many optimized and inexpensive setups are available commercially that can measure thermoelectric parameters in case of thin films. Keeping in view, we have proposed a design to develop an automated setup that can simultaneously measure four-probe electrical conductivity and Seebeck coefficient [9]. In fact, successful estimation of electrical conductivity and Seebeck coefficient of conducting polymer films (under ambient atmosphere conditions) by an in-house built customized setup showed us the way that reliable as well as facile thermoelectric measurements are possible with such a low-cost and simple setup. However, very low value of intrinsic thermal conductivity, though can be useful for high efficiency of thermoelectric materials but at the same time obstructs precise estimation even in laboratory conditions and requires sophisticated instruments. Besides all such investigations/observations, the chapter not only describes various measurement techniques along with basic charge transport mechanisms but also emphasizes the manipulation of structure–property relationship to improve thermoelectric properties [10, 11]. Schematic given in Fig. 1 shows various stages and factors that are to be taken care of to reach the final stage of thermoelectric power generators (TEGs) for commercial applications.

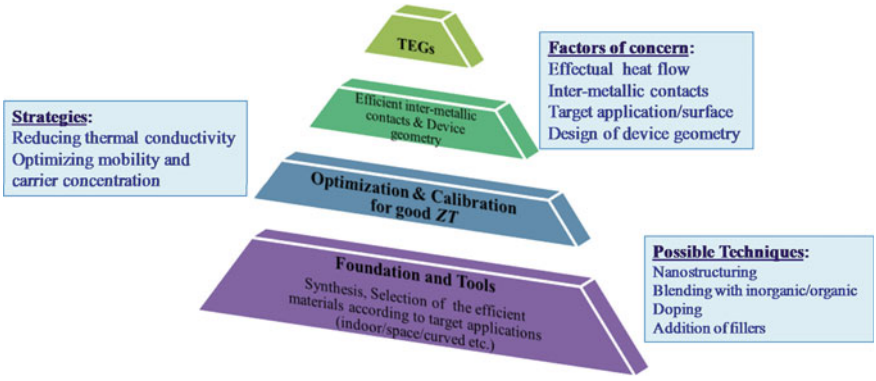

Fig. 1 Schematic showing various stages and factors involved for reaching at the final stage of thermoelectric power generators (TEGs)

Lack of stable and reliable n-type polymers has still been an issue for the design of conventional thermoelectric devices, which make use of both p- and n-type of thermoelements. Therefore, different architectural designs of conducting polymers based 'Organic thermoelectric power generators' (OTEG) that have been already reported in the literature are analysed. In view of the merits and demerits of reported designs of TEGs [12], the study presents a way to design and develop OTEGs using only a single type (i.e. p-type) of thermoelement. A few prototype organic thermoelectric power generators (OTEGs) fabricated using both types of substrate-adherent/free-standing films clearly illustrate that conducting polymers based thermoelectric power generators have the capability of being configured according to the target applications [9].

1.1 Identification of Efficient Thermoelectric Materials

The efficiency (η) with which waste heat can be converted to useful electrical energy by thermoelectric materials is directly related to material parameter termed as the dimensionless figure-of-merit (ZT). The mathematical expression connecting efficiency and figure-of-merit is given in Eq. 1.

$$\eta = \frac{T_h - T_c}{T_h}\left(\frac{\sqrt{1 + ZT_{\text{avg}}} - 1}{\sqrt{1 + ZT_{\text{avg}}} + T_c/T_h}\right) \tag{1}$$

Here T_h and T_c are the respective hot- and cold-end temperatures of thermoelectric materials and T_{avg} is the average temperature of T_h and T_c. The ZT_{avg} is the average figure-of-merit for each thermoelement and it is estimated by Eq. 2 as follows:

$$ZT_{\text{avg}} = \alpha^2 \sigma T/\kappa \tag{2}$$

Here α is the Seebeck coefficient, σ is the electrical conductivity and κ is the thermal conductivity of the material. Thermal conductivity (κ) has two contributions, i.e. electronic (k_e) and lattice (k_l).

In order to obtain high figure-of-merit (ZT) and conversion efficiency (η), certain requirements that need to be fulfilled are: (i) material should exhibit high α to have high voltage output; (ii) high σ is required to have large short circuit current and low Joule heating; and (iii) low κ to have a large temperature difference [4, 6]. Electrical conductivity (σ) since depends upon charge carrier density and mobility can be enhanced through doping; but because charge carrier transport takes place in energy levels close to the Fermi level, doping leads to a decrease in the difference between transport and Fermi levels and thus reduces α [8, 9]. In addition, the thermoelectric performance is also influenced by κ of the materials and according to the Wiedemann–Franz law electronic part of thermal conductivity is given by: $\kappa_e = \sigma LT$ (where L is Lorenz number equal to 2.44×10^{-8} WΩ/K^2 for metals and heavily doped

semiconductors). Therefore, the increase in electrical conductivity (σ) enhances the electronic part of thermal conductivity and such an interdependence of α, σ and κ, does not allow any single material to exhibit favourable properties. Therefore, any approach which can decouple or balance these three parameters (i.e. α, σ and κ) so as to optimize electrical and thermal transport is highly beneficial for designing the material with high ZT_{avg} [2–6]. For instance, in case when doping enhances κ_e, one must think upon to reduce the lattice part of thermal conductivity (κ_l) to achieve a low value of overall thermal conductivity (i.e. κ) [6–8].

1.2 Conducting Polymers: Significance from Thermoelectric Point of View

Conducting polymers are the materials with an extended system of conjugated carbon–carbon double bonds. This existence of bond alternation creates band gap which is responsible for semiconducting properties in these materials [6, 13]. In fact conducting polymers have widely been investigated for their applications in light-emitting diodes, field-effect transistors, gas sensors and solar cells [13]. This already exhibited potential of conducting polymers in flexible electronics and sensors serves as a motivation for organic thermoelectric research worldwide. Moreover, conducting polymers have many advantages such as nature friendliness, flexibility, reduced manufacturing and processing cost and can be easily doped or mixed with inorganic materials to tailor the three thermoelectric parameters (α, σ, κ) [6–9]. Therefore, organic semiconductors, in particular conducting polymers, are envisaged as an alternative to inorganic semiconductors for low-temperature (30–100 °C) flexible thermoelectric applications [10–13]. Besides their several other advantages such as scalability, low-cost processing by simple chemical routes can lead to wearable films which can be used to design and develop thermoelectric devices of desirable geometry so as to meet the needs of target surfaces. However, the thermoelectric performance of conducting polymers has still not been thoroughly investigated. Also, it is essential that conducting polymers with both the conduction type should be synthesized because thermoelectric devices require both p- and n-type materials which are to be connected electrically in series and thermally in parallel [6].

The studies on various conducting polymers such as PEDOT:PSS and P3HT have reported the highest value of ZT ~0.42 and 0.47 at room temperature, respectively [14, 15]. PEDOT:PSS with Te core nanocrystals exhibited ZT values ~0.1 at room temperature with power factor ($\alpha^2\sigma$) of ~70 $\mu W/mK^2$ and low thermal conductivity (κ) of ~0.2 W/mK [16]. PEDOT:PSS and Bi_2Te_3 composites yielded $\alpha^2\sigma$ of ~47 $\mu W/mK^2$ at room temperature [17]. Mostly doped conducting polymers are p-type but a n-type organic material is highly needed for practical thermoelectric applications. The n-type organic semiconductors are scarce due to difficulty in their synthesis and having poor air-stability. In a recent study, by combining n-type poly[Nax(Ni-ett)] and p-type

poly[Cux(Cu-ett)], a thermoelectric module composed of 35 n-p couples was demonstrated, which delivered an output voltage of 0.26 V, a current of 10.1 mA and a power of 2.8 μW for temperature difference (ΔT) of 80 K and hot-end temperature of 420 K [18]. Recently n-type conducting polymer poly[N,N0-bis(2-octyl-dodecyl)-1,4,5,8-napthalenedicarboximide-2,6-diyl]-alt-5,50(2,20bithiophene)] (P(NDIOD-T2)) has been studied for organic thermoelectric [19]. The examples discussed here reveal that conducting polymers based thermoelectric devices exhibit strong potential for low-temperature thermoelectric applications.

Therefore, the present chapter is focussed on thermoelectric studies on a wide range of conducting polymers such as polypyrrole (PPy), polyaniline (PANI), Poly(3-hexylthiophene) (P3HT), poly(3,4-ethylenedioxythiophene): polystyrene sulphonate (PEDOT:PSS), polycarbazole and their composites. However, the main disadvantages that exist as of now with conducting polymers are: (i) the parameter (ZT) which determines their thermoelectric performance is very low, typically $\leq$0.4; and (ii) most of the known conducting polymers based thermoelectric materials are p-type and still there is a scarcity of stable n-type materials [6].

2 Measurement Techniques for Estimation of Thermoelectric Properties

There are several issues that need to be taken care while measuring the thermoelectric properties of materials (bulk or film form). In the field of organic thermoelectric research, issues like feeble adherence of films to the substrates, stability up to low-temperature range (<100 °C) for most of the CPs, patternizing of contacts (for making measurement) on film surface, need concern for precise/accurate measurements. Furthermore, a very low value of thermal conductivity in case of conducting polymers, though, results in obtaining high ZT but in turn demands extra attention in measurement procedures; because even the minor power losses and/or environmental disturbances can lead to attenuation of signals being measured.

2.1 Estimation of Electrical Conductivity and Seebeck Coefficient

Among all thermoelectric parameters, the electrical conductivity can be measured most easily. A four-point probe method consisting of four equally spaced electrodes coated on a substrate or another appropriate material is the most convenient technique to estimate electrical conductivity. One set of leads is used to measure voltage while the other one is used to provide current in the sample. Two different sets of leads minimize errors that arise due to the parasitic contact resistance between the film

surface and the probe [6]. While in case of high resistive samples, two probes can be used to measure the conductivity of polymeric films.

Resistance (R) that is obtained from input current and output voltage is used to calculate conductivity (σ) using Eq. 3.

$$R = \frac{l}{\sigma A} \tag{3}$$

where l is the distance between the voltage probes and A is the cross-sectional area of the sample.

A typical setup that can measure electrical conductivity (through four-probe method) and Seebeck coefficient is shown below (Fig. 2). This setup is enclosed in a housing to have closed ambience or vacuum to minimize any sort of environmental disturbances during thermoelectric measurements [9].

2.2 Estimation of Thermal Conductivity

Thermal conductivity measurement techniques can be classified into steady-state and non-steady-state (or transient) methods. Steady-state methods can be used in case only when the temperature of the sample remains constant. The techniques to measure anisotropic heat conduction via steady state in case of stretched polymers of relatively large thickness (more than a few millimetres) have been available since the 1960s. In case of solid materials, heat conduction occurs through both the lattice vibration waves (phonons) and free electrons. The ability of a material to transport heat is estimated by Eq. 4 below.

$$q = \kappa \frac{\mathrm{d}T}{\mathrm{d}x} \tag{4}$$

where q is the heat flux, κ is thermal conductivity having two contributions as κ_l (phonon part) and κ_e (charge carrier part) and $\mathrm{d}T/\mathrm{d}x$ is the temperature gradient.

Steady-state and non-steady-state (or transient) estimation methods are discussed as follow.

2.2.1 Steady-State Methods

Steady-state method is one of the oldest and simplest methods of measurement of thermal conductivity. In this method, a heater is attached to the one end of a polymer sample, while the other end is maintained at a lower temperature resulting in a longitudinal flow of heat (as shown in Fig. 3). On the other hand, proper care should be taken to avoid the flow (loss) of heat in the transverse direction. Absolute or comparative are the two modes by which heat flux can be measured directly or

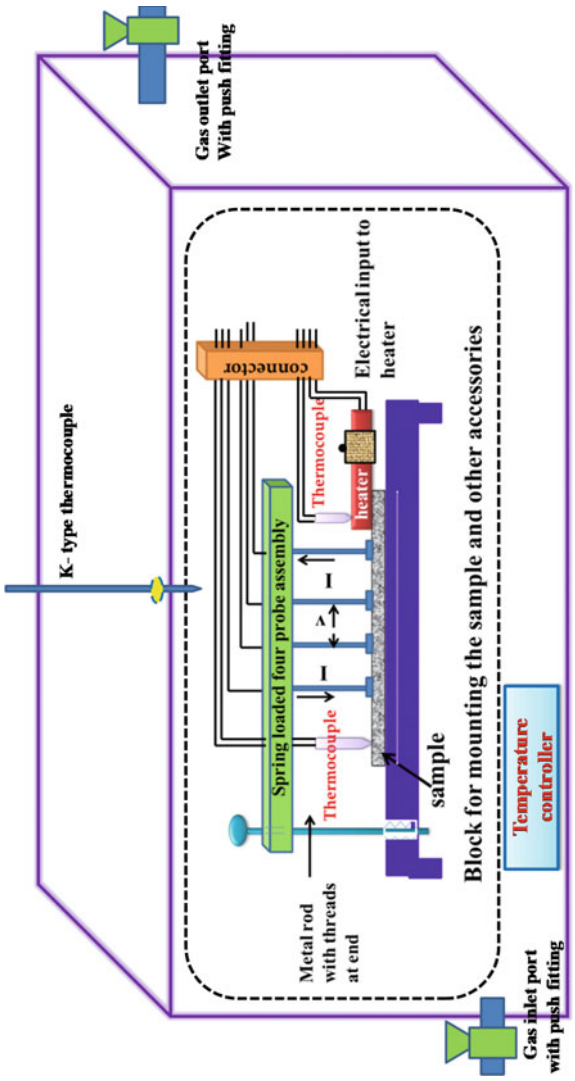

Fig. 2 Setup to measure four-probe conductivity and Seebeck coefficient enclosed in a housing to reduce environmental disturbances

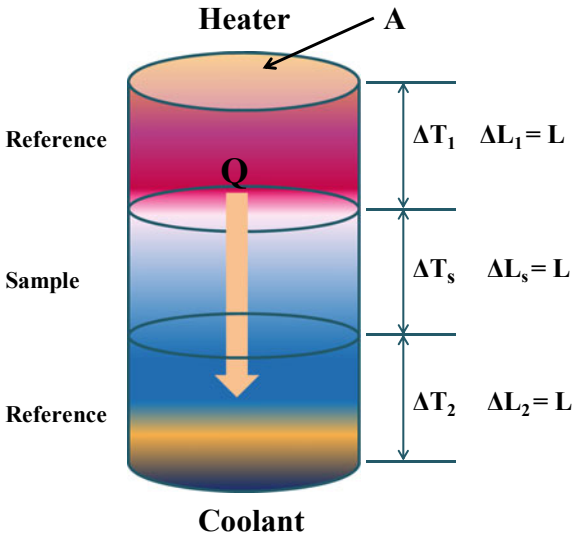

Fig. 3 Axial flow method to measure thermal conductivity

indirectly [20]. When electric power that is supplied to the heater is measured, the method is termed as absolute whereas comparative method estimates heat flux by comparing with the already known value of thermal conductivity of the reference sample. Thus, thermal conductivity along the slab can be calculated by using values of applied steady-state heat flux, and temperature gradient across the sample as shown by Eq. 3.

However, large experimental errors are quite probable due to transverse loss of heat via radiative and air conduction from the sidewalls of the sample. In addition, when this method is used in case of thin films having thicknesses less than a few millimetres, the thermal contact resistances between 'heater/cold plates and the films' and between the 'thermocouple and the films' become comparable to the thermal resistance due to the sample volume; and these contact resistances are highly unknown [21]. Therefore, steady-state characterization technique though, being relatively easy can yield significant uncertainties when the effect of both transverse heat loss and unknown contact resistances are taken into account (while estimating thermal conductivity).

Considering these limitations, earlier in some studies on CP films of thickness ~1 μm, metallic electrodes working as heaters/thermometers were patterned on the sample using lithography technique so that thermal contact resistance between the heaters/thermometers and films was much lowered in comparison to the thermal resistance due to volume of the sample itself. DC current was used to heat the samples to estimate out of plane κ by measuring the Q through I^2R (Joules heating) relation [21].

2.2.2 Transient Methods

Transient methods provide a relatively rapid estimation of κ, and details of various transient techniques are discussed here.

(i) Flash radiometry technique: Choy et al. reported 'flash radiometry technique' as a non-steady-state method for thin samples having thickness less than 150 μm [13, 14]. Schematic diagram of the technique shown in Fig. 4a illustrates that when the front

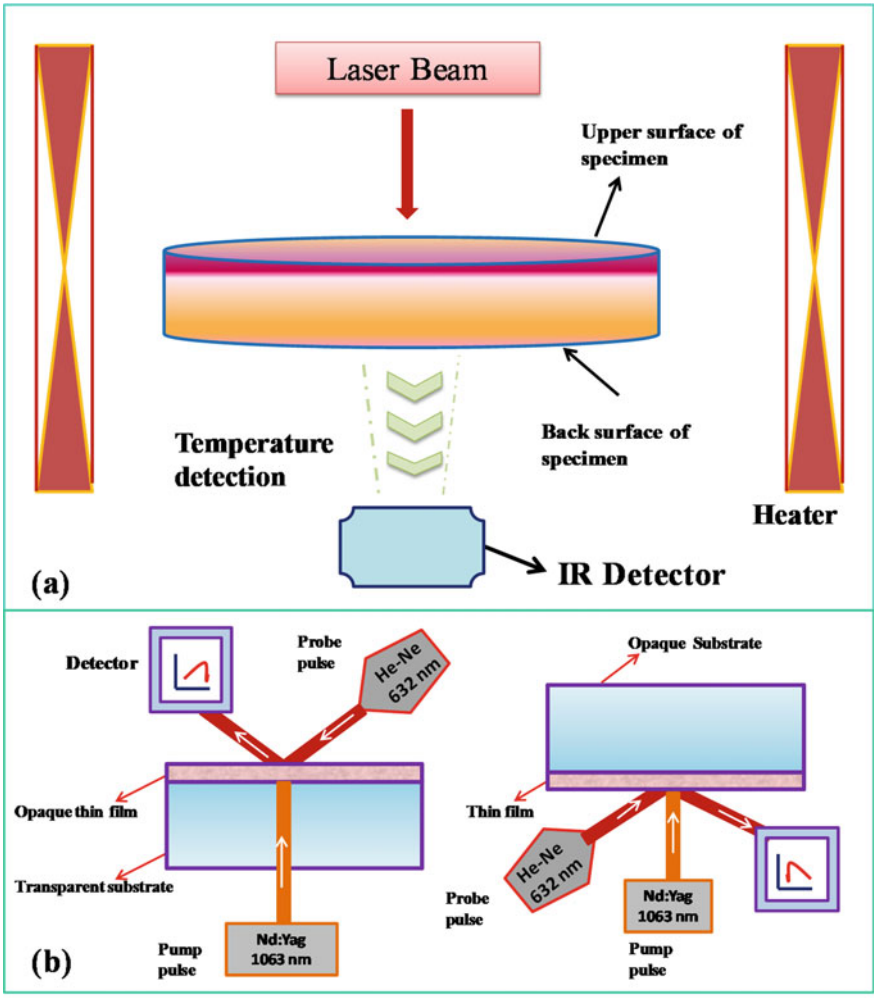

Fig. 4 Schematic showing transient method (laser flash technique) to measure thermal conductivity **a** standard laser flash technique measuring heat waves; **b** laser flash technique for thin films measuring acoustic waves

surface of the sample was irradiated by the laser pulse, heat waves were generated and monitored as a function of time from the rear surface by means of an infrared (IR) detector rather than a thermocouple. This method provides the value of thermal diffusivity (α) normal to the film surface which when used in Eq. 5 determines thermal conductivity (κ) of the polymer.

$$\kappa = C_p \rho \alpha \tag{5}$$

Here C_p and ρ are the specific heat and the density of the polymer, respectively, and C_p can be easily estimated by comparing with a standard sample within the same apparatus.

Laser flash technique described here, though, being useful for free-standing flexible films or pellet samples (bulk material), yet the polymer films deposited on substrates need some other technique because while estimating thermal diffusivity for such films there emerges a substrate contribution. Recently, this issue has been resolved by the company 'Linseis' which has made laser flash technique commercially available for measuring κ of thin films having a thickness from 80 nm to 20 μm shown in Fig. 4b. This technology rather than estimating κ by conventional measurement of thermal diffusivity make use of thermo-reflectance phenomenon. Thermo-reflectance measures the thermal properties by determining the change in reflectance of the surface when a material is heated up. In this method, the acoustic waves generated at the interface are measured by the detector using the peizo-optic effect, whereas standard laser flash relies on the measurement of propagated heat waves. The reflective coefficients are measured as a function of time and compared with standard models that contain coefficients corresponding to various thermal properties.

Two different modes that have been devised by the company to measure κ for thin films:

(a) Rear heating Front detection (RF): In case of a transparent substrate,
(b) Front heating Front detection (FF): In case of a non-transparent substrate where the RF technique is not employable.

However, a single apparatus can be designed to combine features of both RF and FF.

Another important issue that concerns thin film characterization and has been discussed earlier is the anisotropy of thermal conductivity occurring for in-plane and out-of-plane directions. This specifies the need for a method that can provide the thermal conductivities in both of these directions. And the laser flash transient method which minimizes heat loss while measuring thermal diffusivity normal to films suffers from a substantial heat loss till the thermal diffusion reaches the temperature detection point along the film surface [20]. Therefore, this method, though, can effectively measure anisotropy in κ need to consider heat loss occurring parallel to film surface while estimating in-plane thermal conductivity particularly in case of thin films (thickness less than 4 μm).

(ii) Harmonic joule heating and electrical resistance thermometry: The value of in-plane thermal conductivity of CP films can be measured by analysing the transient temperature responses at specific frequency range. This technique relies on the measurement of resistance of the CP films to determine their thermal properties, hence named electrical resistance thermometry [21]. However, sometimes temperature oscillations are also detected by measuring changes in the reflectivity of the metal surfaces. The measurement by harmonic joule heating adopts a similar procedure as used in the 3 omega (3ω) method which has been elaborated here.

The first application of 3 omega method for determining the κ of solid-state samples was demonstrated in 1987. In this method, a microfabricated metal stripe (usually gold) is deposited on the sample surface and it serves both as a heater and a temperature sensor. By passing an AC current of angular frequency ω through this stripe heater some heat is created at the second harmonic frequency (2ω). Since the electrical resistance of the heater stripe is also proportional to the temperature, the temperature oscillations can be measured indirectly by measuring the third component (3ω) of voltage across the heater by using a lock-in amplifier (Fig. 5). It is important to note that the AC current flowing through the heater generates temperature change in heater, and underneath film as well. 3ω method needs an electrically conductive specimen with a temperature-dependent resistance to measure its thermal properties. Whereas for the thermally insulating specimen, the generated heat stays in heater and temperature oscillations are large, hence measuring the temperature oscillations allows accessing of thermal properties of the films lying beneath the heater surface. The expression used in 3ω method to estimate κ of the sample is as follows:

$$\kappa = \frac{V_{h,0}^3 \beta_h}{4\pi t_h R_{h,0} S} \tag{6}$$

Here S is the slope of the third harmonic of voltage as the natural logarithm of the frequencies data. $V_{h,0}$ is the peak amplitude of the heater voltage at the first harmonic frequency, β_h is the temperature coefficient of the resistance (TCR) of the heater, t_h is the thickness of the specimen and $R_{h,0}$ is the heater resistance.

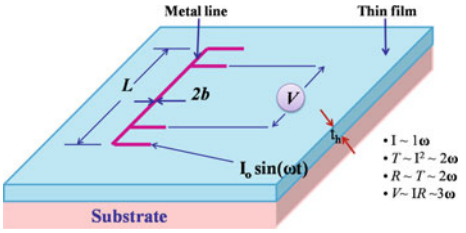

Fig. 5 Schematic showing transient method (thermometry using the electrical method known as the 3ω technique and also the thermo-reflectance technique)

3 Factors Affecting Thermoelectric Performance of Conducting Polymers

From the analysis of measurement techniques and already reported well-known transport mechanism [7–9, 21, 22], it can be said that there are no generalized set of well-defined rules that can be applied to all the conducting polymers while making efforts for enhancing their thermoelectric performances [6, 9]. Before resorting to specific approaches that can be applied to a particular CP, many factors such as its chemical structure, feasibility of carrying out research with compatible dopants, choice of different types of appropriate substrates compatible with the desirable device geometry (like in-plane and out of plane), etc. need to be identified. Such types of factors that can influence TE performance are discussed as follow.

3.1 Structure

Various polymers like polyaniline (PANI), poly(*p*-phenylene vinylene) (PPV), polyacetylene (PA), poly(2,7-carbazolenevinylene), and poly(2,5-dimethoxy phenylenevinylene) (PMeOPV) show different electrical conductivities, thermal conductivities, and figure-of-merits and exhibit various TE performances depending upon the unique characteristics linked to their respective structures. The molecular basis of conductive properties depends upon the conjugation of their bonds. Conductive polymers have continuous backbones of sp^2 hybridized electrons, compared to the sp^3 hybridized covalent bonds of non-conducting polymers. For instance, due to the dependence of thermoelectric performance on polymer structure, P3HT of medium regioregularity ~90% is preferred to regiorandom P3HT as the latter is unable to crystallize. Even high regioregular (~97%) P3HT is not preferred for thermoelectric applications due to its lack of solubility which can result in less promising electrical conductivities [22].

3.2 Concentration

Various studies have been reported where polymer concentration along with dopant affects the charge carrier mobility as well as the charge carrier density. Change in polymer content not only determines the solubility and viscosity but also influences both the Seebeck coefficient and electrical conductivity because of the interaction between dopant atoms and polymer matrix. Variation of κ, σ with respect to dopant concentration shown in Fig. 6 clearly confirms that optimizing the polymer content along with dopant affects thermoelectric parameters in the case of P3HT-Bi_2T_3 composites [23].

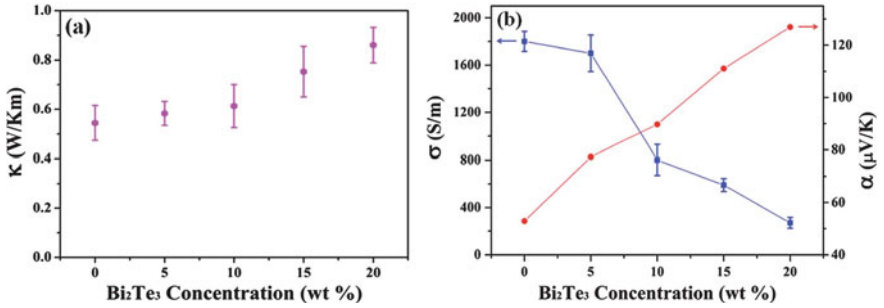

Fig. 6 **a** Thermal conductivity of P3HT–Bi_2Te_3 nanocomposites at room temperature; **b** the electrical conductivity and Seebeck coefficient as a function of the weight ratio of Bi_2Te_3 nanowires in the P3HT–Bi_2Te_3 nanocomposites. The doping level of the P3HT matrix was about 32 wt% and the weight ratio of Bi_2Te_3 nanowires varied from 0 to 20 wt% (Reproduced with the permission from Ref. [23])

3.3 Molecular Weight and Chain Length

It is already well-known that charge carriers' mobility is determined by the molecular weight of the polymers. Thus, controlling the mobility via varying mol wt. can help to tune the electrical conductivity of conducting polymers. Polymers having low molecular weight have shorter chain lengths and despite being more crystalline than polymers with high molecular weight possess low mobility due to barrier of insulating boundaries [7, 24, 25]. On the other hand, the high molecular weight of polymers is the result of longer backbone as well as side chains. In such a case, though, side chains obstruct the conjugation among the chains but can provide a facile path to charge carriers along the backbone by connecting ordered regions more effectively [24, 25]. Moreover, thermal conductivity also shows a reduction with a decrease in polymer chain length. In a study, variation in the length of nanofibres of polythiophene and P3ATs was observed with the length of alkyl side chains (where A = **M**-methyl, **B**-butyl, **H**-hexyl, **O**-octyl, **D**-dodecyl) [25]. An increase in the length of alkyl side chains brought down the value of electrical conductivity from 35 S/cm in case of P3BT to 0.77 S/cm for P3DT. The power factor ~10 $\mu W/mK^2$ achieved in case of P3BT having shortest alkyl chain was found to be 40 times higher than that obtained in case of a polymer having longest alkyl side chain, i.e. P3DT; thus, molecular weight and chain length can be varied to obtain a desirable modification in thermoelectric performances.

3.4 Temperature and Humidity

It can be easily observed from the recent research on organic thermoelectrics that both the temperature and humidity can drastically influence the thermoelectric performances of CPs. Our own experiments on PEDOT:PSS demonstrated that all the thermoelectric parameters are governed by annealing as well as operating temperature because perhaps the temperature affects the carrier density through trapping/release of charge carriers as well as electron–phonon scattering [9]. Electrical conductivity, Seebeck coefficient and power factor, all these three parameters (as shown in Fig. 7) varied with annealing temperature. The PEDOT:PSS films which were annealed at 130 °C exhibited the highest conductivity which increased linearly with temperature in the entire temperature range (shown in Fig. 7a). Whereas, the films annealed at 100, 150 and 170 °C exhibit nearly temperature-independent electrical conductivity in the entire temperature range for operating temperature. Temperature (operating) dependence of Seebeck coefficient (α) for these annealed pristine films is shown in Fig. 7b and in contrast to the other samples, the films annealed at 130 °C exhibit an increase of α from 5 to 9 μV/K with an increase in operating temperature. As a result,

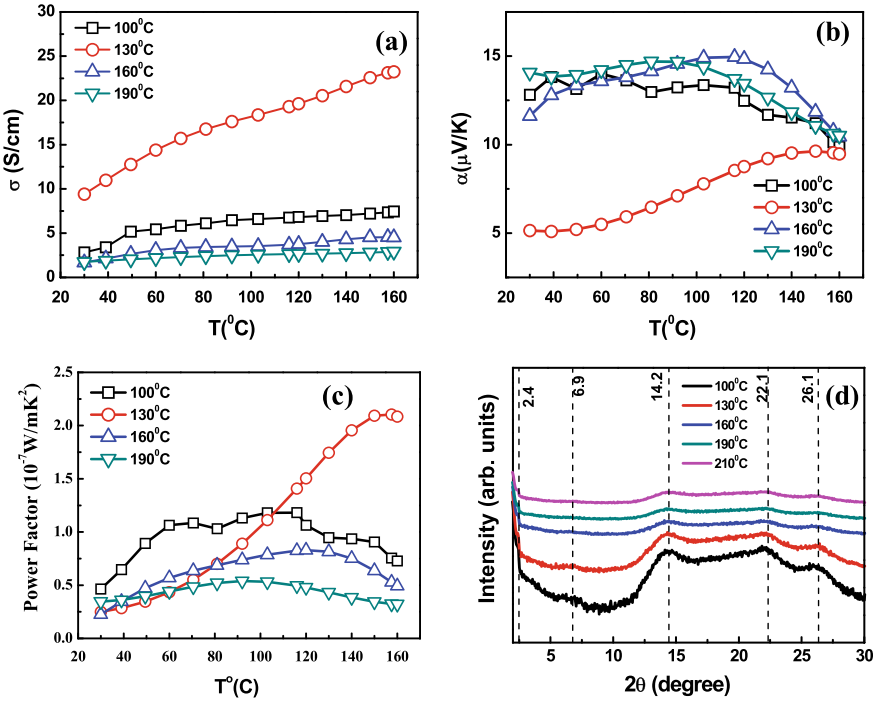

Fig. 7 Temperature dependent **a** electrical conductivity, **b** Seebeck coefficient, **c** power factor and **d** X-ray diffraction data of Pristine PEDOT:PSS films annealed at different temperatures (Reproduced with the permission from Ref. [26])

highest power factor ($\alpha^2\sigma$) of ~2.15 × 10^{-7} W/mK^2 (at 160 °C) was obtained in case of pristine films annealed at 130 °C and it has been mainly attributed to the high σ and moderate α of these samples due to the changes in morphology and conformation of polymer chains. Such a change in morphology as an effect of temperature has also been confirmed by XRD analysis shown in Fig. 7d. The five distinct diffraction peaks at 2θ values of ~2.4°, 6.9°, 14.2°, 22.1° and 26.1°, which correspond to lattice spacings of approximately 38.5, 12.8, 6.4, 4.1, 3.4 Å, respectively, were observed. The peaks observed at 6.9° (corresponding to d ~ 12.8 Å) and 14.2° are attributed to first- and second-order reflections of inter-digited PSS chains [26–28]. Both of these peaks at 6.9° and 14.2° are prominent only for the films annealed at 100 and 130 °C, which suggests that ordering in PSS chains got degraded at higher annealing temperatures.

3.5 Alignment of the Polymer Chains

Alignment is also known to cause an effect on thermoelectric figure-of-merit *ZT* by increasing electrical conductivity in case of CPs. As a result of stretching, it has been found that electrical conductivity can be increased manifold in stretched direction than in case of the perpendicular. For instance, in case of DMSO-mixed PEDOT:PSS, it has been reported that aligned chains enhance carrier mobility and hence, caused an increase in electrical conductivity [9, 26, 29]. Such an improved value of electrical conductivity from 1.5 S/cm of pristine film to 150 S/cm in case of DMSO-mixed film, perhaps could be attributed to the facile motion of charge carriers; and that can be understood as an influence of more aligned/ordered chains of the polymer matrix. This assumption also finds its support from the Raman spectra given in Fig. 8b, which shows that the $C_\alpha = C_\beta$ symmetrical peak corresponding to PEDOT systematically shifts to higher wavenumber with a successive increase in the DMSO content in PEDOT:PSS solution. The blue shift of Raman peak suggests the decrease of bond length, which signifies that PEDOT chains might have rearranged themselves from the curved (benzoid) conformation to (quinoid) stretched/linear form which resulted in greater π–π interactions to further support the alignment of polymer chains [30–32]. Such an enhanced alignment of polymer chains has also been confirmed by AFM images, where random fibrous morphology of pristine films shown in the bottom inset of Fig. 8c got modified by DMSO addition to rearrange in a more aligned fashion (as shown in top inset of Fig. 8c). Schematic shown in Fig. 8a shows that as to how DMSO addition caused alignment of polymer chains to in turn affect thermoelectric performance [26].

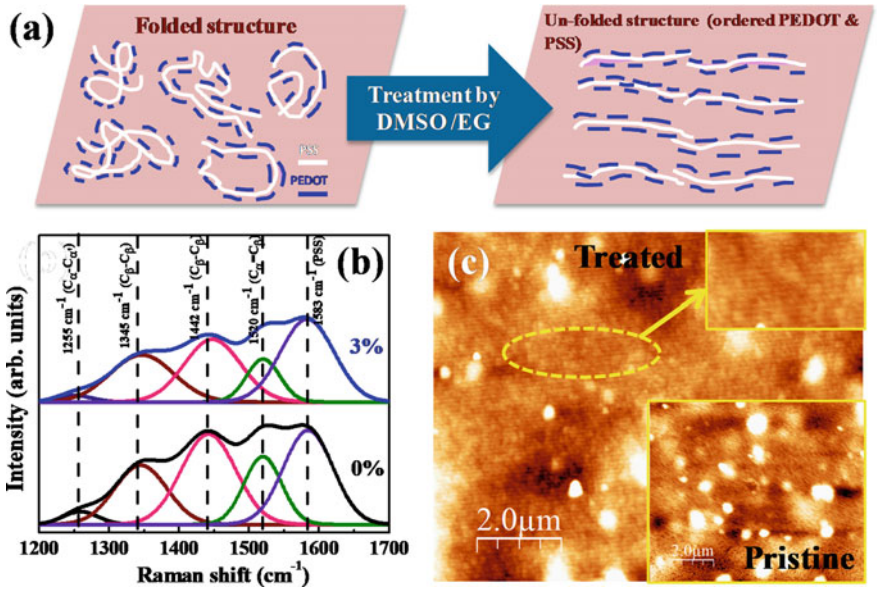

Fig. 8 **a** Schematic showing the unfolding of typical PEDOT:PSS structure to have more ordered/aligned polymer chains, **b** Raman spectra showing a blue shift in case of Pristine (0%) and DMSO-mixed (3%) PEDOT:PSS films, **c** AFM image showing enhanced crystallinity/alignment in DMSO-treated film (Top inset, whereas bottom inset shows the image of Pristine PEDOT:PSS film) (Reproduced with the permission from Ref. [26])

4 Constraints with the Organic Thermoelectric Research

While investigating the many polymers for thermoelectric applications, a lot of challenges emerge not only at the final stage of device development but also at the initial stages of synthesis and fabrication of samples. Some of the constraints that we have come across while carrying out research at our lab are discussed here.

4.1 Long-Term Stability

Most of the organic materials begin to degrade at 150 °C of temperature; hence, their practical use is determined by their thermal stability. On the other hand, inorganic materials are stable over a broad range of temperatures up to 1000 °C. Therefore, organic materials can be the substituent of inorganic materials only in low-temperature applications [6, 10, 33]. Moreover, humidity as well as temperature of the ambience can also influence the stability of organic materials. Tuning the thermoelectric properties via doping can also sometimes makes the conducting polymers less processable and stable. Also, doping of CPs to get efficient n-type nature is not so

easy due to their low electron affinity [34]; hence, most of the CPs are p-type in nature. Further, oxidizing nature of the ambience does not allow n-type polymers to remain stable and thus, scarcity of a stable n-type has become a serious constraint while designing a thermoelectric device of conventional design which requires both p- and n-type of thermoelements. However, many studies have reported the development of n-type polymer through the addition of inorganic materials, metal coordinates compounds, carbon nanotubes, etc. [6, 9, 17, 18].

4.2 Sample Preparation

For depositing environmentally stable polymeric films through solution-processable techniques, a suitable solvent that will not affect stability is also required. Moreover, keeping in view the target applications, the substrate should also be carefully chosen. For instance, the solvent being polar in nature may anchor/interact with the flexible polymeric substrates like Kapton/BOPET and can change the morphology of films to free-standing form [35]. Also, conventional methods such as ball-milling and hot-pressing used for preparing inorganic thermoelectric materials are not appropriate for flexible conducting polymers. Spin-coating and drop-casting methods are usually used to deposit films of organic thermoelectric materials but most effective fabrication methods are still being searched. Whereas, to fabricate organic/inorganic or hybrid polymer composites, simple blending or in situ oxidative/interfacial polymerization/intercalation are mostly used [22, 23, 35, 36]. Moreover, the efficiency of a real device can be much low than those fabricated in the lab because still synthesis techniques that are being preferably used do not produce on a mass scale; and thus, there exists a large variation among different batches of materials [6].

4.3 Measurement Techniques

Precise estimation of thermoelectric parameters is as useful as synthesis of materials. Without having proper and sophisticated techniques of measurement, the identification of desirable material cannot be so easy. For instance, reliable estimation of electrical conductivity needs that the resistance of the organic samples must be several orders of magnitude smaller than that of the substrates so that majority of the current pass through samples/films only. Usually, the four-probe technique should be used preferably to abolish contributions of the current leads or the contacts during the voltage measurements [6, 9]. Besides this, Hall measurement or capacitance–voltage analysis can be used to determine carrier concentration or doping level in CPs [37]. In addition, for better estimation of certain parameters such as Seebeck coefficient and

thermal conductivity, the growth of free-standing organic films (without any substrate contribution) should be promoted. In fact, home-made characterization setups with customized controls that can measure all three parameters simultaneously are highly needed [9, 38].

4.4 Adherence of Films to Substrates

Films deposited on substrates cannot lead to efficient thermoelectric devices unless there is a strong adherence between the film and the substrate. To solve this issue, many times substrates are treated to have anchoring groups so that films get properly adhered to them. However, these days free-standing films are preferred to realize the concept of wearable devices. Sometimes tuning of thermoelectric parameters via doping enhances brittleness of deposited films [38]. So, the concentration of dopant needs to be optimized by using fillers/binding agents to have good mechanical strength along with the improved thermoelectric performance.

4.5 Proper Selection of Metallic Interconnects for Good Electrical/Thermal Contacts

Lack of good electrical contact between organic/inorganic interface in an active composite thermoelectric material, and between active thermoelectric materials (i.e. pure CP or composite) and metal interconnects (for devices), are challenging issues in organic thermoelectrics. In case of organic–inorganic composites, the contact resistance from interfaces can be a reason behind low conductivity. Thus, we need to reduce the contact resistance; one way is to introduce nanostructures into the polymer matrix to have better connectivity [17]. However, excessive doping may lead to an increase in brittleness which might introduce fractures during sample handling and thus, can cause low conductivity [38]. Doping parameters, therefore, require proper optimization in order to offer good electrical performance of the materials. Similarly for device application, the specific contact resistance between metallic interconnects and TE elements should be low (i.e. $\sim 10^{-6}$ to 10^{-7} Ωcm^2). Keeping in view the significance of the interface between the polymer and metallic interconnect, metals having nearly matched work function can be used as an interconnect. For instance, since gold has nearly similar work-function value as of PEDOT:PSS polymer, it was used as a metallic interconnect so as to ensure that the contacts in between PEDOT:PSS thermoelements and with the metal interconnect itself remained Ohmic [26].

5 Strategies for Optimizing Thermoelectric Properties

Designing smart and wearable devices, according to the needs of the modern era, needs novel strategies to optimize thermoelectric properties; so that decoupling of three thermoelectric parameters, i.e. α, σ, κ, can be achieved. Therefore, various strategies that have been employed by other research groups as well as those followed in our laboratory experiments are summarized below.

5.1 Doping

Doping is the easiest and more convenient method to tune the thermoelectric properties of conducting polymers. Properly chosen dopants not only improve the electrical conductivity but can also change the film morphology and conduction type. However, an increase in the concentration of charge carriers caused by doping, though, brings improvement in electrical conductivity but at the same time reduces Seebeck coefficient with an impact on thermal conductivity also; thus, doping has a conflicting impact on the behavioural pattern of these TE parameters [25]. Therefore, to achieve maximum *ZT*, optimum doping level must be identified for most of the CPs [30]. For instance, free-standing films of PPy obtained by interfacial polymerization method were in situ doped by p-toluene sulphonic acid (PTSA) in different concentrations during synthesis. The systematic investigation of thermoelectric properties of free-standing films reveals that morphology as well as the thermoelectric power factor (shown in Fig. 9) can be optimized through controlled doping of PTSA. Similarly, Kim et al. optimized the *ZT* of the PEDOT:PSS mixture by de-doping the portion of unionized insulating dopant (i.e. PSS) using different solvents and thus, achieved a record $ZT = 0.42$ at room temperature [14].

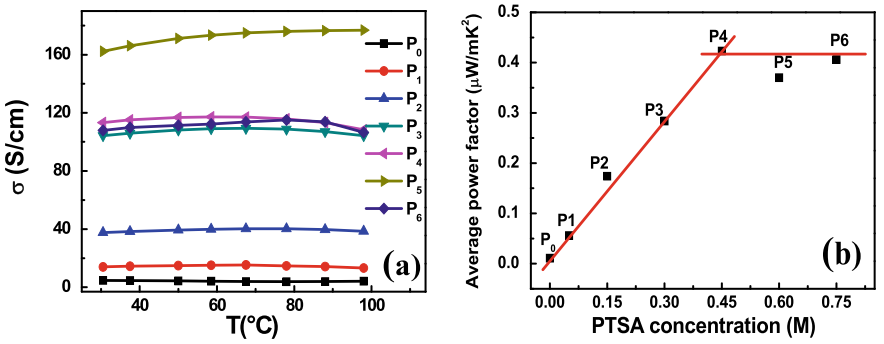

Fig. 9 Temperature dependent **a** electrical conductivity, and **b** variation in average power factor of free-standing PPy films with respect to PTSA concentration (where P0, P1, P2, P3, P4, P5, P6 refers, respectively, to 0.0 M, 0.05 M, 0.15 M, 0.30 M, 0.45 M, 0.60 M, 0.75 M of PTSA concentration) (Reproduced with the permission from Ref. [36])

5.2 *Polymers–Carbon Nanotubes Blends*

CNTs known for their stable one-dimensional nanostructures and excellent electrical and mechanical properties when incorporated into a polymer matrix alter the thermoelectric properties of the materials [39, 41–43]. Contrastingly, we tried to investigate whether treatment with polymers can also modify the properties of the carbon paper made up of MWCNTs. Therefore, these carbon films were treated by drop-casting the polymer polyethyleneimine (PEI) on their surfaces. Temperature-dependent thermoelectric properties of pristine and PEI-modified carbon paper samples are shown in Fig. 10. The temperature dependence of the Seebeck coefficient shown in Fig. 10a suggests that with an increase in PEI content (above 1%) the sign of Seebeck coefficient changes from positive to negative. It indicates that PEI-modified carbon paper behaves like an n-type semiconductor. In fact, it has already been reported that such a transition of conduction from p- to n-type is observed in case of single-walled carbon nanotubes and other polymers by PEI treatment [41, 44, 45]. The n-type conduction in PEI-modified CNTs/polymers has been attributed to the donation of electrons by the electron-rich nitrogen atoms of PEI to the matrix. The electrical conductivity of PEI-modified carbon paper enhances initially up to 5 wt% and after that, it lowers down to a great extent, i.e. below the value obtained in case of pristine carbon paper samples (data shown in Fig. 10b). In another report, an increase in the content of graphene oxide (from zero to 3%) enhanced the electrical conductivity and Seebeck coefficient simultaneously in case of composites of PEDOT:PSS with graphene oxide (GO) after reduction with hydroiodic acid [46]. The improvement is ascribed to the interaction between rGO and polymer matrix and removal of some PSS from the film. The interaction provided a channel for carriers transport and made the PEDOT:PSS chains pack more ordered [39, 46]. However, a unique

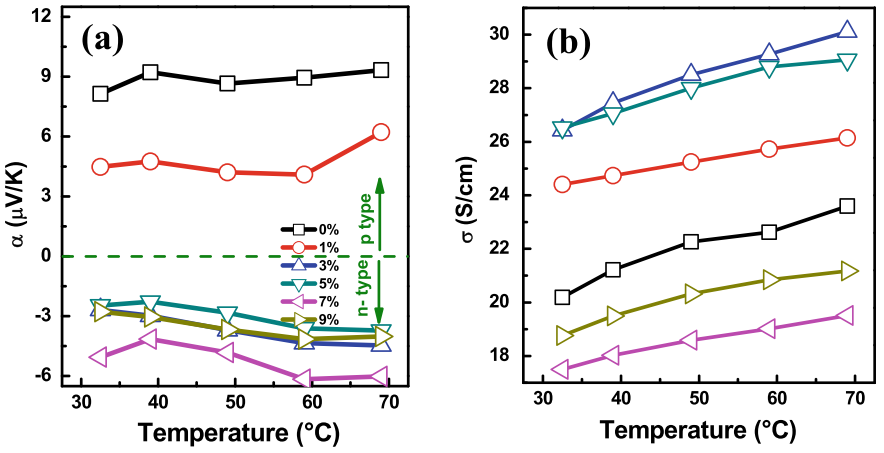

Fig. 10 **a** Seebeck coefficient, and **b** electrical conductivity of polyethylenimine-treated carbon paper thick films

study by Kun Zhang et al. [47] investigated the impact on thermoelectric properties after the addition of a hybrid variety of carbon nanomaterials. Incorporation of the fullerene functionalized graphene ($rGO_xC_{60(30-x)}$) into the PEDOT:PSS caused dual benefits; addition of rGO improved electrical conductivity by increasing the carrier mobility, while C_{60} enhanced the Seebeck coefficient. Thus, future research can look forward to using of a hybrid class of dopants. Such polymer–CNT blends not only improve the thermoelectric properties [39, 46, 47] but also change the conduction type of samples as well [36].

5.3 *Composites of Organic–Inorganic Materials*

Nowadays organic/inorganic composites are being looked as efficient thermoelectric materials because such composites will have advantages of both the realms. Low intrinsic thermal conductivity of polymers if by some means can be integrated with high electrical conductivity of inorganic materials; it can be really helpful for current thermoelectrics. Keeping in view, we synthesized hybrid films of polypyrrole and silver (PPy-Ag) on hydroxylated flexible substrates (BOPET sheet) through eco-friendly photo-polymerization route using UV radiation (~365 nm) and silver nitrate ($AgNO_3$) as photoinitiator [48]. It was observed that in case of PPy-Ag composite films, in situ introduction of Ag particles into the polypyrrole matrix besides enhancing electrical conductivity (from 1.5 to 17.3 S/cm) lowered down the thermal conductivity by one order (0.16–0.002 W/mK) even when these Ag particles are known for their high thermal conductivity (shown in Fig. 11a). Figure 11b shows the embedded Ag nanoparticles embedded in a PPy matrix and actual photograph of PPy-Ag film; bottom inset shows the scattering of phonons through the interface. As

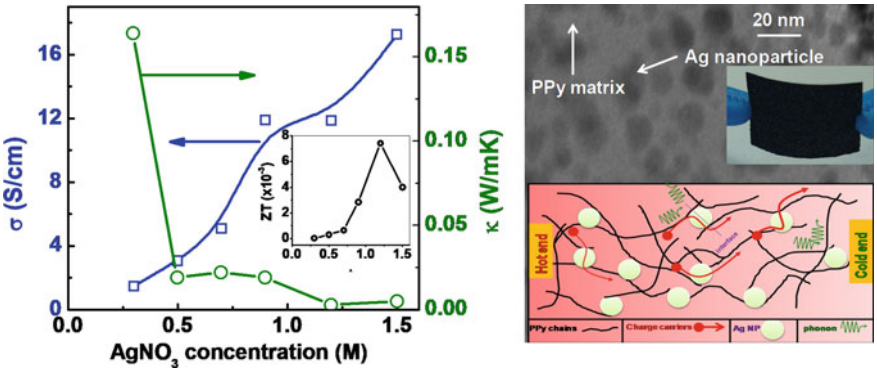

Fig. 11 **a** Thermoelectric properties of PPy–Ag films with $AgNO_3$ concentration (Inset shows the *ZT* variation), **b** SEM image of 1.2 M film with Actual photograph of the PPy–Ag films (whereas bottom inset shows the schematic exhibiting the scattering of phonons through the organic/inorganic interface)

a result, the hybrid PPy-Ag films prepared with 1.2 M of $AgNO_3$ have exhibited the highest *ZT* of ~7.4 × 10^{-3} at 335 K, which is the best value achieved so far, for the PPy-based materials.

On a similar note, we mixed varied concentrations of $Bi_{0.5}Sb_{1.5}Te_3$ (5–15 wt%) to DMSO-mixed PEDOT:PSS for making composite films. Optimizing the inorganic semiconducting alloy not only influenced the thermoelectric properties of PEDOT:PSS to a greater extent but also modified the drop-casted substrate-adherent films to a free-standing form. These synthesized free-standing hybrid films, are indeed, more suitable for developing flexible and wearable thermoelectric power generators to harness the heat of curved surfaces [35]. Moreover, since inorganic materials can be easily doped to have both the conduction types with matching electrical properties, composite films can have an additional advantage to attain n-type conduction through mere optimization of inorganic content. Zhang et al. were able to develop such n- and p-type composites (as shown by Seebeck coefficient values in Fig. 12) much earlier by adding n- and p-type Bi_2Te_3 ball-milled powders to PEDOT:PSS [17]. It was observed that a power factor of 47 μW/mK^2 achieved in case of DMSO-mixed (4%) PEDOT:PSS (CLEVIOS PH1000) enhanced to 131 μW/mK^2 after insertion of ball-milled Bi_2Te_3 particles in the PEDOT:PSS matrix [17]. In fact, these days, collective approaches are needed to bring enhancements in the thermoelectric performance of CPs. With the knowledge of state-of-the-art techniques existing in the field of organic electronics and materials manipulation at the nanoscale, conducting polymers along with their composites can really furnish new dimensions to advanced thermoelectric materials.

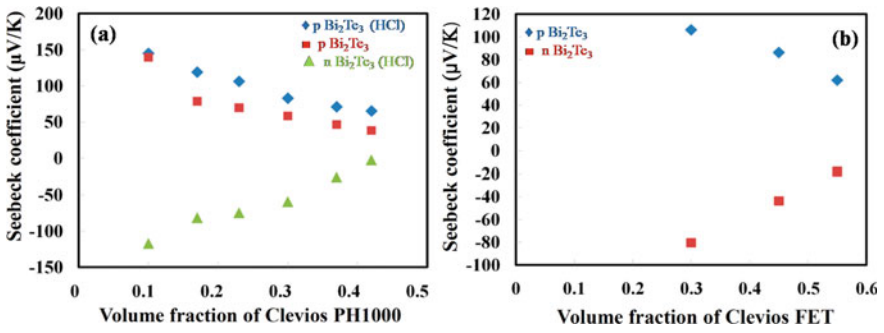

Fig. 12 Seebeck coefficients of **a** Clevios PH1000 mixed with n/p-type Bi_2Te_3 particles (10% volume ratio of PEDOT:PSS); **b** Clevios FET with n/p-type Bi_2Te_3 particles (30% volume ratio of PEDOT:PSS) (Reproduced with the permission from Ref. [17])

5.4 *Nanostructuring*

It has been well-reported that incorporation of nanostructured inorganic materials into the polymer matrix or reducing the polymer to nanodimensions can bring remarkable changes in thermoelectric properties [9, 17, 35]. The highest *ZT* reported till now in the field of inorganic thermoelectrics has been observed in case of nanostructured materials having suppressed κ via phonon scattering centres of hierarchical length scales [49, 50]. Nanodimensional materials when incorporated into the polymer matrix cause reduction in the interfacial resistance because they form proper band alignments with the matrix which can expedite the flow of carriers from the nanoparticles into the matrix. A report by Sahu et al. showed that integration of PEDOT:PSS with various nanostructured chalcogenide materials such as Te and Bi_2Te_3, resulted in high-performance p- and n-type hybrid thermoelectric materials [51]. We have also observed that incorporation of uniformly distributed $Bi_{0.5}Sb_{1.5}Te_3$ in PEDOT:PSS matrix not only helped in the self-peeling of composite films from the substrate (on air-drying) but also improved their electrical conductivity and Seebeck coefficient [35]. The improved electrical conductivity of composite films from 17.5 to 218.3 S/cm (at room temperature and shown in Fig. 13a) found its cause in the strong interaction between organic and inorganic parts. From Fig. 13b, we can easily observe how charge carrier mobility and concentration get affected by varying the doping content. In fact, $Bi_{0.5}Sb_{1.5}Te_3$ nanostructures not only provided better connectivity among polymer chains but due to interaction with PSS, also carried away the detached/additional PSS (which is insulating part) from PEDOT:PSS while settling down; and thus, resulted in better ordering of PEDOT chains as well [35].

Keeping in view the benefits of nanostructuring, we have also tried to use the integrated approach of nanostructuring (mainly used previously for inorganic thermoelectrics) and doping to improve the thermoelectric performance of PPy. Semicrystalline polypyrrole (PPy) nanotubes were synthesized via chemical polymerization method using methyl orange (MO)-$FeCl_3$ as a template for growth and on doping

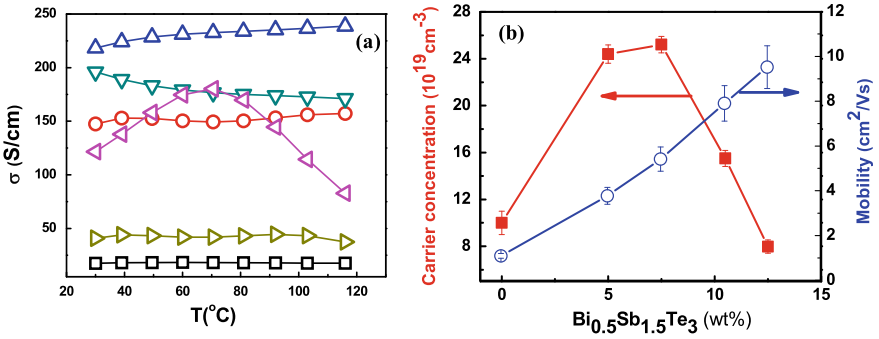

Fig. 13 **a** Temperature dependence electrical conductivity, **b** Hall data of carrier concentration and charge carrier mobility at room temperature (Reproduced with the permission from Ref. [35])

with HCl exhibited high carrier concentration but low charge carrier mobility. Drastic lowering of thermal conductivity (~79%) and enhancement of the Seebeck coefficient caused remarkable improvement in thermoelectric figure-of-merit (i.e. 110% from 1×10^{-3} to 2.1×10^{-3} at 380 K) of HCl doped PPy shown in Fig. 14c, d. This reduction of thermal conductivity has been attributed to whole wavelength scattering of phonons made possible through the hierarchical length scales defect structures (shown in Fig. 14a, b) namely atomic-scale disorder (presence of tensile stress in nanotubes due to large size dopants), nanoscale feature (nanotubular morphology) and mesoscale feature (a few micrometres long grain boundaries formed between PPy nanotubes).

The fact that nanostructures can be more efficient in improving the thermoelectric properties in comparison to their bulk counterpart has also been manifested by comparison of the thermoelectric performance of P3HT in both bulk and nanonet form [40]. Thermoelectric properties of P3HT were enhanced by using a combination of two strategies which included: an increase of electrical conductivity by the growth of dopant nanoparticles on polymer surface; and increase in mobility of charge carriers through engineering of the polymers' molecular structure. As a result, *ZT* of 0.0026 (room temperature) was obtained when P3HT nanonet was doped with

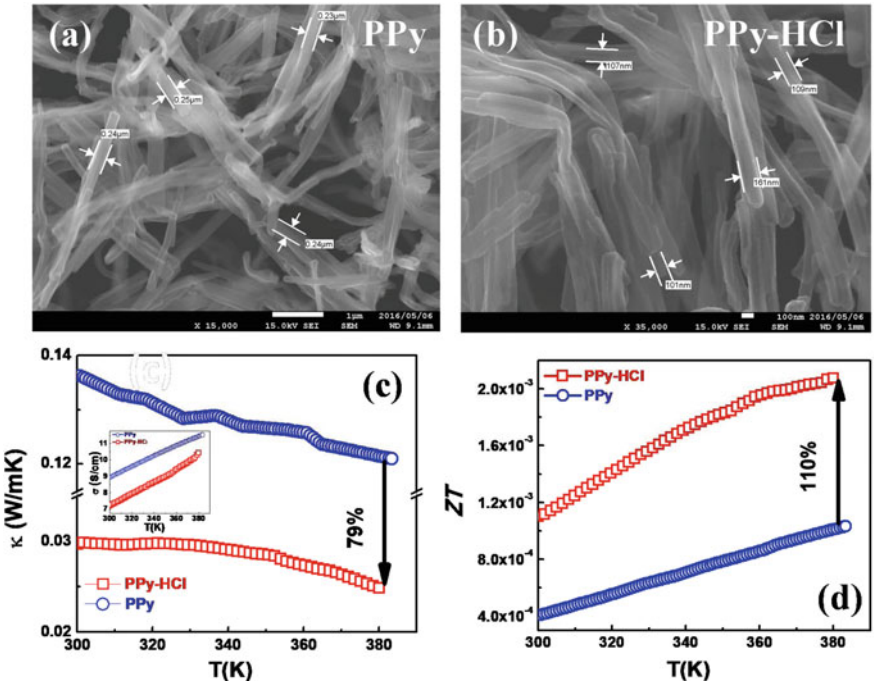

Fig. 14 FE-SEM images **a** pure PPy and **b** HCl-doped PPy nanotube samples, temperature dependence of **c** thermal conductivity (Inset shows electrical conductivity variation), **d** thermoelectric figure-of-merit (*ZT*)

Ag^+ [40]. Therefore, it can be concluded that although organic/inorganic composites can improve thermoelectric properties yet much better thermoelectric performance can be achieved by reaching towards nanoscale.

5.5 *Energy-Filtering Effect*

Energy-filtering phenomenon is the term used to represent the selective flow of charge carriers depending upon their energy through a channel/interface. Organic–inorganic hybrids that possess the advantages of both the domains not only show better connectivity among polymer chains (through nanostructured grains of inorganic materials) resulting in increased mobility but also cause improvement in Seebeck coefficient despite the increase in carrier concentration as a result of doping. This unique feature where an increase in carrier concentration does not reduce the Seebeck coefficient (as α depends on $1/n^{2/3}$) is only exhibited by an interface that is generated either in case of organic–inorganic composites or in reduced graphene oxide–polymer composites; and such an interface provides selective passage to charge carriers. Although organic–inorganic composites have already been discussed yet energy-filtering effect of their interfaces needs to be understood to decouple the strict dependency among the three thermoelectric parameters. A proper energy-filtering interface establishes when there is: (i) a good contact between polymer and nanoparticles; (ii) a similar work function of both the materials to facilitate the transfer of high-energy carriers across the interface. For instance, Bi_2Te_3 and P3HT composites were investigated because a larger work function of Bi_2Te_3 (i.e. ~5.3 eV) in comparison to 4.1 eV of P3HT readily helped the charge carriers to transfer from P3HT to Bi_2Te_3 when there existed no potential barrier due to work-function difference [23]. Band-alignment between P3HT (whose band gap ranges from ~2.0 to < 0.1 eV depending upon the doping level) and Bi_2Te_3 (having band gap ~0.16 eV) determines the height of the interfacial potential barrier [23]. Thus, by manipulating the height of the potential barrier by varying doping levels, carrier scattering at the interface can be optimized to enhance the thermoelectric performance. Moreover, such interfaces kept the thermal conductivity very low (i.e. ~0.86 W/mK even with 20 wt% Bi_2Te_3) due to the effective scattering of the majority of the phonons' wavelength [23].

Similarly, the enhanced power factor of PEDOT/rGO composites ~32.6 $\mu W/mK^2$ can be attributed to size-dependent energy-filtering effect created due to the coating of nanostructured PEDOT:PSS on the rGO [46]. Similarly, in case of PEDOT:PSS/$Bi_{0.5}Sb_{1.5}Te_3$ composites, not only electrical conductivity got improved from 17.5 to 218.3 S/cm but also five times increase in the value of Seebeck coefficient (in comparison to pristine) was observed. In fact, the interface of PEDOT:PSS/$Bi_{0.5}Sb_{1.5}Te_3$, due to a very narrow depletion width of energy barrier as shown in Fig. 15, caused facile transport of holes to increase electrical conductivity. However, the same interface does not allow low-energy charge carriers to tunnel

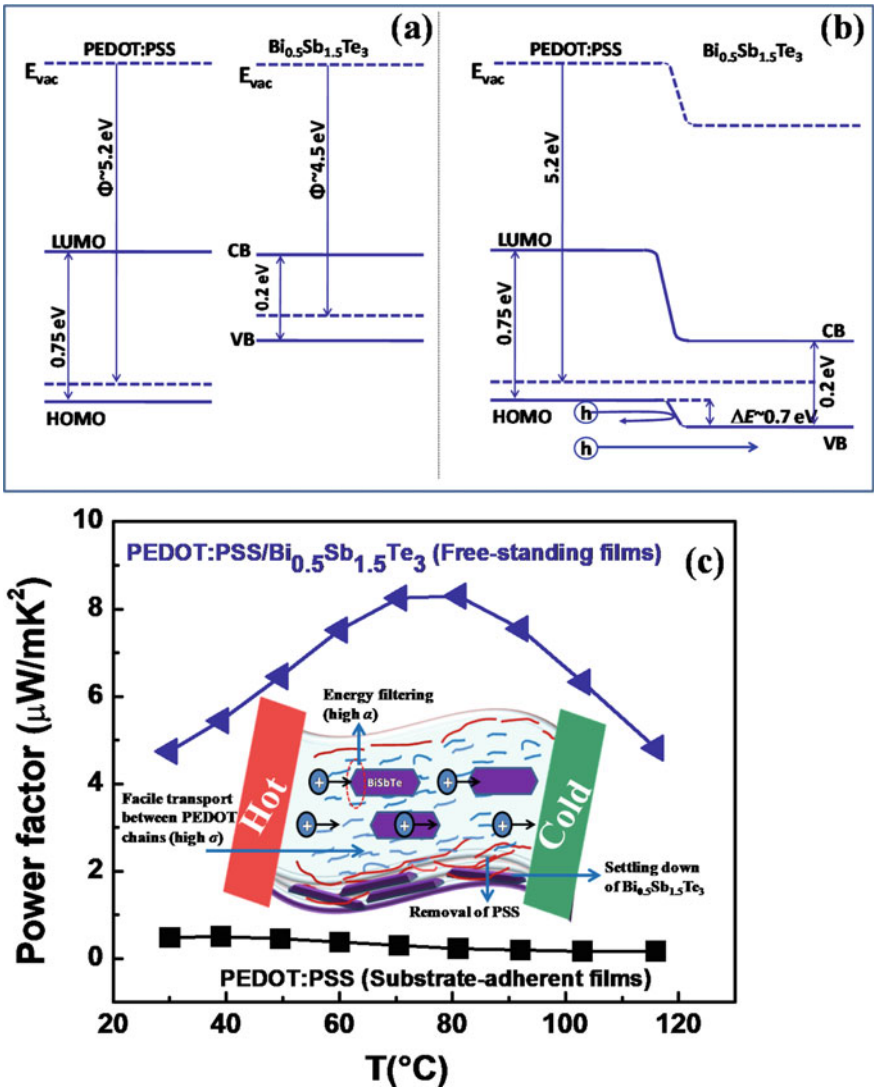

Fig. 15 **a** Equilibrium energy band diagram of PEDOT:PSS and $Bi_{0.5}Sb_{1.5}Te_3$, **b** energy band diagram of PEDOT:PSS/$Bi_{0.5}Sb_{1.5}Te_3$ interface, **c** graph showing temperature-dependent power factor of pristine PEDOT:PSS and composite films (Inset schematic shows the interaction between PEDOT:PSS and $Bi_{0.5}Sb_{1.5}Te_3$ to propose the mechanism behind improved thermoelectric power factor and peeling-off in case of the composite films) (Reproduced with the permission from Ref. [35])

through such a high-energy barrier interface and they get scattered back (pictorially shown in Fig. 15b). Therefore, such selective/filtered energy transport of charge carriers may contribute to the enhancement of the Seebeck coefficient [35].

5.6 Polymer–Polymer Blends (Multilayer Approach)

Recently, a novel technique of combining two or more different conducting polymers has been used to optimize thermoelectric performance in case of PEDOT:PSS/PANI-CSA composites [53]. Multilayer approach followed in these polymer hybrids enhanced electrical conductivity in two ways: firstly, via stretching of PEDOT layer due to underneath PANI-CSA chains and secondly, because of hole diffusion from PANI-CSA layer to the PEDOT:PSS layer. Moreover, the non-variation of Seebeck coefficient was also observed due to the difference in the orbital energy of two polymers which altered the symmetry of the density of states around Fermi level. This bilayer/multilayer approach can be extended to other combinations of polymer systems also for improving their thermoelectric performance [9, 53].

6 Critical Analysis of Reported Organic Thermoelectric Power Generators (OTEGs)

Although the organic thermoelectric research is blooming day by day, still the development of organic thermoelectric power generators has been at the prototype stage. A lot of efforts are still required to lead such prototypes towards full-fledged commercial devices. But, these conducting polymer based thermoelectric devices that have been reported will certainly remain as a landmark for paving the way towards futuristic smart and wearable devices. Design engineering of a thermoelectric power generator determines how much power can be extracted from a thermoelectric material [4]. Usually, a conventional design of TEG consists of a large number of p-type and n-type thermoelements alternately connected electrically in series and thermally in parallel [4]. But in case of organic TEGs, lack of stable n-type polymer puts a constraint on traditional design and OTEGs are designed using only p-type material (as shown in the schematic given in Fig. 16a). However, connecting the hot-end of a former thermoelement to the cold-end of the next can hinder the effectual heat flow via metallic interconnects. And this can eventually reduce the temperature difference across the device which in turn degrades the power output as well as the device efficiency. Besides this, heat flow is also regulated by the thermal contact resistance between heat source and device, and thus, needs to be minimized for efficient transfer of heat from source to the hot-end of the device. Futuristic wearable devices that aim to harness heat from the hot-curved surfaces must be designed after keeping all these constraints in mind. Electrically insulating and thermally conducting adhesives based

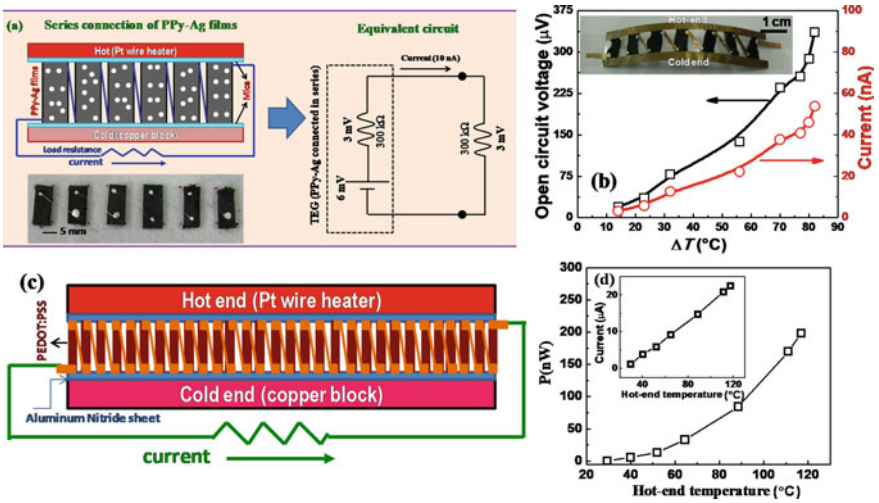

Fig. 16 **a** Schematic showing the practical demonstration of the PPy–Ag films as a thermoelectric power generator when connected electrically in series and thermally in parallel along with its equivalent circuit (lower inset shows the photograph of the TEG) (Reproduced with the permission from Ref. [48]), **b** output characteristics (open-circuit voltage and current generated at the matched load of 3.1 kΩ) of a TEG designed in the form of a wristband using seven numbers of free-standing PPy films (Inset shows the actual photograph of the device) (Reproduced with the permission from Ref. [36]), **c** schematic showing the OTEG based on DMSO-mixed PEDOT:PSS films, **d** power output of the this OTEG as a function of hot-end temperature (Inset shows the current as a function of hot-end temperature) (Reproduced with the permission from Ref. [26])

on Al_2O_3 or AlN can be used to provide a good thermal contact [9]. A few prototype organic thermoelectric devices that have been designed as a result of our experiments along with those reported by other research groups are compiled here; so that the challenges that restrict their commercial use can be identified and analysed.

For instance, six polypyrrole-silver (PPy-Ag) (with Ag concentration ~1.2 M) films were connected electrically in series using silver paint and silver wires. Resistance of individual strip was 50 kΩ; therefore, for a matched load of 300 kΩ, the respective value of open-circuit voltage and current was 6 mV and 10 nA at ΔT ~140 K [48]. Low output power ~30 pW was obtained in comparison to the ~2.8 $\times$ 10^{-7}W which was input heat (Q) to the OTEG (estimated through the relation: $Q = \kappa A(\Delta T/\Delta X)$); and thus, resulted in an efficiency of ~0.01% [48]. However, the output power can be improved by adding a number of stripes and possibly this TEG can be combined with supercapacitors that continuously charge up and operate in burst mode to provide power to an otherwise ideal sensor or RFID tags, etc. While the second form of PPy films based TEG, in which free-standing films were configured to result in a wearable form, exhibits that such flexible films of conducting polymers (PPy in this case) have good potential to harness heat from hot-curved surfaces. But still, the main requirement is to achieve high power output which is still low, i.e. 6.4 pW. For a temperature difference of ~80 °C and matched load resistance of 3.1 kΩ,

the respective value of open-circuit voltage and current was 336 μV and ~46 nA [36].

Figure 16c shows that a large number of thermoelements can be added to enhance the power output of an OTEG. For a temperature difference of ~80 °C (hot-end maintained at ~117 °C), the open-circuit voltage obtained out of PEDOT:PSS films based TEG was ~17.6 mV, while the current of 22.5 μA was estimated at load resistance of 391 Ω and shown in Fig. 16d [26]. An output power of 203 nW obtained using such a simple OTEG that was based on thirty numbers of thermoelements suggests that increase in the number of thermoelements can certainly enhance power output for such applications that need 100–200 μW.

Some of the significant designs that have been reported by other research groups are shown in Fig. 17. Wanq et al. [54] demonstrated the use of a flexible thermoelectric nanogenerator both as a temperature sensor and energy harvester based on Te

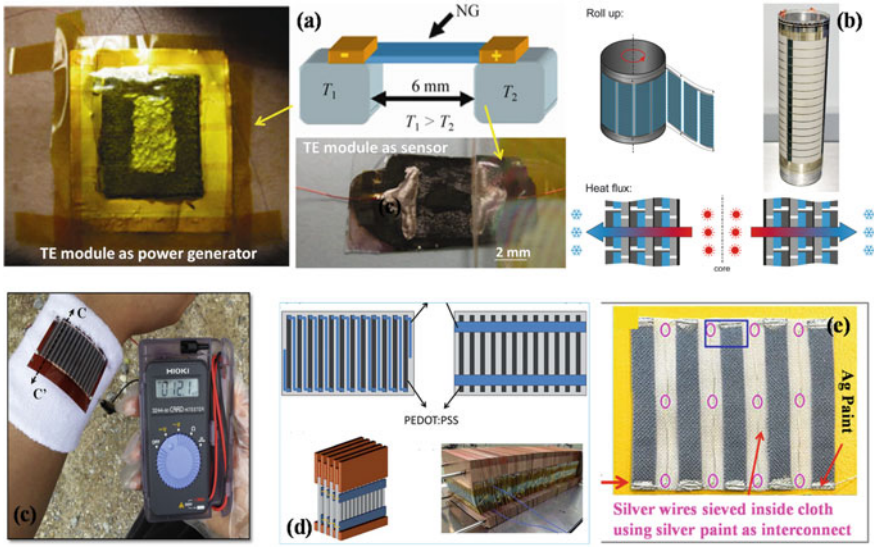

Fig. 17 **a** Schematic diagram showing measurements of the device attached on the human body and as a self-powered temperature sensor (Photographs of a Te-nanowire/P3HT-polymer composite device on a fabric attached with Kapton substrate) (Reproduced with the permission from Ref. [54]), **b** illustration of and picture of the rolled-up final device, Bottom: Illustration of the heat transport in the final setup (Reproduced with the permission from Ref. [55]), **c** performance demonstration of a flexible TEG module exploiting body heat and cross section along with C–C′ (The output voltage of the module with 15 TE couples and the length of 30 mm, using the temperature difference between the body temperature and the ambient air temperature was 12.1 mV at a temperature difference of about 5 K) (Reproduced with the permission from Ref. [56]), **d** schematic representation of the Series and Parallel PEDOT:PSS array, Bottom shows the schematic and actual photograph of the PEDOT:PSS modules sandwiched between copper plates (Reproduced with the permission from Ref. [57]), **e** schematic illustration of a fabric TE power generating unit made of multiple PEDOT:PSS coated strips and photograph of the positive face of the TE generator device (Reproduced with the permission from Ref. [58])

nanowire/P3HT composites (shown in Fig. 17a). Maintaining temperature gradient in case of such TEGs is much tricky because if the substrate is flexible and insulating, we have to find a solution for heat conduction from the human surface in touch with the device (TEG). Roll-to-roll (R2R) technique shown in Fig. 17b provides a remarkable design if its constraints can be removed. It allows quick fabrication of OTEG which can cover a large surface area for practical applications. Moreover, heat loss in such a device is minimized as heat loss by the inner most layer can be absorbed by the next one encapsulating it. However, certain issues with the R2R method such as loss of thermal gradient through the carrier substrate as well as a need and development of thin substrates to reduce bulkiness must be resolved for commercial use [55]. Similarly, screen printing was used to fabricate flexible modules to have a large-area device [56]. Initially, n-type legs were screen-printed on polyimide (PI) substrate using Bi_2Te_3 film and subsequently, Sb_2Te_3 film was printed on the same PI film to form p-type legs. The module having 7 TE couples gave an output voltage of 85.2 mV and the output power density of 1.2 mW/cm^2 at $\Delta T = 50$ K with hot-end temperature ~333 K [56]. Another large-area module was developed by soaking a paper with PEDOT:PSS. The module contained 300 pieces of parallel-connected paper (10 in parallel, 30 in series; Fig. 17d) [57]. Since the power ~50 μW and open-circuit voltage ~40 mV achieved from this module was low, therefore a DC to DC convertor was used to boost the output voltage to ~2.2 V (i.e. sufficient to illuminate an LED). However, paper provide better wettability to PEDOT:PSS than other plastic substrates but at the same time making a large module using such films increases brittleness and degraded the device [57].

Figure 17e shows a fabric-based TEG, for which a commercial cloth was dipped in PEDOT:PSS solution and strips cut from this one were sieved on another cloth using silver wires and paint [58]. However, not all clothes can be used to make fabric-based TEG as breathable aspect and flexibility of the fabric should not be hampered after dipping in polymeric solution. The fabric-based TE module consisting of 5 PEDOT:PSS coated strips resulted in an output voltage of ~4.3 mV at a temperature difference (ΔT) of 75.2 K and when the load resistance matched the internal fabric resistance, the maximum power (P_{max}) was 12.29 nW [58]. Although, this is not the exhaustive list of all the organic TEGs that have been reported till now, but still the important issues of concern that may occur while fabricating such devices can be easily identified by critical analysis of such reports. Furthermore, not many groups have emphasized on the determination of device efficiency. But, the estimation of efficiency is much needed to seek practical use of thermoelectric devices. In short, investigation of various forms of OTEGs from the perspective of futuristic requirements is very beneficial as it can guide us to design the devices depending upon the target surfaces and desirable applications.

7 Summary

Conducting polymers based organic thermoelectric power generators can convert low-temperature natural/waste heat to useful electrical power. Temperature gradients (up to 10–12 °C) lying in natural resources (such as oceans, geothermal sources, etc.) can be used to generate energy. In addition, for low-power applications, the human body's temperature can also serve to create a thermal difference (with the ambience) for being used in thermoelectric applications. Whereas, automotive/instrumental exhausts can also be a source of waste heat which can be tapped with the help of thermoelectric materials to minimize heat loss and reduce global warming. Therefore, conducting polymers with their proven potential in the field of supercapacitors, sensors, and electronic displays, along with their nature friendliness, low thermal conductivity, and ability to emerge as free-standing films, can serve as promising materials for room-temperature thermoelectric applications [9]. Moreover, for this modern era which is striving for smart technologies and wearable devices; conducting polymers owing to their solution processability (that allows facile deposition on various types of large-area flexible substrates) and compatibility to blend with inorganic materials have gained the attention of many research groups worldwide.

In this chapter, we have described the significance of conducting polymers in the field of thermoelectric power generation (from materials to the device status). Measurement techniques to estimate accurate values of thermoelectric parameters have also been emphasized. In addition, factors affecting the thermoelectric performance; challenges that emerge through the whole process of thermoelectric power generation, i.e. beginning from the initial stages of synthesis to final stage of device fabrication; and strategies that need to be followed for optimizing thermoelectric performances; are also described on the basis of results obtained in our experiments as well as by giving examples from other reports. However, since conducting polymers possess the additional advantage of low thermal conductivity, most of the strategies that are employed for enhancing the efficiency of polymeric thermoelectric materials focus on improving the power factors only.

Results of investigation on thermoelectric performances of various conducting polymers such as Polypyrrole, Poly(3,4-ethylenedioxythiophene):poly(styrene sulfonate) i.e. PEDOT:PSS, Poly(3-hexylthiophene) (P3HT) are discussed in relevance to various sections of the chapter. Optimization of thermoelectric properties is shown with the help of results obtained in case of chosen polymers by controlling annealing temperatures, dopant concentrations as well as dopant variations. The influence of the addition of an inorganic material to polymer matrix has also been investigated by synthesizing composite films. In addition, a few experiments that resulted in changing the conduction nature (i.e. from p- to n-type) of CPs-based films are also discussed. Important results that have been obtained as the output of the experiments carried out at our lab on different polymers and already stated in the previous sections of the chapter are summarized as follows:

(i) Polypyrrole: Polypyrrole was investigated in three forms: (i) substrate-adherent films, (ii) free-standing form, (iii) bulk nanostructures. In case of PPy-Ag composite films, in situ introduction of Ag particles into the polypyrrole matrix besides enhancing electrical conductivity (from 1.5 to 17.3 S/cm) lowered down the thermal conductivity by one order (0.16 to 0.002 W/mK) even when these Ag particles possess high thermal conductivity; this lowering of κ has been attributed to scattering of phonons at the organic/inorganic interface. As a result, the highest ZT ~7.4×10^{-3} (at 335 K) was obtained in these composite films [48]. Though the output power obtained from PPy-Ag films based TEG ~30 pW (using 6 strips connected electrically in series and subjected to a temperature difference of 140 K) has been found quite low, yet suggests good prospect for developing organic TEGs as energy harvesting devices [48]. Whereas, investigation of bulk form consisting of nanotubular polypyrrole demonstrated that nanostructuring can also be an effective tool for altering the thermoelectric performance. Improved ZT of ~2.1×10^{-3} (at 380 K) exhibited by HCl-doped nanotubular PPy (mentioned in Sect. 5.4) suggests that thermoelectric performance was optimized through the cumulative effect of doping and nanostructuring; similar to the results obtained in case of PPy-Ag nanocomposite films. Dopant treatment of PPy nanotubes also resulted in the lowering of κ without much affecting the electrical transport; this work provided an important finding that the phonon scattering approach which had been widely used to reduce thermal conductivity in the field of inorganic thermoelectrics could be applied to organic materials also [52]. In case of free-standing films synthesized through interfacial polymerization at the liquid/liquid interface, doping with Tos exhibited remarkable enhancement in electrical conductivity (i.e. from 1.5 to 125.7 S/cm) [36]. Though the Seebeck coefficient in this case was much lower than that observed in case of PPy-Ag films yet the free-standing motif obtained in this work suggests the good potential of PPy films in flexible thermoelectric applications. Therefore, it can be summarized that the variation of the dopant concentration optimizes the thermoelectric properties in the film as well as the bulk form of PPy polymer [9]. Also, various approaches of synthesis can be used to fabricate PPy in the specific form that suits the desirable thermoelectric application.

(ii) Poly (3,4 ethylene-dioxy-thiophene):poly(styrene sulfonate) (PEDOT:PSS): From the experiments carried out with PEDOT:PSS, it was observed that simple addition of organic solvent like DMSO/EG improved the thermoelectric properties. The mechanism behind the power factor enhancement has been attributed to enhanced exposure of PEDOT conductive regions due to the alignment of both the PEDOT and PSS chains; when the insulating PSS got detached from the typical core–shell-type structure under the influence of organic solvents [26]. In addition, we fabricated a flexible thermoelectric generator by using only p-type stripes of polymer PEDOT:PSS similar to the TEG developed using PPy-Ag films; but in this case an array of 30 elements (shown in Fig. 16c) was prepared by drop-casting DMSO-mixed PEDOT:PSS solution through a patterned mask to have a relatively large-area TEG. This array resulted in an output power of 203 nW which indicated that many thermoelements could be clubbed together for enhancing the power output [26].

Whereas, composite films of PEDOT:PSS and $Bi_{0.5}Sb_{1.5}Te_3$, provides an insight that incorporation of $Bi_{0.5}Sb_{1.5}Te_3$ in PEDOT:PSS matrix not only helped in self-peeling of composite films from the substrate (on air-drying) but also improved their power factor. $Bi_{0.5}Sb_{1.5}Te_3$ nanostructures while settling down hold the detached/additional PSS (which is insulating polymer) away from PEDOT:PSS matrix; thus, resulted in better ordering and connectivity of conducting PEDOT chains to cause improvement in the electrical conductivity [35]. Besides this, PEDOT:PSS/$Bi_{0.5}Sb_{1.5}Te_3$ interface of the composites provided the energy-dependent facile pathway for transport of the charge carriers to cause simultaneous enhancement of the Seebeck coefficient. The obtained results certainly exhibit that incorporation of nanostructured inorganic material (i.e. $Bi_{0.5}Sb_{1.5}Te_3$ in this case) in the polymer matrix can be applied as a promising strategy to obtain free-standing films for high-performance flexible thermoelectric devices [35].

(iii) Poly(3-hexylthiophene) (P3HT) and polyethylenimine-treated carbon paper films: In case of P3HT films, doping with ferric chloride not only caused the transition in conduction type but also changed the morphology from substrate-adherent to free-standing form. The huge Seebeck coefficient ~−15000 μV/K (even larger than conventional inorganic materials) with low electrical conductivity was obtained [9]. Whereas, carbon paper (made from multiwalled carbon nanotubes) was synthesized in collaboration with the research group at National Physical Laboratory, New Delhi. The thick film/carbon paper exhibited very low resistance (~1.2 Ω) and was quite sturdy and could be bent many times. While investigating for its thermoelectric properties, it was found that its conduction nature changed from p- to n-type on treatment with polyethylenimine (PEI) [9]. Though the power factor of carbon paper films reduced on treatment with PEI from 0.13 to 0.01 $\mu W/mK^2$, transition of conduction type can be very useful to fabricate a thermoelectric power generator of conventional design (i.e. which makes use of both p- and n-type of thermoelements). These interesting results provide an insight that the morphology, conduction type as well as the thermoelectric properties of conducting polymers can be optimized according to the specific thermoelectric applications.

Moreover, we have also discussed TEGs that were based on films obtained as a result of our research in order to suggest other possibilities of designing OTEGs specific to different target surfaces/applications. These TEGs have been designed either by using the films grown on flexible substrates such as BOPET/KAPTON or films in free-standing form. A few TEGs reported by other research groups have also been discussed to analyse the challenges that may come across during design and development of the thermoelectric devices for practical applications. In this modern era, where emphasize is laid upon smart technologies, such summary of various reported architectural designs of TEGs can pave the way to use conducting polymer based films according to the target surfaces and desirable applications. Results that have been obtained as an outcome of the organic thermoelectric research being carried out world-wide clearly suggest that conducting polymers based films possess good future prospects for energy harvesting applications.

8 Prospective Scope

So far, the reports on thermoelectric applications of various CPs as well as the results obtained by the experiments carried out at our lab suggest that low power factor is the main hurdle in achieving high efficiency. The tuning of doping levels in a CP (in such a way that critical regime of transport can be achieved) may be the best strategy for power factor optimization. However, improvement in power factors is mostly caused by improving electrical conductivity (either by doping or mobility enhancement) without much focus on the Seebeck coefficient. Through optimizing the power factors and taking care of certain issues (shown in Fig. 18), we can surely achieve high efficiency in conducting polymers based thermoelectric devices and think about the use of OTEGs in practical applications.

But, to have high-output voltage from the OTEGs, not only electrical conductivity but the Seebeck coefficient also (of the organic thermoelements) must be high. Nowadays organic–inorganic composites are preferred for improving the Seebeck coefficient in CPs by energy-filtering effect at the interface. But while designing such composites, care has to be taken that the conducting paths should have organic

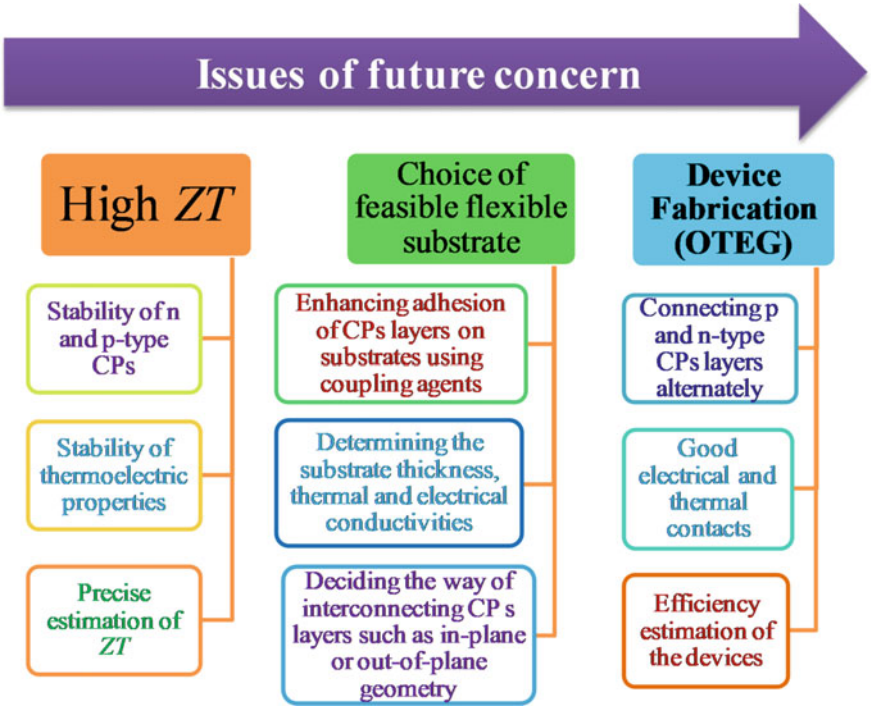

Fig. 18 Schematic revealing issues of future concern that emerge at various stages of organic thermoelectric power generation

and inorganic components with a weighted average of Seebeck coefficients. Moreover, Fermi levels of organic and inorganic components need to be matched to have a facile transport of charge carriers. Future studies should emphasize on careful design of organic/inorganic interface so that high electrical conductivity should not get compromised with a high Seebeck coefficient.

Various strategies that can enhance the thermoelectric properties of a particular CP are mostly applied separately. In the present scenario, we need to adopt a cumulative approach by merging these strategies (mentioned in the schematic shown in Fig. 19) to strengthen the thermoelectric performance of a specific CP. However, to evaluate the thermoelectric performance of synthesized CP/composite films, after the synthesis stage, attempts should be made for the precise estimation of *ZT*. Mostly home-built customized setups used for measurement techniques emphasize the need for developing some standard measurement tools/apparatus. We propose that the establishment of some standards like those existing in the field of photovoltaics is really a significant issue to be looked upon.

With the design and synthesis of high *ZT* organic materials, there comes the challenge of configuring such materials in terms of smart and flexible wearable devices. Effective device geometry needs both p- and n-type of CPs. Though there are many

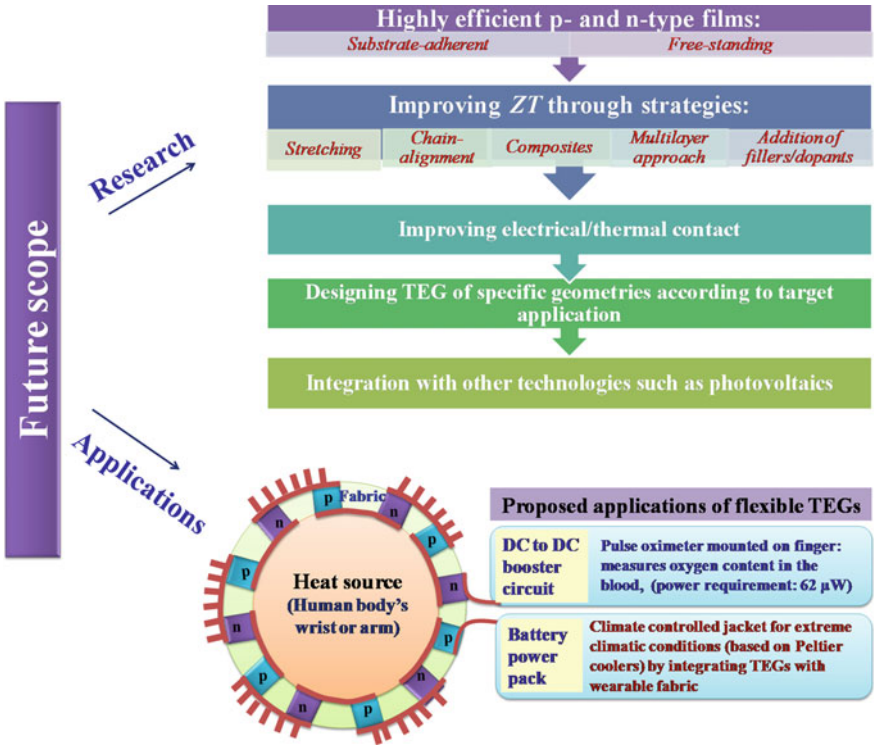

Fig. 19 Schematic showing multidimensional aspects of futuristic organic thermoelectric research

options available for stable CPs with p-type conduction, yet n-types available so far (by doping of two polymers or from co-ordination compounds of metal ligands) do not exhibit enough electrical conductivity and good environmental stability. Therefore, future research should emphasize on development of stable and reliable n-type polymers. In addition, an inexpensive technique that can lead to enormous production on a large scale is yet to be discovered. In this regard, we need to integrate the available tools of large-area electronic displays, photovoltaics, etc. to the field of flexible thermoelectrics.

However, device design and structure make the most significant part to reach the final stage of commercial devices. A decrease in thermoelectric performance due to the degradation of interfacial contact needs to be minimized and proper techniques must be developed to have better interconnects. Anisotropy of both electrical and thermal conductivity should also be considered while carrying out future thermoelectric research. The commercial use of wearable TE devices (having different device geometries) may not only get limited by their low efficiency but also by the level of comfort in using them. Schematic shown in Fig. 19 summarizes the multidimensional future prospects that are available in the field of organic thermoelectrics.

Regardless of so many challenges, the ongoing research in this field certainly ensures that CPs-based thermoelectric power generators (i.e. OTEGs) can be made viable for practical use. However, the presently demonstrated OTEGs have exhibited low efficiency/power output still their deployment can be thought of by using voltage boosters or charging supercapacitors/energy-storage cells which can provide large output in a small flash of time. In summary, inherent features of conducting polymers like low cost, flexibility, non-toxicity, solution processability along with promising outcomes of the ongoing organic thermoelectric research serve as real incentives to look for the deployment of conducting polymers based devices to harness low-temperature heat.

9 Conclusion

The book chapter summarizes the significance of conducting polymers in the field of thermoelectrics that has remained dominated by conventional inorganic materials for many decades. Conducting polymers and their composites, not only, are being looked as promising substitutes of these inorganic materials for room-temperature thermoelectric applications but also have added new dimensions to the device fabrication owing to their flexibility and capability of being patternized on large-area substrates. In this chapter, we have discussed the current status of organic thermoelectric research along with the measurement techniques that are much crucial for identifying promising materials through accurate estimation of thermoelectric parameters. Ongoing research on organic thermoelectrics suggests that the efficiency of polymeric thermoelectric materials can be controlled mainly by tuning their power factors because of their already low intrinsic thermal conductivity. Therefore, various strategies such as doping, chain alignment, addition of fillers/binding agents/inorganic

materials, nanostructuring are described as the causative factors that can optimize the thermoelectric performances of conducting polymers. However, lack of stable n-type polymers, good and efficient thermal and electrical contact, and proper metallic interconnects, are still some of the major challenges that can obstruct the realization of conducting polymers in form of real-life devices. To investigate the future prospects of organic thermoelectric devices, a few prototype thermoelectric power generators based on our own experiments have also been designed and developed along with the critical analysis of already reported architectural designs. Thermoelectric devices based on free-standing conducting polymer films can serve as a real incentive to develop smart and wearable devices for tapping heat from the curved hot surfaces. In short, the book chapter reveals that conducting polymers having inherent features like low cost, flexibility, non-toxicity, solution processability, when integrated with inorganic materials/carbon nanotubes avail benefits of both the components and exhibit remarkably improved thermoelectric performances; and such composites can really serve as new generation promising materials for harnessing natural as well as waste heat of the surroundings.

References

1. C. Han, Z. Li, S. Dou, Chin. Sci. Bull. **59**, 2073 (2014)
2. G. Snyder, E. Toberer, Nat. Mater. **7**, 105 (2008)
3. F. DiSalvo, Science **285**, 703 (1999)
4. D. Aswal, R. Basu, A. Singh, Energ. Convers. Manag. **114**, 50 (2016)
5. J. Bahk, H. Fang, K. Yazawa, A. Shakouri, J. Mater. Chem. C **10**, 1039 (2015)
6. M. Bharti, A. Singh, S. Samanta, D. Aswal, Prog. Mater Sci. **93**, 270 (2018)
7. O. Bubnova, X. Crispin, Energy Environ. Sci. **5**, 9345 (2012)
8. M. He, F. Qiu, Z. Lin, Energy Environ. Sci. **6**, 1352 (2013)
9. M. Bharti, Studies on thermoelectric properties of conducting polymers (Dissertation, University of Mumbai, 2018)
10. R. Kroon, D. Mengistie, D. Kiefer, J. Hynynen, J. Ryan, L. Yu, C. Muller, Chem. Soc. Rev. **45**, 6147 (2016)
11. B. Russ, A. Glaudell, J. Urban, M. Chabinyc, R. Segalman, Nat. Rev. Mater. **1**, 1 (2016)
12. Y. Chen, Y. Zhao, Z. Liang, Energy Environ. Sci. **8**, 401 (2015)
13. D.K. Aswal, J.V. Yakhmi, (eds.) *Molecular and Organic Electronic Devices* (Nova Sciences Publishers, 2010)
14. G. Kim, L. Shao, K. Zhang, K. Pipe, Nat. Mater. **12**, 719 (2013)
15. L. Xu, Y. Liu, B. Chen, C. Zhao, K. Lu, Polym. Compos. **34**, 1728 (2013)
16. K. See, J. Feser, C. Chen, A. Majumdar, J. Urban, R. Segalman, Nano Lett. **10**, 4664 (2010)
17. B. Zhang, J. Sun, H. Katz, F. Fang, R. Opila, A.C.S. Appl, Mater. **2**, 3170 (2010)
18. Y. Sun, P. Sheng, C. Di, F. Jiao, W. Xu, D. Qiu, D. Jhu, Adv. Mater. **24**, 932 (2012)
19. R. Schlitz, F. Brunetti, A. Glaudell, P. Miller, M. Brady, C. Takacs, C. Hawker, M. Chabinyc, Adv. Mater. **26**, 2825 (2014)
20. C. Choy, Polymer **18**, 984 (1977)
21. K. Kurabayashi, Int. J. Thermophys. **22**, 277 (2001)
22. C. Bounioux, D. Pablo, C. Mariano, S. Marisol, A. Goni, Y. Rachel, C. Muller, Energy Environ. Sci. **6**, 918 (2013)
23. M. He, J. Ge, Z. Lin, X. Feng, X. Wang, H. Lu, Y. Yang, F. Qiu, Energy Environ. Sci. **5**, 8351 (2012)

24. O. Bubnova, Thermoelectric properties of conducting polymers (Dissertation, Linkoping University, Sweden, 2013)
25. B. Endrodi, J. Mellar, Z. Gingl, C. Visy, C. Janaky, J. Phys. Chem. C **119**, 8472 (2015)
26. M. Bharti, A. Singh, S. Samanta, A. Debnath, K. Marumoto, D. Aswal, K. Muthe, S. Gadkari, Vacuum **153**, 238 (2018)
27. N. Kim, B. Lee, D. Choi, G. Kim, H. Kim, J. Kim, J. Lee, Y. Kahng, K. Lee, Phys. Rev. Lett. **109**, 106405 (2012)
28. L. Ouyang, C. Musumeci, M. Jafari, T. Ederth, O. Inganäs, ACS Appl. Mater. **7**, 19764 (2015)
29. M. Culebras, C. Gomez, A. Cantarero, J. Mater. Chem. A **2**, 10109 (2014)
30. O. Bubnova, Z. Khan, A. Malti, S. Braun, M. Fahlman, M. Berggren, X. Crispin, Nat. Mater. **10**, 429 (2011)
31. J. Ouyang, Q. Xu, C. Chu, Y. Yang, G. Li, J. Shinar, Polymer **45**, 8443 (2004)
32. S. Sakamoto, M. Okumura, Z. Zhao, Y. Furukawa, Chem. Phy. Lett. **412**, 395 (2005)
33. T. Skotheim, R. Elsenbaumer, J. Reynolds, *Handbook of Conducting Polymers*, 2nd ed. (Marcel Dekker Inc New York NY USA, 1998)
34. C. Dun, C. Hewitt, H. Huang, J. Xu, C. Zhou, W. Huang, Nano Energy **18**, 306 (2015)
35. M. Bharti, A. Singh, G. Saini, S. Saha, A. Bohra, Y. Kaneko, A. Debnath, K. Muthe, K. Marumoto, D. Aswal, S. Gadkari, J. Power Sources **435**, 226758 (2019)
36. M. Bharti, P. Jha, A. Singh, A. Chauhan, S. Misra, M. Yamazoe, A. Debnath, K. Marumoto, K. Muthe, D. Aswal, Energy **176**, 853 (2019)
37. M. Kamarudin, S. Sahamir, R. Datta, B. Long, M. Sabri, S. Said, Sci. World J. (2013). https://doi.org/10.1155/2013/713640-56
38. W. Zheng, P. Bi, H. Kang, W. Wei, F. Liu, J. Shi, L. Peng, Z. Wang, R. Xiong, Appl. Phys. Lett. **105**, 023901 (2014)
39. Z. Zhang, G. Chen, H. Wang, W. Zhai, J. Mater. Chem. C **3**, 1649 (2015)
40. B. Endrodi, J. Mellar, Z. Gingl, C. Visya, C. Janaky, RSC Adv. **4**, 55328 (2014)
41. Z. Wenbin, F. Qingxia, Z. Qiang, C. Le, L. Kewei, G. Xiaogang, Y. Feng, Z. Nan, W. Yanchun, L. Huaping, Z. Weiya, X. Sishen, Nat. Commun. **8**, 14886 (2016)
42. M. Culebras, C. Cho, M. Krecker, R. Smith, Y. Song, C. Gomez, A. Cantarero. J. Grunlan, ACS Appl. Mater. **9**, 6306 (2017)
43. D. Kim, Y. Kim, K. Choi, J. Grunlan, C. Yu, ACS Nano **4**, 513 (2010)
44. E. Munoz, D. Suh, S. Collins, M. Selvidge, A. Dalton, B. Kim, J. Razal, G. Ussery, A. Rinzler, M. Martinez, R. Baughman, Adv. Mater. **17**, 1064 (2005)
45. B. Sun, W. Hong, E. Thibau, H. Aziz, Z. Lu, Y. Li, ACS Appl. Mater. **7**, 18662 (2015)
46. F. Li, K. Cai, S. Shen, S. Chen, Synth. Met. **197**, 58 (2014)
47. K. Zhang, Y. Zhang, S. Wang, Sci. Rep. **3**, 3448 (2013)
48. M. Bharti, A. Singh, S. Samanta, A. Debnath, D. Aswal, K. Muthe, S. Gadkari, Energ. Convers. Manage. **144**, 143 (2017)
49. K. Biswas, J. He, I. Blum, C. Wu, T. Hogan, D. Seidman, V. Dravid, M. Kanatzidis, Nature **489**, 414 (2012)
50. S. Bhattacharya, A. Bohra, R. Basu, R. Bhatt, S. Ahmad, K. Meshram, A. Debnath, A. Singh, A. Sarkar, M. Naveneethan, Y. Hayakawa, D. Aswal, S. Gupta, J. Mater. Chem. A **2**, 17122 (2014)
51. A. Sahu, B. Russ, N. Su, J. Forster, P. Zhou, E. Cho, P. Ercius, N. Coates, R. Segalmane, J. Urban, J. Mater. Chem. A **5**, 3346 (2017)
52. S. Misra, M. Bharti, A. Singh, A. Debnath, D. Aswal, Y. Hayakawa, Mater. Res. Express **4**, 085007 (2017)
53. H. Lee, G. Anoop, H. Lee, C. Kim, J. Park, J. Choi, H. Kim, Y. Kim, E. Lee, S. Lee, Y. Kim, J. Lee, J. Jo, Energy Environ. Sci. **9**, 2806 (2016)
54. Y. Yang, Z. Lin, T. Hou, F. Zhang, Z. Wang, Nano Res. **5**, 888 (2012)
55. R. Søndergaard, M. Hosel, N. Espinosa, M. Jorgensen, F. Krebs, Energy Sci. Eng. **1**, 81 (2013)
56. J. We, S. Kim, B. Cho, Energy **73**, 506 (2014)
57. Q. Wei, M. Mukaida, K. Kirihara, Y. Naitoh, T. Ishida, RSC Adv. **4**, 28802 (2014)
58. Y. Du, K. Cai, S. Chen, H. Wang, S. Shen, R. Donelson, T. Lin, Sci. Rep. **5**, 6411 (2015)

HWCVD: A Potential Tool for Silicon-Based Thin Films and Nanostructures

Rajiv O. Dusane

Abstract Hot-wire chemical vapour deposition technique is the latest tool in the series of low-temperature deposition of thin films by chemical vapour deposition. Since its successful implementation for the preparation of diamond-like films, it has been widely explored for semiconductor thin-film deposition in particular silicon-based thin films. This article gives a detailed report of our efforts to understand this process and its application for depositing thin films of amorphous and microcrystalline silicon as well as depositing silicon nanowires. We also demonstrate that these films and nanowires can be successfully used in devices like solar cells and micro-supercapacitors.

1 Introduction

The importance of various thin films in technology and their significance in the evolution of our knowledge and understanding of material behaviour in two dimensions need not be emphasized. Over the past several decades, different thin-film processing techniques have evolved and matured for their utility on industrial scale albeit depending upon their specific techno-economic capabilities. One such technique that evolved itself in both scope and its utility since its initial stage is the catalytic chemical vapour deposition [1–5] or hot-wire chemical vapour deposition [6–12] or hot-wire chemical vapour processing [13]. The last nomenclature was coined by us because the process was extended beyond the realms of only film deposition. It was shown that the hot wire process is very effective in generating atomic hydrogen by dissociating molecular hydrogen, which could be used for realizing a metal nano template that enables silicon nanowire growth [14]. Also, the generated atomic hydrogen could be used for etching of a-Si-H (amorphous silicon) from mixed phases present in nanocrystalline silicon thin films or around silicon nanowires with core (c-Si)–shell (a-Si) structure [15].

R. O. Dusane (✉)
IIT Bombay, Bombay, India
e-mail: rodusane@iitb.ac.in

S. Kumar and D. K. Aswal (eds.), *Recent Advances in Thin Films*, Materials Horizons: From Nature to Nanomaterials, https://doi.org/10.1007/978-981-15-6116-0_15

The HWCVD process has primarily gained significance as a potential tool to deposit silicon-based thin films after initial work of Matsumara et al. [1–5]. In a large range of experiments, Matsumara et al. showed that HWCVD can deposit high-quality a-Si:H material [1], which then could be also doped both n- and p-type and can be converted to p–i–n devices with photovoltaic conversion efficiency similar to those obtained by the well-established plasma-enhanced CVD (PECVD) [4, 5]. Subsequently, various groups across the globe who were working on PECVD a-Si-H thin films also started exploring the HWCVD. Among these the early one was at NREL, USA who extended the substrate temperature higher than the PECVD process and showed that high-quality a-Si:H with low H-content could be made by employing the HWCVD tool [7]. They also showed that this material was a lot more stable under light illumination [6]. As years passed, many other groups started working on the HWCVD technique and that resulted in the synthesis of other silicon-based thin films like a-SiC:H, a-SiGe:H, a-SiN:H [16–19]. Also, it was shown that microcrystalline silicon (μc-Si:H) films could be made much more easily by this technique [12, 20]. In recent years, our group explored the possibility of using the HWCVD to deposit materials like B_4C and graphene [21, 22]. The capability of the HWCVD to generate a significant amount of atomic hydrogen was extended to develop metal nanotemplates required for the growth of SiNWs.

In this article, it is planned to give a comprehensive information of the HWCVD, its unique features and its utility in depositing ultrathin a-Si:H, microcrystalline silicon, silicon nanowires and their application in solar cells and supercapacitors.

1.1 Features of the HWCVD

Over several decades, plasma-enhanced CVD (PECVD) technique has been the workhorse of the semiconductor industry including thin-film photovoltaics. In this process, the precursor gas like silane (SiH_4) is dissociated via an electron impact dissociation. The PECVD has proved to be a boon to the semiconductor industry as it was now possible to deposit thin films by the CVD route at much lower substrate temperature. It should be noted here that the conventional thermal CVD demands a much higher temperature to be available on the substrate for the dissociation of the precursor. Thus, now it was possible to decouple the dissociation zone (i.e. the plasma) from the deposition (substrate) zone and deposit the material at any desired substrate temperature. The lowering of the substrate temperature now opens up a large number of possibilities like depositing amorphous films [23–26] micro- and nano-crystalline films with a controlled grain size [27–29] and also desired chemical composition.

However, there are a couple of issues with PECVD:

(i) There are a large number of charged and energetic particles like electrons and ions in the plasma environment, which could potentially lead to charge-induced and ion-induced damage to the growing films.

(ii) Any type of plasma instability could lead to dust formation in the plasma, which can lead to heterogeneities in the film and even to the existence of pinholes.

Though the above two limitations are there, PECVD has been very successful for a variety of film deposition.

The search for an alternative which could avoid the above two aspects and still do what the PECVD can, has led to the HWCVD technique getting extended to the semiconductor field from its original success for depositing diamond and diamond-like films.

Prima facie, the HWCVD avoids the formation of charged particles like electrons and ions and also could avoid the dust formation still giving acceptable rates of deposition.

So what is HWCVD? As Fig. 1 shows, it is quite a simple process where a filament of a refractory metal like tungsten or tantalum is heated to high temperature (1600–2000 °C). This leads to the dissociation of the precursor molecules like, say, SiH_4 into the film-forming radicals and the volatiles. The diffusion of these towards the substrate surface along with reactions within the gas phase and subsequent adsorption on the surface accompanied by surface reactions and atomic rearrangement leads to the formation of the film. Successful implementation of this technique was done by Matsumara [1]. The HWCVD technique achieves the primary goal, i.e. decoupling of the dissociation and deposition zones and hence allows low-temperature deposition of the films. In this technique, the filament temperature is analogous to the plasma power and plays a key role in affecting the deposition rate as well as the film quality.

Key differences between PECVD and HWCVD are the following two:

(1) The plasma becomes a volume source of the dissociated radicals while the hot wire is a planar (in case multiple wires) or linear source. (in case of single wire).
(2) Since the plasma contains electrons with a range of energies (the electrons follow a Druyvesteyn distribution), there are different dissociation paths of the precursor molecule depending upon the energy of the electron which strikes the molecule. On the other hand, the hot wire is at one constant temperature and hence offers a unique dissociation path of the precursor.

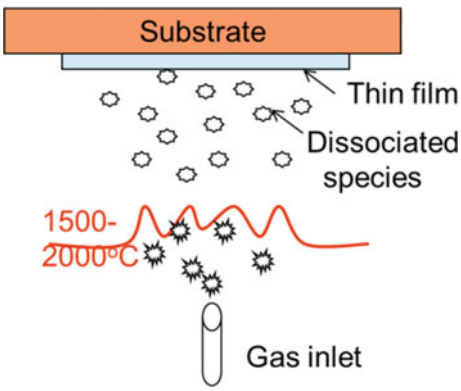

Fig. 1 HWCVD process

Thus considering these two aspects, the HWCVD is quite different in some sense from the PECVD, i.e. it has a bit of a flavour of physical vapour deposition (spatially fixed source in form of the hot filament) as well as also has the characteristics of PECVD (precursor dissociation and gas-phase reactions). Therefore, one can expect a different type of film growth kinetics in the HWCVD process. I will discuss this in more detail in the content of a-Si:H and μc-Si:H film deposition.

Various aspects of the HWCVD technique and its applications to a variety of thin-film material systems have been published by researchers in this field. In fact, a biannual conference is held where new data and findings are reported [30].

Having discussed the general features of the HWCVD tool, now I would like to take two material systems which we have studied over the years. These are

(a) a-Si:H and μc-Si:H.
(b) Si nanowires (SiNWs).

1.2 A-Si:H and μC-Si:H Thin Film Deposition

During the two decades (1985–2005), the thin-film photovoltaic industry was primarily concerned with hydrogenated amorphous silicon (a-Si:H) based solar cells made by PECVD. a-Si:H being a direct band gap semiconductor with high optical absorption became a prime material for thin-film PV [31–34]. However, since a-Si:H is a wide band gap material (E_g ~ 1.65 eV), a large amount of the solar spectrum below 1.7 eV does not get utilized. This led to the concept of tandem solar cells where multiple cells made with absorption layers having different band gaps are deposited in a tandem fashion. Thus alloy films like a-Si:Ge:H (E_g ~ 1.4 eV), a-Si:C:H (E_g ~ 2.2 eV), etc. were synthesized and tandem solar cells having structures like glass/SnO_2/p-a-SiC:H-i-a-SiC:H-n-a-Si:H/p-Si:C:H-i-a-Si:H-n-a-Si:H/p-Si:H-i-SiGe:H-n-a-Si:H/metal were developed [35, 36]. Subsequently, microcrystalline Si (μc-Si:H) was also deposited which has a band gap E_g ~ 1.1–1.3 eV. Then a simple configuration of a micro-morph (glass/TCO/a-Si:H p–i–n/μ-Si:H p–i–n/Metal) was shown to have great promise [37–40]. This solar cell generates power over a much broader solar spectrum and has shown a conversion efficiency of ~11%.

We studied the dependence of the formation kinetics of these two different phases of Si, namely a-Si:H and μc-Si:H when deposited by the HWCVD. We also studied the gas-phase chemistry using quadrupole mass spectrometry (QMS) to understand the correlation between the species generated and the film structure. The kinetics of film formation in a decoupled CVD process like the HWCVD depends upon the following aspects:

(1) Radicals generated primarily due to the dissociation at the heated filament and subsequent desorption into the gas phase.
(2) Secondary gas-phase reactions that occur among the various radicals as they diffuse towards the substrate surface which is heated to the desired temperature (200–350 °C).

(3) Subsequent surface reactions and accommodation on the substrate surface to form the film.
(4) In addition to the above surface, abstractions can also occur due to the impingement of reactive radicals from the gas phase on to the growing film surface leading to the formation of volatile radicals.

Thus, we see that the complete process of film formation is rather complex and interdependent on the various process conditions such as

(1) Precursor gas flow rates.
(2) Dilution with other carriers or reactive gases.
(3) Working pressure.
(4) Filament temperature.
(5) Filament to substrate distance.
(6) Substrate temperature.

The deposition of the various films was carried out in the HWCVD reactor shown in Fig. 2. In order to understand the process better, we also attempted modelling of the process and correlate these results with the QMS data and film properties [41].

Basically, the following simple dissociative reaction takes place at the heated filament surface:

$$SiH_4 \xrightarrow[1600\,^{\circ}C]{Ta} Si + 4H \tag{1}$$

At $T_{Fil} > 1500$ °C, dissociated Si does not stick to the Ta surface but desorbs into the gas phase. Now we have a mixture of H, Si and SiH_4 in the gas phase.

Fig. 2 The single-chamber HWCVD reactor with various control units

Additionally, we may have H_2 if the source gas is diluted with H_2. Thus, there is a possibility of all kinds of reactions taking place within the gas phase. Now as our focus is to deposit both a-Si:H as well as μc-Si:H we concentrate on determining the deposition conditions which will lead to these specific films.

Subsequent to reaction (1), we may have the following reaction between the atomic H generated in (1) and a fresh SiH_4 molecule:

$$SiH_4 + H \rightarrow SiH_3 + H_2 \tag{2}$$

Also, the atomic H can react with SiH_3 as follows:

$$SiH_3 + H \rightarrow SiH_2 + H_2 \tag{3}$$

or two SiH_3 radicals can react to form

$$SiH_3 + SiH_3 \rightarrow SiH_2 + SiH_4 \tag{4}$$

It is interesting to note that one can observe these molecules in the QMS [41]. The study that followed revealed the following scenarios for the two cases of a-Si:H and μc-Si:H deposition:

Case 1: a-Si:H deposition
Conditions: High SiH_4 flow, no H_2 dilution
Observations: $[Si]/[SiH_2] = 0.4$
$[H_2]/[SiH_2] = 100$
Cse 2: μc-Si:H film deposition
Conditions: Low SiH_4 flow, high H_2 dilution
Observation: $[Si]/[SiH_2] = 4$ (one order of magnitude higher)
$[H_2]/[SiH_2] = 1000$

Thus, we see that when there is an abundance of $[SiH_3]$ and $[SiH_2]$ in the gas phase we get a-Si:H deposition, i.e. when the SiH_4 flow is large secondary gas-phase reactions with atomic H are predominant.

However, during μc-Si:H deposition we are having very small SiH_4 flow and hence only the primary reaction dominates and we get Si radicals that yield microcrystalline films. Figure 3a, b shows the Raman spectra of films deposited under the above two conditions. In both depositions, all other parameters were kept the same. Film in (a) is a-Si:H while that in (b) is μc-Si:H. Thus, we see that how the knowledge and understanding of the dissociation and gas-phase chemistry can reproducibly generate films of the desired microstructure. Subsequently, it was shown by Soni et al. [42] that varying the SiH_4 flow rate for a constant high H_2 dilution forms a good process control to obtain either a-SiH or μc-Si:H films.

A further study was undertaken to understand in detail the dependence of the film microstructure on the hydrogen dilution as well as the silane concentration in the gas phase. Raman spectroscopy was primarily used to determine the nature of

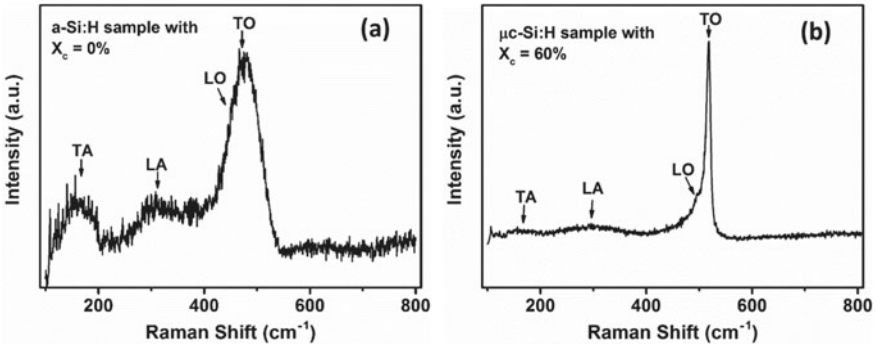

Fig. 3 **a** Characteristic Raman spectrum of a-Si:H sample and **b** Characteristic Raman spectrum of μc-Si:H sample with 60% crystallinity showing different vibrational peaks. (Reproduced from Wadibhasme [43])

the films as it is very sensitive to the presence of any crystalline component in the amorphous films. Figure 4 shows that when SiH_4 is diluted with H_2 the films remain amorphous but improves in quality as reflected by the bond angle deviation [43]. Thus an optimized silane to hydrogen dilution is effective in improving film properties. Figure 5 shows the Raman spectra when the silane to hydrogen ratio is reduced drastically to yield microcrystalline films. We see clearly that there is a transition from amorphous to microcrystalline phase at 10.7% of silane in hydrogen.

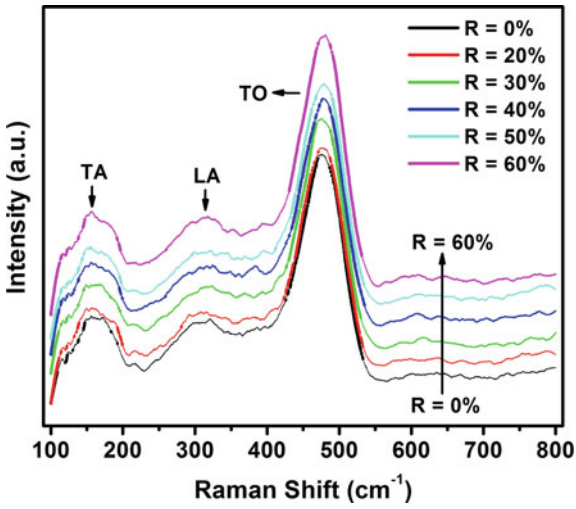

Fig. 4 Raman spectra of a-Si:H thin films deposited at different H_2 dilutions showing position of TO, LA and TA peaks. (Reproduced from Wadibhasme [43])

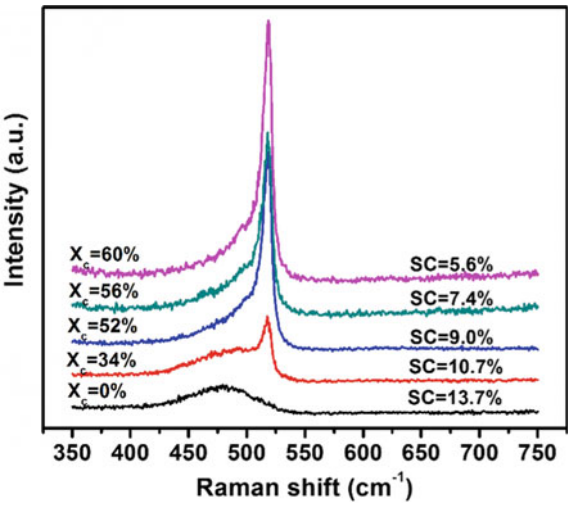

Fig. 5 Raman spectra of μc-Si:H samples deposited on a glass substrate at a different SC showing a shift of TO peak from the crystalline phase (TO peak at 520 cm^{-1}) to amorphous phase (TO peak at 480 cm^{-1}) with an increase in SC. (Reproduced from Wadibhasme [43])

1.2.1 Electronic Properties

The HWCVP deposited a-Si:H films have been shown to be of device quality through a detailed study of their use in different types of solar cells such as single-junction a-Si:H p–i–n solar cells and c-Si/a-Si heterojunction solar cells (SHJ). In order to qualify for implementation in the solar cell device, various properties specific to the application have to be determined. One such characterization is the determination of the gap state density of defects in the amorphous films [43]. This is determined by the constant photocurrent method (CPM) [44–47]. We have carried CPM measurements of a large number of a-Si:H films and determined the density of states (DOS). One such variation is shown in Fig. 6 where the CPM data is plotted for HWCVD a-Si:H films deposited with hydrogen dilution which was varied from 0 to 60%. Figure 7 shows the mid-gap defect density and Urbach energy determined from the CPM data as a function of hydrogen dilution. It clearly shows that diluting the silane with hydrogen leads to a decrease in defect density and lowering of the Urbach energy which is an indication of the spread of mobility edge [48]. The main aim of this study was to develop low-temperature a-Si:H thin films for flexible thin-film solar cells deposited on polyethylene naphtalate (PEN) substrates.

1.2.2 Fabrication of a-Si:H-Based Single-Junction p–i–n Solar Cells

Having worked extensively on the a-Si:H and μc-Si:H film preparation and characterization, we fabricated different single-junction solar cells having both a-Si:H as the absorber layer as well as μc-Si:H as the i-layer, respectively. For this purpose, we designed and commissioned a multi-chamber hot-wire CVD cluster tool which is shown in Fig. 8.

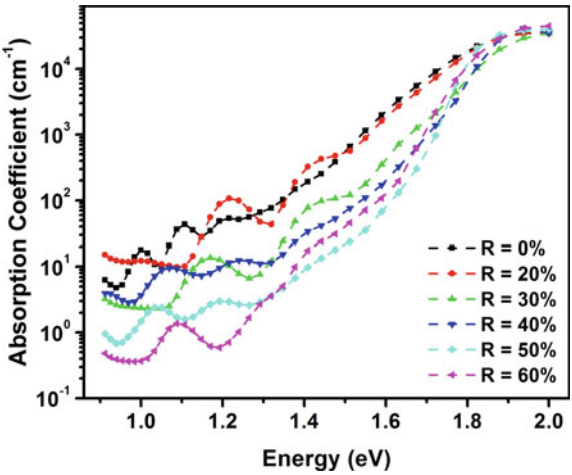

Fig. 6 CPM spectra of a-Si:H thin films prepared at different H_2 dilutions showing comparative absorption coefficient at different photon energy. (Reproduced from Wadibhasme [43])

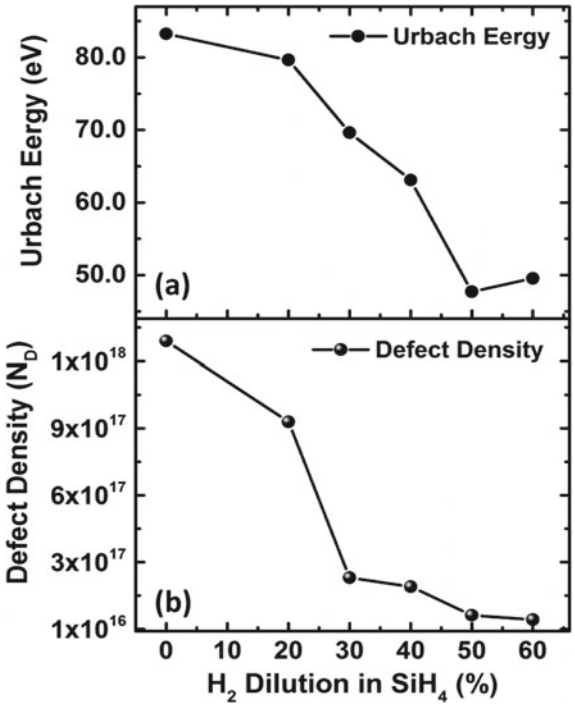

Fig. 7 **a** Urbach energy (E_u) and **b** electronic defect density (N_{dd}) of a-Si:H thin films deposited at different H_2 dilutions. (Reproduced from Wadibhasme [43])

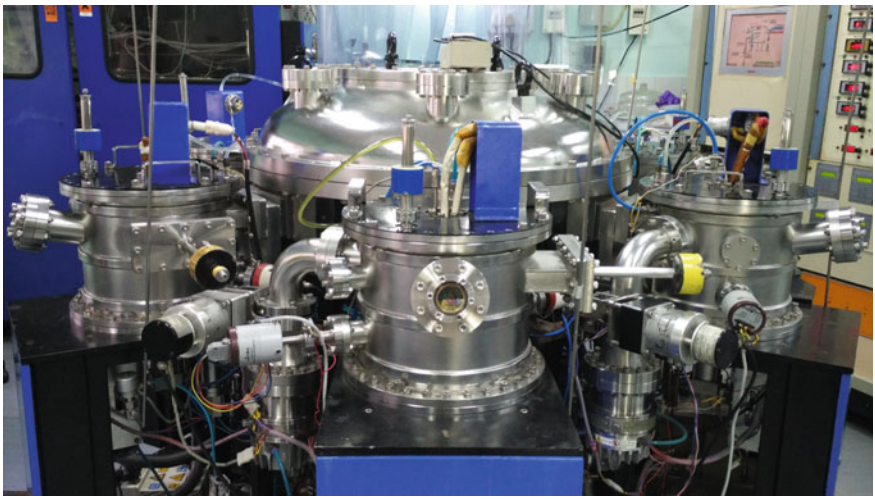

Fig. 8 HWCVD cluster tool used for the deposition of various doped and undoped silicon layers to avoid cross-contamination in the device structure. (Reproduced from Agarwal et al. [53])

This tool has the capability of fabricating multilayer devices without cross-contamination. The tool is semi-automated with a PLC-based control system. Solar cells have been fabricated on transparent conducting oxide (TCO) coated glass, steel foils as well as indium-doped tin oxide (ITO) coated PEN flexible substrates. All the deposition chambers were maintained at the base vacuum of 10^{-7} mbar. Tantalum (Ta) filament of 0.5 mm diameter with four-wire arrangement and covering a surface area of 4.5 cm^2 is used to dissociate the precursors. Pure silane (SiH_4) was used to deposit the intrinsic a-Si:H layer, whereas n-doped and p-doped a-Si:H layers were deposited using phosphine (PH_3—10% diluted in H_2) and di-borane (B_2H_6—10% diluted in H_2) as dopant gases along with pure silane with different gas-phase ratios. All the silicon layers were deposited at a constant substrate temperature (T_s) of 200 °C. The top and bottom aluminium-doped zinc oxide (AZO) thin films were deposited using RF magnetron sputtering. A physical mask with holes of different diameters was used to deposit top AZO to make each dot an individual cell of different area. The p-a-Si:H and p-a-Si:H/AZO layers were deposited separately on the glass substrate for the transmission measurements using UV–Visible spectroscopy measurement. The current–voltage (I–V) characteristics of the solar cells were measured with the help of Keithley 2400 Source metre and AM 1.5 solar simulator at 100 mW/cm^2 intensity. Figure 9 shows the schematic of the a-Si:H p–i–n single-junction solar cell deposited on flexible PEN substrate and Fig. 10 shows the I–V characteristics of the device. We can see that the device shows a fairly good performance though there is a scope for improvement.

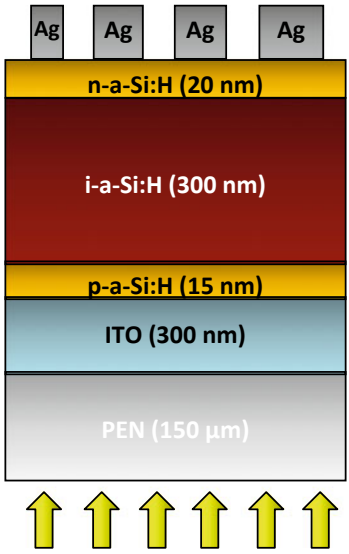

Fig. 9 a-Si:H single-junction cell on PEN substrate. (Reproduced from Wadibhasme [43])

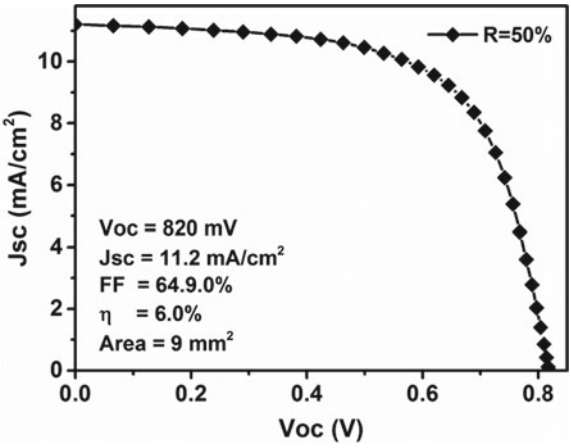

Fig. 10 *I–V* curve of the solar cell shown in Fig. 11. Here the $R = 50$ indicates 50% hydrogen dilution during deposition. (Reproduced from Wadibhasme [43])

1.2.3 Fabrication of Silicon Heterojunction with Intrinsic Thin Layer Solar Cells

Heterojunction solar cells with intrinsic amorphous silicon are the latest solar cells based on c-Si technology. The a-Si:H/c-Si heterojunction in SHJ solar cell is formed by depositing the emitter layer (doped a-Si:H) over the surface of the c-Si substrate. The passivation of dangling bonds that are present on the c-Si surface is an important step prior to emitter layer deposition in this structure [49]. To achieve this, various passivation techniques have been implemented such as atomic hydrogen treatment, wet chemical route and buffer layer depositions. In 1992, for the first time Sanyo

introduced the i-a-Si:H layer in between the c-Si and doped emitter layer [50]. The insertion of i-a-Si:H layer greatly reduces the saturation current density (J_o) and hence increases the open-circuit voltage (V_{oc}) of the device.

There have been different views regarding the nature of the c-Si/a-Si:H interface in terms of its microstructure observed through TEM studies. Centurioni et al. claim that the complete epitaxial intrinsic silicon layer is beneficial for the good performance of SHJ solar cells [51]. Another study shows that if an abrupt c-Si/a-Si:H interface is achieved then it leads to a very good performance of the SHJ solar cells [52]. Thus, a detailed optimization effort involving a systematic variation of the process conditions leading to a control over the c-Si/a-Si:H interface is warranted.

In order to address this issue, we did a detailed study of the c-Si/a-Si:H interface. One parameter which drastically affects film deposition and properties in the HWCVD is the filament temperature. Hence, we varied the filament temperature during the deposition of the intrinsic silicon layer.

The cross-sectional HRTEM images of the i-a-Si:H/c-Si interface prepared at different filament temperatures (T_f) are shown in Fig. 11. When the i-a-Si:H layer is deposited at $T_f = 1550$ °C, we see local epitaxy and crystalline growth up to 5 nm near the c-Si surface as can be seen in Fig. 11a. This is due to the very low deposition rate of a-Si:H film at this T_f favouring the crystalline phase formation during the initial growth of a-Si:H layer on the c-Si wafer. The dissociated gas species have sufficient time to migrate over the c-Si surface to find the lower energy state to enable epitaxial growth. As the T_f increases up to 1650 °C, the deposition rate of the growing film increases which leads to the abrupt a-Si:H/c-Si interface (Fig. 11b). The a-Si:H film starts growing as an amorphous film as soon as the deposition starts and an atomically sharp a-Si:H/c-Si interface is achieved. Further increasing the T_f to 1750 °C leads to a rough a-Si:H/c-Si interface as can be seen in Fig. 11c. The observed roughness at the heterointerface is mainly because of the etching of Si-Si bond due to highly energetic atomic hydrogen present at such high T_f. On further increasing the T_f to 1850 °C, we observe traces of nanocrystallites at the i-a-Si:H/c-Si interface (Fig. 11d). The nucleation of epitaxy/nanocrystallites can be explained by the reconstruction of the amorphous matrix occurring due to the diffusion of hydrogen radicals through the growing film.

Further to investigate the role of these heterointerfaces in the solar cell performance, four single-sided SHJ solar cells were fabricated under the same i-a-Si:H growth conditions as above. Schematic for a single-sided SHJ solar cell fabricated in this study is as shown in Fig. 12. As discussed in detail in [53], the performance of the solar cells exactly follows the condition of the hetero-interface, i.e. the cell deposited at T_f of 1650 °C shows the highest efficiency and other solar cell parameters, while the others are relatively poor in performance.

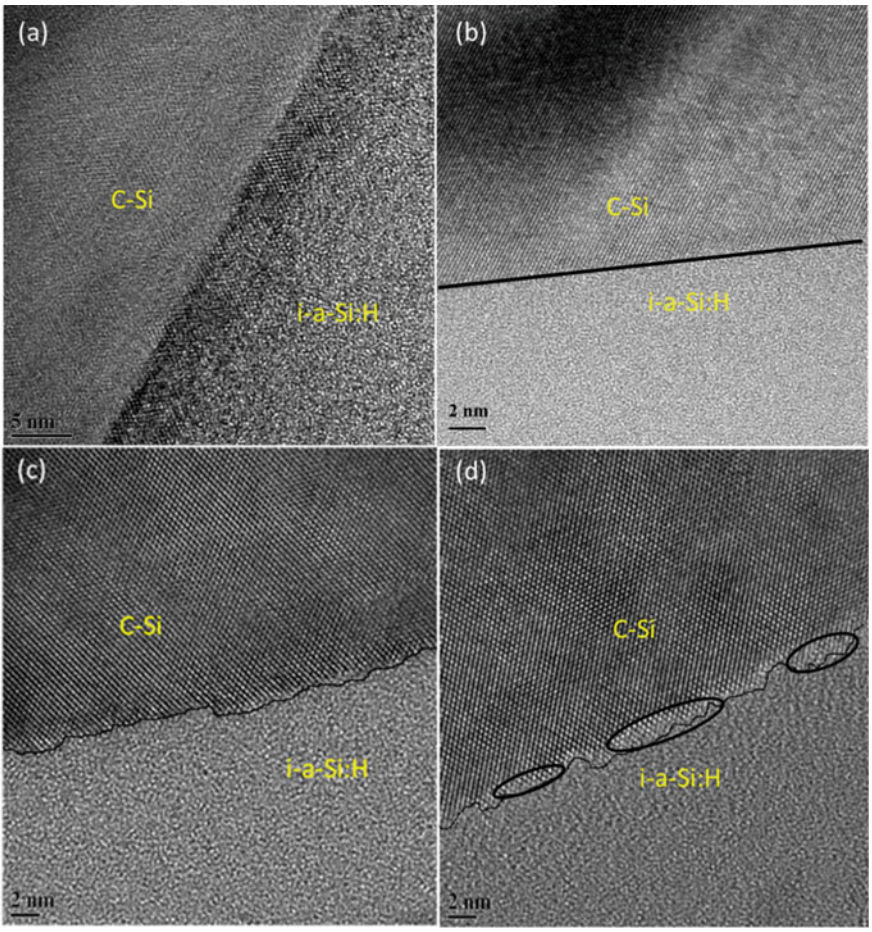

Fig. 11 Cross-sectional HRTEM images of a-Si:H/c-Si interface deposited at different T_f **a** 1550 °C, **b** 1650 °C, **c** 1750 °C, and **d** 1850 °C. In figure (**b**), boundary line represents the abrupt nature of interface separating c-Si and i-a-Si:H part. In both figure (**c**) and (**d**), the solid line indicates the rough nature of interface caused by atomic hydrogen etching. In figure (**d**), encircled areas show nanocrystalline growth. (Reproduced from Agarwal et al. [53])

As seen in Fig. 12b, this structure has a very sharp and abrupt c-Si/a-Si interface thus corroborating our earlier argument that an abrupt amorphous/crystalline interface is necessary for high conversion efficiency. Thus, we see that the HWCVD does not only have the capabilities to allow fabrication of high conversion efficiency solar cells, but also allows one to control the interface microstructure to suit the application.

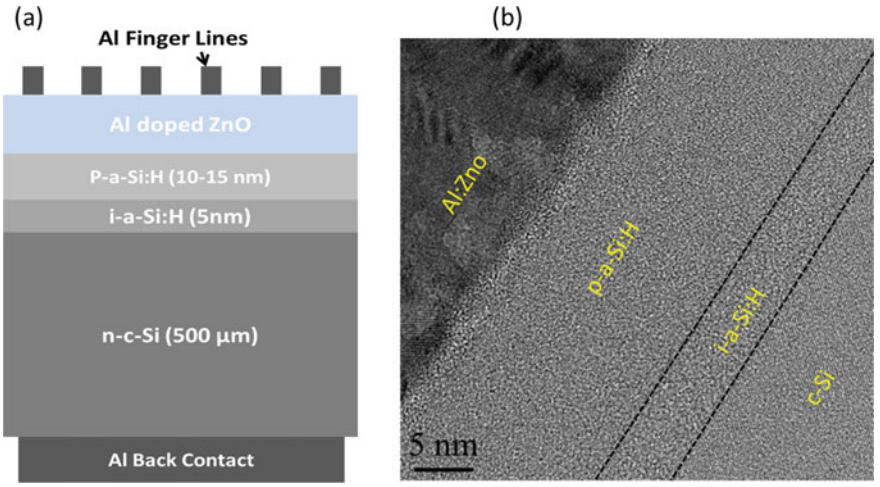

Fig. 12 **a** Schematic of single-sided SHJ solar cell comprising of i-a-Si:H layer followed by doped amorphous and AZO layer. **b** HRTEM cross section of the solar cell. (Reproduced from Agarwal et al. [53])

1.3 Metal Nanotemplate Formation and Silicon Nanowire Growth

Silicon nanowires (SiNWs) have been studied very extensively over the past two decades. The first report of SiNW growth by the vapour–liquid–solid route was by Wagner and Ellis [54]. This is a bottom-up approach to synthesize SiNWs, which is independent of the substrate and hence has a lot of potential in battery and supercapacitor application [55–57].

The SiNWs of course have a great deal of other applications due to the one-dimensional nature and a large surface area [58–60].

The primary mechanism in the VLS process is to offer a seed catalyst in form of a metal nanotemplate under the right process conditions to allow the incoming Si source to lead to the formation of the SiNW [61]. Thus, we see that there are two key things in this process.

(1) The metal nanotemplate.
(2) Flux of a conducive Si source.

A large number of reports exist on the development of the metal nanotemplate with a variety of metals [62–64].

The actual process temperature for the formation of SiNWs is decided by the two participating elements, namely the template metal and the source. This is because the VLS involves the formation of the melt at the eutectic temperature between Si and the metal and subsequent segregation of excess Si in the form of the nanowire (Fig. 13). An alloy of 19% Au and Si% has a melting point of 363 °C. Thus, if

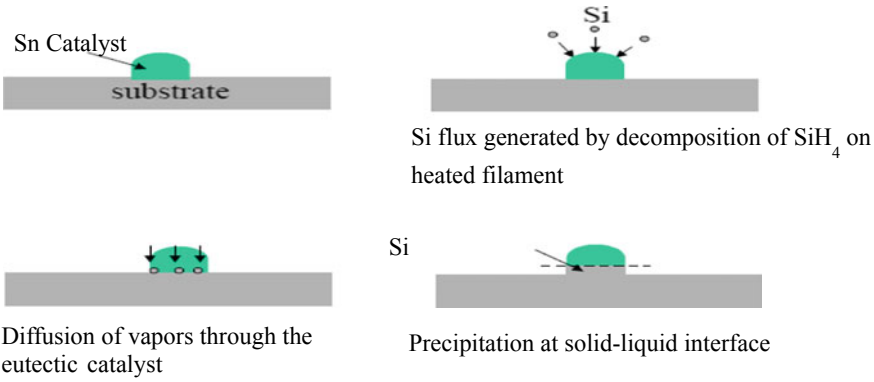

Fig. 13 Cartoon showing the VLS mechanism of silicon nanowire growth with silicon flux. (Reproduced from Soam [69])

silicon atoms are supplied to Au heated to greater than 363 °C it will yield a melt of AuSi alloy. Any additional Si supply leads to the nanowire formation [62–64]. In order to explore the formation of SiNWs at lower temperatures, we used Sn for the metal nanotemplate. Here one more interesting aspect of SiNW growth is to be considered and that is that the SiNW's diameter is closely correlated to the size of the Sn nanotemplate. Thus, the first task is to form the desired Sn nano template. For this, we used the HWCVD process. As we were aware that the hot wire produces a large amount of atomic hydrogen, we utilized this atomic hydrogen to convert a thin Sn film into an Sn nanotemplate as follows. A thin film of approximately 10 nm thickness is deposited on a glass substrate by resistive evaporation. This film is then transferred to the HWCVD chamber and was exposed to atomic H generated by the filament which was heated to 1600 °C for 10 min at a temperature of 200 °C. It is to be noted that the above parameters i.e. the thickness of the initial film, substrate temperature and treatment time affect the nanotemplate size. Thus, we obtain a Sn nanoparticle size from 25 nm to 100 nm. Once the Sn nanotemplate is formed we introduce SiH_4 gas over the heated filament. The SiH_4 gas is dissociated and the Si radical reaches the substrate coated with Sn nanoparticles which is maintained at a temperature between 200 and 350 °C. Subsequently, the Si flux forms the SiSn melt and with continuous Si reaching the substrate the SiNWs start to grow. Figure 14 shows the flowchart of the entire process of synthesizing the nanowires.

Figure 15 depicts the Sn nanotemplate which has been formed for a Sn film under two different process parameters. In Fig. 16, we show the SiNWs synthesized at 200 °C which shows a noodle-like morphology.

However, the morphology is controlled by the process conditions and in Fig. 17, we show SiNWs grown at another set of conditions. In this case, a low pressure was maintained so that the silicon flux is lowered. Under these conditions, we see that the SiNWs are straight grass-like in nature. Hence, we see that the SiNWs are well aligned vertically to the substrate.

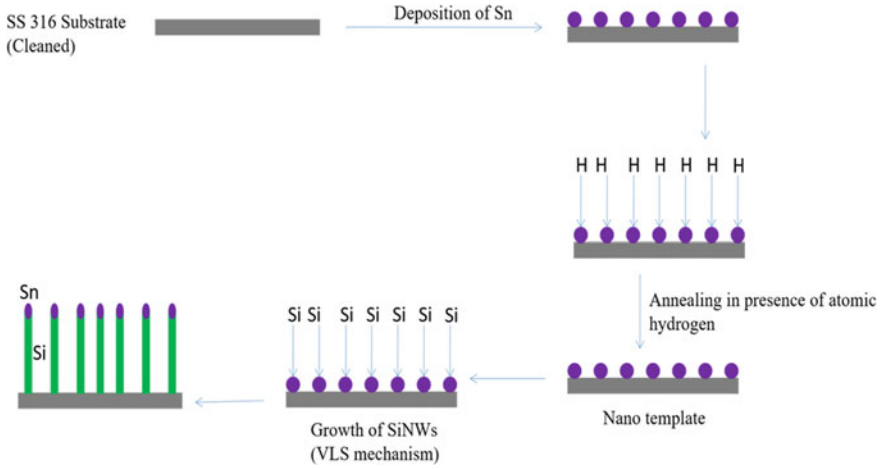

Fig. 14 Flowchart for the growth of silicon nanowires by the HWCVP

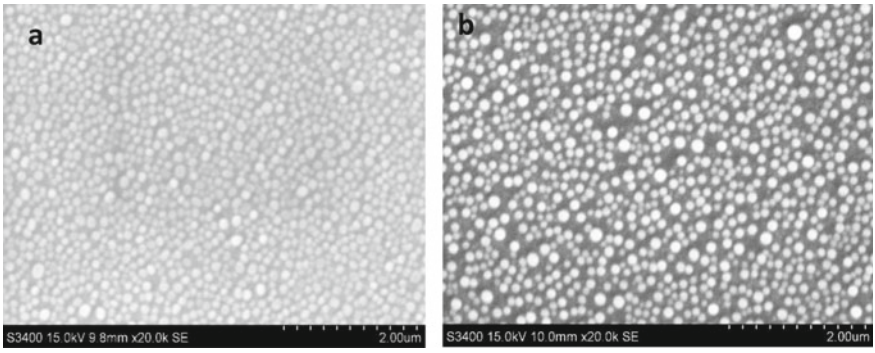

Fig. 15 SEM images of Sn films after H treatment at 200 °C for **a** 1 min and **b** 10 min

There are some interesting features of these SiNWs. They are tapered as we go towards the end away from the substrate. In order to investigate further, we studied the TEM micrograph of the SiNWs. Figure 18 shows a TEM of a tapered nanowire.

In Fig. 19, we show the HRTEM of a single nanowire. In this, we see that the SiNW has a core–shell structure. The core is c-Si and the diameter of the core matches well with the dimension of the Sn nanoparticle. On the periphery, we see a-Si:H being deposited which gives the tapered shape to the nanowire. Thus, we have a SiNW with having c-Si core/amorphous silicon shall structure. This composite nature of the SiNW microstructure has some interesting implications in their application as rechargeable battery electrodes as has been seen in one of our other studies [65]. As was seen the SiNWs having core/shell microstructure show good battery performance in terms of charging/discharging and capacity.

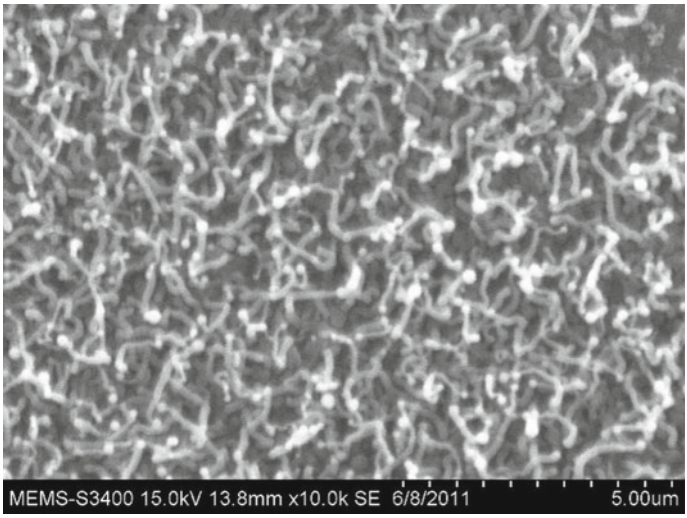

Fig. 16 SEM image of SiNWs synthesized at 200 °C by HWCVD. (Reproduced from Soam et al. [70])

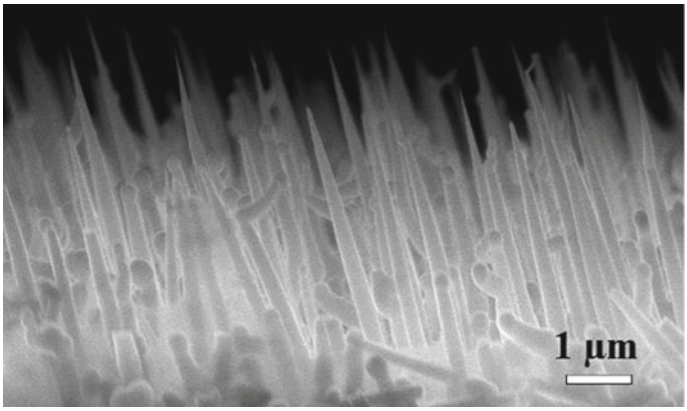

Fig. 17 SiNWs grown at low pressure. (Reproduced from Soam et al. [68])

1.4 Micro-supercapacitor on Chip

The other successful application of the HWCVP-grown SiNWs is the on-chip supercapacitor. After demonstrating that the SiNWs are potential candidates for supercapacitor applications [66, 67], we explored the same to fabricate a micro-supercapacitor on crystalline silicon [68]. The idea was to develop an onboard small storage device that could be used in applications where quick power delivery is required, e.g. signal generated by a sensor to be transferred to a receiver placed

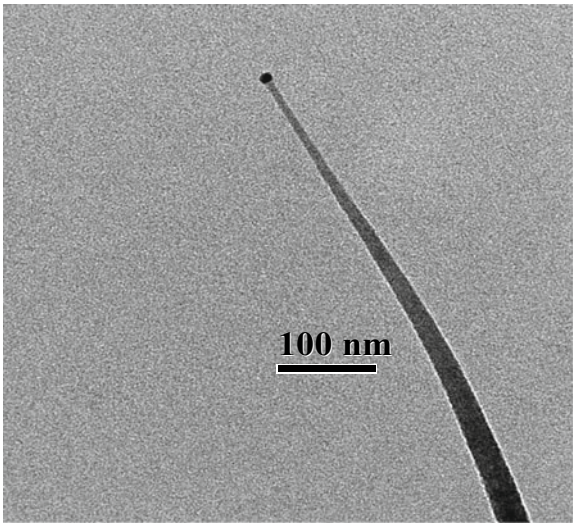

Fig. 18 TEM image of single-tapered nanowire. (Reproduced from Soam et al. [68])

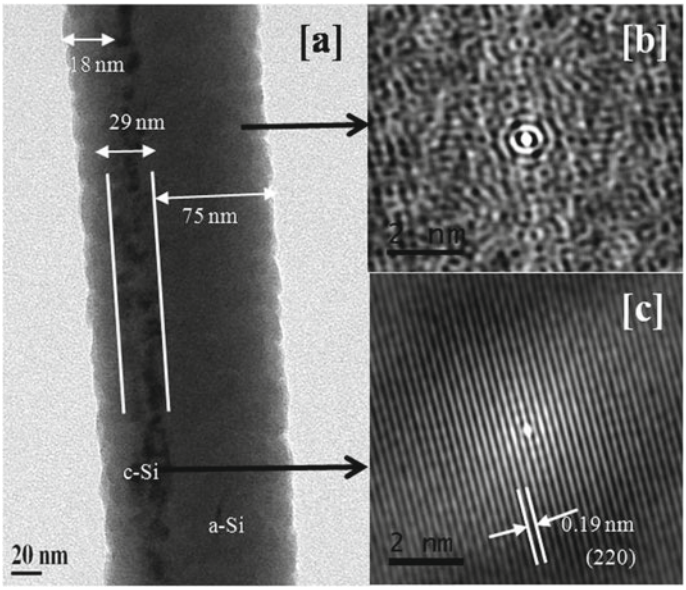

Fig. 19 HRTEM image of a single nanowire exhibiting amorphous shell crystalline core structure. (Reproduced from Soam [69])

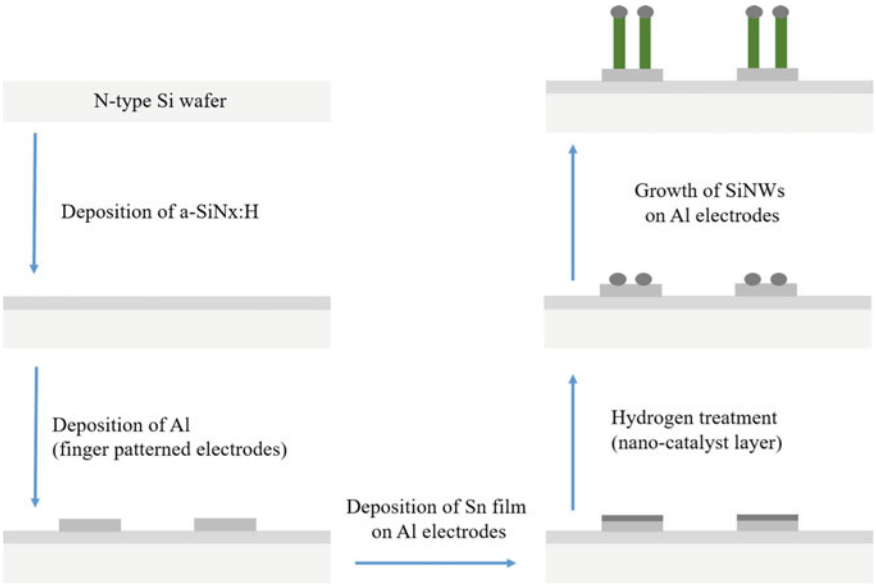

Fig. 20 Full process of growing SiNWs on a silicon wafer. (Reproduced from Soam et al. [68])

away. Such applications are key for the internet of things (IoT) technology. Since the HWCVP growth of SiNWs is at low temperature and can be made locally on silicon wafers, it is compatible with the VLSI process and could be easily implemented. In order to realize the micro-supercapacitor, the following process sequence was adopted.

A standard silicon wafer p-type <100>, 5–10 Ω cm resistivity was cleaned using an established cleaning process and an amorphous silicon nitride film (a-SiN:H) was deposited by the HWCVD to provide an insulating isolation layer for the electrical contacts. Then an aluminium (Al) layer was deposited in the form of a comb-like pattern through a physical mask as shown in Fig. 20.

After that, a thin film of Sn catalyst was deposited on the Al pattern using the same mask. Here it should be mentioned that the Al finger pattern serves as the current collector. The Sn film which is exactly on the Al pattern is then processed to form the Sn nanotemplates and subsequently SiNWs are grown by the process described earlier. The final device structure is shown in Fig. 21 along with the dimensions.

Thus, we have the SiNWs grown exactly on the Al contact pads. Now an ionic electrolyte, namely 1-Ethyl-3-Methylimidozalium bis (Trifluoromethylsulfonyl) imide was filled between the electrodes which form the supercapacitor.

Figures 22a, b shows the performance of the device in terms of its charge retention after 1000 cycles. It is clear that the performance of the device is quite good with a specific capacitance of 38 $\mu F/cm^2$ and a power density of ~108 $\mu W/cm^2$, though a bit lower when compared to devices on SS substrates.

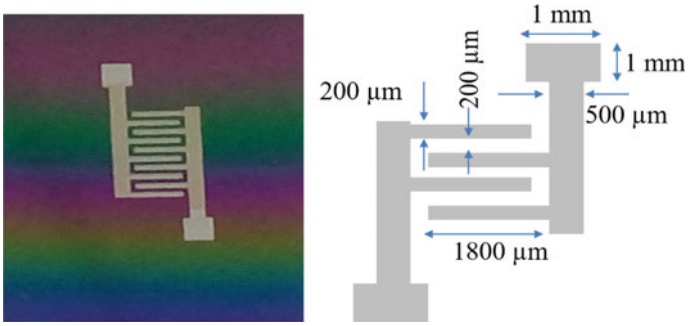

Fig. 21 Digital photograph of SINWs-based micro-supercapacitor and its dimensions. (Reproduced from Soam et al. [68])

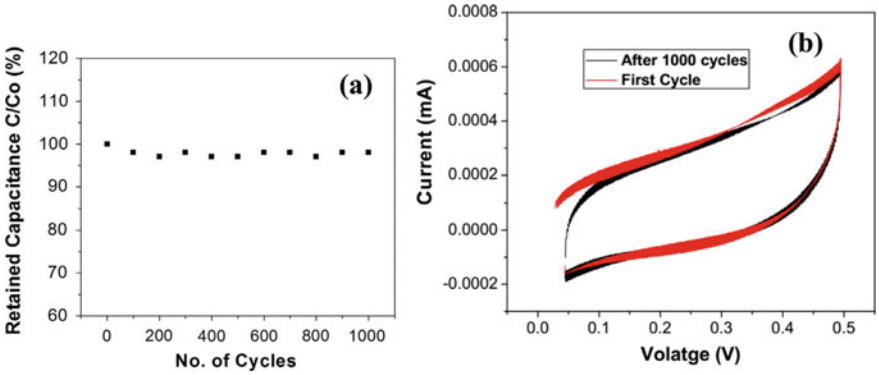

Fig. 22 **a** Cycle stability for SiNWs. The cycle stability was measured by repeating the *CV* curves for 1000 cycles at a scan rate of 100 mV/s and the voltage was fixed to 0.5 V, **b** the *CV* curves for the first cycle and after 1000 cycles. (Reproduced from Soam et al. [68])

Further improvement can be made in these devices by getting better quality SiNWs with a larger surface area. Hence, one can say that the HWCVP offers a low-temperature recipe to deposit SiNWs on any type of substrate as it enables the nanowires to grow at low temperatures.

1.5 Conclusion

Over the years, the HWCVD technique for deposition of silicon-based thin films and nanostructures has been studied widely and it now seems that it has gained the confidence of getting leapfrogged to industrial scale. The simplicity of the process of deposition makes this technique more acceptable compared to other conventional techniques. It also offers a lot of potential to carry out surface nanoengineering since

it can produce active radicals very efficiently. Its scope of application would further get extended to newer material systems like graphene or boron nitride in the coming years.

Acknowledgments The work reported in this article has been contributed by the following researchers in my group, namely Dr. Nagsen Meshram, Dr. Ankur Soam, Dr. Mohit Agarwal and Dr. Nilesh Wadibhasme. The work was carried out with financial support from MNRE and DST, Govt. of India under various schemes.

References

1. H. Matsumura, Study on catalytic chemical vapor deposition method to prepare hydrogenated amorphous silicon. Appl. Phys. **65**, 4402 (1989)
2. H. Wiesmann, A.K. Ghosh, T. McMohan, M. Srongin, a-Si: H produced by high-temperature thermal decomposition of silane. J. Appl. Phy. **50**, 3754 (1979)
3. J. Doyle, R. Robertson, G.H. Lin, M.Z. He, A. Gallagher, Production of high-quality amorphous silicon films by evaporative silane surface decomposition. J. Appl. Phys. **64**, 3215 (1988)
4. H. Matsumura, Catalytic chemical vapor deposition (CLT-CVD) Method to obtain high quality amorphous silicon alloys, in *Amorphous Silicon Technology*, ed. by A. Madan, M.J. Thompson, P.C. Taylor, P.G. LeComber, Y. Hamakawa, Materials Research Society Symp. Proc., vol. 118 (1988), p. 43
5. H. Matsumura, H. Tachibana, Amorphous silicon produced by a new thermal chemical vapor deposition method using intermediate species SiF_2, Appl. Phys. Lett. **47**, 833 (1985)
6. A.H. Mahan, M. Vanecek, A Reduction in the Staebler-Wronski Effect Observed in Low H Content a-Si: H Films Deposited by the Hot Wire Technique. AIP Conf. Proc. **234**, 195 (1991)
7. A.H. Mahan, J. Carapella, B.P. Nelson, R.S. Crandall, I. Balberg, Deposition of device quality, low h content amorphous silicon. J. Appl. Phys. **69**, 6728 (1991)
8. P. Brogueira, J.P. Conde, S. Arekat, V. Chu, Amorphous and microcrystalline silicon films deposited by hot-wire chemical vapor deposition at filament temperatures between 1500 and 1900 °C. J. Appl. Phys. **79**, 8748 (1996)
9. K.F. Feenstra, R.E.I. Schropp, W.F. Van der Weg, Deposition of amorphous silicon films by hot-wire chemical vapor deposition. J. Appl. Phys. **85**, 6843 (1999)
10. M.R. Heintze, H.N. Zedlitz, Wanka, M.B. Schubert, Amorphous and microcrystalline silicon by hot wire chemical vapor deposition. J. Appl. Phys. 79, 2699 (1996)
11. E.C. Molenbroek, deposition of hydrogenated amorphous silicon with the hot-wire technique, Ph.D. thesis, University of Colorado (1995)
12. R.O. Dusane, S.R. Dusane, V.G. Bhide, S.T. Kshirsagar, hydrogenated microcrystalline silicon films produced at low temperature by the hot wire deposition method. Appl. Phys. Lett. **63**, 2201 (1993)
13. R.O. Dusane, Hot wire chemical vapor processing (HWCVP)—a prospective tool for VLSI. Thin Solid Films **516**, 779 (2008)
14. N. Meshram, A. Kumbhar, R.O. Dusane, Synthesis of silicon nanowires using tin catalyst by hot wire chemical vapor processing. Mater. Res. Bull. **48**, 2254 (2013)
15. A. Soam, N. Arya, A. Kumbhar, R. Dusane, Controlling the shell microstructure in a low-temperature-grown SiNWs and correlating it to the performance of the SiNWs-based micro-supercapacitor. Appl. Nanosci. **6**, 1159 (2016)
16. A. Kumbhar, S.B. Patil, S. Kumar, R. Lal, R.O. Dusane, Photoluminescent, wide-bandgap a-Sic: H alloy films deposited by Cat-CVD using acetylene. Thin Solid Films **395**, 244 (2001)

17. S.K. Singh, A.A. Kumbhar, R.O. Dusane, W. Bock, Hot-wire chemical-vapor-deposited nanometer range a-Sic:H diffusion barrier films for ultra large-scale-integrated application. J. J. Vac. Sci. Technol. B24, 543 (2006)
18. B.P. Swain, R.O. Dusane, Effect of substrate temperature on HWCVD deposited a-SiC:H film. Mater. Lett. 61, 4 (2007). https://www.sciencedirect.com/science/journal/0167577X/61/25731
19. P.C. Waghmare, S.B. Patil, A.A. Kumbhar, V.R. Rao, R.O. Dusane, Nitrogen dilution effects on structural and electrical properties of hot-wire-deposited a-SiN: H films for deep-sub-micron CMOS technologies. Thin Solid Films **430**, 189 (2003)
20. R.E.I. Schropp, K.F. Feenstra, E.C. Molenbroek, H. Meiling, J.K. Rath, Device-quality polycrystalline and amorphous silicon films by hot-wire chemical vapor deposition. Philos. Mag. B **76**, 309 (1997)
21. P. Chaudhari, N. Meshram, A. Singh, A. Topkar, R. Dusane, Hot wire chemical vapour deposition (HWCVD) of boron carbide thin films from ortho-carborane for neutron detection application. Thin Solid Films **519**, 4561 (2011)
22. S. Ramakrishna, R.O. Dusane, From a-C to nanographene by chemical nano-engineering. Mater. Chem. Phys. **213**, 177 (2018)
23. R.W. Collins, H. Fujiwara, Growth of hydrogenated amorphous silicon and its alloys. Curr. Opin. Solid State Mater. Sci. **2**, 417 (1997)
24. J.R. Abelson, Plasma deposition of hydrogenated amorphous silicon: studies of the growth surface. Appl. Phys. A **56**, 493 (1993)
25. B.A. Korevaar, G.J. Adriaenssens, A.H.M. Smets, W.H.M. Kessels, H.Z. Song, M.C. van de Sanden, D.C. Schram, High hole drift mobility in a-Si: H deposited at high growth rates for solar cell application. J. Non-Cryst. Solids **266–269**, 380 (2000)
26. B. Rech, T. Roschek, J. Müller, S. Wieder, H. Wagner, Amorphous and microcrystalline silicon solar cells prepared at high deposition rates using RF (13.56 MHz) plasma excitation frequencies. Sol. Energy Mater. Sol. Cells 66, 267 (2001)
27. I. Roca, P. Cabarrocas, A. Fontcuberta, I. Morral, B. Kalache, S. Kasouit, microcrystalline silicon thin films grown by PECVD, growth mechanisms and grain size control. Solid State Phenom. **9**, 257 (2003)
28. R. Carius, T. Merdzhanova, F. Finger, S. Klein, O. Vetterl, A comparison of microcrystalline silicon prepared with plasma enhanced chemical vapor deposition and hot wire chemical vapor deposition: electronic and device properties. J. Mater. Sci. Mater. Electron. **14**, 625 (2002)
29. J.K. Rath, Micro and poly-crystalline silicon materials for thin film photovoltaic devices deposition process and growth mechanism, in *Photovoltaic and Photoactive Materials-Properties, Technology and Application*, NATO Science Series, vol. 280 (2002), p. 157
30. J. E. Bourée, in Seventh international conference on Hot-Wire CVD (Cat-CVD) process, Thin Solid Films, 575, Ed. by Jean-Eric Bourée
31. C. Chittick, J.H. Alexander, H.F. Sterling, The preparation and properties of amorphous silicon. J. Electrochem. Soc. **116**, 77 (1969)
32. W.E. Spear, P.G. Le Comber, Electronic properties of substitutionally doped amorphous Si and Ge. Phil. Mag. **33**, 935 (1976)
33. D.E. Carlson, C.R. Wronski, amorphous silicon solar cell. Appl. Phys. Lett. **28**, 671 (1976)
34. R.A. Street, *Hydrogenated Amorphous Silicon* (Cambridge University Press, New York, 1991)
35. W. Schüttauf, B. Niesen, L. Löfgren, M. Bonnet-Eymard, M. Stuckelberger, S. Hänni, M. Boccard, G. Bugnon, M. Despeisse, F. Haug, F. Meillaud, C. Ballif, amorphous silicon-germanium for triple and quadruple junction thin-film silicon based solar cells. Sol. Energy Mater. Sol. Cells **133**, 163 (2015)
36. S. Okamoto, E. Maruyama, A. Terakawa, W. Shinohara, S. Nakano, Y. Hishikawa, K. Wakisaka, S. Kiyama, Towards large-area, high-efficiency a-Si/a-SiGe Tandem solar cells. Sol. Energy Mater. Sol. Cells **66**, 85 (2001)
37. J. Meier, E. Vallat-Sauvain, S. Dubail, U. Kroll, J. Dubail, S. Golay, L. Feitknecht, P. Torres, S. Fay, D. Fischer, A. Shah, Microcrystalline/micromorph Silicon thin-film solar cells prepared by VHF-GD technique. Sol. Energy Mater. Sol. Cells **66**, 73 (2001)

38. O. Vetterl, F. Finge, R. Carius, P. Hapke, Houben, O. Klut, A. Lambertz, A. Muck, B. Rech, H. Wagner, Intrinsic microcrystalline silicon: a new material for photovoltaics. Sol. Energy Mater. Sol. Cells **62**, 97 (2000)
39. A.V. Shah, J. Meier, E. Vallat-Sauvain, N. Wyrsch, U. Kroll, C. Droz, U. Graf, Material and solar cell research in microcrystalline silicon. Sol. Energy Mater. Sol. Cells **78**, 469 (2003)
40. A.V. Shah, H. Schade, M. Vanecek, J. Meier, E. Vallat-Sauvain, N. Wyrsch, U. Kroll, C. Drozand, J. Bailat, Thin film solar cell technology. Prog. Photovolt: Res. Appl. **12**, 113 (2004)
41. S. Adhikari, A thermodynamic and kinetic investigation of the HWCVD process, Ph.D. thesis (IIT Bombay, 2013)
42. S. Kumar Soni, Study of HWCVD a-Si:H and microcrystalline thin films for application in solar cells, Ph.D. thesis (IIT Bombay, 2013)
43. N. Wadibhasme, Synthesis and characterization of hydrogenated amorphous and microcrystalline thin films for solar cell application, Ph.D. thesis (IIT Bombay, 2016)
44. M. Vanecek, J. Kocka, J. Stuchlik, Z. Kozisek, O. Stika, A. Triska, Density of the gap states in undoped and doped glow discharge a-Si:H. Sol. Energy Mater **8**, 411 (1983)
45. J. Kocka, M. Vanecek, and A. Triska, in *Amorphous Silicon and Related Materials*, ed. H. Fritzsche (World Scientific Publishing Company, 1988), p. 297
46. A. Poruba, A. Fejfar, Z. Remes, J. Springer, M. Vane, J. Kocka, Optical absorption and light scattering in microcrystalline silicon thin films and solar cells. J. Appl. Phys. **88**, 1 (2000)
47. C. Main, S. Reynolds, I. Zrinscak, A. Merazga, Determination of defect densities by constant photocurrent method—comparison of AC and DC methods. Mat. Res. Soc. Symp. Proc. **762**, A19 (2003)
48. P. Alpuim, V. Chu, J.P. Conde, Amorphous and microcrystalline silicon films grown at low temperatures by radio-frequency and hot-wire chemical vapor deposition. J. Appl. Phys. **86**, 3812 (1999)
49. T.H. Wang, E. Iwaniczko, M.R. Page, D.H. Levi, Y. Yan, V. Yelundur, H.M. Branz, A. Rohatgi, Q. Wang, Effective interfaces in silicon heterojunction solar cells, in *Conference Record of the IEEE Photovoltaic Specialists Conference* (2005), p. 955
50. M. Tanaka, M. Taguchi, T. Matsuyama, T. Sawada, S. Tsuda, S. Nakano, H. Hanafusa, Y. Kuwano, Development of new a-Si/c-Si heterojunction solar cells: ACJ-HIT (artificially constructed junction-heterojunction with intrinsic thin layer). Jpn. J. Appl. Phys., Part 1: Regular Papers Short Notes Rev., 3518 (1992)
51. E. Centurioni, D. Iencinella, R. Rizzoli, F. Zignani, Silicon Heterojunction Solar Cell: A New Buffer Layer Concept with Low-Temperature Epitaxial Silicon. IEEE Trans. Electron Devices **51**, 1818 (2004)
52. H. Fujiwara, M. Kondo, Impact of epitaxial growth at the heterointerface of a-Si:H/c-Si solar cells. Appl. Phys. Lett. **90**, 013503 (2007)
53. Mohit Agarwal, Abhijeet Pawar, Nilesh Wadibhasme, Rajiv Dusane, Controlling the c-Si/a-Si:H interface in silicon heterojunction solar cells fabricated by HWCVD. Sol. Energy **144**, 417 (2017)
54. R.S. Wagner, W.C. Ellis, Vapor-liquid-solid mechanism of single crystal growth. Appl. Phys. Lett. **4**, 89 (1964)
55. J.W. Choi, J.M. Donough, S. Jeong, J.S. Yoo, C.K. Chan, Y. Cui, Stepwise nanopore evolution in one-dimensional nanostructures. Nano Lett. **10**, 1409 (2010)
56. F. Thissandier, A.L. Comte, O. Crosnier, P. Gentile, G. Bidan, E. Hadji, T. Brousse, S. Sadki, highly doped silicon nanowires based electrodes for micro electrochemical capacitor applications. Electrochem. Commun. **25**, 109 (2012)
57. F. Thissandier, N. Pauc, T. Brousse, P. Gentile, S. Sadki, Micro ultra-capacitors with highly doped silicon nanowires electrodes. Nanoscale Res. Lett. **8**, 1 (2013)
58. Y. Cui, C.M. Lieber, Functional nanoscale electronic devices assembled using silicon nanowire building blocks. Science **291**, 551 (2001)
59. B. Tian, X. Zheng, T.J. Kempa, Y. Fang, N. Yu, G. Yu, J. Huang, C.M. Lieber, coaxial silicon nanowires as solar cells and nanoelectronic power sources. Nature **449**, 885 (2007)

60. Y. Yang, M.T. McDowell, A. Jackson, J.J. Cha, S.S. Hong, Y. Cui, New nanostructured Li_2S/silicon rechargeable battery with high specific energy. Nano Lett. **10**, 1486 (2010)
61. E.I. Givargizov, Fundamental aspects of VLS growth. J. Cryst. Growth **31**, 20 (1975)
62. M. Jeon, H. Uchiyama, K. Kamisako, Characterization of tin-catalysed silicon nanowires synthesized by the hydrogen radical-assisted deposition method. Mater. Lett. **63**, 246 (2009)
63. Y.J. Xing, D.P. Yu, Z.H. Xi, Z.Q. Xue, Silicon nanowires grown from Au-coated Si substrate. Appl. Phys. A **76**, 551 (2003)
64. H. Uchiyama, M. Jeon, Y. Tomitsuka, K. Maishigi, K. Kamisako, Effect of hydrogen radical treatment and synthesis of Sn-catalysed silicon nanowires at various growth conditions, e-J. Surf. Sci. Nanotech. **7**, 708 (2009)
65. N.P. Meshram, A. Kumbhar, R.O. Dusane, Silicon nanowire growth on glass substrates using hot wire chemical vapour deposition. Thin Solid Films **519**, 4609 (2011)
66. V. Schmidt, J.V. Wittemann, U. Gösele, Growth, thermodynamics, and electrical properties of silicon nanowires. Chem. Rev. **110**, 361 (2010)
67. W. Park, G. Zheng, X. Jiang, B. Tian, C.M. Leiber, Synthesis of millimeter-long silicon nanowires with uniform electronic properties. Nano Lett. **8**, 3004 (2008)
68. M.K. Jangid, A.S. Lakhnot, A. Vemulapally, F.J. Sonia, R.O. Dusane, A. Mukhopadhyay, crystalline core/amorphous shell structured silicon nanowires offer size and structure dependent reversible Na-storage. J. Mater. Chem. A **6**, 3422 (2018)
69. A. Soam, Development of silicon nanowire technology for supercapacitor application, Ph.D. thesis (IIT Bombay, 2017)
70. A. Soam, N. Arya, A. Singh, R. Dusane, Fabrication of silicon nanowires based on-chip micro-supercapacitor. Chem. Phys. Lett. **678**, 46 (2017)

Role of Ultrathin Electron Transport Layers in Performance of Dye-Sensitized and Perovskite Solar Cells

Vibha Saxena

Abstract Dye-sensitized solar cells (DSCs) and perovskite solar cells (PSCs), are emerging and promising technologies amongst third-generation solar cells. Recent breakthroughs in achieving a record efficiency of 11.7% in solid DSCs at 1 sun and 32% at 1,000 lx surpass even the performance of conventional crystalline solar cells. In the context of PSCs, recent developments of new methodologies and materials are promising for achieving high efficiency as well as stability. Charge extraction layers, viz. electron (ETLs) and hole transport (HTLs) layers are important constituents of high efficient DSCs and PSCs. These layers aid in the transport of charges selectively whilst block their counterparts for an efficient solar cell. In general, 100-nm-thick TiO_2 is employed to fabricate DSCs and PSCs using conventional methods, such as spin cast, spray pyrolysis and chemical bath deposition. A thinner and compact charge extraction layer (<50 nm) is desirable to reduce the series resistance and improve the transmittance and thereby the device efficiency. This chapter describes basic concepts underlying the role of ETLs in the device DSCs/PSCs. The basic principle and merits of deposition processes to prepare ultrathin films for PSCs/DSCs are discussed in detail in this chapter. Further, ultrathin ETLs prepared by different methods have been reviewed. Future directions to explore unconventional scalable and simpler technologies in the emerging field of DSCs/PSCs are discussed from the point of view of commercialization and fundamental research.

1 Introduction

Crystalline silicon-based solar cells represent promising renewable alternatives to fossil fuels and currently, wafer-based crystalline Si solar modules dominate more than 90% of the photovoltaic (PV) market [1]. Third-generation solar cells, such as bulk-heterojunction PV, dye-sensitized solar cells (DSCs) and perovskite solar cells (PSCs), represent new concepts and technologies, aiming for high efficient modules

V. Saxena (✉)
Technical Physics Division, Bhabha Atomic Research Centre, Mumbai 400085, India
e-mail: vibhas@barc.gov.in

S. Kumar and D. K. Aswal (eds.), *Recent Advances in Thin Films*, Materials Horizons: From Nature to Nanomaterials, https://doi.org/10.1007/978-981-15-6116-0_16

at substantially low cost. Amongst these technologies, DSCs are very promising PVs due to low cost, non-toxic and earth-abundant materials, simple fabrication techniques, performance under real outdoor conditions, and non-requirement of vacuum technologies. Though the highest power conversion efficiency (PCE) in DSCs reported so far has not gone beyond 14% at lab scale [2] and 10% in the module under 1 sun irradiation, accelerated lifetime tests with high durability efficiencies [3] and best efficiency at low light intensity have continued the research in this area.

A typical liquid electrolyte based DSC consists of a sandwich-type structure of a dye-sensitized TiO_2 (Dye-TiO_2) and a platinized counter electrode filled with a redox electrolyte between these electrodes and have long been considered as potential candidates for cheap, sustainable energy production. Long-term stability issue of liquid-based DSCs paved the path for solid-state DSC (sDSC), where liquid electrolyte is replaced with a hole transporting layer (HTL). However, sDSC did not show high efficiency as achieved in liquid electrolyte based DSCs, reaching a maximum of 7.2% PCE with customized dyes and HTL [4]. Nevertheless, a recent breakthrough in achieving record efficiency of 11.7% at 1 sun irradiation so far in sDSC [5] and 32% at 1,000 lx is particularly promising in terms of stability and efficiency at low light intensity [6]. On the other hand, with perovskites sensitized mesoporous TiO_2 (m-TiO_2) anode, the sDSC have started to show high performances using conventional sDSC architectures as a model system [7] and led to a paradigm shift in this field with a maximum PCE of 20.5% (in >1 cm^2 device area) and record National Renewable Energy Laboratory (NREL)-certified PCE ~25.2% by KRICT/MIT recently [8]. Though PSCs emerged from the DSC architecture containing the perovskite as sensitizer and gave high efficiency, planar-type architectures were also explored [9]. Figure 1 represents the various architectures adopted so far for PSCs together with liquid electrolyte based DSC and sDSC. Despite the difference in architectures in

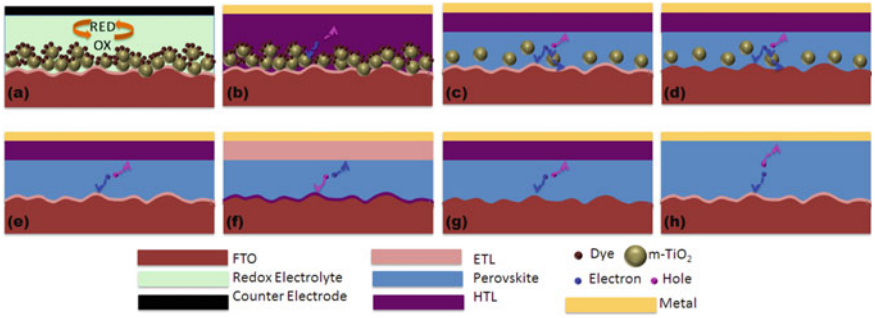

Fig. 1 The device architectures of the **a** liquid-based DSC **b** sDSC, mesoporous **c** PSC with ETL and HTL; and **d** PSC without ETL, Planar **e** normal PSC with ETL and HTL, **f** Inverted PSC with ETL and HTL; **g** normal PSC without ETL; and **h** normal PSC without HTL; *Planar PSCs can be classified as normal and inverted structures depending on which transport (electron/hole) layer (ETL/HTL) is encountered by incident light first*

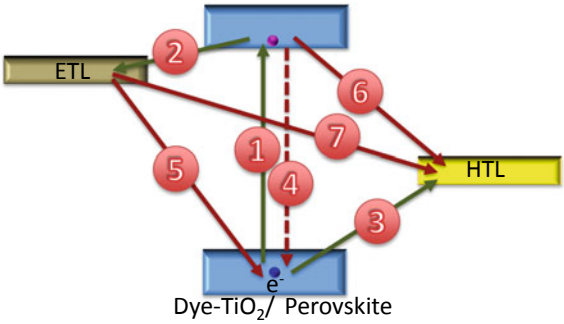

Fig. 2 Charge-transfer processes in DSC/PSC solar cells. The valence band energy (VBE) and the conduction band edge (CBE) of the absorber (dye-sensitized m-TiO_2/perovskite) lie below the HOMO level of HTL and above the CBE of ETL. The CB of widely used TiO_2 as ETL lies at −4.2 eV, and the HOMO of spiro-OMeTAD is at −5.22 eV

both types, the working mechanism in these devices can be divided into four basic phenomena as follows and is illustrated in Fig. 2.

(i) *Light absorption*: The light is absorbed by the dye (or perovskite layer) and exciton is formed as shown by (1) in Fig. 2.
(ii) *Charge separation*: The exciton is then separated due to kinetics in DSCs or due to the electric field in perovskite.
(iii) *Charge transport*: The charge is transported through the mesoporous structure of TiO_2 (or perovskite). Processes (ii) and (iii) are indicated by (2) and (3) in Fig. 2.
(iv) *Charge Collection*: Finally the charge is collected by the respective electrodes.

As illustrated in the figure, for an efficient solar cell, one of the important factors is the charge extraction layer having proper energetic levels in such a way that charges are transported selectively whilst blocking their counterpart. The carrier recombination of electron (or hole) with hole (or electron) is at the transport layer/absorber interfaces; as shown by (5) and (6) in Fig. 2 and/or due to direct contact between TiO_2 and HTL (shown by (7) in Fig. 2). These charge extraction layers called as electron-transport layers (ETLs) and HTLs eventually lead to reduced recombination losses and aid in increasing the open-circuit voltage (V_{OC}) and fill factor (FF) of the device and thereby the efficiency. The ETL (also called compact or blocking layer, BL) have been studied extensively in DSCs, however, little research has been carried out for the perovskite solar cells. Though several researchers reported a PCE of more than 13% for ETL-free devices, the presence of an ETL is essential for a highly efficient and reproducible device, and therefore the choice of ETL/scaffold (only ETL in case of inverted PSCs) for PSC/DSC is vital. An optimum thickness of 100 nm c-TiO_2 film deposited by conventional techniques such as spray pyrolysis and spin coating was used to fabricate sDSCs [10, 11] and PSCs [12, 13]. However, a thinner compact charge extraction layer (50 nm) will result in reduced series resistance and improved

transmittance and therefore subsequently improve the short-circuit current density (J_{SC}) and PCE in PSCs [14] and DSCs [15]. Therefore, it is essential to explore other deposition techniques, such as atomic layer deposition (ALD), electrochemical deposition, sputtering and thermal oxidation, in contrast to conventional solution process techniques (i.e. spin coating, spray pyrolysis) to prepare homogeneous and pinhole-free layers of very low thicknesses. Several reviews have been reported on the use of ETLs in PSCs/DSCs research. In this review, we focus on research carried out using ultrathin ETL (thickness <50 nm) in the field of PSCs and DSCs.

2 Requirement of the Material

An ideal ETL should be able to fulfil the following general criterion before being employed to fabricate PSCs/DSCs:

(i) ***Energy levels and band gap***:
The LUMO (lowest unoccupied molecular orbital) energy level of ETL should match the CBE of the absorber (Dye-TiO_2/perovskite) to facilitate electron transfer and block the hole transport as well as to enhance the built-in potential. Further, a wide band gap material is required so as to get (a) high transparency for efficient light absorption by absorber layer (b) good anti-reflection to minimize light scattering and reflection.
In addition to this, the research has also been carried out to extend the transparency of the material up to UV, which plays a significant role in device stability when operated in outdoor conditions such as higher altitudes and deep space. It is reported that under UV radiation, the oxygen vacancies of TiO_2 reacts with photogenerated holes in TiO_2 producing deep traps for charge recombination and lead to device performance degradation [16].

(ii) ***Morphology***:
A pinhole-free and dense compact layer is essential before incorporating the device fabrication. Other than this, the difference in morphologies of ETL have played an insignificant role in the device performance improvement [17]. Nevertheless, in some cases, the unique morphology of the TiO_2 nanosheets (TNS) had contributed to the hysteresis effect reduction, and therefore it is found to be important for the overall improvement in device performance [18, 19].

(iii) ***Transport properties***:
Ideally, the ETL should have excellent electrical properties in order to maximize the charge collection and to minimize the series resistance of the device. This can be achieved via—(a) Increasing the conductivity by preparing thin films of materials with high mobility and/or high carrier concentration as well as reducing the ETL thickness while processing.
(b) Using interfacial modification, additives or dopants.

Table 1 Electron mobility, conductivity and carrier concentration of some organic/inorganic ETL materials used in PSCs/DSCs

Material	Carrier concentration (cm^3)	Conductivity (S/cm)	Mobility (cm^2/Vs)	Reference
$IC_{60}BA$	–	6.5×10^{-5}	6.9×10^{-3}	Liang et al. [20]
PCBM	–	3.2×10^{-4}	6.1×10^{-2}	
C_{60}	–	2.4×10^{-3}	1.6	
TiO_2	–	1.7×10^{-2}	1.9×10^{-4}	Saito et al. [21]
ZnO	12.5×10^{18}	1.2	15	Bellingeri et al. [22]
Zn_2SnO_4	10^{18}–10^{19}	–	20	Coutts et al. [23]
CdS	4.1×10^{16}	0.68	4.6	Ahmed et al. [24]
SnO_2	–	9.3×10^{-5}	9	Kuang et al. [25]
WO_3	–	0.034	10	Ali et al. [26]
a-Nb_2O_5	6.18×10^{18}	2.053×10^{-5}	20.73	Ling et al. [27]
a-Nb_2O_5	4.076×10^{18}	1.748×10^{-5}	26.77	

(c) Reducing the oxygen vacancies in materials which may act as deep traps for charge recombination.

Table 1 represents the charge transport properties of the most widely used materials for ETL in PSCs/DSCs.

(iv) ***Thickness***:
The thickness of the ETLs has to be optimized to get efficient device performance. An increase in the thickness of the layer will result in reduced electrons transport from the Dye-TiO_2/perovskite layer to the FTO. However, a thin ETL may not cover the FTO effectively, and therefore will result in charge recombination with oxidized dye or perovskite layer. An optimum ETL thickness is a fine balance between hole-blocking behaviour and carrier transport property: full coverage at the cost of increased BL thickness will increase hole-blocking ability but result in carrier transport loss. Depending on the preparation method, the thickness of the ETL has to be optimized to get the best device performance.

(v) ***Structure***:
In conventional methods, a polycrystalline anatase TiO_2 film was prepared as ETL for the fabrication of DSC/PSCs owing to better charge transport properties; lower electron traps density and enhanced transmittance. Amorphous TiO_2 were not employed as ETL in DSCs/PSCs. Recently, an ultrathin (8 nm) amorphous metal oxide along with brookite TiO_2 enormously enhanced photovoltaic efficiency to 21.6% along with high V_{OC} and FF up to 1.18 V and 0.83, respectively [28], owing to outstanding wettability of amorphous TiO_2 against perovskite solution which reduces the interfacial resistance between TiO_2 and perovskite layer. Therefore, the structures of the prepared material need to be investigated before employing in PSCs/DSCs.

(vi) ***Compatibility and stability***:

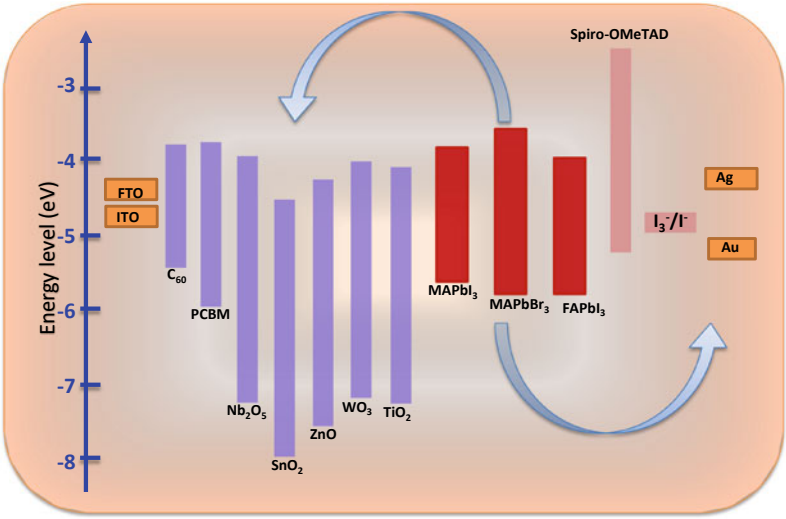

Fig. 3 Energy-level diagram for widely used organic and inorganic materials for ETL in DSCs and PSCs

In order to minimize the degradation owing to moisture and oxygen on PSCs/DSSCs, the research aimed at improving the intrinsic stability of perovskite solar cells. In case of inverted PSCs, ETL is deposited on top of the perovskite layer and thereby acts to protect the underneath layer from oxygen and moisture as well as solvents in the deposition process [29]. Fullerene-based molecules such as C_{60} and [6] -phenyl-C61-butyric acid methyl ester C_{60} (PCBM) have better charge extraction properties than metal oxides and have been widely used as ETL in inverted PSCs. A thin ETL was found to minimize the density of defects as well as overall charge collection at the perovskite/ETL interface, and therefore reduced the charge recombination at the perovskite/ETL interface [30, 31]. Similar findings were obtained for inorganic materials, such as NiO, TiO_2 and ZnO [32]. Figure 3 represents the energy level diagram of organic and inorganic ETLs used in the PSCs and DSCs.

3 Deposition Techniques

Many of the parameters discussed above such as morphology, transport properties and compatibility of compact TiO_2 depend on the fabrication methods, which in turn determines the thickness and roughness of the ETL. The fluorine-doped (FTO) and indium-doped tin oxide (ITO) substrates are invariably used as a transparent conducting oxide in both PSCs and DSCs. Since commercially available FTO/ITO has rough surfaces of about 20–30 nm, it is difficult to prepare the deposition of thin film having ideal ETL properties [18]. Most widely used solution-processable

methods such as spin coating and spray pyrolysis often result in thicker films in order to get continuous and full coverage, and therefore result in enhanced internal resistance of the device and in turn the photovoltaic properties. In order to improve $J_{SC,}$ and therefore the PCE of PSC/DSSC devices, suitable deposition techniques that enable pinhole-free and very thin ETL is essential. The adopted deposition methods for ETL in PSCs/DSCs are summarized in Table 2 and discussed below.

3.1 Solution-Processable Techniques

As stated above, solution-processable techniques such as spin coating and spray pyrolysis have been utilized to prepare continuous and uniform ETL films for DSCs/PSCs. However, these methods result in thick films ~100 nm to achieve optimum device efficiency. Nevertheless, there are a few reports of using spin coating for thinner layer (<50 nm) for ETL preparation and the results are discussed in the following sections.

3.1.1 Spin Coating

Spin coating is a very simple solution-based method, where the precursor of the desired material is spun on the substrate at suitable rpm (Fig. 4). This method is most widely used to deposit thin layers of inorganic and organic materials in the application of solar cells [33]. As stated earlier, the deposition of very thin ETL on FTO is limited due to its surface roughness. In addition, the deposition of very thin ETL results in the formation of a pinhole in the layer, which led to pathways for recombination in the DSCs and PSCs. The optimum thickness reported for achieving high performance in PSC and DSC is 65 nm [14] and 100 nm [11], respectively. Nevertheless, spin coating has been used to deposit a thin and smooth layer in DSCs and inverted PSCs.

Tanvi et al. optimized a very thin spin-coated TiO_2 layer and estimated the blocking behaviour of the prepared ETL as a function of thickness [34]. The blocking behaviour of the prepared films was estimated by recording the cyclic voltammogram (CV). The observed cathodic peak current intensity (I_P) in the CV is related to the reacting area of the electrode (A) according to the Randles–Sevcik equation:

$$I_P = kn^{3/2} AcD^{1/2} \upsilon^{1/2}$$

where n is the number of electrons transferred in the redox couple, υ is the scan rate, D is the diffusion coefficient, c is the redox species concentration and k is the rate constant.

Since all parameters in the above equation are constant, covering the FTO surface with an ETL will decrease the reaction area for the redox couple and thereby result in a reduced I_P. Thus, the ratio of I_P at FTO and ETL can be taken to estimate the surface coverage by ETL, and therefore the blocking effect. Figure 5 shows the blocking

Table 2 Performance of DSCs and PSCs (referred by superscript D and P in the last column) using various ETLs deposited by different methods

Material	V_{OC}	J_{SC}	FF	Control Cell PCE (%)	PCE (%)	Deposition method	Reference
TiO_2	0.77	12.2	56	3.5	5.2	Spin coating	Tanvi et al. [34]^D
	0.9	22.6	51.9	–	13.8		Vivo et al. [37]^P
	1.1	22.6	78.2	14.1	19.4		Shen et al. [38]^P
Brookite TiO_2	1	20.6	70	12.1	14.42		Kogo et al. [36]^P
Amorphous TiO_2	1.14	22.5	79	13.2	20.2		Kogo et al. [28]
TiO_2 QD	1.11	21	76.6	14.4	17.9		Tao et al. [30]^P
SnO_2	1.014	21.24	65.9	–	14.2		Abulikemu et al. [41]^P
C_{60}	0.97	20.2	82	–	16		Chiang and Wu [43]^P
V_2O_5	0.83	16.91	68.1	8.7	9.56	CBD	Elbohy et al. [49]^D
Rutile TiO_2	1.11	17.41	65.6	–	13.03		Yella et al. [51]^P
TiO_2	1.00	19.16	59	–	11.18		Liang et al. [52]^P
SnO_2	1.18	22.37	77		20.46		Anaraki et al. [54]^P
TiO_2	5.32	0.78	75	1.68	3.12	RF sputtering	Braga et al. [56]^D
	1.00	18.8	66	0.3	12.4		Kogo et al. [60]^P
	0.65	11.88	56	3	4.27	RF magnetron	Abdullah and Rusop [61]^D
	1.09	21.97	63	7.6	15.07		Ke et al. [58]^P
	1.09	20.6	54	4.3	12.1		Chen et al. [65]^P
Nb_2O_5	0.71	9.32	68	3.5	4.5		Xia et al. [57]^D
	1.04	22.9	72		17.1		Ling et al. [27]^P

(continued)

Table 2 (continued)

Material	V_{OC}	J_{SC}	FF	Control Cell PCE (%)	PCE (%)	Deposition method	Reference
TiO_2	1.036	23.13	67.87	12.19	15.76	DC magnetron	Huang et al. [59]^{P}
	0.96	18.57	49	–	8.7	Pulsated DC magnetron reactive	Rajmohan et al. [66]^{P}
	0.762	13.95	72	–	7.65	RF reactive magnetron	Chang et al. [62]^{D}
	1.108	20.77	60	3.04	15.88		Mali et al. [67]^{P}
	0.729	13.51	57	4.37	5.57	ICP-assisted DC magnetron	Kim et al. [64]^{D}
C_{60}	1.03	18.6	77.7	–	14.9	Thermal evaporation	Zha et al. [70]^{P}
	0.92	21.07	80	–	15.44		Liang et al. [20]^{P}
	1.06	18.84	74.14	7.88	14.87		Ke et al. [71]^{P}
	1.1	24.04	76.4	–	20.2		Ahn et al. [72]^{P}
	1.08	22.3	75.9	–	18.2		Liu et al. [73]^{P}
TiO_2	1.016	22.35	68	–	15.4		Hwang and Yong [74]^{P}
CdS	0.977	17.54	71	–	12.2		
TiO_2	0.63	16.80	50.7	2.82	5.38	ALD	Li [et al. 85]^{D}
HfO_2	0.71	12.17	55.8		4.83		
ZnO	0.74	9.67	65.8	2.9	4.68		Lu et al. [86]^{D}
TiO_2	1.02	21	71.9	–	15.41		Shalan et al. [87]^{P}
	0.90	19.5	47.75	–	8.40		Wu et al. [79]^{P}
	0.858	14.1	70	9.8	8.4		Di Giacomo et al. [90]^{P}
	1.04	22.8	76.9	16.4	18.3		Lv et al. [92]^{P}
	1.097	19.797	70.614	–	15.33		McCarthy et al. [93]^{P}
SnO_2	1.13	21.56	76.93	–	19.03		Wang et al. [80]^{P}
	1.14	21.3	0.74	–	18.4		Correa Baena et al. [89]^{P}

(continued)

Table 2 (continued)

Material	V_{OC}	J_{SC}	FF	Control Cell PCE (%)	PCE (%)	Deposition method	Reference
	1.08	22.1	75	1.18	17.8		Kuang et al. [25]^{P}
	1.13	22.67	78	19.83	20.03		Lee et al. [94]^{P}
ZnO	0.976	20.4	66	–	13.1		Dong et al. [88]^{P}
	1.02	20.73	76.36	2.55	16.15		Chang et al. [95]^{P}
	0.860	25.62	45.2	11.47	9.97		Kim et al. [91]^{P}
TiO_2	0.74	15.76	69	7.73	8.04	ECD	Wu et al. [97]^{D}
	1.00	20.01	68	10.42	13.60		Su et al. [98]^{P}
	1.00	19.08	70.6	12.03	13.47		Du et al. [99]^{P}
	1.06	20.05	70	12	15.2		Choi et al. [100]^{P}
SnO_2	1.08	19.75	65	10.47	13.88		Chen et al. [101]^{P}
ZnO	0.91	22.6	52.9	–	10.91		Zhang et al. [102]^{P}
TiO_2	0.71	16.48	58	6.94	7.98	EPD	Li et al. [103]^{D}
TNS	0.922	18.5	54		9.4		Li et al. [18]^{P}
TiO_2	0.877	20.12	72.6	11.042	12.812	DC	Hong et al. [105]^{P}
	0.946	19.87	60	12.14	11.47		Huang et al. [107]^{P}
	0.97	13.2	67		8.6		Masood et al. [106]^{P}
SnO_2	0.842	10.55	72.7	5.51	6.46		Kim et al. [64]^{D}
ZnO	0.75	13.46	65.4		6.62		Chou et al. [112]^{D}
WO_3	0.754	14.83	56.07	5.2	6.27	LB	Prakash et al. [111]^{D}

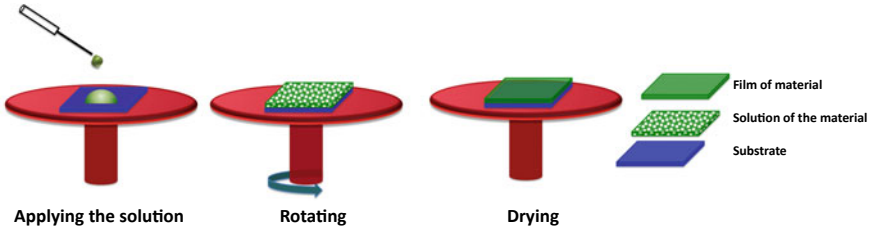

Fig. 4 Schematic of the processes involved in film prepared by the spin-coating method

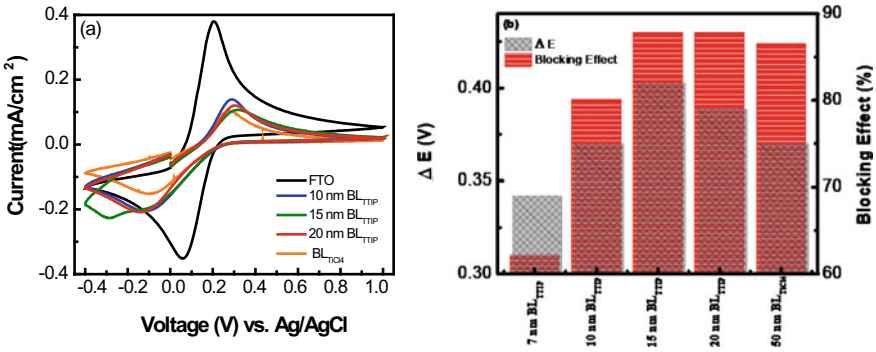

Fig. 5 **a** Cyclic voltammograms of prepared ETLs at a scan rate of 50 mV/s. The voltammogram of FTO substrate is also shown and **b** blocking effect and; peak-to-peak separation (ΔE) of various TiO_2 ETLs

effect of prepared films using this method. Though thicker films (>15 nm) showed good blocking behaviour, the device performance was decreased despite good optical, morphological and blocking properties. On the other hand, thin films ~10 nm resulted in a significant improvement in V_{OC} and J_{SC}, and therefore device efficiency on account of good optical and morphology properties, moderate blocking, enhanced conductivity and more negative shift in the Fermi level are observed. However, for PSCs it was observed that spin-coated TiO_2 possesses many defects such as residual organics and hydroxyl groups, thereby affecting the charge collection properties [35]. A TiO_x ETL deposited by spray pyrolysis along with mesoporous brookite TiO_2 was also used for PSC fabrication [36]. The presence of many hydroxyl groups on the surface of brookite TiO_2 nanoparticles provides an inter-particle connection via dehydration reaction at 150 °C and thus results in a mesoporous layer and device efficiency ~14.3%. When an ultrathin (8 nm) amorphous TiO_x ETL was used along with brookite TiO_2, there was a significant enhancement in PCE [28]. The PSC fabricated with TiO_x/brookite TiO_2 showed high PCE ~21.6% owing to high FF. A study was carried out to compare the TiO_2 (44-66 nm) produced by spin coating of different precursors [37]. The highest PCE ~13.8% was achieved by replacing the commonly used titanium isopropoxide (TTIP) blocking layer precursor with

$TiCl_4$. Further, the lifetime of the PSCs with $TiCl_4$ as a compact layer precursor is significant: 70% of the initial efficiency remained after 4 months of exposure to ambient environment (25 °C, 15% humidity). This was attributed to lower roughness and large crystallite size of prepared $TiCL_4$ as compared with other precursors. It was reported that the doping of TTIP precursor with $TiCl_4$ results in conformal coverage of the spin-coated film (40 nm) on the FTO substrate [38]. The conformal TiO_2 coverage aids in electron transfer and transport, and therefore result in PCE ~20% for 10% $TiCl_4$ doped TiO_2 ETL. In contrast to metal oxides, spin coating was found to be useful to prepare pinhole-free compact layers of controlled thickness using quantum dot (QD) materials such as PbS, CdS and CdSe [39]. Tu et al. utilized crystallized TiO_2 QDs to fabricate a pinhole-free and ultrathin compact layer for PSCs by the spin-coating method [40]. The PSCs based on the TiO_2 QD compact layer offered high PCE of 16.97% as a result of small series resistance and the large shunt resistance of the TiO_2 QD layer. Recently, a facile low-temperature-solution-based microwave-assisted SnO_2 nanocrystals were synthesized for ETL in PSCs [41]. High PCE of 14.2% was obtained due to high transparency and crystallinity.

Other than metal oxides, fullerene derivatives are potential materials for ETL in PSCs. However, film thickness less than 55 nm could not be achieved for high-performance devices due to the fact that in normal PSC meticulous control over uniformity is required due to the fact that these materials dissolved easily in a non-polar solvent like chlorobenzene or toluene, which is a common solvent for perovskite layer [42]. However, a top thin layer of fullerene derivatives, TiO_2 have been used by taking advantage of relatively flat surface perovskite and to improve charge collection and passivation [43, 44]. A relatively thin film of PCBM layer (~55 nm thick) was spin coated on extremely uniform perovskite layers, to demonstrate the efficiency of ~14.1% for a single cell and 8.7% for the module [31]. Other deposition methods were adopted to produce thinner PCBM layers and will be discussed in sections that followed.

Despite being used widely in the fabrication of solution-processed thin films in solar cells, this conventional technique has several drawbacks such as scaling up for large-scale production, difficulty in controlling the thickness and has hardly been used to produce thin layers <50 nm. Scalable technique such as spray pyrolysis often results in thicker films except in a few cases and will not be discussed here [36, 45].

3.1.2 Chemical Bath Deposition (CBD)

CBD comprises a variety of routes for producing ETLs by immersing a substrate in an aqueous precursor solution. The quality of the film can be controlled using various parameters such as solution temperature, pH and concentration. The most used ETLs prepared by the CBD technique were prepared via hydrolysis of $TiCl_4$ resulting in an anatase phase of TiO_2 after sintering. This method has been used both as ETL and as post-treatment of m-TiO_2 and has been found to result in improved J_{SC} in DSCs [46] and extended further to PSCs [47, 48]. Solution-processed passivation of m-TiO_2 with vanadium pentoxide (V_2O_5) was also used in DSCs. Significantly

increased cell efficiency from 8.78 to 9.65% was obtained and was attributed to high charge recombination resistance for V_2O_5-modified ETL as compared with that without V_2O_5 in conventional cells [49]. Lee et al. reported that the rutile phase shows outstanding morphological properties and acts both as an effective electron collector and a recombination blockade [50]. This method was extended further to deposit ETL at low temperature [51]. High PCE ~12.80% was obtained due to a decrease in the series resistance and a significant increase in the recombination resistance at the interface of the TiO_2/perovskite layer and TiO_2/HTL layer. Recently, the CBD was used to prepare ETL (20–310 nm) along with UV/O_3 treatment in planar PSCs at low temperature (<100 °C) [52]. It is found that the surface morphology of the TiO_2 compact layer played a critical role in the device's performance. For low thickness, PCE was low due to incomplete coverage of the TiO_2 layer on the FTO substrate. Over 12% PCE was achieved when the thickness was increased to 60 nm as a result of reduced current leakage and lower series resistance. A systematic investigation on TiO_2 ETL (25–50 nm thickness) prepared by commonly used methods was carried out and their effects on the photovoltaic performance of PSCs were investigated in detail [53]. The CBD method was found to be superior to other methods such as spin coating, sol-gel coating, screen printing. The interconnectivity between the TiO_2 particles and the TiO_2 coverage in the blocking layers is far higher for the ETL prepared by CBD compared with all other studied methods, and therefore results in high PCE ~12.80%. The approach was found to be useful in depositing other ETL materials, SnO_2 [54]. Highly efficient planar PSCs based on SnO_2 ETL showed a PCE close to 21% due to high selectivity and highest reported V_{OC} so far ~1.214 V. In addition to this, PSCs prepared showed great stability retaining more than 82% of the initial efficiency over 60 h and a PCE of 20.7% and opens up a scalable and inexpensive way to deposit high-quality SnO_2 ETL for highly stable and efficient PSCs.

3.2 Physical Vapour Deposition (PVD) Techniques

The thin-film deposition using PVD is obtained by changing the phase of the material from solid to vapour phase by some means and converting this phase to a solid phase on the desired substrate in order to coat. This method, in general, takes place under vacuum or controlled atmospheric condition and have been used in the PSCs/DSCs fabrication as discussed below.

3.2.1 Sputtering

Sputter deposition is a widely used technique to deposit thin and uniform films on desired substrates. In this method, the source (target) material is ion-bombarded resulting in a vapour due to the sputtering of the target material (Fig. 6). The target can be powered in different ways, e.g. direct current (DC) for conductive targets,

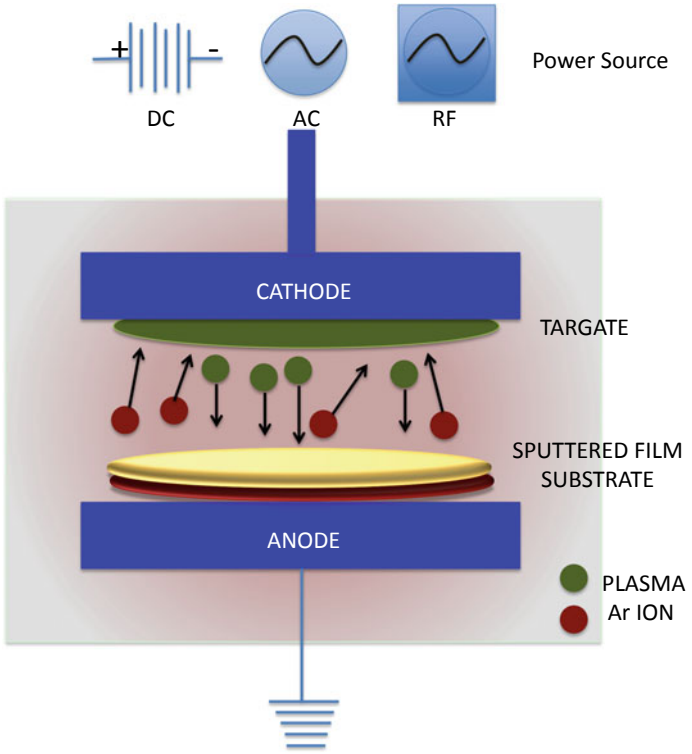

Fig. 6 Schematic of various methods used to sputtering ETL

radio frequency (RF) for non-conductive targets, in addition to various current and/or voltage pulses to the target.

Thin films (5–15 nm) of TiO_2 prepared by thermal oxidation of sputter-coated Ti metal were studied thoroughly to be used as a barrier layer in DSC [55]. The results showed a consistent influence of the thickness and structure of the TiO_2 layers on the DSC performance. The sputtering method produced a smooth compact TiO_2 film in contrast to non-uniform porous TiO_2 film obtained by the conventional method of $TiCl_4$ treatment. To produce an alternative and reliable front contact for DSCs, morphology and composition of a TiO_2 blocking layer (1–5 nm) was studied using a sputtered film of high average transmittance >90% [56]. The ultrathin blocking layer of Ti oxide prevents charge recombination, and improves the overall performance.

Nb_2O_5 deposited by the sputtering method on FTO has been characterized by scanning electron microscopy (SEM), CV and X-ray photoelectron spectroscopy. Thin Nb_2O_5 films work as efficient ETL, by improving V_{OC} and providing enhanced PCE in DSCs [57]. Using RF sputtering in combination with a novel one-step sintering process, TiO_2 porous film over very thin TiO_2 underlayer was produced [58]. Improved PCE of 15.07%, as compared with that of spin-coated film, was achieved in PSCs using this layer as a result of reduced interfacial resistances and were attributed

to higher J_{SC} and FF. Further, TiO_2 films with various crystallinities were prepared without any post-thermal treatments by DC magnetron sputtering. Partly crystalized TiO_2 having with 26.3% crystallinity showed the best device performance (15.76%) as compared with amorphous TiO_2 (13.3%) or anatase TiO_2 (12.9%) [59]. Ultrathin (8 nm) TiO_2 ETL along with brookite m-TiO_2 was also deposited using a low-temperature (150 °C) sputtering for plastic solar cells [60]. The flexible perovskite solar cells prepared exhibited a high PCE ~13.8%.

In order to get higher density plasma and increased deposition rates, sputter deposition was combined with a magnetron source in which positive ions present in the plasma of a magnetically enhanced glow discharge bombard the target. TiO_2 film deposited by RF magnetron sputtering was investigated for DSCs by varying layer thickness (20–80 nm) [61]. The J_{SC} increased when the ETL thickness increased from 40 to 60 nm and was attributed to the lowering of sheet resistance and improvement in the contact resistance between FTO and TiO_2. Moreover, improvement in the electron transport and mobility was obtained resulting in enhanced J_{SC} and PCE ~6.77%. Further deposition by reactive sputtering of TiO_2 was investigated using X-ray diffraction, atomic force microscopy, SEM and UV–Vis spectroscopy in detail [62]. As a result of good crystallinity and increased transmittance J_{SC}, V_{OC} and FF, and therefore PCE increased to 7.65%. In contrast, ETL deposited by reactive DC magnetron sputtering showed different results [63]. Elastic recoil detection analysis and optical measurement showed porosity in the sputtered films, however, good blocking behaviour was observed for these films. A thin layer (~20 nm) improved the FF without affecting other properties of the cell. Further, a low-temperature process was developed by reactive inductively coupled plasma (ICP)-assisted DC magnetron sputtering without substrate heating [64]. The resulting ETL yielded a 47% improvement in the PCE (~6.42%), thereby suggesting effective blocking behaviour of the layer and may be useful for use in flexible devices. Additionally, sputtering was also employed to prepare TiO_2 of controlled thickness by varying deposition time [65]. The 15-min sputtered TiO_2 film (~22 nm) based PSCs showed a PCE of 7.8% with a J_{sc} ~ 16.1 mA/cm^2, FF ~ 51% and V_{OC} ~ 0.95 V. When the deposition time was increased from 15 to 30 min., the J_{SC} and PCE increased to 21.5 mA/cm^2 and 12.1%, respectively. This was attributed to the improved electron collection and effective hole blocking by the TiO_2 layer. Rajmohan et al. used reactive magnetron sputtering for the fabrication of crystalline anatase TiO_2 as ETL at a moderate temperature (150 °C) [66]. The influence of block layer thickness on the photovoltaic performance was investigated and a high performance of 8.7% PCE was obtained for PSCs with a 76-nm-thick TiO_2 blocking layer. RF magnetron sputtering was also employed to prepare compact TiO_2 ETL for flexible PSCs [67]. $MAPb(I_{1-x}Br_x)_3$-based flexible perovskite solar cell showed 15.88% PCE due to extremely uniform (RMS: 7.114 nm) and crystalline perovskite absorbing layer formed on the ETL as well as fast electron transport and reduced recombination as evident by high fill factor (77%).

Other than TiO_2, other semiconducting materials such as ZnO and SnO_2 were also investigated as ETLs for PSCs/DSCs. Intrinsic ZnO films (20–100 nm) prepared by

sputtering, when inserted between the perovskite layer and FTO led to a large reduction of the recombination at this interface. Optimization of the ZnO layer together with that of the perovskite deposition parameters led to PCE of 14.2% [19]. Further, this method enabled the fabrication of a compact ZnO layer (40 nm) based on a highly dense nanorod array [68]. Since the *c*-axis oriented ZnO nanorods were perpendicular to the ITO substrate, electron transport was enhanced and therefore the J_{SC} value (22.4 mA cm^2) and PCE (13.4%). In addition, when the thickness of the ZnO layer increased from 40 to 160 nm, the performance of the devices changed very little and was ascribed to uniform growth and high conductivity of magnetron sputtered ZnO film. Room-temperature RF sputtered SnO_2 film (20–80 nm) was demonstrated as an alternative to TiO_2 and ZnO as an effective and robust ETL for both rigid and flexible PSCs [69]. Despite entire fabrication and characterization processes being carried out in the ambient condition of humidity >65%, good PCE ~12.82 and 5.88% was observed for rigid glass and flexible substrates, respectively. In addition to this, the compatibility of sputtered SnO_2 with vapour-deposited perovskite films was demonstrated via viability and repeatability of acquiring high-quality vapour-deposited perovskite films with large grain sizes and smooth morphology in ambient condition.

3.2.2 Thermal Evaporation

This technique was scarcely used in DSCs on account of the difficulty and thickness of the prepared films. However, this method was used extensively to deposit an ultrathin layer of compact C_{60} films, which is otherwise difficult to deposit by solution-based methods due to the very low solubility of this molecule in common solvents [20]. Efficient metal oxide and annealing-free PSCs were realized by thermal evaporation of both the fullerene C_{60} as the ETL and the perovskite as an absorber [70]. An ultrathin C_{60} layer (5.5 nm) efficiently transfers the electrons and blocks the holes due to the energy-level alignment between C_{60} and FTO electrodes. The C_{60} layer not only operates as ETL but also provides a proper contact with the perovskite layer and improves the crystallinity of film and thereby led to high performance (PCE ~14.9%.). Further, the power conversion efficiency of 15.14% with V_{OC} of 1.08 V and FF ~ 74.51% measured under reverse voltage scanning was obtained for 50-nm-thick C_{60} layer [71]. A 35-nm-thick C_{60} was prepared for normal structure and found to work effectively as ETL [72]. Recently, it was observed that even ultrathin vapour-deposited C_{60} (1 nm) works efficiently in an inverted structure PSC exhibiting a PCE of 18.2% under 1-sun illumination with negligible hysteresis of photocurrent [73]. A systematic investigation with a combination of spatially resolved fluorescence microscopy, impedance spectroscopy and electrical characterization revealed that the role of C_{60} layer is to aid in electron extraction and collection. Further, when TiO_2 ETL was substituted by 20 nm CdS layer deposited by thermal evaporation method, the photostability of PSCs was improved significantly [74]. Despite slightly lower PCE than that of PSC fabricated with TiO_2, stability improved remarkably, maintaining over 90% of the initial efficiency after the continuous sunlight illumination for

12 h. In contrast, the TiO_2 ETL based PSC retains only 18% of the initial efficiency under the same condition. Further increment in CDS thickness, PCE decreased to 10.1%, due to extended length of electron pathways to the bottom FTO electrode, and the decreased incident light to the perovskite layer.

3.2.3 Atomic Layer Deposition (ALD)

ALD has been used to prepare high-quality thin films of inorganic materials such as oxides, nitrides, sulphides, as well as metals. In many deposition methods, reducing the thickness often leads to non-uniform films with pinholes and cracks and thereby to poor blocking behaviour and reduced V_{OC}, FF. Since ALD deposition can be controlled at the sub-nanometer level, deposition of dense and pinhole-free films of thickness ranging from 4 to 15 nm can easily be reproduced. In a typical ALD method, each cycle for the deposition contains four steps: (a) precursor pulse (b) inert gas purge (c) oxidizing pulse followed by (d) inert gas purge (Fig. 7). When the precursors have low chemical reactivity, a hold step is introduced after the precursor pulse so as to trap the precursor in the reactor and to react with the surface-active groups completely. Due to this cyclic surface-controlled growth, ALD inherently offers precise thickness control and conformality over the porous structure and high aspect ratio structures. This technique has been used to prepare blocking layers of materials such as TiO_2, ZnO, Nb_2O_5 [75], Ga_2O_3 [76], HfO_2 [77], Al_2O_3 [78] to be used in DSSCs initially and then extended to PSCs to deposit BLs of TiO_2 [79, 80], [81], MgO-TiO_2 [82], Al_2O_3 [83], ZnO [84].

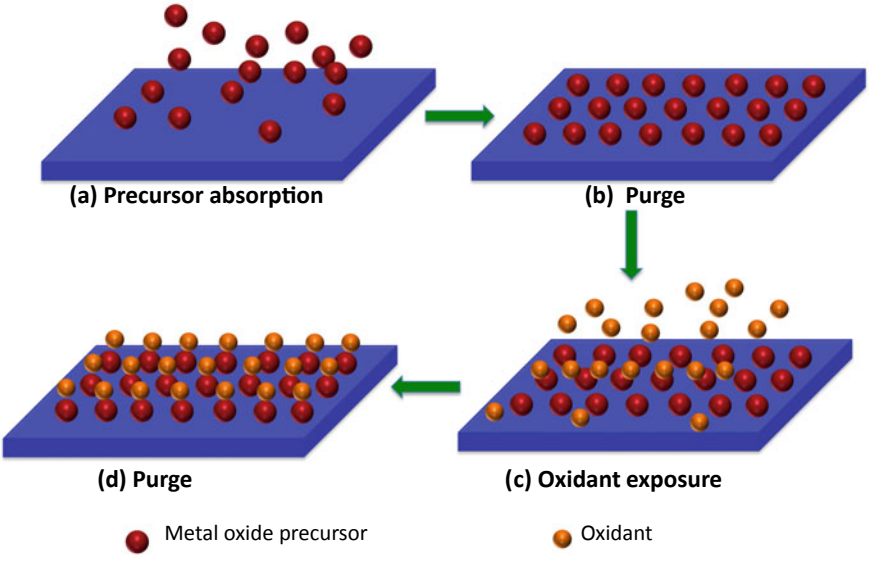

Fig. 7 Schematic presentation of ALD cycle of a binary compound

Li et al. deposited HfO_2 and TiO_2 blocking layers on nanowire surfaces for DSCs via atomic layer deposition (ALD) [85]. They demonstrated that a 1.3nm-thick compact TiO_2 layer between ITO nanowires and the porous TiO_2, avoids the electron recombination and led to efficiency enhancement of more than 90% as compared with sol-gel methods (e.g. $TiCl_4$ treatment). Further, Wu et al. compared the effect of nanoscale pinholes in TiO_2 ETLs, prepared by ALD spin coating and spray pyrolysis, on the device performance. Surface morphology and film resistance studies show that ETL prepared using ALD contains a much lower density of nanoscale pinholes than layers obtained by spin coating and spray pyrolysis methods, and therefore enables a high PCE ~12.56% [79]. Similar to findings in DSSCs, the surface states are suppressed by the deposition of a metal oxide, thereby leading to improved efficiency [86]. ALD deposited ETLs were also employed in DSSCs/PScs without any thermal post-treatment which is suitable for flexible devices. In order to avoid pinholes generated upon thermal treatment during the device fabrication, 1–4-nm-thick TiO_2 layer was deposited over the mesoporous structure, which could prevent electron back reaction effectively, from FTO as well as TiO_2 surface and leading to a PCE 11.5% [47]. Shalan et al. deposited TiO_2 without post-annealing and optimized the thickness of an ETL film [87]. A systematic correlation between the device performance and the surface roughness, conductivity of TiO_2 film and the rate of electron transfer was obtained. Best efficiency, 15.0%, was attained with acceptable reproducibility and stability over a period of 500 h.

ALD method was also extended to explore other semiconductor materials such as SnO_2 [80], ZnO ETLs [88]. ZnO films deposited by ALD show high PCE of 13.1% in perovskite solar cell fabricated with a single-step deposition of the perovskite layer. Interestingly, $CH_3NH_3PbI_3$ was formed at room temperature on the ZnO layer using CH_3NH_3I and $PbCl_2$ precursors, which is in contrast to the reported results [88]. A hysteresis-free PCE >18% with V_{OC} >1.19 V was demonstrated in planar PSCs using SnO_2 ETL at low processing temperatures ~120 °C. This high efficiency was attributed to the favourable alignment of the CB of the perovskite and the ETL. In addition, a deeper conduction band of SnO_2 enabled long-term air stability and improved hysteretic behaviour [89]. Further, plasma-enhanced ALD was utilized to deposit SnO_2 at temperature <100 °C [80]. With C_{60}-self-assembled monolayer passivation, steady-state efficiencies above 18 and 15% were achieved for PSCs fabricated on glass and flexible polymer substrates, respectively.

In addition, low-temperature ALD was utilized to incorporate pinhole-free metal oxide layers into an inverted perovskite solar cell in order to serve both as ETL and passivation layer. In combination with UV-irradiation, PSCs with PCE ~8.4% efficiency, good flexibility and improved stability were reported for ALD-deposited ETL [90]. Further, screen-printable scaffolds and masking/laser patterning procedures enabled the fabrication of perovskite modules on plastic substrates having PCE ~3.1%. A low-temperature (<120 °C) route was used to prepare amorphous TiO_2 ultrathin (12 nm) compact layers for planar PSCs [91]. Room-temperature UV–O_3 treatment produced an ETL which resulted in PSC of efficiency (~9.97%) comparable to crystalline TiO_2 (11.47%) thin films synthesized by higher temperature processing. Further, annealing-free and 20-nm-thick amorphous TiOx film by

ALD method was reported for a flexible PSC exhibiting ~12.2% PCE as a result of fast electron transport [35]. The devices maintained 95% of the initial PCE after 1000 bending cycles for a bending radius of 10 mm. Lately, PSC fabricated using ALD deposited buffer layers, TiO_2 and Al_2O_3 showed significant reduction interfacial charge recombination loss, improvement in interfacial contact, and enhance water resistance, and therefore negligible degradation to the perovskite layer and improved PCE ~18.3% [92]. In addition to TiO_2, amorphous SnO_2 layers fabricated using ALD were also examined for PSCs [93]. Surface morphological and XPS characterization indicate that all ALD films were conformal and pinhole free. However, when incorporated into PSCs, TiO_2 was observed to perform best in a cell with a mesoporous scaffold rather than a planar cell, while SnO_2 displayed promising results when incorporated into a planar cell. The cells with 10 nm SnO_2 exhibited PCE ~18.3 and 15.8% a 0.09 and 0.70 cm^2 area, respectively. Recently, a low-temperature processed ALD SnO_2 was investigated in detail to correlate deposition and/or post-annealing temperature to the properties of the SnO_2 film along with the device performance [94]. It is found that the charge collection from perovskite to SnO_2 is influenced by the downward shift of CB and Fermi level of SnO_2 films, but strongly affected by crystallinity and proper surface passivation of the SnO_2 layer. Additionally, the SnO_2 ETL should be passivated due to metal-like nature of SnO_2. A bilayered ETL of TiO_2/passivated SnO_2 was confirmed to provide better hole-blocking ability than a single passivated SnO_2 layer, which resulted in the further enhanced PCE (20.03%) from 17.75%. A remarkable PCE of 10.8% was demonstrated for air-stable, low-temperature processed ($\leq$100 °C) semitransparent perovskite solar cells (PSCs) by the applications ZnO and Al_2O_3 of ALD technology for use as ETL and encapsulation layer, respectively [95].

Overall, the ALD technique has been widely used in the electron transport layer, passivation layer and encapsulation layer used for DSSCs and PSCs due to its ability to produce a high-quality thin film. For more exhaustive review on the same, the reader may refer to recent review articles dealing with advances and efficiencies achieved in PSCs and DSCs [96]. Despite promising results, ALD is an ultra-high vacuum technique, and therefore an expensive method. This restricts large-scale fabrication of devices and therefore, the commercialization of this technique for enhanced photovoltaic efficiencies.

3.3 Electrochemical Techniques

Electrochemical (ECD) and electrophoretic deposition (EPD) are techniques, which employ electric field to produce compact, uniform and reproducible films of controlled morphology and thickness; of required materials over large areas. These techniques have been widely used to prepare surface cover of PSCs and DSSs due to the versatility, simplicity and cost-effectiveness and are discussed in sections that follow.

3.3.1 Electrochemical Deposition (ECD)

Electrochemically deposited films of TiO_2 were employed as effective ETL in DSCs as well as PSCs. Highly transparent TiO_2 film of thickness 30–50 nm, deposited by galvanostatic technique was shown to act as a blocking layer to inhibit the charge recombination and to improve the electrical contact between FTO and mesoporous TiO_2 film, thereby increasing the PCE from 7.31 to 8.04% [97]. Further Su et al. employed this method to prepare ultrathin TiO_2, which exhibited satisfactory surface coverage even for a thickness of ~29 nm [98]. The structural defects in the prepared layer were thoroughly examined by the CV technique and thereby studied for the blocking effect. The PSC using electrochemically deposited BL showed improved PCE (13.6%) as a result of improved J_{SC} and FF, which were attributed to the suppressed recombination at the FTO surface and minimization of ohmic resistance, respectively. Further, the influence of processing parameters such as electrolyte ingredient and oxidation voltage was investigated to optimize the conditions for TiO_2 layer (20–100 nm) deposited using anodic oxidation [99]. The PSCs fabricated in ambient air and utilizing the optimized TiO_2 as ETL showed higher and repeatable PCE >13%, as compared to its counterpart utilizing conventional high-temperature-processed compact TiO_2 as ETL. The improvement of device performance was attributed to more effective electron collection from the perovskite layer to ETL and the decrease of device series resistance. Choi et al. extensively investigated TiO_2 ETLs (40 nm) prepared by spin coating, sputtering and anodization [100]. They found that spin-coated TiO_2 shows an irregular film thickness, discontinuous areas and poor physical contact between the ETL and the FTO layers and in turn, lowered the charge transport properties through the planar perovskite solar cells. On the other hand, both sputtering and anodization produced a well-defined nanostructured TiO_2 ETL with excellent transmittance, single-crystalline properties, uniform film thickness and defect-free physical contact with FTO, and thereby resulting in outstanding electron extraction and hole blocking in a planar PSCs. In planar perovskite devices, anodized TiO_2 ETL increased the power conversion efficiency by 22% (from 12.5 to 15.2%), as compared with spin-coated TiO_2.

Other than TiO_2, other inorganic materials such as SnO_2, ZnO were also deposited using the electrochemical technique for application in the solar cell. The electrodeposited SnO_2 film endows high crystallinity and conductivity in addition to high transparency across the visible spectrum and shows a high PCE of 13.88% with negligible hysteresis [101]. In contrast to the electrodeposited TiO_2, the electrodeposited crystalline SnO_2 does not need additional seeding layers or post-thermal treatments, and are therefore well suited for flexible devices. This method was further extended to prepare high-quality ZnO thin films (23–1500 nm) by low-temperature electrochemical deposition [102]. The optimized PSCs showed PCE ~11% as a result of reduced recombination.

3.3.2 Electrophoretic Deposition (EPD)

The electrophoretic deposition (EPD) is a low cost, simple and fast method for preparing uniform thin films of controlled thickness using well-dispersed and stable suspensions in an organic solvent or aqueous solutions. However, this method is scarcely reported for preparing ETL in DSCs and PSCs. By using an aqueous suspension of negatively charged TiO_2 nanoparticles with a diameter of ca. 4.5 nm, ETLs were prepared for DSCs via an EPD method [103]. The thickness of the ETLs was adjusted by changing the deposition current and time. For an optimum thickness, PCE ~7.98% was obtained as a result of improved charge collection and reduced recombination. Thinner thin films (8–75 nm) were prepared using two-dimensional (2D) TNS by EPD from a dilute TNS/tetrabutylammonium hydroxide solution. An 8-nm-thick TNS film was found to be sufficient for acting as the compact layer and achieving high efficiency of 10.7% and relatively low hysteresis behaviour [18].

3.4 Dip-Coating Technique

In contrast to the spin-coating method which is a very solution-wasting method for expansive materials, dip-coating is a scalable and low-cost method [104]. A TiO_2 ETL prepared by this method was observed to enhance overall PCE and the performance was found to be better than similar thick film prepared by the spin-coating method [105]. Ultrathin, uniform and pinhole-free (5–50 nm) TiO_2 ETL were prepared from the $TiCl_4$ precursor using the dip-coating method [106]. The thickness of the film was tuned by changing the precursor concentration and is conformably deposited on the FTO for 20–30-nm-thick films. The PCE was improved significantly (from 5.5 to ~8.6%) when the ETL is inserted. The absence or presence of very thin ETL displayed 's-shaped' feature in the negative voltage range of current–voltage curve was attributable to immobilized negative ions at the electron-extracting interface. A very fast dip-coating process was investigated for planar PSCs using TiO_2 ETLs [107]. The prepared film was highly compact and enabled efficient hole blocking as well as deposition of smooth perovskite films with high surface coverage. The performance was nearly identical (12%) to that of a reference device fabricated by conventional spin coating. Moreover, the PSCs showed negligible hysteresis and has the potential to be integrated with the roll-to-roll printing of PSCs. Further, ultrathin SnO_2 layers were deposited on FTO substrate by the layer-by-layer (LBL) utilizing negatively charged SnO_2 nanoparticles and cationic poly(allylamine hydrochloride) [108]. The J_{SC} of DSCs was increased from 8.96 to 10.97 mA/cm^2, whereas the V_{OC} and FF were not changed much with this ETL as compared with conventional ETL. The PCE was enhanced from 5.43 to 6.57% and was attributed to the increased electron diffusion coefficient and the unique CB location of the SnO_2, inducing cascade energy band matching among the CBs of TiO_2.

In contrast to the dipping method, the Langmuir–Blodgett (LB) transfer involves the transfer of a monolayer of amphiphilic molecules adsorbed at the free surface

of the water on a suitable substrate. Both vertical and horizontal dipping can be used to withdraw the substrate at a specific rate. The LB technique is a very useful technique to construct ordered and controlled monomolecular assemblies as well as i to prepare LBL and well-defined multilayer structure on solid substrates. The quality of the deposited film depends on various parameters such as, pH, temperature, substrate, material, dipping speed and deposition type and is illustrated in Fig. 8 for the deposition of metal oxide complex. However, there is scarcely any report on the use of this method for either DSCs or PSCs [109, 110]. Very recently, ultrathin WO_3 films, prepared by UVO-treatment of WO_3-ODA Langmuir–Blodgett multilayer, were used as ETL and blocking layer in DSCs [111]. A dense and uniform compact film with excellent hole blocking; and electron transport properties, crystallinity was prepared. It was reported that PCE of DSCs with optimized WO_3 ETL improved significantly (21%) as compared to those based on conventional TiO_2 ETL. The improvement in the device performance was attributable to improved J_{SC} which is obtained without any accompanying reduction in V_{OC} and FF. The analyses not only reveal that η of DSSCs can be enhanced by employing ultrathin WO_3 LB films as blocking layers but also suggest that the films can possibly be extended further for perovskite and polymer solar cells.

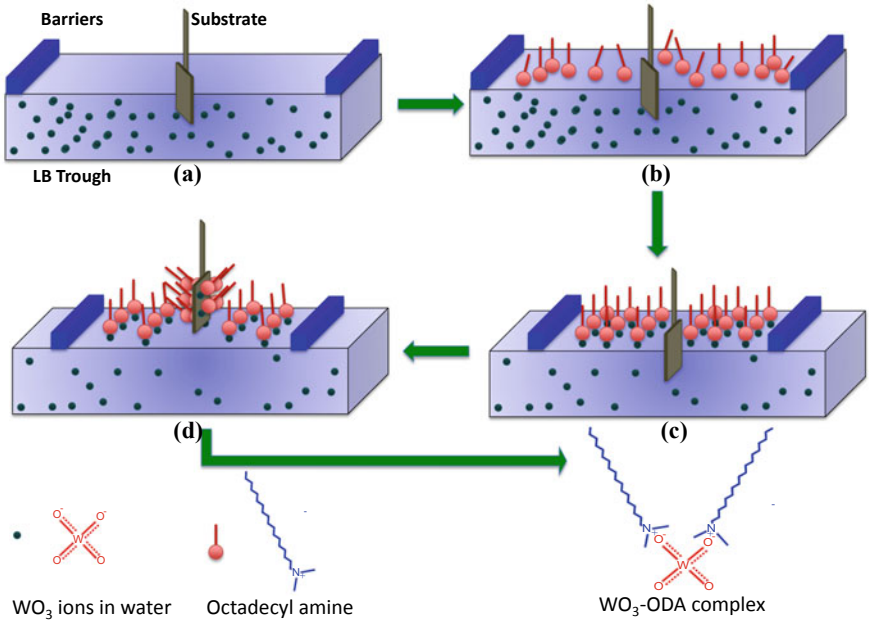

Fig. 8 Schematic of the LB deposition technique: **a** sodium tungstate in water subphase **b** spreading of octadecylamine (ODA) surfactant on air–water interface **c** formation of WO_3-ODA complex at air–water interface and; compression of the monolayer and **d** transfer of monolayer from air–water interface onto the substrate

4 Conclusion

In summary, the ETL plays an important role in the performance of DSCs and PSCs. As discussed in the chapter, a uniform, transparent layer with proper energy level, charge transport and hole-blocking properties is required for efficient working of the device. The ideal ETL should reveal all these favourable properties without compromising thickness so as to keep low series resistance and transparency. It is to be noted that for many deposition processes such as spray pyrolysis and spin coating, lowering the ETL thickness results in poorer uniformity and conformality, and therefore leads to pinholes and cracks. This then results in reduced blocking behaviour and increased charge recombination, and thereby degradation of V_{OC}, FF and long-term stability. Moreover, preparing a pinhole-free conformal ETL becomes more difficult in a large area, which is a requirement for scaling up the DSCs/PSCs technologies for commercial applications. Many of the techniques such as ALD, sputtering reported in the literature for preparation of ultra-thin ETLs in PSCs/DSCs are not scalable and may not be useful from a commercial point of view. A recent demonstration of scalable methods such as dip-coating and LB method for high-quality ultra-thin films are very promising and need to be explored further. For some materials such as TiO_2 QD and SnO_2, high-quality thin films were prepared by even conventional methods such as spin coating and CBD. Therefore, new materials should also be investigated in combination with conventional and new deposition methods to attain ultra-thin film of good quality to be employed as ETLs in PSCs/DSCs.

Acknowledgments The author thanks Dr. K.P. Muthe, Dr. A. Singh and Dr. Sipra Choudhury for their comments and suggestions.

References

1. M. Gul, Y. Kotak, T. Muneer, Energy Explor. Exploit. **34**(4), 485 (2016)
2. K. Kakiage, Y. Aoyama, T. Yano, K. Oya, J.-I. Fujisawa, M. Hanaya, Chem. Commun. **51**(88), 15894 (2015)
3. S. Lepikko, K. Miettunen, A. Poskela, A. Tiihonen, P.D. Lund, Energy Sci. Eng. **6**(3), 187 (2018)
4. J. Burschka, A. Dualeh, F. Kessler, E. Baranoff, N.-L. Cevey-Ha, C. Yi, M.K. Nazeeruddin, M. Grätzel, J. Am. Chem. Soc. **133**(45), 18042 (2011)
5. W. Zhang, Y. Wu, H.W. Bahng, Y. Cao, C. Yi, Y. Saygili, J. Luo, Y. Liu, L. Kavan, J.-E. Moser, A. Hagfeldt, H. Tian, S.M. Zakeeruddin, W.-H. Zhu, M. Grätzel, Energy Environ. Sci. **11**(7), 1779 (2018)
6. Y. Cao, Y. Liu, S.M. Zakeeruddin, A. Hagfeldt, M. Grätzel, Joule **2**(6), 1108 (2018)
7. H.-S. Kim, C.-R. Lee, J.-H. Im, K.-B. Lee, T. Moehl, A. Marchioro, S.-J. Moon, R. Humphry-Baker, J.-H. Yum, J.E. Moser, M. Grätzel, N.-G. Park, Scientific Reports **2**, 591 (2012); M.M. Lee, J. Teuscher, T. Miyasaka, T.N. Murakami, H.J. Snaith, Science **338**(6107), 643 (2012)
8. W.S. Yang, B.-W. Park, E.H. Jung, N.J. Jeon, Y.C. Kim, D.U. Lee, S.S. Shin, J. Seo, E.K. Kim, J.H. Noh, S.I. Seok, Science **356**(6345), 1376 (2017)
9. A. Kojima, K. Teshima, Y. Shirai, T. Miyasaka, J. Am. Chem. Soc. **131**(17), 6050 (2009); A. Gagliardi, A. Abate, ACS Energy Lett. **3**(1), 163 (2018)

10. F. Matteocci, G. Mincuzzi, F. Giordano, A. Capasso, E. Artuso, C. Barolo, G. Viscardi, T.M. Brown, A. Reale, A. Di Carlo, Org. Electron. **14**(7), 1882 (2013); E.J.W. Crossland, N. Noel, V. Sivaram, T. Leijtens, J.A. Alexander-Webber, H.J. Snaith, Nature **495**, 215 (2013); X. Wang, Y. Fang, L. He, Q. Wang, T. Wu, Mater. Sci. Semicond. Process. **27**(1), 569 (2014)
11. P. Docampo, S. Guldin, M. Stefik, P. Tiwana, M.C. Orilall, S. Hüttner, H. Sai, U. Wiesner, U. Steiner, H.J. Snaith, Adv. Func. Mater. **20**(11), 1787 (2010)
12. J.M. Ball, M.M. Lee, A. Hey, H.J. Snaith, Energy Environ. Sci. **6**(6), 1739 (2013)
13. A.K. Jena, A. Kulkarni, T. Miyasaka, Chem. Rev. **119**(5), 3036 (2019)
14. R. Wu, B. Yang, J. Xiong, C. Cao, Y. Huang, F. Wu, J. Sun, C. Zhou, H. Huang, J. Yang, J. Renew. Sustain. Energy **7**(4), 043105 (2015)
15. H. Choi, C. Nahm, J. Kim, J. Moon, S. Nam, D.-R. Jung, B. Park, Curr. Appl. Phys. **12**(3), 737 (2012)
16. M. Saliba, T. Matsui, K. Domanski, J.-Y. Seo, A. Ummadisingu, S.M. Zakeeruddin, J.-P. Correa-Baena, W.R. Tress, A. Abate, A. Hagfeldt, M. Grätzel, Science **354**(6309), 206 (2016)
17. W.J. Nimens, J. Ogle, A. Caruso, M. Jonely, C. Simon, D. Smilgies, R. Noriega, M. Scarpulla, L. Whittaker-Brooks, ACS Appl. Energy Mater. **1**(2), 602 (2018)
18. C. Li, Y. Li, Y. Xing, Z. Zhang, X. Zhang, Z. Li, Y. Shi, T. Ma, R. Ma, K. Wang, J. Wei, ACS Appl. Mater. Interfaces **7**(28), 15117 (2015)
19. W. Hadouchi, J. Rousset, D. Tondelier, B. Geffroy, Y. Bonnassieux, RSC Adv. **6**(72), 67715 (2016)
20. P.-W. Liang, C.-C. Chueh, S.T. Williams, A.K.-Y. Jen, Adv. Energy Mater. **5**(10), 1402321 (2015)
21. J. Saito, T. Oku, A. Suzuki, T. Akiyama, AIP Conf. Proc. **1709**(1), 020027 (2016)
22. E. Bellingeri, D. Marré, I. Pallecchi, L. Pellegrino, A.S. Siri, Appl. Phys. Lett. **86**(1), 012109 (2005)
23. T.J. Coutts, D.L. Young, X. Li, W.P. Mulligan, X. Wu, J. Vac. Sci. Technol., A **18**(6), 2646 (2000)
24. B.A. Ahmed, I.H. Shallal, F.I. Mustafa Al-Attar, J. Phys.: Conf. Series **1032**, 012022 (2018)
25. Y. Kuang, V. Zardetto, R. van Gils, S. Karwal, D. Koushik, M.A. Verheijen, L.E. Black, C. Weijtens, S. Veenstra, R. Andriessen, W.M.M. Kessels, M. Creatore, ACS Appl. Mater. Interfaces **10**(36), 30367 (2018)
26. F. Ali, N.D. Pham, L. Fan, V. Tiong, K. Ostrikov, J.M. Bell, H. Wang, T. Tesfamichael, ACS Appl. Energy Mater. **2**(8), 5456 (2019)
27. X. Ling, J. Yuan, D. Liu, Y. Wang, Y. Zhang, S. Chen, H. Wu, F. Jin, F. Wu, G. Shi, X. Tang, J. Zheng, S. Liu, Z. Liu, W. Ma, ACS Appl. Mater. Interfaces **9**(27), 23181 (2017)
28. A. Kogo, Y. Sanehira, Y. Numata, M. Ikegami, T. Miyasaka, ACS Appl. Mater. Interfaces **10**(3), 2224 (2018)
29. J.A. Christians, P. Schulz, J.S. Tinkham, T.H. Schloemer, S.P. Harvey, B.J. Tremolet de Villers, A. Sellinger, J.J. Berry, J.M. Luther, Nat. Energy **3**(1), 68 (2018)
30. C. Tao, S. Neutzner, L. Colella, S. Marras, A.R. Srimath Kandada, M. Gandini, M.D. Bastiani, G. Pace, L. Manna, M. Caironi, C. Bertarelli, A. Petrozza, Energy Environ. Sci. **8**(8), 2365 (2015)
31. J. Seo, S. Park, Y. Chan Kim, N.J. Jeon, J.H. Noh, S.C. Yoon, S.I. Seok, Energy Environ. Sci. **7**(8), 2642 (2014)
32. W. Chen, Y. Wu, Y. Yue, J. Liu, W. Zhang, X. Yang, H. Chen, E. Bi, I. Ashraful, M. Grätzel, L. Han, Science **350**(6263), 944 (2015); D. Liu, T.L. Kelly, Nat. Photonics **8**, 133 (2013)
33. D.B. Mitzi, L.L. Kosbar, C.E. Murray, M. Copel, A. Afzali, Nature **428**(6980), 299 (2004)
34. Tanvi, V. Saxena, A. Singh, O. Prakash, A. Mahajan, A.K. Debnath, K.P. Muthe, S.C. Gadkari, Solar Energy Mater. Solar Cells **170**, 127 (2017)
35. B.J. Kim, D.H. Kim, Y.-Y. Lee, H.-W. Shin, G.S. Han, J.S. Hong, K. Mahmood, T.K. Ahn, Y.-C. Joo, K.S. Hong, N.-G. Park, S. Lee, H.S. Jung, Energy Environ. Sci. **8**(3), 916 (2015)
36. A. Kogo, Y. Sanehira, M. Ikegami, T. Miyasaka, J. Mater. Chem. A **3**(42), 20952 (2015)
37. P. Vivo, A. Ojanperä, J.-H. Smått, S. Sandén, S.G. Hashmi, K. Kaunisto, P. Ihalainen, M.T. Masood, R. Österbacka, P.D. Lund, H. Lemmetyinen, Org. Electron. **41**, 287 (2017)

38. B. Shen, Z. Hu, K. Sun, C. Lu, Y. Jiang, J. Zhang, Y. Chen, Y. Zhu, Org. Electron. **59**, 177 (2018)
39. J. Gao, C.L. Perkins, J.M. Luther, M.C. Hanna, H.-Y. Chen, O.E. Semonin, A.J. Nozik, R.J. Ellingson, M.C. Beard, Nano Lett. **11**(8), 3263 (2011); A.H. Ip, S.M. Thon, S. Hoogland, O. Voznyy, D. Zhitomirsky, R. Debnath, L. Levina, L.R. Rollny, G.H. Carey, A. Fischer, K.W. Kemp, I.J. Kramer, Z. Ning, A.J. Labelle, K.W. Chou, A. Amassian, E.H. Sargent, Nat. Nanotechnol. **7**, 577 (2012)
40. Y. Tu, J. Wu, M. Zheng, J. Huo, P. Zhou, Z. Lan, J. Lin, M. Huang, Nanoscale **7**(48), 20539 (2015)
41. M. Abulikemu, M. Neophytou, J.M. Barbé, M.L. Tietze, A. El Labban, D.H. Anjum, A. Amassian, I. McCulloch, S. Del Gobbo, J. Mater. Chem. A **5**(17), 7759 (2017)
42. S. Ryu, J. Seo, S.S. Shin, Y.C. Kim, N.J. Jeon, J.H. Noh, S.I. Seok, J. Mater. Chem. A **3**(7), 3271 (2015)
43. C.-H. Chiang, C.-G. Wu, Nat. Photonics **10**, 196 (2016)
44. S. Balasubramanyam, A. Sharma, V. Vandalon, H.C.M. Knoops, W.M.M. Kessels, A.A. Bol, J. Vac. Sci. Technol., A **36**(1), 01B103 (2018)
45. I.P. Liu, W.-H. Lin, C.-M. Tseng-Shan, Y.-L. Lee, ACS Appl. Mater. Interfaces **10**(45), 38900 (2018)
46. N. Fuke, R. Katoh, A. Islam, M. Kasuya, A. Furube, A. Fukui, Y. Chiba, R. Komiya, R. Yamanaka, L. Han, H. Harima, Energy Environ. Sci. **2**(11), 1205 (2009)
47. A.K. Chandiran, A. Yella, M.T. Mayer, P. Gao, M.K. Nazeeruddin, M. Grätzel, Adv. Mater. **26**(25), 4309 (2014)
48. L. Cojocaru, S. Uchida, Y. Sanehira, J. Nakazaki, T. Kubo, H. Segawa, Chem. Lett. **44**(5), 674 (2015)
49. H. Elbohy, A. Thapa, P. Poudel, N. Adhikary, S. Venkatesan, Q. Qiao, Nano Energy **13**, 368 (2015)
50. J.W. Lee, T.Y. Lee, P.J. Yoo, M. Grätzel, S. Mhaisalkar, N.G. Park, J. Mater. Chem. A **2**(24), 9251 (2014)
51. A. Yella, L.P. Heiniger, P. Gao, M.K. Nazeeruddin, M. Grätzel, Nano Lett. **14**(5), 2591 (2014)
52. C. Liang, Z. Wu, P. Li, J. Fan, Y. Zhang, G. Shao, Appl. Surf. Sci. **391**, 337 (2017)
53. C. Zhang, Y. Luo, X. Chen, W. Ou-Yang, Y. Chen, Z. Sun, S. Huang, Appl. Surf. Sci. **388**, 82 (2016)
54. E.H. Anaraki, A. Kermanpur, L. Steier, K. Domanski, T. Matsui, W. Tress, M. Saliba, A. Abate, M. Grätzel, A. Hagfeldt, J.-P. Correa-Baena, Energy Environ. Sci. **9**(10), 3128 (2016)
55. Y. Zheng, S. Klankowski, Y. Yang, J. Li, ACS Appl. Mater. Interfaces **6**(13), 10679 (2014)
56. A. Braga, C. Baratto, P. Colombi, E. Bontempi, G. Salvinelli, G. Drera, L. Sangaletti, Phys. Chem. Chem. Phys. **15**(39), 16812 (2013)
57. J. Xia, N. Masaki, K. Jiang, S. Yanagida, J. Phys. Chem. C **111**(22), 8092 (2007)
58. W. Ke, G. Fang, J. Wang, P. Qin, H. Tao, H. Lei, Q. Liu, X. Dai, X. Zhao, ACS Appl. Mater. Interfaces **6**(18), 15959 (2014)
59. A. Huang, J. Zhu, J. Zheng, Y. Yu, Y. Liu, S. Yang, S. Bao, L. Lei, P. Jin, Sol. Energy Mater. Sol. Cells **163**, 15 (2017)
60. A. Kogo, S. Iwasaki, M. Ikegami, T. Miyasaka, Chem. Lett. **46**(4), 530 (2017)
61. M.H. Abdullah, M. Rusop, J. Alloy. Compd. **600**, 60 (2014)
62. H.-C. Chang, M.-J. Twu, C.-Y. Hsu, R.-Q. Hsu, C.-G. Kuo, Int. J. Photoenergy **2014**, 8 (2014)
63. S.M. Waita, B.O. Aduda, J.M. Mwabora, G.A. Niklasson, C.G. Granqvist, G. Boschloo, J. Electroanal. Chem. **637**(1), 79 (2009)
64. H.-J. Kim, J.-D. Jeon, D.Y. Kim, J.-J. Lee, S.-Y. Kwak, J. Ind. Eng. Chem. **18**(5), 1807 (2012)
65. C. Chen, Y. Cheng, Q. Dai, H. Song, Sci. Rep. **5**, 17684 (2015)
66. G.D. Rajmohan, F.Z. Huang, R. d'Agostino, J. du Plessis, X.J. Dai, Thin Solid Films **636**, 307 (2017)
67. S.S. Mali, C.K. Hong, A.I. Inamdar, H. Im, S.E. Shim, Nanoscale **9**(9), 3095 (2017)
68. L. Liang, Z. Huang, L. Cai, W. Chen, B. Wang, K. Chen, H. Bai, Q. Tian, B. Fan, ACS Appl. Mater. Interfaces **6**(23), 20585 (2014)

69. M. Kam, Q. Zhang, D. Zhang, Z. Fan, Sci. Rep. **9**(1), 6963 (2019)
70. D. Zhao, W. Ke, C.R. Grice, A.J. Cimaroli, X. Tan, M. Yang, R.W. Collins, H. Zhang, K. Zhu, Y. Yan, Nano Energy **19**, 88 (2016)
71. W. Ke, D. Zhao, C.R. Grice, A.J. Cimaroli, J. Ge, H. Tao, H. Lei, G. Fang, Y. Yan, J. Mater. Chem. A **3**(35), 17971 (2015)
72. N. Ahn, K. Kwak, M.S. Jang, H. Yoon, B.Y. Lee, J.-K. Lee, P.V. Pikhitsa, J. Byun, M. Choi, Nat. Commun. **7**, 13422 (2016)
73. D. Liu, Q. Wang, C.J. Traverse, C. Yang, M. Young, P.S. Kuttipillai, S.Y. Lunt, T.W. Hamann, R.R. Lunt, ACS Nano **12**(1), 876 (2018)
74. I. Hwang, K. Yong, ACS Appl. Mater. Interfaces **8**(6), 4226 (2016)
75. E. Barea, X. Xu, V. González-Pedro, T. Ripollés-Sanchis, F. Fabregat-Santiago, J. Bisquert, Energy Environ. Sci. **4**(9), 3414 (2011)
76. A.K. Chandiran, N. Tetreault, R. Humphry-Baker, F. Kessler, E. Baranoff, C. Yi, M.K. Nazeeruddin, M. Grätzel, Nano Lett. **12**(8), 3941 (2012)
77. M. Shanmugam, M.F. Baroughi, D. Galipeau, Thin Solid Films **518**(10), 2678 (2010)
78. T.-C. Tien, F.-M. Pan, L.-P. Wang, C.-H. Lee, Y.-L. Tung, S.-Y. Tsai, C. Lin, F.-Y. Tsai, S.-J. Chen, Nanotechnology **20**(30), 305201 (2009)
79. Y. Wu, X. Yang, H. Chen, K. Zhang, C. Qin, J. Liu, W. Peng, A. Islam, E. Bi, F. Ye, M. Yin, P. Zhang, L. Han, Appl. Phys. Express **7**(5), 052301 (2014)
80. C. Wang, D. Zhao, C.R. Grice, W. Liao, Y. Yu, A. Cimaroli, N. Shrestha, P.J. Roland, J. Chen, Z. Yu, P. Liu, N. Cheng, R.J. Ellingson, X. Zhao, Y. Yan, J. Mater. Chem. A **4**(31), 12080 (2016)
81. J.P. Mailoa, C.D. Bailie, E.C. Johlin, E.T. Hoke, A.J. Akey, W.H. Nguyen, M.D. McGehee, T. Buonassisi, Appl. Phys. Lett. **106**(12), 121105 (2015)
82. G.S. Han, H.S. Chung, B.J. Kim, D.H. Kim, J.W. Lee, B.S. Swain, K. Mahmood, J.S. Yoo, N.-G. Park, J.H. Lee, H.S. Jung, J. Mater. Chem. A **3**(17), 9160 (2015)
83. X. Dong, X. Fang, M. Lv, B. Lin, S. Zhang, J. Ding, N. Yuan, J. Mater. Chem. A **3**(10), 5360 (2015)
84. A.K. Chandiran, M. Abdi-Jalebi, A. Yella, M.I. Dar, C. Yi, S.A. Shivashankar, M.K. Nazeeruddin, M. Grätzel, Nano Lett. **14**(3), 1190 (2014)
85. L. Li, C. Xu, Y. Zhao, S. Chen, K.J. Ziegler, ACS Appl. Mater. Interfaces **7**(23), 12824 (2015)
86. H. Lu, W. Tian, J. Guo, L. Li, Sci. Rep. **5**, 12765 (2015)
87. A.E. Shalan, S. Narra, T. Oshikiri, K. Ueno, X. Shi, H.-P. Wu, M.M. Elshanawany, E.W.-G. Diau, H. Misawa, Sustain. Energy Fuels **1**(7), 1533 (2017)
88. X. Dong, H. Hu, B. Lin, J. Ding, N. Yuan, Chem. Commun. **50**(92), 14405 (2014)
89. J.P. Correa Baena, L. Steier, W. Tress, M. Saliba, S. Neutzner, T. Matsui, F. Giordano, T.J. Jacobsson, A.R. Srimath Kandada, S.M. Zakeeruddin, A. Petrozza, A. Abate, M.K. Nazeeruddin, M. Grätzel, A. Hagfeldt, Energy Environ. Sci. **8**(10), 2928 (2015)
90. F. Di Giacomo, V. Zardetto, A. D'Epifanio, S. Pescetelli, F. Matteocci, S. Razza, A. Di Carlo, S. Licoccia, W.M.M. Kessels, M. Creatore, T.M. Brown, Adv. Energy Mater. **5**(8), 1401808 (2015)
91. I.S. Kim, R.T. Haasch, D.H. Cao, O.K. Farha, J.T. Hupp, M.G. Kanatzidis, A.B.F. Martinson, ACS Appl. Mater. Interfaces **8**(37), 24310 (2016)
92. Y. Lv, P. Xu, G. Ren, F. Chen, H. Nan, R. Liu, D. Wang, X. Tan, X. Liu, H. Zhang, Z.-K. Chen, ACS Appl. Mater. Interfaces **10**(28), 23928 (2018)
93. M. McCarthy, A. Walter, S.-J. Moon, N. Noel, S. O'Brien, M. Pemble, S. Nicolay, B. Wenger, H. Snaith, I. Povey, (Cambridge University Press, 2018) vol. 3, p. 3075 (2018). https://doi.org/10.1557/adv.2018.515
94. Y. Lee, S. Lee, G. Seo, S. Paek, K.T. Cho, A.J. Huckaba, M. Calizzi, D.-W. Choi, J.-S. Park, D. Lee, H.J. Lee, A.M. Asiri, M.K. Nazeeruddin, Adv. Sci. **5**(6), 1800130 (2018)
95. C.-Y. Chang, K.-T. Lee, W.-K. Huang, H.-Y. Siao, Y.-C. Chang, Chem. Mater. **27**(14), 5122 (2015)

96. V. Zardetto, B.L. Williams, A. Perrotta, F. Di Giacomo, M.A. Verheijen, R. Andriessen, W.M.M. Kessels, M. Creatore, Sustain. Energy Fuels **1**(1), 30 (2017); K. Deng, L. Li, Adv. Mater. Interfaces **3**(21), 1600505 (2016); D.H. Kim, M.D. Losego, Q. Peng, G.N. Parsons, Adv. Mater. Interfaces **3**(21), 1600354 (2016); S. Seo, S. Jeong, H. Park, H. Shin, N.-G. Park, Chem. Commun. **55**(17), 2403 (2019)
97. M.-S. Wu, C.-H. Tsai, T.-C. Wei, Chem. Commun. **47**(10), 2871 (2011)
98. T.-S. Su, T.-Y. Hsieh, C.-Y. Hong, T.-C. Wei, Sci. Rep. **5**, 16098 (2015)
99. Y. Du, H. Cai, H. Wen, Y. Wu, L. Huang, J. Ni, J. Li, J. Zhang, ACS Appl. Mater. Interfaces **8**(20), 12836 (2016)
100. J. Choi, S. Song, M.T. Hörantner, H.J. Snaith, T. Park, ACS Nano **10**(6), 6029 (2016)
101. J.-Y. Chen, C.-C. Chueh, Z. Zhu, W.-C. Chen, A.K.Y. Jen, Sol. Energy Mater. Sol. Cells **164**, 47 (2017)
102. J. Zhang, E.J. Juárez-Pérez, I. Mora-Seró, B. Viana, T. Pauporté, J. Mater. Chem. A **3**(9), 4909 (2015)
103. X. Li, Y. Qiu, S. Wang, S. Lu, R.I. Gruar, X. Zhang, J.A. Darr, T. He, Phys. Chem. Chem. Phys. **15**(35), 14729 (2013)
104. L. Yao, J. He, J. Mater. Chem. A **2**(19), 6994 (2014)
105. S. Hong, A. Han, E.C. Lee, K.-W. Ko, J.-H. Park, H.-J. Song, M.-H. Han, C.-H. Han, Curr. Appl. Phys. **15**(5), 574 (2015)
106. M.T. Masood, C. Weinberger, J. Sarfraz, E. Rosqvist, S. Sandén, O.J. Sandberg, P. Vivo, G. Hashmi, P.D. Lund, R. Österbacka, J.-H. Smått, ACS Appl. Mater. Interfaces **9**(21), 17906 (2017)
107. L. Huang, C. Li, X. Sun, R. Xu, Y. Du, J. Ni, H. Cai, J. Li, Z. Hu, J. Zhang, Org. Electron. **40**, 13 (2017)
108. Y.J. Kim, K.H. Kim, P. Kang, H.J. Kim, Y.S. Choi, W.I. Lee, Langmuir **28**(28), 10620 (2012)
109. N. Ibrayev, E. Seliverstova, A. Zhumabekov, IOP Conf. Series: Mater. Sci. Eng. **447**, 012068 (2018)
110. A. Aoki, S. Fukayama, Electrochemistry **78**(2), 178 (2010)
111. O. Prakash, V. Saxena, S. Choudhury, Tanvi, A. Singh, A.K. Debnath, A. Mahajan, K.P. Muthe, D.K. Aswal, Electrochimica Acta **318**, 405 (2019)
112. C.-S. Chou, F.-C. Chou, J.-Y. Kang, Powder Technol. **215–216**, 38 (2012)

Optical Optimization of Thin-Film Polymer Solar Cells

Sanjay Tiwari and Ralph Gebauer

Abstract Photovoltaics are now slowly replacing fossil fuels, aiming at higher efficiencies and lower costs to bring PV to cost parity with grid electricity. Solar energy is a clean and renewable energy, which is generated from the natural source sun. Solar cells are devices that convert solar energy into electricity, either directly via the photovoltaic effect, or indirectly by first converting the solar energy to heat or chemical energy. Both inorganic and organic types of solar cells are available. Unfortunately, the solar cells dominating the market are all made of inorganic materials requiring expensive and complicated manufacturing processes and have limited applications basically to the rooftops. One of the promising alternatives to inorganic solar cells is the polymer ones. Polymer solar cells (PSCs) are attracting interest as potential sources of renewable and clean energy because of their attractive advantages of low-cost large-area fabrication on lightweight flexible substrates. Though the efficiency of polymer devices have not yet reached those of their inorganic counterparts ($\approx$10–24%); the perspective of low cost, low temperature and energy processing, low material requirement, can be used on a flexible substrate, can be shaped to suit architectural applications are some advantages of polymer solar cell that drives the development of polymer photovoltaic devices further in a dynamic way. This chapter is devoted to the optimization of layer thickness in a polymer photovoltaic cell. It presents the applied calculation method which is based on the optical transfer matrix 2×2 formalism. Optical modelling results show that the distribution of light energy determined by optical interference and optimization of thickness of each layer in the OPV would help in the improvement of its performance. The influence of thickness of active layer, electron transport layer and hole transport layer on the normalized modulus squared of optical electric fields distribution inside devices and on the distributions of exciton generation rate and hence current density has been investigated.

S. Tiwari (✉)
Photonics Research Laboratory, S.O.S. in Electronics & Photonics, Pt. Ravishankar Shukla University, Raipur 492010, India
e-mail: stiwari@fulbrightmail.org

R. Gebauer
The Abdus Salam International Centre for Theoretical Physics (ICTP), Strada Costiera 11, 34151 Trieste, Italy
e-mail: rgebaur@ictp.it

S. Kumar and D. K. Aswal (eds.), *Recent Advances in Thin Films*, Materials Horizons: From Nature to Nanomaterials, https://doi.org/10.1007/978-981-15-6116-0_17

A mapping of total and useful absorbed energy and parasitic absorption have been done which helps in accurate measurement of IQE and EQE. The distribution of exciton generation rate has been predicted by modelling.

Keywords Optical modelling · Numerical simulation · Polymer photovoltaic (OPV) · Polymer solar cell (PSC) · Bulk heterojunction · Complex index of refraction · Transfer matrix formalism

1 Introduction

Energy is central to nearly every major challenge and opportunity the world faces today, so the energy consumption has been consistently increasing globally over the past 70 years. The mean global energy consumption rate was 13.5 terawatt (TW) in the year 2000 and the projection is that the global energy demand in 2050 will more than double to 27.6 TW. The social and economic development and human welfare and health improvement depends on energy and its related services. The consumption of fossil fuels as energy resource accounts for the majority of global anthropogenic greenhouse gas emissions, which are responsible for global warming (Fig. 1) [1–5].

The major challenge before humanity is to find a way forward that simultaneously addresses issues of energy supply and saving, energy security, energy access, climate change, reduction of environmental and health impacts and economics. The need for sustainable energy and improved energy efficiency are at the centre of attention as never before. The United Nations (UN) has adopted 17 Sustainable Development Goals (SDGs), which are the blueprint to achieve a better and more sustainable future for all to transform the world by 2030. SDG 7 aims at ensuring access to affordable, reliable, clean, sustainable and modern energy for all. Sustainable energy is an opportunity to transform lives, economies and the planet [6].

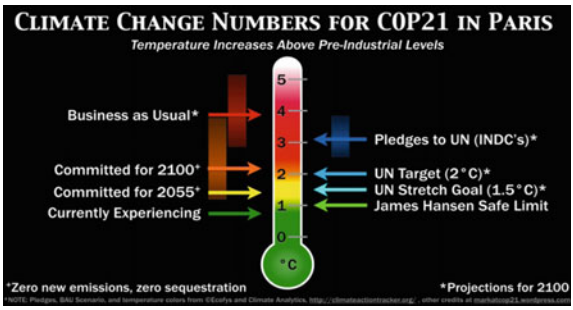

Fig. 1 Climate Change numbers: 1.5° strategies require greenhouse gas emissions to be negative well before 2100, 2° would need to half emissions by mid-2030s (this is to the level of the early 1970s), be at zero by 2080 and rises >2 °C look likely, unless there is a real international appetite to change emission paths, and quickly (2)

At earth's surface, average solar energy is ~3.8 × 10^{24} J/year which is more than our global energy consumption by a factor of 10^4 which is around 3 × 10^{20} J/year(2014) [7]. UN report says that despite tremendous progress, 13% of the global population still lacks access to modern electricity and 3 billion people rely on wood, coal, charcoal or animal waste for cooking and heating. As energy demand continues to rise, SDG 7 targets to increase substantially the share of renewable energy in the global energy [6]. Renewable energy is the most effective key to bridge the gap between demand and supply of energy and especially fight against climate change. Sustainable and affordable energy production persists as one of the great technological problems remaining for humanity to solve. Traditional energy sources, primarily fossil fuels, are unsustainable, since there is essentially a finite amount of them remaining on the planet [8, 9]. Even if the cost of collecting and processing fossil fuels could be diminished, the fact remains that eventually humans have to shift to predominantly renewable energy sources. Many have argued that solar power is the most promising renewable energy source [10–13] and several technologies, specifically photovoltaics and concentrated solar power, have been developed to harness that power. However, these technologies are still too costly to justify a wholesale shift away from traditional energy sources [14, 15]. To expedite the shift towards renewable energy technology, a new class of photovoltaic devices based on organic polymer materials has garnered significant research effort in the preceding decades [16–20]. These devices are in contrast to traditional photovoltaics, which are based on inorganic semiconductors.

Polymer solar cells (PSCs) also named as plastic solar cells are a promising alternative energy for harnessing solar energy because of their composition from abundant lightweight environment-friendly materials and the availability of large-scale, low-energy, solution-processable fabrication methods [21–25]. They may serve as an economically viable renewable energy technology due to speedy progress in efficiency along with scalable manufacturing [26–29]. As the power conversion efficiency of Polymer photovoltaics is drastically increasing and recently reached 11–13.2%, the academia and industry both are taking great interest in OPV technology [30–34].

The photovoltaic effect is the mechanism of direct conversion of the energy of an absorbed photon into electrical energy. The absorption of photon results in the generation of an electron–hole pair; then these free charge carriers are collected by respective electrodes due to the internal field generated by the electrodes work-function difference. The DC power is converted to AC power with an inverter and can be used to power local loads. Polymer solar cell use conjugated polymers as light absorber, electron donor, acceptor, and/or hole transporting material. An organic solar cell is a photovoltaic cell that uses organic electronics—a branch of electronics that deals with conductive polymers or small organic molecules for light absorption and charge transport. Polymer solar cells are built from thin films (typically 100 nm) of organic semiconductors as shown in Fig. 2.

The optical absorption coefficient of polymer molecules is high, so a large amount of light can be absorbed with a small amount of materials. The main disadvantages associated with polymer photovoltaic cells are low efficiency, low stability and low

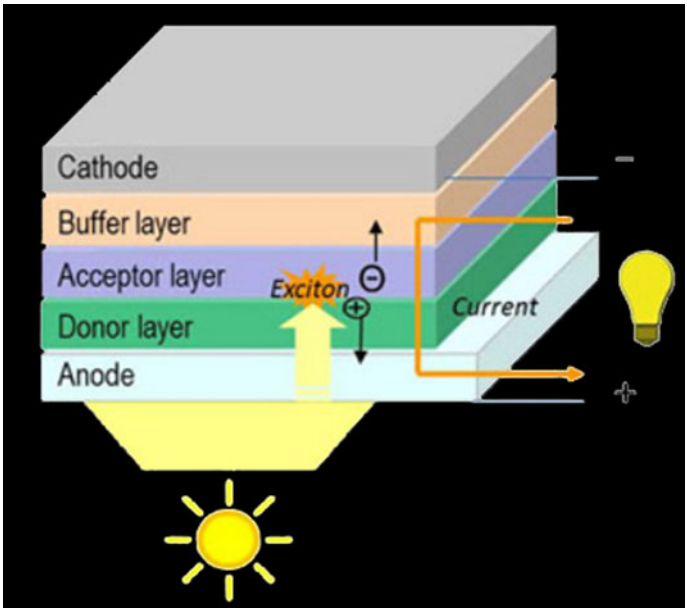

Fig. 2 Device structure of a polymer solar cell. The polymer film may comprise one or more semiconducting layers, a blend or a combination of these

strength compared to inorganic photovoltaic cells. In a bilayer OPV cell, sunlight is absorbed in the photoactive layers composed of donor and acceptor semiconducting polymer materials to generate photocurrents. The donor material (D) donates electrons and mainly transports holes and the acceptor material (A) withdraws electrons and mainly transports electrons.

1.1 Why Polymer Photovoltaic?

The displays and lighting systems based on organic and polymer light-emitting devices are doubtlessly driving the market of polymer semiconductors whereas organic photovoltaics are slowly and steadily moving ahead. Polymer-based solar cells represent a transformative technology with great potential for extremely high-throughput manufacturing at very low cost, and are made from non-toxic, earth-abundant materials with low-energy inputs. They have the potential to serve as lightweight, flexible, conformal and low-cost solid-state power sources. However, their performance must be improved before they can be viable for commercial applications [35].

Current state-of-the-art OPVs exhibit power conversion efficiency (PCE) of ~9% in small size (higher for tandem cells by tuning material properties, such as band gap, charge mobility and energy levels to optimize the light absorption, charge transport, and photovoltage. Developing these optimal materials remains challenging and continuous improvements in material design and chemical synthesis are urgently needed.

1.1.1 Advantages of Polymer Solar Cells

- The PSCs can be processed easily over a large area using spin coating, doctor blade techniques (wet-processing), evaporation through a mask (dry processing) and printing.
- Low cost: The energy consumed to develop a polymer solar cell is less than the amount required for conventional inorganic cells.
- Low weight.
- Flexible substrate: Mechanical flexibility and transparency.
- Band gap tunability: Band gap of polymer materials can be easily tuned chemically by incorporation of different functional groups.

The flexibility in PSC permits

- Compatibility with roll-to-roll fabrication (rapid fabrication low cost).
- Compatible with lightweight substrates (i.e. plastics)—typically flexible.
- New applications, e.g. integration with fabrics are possible.

Solar cell technologies are traditionally divided into three generations. The concept of third-generation PV technologies was originally developed by Martin Green of the University of New South Wales as described in Fig. 3 [30, 36]. Third-generation PV technologies may overcome the fundamental limitations of the photon-to-electron conversion in single-junction devices as able to surpass the Shockley–Queisser limit and, thus, improve both their efficiency and cost. Third-generation thin-film photovoltaic (PV) solar devices are beginning to emerge in the marketplace after approximately 20 years of research and development. The third-generation technology includes polymer cells and nanostructures, dye-sensitized cells and multi-junction III/V cells.

The purpose of this chapter is to introduce the concept of BHJ solar cells, numerically simulate the optical properties of BHJ solar cells and present an overview of optical optimization of Bulk heterojunction polymer solar cells. First, the physics involved in the functioning of BHJ photovoltaic is described. Then, the transfer matrix method used for optical modelling of thin-film solar cells is analysed. Afterwards, our preliminary results on optical simulations of PCDTBT: PCBM-inverted BHJ solar cells are presented. Finally, the chapter ends with a summary and outlook.

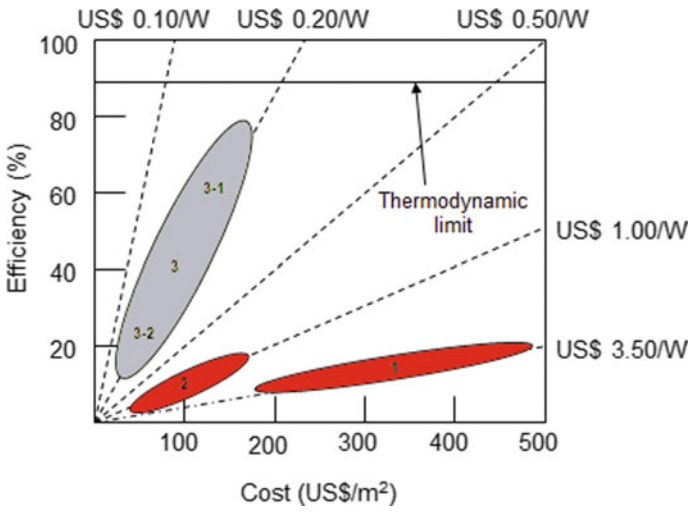

Fig. 3 Cost-efficiency analysis for first-, second- and third-generation PV technologies (labelled 1, 2 and 3, respectively). Region 3-1 depicts very-high-efficiency devices that require novel mechanisms of device operation. Region 3-2 (the region in which polymer PV devices lie) depicts devices with moderate efficiencies and very low costs [30, 36].

1.2 Materials for PSC

Polymer solar cells mainly consist of two polymer materials [7, 8] one of which is a donor (gives electron) and the other is an acceptor (accepts electrons). The conjugated polymer donors and the fullerene derivative acceptors are the key materials for high-performance PSCs. In order to achieve high efficiency, it is necessary to have acceptor and donor materials with optimized properties, such as balanced energy level, efficient exciton dissociation, ideal phase separation and morphology, complementary absorption spectrum compared to the donor, sufficient electron mobility, feasible synthesis, low cost and good solution processability [37–39].

Fullerene derivatives have been the predominant type of acceptors since the first BHJ solar cell was ever reported [40, 41]. Conjugated polymers like MDMO-PPV (poly[2-methoxy-5-(3,7-dimethyloctyloxy)]-1,4-phenylenevinylene), P3HT (poly(3 hexylthiophene-2,5-diyl) and PFB (poly(9,9′-dioctylfluorene-co-bis-*N,N*'-(4-butylphenyl)-bis-*N,N*'- phenyl 1,4-phenylenediamine) act as donors and fullerenes, perylene and its derivatives like F8TB (poly(9,9′- dioctylfluoreneco-benzothiadiazole) and PCBM (1-(3 methoxycarbonyl) propyl-1-phenyl[6,6]C61) act as acceptors [42–44]. Some donor and acceptor materials are shown Fig. 4. Non-fullerene types of acceptors, however, started to emerge recently as a potential substitute to the expensive fullerene derivatives.

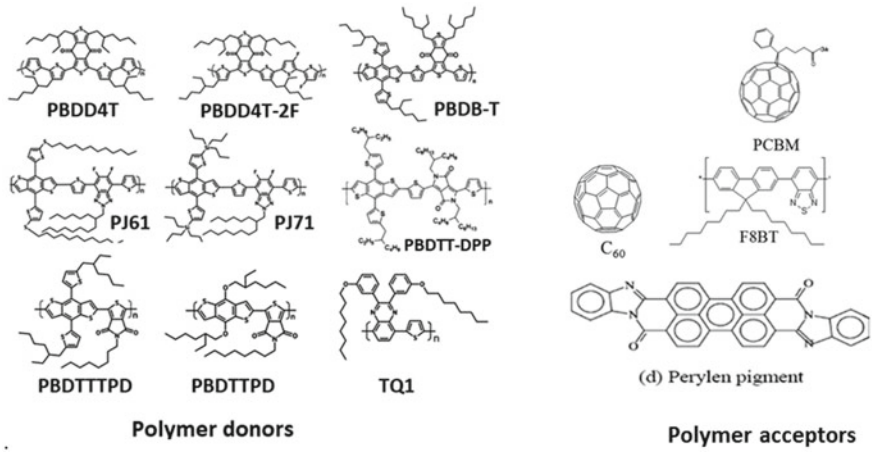

Fig. 4 Donor and acceptor materials for BHJ Polymer solar cell

1.3 Physics of Polymer Solar Cells

Exciton generation, migration and dissociation are major processes that play a key role in the design and operation of many organic optoelectronic devices. In polymer semiconductors, absorption of photons leads to the creation of bound electron–hole pairs (excitons) rather than free charges. These excitons carrying energy but no net charge may *diffuse* to dissociation sites, where their charges can be separated. The separated charges then need to travel to the respective device electrodes to provide voltage and be available for injection into an external circuit.

When the light beam passes through the transparent anode to the donor, the photon is absorbed in the light-absorbing polymeric layer. An electron is excited from the highest occupied molecular orbital (HOMO) to the lowest unoccupied molecular orbital (LUMO), creating a bound electron–hole pair due to Coulombic attraction, known as an exciton which is specifically Frenkel exciton. The binding energy of Frenkel exciton is generally large (0.1–1.0 eV) and the built-in electric field strength is usually insufficient to dissociate the exciton directly [43]. As such, the dissociation occurs almost exclusively at the interface between the donor and acceptor [45], which has different electron affinities and ionization potentials [46]. Thus, after excitation, the exciton diffuses to the donor–acceptor interface. There, the excited electron is transferred to the LUMO of the acceptor, and the energy difference between the LUMOs of the donor and acceptor drives the dissociation of the exciton into free charge carriers. The free hole and electron are then collected by the anode and the cathode, respectively.

In polymer solar cells, the basic four processes involved in converting the sunlight to electricity in OSC are (1) exciton generation via photon absorption; (2) exciton diffusion at a donor/acceptor interface; (3) charge transfer at the interface and charge dissociation into free charge carriers; and (4) charge transport to each electrode as

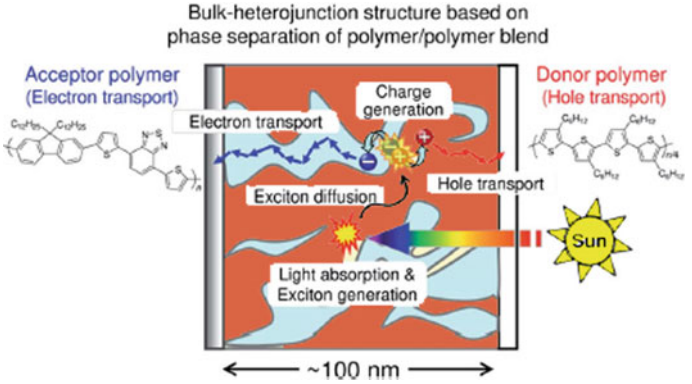

Fig. 5 Photovoltaic conversion processes in polymer/polymer blend solar cells [47] [CC BY-NC 3.0]

depicted in Fig. 5 [47]. These processes are characterized by an efficiency described as

(a) Photon absorption efficiency (η_A): Exciton generation by absorption of light
(b) Exciton diffusion efficiency (η_{ED}); Exciton diffusion over ~L_D (~20 nm)
(c) Charge separation efficiency or Charge-transfer reaction (η_{CT}); Exciton dissociation by rapid and efficient charge transfer
(d) Charge collection efficiency (η_{CC}); Charge extraction by the internal electric field.

The efficiencies of these four processes determine the external quantum efficiency (EQE) of the solar cell [48]. It is also known as incident-photon-to-current collection efficiency (IPCE), which is the number of electrons produced by a solar device for each incident photon. The external quantum efficiency may be expressed as

$$\eta_{EQE} = \eta_A \eta_{IQE} = \eta_A \eta_{ED} \eta_{CT} \eta_{CC} \tag{1}$$

The four basic physical processes responsible for OPV operation are summarized as follows.

1.3.1 Absorption of Photons

Photons with energy equal to the band gap energy are absorbed to create free electrons. Photons with less energy than the band gap energy pass through the material. In most polymer devices, only a small portion of the incident light is absorbed for the following reasons:

- The band gap of polymers is too high. A band gap of 1.1 eV (1100 nm) is required to absorb 77% of the solar radiation on earth whereas the semiconducting polymers have band gaps generally higher than 2.0 eV (600 nm) limiting the possible absorption to about 30%.
- The typically low charge carrier and exciton mobilities require layer thickness in the order of 100 nm and the polymer layer is suitable for PV applications as it is too thin. Fortunately, the absorption coefficient of polymer materials is generally much higher than indirect semiconductors as Si so that only about 100 nm thickness is necessary to absorb between 60 and 90% if a reflective back contact is used. The thin layer thickness also permits low electrical resistance and high built-in internal field.
- More investigations on reflection losses in the polymer materials are required. Anti-reflection coatings as used may prove useful to reduce reflection losses once other losses such as recombination become less dominant.

1.3.2 Exciton Diffusion

In polymer solar cells, charge generation often occurs only at an interface, forcing the exciton to migrate from the point of photogeneration in order to be dissociated into its constituent charge carriers. If the dissociation site may be at the other end of the semiconductor, their diffusion length should be at least equal to the required layer thickness otherwise they recombine and result in low power conversion efficiency. Exciton diffusion ranges in polymers and pigments are typically around 10 nm. However, some pigments like perylenes are believed to have exciton diffusion lengths of several 100 nm [49].

1.3.3 Charge Separation

Optimizing charge separation or dissociation of the strongly bound, photoexcited excitons in the polymer material blend is the key to OSC efficiency and the decisive mechanism for generating free charge carriers in an organic solar cell. As the organic semiconductors possess low dielectric constant, light absorption by an OPV cell generates Frenkel excitons, i.e. hole–electron pairs tightly bounded by strong Coulombic attraction with binding energies of several hundreds of milli electron volts, which require a high electric field to dissociate. This dissociation must occur on a time scale, which is short compared to all other processes. Charge occurs at polymer/metal interfaces, impurities (e.g. oxygen) or between materials with sufficiently different electron affinities (EA) and ionization potentials (IA). In the latter one, the material can then act as electron acceptor (A) while the other keeps the positive charge and is referred to as electron donor (D) as it *donates* the electron to A (Fig. 6). If the difference between IA and EA is not sufficient, the exciton may just hop onto the material with the lower band gap without splitting up its charges. Eventually, it will recombine without contributing charges to the photocurrent [49–51].

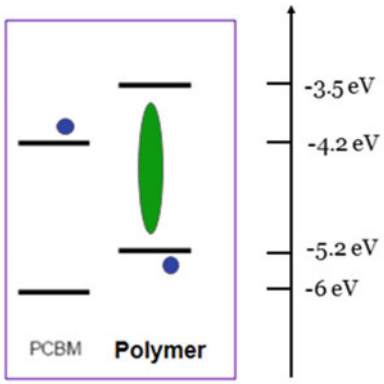

Fig. 6 Donor and acceptor LUMO energy offset is the driving offset which is an ultrafast phenomena

1.3.4 Charge Transport and Charge Collection

The photovoltaic performance of organic solar cells can be enhanced by understanding charge transport. The transport of charges is affected by recombination as they move towards electrodes—particularly if the same material serves as a transport medium for both electrons and holes. The charge transport is hindered by its interaction with atoms or other charges which slow down the mobility and thereby limit the current.

The charges, in general, have to overcome the potential barrier of a thin oxide layer in order to enter an electrode material with a relatively low work function (e.g. Al, Ca). In addition, the metal may have formed a blocking contact with the semiconductor so that they cannot immediately reach the metal [52].

The flowchart of basic physical processes occurring in polymer solar cell is depicted in Fig. 7.

1.4 Modes of Operation

Three different modes of operation are—short-circuit condition, flat band condition, open-circuit condition.

1.4.1 Short-Circuit Condition

Generally, the work function of the anode is considerably higher as compared to the work function of cathode. The short-circuit condition as shown in Fig. 8a requires that the Fermi levels of the two electrodes must align to ensure zero potential across the device. This generates an electrical field, which leads to a drift current that aids the diffusion current. Hence, the total current is maximum in the device under this condition and is called short-circuit current (I_{sc}). This is the upper limit on the amount

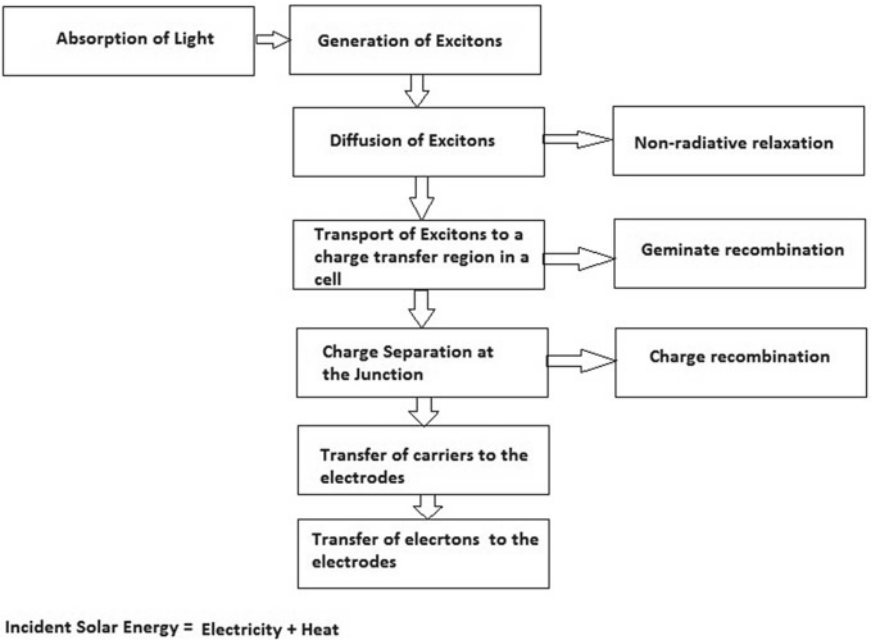

Fig. 7 Flowchart of processes in polymer solar cell. Light which is not converted to electricity is converted to heat and eventually contributes to damage

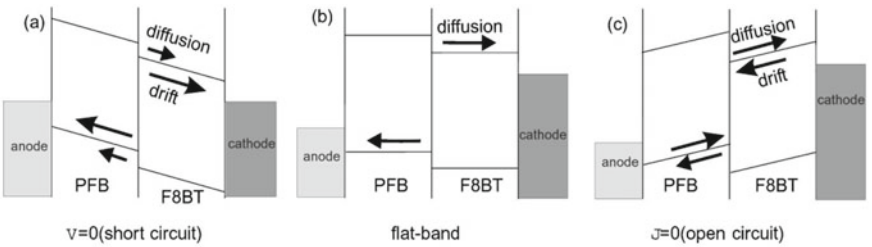

Fig. 8 Band diagram of a photovoltaic device is shown **a** at short circuit **b** under flat band **c** at open circuit

of current that a device can deliver under solar cell operation. This depends on the intensity of the incident light.

1.4.2 Flat-Band Condition

As shown in Fig. 8b this situation arises when the applied voltage is equal to the work-function difference of the cathode and anode. In this condition drift current is zero because there is no electric field within the device. But because of light generated

carriers at the polymer–polymer interface, there is a carrier gradient which leads to the diffusion current. Hence, the total current is non-zero in this condition.

1.4.3 Open-Circuit Condition

This condition is shown in Fig. 8c. Now if the light is made to fall on the device in this condition, it will ultimately lead to creation of charges, which due to diffusion will move towards the electrodes. Hence, there is a clear tendency for diffusion current to flow. But due to open circuit between two electrodes, a steady-state current cannot flow. Therefore, this diffusion current has to be balanced by an equal and opposite drift current. There has to be a finite field inside the bulk to make this drift current flow. So there has to be some external voltage applied between the two electrodes. This voltage is called open-circuit voltage (V_{OC}), which is an important parameter in determining the efficiency of the device.

1.5 Device Architectures

The significant improvement of PSC device performance has been accomplished by introducing various OPV device architectures. The four different architectures [9] are as follows.

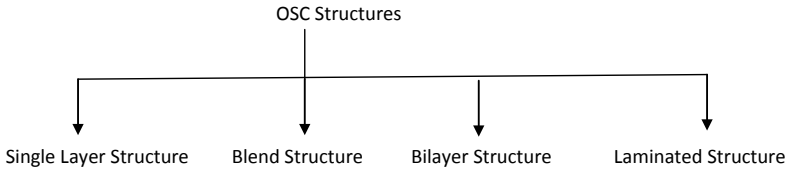

1.5.1 Single-Layer Structure

In the single-layer OSC structure, a layer of active organic or polymer electronic materials (**may be electron donor or electron acceptor type**) are made by sandwiching between two metallic contacts, typically a layer of indium tin oxide (ITO) with high work function and a layer of low work-function metal such as Al, Mg or Ca as shown in Fig. 9. Excitons created in the active material may diffuse and separate, hole and electron are collected by the respective electrode. The difference of work function between the two conductors sets up an electric field in the polymer layer. In practice, single-layer polymer photovoltaic cells have low quantum efficiencies (<1%) and low power conversion efficiencies (<0.1%). The reason for low performance is the insufficient electric field resulting from the difference between the two conductive electrodes and unable to break up the tightly bounded photogenerated Frenkel excitons which require a high electric field to dissociate. The photoactive region is often very thin and since both positive and negative photoexcited charges

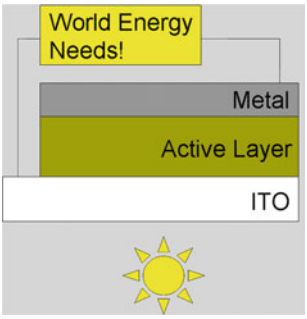

Fig. 9 Single-layer OSC structure

travel through the same material recombination losses are generally high. Often the electrons recombine with the holes rather than reaching the electrode. This problem may be circumvented with the multilayer polymer photovoltaic cells.

1.5.2 Bilayer Structure

The bilayer or planar heterojunction polymer solar cell structure shown in Fig. 10a consists of donor and acceptor layers deposited sequentially to form a heterojunction interface. The bilayer structure is able to tune the properties of the donor and the acceptor both to maximize charge separation and allow absorption in both layers by suitable matching to the solar spectrum. The donor and acceptor layers of materials have differences in electron affinity and ionization energy, resulted in the generation of electrostatic forces at the interface between the two layers. The materials are chosen properly to make the differences large enough, so these local electric fields are

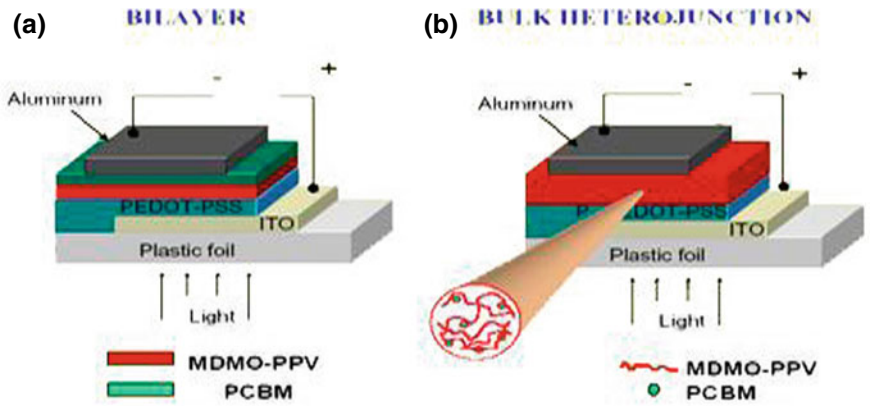

Fig. 10 **a** Bilayer structure of OSC; **b** bulk heterojunction PSC

strong, which may break up the excitons much more efficiently than the single-layer photovoltaic cells do. The acceptor material accepts electrons so it has higher electron affinity and ionization potential and the donor layer have electron affinity lower than the acceptor layer to release electrons. This structure is also called a planar donor–acceptor heterojunction. The absorption results in the creation of Frenkel exciton with energy lower than the HOMO–LUMO band gap by a value exactly equal to the exciton binding energy. The work-function difference between the cathode and anode materials is built-in voltage Vbi and is ideally equal to the open-circuit voltage V_{OC} of the SC.

The charge separation efficiency of bilayer solar cell structure is restricted by the small interfacial area, which requires that a photogenerated exciton must be formed close to a donor–acceptor interface to have a chance of separating before it decays to its ground state. The diffusion length of excitons in polymer electronic materials is typically on the order of 10 nm. However, typically a polymer layer needs a thickness of at least 100 nm to absorb enough light. At such a large thickness, only a small fraction of the excitons can reach the heterojunction interface.

1.5.3 Blend Structure or Bulk Heterojunction Solar Cell

The drawback of constraint on device thickness of bilayer structure due to small interfacial as a consequence of the small exciton diffusion lengths in organic materials has been resolved in the bulk heterojunction structure of polymer solar cell.

In bulk heterojunction photovoltaic cells, the electron donor and acceptor are mixed together, forming a polymer blend resulting in a film with a high interfacial surface area as shown in Figs. 10b and 11. In practice, a conventional BHJ polymer solar cell is made by subsequently depositing a hole extracting (or transport) layer (HEL or HTL), an active layer, an electron extracting (or transport) layer (EEL or ETL) and a metal layer on an indium tin oxide (ITO) covered glass substrate.

Polymer solar cells depend on heterojunction resulting from the contact of a donor (D) and an acceptor (A) material. The absorption of solar photons results in the creation of excitons, which diffuse to the D/A interface where they are dissociated into free holes and electrons by the electric field. Charge carriers within drift distance reach electrodes and create short-circuit current I_{SC}. In addition, the 'photodoping' *leads to* the splitting of Fermi levels and thus creates open-circuit voltage V_{OC}. This

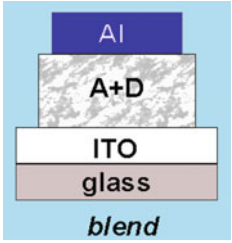

Fig. 11 Blend OSC structure

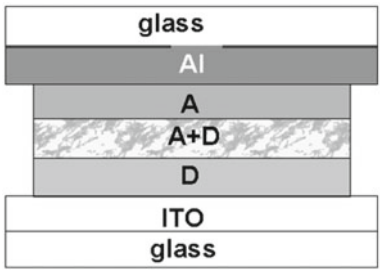

Fig. 12 Polymer/PCBM interpenetrating system

type of heterojunction can be created by two types of architectures, namely bilayer heterojunction and bulk heterojunction solar cells. The bulk heterojunction structure has the advantage of low-cost, easy fabrication and higher conversion efficiency due to high D/A interface. In bulk heterojunction structure, a percolating pathway for the hole and electron transporting phase to the electrodes is needed in order that the separated charge carriers can reach their corresponding electrodes [34].

BHJ approach is used in order to reach an efficient charge carrier generation by creating interpenetrating networks of electron-donating and -accepting materials in a bulk volume—for instance, a polymer–fullerene blend. With the two components interpenetrating one another, an exciton will never be far from the interface. It exhibits a donor–acceptor phase separation that each donor–acceptor interface is within a distance less than the exciton diffusion length of each absorbing site (Fig. 12) [30, 52–57].

1.5.4 Laminated Structure

In this type of photovoltaic cell shown in Fig. 13, the electron donor and acceptor are mixed together, but in such a way that the gradient is gradual and is sandwiched between the donor and acceptor layer. This architecture combines the short electron travel distance in the dispersed heterojunction with the advantage of the charge gradient of the bilayer technology. The drawback is that certain mechanical properties of the polymer semiconductors are required (low-glass transition temperature) to form the intermixed layer [34].

The time line of the polymer solar cell is portrayed in Fig. 14 [58].

1.6 Parameters of Polymer Solar Cells

When a solar cell is exposed to light, it will respond to different input voltages with different currents produced, creating a typical current density versus voltage (J vs. V) curve as the one shown in Fig. 15 [2]. The main parameters that are used to characterize the performance of solar cells are the peak power $P_{\max}$, the short-circuit current density J_{sc}, the open-circuit voltage V_{oc} and the fill factor FF. These parameters are

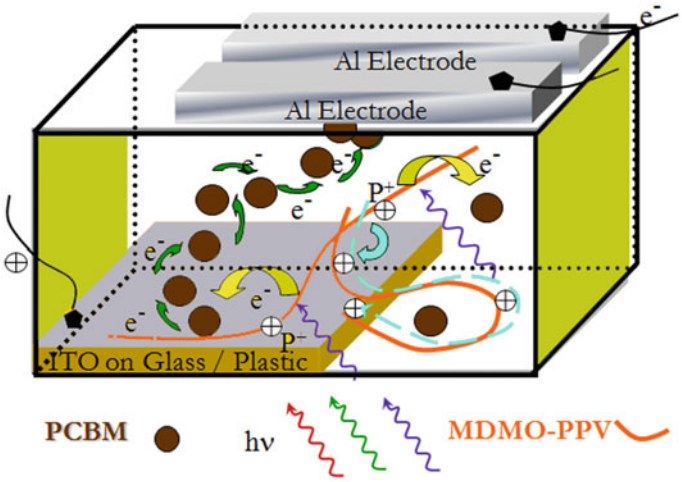

Fig. 13 Laminated structure of OSC

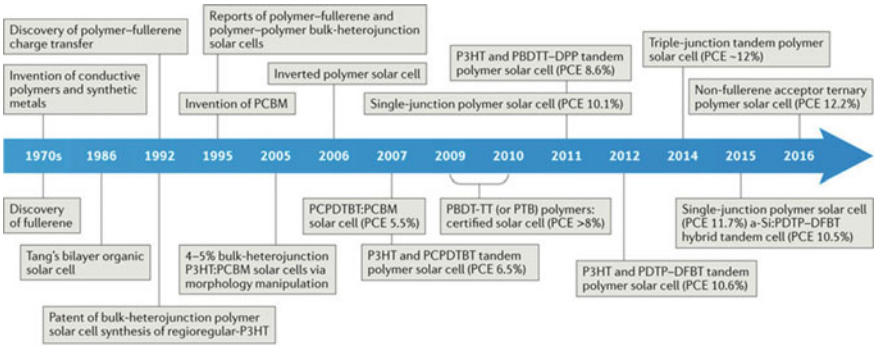

Fig. 14 Polymer solar cell in time line (Courtesy Nature Review Material) [58]

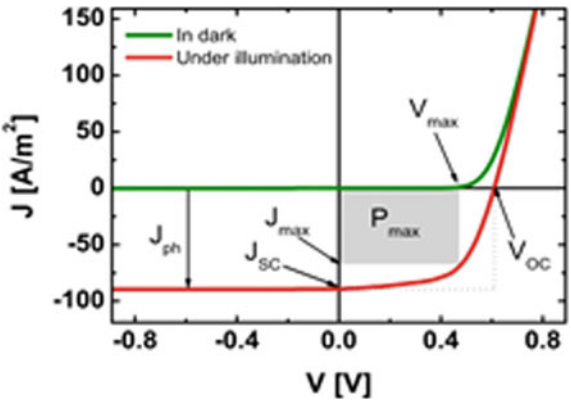

Fig. 15 I–V curve showing J_{sc}, V_{oc} and P_m

determined from the illuminated J-–V characteristic [30]. The conversion efficiency η can be determined from these parameters.

A set of common test conditions and methods for measuring the electrical performance parameters of photovoltaic cells for a reliable measurement of the J–V characteristics are specified by National ASTM standard E948 and international IEC standard 60904-1 [30]. The Standard Testing Conditions (STC) are

1. Temperature of the device under test (DUT) must be 25 ± 1 °C,
2. Spectral distribution of the light must be AM1.5 ± 25%,
3. Irradiance measured at the plane of the solar cell must be 1 Sun ± 2%.

The Sun is a unit of irradiance, one of which is equivalent to 1000 W/m^2 or 100 m W/cm^2. The amount of atmosphere through which sunlight passes to reach a given location on earth is called Air Mass (AM) and varies with that location's air pressure, elevation, latitude, date and time of day. In a given day, AM is minimum when the sun is at its zenith and largest near the horizons.

1.6.1 Short-Circuit Current

The short-circuit I_{sc} is the current that flows through the external circuit when the electrodes of the solar cell are short-circuited. The short-circuit current of a solar cell depends on the photon flux incident on the solar cell, which is determined by the spectrum of the incident light. The short-circuit current density J_{sc} measures the number of charges exiting the cell per unit time and area. For standard solar cell measurements, the spectrum is standardized to the AM1.5 spectrum. The I_{sc} depends on the area of the solar cell. The charges are drifting because of the internal field. In practice often the short-circuit current density J_{sc} is used to describe the maximum current delivered by a solar cell in order to get rid of dependency of solar area onto I_{sc}. J_{sc} is determined by the number of photons absorbed (the number of photoexcitations), the quantum efficiency for charge separation and the transport of the charge carriers through the material. The main parameters which influence J_{sc} are the light absorption by the cell, a function of the absorption profile of the materials, absorption profile of the materials, the film thickness and optical confinement effects, the blend microstructure, and the efficiency of charge generation at the donor–acceptor heterojunction. The behaviour of the short-circuit current can give information as to the dominant recombination mechanisms within the device. If the proportion of excitons that recombine is independent of intensity, i.e. independent of the number of excitons present, then a linear intensity dependence of the short-circuit current will be observed. This case is known as monomolecular (geminate) recombination. If free electrons and holes recombine then the process is dependent on both the electron density and the hole density. This is known as bimolecular recombination and the current shows a square root dependence on intensity in this case [30, 59, 60].

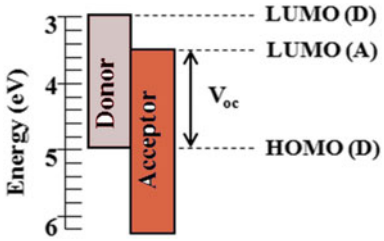

Fig. 16 Band diagram of a donor–acceptor combination showing HOMO and LUMO offsets

1.6.2 Open-Circuit Voltage

The open-circuit voltage V_{oc} is the voltage at which no current flows through the external circuit. It is the maximum voltage that a solar cell can deliver. V_{oc} corresponds to the forward bias voltage, at which the dark current density compensates the photocurrent density. V_{oc} depends on the photogenerated current density. V_{oc} is determined by the difference in the quasi-Fermi levels of the phase-separated donor and acceptor domains.

The open- circuit voltage is given by

$$V_{oc} = E_{\text{fullerene}}(LUMO) + E_{\text{polymer}}(HOMO) + \frac{k_B}{e}\left\{\ln\left(\frac{n_e n_h}{N_c^2}\right)\right\} \tag{2}$$

where n_e and n_h are the electron and hole densities, respectively; and N_c is the corresponding density of states near the fullerene lowest unoccupied molecular orbital (LUMO) and the polymer highest occupied molecular orbital (HOMO), assumed (for simplicity) to be equal. V_{oc} is depicted in the band diagram of a donor–acceptor combination showing HOMO and LUMO offsets in Fig. 16. In principle, V_{oc} can be increased by the difference in work functions of the anode and cathode. However, the use of interlayers (electron transport/hole blocking and hole transport/electron blocking) tends to decouple the open-circuit voltage from the difference in the anode and cathode work functions [61].

1.6.3 Maximum Power Point (P_m or W_p)

The maximum power generated by a solar cell under standard test conditions (STC) is the maximum power point and also called peak power. Normally, the maximum power point for a *V-I* curve of a solar cell occurs at the knee point of the curve. Mathematically, it is expressed as

$$P_m = V_m \times I_m \tag{3}$$

1.6.4 Fill Factor

The FF is a measure of the closeness of the solar cell I–V curve to the ideal rectangular shape. It is beneficial to have FF as close to unity as possible. FF is thus given by the ratio of the dark grey and light grey areas in Fig. 15. The open-circuit voltage and short-circuit current conditions cannot be satisfied simultaneously, and therefore the maximum power that can be extracted from the device is less than $I_{sc}V_{oc}$ [30]. The fill factor is the ratio between the maximum power ($P_{\max} = J_{\max} \,.\, V_{\max}$) generated by a solar cell and the product of V_{oc} with J_{sc} and is illustrated in Fig. 15. It is a measure of the quality of a photovoltaic cell and determined by the series resistance of the cell, and therefore by the mobilities of the charge carriers in the organic material. Typical values of the filling factor are 0.75–0.85 for Si cells and 0.3–0.4 for good polymer-based organic solar cells [30, 62, 63]. In polymer photovoltaics fill factors are still small, around 0.3 or 0.4 for device, compared to silicon devices which have fill factors of between 0.7 and 0.8 [30, 62, 63]. Mathematically, the fill factor is described by

$$FF = \frac{V_{\max} \times J_{\max}}{V_{oc} \times J_{sc}} \tag{4}$$

where $V_{\max}$ and $J_{\max}$ are the voltage and current density in the MPP, respectively. Max is the point on the J–V characteristic of the solar cell, at which the solar cell has the maximal power output. It is found that the fill factor of photovoltaic devices depends strongly on (a) the charge transport characteristics of the photoactive blend and (b) charge transfer through the interfaces between the active layer and the electrodes. In general, reasonably high fill factors can be obtained only for the systems where electron and hole mobilities are balanced in the photoactive blend (means close to each other as much as possible) [30, 64–67]. At the same time, the energy levels of buffer layers and work functions of the electrode materials have to be well aligned to facilitate the collection of each type of charge carrier. Bimolecular recombination also influences the fill factor, which is further determined by the parasitic resistances in the device (series resistance and shunt pathways).

1.6.5 Power Conversion Efficiency

The maximum power rectangle depicted in Fig. 15 is the maximum output power of the device. The power conversion efficiency is the ratio of the maximum power output to the power input. As mentioned above, solar cells are measured under the STC, where the incident light is described by the AM1.5 spectrum and has irradiance around 1000 W/m^2. The power conversion efficiency, more commonly known as the efficiency of a solar cell, is the ratio of the maximum power generated by the solar cell to the incident radiant energy (also called solar constant). The solar constant actually varies by about 0.3% over the 11-year solar cycle but averages about 1368 W/m^2 [30].

$$\eta = \frac{P_{out}}{P_{in}} = \frac{P_{\max}}{P_{light}} = FF \times \frac{V_{oc} \times J_{sc}}{P_{light}} \tag{5}$$

where P_{in} is the power density of the incident light and P_{out} is the electric power generated by the cell at the maximum power point. The incident light power density is usually standardized to the AM 1.5 G spectrums.

The performance parameters, the short-circuit current I_{sc}, the open-circuit voltage V_{oc}, the maximum power point P_m, are derived from mathematical fits to different portions of the I–V curve. The parameters V_{oc} and I_{sc} are the intercepts of least-square fitted lines. Pm is the point at which the derivative with respect to voltage is zero, for a fifth-order polynomial fit to power, the product of current and voltage. Fitting helps to reduce measurement noise.

1.6.6 External Quantum Efficiency and Internal Quantum Efficiency

In order to understand the conversion efficiency as a function of the wavelength of light impingent on the cell, the QE measurement is critical for materials research and cell design. In solar cells, internal quantum efficiency (IQE) is the ratio of the number of charge carriers extracted from the cell to the number of photons absorbed in the active layer at a given wavelength. Internal quantum efficiency (IQE) is a useful device metric, which measures a solar cell's ability to convert photons absorbed within the active material into electrons, and allows for diagnosis of charge collection and absorption problems. The external quantum efficiency is expressed as the ratio of the number of incident photons and the number of charge carriers output to the external circuit. The electrons are calculated from J_{SC} and the photons are calculated from the incident optical power and its optical spectrum. EQE is smaller than IQE for the conversion of the absorbed photons into charge carriers within the cell, because it takes into account losses due to reflection, recombination and scattering.

In organic photovoltaic devices, absorbed photons create excitons and these may be dissociated into separate charges which can be collected at the electrodes. The number of photons absorbed at a given wavelength is, therefore, causally linked to the number of electrons collected at the external circuit which is proportional to the EQE.

EQE and IQE are related as

$$IQE = \frac{EQE}{1 - R} \tag{6}$$

EQE represents the fraction of *incident* photons that are being converted to electrons in the device whereas IQE is the fraction of absorbed photons that are being converted to electrons in the device. In general, IQE is higher than EQE and may attain a value of 100% for a given device because the factor $1 - R$ is always less than 1. The decisive requirement for optimizing efficiency is to achieve balanced carrier mobilities for both holes and electrons so that both charge carriers can be collected

equally. Thus far, hole mobility is still one of the main hurdles in the performance of PSCs.

1.6.7 Incident-Photon-to-Current Conversion Efficiency (IPCE)

The IPCE is determined by the number of electrons leaving the device under short-circuit condition per time and area divided by the number of photons incident per time and area. Generally, IPCE is a measure of the external quantum efficiency, as it includes losses due to reflection at the surface or transmission through the device. Subtracting these two loss channels would lead to the internal quantum efficiency, which is, however, seldom used to compare solar cells.

Measurements are an important tool in the understanding of solar cells. Such measurements are used to correlate the discrete efficiency of the cell as a function of wavelength with the short-circuit current measurements of cells under one sun illumination. Furthermore, since the measurements are steady state, they can be used to determine other important properties of the cell such as the diffusion length. A typical incident-photon-to-current conversion efficiency (IPCE) curve is depicted in Fig. 17.

The IPCE is expressed as

$$IPCE = \frac{\text{no. of electrons through the external circuit}}{\text{no. of photons incident}}$$

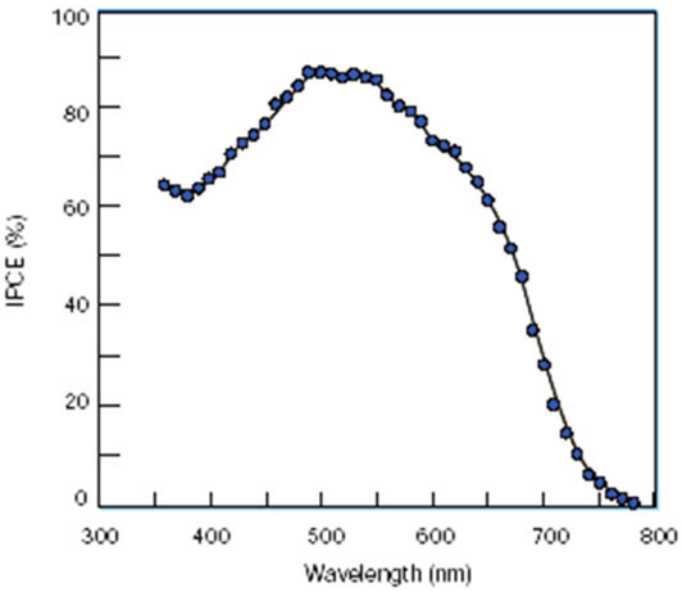

Fig. 17 Incident-photon-to-current conversion efficiency (IPCE)

$$= \frac{[1240\ \text{eV nm}]\,[photocurrent\ density\ (\mu\text{A cm}^{-2})]}{[wavelength\ (\text{nm})]\,[irradiance\ (\text{mW cm}^{-2})]} \tag{7}$$

The data from the IPCE measurements can be used to estimate the short-circuit current at AM1.5 light according to

$$I_{sc} = \int_{\lambda_1}^{\lambda_n} \left[IPCE(\%) \cdot n_p \cdot e \cdot d\lambda \right] \tag{8}$$

where

I_{sc} is the short circuit current in cm^{-2},
IPCE is in percent,
n_p is the number of photons in the wavelength interval *d,*
e is the charge on an electron.

1.7 Numerical Simulation Methods for Optical Modelling of Polymer Solar Cells

Numerical simulation of optical and electrical behaviour of solar cells and other optoelectronic devices has been employed as an essential tool for device structure optimization, obtaining insight into their physical operation and for the development of new ones [68–74]. Simulation of PSC devices can be divided into two parts, optical modelling for coupling of light into a multilayer structure and secondly the extraction of charges which is based on an electrical model. The numerical model of polymer solar cell simulates the generation of photoinduced excitons, excitons diffusion, free charges generation and recombination, charge carriers transfer and charges extraction [75, 76]. The generation of photoinduced excitons is dependent on optical absorption and electromagnetic field distribution inside the device, so this process is stimulated by the optical model [76–83].

Optical modelling thus enables a quantitative comparison of optical performance of alternative materials, the optimization of the physical structure of the device, the analysis of loss mechanisms and the calculation of the generation profile for electrical modelling. It is an important tool in the analysis of loss mechanisms, optical enhancement and carrier generation, because it is difficult to determine the light absorption profile experimentally. From the optical point of view, thin-film polymer solar cells are multilayer structures including thin layers, where the thicknesses are in the range of light wavelengths. Therefore, interference effects between forward- and backward-going (reflected) light have to be considered in the analysis. The interfaces between the layers are usually rough leading to some light scattering in the structure.

Today various numerical methods of rigorously solving the equations have been applied in optical modelling of thin-film solar cells [80, 84–90]. Most popular optical modelling methods are

- finite-difference time domain,
- finite element method,
- finite integration technique,
- rigorous coupled-wave analysis,
- transfer matrix method.

1.7.1 Transfer Matrix Formalism

In this section, the optical analysis of thin-film polymer solar cells has been carried out using a one-dimensional transfer matrix model. Transfer matrix model has been used to calculate optical interference and absorption in multilayer stacks and transmission and reflection are calculated for each interface in the stack as well as attenuation in each layer. This model does not take into account scattering and normal incidence is assumed. When light is incident on a multilayer planar stack, it is reflected, refracted and absorbed in a way that can be derived from the Fresnel equations and matrix formulae could be employed to calculate optical intensity in multiple thin layers [79, 83, 84, 90–92]. Realistic complex refractive indexes were used to describe the optical properties of the layers.

As depicted in Fig. 18, there are m layers between two semi-infinite layers 0 and $m + 1$. 0 represents the transparent substrate and layer $m + 1$ is air. For applying the theory, some assumptions are the following:

(a) layers of PSCs are homogeneous and isotropic, parallel and flat interfaces, and
(b) the incident light is a plane wave normal to the substrate interface.

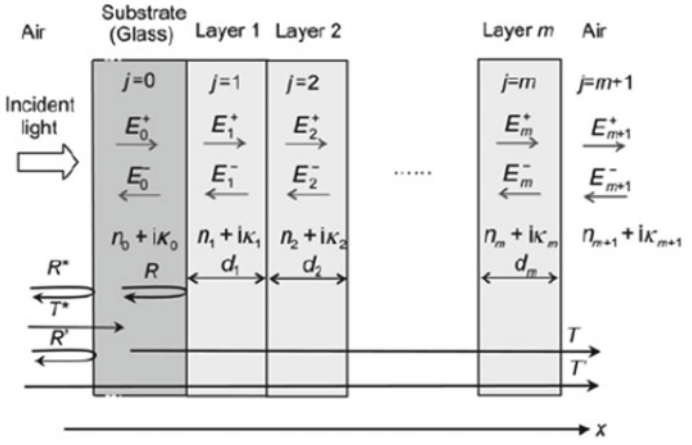

Fig. 18 Geometry of a general multilayer structure for transfer matrix formalism

The transfer-matrix method is based on Maxwell's equations; where there are continuity conditions for the electric field across boundaries from one medium to the next. The electric field for the final layer can be derived using a matrix operation, if it is known for the initial layer. A stack of layers can then be represented as a system matrix, which is the product of the individual layer matrices. The final step of the method involves converting the system matrix back into reflection and transmission coefficients. Based on these assumptions a one-dimensional model is proper to calculate the optical electric field [78, 79]. The layers ($j = 1, 2, \ldots, m$) in polymer thin film solar cells are considered to be embedded between two semi-infinite layers ($j = 0, j = m + 1$). Since the glass substrate is much thicker compared to the light coherent length, light transmission through it should not be calculated by wave interference, but rather be taken into account by reflection and transmission rates [79]. Each layer is described by its complex index of refraction, $\tilde{n}_j = n_j + i\kappa$ which is a function of wavelength (λ), and thickness of the layer (d_j).

As depicted in Fig. 18, the incident light enters along the x-direction from the left side and is reflected at the interfaces inside the device, so a backward light wave is generated. The forward and backward light waves are described with a positive superscript and a negative superscript, respectively, e.g., at a position x in layer j, and the forward and backward light electric fields are described by $E_j^+(x)$ and $E_j^-(x)$, respectively. The light propagation across an interface between layers j and k is described by the 2×2 matrix:

$$I_{jk} = \frac{1}{t_{jk}} \begin{bmatrix} 1 & r_{jk} \\ r_{jk} & 1 \end{bmatrix} \tag{9}$$

where $r_{jk} = \frac{(\tilde{n}_j - \tilde{n}_k)}{(\tilde{n}_j + \tilde{n}_k)}$ and $t_{jk} = \frac{2\tilde{n}_j}{(\tilde{n}_j + \tilde{n}_k)}$ are Fresnel complex reflection and transmission coefficients, respectively. A phase shift of light and absorption caused by propagating through layer j is described by the 2×2 matrix called layer matrix L_j.

$$L_j = \begin{bmatrix} e^{-i\xi_j d_{aj}} & 0 \\ 0 & e^{i\xi_j d_{aj}} \end{bmatrix} \tag{10}$$

where $\xi_j = \left(2\pi/\lambda\right)\tilde{n}_j$. The electric field between the substrate ($j = 0$) and ambient side ($j = m + 1$) is given by the total system transfer matrix S

$$\begin{bmatrix} E_0^+ \\ E_0^- \end{bmatrix} = S \begin{bmatrix} E_{m+1}^+ \\ E_{m+1}^- \end{bmatrix} \tag{11}$$

where S is the product of all interface and layer matrices that light propagates through orderly as

$$S = \begin{bmatrix} S_{11} & S_{12} \\ S_{21} & S_{22} \end{bmatrix} = \left(\prod_{v=1}^{m} I_{(v-1)} L_v \right) \cdot I_{m(m+1)} \tag{12}$$

The total transmission coefficient (t) and reflection coefficient (r) are given as

$$t = \frac{E_{m+1}^{+}}{E_0^{+}} = \frac{1}{S_{11}} \tag{13}$$

$$r = \frac{E_0^{-}}{E_0^{+}} = \frac{S_{21}}{S_{11}} \tag{14}$$

Within layer $j = 0$ and $j = m + 1$, the total transmissivity and reflectivity is given as

$$T = |t|^2 \frac{n_{m+1}}{n_0} \tag{15}$$

$$R = |r|^2 \tag{16}$$

The absorption efficiency of the whole device is expressed as $n_A = 1 - T^{/} - R^{/}$, where

$$T^{/} = \frac{T^* T}{1 + R^* R} \tag{17}$$

$$R^{/} = \frac{R^* + R}{1 + R^* R} \tag{18}$$

According to Fresnel's relation for transmission and reflection $T^* = \left| \frac{2}{1+n_0} \right|^2$ and $R^* = \left| \frac{1-n_0}{1+n_0} \right|^2$.

The total electric field at an arbitrary position $x (0 \leq x \leq d_j)$ inside layer j is given by

$$E_j(x) = E_j^{+}(x) + E_j^{-}(x) = \left(t_j^{+} e^{i\xi_j x} + t_j^{-} e^{-i\xi_j x} \right) E_0^{+} = t_j^{+} \left(e^{i\xi_j x} + r_j^{//} e^{i\xi_j x (2d_j - x)} \right) E_0^{+} \tag{19}$$

At a given position, the number of excitons generated is directly dependent on the energy absorbed by the material. Based on the concept of Poynting vector, the time-averaged absorbed power is given as [88]

$$Q_j(x) = \frac{4\pi c \varepsilon_0 k_j n_j}{2\lambda} \left| E_j(x) \right|^2 = \frac{1}{2} c \varepsilon_0 \alpha_j n_j \left| E_j(x) \right|^2 \tag{20}$$

where c is the speed of light, ε_0 is the permittivity of free space and $\alpha_j = 4\pi kj/\lambda$ is the absorption coefficient. The photon absorption of glass is strong below 300 nm

and polymer materials hardly absorb photons beyond 1100 nm. Thus for PSCs, the time-averaged light energy dissipation $Q(x)$ is integrated over this wavelength range as

$$Q(x) = \int_{300}^{1100} Q(x, \lambda) d\lambda \tag{21}$$

It indicates that the energy absorbed at position x in the layered structure is proportional to the product of the modulus squared of the electric field $\left|E_j(x)\right|^2$, the refractive index n_j, and the absorption coefficient α_j

$$\alpha_j = \frac{4\pi k_j}{\lambda} \tag{22}$$

at the actual position x. Thus, the number of excited states in a layer is proportional to the number of absorbed photons and, hence, $|E(x)|^2$ versus position x in the film directly represents the production of excited states at each point [88, 93–95].

The imaginary part of the complex refractive index is called the extinction coefficient and higher its value, the more quickly light gets absorbed as it transports through the material. The extinction coefficient k_j is different at different frequencies. The optical constants of polymer blend and other layers generally depend on doping density and deposition technique, solvent, post-annealing temperature and time, and of course material quality (contamination and regio-regularity).

The current and reflection loss is computed by integrating the product of the optical absorbance and AM 1.5 spectral photon flux over the spectral range from 305 to 1490 nm (Fig. 19). This range of wavelength is chosen to cover the whole range

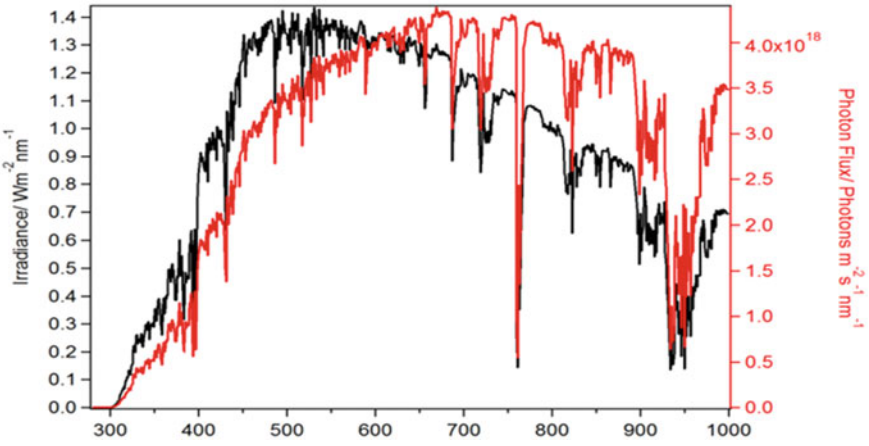

Fig. 19 Solar spectrum

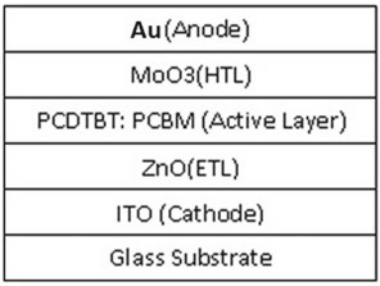

Fig. 20 A typical BHJ-Inverted polymer solar cell structure

for the absorption of the photons by the absorber layer. Figures 3 and 4 show the dependence of the current and the reflection loss of the solar cell on the thickness of the absorber layer.

As mentioned in the earlier section, organic semiconductors generally have high absorption coefficients (~10^5 cm^{-1}) but their absorption tends to occur in fairly narrow bands. Therefore, materials with increased absorption at long wavelengths are desirable for OPV applications and are mostly based upon low-band-gap polymers [96, 97]. The photocurrent is produced in the solar cell due to the absorption of photons. It is a function of the device thickness, the fraction of absorbed photons, depending on the optical field distribution within the device and the free carrier generation yield. The current and the loss tend to become "independent/unaffected" due to the increase in the thickness of the layer after the thickness of 2 μm [98]. They reach this point where a minor increase in the thickness does not lead to a major increase/decrease in the current/loss. Thus the intended thickness of the absorber layer is chosen to be 2 μm.

In this chapter optical simulation of a typical BHJ-inverted polymer photovoltaic cell device structure consisting of a glass substrate/ITO/ZnO/PCDTBT: PC70BM/MoO_3/Au has been done (Fig. 20). The thickness of the glass substrate is not important as it is thick enough that interference effects have practically no effect. Typical thicknesses for the remaining layers are (in nm), 200/60/250/10/100. The target is the visible spectrum where the materials absorb (~350 nm – ~800 nm) and observe the interference patterns of 400, 500 and 600 nm light within the device.

1.7.2 Simulation of the Optical Electric Field Inside the Device

Thin-film theory in matrix formalism enables the extraction of the impact of reflection and interference on the optical electric field E as a function of depth into the device [30, 87]. The model lets us predict, for example, an optimal blend thickness when light is assumed to be both polychromatic and distributed following solar irradiation. It is also possible to see the sensitivity for the variation from this value. The optic electric field distribution inside a simple device for monochromatic irradiation and normal incidence is depicted in Fig. 21. $|E|^2$ is continuous at the layer interfaces. The high wavelengths, 550 and 650 nm, create standing wave behaviour as the polymer is not

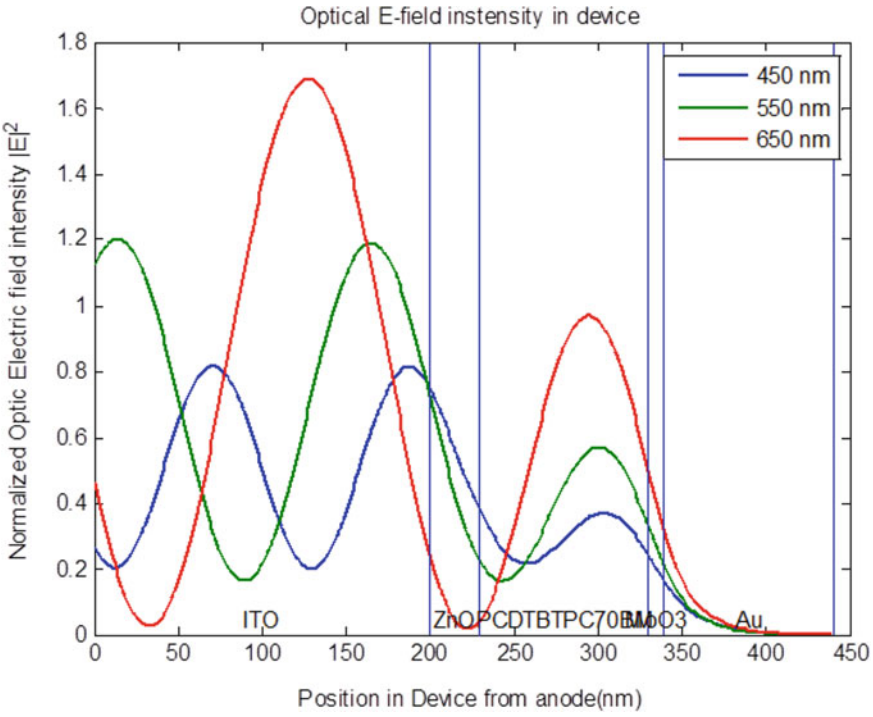

Fig. 21 The optic electric field distribution inside a device for monochromatic irradiation and normal incidence

absorbing. Reflection and interference are indeed dominating features. It is possible to choose the illumination wavelength in order to focus the E-field to certain positions inside the film [74].

The incoming irradiation redistribution on reflection and layer-wise absorption for the structure is shown in Fig. 22. In order to optimize the performance of a solar, it is necessary to measure the sources of optical losses within the device. Generally, a loss of ∼4% occurs due to reflection at the air–glass interface [30, 91]. The other sources of loss are plotted in Fig. 22 as functions of incident light wavelength. The greatest source of loss is due to reflection out of the device. Incident radiation is reflected off at each of the interfaces glass–ITO, ITO–ZnO, etc. Reflection here considers all of the light coming back from the device after multiple reflections within the layer stack [30]. The exciton generation rate in active PCDTBT: PC70BM inverted BHJ solar cell is depicted in Fig. 23.

The mapping of total, parasitic and useful absorbed energy is shown in Figs. 24 and 25, for PBDTTPD: PC70BM BHJ solar cell. The major portion of optical energy is absorbed by blend which is quite high till 550 nm and its absorption extends beyond 800 nm. The optical field distribution and photogenerated carrier profile are influenced by parasitic absorptions and optical interference in non-active layers.

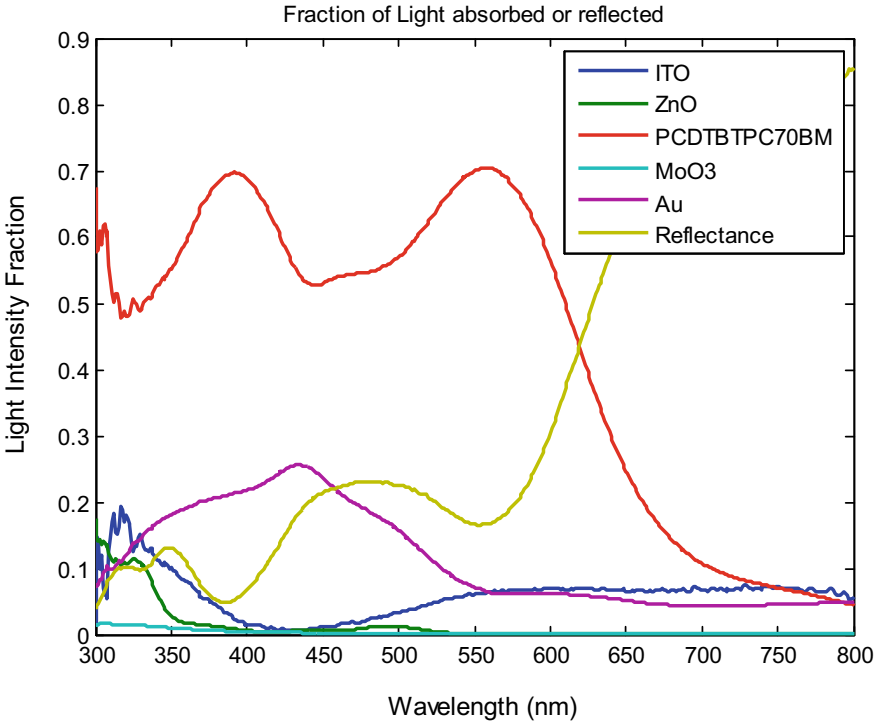

Fig. 22 Redistribution of the incoming irradiation on reflection and layer-wise absorption for structure

When the absorption of the blend decreases, reflection losses start growing. It is also evident that the parasitic absorption in ITO and ZnO increases with an increase in the wavelengths.

1.7.3 Optimization of Thickness of Active Layer of PCDTBT: PC70BM Based Inverted BHJ Solar Cell

Since the layer thicknesses employed in organic solar cells are comparable to the wavelength of light, interference effects are important, and these can be manipulated to enhance optical absorption in the active layer. Therefore, the main issue to design the polymer solar cells is to determine the optimum active layer thickness that represents the best compromise between strong light absorption and efficient charge carrier collection. The optimum absorber thicknesses are often limited to ~100 nm and less as the polymer solar cells have low mobility-lifetime products. If the absorber layer is thick, it leads to increased collection losses of charge carriers due to non-geminate recombination that neutralizes the gain in absorptance in most cases. The polymer cells are strongly affected by interference effects because of the

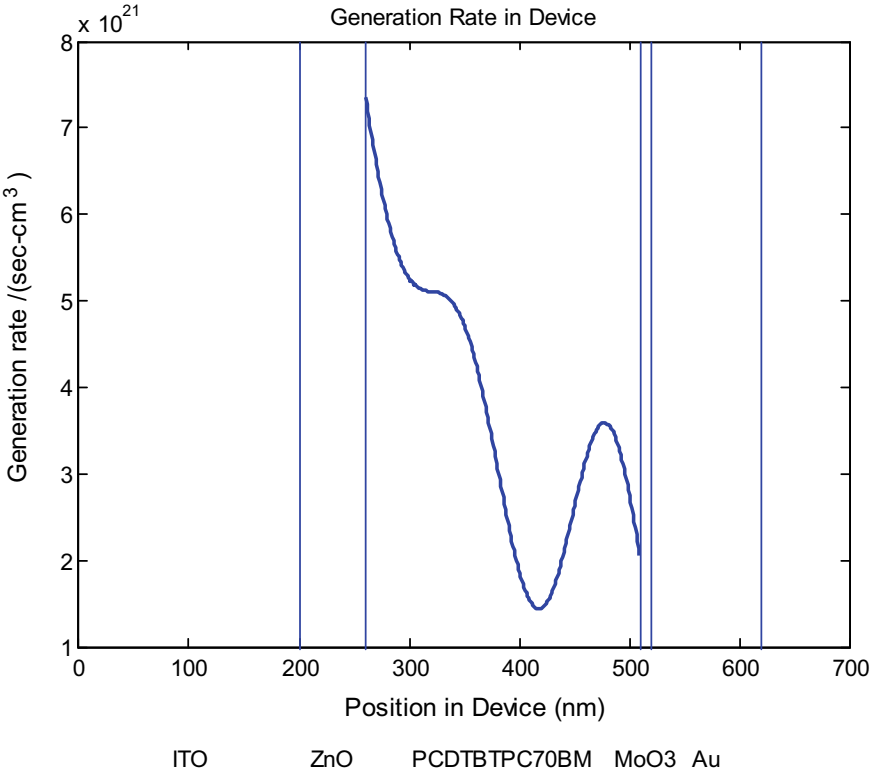

Fig. 23 Exciton generation rate in active PCDTBT: PC70BM BHJ solar cell

smooth interfaces and low thicknesses. Hence, the device optimization of polymer solar cells becomes further tedious.

If it is assumed that all the photogenerated excitons are converted to photocurrent, i.e. 100% IQE at all wavelengths, the maximum photocurrent can be estimated as the exciton generation rate. The variation of J_{sc} as a function of active layer thickness is depicted in Fig. 26. Because the optical absorption depends on the thickness of device, the J_{sc} increases with an increase in thickness. The current J_{sc} decreases after reaching optimum thickness because the risk for trapping increases with the distance travelled. A slight decrease is observed for higher thickness devices that may also be due to higher series resistance. It is found that the experimental saturated photocurrent follows the variation of calculated $J_{\max.}$

The device thickness optimization is an important result in designing of polymer solar cell. Since the incident light is an AM1.5 spectrum with a broad wavelength distribution, the interference maxima and minima are wavelength specific. Although large active layer thickness can improve the short-circuit current density and external

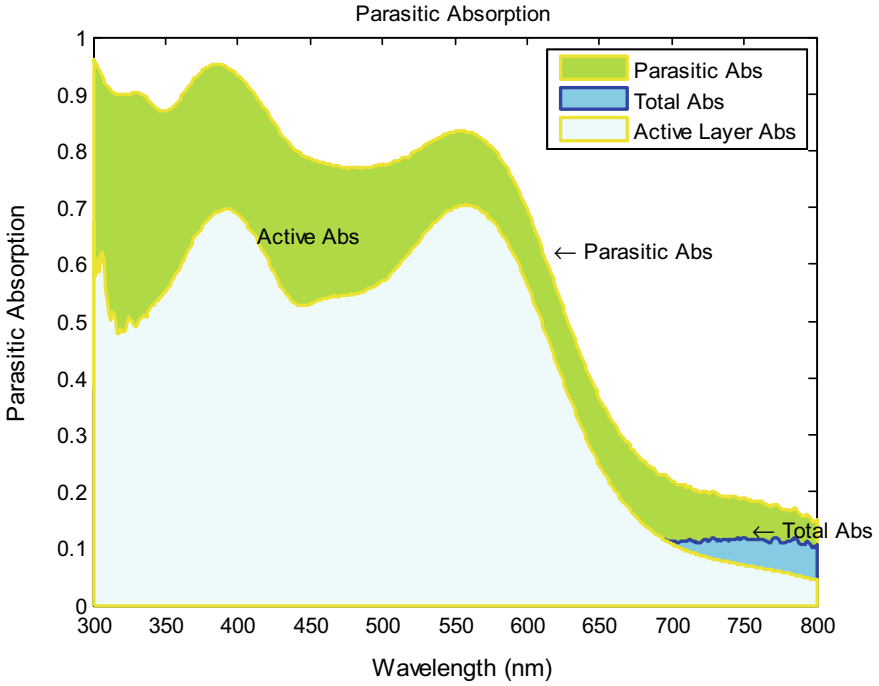

Fig. 24 Area absorption profile in PCDTBT: PC70BM layer of BHJ solar cell

quantum efficiency, thicker devices require higher mobility to ensure the separated charges to reach their respective electrodes. It is also difficult to deposit thick homogenous active layer by spin-coating method.

The photon absorption has several peaks in the plot of absorbed photons versus the thickness of the active layer due to interference between incident and reflected light from Au or Ag mirror electrode at the back of device. The peaks at around 50 and 180 nm in the absorption of photons are attributed to strong constructive interference. The interference caused by the gold anode leads to an oscillatory behaviour of the light absorption and thus J_{sc} on the active layer thickness.

The variation in J_{sc} with HTL layer thickness in Fig. 27 and Variation in J_{sc} with ETL layer thickness in Fig. 28 helps in optimization of thickness of MoO_3 and ZnO layer.

1.7.4 Optimization for High-Efficiency Polymer Solar Cells

The initiatives which should be taken for enhancing the efficiency of BHJ polymer solar cells are the following:

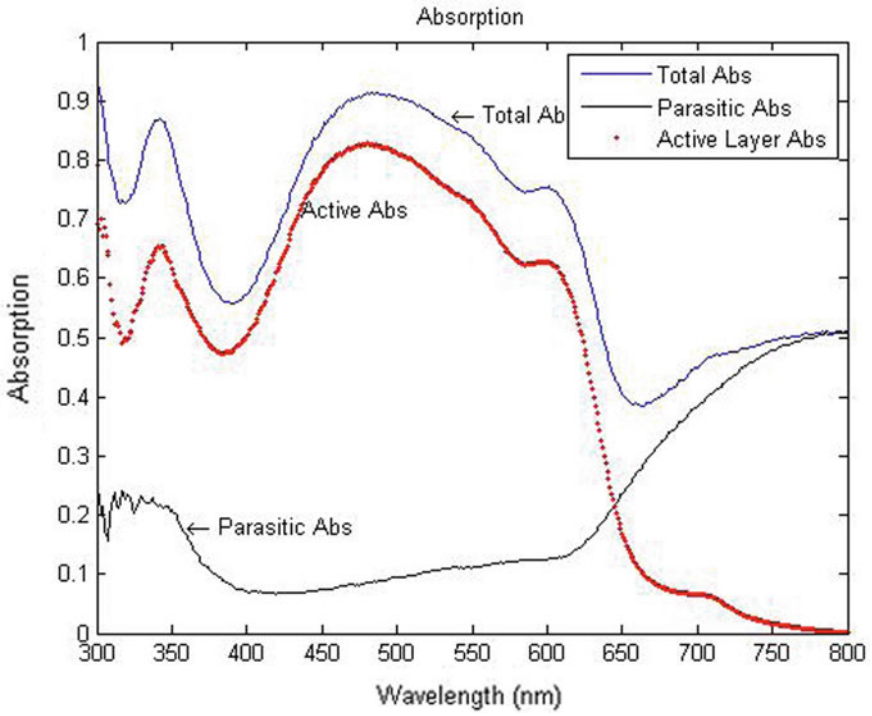

Fig. 25 Absorption profile in PCDTBT: PC70BM BHJ solar cell

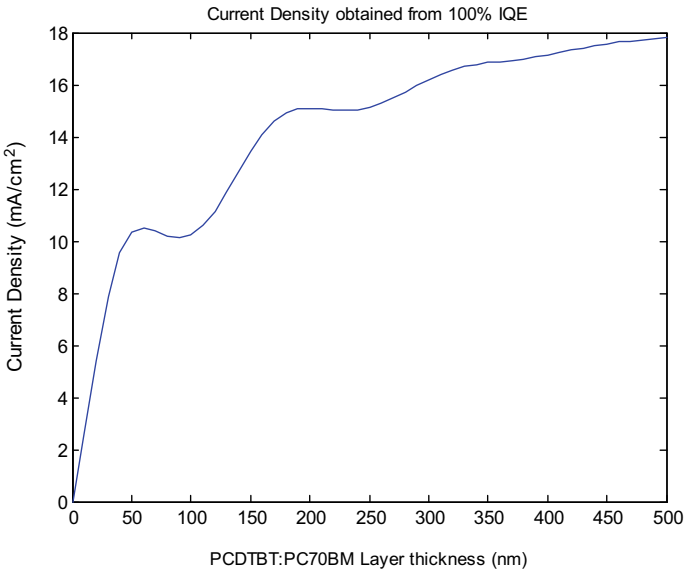

Fig. 26 Variation in *Jsc* with PCDTBT: PC70BM Blend thickness for active layer optimization

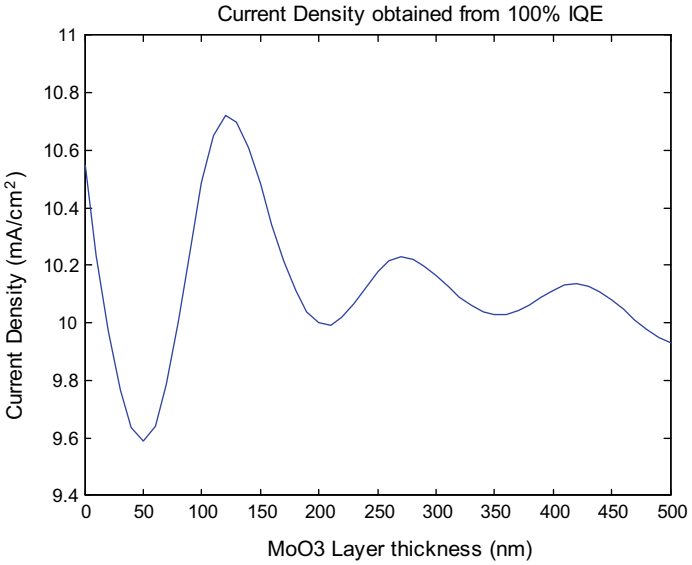

Fig. 27 Variation in *Jsc* with HTL layer thickness

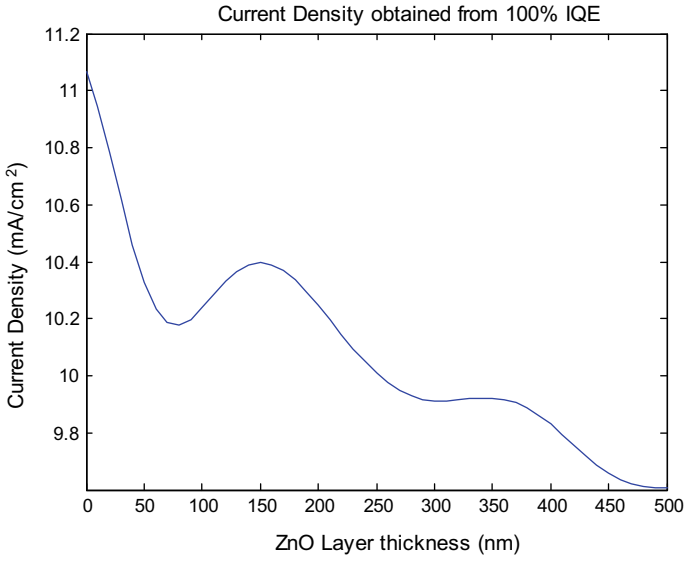

Fig. 28 Variation in *Jsc* with ETL layer thickness

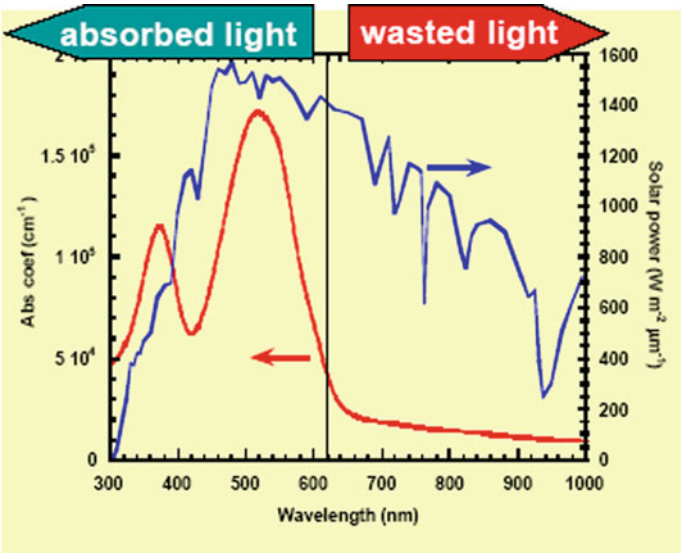

Fig. 29 Optimization to absorb solar radiation

i. **Selection of Conjugated polymer with low band gap**: Maximum photon flux of sun = 700 nm
E_g = 1.24/0.7= 1.77 [eV] which results in maximum absorption of photon of sun as shown in Fig. 29. The material properties should match the solar spectrum and can be processed from non-toxic solvents and amenable to rapid processing. It should also be noted that the decrease in the material band gap to increase the number of photons absorbed may also decrease the driving force for charge separation and lead to a decrease in the yield of photogenerated charges [97].
ii. **Bulk heterojunction morphology**: The exciton diffusion length of conjugated polymer should be below 20 nm [99].
iii. **High carrier mobility**: The electron and hole mobility of conjugated polymer should be high.
iv. **For high I_{sc},** optimization of the transport property (mobility) is necessary. **For high V_{oc}**, tuning of the electronic energy level of the donor–acceptor system is required; V_{oc} may be increased by increasing the energy level offset at the interface by either lowering the donor HOMO or raising the acceptor LUMO. V_{oc} of ~2 V observed in polymeric donor–acceptor system
v. **For high fill factor**, optimization of the contacts and morphology and lowering of serial resistance

$$\eta = \frac{J_{sc} V_{oc} FF}{P_S} \times 100 \tag{23}$$

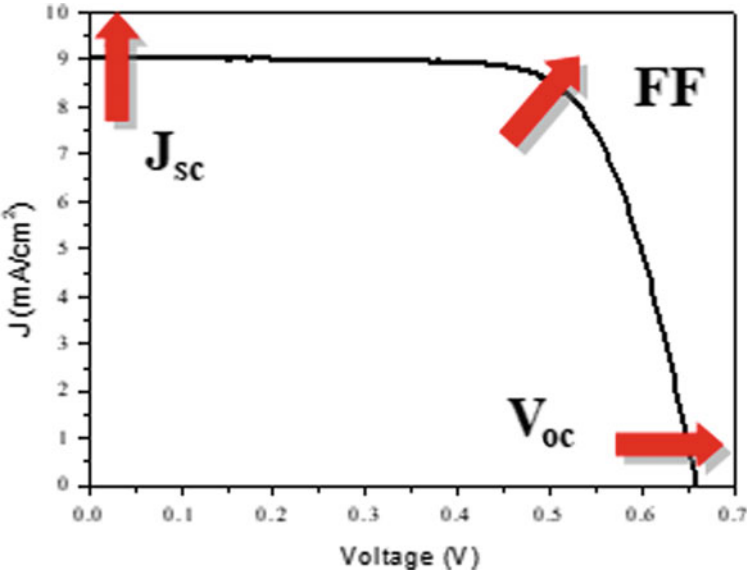

Fig. 30 Enhancing devices efficiency by increasing J_{sc}, V_{oc} and FF

In order to increase the efficiency of BHJ PSC, Jsc, Voc and FF should be increased as depicted in Fig. 30.

vi. It is possible to influence V_{OC}, I_{SC}, FF and efficiency by properly optimizing the electrical and photoelectrical properties of Polymer molecules. To enhance cell performance and stability, interfacial layers between the active layer and electrode could be used.

vii. The improvement in the nanoscale morphology and development of novel low bandgap materials may lead to power conversion efficiencies approaching 10%.

viii. Tandem structures presents a viable solution to boost the efficiency of OSC to more than 15%, compared to the 10% limit of single layer bulk heterojunction devices.

ix. Light trapping mechanisms to enhance the photon path length on thin active layers of polymeric materials can be achieved with simple patterning technique [96, 97] or by use of grating structures [100], microlenses [101, 102], and pattern metal electrodes to induce plasmonic effects [103].

x. High efficiency in PSC can be achieved by efficient charge transfer at small frontier molecular orbital offsets between donor and acceptor.

xi. Optimization of thickness and annealing temperature is crucial to achieve the higher efficiency in PSC.

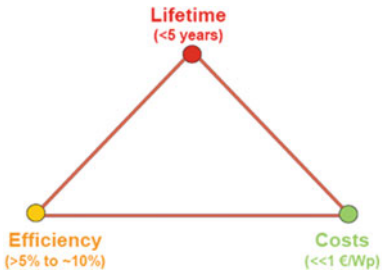

Fig. 31 Parameters and technological goals

xii. The interface between the electrodes and the active layer must be optimized to provide an good ohmic contact and it requires careful selection of the electrode materials. Generally higher-work-function anodes or lower-work-function cathodes to contact to the new low-band-gap active materials are suitable for efficient PSCs.

1.8 Challenges

The major challenge for PSCs is improving efficiency, reducing materials cost and search for low cost, transparent, flexible electrodes. The challenges are also to improve stability specially photostability of polymer semiconductors and interface stability (delamination at soft contacts) and blocking water/oxygen ingress particularly on flexible substrates. The boost in efficiency and device stability are the biggest challenges that must be solved before the commercial application of organic solar cells.

Therefore, the most important parameters of every solar technology are efficiency, lifetimes and costs (Fig. 31) [104]. Today, a large number of OSCs are demonstrating >10% efficiency, recently reaching a milestone of 17% [105]. The actual application defines which parameter or combination of parameters is more or less important. The OPV features like flexibility, weight, transparency are not sufficient to constitute a relevant competitive advantage.

2 Summary and Outlook

Polymer PV devices are widely recognized as one of the most promising low-carbon technologies for the generation of electricity with the potential to provide very environmentally friendly, flexible, low cost, relatively lower installation time and cost, lightweight, low carbon footprint with a short energy payback time and suitability for roll-to-roll printing process based renewable energy for a wide range of applications. In order to put polymer solar cells on equal footing with their inorganic counterparts, the challenge is to enhance its efficiency, stability, lifetime and suitable flexibles.

The power conversion efficiency of the most efficient polymer cells has recently increased to over 10%. It is necessary to identify the factors limiting the device efficiency for further improvement in performance. For these devices to be commercially viable, three important areas must be addressed. It is required to develop robust, thermally stable transparent flexible substrates. Roll to roll coating, film technologies compatible with industrial applications, encapsulation and patterning issues are to be improved.

Optical modelling is a useful tool for the optimization and improvements of thin-film polymer solar cells. It provides insight into internal optics and provides a basis for further optimizations of the structures. The distribution of light energy determined by optical interference and optimization of thickness of each layer in the OPV would help in the improvement of its performance. The limited charge carrier mobility in polymer semiconductors requires the active layer of polymer solar cells to be thin. Although large active layer thickness can improve the short-circuit current density and external quantum efficiency, thicker devices require higher mobility to ensure the separated charges to reach their respective electrodes. Optical modelling helps in thickness optimization. The optical modelling tool requires modifications to incorporate the effect of scattering in the solar cells and due to roughness at the interface the light scatters in different directions which cannot be calculated by applying the basic principles of the reflection and refraction. The optimization of device performance requires maximization of the area of the interface between the electrodes and the organic semiconductors.

The optimization of light distribution and improving the stability of the solar cell requires additional transparent layers at the interfaces between the electrodes and the light-harvesting organic semiconductor layer which must conduct charges to the electrodes. The composites of insulators and conducting nanoparticles such as carbon nanotubes, graphene fragments or metal nanoparticles can serve this purpose.

Eventually, the high efficiency along with long-term stability of polymer solar cells could be reached through a perfect optimization of materials properties, morphology and device architectures. It is, therefore, important to motivate interdisciplinary research in material synthesis, thin-film technology, photo physics and device technology to develop an ideal prototype. Organic solar cells are very close to being commercialized with potential applications in rapidly growing areas as electric vehicles and for integration into windows on buildings as it supports flexible curved surfaces and are very lightweight and colour-tuneable, where silicon technology is misfit. There are still a lot of obstacles for OPV researchers to conquer, but more opportunities in the future. The best has not arrived **yet**.

Acknowledgements The author (ST) is thankful for financial support by the Defence Research & Development Organisation, Ministry of Defence, GOI and the extended support of the Abdus Salam ICTP, Italy through Sr. Associateship.

References

1. T.F. Stocker, D. Qin, G. K. Plattner, M. Tignor, S.K. Allen, J. Boschung, A. Nauels, Y. Xia, V. Bex, P.M. Midgley (eds.), *Climate Change 2013: The Physical Science Basis* (Cambridge University Press, Cambridge, NY, USA, 2015), pp. 1535
2. M. Dixon, Climate Change Numbers for COP21 in Paris, Markatcop21 (2015)
3. M.S. Dresselhause, I.L. Thomas, Nature **414**, 332 (2001)
4. F.C. Krebs, *Polymer Photovoltaics A Practical Approach* (SPIE Press, Bellingham, 2008), p. 15
5. N. Grossiord, M.J. Kroon, R. Andriessen, P.W.M. Blom, Org. Electron. **13**, 432 (2012)
6. Independent Group of Scientists appointed by the Secretary-General, *Global Sustainable Development Report 2019: The Future Is Now—Science for Achieving Sustainable Development* (United Nations, New York, 2019)
7. T.M.W.J. Bandaraand, J.L. Ratnasekera, Polymer electrolytes: characterization techniques and energy applications, in ed. by T. Winie, A.K. Arof, S. Thomas (Wiley VCH, Germany, 2020), p. 300
8. S. Shafiee, E. Topal. Energy Policy **37**, 181 (2009)
9. *Key World Energy Statistics* (International Energy Agency, 2009)
10. M.Z. Jacobson, M.A. Delucchi, Z.A.F. Bauer, S.C. Goodman, W.E. Chapman, M.A. Cameron, C. Bozonnat, L. Chobadi, H.A. Clonts, P. Enevoldsen, J.R. Erwin, S.N. Fobi, O.K. Goldstrom, E.M. Hennessy, J. Liu, J. Lo, C.B. Meyer, S.B. Morris, K.R. Moy, P.L. O'Neill, I. Petkov, S. Redfern, R. Schucker, M.A. Sontag, J. Wang, E. Weiner, A.S. Yachanin, Joule **1**, 1 (2017)
11. A. Hu, S. Levis, G.A. Meehl, W. Han, W.M. Washington, K.W. Oleson, B.J. van Ruijven, M. He, W.G. Strand, Impact of solar panels on global climate. Nat. Clim. Chang. **6**, 290–294 (2016). 10.1038/nclimate2843
12. V. Masson, M. Bonhomme, J.L. Salagnac, X. Briottet, A. Lemonsu, Solar panels reduce both global warming and urban heat island. Front. Environ. Sci. **2**(14), 1 (2014). https://doi.org/10.3389/fenvs.2014.00014
13. D.P. van Vuuren, E. Stehfest, M.G.K. den Elzen, T. Kram, J.V. Vliet, S. Deetman, M. Isaac, K.K. Goldewijk, A. Hof, A.M. Beltran, R. Oostenrijk, B. van Ruijven, RCP2.6: Exploring the possibility to keep global mean temperature increase below 2 °C. Clim. Dynam. **109**, 95 (2011)
14. H.H. Rogner, R.F. Aguilera, C. Archer, R. Bertani, S.C. Bhattacharya, M.B. Dusseault, L. Gagnon, H. Haberl, M. Hoogwijk, A. Johnson, M.L. Rogner, H. Wagne, *Global Energy Assessment-Toward a Sustainable Future* (Cambridge University Press, Cambridge, UK and New York, NY, USA and the International Institute for Applied Systems Analysis, Laxenburg, Austria, 2011), p. 423.
15. P.V. Kamat, J. Phys. Chem. **111**, 2834 (2007)
16. Renewable Energies: The Promise of Organic Solar Cells (CNRS, ScienceDaily,2009). www.sciencedaily.com/releases/2009/04/090409151444.htm. Accessed 3 Jan 2018
17. T. Rousseau, A. Cravino, T. Bura, G. Ulrich, R. Ziessel, J. Roncali, J. Mater. Chem. **19**(16), 2298 (2009). https://doi.org/10.1039/b903189h
18. G. Martin, Third generation photovoltaics advanced solar energy conversion, in *Springer Series in Photonics*, vol. 12 (Springer, Berlin, Heidelberg, 2003)
19. M. Bazilian, I. Onyeji, M. Liebreich, I. MacGillI, J. Chase, J. Shah, D. Gieleng, D. Arenth, D. Landfeari, S. Zhengrongj, Re-considering the economics of photovoltaic power. Renew. Energy **53**, 329–338 (2013). https://doi.org/10.1016/j.renene.2012.11.029
20. R.C. Chiechi, R.W.A. Havenith, J.C. Hummelen, L.J.A. Koster, M.A. Loi, Modern plastic solar cells: materials, mechanisms and modelling. Mater. Today **16**(7/8), 281–289 (2013)
21. T.Y. Huang, D. Patra, Y.S. Hsia, S.H. Chang, C.G. Wu, K.C. Ho, C.W. Chu, Efficient ternary bulk heterojunction solar cells based on small molecules only. J. Mater. Chem. **A 3,** 10512–10518 (2015). 10.1039/C5TA00592B

22. S.S. Sun advances in solar energy: an annual review of research and development in renewable energy technologies recent progress of organic photovoltaic, in ed. by D. Yogi Goswami (American Solar Energy Society, Inc., Boulder, CO, 2007), pp. 74–98
23. J.G. Hedley, A. Ruseckas, I.D.W. Samuel, Light harvesting for organic photovoltaics . Chem. Rev. **117**(2), 796–837 (2017). https://doi.org/10.1021/acs.chemrev.6b00215
24. G. Malliaras, R.H. Friend Phys. Today **58**(5), 53(2005)
25. L.Ye, J. Hou, Organic optoelectronic materials, in ed. by Y. Li (Springer International Publishing, Switzerland, 2015), pp. 195–239
26. J. Bisquert, *The Physics of Solar Cells: Perovskites, Organics, and Photovoltaic Fundamentals*s, 1st edn. (CRC Press, 2017), pp. 46–63
27. K.M. Pelzera, S.B. Darling, Mol. Syst. Des. Eng. **1**, 10 (2016)
28. C.V. Brabec, V. Dyakonov, *Organic Photovoltaics: Materials, Device Physics, and Manufacturing Technologies*, 2nd edn. (Wiley-VCH, 2014), pp. 67–86
29. T.D. Thomas, D.T. Smith, Renew. Sust. Energ. Rev. **80**, 1372 (2017)
30. S. Tiwari, J.V. Yakhmi, S.A. Carter S.A., J.C. Scott, Handbook of ecomaterials, in ed. by L. Martínez, O. Kharissova, B. Kharisov (Springer, Cham, 2019), p. 1. 10.1007/978–3–319–48281–1_66–1
31. Yu. Zhong, M.T. Trinh, R. Chen, G.E. Purdum, P.P. Khlyabich, M. Sezen, O.S. Melda, H. Zhu, B. Fowler B., Zhang, W. Wang, C.Y. Nam, M.Y. Sfeir, C.T. Black, M.L. Steigerwald, Y.L. Loo, F. Ng, X.Y. Zhu, C. Nuckolls, Nat. Commun. **6**, 8242 (2015). 10.1038/ncomms9242
32. W. Zhao, W.S. Li, H. Yao, S. Zhang, Y. Zhang, B. Yang, J. Hou, J. Am. Chem. Soc. **139**(21), 7148–7151 (2017). 10.1021/jacs.7b02677
33. V.M.L. Corre, A.R. Chatri, N.Y. Doumon, L.J.A. Koster, Adv. Energy Mater. **7**, 1701138 (2017)
34. L. Zuo, J. Yu, X. Shi, F. Lin, W. Tang, A. K. Jen. Adv. Mater. **29**(34), 702547 (2017)
35. S. Tiwari, T. Tiwari, S.A. Carter, J.C. Scott, J. Yakhmi, Handbook of ecomaterials, in ed. by L. Martínez, O. Kharissova, B. Kharisov (Springer, Cham, 2018), p. 1103. 10.1007/978-3-319-48281-1_59-1
36. G. Martin, Third generation photovoltaics advanced solar energy conversion, in *Springer Series in Photonics*, vol. 12 (Springer, Berlin, Heidelberg, 2003), pp. 121–138. 10.1007/b137807
37. A. Facchetti, Mater. Today **16**(4), 123 (2013)
38. M.C. Scharber, N.S. Sariciftci, Prog. Polym. Sci. **38**(12), 1929 (2013)
39. D.M. Stoltzfus, J.E. Donaghey, A. Armin, P.E. Shaw, P.L. Burn, P. Meredith, Chem. Rev. **116**(21), 12920–12955 (2016). https://doi.org/10.1021/acs.chemrev.6b00126
40. E.M. Perez, Pure Appl. Chem. **83**(1), 201 (2011)
41. G. Dennler, M.C. Scharber, C.J. Brabec, Adv. Mater. **21**, 1323 (2009)
42. C.J. Brabec, N.S. Sariciftci, J.C. Hummelen, Adv. Funct. Mater. **11**, 15 (2001)
43. B.C. Thompson, J.M. Frechet, J. Angew, Chem. Int. Ed. **47**(1), 58(2008)
44. Y. Li, Y. Zou, Adv. Mater. **20**, 2952 (2008)
45. H. Hoppe, N.S. Sariciftci, J. Mater. Res. **19**(7), 1924 (2004)
46. Y. Liang, Z. Xu, J. Xia, S.T. Tsai, Y. Wu, G. Li, C. Ray, L. Yu, Adv. Mater. **22**(20), E135 (2010)
47. H. Benten, D. Mori, H. Ohkita, S. Ito, Recent research progress of polymer donor/polymer acceptor blend solar cells. Mater. Chem. A **4**, 5340–5365 (2017). https://doi.org/10.1039/c5ta10759h
48. G. Li, R. Zhu, Y. Yang, Nat. Photon. **6**(3), 153 (2012)
49. J. C. Nolasco, A. Castrocarranza, B. Iniguez, J. Pallares, M. Estrada, Int. J. High Speed Electron. Syst. **20**(04), 749 (2012)
50. A. Pivrikas, N.S. Sarıçiftçi, G. Juška, R. Österbacka, A review of charge transport and recombination in polymer/fullerene organic solar cells. Prog. Photovolt. Res. Appl. **15**(8), 677 (2007). 10.1002/pip.79
51. J.G. Hedley, A. Ruseckas, I.D.W. Samuel, Light harvesting for organic. Photovoltaics. Chem. Rev. **117**(2), 796–837 (2017). 10.1021/acs.chemrev.6b00215

52. G. Yu, J. Gao, J.C. Hummelen, F. Wudl, A.J. Heeger, Science **270**, 1789 (1995)
53. J.J.M. Halls, C.A. Walsh, N.C. Greenham, E.A. Marseglia, R.H. Friend, S.C. Moratti, A.B. Holmes, Nature **376**(6540), 498 (1995)
54. J. Peet, J.Y. Kim, N.E. Coates, W.L. Ma, D. Moses, A.J. Heeger, G.C. Bazan Efficiency enhancement in low-bandgap polymer solar cells by processing with alkane dithiols. Nat. Mater. **6**(7), 497–500 (2007). 10.1038/nmat1928; http://dx.doi.org/10.1038/nmat1928
55. J.K. Lee, W.L. Ma, C.J. Brabec, J. Yuen, J.S. Moon, J.Y. Kim, K. Lee, G.C. Bazan, A.J. Heeger, Processing additives for improved efficiency from bulk heterojunction solar cells. J. Am. Chem. Soc. **130**(11), 3619–3623 (2008). 10.1021/ja710079w88M
56. L.J.A. Koster, V.D. Mihailetchi, H. Xie, P.W.M. Blom, Origin of the light intensity dependence of the short-circuit current of polymer/fullerene solar cells. Appl. Phys. Lett. **87**(20), 203502 (2005). 10.1063/1.2130396
57. Y. Long, L. Sunsun, H. Jianhui, Polymer photovoltaics: materials, physics, and device engineering, in ed. by F. Huang, H.-L Yip, Y. Cao, 1st edn. (Royal Society of Chemistry, 2015), p. 32
58. G. Li, W.H. Chang, Y. Yang, Low-bandgap conjugated polymers enabling solution-processable tandem solar cells Nat. Rev. Mater. (2017). https://doi.org/10.1038/natrevmats.2017.43
59. D.W. Sievers, V. Shrotriya, Y. Yang, J. Appl. Phys. **100**, 114509 (2006)
60. N.K. Persson, O. Inganas, Organic photovoltaics: mechanisms, materials and devices, in ed. by S.S. Sun, N.S. Sariciftci (CRC Press, Boca Raton, Fl, 2005), p. 107
61. W. Tress, *Organic Solar Cells Theory, Experiment, and Device Simulation* (Springer International Publishing, Cham, 2014). 10.1007/978–3–319–10097–5
62. S.R. Cowan, A. Roy, A.J. Heeger, Phys. Rev. B **82**, 245207 (2010)
63. P.E. van Hutten, V.V. Krasnikov, G. Hadziioannou, Conjugated polymer and molecular interfaces: science and technology for photonic and optoelectronic application, in ed. by W.R. Salaneck, K. Seki, A. Kahn, J.J. Pireaux (Marcell Dekker, CRC Press, 2001), p. 113
64. M. Zhang, H. Wang, H. Tian, Y. Geng, C.W. Tang, Adv. Mater. **23**, 4960 (2011)
65. V.D. Mihailetchi, J. Wildeman, P.W.M. Blom, Phys. Rev. Lett. **94**, 126602 (2005)
66. W. Tress, A. Petrich, M. Hummert, M. Hein, K. Leo, M. Riede, Appl. Phys. Lett. **98**, 063301 (2011)
67. R. Swami, S. Tiwari, Recent Advances in Photovoltaic under Materials. Research Foundation Series Materials Research Forum LLC (2017), p. 334. https://dx.doi.org/10.21741/9781945291371-12
68. V. Quaschning, R. Hanitsch, Sol. Energy **56**(6), 513 (1996)
69. A. Reinders, P. Verlinde, W. van Sark, A. Freundlich, Photovoltaic solar energy: from fundamentals to applications, in ed. by P. Altermatt (Wiley, 2017). 10.1002/9781118927496.ch15
70. F. Liu, J. Zhu, J. Wei, Y. Li, M. Lv, S. Yang, B. Zhang, J. Yao, S. Dai, Appl. Phys. Lett. **104**, 253508 (2014)
71. S. Tiwari, N.C. Greenham, D. Kabra, Numerical simulation of single layer polymer light-emitting diodes. Opt. Quantum Electron. **40**(14), 1267–1272 s(2009)
72. W.Hu, E. Avrutin, J. Javaloyes, S. Sujecki, M. Swillam, Introduction to the special issue on numerical simulation of optoelectronic devices NUSOD'14. Opt. Quantum Electron. **47**(6), 1291–1292 (2015)
73. R. Stangl, C. Leendertz, J. Haschke, Solar Energy, in ed. by R.D. Rugescu (IntechOpen Limited, London, UK, 2010), p. 321. 10.5772/8073
74. S. Tiwari, S. Carter, J.C. Scott, Optical simulation of quantum dot thin film solar cells. IEEE Recent. Adv. Photon. 14651212 (2014). 10.1109/WRAP.2013.6917711
75. J. Krc, M. Topic, *Optical Modeling and Simulation of Thin-Film Photovoltaic Devices*, 1st edn. (CRC Press, 2013), pp. 3–34
76. A. Čampa, J. Krč, M. Topič, Analysis and optimization of microcrystalline silicon solar cells with periodic sinusoidal textured interfaces by two-dimensional optical simulations. J. Appl. Phys. **105**(8) (2009). 10.1063/1.3115408
77. A.K. Ghosh, T. Feng, J. Appl. Phys. **49**(12), 5982 (1978)

78. E. Gondek, Optical optimization of organic solar cell with bulk heterojunction. Opto−Electron. Rev. **22**(2), 77–85 (2014). 10.2478/s11772−014−0180−4
79. X. Zhao, B. Mi, Z. Gao, W. Huang, Sci. China Phys. Mech. Astron. **54**(3), 375–387 (2011). https://doi.org/10.1007/s11433-011-4248-6
80. S.F. Rowlands, J. Livingstone, C.P. Lund, Sol. Energy **76**(1–3), 301 (2004)
81. Y.M. Nam, J. Huh, W.H. Jo, Sol. Energy Mater. Sol. Cells **94**, 1118 (2010)
82. A.J. Moulé, J.B. Bonekamp, K. Meerholz. J. Appl. Phys. **100**, 094503 (2006)
83. P.P. Gunaicha, Optical modelling of solar cells. Theses and dissertations, The University of Toledo Digital Repository 325 (2012)
84. L.A.A. Pettersson, L.S. Roman, O. Inganäs, J. Appl. Phys. **86**(1), 487 (1999)
85. O. Heavens, *Optical Properties of Thin Solid Films* (Dover, 1991), pp. 46–95
86. G.F. Burkhard, E.T. Hoke, M.D. McGehee Adv. Mater. **22**, 3293 (2010)
87. W. Tress, *Modelling Organic Solar Cells: Theory, Experiment, and Device Simulation* (Springer International Publishing, Switzerland, 2015), pp. 215–271. 10.1007/978–3–319–10097–5
88. M.R. Merad Boudia, A. Cheknane, B. Benyoucef, A.M. Ferouani, H.S. Hilal, Evol. Trends Eng. Technol. **3**, 30 (2014)
89. S. Jung, K.Y. Kim, Y.I. Lee, J.H. Youn, H.T. Moon, J. Jang, J. Kim, Jpn. J. Appl. Phys. **50**, 122301 (2011)
90. P. Peumans, A. Yakimov, S.R. Forrest, J. Appl. Phys. **93**(7), 3693 (2003)
91. C.H. Poh, L. Rosa, S. Juodkazis, P. Dastoor, Opt. Mater. Express **1**(7), 1326 (2011)
92. H. Hoppe, N. Arnold, N.S. Sariciftci, D. Meissner, Sol. Energy Mater. Sol. Cells **80**(1), 105 (2003)
93. H. Hoppe, N. Arnold, D. Meissner, N.S. Sariciftci, Thin Solid Films **451–452**, 589 (2004)
94. A. Cheknane, T. Aernouts, M. MeradBoudia, Revue des Energies Renouvelables ICRESD-07, Tlemcen, 267 (2007)
95. J.A. Barker, C.M. Ramsdale, N.C. Greenham, Phys. Rev. B **67**, 075205 (2003)
96. C.D. Smith, J. Nelson, Y. Li, Organic solar cells (2018), pp. 567–597. 10.1016/B978–0–12–809921–6.00015-X
97. C.D. Smith, J. Nelson, *Solar Cells Materials, Manufacture and Operation*, 2nd edn., in ed. by A. McEvoy, L. Castañer, T. Markvart (Elsevier Science, 2013). 10.1016/C2011–0–07789-X
98. P. Cusumano, C. Arnone, M. A. Giambra, A. Parisi, Electronics **9**, 70 (2020). 10.3390/electronics9010070
99. L. Lu, T. Zheng, Q. Wu, A.M. Schneider, D. Zhao, L. Yu, Chem. Rev. **115**, 12666 (2015). https://doi.org/10.1021/acs.chemrev.5b00098
100. M. Niggemann, M. Glatthaar, A. Gombert, A. Hinsch, V. Wittwer, Thin Solid Films **451–452**, 619 (2004)
101. S.D. Zilio, K. Tvingstedt, O. Inganäs, M. Tormen, Microelectron. Eng. **86**(4–6), 1150 (2009)
102. K. Tvingstedt, S.D. Zilio, O. Inganäs, M. Tormen, Opt. Express **16**(26), 21608 (2008)
103. T.H. Reilly, J. v.de Lagemaat, R.C. Tenent, A.J. Morfa, K. L. Rowlen, Appl. Phys. Lett. **92**(24), 243304 (2008)
104. S. Gunes, Energy efficiency and renewable energy through nanotechnology, in ed L. Zhang (Springer, London, 2011). 10.1007/978–0–85729–638–2
105. A. Cominetti, G. Serrano, A. Savoini, C. Carbonera, F. Melchiorre, S. Perucchini, A. Congiu, G. Corso, R. Barbieri, E. Trippodo, A. Caneschi, R. Po, physica status solidi (a), 1901023 (2020)

Nanostructured Black Silicon for Efficient Thin Silicon Solar Cells: Potential and Challenges

Sanjay K. Srivastava, Prashant Singh, Avritti Srivastava, P. Prathap, Sushil Kumar, C. M. S. Rauthan, and D. K. Aswal

Abstract The world's energy system is at crossroads as the natural fossil fuels are becoming increasingly unavailable and more expensive. Thus, the usage of various renewable energy (RE) sources to provide environmentally benign, economically feasible and sustainable energy supply is drawing more attention to meet ever-increasing energy demands. Among the various RE sources, solar energy has the potential to provide energy independence and security of supply to every economy. Among the possible solutions, the deployment of photovoltaic (PV) modules to directly convert solar radiation into electricity is one of the best choices. The PV is one of the promising technologies to provide a feasible carbon-free route to replacing nonrenewable power sources worldwide. However, the limited performance to cost ratio for the present market-dominating silicon (Si) wafer PV modules restricts large-scale civil utilization of solar electricity. One of the basic costs for Si PV cells is the starting Si wafer itself, which requires several extensive purification to maintain the reasonable performance of the device. Thus, developing PV devices of high performance to cost ratio has always been in demand. Researchers are trying to explore solar cell designs via an unconventional method, aiming at cost reduction and performance improvement. One of the growing potential approaches is PV designs based on nano-architectured materials with low cost and advanced optical and electrical management properties. Micro-and nanostructured Si surfaces are well known for their applications in Si micro-and optoelectronic devices, particularly in solar PV. A particular class of nanostructured silicon is called black silicon. The black Si concept is a promising approach to eliminate front surface reflection (<2% in broad spectral range) omnidirectionally in PV devices without the need for a conventional anti-reflection coatings (ARC). Besides, strong light-trapping can also be achieved for weakly absorbed photons with energies close to the absorption edge of Si and might lead to both an increase in efficiency as well as a reduction in the fabrication costs of solar cells. The nanostructured black Si surfaces, suitable for solar cell applications, have been fabricated by various methods such as metal-assisted wet-chemical etching (MACE), dry reactive ion etching (RIE), etc. In the chapter, a brief introduction of PV

S. K. Srivastava (✉) · P. Singh · A. Srivastava · P. Prathap · S. Kumar · C. M. S. Rauthan · D. K. Aswal
CSIR-National Physical Laboratory, New Delhi 110012, India
e-mail: srivassk@nplindia.org; sksrivastava78@gmail.com

S. Kumar and D. K. Aswal (eds.), *Recent Advances in Thin Films*, Materials Horizons: From Nature to Nanomaterials, https://doi.org/10.1007/978-981-15-6116-0_18

technology is presented along with the current status of Si wafer based solar cells. Various challenges/losses associated with conventional solar cell technology with an emphasis on addressing the optical/reflection losses are also discussed. Efforts made to minimize these losses with an emphasis on minimization of reflection losses through nanostructuring schemes are discussed. Moreover, an attempt is made to present a review on the recent progress of black Si research for solar cell technologies. First, MACE technique for the preparation of black Si is discussed in detail along with a brief critical analysis with respect to advantages and disadvantages for solar PV applications. The applications of black Si in solar cells and the progress over the years are then summarized. In addition, one of the major challenges of black Si cell is enhanced surface recombination which imposes a critical limit to solar cell efficiency especially in thinner solar cells. Hence, an efficient black Si solar cell can only be obtained if an optimal trade-off between light absorption gain and electrical losses (due to recombination) is achieved for the black Si-based PV technology. The dielectric thin films play a critical role in effective surface passivation of the black Si surfaces. Therefore, the current status of passivation schemes and challenges for black Si solar cell technology is also highlighted. Moreover, the current status of black Si solar cells concepts employing both monocrystalline, multicrystalline Si as well as the concept of thin/flexible silicon solar cells towards high-efficiency solar cells is reviewed critically. Finally, conclusions and future prospects of the black Si concept is outlined wherein it is envisaged that nanostructured black Si will play a key role in cost-effective and efficient solar photovoltaic devices in days to come.

1 Introduction

Modern society largely depends on energy consumption and energy for civilization is like food for humans. The energy is used for heating in our houses, transport, goods production, communication, food, and even for everything like reading this chapter. Energy is never produced --it is always converted from one form to another to make it a more usable form of energy. Humanity developed many different methods of energy conversion. The most prosperous and technologically developed countries consume the most energy per inhabitant [1]. However, their economies are relatively stable and do not show rapid growth and, therefore, an increase in power consumption. While developing countries, according to the World Energy Outlook (WEO) [2], display 30% growth of energy consumption and at the same time these countries have the highest birth rate leading to an increase in the global population. In May 2017, the world population was 7.5 billion people [3] and consumed 12.3 TW of power [4], and by 2050 the world population would be around 10 billion [5, 6] with the projected energy need for 18–20 TW or 16–18 billion tonne of oil equivalent (toe); (1 toe = 11.63 MW) [4]. It is the so-called supply–demand energy challenge and it could be and would be solved by increasing the total energy production [1]. A second challenge is that our energy infrastructure heavily depends on fossil fuels, like oil, coal and gas. Fossil fuel resources, due to our intensive use, would be depleted in

a while. Furthermore, by burning fossil fuels, we produce greenhouse gases (GHGs) like carbon dioxide, methane, nitrous oxide, hydrofluorocarbons, perfluorocarbons, sulphur fluoride, etc. in the atmosphere. This has led to increased entrapment of insolation in the atmosphere which has increased the earth's global average temperature by ~1 °C over the period 1885–2016. Increase in temperature is having a range of effects such as sea-level rise, putting some of the biggest metropolis such as New York, Mumbai, etc. at the risk of inundation; increase in the frequency of extreme weather events; adverse impact on agricultural output in relatively more productive lower latitude areas due to disturbance in the climatic pattern; retreat of glaciers such as arctic sea ice which in turn is increasing GHGs emission and worsening the scenario; increasing oceanic temperature leading to migration of fishes to higher latitudes; acidification of ocean leading to coral bleaching; adversely affecting human health, etc. [7–11]. There have been educated speculations about the extinction of human species itself in not-so-distant future as survival, and extinction, of human species is inextricably linked to the health of the planetary ecosystem which appears to be in irreversible decline [12]. All these horrific changes are in part due to the consumption of fossil fuels, which emit GHGs as undesirable by-products [13]. These changes forced world leaders to engage in discussions to take coordinated measures to reduce the consumption of fossil fuels in particular and stop climate change in its tracks. At the 21st Conference of Parties, world leaders committed themselves to hold the global average temperature increase to well below 2 °C above pre-industrial levels and pursue efforts to limit the increase to 1.5 °C [14].

1.1 Photovoltaics as an Alternative Energy Source

Any viable and sustainable effort at reducing GHGs emission has to take into account the aspiration of developing and least developed countries to attain living standards comparable to industrialized countries of North which is resource intensive and puts a higher premium on energy. Thus not only humanity has to evolve alternative, environmentally benign sources of energy, to fight the menace of climate change, but also transition to a socio-economic system where the marginal environmental cost to economic growth is progressively lower and lower. Realization of former goal hinges around harnessing energy sources that do not emit GHGs which undoubtedly are renewable sources of energy. The renewable energy could solve all of the above challenges. Renewable energy carriers are energy carriers that can be replenished by natural processes at the rate comparable to or faster than human consumption. Hydro, wind and solar energy are renewable energy resources. However, sources such as hydroelectricity, nuclear do not enjoy public trust due to understandable safety issues. Public suspicion of nuclear power has become more pronounced due to an accident at Fukushima Daichi nuclear plant in Japan. Increasing the frequency of extreme weather events is posing a serious risk to the viability of dams and hydroelectric power plants. These are also prone to geological activities.

Earth intercepts around 1,73,000 TW of solar energy continuously which is more than 10,000 times the entire planet's energy consumption [15]. Thus there is only a need for technological capability to harness it. Thus solar energy especially solar photovoltaic (PV) emerges as a mature and trustworthy technology in a bigger bracket of renewable energy technologies. That is the reason why it has witnessed an average annual growth rate of 50% in recent years [16]. Solar photovoltaic (SPV) is particularly important in solar energy technologies as it is quite easier to install it at an individual/household level and hence entire power evacuation infrastructure is not needed which requires huge upfront capital investment. The cost of solar cell electricity can be lowered by decreasing the production cost increasing power output. For PV to be competitive, the cost of modules should be below 1$/W and cells price—below 30 cents/W. The global PV industry is experiencing a rapid growth with a global installed capacity of 97.5 GWp in 2017 alone and a cumulative installed capacity of 405 GWp at the end of 2017 [17] with a compound annual growth rate of ~24% from 2010 to 2018 and 505 GWp at the end of 2018 [18]. The annual global market for PV increased only slightly in 2018, but enough to surpass the 100 GWp level (including on- and off-grid capacity) for the first time. Cumulative capacity increased approximately 25% to at least 505 GW; this compares to a global total of around 15 GW only a decade earlier (See Fig. 1). Despite the single-digit growth rate of the global market in 2018, solar PV has become the world's fastest growing energy technology, with gigawatt-scale markets in an increasing number of countries. Demand for solar PV is spreading and expanding as it becomes the most competitive option for electricity generation in a growing number of markets—for residential and commercial applications and increasingly for utility projects [18].

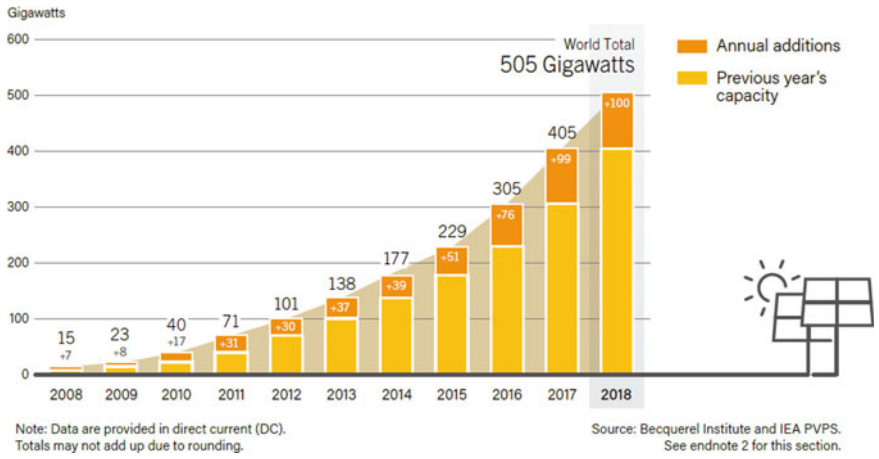

Fig. 1 Solar PV global capacity and annual addition, 2008–2018 [18]

1.2 Why Silicon Photovoltaic?

Silicon (Si)-based SPV have emerged as one of the most attractive pillars of clean energy architecture. This is mainly because of four reasons: stable power output over more than two decades; silicon being second most abundant material in earth's crust; non-toxicity of Si in bulk and; readymade technical know-how of Si due to pioneering efforts of the microelectronics industry. Also, despite initial promises, thin film based solar cells have not been up to expectation and the SPV market is still dominated by crystalline (c) and multicrystalline (mc) silicon based solar cells. In the recent past due to price reduction across the entire value chain combined with larger packing fraction of mc-Si solar cells at the module level, mc-Si based solar cells are outpacing c-Si-based solar cells, despite c-Si having edge over mc-Si at cell level due to recombination in latter at the grain boundaries, for a similar level of technology deployment [19]. Figure 2a shows the price trend for silicon-based solar cells, and it has exponentially decreased since 1977. The cumulative PV capacity over the past decades allowed PV module cost reduction. This dependency is represented as logarithmic Swanson's Law learning curve in Fig. 2b [20]. The price drop for silicon over time became possible due to the fact that Si had been dominating materials and technology in the semiconductor industry as well as in the photovoltaic industry for several decades. Si shared more than 90% of the total PV market splitting it shares between different Si-based technologies: multicrystalline Si (mc-Si) (60.8%), monocrystalline Si (c-Si) (32.2%), amorphous Si (a-Si) (0.3%) in 2017 according to Fig. 3 [17]. The total share of thin-film technologies is 4.5% in which CdTe has the maximum share (2.3%), followed by CIGS (1.9%) and last is a-Si (0.3%). Such significant market shares led to the development of different Si-based PV technologies and cell designs with efficiency above 20% up to 26.7% [21].

Nevertheless, many different promising PV technologies could promise a combination of high power conversion efficiency and low production cost, but Si has a

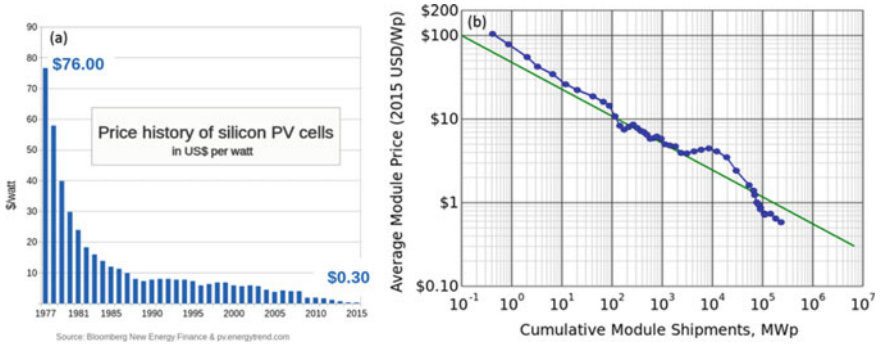

Fig. 2 **a** Price reduction for silicon PV cells since mass production started in 1977 till 2015, **b** Swanson's learning curve for silicon PV modules [20]

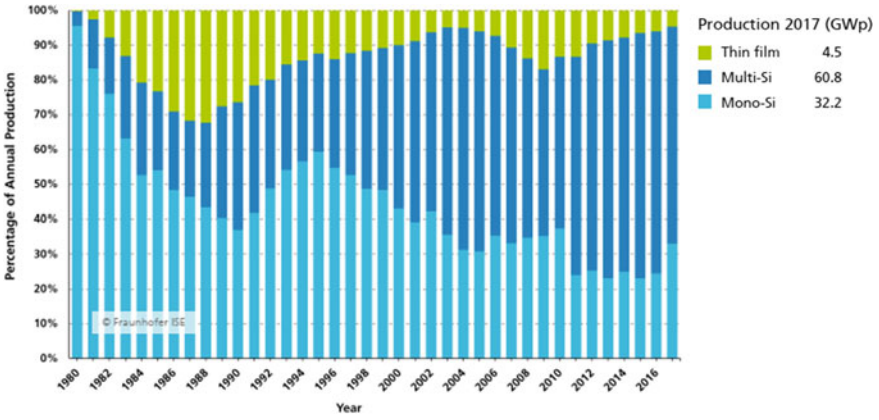

Fig. 3 Global PV production by technology: Percentage of the global annual production of PV by technology (from 1980 to 2017) [17]

huge potential for its further usage in the PV industry. Development of new technologies that could optimize one or another parameter (either to improve efficiency or reduce production cost or both) will keep Si as a PV market dominant further at least for several decades. Thus, Si solar cells are the most promising technology as a renewable energy source that can guarantee a sustainable future for us and our future generations.

2 Solar Cell: Basics

2.1 Solar Cell Basic Structure

Basic structure of a typical p-n junction silicon solar cell is shown schematically in Fig. 4a. Immense work has been done on solar cells and its operation is well understood. A device must have three properties to behave as solar cells:

(1) device must be able to absorb incident radiation to generate excess, unbound and mobile electron and hole pairs,
(2) a steady population of electrons and holes has to be maintained by suppressing their recombination before they get collected,
(3) the electron and hole pairs must be spatially separated at the space charge region (diffused p-n junction) or Schottky junction and eventually collected by electron and hole collection terminals to drive current through the external circuit.

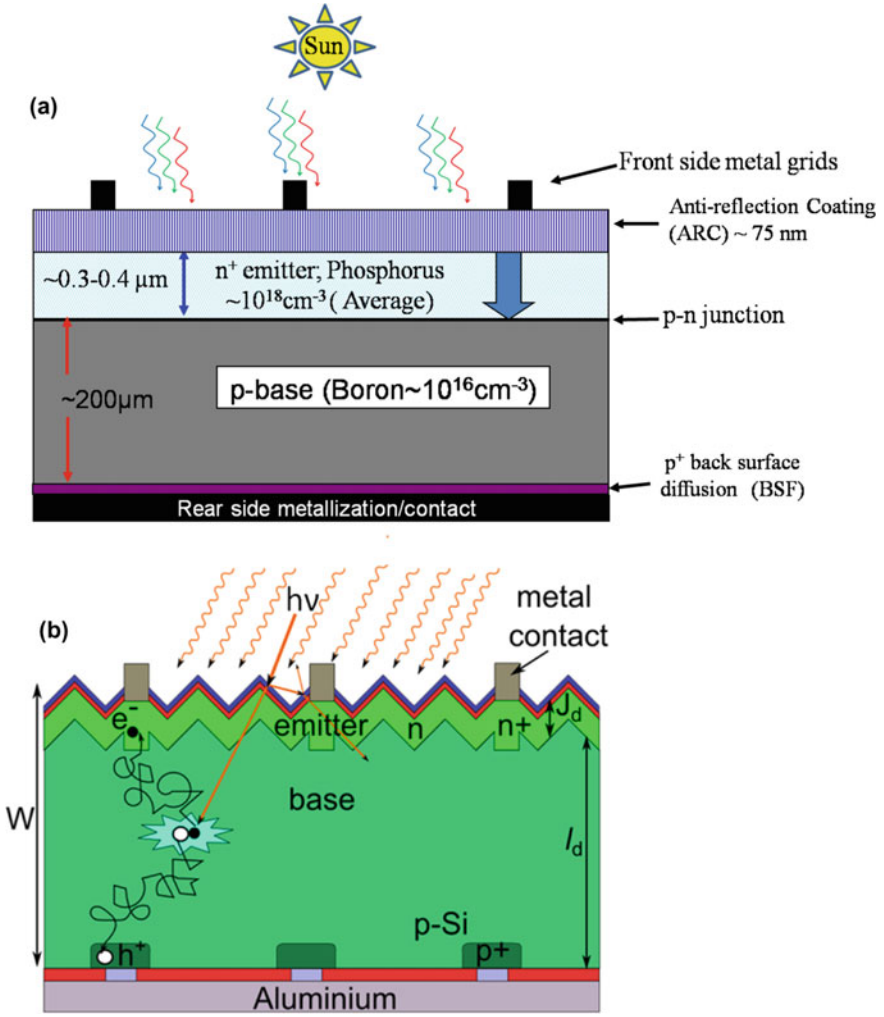

Fig. 4 **a** Schematic of a typical basic structure of flat-plate (planar) p–n junction silicon solar cell. All the layers are labelled. **b** Schematic of an advanced Si solar cell with ARC and surface (μ-pyramids) texturing. In this scheme, typical cell thickness, W = 200 μm, is used to absorb the light and the charge carriers collection is primarily from the diffusion region (l_d) where $l_d >> J_d$, the junction drift region. Further, the light absorption and carriers collection in the same direction (longitudinal to the solar cell surface). Also, the concept of front and back surface passivation is employed. Instead of full area BSF, localized BSF (p^+) is used in the rear side. And selective emitter (high doping under the metal contacts and relatively light doping in light active regions) is also used **b**. Reprinted/adapted by permission from Springer: Ref. [332], Copyright (2016)

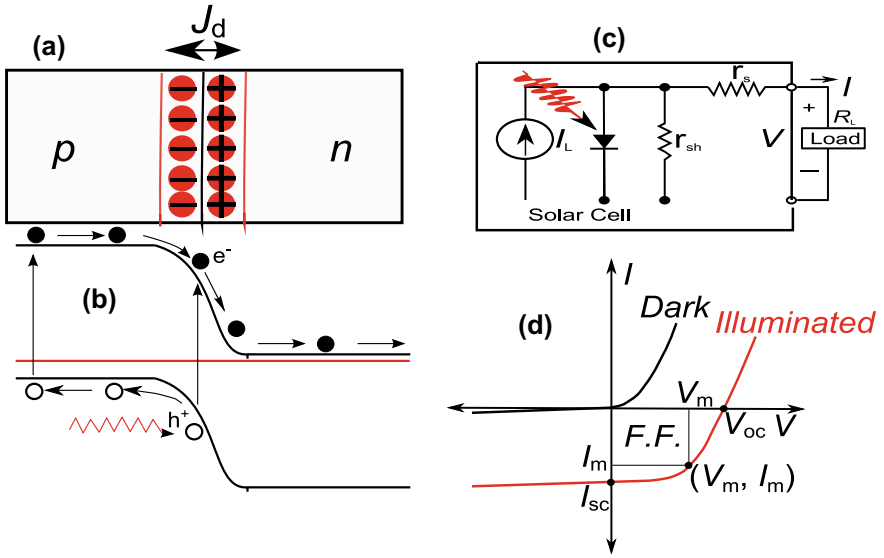

Fig. 5 **a** Top is schematic of a p–n junction showing depletion region (J_d) with ionized immobile dopant charges; **b** bottom is the correspondent energy-band diagram. Incident light creates an electron–hole pair that is swept across the junction by the in-built drift electric field to the charge-neutral regions. **c** An equivalent circuit of a practical solar cell connected to an external load (R_L). In the circuit, parasitic resistances, series (r_s) and shunt (r_{sh}) are also shown. **d** Typical I–V characteristics of a p–n junction solar cell under dark and illumination conditions. The solar cell's basic performance parameters are also shown in the I–V characteristics. Reprinted/adapted by permission from Springer: Ref. [332], Copyright (2016)

The quality or performance solar cell is evaluated by using its dark and illuminated I–V (or J–V) characteristics. There are different performance parameters such as open-circuit voltage, short-circuit current, fill factor, dark saturation current, maximum power point and power conversion efficiency (PCE).

The solar cell operation principle can be understood from Fig. 5. It is based on an unbiased p-n junction diode connected to a load (R_L) to generate power [22, 23]. There is a region of high (in-built) electric field, called the depletion region (labelled as J_d), at the junction of the p- and n-type semiconductors where photo-generated charge carriers (electrons and holes) are separated by the in-built electric field, producing a current. In addition, carriers generated in either the p- or n-type regions within a minority charge carrier diffusion length (I_d) of the depletion region can be collected at the junction and contribute to the total current. The key criteria for efficient solar cells are high absorption of the incident light in the active region of carrier collection and minimal loss of carriers due to recombination (bulk and surface defects). Conventional wafers-based crystalline silicon solar cells rely primarily on thick diffusion regions (~200 μm), compared to the much thinner drift region (J_d), for carrier collection as schematically illustrated in Fig. 4b. This scheme is inevitable due to the poor absorption of light by silicon across the solar spectrum [22], and

therefore relatively thick Si is used to absorb the incident light effectively in a wide spectral range. However, as illustrated in the cross-sectional view of typical high-efficiency planar silicon solar cell geometry (Fig. 4b), the charge carriers generated away from the junction have to diffuse long distances to reach the junction (without recombination) for collection, and therefore requires large diffusion length. This requirement restricts the quality of the silicon materials to be reasonably high. Thus, high-efficiency silicon solar cells require defect-free material with long minority carrier lifetimes (or large diffusion lengths). The current record efficiency under terrestrial illumination conditions (AM 1.5 G, 100 mW/cm^2) for silicon solar cell is 26.7% [21]. This efficiency is quite close to the maximum theoretical efficiency ~31% predicted for a single-junction solar cell by Shockley–Queisser, also known as Shockley–Queisser limit [22]. However, the fabrication costs are quite high for such record efficiency cells. Commercial silicon solar cells' efficiency typically ranges from ~17 to 23% depending on solar cell structure and design [21, 24, 25].

2.2 Solar Cell Basic Parameters

The expression for net current (I) flowing across the load can be expressed as

$$I = I_{\mathrm{L}} - I_0\{\exp(q(V + \mathrm{Ir_s})/\mathrm{nkT}) - 1\} - (V + \mathrm{Ir_s})/r_{\mathrm{sh}}\}$$

I_{SC}: short-circuit current; J_{sc}: short-circuit current density

I_{L}: light generated current,

I_0: dark saturation current,

$V_{\mathrm{OC}} = \mathrm{kT/q}\{\ln(I_{\mathrm{L}}/\mathrm{I_o}) + 1\}$: open-circuit voltage {since at V_{oc}, $I = 0$)

where k is Boltzman's constant, T temperature in Kelvin, q as the electronic charge.

V_{m} and I_{m}: Operating point yielding the maximum power output

Fill Factor ($F.F.$) = $V_{\mathrm{m}}\, I_{\mathrm{m}}/V_{\mathrm{OC}}\, I_{\mathrm{SC}}$

Power conversion efficiency (η):

$$\eta = P_{\max}/P_{\mathrm{in}} = V_{\mathrm{m}} I_{\mathrm{m}}/P_{\mathrm{in}} = F.F.V_{\mathrm{OC}} I_{\mathrm{SC}}/P_{\mathrm{in}}$$

In solar cell operation, generally, the key aim is to generate power by (1) generating a large short-circuit current, I_{sc}, (2) a large open-circuit voltage, V_{oc} and (3) minimize parasitic power loss mechanisms (particularly series and shunt resistances), and therefore maximize the fill factor ($F.F.$) [22, 23].

2.2.1 Open-Circuit Voltage

The open-circuit voltage (V_{oc}) is the voltage at which no current flows through the external circuit. It is the maximum voltage available from the device when the circuit

current is zero, and it defines the operating regime of the solar cell. A solar cell delivers power only in the region from 0 to V_{oc}. The above equation shows that V_{oc} depends on the saturation current (I_0) of the solar cell and the photogenerated current (I_L). While I_L typically has a small variation, the key effect is the saturation current, since this may vary by orders of magnitude. The saturation current depends on the recombination in the solar cell. In devices where minority carrier lifetime is low (caused by poor quality material, flawed processing steps or device design, etc.) its open-circuit voltage tends to be low and vice versa.

2.2.2 Short-Circuit Current

The short-circuit current, $I_{sc,}$ is the current that flows through the external circuit when the electrodes of the solar cell are short-circuited. The short-circuit current of a solar cell depends on the photon flux density incident on the solar cell, which in turn is determined by the spectrum of the incident light. I_{sc} depends upon the area of the solar cell and hence it is an extensive variable. I_{sc} is divided by the area of solar cell to arrive at short-circuit current density (J_{sc}), which is an intensive variable.

2.2.3 Fill Factor (FF)

The purpose of a solar cell is to deliver power to an external device or load such as a bulb. The fourth quadrant of the illuminated I–V curve (see Fig. 5d) shows the regime under which solar cell can deliver power. In this quadrant, a point can be found where the power reaches its maximum value. This point is called the maximum power point (P_{max}). The fill factor is defined as the ratio of the maximum output power ($V_{mp} \times I_{mp}$) to the product of V_{oc} and I_{sc}. V_{mp} and I_{mp} represent the maximum voltage and maximum current at the point on the illuminated I–V curve the cell delivers maximum electrical power to the external circuit. The fill factor *(FF)* is a measure of the diode characteristic of the solar cell. The higher the number, the more ideal the diode is. Ideally, the fill factor should be unity, but due to transport (parasitic resistances) and recombination losses, its value gets reduced. The direct relation of *FF* with current density indicates that it is greatly affected by the mobility of the charge carriers. In order to obtain a high fill factor, the shunt resistance of a photovoltaic device has to be very large, in order to prevent leakage currents, and series resistance has to be very low. As such the value of series resistance and shunt resistance for an ideal solar cell are zero and infinite, respectively.

2.2.4 Dark Current

The dark current is the current through the diode when no light is incident on the device. This current is due to the ideal diode current, the generation/recombination of carriers in the depletion region and any surface leakage, which occurs in the diode.

When a load is applied in forward bias, a potential difference develops between the terminals of the cell. This potential difference drives a current, which acts in the opposite direction to the photocurrent, and the net current is reduced from its short-circuit value. This reverse current is usually called dark current in analogy with the current $I_{\text{dark}}(V)$, which flows across the device under an applied voltage in the dark. Solar cells behave like a diode in the dark, admitting a much larger current under the forward bias ($V > 0$) than under reverse bias ($V < 0$). Larger the dark current lower is the device performance, i.e. its ability to deliver power. The dark current is an indirect manifestation of lower minority carrier lifetime (poor semiconductor material), poor solar cell design and processing.

2.2.5 Power Conversion Efficiency

The power conversion efficiency (PCE) or simply efficiency (η) is the most widely used parameter to assess the performance of a solar cell. It is defined as the ratio of the maximum output electrical power to the total incident solar power density (P_{in}). The PCE depends on the intensity of the incident light on the device, temperature of the device, minority carrier lifetime, design of the solar cell and the ability of the device to harness the incident energy. Power conversion efficiency of the solar cell reflects the capability of the solar cell to convert the incident light into electrical power.

2.2.6 Maximum Power Point (P_{max}, V_{mp}, I_{mp})

As discussed above, the maximum power point is the point on the illuminated I–V (or J–V) curve of the solar cell where the product of voltage (V) and current density (J) or current (I) is the maximum. At this point, the device delivers the maximum power.

2.2.7 Standard Test Conditions (STC) for Solar Cells

The efficiency of a solar cell depends upon the host of parameters. To establish a scientific comparison of the performance of different solar cells and also to estimate the capability of the solar cell to deliver power, the standard test conditions have been designed. These test conditions are based on a spectral distribution, reflection of the emission spectrum of the sun, measured on a clear sunny day with a radiant intensity of 100 mW/cm^2 (or 1000 W/m^2) that is received on a tilted plane surface with an angle of incidence of 48.2°. This spectrum that also counts for a model atmosphere containing specified concentrations of, e.g. water vapour, carbon dioxide and aerosol is referred to as an 'Air Mass 1.5 Global' (AM1.5G, IEC 60904-3) spectrum. These standard test conditions also include a measuring cell temperature of 25 °C.

2.3 Solar Cell Losses

2.3.1 Quantum Losses

This mode of loss is due to inefficient utilization of solar spectrum by Si-based solar cells. This limitation arises due to the band gap of the semiconductor. Si has 1.12 eV band gap. Therefore, photons having energy less than 1.12 eV are of no use in solar cell output. Similarly, the extra energy of photons having high energy (>1.12 eV) is lost in non-radiative losses producing heat in the device only.

2.3.2 Recombination Losses

Incident radiation with energy higher than 1.12 eV excites an electron from the valence band to the conduction band of Si substrate. This process generates two charged particles of opposite polarity; electron in the conduction band and hole in the valence band. These generated electron and hole pairs are then separated by either diffused junction (p–n) or Schottky junction and collected at the terminals for doing work in the external circuit. However, all the electron–hole pairs generated, by the incident radiation, do not get collected at the terminals due to the recombination of electron and hole pairs before getting separated and eventually collected. Thus recombination process does not allow the generated electron–hole pairs to reach the terminal and contribute to the current thus lowering the device efficiency. Based on recombination sites it can be divided into two types; (i) surface recombination and; (ii) bulk recombination.

Surface recombination occurs at both the front and rear side of the substrate. Si has four valence electrons. Si atoms present at the surface has one non-bonded electron and three covalently bonded. Dangling bonds of Si become diversion route for the generated electron–hole pair and reduction in current in the external circuit. Short-wavelength radiation is absorbed near the front of the Si substrate. Therefore, front surface recombination is relatively more effective in lessening current than other recombination modes. To avoid this recombination front surface is usually passivated through application of SiO_2, SiN_x, etc. A Similar process operates at the rear side of the device to lessen the total current. Rear side recombination is lessened through the application of back surface field (BSF), which suppresses the diffusion of minority carriers towards the back surface and their recombination with the unpassivated dangling Si bonds. Bulk recombinations are those which occur within the Si substrate due to various structural defects and other impurity related defects.

2.3.3 Resistive Losses

A solar cell possesses both shunt and series resistance, which lowers the fill factor of the device and hence the power conversion efficiency of the solar cell. These are also known as parasitic resistive losses. Low shunt resistance is a processing flaw and negatively impacts the performance of the device and also the life cycle of it. Series resistance of the device is required to be lower for optimum power conversion efficiency. It is determined by the top contact design and material, emitter resistance, resistance of the bulk material and the back contact of the device. If the bus bar and the fingers of the top contact are widely spaced reflection losses are lower and the series resistance is higher. On the other hand, if the bus bar and the top contact are closely spaced then reflection losses are higher but series resistance is higher. Thus, there is a trade-off between the reflection losses, to be discussed in the next section, and series resistance.

2.3.4 Reflection Losses

Polished planar silicon surface, with characteristic silver-grey colour, both monocrystalline and multicrystalline, have ~36–38% of solar weighted reflectance (SWR) in the spectral range, 300–1100 nm, the spectral range is useful for silicon-based solar cells. This implies that more than one-third of insolation over these surfaces/substrates is reflected back without contributing anything to energy production. The reflection loss is one of the major limiting factors for silicon solar cell performance (on efficiency). Monocrystalline and multicrystalline silicon require different but similar approaches to suppress reflection and enhance the absorption of the incident radiation.

3 Conventional Methods of Light Tapping/Harvesting in Silicon Solar Cells: *Microscale Textures and Anti-reflection Coatings*

As mentioned in the previous section both mono- and multicrystalline silicon reflect more than one-third of the incident radiation which prevents the solar cell from achieving its potential efficiency [26–29]. Three broad strategies are adopted for the reduction of reflectivity of mono- and multicrystalline silicon; application of a quarter-wavelength layer of dielectric such as silicon nitride, titanium oxide, etc., to reduce reflection (also called as anti-reflection coatings), modification of surface topography of both mono- and multicrystalline silicon and a suitable combination of both [30]. Among these, the combination of microscale texturing and the anti-reflection coating is the most common. However, the quarter-wavelength structures

of the dielectrics are resonant structure and work effectively only in a limited spectral range [30]. These are unstable and expensive to fabricate both in terms of material and time. These also require handling of life-threatening gases such as silane which further raises the budget of the process. Modification of surface topography is comparatively cheaper though it leads to manifold enhancement in the surface area and the number density of dangling bonds, and therefore requires passivation which again invites either use of silicon dioxide or silicon nitride or such other layers [30]. Surface modification is accomplished through "top-down" and "bottom-up" approaches" depending upon whether the surface topography is modified through etching out selected/predefined regions of the substrate or some structure is assembled from scratch, respectively. Surface modification can also be divided into physical and chemical processes depending upon the method adopted to modify the surface topography [31].

The wet chemical approaches, among several available approaches, are the most common ones, and are used for the surface modification of silicon and have been adopted to fabricate randomly distributed, microstructures over Si surface [26–29]. These can be periodic structures predefining patterns using masks and random such as uncontrolled wet etching without predefining any pattern. Periodic microstructures are advantageous in lowering reflectivity over non-periodic ones [32]. But the non-periodic are easier to fabricate than periodic microstructure. Microstructures have been able to bring down the SWR to ~12–14% [26–29]. However, 12% is still a major loss and to lower down weighted reflectivity further nanoscale texturing, to be discussed in the next section, is used. The microscale texturing of monocrystalline Si (c-Si) is carried out in aqueous alkaline solution (such as KOH, NaOH, etc.) containing some moderator such as isopropyl alcohol (IPA) in controlled condition. This produces micro-pyramids of random size and distribution on the silicon surface and can reduce SWR to 12–14% in 300–1100 nm spectral range (see Fig. 6). However, the conventional alkaline texturing scheme of c-Si cannot be applied to multicrystalline Si (mc-Si) [33, 34], which is increasingly outpacing c-Si [35], due to random orientation of grains and hence there is a major lacuna in this approach.

For mc-Si, the acidic texturing technique is being used, similar to microtexturing of c-Si, which leads to randomly oriented hemispherical structures on the micrometre scale [33, 34]. This is called 'stain etching' (or acidic etching), which uses a solution of hydrofluoric acid and nitric acid, both in comparable amounts, and sometimes acetic acid is also added to moderate the reaction rate [29, 30]. If the concentration of nitric acid (HNO_3) is higher than hydrofluoric (HF) acid, then isotropic etching of wafer takes place and this etching solution is used to remove the wire and saw damages from the silicon wafer surfaces (see Fig. 7). In the acidic etching approach, the SWR as low as 20–25% could be achieved in the spectral range 300–1000 nm [33, 34].

It is clear that only the microtexturing schemes discussed above (in both c-Si and mc-Si) is not sufficient to reduce the reflection losses to a minimum. As a consequence, the microtextured substrate is used in combination with vacuum coating of quarter-wavelength single or multiple (stack) layers of dielectric thin films such as silicon nitride (SiN_x) or titanium oxide (TiO_x), etc., which also passivates the surface

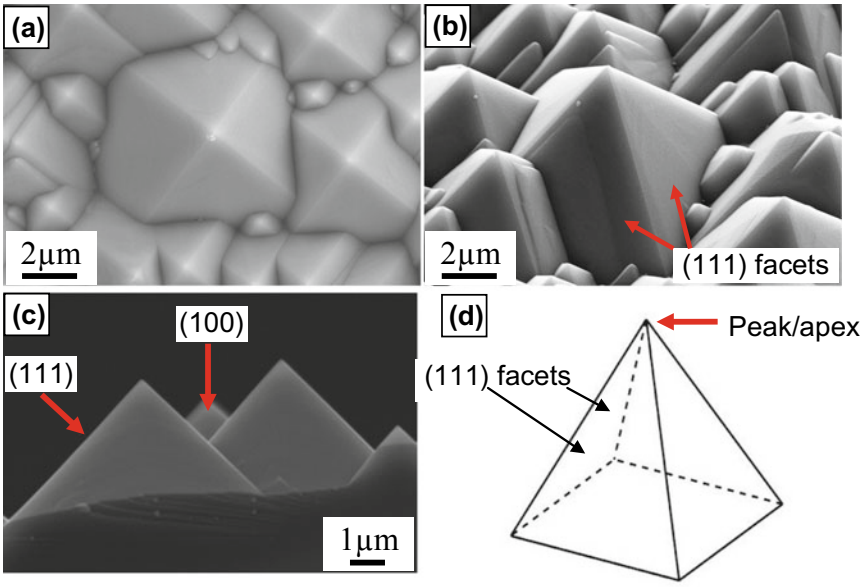

Fig. 6 Typical alkaline textured micro-pyramids on silicon (100) wafers. SEM images of micro-textured Si (100) samples; **a** top planar view, **b** tilted (45°) view, and **c** cross-sectional view of the micro-pyramids formed after 60 min texturization in aq. KOH solution. **d** outline of a typical pyramid indicating the four facets (111) and the apex (peak). Reprinted by permission from Springer [Journal of Materials Science] Ref. [29], Copyright (2014)

[36, 37]. Thickness of these dielectrics is taken as one-fourth of the wavelength of the incident light, where photon flux is the maximum and hence the impact of the dielectric is optimum [36, 37]. These layers are expensive, strongly spectral and angular dependent of incoming radiation and hence not the ultimate option. Nevertheless, the microtexturing combined with an anti-reflection (AR) layer is industry standard at present. The plasma-enhanced chemical vapour deposition (PECVD) based silicon nitride (SiN_x) of thickness ~70–80 nm is generally used as an AR coating (ARC) in the industrial solar cell production process though it is costly, hazardous and non-environmental friendly.

Further, conventional wet texturing, as mentioned above, the technique involves the creation of random sized (5–15 μm) microstructures both in vertical as well as lateral (base) direction distributed randomly over the entire Si wafers. This puts a lower limit on wafer's thickness over which conventional etching facilitated solar cell can be fabricated; which eventually puts a lower limit on the processing cost also. Besides, it also creates a problem along the edges. The silicon wafer cost constitutes around 40–50% of total module cost and hence is a reasonable target for price reduction [38]. This can be done in two ways; wafer thinning and/or increasing impurity tolerance of wafers as purification of wafer from metal grade to solar grade involves considerable cost. Thinning of wafer means corresponding loss of solar radiation as

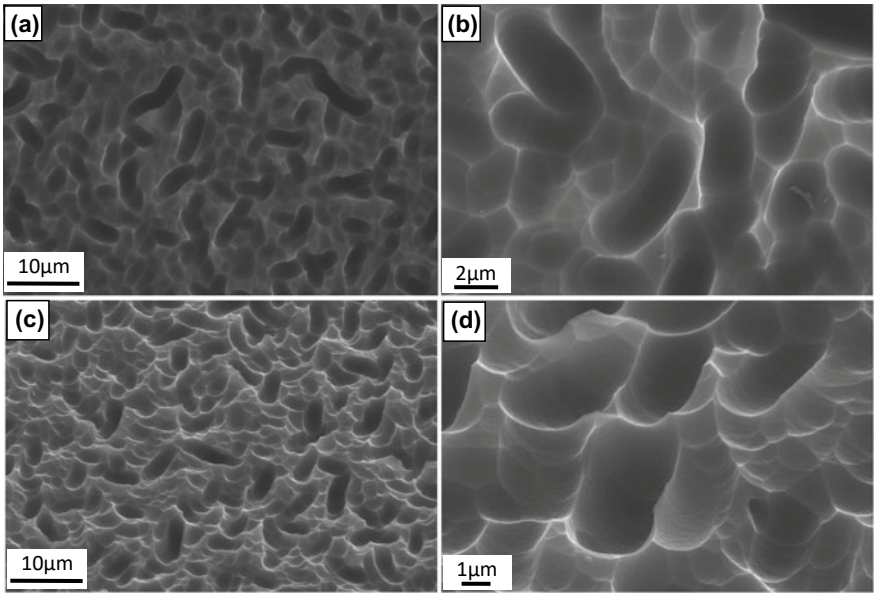

Fig. 7 Typical SEM images of microscale textured mc-Si wafers (using the acidic texturing scheme in $HNO_3/HF/H_2O$) used in conventional industrial mc-Si solar cells which show the random microscale pits; **a** low magnification top view, **b** magnified view of a section of surface shown **a**; **c** low magnification image in 45° tilted view, **d** magnified 45° tilted view of a section of the surface shown **c**

thinner wafers would not be able to absorb long-wavelength radiations. This necessitates an architecture that is able to considerably enhance radiation absorption even in ultra-thin wafers so that wafer can be thin down without loss of photons. A variety of architectures have emerged which performs this job admirably. These include arrays of nanowires, nanocones, nanopillars, nanorockets, porous silicon, etc. on the silicon wafer surface [31] collectively classified as 'nanostructured silicon' or more specifically 'nanostructured black silicon' owing to extremely low light reflection from these surfaces.

4 Nanostructured Black Silicon Concept

As described earlier, the solar PV is one of the promising technologies to provide the most feasible carbon-free route to displacing TW of nonrenewable or fossil sources based power consumed worldwide. The continuous improvement of the cost–performance ratio for solar cells is a driving force for the sustained growth of PV deployment. It is well accepted in the PV industry that the silicon wafer cost constitutes around 40–50% of total PV module cost and hence is a reasonable target for price reduction [38]. Reducing silicon wafer thickness is an effective method to decrease

the material cost of wafer-based solar cells. However, as the wafers become very thin, conventional wet etching methods are no longer equally effective for texturing wafer surfaces and reducing the surface reflection of the incident radiation. New methods to develop highly absorbent textured silicon surfaces are thus required. Nanostructured silicon surfaces are well known for their applications in Si micro-and optoelectronic devices, particularly in solar PV [7]. A particular class of nanostructured Si is 'black silicon'. Black silicon consists of a nanostructured surface layer (up to few hundreds of nanometers), which effectively minimizes the reflection of incident light in broad spectral range, and therefore giving the surface 'black' appearance, instead of the typical silver-grey appearance of planar Si wafers. This unique property makes black silicon a promising solution for the ARC of silicon solar cells [39–46]. Moreover, these nanostructures are promising building blocks for next-generation photovoltaic (PV), optoelectronic and photonic devices [47–54]. Black silicon can also be used to make ultra-thin and flexible wafers based solar cells and reduce wafer impurity levels. Such device structures have opened new avenues for thin and low-grade Si-based solar cells on flexible/glass substrates [54, 55]. In addition to PV, several other technological applications of black Si, such as in, thermoelectric systems [56], micro-electro-mechanical systems (MEMS) [57], lithium batteries [58], chemical sensors and biosensors [59, 60], field-effect transistors [61], photodetectors [62] and light-emitting diodes [63] and other optoelectronic and photonic devices [39–55, 64, 65], H_2 production by the photoelectrochemical splitting of water [66], as a "self-cleaning" surface [67–72] and many more are being explored extensively.

As stated earlier, the black Si has been material of interest in solar cell research, particularly as a highly absorbent textured front surface. Over the past decade, several new black Si fabrication techniques have emerged and some of those also got matured. Significant developments in the effective implementation of black Si concept in different conventional and innovative solar cell architectures have been made having strong potential for increasing power conversion efficiency (PCE) of the Si solar cells at a relatively lower cost [26, 39–46, 73–90]. In parallel, the global PV industry is experiencing rapid growth with a global installed capacity of 97.5 GWp in 2017 alone and >100 GWp in 2018 and a cumulative installed capacity of 405 GWp at the end of 2017 and 505 GWp at the end of 2018 [17]; with a compound annual growth rate of ~24% from 2010 to 2018 [18]. Undoubtedly, solar PV has become the world's fastest growing energy technology, with gigawatt-scale markets in an increasing number of countries. At the same time, there is strong belief and consensus in the PV community to identify the value products, especially quality PV cells and modules (the building block of a PV system) and promote the new concepts to improve the cost-to-performance ratios of solar modules which consequently pave the way for innovative concepts like black silicon-based solar photovoltaic devices.

In this chapter, a review of the recent progress of black Si research for solar cell technologies is presented. Different black Si fabrication techniques are introduced very briefly with more emphasis on the recently developed method, namely 'MACE'—metal-assisted wet chemical etching, followed by its brief critical analysis with respect to advantages and disadvantages for solar PV applications. The main challenges of applying black silicon for high-efficiency solar cells and the possible

ways to circumvent those are also highlighted along with the efforts made in this regard during the past decade. The surface passivation of the black silicon surface is the most critical component in its effective implementation towards high-efficiency black silicon solar cells, and therefore different surface passivation schemes based dielectric thin films are also discussed. The latest development in mc-Si solar cells employing the MACE black silicon is also reviewed. The application of black silicon towards the development of thin silicon solar cells is discussed with the recent progress made to this end. Finally, conclusions and future prospects of the MACE nanostructured black silicon concept for photovoltaic is outlined wherein it is envisaged that nanostructured black Si will play an increasingly important role in cost-effective and efficient solar photovoltaic devices and technology in the coming years not only in the conventional monocrystalline and multicrystalline silicon wafers based solar cells but also in the thin/flexible silicon solar cells.

4.1 Fabrication of Nanostructured Black Si Surface

In general, there are two main approaches for the black silicon formation, namely 'bottom-up' and 'top-down'. Several bottom-up methods such as the vapour–liquid–solid, popularly known as 'VLS' method [43, 91–94], based on chemical vapour deposition [54, 95], molecular beam epitaxy [96], laser ablation [97, 98], thermal evaporation [99, 100] or a few more options [101, 102], have been successfully developed to prepare silicon nanostructures. However, these processes generally require complex and expensive equipment, with which processing is done at relatively high temperatures under vacuum using templates and hazardous silicon precursors. These features make the processes time-consuming and expensive, and therefore limit their suitability for several applications. Besides, nanostructures fabrication over a large area is difficult to achieve. Owing to these limitations, the bottom-up approaches, which are not feasible for solar cell applications, and not discussed here. In the top-down approach, over recent years, a range of black Si fabrication processes has been developed, namely 'MACE'; Reactive ion etching (RIE); conventional electrochemical etching and stain/acidic etching and femtosecond laser-based etching [89, 103–118]. Methods like RIE [112] and/or lithography [113], etc., are little complex, expensive (owing to the use of vacuum components) and time-consuming. In addition, fabrication of homogeneous nanostructures on a large area with high throughput is relatively difficult [89, 112–119]. Moreover, RIE also causes significant surface damage to the silicon wafers, and hence enhanced surface recombination of charge carriers [120, 121]. Similarly, the laser-based etching process is also relatively slow in comparison to other etching techniques, especially on an industrial scale. In addition, laser-induced material damage can be quite substantial; and is of great concern, especially, for solar cell applications.

The MACE method is rather free from all these limitations. It is a simple, room-temperature and solution-based process that enables the formation of nanostructured black surface on a wafer scale and in a batch line [90, 122]. Hence, the focus of

the chapter is on metal-assisted chemical etching for the fabrication of black silicon surface and its application in PV devices. Black silicon surface, consisting of both aperiodic (randomized) and periodic arrays of silicon nanostructures can be fabricated by this process. However, for periodic arrays of nanostructures, an additional lithographic process employing colloidal or nanospheres lithography, etc. is essential prior to the MACE process [122, 123]. On the other hand, the conventional MACE process results in an aperiodic array of nanostructures. Herein, the scope of this chapter is limited to random nanostructures based black silicon surfaces only.

4.2 Metal-Assisted Chemical Etching

This process is based on the etching of silicon in aqueous hydrofluoric acid (HF) in the presence of an oxidative agent, and catalyzed by noble metals, to form micro-/nanostructured surfaces with various morphologies [122, 124–129]. In the MACE process, there are two known approaches; (a) single-step MACE, and (b) two-step MACE. The former is a self-controlled process and simply involves placing of a clean silicon wafer in an aqueous solution of HF containing metal ions such as Ag, Au, Fe, Cu, etc. [122, 130–133] whereas in the latter case, metal (Ag, Au) particles are first deposited either by a wet chemical process (electroless deposition) in solution or by a physical vapour deposition (such as sputtering, thermal and electron beam evaporation) under vacuum followed by placing of metal nanoparticles coated silicon wafer in the etching solution (an aqueous solution of HF and H_2O_2) to fabricate nanostructured black Si surface [134–137]. The schematic of the experimental setup commonly used for single- or two-step MACE process is presented in Fig. 8. The fabrication of black silicon by MACE has been extensively reported wherein most of the studies are based either on Ag-assisted MACE process [122, 125, 130, 131, 134–138] or the Au-assisted MACE process [75–79, 82, 83, 122, 132–135]. In addition to Ag and Au, metals such as Fe, Cu, Pt, etc., have also been used (as catalytic agent) for the fabrication of black Si surfaces by MACE method [81, 132–135, 139–142]; however, the investigations are limited. Among the noble metals, Au and Ag are the two most popular choice for the MACE as they can easily be deposited onto the surface in solution (i.e. via electroless deposition and electrodeposition) [82, 83, 87,

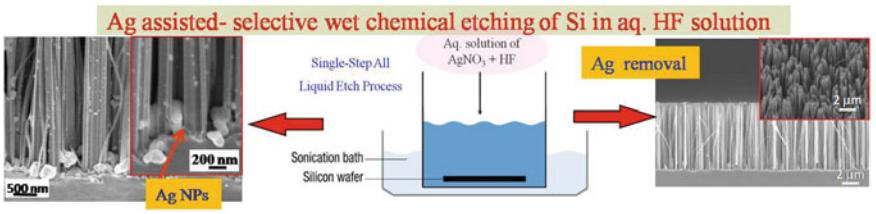

Fig. 8 Schematic of metal-assisted wet chemical etching setup for fabrication of nanostructured black Si surfaces

122, 124, 125, 131] as well as under vacuum (i.e. via sputtering, thermal and e-beam evaporation) [122, 136]. Among all, the majority of MACE investigations are based on the Ag-assisted process. One possible reason for the preference of Ag as a catalyst over others could be due to its advantages such as redox potential of Ag^+/Ag system is overlapping with Si valence band (VB), and therefore ease the silicon etching by the self-sustained MACE process [122, 124, 134, 135, 138]. Other possibilities may be related to avoiding the side effects of Au, Fe, Cu, etc. on the electronic properties of the resulting nanostructured Si; since these metals are known to have deep-level impurities and have adverse effect on the electronic properties (particularly lifetime of minority charge carriers) of silicon-based devices. The minority charge carrier lifetime is a very critical parameter for solar cells applications [143–145]. The etch bath in the Ag-assisted MACE process consists of an aqueous HF solution containing Ag^+ ions (typically, aq. $AgNO_3$ solution). This bath is also known as oxidizing HF solution. In general, fabrication of black silicon is carried out on both p- and n-type silicon wafers with a doping density of 1–10 Ω cm in a beaker using aqueous HF (~5.0 mol/L) solution containing ~0.02 mol/L $AgNO_3$ at room temperature. Most of the reports are focused on silicon wafers with (100) crystal orientation [122, 125, 130, 131, 134–138], as silicon wafers with these electronic properties and crystal orientations are preferred for PV applications. However, the effect of doping properties of silicon wafers and crystal orientation on the formation of nanostructured black silicon containing different morphologies such as silicon nanowires (Si NWs), porous silicon nanowires (p-Si NWs), conical wires, zig-zag nanowires, nanoscaled textures or nanopillars, porous silicon, etc. have also been investigated using (100), (110), (111) oriented silicon wafers under different etch parametric conditions [146–153].

In general, the MACE method consists of the following sequential steps for black silicon fabrication. (i) Prior to the etching, the wafers are sequentially cleaned with acetone, IPA, de-ionized (DI) water and boiling in piranha solution (H_2SO_4:H_2O_2 = 3:1 by volume, for 30–60 min); (ii) the wafers are then rinsed thoroughly with de-ionized water followed by dipping in 5–10% HF solution to remove silicon oxides (either native or grown during the process on the surface); (iii) cleaned silicon wafers are then immersed in the etching solution for the desired time duration for etching; and (iv) Finally, removal/etching of the residual/deposited Ag particles from the Si samples. This can be achieved by treating the samples in NH_4OH:H_2O_2 or HNO_3 solution [122, 125, 130, 131, 134–138], followed by rinsing in DI water copiously and drying. Recently, Srivastava et al. have reported that single step Ag-assisted MACE provides a wide range of flexibility in the processing parameters for fabrication of silicon nanostructures especially aligned vertical Si NW array based black silicon [125]. In this article, they carried out extensive investigations on the influence of all the etch parameters such as etch time, etch bath temperature, etch bath components, like HF and $AgNO_3$ concentrations and also the surface area of the silicon samples under a given etch conditions on the formation of the Si NWs array. Another very important feature of this method is that it is a room temperature beaker process and there is no limitation on the size of the wafers. Further, Kumar et al. have reported wafer-scale fabrication of black silicon [131]. With the suitable design

of the setup, it can easily be scaled-up for large-scale fabrication of black silicon in the batch process [154, 155]. Srivastava and co-workers have also reported the fabrication of black silicon surfaces by silver assisted two-step MACE process on both monocrystalline and multicrystalline silicon wafers on small-sized samples as well as on industrial scaled 125 × 125 mm^2 (mono-Si) and 156 × 156 mm^2 on multi-Si wafers [19, 87, 88] for solar cell applications. So far, the technique has been thoroughly investigated and also reviewed in the literature [122, 124–129]. Here, a brief summary of the process, its mechanism and importance from the solar cell perspective is presented. The MACE process mechanism is explained with the example of Ag-assisted etching. However, in general, the MACE process assisted by other noble metals, like Au/Pt/Cu, also works on a similar principle.

4.2.1 Single-Step Etch Process

Catalytic activity of Ag nanoparticles is well known in the electrochemical etching of silicon in HF solution where deep cylindrical nanoholes were produced in (100) silicon using Ag nanoparticles as a catalyst by Li and Bohn in 2000 and named the process as 'metal-assisted chemical etching' of silicon [124]. The mechanism of formation of nanostructured black Si surface can be understood considering it as a self-assembled Ag-induced selective etching process based on localized microscopic electrochemical cell model. It works on the continuous galvanic displacement of Si by Ag^+ ions via $Ag^+ \rightarrow Ag$ reduction on the Si surface and hence forming numerous local nano-electrochemical cells on the Si surface. The deposited Ag nuclei and then nanoparticles act as 'cathode' and the Si surface in contact with the Ag nanoparticles as 'anode'. In brief, Ag^+ ions get reduced to Ag onto the Si surface by injecting holes (h^+) into the Si valence band and oxidizing the Si surface locally in contact with Ag nanoparticles. The oxidized Si surface is subsequently etched away by HF. The complete self-controlled redox reaction occurring in aq. HF + $AgNO_3$ etch bath on the Si surface can be divided into two parts: cathode and anode reactions which are stated below [122, 125, 131, 135].

At cathode site:

$$Ag^+ + e^-(VB) \rightarrow Ag(s)$$

At anode site:

$$Si(s) + 2H_2O \rightarrow SiO_2 + 4H^+ + 4e^-(VB)$$

$$SiO_2(s) + 6HF \rightarrow H_2SiF_6 + 2H_2O$$

The initial reduction of Ag^+ ions results in Ag nuclei which act as a catalytic site for subsequent cathodic reactions. Subsequently, Ag^+ ions get reduced to Ag

preferably on the Ag nuclei, and therefore forming nanoclusters/nanoparticles (but not on the uncovered Si surface) by electron transfer from the underlying wafer (since Ag is relatively highly electronegative than the silicon and hence provide easy injection path for holes). In the next step, agglomeration of Ag nanoclusters occurs to form dendritic structures, a non-compact Ag layer, as shown in Fig. 9 (refer to SEM images (e) and (f) indicating Ag nanoparticles in the bottom of the pores and Ag-dendrites on the top surface of Si NW arrays)), which lead to selective oxidation and dissolution of Si in the aqueous HF + $AgNO_3$ solution. Once the Ag nanoclusters get trapped into the silicon pores they move deeper and deeper by the continuous formation of SiO_x underneath the metal particles and the corresponding removal action by the HF resulting in the one-dimensional nanostructures and the process is continued until terminated. The complete etching process by the Ag-assisted MACE method using HF and $AgNO_3$ solution can be represented in five basic steps and are

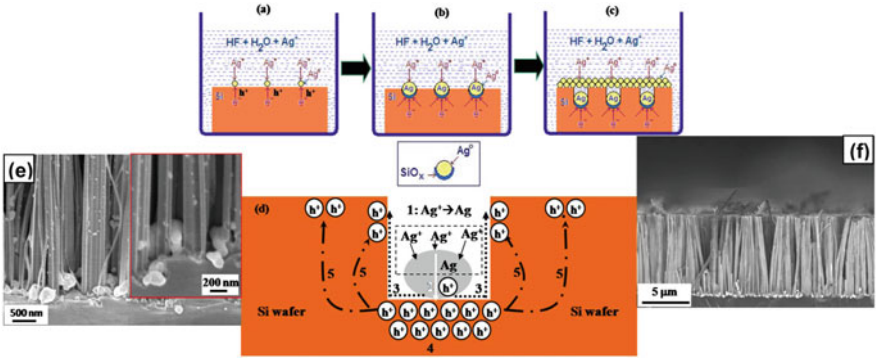

Fig. 9 Schematic presentation of silver assisted selective etching mechanism of silicon wafers leading to different silicon nanostructured surface in a typical single-step Ag–assisted MACE process in aq. HF/$AgNO_3$ etch bath. Representation of cross-sectional SEM image (shown left) of as-prepared black Si indicates the Ag nanoparticles at the bottom of the pores and image (shown right) shows the presence of dendritic Ag morphology on nanostructured Si surface along with the Ag nanoparticles in the bottom of the pores and along the nanostructures surfaces. **a** Reduction of Ag^+ ions to elemental Ag via hole (h^+) injection into the VB of Si, leading to the formation of Ag nuclei at the Si surface, and simultaneously hole injection into the Si substrate, oxidizing the Si to SiO_x. **b** Growth of Ag nuclei into large particles with increasing etching time, oxidative dissolution of Si atoms (in presence of HF) under the Ag particles and sinking of the particles into the Si substrate. **c** The charge transfer preferentially occurring at the etching front (Ag/Si interface) and vertical propagation for the Ag/Si interface. **d** Schematic representation of the complete etching mechanism of Si in aqueous HF/$AgNO_3$ solution: (1) reduction of (Ag^+) to elemental Ag at the silicon surface; (2) injection of holes (h^+) into the Si valence band at the Ag/Si interface, oxidation of Si at the Ag/Si interface and dissolution of oxides by HF; (3) diffusion/migration of the etchants (HF) and by-products (H_2SiF_6) along the Ag/Si interface; (4) preferential charge transfer at the Ag/Si interface leading to faster etching of the Ag/Si interface as compared to non Ag regions and vertical propagation of the Ag/Si interface (i.e. the pore bottom); and (5) diffusion/migration of excess holes at the Ag/Si interface to off-Ag regions (sidewalls) leading to porous sidewalls of MACE Si nanostructures. Srivastava et al. [125]

presented schematically in Fig. 9d. A similar analogy can be applied to other metals such as Au, Pt, etc. based MACE processes.

The nanostructure array or black silicon surface layer of desired depth can be produced by controlling the etch time and temperature for a given etch-solution composition and sample size. It has been shown that the surface area of the Si samples exposed in the etch-solution has a strong influence on the etch kinetics of the process. Generally, the higher $AgNO_3$ and HF concentrations lead to side etching and tapering of nanostructures. Shallow (short length) and well-aligned nanostructures in the black silicon surface could be made at lower $AgNO_3$ and HF concentrations, which may be important for PV device applications [42]. It has been observed that the morphology of the nanostructures (lateral dimension or diameter) and their distribution depends on the dimension and distribution of the Ag nanoparticles formed on the Si surface. However, it is difficult to control the cluster size in such a self-assembled MACE process. In practice, controlling the diameters of nanostructures in a single-step MACE process (without using any lithography process/templates) is rather difficult. Even though based on experimental observations, efforts have been made to develop a model that can estimate the distribution and diameter of the nanostructures by this method [156]. It is also important to note that the MACE method, despite the process being strictly anisotropic in nature, owing to grain orientation dependent nanostructures orientation and morphology, can be applied to produce nanostructures on mc-silicon substrates also [125].

4.2.2 Two-Step MACE Process

In a two-step MACE process, also, the electroless etching process takes place due to the catalytic action of the metal nanoparticles (Ag or Au nanoparticles) deposited on the cleaned silicon surface, either by the electroless wet method [87, 88, 122] or a PVD method [78, 136], in the presence of an oxidizing agent like H_2O_2. In a typical two-step MACE process, a silicon wafer, partly covered by noble metal nanoparticles, is immersed in a solution of HF and an oxidative agent [122, 157–159]. Vacuum deposition, of course, offers better control over the metal film morphology, while electroless deposition is a simpler process and can be adopted when the requirement on silicon surface morphologies is less stringent [122]. From the viewpoint of large-scale production for industry application where batch processes are preferred, the electroless deposition may be the choice. For electroless deposition of metal nanoparticles, a compound containing Au- or Ag-ions such as $AgNO_3$ or $HAuCl_4$, is added to an aqueous HF solution. In contact with the silicon surface, the noble metal ions (Ag^+ or Au^+) acquire electrons from the silicon valence band (VB) and are reduced to form the seed nuclei which grow into nanoparticles. Concurrently, these ions inject holes underneath the silicon causing its oxidation locally into SiO_x, which are subsequently removed by HF [122]. The metal-coated wafers once immersed in HF solution in presence of an oxidizing agent, the etching process continues similar to single-step process, wherein continuous galvanic displacement of Si (assisted by metal nanoparticles) occurs via formation of local nano-electrochemical cells on the

silicon surface. The metal (like Ag) nanoparticles act as cathode and silicon surface in contact with the metal nanoparticles as an anode. The H_2O_2 acts as an oxidizing agent and injects hole in the Si valence band facilitated by Ag nanoparticles [124]. The local cathode and anode reactions can be presented as following after Li and Bohn [124] work on metal-catalyzed porous silicon formation:

Cathode reaction (at Ag sites):

$$2H_2O_2 + 2H^+ \rightarrow 2H_2O + 2h^+,$$

$$2H^+ + 2e^- \rightarrow H_2 \uparrow,$$

Anode reaction (at Si sites):

$$Si + 4h^+ + 4HF \rightarrow SiF_4 + 4H^+,$$

$$SiF_4 + 2HF \rightarrow H_2SiF_6,$$

The generation of h^+ from H_2O_2 and the reduction of H^+ to form H_2, both are facilitated by the Ag particles. Silicon surface in contact with Ag is locally oxidized which is subsequently etched away by HF. The whole process is self-controlled. By the continuous formation of SiO_x underneath the metal particles and the corresponding removal action by the HF, the metal nanoparticles sink into the silicon and create porous structures [122]. The depth of these pores is proportional to the etching time [88]. Once the desired surface structures are created, the metal nanoparticles are removed by another etchant, such as in ammonia and H_2O_2 solution or HNO_3, followed by a thorough cleaning process. The sequential process steps of the Ag-assisted two-step MACE is schematically presented in Fig. 10a with corresponding representative SEM images supporting the morphology/surface structures of each process step. Based on the above discussion, the noble metal-assisted MACE process, in general, can be represented in Fig. 10b.

The advantage with the two-step MACE is that simultaneous deposition of a thick metal layer (like Ag-dendrites in the case of Ag-assisted process or Au film in case of Au-assisted process) can be avoided. Only a thin layer of metal nanoparticles initially deposited on silicon surface does the job which is rather easy to etch out in a suitable metal etchant solution and the probability of traces of metal in the black silicon surface is less which is very important for its PV applications. Also, the two-step process in the presence of an oxidizing agent is relatively faster than the corresponding single step Ag/Au-assisted process [19, 30, 87, 88, 125, 131].

As discussed above, the metal catalysis plays a key role during the chemical etching process. Koynov et al. showed that without metal catalysis, the etching speed was very low (1 nm/min) [78]. In contrast, this speed was greatly increased by the addition of Au; 250 nm high-hillock structures were fabricated within 50–90 s [76]. Similarly, Srivastava and co-workers [19, 87, 88] showed that the nano-texturing

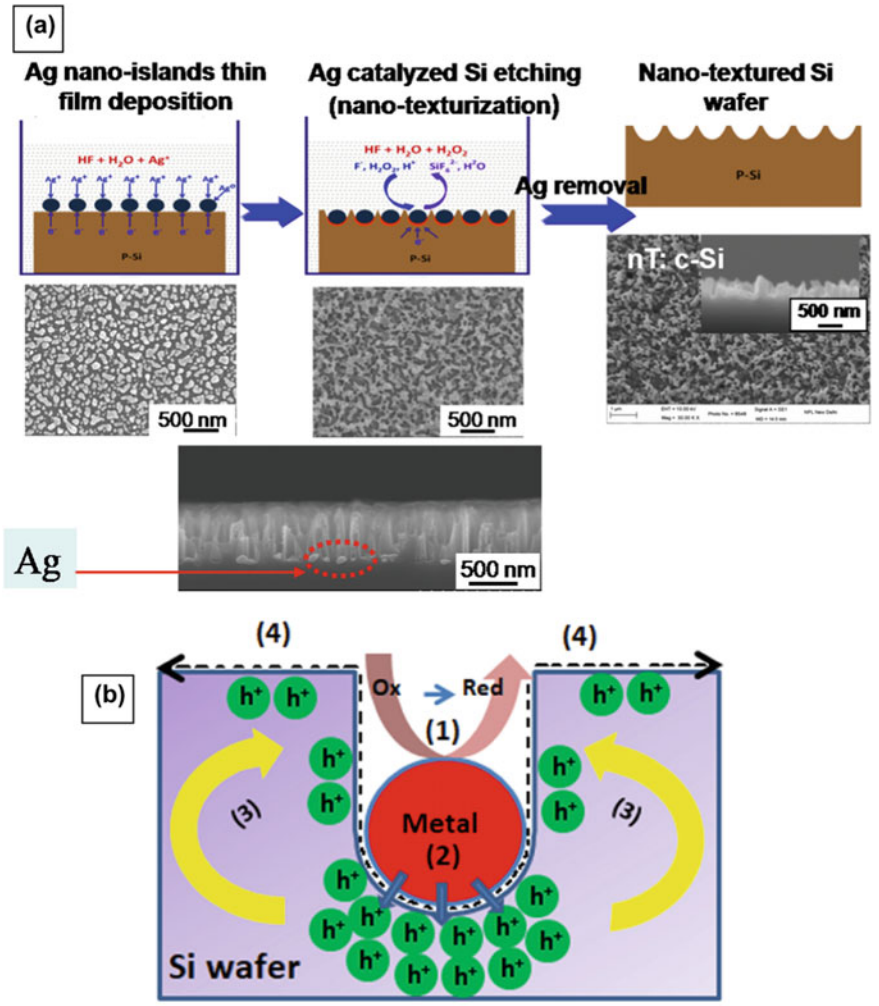

Fig. 10 **a** Sequential steps of a typical two-step MACE process assisted by silver nanoparticles; The surface morphology of resulting Si surface corresponding to each step is also shown below the schematic of each step for better understanding. The Ag nanoparticles in the bottom of the resulted nanostructured Si are also shown as an indicator of Ag-assisted/induced localized etching of the Si surface resulting in the nanostructured surface. **b** An illustrative of the MACE process; (1) the reduction of an oxidative agent (such as Ag^+ ions or H_2O_2) catalyzed by a noble metal particle; (2) the injection of the holes generated during the reduction reaction into the silicon substrate, with the highest hole concentration underneath the metal particle; (3) the migration of the holes to silicon sidewalls and surfaces; (4) the removal of oxidized silicon by HF

process was strongly dependent on etching time and initial thickness of the Ag film deposited by electroless metal deposition. The etching of the polished silicon without metal ions (Ag) in the same solution (H_2O:HF:H_2O_2) was very slow. Consequently, the size and shape of deposited metal particles largely determine the morphologies of the etched surface, since the silicon underneath this metal catalyst is etched much faster. By varying the surface coverage and distance between metal particles, one can create a wide range of surface nanostructures, from black Si layers to nanowires [78, 87, 88, 136, 160]. A typical surface morphology of the nano-structured c-Si and mc-Si surfaces by a two-step Ag-assisted MACE is shown in Fig. 11. From Fig. 11a it can be seen that a surface with nanopores of diameter 50–200 nm and a vertical depth of ~300–500 nm is obtained in the nanostructured c-Si surfaces in 30 s. The cross-sectional view also indicates that the nano-textured surface has graded density structure similar to that obtained by Koynov and co-workers [78] and Branz and co-workers [79] using the Au as etching catalyst. The Ag catalyzed nanostructuring process is equally effective in mc-Si also (see Fig. 11b), which is difficult in the conventional anisotropic alkaline texturing process. The process can easily be scaled-up to produce a low reflective black surface over the entire area of industrial wafers dimensions like 125 × 125 mm^2 (c-Si) and 156 × 156 mm^2 (mc-Si) wafers. A representative digital image of such a black surface is shown in Fig. 12. This clearly demonstrates the versatility of the MACE nano-texturing process for both c-Si and mc-Si.

In summary, the MACE is a simple, fast, low cost and versatile technique for fabricating a wide range of nanostructures with minimal capital equipment requirements. The morphologies of the resulting Si surfaces can be controlled by varying the process parameters such as the size, shape and surface coverage of the noble metal nanoparticles, etchant concentration, etching time and temperature [125, 160, 161]. This etching technique can be applied to monocrystalline (c-Si)/multicrystalline (mc-Si)/polycrystalline (thin layer), and even for amorphous Si (a-Si) [19, 78, 87, 88, 162, 163]. The technique has drawn tremendous interest during the past decade,

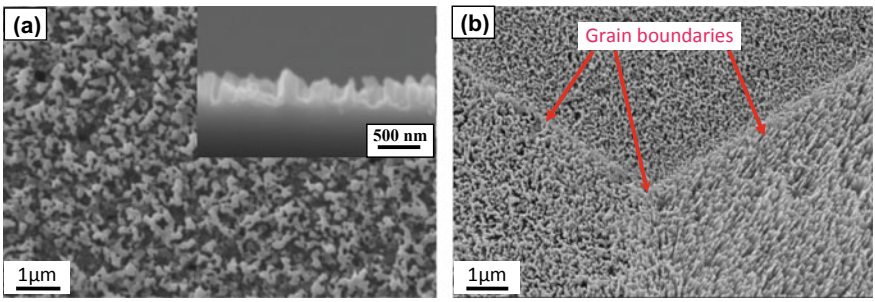

Fig. 11 SEM images of nanotextured silicon surfaces. **a** nanotextured black mono-Si (magnified cross-sectional view is shown in the inset), **b** nanotextured black mc-Si showing uniform texturing in a given grain however, the texturing rate and morphology are grain orientation dependent. The grain boundaries are also indicated by arrows

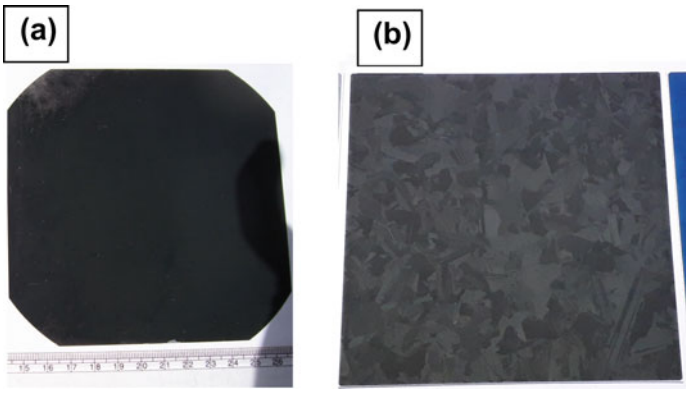

Fig. 12 Representative digital image of a MACE nanostructured Si wafers of **a** 125 × 125 mm^2 pseudo square c-Si and **b** 156 × 156 mm^2 mc-Si wafer showing that the Ag catalyzed nanotexturing process is suitable for industrial silicon wafers

especially in a research context, and remains a mainstream etching method. From a solar cell perspective, a great success is made in effective implementation of this process in fabrication of high-efficiency silicon solar cells (both in c-Si and mc-Si) from lab level to large-scale industrial sized wafers, which will be briefly reviewed in the following section; addressing all the issues in effective implementation of the MACE black Si solar cell technology, its present status and future perspectives. Prior to that, the excellent light-harvesting properties of the MACE nanostructured black silicon surface and its basic principles are outlined briefly in the following section.

5 Anti-reflection Properties of Black Silicon Surface: *Light Trapping and Enhanced Optical Absorption in Black Si*

5.1 Black Silicon on Bulk Silicon Wafer

The optical absorption properties of solar cells in the solar spectrum are important in determining cell efficiency. For example, polished silicon surface has a high natural reflectivity (>35%) with a strong spectral dependence, and therefore minimization of reflection losses is a prerequisite for efficient Si solar cells [23]. To achieve this, as discussed before, the top surface of the Si solar cell is typically textured or coated with an AR layer. Anisotropic etching in aqueous alkaline solution (such as using KOH or NaOH) is a standard process for c-Si and is widely applied in Si-wafer based PV industry. Such an approach of surface-texturing of Si forms densely packed random micro-pyramids which results in the reduction of reflection losses in a broad spectral range [164, 165]. With this process, reflection losses can be reduced to ~11%. For further reduction of reflection (~2–3%), anti-reflection coating (ARC) based on

quarter-wavelength transparent layers of dielectrics such as SiO_x, TiO_x or Si_xN_y is used [164, 165]. Such ARCs have resonant structures and work effectively only in a limited spectral range and specific angles of light incidence. As introduced in Sect. 3, the optical losses in thick wafer-based solar cells is primarily addressed by reducing front surface reflection, via combined use of ARCs and surface texturing. The surface textures additionally act as a light-trapping medium and improve light absorption in the long-wavelength range. The industry has traditionally used wet etching to develop textures on Si solar cells because of its low cost, high etching rate and good uniformity across large areas [166]. In c-Si (100) wafers, alkaline wet etching is often adopted to form random micro-pyramidal structures that are 5–15 μm deep for light scattering and AR applications, resulting in a weighted reflectance of 12–14% on wafer-scale without AR coating (see Fig. 6 of Sect. 3) [76, 167]. Reducing the sizes of these pyramidal structures, i.e. to 4–6 μm in depth, could lower the weighted solar reflectance to 11.4–12.2% [168]. By adding a quarter-wavelength AR coating, typically made from SiO_2 or SiN_x, the fraction of reflected photons can be further reduced to 3% or less for this type of textures. Alkaline etching is anisotropic and creates undesirable steps along the grain boundaries in mc-Si wafers (see Fig. 7 of Sect. 3). Consequently, for mc-Si wafer solar cells, the most common one available in the market, isotropic acidic texturing is often employed, which results in a weighted reflectance of 20–25% (in 300–900 nm) on wafers without AR coating [166, 169–171]. On mc-Si wafers, dielectric layers are also used to improve the passivation and AR properties; this results in a weighted reflectance down to 6–7%. However, it is a common trend in solar cell technology to produce ever thinner solar wafers, for reducing material cost and relaxing the requirements on wafer impurity levels and associated carrier diffusion lengths [172, 173]. As wafer thickness decreases, it becomes increasingly difficult to undertake the conventional wet etching, owing to its deep etching profile and relatively large wastage of Si material. The conventional etching techniques, in general, are not appropriate on very thin wafers (<10 μm) [121], yet, ARC and particularly light trapping is critical for the photon management of these thin wafers [174, 175]. An alternative way is to use the MACE nanostructured black Si concept. The MACE nanostructured black silicon possesses several unique optical properties owing to their high surface areas and structural features smaller than the wavelength of light and therefore have potential applications in solar cells to replace the conventional microtexturing schemes.

In the recent past, excellent anti-reflection or light-trapping properties of the MACE nanostructured black silicon has been reported by many groups [19, 26, 30, 39, 86–90, 125, 155, 176–187]. For example, Peng et al. reported that black silicon consisting of Si NW arrays fabricated on c-Si wafers drastically suppress light reflection (<1.4%) over 300–600 nm spectral range [39]. Srivastava and co-workers performed systematic investigations on the AR property of the Si NWs fabricated by the MACE method for different arrays length (or black silicon layer depth) [19, 30, 88]. The hemispherical reflectance of the nanostructured Si (both c-Si and mc-Si) by Ag-based MACE is shown in Fig. 13a along with the reflectance of the polished planar Si wafers. The reflectance plot of a typical microtextured c-Si is also shown in the figure for the sake of comparison. The reflection spectrum

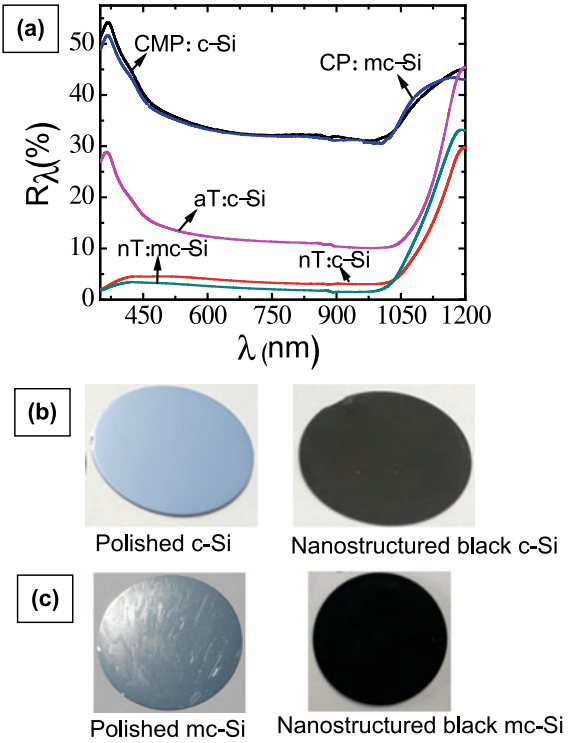

Fig. 13 **a** Reflectance (R_λ) versus wavelength (λ) curves of polished (c- and mc-) Si, KOH textured-Si, MACE nanostructured c-Si and mc-Si surfaces. CMP: chemically mechanically polished; CP: chemically polished; aT:alkaline textured; nT: nanostructured. **b** Digital images of a polished c-Si and MACE nanostructured black c-Si surfaces, **c** Digital images of a polished mc-Si and MACE nanostructured black mc-Si surfaces (MACE nanostructured c-Si and mc-Si wafer on 50 mm diameter)

of the polished (both c-Si and mc-Si) surface shows the typical high R_λ (~34%) whereas average reflectance achieved in alkaline textured c-Si (aT:c-Si) is ~12% in the 400–1000 nm wavelength range. In the case of nano-textured silicon samples, the average R_λ is reduced to less than 4% for c-Si surfaces and ~3% for the mc-Si in the 400–1000 nm range. This clearly demonstrates that nanostructured black silicon drastically suppresses light reflection over a broad spectral range. Srivastava and co-workers have also observed that reflectance decreases with increase in nanostructure arrays length and reaches a minimum of ~1.5% in the 300–600 nm range and ~4% in the spectral range 600–1000 nm in the samples etched for 15 min or more (corresponding to the nanostructure arrays length of ~4 μm or more) [30]. Digital images of the nanostructured Si wafers (on 50 mm diameter) are also shown in Fig. 13b and c along with that of a polished silicon surface for comparison. The black appearance of the surfaces clearly confirms the very low surface reflectance of the nanostructured Si (both in c-Si and mc-Si wafers). The excellent AR property of the nanostructure arrays confers them as a potential candidate for an effective AR layer in silicon solar cells. Till date, a number of articles have been reported on the MACE nanostructured black Si solar cells exploiting their efficient light-trapping/anti-reflection characteristics and will be discussed later. It is also obvious that the black silicon nanoscale texturing by MACE is equally effective in mc-Si wafers for light trapping irrespective of grain-dependent orientation (or anisotropic etching characteristics of the MACE).

In case of mc-Si, the texture depth ≤500 nm is sufficient for effective light trapping [19, 88].

The excellent AR or light-trapping property of the black Si surface has been attributed to the followings: (i) highly rough surfaces and network assembly of the nanostructures may lead to strong light scattering interactions among the nanostructures making light to travel path many folds than the black surface layer thickness which eventually lead to almost complete light trapping and its absorption in contrast to the light striking the planar silicon surface only once [30, 39, 177, 178], (ii) the nanostructured black silicon surfaces have morphological features similar to sub-wavelength structures (SWSs) surface which can suppress the reflection loss over a wide spectral range [188–197], also (iii) the black Si surface has varying porosity from top (air–black Si interface) to the bottom end of the black Si (black Si–Si substrate interface), where the porosity gradient causes a graded refractive index layer from top to bottom (refractive index 'n' increases with decrease in porosity in the black Si layer) [30, 78, 155, 184, 185, 187, 198–201] which closely resembles a multilayer ARC [30, 199]. The concept of graded refractive index incorporating Si nanostructures indicating the two interfaces is illustrated schematically in Fig. 14a. All the above features hold true irrespective of c-Si and mc-Si based nanostructured black Si layer and the same is presented schematically in Fig. 14b. In the effective refractive index medium region, the substrate material (Si) is mixed with air on a sub-wavelength scale. A constant porosity in the black Si layer leads to a step change in refractive index from air to black Si, and then to bulk silicon. This layer is equivalent to a lower refractive index material effectively. The effective refractive index of the layer at any depth (z) can be estimated by knowing the porosity gradient at level z (i.e. filling fraction of Si $ff(z)$ and air) as below:

$$n_{\text{eff}} = n_{\text{si}} \times ff(z) + n_{\text{Air}}[1 - ff(z)]$$

where $0 \leq ff(z) \leq 1$ and hence n_{eff} can be between 1 and n_{Si} leading to gradient refractive index as indicated schematically in Fig. 14a and b. By creating a porosity gradient, a smoother transition in the refractive index from air to bulk silicon (see Fig. 14a and b) can be achieved. No abrupt interface between air and Si leads to almost no reflection. Since it does not rely on interference as in the case of resonant AR coatings, anti-reflection properties of black silicon surface are good at all angles, i.e. it is omnidirectional (will be discussed with examples in Sect. 5.4). These black Si layers lead to a maximum reduction in reflectance [199, 202–204] and the overall reflectance improves as the thickness of the black Si layer increases and as the feature size of the nanostructured silicon becomes smaller [40, 205] The effective medium theory predicts that a 200–300 nm thick textured graded-index layer is sufficient to almost completely suppress the reflectance across the whole solar spectrum (above the silicon band gap) [19, 30, 39, 202]. Consequently, by increasing its thickness and reducing its feature size, the black Si demonstrates comparable, and even superior, low reflection as compared to the conventional single layer (such as SiN_x) and double layer (such as TiO_2/MgF_2) AR coatings [206] with a reflectance of less than 1% over a broadband [205, 207]. Therefore, the black Si helps to reduce reflectance in different

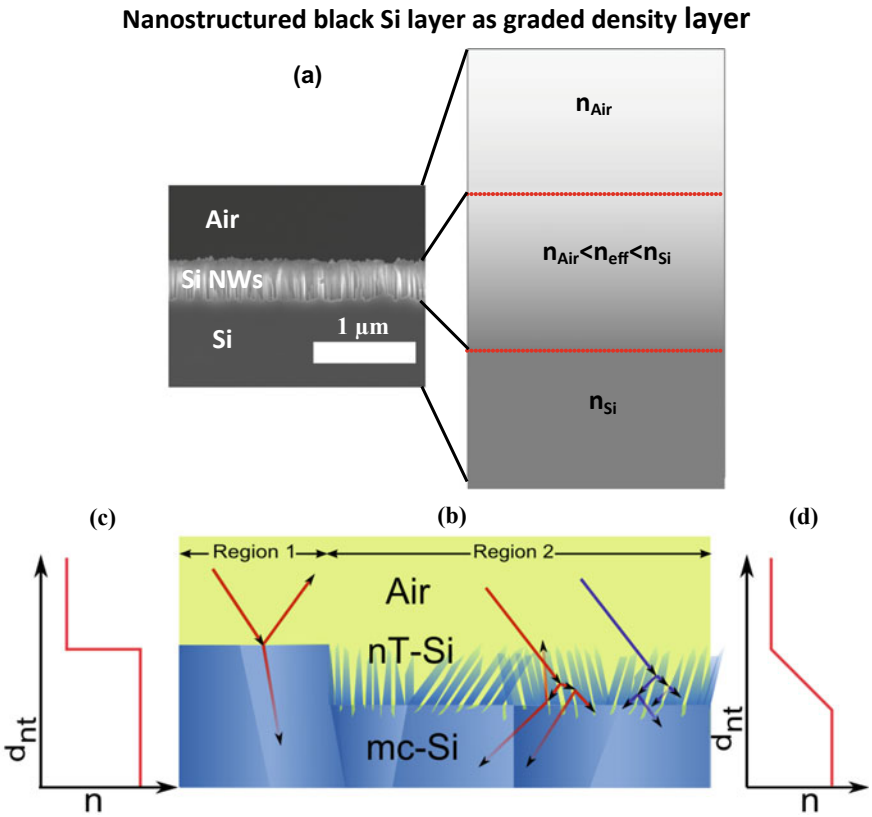

Fig. 14 **a** Schematic representation of graded density layer (and hence graded refractive index) behaviour of Si NSs arrays layer. The symbols n_{air}, n_{Si} and n are the refractive indices for air, silicon and the Si NSs layer, respectively. **b** Schematic presentation of air/mc-Si interface (Region 1) and corresponding abrupt change of the refractive index (n) at the interface **c**, schematic presentation of air/mc-Si interface after introducing nT-mc-Si layer (Region 2) causing a gradual change in effective refractive index and therefore enhanced trapping of light or absorption **d** Reprinted from Ref. [19]. Copyright (2015), with permission from Elsevier

ways, depending on the size and shape of its surface nanoscale textures. First, there is a reflection reduction because of multiple interactions of light with the textured surface; Second, when the size of the texture features is large compared to the wavelength of the solar spectrum, surface scattering is responsible for an elongated light path and enhanced absorption [26, 174]; Third, the surface feature sizes are so small that the surface essentially acts as an effective index medium [202]. In this case, a smooth refractive index transition from air to bulk silicon, via the nanostructured surface, results in an effectively graded-index AR coating (Fig. 14a and b, respectively, for c-Si and mc-Si).

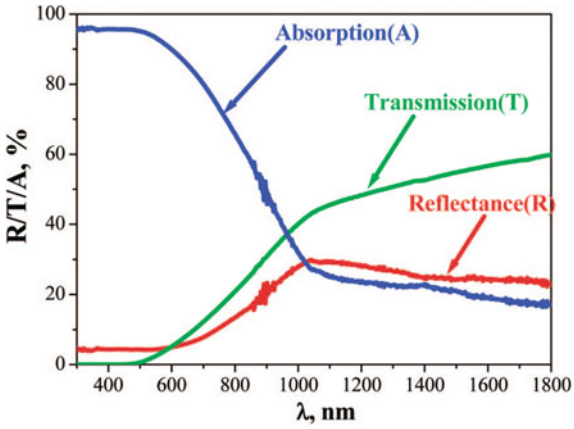

Fig. 15 Optical transmission (T), reflectance (R) and absorption (A = 1−T−R) of Si NWs prepared by etching of ~2.7 μm thick mc-p^+nn^+-Si layers on glass. Reprinted with permission from Ref. [55], Copyright (2009) American Chemical Society

5.2 *Black Si Thin Film Supported on Glass Substrates*

The MACE method has also been used to fabricate the black surface on thin silicon films supported on glass substrates to examine the excellent light-harvesting quality of such surfaces for thin solar cell concepts. The optical absorption properties of such black surface films fabricated on glass substrates by MACE have been measured by Tsakalakos and co-workers [176] and Sivakov and co-workers [55]. The nanostructured (Si NW) Si films on glass exhibited very low reflectance (<10% in the spectral range 300–800 nm, strong broadband optical absorption (>90% at 500 nm) and an optical absorption much higher than non-structured Si thin films of the equivalent thickness (as shown in Fig. 15). The enhanced broadband absorption has been attributed to the strong resonance among the vertical Si NW arrays, while the observed enhanced absorption is partly due to the high-density surface states in the nanostructured film [55, 176].

Similarly, MACE based nanostructured black Si has been very successfully produced in ultra-thin silicon wafers with excellent light-trapping properties for ultra-thin silicon-based PV devices [78, 162, 163, 173, 208–214], which will be discussed in detail in Sect. 9.

5.3 *Theoretical Modelling/Simulation of AR/Light Trapping for MACE Black Si Surfaces*

As discussed above with the help of experimental observations, it is no doubt that the optical properties of the nanostructured Si layer are strikingly different from those of Si bulk wafer and thin films. Detailed simulation of the optical properties of Si NWs has been performed by several research groups looking at their potential application in efficient and cost-effective solar PV devices or Si NW-based solar cells [215–218].

However, most of these simulations/analyses have been done for ordered Si NWs. For example, Hu and co-workers simulated the effects of NWs diameter, length and filling ratio on the absorptance of the NW arrays [215]. They found that NW arrays with moderate filling ratios have much lower reflectance compared to the thin films of equivalent thicknesses. Lin and co-workers used the transfer matrix method (TMM) to calculate the optical absorptance of Si NW arrays [217]. It was found that for a fixed filling ratio, significant optical absorption enhancement occurred when the lattice constant was increased from 100 to 600 nm. The enhancement was attributed to an increase in field concentration within the NW as well as the excitation of guided resonance modes. It was also shown that an optimized Si NW array with a lattice constant of 600 nm and a wire diameter of 540 nm had a 72.4% higher ultimate efficiency than any Si thin film of equal thickness.

Similarly, there have been some efforts made to simulate the optical properties for aperiodic Si NW arrays. For example, Bao and co-workers numerically investigated the optical properties for vertical Si NW arrays with three types of structural randomness, random position, diameter and length [219]. It was shown that the NW arrays with random position exhibited slight absorption enhancement, while those with random diameter or length exhibited significant absorption enhancement, which was attributed to the stronger optical scattering in a random structure. Further, it was also shown that Si NW arrays structural randomness could further enhance optical absorption compared to ordered NW arrays [219]. Rigorous coupled-wave analysis (RCWA) has also been widely used to simulate the experimental observations of excellent light trapping of the vertical Si NW arrays [155, 186, 220]. For example, Xie and co-workers have experimentally found that the reflectance can be significantly suppressed (<1%) over a wide solar spectrum (300–1000 nm) in the as-prepared Si NW arrays [220]. Using the bundled model, they used RCWA to simulate the reflectance in Si NW arrays, and found that the calculated results were in good agreement with the experimental data.

5.4 Omnidirectional Light-Trapping Properties

In addition to excellent AR property, the nanostructured black Si also exhibit other favourable AR properties, including omni-directionality and polarization-insensitivity [155, 220]. Critical features of the AR coatings such as broadband, angular insensitive, and polarization-insensitive characteristics have been demonstrated in the Si NW arrays based black Si under both unpolarized and polarized light by Chang and co-workers [155]. The effective elimination of spectral and angular reflection was accounted to the fact that controlled geometrical configurations such as density of Si NW arrays and interfaces of air/NW arrays layers and NW arrays layers/substrate, which resulted in an intermediate transition region, exhibited a favourable gradient of effective refractive index. The smooth refractive index gradient of Si NW arrays due to increased interface roughness and decreased filling fraction was shown to be critical to considerable reflection elimination, leading

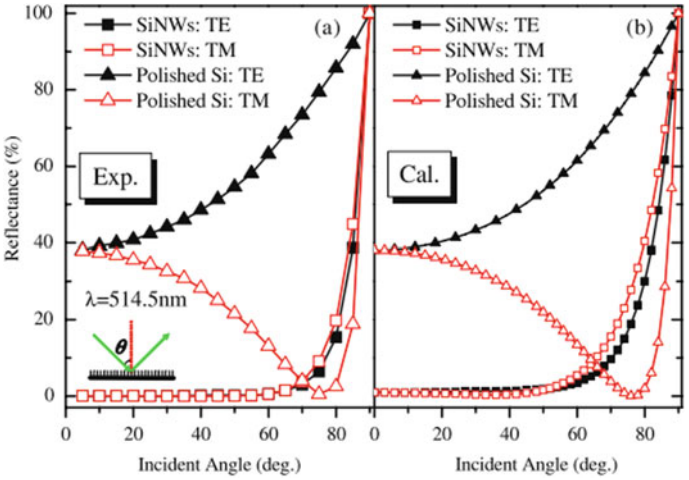

Fig. 16 **a** Measured and **b** RCWA-calculated reflectance of the 800 nm long Si NWs versus the incident angle for s-(TE) and p-polarized (T) light of 514.5 nm wavelength. Results for the polished Si are also presented for comparison. The incident angle (θ) is defined as in the inset in (**a**). Ref. [220] © IOP Publishing. Reproduced by permission of IOP Publishing. All rights reserved

to the excellent broadband and omnidirectional AR characteristics of the aperiodic Si NW arrays. They could achieve the averaged specular and diffuse reflectance of the NWs arrays as low as 0.03% and 1.46%, respectively, within the wavelength ranges of 200–850 nm. Also, TE and TM reflectance as low as 0.1% was measured at a wavelength of 528 nm for the angle of incidence up to 55° [155]. Other studies also sound similar conclusions about the AR properties of the black Si [75, 76]. Furthermore, the polarization and angular dependence of the MACE black Si have also been confirmed by Xie et al. [220] demonstrating a low reflectance up to a large incident angle of ~80° (see Fig. 16).

6 Solar Cell Application of Black Silicon

To exploit the excellent light trapping properties of the MACE nanostructured black silicon for solar cells, Peng and co-workers, in 2005, first reported Si NW arrays based p–n junction solar cells employing the conventional fabrication protocol [39]. They fabricated the solar cells using the following processing sequence: (i) fabrication of black Si on p-type Si wafers; (ii) RCA (the Radio Corporation of American) cleaning to remove the residual metal and organic contaminants followed by removal of SiO_x in a buffered HF solution; (iii) formation of thin emitter (n^{++} layer) in black Si via phosphorous (P) diffusion at >900 °C; (iv) evaporation of an Al layer onto the rear Si surface and removal of the rear parasitic p-n junction; and (v) deposition of Ti/Pd/Ag grid contacts onto the frontside of black Si. Such a solar cell on a c-Si

substrate exhibited a V_{oc} of 548.5 mV and an F.F. of 65%, giving $\eta = 9.31\%$ under AM 1.5 G illumination, which was lower than that of a planar solar cell fabricated in the same batch but without black Si surface. The low power conversion efficiency (PCE) was mainly attributed to the surface or interfacial recombinations, high series resistance and low-current-collection efficiency of the front-grid electrodes. Later, Fang and co-workers, in 2008, fabricated solar cells on slantingly aligned Si NWs based black Si on a Si (111) substrates, which yielded an improved PCE of 11.37% [221]. Though, this efficiency was still lower than that of the planar solar cell fabricated under identical processing conditions. The improved device performance was attributed to the combined effects of excellent AR properties of the black Si and better electrical contacts as compared to the vertical Si NW arrays used in earlier approach [39] by Peng and co-workers. However, the high surface recombination of minority carriers in black silicon remained the main challenging issues to the solar cell performance. Also, the Si NWs in the black Si layer have a tendency to be bunched/bundled, particularly for longer lengths, which affect the optical as well as solar cell characteristics. To address this, Jung and co-workers, in 2010, demonstrated that vertical and tapered Si NWs prepared using MACE process followed by post-KOH treatment were very promising for solar cells because of their strong light trapping ability [187]. It was shown that compared to the bunched NW arrays, tapered Si NWs could further suppress the optical reflectance over a broad spectral range due to a gradual transition of the effective refractive indices. The PCE of the tapered Si NW solar cell was reported higher than that of bunched NWs arrays processed in the same batch. However, the cell efficiency was quite low (~6.56%) as compared to that achieved earlier by Peng et al. [39] and Fang et al. [221].

It is to be noted that in most of the efforts made in MACE prepared Si NW arrays based solar cells discussed earlier used vertical Si NWs directly on Si wafers [39, 187, 221]. In such cases, the metal contact quality was rather poor due to non-compact contacts between electrodes and Si NW arrays and thus might lead to a significant electrical loss. Fang and co-workers tried to overcome the problem by fabricating solar cells on slantingly aligned Si NW arrays on p-type Si (111) substrate [221]. However, highly compact contacts could not even be made on slantingly aligned SiNW arrays also compared to that on a planar silicon surface made in the conventional silicon solar cells. Kumar and co-workers, in 2011, tried to address the problem of metal contacts on Si NW arrays surface by fabricating Si NW arrays selectively in the active area (i.e. emitter exposed to light) of the solar cell and keeping metal grid pattern on the planar surface [41]. The n^+-p-p^+ structure based solar cells were fabricated by conventional cell fabrication protocol (similar to that used by Peng and co-workers [39] except selective Si NWs fabrication) [26, 41]. In this approach, they improved the quality of front metal electrodes of the black Si nanostructures based solar cells while retaining the excellent AR property of the cell. The J_{sc} increased significantly to 37 mA/cm^2 but V_{oc} decreased marginally (544 mV) as compared with the cell made on planar Si substrates (without Si NWs). The efficiency (13.7%) realized was improved by absolute 1% compared with a cell made on planar Si substrates (without Si NWs) which was basically attributed to enhanced light absorption due to Si NW arrays. They also concluded that low efficiency of Si

NW arrays cell was due to enhanced recombination losses caused by the large surface area of the Si NWs. Though the steps introduced for protecting metal grid patterns (via simple photolithographic steps) resulted in improved solar cell performances, it required a high degree of accuracy of alignment of metal grid patterns deposition on the pre-patterned black Si substrates. Also, the large scale implementation of such a process involves additional cost and may not be the preferred choice.

In another approach to improve the performance of black Si solar cell, controlling the surface recombination losses associated with black silicon emitter surface (highly doped n^+-region) is critical. Um and co-workers, in 2014, demonstrated a self-aligned selective emitter successfully integrated into an antireflective Si NW solar cell [222]. The formation of a selective emitter in c-Si solar cells improves PCE by decoupling emitter regions for light absorption (moderately doped) and metallization (degenerately doped). Using the single-step MACE, they prepared NW arrays based black Si selectively in the light-absorbing areas between top-metal grids while selectively retaining Ohmic contact regions underneath the metal grids. They observed a remarkable ~40% enhancement in blue responses of internal quantum efficiency (IQE), corresponding to a PCE of 12.8% in comparison to the 8.05% of a conventional NWs based black Si solar cell. A similar concept was also demonstrated by Chen and co-workers, in 2011, wherein a simple and convenient double-step diffusion process for forming a highly doped n^+ region at the tips of the Si NW arrays was reported [223]. With this approach, the electrode-contact enhancement was achieved reducing effectively the series resistance which eventually leads to an increase in the J_{sc} in the cell. They could achieve a 40.2% increase in J_{sc} in two-step diffused processed solar cells as compared to that synthesized by one-step diffusion process. Similarly, a large number of solar cells with MACE based black Si as ARC layers have been fabricated [19, 26, 41, 73–76, 79–82, 86–88, 90, 162, 222, 224–241] in the past decade with efficiencies starting from as low as <9% to more than 20% in conventional thick silicon ($\geq$180 μm) wafers-based technology mostly by using the standard solar cell fabrication protocol, not only using the c-Si [26, 41, 73, 75–88, 90, 221–234, 236] but also on mc-Si wafers [19, 74, 78, 163, 235, 237–241]. Several aspects of black Si have been investigated such as influence of black Si layer thickness, aspect ratio of nanostructures, their distribution density, etc. including a few on large area (e.g. 125 mm × 125 mm or 156 mm × 156 mm) black silicon based solar cells with prime objective to produce efficient black Si solar cells [73, 224–233]. The majority of these black silicon solar cells have, in general, similar design as used in a conventional silicon solar cell (see Fig. 4 of Sect. 2), in which a p–n junction is formed near the front surface of a c-Si or mc-Si wafer and metal contacts are screen-printed or deposited by a PVD technique on both the front- and rear-surfaces followed by sintering for Omic contacts. However, the random alkaline/acid textured micro-surface in conjunction with a single-layer AR coating (like SiN_x) in conventional solar cells were replaced by a MACE black Si layer (in addition to a thin passivation layer of SiN_x, SiO_x, Al_2O_3 or their stacks) in black Si solar cells. Although black silicon offers excellent optical performance, no doubt, its electrical performance in solar cells is, on the whole, as expected is not straightforward but quite poor. The

black Si solar cells, in general, show lower PCE when compared with the conventional standard microtextured Si surfaces+single layer ARC processed under similar conditions [73, 242–244]. For example, Oh and co-workers reported PCE of 18.2% on <1 cm^2 cell area. But it was slightly lower than the standard control cells (18.6%); with random pyramidal textured surfaces, single-layer ARC fabricated under similar conditions [73]. Of course when compared with the cell made on the polished silicon surface (13.1%), the black cell performance was significantly much higher. Similarly, Kumar and co-workers [41] as well as Srivastava and co-workers [19, 86–88] reported improved PCE (by >1% absolute) in black Si solar cells as compared to that of the planar control cells (without any standard texturing and ARC) processed under the same batch. These results re-iterated that black cell can work as an effective light trapping medium or ARC.

So, in majority of the cases, it has been observed that black silicon reduces the reflectance of solar cells significantly but this optical gain does not improve the overall performance of the solar cells such as PCE, quantum efficiency, etc. The solar cells' performance parameters are strongly influenced by the thickness of the nanostructured layer, their aspect ratio of the nanostructures and density. Researchers have unanimously pointed out the concern of increased recombination losses (both bulk as well as surface recombination) of charge carriers, and the parasitic resistance (series and shunt resistance) due to enhanced surface area. Indeed, an increase in these parameters has a negative effect on the performance of the solar cells in contrast to the expected improvement due to the enhanced optical absorption. Therefore, the design principle of the black Si-based solar cell is that the ultra-low reflectance is not the only pursuit but optimizing the surface passivation, improving the electrode-contact property must also be considered for high-efficiency black Si surface based solar cells. There are investigations which shows that the performance of the black Si solar cells near the top emitter surface is very poor as compared to rest (planar) part of the device [234], and has been suggested that top thin section of the nanostructured layer (diffused emitter, n^+ or p^+ depending on the solar cell design) is effectively equivalent to an electronically 'dead' layer [75, 76]. In a summary, undoubtedly, the main culprits for the poor solar cell performance of the nanostructured black surface have been attributed to the following causes: (1) the enhanced surface area resulting in increased surface recombination of photo charge carriers; (2) relatively high and non-uniform emitter doping, leading to substantial Auger recombination and/or shunting, and increased leakage currents; (3) high parasitic losses (due to relatively poor metal contacts on the nanostructured surface). Also, the surface recombination may be critical, considering the non-conformal dielectric coatings on rough surfaces by conventional passivation techniques (PECVD-based SiNx in standard cell fabrication process) [73, 90]. Oh and co-workers showed that in high doping regions, Auger recombination is a dominating factor for carrier losses in black Si solar cells, while the surface recombination dominates only in low doping regions; and both surface and Auger recombination mechanisms are important in the medium doping region (sheet resistance of 90–210 Ω/m) [73]. The problem of low shunt resistance and high leakage current due to non-uniform doping in the black Si was demonstrated by Hsu and co-workers based on electroluminescence (EL) imaging

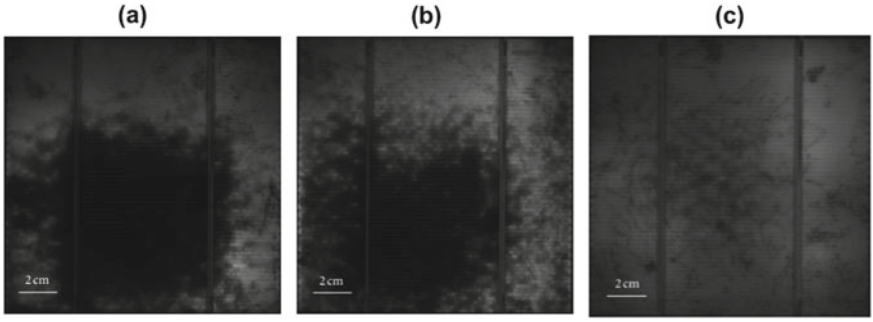

Fig. 17 6" mc-Si PV solar cells with surface texture using 1 μm, 600 nm, and 100 nm thick nanorods (black-nanostructured layer thickness) shown from **a** to **c** are tested by electroluminescence (EL) to investigate the doping uniformity in cells. The lateral nonuniform doping introduces defects (the dark regions) in solar cells, largely suppressing the minority carrier lifetime and the IR light irradiation. The solar cell decorated with 100-nm-thick nanorods has relatively few dark areas, showing the better doping uniformity. Adopted from Ref. [235]; Open Access

of the cells with different Si nanorods length [235] (see Fig. 17). They fabricated MACE-based black mc-Si consisting of different nanorod length on 600 wafers (size 156 mm × 156 mm), and produced solar cells using standard fabrication procedures. They found that black Si with longer nanorods led to more widespread non-uniform doping, largely suppressing the luminescence in silicon solar cells and exhibiting more dark areas (Fig. 17a and b) as compared to that having the shorter (100 nm) nanorods indicating a more uniform doping profile (Fig. 17c).

Moreover, making good metal contacts on nanostructured surfaces in black Si is always challenging. This is true with conventional microtextured Si (tip of the random pyramids in case of c-Si or tips of the hemispherical micro-pits in mc-Si). In case of black Si, the metal (coated either by any PVD or screen printed technique) cannot completely fill pores between nanostructures resulting in poor contact [245]. Examples of conventional screen printed Ag contacts on black Si are shown in Fig. 18 (SEM images) and Ti/Ag layer by thermal evaporation method are shown in Fig. 19. In addition, the black Si surfaces also have "self-cleaning" or super-hydrophobic properties, posing significant difficulties for screen printed metal contacts [67–72, 245] (see SEM images in Fig. 18). As mentioned earlier, the conformal deposition of a passivation layer, such as SiN_x, on black Si is challenging; and the non-uniform thickness of the SiN_x layer on the nanostructured Si surface makes the contact formation (metal fire through) even more challenging. For example, the silver paste cannot etch through the relatively thicker SiN_x layer deposited in the pores of the nanostructures at optimized process temperature for conventional silicon surfaces, thus raising contact resistance and hence affecting the fill factor [244]. These factors are largely responsible for the overall lower PCE of the black Si solar cells as compared to that of standard solar cells with conventional surface texturing scheme when processed under identical conditions. Quite often, the electrical losses of the

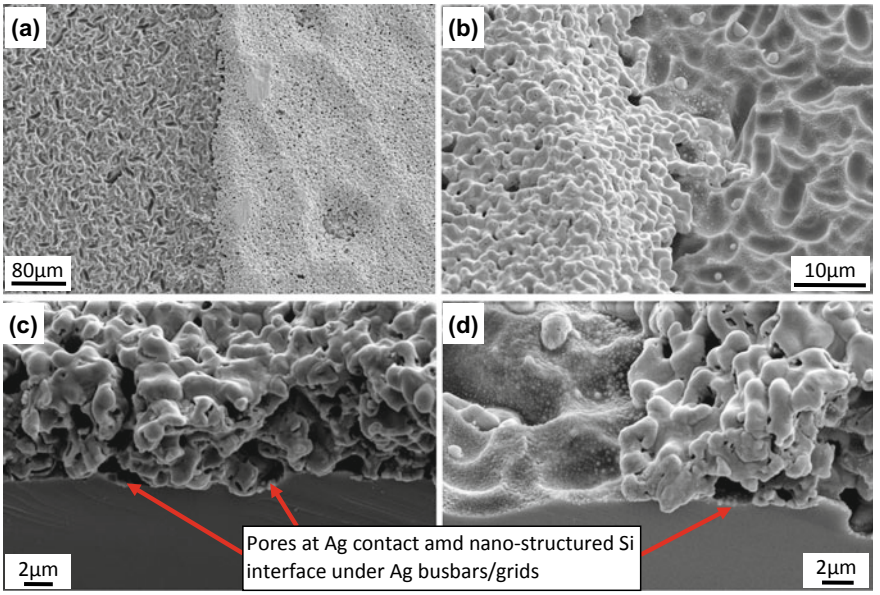

Fig. 18 **a** SEM images of screen printed and fired metal contacts on the MACE nanostructured black surface silicon solar cells, **a** top view showing Ag bus bar and the nano-microtextured surface of mc-Si, **b** magnified view of the Ag bus bar, **c** and **d** tilted view (45°) of the Ag contacts (bus bar/fingers/grids) at the edge (shown by arrows) indicating gaps (non-compactness or porosity of the Ag layer and nanostructured Si surface interfaces) resulting into high contact and series resistances and hence the lower fill factor

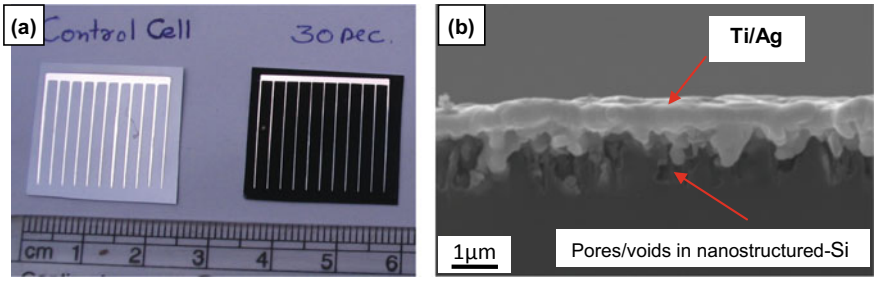

Fig. 19 **a** Digital images of planar control (shining grey surface) and nanostructured black surface Si based solar cells, **b** cross-sectional SEM view of Ti/Ag contact (deposited by metal evaporation method) on nanostructured Si solar cells showing non-contacts of metal grids and nanostructured Si interfaces

black-nanostructured Si surfaces cannot be compensated by their optical gain unless until these issues are addressed effectively.

Another way of assessing the performance of the solar cells with respect to the different spectral range of incident radiation (which also in a way shows the relative

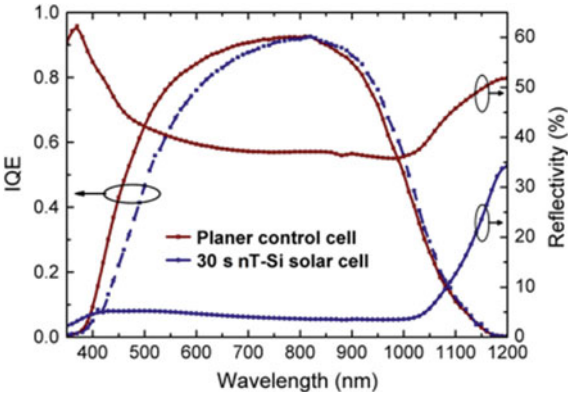

Fig. 20 IQE and reflectance curves for planar control and 30 s nanostructured-Si solar cells. A marginal decrease in the IQE of the nanostructured Si solar cell compared with the control planar cell can be seen in the short-wavelength region Reprinted from Ref. [88]. Copyright (2012), with permission from Elsevier

contributions of the different parts of the solar cells across the thickness of the solar cell from frontside to rear) is to study the quantum efficiency (QE) of the solar cells. As different energy photons are absorbed at different depths of the solar cell. Short-wavelength photons are strongly absorbed in the top layer of a silicon wafer, i.e. in the nanostructured black Si layer, while longer wavelength photons are absorbed in the middle or near the rear side depending on their energy. The QE of the black Si solar cells is especially poor in the short-wavelength region which is often termed as blue response of the solar cell [19, 41, 73, 88, 208, 245]. For example, a typical IQE (internal quantum efficiency) plot of the black Si solar cell is compared with that of a control planar cell (without any surface passivation layer in both cases) in Fig. 20 [19, 41, 88]. This is a typical characteristic of the black Si solar cells. Such spectral response (or quantum efficiency) of the black Si is again confirmation of electrical losses associated with the nanostructured black Si owing to the enhanced surface area and surface defects, heavy doping and the associated surface and Auger recombination in the black Si emitters as discussed above.

In the following section, the above issues of the black Si have been discussed in little more details along with the efforts made by different groups to circumvent these issues effectively. Besides, other possible ways of overcoming the problems for the development of high-efficiency black Si solar cells and its integration in the industrial line for the full exploitation of such a novel concept are also discussed.

7 Challenges and Way Forward to Improve Black Si Solar Cell Performances

7.1 Surface Passivation and Passivation Methods: Role of Dielectric Thin Films

Crystalline silicon is an indirect semiconductor and hence recombination losses in this material occur largely via defect levels within the band gap. These defects are located within the volume and at the surfaces of the sample (called as bulk and surface defects, respectively). Owing to the involvement of non-silicon atoms, the situation is more complicated at the Si surface [246]. The surface represents the largest possible disturbance of the symmetry of the crystal lattice and hence, due to non-saturated ('dangling bonds'), a large density of defects ('surface states') within the band gap exists at the surface of the crystal. These dangling bond defects can be divided into intrinsic and extrinsic defects. There are typically additional processing related extrinsic surface defects, for instance, due to dislocations or chemical residues and metallic depositions on the surface. In order to keep surface recombination losses at c-Si surfaces at tolerable levels, they must be electronically well passivated. In the case of solar cells, the chosen surface passivation scheme must be long-term stable (>20 years), and if applied to the illuminated cell surface, stable against the ultraviolet (UV) photons of sunlight [247]. There are two fundamentally different types of surfaces in a c-Si solar cell: metallized and non-metalized surfaces (refer to Fig. 4 of Sect. 2 for basic solar cell structure). Metal–silicon interfaces feature very high surface recombination and hence need to be carefully designed to avoid excessively large recombination losses. Similarly, in order to ensure a good short-wavelength (or blue) response of the solar cell, the illuminated non-metalized surface regions (the front surface) need to be well passivated and not too heavily doped in order to avoid the formation of a 'dead layer' (electronically). The importance of the passivation of both cell surfaces (front and rear, both light active and metallized silicon surfaces) is well recognized and advances in the passivation of both cell surfaces led to the first c-Si solar cells with 1-sun PCE above 20% in the 1980s [247–249]. Therefore, effective surface passivation is critical to realizing high-efficiency Si solar cells and is becoming ever more important as wafer thicknesses are reduced and bulk Si quality improves [247, 250–253]. The well-established Si-based passivation layers are SiO_2 [254], SiN_x [255], a-Si:H [256], and more recently Al_2O_3 [257–261] has drawn significant interest in the field. The mechanism of surface passivation is generally understood to involve a reduction in the number of interface states (called as 'chemical' passivation) and/or suppression of the concentration of either electrons or holes at the semiconductor surface (generally called as 'field-effect' passivation). In general, effective passivation of Si solar cells almost always involves a combination of these two mechanisms. Several reviews on passivation of silicon solar cells have been reported [247, 250–253] and a fundamental of surface passivation is well discussed by Armin and co-workers [247].

As discussed earlier, for black Si, owing to the feature sizes of the nanostructures, the surface area (surface to volume ratio) is significantly larger than that of a planar or conventional microtextured counterpart (i.e. bulk silicon surface). Hence, an effective passivation becomes extremely critical for the black Si solar cells. In the following section, some of the popular silicon-based passivation layers (dielectric layers), namely SiO_2, SiN_x, and amorphous Si (a-Si) or hydrogenated a-Si (i.e. a-Si:H) and the recent very promising materials, Al_2O_3, are briefly introduced in view of their characteristics for silicon surface passivation and their suitability for the black silicon surfaces. In this line, a comprehensive and critical review of the surface passivation of black Si solar cells is reported by Liu and co-workers [90].

7.1.1 Silicon Nitride

Silicon nitride (SiN_x) thin films deposited by PECVD is currently the industrial standard used to passivate the n-type emitter of p-type silicon solar cells (n^+-p-p^+ structure). It is deposited onto silicon using ammonia (NH_3) and silane (SiH_4) mixtures by PECVD at ~400 °C [262]. The relative weight of silicon and nitrogen can be adjusted by changing the flow rates of NH_3 and SiH_4. The nitrogen (N_2) may also be added into the gas mixture in order to lower the silicon content, which improves the etching rate of SiN_x (for forming the metal contact), minimize its UV light absorption, and maintain a high minority lifetime [37]. In Si-rich SiNx, the passivation is mainly governed by chemical passivation, i.e. by reducing the number of surface dangling bonds. As the nitrogen content increases, a high density of fixed positive charge ($Q_f \sim 10^{12}$ cm^{-2}) develops [260, 263]. This positive interfacial charge is beneficial for passivating n-Si through field-effect passivation. Essentially, an accumulation layer is created near the silicon surface due to the positive charge; thereby reducing the minority carrier concentration at the surface [260]. Owing to its good chemical passivation and positive interfacial charge, SiN_x passivation works for n-Si of arbitrary doping concentrations, and lightly doped p-Si; but it is less ideal for heavily doped p-Si [257] Based on SiN_x passivation, very low surface recombination rate of 6 and 15 cm/s have been reported for ~1 Ω-cm n-Si and p-Si, respectively [264–266]. Since solar cell emitters are always heavily doped and SiN_x does not work for p^+-Si, its passivation is limited to p-type solar cells (with n^+ emitters). In addition to its role of passivation, a quarter-wavelength thick SiN_x film also acts as an AR layer and is commonly used in commercial solar cells. The SiN_x has been employed for passivating n^+ black Si emitters in MACE nanostructured black Si solar cells [74, 90, 242]. In some of the early demonstrations on black Si, Liu and co-workers [242] observed significant improvement in black Si solar cell efficiency from 11.5 to 14.9%. Also, it has been observed that relatively thicker SiNx provides better passivation for black Si surfaces [267]. But a thick SiN_x film also increases serial resistance for screen printed metal contacts as discussed earlier. Therefore, a trade-off (in SiN_x thickness, low resistance metal contacts and better surface passivation) is required to maintain the overall optimal performance [267]. Also, since SiN_x is, generally, deposited by PECVD, its surface conformality is relatively poor for high

aspect ratio black Si. Nevertheless, given the trend towards the lower cost (but also lower quality) Si materials such as mc-Si, thin-film polycrystalline Si, the SiNx is one of the most promising surface passivation methods for surface passivation of the Si surfaces in conventional Si solar cells as this material, besides reducing surface recombination and reflection losses, additionally provide a very efficient passivation of bulk defects [247]. Despite few issues of non-conformality and related aspects, there have been several successful examples of a quite effective passivation of black silicon solar cells with SiN_x alone or in stack with other dielectrics such as SiO_2 or Al_2O_3 which will also be discussed in Sect. 7.1.5.

7.1.2 Hydrogenated Amorphous Silicon (a-Si:H)

Hydrogenated amorphous Si (a-Si:H) thin film is another important passivation material that can be deposited via PECVD at a relatively low temperature between 200 and 250 °C [268]. The a-Si:H can provide excellent passivation of Si surfaces and also enables the electrical contacting of Si wafers at the same time. Furthermore, the use of amorphous-crystalline silicon heterojunctions (a-Si:H/c-Si-SHJ) is a proven concept for high-efficiency silicon solar cells [269]. It forms a good interface to c-Si, thus provide strong chemical passivation, and can be used to passivate both p- and n-Si in conjunction with hydrogen annealing [257, 268–272]. Silicon surface recombination velocities (SRVs) as low as 2 cm/s have been demonstrated with a-Si passivation [260]. While employed in solar cells, minority carrier lifetimes greater than 5 ms and V_{oc} up to 738 mV have been demonstrated with post-deposition plasma-hydrogenation and annealing [273]. Later, V_{oc} up to 750 mV was also reported by Taguchi and co-workers [269]. The combination of the excellent optical properties of black Si with the high-quality surface passivation of a-Si becomes even more interesting as the a-Si:H/c-Si-technology moves towards thinner wafers in order to realize even higher V_{oc} [274]. However, a-Si strongly absorbs in the visible region of the solar spectrum, and is not thermally stable [257, 270–272]. Owing to the use of PECVD, the conformality of a-Si on black Si is challenging. Therefore, though a-Si:H has been quite useful in high-efficiency structure such as 'HIT'/SHJ solar cells [269, 273, 274], there have been very limited studies reporting a-Si:H passivation of black silicon solar cells. For example, Mews and co-workers reported excellent passivation of MACE black Si surfaces by thin a-Si layers deposited with PECVD achieving the minority charge carrier lifetimes of 1.3 ms, and an implied V_{oc} of 714 mV [275]. Furthermore, they also showed a gain in the QE for wavelengths >600 nm, as compared to random textured solar cells, eventually leading to 17.2% efficient a-Si:H/c-Si-SHJ solar cells with black silicon textures [275]. Very recently, Iandolo and co-workers also reported a-Si:H passivation of black Si surface however, the black Si texturing was performed by RIE [276]. They demonstrated minority lifetime over 1.5 ms for the best black Si surfaces, corresponding to over 700 mV of implied V_{oc}, values higher than on reference surfaces prepared by KOH texturing. Fabrication of solar cells resulted PCE of 16.1% for black Si, much lower as compared to 18.5% for KOH reference cell. The QE measurements revealed that

the black Si cells lose ~0.5 mA cm^{-2} of J_{sc} in the visible and of 0.8–1 mA cm^{-2} in the IR region [276].

7.1.3 Thermal Silicon Oxide (SiO_2)

Thermal oxide (SiO_2) provides very good chemical passivation, reducing silicon interfacial defects to ~10^9 eV^{-1} cm^{-2} [260, 263, 277]. It also contains a small amount of positive fixed charges with a density of 10^{10} to 10^{11} cm^{-2}, and therefore have capability to provide a weak field-effect passivation [260, 263]. It can be used to passivate either n- or p-Si of arbitrary doping concentrations with excellent surface conformality. The primary drawback of thermal oxide passivation concerns its high processing temperature (850–1100 °C). Consequently, only c-Si with low impurities is suitable for this process [278]. In mc-Si, such a high processing temperature leads to the diffusion of impurities from grain boundaries to the bulk. The SiO_2 is thus not preferred for mc-Si, owing to both performance and cost/throughput considerations [262]. Moreover, the dopants in the emitter are drawn into the oxide layer, changing the doping profile and potentially degrading solar cell efficiencies during high-temperature thermal oxidation in some cases [243]. Various strategies have been developed to circumvent this high-temperature problem. For example, SiO_x can be deposited via low-temperature PECVD. This layer, however, has poorer passivation performance in comparison to thermal SiO_2, but its properties can be improved by capping another dielectric layer such as amorphous SiN_x (a-SiN_x) or Al_2O_3 layers [260]. Alternatively, low-temperature wet oxidation (at 800 °C) is also an alternative to high-temperature dry oxidation [279] which can provide good passivation. Owing to its good surface conformality, the SiO_2 has been employed to passivate n^+ emitters in black Si [73, 75, 280]. Oh and co-workers have also used SiO_2 to passivate the MACE nanostructured black silicon surface in their record (at that point of time) lab PCE of 18.2% black Si solar cell [73].

7.1.4 Aluminium Oxide

Aluminium oxide (Al_2O_3) is an excellent surface passivation dielectric material, and can be deposited on silicon via several methods, such as atomic-layer deposition (ALD), PECVD and pulsed laser deposition [260, 281]. The ALD has properties of excellent surface conformality for complex surface morphologies like the black silicon ones (see Fig. 22 of Si NWs and ALD-Al_2O_3 coated Si NWs, reproduced from [80]). In an ALD process of Al_2O_3 deposition, an aluminium precursor, typically $Al(CH_3)_3$, and an oxidative agent, typically H_2O, are introduced into the reaction chamber sequentially [278]. The deposition of $Al(CH_3)_3$ or H_2O is a self-limiting process; in which a monolayer of these molecules covers the entire substrate surface, upon which further deposition of the same type of molecules is prevented. Hence, sequential deposition of an $Al(CH_3)_3$ or H_2O monolayer, and their reactions lead

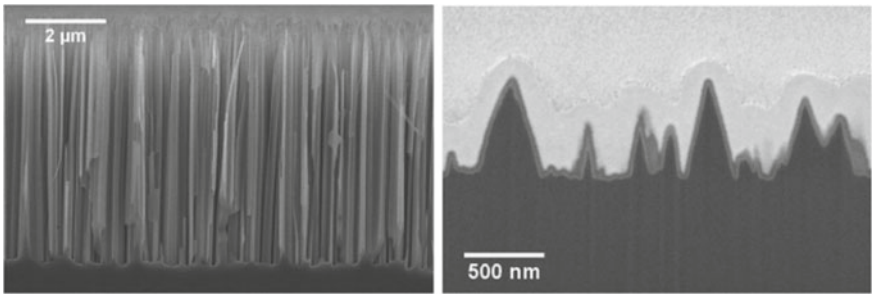

Fig. 22 **a** SEM image of passivated long nanowires (NWs) fabricated in a 10 min long Ag-MACE etching step. The NWs are conformally coated with 35 nm Al_2O_3 and have lengths of ~6 µm and diameters of about 50–150 nm. Due to the scale, the passivation layer is not well visible. **b** Cross section of the Au-MACE-structured black Si nanocones (NCs). The black surface is passivated with a 35 nm thick layer of Al_2O_3 (grey), followed by the ZnO:Al coating (white contrasts) for better visibility. A Pt protection layer was placed on top (light grey)-indicating perfect example of conformal coating of complex structures like black Si by ALD. Reproduced after permission from Ref. [80], © 2014 WILEY-VCH Verlag GmbH & Co. KGaA, Weinheim

to the formation of an atomic layer of Al_2O_3 in each cycle. Consequently, excellent thickness and uniformity control and great conformality over large area can be achieved [260]. In addition to H_2O, O_3 or O_2 plasma is often added to the reaction chamber as an alternate oxidant source. As a result, ALD process is classified into two categories; Thermal ALD wherein either H_2O or O_3 is used as an oxidation source and plasma-assisted ALD (PE-ALD) in which O_2 plasma is used as oxidation source [260, 278]. However, the deposition rate of PE-ALD is 30% faster in comparison to that of thermal ALD, owing to more active oxygen radicals and a shorter purging time [257, 260, 278]. Further, the PE-ALD offers lower impurity levels, and better quality, especially at low temperatures [260] and provides good passivation, which is almost independent of temperature (200–300 °C range) [278].

Since 2006, passivation by ALD deposited Al_2O_3 has been studied extensively for its outstanding performance on highly doped p-type Si [257, 258, 282]. It has been shown that very thin layers of Al_2O_3 are sufficient to obtain very low SRVs [283–286]. The Al_2O_3 offers a unique combination of two complementary passivation effects: first, the coated layer contains a quite high number of negative fixed charges [263] (up to $Q_{fix} = -1 \times 10^{13}$ cm^{-2}) that lead to a very strong field-effect passivation, and second, the interface exhibits a very good chemical quality with interface defect densities as low as $D_{it} = 4 \times 10^{10}$ $eV^{-1}cm^{-2}$ [79, 287]. As a result, the surface passivation of silicon solar cells by Al_2O_3 is considered a key technology in future industrial high-efficiency solar cell production [288]. The interfacial defect density between Al_2O_3 and Si is estimated to be ~10^{11} eV^{-1} cm^{-2}, [263], which is higher than that offered by thermal SiO_2 (10^9 to 10^{10} eV^{-1} cm^{-2}). However, Al_2O_3 exhibits a stronger field-effect passivation due to a larger Q_{fix}, up to ~10^{13} cm^{-2} [257, 263, 278]. This value is much higher than that in SiO_2, (Q_{fix} ~ 10^{10} to 10^{11} cm^{-2}).

Consequently, very low SRVs of 2 cm/s and 13 cm/s have been reported for low resistivity n-Si and p-Si wafers, respectively [257]. These values are comparable to those offered by state-of-the-art thermal oxide passivation. Because of its relatively low D_{it} (chemical passivation), Al_2O_3 has also been employed to passivate n^+-emitters and offers good performance, although SiO_2/Al_2O_3 stacks without negative charges are likely preferable [233, 260, 289]. Similar to SiN_x, Al_2O_3 (with a refractive index of 1.60–1.65 for 2 eV light can also serve as an AR layer [257, 290].

The ALD-Al_2O_3 has excellent thickness control, good step coverage and conformality, low defect density, high uniformity over a large area, good reproducibility and low deposition temperature [233]. The primary drawback of ALD-Al_2O_3 is related to its slow growth rate (~0.5–1.5Å per cycle, each cycle takes several seconds). However, several industrial processes have been developed to address this concern [260]. The ALD-Al_2O_3 is an attractive black Si passivation option, owing to its excellent conformality on nanostructures (see Fig. 22) and has been investigated by several research groups [233]. Thermal ALD Al_2O_3 passivation has been applied to black Si solar cell with an n^+-emitter by Wang and co-workers [233]. The excellent passivation improved the carrier lifetime from 1.05 to 18.1 μs, leading to a high PCE of 18.2%. In addition, the nanostructured black silicon wafer covered with the Al_2O_3 layer exhibited a total reflectance of ∼1.5% in a broad spectral range (400–800 nm). Consequently, an 8% increment of J_{sc} and 10.3% enhancement of efficiency were achieved due to the ALD-Al_2O_3 surface passivation [233].

7.1.5 Stacked Dielectric Layers for Effective Surface Passivation of Black Silicon Solar Cells

As seen above, a number of attempts have been made to develop effective surface passivation schemes employing single layer or double layer stacking of dielectrics such as SiO_x, SiN_x, $SiO_x + SiN_x$, ALD-$Al_2O_3$for black Si [71, 75, 231, 233, 235, 241, 291, 292]. However, every dielectric passivation material has limitations. For example, the positive fixed charge in SiN_x degrades its passivation effect on a p^+-emitter; and the performance of Al_2O_3 is less ideal on an n^+-emitter. A stacked dielectric layer, however, can be employed to avoid these drawbacks. For instance, a SiO_2/Al_2O_3 stacked layer removes the negative fixed charge associated with Al_2O_3, and offers an improved passivation performance on n-Si [260]. In addition to tuning the fixed interfacial charge density, a stacked layer may also boost chemical passivation, such as in the case of SiO_2/SiN_x. In this stacked passivation layer, a SiO_2 layer >10 nm is required to provide a good interface to silicon; during the deposition of SiN_x, further hydrogenation helps to passivate the dangling bonds at the Si/SiO_2 interface, leading to an impressive passivation effect. The SiO_2/SiN_x stack also greatly improves the thermal stability of the dielectric layer; this feature is critical for solar cell fabrication, since solar cells have to go through a few high-temperature processes. Nevertheless, thermal oxide in this stacked layer is fabricated at high temperature and is not desirable. Stacked Al_2O_3/SiN_x layers have also been employed for both passivation and AR effects on p-Si. In particular, Al_2O_3 may be deposited by PECVD instead

of ALD on planar wafers to minimize cost and increase throughput. Duttagupta and co-workers showed that in the PECVD AlO_x/SiN_y stacked layer on a p^+ emitter, 5 nm AlO_x was enough for the passivation effect; the additional 65 nm SiN_x enhanced the AR effects and resulted in reduced weighted reflectance of 2.3% in the 300–1000 nm range [292]. When used in black Si solar cells, one additional concern on the dielectric passivation layer regards its surface conformality. The SiO_2/SiN_x has thus been adopted by several research groups [232, 235, 264]. One of the obvious reasons for preference of SiO_2 is its great surface conformality with Si irrespective of surface morphology. For example, Lin and co-workers have demonstrated an effective and industrially compatible technique of dielectric passivation to improve the electrical properties of Si NW based black Si solar cells without compromising with the optical properties of the black Si [231]. It was shown that the SiN_x-based passivation could reduce defect state density quite effectively and also suppressed the Auger recombination due to the well-known surface passivation and hydrogen-diffusion-induced bulk passivation. They further combined the SiN_x with the SiO_2 (SiO_2/SiN_x stack) to obtain the best Shockley–Read–Hall (SRH) and Auger recombination suppression in the black Si solar cells to realize the high-performance solar cells with a PCE of 17.11% on a large size of 125 mm × 125 mm. Interestingly they tried single-layer SiN_x, SiO_2 and then a stack of SiO_2/SiN_x and found that the stack of SiO_2/SiN_x exhibited the best passivation of the black Si surface and hence resulted in the best electrical outputs in terms of the solar cell efficiency. The schematic of the proposed passivation schemes and cell fabrication protocol used by Lin and co-workers are presented in Fig. 23 [231].

In the same line, Liu and co-workers showed that SiN_x could not completely cover the black Si surface, resulting in a PCE of only 14.9% [242]. By inserting an additional thermal SiO_2 layer (of 20 nm) between bulk silicon and SiN_x (of 60 nm), the surface coverage and associated passivation effect were improved significantly; consequently, the solar cell PCE increased to 15.8%. Similarly, Zhao and co-workers investigated the performance of black Si solar cells with a single and double stack layer of dielectrics passivation on a large area (156 mm × 156 mm) [232]. It was observed that the PCE of black Si solar cells without passivation could be only 13.8% which was enhanced to 16.1% and 16.5%, respectively, with SiO_2 and SiN_x:H passivation of Si NWs surfaces. Further, the passivation by SiO_2/SiN_x:H stacks exhibited better efficiency (17.1%) as compared to single dielectric layer based surface passivation of black silicon solar cells. It was suggested that the SiO_2/SiN_x:H stacks layer decreased the Auger recombination through reducing the surface doping concentration and surface state density of the Si/SiO_2 interface, and SiN_x:H layer suppresses the SRH recombination in the Si NWs based silicon solar cell yielding the best electrical performance. Similarly, Zhao and co-workers also found that their solar cells passivated by the stacked layer of SiO_2/SiN_x offered higher PCE (17.1%), in comparison to those passivated either by SiO_2 (16.1%) or SiN_x (16.5%) alone [232]. Interestingly, Zhao and co-workers also noticed that thermal oxidation reduced emitter doping concentration, which is beneficial for minimizing Auger recombination in an over-heavily doped emitter [232]. However, high-temperature thermal oxidation is undesirable, especially for mc-Si solar cells. Therefore, Hsu and co-workers adopted

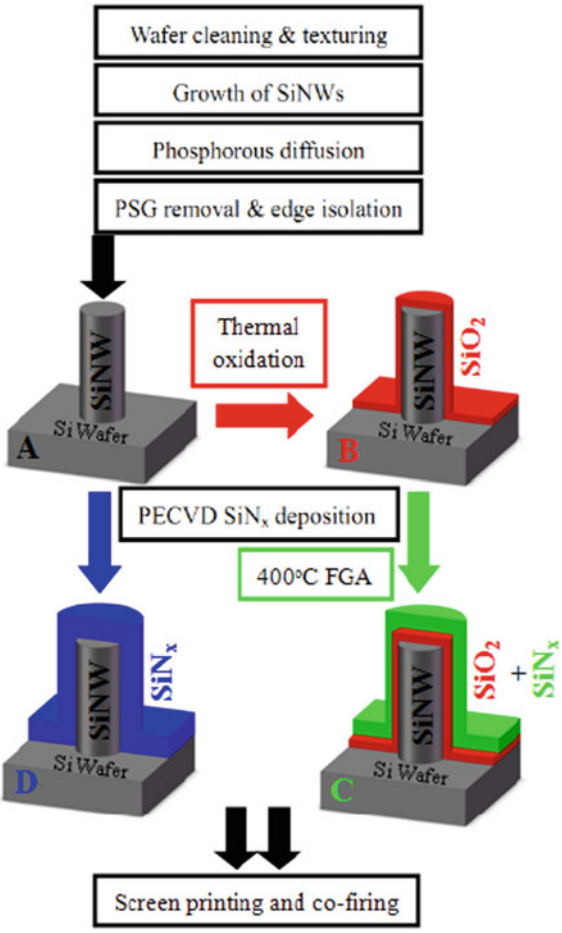

Fig. 23 Schematic fabrication process diagrams of the SiNW based solar cells with different passivations for series **a** (in black, bare SiNWs without dielectric shell); **b** (in red, thermal oxidation of ~10 nm SiO_2 layer); **c** (in green, thermal oxidation ~10 nm SiO_2 layer combined with 60 nm SiN_x deposition); and **d** (in blue, 70 nm SiN_x deposition only). Ref. [231] © IOP Publishing Reproduced by permission of IOP Publishing. All rights reserved

a trade-off strategy by performing a quick thermal anneal followed by PECVD SiN_x growth on an n^+-emitter. With a hydrogenated SiO_2 (5 nm)/SiN_x (50 nm) stack, the minority carrier lifetime increased substantially from 1.8 to 7.2 μs for a 100 nm-long nanorod-coated solar cell and a high PCE of 16.38% was achieved [235]. Instead of thermal oxide, Wong and co-workers passivated their nanostructured n^+-emitter with 20 nm ALD-Al_2O_3 to achieve good surface conformality, followed by 70 nm PECVD SiN_x resulting in a PCE of 16.5% [71]. In summary, the stack layer of Al_2O_3/SiN_x or SiO_2/SiN_x performs better for nanostructured black Si solar cell passivation as compared to a single layer of Al_2O_3, SiN_x or SiO_2.

7.2 Control of Optimal Thickness of Black Si Layer

A thicker nanostructured layer is required to minimize the surface reflectance, however, such a surface structure results in a significantly enhanced surface area for recombination and poses considerable challenges for dopant doping and metal contact formation [19, 41, 88]. In order to attain an improved solar cell performance, the thickness of the nanostructured layer must be tightly controlled. To overcome the issue, several optimal thickness values have been suggested. For example, Yuan et al. found that a thickness ~500 nm yielded the highest solar cell efficiency [75]. Similarly, Srivastava and co-workers [19, 88] also found <500 nm thickness of the black silicon layer was sufficient for improved solar cell performance both in c-Si and mc-Si wafers. Oh and co-workers reported a high efficiency of 18.2%, for black silicon layer thicknesses of <400 nm [73]. Very recently, Zhang and co-workers studied the influence of Ag-ion concentration on the performance of mc-Si silicon solar cells textured by MACE to optimize the Ag-ion concentration required for the optimum trade-off between optical gain and solar cell performance (electrical parameters) in diamond wire sawn (DWS) mc-Si wafers [241]. With the increasing of Ag-ion concentration, the light-trapping capabilities keep improving, however, the solar cell's electric performances deteriorated dramatically when Ag-ion concentration reached a certain value. For an optimum Ag-ion concentration value, the black mc-Si solar cell's performance was enhanced and an efficiency of 18.94% was obtained for a large size of 156.75 mm × 156.75 mm wafer. An absolute efficiency of 0.5% was improved in MACE black mc-Si solar cells as compared to the conventional acidic textured DWS mc-Si solar cell. It shows the necessity of controlling the Ag-ion concentration in the MACE of black silicon. They concluded that low concentration of Ag-ion followed by shallow nanopores which have bad optical harvesting, while high Ag-ion concentration leads to overcrowded deep nanopores and deteriorates mc-Si solar cell's performances. Overall, the optimal thickness for nanostructured black silicon layer may be considered taking into account the fact that electrical issues are properly addressed, i.e. by applying surface passivation and doping strategies suitable to the nanostructured surface. Therefore, the conflicting optical and electrical needs of MACE black Si requires a trade-off in the optimized morphologies for solar cell applications [241].

7.3 Achieving Metal and Other Surface Defects Free Clean Surface

Surface cleaning of the MACE black silicon is another challenge for efficient black silicon solar cells. As, black Si formation, in addition to enlarging the surface area, also creates a considerable number of defects within a nanostructured surface; a thorough cleaning or post-etching process is essential to remove these defects. In MACE black silicon, shallow nanostructuring is always preferred and advantageous

in several ways (as discussed above an optimal depth of nanostructuring should be used in order to minimize the surface area and other surface issues in solar cell fabrication processing). Deep or longer etching creates a sub-oxidized surface with a significant number of surface defects, the surface of the chemically etched nanostructures is very rough (surface states/porous layer with a size of 2–5 nm). This surface porosity has little impact on the optical reflectance of the black Si, however, causes a substantial increase in its surface area. Furthermore, it is likely that a small trace of metal ions/particles diffuse into silicon during the black Si fabrication. This issue becomes even more vital if a high-temperature process (e.g. doping, contact firing) follows the black Si formation. Algasinger and co-workers performed a modified RCA cleaning, successfully removing the surface defects and gold nanoparticles used for the MACE [208]. This cleaning procedure also etched away the small nanoprotrusions. The reduced surface area makes the surface passivation much easier to implement. Consequently, they could achieve a higher carrier lifetime after passivating the cleaned black Si surface by ALD-Al_2O_3 [208]. Similarly, surface cleaning using a diluted alkaline solution (KOH, NaOH or TMAH) or chemical polishing of the surface by any other suitable etching bath post MACE process has also been used by several groups and is very effective in removing the surface defects/protrusions along with other surface impurities. Yue and co-workers used additional 30 s treatment of MACE black mc-Si to achieve 18.03% efficient black mc-Si solar cells on 156 mm × 156 mm wafers which was 0.64% absolute higher than the conventional mc-Si solar cell (17.39%) and much higher (by 1.79% absolute) than black mc-Si solar cell without NaOH treatment [237]. Though, there was a marginal increment in the surface reflectance of the black mc-Si after NaOH treatment (5.45% as compared to 2.03% in as-prepared black mc-Si surface) (see Fig. 24). The gain in electrical performance was significant. This was primarily due to the removal of the surface defects/residues after the MACE process [237].

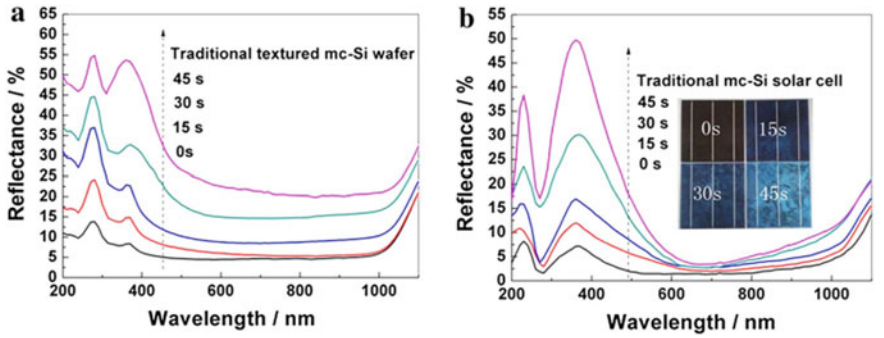

Fig. 24 Reflectance curves: **a** Ag-assisted etched mc-Si with NaOH treatment of different time and traditional textured mc-Si wafer; **b** solar cells using the samples in **a** as substrate wafers. Inset in **b** is photos of the four black mc-Si solar cells Reprinted by permission from Springer Ref. [237], Copyright (2014)

This has been the highest absolute gain in efficiency by applying black Si concept in any solar cells as compared to their counterpart processed in the same conditions (both on c-Si or mc-Si). Interestingly they used only SiN_x layer as passivation for the black Si surfaces. It is possible to improve the performance even better by applying a suitable stacks (SiO_2/SiN_x or Al_2O_3/SiN_x) passivation layer. In the same line, Lin and co-workers [238] demonstrated a certified conversion efficiency of 17.75% on large size (156 mm × 156 mm) silicon cells, which was ~0.3% higher than the acid textured counterparts. This was higher-than-traditional output performance of nanostructured black mc-Si solar cells through a trade-off between optical and electrical performances (as discussed above) by controlling surface reflectance, surface area enhancement via the treatment of mc-Si black surface with post-MACE NaOH treatment to control the nanostructure geometrical parameters. These examples, certainly, are very promising and open potential prospects for the mass production of the MACE nanostructured black Si solar cells with improved performances. Of course, it was also due to the fact that they used effective surface passivation schemes.

7.4 Optimal Emitter Design and Doping Profile Control

The high-temperature dopant (such as phosphorus/boron) diffusion parameters for making emitters that are optimized for the conventional textured (microtextured or planar) surfaces may not be directly applicable in the case of MACE nanostructured black Si. The increased surface area of the nanostructured surface may cause a high dopant diffusion rate at the same temperature as compared to the planar or the conventional textured silicon surfaces. In general, the higher doping concentration (lower sheet resistance of the emitter) in black silicon is observed as compared to planar silicon processed under identical conditions. For example, Zhong and co-workers compared the resistance of a black Si wafer and a planar wafer with the same doping conditions and found that the black Si had a lower resistance, indicating a higher level of doping [171]. Therefore, a lower doping temperature and time should be employed in case of black silicon in order to control the black Si doping concentration and minimize Auger recombination [171]. Alternatively, etch-back process of the diffused emitter can also be employed in a controlled manner by suitable etchants like KOH, NaOH/LiOH or TMAH) to remove few tens of nanometers from the top surface which can etch out the heavily diffused surfaces (‘dead’ layer) and in a way the emitter properties can be tailored as per the demands of the black silicon solar cells. This approach was adopted by Oh and co-workers [73]. They performed doping at 850 °C with a subsequent anisotropic TMAH etch procedure. They could overcome two issues with this short TMAH treatment of black Si surface post-emitter formation: (i) removal of highly doped (dead layer) on the emitter surface (front surface) of the black Si; (ii) relative reduction of the total surface area which was primarily caused by reduction in the nanostructured layer thickness and an increase of its surface feature size. However, this step (TMAH etching) resulted in a marginal

increase of reflectance (as also discussed earlier). Consequently, they could minimize the surface recombination and Auger recombination with the realization of the 18.2% black Si solar cell performance which was the highest ever in black Si at that point of time [73], though it was only on <1 cm^2 area of the sample. Similarly, Zhao and co-workers achieved 17.3% efficient black silicon solar cells without AR coating via short TMAH etching after the formation of the diffused emitter in the MACE black Si [236]. They also claimed that black Si nanostructures modification by TMAH suppressed the surface recombination and Auger recombination at and near the emitter surface, leading to increase in the effective minority carrier lifetime of the black Si solar cells from 10.7 to 20.8 μs and hence the improved QE in blue region, the main limiting factor for the efficiency of black Si solar cells. In this line, Li and co-workers employed both surface engineering of the MACE Si both pre-and post-emitter diffusion (or after MACE and after emitter diffusion) by dilute bath of KOH for short duration [293]. They showed that black-Si wafers with a 15 s KOH etching after MACE and an additional 30 s KOH modification after the diffusion exhibited better performance as a compromise between low surface recombination and low reflectance. They showed significant improvement in the performance of the solar cells (PCE:17.7%) after two steps KOH treatment as compared to only 15.3% without any KOH treatment with a 10 nm SiO_2 passivation and screen-printed contacts. Interestingly, they could achieve PCE of 18.5% after applying SiO_2(10 nm)/SiN_x(45 nm) stack layer passivation scheme in p-type 156 mm × 156 mm black Si solar cells. Therefore, via incorporating the optimized stack passivation scheme of SiO_2/SiN_x, the surface morphology modification and emitter optimization technique, their black silicon solar cells obtained a large improvement of 3.7% in average PCE compared to standard black silicon solar cells without any optimization [293].

Another approach to avoid the heavy doping issue associated with black Si is to perform emitter formation (doping the wafer with P/B) prior to the MACE nanostructuring. This approach has been successfully adopted by few groups [74, 232, 294]. Nevertheless, a high doping concentration at the emitter is likely to change the surface morphology of the resulting black Si. For example, observation of highly porous silicon nanostructures formation in heavily doped silicon is very common [149–153] and also the doping profile (dopant concentration) varies with the junction depth (emitter thickness) which may cause different morphology and surface features in the black silicon across the black silicon layer. Moreover, in MACE, the surface feature size tends to increase in line with the doping level of the silicon substrate, and the impact of doping on the etching rate is not yet fully understood [122]. The possibility of control of etching is difficult to protect the junction on large area as there is always variation in doping level across the wafer, though small (in case of the highly uniform and controlled doping). As the MACE process is self-controlled, therefore puncturing/shunting of the p–n junction could be a serious issue (for a shallow emitter of ≤400 nm with variation in doping profile across the wafer and hence different etching rate at a given condition). Further work is thus required before a wider deployment of this doping approach can be adopted.

7.5 *Optimal Metal Contacts*

Currently, metal electrodes designs on solar cells are optimized as per the standard microtextured and ARC surfaces. However, the black silicon, surface due to enhanced surface area, has higher surface resistance compared to that of a planar surface of conventional solar cell [295]. Consequently, it would be essential to optimize the metal grids (fingers and busbars) design and also fine-tuning of the metal contact formation process parameters, particularly the fire through contacts of screen-printed contacts, in view of the optimal dielectric layer on the surface (both in front and rear side) in the black Si solar cells to enhance the charge collection efficiency.

In summary, it is obvious that in spite of excellent optical performance, the efficiency of a solar cell with nanostructure texturing is limited by enhanced surface recombinations due to increased surface area. Nevertheless, in some of the latest developments, as discussed in few examples above, the black Si solar cells have now started outperforming the conventional/standard microtextured solar cells processed under similar protocols [237, 238]. This is becoming possible owing to continuous efforts made to address the above-mentioned challenges via optimal surface morphology, emitter properties, effective surface passivation (stack layer) and metal contacts suiting the nanostructured black Si.

8 Multi-scaled Textured Black Si Solar Cells: *Recent Developments Employing MACE Process*

In the past couple of years, the multi-scale texturing (also quite often referred as dual texturing, binary texturing, hierarchical texturing, etc. in the literature) which consists of the application of black silicon nanostructures on microtextured (alkaline textured random micro-pyramids in c-Si or acid textured micro-pits in case of mc-Si) have been introduced with quite promising PV performances in large-sized (156 mm $\times$ 156 mm) wafers [83, 240, 296–299]. A typical example of multi-scaled textures based black Si surfaces (both in mc-Si and c-Si) are shown in Fig. 25. The significant developments have been made to this end achieving ~18.5% in mc-Si [296] and >20.0% in c-Si [298] black Si solar cells with a potential to go past 20.0% in both mc-Si and c-Si. In some recent cases, the black Si cells are outperforming the standard c-Si and mc-Si solar cells and hence seem very promising in large-scale deployment of the black silicon concept in the PV industry in near future.

Moreover, the MACE black Si concept is also drawing a lot of interests not only in R&D but also in the PV industry for its potential superiority to replace the conventional acid texturing process for the new technology of mc-Si solar cells based on diamond wire sawn (DWS) mc-Si wafers [239–242, 300–305]. It is noteworthy that acid texturing process is an industry standard for saw wire cut/slurry based mc-Si wafers. The DWS mc-Si is expected to be the mainstream wafering technology in the Si-based PV industry in the coming years. The DWS technique has several advantages

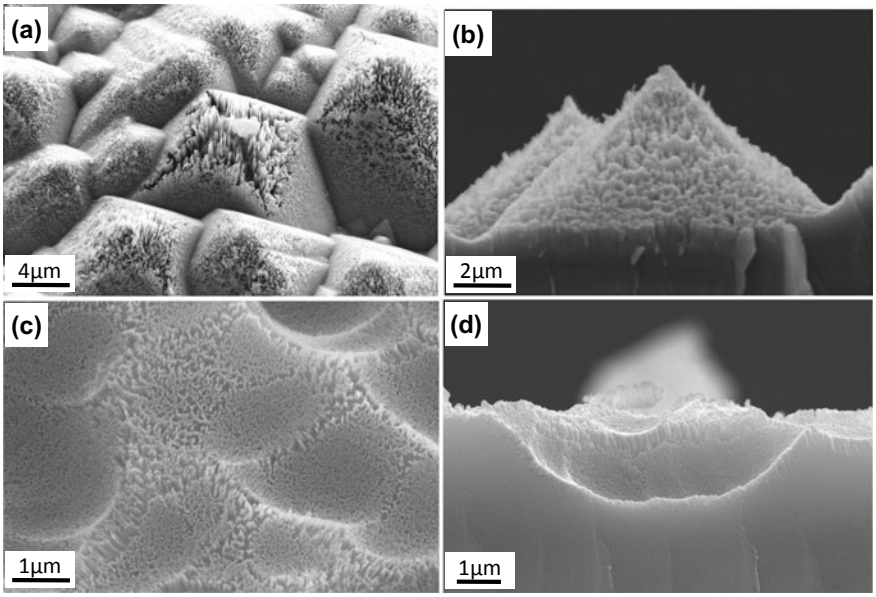

Fig. 25 Representative SEM images of Ag-assisted MACE-based binary (nano/microstructured) texture silicon surfaces; **a** and **b** binary textured Si surface on c-Si; and **c** and **d** binary textured Si surface on mc-Si. Images in **a** and **c** are 45° tilted and in **b** and **d** are in a cross-sectional view

such as larger output of wafers per ingot, higher precision enabling production of thinner wafers, lower environmental impact, easier recovery of silicon kerf loss and less surface mechanical damages [240, 300–302]. In recent years, DWS mc-Si wafers have been used in the PV industry because of its relatively lower cost (owing to the DWS technology), as compared to that of slurry-wire-sawn (SWS) mc-Si wafers [303]. However, there is no effective method for texturing the DWS mc-Si to decrease light reflection and to improve the PCE. Thus, the large scale use of DWS mc-Si wafer is limited in the PV industry [305]. However, the MACE black silicon technology is a promising approach to fabricate the nanosized textures on the DWS mc-Si's surface [90, 282, 305].

Black silicon with nanosized textures is very important to the DWS mc-Si solar cell due to its low reflectivity. For example, Su and co-workers found that in order to improve the PCE of DWS mc-Si solar cell with nanosized textures, the textures' morphologies must be modified by acid etching [240, 300]. The acid etching is the defect removal etching process. A DWS mc-Si solar cell with modified nanosized textures was successfully obtained by MACE and suitable acid etching process, whose reflectivity was lower than that of a DWS mc-Si solar cell prepared by conventional acidic texturizing. The highest PCE of 19.07% was achieved with a 0.6% (absolute) gain in the PCE of MACE black DWS mc-Si solar cell, as compared to that of the DWS mc-Si solar cell using the conventional acidic texturizing. These results are quite important as traditional acidic etching could not create a low reflectivity

structure on the DWS mc-Si, but MACE technique could decrease the reflectivity through nanostructures. Meanwhile, the efficiency of solar cells fabricated by traditional acidic etching techniques has reached the ceiling, and the MACE technique has the potential to further improve the performances of solar cells. Further, improvement of the cell performance can be realized by optimizing diffusion and passivation and other critical aspects suiting to the black Si nanostructured surface on DWS mc-wafers.

9 Crystalline Silicon Thin Films Solar Cells Based on Black Silicon

As discussed earlier, while black Si poses several challenges such as in performing doping, forming good Si/metal contact and increased surface recombination, novel cell designs can be adopted to mitigate these problems. Of course, the terrestrial PV market is currently dominated by crystalline silicon wafers (c-Si and mc-Si). Also, as described earlier, for a conventional Si solar cells, the active Si layer has to be sufficiently thick ($\geq$180 μm) in order to harvest incident photons significantly. However, due to its material intensiveness (thick and quality material), it is always difficult to reach the cost levels required for a widespread application of PV with the current wafer-based technology. An alternative is to use thinner silicon wafers/films and develop a strategy for thin silicon solar cells. Therefore, one possible route to reduce the cost of silicon PV is to develop thin-film solar cells (thickness <30 μm) or even ultra-thin solar cells (thickness <10 μm), by significantly decreasing the consumption of Si during solar cell fabrication. Thin solar cells also offer many other advantages, such as lightweight, mechanical flexibility and easy integration with a diverse range of substrate materials [172, 306–308]. Surface texture of ultra-thin silicon via alkaline or acid wet etching requires the usage of a photolithography-defined mask [309] and is not considered to be industrially compatible [310]**.** Hence, the limitation of wet etching in thin silicon solar cells presents a good opportunity for developing black silicon texture. Experiment and theory have shown that black Si enables efficient broadband absorption of light, less than 1% of the Si material (having black silicon surface) would have the same absorption efficiency as in the conventional Si-wafer based devices. The reduced Si materials requirement in black Si solar cells would decrease the production cost, since the Si material is a major cost for Si-based PV cells.

9.1 Nanostructured Black Si Thin-Film Solar Cells on Cheap Glass Substrates

The polycrystalline silicon thin-film solar cells on supporting materials like glass is quite promising as glass is a cheap, transparent, electrically insulating, long-term stable, readily available and already a standard component in the PV modules. However, the drawback of glass sheets is their limited thermal stability, excluding the use of lengthy high-temperature (>650 °C) processing steps during solar cell fabrication. A group at Helmholtz-Zentrum Berlin für Materialien und Energie-Institut für Silizium-Photovoltaik, Berlin, Germany has done outstanding work towards the development of polycrystalline silicon on glass substrates for thin silicon photovoltaic devices [78, 311–316]. The material processing has been thoroughly reviewed by the group for thin-film solar cells.

The MACE process for black silicon is applicable even on thin film as well (both in amorphous Si and microcrystalline) [78, 163]. However, the work employing thin Si solar cell concept using MACE-based nanostructured black Si on glass substrates are though limited but have shown promising results. In this concept of solar cells, the nanostructured layer is made by MACE on thin layers of doped mc-Si (prepared by laser crystallization or e-beam crystallization). These structures enable the use of low-cost substrates like glass [55, 317, 318]. For example, Sivakov and co-workers demonstrated such a solar cell employing nanostructured mc-Si in p^+-n-n^+ junctions on glass substrates, as shown in Fig. 26 [55]. They first fabricated a large-grained 2.5–3 μm thick multicrystalline p^+-n-n^+ Si layer stack on a glass substrate by e-beam evaporation deposition followed by laser crystallization. The mc-Si layer (on glass) with p^+-n-n^+ junctions was then nanostructured by MACE process in HF + $AgNO_3$ solution. The solar cells exhibited a maximum V_{oc} of 450 mV and a J_{sc} of 40 mA cm^{-2} resulting in overall PCE of 4.4% under AM 1.5G illumination. It was suggested that severe shunting and large series resistance were responsible for the relatively low device performance. In this series, a group at IPHT Jena, Germany has made significant development [317, 318]. Jia and co-workers, fabricated a multiple core–shell NW based HIT solar cell with a thickness of less than 10 μm. In this device structure, the NWs were etched into n-doped, laser crystallized mc-Si thin films prepared on glass and covered by the intrinsic and p-doped shells of a-Si resulting in a radial p–n junction geometry [317, 318]. They reported an efficiency of 8.8% with a V_{oc} of 530 mV in such cells on glass substrates. The nanostructures (Si NWs) were fabricated by MACE of an n-type, 8 μm thick laser crystallized mc-Si Si thin film on glass [317]. PECVD was used to deposit an a-Si hetero-emitter around the nanostructures. In this device structure, the ALD-based Al_2O_3 passivation layer was also utilized. Finally, aluminium doped zinc oxide (ZnO:Al) was conformally deposited as a transparent conducting oxide (TCO) on the black silicon surface to have a planar transparent conducting layer. Later, the same group realized 10% efficient prototype solar cell employing similar black Si nanostructured surface on a polycrystalline (pc)-Si thin film with a thickness of only 8 μm formed on glass [317]. By improved nanostructruing process (via cleaning of the metal contamination from the MACE),

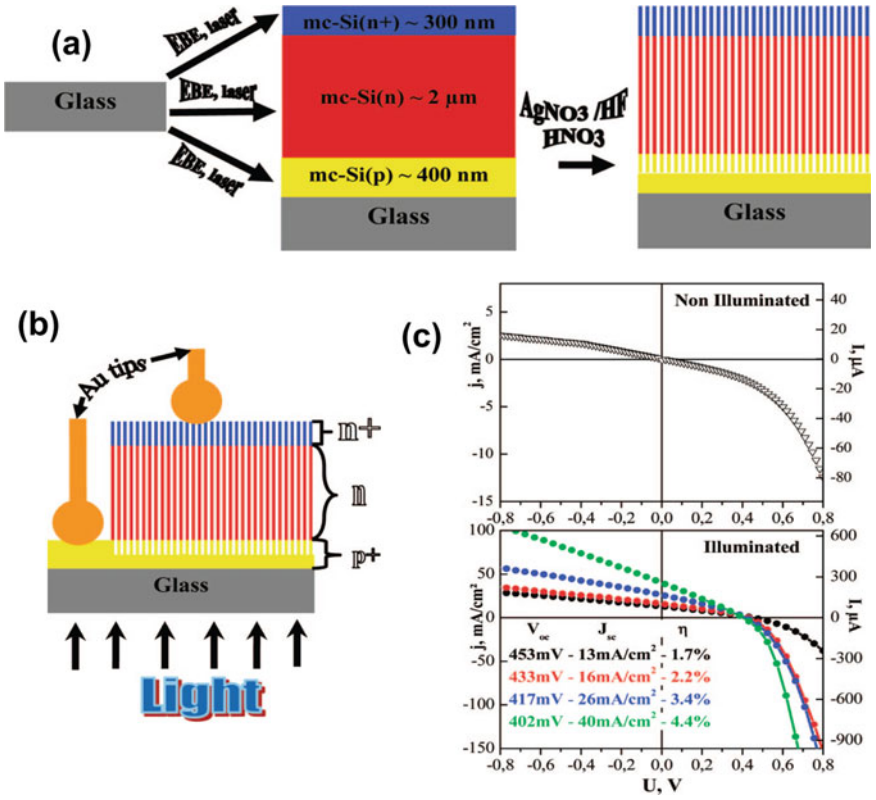

Fig. 26 **a** Schematic cross-sectional view of the mc-Si p-n junction layer stack on a glass substrate (left) and the SiNWs after wet chemical etching (right). **b** Schematic representation of the I–V curve measurements of SiNW based p-n junctions. (c) Non-illuminated and illuminated (AM1.5) I–V curves of SiNWs etched into a mc-p^+−n−n^+-Si layer on glass. SiNW are irradiated through the glass substrate (superstate configuration) and contacted by metal tips at four different sample positions. The right-hand scale gives real measured current values and the left-hand scale current density values. Reprinted with permission from Ref. [55], Copyright (2009) American Chemical Society

effective passivation by a-Si:H emitter as well as by an ultra-thin Al_2O_3 tunnel layer on the emitter surface, and by appropriate design of the cell structure (superstrate configuration), the detrimental effects related to the nanostructures could be avoided while retaining the light trapping properties of the black Si layer. Though the PCEs of such solar cells are not so impressive at present compared to the conventional planar silicon solar cells, nevertheless, such solar cells with nanostructured thin Si as effective light absorber on cheap glass substrates could impact next generation PV technologies, particularly, the device cost.

9.2 Silicon Wafer Based Thin Solar Cells Employing Black Silicon

Reducing Si wafer thickness in the PV industry has always been the main focus of lowering the overall cost. Further benefits such as short collection lengths and improved V_{oc} can also be achieved by Si thickness reduction. However, the problem with thin films is poor light absorption. One way to decrease optical losses in solar cells is to minimize the frontside reflection. This approach can be applied to front-contacted ultra-thin crystalline Si solar cells to increase the light absorption. Utilization of black silicon (especially Si NWs) to minimize frontside reflection in wafer-based ultra-thin Si solar cells has been reported. For example, ultra-thin, Si solar cells with black Si in interdigitated back-contacted (IBC) structures have been successfully demonstrated [319, 320]. Moreover, ultra-thin Si wafers fabricated via KOH etching, exhibited excellent mechanical flexibility and bendability. Double-sided nanotextured pyramidal design was used for light trapping in these ultra-thin Si films and extensive improvement in light absorption was demonstrated [321]. Very recently, Aurang and co-workers used NW structures based black Si in conventional front-contacted ultra-thin Si solar cell structures [322]. Aurang and co-workers demonstrated, homojunction solar cells using ultra-thin and flexible single-crystal Si wafers (see Fig. 27). In this work, KOH etched ultra-thin Si wafers with thicknesses of 20 ± 0.2 μm were used to fabricate homojunction solar cells. In order to improve the weak light absorption of ultra-thin Si wafers, the MACE Si NWs were made in solar cell surface. In order to optimize the top contact design, photolithography was employed to pattern Si NWs so that the top contact areas are protected from the NWs etching during the MACE process, similar to the approach developed by Kumar and co-workers [41] to improve the top contact in NW solar cells wherein the contact area was protected from MACE etching. A relative improvement of 56%

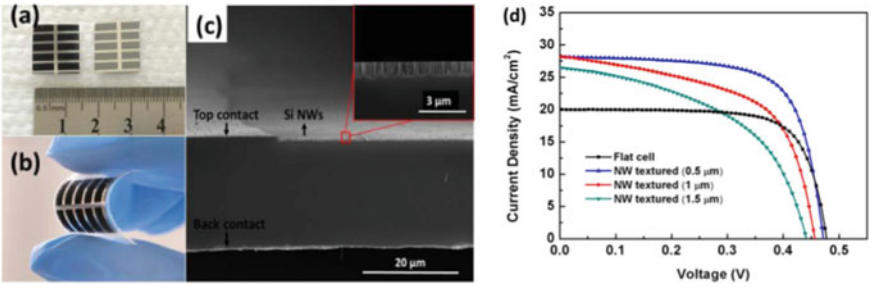

Fig. 27 **a** Photograph of fabricated ultra-thin Si solar cell with NWs or black Si (left) and without NWs or black Si (right). **b** Photograph of the flexible nature of the black Si textured Si solar cell on polyethylene terephthalate (PET) **c** Cross-sectional SEM image of fabricated black Si ultra-thin Si solar cell **d** J–V curves of the ultra-thin Si solar cells decorated with different lengths of NWs (thickness of black Si layer). Ref. [322] © IOP Publishing. Reproduced by permission of IOP Publishing

in the reflectivity was observed for ultra-thin Si wafers with a thickness of 20 ± 0.2 μm upon NW texturization. With an optimal NW length and top contact design, they could achieve a relative enhancement of 23 ± 5% in the PCE with a maximum device efficiency of 9.6 ± 1% in black Si based ultra-thin silicon wafer solar cells as compared to 7.8 ± 0.6% in flat ultra-thin solar cells without black Si [322].

In the same line, Hadibrata and co-workers reported even thinner silicon wafer based ultra-thin (only 8 μm thick) silicon solar cells with an efficiency of 9.60% [212]. MACE nanostructured black silicon surface produced a broadband reflection <10%. Despite the excellent optical performance, a moderate short-circuit current (J_{sc}) of 25.44 mA/cm^2 was achieved. As usual, relatively poor QE in the blue spectral region was associated with carrier recombination at the enhanced surface and by the Auger process. Moreover, relatively low QE was also observed in the long-wavelength region of the spectrum which was accounted for parasitic absorption at the back contact. Based on optical simulations, they showed that planarization of the rear Si surface (or introducing a BSR surface) and a low refractive index dielectric spacer between Si and the rear metal could significantly reduce the parasitic absorption in the metal, resulting in J_{SC} values over 35 mA/cm^2 [212]. In another similar approach, Tang and co-workers proposed Cu-assisted chemical etching of bulk c-Si (similar to KOH-based wafer thinning process); a relatively rapid method to obtain 45 μm ultra-thin flexible c-Si solar cells with asymmetric front and back light-trapping structures and achieved 17.3% efficient flexible solar cells in 45 μm ultra-thin flexible c-Si solar cells by MACE [214]. In this work, they reported a simple method to realize rapid thinning and texturing of bulk c-Si at room temperature by varying the ρ (= [HF]/([HF] + [H_2O_2])) values during the Cu-MACE process and achieved etch rate of ~30 μm/min under optimized conditions of ρ values. For solar cell, they used two sequential etch process (i.e. to achieve asymmetric front and back light trapping structures) consisting of (i) thinning in the ($\rho = 95\%$) followed by texturing in ($\rho = 60\%$) solution successively (see Fig. 28 for representative SEM images of the 45 μm c-Si samples with asymmetric front and back light trapping structures). A high J_{sc} (36.12 mA/cm^2) and PCE (17.3%) were achieved. The results were respectively 1.09 mA/cm^2 and 0.4% higher than the corresponding values in a 45 μm c-Si with a flat back surface (see Fig. 29 showing a digital image of a 45 μm c-Si flexible solar cell (a) and the corresponding PV performances in (b), (c) and (d)) [214].

In a slightly different solar cell design structure, Song and co-workers [323] created a planar black silicon structure that uses SiN_x-ARC on the frontside to optimize the visible absorption without deteriorating the electronic properties by having a nanostructured surface (see Fig. 30). It also has an integrated grating structure at the backside (BS) of the solar cell for the optical path enhancement which needs to compensate insufficient NIR absorption due to the 50 μm thickness of the solar cell. Here also, thin silicon wafers were produced by KOH etching of conventional CZ-Si wafers. An ALD-based ultra-thin (~4 nm) ZnO film was used as the tunnel oxide for the nanostructured backside solar cells in such thinner c-Si solar cell structure. The proposed tunnel-oxide passivated contacts (TOPC) approach increased the PCE by ~24%, in which the ZnO film successfully passivated the defect states and improved hole flows via surface band bending. The TOPC introduced effectively passivated

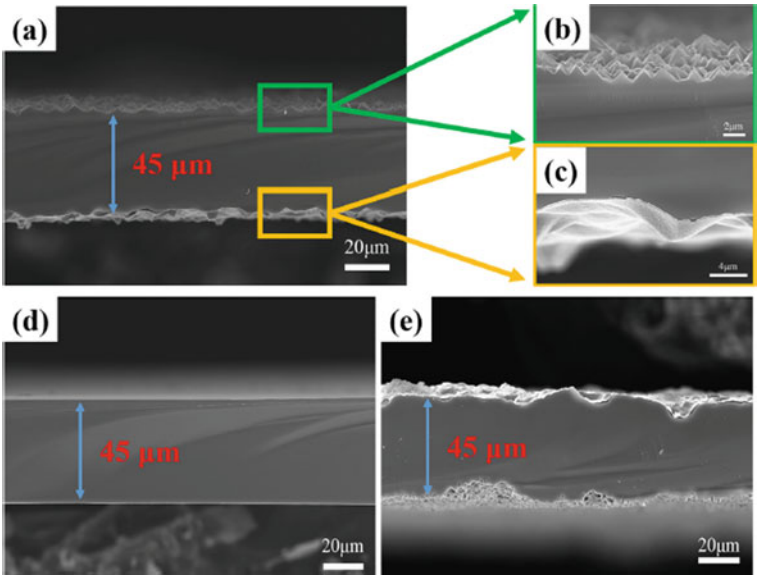

Fig. 28 **a** Cross-sectional SEM image of 45 µm c-Si solar cell with asymmetric structures, Green and yellow boxed regions are shown in **b** and **c**, respectively, **d** Cross-sectional SEM images of flat (F-flat +B-flat), **e** Cross-sectional SEM images of Etc-95 (F-95 +B-95) samples. Reprinted from Ref. [214] Copyright (2018), with permission from Elsevier

the large amount of unpassivated Si dangling bonds, which seriously hinders the flow of charge carriers when direct metal contact is made onto the nanostructured Si. The highest PCE of 13.1% was achieved for an optimized ZnO layer passivation, a significant step towards a thin black Si technology [324]. They also applied a nanostructured black layer on the front-side, however, IQE of the backside (B) NS Si surface was found much better as compared to that in front nanostructured surface structure of the cell in the entire spectral range of interest. It is to be noted that a back surface field (BSF) of p^+ was also used in this cell design to reduce back surface recombination [323].

In another slightly different novel approach, the black silicon has been used in a back-contact back-junction (BCBJ) solar cell design, wherein the active junction is also formed at the backside and the interdigitated metal contact is built on a flat substrate surface in the backside itself and the black silicon layer is used in the frontside as an effective light trapping media (see Fig. 31). The BCBJ design has been used successfully in conventional thicker silicon solar cells [324, 325]. For example, Jeong and co-workers have shown that the benefits of this design (all back contact) are even more significant in thin solar cells, avoiding the doping and contact formation problems associated along with the Auger and surface recombinations with the black Si [211]. Consequently, a PCE of 13.7% was realized in an ultra-thin solar cell (thickness <10 µm) as compared to 10.9% in a planar solar cell with AR coatings in this design [211].

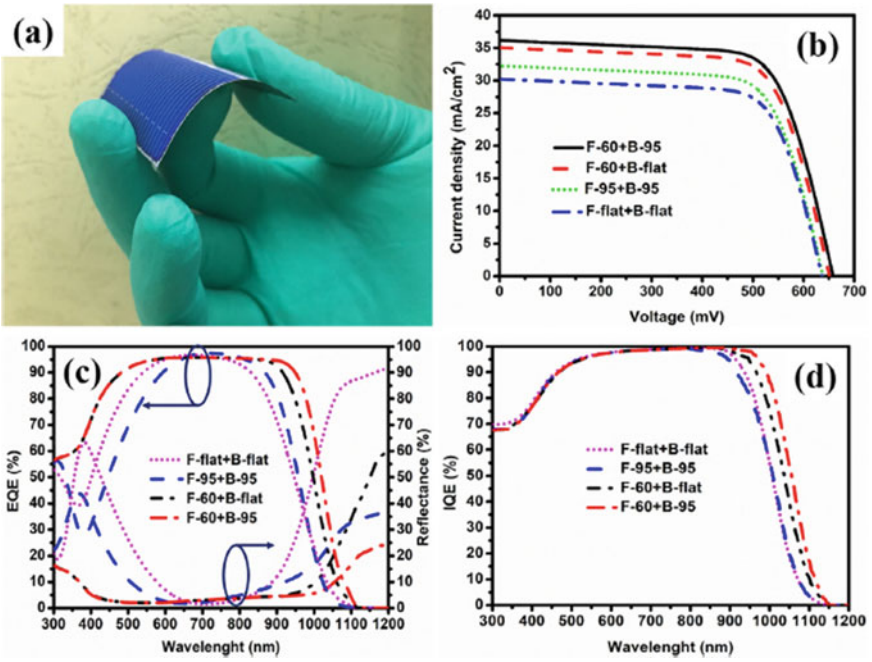

Fig. 29 **a** Photograph of 45 μm c-Si solar cell with asymmetric structures (F-60 + B-95) in a flexible state. **b** J–V curve of 45 μm c-Si solar cell with different surface conditions. **c** Surface reflectance and EQE of 45 μm c-Si solar cell with different surface conditions. **d** IQE of 45 μm c-Si solar cell with different surface conditions. Reprinted from Ref. [214] Copyright (2018), with permission from Elsevier

In contrast to the above, the p–n junction is also formed at the flat rear side, while the front metal contact is still built on black Si. However, a front surface field (FSF) has been created (similar to BSF in the rear side of the conventional solar cell) via heavy boron doping, in order to reduce surface recombination. Such design was adopted by Chan and co-workers in fabricating ~5.7 μm thick black Si solar cells (see Fig. 32) [173]. It should be pointed out here that an FSF may also be incorporated into a BCBJ cell. In addition to its role in reducing surface recombination, an FSF also improves lateral base conductivity and enhances cell stability against the UV radiation in BCBJ solar cells [326–328]. By incorporating a diffuse back surface reflector (BSR) into a black Si surface, Chan and co-workers showed that the solar cell efficiency got improved from 6.9% to 11.4% [173]. It is also to be emphasized that for thin solar cells, light trapping becomes critical for photon management, in addition to AR properties [329–331]. Hence, additional light trapping structures become essential to enhance the efficiencies of this type of thin solar cell. A backside metal-based reflector was also used by IPHT Jena group [318].

In summary, there have been several examples of ultra-thin silicon solar cells employing MACE nanostructured black Si as an effective light trapping media (in

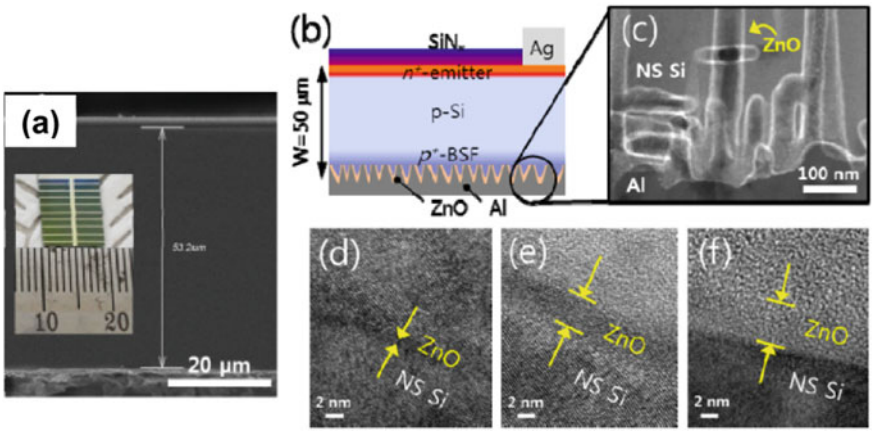

Fig. 30 **a** Cross-section SEM image of 50 μm-thin black-nanostructured Si Solar cell, a digital image of 50 μm-thin black-nanostructured Si Solar cell showing an active area of 0.9 cm^2; **b** A cell structure showing the ZnO-passivated contacts integrated with backside NS (B-NS). Cross-sectional TEM images showing **c** the Al/ZnO/NS/Si contact, and **d**–**f** various thicknesses (1.4, 4.3, 7.2 nm) of ALD ZnO deposited on NS surfaces Reprinted/Adapted with permission from Ref. [323] © The Optical Society

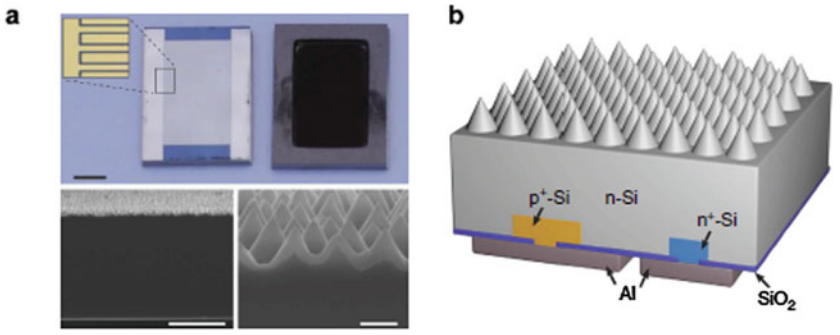

Fig. 31 Ultra-thin Si nanocone solar cell, **a** Optical image of the back (top, left) and front (top, right) side of the 10 μm thick Si solar cell. Inset shows the optical microscope image of the interdigitated metal electrodes. SEM images of a cross-sectional view of the device (bottom, left) and the cross-sectional view of the nanocones (bottom, right). **b** Schematic illustration of the device in BCBJ structure Reprinted by permission from Nature [Nature Communication] Ref. [211] Copyright (2013)

different solar cell design structures) supported on glass or flexible geometry with quite reasonable power conversion efficiencies. The progress is quite significant and a lot of efforts are made to improve the performance even better. There are still several challenges to be addressed including the effective passivation, stability and scalability of the concept for large-scale application. Nevertheless, the concept is promising and these ultra-thin c-Si solar cells (≤50 μm) are believed to find

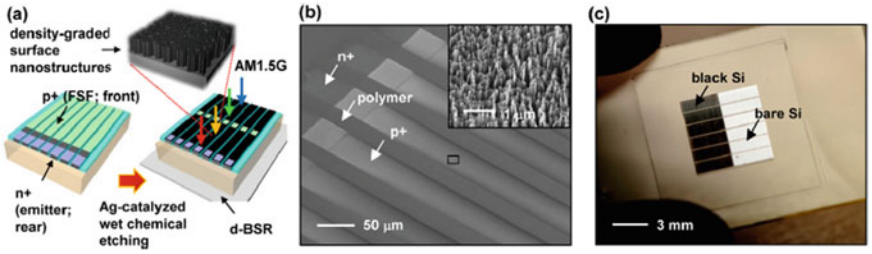

Fig. 32 **a** Schematic illustration of fabrication procedures for ultra-thin (~6 μm), black–Si solar microcells, where density graded surface nanostructures were incorporated on their front surface through Ag-MACE. A phosphorus-doped emitter (n^+) was placed at the near-surface of microcells while a boron-doped surface field region (p^+) formed at the front surface. **b** Tilt-view SEM image of ultra-thin black Si microcells embedded in a thin layer of photocurable polymers coated on a glass substrate. Inset: magnified view of the nanostructured surface of microcells. **c** Photographic image of a printed array of ultra-thin Si microcells on a glass substrate, where half of the cell area appears dark due to the suppression of front surface reflection through black Si implementation. Reprinted from Ref. [173] with the permission of AIP Publishing

applications in several special circumstances such as military, aerospace, etc. in the future due to their flexibility and high specific power density, in addition to the conventional applications for low-cost PV devices and thus is attracting a great deal of research interests.

10 Concluding Remarks and Future Prospects

In this chapter nanostructured silicon prepared by metal-assisted chemical etching and their application in solar cells have been reviewed including the flexible thin Si solar cells concept. It is no doubt that the MACE nanostructured black Si has lots of potential for high-efficiency solar cells both on conventional Si wafers as well as in thin Si solar cell concepts. The MACE is a simple, low cost yet effective and versatile technique to produce black Si surface on industrial size wafers. The process is equally effective both on monocrystalline and multicrystalline Si wafers. By judiciously controlling the MACE process parameters, a wide range of surface morphologies can be created with a high degree of control. Moreover, the MACE holds a great promise for large-scale industrial deployment, owing to its simple experimental setup and fast etching rate. The method can produce nanostructured black Si surface having very low reflectance down to <2% in broad spectral range with excellent omnidirectional light trapping ability owing to enhanced optical path length of the incident radiation in the nanostructured Si layer and smooth refractive index transitions from air to bulk silicon. Moreover, the surface also offers polarization-independent light trapping. The MACE black Si has been employed in the development of high-efficiency solar cells in a variety of cell designs and process sequences depicting great potential of the concept. However, while the black Si offers superior optical performance,

there are several issues related to effective implementation of the nanostructures, primarily caused by the enhanced surface area, it has poor electrical characteristics which have determining influence on the overall power conversion efficiencies of the black Si solar cells. Also, the porous surface in black Si leads to increased surface recombination, causes high and sometimes non-uniform doping concentrations, and poses significant challenges for forming a good silicon/metal contact. Consequently, improved fabrication processes are essential to balance the optical gains and electrical losses of the black Si in order to achieve high solar cell efficiencies. Nevertheless, as a result of continuous efforts around the world over the years, the black Si solar cell concept has become a reality. Starting from below 10% PCE a decade ago, the concept has come up a long way. While the efficiencies of black Si solar cells, in general, remain below those of conventional silicon solar cells, there has been significant progress in implementing the strategies suitable for the black silicon surfaces and hence improving the cell efficiencies continuously. Efficiencies >20% in c-Si and >19% in c-Si have been demonstrated in industrial-size wafers and the concept is maturing to be deployed in the production line. Overcoming the basic challenges, there have been few examples in which black Si has outperformed the conventional silicon solar cells processed under identical conditions.

Furthermore, the incorporation of black Si in the thin Si solar cell concept has also been gaining significant interest. PCE close to 10% has been achieved even in ultra-thin Si solar cells (20μ thin) employing the black Si concept for light trapping. The performance of MACE-based Si cells on glass has also reached a promising level of >10% PCE (though on a small area) which is quite encouraging for the next-generation PV technologies. These techniques may potentially improve solar cell efficiencies or reduce material costs. It is worth adding that black Si texturing methods are likely to play an important role in mc-Si and ultra-thin solar cells, especially where conventional wet etching methods fail as cell thicknesses decrease. For such cell concepts, surface passivation is extremely important and therefore, dielectric layers of SiN_x, SiO_2, a-Si, Al_2O_3 alone or their stacks are very important for the success of this technology. The Al_2O_3 is finding a lot of interests in black silicon solar cells. Most of the record efficiency solar cells have been achieved employing either Al_2O_3/SiN_x or SiO_2/SiN_x stacks as a surface passivation layer. Particularly, Al_2O_3 owing to its superior passivation properties is expected to play a vital role in the development of high-efficiency black Si solar cells.

However, despite the phenomenal progress during the past decade, the full potential of the MACE nanostructured black Si solar cells is yet to be realized. One obvious cause could be due to the fact that most of the current fabrication methods of the black Si solar cells are largely based on conventional solar cell processing technologies which may not suit the nanostructured Si surfaces directly. Fine-tuning of the process parameters is therefore required to improve their cell efficiencies further and realize the full potential of the concept. Some important aspects which should be considered while designing an efficient nanostructured black silicon solar cell are summarized below:

- A trade-off between nanostructures' morphology, using low aspect ratio nanostructures in the black silicon layer and low reflection is essential for obtaining high efficiency and requires optimization of the process. Therefore, the nanostructures of the lower aspect ratio should be employed to balance the optical gain and electrical losses.
- Getting rid of the porous Si on the surface of the nanostructures in black Si by MACE is a must as this porous layer leads to a dead region (after emitter diffusion) degrading the blue response of the cell and the PCE. Therefore, thorough removal of surface defects is critical to maximizing carrier lifetime. A modified dopant diffusion strategy should be developed to minimize the surface losses (avoiding dead layer, reducing Auger recombination in the surface layer and other surface recombinations) for the improvement of the blue response. Due to enhanced area, very effective passivation is extremely essential in black Si, improvised dielectric layer scheme must be applied in combination with other cell process parameters for optimum cell efficiency.
- Metal contact architectures must be optimized as per the requirement of the nanostructured black Si possibly by a finer and denser metal grid for higher charge collection efficiency.
- The nanostructures morphology should also be designed for optimal performance in the module/finished cell. For example, an oxide is always formed during dopant diffusion which changes the nanostructures' morphology. Also, depending on the type of SiN_x or other passivation schemes, the optimal geometry of the nanotexture varies. In general, the optimized nanostructuring process will depend on the details of the rest of the cell and possible module assembly processes.
- The nanostructure should be optimized for reliability and not just the efficiency. For example, different nanostructures result in different adhesion of metal fingers and bus bars to the cell. Therefore, long-term reliability of such black cell technology should also be taken into account in addition to high efficiency.
- Black silicon could enable cells designs without SiN_x and with just using SiO_2 or Al_2O_3 to passivate the surface, since an AR layer is not required with black Si. This cell design is especially relevant for higher efficiency designs that currently use both a passivating layer and an AR coating.
- The MACE can also be designed for a singled sided texturing process leaving the rear surface planar for high-efficiency cell designs.

By undertaking the above improvements, it is likely that the efficiency of the black Si solar cells will advance even further in the near future, with $a > 20\%$ efficient solar cell concept recently achieved and visioned for even higher values. In particular, with a better understanding of the carrier loss mechanisms and improvements in cell design and fabrication strategies, the efficiency of black Si solar cells will continue to increase in the future. Looking at the enormous efforts being put around the world, the MACE-based black cell photovoltaic technology is certainly going to be a reality in the PV industry in the near future.

Acknowledgments Authors would like to acknowledge the financial support by the Council of Scientific and Industrial Research (CSIR), India CSIR-TAPSUN project (Grant code: NWP-55) and CSIR YSA Research project (Grant code: OLP 142732; P-81-113).

References

1. A.H.M. Smets, K. Jäger, O. Isabella, R.V. Swaaij, M. Zeman, *Solar Energy: The Physics and Engineering of Photovoltaic Conversion, Technologies and Systems*, Kindle edn. (UIT Cambridge Ltd., UK, 2016)
2. U.S. Energy Information Administration, International Energy Outlook 2016-Electricity 0484, 1 (2016). www.eia.gov/forecasts/ieo/pdf/0484(2016).pdf
3. Worldometers, World Population Clock. (2017). http://www.worldometers.info/world-population/. Accessed 20 Dec 2019
4. British Petroleum. BP energy outlook. (2017). https://www.bp.com/content/dam/bp/business-sites/en/global/corporate/pdfs/energy-economics/energy-outlook/bp-energy-outlook-2017.pdf
5. World Population Prospects: 2015 Revision. (2015). https://www.un.org/en/development/desa/publications/world-population-prospects-2015-revision.html
6. J.E. Cohen, Science **302**, 1172 (2003). https://doi.org/10.1126/science.1088665
7. J.F. Morton, Proc. Natl. Acad. Sci. U.S.A. **104**, 19680 (2007)
8. C. Parmesan, G. Yohe, Nature **421**, 37 (2003)
9. M. Edwards, A.J. Richardson, Nature **430**, 881 (2004)
10. C. Rosenzweig, M.L. Parry, Nature **367**, 133 (1994)
11. N. Klein, *This Changes Everything: Capitalism vs. the Climate* (Simon & Schuster, New York, 2014)
12. N. Mukherji, Economic Political Weekly **51**(32), 30 (2016)
13. IPCC, 2007: Summary for Policymakers, in *Climate Change 2007: The Physical Science Basis. Contribution of Working Group I to the Fourth Assessment Report of the Intergovernmental Panel on Climate Change*, eds by S. Solomon, D. Qin, M. Manning, Z. Chen, M. Marquis, K.B. Averyt, M. Tignor and H.L. Miller (Cambridge University Press, Cambridge, UK and New York, NY, USA)
14. T. Jayaraman, T. Kanitkar, Economic Political Weekly **51**(3), 10 (2016)
15. D.L. Chandler, *Vast amounts of solar energy radiate to the Earth, but tapping it cost-effectively remains a challenge*. (2011). https://phys.org/news/2011-10-vast-amounts-solar-energy-earth.html. Accessed 20 December 2019
16. U.N. Sushma, A. Nupur, *Cheap Renewable Energy is Killing India's Coal-Based Power Plants*. https://qz.com/india/1272394/cheap-solar-and-wind-energy-prices-are-killing-indias coal-power-plants. Accessed 9 May 2018
17. Photovoltaics Report, *Fraunhofer Institute for Solar Energy Systems* (ISE, Freiburg, 2019). www.ise.fraunhofer.de
18. Solar PV Markets, in *Global Status Report 2019-Renewables*. https://www.ren21.net/wp-content/uploads/2019/05/gsr_2019_full_report_en.pdf
19. S.K. Srivastava, P. Singh, M. Yameen, P. Prathap, C.M.S. Rauthan, Vandana, P.K. Singh, Sol. Energy **115**, 656 (2015)
20. C. Kost, J.N. Mayer, J. Thomsen, N. Hartmann, C. Senkpiel, S. Philipps, S. Nold, S. Lude, N. Saad, T. Schlegl, *Levelized Cost of Electricity Renewable Energy Technologies* (Fraunhofer Institute for Solar Energy Systems ISE, Freiburg, 2013), p. 50
21. M.A. Green, Y. Hishikawa, E.D. Dunlop, D.H. Levi, J. Hohl-Ebinger, M. Yoshita, A.W.Y. Ho-Baillie, Prog. Photovolt. Res. Appl. **27**(53), 3 (2019)
22. J. Nelson, *The Physics of Solar Cells* (Imperial College Press, London, 2003)

23. M.A. Green, *Silicon Solar Cells: Advanced Principles and Practice* (Bridge Printery, Sydney, 1995)
24. C.A. Wolden, J. Kurtin, J.B. Baxter, I. Repins, S.E. Shaheen, J.T. Torvik, A.A. Rockett, V.M. Fthenakis, E.S. Aydil, J. Vac. Sci. Technol. A **29**, 030801 (2011)
25. C. Battaglia, A. Cuevas, S.D. Wolf, Energy Environ. Sci. **9**, 1552 (2016)
26. M. Yameen, S.K. Srivastava, P. Singh, K. Turan, P. Prathap, Vandana, C.M.S. Rauthan, P.K. Singh, J. Mater. Sci. **50**, 8046 (2015)
27. P. Singh, S.K. Srivastava, B. Sivaiah, S. Laxmi, P. Prathap, C.M.S. Rauthan, J. Mater. Sci.: Mater. Electron. **29**(6), 5087 (2018)
28. P. Singh, S.K. Srivastava, B. Sivaiah, P. Prathap, C.M.S. Rauthan, Sol. Energy **170**, 221 (2018)
29. P. Singh, S.K. Srivastava, M. Yameen, B. Sivaiah, V. Prajapati, P. Prathap, S. Laxmi, B.P. Singh, Vandana, C.M.S. Rauthan, P.K. Singh, J. Mater. Sci. **50**(20), 6631 (2015)
30. S.K. Srivastava, D. Kumar, P.K. Singh. M. Kar, V. Kumar, M. Hussain, Sol. Energy Mater. Sol. Cells **94**, 1506 (2010)
31. V. Schmidt, J.V. Wittemann, S. Senz, U. Gósele, Adv. Mater. **21**, 2681 (2009)
32. C. Lin, N. Huang, M.L. Povinelli, Opt. Express **20**(1), A125 (2012)
33. V.Y. Yerokhov, R. Hezel, M. Lipinski, R. Ciach, H. Nagel, A. Mylyanych, P. Panek, Sol. Energy Mater. Sol. Cells **72**, 291 (2002)
34. P. Panek, M. Lipiński, J. Dutkiewicz, J. Mater. Sci. **40**, 1459 (2005)
35. Crystalline Silicon Technology-Current Status and Outlook, International Technological Roadmap for Photovoltaic (ITRPV), 8th edition, 2017. www.itrpv.net; http://re100.eng.anu.edu.au/resources/assets/1705ITRPVEighthEdition2017.pdf
36. H. Nagel, A.G. Aberle, R. Hezel, Optimised antireflection coatings for planar silicon solar cells using remote PECVD silicon nitride and porous silicon dioxide. Prog. Photovolt. Res. Appl. **7**, 245 (1999). https://doi.org/10.1002/(SICI)1099-159X(199907/08)7:4<245::AID-PIP255>3.0.CO;2-3
37. J. Schmidt, M. Kerr, A. Cuevas, Semicond. Sci. Technol. **16**, 164 (2001)
38. M. Dutta, L. Thirugnanam, N. Fukata, *Si nanowire solar cells: principles, device types, future aspects, and challenges* (Springer, Cham, 2018), pp. 299–329
39. K.Q. Peng, Y. Xu, Y. Wu, Y. Yan, S.T. Lee, J. Zhu, Small **1**, 1062 (2005)
40. E. Garnett, P. Yang, Nano Lett. **10**, 1082 (2010)
41. D. Kumar, S.K. Srivastava, P.K. Singh, M. Husain, V. Kumar, Sol. Energy Mater. Sol. Cells **95**, 215 (2011)
42. B.M. Kayes, H.A. Atwater, N.S. Lewis, J. Appl. Phys. **97**, 114302 (2005)
43. M.D. Kelzenberg, S.W. Boettcher, J.A. Petykiewicz, D.B. Turner-Evans, M.C. Putnam, E.L. Warren, J.M. Spurgeon, R.M. Briggs, N.S. Lewis, H.A. Atwater, Nat. Mater. **9**, 239 (2010)
44. B. Ozdemir, M. Kulakci, R. Turan, H.E. Unalan, Appl. Phys. Lett. **99**, 113510 (2011)
45. E.A. Dalchiele, F. Martín, D. Leinen, R.E. Marotti, J.R. Ramos-Barrad, J. Electrochem. Soc. **156**, K77 (2009)
46. L.J. Chen, J. Mater. Chem. **17**, 4639 (2007)
47. X.Y. Zhao, C.M. Wei, L. Yang, M.Y. Chou, Phys. Rev. Lett. **92**, 236805 (2004)
48. Y. Huang, X.F. Duan, C.M. Lieber, Small **1**, 142 (2005)
49. S.M. Koo, Q. Li, M.D. Edelstein, C.A. Richter, E.M. Vogel, Nano Lett. **5**, 2519 (2005)
50. D. Li, Y. Wu, P. Kim, L. Shi, P. Yang, A. Majumdar, Appl. Phys. Lett. **83**, 2934 (2003)
51. Y. Cui, C.M. Lieber, Science **291**(80), 851 (2001)
52. G. Brönstrup, N. Jahr, C. Leiterer, A. Csäki, W. Fritzsche, S. Christiansen, ACS Nano **4**, 7113 (2010)
53. K.Q. Peng, S.T. Lee, Adv. Mater. **23**, 198 (2011)
54. L. Tsakalakos, J. Balch, J. Fronheiser, B.A. Korevaar, O. Sulima, J. Rand, Appl. Phys. Lett. **91**, 233117 (2007)
55. V. Sivakov, G. Andrä, A. Gawlik, A. Berger, J. Plentz, F. Falk, S.H. Christiansen, Nano Lett. **9**, 1549 (2009)
56. A.I. Hochbaum, R.K. Chen, R.D. Delgado, W. Liang, E.C. Garnett, M. Najarian, A. Majumdar, P. Yang, Nature **451**, 163 (2008)

57. G. Barillaro, A. Nannini, M. Piotto, Sensors Actuators A **102**, 195 (2002)
58. C.K. Chan, H. Peng, G. Liu, K. McIlwrath, X.F. Zhang, R.A. Huggins, Y. Cui, Nat. Nanotechnol. **3**, 31 (2008)
59. Y. Cui, Q. Wei, H. Park, C.M. Lieber, Science **293**, 1289 (2001)
60. S. Singh, J. Zack, D. Kumar, S.K. Srivastava, Govind, D. Saluja, M.A. Khan, P.K. Singh, Thin Solid Films. **519**, 1151 (2010)
61. J. Goldberger, A.I. Hochbaum, R. Fan, P. Yang, Nano Lett. **6**, 973 (2006)
62. J. Bae, H. Kim, X.M. Zhang, C.H. Dang, Y. Zhang, Y.J. Choi, A. Nurmikko, Z.L. Wang, Nanotechnology **21**, 095502 (2010)
63. F. Qian, S. Gradečak, Y. Li, C.Y. Wen, C.M. Lieber, Nano Lett. **5**, 2287 (2005)
64. M. Steglich, M. Zilk, F. Schrempel, A. Tünnermann, E.B. Kley, Appl. Phys. Lett. **102**, 111110 (2013)
65. M. Steglich, M. Zilk, A. Bingel, C. Patzig, T. Käsebier, F. Schrempel, E.B. Kley, A. Tünnermann, J. Appl. Phys. **114**, 183102 (2013)
66. J. Oh, T.G. Deutsch, H.C. Yuan, H.M. Branz, Energy Environ. Sci. **4**, 1690 (2011)
67. D. Qi, N. Lu, H. Xu, B. Yang, C. Huang, M. Xu, L. Gao, Z. Wang, L. Chi, Langmuir **25**, 7769 (2009)
68. Y. Xiu, S. Zhang, V. Yelundur, A. Rohatgi, D.W. Hess, C.P. Wong, Langmuir **24**, 10421 (2008)
69. B.S. Kim, S. Shin, S.J. Shin, K.M. Kim, H.H. Cho, Langmuir **27**, 10148 (2011)
70. J. Seo, S. Lee, H. Han, Y. Chung, J. Lee, S.D. Kim, Y.W. Kim, S. Lim, T. Lee, Thin Solid Films **527**, 179 (2013)
71. Y. Liu, A. Das, Z. Lin, I.B. Cooper, A. Rohatgi, C.P. Wong, Nano Energy **3**, 127 (2014)
72. S. Shen, C.P. Wong, I.E.E.E. Trans, Components. Packag. Manuf. Technol. **8**(1), 140 (2018)
73. J. Oh, H.C. Yuan, H.M. Branz, Nat. Nanotechnol. **7**(11), 743 (2012)
74. Y. Wang, Y.P. Liu, T. Lai, H.L. Liang, Z.L. Li, Z.X. Mei, F.M. Zhang, A. Kuznetsov, X.L. Du, RSC Adv. **3**, 15483 (2013)
75. H.C. Yuan, V.E. Yost, M.R. Page, P. Stradins, D.L. Meier, H.M. Branz, Appl. Phys. Lett. **95**(12), 123501 (2009)
76. F. Toor, H.M. Branz, M.R. Page, K.M. Jones, H.C. Yuan, Appl. Phys. Lett. **99**(10), 103501 (2011)
77. X. Ao, X. Tong, D.S. Kim, L. Zhang, M. Knez, F. Müller, S. He, V. Schmidt, Appl. Phys. Lett. **101**, 111901 (2012)
78. S. Koynov, M.S. Brandt, M. Stutzmann, Appl. Phys. Lett. **88**, 203107 (2006)
79. H.M. Branz, V.E. Yost, S. Ward, K.M. Jones, B. To, P. Stradins, Appl. Phys. Lett. **94**(23), 231121 (2009)
80. M. Otto, M. Algasinger, H. Branz, B. Gesemann, T. Gimpel, K. Füchsel, T. Käsebier, S. Kontermann, S. Koynov, X. Li, V. Naumann, J. Oh, A.N. Sprafke, J. Ziegler, M. Zilk, R.B. Wehrspohn, Adv. Opt. Mater. **3**(2), 147 (2014)
81. F. Toor, J. Oh, H.M. Branz, Prog. Photovolt. Res. Appl. **23**(10), 1375 (2015)
82. H.C. Yuan, V.E. Yost, M.R. Page, L. Roybal, B. To, P. Stradins, D.L. Meier, H.M. Branz, in *Proceedings of the* 34th *IEEE Photovoltaic Specialists Conference (PVSC)* (Philadelphia, USA, 2009), p. 000141
83. F. Toor, M.R. Page, H.M. Branz, H.C. Yuan, in *Proceedings of the* 37th *IEEE Photovoltaic Specialists Conference (PVSC)* (Washington, USA, 2011), p. 000020
84. M. Halbwax, T. Sarnet, P. Delaporte, M. Sentis, H. Etienne, F. Torregrosa, V. Vervisch, I. Perichaud, S. Martinuzzi, Thin Solid Films **516**, 6791 (2008)
85. P. Repo, J. Benick, V. Vähänissi, J. Schön, G. Von Gastrow, B. Steinhauser, M.C. Schubert, M. Hermle, H. Savin, Energy Procedia **38**, 866 (2013)
86. S.K. Srivastava, D. Kumar, P.K. Singh, V. Kumar, in *Proceedings of the* 34th *IEEE Photovoltaic Specialists Conference (PVSC)* (Philadelphia, USA, 2009), p. 001851
87. S.K. Srivastava, D. Kumar, P. Sharma, Vandana, P.K. Singh, in *Proceedings of the 26th EUPVSEC* (Hamburg, Germany, 2011), p. 1699. https://doi.org/10.4229/26theupvsec2011-2bv.3.35

88. S.K. Srivastava, D. Kumar, Vandana, M. Sharma, R. Kumar, P.K. Singh, Sol. Energy Mater. Sol. Cells **100**, 33 (2012)
89. S.W. Schmitt, G. Brönstrup, G. Shalev, S.K. Srivastava, M.Y. Bashouti, G.H. Döhler, S.H. Christiansen, Nanoscale **6**, 7897 (2014)
90. X. Liu, P.R. Coxon, M. Peters, B. Hoex, J.M. Cole, D.J. Fray, Energy Environ. Sci. **7**, 3223 (2014)
91. R.S. Wagner, W.C. Ellis, Appl. Phys. Lett. **4**, 89 (1964)
92. J. Westwater, D.P. Gosain, S. Tomiya, S. Usui, H. Ruda, J. Vac. Sci. Technol. B **15**, 554 (1997)
93. L. Latu-Romain, C. Mouchet, C. Cayron, E. Rouviere, J.P. Simonato, J. Nanopart. Res. **10**, 1287 (2008)
94. C.L. Cheng, C.W. Liu, J.T. Jeng, B.T. Dai, Y.H. Lee, J. Electrochem. Soc. **156**, H356 (2009)
95. Y. Li, H. Yu, J. Li, S.M. Wong, X.W. Sun, X. Li, C. Cheng, H.J. Fan, J. Wang, N. Singh, Small **7**, 3138 (2011)
96. B. Fuhrmann, H.S. Leipner, H.R. Höche, L. Schubert, P. Werner, U. Gösele, Nano Lett. **5**, 2524 (2005)
97. A.M. Morales, C.M. Lieber, Science **279**, 208 (1998)
98. Y.H. Yang, S.J. Wu, H.S. Chiu, P.I. Lin, Y.T. Chen, J. Phys. Chem. B **108**, 846 (2004)
99. H. Pan, S. Lim, C. Poh, H. Sun, X. Wu, Y. Feng, J. Lin, Nanotechnology **16**, 417 (2005)
100. S.K. Srivastava, P.K. Singh, V.N. Singh, K.N. Sood, D. Haranath, V. Kumar, Physica E **41**, 1545 (2009)
101. S.D. Hutagalung, K.A. Yaacob, A.F.A. Aziz, Appl. Surf. Sci. **254**, 633 (2007)
102. J.D. Holmes, K.P. Johnston, R.C. Doty, B.A. Korgel, Science **287**, 1471 (2000)
103. P. Menna, G.D. Francia, V.L. Ferrara, Sol. Energy Mater. Sol. Cells **37**, 13 (1995)
104. L. Stalmans, J. Poortmans, H. Bender, M. Caymax, K. Said, E. Vazsonyi, J. Nijs, R. Mertens, Prog. Photovolt. Res. Appl. **6**, 233 (1998)
105. V.Y. Yerokhov, I.I. Melnyk, Renew. Sustain. Energy Rev. **3**, 291 (1999)
106. R.R. Bilyalov, R. Lüdemann, W. Wettling, L. Stalmans, J. Poortmans, J. Nijs, L. Schirone, G. Sotgiu, S. Strehlke, C.L. Clément, Sol. Energy Mater. Sol. Cells **60**, 391 (2000)
107. V.V. Iyengar, B.K. Nayak, M.C. Gupta, Sol. Energy Mater. Sol. Cells **94**, 2251 (2010)
108. B.K. Nayak, V.V. Iyengar, M.C. Gupta, Prog. Photovolt. Res. Appl. **19**, 631 (2011)
109. V.V. Iyengar, B.K. Nayak, K.L. More, H.M. Meyer, M.D. Biegalski, J.V. Li, M.C. Gupta, Sol. Energy Mater. Sol. Cells **95**, 2745 (2011)
110. K.C. Phillips, H.H. Gandhi, E. Mazur, S.K. Sundaram, Adv. Opt. Photon. **7**, 684 (2015)
111. Z. Sun, M.C. Gupta, in *Proceedings of the 43rd IEEE Photovoltaic Specialists Conference (PVSC)* (Portland, Oregon, USA, 2016), p. 0713
112. Y.Q. Fu, A. Colli, A. Fasoli, J.K. Luo, A.J. Flewitt, A.C. Ferrari, W.I. Milne, J. Vac. Sci. Technol. B **27**, 1520 (2009)
113. R.V. Martínez, J. Martínez, R. Garcia, Nanotechnology **21**, 245301 (2010)
114. S.W. Schmitt, F. Schechtel, D. Amkreutz, M. Bashouti, S.K. Srivastava, B. Hoffmann, C. Dieker, E. Spiecker, B. Rech, S.H. Christiansen, Nano Lett. **12**, 4050 (2012)
115. A. Smyrnakis, E. Almpanis, V. Constantoudis, N. Papanikolaou, E. Gogolides, Nanotechnology **26**, 085301 (2015)
116. H. Jansen, H. Gardeniers, M.D. Boer, M. Elwenspoek, J. Fluitman, J. Micromech. Microeng. **6**, 14 (1996)
117. V.M. Donnelly, A. Kornblit, J. Vac. Sci. Technol. A **31**(5), 050825 (2013)
118. M. Steglich, T. Käsebier, M. Zilk, T. Pertsch, E.B. Kley, A. Tünnermann, J. Appl. Phys. **16**, 173503 (2014)
119. K.N. Nguyen, P. Basset, F. Marty, Y.L. Wang, T. Bourouina, J. Appl. Phys. **113**, 194903 (2013)
120. S. Schaefer, R. Lüdemann, J. Vac. Sci. Technol. A **17**, 749 (1999)
121. S.H. Zaidi, D.S. Ruby, J.M. Gee, I.E.E.E. Trans, Electron Devices **48**, 1200 (2001)
122. Z. Huang, N. Geyer, P. Werner, J.D. Boor, U. Gösele, Adv. Mater. **23**, 285 (2011)
123. K. Peng, M. Zhang, A. Lu, N.B. Wong, R. Zhang, S.T. Lee, Appl. Phys. Lett. **90**, 163123 (2007)
124. X. Li, W. Bohn, Appl. Phys. Lett. **77**, 2572 (2000)

125. S.K. Srivastava, D. Kumar, S.W. Schmitt, K.N. Sood, S.H. Christiansen, P.K. Singh, Nanotechnology **25**, 175601 (2014)
126. C.H. Hsu, J.R. Wu, Y.T. Lu, D.J. Flood, A.R. Barron, L.C. Chen, Mater. Sci. Semicond. Process. **25**, 2 (2014)
127. F. Toor, J.B. Miller, L.M. Davidson, W. Duan, M.P. Jura, J. Yim, J. Forziati, M.R. Black, Nanoscale **8**(34), 15448 (2016)
128. F. Toor, J.B. Miller, L.M. Davidson, L. Nichols, W. Duan, M.P. Jura, J. Yim, J. Forziati, M.R. Black, Nanotechnology **27**, 412003 (2016)
129. M. Li, Y. Li, W. Liu, L. Yue, R. Li, Y. Luo, M. Trevor, B. Jiang, F. Bai, P. Fu, Y. Zhao, C. Shen, J.M. Mbengue, Mater. Res. Bull. **76**, 436 (2016)
130. K.Q. Peng, Y.J. Yan, S.P. Gao, J. Zhu, Adv. Mater. **14**, 1164 (2002)
131. D. Kumar, S.K. Srivastava, P.K. Singh, K.N. Sood, V.N. Singh, N. Dilawar, M. Husain, J. Nanopart. Res. **12**, 2267 (2010)
132. K. Peng, J. Zhu, J. Electroanal. Chem. **558**, 35 (2003)
133. K. Peng, J. Zhu, Electrochim. Acta **49**, 2563 (2004)
134. K. Peng, Y. Wu, H. Fang, X. Zhong, Y. Xu, J. Zhu, Angew Chemie **44**, 2737 (2005)
135. K. Peng, J. Hu, Y. Yan, Y. Wu, H. Fang, Y. Xu, S. Lee, J. Zhu, Adv. Funct. Mater. **16**, 387 (2006)
136. H. Fang, Y. Wu, J. Zhao, J. Zhu, Nanotechnology **17**, 3768 (2006)
137. K. Peng, H. Fang, J. Hu, Y. Wu, J. Zhu, Y. Yan, S.T. Lee, Chem. Eur. J. **12**, 7942 (2006)
138. T. Qiu, X.L. Wu, Y.F. Mei, G.J. Wan, P.K. Chu, G.G. Siu, J. Cryst. Growth **277**, 143 (2005)
139. Y.T. Lu, A.R. Barron, J. Mater. Chem. A **2**, 12043 (2014)
140. Y. Cao, Y. Zhou, F. Liu, Y. Zhou, Y. Zhang, Y. Liu, Y. Guo, ECS J. Solid State Sci. Technol. **4**, 331 (2015)
141. Y. Wang, L. Yang, Y. Liu, Z. Mei, W. Chen, J. Li, H. Liang, A. Kuznetsov, D. Xiaolong, Sci. Rep. **5**, 10843 (2015)
142. Y. Wang, Y. Liu, L. Yang, W. Chen, X. Du, A. Kuznetsov, Nanoscale **9**, 907 (2017)
143. S.K. Gandhi, *VLSI Fabrication Principles: Silicon and Gallium Arsenide* (Wiley, New York, 1983)
144. W.M. Bullis, Solid State Electron. **9**, 143 (1966)
145. C.D. Cañizo, I. Tobías, R. Lago-Aurrekoetxea, A. Luque, J. Electrochem. Soc. **149**, G522 (2002)
146. M.L. Zhang, K.Q. Peng, X. Fan, J.S. Jie, R.Q. Zhang, S.T. Lee, N.B. Wong, J. Phys. Chem. C **112**, 4444 (2008)
147. Z. Huang, T. Shimizu, S. Senz, Z. Zhang, X. Zhang, W. Lee, N. Geyer, U. Gösele, Nano Lett. **9**, 2519 (2009)
148. V.A. Sivakov, G. Brönstrup, B. Pecz, A. Berger, G.Z. Radnoczi, M. Krause, S.H. Christiansen, J. Phys. Chem. C **114**, 3798 (2010)
149. S. Li, W. Ma, Y. Zhou, X. Chen, Y. Xiao, M. Ma, W. Zhu, F. Wei, Nanoscale Res. Lett. **9**, 196 (2014)
150. A.I. Hochbaum, D. Gargas, Y.J. Hwang, P. Yang, Nano Lett. **9**(10), 3550 (2009)
151. W.K. To, C.H. Tsang, H.H. Li, Z. Huang, Nano Lett. **11**, 5252 (2011)
152. N. Geyer, N. Wollschläger, B. Fuhrmann, A. Tonkikh, A. Berger, P. Werner, M. Jungmann, R.K. Rehberg, H.S. Leipne, Nanotechnology **26**, 245301 (2015)
153. L.U. Vinzons, L. Shu, S. Yip, C.Y. Wong, L.L.H. Chan, J.C. Ho, Nanoscale Res. Lett. **12**, 385 (2017)
154. W. Wang, D. Li, M. Tian, Y.C. Lee, R. Yang, Appl. Surf. Sci. **258**, 8649 (2012)
155. H.C. Chang, K.Y. Lai, Y.A. Dai, H.H. Wang, C.A. Lin, J.H. He, Energy Environ. Sci. **4**, 2863 (2011)
156. C.Y. Chen, C.S. Wu, C.J. Chou, T.J. Yen, Adv. Mater. **20**, 3811 (2008)
157. S. Yae, Y. Morii, N. Fukumuro, H. Matsuda, Nanoscale Res. Lett. **7**(1), 352 (2012)
158. K. Nishioka, S. Horita, K. Ohdaira, H. Matsumura, Sol. Energy Mater. Sol. Cells **92**, 919 (2008)

159. S. Yae, Y. Kawamoto, H. Tanaka, N. Fukumuro, H. Matsuda, Electrochem. Commun. **5**, 632 (2003)
160. Y.T. Lu, A.R. Barron, Phys. Chem. Chem. Phys. **15**, 9862 (2013)
161. Y. Matsui, S. Adachi, J. Appl. Phys. **113**, 173502 (2013)
162. S. Koynov, M.S. Brandt, M. Stutzmann, Phys. Status Solidi—Rapid Res. Lett. **1**, R53 (2007)
163. S. Koynov, M.S. Brandt, M. Stutzmann, J. Appl. Phys. **110**, 043537 (2011)
164. P.K. Singh, R. Kumar, M. Lal, S.N. Singh, B.K. Das, Sol. Energy Mater. Sol. Cells **70**, 103 (2001)
165. J. Zhao, A. Wang, M.A. Green, F. Ferrazza, Appl. Phys. Lett. **73**, 1991 (1998)
166. Y.T. Cheng, J.J. Ho, S.Y. Tsai, Z.Z. Ye, W. Lee, D.S. Hwang, S.H. Chang, C.C. Chang, K.L. Wang, Sol. Energy **85**, 87 (2011)
167. A.K. Chu, J.S. Wang, Z.Y. Tsai, C.K. Lee, Sol. Energy Mater. Sol. Cells **93**, 1276 (2009)
168. P.K. Basu, D. Sarangi, K.D. Shetty, M.B. Boreland, Sol. Energy Mater. Sol. Cells **113**, 37 (2013)
169. K. Kim, S.K. Dhungel, S. Jung, D. Mangalaraj, J. Yi, Sol. Energy Mater. Sol. Cells **92**, 960 (2008)
170. B.G. Díaz, R.G. Lemus, B.D. Herrera, N. Marrero, J.M. Ramos, D. Borchert, Mater. Sci. Eng. B **159**, 295 (2009)
171. S. Zhong, B. Liu, Y. Xia, J. Liu, J. Liu, Z. Shen, Z. Xu, C. Li, Energy Procedia **14**, 505 (2012)
172. Y. Yao, E. Brueckner, L. Li, R. Nuzzo, Energy Environ. Sci. **6**, 3071 (2013)
173. L. Chan, D. Kang, S.M. Lee, W. Li, H. Hunter, J. Yoon, Appl. Phys. Lett. **104**, 223905 (2014)
174. M. Kroll, M. Otto, T. Käsebier, K. Füchsel, R. Wehrspohn, E.B. Kley, A. Tünnermann, T. Pertsch, in *Proceedings of the Photonics for Solar Energy Systems IV (*Brussels, Belgium, 2012). https://doi.org/10.1117/12.922380
175. A. Ingenito, O. Isabella, M. Zeman, ACS Photon. **1**, 270 (2014)
176. L. Tsakalakos, J. Nanophoton. **1**, 013552 (2007)
177. Y. Kato, S. Adachi, J. Electrochem. Soc. **158**, K157 (2011)
178. R.C. Wang, C.Y. Chao, W.S. Su, Acta Mater. **60**, 2097 (2012)
179. C.Y. Chen, W.J. Li, H.H. Chen, Chem. Phys. Chem. **13**, 1415 (2012)
180. N. Nafie, M.A. Lachiheb, M. Bouaich, Nanoscale Res. Lett. **7**, 393 (2012)
181. T. Yamaguchi, T. Shimizu, Y. Morosawa, K. Takase, T. L. Chen, S. M. Lu, H. C. Chien, S. Shingubara, Jpn. J. Appl. Phys. **53**, 06JF10 (2014)
182. M.A. Lachiheb, M.A. Zrir, N. Nafie, O. Abbes, J. Yakoubi, M. Bouaïcha, Sol. Energy **110**, 673 (2014)
183. Z. Zuo, K. Zhu, G. Cui, W. Huang, J. Qu, Y. Shi, Y. Liu, G. Ji, Sol. Energy Mater. Sol. Cells **125**, 248 (2014)
184. Y.J. Hung, S.L. Lee, K.C. Wu, Y. Tai, Y.T. Pan, Opt. Express **19**, 15792 (2011)
185. Y.J. Hung, S.L. Lee, K.C. Wu, Y.T. Pan, IEEE Photon. J. **3**, 617 (2012)
186. T.H. Pei, S. Thiyagu, Z. Pei, Appl. Phys. Lett. **99**, 153108 (2011)
187. J.Y. Jung, Z. Guo, S.W. Jee, H.D. Um, K.T. Park, J.H. Lee, Opt. Express **18**, A286 (2010)
188. S. Wang, X.Z. Yu, H.T. Fan, Appl. Phys. Lett. **91**, 061105 (2007)
189. M.E. Motamedi, W.H. Southwell, W.J. Gunnin, Appl. Opt. **31**, 4371 (1992)
190. K. Hadobás, S. Kirsch, A. Carl, M. Acet, E.F. Wassermann, Nanotechnology **11**, 161 (2000)
191. C.H. Sun, W.L. Min, N.C. Linn, P. Jiang, B. Jiang, Appl. Phys. Lett. **91**, 231105 (2007)
192. Z. Yu, H. Gao, W. Wu, H. Ge, S.Y. Chou, J. Vac. Sci. Technol. B **21**, 2874 (2003)
193. G. Zhang, J. Zhang, G. Xie, Z. Liu, H. Shao, Small **2**, 1440 (2006)
194. Y. Kanamori, E. Roy, Y. Chen, Microelectron. Eng. **287**, 78 (2005)
195. P. Lalanne, G.M. Morris, Nanotechnology **8**, 53 (1997)
196. Y. Kanamori, M. Sasaki, K. Hane, Opt. Lett. **24**, 1422 (1999)
197. H. Sai, H. Fujii, K. Arafune, Y. Ohshita, M. Yamaguchi, Y. Kanamori, H. Yugami, Appl. Phys. Lett. **88**, 201116 (2006)
198. C.C. Striemer, P.M. Fauchet, Appl. Phys. Lett. **81**, 2980 (2002)
199. M.L. Kuo, D.J. Poxson, Y.S. Kim, F.W. Mont, J.K. Kim, E.F. Schubert, S.Y. Lin, Opt. Lett. **33**, 2527 (2008)

200. L. Tian, K.B. Ram, I. Ahmad, L. Menon, M. Holtz, J. Appl. Phys. **97**, 026101 (2005)
201. L.L. Ma, Y.C. Zhou, N. Jiang, X. Lu, J. Shao, W. Lu, J. Ge, X.M. Ding, X.Y. Hou, Appl. Phys. Lett. **88**, 171907 (2006)
202. R.B. Stephens, G.D. Cody, Thin Solid Films **45**, 19 (1977)
203. K.H. Kim, Q.H. Park, Sci. Rep. **3**, 1062 (2013)
204. M. Chen, H.C. Chang, A.S.P. Chang, S.Y. Lin, J.Q. Xi, E.F. Schubert, Appl. Opt. **46**, 6533 (2007)
205. S. Chattopadhyay, Y.F. Huang, Y.J. Jen, A. Ganguly, K.H. Chen, L.C. Chen, Mater. Sci. Eng. R Rep. **69**, 1 (2010)
206. P. Singh, S.N. Sharma, N.M. Ravindra, JOM **62**, 15 (2010)
207. M.J. Huang, C.R. Yang, Y.C. Chiou, R.T. Lee, Sol. Energy Mater. Sol. Cells **92**, 1352 (2008)
208. M. Algasinger, J. Paye, F. Werner, J. Schmidt, M.S. Brandt, M. Stutzmann, S. Koynov, Adv. Energy Mater. **3**(8), 1068 (2013)
209. W. Huang, Y. Xue, X. Wang, X. Ao, Opt. Mater. Express **5**, 1482 (2015)
210. F. Wang, H. Yu, J. Li, X. Sun, X. Wang, H. Zheng, Opt. Lett. **35**(1), 40 (2010)
211. S. Jeong, M.D. McGehee, Y. Cui, Nat. Commun. **4**, 2950 (2013)
212. W. Hadibrata, F. Es, S. Yerci, R. Turan, Sol. Energy Mater. Sol. Cells **180**, 247 (2018)
213. J.W. Song, Y.H. Nam, M.J. Park, B. Yoo, J.S. Cho, R.B. Wehrspohn, J.H. Lee, Opt. Express **24**(18), A1224 (2016)
214. Q. Tang, H. Shen, H. Yao, K. Gao, Y. Jiang, W. Yang, Y. Liu, Sol. Energy **170**, 263 (2018)
215. L. Hu, G. Chen, Nano Lett. **7**, 3249 (2007)
216. J.S. Li, H.Y Yu, S.M. Wong, G. Zhang, X. Sun, P.G.Q. Lo, D.L. Kwong, Appl. Phys. Lett. **95**, 033102 (2009)
217. C. Lin, M.L. Povinelli, Opt. Express **17**, 19371 (2009)
218. R.A. Street, W.S. Wong, C. Paulson, Nano Lett. **9**, 3494 (2009)
219. H. Bao, X. Ruan, Opt. Lett. **35**, 3378 (2010)
220. W.Q. Xie, J.I. Oh, W.Z. Shen, Nanotechnology **22**, 065704 (2011)
221. H. Fang, X. Li, S. Song, Y. Xu, J. Zhu, Nanotechnology **19**, 255703 (2008)
222. H.D. Um, K.T. Park, J.Y. Jung, X. Li, K. Zhou, S.W. Jee, J.H. Lee, Nanoscale **6**, 5193 (2014)
223. C. Chen, R. Jia, H. Li, Y. Meng, X. Liu, T. Ye, S. Kasai, H. Tamotsu, N. Wu, S. Wang, J. Chu, Appl. Phys. Lett. **98**, 143108 (2011)
224. H. Li, R. Jia, C. Chen, Z. Xing, W. Ding, Y. Meng, D. Wu, X. Liu, T. Ye, Appl. Phys. Lett. **98**, 151116 (2011)
225. J.Y. Jung, Z. Guo, S.W. Jee, H.D. Um, K.T. Park, M.S. Hyun, J.M. Yang, J.H. Lee, Nanotechnology **21**, 445303 (2010)
226. C. Chen, R. Jia, H. Yue, H. Li, X. Liu, D. Wu, W. Ding, T. Ye, S. Kasai, H. Tamotsu, J. Chu, S. Wang, J. Appl. Phys. **108**, 094318 (2010)
227. S.H. Baek, H.S. Jang, J.H. Kim, Curr. Appl. Phys. **11**, S30 (2011)
228. C. Chen, R. Jia, H. Yue, H. Li, X. Liu, T. Ye, S. Kasai, H. Tamotsu, N. Wu, S. Wang, J. Chu, B. Xu, J. Vac. Sci. Technol. B **29,** 021014 (2011)
229. B.R. Huang, Y.K. Yang, T.C. Lin, W.L. Yang, Sol. Energy Mater. Sol. Cells **98**, 357 (2012)
230. M. Kulakci, F. Es, B. Ozdemir, H.E. Unalan, R. Turan, IEEE J. Photovolt. **3**, 548 (2013)
231. X.X. Lin, X. Hua, Z.G. Huang, W.Z. Shen, Nanotechnology **24**, 235402 (2013)
232. Z. Zhao, B. Zhang, P. Li, W. Guo, A. Liu, Int. J. Photoenergy. **2014**(683654), 6 (2014). https://doi.org/10.1155/2014/683654
233. W.C. Wang, C.W. Lin, H.J. Chen, C.W. Chang, J.J. Huang, M.J. Yang, B. Tjahjono, J.J. Huang, W.C. Hsu, M.J. Chen, A.C.S. Appl, Mater. Interfaces **5**, 9752 (2013)
234. C.H. Lin, D.Z. Dimitrov, C.H. Du, C.W. Lan, Phys. Status Solidi C **7**, 2778 (2010)
235. W.C. Hsu, Y.S. Lu, J.Y. Chyan, J.A. Yeh, Int. J. Photoenergy. **2012**(197514), 7 (2012). https://doi.org/10.1155/2012/197514
236. Z. Zhao, P. Li, Y. Wei, C. Lu, X. Tan, A. Liu, Sol. Energy **110**, 714 (2014)
237. Z. Yue, H. Shen, Y. Jiang, W. Chen, Q. Tang, J. Jin, T. Pu, J. Luo, F. Kong, C. Rui, J. Cai, Appl. Phys. A **116**, 683 (2014)

238. X.X. Lin, Y. Zeng, S.H. Zhong, Z.G. Huang, H.Q. Qian, J. Ling, J.B. Zhu, W.Z. Shen, Nanotechnology **26**, 125401 (2015)
239. J. Jin, H. Shen, P. Zheng, K.S. Chan, X. Zhang, H. Jin, IEEE J. Photovolt. **7**, 1264 (2017)
240. G. Su, R. Jia, X. Dai, K. Tao, H. Sun, Z. Jin, X. Liu, IEEE J. Photovolt. **8**(4), 937 (2018)
241. P. Zhang, R. Jia, K. Tao, S. Jiang, X. Dai, H. Sun, Z. Jin, Z. Ji, X. Liu, C. Zhao, H. Liu, Y. Zhao, L. Tang, Sol. Energy Mater. Sol. Cells **200**, 109983 (2019)
242. Y. Liu, T. Lai, H. Li, Y. Wang, Z. Mei, H. Liang, Z. Li, F. Zhang, W. Wang, A.Y. Kuznetsov, X. Du, Small **8**, 1392 (2012)
243. W.F. Liu, J.M. Bian, Z.C. Zhao, Y.L. Luo, Z. Yuan, B.Y. Zhang, A.M. Liu, ECS Solid State Lett. **2**, Q17 (2013)
244. S. Zhong, B. Liu, Y. Xia, J. Liu, J. Liu, Z. Shen, Z. Xu, C. Li, Sol. Energy Mater. Sol. Cells **108**, 200 (2013)
245. Y. Xia, B. Liu, J. Liu, Z. Shen, C. Li, Sol. Energy **85**, 1574 (2011)
246. A.G. Aberle, *Crystalline Silicon Solar Cells-Advanced Surface Passivation and Analysis* (Centre for Photovoltaic Engineering, University of NSW, Sydney, Australia, 1999)
247. A.G. Aberle, Prog. Photovolt. Res. Appl. **8**, 473 (2000)
248. A.W. Blakers, M.A. Green, Appl. Phys. Lett. **48**, 215 (1986)
249. R.R. King, R.A. Sinton, R.M. Swanson, in *Proceedings of the 20th IEEE Photovoltaic Specialists Conference (PVSC), (1988)* (Las Vegas, USA, 1988), p. 0538
250. M.Z. Rahman, S.I. Khan, Mater. Renew. Sustain. Energy **1**, 1 (2012). https://doi.org/10.1007/s40243-012-0001-y
251. J. Schmidt, R. Peibst, R. Brendel, Sol. Energy Mater. Sol. Cells **187**, 39 (2018)
252. L.E. Black, B.W.H. van de Loo, B. Macco, J. Melskens, W.J.H. Berghuis, W.M.M. Kessels, Sol. Energy Mater. Sol. Cells **188**, 182 (2018)
253. M.A. Green, Prog. Photovolt. Res. Appl. **17**, 183 (2009)
254. J. Zhao, A. Wang, M.A. Green, Prog. Photovolt. Res. Appl. **7**, 471 (1999)
255. C. Leguijt, P. Lölgen, J.A. Eikelboom, A.W. Weeber, F.M. Schuurmans, W.C. Sinke, P.F.A. Alkemade, P.M. Sarro, C.H.M. Marée, L.A. Verhoef, Sol. Energy Mater. Sol. Cells **40**, 297 (1996)
256. M. Schaper, J. Schmidt, H. Plagwitz, R. Brende, Prog. Photovolt. Res. Appl. **13**, 381 (2005)
257. B. Hoex, S.B.S. Heil, E. Langereis, M.C.M. Van De Banden, W.M.M. Kessels, Appl. Phys. Lett. **89**, 042112 (2006)
258. G. Agostinelli, A. Delabie, P. Vitanov, Z. Alexieva, H.F.W. Dekkers, S.D. Wolf, G. Beaucarne, Sol. Energy Mater. Sol. Cells **90**, 3438 (2006)
259. G. Dingemans, W.M.M. Kessels, ECS Trans. **41**(2), 293 (2011)
260. G. Dingemans, W.M.M. Kessels, J. Vac. Sci. Technol. A **30**, 040802 (2012)
261. N. Vandana, J. Batra, R. Gope, J. Singh, S. Panigrahi, P. Tyagi, S.K. Pathi, C.M.S. Srivastava, P.K. Rauthan, Singh. Phys. Chem. Chem. Phys. **16**, 21804 (2014)
262. A.G. Aberle, Sol. Energy Mater. Sol. Cells **65**, 239 (2001)
263. B. Hoex, J.J.H. Gielis, M.C.M. Van De Sanden, W.M.M. Kessels, J. Appl. Phys. **104**, 113703 (2008)
264. J. Schmidt, M. Kerr, Sol. Energy Mater. Sol. Cells **65**, 585 (2001)
265. M.J. Kerr, A. Cuevas, Semicond. Sci. Technol. **17**, 166 (2002)
266. T. Lauinger, J. Schmidt, A.G. Aberle, R. Hezel, Appl. Phys. Lett. **68**, 1232 (1996)
267. B. Liu, S. Zhong, J. Liu, Y. Xia, C. Li, Int. J. Photoenergy. **2012**(971093), 5 (2012)
268. S. Dauwe, J. Schmidt, R. Hezel, in *Proceedings of the 29th IEEE Photovoltaic Specialists Conference (PVSC)* (New Orleans, USA, 2002), p. 001246
269. M. Taguchi, A. Yano, S. Tohoda, K. Matsuyama, Y. Nakamura, T. Nishiwaki, K. Fujita, E. Maruyama, IEEE J. Photovolt. **4**(1), 96 (2014)
270. M. Taguchi, K. Kawamoto, S. Tsuge, T. Baba, H. Sakata, M. Morizane, K. Uchihashi, N. Nakamura, S. Kiyama, O. Oot, Prog. Photovolt. Res. Appl. **8**, 503 (2000)
271. M. Garín, U. Rau, W. Brendle, I. Martín, R. Alcubilla, J. Appl. Phys. **98**, 093711 (2005)
272. S. Olibet, E.V. Sauvain, C. Ballif, Phys. Rev. B Condens. Matter Mater. Phys. **76**, 035326 (2007)

273. B. Stegemann, J. Kegel, M. Mews, E. Conrad, L. Korte, U. Stürzebecher, H. Angermann, Energy Procedia **38**, 881 (2013)
274. T. Mishima, M. Taguchi, H. Sakata, E. Maruyama, Sol. Energy Mater. Sol. Cells **95**(1), 18 (2011)
275. M. Mews, C. Leendertz, M. Algasinger, S. Koynov, L. Korte, Phys. Status Solidi-Rapid Res. Lett. **8**, 831 (2014)
276. B. Iandolo, M. Plakhotnyuk, R.S. Davidsen, E. Stamate, O. Hansen, S. Nunomura, in *Proceedings of the IEEE 7th World Conference on Photovoltaic Energy Conversion (WCPEC 2018)—A Joint Conference of 45th IEEE PVSC, 28th PVSEC and 34th EU PVSEC* (2018), p. 2135
277. H. Jin, K.J. Weber, N.C. Dang, W.E. Jellett, Appl. Phys. Lett. **90**, 262109 (2007)
278. B. Hoex, J. Schmidt, P. Pohl, M.C.M. Van De Sanden, W.M.M. Kessels, J. Appl. Phys. **104**, 044903 (2008)
279. O. Schultz, S.W. Glunz, G.P. Willeke, Prog. Photovolt. Res. Appl. **12**, 553 (2004)
280. R. Khandelwal, U. Plachetka, B. Min, C. Moormann, H. Kurz, Microelectron. Eng. **111**, 220 (2013)
281. M.B. Rabha, M. Salem, M.A. El Khakani, B. Bessais, M. Gaidi, Mater. Sci. Eng. B **178**, 695 (2013)
282. B. Hoex, J. Schmidt, R. Bock, P.P. Altermatt, M.C.M. Van De Sanden, W.M.M. Kessels, Appl. Phys. Lett. **91**, 112107 (2007)
283. J. Schmidt, B. Veith, R. Brende, Phys. Status Solidi-Rapid Res. Lett. **3**, 287 (2009)
284. G. Dingemans, R. Seguin, P. Engelhart, M.C.M. van de Sanden, W.M.M. Kessels, Phys. Status Solidi-Rapid Res. Lett. **4**, 10 (2010)
285. A. Richter, J. Benick, M. Hermle, S.W. Glunz, Phys. Status Solidi-Rapid Res. Lett. **5**, 202 (2011)
286. B. Veith, F. Werner, D. Zielke, R. Brendel, J. Schmidt, Energy Procedia **8**, 307 (2011)
287. G. Dingemans, A. Clark, J.A. Van Delft, M.C.M. Van De Sanden, W.M.M. Kessels, J. Appl. Phys. **109**, 113107 (2011)
288. J. Schmidt, F. Werner, B. Veith, D. Zielke, S. Steingrube, P.P. Altermatt, S. Gatz, T. Dullweber, R. Brendel, Energy Procedia **15**, 30 (2012)
289. B. Hoex, M.C.M. van de Sanden, J. Schmidt, R. Brendel, W.M.M. Kessels, Phys. Status Solidi-Rapid Res. Lett. **6**, 4 (2012)
290. L.Q. Zhu, Y.H. Liu, H.L. Zhang, H. Xiao, L.Q. Guo, Appl. Surf. Sci. **288**, 430 (2014)
291. L.E. Black, K.R. McIntosh, I.E.E.E. Trans, Electron Devices **57**, 1996 (2010)
292. S. Duttagupta, F. Lin, K.D. Shetty, A.G. Aberle, B. Hoex, Prog. Photovolt. Res. Appl. **21**, 760 (2013)
293. P. Li, Y. Wei, X. Tan, X. Li, Y. Wang, Z. Zhao, Z. Yuan, A. Liu, RSC Adv. **6**, 104073 (2016)
294. Z. Shen, B. Liu, Y. Xia, J. Liu, J. Liu, S. Zhong, C. Li, Scr. Mater. **68**, 199 (2013)
295. R.J. Martín-Palma, L. Vázquez, J.M. Martínez-Duart, M. Schnell, S. Schaefer, Semicond. Sci. Technol. **16**, 657 (2001)
296. X. Ye, S. Zou, K. Chen, J. Li, J. Huang, F. Cao, X. Wang, L. Zhang, X.F. Wang, M. Shen, X. Su, Adv. Funct. Mater. **24**, 6708 (2014)
297. Z.G. Huang, X.X. Lin, Y. Zeng, S.H. Zhong, X.M. Song, C. Liu, X. Yuan, W.Z. Shen, Sol. Energy Mater. Sol. Cells **143**, 302 (2015)
298. Z. Huang, X. Song, S. Zhong, H. Xu, W. Luo, X. Zhu, W. Shen, Adv. Funct. Mater. **26**, 1892 (2016)
299. I.R. Putra, J.Y. Li, C.Y. Chen, Appl. Surf. Sci. **478**, 725 (2019)
300. G. Su, X. Dai, K. Tao, H. Sun, R. Jia, Z. Jin, X. Liu, H. Liu, S. Liu, C. Xu, Y. Cao, Y. Zhao, H. Qu, B. Liu, B. Chen, Sol. Energy **170**, 95 (2018)
301. K. Chen, J. Zha, F. Hu, X. Ye, S. Zou, V. Vähänissi, J.M. Pearce, H. Savin, X. Su, Sol. Energy Mater. Sol. Cells **191**, 1 (2019)
302. Y.C. Niu, H.T. Liu, X.J. Liu, Y. Sen Jiang, X.K. Ren, P. Cai, T.G. Zhai, Mater. Sci. Semicond. Process. **56**, 119 (2016)

303. A. Holt, A. Thøgersen, C. Rohr, J.I. Bye, G. Helgesen, Ø. Nordseth, S.A. Jensen, L. Norheim, Ø. Nielsen, in *Proceedings of the 35th IEEE Photovoltaic Specialists Conference (PVSC)* (Honolulu, HI, USA, 2010), p. 003501
304. C. Zheng, H. Shen, T. Pu, Y. Jiang, Q. Tang, W. Yang, C. Chen, C. Rui, Y. Li, IEEE J. Photovolt. **7**, 153 (2017)
305. R. Wehrspohn, A.N. Sprafke, J. Opt. Soc. Amer. B **3**(2), 147 (2014)
306. J. Yoon, A.J. Baca, S. Il Park, P. Elvikis, J.B. Geddes, L. Li, R.H. Kim, J. Xiao, S. Wang, T.H. Kim, M.J. Motala, B.Y. Ahn, E.B. Duoss, J.A. Lewis, R.G. Nuzzo, P.M. Ferreira, Y. Huang, A. Rockett, J.A. Rogers, Nat. Mater. **7**, 907 (2008)
307. A.J. Baca, K.J. Yu, J. Xiao, S. Wang, J. Yoon, J.H. Ryu, D. Stevenson, R.G. Nuzzo, A.A. Rockett, Y. Huang, J.A. Rogers, Energy Environ. Sci. **3**, 208 (2010)
308. J. Yoon, L. Li, A.V. Semichaevsky, J.H. Ryu, H.T. Johnson, R.G. Nuzzo, J.A. Rogers, Nat. Commun. **2**, 343 (2011)
309. A. Mavrokefalos, S.E. Han, S. Yerci, M.S. Branham, G. Chen, Nano Lett. **12**, 2792 (2012)
310. D.M. Powell, M.T. Winkler, H.J. Choi, C.B. Simmons, D.B. Needleman, T. Buonassisi, Energy Environ. Sci. **5**, 5874 (2012)
311. C. Becker, D. Amkreutz, T. Sontheimer, V. Preidel, D. Lockau, J. Haschke, L. Jogschies, C. Klimm, J.J. Merkel, P. Plocica, S. Steffens, B. Rech, Sol. Energy Mater. Sol. Cells **119**, 112 (2013)
312. S. Gall, B. Rech, Sol. Energy Mater. Sol. Cells **119**, 306 (2013)
313. D. Amkreutz, J. Haschke, T. Häring, F. Ruske, B. Rech, Sol. Energy Mater. Sol. Cells **123**, 13 (2014)
314. D. Amkreutz, J. Haschke, S. Kuhnapfel, P. Sonntag, B. Rech, IEEE J. Photovolt. **4**, 1496 (2014)
315. S. Kühnapfel, S. Gall, B. Rech, D. Amkreutz, Sol. Energy Mater. Sol. Cells **140**, 86 (2015)
316. P. Sonntag, N. Preissler, M. Bokalič, M. Trahms, J. Haschke, R. Schlatmann, M. Topič, B. Rech, D. Amkreutz, Sci. Rep. **7**, 873 (2017)
317. G. Jia, A. Gawlik, J. Bergmann, B. Eisenhawer, S. Schonherr, G. Andra, F. Falk, IEEE J. Photovolt. **4**, 28 (2014)
318. G. Jia, G. Andrä, A. Gawlik, S. Schönherr, J. Plentz, B. Eisenhawer, T. Pliewischkies, A. Dellith, F. Falk, Sol. Energy Mater. Sol. Cells **126**, 62 (2014)
319. X. Fang, Y. Li, X. Wang, J. Ding, N. Yuan, Sol. Energy **116**, 100 (2015)
320. H. Savin, P. Repo, G. Von Gastrow, P. Ortega, E. Calle, M. Garín, R. Alcubilla, Nat. Nanotechnol. **10**, 624 (2015)
321. S. Wang, B.D. Weil, Y. Li, K.X. Wang, E. Garnett, S. Fan, Y. Cui, Nano Lett. **13**, 4393 (2013)
322. P. Aurang, R. Turan, H.E. Unalan, Nanotechnology **28**, 405205 (2017)
323. J.W. Song, Y.H. Nam, M.J. Park, B. Yoo, J.S. Cho, R.B. Wehrspohn, J.H. Lee, Opt. Express **24**, A1224 (2016)
324. R. Woehl, J. Krause, F. Granek, D. Bir, IEEE Electron Device Lett. **32**, 345 (2011)
325. C. Gong, E. Van Kerschaver, J. Robbelein, T. Janssens, N. Posthuma, J. Poortmans, R. Mertens, I.E.E.E. Electron, Device Lett. **4**, 2950 (2010)
326. F. Granek, M. Hermle, D.M. Huljić, O. Schultz-Wittmann, S.W. Glunz, Prog. Photovolt. Res. Appl. **17**, 47 (2009)
327. M. Hermle, F. Granek, O. Schultz, S.W. Glunz, J. Appl. Phys. **103**, 054507 (2008)
328. F. Granek, C. Reichel, Sol. Energy Mater. Sol. Cells **94**, 1734 (2010)
329. C. Trompoukis, O. El Daif, V. Depauw, I. Gordon, J. Poortmans, Appl. Phys. Lett. **101**, 103901 (2012)
330. M. Peters, M. Rüdiger, H. Hauser, M. Hermle, B. Bläsi, Prog. Photovolt. Res. Appl. **20**, 862 (2012)
331. A. Bozzola, M. Liscidini, L.C. Andrean, Prog. Photovolt. Res. Appl. **22**, 1237 (2014)
332. S.K. Srivastava, C.M.S. Rauthan, V. Kumar, P.K. Singh, *in Advances in Nanomaterials*, ed. by Z.H. Khan, M. Husain. Advanced Structured Materials, STRUCTMAT, vol. 79 (Springer, Berlin, 2016), p. 329

Chemiresistive Sensors for H_2S Gas: State of the Art

Niranjan Ramgir, Ankita Pathak, K. R. Sinju, Bhagyashri Bhangare, A. K. Debnath, and K. P. Muthe

Abstract Hydrogen sulphide (H_2S) is a colourless, corrosive, flammable and toxic gas with a typical rotten egg smell. Although it has demonstrated wide commercial utility, especially in food processing industry, coal gasification plants and oil refineries, its adverse effect on both environment and human health demands its monitoring and careful usage. It has the ability to block cellular respiration owing to its interaction with iron that is present in the cytochrome enzymes of the mitochondria. Exposure to higher concentrations can adversely affect the nervous and other systems in the body. Consequently, its short-term (15 min) and long-term (8 h) exposure limits have been set to 15 and 10 ppm, respectively. Chemiresistive sensor is one of the simplest sensors that has demonstrated a tremendous potential for H_2S detection in various concentration ranges. It works on the simple principle of resistance change of the sensor due to chemical reaction of H_2S with the sensor surface. The present chapter focuses on the recent advances in the field of chemiresistive sensors for H_2S detection. Care has been taken to give a complete insight about H_2S: its source, applications, dangerous effects and different means of detection. With the upsurge in nanoscience, novel sensor morphologies have been realized with enhanced sensor responses. This chapter will try to cover most of the important works carried out for H_2S detection highlighting the sensor with a potential for commercial application. The chapter will conclude highlighting the challenges that need to be addressed to realize practical application and discussing the future of chemiresistive sensors for H_2S detection.

Keywords Chemiresistive sensors · H_2S · Metal oxides · Nanostructures · Nanotechnology

N. Ramgir (✉) · A. Pathak · K. R. Sinju · B. Bhangare · A. K. Debnath · K. P. Muthe
Technical Physics Division, Bhabha Atomic Research Centre, Mumbai 400085, India
e-mail: niranjanpr@yahoo.com

A. Pathak · K. R. Sinju · A. K. Debnath · K. P. Muthe
Homi Bhabha National Institute, Anushaktinagar, Mumbai 400085, India

S. Kumar and D. K. Aswal (eds.), *Recent Advances in Thin Films*, Materials Horizons: From Nature to Nanomaterials, https://doi.org/10.1007/978-981-15-6116-0_19

1 Introduction

Earth's atmosphere comprises of mixture of gases that provides not only the air we breathe, but also makes life possible in several ways. Besides natural gases that are necessary to sustain life, the atmosphere includes natural and man-made particles and gases that when achieve excessive concentrations can cause serious toxicological effects detrimental for human health and planet as a whole. Both natural and man-made sources contribute to rising pollution levels. These sources are commonly classified into three broad groups: primary, secondary and re-emission sources. A primary source is the one that causes direct emissions into the atmosphere; for example, ash from volcanic eruptions and pollutants released from vehicle exhausts and industries. Secondary sources are the ones that result from the reaction of primary pollutants in air, e.g. ground level ozone. Finally, re-emission sources that result from primary or secondary pollutants deposit on the Earth's terrestrial or aquatic surfaces, followed by re-emission to the atmosphere [1]. Some of the common sources of pollutants are listed below [2]:

- Combustion of fossil fuels, in electricity generation, industry, transport and households.
- Oil and gas industries release several gases such as CO_2, NO_2, H_2S, volatile organic compound (VOC) and silica particles [3].
- Paper and pulp mills produce chlorine and chlorine-based materials, sulphur, H_2S and SO_2 [4].
- Mining industries produce metals like Cu, Pb, Zn, Cd, As, etc. as well as gases (CO_2, NO_2, SO_2), particulate matter emissions, sewage waters and solid wastes [5].
- Agriculture pollutants include biotic and abiotic by-products of farming.
- Waste treatment plants lead to release of VOCs and noxious gases like CH_4, CO_2 and NH_3 [6].
- Natural sources include volcanic eruptions, wind-blown dust, sea salt spray and emissions of VOCs from plants.
- Indoor pollutants—cooking and heating appliances, tobacco smoke and vapours from building materials, paints, furniture, etc.
- Radon, natural radioactive gas released from radioactive decay in the Earth's crust is an indoor pollutant and can be found concentrated in basements [7].

Pollution has serious toxicological impact on human health and environment [8]. Extend of effect is dependent on the nature of gas and its concentration. Generally, exposure leads to coughing, wheezing, nausea, irritation to eyes, nose and throat. Prolonged exposure may lead to impaired lung function, birth defects, reduced fertility, damage to nervous system, cardiovascular system and sometimes even cancer. Hardening of the arteries has also been observed in certain cases, and it may increase the risk of heart attack and strokes [9]. Exposure to higher concentration has adverse effect on nervous system leading to psychiatric disorders [10], neurological complications like neuroinflammation [11], degenerative brain diseases

Table 1 Exposure limits of various toxic gases

Gas	LTEL (ppm)	STEL (ppm)
H_2S	**10**	**15**
CO	50	300
NO_X	3	5
NH_3	25	35
SO_2	2	5
Cl_2	0.5	1
CH_3OH	200	250
HCl	–	5

such as Parkinson's [12], Alzheimer's and schizophrenia [13]. Exposure to air pollution early in life may lead to autism and its related disorders in foetus and children [14–16]. In some cases, severe effects like emphysema [17], chronic bronchitis [18] and lung cancer [19–21] have also been observed.

The impact of gas on human health is strongly dependent on the gas and its exposed concentration. To ensure safe and healthful working conditions, permissible exposure limits (PEL) have been established by controlling authorities like occupational safety and health administration (OSHA). For chemicals, the chemical regulation is usually expressed in parts per million (ppm) and/or milligrammes per cubic metre (mg/m^3). For the work place, exposure limits are set in terms of short-term (STEL-15 min) and long-term exposure limits (LTEL-8 h). The LTEL is the maximum exposure allowed over an eight-hour period and referred to as eight-hour time-weighted average (TWA). Some of the common toxic gases and their exposure limits are shown in Table 1. According to a report of United States Environmental Protection Agency [22] compiled by Sydney Miner, totally 30 such pollutants have been identified and investigated thoroughly for their abatement. Hydrogen sulphide is one such pollutant present in nature having severe deleterious effect on humans as well as on ecosystem. The present chapter is mainly focussed on H_2S gas: its sources, distribution, harmful effects and control technology for its abatement.

2 Need for H_2S Sensor

In eighteenth century, a Swedish chemist, Carl Wilhelm Scheele while treating Ferrous sulphide with a mineral acid observed rank odour which he called *Schwefelluft* (sulphur air) and referred as *stinkende* (stinking or foetid) [23]. He extensively studied H_2S and accordingly is credited with the discovery of chemical composition of Hydrogen Sulphide [24]. H_2S is a colourless, highly toxic chalcogen hydride gas having characteristic rotten eggs foul odour. It is referred as a broad-spectrum toxicant as it can affect different tissues and organs. It is very reactive, poisonous, corrosive and flammable gas. It is slightly denser than air and soluble in water and organic solvents. It easily reacts with metal ions forming metal sulphides that are dark coloured and insoluble solids.

2.1 H_2S Sources

- It occurs naturally in ground water [25] and is formed from decomposition of underground organic matter deposits such as decaying plant material. It is often present in wells drilled in shale or sandstone, or near coal or peat deposits or oil fields. H_2S gas is one of the major gases present in geothermal fluids and is an inevitable part of high-temperature geothermal power production [26–28].
- H_2S is often produced in the microbial breakdown of organic matter under anaerobic conditions such as in swamps and sewers [29]. Sulphate-reducing bacteria (such as salmonella) and some archea obtain energy by oxidizing organic matter or hydrogen with sulphates, producing H_2S. They perform anaerobic respiration utilizing sulphate (SO_4^{2-}) as terminal electron acceptor, reducing it to H_2S [30, 31]. These microorganisms are prevalent in low-oxygen environments, such as in swamps and standing waters. Other anaerobic bacteria liberate H_2S when they digest sulphur-containing amino acids, for instance during the decay of organic matter. Wherever sulphur comes into contact with organic material, especially at high temperatures, H_2S gas is released. As H_2S is formed during the decay of organic matter, waste water treatment plants, landfills and tanneries are also important H_2S-emitting sources [32].
- While sulphur is a constituent of most kerogens, elemental sulphur is a common component of sediments that have been dysaerobic or anoxic. During the hydrocarbon generation process, both the organic and elemental sulphur can form H_2S and free organic sulphur compounds.
- It is emitted as low-temperature volcanic gas dissolved in the silicate liquid, present in a coexisting gas phase at depth, or from the breakdown of sulphur-bearing minerals [33].
- It is a by-product of many useful industrial processes such as rayon manufacturing, wood pulp processing and production of elemental sulphur, sulphuric acid and heavy water. In particular, Kraft process employed in many paper mills, which involves use of sodium hydroxide and sodium sulphide results in H_2S emission [34]. Heavy water plants use H_2S gas to produce heavy water (D_2O) in H_2O–H_2S isotopic exchange process known as Girdler Sulphide (G-S) process. Any leakage will be harmful for working personnel and increase toxicity in the surrounding area and accordingly demand its continuous monitoring.

2.2 Girdler Sulphide (G-S) Process for Heavy Water Production

G-S process is an industrial production method for filtering heavy water out of natural water. In nuclear fission reactor, neutrons emitted in fission reaction need to be slowed down to thermal energies for effective or controlled chain reaction. Accordingly, different moderators, namely, light water, heavy water (D_2O), solid graphite,

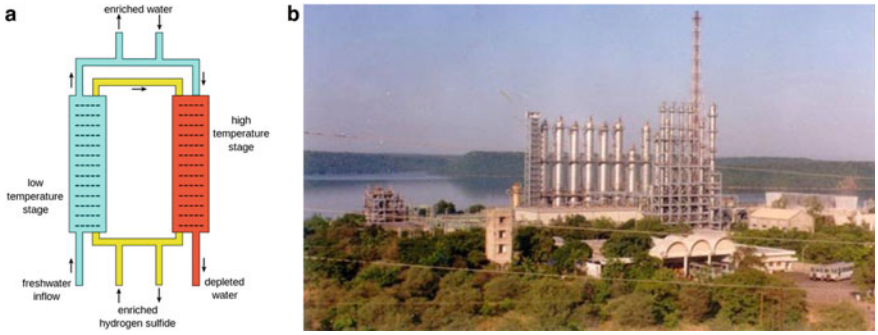

Fig. 1 **a** Schematic showing G-S process and **b** photograph of HWP Manuguru

beryllium and beryllium oxide are used in the reactors. Ideal moderators should have high neutron scattering cross section and very low absorption cross section. D_2O is used as moderator in CANDU (Canada deuterium uranium) designs based pressurized heavy water reactors. Molecules of D_2O are separated from H_2O in G-S process also known as Geib–Spevack (G-S) process. This method is based on the isotopic exchange process between H_2S and H_2O ('light' water) that produces D_2O. The first such facility of India's Heavy Water Board to use the G-S process is at Rawatbhata near Kota, Rajasthan; this was followed by a larger heavy water plant (HWP) at Manuguru, Andhra Pradesh. Figure 1 shows the schematic of the G-S process and the photograph of the HWP at Manuguru. It consists of two separate sieve tray columns, one maintained at 30 °C known as the 'cold tower' and the other at 130 °C known as the 'hot tower'. The equilibrium reaction governing the production of D_2O is given as

$$\mathbf{H_2O + HDS \rightleftharpoons HDO + H_2S} \tag{1}$$

Difference in equilibrium constant at two temperatures leads to the enrichment of deuterium in heavy water. In G-S process, H_2S gas is used in large quantities as carrier gas to extract deuterium content from water. The normal inventory of H_2S in Kota Plant is of the order of 200 tonnes in process and 50 tonnes in storage, whereas Manuguru Plant with double stream will have about 400 tonnes in process and 50 tonnes in storage. The safe handling of such large quantities of H_2S gas poses a major problem. Due to acute toxic effects, the exposed person may lose consciousness very fast and cannot come out of high concentration zone. Use of self-contained breathing apparatus is a must for persons working in H_2S-prone zone. Also as H_2S is highly corrosive as well and causes embrittlement, the selection of materials is to be done keeping this aspect in mind (Table 2).

Table 2 Concentrations of H_2S at different sources

Concentration	Sources
80–160 ppb	Normal halitosis [35, 36]
160–250 ppb	Weak halitosis
>250 ppb	Strong halitosis
0.0002 ppm	Average in ambient air [37]
>0.05 ppm	Near geothermal activity
0.13 ppm	Paper and pulp mill
25.5 ppmv	Human flatus
0.05–20 ppm	Kraft mills [38]
0.3–7.8 ppm	Viscose rayon plants [39]

2.3 Hazardous Effects of H_2S Gas

- Corrosion of metals—H_2S can lead to rapid and extensive damage to metals, including uniform corrosion, pitting and stepwise cracking.
- Exposure to H_2S affects respiratory as well as nervous system.
- Exposure to low concentrations may cause irritation to the eyes, nose, sore throat, cough, nausea, shortness of breath and fluid in the lungs (pulmonary oedema) [40].
- Long-term low-level exposure causes fatigue, headaches, poor memory and tiredness.
- Short-term high-level exposure may lead to loss of breathing, cortical pseudolaminar necrosis [41], cerebral oedema and degeneration of basal ganglia [42].
- The health effects of H_2S depend on several factors, namely concentration and duration of exposure. Table 3 summarizes the effect of H_2S at different exposure concentrations [43].

Table 3 Effect of H_2S at different concentrations

H_2S concentration (ppm)	Effect
0.0047	Gas recognition threshold (Rotten gas smell)
10–20	Threshold concentration for eye irritation
50–100	Serious eye damage
150–250	Olfactory nerve paralyzed and sense of smell disappears
320–530	Pulmonary oedema with risk of death
530–1000	Strong CNS stimulation, hyperpnoea followed by respiratory arrest
>800	Lethal concentration for 50% of humans for 5 min exposure (LC50)
1000–2000	Immediate collapse with paralysis of respiration even after inhalation of single breath

2.4 Major Incidents in the History Showing Deleterious Effects of H_2S

- During World War I in 1916, British Army used H_2S as chemical weapon [44].
- In 1975, during an oil drilling operation in Denver City, Texas, accidental H_2S release caused nine casualties [45].
- On September 2005, three crewmen died due to sewage line leak in the propeller room of a Royal Caribbean Cruise Liner docked in Los Angeles [46, 47].
- In 2006, a dump of toxic waste containing H_2S caused 17 deaths and thousands of illnesses in Abidjan, on the West African coast.
- In 2014, H_2S levels as high as 83 ppm have been observed at a newly built mall in Thailand at the Siam Square area. Exposure had caused health complications such as sinus inflammation, difficulties in breathing and eye irritation to shop tenants. Defective treatment and disposal of waste water in the building [48] was attributed to the observed high concentration.
- In January 2017, three utility workers in Key Largo, Florida, died within seconds of descending into a narrow space beneath a manhole cover to check a section of paved streets; the hole had H_2S and CH_4 gas created from years of rotted vegetation [49, 50].

Thus, it is evident that there is an urgent need to opt suitable methods and techniques to detect H_2S both quantitatively and qualitatively. In this direction, sincere efforts are made by the researchers around the globe to develop gas sensing devices using different materials and novel detection techniques.

3 Different Techniques for H_2S Detection

Human olfactory system is an excellent sensor that can detect very low concentrations of odorant molecules almost instantaneously. This has been assigned to the presence of several million olfactory receptor cells in the nasal cavity. For example, towards H_2S that have a characteristic rotten egg smell, the gas recognition threshold is just 4.7 ppb. Even with such high sensitivity for odorant molecules, most of the toxic gases are either detectable at higher concentrations or undetectable at all. Thus, the development of highly sensitive yet economical sensors is in great demand for real-time and online monitoring of hazardous gases. For H_2S detection, some of the analytical and standardized methods are based on colorimetric and chromatographic techniques. To determine this noxious gas in environmental samples, these methods have been frequently employed. For example, to perform complete compositional measurements and detect the concentration of H_2S in oil and gas reservoir, conventional techniques such as Gas chromatography and Lead acetate tape method (colorimetry) are used to analyse the fluid sample from the reservoir [51, 52].

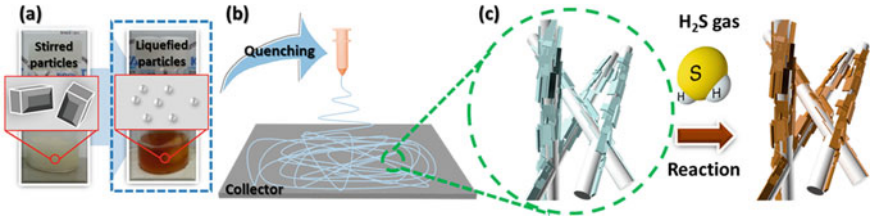

Fig. 2 Schematic illustrations of **a** high-temperature stirring (HTS), **b** electrospinning for synthesis of $Pb(Ac)_2$@NFs and **c** colour change of $Pb(Ac)_2$@NFs on exposure to H_2S. Reprinted with permission from J. H. Cha et al. Anal. Chem., 90 (2018), 8769–8775 copyright @ ACS

3.1 Colorimetry

Colorimetric technique is one of the conventional techniques used for the measurement of H_2S concentration in air [53]. It is inexpensive, simple to operate and used frequently in industries. Specific volume of target gases can be checked simply by observing the colour change in various chemicals. The depth and length of the colour change determines the corresponding concentration of gas in the sample [54, 55]. This method is generally considered to be subjective and semi-quantitative as is based on the human eye perception. Also it can be easily interfered by other chemicals, e.g. NO_2, SO_2 and various mercaptans [56]. Besides, it is highly sensitive to temperature and humidity, thus having limited shelf life. Lead acetate tape method is based on the reaction of H_2S with lead acetate impregnated paper tape to form lead sulphide [57, 58] that appears as a brown stain on the paper tape. The greater the amount of H_2S, the darker the stain is. J. H. Cha et al. have shown the sub-ppm detection of H_2S using lead acetate anchored nanofibres and employed the same for the diagnosis of Halitosis [59]. Figure 2 shows the schematic illustration of the synthesis of lead acetate anchored nanofibres and the colour change upon exposure to H_2S. The main advantage of the sensor is that it does not require any power for its operation. But due to its complexity and long detection time, it is hardly used for in situ measurements. In particular, as online analyser, additional components include a light source to illuminate the tape where the reaction occurs and a light detector to monitor the reflection of the source from the tape [60]. The rate of staining on the tape determines the H_2S concentration.

3.2 Gas Chromatography

Another commonly used conventional technique is Gas chromatography (GC) that involves the flow of carrier gas containing sample through a column (e.g. Poropack for sulphur compounds) which is maintained at constant temperature and pressure [61–63]. Identity of a given component is determined on the basis of the time it takes to pass through the column. Area under the peak of the detected signal will give the

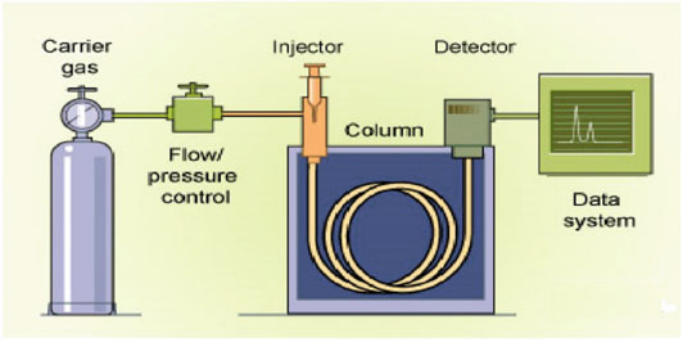

Fig. 3 Schematic representation of the basic gas chromatograph system

concentration of the gas by comparing it with premeasured area of known concentration of the gas. Figure 3 shows schematics of the simple gas chromatography system. Similar techniques such as high-performance liquid chromatography [64] (HPLC) and ion chromatography [65] with high sensitivity towards low concentrations of toxic gases and vapours are also available. However, disadvantages such as complex sample preparation, long detection time and high cost limit their usage.

Both the conventional methods, i.e. colorimetry and chromatography, suffer from numerous disadvantages that include complex laboratory procedures, very small shelf life, need of frequent replacement and difficulty in real-time measurements [66]. Also these methods involve a multistage protocol starting from sampling and going to final determination. As such, the approaches are not convenient to track down short-term variations in behaviour due to the uncertain dynamics of the varying environmental conditions [67].

3.3 Electrochemical Sensor

Electrochemical sensors are powerful tools to achieve real-time information in in situ measurements of chemical composition without sampling unlike conventional techniques [68, 69]. High sensitivity, low power consumption, miniaturization and direct linear current output to gas concentration are some of its advantages. Depending on electrolyte, these sensors can operate in wide temperature range from −30 to 1600 °C with liquid electrolyte up to 140 °C and solid electrolyte >500 °C [70]. Sensors with liquid electrolyte are rather bulky and easy to be dried. Also, there is high chance of leakage of electrolyte which may corrode the device and impair its function. These sensors work in different modes depending on the type of signal transduction, i.e. amperometric (change of current), potentiometric (change of membrane potential) [71], impedimetric (change of impedance) or conductometric (change of conductance) [72]. Figure 4 shows the schematics of the amperometric and the poten-

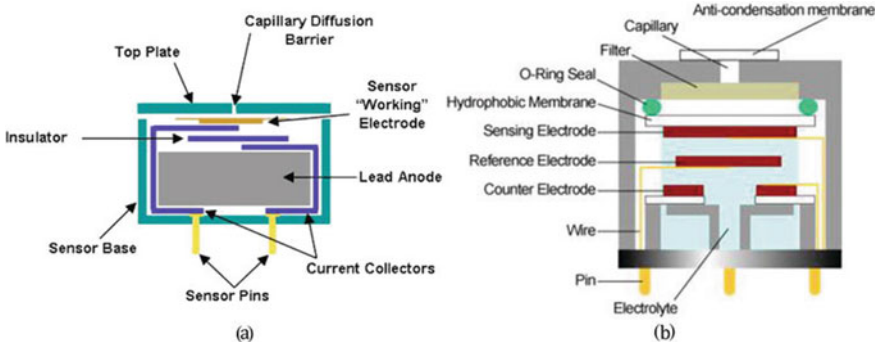

Fig. 4 Schematic representation of the **a** Amperometric and **b** Potentiostatic cell sensor

tiostatic cell sensors. Schiavon et al. have demonstrated an ion exchange membrane based H_2S sensor with high sensitivity and fast response [73]. Porous silver electrode supported on ion exchange membrane that serves as solid polymer electrolyte significantly enhances the sensor response. In another study, Yu et al. show that the Nafion membrane pretreated with conc. H_2SO_4 exhibits superior and more stable H_2S response than untreated membrane [74]. Treatment with H_2SO_4 increases the water-preserving ability of membrane, thus giving sensitivity of 2.9 μA/ppm with response time of 9 s and detection limit of 0.1 ppm.

Reaction kinetics slows down with temperature and thus limits the operable temperature range of the sensor. Operation in low-oxygen environments also alters the performance in sensors where oxidation of the target gas takes place at the sensing electrode. The significant reduction or even elimination of the narrow operating temperature range of electrochemical sensors has taken away the principal argument for the use of solid-state sensors in their place.

3.4 Mass-Sensitive Sensor

Surface acoustic wave (SAW) sensors are a type of mass-sensitive sensor [75, 76]. Their sensing principle depends on the detection of frequency variation of surface acoustic wave excited on quartz or piezoelectric substrate in the presence of analyte gas. Wang et al. had developed SAW sensor using SnO_2/CuO composite film on $YXLiTaO_3$ substrate [77]. In the presence of H_2S gas phase, velocity of acoustic wave changes due to mass loading and acousto-electric effect, which creates frequency shift in the SAW device. As shown in Fig. 5, the sensor showed switch-like response (55 s) and recovery (45 s) with a large frequency response of 230 kHz for 20 ppm H_2S at working temperature of 160 °C.

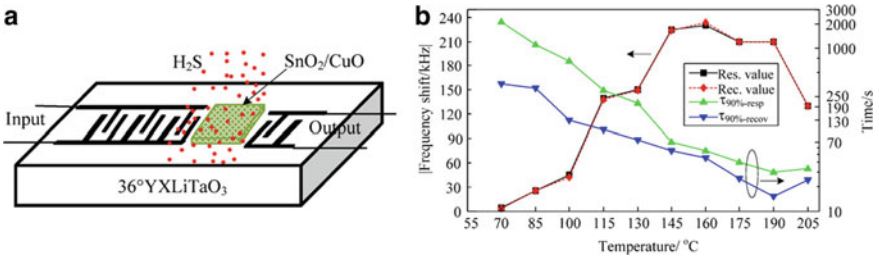

Fig. 5 **a** Scheme of the SnO_2–CuO films coated SAW H_2S sensor. **b** The sensing properties vs. operating temperatures of the present SAW sensor towards 20 ppm concentration of H_2S. Reprinted with permission from X. Wang et al. Sens. Actuators B 169, (2012) 10–16. Copyright @ Elsevier

3.5 Optical Sensors

Surface plasmon resonance (SPR) belongs to the category of optical sensor [78, 79]. Their sensing mechanism depends on the detection of change in SPR signal which is proportional to the refractive index close to the sensor surface that is directly related to the amount of gas molecules present on the surface. An SPR-based fibre optic H_2S sensor using thin ZnO layer over copper film as the sensing material was reported by Taabassum et al. [80]. The sensor works on the principle of change in the refractive index of the ZnO due to H_2S interaction. The unpolarized light from a polychromatic source is launched from one end of the fibre and the corresponding SPR spectrum is recorded at the other end (Fig. 6). The recorded SPR spectrum exhibits a shift in the resonance wavelength with respect to H_2S concentration (0–100 ppm) (Fig. 6). Increase in H_2S concentration causes the curve to shift towards red wavelength. This is due to change in dielectric constant of ZnO with respect to H_2S. High sensitivity of this sensor over other metal oxide coated sensor justified the selection of ZnO as

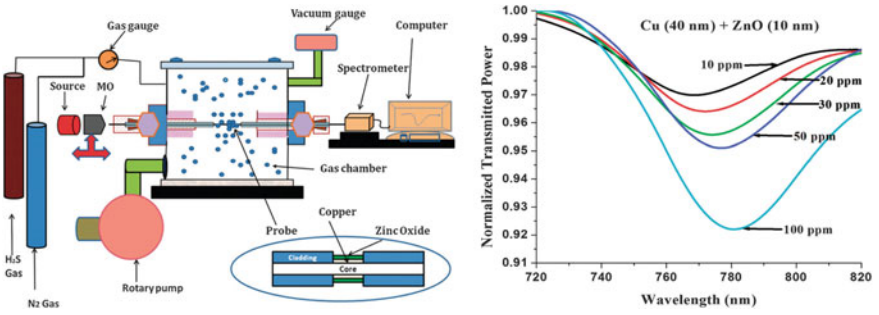

Fig. 6 Schematic diagram of the experimental gas sensing set-up. SPR spectra of the fibre optic SPR probe for different H_2S concentrations. The probe has layers of copper (40 nm) and zinc oxide (10 nm). Reprinted with permission from R. Tabassum et al. Phys. Chem. Chem. Phys. 15 (2013), 11868–11874. Copyright @ RSC

the sensing material. Sensor possesses maximum sensitivity with a film of 10 nm thickness with response and recovery time of around 1 min.

3.6 Chemiresistive Sensors

Chemiresistive sensors are among the simplest and most popular sensor types based on the simple principle of change in electrical resistance of the sensors due to chemical reaction happening on the sensor surface. Direction of change in resistance depends on the nature of material (p or n-type) and the oxidizing or reducing nature of the gas. To characterize the sensor performance, a set of parameters is defined and is listed below [81, 82]:

- **Sensor response**—it is the sensing characteristic that perceives the variation in the physical and/or chemical properties of the sensing material when exposed to gas. For chemiresistive sensor, it is defined as

  (a) the ratio of resistance in air to gas, i.e. $S = \frac{R_a}{R_g}$ or $S = \frac{R_g}{R_a}$ depending on the nature of gas
  (b) In terms of percentage, it is given by ratio of change in resistance to that of air

$$S(\%) = \frac{\left(R_a - R_g\right)}{R_a} \times 100$$

- **Sensitivity**—it is defined as the change of measured signal per analyte concentration.
- **Selectivity**—it is the capacity of a sensor to discriminate between gases in a mixture. Good sensor should have high sensitivity towards a particular gas while remaining almost insensitive to other test gases. Selectivity factor (k) is defined as

$$K = \frac{\text{Sensitivity of sensor to target gas}}{\text{Sensitivity of sensor to interfering gases}}$$

- **Stability**—it is the ability of the sensor to maintain its properties, i.e. sensitivity, selectivity, response and recovery and provide reproducible results when operated for long durations.
- **Response Time**—it is the time required for resistance to attain a fixed percentage (usually 90%) of the saturation value after exposure to test gas (Fig. 7).
- **Recovery time**—it is the time required for sensor to recover to 10% of the original resistance when exposed to clean air for recovery after exposure to target gas.
- **Detection Limit**—it refers to the lowest analyte concentration that can be detected under given conditions, particularly temperature.

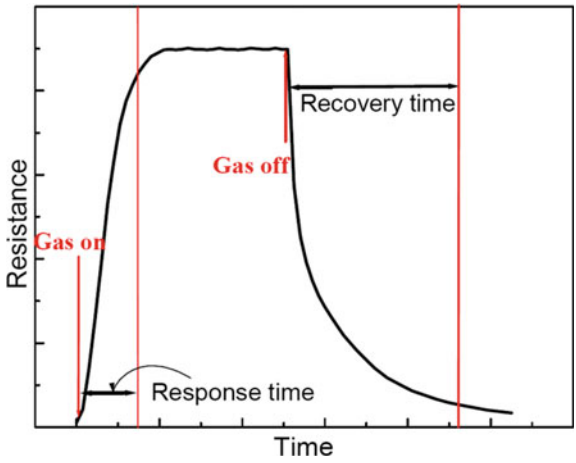

Fig. 7 Typical response curve of n-type semiconductor for oxidizing gas

4 Ideal Characteristics of Gas Sensor

One of the main selection criteria for the sensor to be an ideal one for commercial deployment is the satisfaction of '4-S selection criteria'. Herein, each S stands for Sensitivity, Selectivity, Stability and Suitability. An ideal chemical sensor would possess high sensitivity, selectivity for particular gas, long-term stability, low detection limit, short response and recovery time and long shelf life. In applications, the importance of sensor lies in its precision and ability to sense gas for large number of cycles without hysteresis. A good sensor should show invulnerability towards various interferences like humidity, dust and vibrations. Low operating temperature materials are preferred for integration with electronic circuits. Sensors working at elevated temperatures increase power consumption, and requirement of heating element makes device bulkier and affects sensor life. The criteria for suitability come from the economic point of view. The sensor should be cost-effective from both industry and user's point of view. The above-mentioned sensor performance parameters are necessary to carry research from laboratory scale to complete device at commercial scale.

5 Chemiresistive Sensors: Techniques for Gas Sensing Measurements

For chemiresistive sensors, the response curves are measured by recoding the resistance values continuously as a function of time before and after exposure to known concentration of target gas. The response curves are recorded using either static or dynamic environment method as schematically represented in Fig. 8.

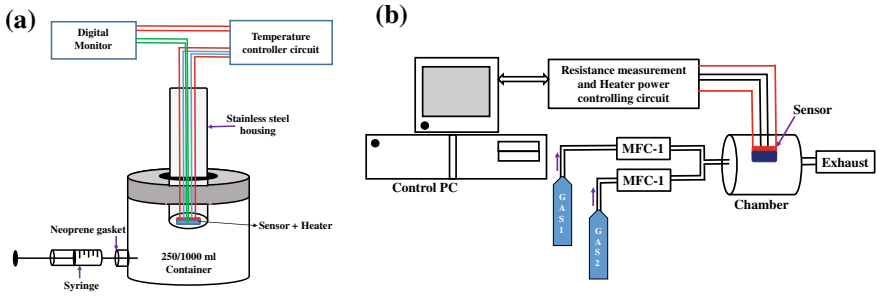

Fig. 8 Schematics of the sensor testing method **a** Static and **b** Dynamic environment method

5.1 Static Environment Method

In this method, the sensing element is placed inside the test chamber of known volume having a provision for gas inlet. When the resistances of the sensors become almost stable in air, the target gas with known concentration is introduced into the test chamber through the gas inlet using a syringe. The final gas concentration is determined by the volume ratio of the injected gas to air in the test chamber under standard atmospheric pressure. The resistance values of sensor are recorded as a function of time till it reaches saturation, and then the recovery is studied by removing the gas chamber and exposing the sensor to ambient air. Measured resistance values are used to calculate the sensor response, response and recovery times and sensitivity of the test sample.

5.2 Dynamic Environment Method

It measures the resistance values under continuous flow of target gas containing desired concentration of test gas. It uses mass flow controllers (MFC) for both target and reference gases. Thus, the desired concentration of analyte gas is achieved by mixing it with reference gas (preferably N_2 or Ar) using MFCs. The main advantage of this dynamic method over static method is that the sensor response can be recorded repeatedly at different concentrations.

The sensing performance of an element is a strong function of operating temperature; hence, in both the systems, sensor is attached to a heater whose temperature is controlled by attached temperature controller circuit.

6 Gas Sensing Mechanism in Chemiresistive Sensors

6.1 Pristine Metal Oxides

Metal oxides (MOs) are intrinsically insulating in nature; but due to the presence of inherent vacancies, they behave as semiconductors and referred to as metal oxide semiconductors (MOS). They can be either n- or p-type depending on the type of vacancies present. MOS with metallic vacancies behaves as p-type semiconductor, e.g. CuO, NiO, etc. and the one with oxygen vacancies behaves as n-type semiconductor, e.g. SnO_2, ZnO, Fe_2O_3, etc. The inherent non-stoichiometry and the ability to precisely tailor the electronic properties make MOS the most popular materials for detection of hazardous gases. Accordingly, they have been exhaustively investigated for detection of various toxic gases. MOS sensors were first used commercially in the 1960s as household gas alarms in Japan under the names of *Taguchi* (the inventor) or *Figaro* (company's name) [83]. Their sensing mechanism also depends on the changes of resistances induced by the adsorption of gases.

In chemiresistive sensors, change in resistance due to interaction of target analyte at the surface leads to a detectable signal. This resistance variation is the result of change in free charge carrier concentration in the sensing material caused by adsorption of gas molecules on the surface. Under ambient conditions, oxygen present in the atmosphere due to their high electronegativity traps electrons from the conduction band of sensing material and gets physisorbed on the surface in the form of O_2^-, O^- or O^{2-} species. Depending on the substrate or operating temperature, the adsorbed oxygen on the sensor surface undergoes following reactions:

$$\mathbf{O_2} + \mathbf{e^-} \rightarrow \mathbf{O_2^-} \quad (\mathrm{RT} - 100\,^\circ\mathrm{C}) \tag{2}$$

$$\mathbf{O_2^-} + \mathbf{e^-} \rightarrow 2\mathbf{O^-} \quad (100 - 300\,^\circ\mathrm{C}) \tag{3}$$

$$\mathbf{O^-} + \mathbf{e^-} \rightarrow \mathbf{O^{2-}} \quad (\mathrm{T} > 300\,^\circ\mathrm{C}) \tag{4}$$

This leads to the formation of space charge region at the grain boundaries, which changes the resistance of the material due to change in free charge carrier concentration. Abstraction of electron will form electron-depleted layer in n-type MOS and accumulation layer in p-type MOS. As the concentration of electrons in depletion region is lower than in the bulk region in n-type semiconductor, the resistance in depletion region is higher than the bulk. While holes being the majority carrier in p-type MOS, resistance of accumulation region is lower than the core region. Now, H_2S gas is reducing in nature and has the tendency to donate electrons. Hence, upon H_2S exposure, oxygen physisorbed on the sensor surface reacts with H_2S causing reinjection of the trapped electrons back to MOS, thereby increasing the charge carrier concentration. This causes the modulation of the resistance of the sensor material. Released electrons reduce the width of both depletion and accumulation region, thus

decreasing and increasing the resistance of n- and p-type MOS, respectively. Reaction between H_2S and adsorbed oxygen is expressed by the following reactions:

$$H_2S + 3\mathbf{O}^- \rightarrow SO_2 + H_2O + 3\mathbf{e}^- \tag{5}$$

$$2H_2S + 3\mathbf{O}_2^- \rightarrow 2H_2O + 2SO_2 + 6\mathbf{e}^- \tag{6}$$

$$H_2S + 3O^{2-} \rightarrow H_2O + SO_2 + 6\mathbf{e}^- \tag{7}$$

6.1.1 Potential Barrier Model

Conduction mechanism occurring on the sensor surface can be physically explained by Band theory which is one of the most established and widely accepted models. Sensor surface is composed of metal oxide grains which adsorb ambient oxygen leading to creation of depletion layer in their boundaries which are devoid of free charge carriers. However, ample electrons are present in the bulk of the sample. For electrons to flow from one grain to another, they need to cross this insulating barrier present at the grain boundaries. This insulating layer leads to the band bending and forms surface potential barrier which needs to be overcome by the electrons for conduction to take place. This potential barrier is associated with the electric field developed due to positively charged immobile ions in the insulating layer and negatively charged oxygen ions at the surface. This space charge layer is characterized by two parameters, thickness (L_s) and height of surface potential (V_s). This thickness and height of band bending depends on the surface charge. By solving one-dimensional Poisson's equations, V_s is expressed by

$$\boldsymbol{V_s = \frac{2\pi q^2 N_s^2}{\varepsilon N_d}} \tag{8}$$

where ε is dielectric constant, N_d is the concentration of donor impurity, q is the surface state charge and N_s is the concentration of surface charge states.

The space charge layer thickness is given by

$$\boldsymbol{L_s = L_D\sqrt{\frac{eV_s^2}{KT}}} \tag{9}$$

where K is Boltzmann constant, T is the temperature and L_D is the Debye length expressed as

$$\boldsymbol{L_D = \sqrt{\frac{\varepsilon KT}{2\pi e^2 N_d}}} \tag{10}$$

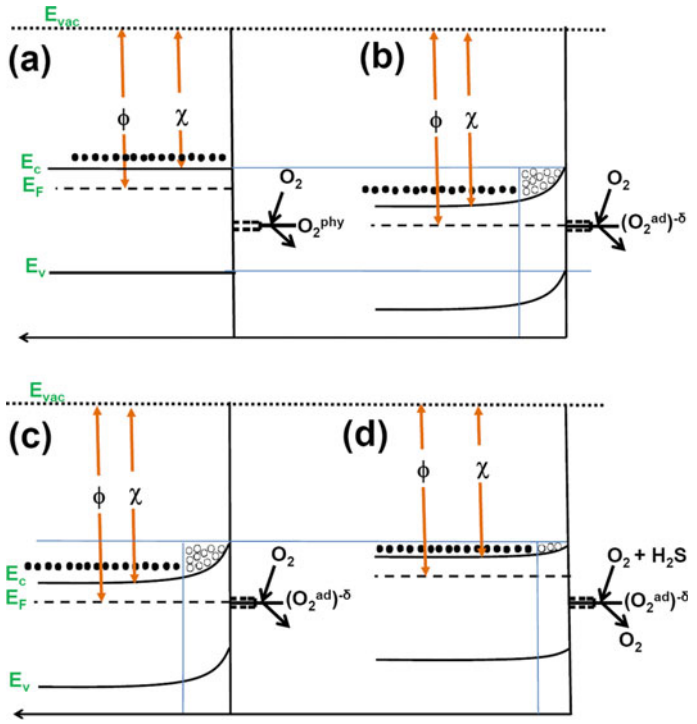

Fig. 9 Schematic representation of the band bending due to oxygen **a** and **b**, and H_2S adsorption in n-type MOS **c** and **d**

The concentration and type of adsorbed oxygen determines the height of potential barrier. Concentration of oxygen adsorbed strongly depends on the sensing temperature and specific surface area of the sensor. On exposure to H_2S, height of band bending, i.e. potential barrier, decreases [84]. Now, the surface layers are again enriched with charged carriers and form a complex interlacing of conduction channel which reduces the resistance of the sensor. Thus, the decrease in barrier height decides the sensor response. Figure 9 shows the band bending due to oxygen adsorption on the sensor surface (a) and (b), and decrease in potential barrier on exposure to H_2S (c) and (d). Here, ϕ and χ stand for work function and electron affinity, respectively, while E_v, E_F, E_c and E_{vac} represent valence band edge, Fermi level, conduction band edge and vacuum level, respectively.

6.1.2 For p-type Semiconductor Films

In addition to oxygen adsorption and desorption, many other processes that significantly contribute to the sensor response are also possible. These processes are strongly dependent on the type of sensing material and the target gas. For example,

CuO, which is a p-type semiconductor, is found to be highly sensitive towards H_2S due to dissociative adsorption. The bond energy of H–SH is merely 381 kJ/mol and is smaller than the other inorganic and most of the organic gases. Hence, H–SH bond can easily be broken [85]. Cu^{2+} cations present in CuO have more favourable kinetics for H_2S dissociation. First, H_2S is decomposed to H–SH and subsequently H–S further breaks into S and H atoms. This sulphur replaces oxygen in CuO forming CuS, as depicted in Eq. 11.

$$CuO + H_2S \rightarrow CuS + H_2O- \tag{11}$$

Due to the formation of CuS, which is metallic in nature, there is a sharp decrease in resistance [86]. Figure 10 shows the band diagram when CuO is exposed to different concentration of H_2S. In air (before exposing to H_2S), the grains of CuO films absorb oxygen from air and form surface states. These surface states created by adsorbed oxygen species (O_2^-) allow electrons to be excited from valence band (VB) and induce holes in p-type CuO grains. When low-concentrated H_2S gas reaches CuO grains, it reacts with O_2^-, and the released electrons recombine with the holes in the VB, and thereby, causing an increase in the film resistance. At high concentration, H_2S reacts with the CuO and forms CuS layers at the surface of CuO grains, which enhances the electrical connectivity between the adjacent CuO grains, and hence, decreases the film resistance.

In spite of innumerable advantages, poor selectivity, sluggish response kinetics and poor stability limit the applications of pristine MOS sensors. To overcome these limitations, different approaches such as surface modification by addition of noble catalytic metal (Pt, Pd, Au, Ni) [87–91] and metal oxides of Cu, Fe and Co [92–94], doping and use of multi-compositional structures have been employed to improve the gas sensing properties.

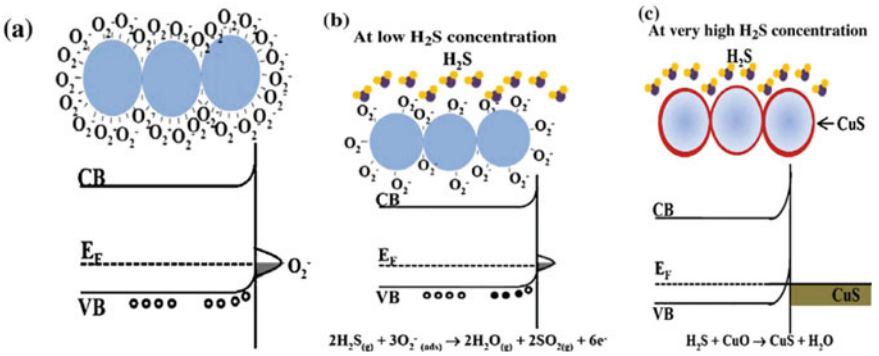

Fig. 10 Schematics and band diagrams showing different stages before **a** and after the CuO films were exposed to H_2S gas of **b** low and **c** high concentrations

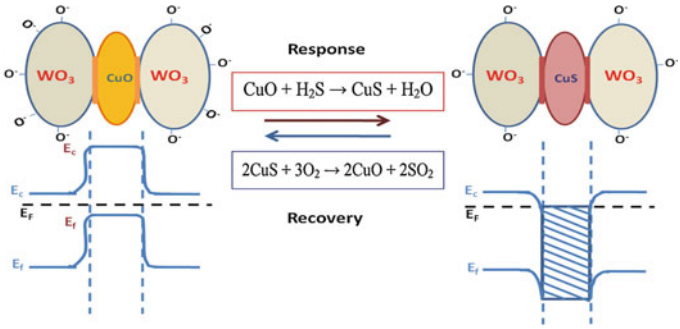

Fig. 11 H_2S sensing mechanism in CuO-modified WO_3 thin films

6.1.3 p–n Heterojunction MOS

Modification of n-type material with other p-type material leads to the formation of random p–n heterojunctions in the sensing material [84, 95–97]. This leads to the enhancement of the sensitivity of the resultant material as compared to their pristine counterparts. For example, Ramgir et al. observed improved sensing results when n-type WO_3 thin films were modified by p-type CuO, thus creating randomly distributed nano p–n junction over the entire surface of the sensor film [98]. Formation of these nano p–n junctions increases the net resistance of the sensor. Due to difference in the fermi level of the two materials, depletion region formed at the interface causes band bending, thus increasing the potential barrier for electron conduction. Also, modification with CuO increases adsorbed oxygen species on the surface. Exposure to H_2S removes surface oxygen species, thus releasing large number of electrons which reduces the resistance of pristine WO_3 and increases the resistance for p-type CuO [99]. But at elevated temperature dominant interaction of H_2S with CuO leads to the formation of CuS, which will transform barrier-like p–n junction between CuO and WO_3 into metal–semiconductor junction between CuS and WO_3. This eventually reduces the potential barrier and facilitates the flow of electron between CuO and WO_3 grains. Figure 11 represents the sensing mechanism of CuO-modified WO_3 films. Sensing mechanism was further corroborated with the observation of changes in work function (φ) of the sensing material measured using Kelvin probe technique. Figure 12 shows the increase in work function of CuO-modified WO_3 film which supports the formation of potential barrier between them. Decrease in work function after H_2S exposure by 0.2 eV supports the formation of metallic CuS.

6.1.4 Noble Metal Decorated MOS

Decoration of MOS by noble metals which are highly effective oxidation catalyst enhances the sensitivity of the material by combining the gas sensitivity of the MOS and the catalytic properties of noble metals (Pt, Au, Pd and Ag) [100–104]. They

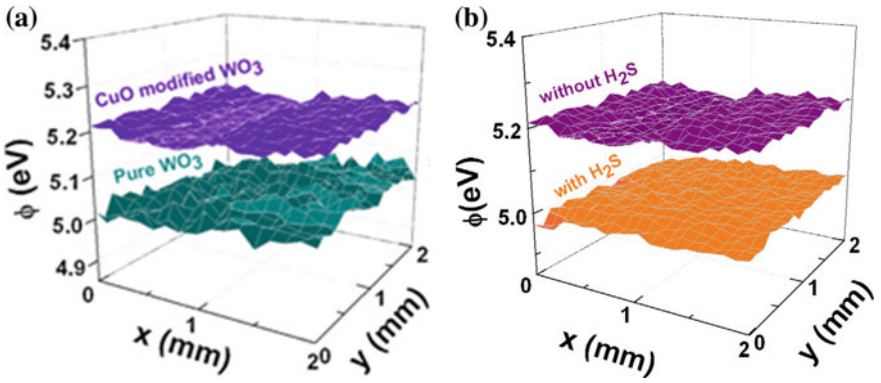

Fig. 12 Work function area map for 2 × 2 mm recorded for **a** pure and CuO-modified WO_3 thin films and **b** change in work function of CuO-modified WO_3 films upon exposure to 50 ppm H_2S

are often anchored as isolated islands on the surfaces of MOS and increase the effective surface area, thereby the sensor response. They also contribute towards the lowering of the operating temperatures for sensing and improvement of the selectivity towards a particular gas and response kinetics of the sensor. These sensitizers enriched the surface with additional absorption sites and catalytic sites for enhanced surface reactions [105]. Effect of incorporation of noble metal on MOS can be conceptualized in two ways. One is based on the electronic variations and other on chemical process.

Electronic Effects

These include formation of nanoSchottky type barrier junction between metal and semiconductor. When ϕ of metal is more than χ of semiconductor, electrons flow from semiconductor to metal creating positively charged depletion region near n-type semiconductor surface and excess of negative charge on metal. The resultant charge separation creates potential barrier at the interface where barrier height depends on the interaction between metal and semiconductor. The created barrier properties can easily be altered by various interactions such as oxygen adsorption and desorption and exposure to target gas at the interface. Modulation of this potential barrier due to various interactions at the interface is responsible for enhanced sensing performances.

Chemical Process

In chemical process, the addition of noble metal increases the concentration of reactants at the surface and lowers the activation energy for the reaction. They catalytically promote the dissociation of molecular oxygen and target molecules and subsequently spill over the reaction products onto metal oxide. This spill over effect accelerates the reaction resulting in higher sensitivities and faster response [106]. For example,

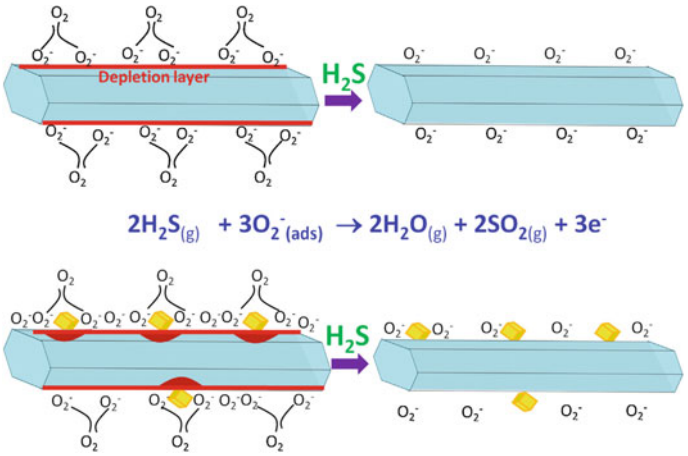

Fig. 13 H_2S sensing mechanism in Au-modified ZnO NWs. Reprinted with permission from N. S. Ramgir et al. Sens. Actuators B 186 (2013) 718–726. Copyright @ Elsevier

modification of ZnO nanowires (NWs) by thin Au layer [90] showed enhanced sensor response towards H_2S due to formation of Schottky barrier type junction between Au and ZnO NWs over the surface. Alteration of barrier properties due to adsorption and desorption of oxygen and target analytes leads to enhanced sensor response. Also catalytic dissociation of oxygen molecules by Au and their migration onto the sensor surface significantly increases the quantity of oxygen ions on the surface, thus creating additional active sites (Fig. 13). Thus, the results inferred the contribution of both electronic and chemical process towards enhanced response and response kinetics of the semiconductor.

In another study by Kolmakov et al., effect of Pd catalyst on SnO_2 NWs and nanobelts (NBs) was investigated [107]. Improved response by adding Pd was attributed to the modulation of the nanoSchottky barriers formed. This variation in barrier height is attributed to the changes in the oxidation state of the Pd and corresponding oxygen adsorption and desorption.

7 Recent Advances in H_2S Gas Sensors: State of the Art

For practical applications, highly sensitive, selective, fast, inexpensive and miniaturized gas sensors with long-term stability is highly desired. This has led to the widespread research for suitable materials and techniques to achieve improved sensing properties. Different techniques employed for H_2S detection as discussed earlier have their own advantages and limitations and are also application specific. Among them, chemiresistive sensors are widely investigated worldwide due to their simple design, compact size, high sensitivity, cost-effectiveness and long-term

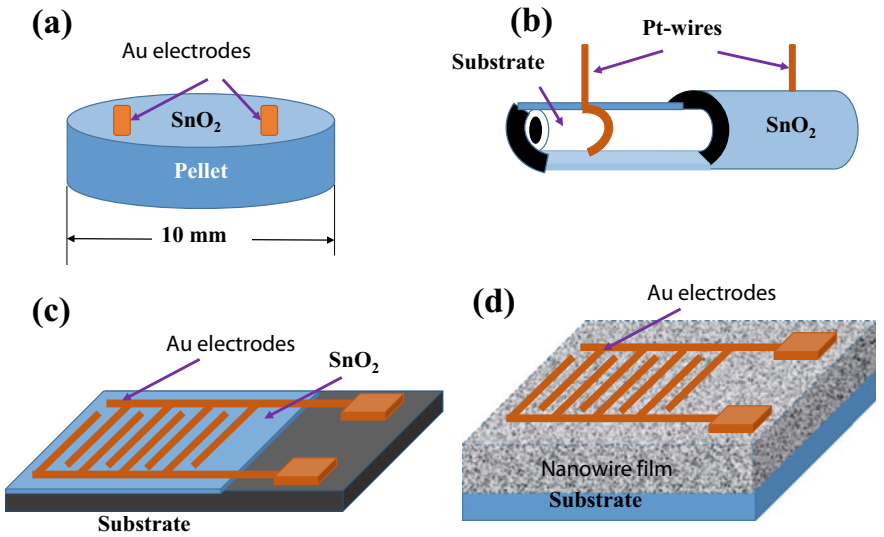

Fig. 14 Different sensing configurations **a** Pellets, **b** Thick films, **c** Thin films and **d** Nanostructures (nanowires)

stable performance. Many inorganic and organic materials are widely exploited by researchers to achieve the best sensing parameters, among which MOS comes out to be the most popular choice as sensing element. Sensing elements of chemiresistive gas sensor have been investigated in different forms, namely (i) sintered pellets, (ii) thick films, (iii) thin films and more recently into (iv) nanostructured form, as shown in Fig. 14.

Recently, materials in nanomorphologies are widely investigated for gas sensing applications due to their high specific surface area compared to conventional microsensors. Low weight, miniaturized integration, tunable surface reactivity, good chemical and thermal stability are some of the advantages of these materials which make them favourable for gas sensing applications. Table 4 shows some examples of H_2S gas sensor based on different materials, morphologies and their synthesis routes along with their sensing parameters. Some of the routes adopted to improve H_2S sensing based on different materials and techniques will be discussed below.

7.1 SnO_2–CuO Based H_2S Sensors

SnO_2, a wide band gap (3.6 eV) n-type semiconductor, is the most popular material investigated for gas sensing. Sensors based on SnO_2 show good sensitivity for many reducing gases and often suffer from the drawback of poor selectivity. Long-term stability is another serious issue as sensitivity degrades over long period of operation. As discussed earlier, selectivity and stability are pivotal criteria that need

Table 4 Different materials for H_2S detection

Material	Synthesis route	Gas (ppm)	Response (R_a/R_g)	T (°C)	t_{res}/t_{rec} (s)	LDL (ppm)	Reference
CuO–MoS_2	Layer-by-layer self-assemble	30	61	RT	26 /18	–	Zhang et al. [108]
CeO_2 NWs	Hydrothermal	50	44	RT	100/260	<1	Li et al. [109]
Ti–ZnO	Chemical spray pyrolysis	30	37	200	5/15	5	Shewale and Yu [110]
ZnO	Carbothermal evaporation	20	2	500	35/390	–	Mortezaali and Moradi [111]
Pillar-shaped ZnO NRs	Spray pyrolysis	100	61.7 (ΔG/Ga)	50	4/60	10	Shinde et al. [112]
MoO_3–RGO hybrid	hydrothermal	40	59	110	9/7	5	Bai et al. [113]
Fe–MoO_3	hydrothermal	100	184.1	270	15/34	10	Ouyang et al. [114]
RGO–SnO_2	Electrospinning	5	34	200	3.3/1.9 min	1	Choi et al. [115]
WO_3 hemitubes/graphene	–	1	5.6	300	12.5/1.6	100 ppb	Choi et al. [116]
Three-dimensional RGO/h-WO_3 composites	hydrothermal	1	10.80	330	7/55	10 ppb	Shi et al. [117]
CuO (10 nm): ZnO NWs	Hydrothermal	10	40	200	6/30 min	5	Datta et al. [118]
Mixed compounds SnO_2–CeO_2	Electrospinning	20	90	210	24/91 s	1	Qin et al. [119]
Flower-like hierarchical ZnO	hydrothermal	10	20	150	–	10	Cao et al. [120]
ZnO nanostructures	Carbothermal	20	80%	300	35/390	–	Mortezaali and Moradi [111]

(continued)

Table 4 (continued)

Material	Synthesis route	Gas (ppm)	Response (R_a/R_g)	T (°C)	t_{res}/t_{rec} (s)	LDL (ppm)	Reference
Nanocrystalline ZnO thin films	Advanced spray pyrolysis	20	0.3 (ΔG/Ga)	300	<13/<24	20	Shewale et al. [121]
Single ZnO NW	Reactive vapour deposition	100	1	RT	–	100	Liao et al. [122]
ZnO NR	Hydrothermal	50	2	300	–	50	Kim and Yong [123]
ZnO microstructures	Solution route	1000 ppb	51	220	123/349	50 ppb	Diao et al. [124]
Pt–Fe_2O_3	Chemical co-precipitation	10	147.5	160	–	10	Wang et al. [125]
Pd–Fe_2O_3	Chemical co-precipitation	10	46.6	160	–	10	Wang et al. [126]
Ag–Fe_2O_3	Chemical co-precipitation	100	220	160	42/26	60	Wang et al. [127]
Au–Fe_2O_3	Electron-beam evaporation and RF sputtering	10	538% ((Gg − Ga)/Ga) × 100	250	1.65/27 min	10	Balouria et al. [128]
Zn_2SnO_4 octahedra	Hydrothermal	100	172.5	170	–	5 ppb	Xu et al. [129]
TiO_2 thin film	Bar coating	200	26.55	300	–	5	Sun et al. [130]
SnO_2 NRs	Solvothermal reaction	50	120	350	7 /9	5	Xu et al. [131]
Au/SWNT	Electrodeposition	20 ppb	0.07%	RT	6–8 /10 min	3 ppb	Mubeen et al. [132]
Fe_2O_3 thin films	Electron-beam evaporation	10	250%	250	64 s/6.5 min	1	Balouria et al. [133]

(continued)

Table 4 (continued)

Material	Synthesis route	Gas (ppm)	Response (R_a/R_g)	T (°C)	t_{res}/t_{rec} (s)	LDL (ppm)	Reference
WO_3 nanoparticles	Advanced Reactive gas deposition	35	3500 Ggas/Gair	RT	Several minutes/several hours	5	Reyes et al. [134]
In-doped ZnO thin films	Spray pyrolysis technique	1000	13,000	250	2 s/4 min	200	Badadhe and Mulla [135]
ZIF-8 particle-loaded ZnO NR hybrid	Self-template method	10	52.1%	RT	7 min/-	50 ppb.	Wu et al. [136]
Colloidal zinc oxide QDs	Colloidal method	50	113.5	RT	16/820	10	Zhang et al. [137]
ZnO QDs	Wet chemical	68.5	567	90	~165/378	–	Deng et al. [138]
ZnO NRs	Two-step solution approach	1	11	RT	500/360	–	Qi et al. [139]
ZnO	Spray pyrolysis	100	110	RT	25/150	25	Mani and Rayappan [140]
ZnO films	CVD	20	80%	300	35/390	–	Mortezaali and Moradi [111]
ZnO NTP with CuO	Carbothermal	20	1.2	250	Few minutes	10	Kaur et al. [141]
Indium-doped ZnO (IZO) thin film	Spray pyrolysis	1000	13,000	250	2 s/4 min	100	Badadhe and Mulla [135]
Cu-doped ZnO nanofibres	electrospinning	10	18.5	230	18/20	1	Zhao et al. [142]
CuO nanoparticle decorated ZnO NR	Hydrothermal	100	40	100	120/-	–	Wang et al. [143]
ZnO–CuO thick film	Liquid phase co-precipitation method	50	20	108	13/5	–	Hu et al. [144]

(continued)

Table 4 (continued)

Material	Synthesis route	Gas (ppm)	Response (R_a/R_g)	T (°C)	t_{res}/t_{rec} (s)	LDL (ppm)	Reference
CuO–ZnO composite hollow spheres	Hydrothermal	5	32.4	336	47/-	1	Kim et al. [145]
ZnO NRs	CVD	5	581	RT	~1000/3700	1	Hosseini et al. [146]
ZnO NWs	Hydrothermal	20	1.15	150	~120/40	50 ppb	Huang et al. [147]
ZnO NR	Solvothermal synthesis	100	122	150	–	–	Meng et al. [148]
ZnO thick film	Chemical route	10	376	200	~30/50	–	Shinde et al. [149]
Cu-doped ZnO powder	RF sputtering	5	65%	250	~25/100	2.5	Girija et al. [150]
WO_3–CuO composites	–	5 ppm	105.2	80	42	–	He et al. [151]

SWNT: single-walled carbon nanotubes, CVD: chemical vapour deposition, NWs: nanowires, NRs: nanorods, NTP: nanotetrapods, QDs: quantum dots, ZIF-8: Zeolitic imidazolate framework-8.

to be satisfied so as to make sensor ready for commercialization. In order to get the desired properties in a sensor or improve the above-mentioned characteristics, different approaches were investigated. For example, Tamaki et al. have investigated the influence of various metal oxide sensitizers on H_2S sensing properties of SnO_2 and found that incorporation of CuO into SnO_2 matrix drastically improves the H_2S sensing properties [92]. Importantly, the sensor was found to be highly selective and almost insensitive to many other gases [152]. The thick film based H_2S sensors were realized using impregnation method, and it showed sensitivity of 3.5×10^4 towards 50 ppm H_2S at 200 °C with response time between 5 and 15 min. Proposed sensing mechanism considers CuO to be dispersed as fine particle on the surface of SnO_2, thus forming p–n junction at each interface. The response time of the sensors comes out to be large enough from application of view. In thick sensing layer, H_2S gas molecules mostly interact with the oxygen in the outer region of the element, and core region remains unexploited. As sensing is a surface phenomenon and the response time is found strongly dependent on the diffusion of gas into the sensor material, hence, most of the research nowadays is based on the use of either thin films or nanostructure-based sensors to achieve better response kinetics. Same group demonstrated a thin film based H_2S sensors for detection of dilute concentrations [94]. With thin film as sensing element, gas diffusion occurs but depends very much on the microstructure of the film. To achieve optimum microstructure, low-pressure evaporation methods were used for preparation of SnO_2 and SnO_2–CuO thin films by simultaneous evaporation of metallic Sn and Cu followed by calcination. After addition of CuO, film exhibits very high sensitivity with the detection limit close to 0.02 ppm at 300 °C.

As discussed above, SnO_2–CuO is noted to be an established material for H_2S sensing, but long-term stability studies revealed drift in sensor characteristics (low sensitivity and slower response) on prolonged exposure to industrial environment. Accordingly, the mechanism of drift in this system was investigated in detail by Katti et al. [153]. In particular, XPS measurements were performed on prolonged H_2S-exposed samples. The XPS study confirms the formation of CuS on H_2S-exposed samples; the moisture-exposed films shows shift in Cu $2P_{3/2}$ peak indicating formation of $Cu(OH)_2$. It was concluded further that the larger response time after prolonged exposure could be attributed to slow reaction rate between H_2S and $Cu(OH)_2$ as shown in reactions below:

$$CuO + H_2O \rightarrow Cu(OH)_2 \tag{12}$$

$$Cu(OH)_2 + H_2S \rightarrow CuS + 2H_2O \tag{13}$$

It further showed that the degraded sensors' performance can easily be rejuvenated by either exposing the sensor to a high H_2S dose or heating at elevated temperatures. Growth kinetics of the sensing film and the nature of dispersal and quantity of the catalyst influence the response characteristics for H_2S gas sensor to a great extent

[154, 155]. An improvement in operating temperature and higher sensor response has been reported when CuO is dispersed as a catalyst either in the form of islands or as continuous layer on the surface of SnO_2 film prepared by sputtering [156, 157]. In another study, porous SnO_2–CuO multilayered structure synthesized using pulsed laser deposition (PLD) technique showed a maximum response of 2.7×10^4 at 140 °C towards 20 ppm H_2S with response time of just 2 s [158].

7.2 Other Metal Oxides for H_2S Sensing

After getting remarkable improvement in sensor response and other parameters using SnO_2–CuO composite, scientists investigated other materials also to look for better response towards H_2S. Cupric oxide (CuO) is a p-type narrow band gap (1.2 eV) semiconductor and exhibits low electrical resistance [159]. It has been intensively studied owing its superior response to H_2S, [160] and formation of heterojunction with other n-type semiconductor materials like ZnO, TiO_2 and Fe_2O_3. Of these, ZnO is another wide band gap (3.37 eV) n-type semiconductor which is extensively investigated for gas sensing applications. It exhibits excellent optical, electrical and piezoelectric properties and are highly stable and biocompatible in nature. ZnO offers the advantages of exhibiting most diverse nanomorphologies such as nanowires, nanaorods, nanofibres and nanobelts. For H_2S sensing, Kaur et al. investigated CuO-functionalized ZnO nanotetrapods (NTPs) synthesized using carbothermal reduction method [141, 161]. Thick films of CuO-modified ZnO NTPs exhibited a sensor response of 17 as compared to 1.5 for pure ZnO towards 50 ppm H_2S at an operating temperature of 50 °C. In a recent research, Fe_2O_3 nanoparticles decorated CuO nanorods (NRs) have shown the potential to detect low concentration of H_2S, especially for the diagnosis of Halitosis [162]. The breath of sufferers of halitosis contains 0.1 to 0.5 ppm of H_2S [163]. In this research, Fe_2O_3 NPs prepared by hydrothermal route were spin coated on CuO NRs synthesized using thermal.

7.3 Metal–Semiconductor H_2S Sensor: Fe as Sensitizer

As explained earlier, addition of metal as sensitizers significantly improves the sensing characteristics. In particular, Cu and Fe have been demonstrated as highly sensitive material for H_2S gas sensing. But CuO has a tendency to form $Cu(OH)_2$ in presence of moisture leading to sluggish response kinetics for H_2S, often causing sensor to enter into sleep mode. Iron oxide on the other hand is a very stable solid solution with SnO_2 and does not have the tendency of going into sleep mode. Ramgir et al. reported the effect of Fe modification on H_2S sensing properties of rheotaxially grown and thermally oxidized (RGTO) SnO_2 thin films [164]. The sensor film with 0.64% of Fe exhibited maximum sensor response of 14.5 towards 10 ppm of H_2S at 225 °C with response and recovery time of 90 and 98 s, respectively. XPS

studies revealed that Fe exists in the form Fe_3O_4 over SnO_2 surface and forms low band gap FeS upon H_2S exposure leading to significant improvement in sensing characteristics.

7.4 Room-Temperature Operating H_2S Sensors

In spite of numerous benefits of MO-based gas sensors such as high sensitivity, easy production and low cost, their high operating temperature (>100 °C) sets a huge limitation for achieving wide industrial applications. High temperature implies high power consumption and requirement of heating element that leads to difficulty in integration and miniaturization. Besides, prolonged high-temperature operation results in thermally induced grain growth which degrades the sensor performances. These limitations have kicked the research in the direction of low temperature preferably room-temperature operating gas sensors. Many researchers are investigating novel materials and techniques for room-temperature operation.

7.4.1 Inorganic–Organic Hybrid Sensors

Nanocomposites or nanohybrids are an excellent class of novel functional materials for sensing applications. Herein, the advantages offered by the individual components are retained, and novel functionalities are introduced which have been exploited for several applications including gas sensing. Recently, graphene and its derivatives such as reduced graphene oxide (rGO) have been widely explored for gas sensing due to their interesting properties like high specific surface area, excellent thermal conductivity, excellent electron transport capabilities and high Young's modulus. Accordingly, nanocomposites of rGO with other materials have been studied for possible gas sensing application. For example, Song et al. demonstrated a high-performance room-temperature gas sensors based on SnO_2 quantum wire—rGO nanocomposites [165]. Here, one-step colloidal synthesis technique was used to control the quantum confinement of SnO_2 by tuning the reaction time due to steric hindrance effect of rGO. Sensor developed with 8 h reaction time exhibited highly sensitive and selective response of around 33 in just 2 s towards 50 ppm H_2S at room temperature with full recovery. Here, SnO_2 quantum wire provides enhanced surface area for gas adsorption, while rGO served as electron acceptors from SnO_2 quantum wires.

In another study, flexible gold (Au)–cobalt phthalocyanine (CoPc) heterojunction thin films exhibited excellent room-temperature H_2S detection capability [166]. CoPc films were deposited on flexible BOPET substrate using molecular beam epitaxy (MBE) at substrate temperature of 100 °C. A portion of CoPc film is modified by a thin Au layer (1 nm) at room temperature. Enhanced response of Au–CoPc is attributed primarily to the formation of hole accumulation layer in CoPc due to Au and secondly to the role of Au as catalyst for the dissociation of oxygen molecules by

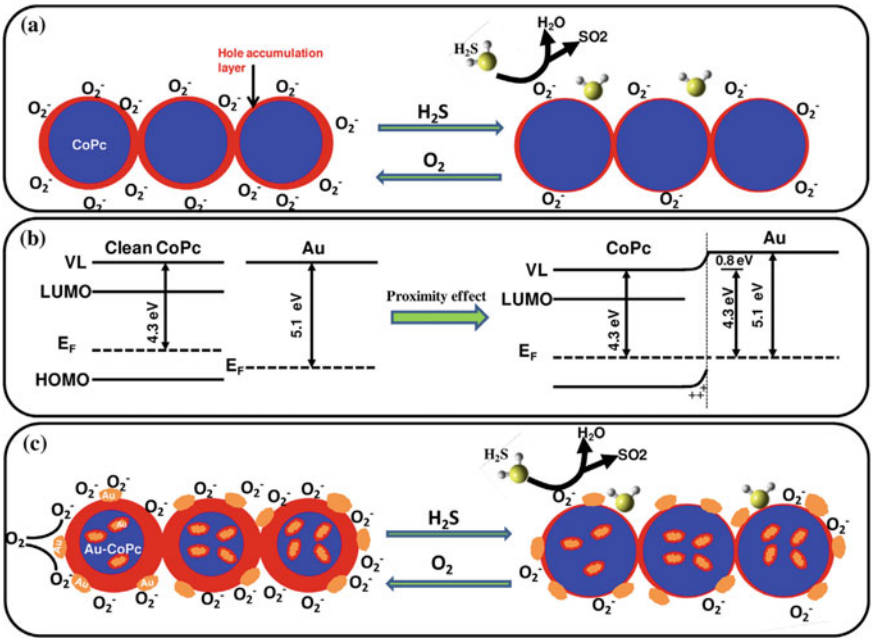

Fig. 15 Schematic diagram showing H_2S sensing mechanism for **a** pure CoPc film **b** energy band diagram for CoPc and Au as individual and in close proximity and **c** Au–CoPc. Reprinted with permission from A. Kumar et al., Sens. Actuators B 206, 653 (2015). Copyright @ Elsevier

spill over effect onto the sensor surface as shown schematically in Fig. 15. Both the effects increase the hole density in Au–CoPc which enhances response in presence of H_2S whose reducing nature decreases the width of accumulation region. Being flexible in nature, authors also studied the sensing characteristics at different bending radii and found it to be stable for bending radius >20 mm.

7.4.2 Organic–Organic Hybrid Gas Sensor

Recently, demands for flexible sensors are growing rapidly both for personal and industrial applications. In one report, flexible H_2S gas sensor based on polyaniline–polyethylene oxide (PAni–PEO) nanofibres doped by camphorsulfonic acid (HCSA) was presented [167]. Here, PEO acts as binder in solution to increase the solution viscosity and helps in the formation of continuous nanofibres web. Nanofibres were directly written on the paper and polyimide substrates by electrospinning method. Sensor showed around 5, 13.5 and 25% response towards 1, 5 and 10 ppm H_2S, respectively, with average response and recovery time of 120 and 250 s, respectively, at room temperature. Formation of high quality nanofibres web on the electrode provides high surface area to volume ratio facilitating fast adsorption and desorption of H_2S. Sensor was found to be highly selective and showed good stability over time.

Also, almost identical response after 1000 bending cycles were obtained, thereby emphasizing the high flexibility and robustness of sensor for wearable applications.

8 Effect of Morphology on H_2S Sensing

In recent years, gas sensors based on nanostructures have attracted much attention due to their various advantageous features such as large surface area to volume ratio, high crystallinity, high integration density, low power consumption and tunable surface reactivity. Also, for nanostructures, Debye length is comparable to size and hence superior sensitivity to chemical surface process is obtained. With the upsurge in nanoscience and nanotechnology, materials have been synthesized into numerous novel nanomorphologies such as nanoparticles, nanorods, nanobelts and nanoflowers. Control over morphology implies control over surface interactions, thereby tunable sensor characteristics. Few such results of different nanoforms are discussed below.

8.1 Nanoparticles

This is the simplest form of nanomaterials. The reduction in the size of the material has been demonstrated to result in improved response characteristics attributed to the increased surface area to volume ratio. The sensor response was found to increase exponentially when the size of the material falls below 25 nm. At this low-dimensional scale, the number of atoms residing on the sensor surface is larger than that in the bulk and hence implies more interaction with the target gases and more sensitivity. For example, Ag-doped αFe_2O_3 nanoparticles exhibited high sensitivity and selectivity towards H_2S at 160 °C [127]. More number of active reaction sites made available due to nanodimensions has resulted in enhanced response characteristics.

Recently, perovskite oxides emerged as an important group of gas sensing materials owing to their great sensitivity and stability in harsh environments and outstanding affordability of high doping concentration, high temperature and corrosivity. For instance, $BaTiO_3$ thick film sensors were found to be highly sensitive and selective for H_2S gas but only towards higher concentration (100 ppm) [168]. As base resistance of developed sensor is very high which is not ideal for gas sensing, nanostructures of perovskite were explored for improved results. Huang et al. investigated effect of αFe_2O_3 on sensing properties of Ce-doped $BaTiO_3$ ($Ba_{0.99}Ce_{0.01}TiO_3$) nanoparticles (30-60 nm) prepared by co-precipitation method [169]. A highly sensitive sensor towards low concentration of H_2S (400 ppb) giving response of 2.91 at 150 °C with very fast response and recovery ($T_{res} = 45$ s and $T_{rec} = 124$ s) was obtained. The enhanced sensing performance was mainly attributed to the catalytic effect of αFe_2O_3 distributed on the surface of $Ba_{0.99}Ce_{0.01}TiO_3$.

8.2 Nanoflowers

Vertically aligned ZnO rods with flower-like morphology exhibited a very high response and selectivity towards H_2S [146]. Authors used simple carbothermal reduction and vapour phase transport (CTR-VPT) method to produce high quality nanostructures. The prepared samples exhibited good crystallinity with preferential *c*-axis orientation and considerable quantity of oxygen vacancies. Large number of vacancies leads to enhanced oxygen adsorption which increases the probability of interaction with the target gas molecules at the surface. Sensor exhibits very high response of 296 at 1 ppm with excellent selectivity at room temperature. Presence of considerable concentration of oxygen vacancies, large effective surface area of the nanostructures and presence of interface layer are responsible for such high performance of the sensor.

8.3 Nanowire

To probe one-dimensional nanostructures of CuO for gas sensing applications at room temperature, CuO nanowires were synthesized by thermal oxidation of copper foil at 675 °C. Kaur et al. investigated NWs in three different configurations, namely isolated NW aligned between two electrodes, grown CuO flakes consisting of vertical NW and CuO NW thin films [170]. Among them, isolated NW showed high sensitivity (200%) with fast response (30 s) and recovery (60 s) at room temperature. CuO flakes showed very slow recovery at lower concentration and incomplete recovery at higher concentrations. Although p-type in nature, isolated NWs after a slight increase show decrease in resistance on exposure to H_2S. Authors suggested that formation of CuS which is metallic in nature might be the reason for decrease in resistance. For CuO NW thin film also, recovery was found to be very slow.

8.4 Nanosized Core Shell Structures

As already discussed, p–n junction between n-type SnO_2 and p-type CuO has been reported to be highly sensitive towards H_2S. Xue et al. reported one-dimensional nanosized core/shell p–n junctions formed between n-type SnO_2 nanorods coated with p-type CuO nanoparticles [171]. TEM studies shows that p–n junctions are uniformly distributed along the length of nanorods with average diameter of CuO nanoparticles around 4 nm. Sensor showed highest sensitivity (9.4×10^6) towards 10 ppm of H_2S at 60 °C. Enhanced response was attributed to the small size effect of nanostructures, and the conversion of CuO–SnO_2 p–n junction to CuS–SnO_2 ohmic contact. More precisely, exposure to H_2S leads to the formation of metal–semiconductor junction, thus reducing the overall sensor resistance.

9 Summary and Future Scope

H_2S, although less ubiquitous, has been identified as one of the major contaminants having severe pernicious effect on our ecosystem and mankind. Due to its toxic effects and wide occurrence in various natural and man-made settings, it has often been targeted as one of the key pollutant gases for regulation. The present chapter discussed the various repercussions of H_2S that has led researchers globally to investigate accurate tools for its quantification under real situations. Different possible techniques like chromatography, colorimetry, electrochemical, chemiresistive, optical and mass-sensitive sensors were explored for real-time monitoring and leakage detection. For commercial applications, sensors should satisfy the '4-S criteria' possessing high sensitivity, selectivity, stability and suitability. Every sensing technique has its own advantage and limitation. This chapter is focussed on chemiresistive sensors which are most popular and widely investigated due to their high sensitivity, low cost, low power consumption, wide detection ranges, possibility of miniaturization and long-term stability. Metal oxides such as SnO_2, ZnO and WO_3 are the most popular choice for detection of hazardous gases. In pristine form, selectivity and long-term stability limit their practical applications. Hence, they are often modified with other metal oxides, noble metals, organic materials and multi-compositional structures to achieve improved sensor response. Formation of heterojunction between different MOS has demonstrated a great potential for achieving superior H_2S sensing properties. CuO and Fe_2O_3 are highly noted semiconductors for H_2S detection due to their catalytic effect as well as formation of sulphides on exposure to H_2S. Organic materials have also been reported for H_2S detection. They offer advantage of low-temperature sensing but contain drawbacks of poor long-term stability and sensitivity. Nanomorphologies such as NP, NW, NF, NRs, etc. are emerging as promising candidates for high-performance H_2S gas sensors. They offer very high surface area for oxygen and H_2S adsorption, thus increasing the number of active sites on surface leading to improved response characteristics. Materials with porous structures are another popular choice for sensing as they offer high surface area for adsorption, and enhanced diffusion due to porosities allows utilization of bulk sites as well. Many studies have reported the H_2S sensitivity of ternary and quaternary oxides, such as ferrite and perovskite materials. Unfortunately, these compounds in comparison to classical MOS offers much lower response. These materials need to be thoroughly investigated to enhance their sensing performance. In spite of their wide popularity, classical sensors still deals with some drawbacks, among which high operating temperature is one which limits their applications in potentially hazardous situations. Also high temperature leads to difficulty in integration and miniaturization for industrial applications. Nanoscience and technology provides numerous opportunities to develop next generation gas sensors with enhanced performances. Recently, different materials in nanodimensions are widely exploited, where size and morphology of the material greatly influence its thermodynamic and kinetic behaviour. Room-temperature operated sensors simplify the sensor design, gaining practical flexibility to realize cost-effective and miniaturized devices. Importantly,

these sensors have numerous applications for societal benefits, especially for medical applications where flexible wearable devices are needed for real-time medical diagnosis. Wearable sensors are future for personal as well as industrial monitoring of H_2S and other toxic gases hazardous to human health. Future research in this field demands more sensitive, robust and stable sensors that can operate consistently in harsh environmental conditions. With further advances in the field of nanoscience and nanotechnology, more sensitive, selective, stable and suitable MOS-based H_2S gas sensors with potential for commercial deployment are expected in the near future.

References

1. https://www.ncbi.nlm.nih.gov/books/NBK368029/
2. https://www.eea.europa.eu/themes/air/air-pollution-sources
3. X. Xu, Y. Chen, Int. J. Environ. Stud. **73**(3), 422 (2016)
4. K.B. Ince, Z. Cetecioglu, O. Ince, Pollution prevention in the pulp and paper industries. Environmental Management in Practice (2011)
5. S. Dudka, D.C. Adriano, J. Environ. Quality **26**(3), 590 (1997)
6. M.F. Hamoda J. Environ. Sci. Health, Part A, **41**(1), 77 (2006)
7. *WHO Handbook on Indoor Radon: A Public Health Perspective* (World Health Organization, Geneva, 2009)
8. A. Ghorani-Azam, Z. BamdadRiahi, M. Balal-Mood, J. Res. Med. Sci. **21**, 65 (2016)
9. S.S. Yamamoto, R. Phalkey, A.A. Malik, Inter. J. Hyg. Environ. Health **217**(2–3), 133 (2014)
10. V. Sass, N. Kravitz-Wirtz, S.M. Karceski, A. Hajat, K. Crowder, D. Takeuchi, Health Place **48**, 72 (2017)
11. L. Calderón-Garcidueñas, A. Mora-Tiscareño, E. Ontiveros, G. Gómez-Garza, G. Barragán-Mejía, J. Broadway, S. Chapman, G. Valencia-Salazar, V. Jewells, R.R. Maronpot, C. Henríquez-Roldán, B. Pérez-Guillé, R. Torres-Jardón, L. Herrit, D. Brooks, N. Osnaya-Brizuela, M.E. Monroy, A. González-Maciel, R. Reynoso-Robles, R. Villarreal-Calderon, A.C. Solt, R.W. Engle, Brain Cogin. **68**(2), 117 (2008)
12. L. Calderón-Garcidueñas, A.C. Solt, C. Henríquez-Roldán, R. Torres-Jardón, B. Nuse, L. Herritt, R. Villarreal-Calderón, N. Osnaya, I. Stone, R. García, D.M. Brooks, A. González-Maciel, R. Reynoso-Robles, R. Delgado-Chávez, W. Reed, Toxicol. Pathol. **36**(2), 289 (2008)
13. L. Attademo, F. Bernardini, R. Garinella, M.T. Compton, Schizophrenia Res. **181**, 55 (2017)
14. Y.-C. Chang, R. Daza, R. Hevner, L.G. Costa, T.B. Cole, Brain, Behav. Immun. **78**, 105 (2019)
15. A.L. Roberts, K. Lyall, J.E. Hart, F. Laden, A.C. Just, J.F. Bobb, K.C. Koenen, A. Ascherio, M.G. Weisskopf, Environ. Health Perspect. **121**, 978 (2013)
16. H.E. Volk, F. Lurmann, B. Penfold, I. Hertz-Picciotto, R. McConnell, JAMA Psychiatry **70**, 71 (2013)
17. H.S. Lee, C.G. Lee, D.H. Kim, H.S. Song, M.S. Jung, J.Y. Kim, C.H. Park, S.C. Ahn, S.D. Yu, Ann. Occup. Environ. Med. **28**(1), 17 (2016)
18. J. Sunyer, D. Jarvis, T. Gotschi, R. Garcia-Esteban, B. Jacquemin, I. Aguilera, N. Kunzli, Ann. Occup. Environ. Med. **63**(12), 836 (2006)
19. W. Zhang, C.N. Qian, Y.X. Zeng, Chin J. Cancer **33**, 173 (2014)
20. A.J. Cohen, Thorax **58**(12), 1010 (2003)
21. S.P. Eckel, M. Cockburn, Y.-H. Shu, H. Deng, F.W. Lurmann, L. Liu, F.D. Gilliland, Thorax **71**(10), 891 (2016)
22. https://nepis.epa.gov/Exe/ZyPURL.cgi?Dockey=9100805J.TXT
23. https://www.americanscientist.org/article/a-short-history-of-hydrogen-sulfide

24. C.W. Scheele, ChemischeAbhandlung von der Luft und demFeuer (Chemical treatise on air and fire) (Upsala, Magnus Swederus, Sweden, 1777), § 97: Die stinckendeSchwefelLuft (The stinking sulfur air [i.e., gas]), pp. 149–155
25. A. Mukhopadhyay, A. Al-Haddad, M. Al-Otaibi, M. Al-Senafy, Environ. Geo. **52**(6), 1151 (2006)
26. B.M. Juliusson, I. Gunnarsson, K.V. Matthiasdottir, S.H. Markusson, B. Bjarnason, O. Sveinsson, T. Gislason, H. H. Thorsteinsson, Tackling the challenge of H_2S emissions, Reykjavik Energy, Baejarhalsi 1, 110 Reykjavik, Iceland, in *Proceedings World Geothermal Congress 2015* (Melbourne, Australia, 19–25 April 2015)
27. A. Bassani, D. Previtali, C. Pirola, G. Bozzanoa, I.S. Nadezhdin, A.G. Goryunov, F. Manentia, P.D. Milano, H_2S in geothermal power plants: from waste to additional resource for energy and environment. The Italian Association of Chemical Engineering
28. S. D'Imperio, C.R. Lehr, H. Oduro, G. Druschel, M. Kuhl, T.R. McDermott, Appl. Environ. Microbio. **74**(18), 5802 (2008)
29. JPAFMAT 2008; 8(1). ISSN 0972-5687
30. G. Muyzer, A.J.M. Stams, Nat. Rev. Microbio. **6**(6), 441 (2008)
31. E.-D. Schulze, H.A. Mooney, *Biodiversity and Ecosystem Function* (Springer, 1993), pp. 88–90. ISBN 9783540581031
32. L. Zhang, P. De Schryver, B. De Gusseme, W. De Muynck, N. Boon, W. Verstraete, Water Res. **42**, 1 (2008)
33. C. Oppenheimer, B. Scaillet, R.S. Martin, Mineralogical Soc. **73**, 363 (2011)
34. T.L.C. de Souza, JAPCA **38**, 792 (1988)
35. M. Baharvand, Z. Maleki, S. Mohammadi, K. Alavi, E. Moghaddam, J. Contemp. Dent. Pract. **9**, 76 (2008)
36. A.C. Donaldson, M. Riggio, H. Rolph, J. Bagg, P. Hodge, Oral Dis. **13**, 63 (2007)
37. Hydrogen Sulfide, Geneva, World Health Organization, 1981 (Environmental Health Criteria, No. 19)
38. J. Kangas, P. Jappinen, H. Savolainen, Am. Ind. Hyg. Asso. J. **45**(12), 787 (1984)
39. T. Higashi, T. Toyama, H. Sakurai, M. Nakaza, K. Omae, T. Nakadate, N. Yamaguchi, Ind. Health **21**(4), 281 (1983)
40. J. Lindenmann, V. Matzi, N. Neuboeck, B. Ratzenhofer-Komenda, A. Maier, F.M. Smolle-Juettner, Diving Hyperbaric Med. **40**(4), 213 (2010)
41. W. Rumbeiha, E. Whitley, P. Anantharam, D.-S. Kim, A. Kanthasamy, Ann. New York Aca. Sci. **1378**(1), 5 (2016)
42. M. Matsuo, J.W. Cummins, R.E. Anderson, Arch. Neurol. **36**, 451 (1979)
43. H. Savolainen, Nordiskaexpertgruppen f6r gransvardesdokumentation. 40. Dihydrogensulfid [Nordic expert group for TLV evaluation. 40. Hydrogen sulfide], Arbetaochhdlsa, **31**, 1 (1982)
44. C.H. Foulkes, *Gas! The Story of the Special Brigade* (Naval Military, 2001), p. 105. ISBN 978-1-84342-088-0
45. H. Swindle, The deadly smell of success. Texas Monthly, June 1975. Accessed 14 Dec 2010
46. "LA County Department of Public Health" (PDF). County of Los Angeles: Department of Public Health
47. H. Becerra, D. Pierson, (2005-09-03). "Gas Kills 3 Crewmen on Ship". Los Angeles Times
48. "Do not breathe: Dangerous, toxic gas found at Siam Square One". *Coconuts Bangkok*. Coconuts Media. 2014-10-21. Accessed 20 Nov 2014
49. C. Rabin, D. Goodhue, (16 January 2017). "Three Keys utility workers die in wastewater trench". Miami Herald. Accessed 28 Apr 2017
50. "One by one, 3 utility workers descended into a manhole. One by one, they died". www.washingtonpost.com
51. B. Dai, C. Jones, M. Pearl, M. Pelletier, M. Myrick, Sensors, **18**(7), 2006 (2018)
52. H. Elshahawi, M.N. Hashem, Accurate measurement of the hydrogen sulfide content in formation fluid samples-case studies, in *SPE Annual Technical Conference and Exhibition, 9–12 October* (Dallas, Texas, 2005). Document ID SPE-94707-MS
53. https://www.azom.com/article.aspx?ArticleID=14087

54. S.B. Reddy, (2016, July 25). Pulsed Fluorescence SO_2, H_2S, CS Analyzer Working Principle. Retrieved December 30, 2016, from Instrumentation Tools website
55. Interscan Corporation. Detector Tubes and When to Use Them. Retrieved 29 Dec 2016, from Interscan Corporation website
56. RAE Systems, *Gas Detection Tubes and Sampling Handbook*. Retrieved 29 Dec 2016, from RAE Systems website
57. R.M. Bethea Comparison of hydrogen sulfide analysis techniques, J. Air Pollut. Control Asso. **23**, 710 (1973)
58. P.J. Moore, R.W. Spitler, Hydrogen sulfide measurement and detection, in *Thermo Electron Corporation, 2003 Proceedings American School Of Gas Measurement Technology*
59. J.-H. Cha, D.-H. Kim, S.-J. Choi, W.-T. Koo, I.-D. Kim, Anal. Chem. **90**(15), 8769 (2018)
60. https://pdfs.semanticscholar.org/6edc/acbc5f18890daa9f23e16223185ad1ca507e.pdf
61. V. Vitvitsky, R. Banerjee, Meth. Enzymology **554**, 111 (2015)
62. H.J. Rath, J. Wimmer, Chromatographia **13**(8), 513 (1980)
63. H.J. Cortes, B. Winniford, J. Luong, M. Pursch, J. Sep. Sci. **32**, 883 (2009)
64. W. Xiao, P.J. Oefner, Hum. Mutat. **17**, 439 (2001)
65. P.R. Haddad, P.N. Nesterenko, W. Buchberger, J. Chromatogr. A **1184**(1), 456 (2008)
66. A. Mirzaei, S.G. Leonardi, G. Neri, Ceram. Int. **42**, 15119 (2016)
67. S.K. Pandey, K.-H. Kim, Environ. Sci. Technol. **43**, 3020 (2009)
68. A.V. Kroll, V. Smorchkov, A.Y. Nazarenko, Sens. Actuators, B **21**(2), 97 (1994)
69. M. Khan, M. Rao, Q. Li, Sensors **19**(4), 905 (2019)
70. U. Guth, W. Vonau, J. Zosel, Meas. Sci. Tech. **20**(4), 042002 (2009)
71. I. Cretescu, D. Lutic, L.R. Manea, Electrochem. Sensors Tech. (2017). https://doi.org/10.5772/intechopen.68512
72. D. Antuña-Jiménez, G. Díaz-Díaz, M. C. Blanco-López, M.J. Lobo-Castañón, A.J. Miranda-Ordieres, P. Tuñón-Blanco, Molecularly imprinted electrochemical sensors; past, present and future, in *Molecul. Imprinted Sensors: Overview and Applications*, ed. by S. Li. S.A. Piletsky, J. Lunec (Elsevier, Oxford, 2012), p. 1
73. G. Schiavon, G. Zotti, R. Toniolo, G. Bontempelli, Anal. Chem. **67**(2), 318 (1995)
74. C. Yu, Sens. Actuators, B **86**(2–3), 259 (2002)
75. M. Wu, G.Z. Xie, Y. Zhou, H.L. Tai, Appl. Mech. Mat. **651–653**, 191 (2014)
76. W. Luo, Q. Fu, D. Zhou, J. Deng, H. Liu, G. Yan, Sens. Actuators, B **176**, 746 (2013)
77. X. Wang, W. Wang, H. Li, C. Fu, Y. Ke, S. He, Sens. Actuators, B **169**, 10 (2012)
78. E. Della Gaspera, M. Guglielmi, S. Agnoli, G. Granozzi, M.L. Post, V. Bello, G. Mattei, A. Martucci, Chem. Mater. **22**(11), 3407 (2010)
79. S.P. Usha, S.K. Mishra, B.D. Gupta, Sens. Actuators, B **218**, 196 (2015)
80. R. Tabassum, S.K. Mishra, B.D. Gupta, Phys. Chem. Chem. Phys. **15**(28), 11868 (2013)
81. D.K. Aswal, S.K. Gupta (Eds.), *Science and Technology of Chemiresistive Gas Sensors* (Nova Science Publisher, NY, USA, 2007). ISBN-13: 978-1-60021-514-8
82. V.E. Bochenkov, G.B. Sergee, Laboratory of low temperature chemistry, sensitivity, selectivity, and stability of gas-sensitive metal-oxide nanostructures. Department of Chemistry, M.V. Lomonosov Moscow State University, Moscow 119991, Russia
83. N. Taguchi, Gas detecting devices. U.S. Patent 3,631,436, 28 December 1971
84. N. Datta, N.S. Ramgir, S. Kumar, P. Veerender, M. Kaur, S. Kailasaganapathi, A.K. Debnath, D.K. Aswal, S.K. Gupta, Sens. Actuators, B **202**, 1270 (2014)
85. C. Wang, X. Chu, M. Wu, Sens. Actuators, B **113**, 320 (2006)
86. N.S. Ramgir, S.K. Ganapathi, M. Kaur, N. Datta, K.P. Muthe, D.K. Aswal, S.K. Gupta, Sens. Actuators, B **151**(1), 90 (2010)
87. X.-Y. Xue, Z.-H. Chen, L.-L. Xing, C.-H. Ma, Y.-J. Chen, T.-H. Wang, J. Phys. Chem. C **114**(43), 18607 (2010)
88. X. Xue, Z. Chen, C. Ma, L. Xing, Y. Chen, Y. Wang, T. Wang, J. Phys. Chem. C **114**(9), 3968 (2010)
89. Z. Bai, C. Xie, M. Hu, S. Zhang, Physica E **41**(2), 235 (2008)

90. N.S. Ramgir, P.K. Sharma, N. Datta, M. Kaur, A.K. Debnath, D.K. Aswal, S.K. Gupta, Sens. Actuators, B **186**, 718 (2013)
91. C. Jin, T. Yamazaki, K. Ito, T. Kikuta, N. Nakatani, Vacuum **80**(7), 723 (2006)
92. J. Tamaki, T. Maekawa, N. Miura, N. Yamazoe, Sens. Actuators B **9**(3), 197 (1992)
93. J. Liu, X. Huang, G. Ye, W. Liu, Z. Jiao, W. Chao, Z. Zhou, Z. Yu, Sensors **3**(5), 110 (2003)
94. J. Tamaki, K. Shimanoe, Y. Yamada, Y. Yamamoto, N. Miura, N. Yamazoe, Sens. Actuators B **49**(1–2), 121 (1998)
95. N. Datta, N.S. Ramgir, M. Kaur, S. KailasaGanapathi, A.K. Debnath, D.K. Aswal, S.K. Gupta, Sens. Actuators, B **166–167**, 394 (2012)
96. I. Giebelhaus, E. Varechkina, T. Fischer, M. Rumyantseva, V. Ivanov, A. Gaskov, S.J. Mathur, Mater. Chem. A **1**(37), 11261 (2013)
97. F. Shao, M.W.G. Hoffmann, J.D. Prades, R. Zamani, J. Arbiol, J.R. Morante, E. Varechkina, M. Rumyantseva, A. Gaskov, I. Giebelhaus, T. Fischer, S. Mathur, F. Hernández-Ramírez, Sens. Actuators B **181**, 130 (2013)
98. N.S. Ramgir, C.P. Goyal, P.K. Sharma, U.K. Goutam, S. Bhattacharya, N. Datta, M. Kaur, S. Kailasaganapathi, A.K. Debnath, D.K. Aswal, S.K. Gupta, Sens. Actuators B **188**, 525 (2013)
99. E.P.S. Barrett, G.C. Georgiades, P.A. Sermon, Sens. Actuators, B **1**(1–6), 116 (1990)
100. Y. Lu, J. Li, J. Han, H.-T. Ng, C. Binder, C. Partridge, M. Meyyappan, Chem. Phys. Lett. **391**, 344 (2004)
101. D. Wang, Z. Ma, S. Dai, J. Liu, Z. Nie, M.H. Engelhard, Q. Huo, C. Wang, R. Kou, J. Phys. Chem. C **112**, 13499 (2008)
102. D. Haridas, K. Sreenivas, V. Gupta, Sens. Actuators, B **133**, 270 (2008)
103. A.M. Ruiz, A. Cornet, K. Shimanoe, J.R. Morante, N. Yamazoe, Sens. Actuators, B **108**, 34 (2005)
104. C.R. Henry, C. Chapon, C. Duriez, J. Chem. Phys. **95**, 700 (1991)
105. N. Barsan, M. Schweizer-Berberich, W. Göpel, Anal. Chem. **365**(4), 287 (1999)
106. C. Li, L. Li, Z. Du, H. Yu, Y. Xiang, Y. Li, Y. Cai, T. Wang, Nanotechnology **19**(3), 035501 (2007)
107. A. Kolmakov, D.O. Klenov, Y. Lilach, S. Stemmer, M. Moskovits, Nano Lett. **5**(4), 667 (2005)
108. D. Zhang, J. Wu, Y. Cao, Sens. Actuators B **287**, 346–355 (2019)
109. Z. Li, X. Niu, Z. Lin, N. Wang, H. Shen, W. Liu, K. Sun, Y.Q. Fu, Z. Wang, J. Alloys Comp. **682**, 647 (2016)
110. P.S. Shewale, Y.S. Yu, J. Alloys Comp. **684**, 428 (2016)
111. A. Mortezaali, R. Moradi, Sens. Actuators, A **206**, 30 (2014)
112. S.D. Shinde, G.E. Patil, D.D. Kajale, V.B. Gaikwad, G.H. Jain, J. Alloys Comp. **528**, 109 (2012)
113. S. Bai, C. Chen, R. Luo, A. Chen, D. Li, Sens. Actuators, B **216**, 113 (2015)
114. Q.-Y. Ouyang, L. Li, Q.-S. Wang, Y. Zhang, T.-S. Wang, F.-N. Meng, Y.-J. Chen, P. Gao, Sens. Actuators, B **169**, 17 (2012)
115. S.-J. Choi, B.-H. Jang, S.-J. Lee, B.K. Min, A. Rothschild, I.-D. Kim, A.C.S. Appl, Mater. Interfaces **6**(4), 2588 (2014)
116. S.-J. Choi, F. Fuchs, R. Demadrille, B. Grévin, B.-H. Jang, S.-J. Lee, J.-H. Lee, H.L. Tuller, I.I.-D. Kim, A.C.S. Appl, Mater. Interfaces **6**(12), 9061 (2014)
117. J. Shi, Z. Cheng, L. Gao, Y. Zhang, J. Xu, H. Zhao, Sens. Actuators, B **230**, 736 (2016)
118. N. Datta, N. Ramgir, M. Kaur, S. Kailasa Ganapathi, A.K. Debnath, D.K. Aswal, S.K. Gupta, Sens. Actuators B **166–167**, 394 (2012)
119. W. Qin, L. Xu, J. Song, R. Xing, H. Song, Sens. Actuators, B **185**, 231 (2013)
120. Y. Cao, X. Hu, D. Wang, Y. Sun, P. Sun, J. Zheng, J. Ma, G. Lu, Mater. Lett. **69**, 45 (2012)
121. P.S. Shewale, G.L. Agawane, S.W. Shin, A.V. Moholkar, J.Y. Lee, J.H. Kim, M.D. Uplane, Sens. Actuators, B **177**, 695 (2013)
122. L. Liao, H.B. Lu, J.C. Li, C. Liu, D.J. Fu, Y.L. Liu, Appl. Phys. Lett. **91**(17), 173110 (2007)
123. J. Kim, K. Yong, J. Phys. Chem. C **115**(15), 7218 (2011)
124. K. Diao, M. Zhou, J. Zhang, Y. Tang, S. Wang, X. Cui, Sens. Actuators, B **219**, 30 (2015)

125. Y. Wang, S. Wang, Y. Zhao, B. Zhu, F. Kong, D. Wang, S. Wu, W. Huang, S. Zhang, Sens. Actuators, B **125**(1), 79 (2007)
126. Y. Wang, F. Kong, B. Zhu, S. Wang, S. Wu, W. Huang, Mater. Sci. Eng., B **140**(1–2), 98 (2007)
127. Y. Wang, Y. Wang, J. Cao, F. Kong, H. Xia, J. Zhang, B. Zhu, S. Wang, S. Wu, Sens. Actuators B **131**(1), 183 (2008)
128. V. Balouria, N.S. Ramgir, A. Singh, A.K. Debnath, A. Mahajan, R.K. Bedi, D.K. Aswal, S.K. Gupta, Sens. Actuators, B **219**, 125 (2015)
129. T.-T. Xu, X.-F. Zhang, Z.-P. Deng, L.-H. Huo, S. Gao, Polyhedron **151**, 510 (2018)
130. G.-J. Sun, H. Kheel, J.K. Lee, S. Choi, S. Lee, C. Lee, Surf. Coatings Tech. **307**, 1088 (2016)
131. J. Xu, D. Wang, L. Qin, W. Yu, Q. Pan, Sens. Actuators, B **137**(2), 490 (2009)
132. S. Mubeen, T. Zhang, N. Chartuprayoon, Y. Rheem, A. Mulchandani, N.V. Myung, M.A. Deshusses, Anal. Chem. **82**(1), 250 (2010)
133. V. Balouria, A. Kumar, S. Samanta, A. Singh, A.K. Debnath, A. Mahajan, D.K. Aswal, S.K. Gupta, Sens. Actuators, B **181**, 471 (2013)
134. L.F. Reyes, A. Hoel, S. Saukko, P. Heszler, V. Lantto, C.G. Granqvist, Sens. Actuators, B **117**(1), 128 (2006)
135. S.S. Badadhe, I.S. Mulla, Sens. Actuators, B **143**(1), 164 (2009)
136. X. Wu, S. Xiong, Y. Gong, Y. Gong, W. Wu, Z. Mao, Q. Liu, S. Hu, X. Long, Sens. Actuators, B **292**, 32 (2019)
137. B. Zhang, M. Li, Z. Song, H. Kan, H. Yu, Q. Liu, H. Liu, Sens. Actuators, B **249**, 558 (2017)
138. J. Deng, Q. Fu, W. Luo, X. Tong, J. Xiong, Y. Hu, Z. Zheng, Sens. Actuators, B **224**, 153 (2016)
139. G. Qi, X. Lu, Z. Yuan, RSC Advances **6**(51), 45660 (2016)
140. G.K. Mani, J.B.B. Rayappan, Mater. Lett. **158**, 373 (2015)
141. M. Kaur, K. Ganapathi, V. Mukund, C. Jain, N.S. Ramgir, N. Datta, S.K. Gupta, Mater. Chem. Phys. **143**(3), 1319 (2014)
142. M. Zhao, X. Wang, L. Nin, J. Jia, X. Li, L. Cao, Sens. Actuators B **156**(2), 588 (2011)
143. L. Wang, Y. Kang, Y. Wang, B. Zhu, S. Zhang, W. Huang, S. Wang, Mater. Sci. Eng., C **32**(7), 2079 (2012)
144. Y. Hu, X. Zhou, Q. Han, Q. Cao, Y. Huang, Mater. Sci. Eng., B **99**(1–3), 41 (2003)
145. S.-J. Kim, C.W. Na, I.-S. Hwang, J.-H. Lee Sens. Actuators B **168**, 83 (2012)
146. Z.S. Hosseini, A.I. Zad, A. Mortezaali, Sens. Actuators B **207**, 865 (2015)
147. H. Huang, P. Xu, D. Zheng, C. Chen, X. Li, J. Mater. Chem. A **3**(12), 6330 (2015)
148. F. Meng, G. Zhao, H. Zhang, Nanosci. Nanotech. Lett. **5**(9), 1012 (2013)
149. S.D. Shinde, G.E. Patil, D.D. Kajale Inter. J. Smart Sens. Intell. Sys., **5**, 277 (2012)
150. K.G. Girija, K. Somasundaram, A. Topkar, R.K. Vatsa, J. Alloys Comp. **684**, 15 (2016)
151. M. He, L. Xie, X. Zhao, X. Hu, S. Li, Z.-G. Zhu, J. Alloys Comp. **788**, 36 (2019)
152. T. Maekawa, J. Tamaki, N. Miura, N. Yamazoe, Chem. Lett. **20**(4), 575 (1991)
153. V.R. Katti, A.K. Debnath, K.P. Muthe, M. Kaur, A.K. Dua, S.C. Gadkari, S.K. Gupta, V.C. Sahni, Sens. Actuators, B **96**(1–2), 245 (2003)
154. M. Verma, A. Chowdhuri, K. Sreenivas, V. Gupta Thin Solid Films, **518**(24), e181 (2010)
155. A. Khanna, R. Kumar, S.S. Bhatti, Appl. Phys. Lett. **82**(24), 4388 (2003)
156. A. Chowdhuri, S.K. Singh, K. Sreenivas, V. Gupta, Sens. Actuators, B **145**(1), 155 (2010)
157. R. Vasiliev, M. Rumyantseva, N. Yakovlev, A. Gaskov, Sens. Actuators, B **50**(3), 186 (1998)
158. M.K. Verma, V. Gupta, Sens. Actuators, B **166–167**, 378 (2012)
159. Y. Min, T. Wang, Y. Chen, Appl. Surf. Sci. **257**(1), 132 (2010)
160. S.-W. Choi, A. Katoch, J. Zhang, S.S. Kim, Sens. Actuators, B **176**, 585 (2013)
161. L. Zanotti, D. Calestani, M. Villani, M. Zha, A. Zappettini, C. Paorici, Crys. Res. Tech. **45**(6), 667 (2010)
162. S. Park, Z. Cai, J. Lee, J.I. Yoon, S.-P. Chang, Mater. Lett. **181**, 231 (2016)
163. F.E. Annanouch, Z. Haddi, S. Vallejos, P. Umek, P. Guttmann, C. Bittencourt, E. Llobet, ACS Appl. Mater. Interfaces **7**(12), 6842 (2015)

164. N.S. Ramgir, N. Datta, S. Kumar, S. Kailasaganapathi, U.V. Patil, N. Karmakar, A.K. Debnath, D.K. Aswal, D.C. Kothari, S.K. Gupta, Mater. Chem. Phys. **156**, 227 (2015)
165. Z. Song, Z. Wei, B. Wang, Z. Luo, S. Xu, W. Zhang, H. Liu, Chem. Mater. **28**(4), 1205 (2016)
166. A. Kumar, N. Joshi, S. Samanta, A. Singh, A.K. Debnath, A.K. Chauhan, D.K. Aswal, S.K. Gupta, Sens. Actuators, B **206**, 653 (2015)
167. S. Mousavi, K. Kang, J. Park, I. Park, RSC Adv. **6**(106), 104131 (2016)
168. G.H. Jain, L.A. Patil, M.S. Wagh, D.R. Patil, S.A. Patil, D.P. Amalnerkar, Sens. Actuators B **117**(1), 159 (2006)
169. H.-M. Huang, H.-Y. Li, X.-X. Wang, X. Guo, Sens. Actuators, B **238**, 16 (2017)
170. M. Kaur, K. Ganapathi, N. Datta, K.P. Muthe, S.K. Gupta, Int. J. Nanosci., **10**(04n05), 733 (2011)
171. X. Xue, L. Xing, Y. Chen, S. Shi, Y. Wang, T.J. Wang, Phys. Chem. C **112**(32), 12157 (2008)

Substituted Phthalocyanine-Based Nanostructured Materials for Room-Temperature Gas Sensing Applications

Aman Mahajan, Rajan Saini, and R. K. Bedi

Abstract In recent years, environment monitoring is one of the prerequisites for the welfare of human beings. Environment monitoring leads to the development of sensors that can detect the presence of harmful/toxic gases and vapours. For the detection of poisonous gases, various studies have been reported over the last few years using nanostructured thin films based on various semiconducting oxides, conducting polymers and organic molecules. Among different organic materials, metallo-phthalocyanines (MPcs) based materials are regarded as excellent sensing material, as their electrical conductivity significantly changes on interaction with oxidizing/reducing gases. Sometimes small response characteristics of these sensors at room temperature become a limitation and can be overcome by exploring long-range molecular nanostructure with high surface/volume ratio. In this chapter, we have systematically discussed the development of cost-effective, highly sensitive and reproducible phthalocyanine-based room-temperature chemiresistive sensors capable of detecting harmful/toxic gases up to ppb levels. The primary emphasis will be laid on the formation of different phthalocyanine-based nanostructures, including nanowires, nanoflowers and nanobelts for sensing applications.

1 Introduction

With the advent of industrialization, humankind has made enormous progress in day-to-day life within a short period. Growth at this rapid pace, however, has resulted in increasing environmental pollution and degradation of nature at an unprecedented

A. Mahajan (✉)
Department of Physics, Guru Nanak Dev University, Amritsar 143005, India
e-mail: dramanmahajan@yahoo.co.in; aman.phy@gndu.ac.in

R. Saini
Department of Materials Science and Engineering, Rutgers—State University of New Jersey, Piscataway, NJ 08854, USA

R. K. Bedi
S. I.E. T, Ram Tirath Road, Amritsar 143107, India

S. Kumar and D. K. Aswal (eds.), *Recent Advances in Thin Films*, Materials Horizons: From Nature to Nanomaterials, https://doi.org/10.1007/978-981-15-6116-0_20

scale. Rising awareness about clean air for the welfare of living beings has led to the creation of strict legislations set-up by competent authorities to limit the exposure to toxic gases at the workplace. Thus, highly efficient gas sensors are required, which can detect hazardous gases emitted from vehicles and industries well below the occupational exposure limit (OEL) (Table 1). Presently, the available gas sensors can be classified into different types based on their operating principle. The main categories of sensors are calorimetric sensors, quartz crystal microbalance sensors, acoustic sensors, chemiresistive sensors, capacitance sensors, etc. (Table 2). Among these, chemiresistive gas sensors are comparatively more economical, portable, highly sensitive, selective and reproducible. In these sensors, the electrical resistance of sensing material changes exceptionally on exposure to the target gas analytes that provide information regarding the nature and concentration of gas. A good quality chemiresistive gas sensor should be easily fabricated and have low operational cost and compact size with higher gas sensing response characteristics.

Till now, various materials such as metal oxides, inorganic compounds and hybrid materials have been used in chemiresistive sensors for the detection of NH_3, NO_2,

Table 1 Long-term exposure limits (LTEL) for 8 h and short-term exposure limits (STEL) for 10 min of some toxic gases [20]

Gas/vapour	LTEL (ppm)	STEL (ppm)	Features
Ammonia (NH_3)	25	35	Colourless gas having a pungent odour
Carbon monoxide (CO)	50	300	Colourless, odourless and tasteless gas
Hydrogen sulphide (H_2S)	10	15	Poisonous, corrosive and flammable gas having a foul odour of rotten eggs
Ethyl alcohol (C_2H_5OH)	1000	–	Volatile, flammable and colourless liquid having a slight characteristic odour
Liquefied petroleum gas (LPG)	1000	1000	Colourless gas having a characteristic smell of added odorizing agent
Nitric oxide (NO)	25	25	Colourless, non-flammable gas
Nitrogen dioxide (NO_2)	0.5	1	Reddish brown gas having a pungent odour
Nitrous oxide (N_2O)	25	–	Colourless, non-flammable gas having a slightly metallic scent and taste, commonly known as laughing gas
Sulphur dioxide (SO_2)	2	5	Toxic gas having a pungent and irritating smell
Chlorine (Cl_2)	0.5	1	Pale yellow-green gas, severely irritating
Carbon dioxide (CO_2)	5000	30000	Colourless, odourless gas

Table 2 List of gas sensors with their corresponding detection principles [20]

Types of sensors	Gas sensor	Detection principle
Solid-state sensors	Chemiresistive	Change in resistance
	Chemical field-effect transistors	Change in current–voltage (I–V) curves
	Calorimetric	Rise in temperature resulting from the oxidation process on a catalytic element
	Potentiometric	Change in the potential difference (voltage) across the working electrode and the reference electrode
	Amperometric	Change in the current of an ionic conductor due to gas diffusion
Mass sensitive sensors	Acoustic	Change in frequency of surface-acoustic waves (SAW) excited on quartz or piezoelectric substrate
	Microelectromechanical systems (MEMS) based sensors	Change in mechanical bending of micro or nanocantilevers
	Surface plasmon resonance (SPR)	Change in SPR signals is proportional to the refractive index close to the sensor surface and is, therefore, related to the number of bound gas molecules
Optical sensors	Optodes	Change in optical properties like absorbance, reflectance, luminescence, light polarization or Raman lines

NO, H_2S, Cl_2, alcohols and volatile organic compounds (VOCs), etc. [1–3]. Among them, metal oxides such as ZnO, TiO_2, SnO_2, Cr_2O_3, FeO_3 and CoO have been considered as promising candidates for sensor applications owing to their unique physical and chemical properties, high tunability, abundant availability and inexpensiveness. Nevertheless, they operate at high temperatures (300–500 °C) which increase power consumption, and equipping the sensor with an inbuilt heater makes it a costly affair [4–7]. Additionally, analytes having low boiling point can inflame easily at high temperatures leading to the need for room-temperature sensors [8]. Also, room-temperature gas sensors exhibit reproducible response kinetics for long periods.

In past few decades, organic materials have achieved significant consideration as suitable candidates for room-temperature gas sensors because of their sensing response in parts per billion range [9] and the ability to easily tune the sensing characteristics by making substitutions to organic molecules. Phthalocyanines (Pcs) have emerged as potential candidates amongst organic materials due to their easily

tunable physicochemical properties even at room temperature [10–13]. This property makes them superior to metal oxides and other inorganic materials based sensors where the high operational temperature is a prerequisite. Moreover, the sensitivity of Pcs-based room-temperature sensors can be tailored by the substitution of different peripheral/non-peripheral substituents which increases the solubility of Pc molecules in various organic solvents [14] and replacing central metal ions by other metal ions [15–17] for detecting different harmful gases like NH_3 and NO_2 [14, 18, 19].

The present chapter presents an overview of the characterization and application of substituted Pcs-based materials for the fabrication of cost-effective and ppb-level room-temperature gas sensors. Different nanostructures of substituted Pcs (nanobelts, nanowires and nanoflowers) were synthesized by self-assembly technique. It is demonstrated that these nanostructures were highly sensitive and selective at room temperature. The gas sensing kinetics of sensors is thoroughly discussed herein based on Raman and XPS studies. The chapter has been systematically divided into different sections covering Pcs and their applications, Pcs-based chemiresistive gas sensors, nanostructures of Pcs and demonstration on synthesis, characterization and gas sensing properties of substituted Pcs.

2 Phthalocyanines and Their Applications

Pcs are metal–organic semiconductors (Fig. 1) with two-dimensional 18 π-electron aromatic macromolecules consisting of four isoindole units connected via nitrogen atoms. They have received considerable attention owing to their peculiar spectroscopic, photoelectric and redox properties. Thus, Pcs-based materials have been extensively used in various fields from dyes to molecular electronic technology such as electrophotography, optical data storage systems, gas sensing devices, photovoltaic cells, fuel cells, and electrochromic displays [21, 22]. Due to high architectural flexibility and chemical stability of Pcs, their physical, optoelectronic and chemical properties can be altered over a broad range.

The easy substitution of different functional groups in the Pc ring as well as replacement of the central metal ion by more than 70 elements imparts exceptional properties to Pc molecules. A commonly used derivative of Pc is 1:1 (metal ion: macrocycle) type, e.g. copper phthalocyanine (CuPc) and zinc phthalocyanine (ZnPc). Small monovalent ions such as Li^+ form 2:1 complexes (Li_2Pc), while larger ions like rare-earth metals forming 1:2 complexes ($EuPc_2$) have also been reported in the literature [24].

Nowadays, most of the devices use ordered and a reproducible thin film of various materials which can be prepared using different deposition techniques. Pcs thin films research, with controlled growth and uniformity, has been focused on optimizing their electronic as well as optical properties. Multiple methods have been adopted to

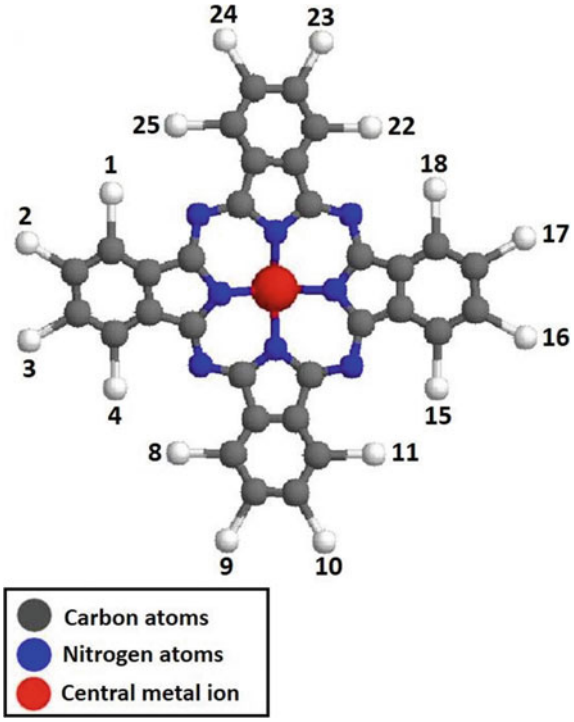

Fig. 1 Chemical structure of phthalocyanine molecule representing peripheral (2, 3, 9, 10, 16, 17, 23, 24) and non-peripheral (1, 4, 8, 11, 15, 18, 22, 25) positions [23]

prepare thin films of Pcs such as physical techniques including physical vapour deposition, glow discharge sputtering, thermal evaporation, molecular beam epitaxy, sputtering and solution-processable techniques like drop-casting, self-assembled monolayer, Langmuir–Blodgett, spin coating, dip coating, etc. [12, 25–27]. Thin films of unsubstituted MPcs have been intensively prepared using vapour deposition techniques as they are insoluble in organic solvents [28]. The addition of substituents on available active sites of 16 benzenoid rings in unsubstituted Pcs increases the number of known derivatives beyond any bounds. These active sites are available either at peripheral (2, 3, 9, 10, 16, 17, 23, 24) or non-peripheral (1, 4, 8, 11, 15, 8, 22, 25) positions (Fig. 1). The substitutions increase the solubility of the ring system in organic solvents and tune the wavelength of the visible region absorption band known as the Q band [29]. Attachments of solubilizing groups like alkyl (C_nH_{2n+1}) or alkoxy (OC_nH_{2n+1}) side chains at active sites for substitutions made Pcs molecules soluble in organic solvents [24] leading to the processing of these Pcs molecules in thin films using spin coating and self-assembly techniques [25, 30]. Thus, the different central metal ions and substituents on Pcs rings remarkably affect their molecular packings and effectively tune the electronic properties of the macrocycle in the solid-state [31].

3 Phthalocyanines-Based Chemiresistive Gas Sensors

Pcs, with their recognitions mentioned above, have been extensively studied as chemiresistive gas sensors for detecting various harmful gases such as O_3, NO_2, Cl_2, NO, NH_3, VOCs, alcohols, etc. [27]. Pcs behave as insulators in dark, high-vacuum environments and change to semiconducting nature when exposed to air due to the oxidation of Pc film via metal centres forming superoxides [32]. Pc film conductivity decreases when it interacts with reducing gases like NH_3, and conductivity increases on interaction with oxidizing gases like NO_2, Cl_2, etc. [33–35]. The gas sensing kinetics is explained through charge-transfer reactions between analytes and Pc films [15]. The nature of the Pc film, whether single crystalline, polycrystalline or amorphous affects the degree of interaction of the gas. For instance, the gas sensing response of amorphous CuPc is higher in comparison to polycrystalline film owing to weak molecular stacking [36]. Moreover, the gas sensing parameters of MPc films depend upon film thickness, substrate temperature, nature of substrate, sensing and annealing temperature.

Recently, sublimed thin films of metal-free (H_2Pc) and unsubstituted MPcs (M=Fe, Co, Cu and Zn) have been investigated for detecting O_2, NO, NO_2 and NH_3 analytes. Gas sensing parameters of several vacuum sublimated MPc (M=Pb, Zn, Cu, Ni, Co and Fe) films at different temperatures have also been studied for detecting the low concentration of NO_2, NO, F_2, BCl_3, BF_3, NH_3, H_2S, SO_2 and HCl [9]. Hydrogen sensor based on CuPc and palladium (Pd) admixture with the detection limit below 1 ppm H_2 at an operating temperature of 95 °C has been reported [37–39].

Most of the reports available in the literature correspond to the parts per million (ppm) level of various toxic gases but only a few reported on parts per billion [40–42] level detection of toxic gases.

4 Nanostructures of Phthalocyanines

Recently, nanostructures of metal oxides, inorganic and organic materials have been extensively investigated for their potential in detecting harmful gases. Among them, nanostructures of organic materials have been considered for gas sensing applications due to the low cost for material synthesis, high flexibility and ease of large-area production as well as compatibility with lightweight flexible plastic substrates [43–45]. The use of nanostructures with a large surface to volume ratio is found to overcome the poor gas sensing performance of room-temperature gas sensors [43, 44, 46, 47]. Organic physical vapour deposition technique has been used for the synthesis of nanoribbons and nanowires of various MPcs (M=Cu, Ni, Fe, Co, Zn) and F_{16}CuPc.

Owing to poor solubility of Pc molecules in organic solvents, thin films of nanostructured unsubstituted Pcs have been prepared using OPVD, organic

molecular beam epitaxy and vacuum evaporation technique with a limitation of high fabrication cost [48–51]. Substituted Pcs nanostructures have been synthesized using solution processing based techniques as they are soluble in organic solvents [17, 52, 53]. Out of different solution processing techniques, namely solvothermal, template-assisted method and electrochemical method, self-assembly is considered to be the simplest method for the controlled growth of long ordered nanostructures with large surface area [54]. Nanobelts of metal-free 2,3,9,10,16,17,23,24-octakis (isopropylthio)phthalocyanine H_2Pc(β-SC3H7)8 and its derivatives like CuPc(β-SC3H7)8 and PbPc(β-SC3H7)8 [55], 1D microwires of $CuPcOC_4$ [56], nanofibres of metal-free alkoxy-substituted phthalocyanine derivative 2,3,9,10,16,17,23,24-octakis(octyloxy)-29H,31H-phthalocyanine [53], nanobars of copper(II) 1,4,8,11,15,18,22,25-octabutoxy-29H,31H-phthalocyanine, two-dimensional films of copper(II) 2,3,9,10,16,17,23,24-octakis(octyloxy)-29H,31H phthalocyanine [50] and nanostructures of tris(phthalocyaninato) terbium triple-decker [(Pc)TbPc(OC8H17)8 Tb(Pc)] [57] have been prepared via self-assembly technique.

Keeping these reports into consideration, a demonstration on the fabrication of Pc nanostructures and their application as room-temperature ppb-level gas sensors [40–42] has been planned which will provide an understanding of enhancement of gas sensing parameters at room temperature.

5 Synthesis, Characterization and Gas Sensing Properties of Substituted Phthalocyanines

In this section, growth and gas sensing applications of nanostructured substituted Pcs, namely $ZnPcOC_4$, $CuPcOC_4$, $ZnPcOC_8$ and $CuPcOC_8$ (Fig. 2), have been demonstrated to understand the possible reasons behind the formation of nanostructures and how they help in improving the gas sensing performance. The thorough experiments performed, and results obtained have been discussed below.

5.1 Growth of Substituted Phthalocyanine-Based Nanostructures

The Pc-based nanostructures have been fabricated by self-assembly process under closed environmental conditions. To achieve this, their solutions in organic solvents have been prepared and subsequently, filtered through a polytetrafluoroethylene (PTFE) membrane. The prepared solutions were drop-casted onto well-cleaned substrates in a closed environment of solvent vapours (Fig. 3).

The XRD patterns of $ZnPcOC_8$ nanostructures (Fig. 4) sample revealed two diffraction peaks corresponding to the intercolumnar spacing of Pc molecules (4.2°)

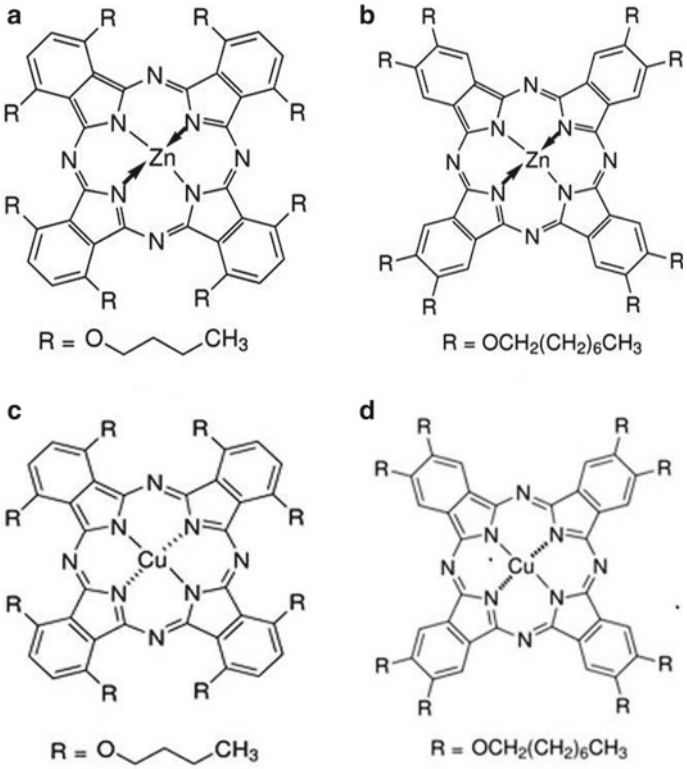

Fig. 2 Chemical structure of **a** $ZnPcOC_4$, **b** $ZnPcOC_8$, **c** $CuPcOC_4$, **d** $CuPcOC_8$ [23]

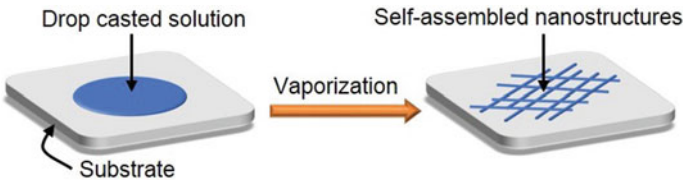

Fig. 3 Schematic representation of surface-supported self-assembly phenomenon [23]

and the intracolumnar π–π interactions between two neighbouring Pc molecules (26°) [58]. Similar diffraction peaks were observed for $ZnPcOC_4$ nanostructures [41]. However, in case of $CuPcOC_8$ (Fig. 4) and $CuPcOC_4$, the diffraction peak around 20–30° was found to be absent indicating the lack of π–π interactions periodicity [41, 42, 58].

Further, the SEM image of $ZnPcOC_8$ nanostructured film (Fig. 5a) showed the formation of long-range nanowires (NWs) grown parallel to the substrate. The uniformly developed network of nanofibers (NFs) onto the glass substrate was

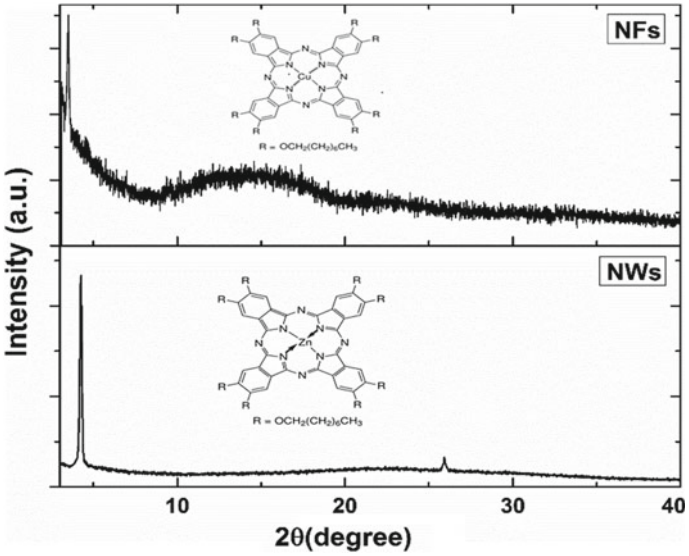

Fig. 4 XRD pattern and structure of $ZnPcOC_8$ (NWs) and $CuPcOC_8$ (NFs) [41]

observed in the case of $CuPcOC_8$ nanostructured films (Fig. 5b), while the formation of nanobelts (NBs) and NWs was seen in $ZnPcOC_4$ and $CuPcOC_4$ films, respectively (Fig. 5c, d).

The UV-visible spectrum of Pcs consists of two bands: higher energy "B-band" (250–500 nm) arising from the highest occupied molecular orbital (HOMO) a2u to lowest unoccupied molecular orbital transition (LUMO) e.g., and the lower energy "Q-band" (550–800 nm) which is attributed to transition from HOMO a1u to LUMO, e.g. [14]. $ZnPcOC_8$ NWs film possessed higher energy B-band at 358 nm and broad Q-band at 602 and 665 nm (Fig. 6). In comparison to $ZnPcOC_8$/Toluene solution, the aggregation of Pc molecules in film led to the broadening of absorption bands [14]. Also, Q band of NBs was found to be blue shifted from 602 to 665 nm representing the formation of H-aggregates of molecules in NWs and co-facial stacking of $ZnPcOC_8$ molecules (Fig. 6) [24]. Further, absorption spectra for $CuPcOC_8$ NFs depicts the position of B and Q band at 342, and 609 and 674 nm, respectively, as seen in Fig. 6. In comparison to $CuPcOC_4$ solution (Fig. 6), similar blue shifting of Q band was also observed due to the co-facial stacking of molecules in $CuPcOC_8$ NFs. Same results have been obtained for $ZnPcOC_4$ and $CuPcOC_4$ nanostructured films [41, 42].

The growth behaviour of organic nanostructures can be described in terms of molecule–substrate interactions and molecule–molecule interactions [49]. In $ZnPcOC_8$ NWs films, parallel growth of NWs had taken place concerning the substrate due to the supremacy of molecule–substrate interactions. Long-range horizontal columns were formed by piling up of molecules which migrates from the nearby surface. Such columns are assembled to form an NW. While in the case

of $CuPcOC_8$, molecule–molecule interactions were dominant during the formation of nanoribbons resulting in their inclined growth concerning the substrate surface [49]. Co-facial stacking of $CuPcOC_8$ molecules indicated by a blue shift of Q bands suggested that initially deposited molecules acted as nucleation seeds for further growth of columns due to molecule–molecule interactions dominance. Several such tilted columns assembled together forming a nanoribbon. Likewise, molecule–substrate interactions were stronger than molecule–molecule interactions in case of $ZnPcOC_4$ NBs such that at the initial stage of growth NBs were grown parallel to substrate surface. Further, during the evaporation of the solution, the layer-by-layer growth process occurred via π–π interactions resulting in the formation of

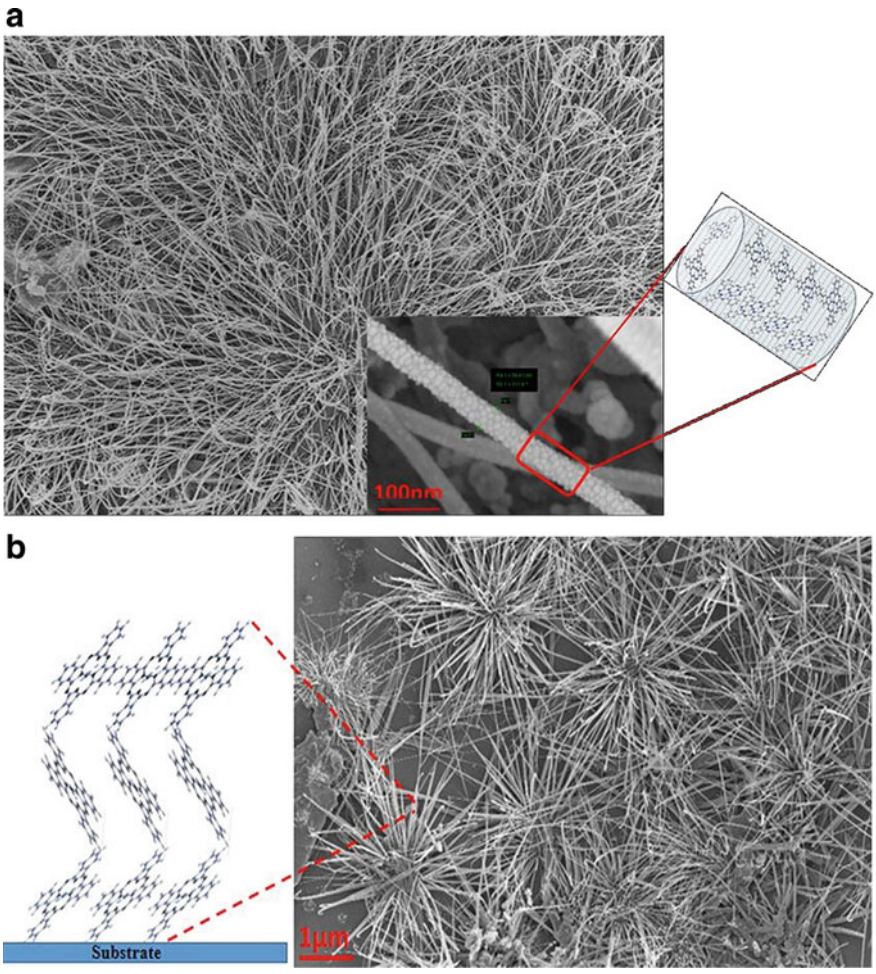

Fig. 5 SEM image and formation schematic of **a** $ZnPcOC_8$ NWs, **b** $CuPcOC_8$ NFs, **c** $ZnPcOC_4$ NBs, **d** $CuPcOC_4$ NWs [40–42]. Reproduced by permission of The Royal Society of Chemistry

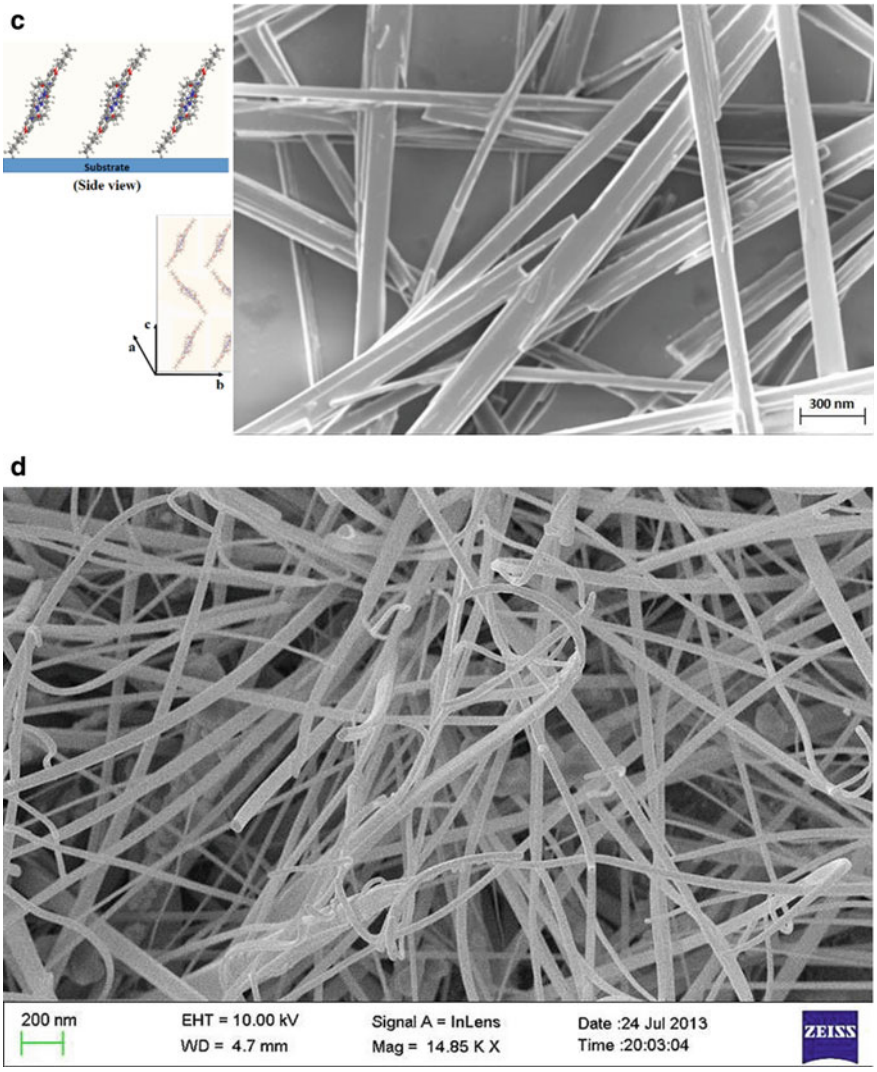

Fig. 5 (continued)

NBs. Similarly, for $CuPcOC_4$ sample, the dominance of molecule–substrate interactions resulted in lateral growth of NWs and blue shift in Q band. However, the lack of π–π interactions resulted in the absence of diffraction peak around 20–30°.

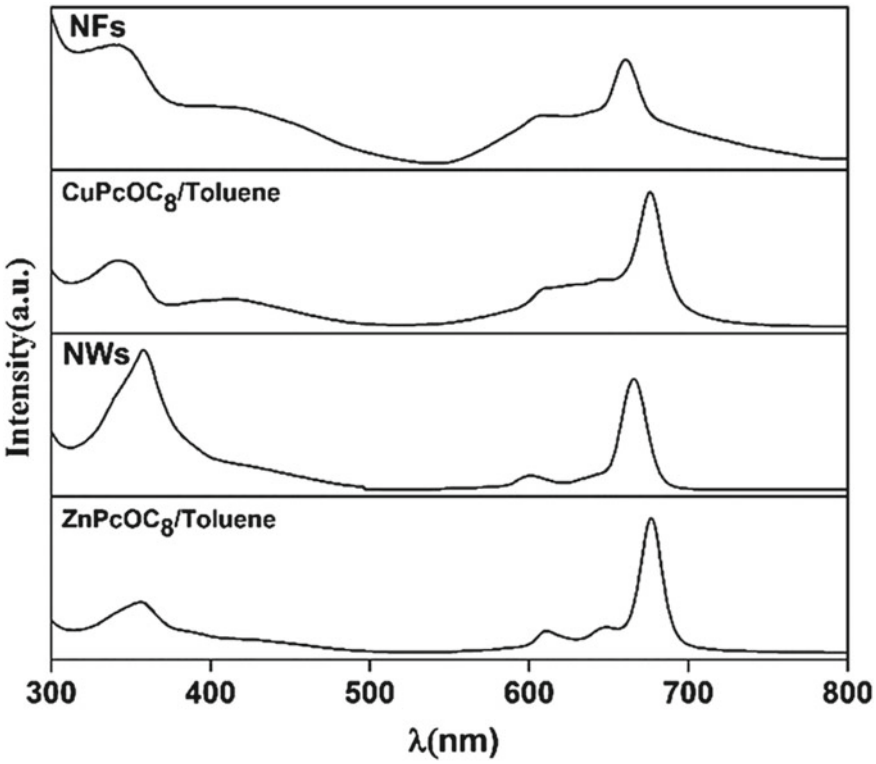

Fig. 6 UV–visible absorption spectrum of $ZnPcOC_8$ NWs, $ZnPcOC_8$/Toluene solution, $CuPcOC_8$ NFs and $CuPcOC_8$/Toluene solution [40]. Reproduced by permission of The Royal Society of Chemistry

5.2 Gas Sensing Studies of Phthalocyanine Nanostructures

It is well established that the p-type behaviour of Pc films results from the adsorption of ambient oxygen-forming MPc^+ and O^- species on its surface [13, 15]. To study the gas sensing properties of films at room temperature (25 °C and 50% relative humidity), two gold pads (50 nm thick, dimensions 5 mm × 5 mm with separation of 1 mm) were thermally evaporated onto the film sample by using a shadow mask to fabricate sensors. The sensors were kept in the test chamber under a constant bias of 5 V for a few hours to achieve a stable baseline value of sensor conductance. To ascertain the selectivity of the fabricated sensors, they were exposed to 500 ppb of Cl_2, NO_2, NO and NH_3 gases, and their corresponding histograms are presented in Fig. 7 a–d. Since all the nanostructured sensors were found to be highly selective for Cl_2 at room temperature, their response curves were recorded by exposing them to Cl_2 in the concentration range of 5–1500 ppb. It has been found that all the sensors exhibited good reversibility for Cl_2 concentration under investigation. For $ZnPcOC_8$

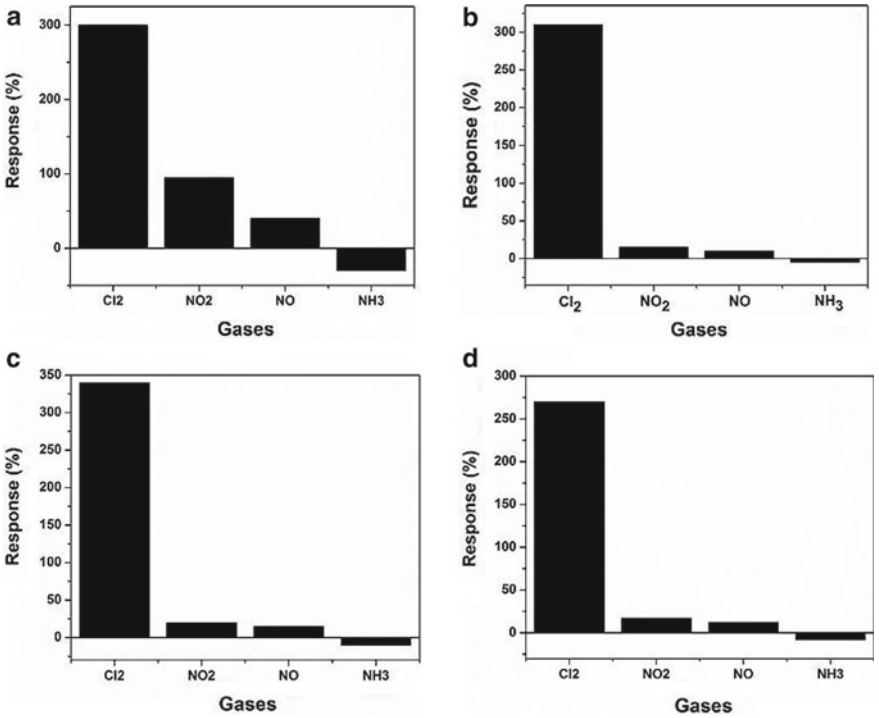

Fig. 7 Response histogram corresponding to **a** $ZnPcOC_4$ NBs, **b** $CuPcOC_4$ NWs, **c** $ZnPcOC_8$ NWs, **d** $CuPcOC_8$ NFs based sensors [40–42]. Reproduced by permission of The Royal Society of Chemistry

NWs and $CuPcOC_8$ NFs sensor, the response curve and dependence of response on Cl_2 concentration is presented in Fig. 8a, b. The Cl_2 response characteristics of $ZnPcOC_4$ NBs and $CuPcOC_4$ NWs are listed in Table 3 [40–42].

Further, the response time of sensors decreased, while recovery time was found to increase with increasing Cl_2 concentration. Comparison of obtained results of nanostructured sensors with the literature [13, 59–64] suggests that Pc nanostructure sensors seem to be superior for room-temperature Cl_2 detection.

Since water vapours act as a donor type impurity to the Pc films, the role of humidity in Cl_2 sensing characteristics of sensors is inevitable at room temperature [65]. The effect of relative humidity on room-temperature Cl_2 sensing characteristics of nanostructured sensors was studied in the relative humidity range 10–80%. The variation in response was found to be very small, i.e. humidity had negligible effect on the Cl_2 response of nanostructures based sensors that make these nanostructures a suitable material as room-temperature Cl_2 sensors [40–42].

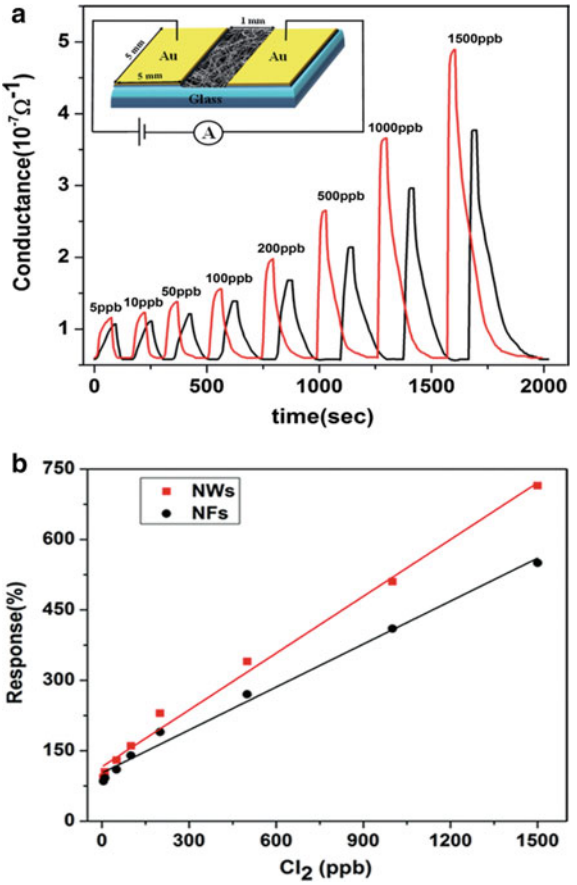

Fig. 8 **a** Response curve of $ZnPcOC_8$ NWs (red curve) and $CuPcOC_8$ NFs (black curve) sensors towards different concentrations of Cl_2, **b** Linear variation of $ZnPcOC_8$ NWs (red curve) and $CuPcOC_8$ NFs (black curve) sensors response with Cl_2 concentration [40]. Reproduced by permission of The Royal Society of Chemistry

Table 3 Cl_2 response of phthalocyanine nanostructures based sensors [23]

Cl_2 concentration (in ppb)	$ZnPcOC_4$ NBs response (%)	$ZnPcOC_8$ NWs response (%)	$CuPcOC_4$ NWs response (%)	$CuPcOC_8$ NFs response (%)
5	90	93	91	85
10	100	105	102	92
50	122	130	126	110
100	155	160	157	140
200	211	230	222	190
500	300	340	328	270
1000	450	510	490	410
1500	655	715	670	550

5.3 Adsorption Kinetics of Phthalocyanine-Based Room-Temperature Sensors

Elovich model has been used to study the adsorption kinetics of Cl_2 on nanostructures. According to this model, the adsorption rate of gas on the heterogeneous solid surface decreases with time due to an increase in surface coverage following the Elovich equation [66, 67]

$$\frac{d\theta}{dt} = \alpha e^{-\beta\theta} \tag{1}$$

where θ is the amount of adsorbed gas at time t, α represents initial adsorption rate and β measures the extent to which the film surface has been screened by the potential barrier for successive adsorption [13]. Assuming that the sensor conductance (ΔC) changes proportionally with respect to the amount of adsorbed Cl_2 molecules (θ), (1) can be rewritten as

$$\frac{d(\Delta C)}{dt} = ae^{-b\Delta C} \tag{2}$$

where a and b are constants. In integral form, (2) can be converted to

$$\Delta C = \left(\frac{2.3}{b'}\right)\log(a'b') + \left(\frac{2.3}{b'}\right)\log(t) \tag{3}$$

where a' and b' are constants. Variation of ΔC versus log (t) for different Cl_2 concentrations has been considered to describe the Cl_2 adsorption on the surface of nanostructures (Fig. 9). Initially, ΔC increased linearly with time before slowing down on reaching adsorption equilibrium, which indicates that the increase in surface coverage

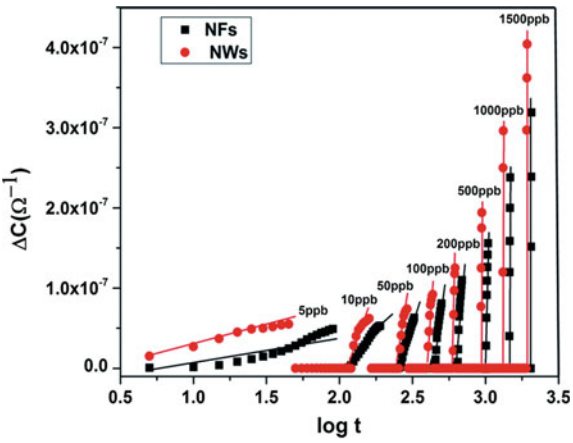

Fig. 9 Plot of ΔC versus log (t) of $ZnPcOC_8$ NWs (red curve) and $CuPcOC_8$ NFs (black curve) [40]. Reproduced by permission of The Royal Society of Chemistry

decreased the adsorption rate. Further, values of constant b' (slope $= 2.3/b'$) determined from Elovich plots increased with increase in Cl_2 concentration suggesting that at higher Cl_2 concentration, the reaction between Cl_2 and film became faster, resulting in quicker film surface coverage.

5.4 *The Gas Sensing Mechanism of Phthalocyanine-Based Sensors*

To explore the interaction mechanism between Cl_2 and nanostructured film samples, Raman and XPS measurements were carried out after exposing the samples to Cl_2. The XPS spectra of $ZnPcOC_8$ NWs before and after exposure (Fig. 10) depict characteristics Zn-2p (1022 eV−Zn-2p3/2 & 1045 eV−Zn-2p1/2), O-1 s (533 eV), N-1 s (399 eV) and C-1 s (286 eV) peaks [13]. No change in the spectrum of core level C-1 s

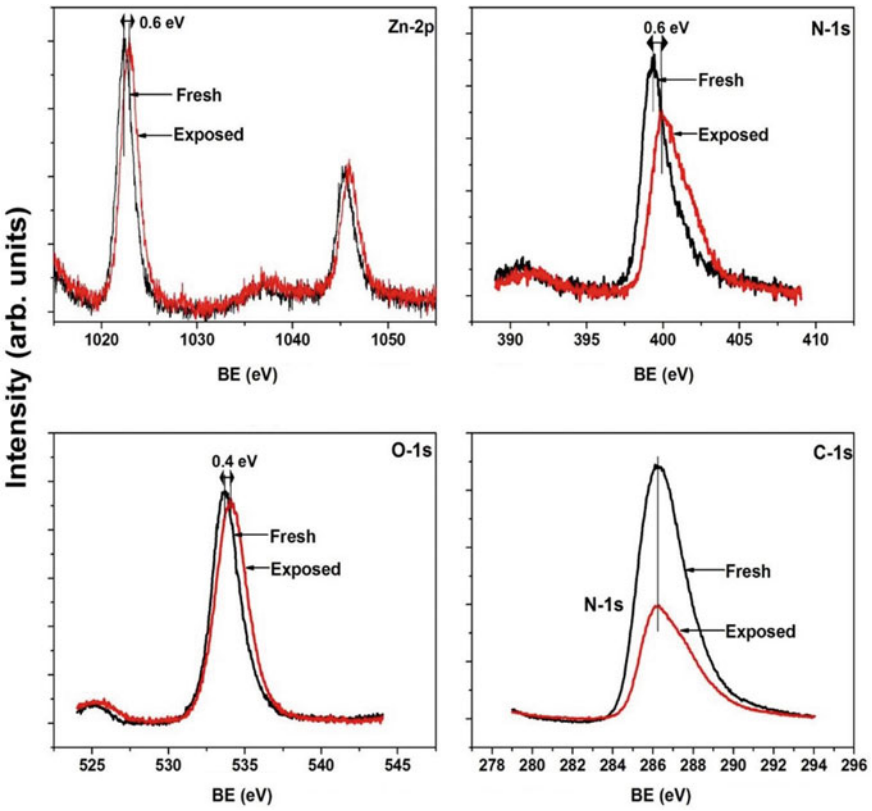

Fig. 10 XPS spectra of Zn-2p, N-1 s, O-1 s and C-1 s peaks of $ZnPcOC_8$ NWs recorded before and after exposure to 25 ppm of Cl_2 [40]. Reproduced by permission of The Royal Society of Chemistry

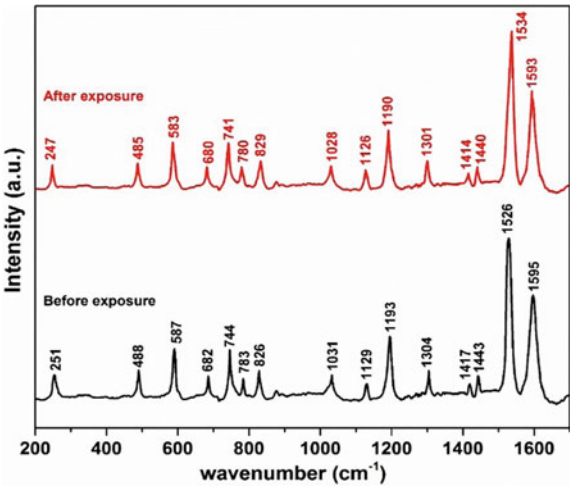

Fig. 11 Raman spectra of $ZnPcOC_8$ NWs obtained before and after exposing the films to 25 ppm of Cl_2 [40]. Reproduced by permission of The Royal Society of Chemistry

after gas exposure was seen. However, a peak shift of 0.3 and 1.1 eV towards higher B.E. side was observed for O-1 s and Zn-2p peak, respectively. Thus, it is evident from the extent of shift that central metal atom Zn act as the predominant adsorption site for Cl_2. A similar shift was also observed in N-1 s peak after Cl_2 exposure since metal ions are directly connected to the nitrogen atoms. Similar peak shift of central metal atom was observed in $CuPcOC_8$ NFs (0.6 e V), $ZnPcOC_4$ NBs (0.6 eV) and $CuPcOC_4$ NWs (1.3 eV) suggesting that central metal ions of Pc molecules were the main sites of interaction for Cl_2 [40–42].

In the case of Raman spectra, also, there were shifts in positions and change in intensities of some bands after Cl_2 exposure. For $ZnPcOC_8$ NWs (Fig. 11), the typical metal–nitrogen bond positioned at 153 cm^{-1} was shifted to 145 cm^{-1} and the macrocyclic bands observed at 593, 751, 832, 1120, 1281, 1384 and 1422 cm^{-1} were shifted by 4 cm^{-1}. While the characteristic central metal ion band positioned at 1507 cm^{-1} was shifted by 10 cm^{-1} indicating that Cl_2 molecules preferred to bind with a central metal ion, i.e. Zn^{+2}. Since this band is characterized by the large displacement of C–N–C bridge bonds of Pc ring and is identified as highly sensitive to the changes in metal ion environment [68]. Similar major peak shifts corresponding to metal–nitrogen bond were observed for $CuPcOC_8$ NFs, $ZnPcOC_4$ NBs and $CuPcOC_4$ NWs samples [40–42]. Therefore, both Raman and XPS studies confirmed that central metal ions were the main sites for Cl_2 interaction.

6 Conclusion

In conclusion, although MPcs have been around for the past few decades, they still keep attracting a great deal of interest due to their exceptional properties. Gas sensors based on these Pcs, both substituted and unsubstituted, have enormous potential in everyday life. As of today, many toxic gases and vapours can be effectively detected by gas sensors based on MPcs. Indeed, they are regarded as superior to the conventional metal oxides based sensors as they can work at room temperature in contrast to the latter category, which shows gas sensing ability at high temperatures. Further, as demonstrated, Pc-based gas sensors show excellent selectivity with high response and reversibility even at room temperature. Herein, we have discussed the gas sensing characteristics of self-assembled nanostructured thin films based on MPcs. It has been revealed that the fabricated sensors were highly selective and sensitive towards Cl_2 at room temperature with a detection limit as low as 5 ppb. Further, it has been observed that the central metal ions of Pcs directly interact with the molecules of the test gas, and thus influence the sensing characteristics of fabricated thin films. However, there are still several issues, including

(a) synthesis of pure and substituted Pcs is still challenging and costly,
(b) their properties can easily vary depending on the preparation techniques, substitutions and nature of metal ion used,

which need to be addressed before their large-scale application.

References

1. K. Shimizu, I. Chinzei, H. Nishiyama, S. Kakimoto, S. Sugaya, W. Matsutani, A. Satsuma, Sensors Actuators B Chem. **141**, 410 (2009)
2. B. Wolpert, O.S. Wolfbeis, V.M. Mirsky, Sensors Actuators B Chem. **142**, 446 (2009)
3. A. Afzal, N. Cioffi, L. Sabbatini, L. Torsi, Sensors Actuators B Chem. **171–172**, 25 (2012)
4. S. Nakata, H. Okunishi, Appl. Surf. Sci. **240**, 366 (2005)
5. Y. Jia, L. He, Z. Guo, X. Chen, F. Meng, T. Luo, M. Li, J. Liu, J. Phys. Chem. C **113**, 9581 (2009)
6. A. Hackner, A. Habauzit, G. Müller, Sensors Actuators B Chem. **146**, 433 (2010)
7. X. Wang, S. Qiu, C. He, G. Lu, W. Liu, J. Liu, RSC Adv. **3**, 19002 (2013)
8. N.G. Patel, P.D. Patel, V.S. Vaishnav, Sensors Actuators B Chem. **96**, 180 (2003)
9. T.A. Jones, B. Bott, Sensors Actuators **9**, 27 (1986)
10. R. Zhou, F. Josse, W. Göpel, Z.Z. Öztürk, Ö. Bekaroğlu, Appl. Organomet. Chem. **10**, 557 (1996)
11. L. Valli, Adv. Colloid Interface Sci. **116**, 13 (2005)
12. N. Padma, A. Joshi, A. Singh, S.K. Deshpande, D.K. Aswal, S.K. Gupta, J.V. Yakhmi, Sensors Actuators B Chem. **143**, 246 (2009)
13. A. Kumar, A. Singh, A.K. Debnath, S. Samanta, D.K. Aswal, S.K. Gupta, J.V. Yakhmi, Talanta **82**, 1485 (2010)
14. B. Wang, X. Zhou, Y. Wu, Z. Chen, C. He, X. Zuo, Sensors Actuators B Chem. **161**, 498 (2012)
15. F.I. Bohrer, C.N. Colesniuc, J. Park, M.E. Ruidiaz, I.K. Schuller, A.C. Kummel, W.C. Trogler, J. Am. Chem. Soc. **131**, 478 (2009)

16. J. Zhao, L.-H. Huo, S. Gao, H. Zhao, J.-G. Zhao, N. Li, Sensors Actuators B Chem. **126**, 588 (2007)
17. J. Gao, G. Lu, J. kan, Y. Chen, M. Bouvet, Sensors Actuators B Chem. **166–167**, 500 (2012)
18. A. Cole, R.J. McIlroy, S.C. Thorpe, M.J. Cook, J. McMurdo, A.K. Ray, Sensors Actuators B Chem. **13**, 416 (1993)
19. Y. Wang, N. Hu, Z. Zhou, D. Xu, Z. Wang, Z. Yang, H. Wei, E.S.-W. Kong, Y. Zhang, J. Mater. Chem. **21**, 3779 (2011)
20. A.K. Sharma, D.A. Mahajan, *Preparation and Characterization of Carbon Nanotubes/Phthalocyanines Based Hybrid Materials for Gas Sensing Applications* (Guru Nanak Dev University, 2018)
21. A.W. Snow, W.R. Barger, A.B.P.L.C.C. Leznoff, *Phthalocyanine Films in Chemical Sensors* (VCH, Cambridge, 1989)
22. N.B. McKeown, *Phthalocyanine Materials* (Cambridge University Press, 1998)
23. R. Saini, D.R.K. Bedi, *Study of Phthalocyanine Based Materials for Device Applications* (Guru Nanak Dev University, 2014)
24. B.M. Hassan, H. Li, N.B. McKeown, J. Mater. Chem. **10**, 39 (2000)
25. T. Basova, E. Kol'tsov, A.K. Ray, A.K. Hassan, A.G. Gürek, V. Ahsen, Sensors Actuators B Chem. **113**, 127 (2006)
26. G. Maggioni, S. Carturan, M. Tonezzer, M. Bonafini, A. Vomiero, A. Quaranta, C. Maurizio, F. Giannici, A. Scandurra, F. D'Acapito, G. Della Mea, and O. Puglisi, Chem. Mater. **18**, 4195 (2006)
27. H. Gupta, R.K. Bedi, A. Mahajan, J. Appl. Phys. **102**, 73502 (2007)
28. A.B.P.L.C.C. Leznoff, *Phthalocyanines, Properties and Applications* (VCH, Cambridge, 1989)
29. P.B.J. Simon, A.B.P.L.C.C. Leznoff, *No Title* (VCH, Cambridge, 1993)
30. R.H. Tredgold, J. Mater. Chem. **5**, 1095 (1995)
31. C.G. Claessens, U. Hahn, T. Torres, Chem. Rec. **8**, 75 (2008)
32. J.-J.A.J. Simon, *Molecular Semiconductors* (Springer, Berlin, Heidelberg, 1985)
33. R.L. van Ewyk, A.V Chadwick, J.D. Wright, J. Chem. Soc. Faraday Trans. 1 Phys. Chem. Condens. Phases **76**, 2194 (1980)
34. Y. Sadaoka, T.A. Jones, W. Göpel, Sensors Actuators B Chem. **1**, 148 (1990)
35. T. Miyata, T. Minami, Appl. Surf. Sci. **244**, 563 (2005)
36. M. Masui, M. Sasahara, T. Wada, M. Takeuchi, Appl. Surf. Sci. **92**, 643 (1996)
37. M. Passard, A. Pauly, J.P. Blanc, S. Dogo, J.P. Germain, C. Maleysson, Thin Solid Films **237**, 272 (1994)
38. C. Maleysson, D. Bouchepillon, O. Tomas, J.P. Blanc, S. Dogo, J.P. Germain, M. Passard, A. Pauly, Thin Solid Films **239**, 161 (1994)
39. V. Uwira, A. Schütze, D. Kohl, Sensors Actuators B-Chem. **26**, 153 (1995)
40. R. Saini, A. Mahajan, R.K. Bedi, D.K. Aswal, A.K. Debnath, Sensors Actuators B Chem. **203**, 17 (2014)
41. R. Saini, A. Mahajan, R.K. Bedi, D.K. Aswal, A.K. Debnath, Sensors Actuators B Chem. **198**, 164 (2014)
42. R. Saini, A. Mahajan, R.K. Bedi, D.K. Aswal, A.K. Debnath, RSC Adv. **4**, 15945 (2014)
43. L. Zang, Y. Che, J.S. Moore, Acc. Chem. Res. **41**, 1596 (2008)
44. J. Kim, C.R. Park, S. Yim, RSC Adv. **2**, 963 (2012)
45. C. Zhang, L. Jing, S. Lin, Z. Hao, J. Tian, X. Zhang, P. Zhu, ChemPhysChem **14**, 3827 (2013)
46. S. Maldonado, E. García-Berríos, M.D. Woodka, B.S. Brunschwig, N.S. Lewis, Sensors Actuators B Chem. **134**, 521 (2008)
47. R. Saini, A. Mahajan, R.K. Bedi, S. Kumar, Sensors Actuators B Chem. **147**, 122 (2010)
48. S. Karan, B. Mallik, J. Phys. Chem. C **111**, 7352 (2007)
49. A.K. Debnath, S. Samanta, A. Singh, D.K. Aswal, S.K. Gupta, J.V. Yakhmi, S.K. Deshpande, A.K. Poswal, C. Sürgers, Phys. E Low-Dimens. Syst. Nanostruct. **41**, 154 (2008)
50. B. Wang, Z. Li, X. Zuo, Y. Wu, X. Wang, Z. Chen, C. He, W. Duan, J. Gao, Sensors Actuators B Chem. **149**, 362 (2010)
51. H.-Z. Chen, L. Cao, H.-B. Zhou, Y. Rong, M. Wang, J. Cryst. Growth **281**, 530 (2005)

52. Z. Guo, B. Chen, M. Zhang, J. Mu, C. Shao, Y. Liu, J. Colloid Interface Sci. **348**, 37 (2010)
53. V. Duzhko, K.D. Singer, J. Phys. Chem. C **111**, 27 (2007)
54. J.A.A.W. Elemans, R. van Hameren, R.J.M. Nolte, A.E. Rowan, Adv. Mater. **18**, 1251 (2006)
55. Z. Hao, X. Wu, R. Sun, C. Ma, X. Zhang, ChemPhysChem **13**, 267 (2012)
56. Y. Zhang, Z. Zhang, Y. Zhao, Y. Fan, T. Tong, H. Zhang, Y. Wang, Langmuir **25**, 6045 (2009)
57. P. Zhu, Y. Wang, M. Ren, X. Zhao, X. Zhang, Inorganica Chim. Acta **392**, 10 (2012)
58. S. Takami, S. Furumi, Y. Shirai, Y. Sakka, Y. Wakayama, J. Mater. Chem. **22**, 8629 (2012)
59. A. Joshi, D.K. Aswal, S.K. Gupta, J.V. Yakhmi, S.A. Gangal, Appl. Phys. Lett. **94**, 103115 (2009)
60. A. Chaparadza, S.B. Rananavare, Nanotechnology **19**, 245501 (2008)
61. S. Jain, A.B. Samui, M. Patri, V.R. Hande, S.V. Bhoraskar, Sensors Actuators B Chem. **106**, 609 (2005)
62. D.R. Patil, L.A. Patil, Sensors Actuators B Chem. **123**, 546 (2007)
63. S.-T. Jean, Y.-C. Her, J. Appl. Phys. **105**, 24310 (2009)
64. A. Altindal, Z.Z. Öztürk, S. Dabak, Ö. Bekaroğlu, Sensors Actuators B Chem. **77**, 389 (2001)
65. T. Sizun, M. Bouvet, J.-M. Suisse, Talanta **97**, 318 (2012)
66. R. Tongpool, S. Yoriya, Thin Solid Films **477**, 148 (2005)
67. W. Yang, L. Liu, Z. Zhou, C. Qiu, P. Ma, H. Liu, W. Xu, New J. Chem. **37**, 2758 (2013)
68. M. Szybowicz, J. Makowiecki, J. Mater. Sci. **47**, 1522 (2012)

Hybrid Flexible Sensor

V. B. Patil

Abstract A novel flexible, ultra-sensitive, selective and room temperature operable polyaniline-based hybrid (PAni/α-Fe_2O_3 PAni/WO_3) ammonia (NH_3) gas sensors were developed onto a flexible polyethylene terephthalate (PET) substrate by in-situ polymerization process. The observations were recorded to 100 ppm fixed level for various gases including NO_2, CH_3OH, C_2H_5OH, NH_3 and H_2S through monitoring the change in resistance of the developed sensor. The flexible (PAni/α-Fe_2O_3 PAni/WO_3) hybrid sensor demonstrated better selectivity towards NH_3. The synergistic response of the flexible hybrid sensors was remarkable than that of the PAni and α-Fe_2O_3 and WO_3 alone; indicating the effective improvement in the performance of PAni flexible sensor on nanocomposite process. Moreover, the flexible sensor detected NH_3 at low concentration (5 ppm) with a fast response (27 s) and very short recovery time (46 s). Further, PAni/α-Fe_2O_3 and PAni/WO_3 hybrid flexible sensor films were characterized by X-ray diffraction, field-emission scanning electron microscopy, UV–visible and Raman spectroscopy, Fourier transform infrared and X-ray photoelectron for structural analysis, morphological evolution, optical and surface related studies.

1 Introduction

In recent days, the development of stretchable and flexible sensors for array of functions has been accelerated by fast advances in materials and processing methods. Flexible sensors are attracting more interest due to their fascinating properties like flexibility, low cost, lightweight, shock resistance, smoothness, etc. Flexible sensors hold great assure for variety of appliances in several fields including medicine, communication, personal safety, environmental monitoring, energy storage and poisonous pollutant detection for human health [1]. The fundamental advantage of flexible sensor is that it can operate at room temperature and can be situated in compact places which make it portable, trouble-free and economical [2].

V. B. Patil (✉)
School of Physical Sciences, Solapur University, Solapur 413255, MH, India
e-mail: drvbpatil@gmail.com

S. Kumar and D. K. Aswal (eds.), *Recent Advances in Thin Films*, Materials Horizons: From Nature to Nanomaterials, https://doi.org/10.1007/978-981-15-6116-0_21

The flexibility of sensors affords its interaction with the target system in order to advance the reliability and stability of the tests. The development of flexible substrate-based sensor leads to the production of wearable, transportable and hand-held consumer electronics [3, 4]. Mechanical flexibility and lightweight property of flexible sensors offer an extensive range of narrative and low-cost appliances [5]. The advantage of plastic substrate-based flexible sensor is that they can be placed in compact places and operate at room temperature, which not only avoids the heating assembly but also makes it simple, cheap and portable.

In order to develop simple and cost-effective gas sensors, a chemical oxidative in-situ polymerization method is implemented, which also improves the detection limit of sensor at lower concentration of gas. The main benefit of flexible substrate is that it can be placed in compact places without fracture of the sensor. The in-situ chemical oxidative polymerization method is most beneficial, because huge number of films can be deposited in a single batch without overwhelming time and chemicals. The gas-sensing performance of polyaniline sensor can be enhanced in terms of sensitivity, selectivity and response/recovery times by incorporating tungsten oxide nanoparticles. Polyaniline hybrid nanocomposite was prepared by adding WO_3 nanoparticles into the PAni template.

Nowadays, environmental pollution has been seriously increased due to toxic gases, such as NH_3, nitrogen dioxide (NO_2), carbon monoxide (CO) and sulphur dioxide (SO_2), leading to environmental imbalance. In order to monitor these gases, large efforts have been done to fabricate a variety of sensors useful in different fields such as agriculture, food, medicine and industries. NH_3 is one of the major toxic pollutants in air which causes adverse effects on human being and environment as well. Therefore, it is essential to detect highly toxic NH_3 gas and for the same, a room temperature operated low cost, reliable and highly sensitive gas sensor system should be developed. Many organic and inorganic materials have been widely explored as sensing materials due to their promising characteristics. In recent years, conducting polymers has attracted significant attention in the field of chemical sensors [6–8].

Nowadays, plastic substrate-based NH_3 sensors are attracting more attention, due to their intriguing properties including flexibility, shock resistance, lightweight and softness. They have a wide variety of applications in many fields including communication, environmental monitoring, industrial process, chemical processes, personal safety, energy storage and toxic pollutant detection for human health [9]. Development of gas sensor includes not only to improve its detection limit at lower concentration of gas but also to incorporate simple and inexpensive processes. Current demonstrates highly selective and sensitive polyaniline-based sensor films deposited on flexible polyethylene terephthalate (PET) substrate by in-situ polymerization process. The advantage of flexible substrate is that it cannot break even if it bends and can be placed in compact places. Polyaniline (PAni) is deposited on polyethylene terephthalate (PET) substrate by very simple in-situ chemical oxidative polymerization method. The in-situ deposition method is most advantageous, because large number of films can be deposited in a single run without consuming time and chemical. Further, the sensing performance of polyaniline sensor can be improved in terms

of selectivity, sensitivity and response/recovery times by incorporating α-Fe_2O_3 and WO_3 nanoparticles.

2 Experimental Aspects

2.1 Polyaniline (PAni) Flexible Sensor

2.1.1 Preparation of PAni Flexible Sensor Films

Polyaniline flexible sensors were prepared by depositing polyaniline on flexible polyethylene terephthalate (PET) substrate by in-situ chemical oxidative polymerization method. Polyaniline synthesized at room temperature. The detailed synthesis procedure is explained as follows:

Initially, aniline was added in a beaker containing 1 M HCl and stirred for 10 min on magnetic stirrer for complete liquefy. Ammonium persulphate (APS) was used as a solvent also dissolved in 1 M HCl solution and transferred drop wise in to the monomer (aniline) solution. Thin films of PAni were in-situ deposited on polyethylene terephthalate (PET) substrate, which was dipped vertically into the reaction mixture. The polymerization reaction was carried out for 7 h stirring. After the termination of polymerization process, films were removed from the polyaniline solution and washed with distilled water. Deposited green coloured polyaniline on the flexible substrate was the emeraldine salt form (ES). The emeraldine salt form of polyaniline was terminated to emeraldine base with treatment of 0.1 M ammonia solution. The whole process was carried out at room temperature.

The schematic for the deposition of PAni on PET substrate with its chemical reaction is shown in the following Fig. 1.

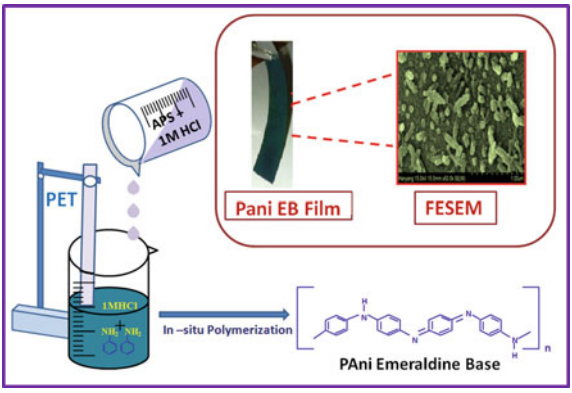

Fig. 1 Schematic synthesis of PAni flexible sensor

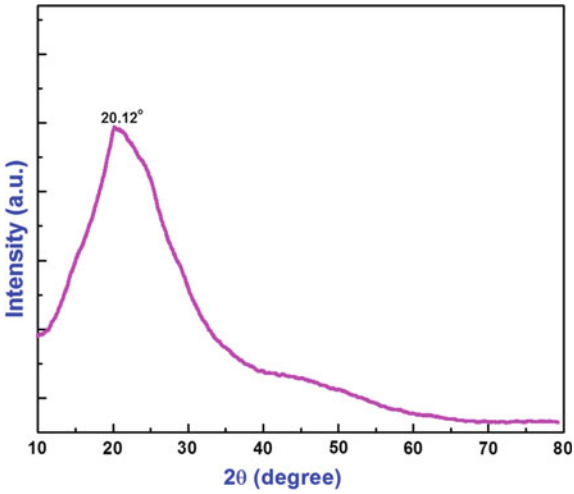

Fig. 2 XRD pattern of PAni flexible film

2.1.2 X-Ray Diffraction (XRD)

Figure 2 shows the XRD pattern of PAni flexible film. A broad diffraction peak in the range of $2\theta = 15-35°$ was observed for PAni flexible and is presented in Fig. 2. This peak shows the characteristics of amorphous nature of the emeraldine base form of PAni [9].

2.1.3 Fourier Transform Infrared Spectroscopy (FTIR) of PAni Flexible Film

FTIR spectroscopy provides valuable information about chemical structure and formation of PAni. FTIR spectra of PAni flexible films prepared by in-situ polymerization method at room temperatures was recorded in the range of 400−4000 cm^{-1} and presented in Fig. 3. The peaks observed at 802, 804 and 801 cm^{-1} for PAni flexible sensor are due to out of plane deformation of C–H in para-disubstituted benzene rings present in PAni. The peaks at 1450, 1496 and 1472 cm^{-1} are due to C–C stretching of benzenoid ring. The peaks at 1559, 1591 and 1557 cm^{-1} are the characteristics peak of C=C stretching of quinoid ring present in PANi. Moreover, Fig. 3 shows all the prominent FTIR peaks of PAni flexible sensor with their assignment. Thus the FTIR spectra confirmed the formation of PAni.

2.1.4 Field Emission Scanning Electron Microscopy (FESEM)

Surface morphology of PAni flexible film prepared at room temperature was carried using FESEM micrographs. A close look of FESEM micrograph of PAni synthesized

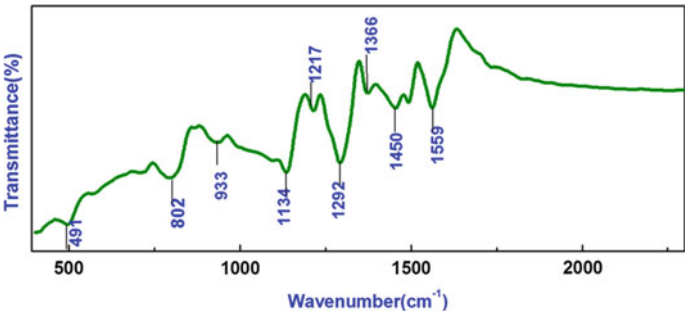

Fig. 3 FTIR spectroscopy of PAni flexible film

Fig. 4 FESEM images of PAni flexible film

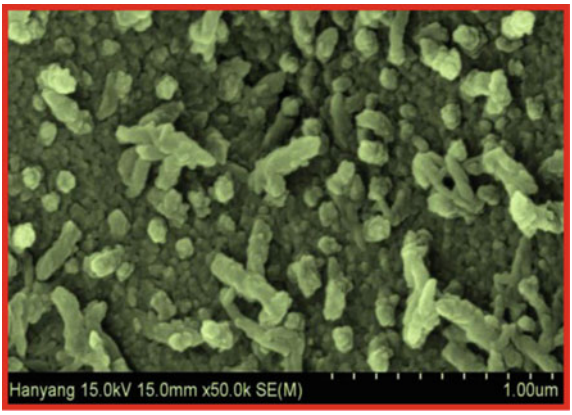

room temperature in Fig. 4 demonstrates dispersion of broken PAni fibres in the sea of granular PAni matrix. The advantage of such type of morphology is that it can provide high surface to volume ratio which can easily diffuse adsorbed gas molecules, into and out of the film structure [10]. This is the essential condition for gas sensing applications [11].

2.1.5 Gas Sensing Properties of Flexible PAni Sensor

In order to compute the response for different gases, the change in resistance of PAni flexible films was measured in presence of air and test gas ambient. In order to measure the response in terms of change in resistance two silver electrode contacts, 1 cm apart from each other were made on flexible film. Keithley electrometer (Model: 6514) was used to gauge the change in resistance. All the gas sensing study was carried out at room temperature in a home-built airtight stainless steel chamber (Volume: 250 cc) containing sample holder geometry. Different test gases such as NH_3, H_2S, CH_3OH, NO_2 and C_2H_5OH were procured from Space Cryo Gases Pvt.

Ltd., India in the form of gas-filled canisters (Volume: 0.5 L) with 1000 ppm concentration. A known concentration of gas in chamber was injected by using the syringe. Recovery of the sensors was achieved by opening the lid of stainless still chamber. The changes in the resistance of flexible films were recorded as function of time via computer interfaced 6514 Keithley electrometer. The response of flexible PAni sensor was calculated using as follows:

$$\text{Response } (\%) = \frac{R_a - R_g}{R_a} \times 100$$

where R_a is the resistance of sensor in presence of air and R_g is the resistance of sensor in presence of target gas.

2.1.6 Selectivity of PAni Flexible Sensor

Selectivity is the ability of a sensor that can distinguish one kind of gas among the different kinds of gases. Figure 5 shows the histogram of selectivity study of prepared flexible PAni sensor film against different toxic gases including NH_3, C_2H_5OH, H_2S, CH_3OH and NO_2 with each having 100 ppm concentration operating at room temperature. As seen in Fig. 3, flexible PAni film found to be highly selective and sensitive to NH_3 gas compared to other test gases. This confirmed the selectivity of flexible PAni sensor film for NH_3 gas. The porous structure provides higher surface area to volume ratio, which leads to increase in the surface area for the adsorption of gas molecules as well as offers more chemical reactions to arise at the interface and eventually results in increase in gas response [12].

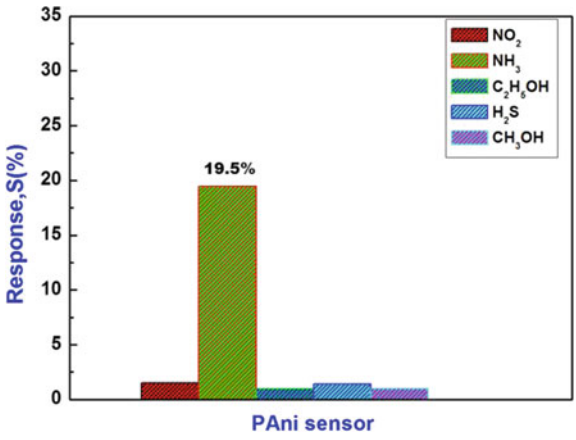

Fig. 5 Selectivity study of flexible PAni film towards different gases

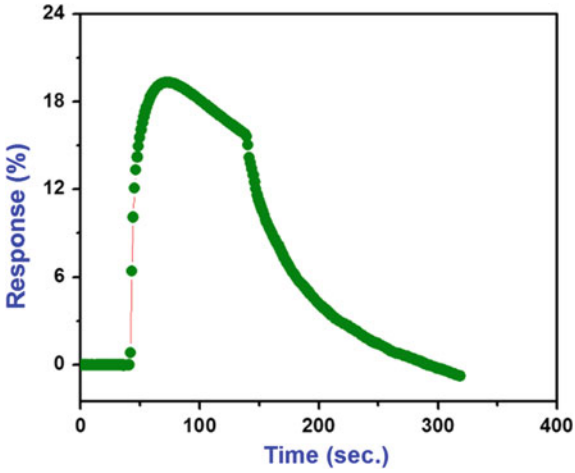

Fig. 6 Gas response study of PAni Sensor

2.1.7 Gas Response of PAni Flexible Sensor

Figure 6 shows the plot of response as a function of time for PAni flexible sensor towards 100 ppm of NH_3 gas. It should be noted that the flexible sensor film is capable to sense NH_3 gas at room temperature. Sudden increase in resistance value was observed upon interaction of NH_3 gas with very fast response (20 s) and recovery time (220 s).

2.1.8 Gas Sensing Mechanism

It is seen that resistance increases with respect to time when the PAni sensor is exposed to NH_3 gas. This increase in PAni sensor resistance after exposure to NH_3 gas can be attributed to the interaction between the reactive sites of PAni sensitive layer and NH_3 gas molecules. Here we have used PAni emeraldine base which is in the state of half oxidized and half reduced. Therefore, PAni (EB) has neutral state, when PAni (EB) sensor is exposed to NH_3 gas, due to reducing nature of NH_3 (electron-donating property) it can accept H^+ ions from PAni (EB) and forms ammonium ion, this again decreases the doping level of PAni [13] and PAni is converted into pernigraniline base (fully oxidized) form [14]. Due to the loss of H^+ ions, density of electrons gets increased and PAni becomes more negative, due to this resistance of PAni sensor increases and the conductivity decreases [15, 16]. The pernigraniline base is unstable state of PAni, because when PAni sensor is exposed to air, it can capture hydrogen from ammonium ion and restore its initial doping level of PAni (EB) [17, 18]. This added H^+ ion forms N–H bond due to this resistance of sensor decreases [19, 20] and attains initial baseline resistance value. The possible reaction is schematically shown in Fig. 7.

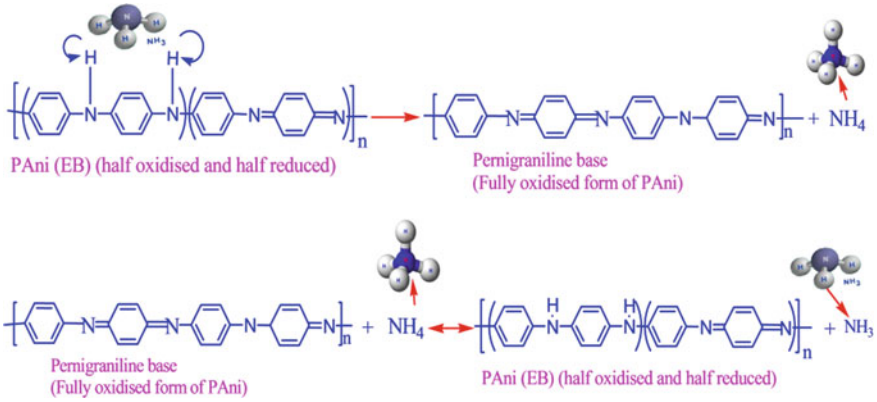

Fig. 7 Gas sensing mechanism of PAni flexible sensor to NH_3 gas

As discussed above the interaction between PAni and NH_3 was occurred at room temperature and showed remarkable results. Therefore, it is concluded that PAni operates better at room temperature and shows good NH_3 sensitivity.

2.2 PAni/α-Fe_2O_3 Hybrid Nanocomposite Flexible Sensor

2.2.1 Deposition of PAni/α-Fe_2O_3 by in-Situ Polymerization

Flexible PAni/α-Fe_2O_3 hybrid nanocomposite flexible films were deposited on polyethylene terephthalate (PET) substrate by in-situ polymerization process. In order to achieve the better performance of PAni sensor films, polyaniline was chemically modified by adding α-Fe_2O_3 (50 wt%) filler particles in the PAni matrix during de-doping of PAni. Schematic diagram in Fig. 8 demonstrates the detailed process for the preparation of PAni/α-Fe_2O_3 hybrid nanocomposite flexible films.

2.2.2 X-Ray Diffraction (XRD)

Figure 9b shows the XRD patterns of as-synthesized PAni/α-Fe_2O_3 nanocomposite flexible films. From the XRD pattern of pure PAni, single broad diffraction peak (Fig. 2) with a small shoulder peak in the range of $2\theta = 20-30°$ was evidenced. Which is higher in enclosed area and intensity, but in the case of composite, i.e. PAni/α-Fe_2O_3 (Fig. 9a) several new planes were evidenced. The broad nature of XRD pattern clearly indicated amorphous behaviour of prepared PAni. XRD pattern of α-Fe_2O_3 is in Fig. 9b was crystallized in hexagonal phase [21]. All the peaks well matched with the JCPDs data card no. 85-0985. In the present case, the change in peak position of PAni may be due to a change of its structure when composite

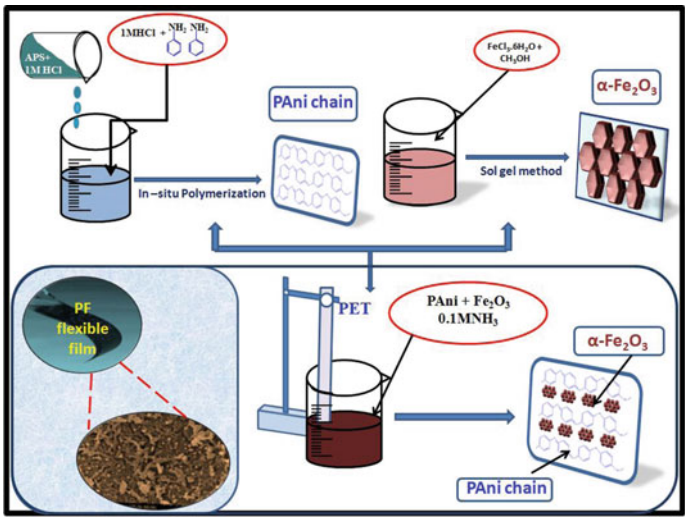

Fig. 8 Schematic diagram for preparation of PAni/α-Fe_2O_3 flexible sensor film

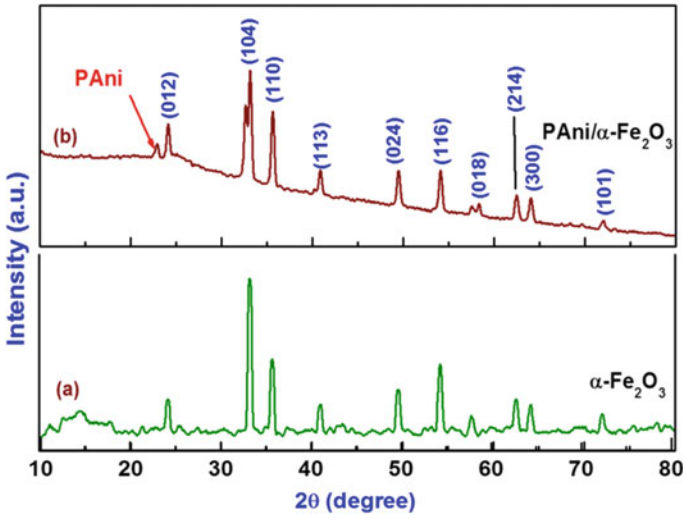

Fig. 9 XRD pattern of **a** α-Fe_2O_3 and **b** PAni/α-Fe_2O_3 hybrid nanocomposite flexible film

is formed. The other peaks of PAni/α-Fe_2O_3 hybrid nanocomposite were similar to the peaks observed in XRD pattern of α-Fe_2O_3 [21], confirming the type of α-Fe_2O_3 crystal structure which was well-maintained after preparing composite in base media. The XRD result showed the presence of two different phases, i.e. PAni and α-Fe_2O_3, supporting for the formation of PAni/α-Fe_2O_3 nanocomposite.

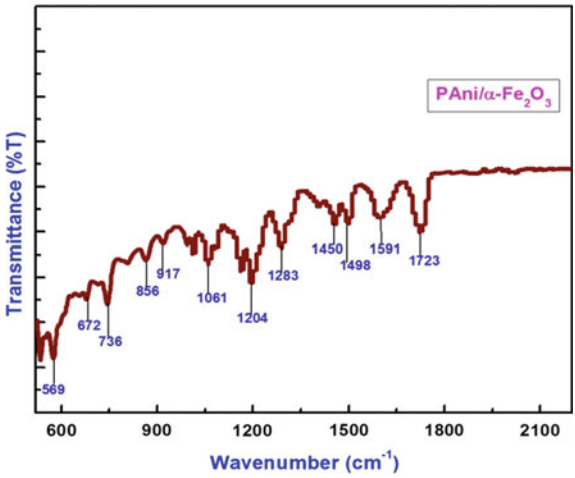

Fig. 10 FTIR spectra of PAni/α-Fe_2O_3 hybrid nanocomposite flexible film

2.2.3 Fourier Transform Infrared Spectroscopy (FTIR)

To identify the presence of α-Fe_2O_3 in the composite and to observe the association between the PAni and the α-Fe_2O_3, FTIR spectra of flexible PAni/α-Fe_2O_3 hybrid nanocomposite flexible film was recorded. The FTIR spectra of PAni/α-Fe_2O_3 hybrid nanocomposite flexible film is as shown in Fig. 10. The peak at 569 cm^{-1} is the characteristic of the Fe-O stretching vibration, clearly supported for the presence of α-Fe_2O_3 in PAni matrix and shift of peak suggested the interaction of α-Fe_2O_3 with polyaniline [22–24]

2.2.4 Field Emission Scanning Electron Microscopy (FESEM)

Figure 11 shows the FESEM micrographs of α-Fe_2O_3, and PAni/α-Fe_2O_3 nanocomposite flexible films prepared by in-situ polymerization process. Figure 11a shows the FESEM micrograph of α-Fe_2O_3 film prepared from a powder annealed at 700 °C. The particles are elongated-type with few reminiscences of the hexagonal corundum structure of α-Fe_2O_3. From Fig. 11b it is seen that α-Fe_2O_3 nanoparticles are embedded within the net-like structure consisting of PAni fibres. The FESEM micrograph of PAni/α-Fe_2O_3 hybrid nanocomposite suggesting a significant change in the original individual morphologies. As a consequence, PAni/α-Fe_2O_3 hybrid nanocomposite film (Fig. 11b) possessed both well-defined forms, i.e. PAni and α-Fe_2O_3, implying a highly micro-porous structure. Such a porous structure can provide a path for insertion and extraction of gas molecules and ensure high rate of reaction.

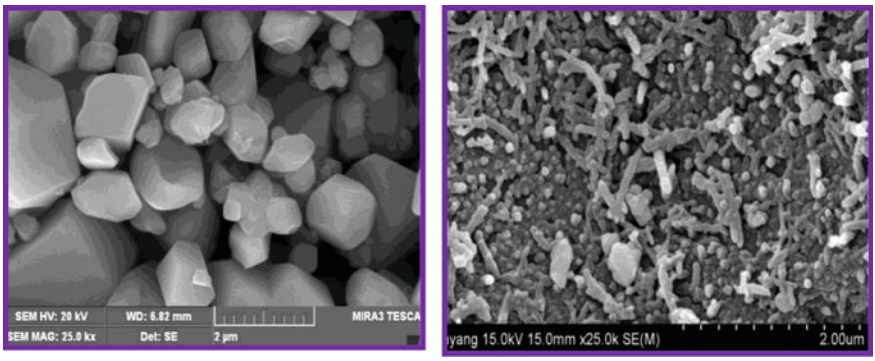

Fig. 11 FESEM images of **a** α-Fe_2O_3 and **b** PAni/α-Fe_2O_3 (50%) hybrid nanocomposite flexible film

2.2.5 Gas Sensing Study of PAni/α-Fe_2O_3 Hybrid Nanocomposite Flexible Sensor

Gas sensing test of prepared PAni/α-Fe_2O_3 hybrid nanocomposite film was carried out in terms of selectivity, sensitivity and response/recovery times at room temperature. The sensing performance was measured under different concentrations of analyte species.

2.2.6 Selectivity of PAni/α-Fe_2O_3 Hybrid Nanocomposite Flexible Sensor

High selectivity is an important parameter for excellent working of sensor. To confirm the selectivity of the sensor to a particular gas, chemo-resistive properties were studied for PAni and PAni/α-Fe_2O_3 hybrid nanocomposite flexible sensors by exposing sequentially for different gases. Selectivity study of PAni/α-Fe_2O_3 hybrid nanocomposite flexible sensor was performed for NH_3, H_2S, C_2H_5OH, CH_3OH and NO_2 at 100 ppm concentration of each gas and given in Fig. 12. Resistance of PAni flexible sensor was not changed to C_2H_5OH and CH_3OH gases, hence, the response was considered to be zero, confirming that these gases are not interacting with the PAni flexible sensor. But when PAni flexible sensor was exposed to NO_2 and H_2S gases, it showed responses of 3% and 0.5%, respectively, considerably lower as compared to NH_3 (39%) gas.

Selectivity study clearly supported that PAni/α-Fe_2O_3 hybrid nanocomposite flexible sensor is more selective to NH_3 than other test gases and exhibited higher selectivity to NH_3 when compared to pure PAni. After addition of α-Fe_2O_3 nanoparticles in PAni matrix, quinoid structure (higher conjugation) of PAni is transformed into benzenoid structure (lower conjugation) and made it more selective to target NH_3 gas [25].

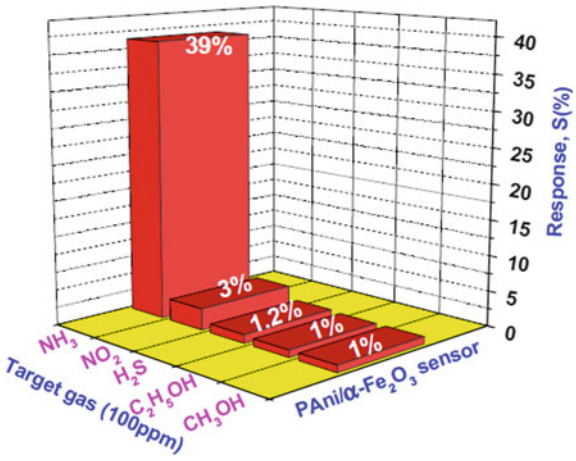

Fig. 12 Selectivity of PAni/α-Fe_2O_3 flexible sensor to 100 ppm of oxidizing and reducing gases

2.2.7 NH_3 Gas Response Study of PAni/α-Fe_2O_3 Hybrid Nanocomposite Flexible Sensor

The performance of PAni/α-Fe_2O_3 hybrid nanocomposite flexible sensor is determined by measuring the sensor response for different ammonia gas concentrations at room temperature (35 °C). Figure 13 reveals that PAni/α-Fe_2O_3 hybrid nanocomposite flexible sensor is sensitive to very low concentration (10 ppm) of NH_3. From Fig. 13 it is exposed that the response of PAni/α-Fe_2O_3 hybrid nanocomposite flexible sensor is increased with rising NH_3 gas concentration. At higher concentration of ammonia (100 ppm), it showed not only the maximum response (39%) but also

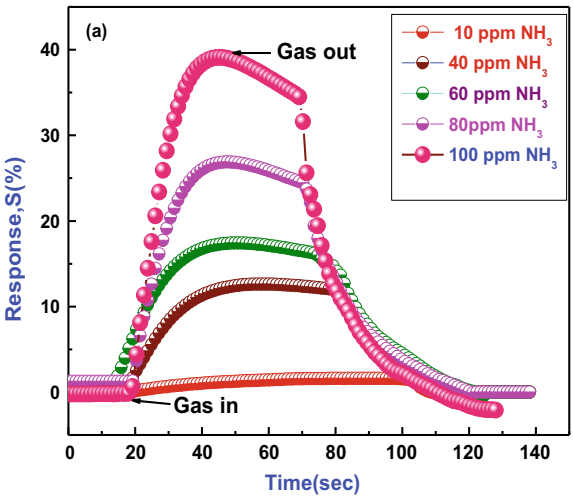

Fig. 13 Plot of response versus NH_3 concentration (10–100 ppm) PAni/α-Fe_2O_3 hybrid nanocomposite flexible sensor

very short response time (27 s), with increase in concentration the number of gas molecules interacting with sensor surface increases as well.

2.3 PAni-WO_3 Flexible Sensor

2.3.1 Fabrication of Flexible PAni-WO_3 Sensor Films

PAni–WO_3 nanocomposite sensors were prepared on flexible PET substrate by in-situ chemical oxidative polymerization route using aniline (C_6H_7N) as monomer and ammonium persulfate [$(NH_4)2S_2O_8$] as an oxidant in hydrochloric acid (HCl) solution, resulting procedure is as follows: 0.1 M APS was added into an aqueous mixture containing 0.2 M C_6H_7N and 1 M HCl and then kept at room temperature for 7 h followed by continuous stirring. After polymerization, a green precipitate of the emeraldine salt form of PAni was formed. Subsequently, de-doping of the emeraldine salt was done through 0.1 M ammonia solution and at the same instant flexible PET substrates were immersed in the solution.

Tungsten oxide (WO_3) nanoparticles (NPs) were synthesized by sol-gel method from tungsten hexachloride (WCl_6) and methanol (CH_3OH). The reaction mixture of WCl_6 and CH_3OH was stirred vigorously at 60 °C for 2 h, leading to the formation of a gel. This gel was further heated for 15 min to obtain powder and then dried in air under an IR lamp for 1 h. The resulting powder was annealed at 700 °C for 1 h in air to obtain nanocrystalline WO_3 powder. As-synthesized WO_3 nanoparticles (10–50 wt%) are incorporated into the PAni matrix at the time of de-doping of PAni and stirred for 3 h for the formation of resulting nanocomposite on PET substrate.

2.3.2 X-Ray Diffraction (XRD)

Figure 14 shows the XRD pattern of pure PAni, WO_3 and flexible PAni–WO_3 hybrid nanocomposite films. Figure 14a represents the XRD pattern of WO_3. Observed

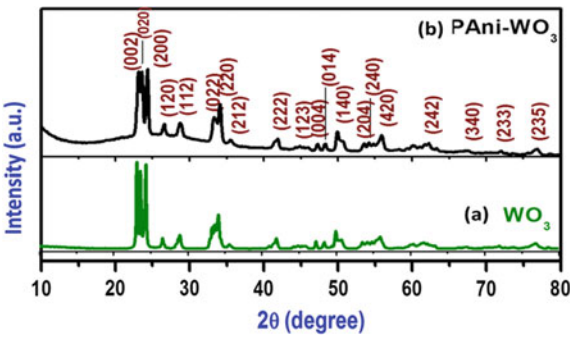

Fig. 14 XRD pattern of **a** WO_3 and **b** PAni–WO_3 hybrid nanocomposite flexible film

diffraction peaks indicate the formation of pure orthorhombic WO_3 with lattice constants a = 7.301 Å, b = 7.521 Å and c = 7.687 Å. All diffraction peaks along with lattice constants are indexed well with the JCPDS file number 71-0131. The XRD pattern of PAni–WO_3 hybrid nanocomposite (Fig. 14b) suggests that the prominent diffraction peaks of WO_3 are also present in PAni–WO_3 nanocomposites, indicating that the crystallization performance of WO_3 was not influenced because of PAni. It confirms that no chemical transformation in the WO_3 occurs upon mixing them with PAni. The broad peak of PAni was found to overlap with the large diffraction intensities of (002), (020) and (200) crystal faces of WO_3. The increase in intensities of PAni–WO_3 hybrid nanocomposite suggests that the WO_3 NPs are highly dispersed in the PAni matrix.

2.3.3 Field Emission Scanning Electron Microscopy (FESEM)

The field emission scanning electron microscopy (FESEM) was carried out to study the surface morphology of WO_3 and PAni-WO_3 (50 wt%) flexible films. Figure 15 shows the FESEM images of WO_3 and in-situ chemical oxidative mediated flexible PAni–WO_3 (50%) hybrid nanocomposite films. Figure 15a shows the FESEM micrograph of WO_3 prepared by sol-gel method, demonstrating approximately spherical shaped WO_3 nanoparticles of the size of 50–100 nm diameters are uniformly distributed with porous morphology. FESEM micrograph of PAni–WO_3 (50%) hybrid nanocomposite flexible film (Fig. 15b) shows that the WO_3 nanoparticles are well embedded within the mesh-like nanofiber structure of PAni matrix, signifying a considerable variation of the individual morphologies of PAni and WO_3. FESEM micrographs undoubtedly show that the morphology of hybrid nanocomposites is considerably affected due to the different loadings concentration of WO3 nanoparticles in PAni template. Incorporation of WO_3 nanoparticles in the PAni matrix leads to a highly micro-porous morphology, which is advantageous for enhancing gas sensing properties by appropriating insertion and extraction of gas molecules.

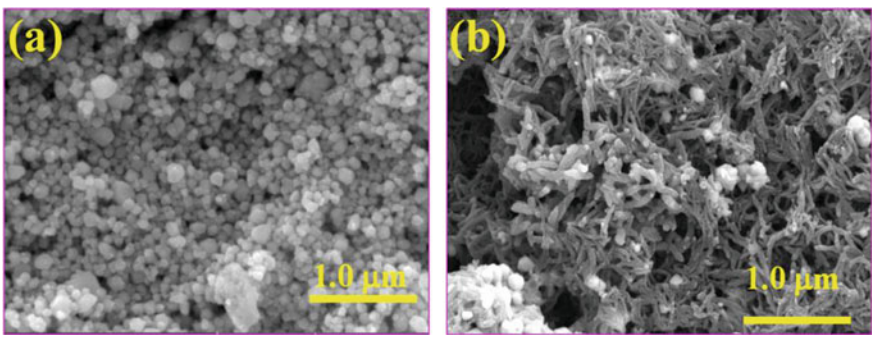

Fig. 15 FESEM images of **a** WO_3 and **b** PAni–WO_3 (50 wt%) hybrid nanocomposite flexible films

2.3.4 Gas Sensing Properties

The gas sensing activities of hybrid PAni-WO_3 flexible sensors were precisely investigated using custom-developed room temperature gas sensing set up coupled with programmable electrometer. (KEITHLEY 6514). The gas sensing parameters in terms of selectivity, reproducibility, response, response/recovery times, stability for different concentrations of selective gas for PAni–WO_3 hybrid nanocomposites flexible are tested for oxidizing and reducing gases. The known concentration of gas was taken from gas canister containing 1000 ppm as total concentration of gas and it was injected into the gas chamber with the help syringe. On exposure to gas the sensor resistance increased, attained stable state value and started to decrease on exposure to air.

2.3.5 Response to Various NH_3 Concentrations of PAni–WO_3 (50%) Hybrid Nanocomposite Flexible Sensor

The dynamic (time-dependent) gas response profile of PAni–WO_3 (50%) hybrid nanocomposite flexible sensor towards 1–100 ppm concentration of NH_3 gas is shown in Fig. 16. The dynamic response plot shows that the increase in concentration of NH_3 gas leads to increase in the response of hybrid sensor. Moreover, PAni-WO_3 (50%) hybrid flexible sensor is sensitive to very low 1 ppm concentration of NH_3 gas with reasonable response of 9%. At higher concentration of NH_3 (100 ppm), sensor showed a maximum response of 121% along with a short response time of 32 s. At higher concentration, NH_3 gas molecules cover a maximum surface area of sensor and consequently more and more NH_3 molecules participated in surface reactions. Thus, increasing surface reactions leads to higher response. On the other hand, NH_3 gas molecules cover minimum surface area at lower concentration and therefore less surface reactions occur at the sensor surface, resulting in low response.

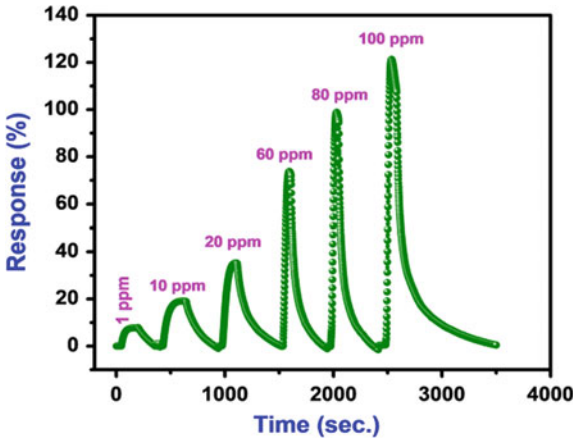

Fig. 16 Response study of flexible PAni–WO_3 (50%) hybrid nanocomposites to 5–100 ppm of NH_3 gas

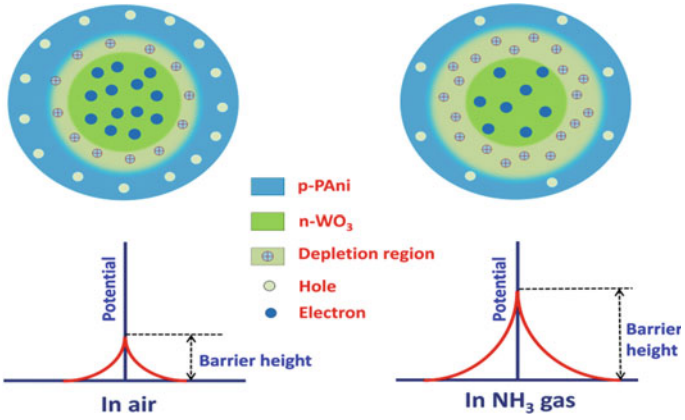

Fig. 17 Schematic sensing model of flexible PAni–WO_3 hybrid nanocomposite sensor when exposed to air and NH_3 gas at room temperature

2.3.6 Gas Sensing Mechanism

In case of pure PAni sensor, the response is mainly attributed to the protonation and deprotonation resulting from adsorption and desorption of NH_3 gas molecules, respectively. Herein, emeraldine salt form of PAni is converted to emeraldine base form on exposure to NH_3 gas on sensor surface. Consequently, increase in resistance occurred because of decrease in hole density in PAni [26, 27]. For hybrid films apart from the above-mentioned mechanism, the gas sensing is predominantly based on the trapping of NH_3 gas molecules in nanocomposite and the change in the surface resistance of the nanocomposites when the gas adsorb and react with it. Figure 17 represents the schematic sensing model of PAni-WO_3 hybrid flexible sensor when exposed to air, and NH_3 gas at room temperature. The PAni–WO_3 hybrid nanocomposite is more porous due to insertion of WO_3 nanoparticles in the PAni matrix, as observed from FESEM, producing oxygen chemisorptions centres with localized donor and acceptor states on the surface of the film. These centres are filled by adsorbing oxygen from atmospheric air. During polymerization of polyaniline, the p-n heterojunction has formed between p-type PAni and n-type WO_3. When the nanocomposite was exposed to air, the surface of PAni was covered with chemisorbed oxygen at room temperature. Due to electron and hole transfer between PAni and WO_3, a depletion layer is formed at the interface of PAni and WO_3, resulting into formation of heterojunction barrier (shown in Fig. 17). PAni is a p-type material, since majority charge carriers are holes. PAni is a host material in PAni–WO_3 hybrid nanocomposite sensor; therefore, it contributes to a major part in gas sensing mechanism. As NH_3 is a reducing gas hence it has electron-donating property. When the PAni-WO_3 hybrid flexible sensor is exposed to NH_3 gas at room temperature, the free electrons, released due to interaction between NH_3 molecules and chemisorbed oxygen, neutralize the holes due to electron-hole combination resulting in decrease in

the hole concentration in PAni. This reduces the carrier concentration of the heterojunction, and potential barrier height increases followed by increase in the resistance of hybrid nanocomposite sensor [28].

3 Conclusion

PAni, PAni/α-Fe_2O_3 and PAni–WO_3 hybrid nanocomposite flexible sensor films were synthesized successfully by in-situ chemical oxidative polymerization method and characterized by various techniques for structural, chemical and morphological properties. XRD pattern revealed the presence of both the phases of amorphous PAni and crystalline α-Fe_2O_3. Structural analysis confirmed the presence of both the amorphous (PAni) and crystalline phases (WO_3) and in the PAni–WO_3 hybrid nanocomposite. FTIR spectra showed characteristic peak of C–N stretching of primary aromatic amine ring at 1283 cm^{-1}. Peak of C=N stretching of aromatic ring is aroused at 1490 cm^{-1}. FESEM micrograph showed that α-Fe_2O_3 nanoparticles are embedded within the net-like structure consisting of PAni fibres in the case of PAni/α-Fe_2O_3 hybrid nanocomposite, suggesting a significant change in the original individual morphologies. Morphological investigation showed that the PAni-WO_3 hybrid flexible film exhibits porous and fibrous structure which is more favourable for enhancing gas sensing properties of hybrid nanocomposite. The sensing parameters like response, response/recovery times, dynamic response were determined for the NH_3 concentrations from 5 ppm to 100 ppm range. The PAni-WO_3 hybrid flexible sensor showed a maximum response of 121% with short response time of 32 s. The used synthesis strategy is scalable and commercial approach to fabricate flexible PAni–Fe_2O_3 and PAni–WO_3 hybrid nanocomposite sensors, which can open inventive pathways for the development of other PAni-based hybrid nanocomposite materials appropriate for toxic NH_3 detection, which is a subject of ongoing research study.

References

1. P. Kubersky, T. Syrovy, A. Hamacek, S. Nespurek, J. Stejskal, Proc. Eng. **120**, 614–617 (2015)
2. A. Arena, N. Donato, G. Saitta, A. Bonavita, G. Rizzo, G. Neri, Sens. Actuators B **145**, 488–494 (2010)
3. K. Mitsubayashi, Y. Wakabayashi, D. Murotomi, T. Yamada, T. Kawase, S. Iwagaki, I. Karube, Sens. Actuators B **95**, 373–377 (2003)
4. K. Parikh, K. Cattanach, R. Rao, D.S. Suh, A. Wu, S.K. Manohar, Sens. Actuators B **113**, 55–63 (2006)
5. P.G. Su, C.T. Lee, C.Y. Chou, K.H. Cheng, Y.S. Chuang, Sens. Actuators B **139**, 488–493 (2009)
6. P.S. Shewale, V.B. Patil, S.W. Shin, J.H. Kim, M.D. Uplane, Sens. Actuators B **186**, 226 (2013)
7. N. Guernion, R.J. Ewen, K. Pihlainen, Synth. Met. **126**(2–3), 301 (2002)

8. B.T. Raut, M.A. Chougule, S.R. Nalage, D.S. Dalavi, S. Mali, P.S. Patil, V.B. Patil, Ceram. Inter. **8**(7), 5501 (2012)
9. M.C. Mcalpine, H. Ahmad, D. Wang, J.R. Heath, Nat. Mater. **6**, 379 (2007)
10. J.P. Pouget, Macromolecules **24**, 779 (1991)
11. S. Virji, J. Huang, R.B. Kaner, B.H. Weiller, Nano Lett. **4**, 491 (2004)
12. S.T. Navale, G.D. Khuspe, M.A. Chougule, V.B. Patil, Ceram. Interfaces **40**, 8013 (2014)
13. H. Tai, Y. Jiang, G. Xie, J. Yu, X. Chen, Sens. Actuators, B 18, 644 (2007)
14. A. Airoudj, D. Debarnot, B. Beche, F. Poncin, Anal. Chem. **80**, 9188 (2008)
15. P. Barta, T. Kugler, W.R. Salaneck, A.P. Monkman, J. Libert, R. Lazzaroni, J.L. Bredas, Synth. Met. **93**, 83 (1998)
16. H. Bai, G. Shi, Sensors **7**, 267 (2007)
17. D. Xie, Y.D. Jiang, W. Pan, D. Li, Z.M. Wu, Y.R. Li, Sens. Actuators, B **81**, 158 (2002)
18. S. Virji, R.B. Kaner, B.H. Weiller, J. Phys. Chem. B **110**, 22266 (2006)
19. J. Huang, S. Virji, B.H. Weiller, R.B. Kaner, J. Am. Chem. Soc. **125**, 314 (2003)
20. Y. Liao, C. Zhang, Y. Zhang, V. Strong, J. Tang, X.G. Li, K.K. zadeh, E.M.V. Hoek, K.L. Wang, R.B. Kaner, Nano Lett. **11**, 954 (2011)
21. J. Huang, S. Virji, B.H. Weiller, R.B. Kaner, Chem. Eur. J. **10**, 1314 (2004)
22. G.D. Khuspe, S.T. Navale, D.K. Bandgar, R.D. Sakhare, M.A. Chougule, V.B. Patil, Electron. Mater. Lett. **10**, 191 (2014)
23. C. Yang, J. Du, Q. Peng, R. Qiao, W. Chen, C. Xu, Z. Shuai, M. Gao, J. Phys. Chem. B **113**, 5052 (2009)
24. V.A. Khatil, S.B. Kondawar, V.A. Tabhane, Anal. Bioanal. Electrochem. **3**, 614 (2011)
25. K.R. Reddy, K.P. Lee, A.I. Gopalan, J. Appl. Polym. Sci. **106**, 1181 (2007)
26. S.J. Park, O.S. Kwon, J.E. Lee, J. Jang, H. Yoon, Sensors **14**, 3604 (2014)
27. Z.F. Li, F.D. Blum, M.F. Bertino, C.S. Kim, S.K. Pillalamarri, Sens. Actuators B **134**, 31–35 (2008)
28. R. Arora, A. Srivastav, U.K. Mandal, Inter. J. Modern Eng. Res. **2**, 2384–2395 (2012)

Vanadium Oxide Thin Films for Optical and Gas Sensing Applications

Ravish Kumar Jain and Atul Khanna

Abstract The transition metal-oxides are a versatile class of materials with numerous applications. In this chapter, the optical and gas sensing properties of the vanadium oxide thin films have been reviewed keeping in view their applications in energy efficient optical windows and solid state gas sensors. Vanadium exists in variable valence states and exhibit Magneli pahses such as VO_2, V_2O_3, V_6O_{13}, V_2O_5 etc. VO_2 and V_2O_5 are the two most widely studied oxides of vanadium among all of its Magneli phases. VO_2 thin films exhibit metal–insulator transition close to room temperature (68 °C) and find application as thermo-chromic coatings. The changes in the electrical conductivity of V_2O_5 are reported to take place at higher temperatures and are attributed to the creation of oxygen defects and temporary distortion in the structure without any structural phase transition. The changes in optical transmittance of V_2O_5 with temperature are very small as compared to VO_2. However, better thermodynamic stability of V_2O_5 over VO_2 has inspired the research on enhancing the temperature dependent optical properties of the V_2O_5 films, and a correlation between their short-range structural properties and the temperature dependent optical transmission has been found. The results of the previous research carried out on vanadium oxide thin films are discussed in this chapter. V_2O_5 is a good gas sensing material since it shows large changes in the electrical resistance in the presence of some gases. The gas sensing mechanisms and various methods and parameters that have been used to tailor the sensor signal and response time towards different gases are discussed. The atomic structure, surface morphology and composition of the films play important role in determining the gas sensing characteristics. The information provided in this article shows that the physical properties of the V_2O_5 thin films can be modified significantly for their applications as thermo-chromic coatings and gas sensors.

R. K. Jain · A. Khanna (✉)
Sensors and Glass Physics Laboratory, Department of Physics, Guru Nanak Dev University, Amritsar 143005, Punjab, India
e-mail: atul.phy@gndu.ac.in

S. Kumar and D. K. Aswal (eds.), *Recent Advances in Thin Films*, Materials Horizons: From Nature to Nanomaterials, https://doi.org/10.1007/978-981-15-6116-0_22

1 Introduction

Transition metal-oxide thin films are one of the most interesting class of materials with important physical properties such as optical transparency, wide band gap, thermo-chromism, electro-chromism, photo-chromism, gaso-chromism, magnetism, magnetoresistance, multiferroicity and optoelectronic properties that lead to a variety of potential applications of these materials [1–21]. The scientifically and technologically important materials from transition metal-oxide family are: TiO_2, WO_3, MoO_3, VO_2, V_2O_5, ZnO, HfO_2, ZrO_2, Nb_2O_5, Cr_2O_3, MnO_2,FeO, Fe_2O_3, CoO, etc. The transition metal-oxide films find applications in thin-film solar cells, electronic and optoelectronic devices, infra-red detectors, night vision cameras, memory devices, gas sensors, smart and self-cleaning windows, chromogenic window coatings, hydrophobic protective coatings, high-k dielectrics, wear resistant coatings, luminescent devices, magnetic field sensors, etc. [1–5, 7, 8, 18, 19, 21–37]. TiO_2 is widely investigated for its applications in thin-film solar cells as an electron transport layer [22]. MoO_3, WO_3 and V_2O_5 films have been used as electro-chromic coatings for making energy efficient windows [1, 5]. Transition metal-oxide films are excellent materials for gas sensing application. A variety of gases such as carbon monoxide (CO), carbon dioxide (CO_2), nitrogen dioxide (NO_2), hydrogen sulphide (H_2S), hydrogen (H_2), ethanol (C_2H_5OH), acetone (C_3H_6O), ammonia (NH_3), methane (CH_4), propane (C_3H_8), etc. can be sensed by these films [31–33]. Hafnia (HfO_2) films have been studied for their potential to act as hydrophobic, anti-reflective and protective top coatings [26]. HfO_2 and zirconia (ZrO_2) coatings have also been explored as highly insulating layers for gate-dielectrics [34, 35]. The transition metal-oxides are bestowed with a variety of properties owing to their electronic configuration with partially filled d-orbitals and highly correlated electron system. In addition, the hybridization of p-energy states of oxygen with d-orbitals of metal strongly influences the electronic structure [38–40]. The sub-oxides of the transition metals are known, to possess metallic character which is supposed to be due to the extension of non-bonding t_{2g} to overlap and form a narrow-conduction band [41]. The transport properties of the transition metal-oxides are governed mainly by two types of energy gaps: Mott-Hubbard gap that is related to the correlated electrons of d-orbital (d-d gap) and charge transfer gap that arises due to the hybridization of d-and p-energy states of transition metal and oxygen ions, respectively (d-p gap).

In general, the transition metals with less than half-filled d-orbital configuration form Mott-insulator type of materials and transition metals with more than half-filled d-orbital configurations form charge transfer type of materials [42]. The detailed description of theoretical models used to explain the peculiar electrical transport properties and metal–insulator transformation in the transition metal-oxides is given by Imada et al. in their comprehensive review article [42]. The d-d gap Mott-insulator materials can be made to transform into d-p gap charge transfer materials by a change of chemical composition (doped/composite materials) according to the desired application requirements [42]. The electrical properties of the materials change abruptly when energy equivalent to any of these gaps is available to the material in the form of heat, light or electrical potential and therefore such materials are

thermo-chromic, photo-chromic and electro-chromic, respectively. Various methods are being explored to tailor these energy states for the desired applications [43–46].

There are several methods available for the synthesis of transition metal-oxide thin films which can be broadly classified into two categories: chemical and physical routes. The chemical methods include chemical vapour deposition, spin-coating, dip-coating, spray pyrolysis, etc. whereas, the physical deposition methods include thermal evaporation, electron beam evaporation, magnetron-sputtering, pulsed laser deposition and molecular beam epitaxy, etc. [3–8, 11, 27–29, 31, 32]. The physical deposition methods are preferred because these are cleaner and more compatible for large scale production as well as for integrated device fabrication, as compared to chemical methods. In the last few decades, the effects of various deposition parameters such as base and working pressure, substrates, substrate-temperature, deposition rate, film thickness, partial pressure of suitable gases, etc. have been studied by a large number of researchers and the results of their studies have lead to the fine control over various physical properties of the transition metal-oxide thin films. Nowadays, to further extend the limits of physical properties of various thin films and discover newer properties and phenomena, the combination of materials, multilayer stacking, patterning by lithography and etching techniques, etc. are being explored. Doping of different materials into the host matrix films and nano-structuring of the surface are the two leading methods to tailor the chromogenic properties of the materials.

2 Physical Properties and Applications of Vanadium Oxide Thin Films

This chapter focuses on the versatile vanadium oxide thin films, their crystal structure, optical and electrical properties along with their potential applications.

2.1 Chromogenic Properties of Vanadium Oxide Films

An interesting property of the transition metal-oxides such as vanadium oxide, molybdenum oxide, titanium oxide is the existence of their sub-stochiometric oxides, also known as Magneli phases. Vanadium exhibits highest number of Magneli phases that include VO_2, V_2O_3, V_5O_9, V_6O_{13}, V_2O_5, etc. [33]. This interesting property to exist in multiple valence states has always attracted the attention of materials scientists towards vanadium oxide and other such transition metal-oxides. Out of the various oxides of vanadium, VO_2 and V_2O_5 possess very interesting and useful chromogenic properties. VO_2 films show large thermo-chromic behaviour and V_2O_5 films possess electro-chromic properties [1, 2]. Granqvist presented an overview of the potential materials that can be used as energy efficient window coatings [1, 2]. The materials that exhibit abrupt changes in the electrical conductivity with some stimulus can be used for various applications such as thermal and optical switching.

VO_2 is a very good example of materials which shows thermo-chromic effect at 68 °C in bulk samples [1, 2]. VO_2 changes from low-temperature monoclinic structure which is semi-conducting or low conductivity phase to high-temperature rutile structure which is metallic or high conductivity phase at 68 °C, and this process is reversible [1, 2, 43]. The change in the electrical properties is accompanied by large change in optical properties such that the films have high transmittance in the infra-red range for the low-temperature monoclinic phase and high reflectance (i.e. low transmittance) for infra-red rays in the high-temperature rutile phase. VO_2 exhibits the highest change in optical transmittance with temperature and it has transition temperature near to room temperature (~68 °C). Although, VO_2 has a good potential to be used as thermo-chromic coating, there are some difficulties that need to be resolved to make it suitable for applications. The basic requirements of a film to be used as energy efficient thermo-chromic coating are high luminous transmittance (T_{lum}), high solar modulating ability (ΔT_{sol}) and low transition temperature (T_c) [43]. Qian et al. have fabricated the films with periodicity of 210 nm, 440 nm, 580 nm and 1000 nm by dip-coating method on silica substrates patterned by reactive ion etching for which 2D polystyrene colloidal crystals were used as mask (Fig. 1) [43]. A significant difference in optical transmittance of patterned and planer VO_2 films at 25 and 90 °C (indicative of metal–insulator transition) and enhancement in the luminous and the infra-red transmission for VO_2 film with a periodic structure (moth-eye nanostructure) at both high and low temperatures has been reported (Fig. 2b) [43]. With a periodicity smaller than the wavelength of the light, anti-reflection action is produced and the transmittance is enhanced by about 10% along with increase in solar modulation of about 24.5% [43]. 3D AFM images and AFM cross-section profiles of VO_2 films with different periodicities and scanning electron microscopic cross-section image of film with periodicity 210 nm (Fig. 3) show uniform array of the tapered nanostructures grown perpendicular to the substrate without any fragments or clusters between the arrays [43].

Thin-film thickness and substrate temperature during deposition are two very important growth parameters that control the structural, optical, electrical and phase-transition properties of the films. Yang et al. have systematically studied the effect of thickness on the optical parameters of phase transition [47]. VO_2 films were prepared without substrate heating by DC magnetron-sputtering using V_2O_3 target, 200 W DC power, Ar and oxygen flow rates of 35 sccm and 15 sccm, respectively and then heat treated in vacuum at 450 °C for 5 min to obtain crystalline VO_2 films. Deposition time was changed to vary the thickness keeping all other parameters same. Large increase in solar modulation property was observed with an increase in thickness up to 90 nm and it decreased with further increase in the film thickness. Also the luminous transmittance value was 36.4% for 90 nm film (wavelength range: 380–780 nm) which is highest among all samples. It was reported that the value of transition temperature varied with thickness and it was different in the cooling and heating cycles. The heating rate was regulated by the temperature controller, but the cooling was natural and the rate of heat dissipation was different for different thicknesses and the variations in transition temperature values was more during cooling cycle [47]. The variation in T_c values indicates that the transition is not sharp which may be due

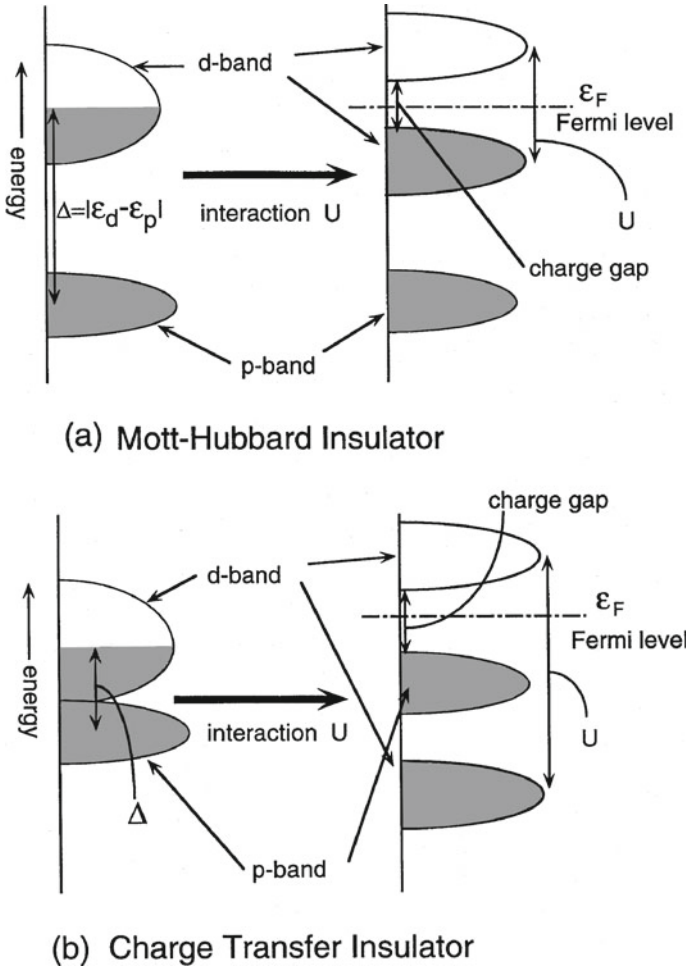

Fig. 1 Energy levels depicted schematically for **a** Mott-Hubbard insulator **b** Charge transfer insulator [42]. Reprinted figure with permission from: [42]. Copyright (1998) by American Physical Society

to the polycrystalline nature or phase impurity or stoichiometry variation, study of which was lacking [47].

The substrate temperature is another important synthesis parameter that plays a crucial role in determining the cost effectiveness and the compatibility of the process for large scale production. The use of lower substrate temperatures, during deposition decreases the cost of synthesis and provides higher compatibility for mass production. Gu et al. have shown that addition of Gd in VO_2 in certain limited amount reduces the transition temperature and minimum value of T_c in their report was ~54 °C for Gd/(V + Gd) ratio of 0.03 [44]. With further increase in this ratio, i.e. Gd concentration, the semiconductor to metal transition disappeared. They attributed this reduction

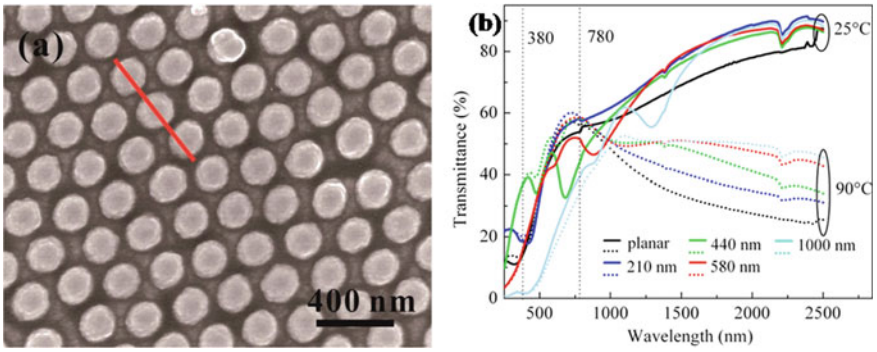

Fig. 2 **a** Top view (scanning electron microscopic image) of the moth-eye structured VO_2 film surface with 440 nm period. **b** Transmission spectra of samples showing two difference transmittance states at 25 and 90 °C. Reprinted (adapted) with permission from Ref. [43]. Copyright 2014 American Chemical Society

in transition temperature to the decrease in grain size of the film with addition of Gd, suggesting that the grain size has strong influence on the transition temperature [44]. The disappearance of the transition is ascribed to the fact that addition of Gd weakens the dimerization, *i.e.* V-V bond formation and hinders the d-d band splitting in vanadium, narrowing the band gap, which is the cause of transition. Also 4f energy states of Gd appear above the vanadium d bands, so increasing the amount of Gd will increase these states and eventually the band gap will vanish [44]. Hu et al. have reported the fabrication of porous VO_2 films by sol-gel spin-coating method with metal–insulator transition temperature (T_c) of 55 °C. The value of T_c is significantly lower than that of the bulk VO_2 (68 °C) and is attributed to the inhomogeneous strain in the film caused by the porous structure [45]. The transition temperature was further reduced with the addition of W as a dopant and T_c value as low as 28 °C for 2 at.% W-dopant have been reported. But along with T_c, the solar modulating ability (ΔT_{sol}) also decreased with W-doping. The pure film had a solar modulating ability value of 9.4% whereas for 2 at.% W-doped sample, the value was 6.9%. The T_c was calculated using $d(T_r)/dT$ versus T plots, where T is temperature and T_r is transmittance at a fixed wavelength of 2000 nm [45].

The stoichiometry and presence of other oxide phases of vanadium in small quantities influences the transition temperature, sharpness and extent of metal–insulator transition significantly. Ruzmetov et al. fabricated vanadium oxide thin films of 100 nm thickness by reactive sputtering of vanadium target in the presence of Ar and O_2 gases at a working pressure of 10 mTorr and substrate temperature of 550 °C [46]. They varied the oxygen concentration during deposition for different samples that lead to the variation in film stoichiometry and found the formation of small amounts of V_2O_3 and V_2O_5 phases along with the dominant VO_2 phase. Temperature dependent resistance measurements by two-probe method have revealed that both high and low concentrations of oxygen during deposition lead to the disappearance of the phase transition. Only under optimum oxygen content (8.8% of oxygen) the sharp

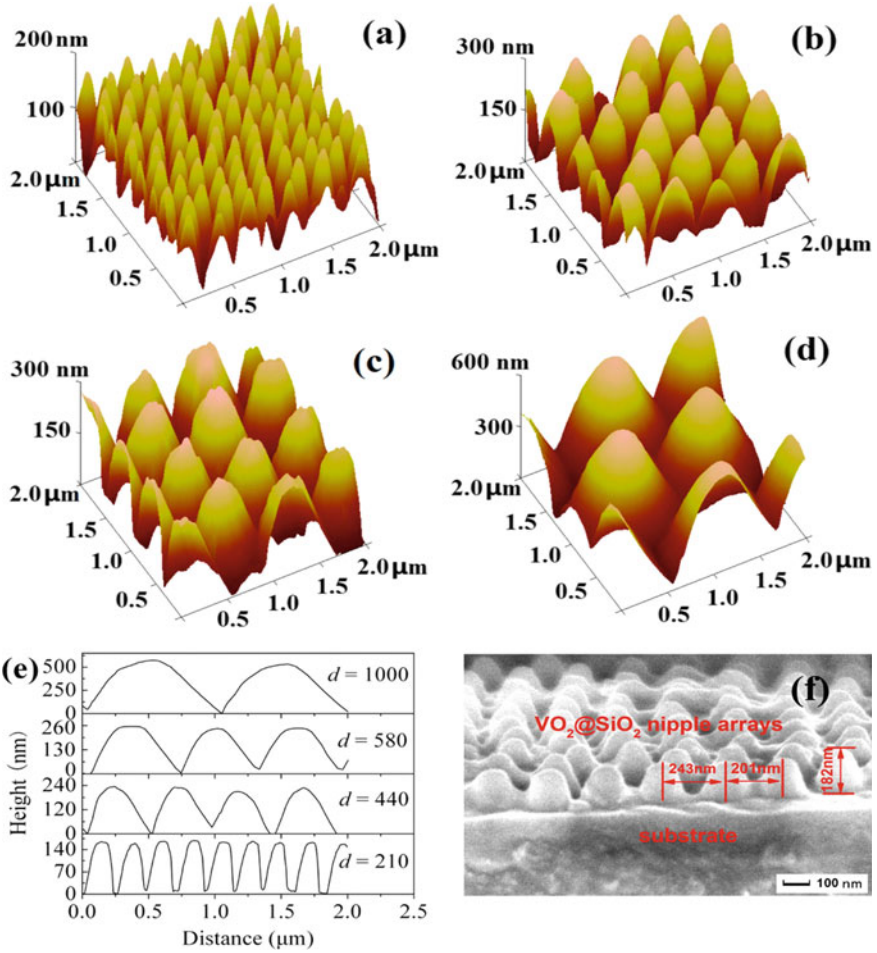

Fig. 3 3D AFM images of patterned VO_2 films with a period of **a** 210 nm, **b** 440 nm, **c** 580 nm and **d** 1000 nm. **e** AFM cross-section profiles of the samples. **f** SEM cross-sectional image of film with a period of 210 nm. Reprinted (adapted) with permission from Ref. [43]. Copyright 2014 American Chemical Society

transition occurred at 75 °C [46]. The presences of other phases of vanadium oxide do not contribute to the phase transition and hence the sharpness of the transition decreased and eventually it vanished [46]. It can be concluded from this study that the presence of VO_2 phase is essential for the proper functioning of the film as a thermo-chromic coating. VO_2 phase is unstable and starts forming higher oxides when it comes in contact with oxygen in the air due to which practical application of such coatings is very difficult as the performance of the coating degrades rapidly. Therefore, it is important to explore V_2O_5 films for thermo-chromism because it possesses the highest thermodynamic stability among all the oxides of vanadium.

2.2 Study of Effects of Temperature on Raman and UV-Vis Spectra of V_2O_5 Film

VO_2 is thermodynamically unstable and changes to higher and more stable oxides of vanadium upon exposure to the air or oxygen, thus making it difficult to use for practical applications. This factor has motivated the search of reversible change in transmittance in most stable oxide of vanadium, i.e. vanadium pentoxide (V_2O_5). Kang et al. have reported a large change in the electrical properties of V_2O_5 films with temperature in the range 250–280 °C [48]. This metal–insulator transition is not accompanied by any complete structural phase transition, hence, it is not a Mott transition [49]. Some reversible change in short-range structure of the films may be responsible for such a behaviour.

A study on the structural, optical and electrical properties of orthorhombic V_2O_5 films was conducted by Jain and Khanna to explore the presence of temperature dependent changes in optical transmittance and its probable cause [50]. V_2O_5 films of different thicknesses were prepared by thermal evaporation method with *in situ* substrate heating at 350 °C. The films were characterized by *in situ* temperature dependent UV-vis spectroscopy and *in situ* temperature dependent Raman spectroscopy at ambient pressure. It was found that on heating in air, the transmittance of the film decreased with a time lag of ~10 min and on cooling, the film tends to attain its original optical transmittance back again with a time lag of ~20 min (Fig. 4) [50]. The average transmittance was calculated by using Eq. 1 [50] and it was found that the change in the mean transmittance in the wavelength range: 200–1100 nm was 1.1%, 0.7% and 0.4% for films of thicknesses 78 nm, 88 nm and 119 nm, respectively. This change was 2–3% in the near IR region, i.e. for wavelength range: 700–1100 nm [50].

$$< \mathrm{T} > = \frac{\int T(\lambda) d\lambda}{\int d\lambda} \tag{1}$$

The Raman spectra of the films show that the broadening of two peaks at 283 and 305 cm^{-1} corresponding to bending vibrations of V = O bonds and triply coordinated oxygen bonds occurs with increase in temperature and the peaks regain their shape on cooling (Fig. 5) [50]. This Raman peak broadening effect can be attributed to the formation of multiple phonons of equivalent total energy from single phonon. The time lag in regaining the original shapes of the above mentioned respective peaks is approximately same as that in case of the optical transmittance. This observation leads to the conclusion that there is correlation between the changes in optical and short-range structural properties which determines the thermo-optic behaviour of the films. Thin films of different thickness (78 nm, 88 nm and 119 nm) were studied for this effect and the film with 78 nm thickness was found to show maximum change in transmittance with temperature. These findings suggested that the effect is enhanced for low thickness films [50].

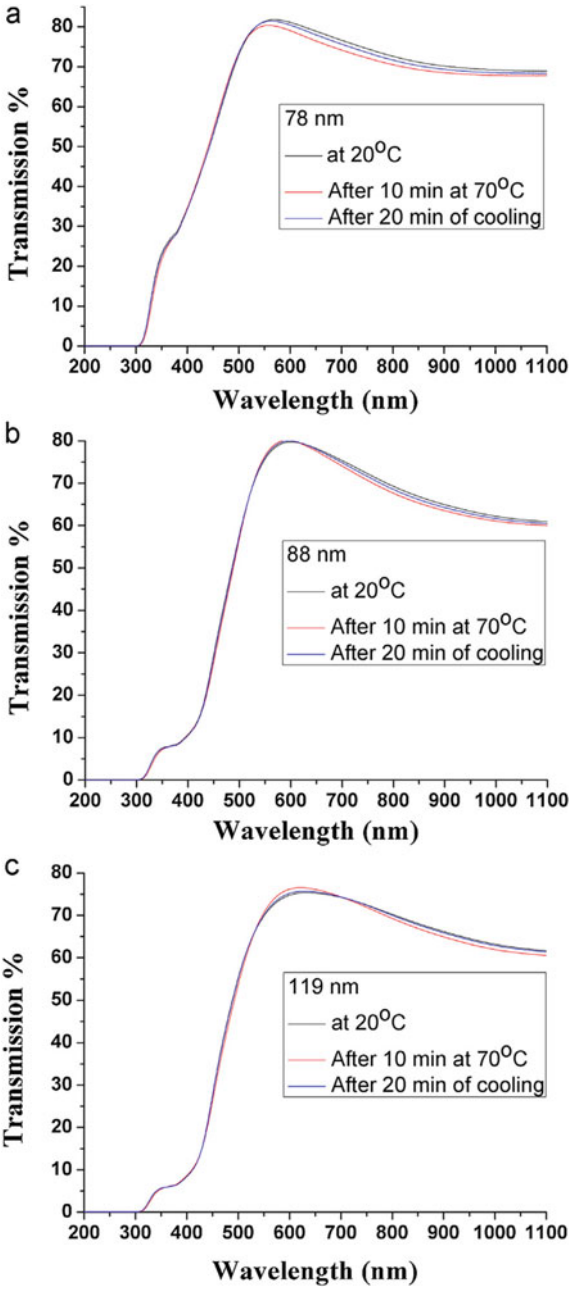

Fig. 4 Transmittance spectra of the samples recorded at 20 °C (black line), after 10 min heating at 70 °C (red line) and after 20 min of cooling to 20 °C (blueline): **a** 78 nm film, **b** 88 nm film, **c** 119 nm film. From Ref. [50] (reproduced with permission from Elsevier)

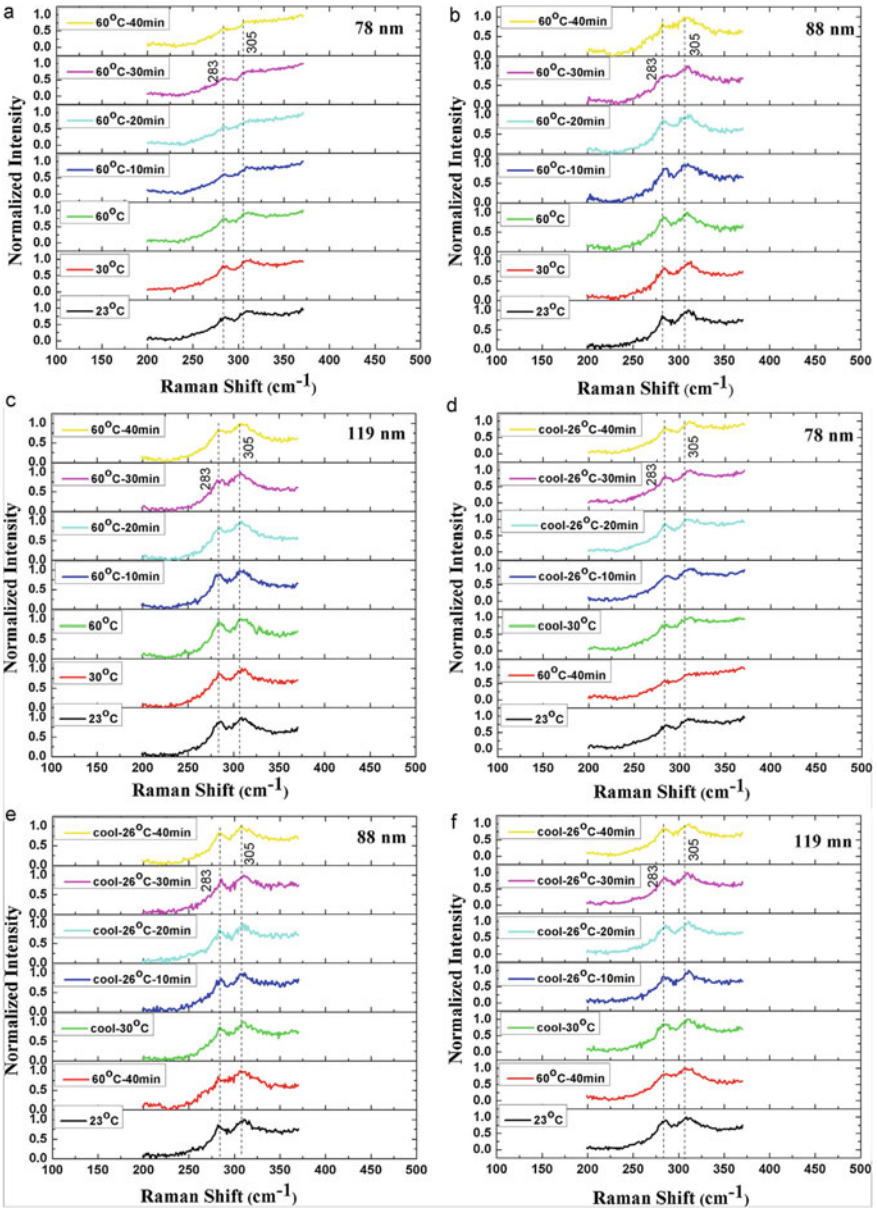

Fig. 5 Raman spectra of films showing changes in the Raman peaks at 285 and 305 cm^{-1} during heating cycle: **a** 78 nm film, **b** 88 nm film, **c** 119 nm film, and during cooling cycle, **d** 78 nm film, **e** 88 nm film, **f** 119 nm film. From Ref. [50] (reproduced with permission from Elsevier)

2.3 Gas Sensing Properties of Vanadium Oxides

V_2O_5 films are good materials for gas sensing applications with its n-type semiconducting nature and d^0 configuration in V^{5+} state which results in active sites available for adsorption of gas molecules. The conductivity of V_2O_5 films (being n-type semiconductor material), increases when it comes in contact with reducing gas that supplies electrons to convert V^{5+} to V^{4+} [33]. V_2O_5 exhibits a variety of morphologies such as nano-fibre, nanorod, nano-tube, hollow-sphere, sheet/flake-like and spindle-shaped structures depending upon synthesis technique and parameters [32, 49, 52–57]. Such nanostructures possess large surface to volume ratio, i.e. high surface area, which enhances the number of available gas adsorption sites. The diversity in morphology of V_2O_5 nanostructures gives it extra advantage to tailor and enhance the gas sensing properties, i.e. it increases the gas-response signal and decreases the response and recovery times.

In this section, we have compiled the results of some of the reported studies made on gas sensing properties of V_2O_5 nanostructures and thin films and also the associated mechanisms given by different authors have been elaborated. V_2O_5 thin films and nanostructures are useful in the detection of NO_2, NH_3, hydrogen, methane, propane, ethanol, 2-propanol, 1-butylamine, etc. [33, 51–55]. Schneider et al. have studied hydrogen, methane and propane sensing with V_2O_5 films of 200 to 600 nm thicknesses, fabricated by reactive RF sputtering of metallic vanadium target [33]. These authors reported better response at a working temperature of 175 °C or more and attributed this observation to the temperature induced deviation from stoichiometry in V_2O_5 films due to creation of oxygen vacancies at higher temperatures. Some of the V^{5+} reduces to V^{4+} to maintain the electrical neutrality of the films and the charge carriers are depleted resulting in the high resistance. On inserting any reducing gas, the adsorbed gas molecules donate electrons into the conduction band that causes the reduction in resistance on gas adsorption, and hence the response [33]. Further they have reported that the vanadium oxide films are more sensitive towards hydrogen as compared to methane or propane [33]. Modafferi et al. have fabricated electro-spun V_2O_5 fibers for the detection of ammonia [51] and claimed the detection limit for ammonia as low as 100 ppb and optimum temperature to be 200–250 °C with a response time of 50 s and recovery time of 350 s. The calcination temperature of 400 °C was assumed to be best suited because calcination at this temperature causes the evaporation of polyvinyl acetate resulting in the hollow and rough morphology of pure phase V_2O_5 fibers thereby increasing the sensing response [51]. The gas sensing mechanism used by them to support their observation involves intermediate layer of adsorbed oxygen on the surface of V_2O_5 fiber layer. Ammonia supplies electrons and reacts with the adsorbed oxygen to form N_2 and H_2O and the electrons donated by ammonia are further transferred to V_2O_5 and the resistance drops [51]. Raible et al. have shown in their study that the V_2O_5 nano-fibers deposited by self-assembly in aqueous solution on Si-substrate are highly sensitive towards organic compound 1-butylamine [52]. They used sophisticated photo- and e-beam lithography for making gold contacts in two different configurations: top

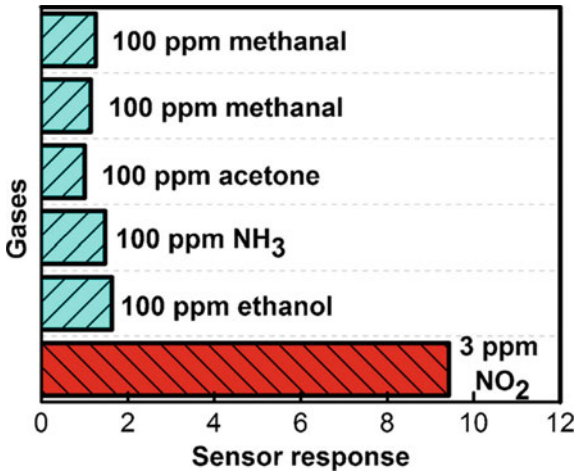

Fig. 6 The bar graphs of responses of thin-film sample sputtered for 60 min towards various gases. From Ref. [53] (reproduced with permission from Elsevier)

electrode and bottom electrode and the latter was found to possess a high response. All the gas sensing studies were performed at room temperature in this work and it was found that the response increases with increase in humidity from 5 to 40% [52]. They speculated that the enhanced response in the presence of increased humidity is due to the formation of thin water layer at the V_2O_5-fiber layer which dissolves the organic amine and speed-up the reaction kinetics by acting as a catalyst. They also tested their samples for the detection of ammonia, 1-propanol and toluene and reasonably good response was observed for ammonia as well [52]. This observation revealed that the sensor is highly selective for ammonia and organic amines. The effect of humidity on response was similar to that for 1-butylamine but no change with humidity was observed in case of 1-propanol and toluene [52]. Yan et al. fabricated the V_2O_5 nanorods on porous silicon (PS) substrates (prepared by etching of Si wafer by HF) by heat treatment of metallic vanadium film deposited by DC magnetron-sputtering and investigated the gas sensing properties of the nano-structured films for NO_2 and NH_3, etc. [53]. The films are reported to be highly selective for NO_2 as shown in Fig. 6. They have performed the sensing measurements for an operating temperature in the range: 25–250 °C and interestingly it was observed that the gas response decreases with an increase in operating temperature which is opposite to the conventional trend [53]. The highest response achieved at 25 °C was attributed to the formation of anti-heterojunction between p-type porous silicon substrate and n-type V_2O_5 nanorod film resulting in a depletion layer. The large surface area possessed by porous silicon and V_2O_5 nanorods results in large number of surface defects (active sites for oxygen adsorption) that facilitates the adsorption of large amount of oxygen at low temperatures. This oxygen adsorption leads to the loss of electrons from V_2O_5 nanorods, increases the band bending (Fig. 7) and results in an inversion layer in which the holes become majority charge carriers converting V_2O_5 nanorod film into p-type layer and hence the resistance decreases on adsorption of NO_2 gas by further withdrawing electrons and increasing hole concentration [53].

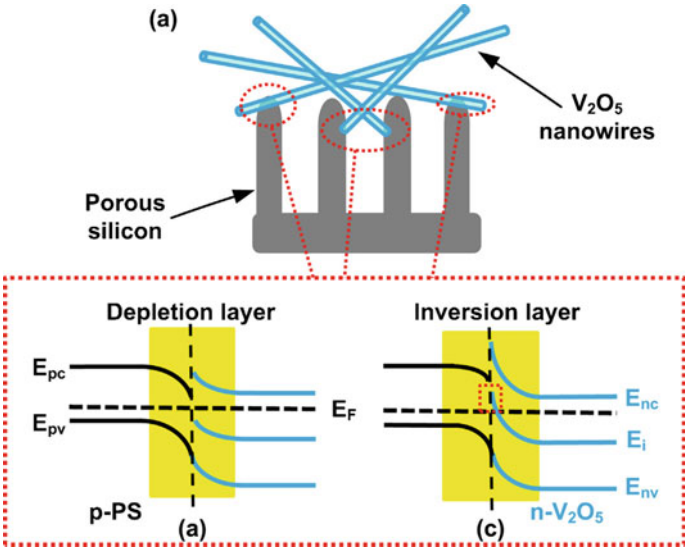

Fig. 7 **a** Depiction of PS/V_2O_5 nanorod structure. Schematic energy-level diagram of PS/V_2O_5 nanorod structure, **b** before and **c** after strong surface adsorption of oxygen. From Ref. [53] (reproduced with permission from Elsevier)

In another research, Mane et al. studied the effects of deposition temperature and working temperature on gas sensing properties of V_2O_5 films prepared by chemical spray deposition [54]. The V_2O_5 film prepared at a deposition temperature of 400 °C was reported to show the highest response (20.3%) for 100 ppm NO_2 (Fig. 8) because of maximum void formation at this temperature which facilitates the gas adsorption [54]. In case of a deposition temperature of 350 °C the nanorod type surface morphology was compact and above 400 °C the formation of micro-sheet type structures in between the nanorods reduces the surface area and gas adsorption [54]. Further they reported the optimum operating temperature for 100 ppm concentration of NO_2 gas is 200 °C (Fig. 9) with a response time of 17 s, recovery time of 185 s. The lower detection limit claimed for NO_2 sensing is 20 ppm [54]. The films deposited at 400 °C were tested towards SO_2, CO_2, H_2S, CO and NH_3 gases at various operating temperatures and found that the response for NO_2 and NH_3 is more as compared to that for other gases when operating temperature was kept at 150 °C or above [54]. At low operating temperature (100 °C), the film deposited at 400 °C substrate temperature was found to be highly selective for NO_2, although the response was lower than that at the operating temperature of 200 °C. In contrast to the results reported by Yan et al., the resistance of the V_2O_5 film increases on exposure of NO_2 gas indicating typical n-type behaviour to oxidising gases [55, 56].

Karthikeyan et al. reported a very fast response and recovery time of 3 s and 10 s, respectively for 5 ppm concentration of 2-propanol by V_2O_5 films [55]. V_2O_5 films were also tested for methanol and ethanol but the response was low. Hence the study concluded that the V_2O_5 film was highly selective for 2-propanol [55].

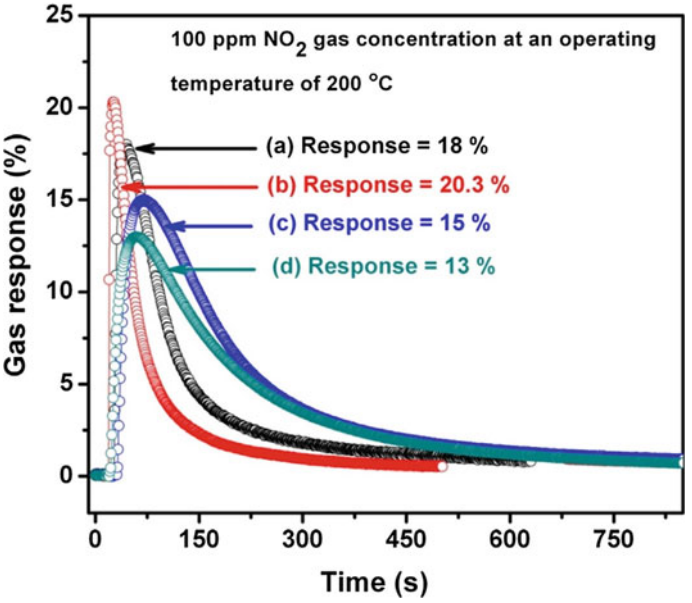

Fig. 8 Response curves of V_2O_5 thin films deposited at substrate temperature of **a** 350 °C, **b** 400 °C, **c** 450 °C and **d** 500 °C for 100 ppm NO_2 gas at a working temperature of 200 °C. From Ref. [54] (reproduced with permission from Elsevier)

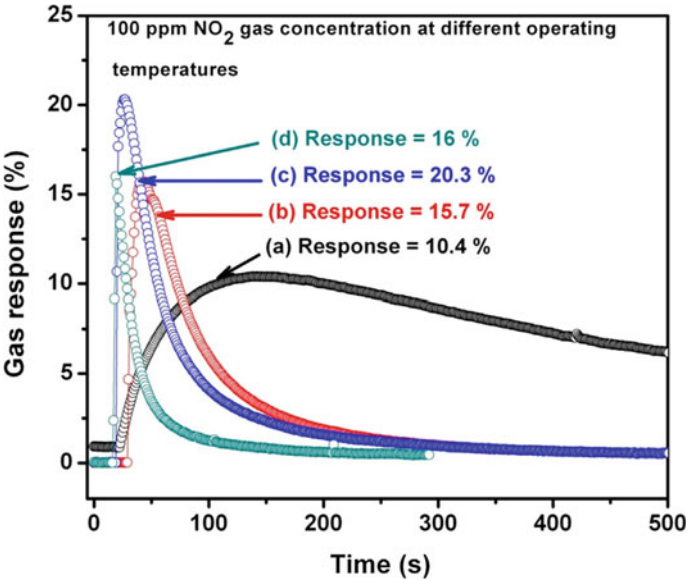

Fig. 9 Response curves of V_2O_5 thin film deposited at a substrate temperature of 400 °C for 100 ppm of NO_2 gas at a working temperature of **a** 100 °C, **b** 150 °C, **c** 200 °C and **d** 250 °C. From Ref. [54] (reproduced with permission from Elsevier)

There are many other reports on gas sensing properties of V_2O_5 films available in literature and still research is continuing to enhance the response and decrease the operating temperature, response time and recovery time. Some of the reports discussed here have presented the comparison of their results obtained with those available in literature. The results of the reports discussed here are summarized in Table 1.

3 Conclusion

The transition metal-oxide films owe their importance in fundamental science and technology to their unique electronic configurations having partially filled d-orbitals, and hybridization of p-orbitals of oxygen with these partially filled d-orbitals. The strongly correlated electrons, the Coulomb interactions of electrons and hybridization with p-orbitals of oxygen result in the redistribution of energy levels that gives rise to d-d type Mott-Hubbard band gap and d-p-type charge transfer band gap. The lower oxides of transition metals show metal–insulator or semiconductor–insulator transition, the characteristic parameters of which can be tailored using different synthesis techniques and parameters. The metal–insulator transition in VO_2 films produces changes in optical transmittance of the film with temperature making it useful as thermo-chromic energy efficient window coatings. Various studies on methods including thickness control, substrate temperature control, doping and porous structure formation to tailor the transmittance, transition temperature, solar modulation ability, etc. have been employed by the scientists and their outcomes were discussed in this chapter. Formation of other higher more stable oxides on exposure to air results in the degradation of the thermo-chromic performance of VO_2 film. Although V_2O_5 films do not show metal–insulator transition, these materials need to be explored for thermo-chromism because they are thermodynamically more stable which is a required property for the consistent performance of the window coatings. A few reports are available in the literature showing that transmittance and electrical properties of V_2O_5 exhibit a temperature dependence without involving any structural phase transitions. Reversible changes in short-range structure of V_2O_5 films are responsible for such behaviour and if this effect can be enhanced by doping or by controlling the surface morphology, it can be utilized for thermo-chromic window coating applications. The correlation between the short-range structural properties of V_2O_5 films and optical transmittance has been reported but the percentage change in transmittance with temperature was too small for practical purposes. Further efforts are required to make V_2O_5 useful as a thermo-chromic coating. Although V_2O_5 has not yet proven to be good thermo-chromic coating but it has a great potential for gas sensing applications. The reports from the literature discussed in this chapter have shown that the V_2O_5 nanostructures have very good response towards NO_2, NH_3 2-propanol and 1-butylamine, etc. and their sensor response, selectivity, response time and recovery time can be easily tailored by modifying the deposition techniques and parameters. This chapter provides the information about the less studied aspects of

Table 1 The summary of the results obtained for the sensing of different gases using various materials and techniques

Gas	Material used	Method of Preparation	Operating temperature	Gas concentration (ppm)	Sensor response $\Delta R/R_{ini}$	Ref.
NH_3	V_2O_5 fibrous film	Sol-gel and electro-spinning	150–250 °C	0.85–2.1	–	[51]
NH_3	V_2O_5 nanofibres	Chemical route	R.T.	10	0.42	[52]
$CH_3(CH_2)_3NH_2$	V_2O_5 nanofibres	Chemical route	R.T.	10	0.18	[52]
H_2	V_2O_5 film	Reactive RF sputtering	150–250°C	10–300	–	[33]
CH_4	V_2O_5 film	Reactive RF sputtering	150–250°C	50–3000	–	[33]
C_3H_8	V_2O_5 films	Reactive RF sputtering	150–250°C	50–3000	–	[33]
NO_2	V_2O_5 nanorods	Magnetron-sputtering	25–250°C	0.25–3	1.65–9.43	[53]
NO_2	V_2O_5 films	Chemical spray deposition	100–250°C	20–100	0.08–0.2	[54]
NO_2	MoO_3-V_2O_5 thin films	Chemical spray deposition	100–250°C	20–120	0.25–0.8	[31]
C_3H_8O	V_2O_5 thin film	DC reactive magnetron-sputtering	–	5–200	2–176	[55]
C_3H_8O	V_2O_5 thin film	DC reactive magnetron-sputtering		200	1.06	[55]
C_3H_8O	V_2O_5 thin film	DC reactive magnetron-sputtering		200	1.45	[55]

V_2O_5 films such as thermo-chromic effect and gas sensing properties. It is important to multiply efforts in realizing thermo-chromic devices based on V_2O_5 as well as in making highly selective, sensitive and low cost solid state gas sensors.

References

1. C.G. Granqvist, Recent progress in thermochromics and electrochromics: A brief survey. Thin Solid Films **614**, 90–96 (2016)
2. C.G. Granqvist, Electrochromics and thermochromics: Towards a new paradigm forenergy efficient buildings. Mater. Today: Proc. **3S**, S2–S11 (2016)
3. H. Ji, D. Liu, H. Cheng, Y. Tao, Large area infrared thermochromic VO_2 nanoparticle films prepared by inkjet printing technology. Sol. Energy Mater. Sol. Cells **194**, 235–243 (2019)
4. C. Hua, G. Yuan, Z. Cheng, H. Jiang, G. Xu, Y. Liu, G. Han, Building architecture of TiO_2nanocrystals embedded in amorphousWO_3 films with improved electrochromic properties. Electrochim. Acta **309**, 354–361 (2019)
5. C.T. Lee, S. Han, Y.X. Zhao, Y.C. Hung, T.H. Hsu, H.Y. Hsieh, K.W. Weng, Synthesis and electrochromic properties of molybdenum oxide films. Surf. Coat. Technol. **363**, 426–429 (2019)
6. A.K. Surca, G. Dražić, M. Mihelčič, Low-temperature V-oxide film for a flexible electrochromic device: Comparison of its electrochromic, IR and Raman properties to those of a crystalline V_2O_5 film. Sol. Energy Mater. Sol. Cells **196**, 185–199 (2019)
7. A.I. Gavrilyuk, Aging of the nanosized photochromic WO_3 films and the role of adsorbed water in the photochromism. Appl. Surf. Sci. **364**, 498–504 (2016)
8. H. Wang, G. Gao, G. Wu, H. Zhao, W. Qi, K. Chen, W. Zhang, Y. Li, Fast hydrogen diffusion induced by hydrogen pre-split for gasochromic based optical hydrogen sensors. Int. J. Hydrogen Energy **44**, 15665–15676 (2019)
9. G. Rizzo, A. Arena, A. Bonavita, N. Donato, G. Neri, G. Saitta, Gasochromic response of nanocrystalline vanadium pentoxide films deposited from ethanol dispersions. Thin Solid Films **518**, 7124–7127 (2010)
10. Y.K. Ho, C.C. Chang, D.H. Wei, C.L. Dong, C.L. Chen, J.L. Chen, W.L. Jang, C.C. Hsu, T.S. Chan, K. Kumar, C.L. Chang, M.K. Wu, Characterization of gasochromic vanadium oxides films by X-ray absorption spectroscopy. Thin Solid Films **544**, 461–465 (2013)
11. Y. Liu, J. Chen, L. Peng, N. Deng, W. Ding, Fabrication and optical property improvement of gasochromic switchable mirror based on Pd/Mg-Nb_2O_5 thin film. Int. J. Hydrogen Energy **44**, 15205–15217 (2019)
12. K. Nishizawa, Y. Yamada, K. Yoshimura, Low-temperature chemical fabrication of Pt-WO_3 gasochromic switchable films using UV irradiation. Sol. Energy Mater. Sol. Cells **170**, 21–26 (2017)
13. W. Qi, G. Gao, G. Wu, H. Wang, Flexible gasochromic films with favorable high temperature resistance and energy efficiency. Sol. Energy Mater. Sol. Cells **195**, 63–70 (2019)
14. K. Ma, J. Lago, F.O. von Rohr, Superconductivity in the η-carbide-type oxides $Zr_4Rh_2O_x$. J. Alloy. Compd. **796**, 287–292 (2019)
15. A.V. Palnichenko, O.M. Vyaselev, A.A. Mazilkin, I.I. Zver'kova, S.S. Khasanov, Metastable superconductivity of W/WO_3 interface. Phys. C: Supercond. Its Appl. **534**, 61–67 (2017)
16. A.V. Palnichenko, I.I. Zver'kova, D.V. Shakhrai, O.M. Vyaselev, Metastable superconductivity of Mo/MoO_{3-x} interface. (2017) **558**, 25–29 (2019)
17. N.P. Novák, Transition metal oxides: Magnetism, in *Reference Module in Materials Science and Materials Engineering*, Elsevier, Amsterdam. https://doi.org/10.1016/b978-0-12-803581-8.02502-9

18. R. Bhardwaj, B. Kaur, J.P. Singh, M. Kumar, H.H. Lee, P. Kumar, R.C. Meena, K. Asokan, K.H. Chae, N. Goyal, S. Gautam, Role of low energy transition metal ions in interface formation in ZnO thin films and their effect on magnetic properties for spintronic applications. Appl. Surf. Sci. **479**, 1021–1028 (2019)
19. S. Lu, C. Li, Y.F. Zhao, Y.Y. Gong, L.Y. Niu, X.J. Liu, T. Wang, Tunable magnetism of 3d transition metal doped $BiFeO_3$. J. Magn. Magn. Mater. **439**, 57–66 (2017)
20. P.D. Battle, Magnetoresistance in transition metal oxides, in *Encyclopedia of Materials: Science and Technology*. ISBN: 0-08-0431526, 5083-5086
21. A. Obstarczyk, D. Kaczmarek, D. Wojcieszak, M. Mazur, J. Domaradzki, T. Kotwica, R. Pastuszek, D. Schmeisser, P. Mazur, M. Kot, Tailoring optical and electrical properties of thin-film coatings based on mixed Hf and Ti oxides for optoelectronic application. Mater. Des. **175**, 107822 (2019)
22. K.S. Anuratha, H.S. Peng, Y. Xiao, T.S. Su, T.C. Wei, J.Y. Lin, Electrodeposition of nanostructured TiO_2 thin film as an efficient bi-functional layer for perovskite solar cells. Electrochim. Acta **295**, 662–667 (2019)
23. Z.W. Chen, C.B. Yao, J.Y. Hu, The nonlinear optical properties and optical transition dynamics of Er-doped ZnO films. Opt. Laser Technol. **119**, 105609 (2019)
24. A. Hernández-Granados, A.N. Corpus-Mendoza, P.M. Moreno-Romero, C.A. Rodríguez-Castañeda, J.E. Pascoe-Sussoni, O.A. Castelo-González, E.C. Menchaca-Campos, J. Escorcia-García, H. Hu, Optically uniform thin films of mesoporous TiO_2 for perovskite solar cell applications. Opt. Mater. **88**, 695–703 (2019)
25. S.H. Tu, H.C. Wu, C.J. Wu, S.L. Cheng, Y.J. Sheng, H.K. Tsao, Growing hydrophobicity on a smooth copper oxide thin film at room temperature and reversible wettability transition. Appl. Surface Sci. **316**, 88–92 (2014)
26. R.K. Jain, Y.K. Gautam, V. Dave, A.K. Chawla, R. Chandra, A study on structural, optical and hydrophobic properties of oblique angle sputter deposited HfO_2 films. Appl. Surf. Sci. **283**, 332–338 (2013)
27. A. Shokuhfar1, M. Alzamani, E. Eghdam, M. Karimi, S. Mastali, SiO_2-TiO_2 nanostructure films on windshields prepared by Sol-Gel Dip-Coating technique for self-cleaning and photocatalytic applications. Nanosci. Nanotechnol. **2**(1), 16–21 (2012)
28. D. Hafedh, K. Kaouther, B.C.L. Ahmed, Multi-property improvement of TiO_2-WO_3 mixed oxide films deposited on 316L stainless steel by electrophoretic method. Surf. Coat. Technol. **326**, 45–52 (2017)
29. B. Guo, D. Wan, A. Ishaq, H. Luo, Y. Gao, Direct synthesis of high-performance thermal sensitive VO_2(B) thin film by chemical vapor deposition for using in uncooled infrared detectors. J. Alloy. Compd. **715**, 129–136 (2017)
30. W. Zhou, Y. Yin, J. Wu, Y. Gao, Z. Huang, Improvements in electrical properties, low frequency noise and detection performance of a Mn-based bilayer thin film infrared detector. Sensors and Actuators A **283**, 196–203 (2018)
31. W. Maziarz, TiO_2/SnO_2 and TiO_2/CuO thin film nano-heterostructures as gas sensors. Appl. Surf. Sci. **480**, 361–370 (2019)
32. A.A. Mane, S.A. Nikam, A.V. Moholkar, NO_2 gas sensing properties of sprayed composite porous MoO_3-V_2O_5 thin films. Mater. Chem. Phys. **216**, 294–304 (2018)
33. K. Schneider, M. Lubecka, A. Czapla, V_2O_5 thin films for gas sensor applications. Sensors and Actuators B **236**, 970–977 (2016)
34. S.S. Jiang, G. He, J. Gao, D.Q. Xiao, P. Jin, W.D. Li, J.G. Lv, M. Liu, Y.M. Liu, Z.Q. Sun, Microstructure, optical and electrical properties of sputtered HfTiO high-k gate dielectric thin films. Ceram. Int. **42**(10), 11640–11649 (2016)
35. G. Xia, S. Wang, Rapid and facile low-temperature solution production of ZrO_2 films as high-k dielectrics for flexible low-voltage thin-film transistors. Ceram. Int. **45**(13), 16482–16488 (2019)
36. S. Sharma, A. Paliwal, M. Tomar, V. Gupta, Multiferroic BFO/BTO multilayer structures based Magnetic field sensor. Physica B **571**, 1–4 (2019)

37. A. Paliwala, M. Tomarb, V. Gupta, Study of optical properties of Ce and Mn doped $BiFeO_3$ thin films using SPR technique for magnetic field sensing. Vacuum **158**, 48–51 (2018)
38. J. Zaanen, G.A. Sawatzky, J.W. Allen, Band Gaps and Electronic Structure of Transition-Metal Compounds. Phys. Rev. Lett. **55**(4), 419–421 (1985)
39. S. Hufner, Mott Insulation in Transition Metal Compounds. Z. Phys. B - Condensed Matter **61**, 135–138 (1985)
40. A. Fujimori, T. Mizokawa, Electronic structure of transition-metal oxides. Curr. Opin. Solid State Mater. Sci. **2**, 18–22 (1997)
41. F.J. Morin, Oxides which show a metal-to-insulator transition at the neel temperature. Phys. Rev. Lett. **3**(1), 34–36 (1959)
42. M. Imada, A. Fujimori, Y. Tokura, Metal-insulator transitions. Rev. Mod. Phys. **70**(4), 1039–1263 (1998)
43. X. Qian, N. Wang, Y. Li, J. Zhang, Z. Xu, Y. Long, Bioinspired Multifunctional Vanadium Dioxide: Improved Thermochromism and Hydrophobicity. Langmuir **30**, 10766–10771 (2014)
44. D. Gu, X. Zhou, Z. Sun, Y. Jiang, Influence of Gadolinium-doping on the microstructures and phase transition characteristics of VO_2 thin films. J. Alloy. Compd. **705**, 64–69 (2017)
45. L. Hu, H. Tao, G. Chen, R. Pan, M. Wan, D. Xiong, X. Zhao, Porous W-doped VO_2 films with simultaneously enhanced visible transparency and thermochromic properties. J. Sol-Gel. Sci. Technol. **77**(1), 85–93 (2016)
46. D. Ruzmetov, S.D. Senanayake, V. Narayanamurti, S. Ramanathan, Correlation between metal-insulator transition characteristics and electronic structure changes in vanadium oxide thin films. Physical Review B **77**, 195442-1–195442-5 (2008)
47. Y. Yang, X. Cao, G. Sun, S. Long, T. Chang, X. Li, P. Jin, Transmittance change with thickness for polycrystalline VO_2 films deposited at room temperature. J. Alloy. Compd. **791**, 648–654 (2019)
48. M. Kang, I. Kim, S. W. Kim,, J. W. Ryu, and H. Y. Park, Metal-insulator transition without structural phase transition in V_2O_5 film, Applied Physics Letters 98(2011) 131907-1-131907-3
49. A. Pergament, G. Stefanovich and V. Andreeev, Comment on "Metal-insulator transition without structural phase transition in V_2O_5film" [Appl. Phys. Lett. 98, 131907 (2011)], Applied Physics Letters 102(2013) 176101-1-176101-3
50. R.K. Jain, A. Khanna, Structural, optical and electrical properties of crystallineV_2O_5 films deposited by thermal evaporation and effects of temperature on UV–vis and Raman spectra. Optik **144**, 271–280 (2017)
51. V. Modafferi, G. Panzera, A. Donato, P.L. Antonucci, C. Cannilla, N. Donato, D. Spadaro, G. Neri, Highly sensitive ammonia resistive sensor based on electrospun V_2O_5 fibers. Sensors and Actuators B **163**, 61–68 (2012)
52. I. Raible, M. Burghard, U. Schlecht, A. Yasuda, T. Vossmeyer, V_2O_5 nanofibres: novel gas sensors with extremely high sensitivity and selectivity to amines. Sensors and Actuators B **106**, 730–735 (2005)
53. W. Yan, M. Hu, D. Wang, C. Li, Room temperature gas sensing properties of porous silicon/V_2O_5 nanorods composite. Appl. Surf. Sci. **346**, 216–222 (2015)
54. A.A. Mane, P.S. Maldar, S.H. Dabhole, S.A. Nikam, A.V. Moholkar, Effect of substrate temperature on physicochemical and gas sensing properties of sprayed orthorhombic V_2O_5 thin films. Measurement **131**, 223–234 (2019)
55. P.S. Karthikeyan, P. Dhivya, P.D. Raj, M. Sridharan, V_2O_5 thin film for 2-Propanol vapor sensing. Materials Today: Proceedings **3**, 1510–1516 (2016)
56. H. Yin, K. Yu, H. Peng, Z. Zhang, R. Huang, J. Travas-Sejdic, Z. Zhu, Porous V_2O_5 micro/nanotubes: Synthesis via a CVD route, single-tube-based humidity sensor and improved Li-ion storage properties. J. Mater. Chem. **22**, 5013–5019 (2012)
57. M. Wu, X. Zhang, S. Gao, X. Cheng, Z. Rong, Y. Xu, H. Zhao, L. Huo, Construction of monodisperse vanadium pentoxide hollow spheres via a facile route and triethylamine sensing property. Cryst. Eng. Comm **15**, 10123–10131 (2013)